Green Energy and Technology

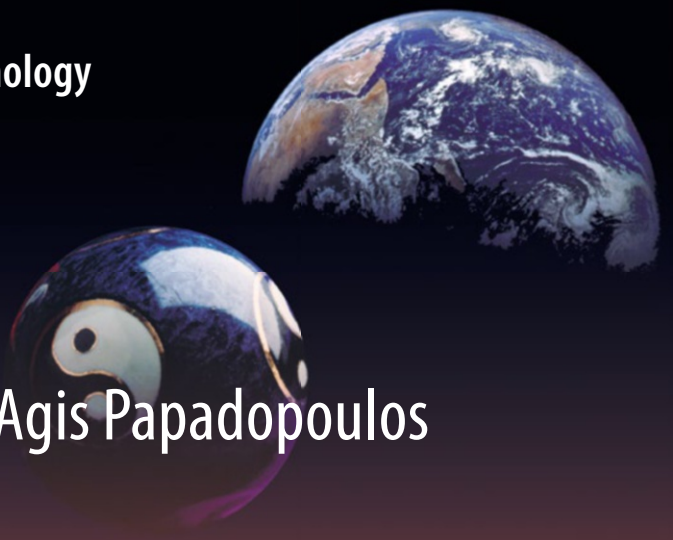

Sandro Nižetić · Agis Papadopoulos
Editors

The Role of Exergy in Energy and the Environment

Springer

Green Energy and Technology

More information about this series at http://www.springer.com/series/8059

Sandro Nižetić • Agis Papadopoulos
Editors

The Role of Exergy in Energy and the Environment

Springer

Editors
Sandro Nižetić
FESB Faculty, LTEF-Head
of Laboratory for Thermodynamics
and Energy Efficiency
University of Split
Split, Croatia

Agis Papadopoulos
Department of Mechanical Engineering
Aristotle University of Thessaloniki
Process Equipment Design Laboratory
Thessaloniki, Greece

ISSN 1865-3529 ISSN 1865-3537 (electronic)
Green Energy and Technology
ISBN 978-3-319-89844-5 ISBN 978-3-319-89845-2 (eBook)
https://doi.org/10.1007/978-3-319-89845-2

Library of Congress Control Number: 2018947194

Printed on acid-free paper

This Springer imprint is published by the registered company Springer International Publishing AG part of Springer Nature.
The registered company address is: Gewerbestrasse 11, 6330 Cham, Switzerland

Preface

Energy remains in the epicentre of the twenty-first century, being the driving force of global economic growth, the firm ground of post-industrial societies' wellbeing but also the main reason behind climate change. What is new is the global scale of energy issues, which affect humanity on an unprecedented extent, leaving the whole world to face complex problems related to energy, environment and economic issues. Today's world population has left a global trace in numerous ways, and we have for sure entered an era of unpredictable events and scenarios, which inevitably bear also hazards. Researchers all over the world have made efforts to obtain knowledge and understanding of the underlying physical phenomena and to provide engineering solutions. Exergy has undoubtedly emerged as novel approach, which is crucial and important for energy and environmental issues and can be developed as a precise and adaptive tool for the effective evaluation of systems, components and processes.

Providing sustainable energy, and in that sense ensuring energy sustainability, is a complex task and it is intertwined with numerous issues which fall within the scope of diverse engineering disciplines such as mechanical, electrical, environmental, chemical as well as other areas that are closely related to sustainability, i.e. energy-related issues. New energy solutions and concepts are needed to bridge current gaps as well as upcoming tasks and issues to enable a sustainable future. The evaluation and consideration of novel energy concepts, systems or components seeks for the application of an exergy approach with a clear interconnection with energy and environmental aspects. The role of exergy is hence undeniable and it should be a starting point for any energy or environmental based analysis; exergy is in that sense a foundation of sustainability.

Rational use of energy and utilization of renewable energy sources are the main tools of energy and environmental policies of the twenty-first century, as well as the prerequisites for mitigating climate change. This volume includes contributions based on selected papers from the 9th International Exergy, Energy and Environment Symposium (IEEES-9) that was held in Split, Croatia, on May 14–17, 2017. The IEEES-9 conference was a multidisciplinary one, covering a variety of topics

and areas related to exergy- and energy-based analyses, addressing environmental and economic issues. The conference attracted researchers, professionals, engineers and scientist from almost 40 countries; more than 200 presentations were given, providing a cross section of the latest research findings, monitoring the progress in basic and applied research and discussing state-of-the-art technological solutions.

Chapters of the book are devoted to analysis of energy and environmental issues in all sectors of the economy, including industrial processes, transportation, buildings and services. Energy sources and technologies considered reach from hydrocarbons to wind and solar and from fuel cells to thermal and electricity storage.

It is the editors' belief that this volume provides theoretical insights, along with case studies and examples, which are useful to the academic community, but also to energy and environmental professionals and decision makers.

Finally, the editors would like to express their sincere appreciation to the authors for their general contribution which made this book possible as well as to the technical team that helped to revise the chapters and prepare them for publication. Dr. Sandro Nižetić would like to acknowledge the general support provided by the Faculty of Electrical Engineering, Mechanical Engineering and Naval Architecture together with the University of Split.

Split, Croatia — Sandro Nižetić
Thessaloniki, Greece — Agis Papadopoulos

Contents

Part II Energy Systems, Components and Applications

Part III Sustainable Energy and the Environment

Contributors

B. Abdulrahman Energy Efficiency Technologies Program (EET), Energy & Building Research Center (EBRC), Kuwait Institute for Scientific Research (KISR), Safat, Kuwait

Mohamed Hany Abokersh The American University in Cairo, Mechanical Engineering Department, New Cairo, Egypt

Askar Absemetov Nazarbayev University, School of Engineering and Graduate School of Business, Astana, Kazakhstan

Aramide Adesina School of Engineering, University of Kwazulu-Natal, Durban, South Africa

J. Aiman University of Science and Technology of China, Department of Precision Machinery and Precision Instrumentation, Hefei, Anhui, People's Republic of China

Daniyar Aitkulov Nazarbayev University, School of Engineering and Graduate School of Business, Astana, Kazakhstan

Charilaos Akasiadis Technical University of Crete, Chania, Greece

Muhammet Vefa Akpınar Karadeniz Teknik Üniversitesi, Civil Engineering Department, Trabzon, Turkey

M. W. Akram University of Science and Technology of China, Department of Precision Machinery and Precision Instrumentation, Hefei, Anhui, People's Republic of China

Ahmad Al Mulla Energy Efficiency Technologies Program (EET), Energy & Building Research Center (EBRC), Kuwait Institute for Scientific Research (KISR), Safat, Kuwait

Fernando Alay École des Mines de Nantes, Department of Energy Systems and Environment, Nantes, France

Ruba Al-Foraih Energy Efficiency Technologies Program (EET), Energy & Building Research Center (EBRC), Kuwait Institute for Scientific Research (KISR), Safat, Kuwait

Ersin Alptekin Department of Mechanical Engineering, Dokuz Eylül University, Izmir, Turkey

Michael Anees IMT Atlantique, Department of Energy Systems and Environment, Nantes, France

Panagiota Antoniadou Department of Mechanical Engineering, Aristotle University of Thessaloniki, Process Equipment Design Laboratory, Thessaloniki, Greece

Mustafa Araz Yasar University, Energy Systems Engineering, Izmir, Turkey

Silvia Arias University of Guadalajara Mexico, Department of Urbanism, Guadalajara, Jalisco, Mexico

Maria Aryblia Renewable and Sustainable Energy Systems Laboratory, School of Environmental Engineering, Technical University of Crete, Chania, Greece

Mustafa Asker Department of Mechanical Engineering, Adnan Menderes University, Aydın, Turkey

Zhuldyz Assylova Nazarbayev University, School of Engineering and Graduate School of Business, Astana, Kazakhstan

Yavuz Ates Yildiz Technical University, Electrical Engineering Department, Istanbul, Turkey

David C. Avila University of Guadalajara Mexico, Department of Urbanism, Guadalajara, Mexico

Elif Merve Bahar Energy Systems Engineering, University of Yalova, Yalova, Turkey

Maria Balouktsi Karlsruhe Institute of Technology, Centre for Real Estate, Karlsruhe, Germany

Sinem Bayar Energy Systems Engineering Department, Kırklareli University, Technology Faculty, Kırklareli, Turkey

Emrah Biyik Yasar University, Energy Systems Engineering, Izmir, Turkey

Maresa Bussa IMT Atlantique, Department of Energy Systems and Environment, Nantes, France

Ozum Calli Ege University, The Graduate School of Natural and Applied Sciences, Izmir, Turkey

Omer Cam Erzincan Binali Yildirim University, Department of Airframes and Powerplants, Erzincan, Turkey

Lucas Chacha École des Mines de Nantes, Department of Energy Systems and Environment, Nantes, France

Georgios Chalkiadakis Technical University of Crete, Chania, Greece

Zhu Changan University of Science and Technology of China, Department of Precision Machinery and Precision Instrumentation, Hefei, Anhui, People's Republic of China

Tomasz Cholewa Lublin University of Technology, Faculty of Environmental Engineering, Lublin, Poland

Frans Coenen University of Twente, Department of Government and Technology for Sustainability, Enschede, The Netherlands

Can Ozgur Colpan Dokuz Eylul University, Faculty of Engineering, Mechanical Engineering Department, Buca, Izmir, Turkey

M. Cruz Castañeda Universidad Politécnica de Madrid, Ingeniería Geológica y Minera, Madrid, Spain

Lorenzo Chacon Ladron de Guevara Andalusian Institute of Technology, Sevilla, Spain

Teodosio del Caño Onyx Solar Energy, Avila, Spain

Atilla G. Devecioğlu Dicle University, Department of Mechanical Engineering, Diyarbakır, Turkey

Kevser Dincer Selcuk University, Faculty of Engineering, Department of Mechanical Engineering, Konya, Turkey

Cristina Dominguez IMT Atlantique, Department of Energy Systems and Environment, Nantes, France

Marco Duran IMT Atlantique, Department of Energy Systems and Environment, Nantes, France

Abdelghani A. Elimam The American University in Cairo, Mechanical Engineering Department, New Cairo, Egypt

Mohamed El-Morsi The American University in Cairo, Mechanical Engineering Department, New Cairo, Egypt

Mohammadreza Emami Selcuk University, Faculty of Engineering, Department of Mechanical Engineering, Konya, Turkey

Hikmet Erbıyık Department of Industrial Engineering, University of Yalova, Yalova, Turkiye

Anil Erdogan Dokuz Eylul University, The Graduate School of Natural and Applied Sciences, Buca, Izmir, Turkey

Mohammad Eslami School of Mechanical Engineering, Shiraz University, Shiraz, Fars, Iran

Emmanuel Essah University of Reading, School of the Built Environment, Reading, UK

Mehmet Akif Ezan Department of Mechanical Engineering, Adnan Menderes University, Aydın, Turkey

Eleni Farmaki Technical University of Crete, School of Environmental Engineering, Renewable and Sustainable Energy Systems Laboratory, Chania, Greece

Maria Frangou Renewable and Sustainable Energy Systems Laboratory, School of Environmental Engineering, Technical University of Crete, Chania, Greece

Anne Dominique Furphy Andalusian Institute of Technology, Sevilla, Spain

Mohamed Gadalla Department of Mechanical Engineering, College of Engineering, American University of Sharjah, Sharjah, United Arab Emirates

Hadi Ganjehsarabi Department of Mechanical Engineering, Erzincan University, Erzincan, Turkey

Justo García-Sanz-Calcedo Graphical Expression Department, University of Extremadura, Badajoz, Spain

Ilyes Ghedjatti Laboratoire des Carburants Gazeux et de l'Environnement, Département de Génie Mécanique, Institut de Génie Civil et Mécanique d'Oran, Université des Sciences et de la Technologie d'Oran Mohamed Boudiaf, Oran, Algeria

Effrosyni Giama Department of Mechanical Engineering, Aristotle University of Thessaloniki, Process Equipment Design Laboratory, Thessaloniki, Greece

Erdin Gokalp Yildiz Technical University, Electrical Engineering Department, Istanbul, Turkey

Justyna Gołębiowska Faculty of Environmental Engineering, Lublin University of Technology, Lublin, Poland

Alfonso G. González Department of Mechanical, Energy and Materials Engineering, University of Extremadura, Mérida, Spain

Ceyda Gunay Dokuz Eylul University, The Graduate School of Natural and Applied Sciences, Buca, Izmir, Turkey

Huseyin Gunerhan Ege University, Faculty of Engineering, Mechanical Engineering Department, Izmir, Turkey

Boudjelal Kadi Hanifi Lafarge Ciment Oggaz, Lafarge Algeria, A Member of LafargeHolcim, Mascara, Algeria

Arif Hepbasli Yasar University, Energy Systems Engineering, Izmir, Turkey

Taehoon Hong Department of Architecture and Architectural Engineering, College of Engineering, Yonsei University, Seoul, Republic of Korea

Thomas Hoppe TU Delft, Department of Multi-Actor Systems, Delft, The Netherlands

Arian Hosseini Industrial Engineering & Management, KTH Royal Institute of Technology, Stockholm, Sweden

Natalia Howaniec Central Mining Institute, Katowice, Poland

Hamid Jamili Ecole des Mines de Nantes, Engineering, Energy Systems and Environment Department, Nantes, France

Yuchen Ji Dalhousie University, Faculty of Agriculture, Department of Engineering, Truro-Bible Hill, NS, Canada

Yi Jin University of Science and Technology of China, Department of Precision Machinery and Precision Instrumentation, Hefei, Anhui, People's Republic of China

Aashis Joshi École des Mines de Nantes, Department of Energy Systems and Environment, Nantes, France

Mandar Kadam IMT Atlantique, Department of Energy Systems and Environment, Nantes, France

Kernyong Kang Korea Institute of Machinery and Materials, Engine Research, Daejeon, Republic of Korea

Dimitris Karakasidis Department of Mechanical Engineering, Aristotle University of Thessaloniki, Process Equipment Design Laboratory, Thessaloniki, Greece

T. Hikmet Karakoc Anadolu University, Faculty of Aeronautics and Astronautics, Department of Airframe and Power plant Maintenance, Eskisehir, Turkey

Karim Khiari Ecole Militaire Polytechnique, LGP, Algiers, Algeria

Sujit Karmakar National Institute of Technology Durgapur, Durgapur, West Bengal, India

S. C. Kaushik Centre for Energy Studies, Indian Institute of Technology Delhi, New Delhi, India

Goutam Khankari National Institute of Technology Durgapur, Durgapur, West Bengal, India

Yongrae Kim Korea Institute of Machinery and Materials, Engine Research, Daejeon, Republic of Korea

Michal Kolovratnik Czech Technical University in Prague, Faculty of Mechanical Engineering, Prague 6, Czech Republic

Choongwan Koo Department of Architectural Engineering, College of Creative Engineering, Kyonggi University, Suwon, Republic of Korea

Murat Koray Piri Reis University, MHVS, Istanbul, Turkey

Dimitrios N. Korres Mechanical Engineering Department, National Technical University of Athens, Athens, Greece

Robert Kostić Zagreb City Holding, Department of Projects and International Cooperation, Zagreb, Croatia

Danurachman Krishana Ecole des Mines de Nantes, Engineering, Energy Systems and Environment Department, Nantes, France

Patrycja Kuna-Gwoździewicz Central Mining Institute, Katowice, Poland

Mehmet Kurban Bilecik Şeyh Edebali University, Electric and Electronic Engineering Faculty, Bilecik, Turkey

Elli Kyriaki Mechanical Engineering, Aristotle University of Thessaloniki, Thessaloniki, Greece

Ravita Lamba Centre for Energy Studies, Indian Institute of Technology Delhi, New Delhi, India

Juan Luis Lechón Onyx Solar Energy, Avila, Spain

Minhyun Lee Department of Architecture and Architectural Engineering, Yonsei University, Seoul, Republic of Korea

Seokhwan Lee Korea Institute of Machinery and Materials, Engine Research, Daejeon, Republic of Korea

Guiqiang Li University of Science and Technology of China, Department of Thermal Science and Energy Engineering, Hefei, Anhui, People's Republic of China

Bernardo Llamas Universidad Politécnica de Madrid, Ingeniería Geológica y Minera, Madrid, Spain

David Lokhat School of Engineering, University of Kwazulu-Natal, Durban, South Africa

Khaled Loubar IMT Atlantique, Systèmes Energétiques et Environnement, Nantes, France

Thomas Lützkendorf Karlsruhe Institute of Technology, Centre for Real Estate, Karlsruhe, Germany

Carlos Laín Universidad Politécnica de Madrid, Ingeniería Geológica y Minera, Madrid, Spain

Rachid Mahmoud Ecole Militaire Polytechnique, LGP, Algiers, Algeria

Matislav Majstrović Energy Institute Hrvoje Požar, Power Transmission and Distribution, Zagreb, Croatia

Ivo Marinić-Kragić Faculty of Electrical Engineering, Mechanical Engineering and Naval Architecture, Univeristy of Split, Split, Croatia

Philippe Martin Lafarge Ciment Oggaz, Lafarge Algeria, A Member of LafargeHolcim, Mascara, Algeria

Zoran Milas Faculty of Electrical Engineering, Mechanical Engineering and Naval Architecture, Univeristy of Split, Split, Croatia

Hossein Moshfegh School of Mechanical Engineering, Shiraz University, Shiraz, Fars, Iran

Medet Mukushev Nazarbayev University, School of Engineering and Graduate School of Business, Astana, Kazakhstan

P. Unnikrishnan Nair Turbopump Division, Liquid Propulsion System Centre, ISRO, Trivandrum, Kerala, India

Rocío Nallim École des Mines de Nantes, Department of Energy Systems and Environment, Nantes, France

Sandro Nižetić Faculty of Electrical Engineering, Mechanical Engineering and Naval Architecture, University of Split, LTEF – Laboratory for Thermodynamics and Energy Efficiency, Split, Croatia

Vaclav Novotny Czech Technical University in Prague, Faculty of Mechanical Engineering, Prague 6, Czech Republic

Jeongyoon Oh Department of Architecture and Architectural Engineering, College of Engineering, Yonsei University, Seoul, Republic of Korea

Armando C. Oliveira University of Porto, Mechanical Engineering, Porto, Portugal

Mine Nazan Kerimak Öner Kocaeli University, Köseköy Vocational School, Department of Food Technology, Kocaeli, Türkiye

Vedat Oruç Dicle University, Department of Mechanical Engineering, Diyarbakır, Turkey

Betül Özer Energy Systems Engineering Department, Kırklareli University, Technology Faculty, Kırklareli, Turkey

Gokçen Ozkara Energy Systems Engineering, University of Yalova, Yalova, Turkey

Süleyman Ozkaynak Maritime Faculty, Piri Reis University, Istanbul, Turkey

Agis M. Papadopoulos Department of Mechanical Engineering, Aristotle University of Thessaloniki, Process Equipment Design Laboratory, Thessaloniki, Greece

Canan Perdahci Kocaeli University, Electrical Engineering, Kocaeli, Turkey

Johanna Pérez École des Mines de Nantes, Department of Energy Systems and Environment, Nantes, France

Jaison Philip Department of Mechanical Engineering, John Cox Memorial C.S.I Institute of Technology, Trivandrum, Kerala, India

Juan Pous Universidad Politécnica de Madrid, Ingeniería Geológica y Minera, Madrid, Spain

Ivan Ramljak P.U "Elektroprivreda HZHB", Development Division, Mostar, Bosnia and Herzegovina

Farshad Ravosh Sharif University of Technology, Mechanical Engineering, Tehran, Iran

K. S. Reddy Heat Transfer and Thermal Power Laboratory, Department of Mechnaical Engineering, Indian Institute of Technology Madras, Chennai, Tamilnadu, India

Bojan Ribić Zagreb City Holding, Department of Projects and International Cooperation, Zagreb, Croatia

Elena Rico Onyx Solar Energy, Avila, Spain

Luis Rojas-Solórzano Nazarbayev University, School of Engineering, Department of Mechanical Engineering, Astana, Kazakhstan

Jesus Rubio Ecole des Mines de Nantes, Engineering, Energy Systems and Environment Department, Nantes, France

Khadidja Safer Laboratoire des Carburants Gazeux et de l'Environnement, Département de Génie Mécanique, Institut de Génie Civil et Mécanique d'Oran, Université des Sciences et de la Technologie d'Oran Mohamed Boudiaf, Oran, Algeria

Mohammad Saghafifar Department of Engineering, University of Cambridge, Cambridge, UK

David R. Salgado Department of Mechanical, Energy and Materials Engineering, University of Extremadura, Badajoz, Spain

T. V. Sanand Turbopump Division, Liquid Propulsion System Centre, ISRO, Trivandrum, Kerala, India

Nikolaos Savvakis Technical University of Crete, Chania, Greece

Zakaria Bekkar Djelloul Sayah Ecole Militaire Polytechnique, LGP, Algiers, Algeria

Mine Sertsöz Anadolu University, Vocational School of Transportatıon, Eskişehir, Turkey

Sedat Sevin Gümüşhane Üniversitesi, Civil Engineering, Gümüşhane, Turkey

Mehdi Shahrestani University of Reading, School of the Built Environment, Reading, UK

Misagh Irandoost Shahrestani University of Tehran, Mechanical Engineering, Tehran, Iran

Li Shao University of Reading, School of the Built Environment, Reading, UK

H. Sharon Heat Transfer and Thermal Power Laboratory, Department of Mechnaical Engineering, Indian Institute of Technology Madras, Chennai, Tamilnadu, India

Adam Smoliński Central Mining Institute, Katowice, Poland

M. Ziya Söğüt Piri Reis University, Maritime Faculty, Istanbul, Turkey

K. J. Sreekanth Energy Efficiency Technologies Program (EET), Energy & Building Research Center (EBRC), Kuwait Institute for Scientific Research (KISR), Safat, Kuwait

Elnara Suanbekova Nazarbayev University, School of Engineering and Graduate School of Business, Astana, Kazakhstan

Abhilash Suryan Department of Mechanical Engineering, College of Engineering Trivandrum, Trivandrum, Kerala, India

Elis Sutlović University of Split, Faculty of Electrical Engineering, Mechanical Engineering and Naval Architecture, Department of Power Engineering, Split, Croatia

Lyes Tarabet Ecole Militaire Polytechnique, LGP, Algiers, Algeria

Mohand Tazerout IMT Atlantique, Systèmes Energétiques et Environnement, Nantes, France

Mohamed Tebbal Laboratoire des Carburants Gazeux et de l'Environnement, Département de Génie Mécanique, Institut de Génie Civil et Mécanique d'Oran, Université des Sciences et de la Technologie d'Oran Mohamed Boudiaf, Oran, Algeria

Ayça Tokuç Department of Architecture, Dokuz Eylul University, Izmir, Turkey

Stavroula Tournaki Technical University of Crete, School of Environmental Engineering, Renewable and Sustainable Energy Systems Laboratory, Chania, Greece

Gabriela Tristan Ecole des Mines de Nantes, Engineering, Energy Systems and Environment Department, Nantes, France

Theocharis Tsoutsos Technical University of Crete, School of Environmental Engineering, Renewable and Sustainable Energy Systems Laboratory, Chania, Greece

Technical University of Crete, Chania, Greece

Hasan Hüseyin Turan Capability Systems Centre, School of Engineering and Information Technology, University of New South Wales, Canberra, Australia

Mehmet Tan Turan Yildiz Technical University, Electrical Engineering Department, Istanbul, Turkey

Christos Tzivanidis Mechanical Engineering Department, National Technical University of Athens, Athens, Greece

Umit Unver Energy Systems Engineering, University of Yalova, Yalova, Turkey

Murat Pasa Uysal Baskent University, Faculty of Commercial Sciences, Ankara, Turkey

Siavash Vaezi Sharif University of Technology, Mechanical Engineering, Tehran, Iran

Monika Vitvarova Czech Technical University in Prague, Faculty of Mechanical Engineering, Prague 6, Czech Republic

Damir Vučina Faculty of Electrical Engineering, Mechanical Engineering and Naval Architecture, Univeristy of Split, Split, Croatia

Enver Yalcin Engineering Faculty of Balikesir University, Mechanical Engineering, Balıkesir, Turkey

Runming Yao University of Reading, School of the Built Environment, Reading, UK

Alibek Yerubayev Nazarbayev University, School of Engineering and Graduate School of Business, Astana, Kazakhstan

Ilhami Yildiz Dalhousie University, Faculty of Agriculture, Department of Engineering, Truro-Bible Hill, NS, Canada

Harun Yilmaz Erzincan Binali Yildirim University, Department of Airframes and Powerplants, Erzincan, Turkey

Ilker Yilmaz Erciyes University, Department of Airframes and Powerplants, Kayseri, Turkey

Agnieszka Żelazna Faculty of Environmental Engineering, Lublin University of Technology, Lublin, Poland

Zarina Zhumanalina Nazarbayev University, School of Engineering and Graduate School of Business, Astana, Kazakhstan

Part I
Energy Analysis and Energy Storage Technologies

Chapter 1
Endorsing Stable and Steady Power Supply by Exploiting Energy Storage Technologies: A Study of Kuwait's Power Sector

Ruba Al-Foraih, K. J Sreekanth, Ahmad Al Mulla, and B. Abdulrahman

1.1 Introduction

1.1.1 Energy Storage Technologies

Energy plays an essential role in the development, economic growth, and advancement of any country. Its future prospects will significantly depend on the long-term availability of energy sources, which are affordable, manageable, storable, and environmentally friendly. Having an uninterrupted source of energy, especially at peak loads, is equally important. In Kuwait, the peak power demand increased from 6000 MW in 1999 to 12,000 MW in 2013 with a total availability supply of about 15,000 MW [1]. The peak demand is expected to reach 27,000 MW by 2030 [2]. Kuwait may, thus, face a shortage in providing a sustainable electric supply especially at peak demands, though there are a number of ways to reduce peak demands especially in summer. One of these solutions is the use of energy storage technologies (ESTs).

Electrical energy cannot be stored directly; therefore, the supply of electricity must be equal to the demand for it. The equal balance of supply and demand has significant operational and cost implications. Generating capacity should be capable of supplying at peak demand, even though this will only be required sporadically. In addition, the inability to store electricity requires the provision of a generating capacity, both in the form of spinning and non-spinning reserves, preserved to account for changes in the amount of load or unplanned deficit of an operating generator.

R. Al-Foraih · K. J. Sreekanth · A. Al Mulla (✉) · B. Abdulrahman
Energy Efficiency Technologies Program (EET), Energy & Building Research Center (EBRC), Kuwait Institute for Scientific Research (KISR), PO Box 24885, Safat 13109, Kuwait
e-mail: ahmulla@kisr.edu.kw

S. Nižetić, A. Papadopoulos (eds.), *The Role of Exergy in Energy and the Environment*, Green Energy and Technology,
https://doi.org/10.1007/978-3-319-89845-2_1

ESTs facilitate us to convert electrical energy to another type of energy that can be stored. The stored energy can then be switched back to electricity when needed. There are different types in which energy can be stored. General examples consist of chemical energy (batteries), kinetic energy (flywheels or compressed air), gravitational potential energy (pumped hydroelectric), and energy in the form of electrical (capacitors) and magnetic fields. These energy storage systems act as a load while the energy is being stored (e.g., while charging a battery) and sources of electricity when the energy is returned to the system. Energy storage is the largely hopeful technology to lessen fuel consumption in the electricity sector. Consistent and reasonable electricity storage is a requirement for using energy in all locations, the incorporation into the electricity system, and the advancement of a potential decentralized energy supply system.

On an international level, pumped storage hydroelectricity (PSH), which is not applicable to Kuwait due to geographical constraints, dominates the grid energy storage. Hence, it could be one potential solution for reducing the investment required for network reliability and maintainability [3]. While, other ESTs' could aid only the integration of future renewable energy sources into the present distribution grid [4], PSH combines the variation in the broad service regulatory surroundings, commercial features, and the domestic purposes. The development of renewable energy as a major and important source of electricity supply, and all united with increasingly meticulous environmental necessities [5–7]. Thermal energy storage could be employed to stack an excess of renewable energy storage (RES) production as presented by Lund [8] or efficiently joint with lesser level use to enhance revenue, as elucidated in Pagliarini [9]. Some explanations have been derived from pioneering views on the use of the thermal storage for electricity storage and generations in occurrences in which PHS or CAES are clarified in Desrues [10]. Estimations among every storage technology that contain distinctiveness, technology development, related markets and technical implementations, were presented by Chen [11], Gonzalez [12], and Kamali [13].

The major objectives of this research study are:

- To study the viability of three major types of EST uses in the electrical energy sector and the various techniques used in understanding the economical assessment of energy storage, pertaining to the substation assembly section
- To use the selected ESTs in the substation section, based on techno-economic analysis results

1.1.2 Electrical Energy Generation and Demand Analysis

The demand for electricity in Kuwait has been increasing at an alarming rate over the past decade. The electrical energy generated by the Ministry of Electricity and Water (MEW) has increased from 38.6 TWh in 2003 to 61.0 TWh in 2013, showing a 58.0% growth in a decade. The MEW estimates that electrical energy generated will

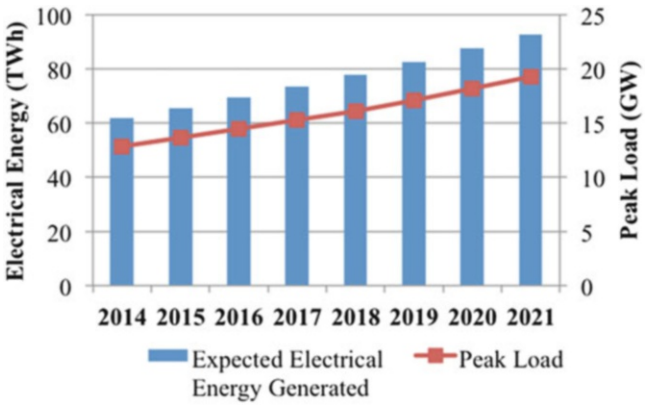

Fig. 1.1 Future estimates of electrical energy generated and peak demand (Source: MEW [14])

Table 1.1 National peak load growth in Kuwait

Year	Peak demand (MW)	Installed capacity (MW)	Mean annual peak load growth during 10 years (%)
1981	2290	2686	–
1992	3460	6898	7.9
2001	6750	9189	9.5
2011	11,220	14,703	5.2

Source: MEW [1]. Electrical energy statistical data yearbook

reach 92.6 TWh with a peak load of 19.2 GW by 2021 compared to 61.0 TWh and 12.1 GW in 2013. Figure 1.1 illustrates the future estimates of the power stations' peak demand and generated electricity.

Kuwait currently ranks as the country with the fourth highest electricity consumption per capita at 16,542 kWh in 2012 [15]. Kuwait's energy consumption is comparable to electricity consumption per capita of industrial countries with extremely cold climates. In 2012, the electricity consumption per capita in Iceland, Norway, Canada, and Finland was around 15 MWh.

Economic prosperity, growing population, urbanization, and heavily subsidized commodities including electricity, as well as harsh, hot weather, are some of the factors that attribute to this growing electrical demand. Peak power demand is experienced in the summer months because of high cooling requirements for buildings. Over 10 years, peak load increased by 61.3%, from 6750 MW in 2001 to 10,890 MW in 2010. The average peak load demand in July was 11,300 MW, a figure that is 100% more than the average peak load demand in January (5270 MW). Table 1.1 illustrates the peak growth over the years.

The dependence of fossil fuel combustion to generate electricity presents severe environmental effects. In 2012, Kuwait was ranked the second highest in the world for carbon dioxide emissions per population (28.1 tons CO_2/population).

1.2 Methodology

This paper aims to examine the viability of certain important types of ESTs used in the electrical energy sector and the various techniques used in understanding the economical assessment of energy storage, in relation to the substation assembly section. It also examines the environmental aspects of implementation of ESTs in the Kuwaiti power sector in relation with the substation section. The ideal use of the selected ESTs in the substation section, based on techno-economic analysis results, will also be looked at.

Two simulation tools, energy storage select (ES-Select) and energy storage computational tool (ESCT), were utilized for the feasibility study. Cash flow, payback, benefit range, and the associated market potential based on various EST implementations were addressed while considering the energy efficiency aspect. ESTs will also contribute toward reducing carbon emission reduction (CER) through the exploitation of electricity as an alternative energy resource particularly in these regions. The present study is, therefore, useful in enhancing the knowledge on ESTs, with the prospective of providing an alternative and sustainable electrical energy supply solution.

The chosen methodology of exploiting ESTs is to use computational tools for representing the incorporation of ESTs within the selected section location of the power system, where it can be connected to bulk generation, transmission and distribution, commercial and industry, and residential users in the most economical way. The two main programs that were chosen for the study and analysis are ESCT and ES-Select.

Five different locations are specified for the ESTs in the grid, namely, central or bulk storage, substation, container/CES fleet, commercial/industrial, and residential/small commercial, related with the corresponding capacities. This is shown in Fig. 1.2. In this paper the substation assembly will be studied.

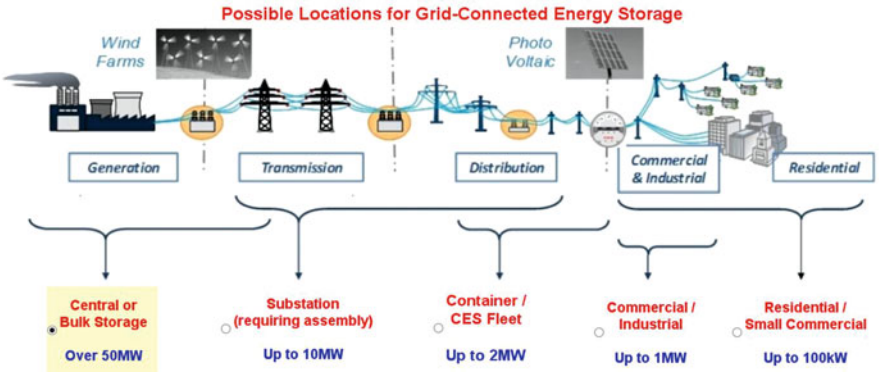

Fig. 1.2 Five possible locations for connecting energy storage to an electric grid

1.2.1 Data Collection of Electrical System in Kuwait

Kuwait's power generation (bulk power generation units), transmission, distribution, and end users' data were collected, which were from different sources such as MEW statistical books and other associated literature, as well as from power generation units. Along with that, the data relating to different ESTs were gathered. The collected and recorded data were used to obtain the seasonal variation of energy use based on climatic conditions for the present electricity generation, transmission, and distribution system. Furthermore, the recorded data analyzed the effect of weather on energy consumption. This data were grouped according to the type and application and used to evaluate and characterize 19 different ESTs' applications mentioned earlier. This was achieved by identifying their employed storage technologies and their applications.

1.3 Results and Discussion

For this paper, the substation assembly section, which is the second location, was examined. The environmental aspects of implementation of ESTs in the Kuwaiti power sector as well as the ideal use of the selected ESTs in the substation section, based on techno-economic analysis results, were studied. Analysis was carried out based on the conditions, and the results of the feasibility criteria are given in Fig. 1.3.

Once the feasibility analysis with weightage is carried out with the utilization factor, the immediate step is to evaluate the financial feasibility of the installation.

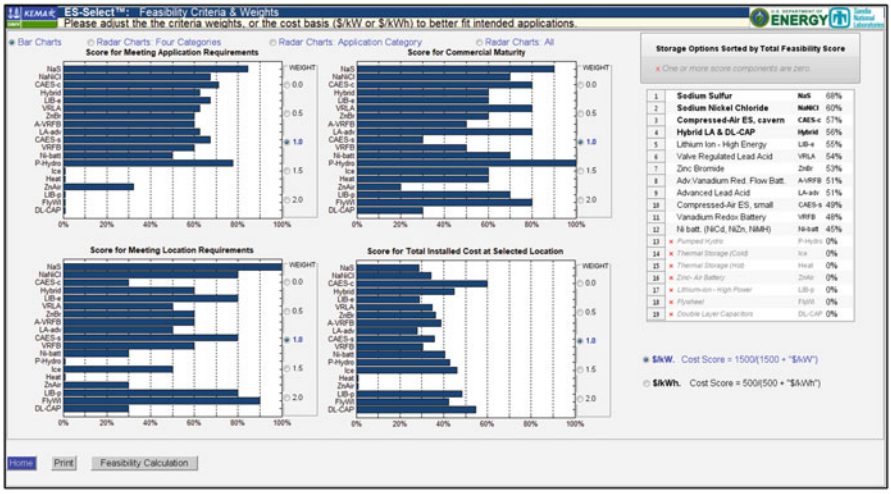

Fig. 1.3 Feasibility criteria analysis of various ESTs with the substation

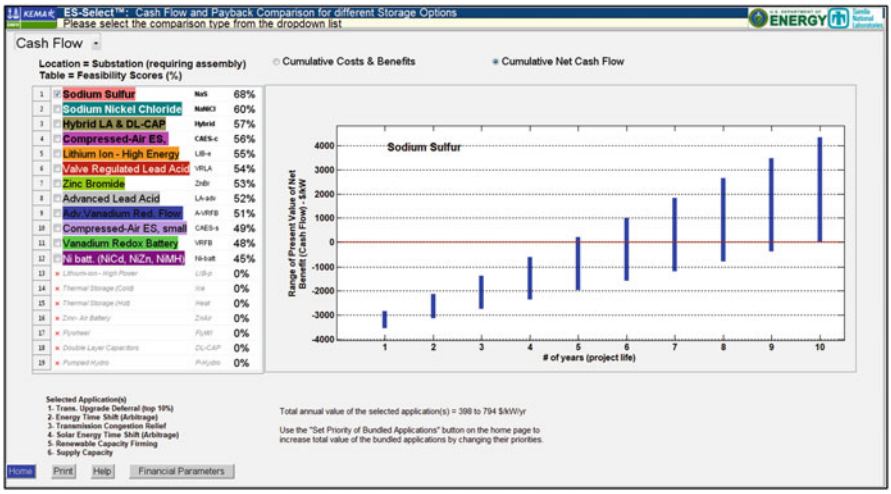

Fig. 1.4 Cumulative net cash flow for substation assembly

For that, the cumulative net cash flow, cumulative costs and benefits, and the total annual value of the selected application are found out.

Net cash flow = cash flows from operating activities (CFO) + cash flows from investing activities (CFI) + cash flows from financing activities (CFF), or net cash flows = CFO + CFI + CFF. (1)

When the net cash flow is calculated, the cumulative costs and the total annual value can be established. Figure 1.4 shows the cumulative net cash flow, and Fig. 1.5 illustrates the cumulative costs and benefits for the substation assembly.

Figure 1.4 shows that the sodium sulfur EST gives maximum benefit with a total annual value of $398 to $794 per kWh with little cumulative annual losses and maintenance costs, and it can be seen that the PV of cumulative annual benefits is very high for the different ESTs selected. Once the total annual value is calculated, the payback period for the installation is estimated to evaluate the time needed to recover the capital investments.

The payback period for the ESTs for the substation assembly location with sodium sulfur EST is 7–8 years whereas that for compressed air EST is only 2–3 years. Hence, based on payback analysis too, it can be seen that the compressed air EST is the most suitable option of EST for substation assembly. This is shown in Fig. 1.6.

Figure 1.7 shows the discharge duration vs. energy efficiency plots for substation location. This plot depicts the behavior of various selected ESTs with these two parameter locations. When it comes to substation location, as seen in Fig. 1.7, it is clear that the compressed air EST has the maximum discharge duration followed by sodium sulfur. Even though Li-ion EST gives maximum energy efficiency, it has minimum discharge duration. Thus, when considering an optimum condition, compressed air EST will yield maximum benefits.

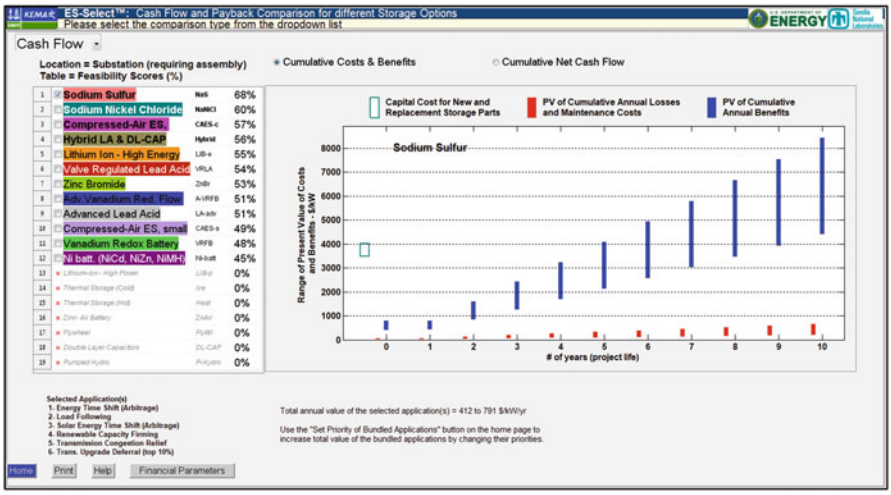

Fig. 1.5 Cumulative costs and benefits for substation assembly

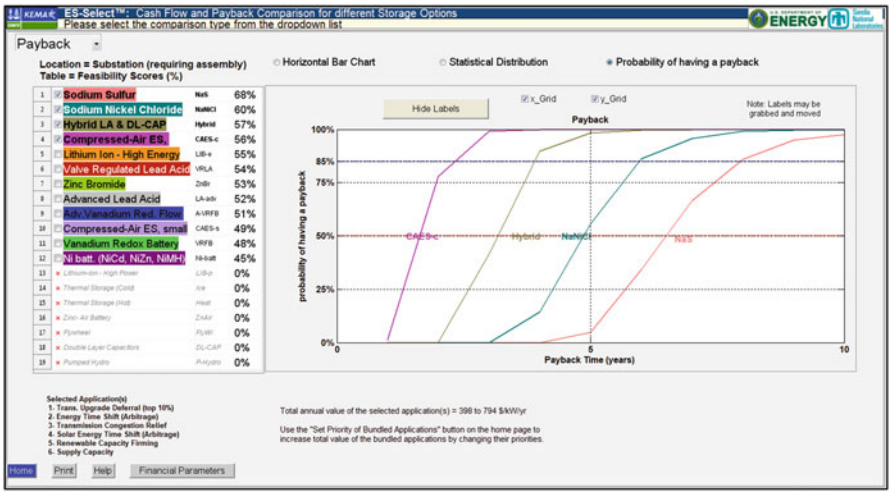

Fig. 1.6 The payback period for the substation EST

These plots illustrate that the sodium sulfur EST and the sodium nickel chloride EST are the primary ESTs for the substation assembly location, which are followed by the CAES EST and the hybrid LA and DL ESTs. Sulfur EST and sodium nickel chloride EST are batteries, whereas the CAES is not. Based on the payback analysis and the cumulative cost and benefit analysis, CAES is one of the better options considering the conditions in Kuwait. At the same time, when the energy efficiency aspect is considered, sodium sulfur is more energy efficient than CAES. From Fig. 1.7, it is evident that sodium sulfur is 90% energy efficient, while CAES is

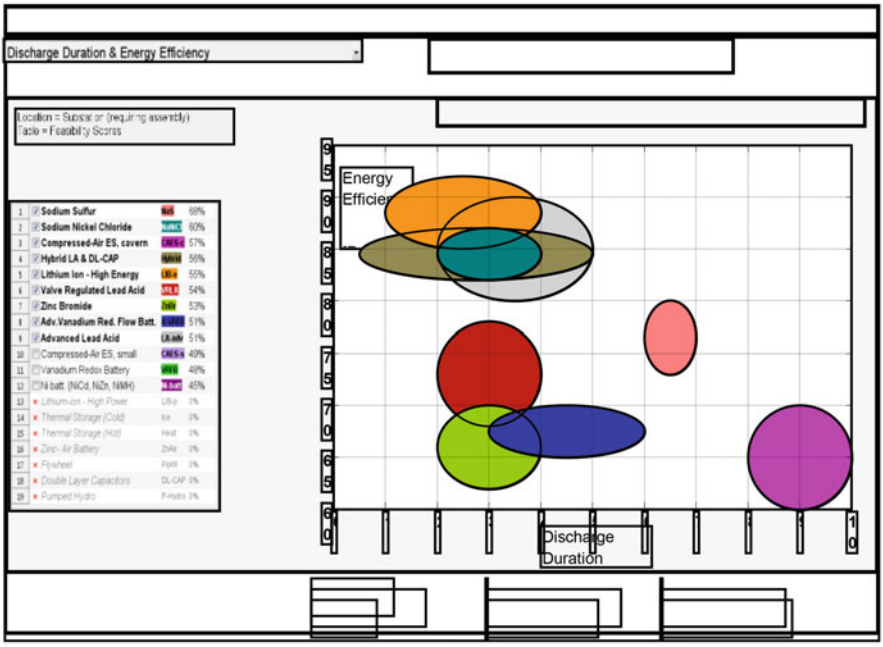

Fig. 1.7 Discharge duration vs. energy efficiency for substation location

70% energy efficient. However, the discharge duration is more for CAES, with 9–10 hours, whereas it is only 3–4 hours for sodium sulfur. For an EST, the discharge duration is a more important parameter than energy efficiency. Therefore, considering all the aforementioned conditions, for the substation assembly sector, compressed air EST is the better and most feasible option, both financially and technically.

1.4 Conclusion

This study aimed at identifying the advantages of ESTs as a step to managing the future energy demand for the State of Kuwait, mainly pertaining to substation sector. The study was intended to assess different forms of ESTs' incorporation into the existing electric power system, particularly those with higher potential related to optimization of power supply, with reference to high demands at peak loads, by utilizing the optimal exploitation of ESTs' within the current power system, relevant to substation. The results showed that the sodium sulfur EST and CAES were the two optimal options when comparing technical and economical aspects such as the net present value, net cash flow, cumulative costs and benefits, payback period, energy efficiency, and discharge duration. The overall feasibility criteria were

evaluated based on the aforementioned features, and it was recognized that compressed air storage is the ideal EST for the Kuwaiti electric power conditions pertaining to the substation sector.

References

1. Ministry of Electricity and Water (MEW), Kuwait (2012) Statistical data book – electricity and water. Ministry of Electricity and Water (MEW), Kuwait
2. Wood M, Alsayegh O (2012) Development of a strategy for the exploitation of renewable energy resources for the State of Kuwait: the future energy demand of the State of Kuwait. Kuwait Inst Sci Res 11178, Kuwait, pp 870–876
3. Koeppel G (2007) Reliability consideration of future energy systems: multi-carrier system and the effect of energy storage; PhD Dissertation submitted to the Swiss Federal Institute of Technology; Diss. ETH No. 17058
4. Smartgrid.gov. https://www.smartgrid.gov (2014) This site is supported by the Office of Electricity Delivery & Energy Reliability within the U.S. Department of Energy
5. Dti Report (2004a) Review of electrical energy storage technologies and systems and of their potential for the UK. DG/DTI/00055/00/00, URN NUMBER 04/1876. UK Department of Trade and Industry, UK, pp 1–34
6. Dti Report (2004b) Status of electrical energy storage systems. DG/DTI/00050/00/00, URN NUMBER 04/1878, UK Department of Trade and Industry, UK, pp 1–24
7. Walawalkar R, Apt J, Mancini R (2007) Economics of electric energy storage for energy arbitrage and regulation. Energy Policy 5:2558–2568
8. Lund H (2005) Large-scale integration of wind power into different energy systems. Energy 30 (13):2402–2412
9. Pagliarini G, Rainieri S (2010) Modelling of a thermal energy storage system coupled with combined heat and power generation for the heating requirements of a University Campus. Appl Therm Eng 30:1255–1261
10. Desrues T, Ruer J, Marty P, Fourmigué JF (2010) A thermal energy storage process for large scale electric applications. Appl Therm Eng 30:425–432
11. Chen H, Cong TN (2009) Progress in electrical energy storage system: a critical review. Prog Nat Sci 19:291–312
12. Diaz-Gonzalez F et al (2012) A review of energy storage technologies for wind power applications. Renew Sust Energ Rev 16:2154–2171
13. Koohi-Kamali S, Tyagi V et al (2013) Emergence of energy storage technologies as the solution for reliable operation of smart power systems: a review. Renew Sust Energ Rev 25:135–165
14. Ministry of Electricity and Water (MEW), Kuwait (2014) Statistical data book – electricity and water. Ministry of Electricity and Water (MEW), Kuwait
15. International Energy Agency (IEA) (2014) Energy storage technology roadmap, technical annex, Paris, International Energy Agency

Chapter 2
Comparison of Aluminum and Copper Particle Critical Diameter Produced in Overhead Line Conductor Clashing

Matislav Majstrović, Elis Sutlović, Ivan Ramljak, and Sandro Nižetić

2.1 Introduction

Wildfires, especially in the dry and hot periods, occur all over the world. Very often conductor clashing of overhead power lines is considered as fire cause. It is possible that during strong, gusting wind, conductors of both low-voltage and high-voltage overhead power lines come in contact with one another causing the flow of short circuit current followed by arcing when the contact is broken as the conductors are separated. In the high-voltage network, arcing is also possible between conductors when they come close enough. After that, ejected metal sparks will fall below, or supported by the wind, in the surrounding area of the power line potentially with a dry vegetation. A major issue is not whether or not such generated particles can initiate a brush or grass fire under certain conditions, because numerous studies have shown this. The main issues are how large the probability of a bushfire ignition is, identifying the parameters that affect ignition as well as how to reduce the risk of bushfire.

M. Majstrović
Energy Institute Hrvoje Požar, Power Transmission and Distribution, Zagreb, Croatia

E. Sutlović (✉)
University of Split, Faculty of Electrical Engineering, Mechanical Engineering and Naval Architecture, Department of Power Engineering, Split, Croatia
e-mail: elis.sutlovic@fesb.hr

I. Ramljak
P.U "Elektroprivreda HZHB", Development Division, Mostar, Bosnia and Herzegovina

S. Nižetić
Faculty of Electrical Engineering, Mechanical Engineering and Naval Architecture, University of Split, LTEF – Laboratory for Thermodynamics and Energy Efficiency, Split, Croatia

S. Nižetić, A. Papadopoulos (eds.), *The Role of Exergy in Energy and the Environment*, Green Energy and Technology,
https://doi.org/10.1007/978-3-319-89845-2_2

The critical diameter is the least diameter of the particle caused by conductor clashing that will, in spite of particle cooling on the way, be sufficient to ignite the biomass on the ground. The model for calculating the critical diameter, used in this paper, takes into account the features of the overhead lines (conductor type, height of conductor clashing place, etc.) and the actual conditions in the environment (ignition temperature and relative humidity of biomass on the ground, wind velocity, etc.).

The aim of this article is to determine the impact of the conductor material (copper and aluminum) on the critical diameter of particle produced in overhead line conductor clashing in the same conditions. In numerical calculations of critical diameter, we use the mathematical model and the appropriate software detailed described in [1].

2.2 Conductor Clashing as a Fire Cause

The problem of ignition of cellulosic fuels caused by overhead line conductor clashing can be divided into three parts, each with its own properties:

- Mechanism of particle emission
- Description of particle flight
- Bushfire ignition after the particle landing

2.2.1 Mechanism of Particle Emission

The researchers have no doubt that during contact of two bare conductors of energized power line or in the case of an arch between them, generated heat can cause melting and vaporization of conductor material, regardless of the metal, aluminum or copper. The pressure from the gasified metal may be high enough to eject the molten metal as small particles, which are then carried away by the wind. The important characteristics of clashing fault are the energy of the arc and the erosion of conductor material. The type of metal influences the problem due to its physical properties and combustion characteristics. On leaving the conductor with some initial speed, a particle falls to the ground under the action of gravity and is also dragged horizontally by the wind.

Several experimental investigations have been conducted on the particle generation and particle flight of different sources under different conditions. In analyzing the results of available experiments, we will focus mostly on the size of generated particles and the temperature of particles during flight.

For the State Electricity Commission of Victoria (SECV) in Australia, some experimental research has been conducted on the ignition potential of particles produced by aluminum conductor clashing [2]. The purpose of the experiments in laboratory conditions (with 240 V and 415 V at a fault current of 100, 300, and

500 A for each voltage level) was to find the size of particles produced by conductor clashes and to measure the temperature as well as the velocity of particles as they leave the conductor. The temperature measured extending about 100 mm from the clash site was 1843 ± 56 °K. Particle sizing showed no significant difference in size distribution with current level (except slightly the size of particles increasing with the increase in current at 240 V level). The majority of generated particles (90%) were less than 0.5 mm in diameter. The maximum size of particle was of the order of 2.5 mm.

Blackburn [3] investigated the arcing characteristics of clashing faults on overhead lines in laboratory experiments for a range of current, for voltage of 240 V and 6.6 kV, and for aluminum and copper conductors. Both high speed and video films were taken to record particle emission. The number and the size of ejected particles were determined by collecting all solid material emitted during clashing. The results show that most (> 50%) of the particles emitted were less than 0.3 mm at each current level. The largest size was 3 mm for copper and 2.5 mm for aluminum. There is not a significant difference in the total number of particles emitted. In contrast to the collision of copper conductors, during collision of aluminum conductors, a larger number of visible particles which soon disappear are observed from high-speed film records.

According to Bushfire Ignition Review [4], SECV (Joynt) also carried out investigations to determine the conditions under which it was likely that clashing copper conductors could cause fires. The testing was done at 240 V and 480 V with currents of 100, 300, and 500 A. The maximum temperatures were observed as high as 2513 K, but due to particle cooling during flight, temperatures were between 1373 K and 1773 K upon impact. The largest particles were up to 1.3 mm in diameter. There were no definitive conclusions about the critical conditions under which copper particles emitted from clashing conductors could cause ignition of grasses, but it was indicated that the largest observed particles (1.3 mm in diameter) could potentially lead to ignition.

According to the same review, Stokes conducted arcing tests which showed that aluminum provided a much more spectacular arc display than did copper because the steel and aluminum molten metal arc product oxidizes in flight with an exothermic reaction.

In our experiments, conductor clashing of aluminum conductors was simulated in two environmental conditions [5]. The first group of the three experiments was performed in the live low-voltage electricity distribution network, and the second group of the three experiments was performed in the laboratory. In these simulations ACSR 25/4 conductors (aluminum conductor steel reinforced with the cross section of 25 mm^2 Al and 4 mm^2 Fe) were used. All was recorded with a high-speed camera. In the live network of 400 V nominal voltage, conductor clashing was simulated as line-to-line short circuit at a height of about 6 m above the ground. The short circuit current value (contact current) at the simulation place was 1700 A. The experiments were carried out with three different fuses with rated currents of 100 A, 125 A, and 160 A. By changing the fuse in each experiment, we obtained different duration of fault according to the time-current characteristic of the fuses. Laboratory

experiments were performed with the contact current of 100 A, 200 A, and 300 A. The amounts of measured values obtained in the first 100 ms have been processed. From the experiment results, it can be seen that the mean values of particle diameters are approximately equal in live network experiments and in laboratory testing. The mean value of the particle diameter slightly increased with increasing contact currents in laboratory experiments (0.675 mm–0.732 mm). The largest particles were up to diameter of 2.5 mm. Empirical data of the frequency of the particle diameters in every experiment were very good approximated by some theoretical probability distribution function (PDF).

2.2.2 Description and Modeling of Particle Flight

Several mathematical models were proposed by various researchers for the determination of the temperature-time history and trajectory of particles of different sizes for various wind conditions. According to the criterion of Glassman who has proposed that for a metal to burn in the gaseous phase, the boiling point temperature of the oxide must be higher than that of the metal, Tse and Fernandez-Pello [6] have explained the differences in the lifetime properties of the particles ejected from copper and aluminum conductors. Since the boiling temperature of copper is higher than that of its oxides, copper can, at best, burn heterogeneously (as a surface reaction). Compared to copper, which is not known to burn by itself in atmospheric air, aluminum is less dense, has lower melting and boiling temperatures, and burns well in air in the gas phase.

2.2.2.1 Copper Particles

In the case of copper power lines, Tse and Fernandez-Pello [6] concluded that ejected particles most likely emerge molten but not burning. Immediately after creation, the copper particles cool down by convection and radiation as they are carried away by the wind. In their numerical model of computation of copper particle trajectories as well as temperature variation for different initial particle diameters (0.5 mm–2 mm), the copper particles are taken to be initially in the solid phase at the melting temperature (1356 °K). It is assumed that the power lines are at a height of 10 m above the ground.

2.2.2.2 Aluminum Particles

Modeling the flight of aluminum particles has always caused more doubt for researchers. Although the explanation of the aluminum particle generation and the simple models of trajectories of such spark on the basis of their own experiments has

been introduced in the aforementioned works [2, 3], more complex models have been proposed in the later works.

Mills and Hang [7] describe aluminum power cable arcing as a bright flash, sparks, and, later, a puff of white smoke. The sparks fall toward the ground but most, if not all, seem to disappear before reaching the ground. In the explanation of trajectories of sparks from arcing aluminum power cables, they indicate that the arc delivers sufficient heat to the metal underneath the point of arc attachment to raise the metal surface to its boiling point and to vaporize a significant fraction of the metal removed. Upon contact with air, this vapor burns rapidly in a very high-temperature flame (the characteristic flash) to form aluminum oxide Al_20_3, which condenses as small aerosol particles (the puff of smoke). The localized high pressure causes ejection of molten aluminum as small droplets. These droplets can have initial temperatures ranging between the surface temperature (2730 K) and the melting point of aluminum (930 K). Some of these droplets will ignite and burn, while others will simply fall to the ground, cooling off on the way. So there are two potential brush fire ignition sources: molten or solidified droplets of aluminum which did not ignite (the majority of the droplets ejected) and burning droplets (sparks) which reach the ground.

- Below the ignition temperature for an aluminum droplet (about 2300 K), which corresponds to the melting point of aluminum oxide Al_20_3, the accumulation of solid oxide on the droplet surface inhibits the contacting of oxygen and aluminum, and the oxidation process is relatively slow.
- If the oxide is molten, the oxidation process can then be rapid enough in which the heat of oxidation released is sufficient to balance the heat losses by convection and radiation. These droplets will burn until all the metal is consumed or until they reach the ground. The initial size of a droplet determines its lifetime, and only the larger droplets may be able to reach the ground below a power distribution cable before burning up.

A model of aluminum droplet combustion is proposed and used to calculate combustion rates, lifetimes, and trajectories of such sparks for various wind conditions. The results show that for the arcing cables 10 m above ground level, sparks of about 1 mm initial diameter can reach the ground before burning up so ignition of dry brush is quite possible.

Tse and Fernandez-Pello [6] agree with the explanation of Mills and Hang [7] and use their own model to calculate trajectories, combustion rates, and lifetimes of aluminum burning sparks of different sizes (diameters of 0.5 mm, 1 mm, 1.5 mm, and 2 mm) for various wind conditions. It is assumed that the power lines are at a height of 10 m above the ground. Aluminum particles are assumed to be ejected at a speed of 1 m/s for a wind speed of 48. 3 km/h. All of the particles are at their boiling temperatures throughout their flight paths. Simulation results show that the 1.5 mm diameter particles do not burn out before impact for the assumed conditions. For the burning particles that reach the ground, the smaller particles travel farther horizontally but also bring less total amounts of heat to their locations of impact.

Rallis and Mangaya [8] in their article complement the abovementioned articles [6, 7] and focus their investigation on the majority of the ejected droplets of aluminum which did not ignite. They assumed that if such a particle falls into dry veld grass while its temperature was between 300 and 400 °C or above, it could cause ignition of the grass. A series of computational calculation of distances traveled before reaching ground and corresponding particle temperatures for a different set of input parameters were carried out. Two initial temperatures have been used: 900 K and 1700 K, particle diameter of 0.5 mm to 5.5 mm (step 0.5 mm), etc. Simulation results indicate that the initial temperature of the particles is the most dominant parameter. In most sets of input parameters, some of the particles would be hot enough to ignite the grass so the probability of a fire being initiated by hot particles ejected into a high-velocity wind as a result of short circuiting of high-voltage overhead transmission lines is high.

Psaros et al. [9] have also suggested a model for the temperature calculation of the molten (but not burning) aluminum particles ejected from low-voltage bare conductors during their flight. The differential equation of the temperature vs. time is solved with an assumption that the particle does not radiate, and only the change of temperature due to convection is examined. The arithmetic example emulates an incandescent particle ejected from bare aluminum conductors at a height of 10 m when the air velocity was 20 ms^{-1}. Created particles are considered to have an initial temperature of 933 K (the melting point of aluminum) and diameter of 0.5 mm. The conclusion is that there is no risk of fire ignition in such conditions because the temperature of the particles when they hit the ground would be in the order of 400 K.

All the above models of aluminum particle flight calculated the temperature-time history of particles of a certain size under given conditions because the particle temperature and the particle diameter when they reach the ground are the dominant parameters to determine whether the particles can ignite the biomass on the ground. Whereas Mills and Hang as well as Tse and Fernandez-Pello deal with the burning particles of aluminum and search whether or not a spark of prescribed initial size can indeed reach the ground, Rallis and Mangaya as well as Psaros et al. deal with molten aluminum particles which are cooled off on the way to the ground. In the first case, since burning particles lose mass and volumes, the key parameter is the initial particle size. In the second case, the mass and the volume of the particles are taken as constant due to negligible evaporation so the initial temperature of the particles has the greatest impact on results, and therefore the conclusions of the last two described models are different.

It is interesting that in the all numerical examples of the above models, the researchers assumed the height of the conductor clashing of about 10 m above the ground, and no one varies this parameter.

2.2.3 *Ignition of the Biomass after Particle Landing*

Particular studies have examined what happens after hot particles reach the ground and which parameters, in addition to the size and the temperature of the particles, are important to the ignition process. Although the ignition scenario of biomass on the ground is not the subject of this paper, let us mention that some studies that deal with this issue are described in the aforementioned reports [2, 4]. In addition to the particle temperature and the particle size upon contact with the ground, calculated in simulation model of particle flight, Coldham [2] considers other factors affecting ignition like fuel factors (the moisture content, the density, and the size of fuel materials) as well as meteorological factors (the air temperature, the humidity, and the wind speed). He concludes that the moisture content of a fuel is the most critical parameter in determining the probability of ignition. Recent work by Zak [10] also gives a good overview of the conducted research in this field, with both experimental and theoretical approaches used to understanding the physics underlying the ignition process.

Our mathematical model for the calculation of the particle size that has sufficient heat and temperature to cause ignition of flammable material on the ground [1] is based on our experiment results of aluminum conductors clashing on a real network at the height of 6 m above the ground. In these experiments, which lasted until the fuse did not blow at the beginning of the transmission line, we did not notice burning aluminum particles reaching the ground still burning. Probably, it is possible that some particles of burning aluminum reach the ground especially in the case of small height of conductor clashing site. However, this model is focused on those more numerous aluminum particles as well as copper particles which are not ejected burning and which are cooled down on the way to the ground. The model observes the amount of heat carried by the particles as a criterion for ignition taking into consideration the characteristics of cellulosic fuel under the power line.

We now investigate the probability of the conditions for the occurrence of fire based on the PDF function of the particle size, the critical diameter of the particles upon impact with the ground, and the duration of a conductor clashing in an electrical network.

2.3 Results and Discussion

In order to investigate the impact of conductor material (copper and aluminum) on the critical diameter of particle produced in the overhead line conductor clashing, we have performed a series of numerical calculations of the critical radius in the same conditions. According to the experiments and the theoretical models previously mentioned, the initial temperature of non-burning aluminum particles is bounded by the aluminum and aluminum oxide melting points, while the initial temperature of copper particles is bounded by the melting and vaporization points of copper. Numerical calculations were carried out for both copper and aluminum conductors

for these two endpoints with the same values of other parameters, in case of windless as well as strong wind conditions.

In all cases it is assumed that the metal particles fell on the cap of the pine needles under energized overhead power line with the following characteristics:

The mass of pine needles' dry cap	0.005 × 10–3 kg
The specific heat capacity of pine needles' dry cap	1.8 kJ/(kg K)
The ignition temperature of pine needles' dry cap	593.15 K

It is also assumed that pine needles have a low value of the thermal conductivity.

The moisture content of the fuel as the most critical parameter in determining the probability of ignition is varied in all cases in the range from 0% to 100% by step of 20%.

Meteorological factors are assumed as follows:

The ambient temperature	293.15 K
The wind velocity in vertical direction	0.0 m/s
The wind velocity in horizontal direction	0.0 m/s
The wind velocity in horizontal direction (two cases):	
Windless	0.0 m/s
Strong wind	30.0 m/s

For copper particles the following are assumed:

The specific density of particle material	8933.0 kg/m^3
The specific heat capacity of particle material	385.0 J/(kg K)
The temperature of particle material on the clashing site (two cases):	
The lowest (melting point of cu)	1357.0 K
The highest (just before evaporation)	2835.0 K

For aluminum particles the following are assumed:

The specific density of particle material	2700.0 kg/m^3
The specific heat capacity of particle material	920.0 J/(kg K)
The temperature of particle material on the clashing site (two cases):	
The lowest (melting point of Al)	931.0 K
The highest (melting point of Al2O3)	2300.0 K

The height of the conductor clashing point over the needle cap on the ground, according to the common height of the towers of overhead power lines in the transmission and distribution network, is varied in all cases in the range from 5 m to 30 m, by the step of 5 m.

The results of the critical diameter calculations for aluminum and copper conductors for different values of the wind velocity in horizontal direction as well as initial particle temperature are presented in eight tables (Tables 2.1, 2.2, 2.3, 2.4, 2.5, 2.6, 2.7, and 2.8).

Table 2.1 The critical diameter of copper particle in mm ($v = 0$ m/s, Tp = 1357.0 K)

	Height of Cu conductor clashing [m]					
Relative humidity [%]	5	10	15	20	25	30
0	1.47	1.60	1.70	1.80	1.88	1.97
20	1.58	1.70	1.80	1.90	1.98	2.06
40	1.67	1.79	1.89	1.99	2.07	2.15
60	1.76	1.88	1.97	2.06	2.15	2.22
80	1.83	1.95	2.05	2.13	2.22	2.29
100	1.90	2.02	2.11	2.20	2.28	2.36

Table 2.2 The critical diameter of copper particle in mm ($v = 0$ m/s. Tp = 2835.0 K)

	Height of Cu conductor clashing [m]					
Relative humidity [%]	5	10	15	20	25	30
0	1.13	1.24	1.33	1.41	1.48	1.55
20	1.21	1.32	1.41	1.49	1.56	1.62
40	1.28	1.39	1.48	1.56	1.63	1.69
60	1.34	1.45	1.54	1.62	1.68	1.75
80	1.40	1.51	1.59	1.67	1.74	1.80
100	1.45	1.56	1.64	1.72	1.79	1.85

Table 2.3 The critical diameter of aluminum particle in mm ($v = 0$ m/s. Tp = 931.0 K)

	Height of Al conductor clashing [m]					
Relative humidity [%]	5	10	15	20	25	30
0	2.17	2.38	2.58	2.76	2.93	3.09
20	2.65	2.85	3.02	3.18	3.34	3.48
40	3.00	3.18	3.34	3.49	3.63	3.77
60	3.27	3.44	3.60	3.74	3.88	4.01
80	3.50	3.67	3.82	3.95	4.09	4.21
100	3.70	3.86	4.01	4.14	4.27	4.39

Table 2.4 The critical diameter of aluminum particle in mm ($v = 0$ m/s. Tp = 2300.0 K)

	Height of Al conductor clashing [m]					
Relative humidity [%]	5	10	15	20	25	30
0	1.38	1.53	1.66	1.78	1.88	1.98
20	1.67	1.82	1.94	2.05	2.15	2.24
40	1.88	2.02	2.14	2.24	2.34	2.43
60	2.04	2.18	2.29	2.40	2.49	2.58
80	2.17	2.31	2.43	2.53	2.62	2.71
100	2.29	2.43	2.54	2.64	2.73	2.82

Table 2.5 The critical diameter of copper particle in mm ($v = 30$ m/s, Tp = 1357.0 K)

	Height of Cu conductor clashing [m]					
Relative humidity [%]	5	10	15	20	25	30
0	1.65	1.79	1.91	2.01	2.10	2.18
20	1.76	1.90	2.01	2.11	2.19	2.28
40	1.85	1.99	2.10	2.19	2.28	2.36
60	1.93	2.07	2.18	2.27	2.35	2.43
80	2.00	2.14	2.25	2.34	2.42	2.50
100	2.07	2.21	2.31	2.40	2.48	2.56

Table 2.6 The critical diameter of copper particle in mm ($v = 30$ m/s, Tp = 2835.0 K)

	Height of Cu conductor clashing [m]					
Relative humidity [%]	5	10	15	20	25	30
0	1.25	1.37	1.47	1.54	1.62	1.68
20	1.33	1.45	1.54	1.62	1.69	1.76
40	1.40	1.52	1.61	1.69	1.76	1.82
60	1.46	1.58	1.67	1.75	1.82	1.88
80	1.52	1.64	1.73	1.80	1.87	1.93
100	1.57	1.69	1.77	1.85	1.92	1.98

Table 2.7 The critical diameter of aluminum particle in mm ($v = 30$ m/s, Tp = 931.0 K)

	Height of Al conductor clashing [m]					
Relative humidity [%]	5	10	15	20	25	30
0	2.43	2.68	2.89	3.08	3.26	3.43
20	2.91	3.13	3.32	3.49	3.65	3.80
40	3.24	3.45	3.63	3.79	3.94	4.08
60	3.51	3.71	3.88	4.03	4.17	4.31
80	3.73	3.93	4.09	4.24	4.38	4.51
100	3.93	4.13	4.28	4.43	4.56	4.68

Table 2.8 The critical diameter of aluminum particle in mm ($v = 30$ m/s, Tp = 2300.0 K)

	Height of Al conductor clashing [m]					
Relative humidity [%]	5	10	15	20	25	30
0	1.50	1.66	1.79	1.90	2.01	2.11
20	1.80	1.95	2.07	2.18	2.28	2.37
40	2.00	2.15	2.27	2.37	2.47	2.56
60	2.17	2.31	2.43	2.53	2.62	2.71
80	2.30	2.45	2.56	2.66	2.75	2.84
100	2.42	2.56	2.68	2.78	2.87	2.95

Also the results of the critical diameter calculations in windless conditions for copper conductors with particle initial temperature of 1357.0 K (conditions as in Table 2.1) as well as for aluminum conductors with particle initial temperature of 931.0 K (conditions as in Table 2.3) are presented graphically in Figs. 2.1 and 2.2, respectively.

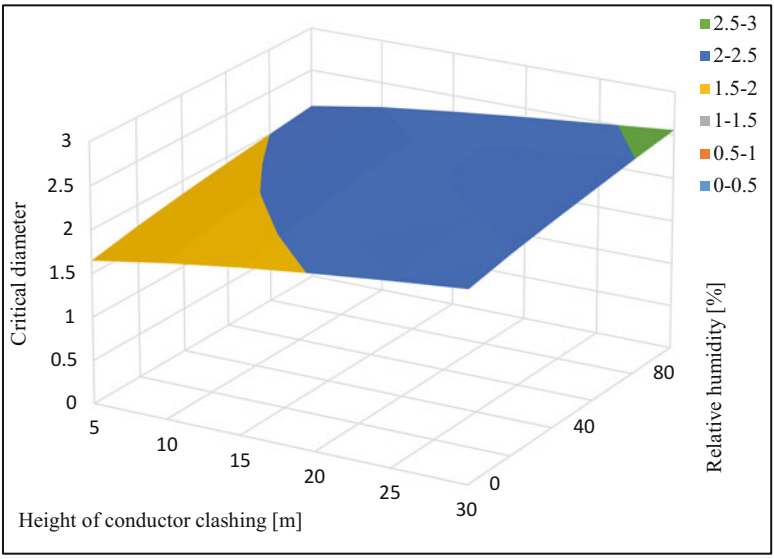

Fig. 2.1 The critical diameter of copper particle in mm ($v = 0$ m/s, $T_p = 1357.0$ K)

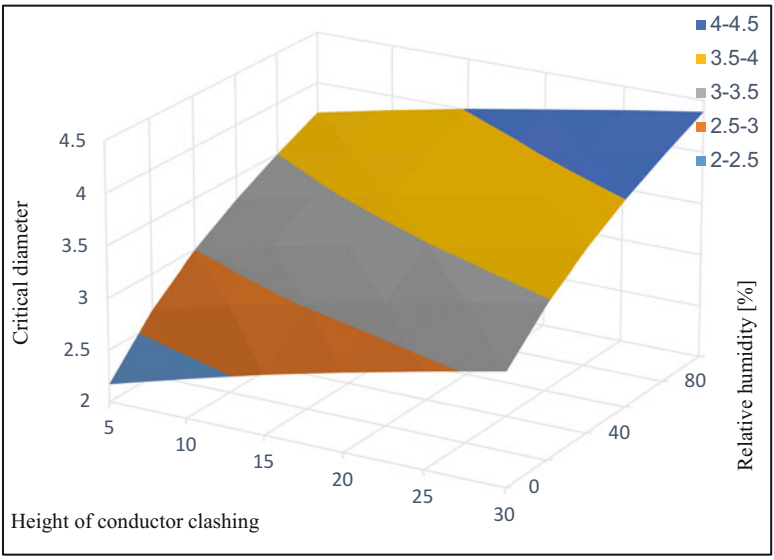

Fig. 2.2 The critical diameter of aluminum particle in mm ($v = 0$ m/s, $T_p = 931.0$ K)

Analyzing the results of the critical diameter calculations, it can be concluded:

- The critical diameter of the particles, in some cases and in some condition, for both copper and aluminum conductors, can be less than 2.5 mm, which is noticed as the largest diameter of the particles in several abovementioned experiments (evident from the overall results).
- The critical diameter of the metal particles increases with increasing the biomass relative humidity and with increasing the height of the conductor clashing point over the ground (evident by observing any of the eight tables). This impact is significant.
- The critical diameter of the particles, for both copper and aluminum conductors, decreases with increasing the initial temperature of the ejected particles (evident by observing together Tables 2.1 and 2.2 or Tables 2.3 and 2.4). This impact is also significant.
- The critical diameter of the metal particles increases with increasing the wind speed (evident by observing together Tables 2.1 and 2.5 or Tables 2.4 and 2.8). This impact, for both copper and aluminum conductors, is little. With increasing the wind speed, the time of particle flight and the particle trajectories (with better cooling on the way) are also increasing. Although the conductor clashing occurs in strong wind conditions, it is possible that after clashing caused by gust, wind suddenly reduced.
- The critical diameter of the metal particles for all cases in the same conditions is lower for copper than for aluminum conductors (observing together Tables 2.1 and 2.3 or Tables 6 and 8). "The same conditions" means the minimum or the maximum possible initial temperature of ejected particles for both copper and aluminum conductors. The main reasons why the critical diameter of copper particles is always less than the corresponding critical diameter of aluminum particles are higher initial temperature of copper particles and higher density of copper even though aluminum has higher specific heat capacity.

2.4 Conclusions

Hot metal particles generated during conductor clashing of energized overhead line may initiate the ignition of vegetation under power lines in some conditions. Several experimental studies on the generation of particles and several mathematical models of particle flight are discussed.

The critical diameter is the least diameter of the particle which will, in spite of particle cooling on the way, be sufficient to ignite the biomass on the ground. The results of numerical calculations for different sets of input parameters showed that the critical diameter of particle ejected during copper conductor clashing is always smaller than the corresponding critical diameter of the non-burning particle ejected during aluminum conductor clashing. A smaller particle critical diameter means greater possibility of initiating a fire. The biomass relative humidity, the height of

conductor clashing point over the ground, and the initial temperature of the ejected particles have great influence on the critical diameter of the metal particles.

From the results it can also be seen that in some conditions, for both copper and aluminum conductors, the critical diameter of the particles is less than 2.5 mm, which is noticed as the largest diameter of the particles in several experiments.

References

1. Majstrovic M, Sutlovic E, Ramljak I (2017, March) Critical diameter of particles produced in overhead line conductor clashing. Appl Therm Eng 114:713–718
2. Pleasance GE, Hart JA (1977) An examination of particles from conductor clashes as possible sources of bushfire ignition, Laboratory report. State Electricity Commission of Victoria
3. Blackburn TR (1985) Conductor clashing characteristics of overhead lines. In: Electric energy conference (1985 Newcastle, N.S.W.): Modern trends in the generation, transmission, distribution and utilisation of electrical energy. The Institution of Engineers Australia, pp 212–216
4. Coldham D (2011) Bushfire ignition from electric faults – a review of technical literature, report no: HCL/2010/440–final. HRL Technology Pty Ltd, Melbourne
5. Ramljak I, Majstrović M, Sutlović E (2014) Statistical analysis of particles of conductor clashing. In: ENERGYCON 2014 conference. IEEE International, Cavtat, Croatia, pp 638–643
6. Tse DS, Fernandez-Pello A (1998) On the flight paths of metal particles and embers generated by power lines in high winds-a potential source of wildland fires. Fire Saf J 30:333–356
7. Mills AF, Hang X (1984, May) Trajectories of sparks from arcing aluminum power cables. Fire Technol 20:5–14
8. Rallis JC, Mangaya BM (2002) Ignition of weld grass by hot aluminum particles ejected from clashing overhead transmission lines. Fire Technol 38:81–92
9. Psarros EG, Polykrati AD, Karagiannopoulos CG, Bourkas PD (2009) A model for calculating the temperature of aluminum particles ejected from overhead low-voltage lines owing to a short circuit. Int J Wildland Fire 18:722–726
10. Zak CD (2015) The effect of particle properties on hot particle spot fire ignition, PhD. Thesis, UC Berkeley, USA

Chapter 3
Investigation of an Optimal Operating Condition for a Micro Combustor Regarding Basic Thermophotovoltaic System Requirements

Harun Yilmaz, Omer Cam, and Ilker Yilmaz

3.1 Introduction

Micropower generation systems have growing interest based on the recent developments in microelectromechanical systems (MEMS). Day after day, these systems become more practical for production and appear more in daily life [3, 4]. Electrical energy needed for such systems can be supplied through a micro thermophotovoltaic (MTPV) cell which utilises convective and radiative heat from combustion in a micro combustor [5]. Using hydrogen or hydrocarbon-fuelled micro combustors instead of chemical batteries as a power source offer many benefits. First of all, energy densities of hydrogen or hydrocarbon fuels are much higher than that of the chemical batteries, even with low energy conversion ratio of hydrocarbons to power [5, 6]. It also assures longer lifetime and lower weight of the overall system compared to electrical or mechanical devices in which batteries are used as a power source [6].

Regarding these benefits, the subject of using hydrocarbon-fuelled micro combustors in MEMS was experimentally and numerically studied by many researchers. Zarvandi et al. tried to modify and improve premixed CH_4/air flames by using hydrogen as an additive in a micro-stepped tube. They used a high-order 2D code to calculate effects of additive, inlet velocity and heat losses on temperature patterns and combustion process itself in the combustor. They concluded that hydrogen addition has a great impact on combustion characteristics by means of increasing radical concentrations, ensuring flame presence under certain circumstances and

H. Yilmaz (✉) · O. Cam
Erzincan Binali Yildirim University, Department of Airframes and Powerplants, Erzincan, Turkey
e-mail: hyilmaz@erzincan.edu.tr

I. Yilmaz
Erciyes University, Department of Airframes and Powerplants, Kayseri, Turkey

S. Nižetić, A. Papadopoulos (eds.), *The Role of Exergy in Energy and the Environment*, Green Energy and Technology,
https://doi.org/10.1007/978-3-319-89845-2_3

improving temperature distribution [3]. Li et al. numerically investigated effects of combustor size, combustor geometry, inlet velocity and wall boundary conditions on premixed CH_4/air flames. Results showed that under a certain flow velocity, the larger the combustor, the higher the flame temperature is, and planar combustor provides higher flame temperature than its cylindrical counterpart [7]. Lei et al. numerically studied flame stability characteristics such as quenching distance and flammability limits in a micro combustor. For this purpose, they constructed a micro combustor model with EGR (exhaust gas recirculation). It was founded that quenching distance reduces and flammability limits increase with EGR [5]. Mixing condition of fuel and oxidiser is very important for non-premixed combustion with respect to flame characteristics and emissions. Jiaqiang et al. performed both numerical and experimental studies to investigate mixing conditions and combustion performances of non-premixed hydrogen/air flames in a novel micro combustor. It was shown that mixing condition can be developed by adding more pipes to combustor, and thermal power is highly related to combustion performance [4]. In a micro combustor, high surface to volume ratio is a desirable geometric property due to the high radiation flux per unit volume of this kind of structures. Motivated by this, Pan et al. proposed a novel TPV power generator which utilises a micro parallel plate combustor. They built an experimental setup to understand effects of hydrogen/oxygen mixing ratio, volumetric flow rate of hydrogen and nozzle geometry on combustor performance. They also investigated flame initiation limits for two different combustors. It was concluded that increasing hydrogen flow rate reduces combustion performance by shortening flame residence time, lean flammable limit increases with reducing combustor size and barely oxygen rich mixtures result with higher wall temperature. Lastly, rectangular nozzle was found to be better than circular nozzle in point of combustion efficiency [8]. Su et al. carried out simulation studies to understand the impact of combustor design on the performance of MTPV systems by varying combustor channel. They implemented five cylindrical channels to the combustor model and concluded that wall temperature profiles become more uniform, and radiation energy efficiency increases with multichannel arrangement compared to single-channel combustor [9]. Tang et al. built an experimental setup to determine availability of three different hydrocarbons, namely, methane, propane and hydrogen, with regard to flame placement, outer wall temperature profiles and quenching distance in micro combustors. It was reported that hydrogen has higher flammability limits than methane and propane, increasing flow rate moves methane and propane flame placements towards combustor outlet, methane provides the most uniform wall temperature distribution for the same thermal power and hydrogen has the lowest quenching distance [10]. Sakurai et al. developed a micro combustor and tested it at propane lean equivalence ratio conditions to analyse combustion characteristics. It was observed that increasing amount of preheating of unburned mixture improves flame stability, carbon monoxide and total hydrocarbon emissions are sensitive to heat losses and NO_x emission can be reduced by complete burning [11]. Raimondeau et al. simulated flame propagation in microchannels using a 2D parabolic code that takes multicomponent transport, heat loss and radical-wall interaction into consideration. At the inlet of the combustor, heat loss and radical-wall interactions were found to effect flame propagation [12].

In this study, an experimentally tested micro combustor [2] model was built, and effects of equivalence ratio and thermal power on combustion and emission behaviour of premixed hydrogen/air flames were analysed to find an optimal operating condition with respect to basic thermophotovoltaic system requirements which are high and uniform temperature distribution at the outer wall of the combustor.

3.2 Numerical Setup

3.2.1 Combustor Structure

A 3D micro planar combustor model was built, and combustion process in this combustor was simulated using ANSYS-Fluent CFD code [13]. Dimensions of the combustor are 18 mm in length, 9 mm in width and 3 mm in height. Thickness of the combustor wall is 0.5 mm, so inlet of the flow area has a 2 mm height. Combustor geometry can be seen in Fig. 3.1.

3.2.2 Mathematical Model

In this study, premixed hydrogen/air combustion was simulated at different equivalence ratios (0.8, 1.0 and 1.2) and thermal powers (50 W, 100 W, 150 W and 200 W). Steady-state forms of the basic governing equations (continuity, momentum, energy and species) were solved. Assumptions made for simulation studies: energy flux due to mass concentration gradients, work done by pressure and viscous forces, gas radiation, surface reactions were neglected and lastly, no slip boundary

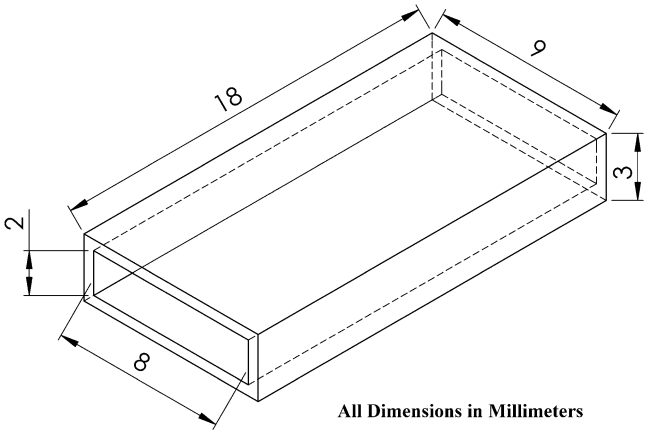

Fig. 3.1 Combustor geometry [2]

condition at the combustor wall was implemented. EDC (eddy dissipation concept) model was used as combustion model, and reaction scheme includes 9 species and 19 steps. Yılmaz et al. investigated effects of different turbulence models on combustion characteristics of premixed hydrogen/air flames in a micro combustor and pointed out that RNG k-ε model gives better simulation results [1] so turbulence model used in this study is RNG k-ε. Reaction scheme of hydrogen/air combustion can be found in Ref. [14].

3.2.3 Governing Equations

Continuity equation can be written as

$$\frac{\delta\rho}{\delta t} + \nabla.\left(\rho\,\vec{v}\right) = 0 \tag{3.1}$$

Conservation of momentum

$$\frac{\delta}{\delta t}\left(\rho\,\vec{v}\right) + \nabla.\left(\rho\,\vec{v}\vec{v}\right) = -\nabla p + \nabla.\left(\bar{\bar{\tau}}\right) + \rho\,\vec{g} + \vec{F} \tag{3.2}$$

p, static pressure; $\bar{\bar{\tau}}$, stress tensor; $\rho\,\vec{g}$, gravitational body force; $\vec{F}$, external body force.

Stress tensor

$$\bar{\bar{\tau}} = \mu\left[\left(\nabla\vec{v} + \nabla\vec{v}^{T}\right) - \frac{2}{3}\nabla.\,\vec{v}I\right] \tag{3.3}$$

μ, molecular viscosity; I, unit tensor.

Energy equation

$$\frac{\delta}{\delta x_j}\left(\rho u_j h + F_{hj}\right) = u_j\frac{\delta p}{\delta x_j} + \tau_{ij}\frac{\delta u_i}{\delta x_j} \tag{3.4}$$

h, enthalpy of gas composition; F_{hj}, energy flux of the x_j direction; τ_{ij}, stress tensor; u_j, velocity component; ρ, density.

Energy conservation equation of wall

$$\frac{\delta(\lambda_w \delta T)}{\delta x_i^2} \tag{3.5}$$

λ_w, thermal conductivity.

Ideal gas equation [15]

$$p = \rho R_0 T\sum\frac{mi}{Mi} \tag{3.6}$$

R_0, universal gas constant; Mi, molar mass of species i [16].

Species transport equation

$$\frac{\delta}{\delta t}(\rho Y_i) + \nabla.\left(\rho \vec{v} Y_i\right) = -\nabla \vec{J}_i + R_i \tag{3.7}$$

Y_i, mass fraction of species i; R_i, net production rate of species i via chemical reactions; $\vec{J}_i$, diffusion flux of species i.

Diffusion flux of species i can be defined as

$$\vec{J}_i = -\left(\rho D_{i,m} + \frac{\mu_t}{Sc_t}\right) \nabla Y_i - D_{T,i} \frac{\nabla T}{T} \tag{3.8}$$

Sc_t, turbulent Schmidt number $\left(\frac{\mu_t}{\rho D_t}\right)$; μ_t, turbulent viscosity; D_t, turbulent diffusivity; $D_{i,\ m}$, mass diffusion coefficient for species i; $D_{T,\ i}$, thermal diffusion coefficient.

Source term R_i can be computed by Eddy dissipation concept model

$$R_i = \frac{\rho(\varepsilon^*)^2}{\tau^*\left[1 - (\varepsilon^*)^3\right]} \left(Y_i^* - Y_i\right) \tag{3.9}$$

Length scale of fine fractions is computed as follows

$$\varepsilon^* = C_\varepsilon \left(\frac{v\varepsilon}{k^2}\right)^{1/4} \tag{3.10}$$

Over τ^* (time scale), species are supposed to react in fine structures. Reaction rates are specified by the Arrhenius rates and are integrated using ISAT algorithm [1, 14].

$$\varepsilon^* = C_\tau \left(\frac{v}{\varepsilon}\right)^{1/2} \tag{3.11}$$

C_ε, volume fraction constant (2.1377); C_τ, time scale constant (0.4082) [17, 18].

3.2.4 *RNG* k-ε *Turbulence Model*

Transport equations for the RNG k-ε model

Turbulence kinetic energy, k, and its dissipation rate, ε.

$$\frac{\partial}{\partial t}(\rho k) + \frac{\partial}{\partial x_i}(\rho k u_i) = \frac{\partial}{\partial x_j}\left(\alpha_k \mu_{\text{eff}} \frac{\partial k}{\partial x_j}\right) + G_k + G_b - \rho\varepsilon - Y_M + S_k \tag{3.12}$$

and

$$\frac{\partial}{\partial t}(\rho\varepsilon) + \frac{\partial}{\partial x_i}(\rho\varepsilon u_i) = \frac{\partial}{\partial x_j}\left(\alpha_\varepsilon \mu_{\text{eff}} \frac{\partial \varepsilon}{\partial x_j}\right) + C_{1\varepsilon}\frac{\varepsilon}{k}(G_k + C_{3\varepsilon}G_\text{b}) - C_{2\varepsilon}\rho\frac{\varepsilon^2}{k} - R_\varepsilon + S_\varepsilon \tag{3.13}$$

In these equations, G_k, generation of turbulence kinetic energy due to the mean velocity gradients; G_b, generation of turbulence kinetic energy due to the buoyancy; Y_M, contribution of the fluctuating dilatation in compressible turbulence to the overall dissipation rate; $C_{1\varepsilon}$, $C_{2\varepsilon}$ and $C_{3\varepsilon}$ are constants; α_k and α_ε are inverse effective Prandtl numbers for k and ε; S_k and S_ε are user-defined source terms. μ_{eff}, effective viscosity [13].

RNG k-ε model has an additional term in the ε equation which is

$$R_\varepsilon = \frac{C_\mu \rho \eta^3 (1 - \eta/\eta_0)}{1 + \beta\eta^3}\frac{\varepsilon^2}{k} \tag{3.14}$$

Where $\eta \equiv S_k/\varepsilon$, $\eta_0 = 4.38$, $\beta = 0.012$.

3.3 Boundary Conditions

Premixed hydrogen air mixture enters combustor through the inlet at ambient pressure and temperature. So, mass flow inlet boundary condition was employed at the combustor inlet. Mass flow rates were specified based on the thermal power, and mass fraction of each species was calculated depending on the equivalence ratio. At the outlet, pressure outlet boundary condition was chosen. Hydraulic diameter and turbulent intensity of the inlet and outlet are 3.2 mm and 5%, respectively. Taking radiation and convection heat transfer to the surrounding area into consideration, mixed thermal condition was chosen for all walls. Wall emissivity and convective heat transfer coefficient were set as 0.65 and 15 W/(m^2-K), respectively. Convergence criteria for all species, momentum, energy and continuity were set as 10^{-6}. Calculation methods of important modelling parameters are tabulated in Table 3.1.

3.4 Mesh Independency Study

To construct a mesh structure that includes minimum number of element for an accurate simulation and to reduce computational time and effort, a mesh independency study was carried out. For this purpose, five mesh structures with different number of elements (31,104, 90,640, 248,832 and 486,000 elements) were formed, and predicted centreline temperature profiles were compared (Fig. 3.2). To save computational time and effort, mesh structure with 248,832 elements was chosen.

Table 3.1 Calculation methods of important modelling parameters [19]

Parameters	Methods
Discretisation	Second-order upwind
Mixture physical properties	Density: incompressible ideal gas law Specific heat: mixing law Thermal conductivity: mass-weighted mixing law Viscosity: mass-weighted mixing law Mass diffusivity: kinetic theory
Species physical properties	Specific heat: piecewise of polynomial fitting of temperature Thermal conductivity: kinetic theory Viscosity: kinetic theory

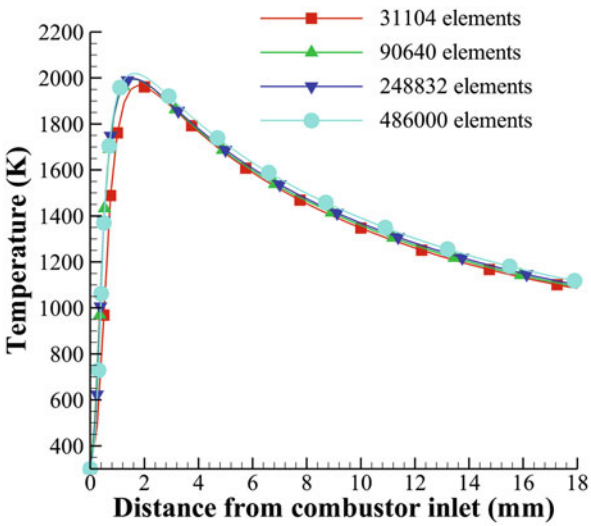

Fig. 3.2 Mesh independency study

3.5 Model Validation

In order to check out availability of the combustor model, data obtained from experimental and numerical studies of Ref. [2] was used. Temperature distribution profiles at outer wall centreline of the micro combustor showed a good agreement with published data by means of trend and value. Results of this study are illustrated in Fig. 3.3. At 900 ml/min hydrogen flux, our model predicts nearly the same temperature values with the experimental study at the points which are 2 and 16 mm away from combustor inlet. At 600 ml/min hydrogen flux, predicted and experimental values are very close at a position near combustor inlet, but towards the outlet of the combustor, predicted values differ from the experimental values.

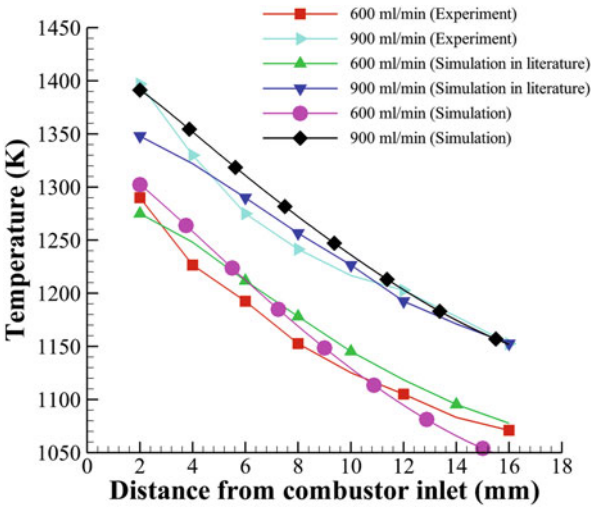

Fig. 3.3 Validation of numerical model

3.6 Results and Discussions

Wall temperature distribution of micro combustors can highly effect the amount of electrical power generated by MTPV systems. The most effective and immediate way of providing high power output is increasing wall temperature [8, 20]. Improving heat transfer characteristics can also enhance the performance of MTPV systems. In Fig. 3.4, outer wall temperature distributions at different equivalence ratios and hydrogen fluxes can be seen. Irrespective of thermal power of the combustor, highest temperature distributions are at stoichiometric conditions, and wall temperature distributions show an agreement in terms of trend at 1.0 and 1.2 equivalence ratios. With excess air, trend of wall temperature profile differs. At the inlet of the combustor, temperature values at 1200 ml/min, 900 ml/min and 600 ml/min hydrogen fluxes ($\phi = 0.8$) are very close to stoichiometric conditions, but towards the outlet of the combustor, some discrepancies become apparent in terms of trend and value. At 300 ml/min hydrogen flux, wall temperature distributions at 1.0 and 0.8 equivalence ratios have the best agreement.

When we examine temperature contours at centreline plane of the combustor at 300 ml/min hydrogen flux for 0.8 and 1.0 equivalence ratios (Fig. 3.5), it can be seen that flame shapes are different. At 0.8 equivalence ratio, flame front moves backward and becomes sharper, but reaction zone distributions do not change much. Predicted maximum temperature values are 1873 K and 1996 K at 0.8 and 1.0 equivalence ratios, respectively, but mean temperature value at the outer wall of the combustor is 1065 K at both equivalence ratios. Because wall temperature distributions have nearly the same uniformity, outer wall mean temperature values are the same, and reaction zone distributions do not change much at both equivalence ratios; this agreement makes sense.

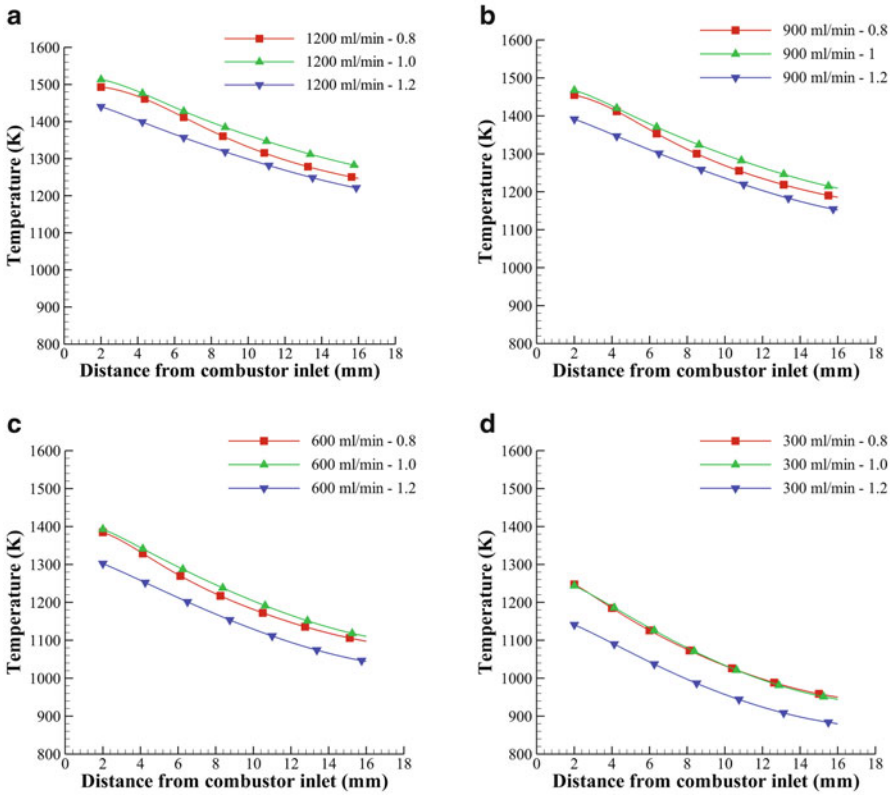

Fig. 3.4 Temperature distributions at the centreline of the outer wall of the combustor. Combustor thermal powers: (**a**) 200 W, (**b**) 150 W, (**c**) 100 W, (**d**) 50 W

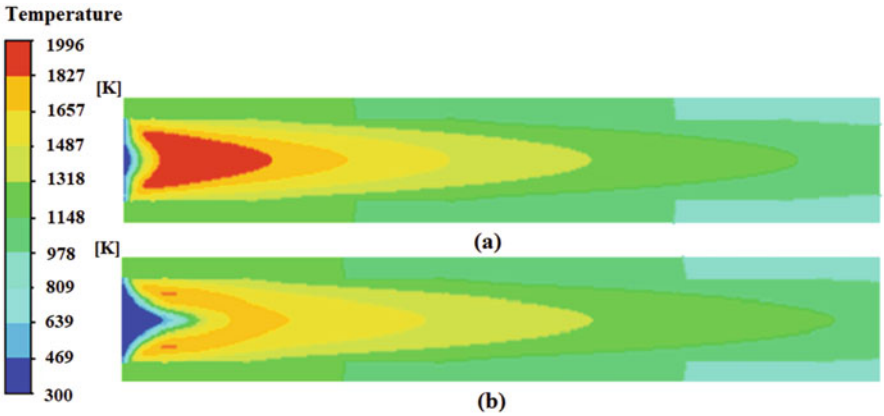

Fig. 3.5 Temperature contours at the centreline plane of the combustor. (**a**: $\phi = 1.0$, **b**: $\phi = 0.8$)

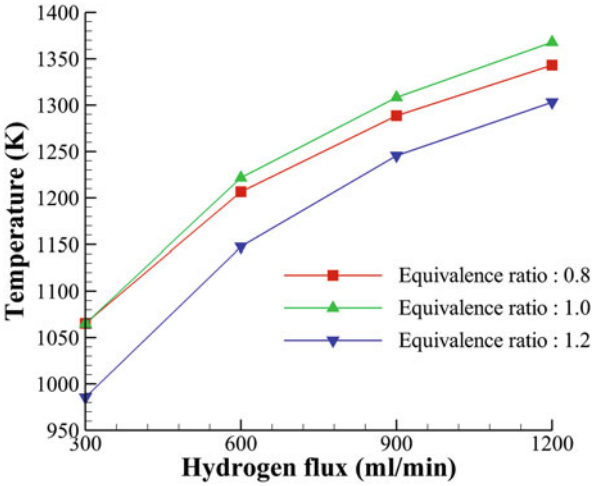

Fig. 3.6 Change of outer wall mean temperature value with thermal power and equivalence ratio

With respect to heat transfer principles, the driving force of the heat transfer is flame, or mixture temperature and the amount of heat transferred effects outer wall temperature distribution of a combustion device. Temperature increment improves the conversion rate of chemical energy to utilisable radiation energy. But, temperature resistance of the combustor material limits this temperature increment. Uniformity of temperature distribution is also very important by means of reducing thermal stresses on material surface and increasing service life of the combustor [2].

In Fig. 3.6, change of outer wall mean temperature value with thermal power and equivalence ratio can be seen. The highest mean temperature value is at 1200 ml/min hydrogen flux which provides 200 W thermal power, and at stoichiometric conditions. As the thermal power reduces and equivalence ratio increases, outer wall mean temperature value reduces. At 0.8 and 1.0 equivalence ratios, outer wall mean temperature values are very close. By examining temperature contours at outer wall of the combustor, it is founded that the most uniform temperature distribution is at 1200 ml/min hydrogen flux and 1.2 equivalence ratio. As the equivalence ratio and hydrogen flux reduce, this uniformity diminishes.

Outer wall mean temperature value must be higher than 1200 K to meet basic operating necessity of MPTV systems. Because radiant energy needed for MPTV systems is highly related to outer wall mean temperature value [19]. At 300 ml/min hydrogen flux, outer wall mean temperature value is less than 1200 K for all equivalence ratios tested (Fig. 3.6). On the other hand, basic operating necessity can be barely met at 600 ml/min hydrogen flux. So, for an effective operation, hydrogen flux for this combustor must be higher than 600 ml/min. With respect to outer wall mean temperature value and uniformity of temperature distribution, this combustor must operate at 1.0 equivalence ratio and 1200 ml/min hydrogen flux.

For micro combustors, key issues are to obtain steady combustion, uniform outer wall temperature distribution and high radiant energy output [19]. In Fig. 3.7,

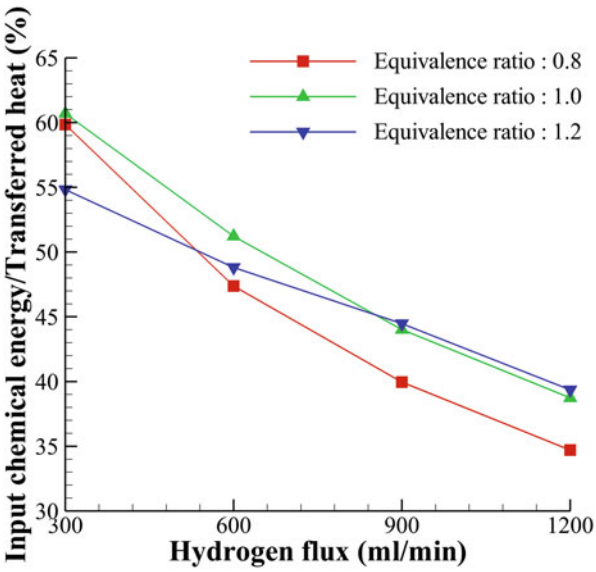

Fig. 3.7 Conversion rate of input chemical energy to total transferred heat at different equivalence ratios

conversion rate of input chemical energy to total transferred heat (in percentage) at different equivalence ratios and hydrogen fluxes can be seen. Maximum conversion ratio can be achieved at 1.0 equivalence ratio and 300 ml/min hydrogen flux. As the hydrogen flux increases, conversion ratio decreases. With less air, conversation ratio is better at high hydrogen fluxes, but incomplete combustion will reduce the efficiency of the micro combustor. With only regard to conversion ratio of input chemical energy to total heat transfer, optimal operating conditions for this combustor are 1.0 equivalence ratio and 600–900 ml/min hydrogen flux.

In Fig. 3.8, temperature profiles along the centreline of the combustor at different hydrogen fluxes and equivalence ratios can be seen. Because of the high burning rate of hydrogen, chemical reactions take place in a short distance near combustor inlet. As the hydrogen flux increases, the place where maximum temperature occurs moves away from combustor inlet, and maximum temperature gets a higher value. Transition from minimum temperature to maximum temperature actualizes nearly 5 mm away from the combustor inlet in the worst case, and then temperature values along the combustor reduce because of the heat losses to the environment and heat absorption of combustor walls. As the hydrogen flux increases, temperature decrement declines, and temperature distribution along the centreline of the combustor becomes more uniform. At 0.8 equivalence ratio, maximum temperature values are 1686 and 1773 K at 300 and 1200 ml/min hydrogen fluxes, respectively. Although the difference between peak temperature values is 89 K, outer wall mean temperature value is 300 K higher at 1200 ml/min hydrogen flux. At 1.0 equivalence ratio, maximum temperature values are 1996 and 2086 K at 300 and 1200 ml/min hydrogen fluxes, respectively. The differences between maximum temperature values and outer wall mean temperature values are 90 K and 300 K in return,

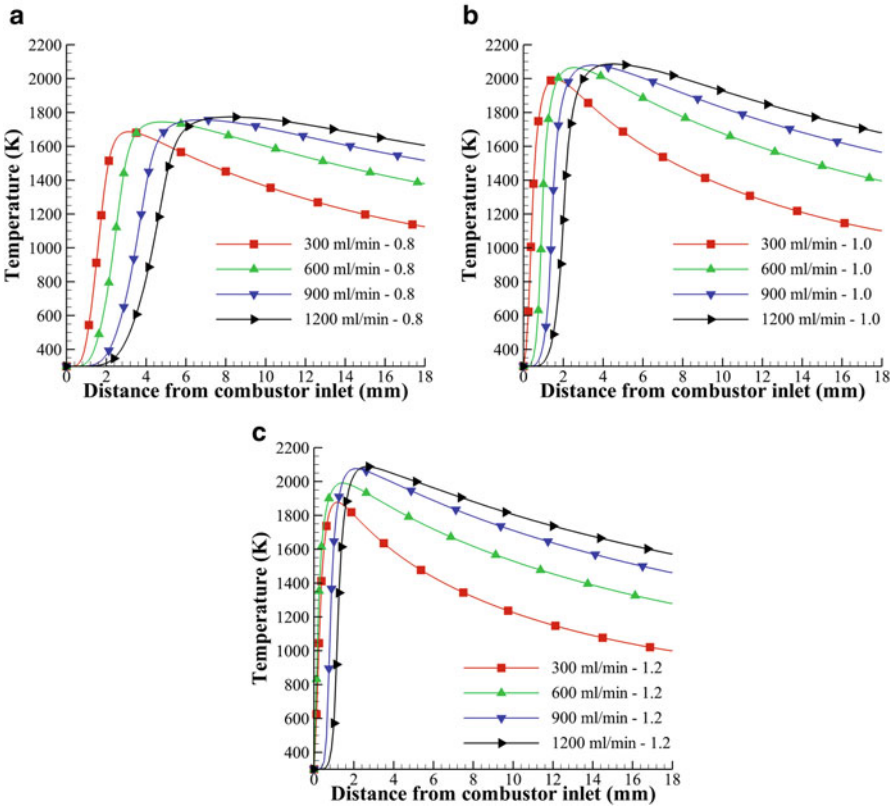

Fig. 3.8 Temperature distributions along the centreline of the combustor. Equivalence ratios: (**a**) 0.8, (**b**) 1.0, (**c**) 1.2

respectively. At 1.2 equivalence ratio, reaction takes place in a very short distance from combustor inlet, but temperature decrement along the flow direction is a lot. Because outer wall mean temperature values are nearly the same at 0.8 and 1.0 equivalence ratios (1343 K and 1367 K), and temperature distribution is more uniform at 0.8 equivalence ratio, optimal operating conditions for this combustor are 0.8 equivalence ratio and 1200 ml/min hydrogen flux.

In Fig. 3.9, NO_x formation profiles along the centreline of the combustor can be seen. As the hydrogen flux and equivalence ratio increase, depending on the temperature increment, the amount of NO_x formed and peak NO_x values increase. At 900 ml/min hydrogen flux, NO_x quantity emanated from the exhaust of the combustor and peak NO_x value are higher than the case in which hydrogen flux is 1200 ml/min. This maybe because of the reversible reactions. NO formed in one reaction can be destroyed in another reaction. With only respect to NO_xemissions, this combustor should operate at 0.8 equivalence ratio and 300 ml/min hydrogen flux.

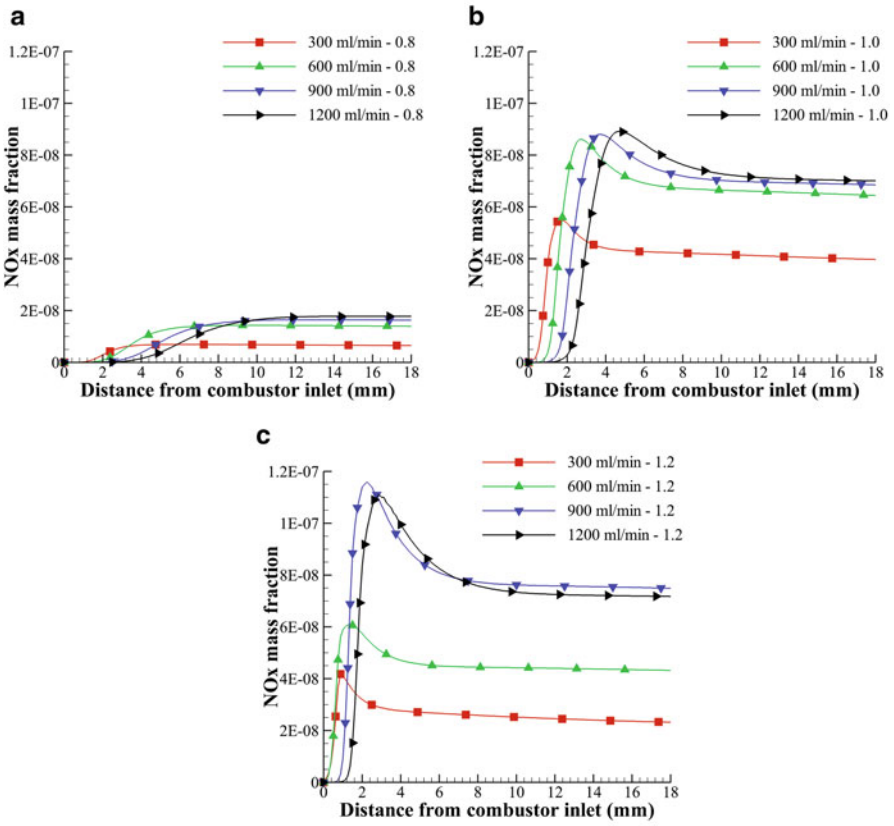

Fig. 3.9 NO_x formation along the centreline of the combustor. Equivalence ratios: (**a**) 0.8, (**b**) 1.0, (**c**) 1.2

3.7 Conclusions

In this study, effects of thermal power and equivalence ratio on combustion and emission behaviour of premixed hydrogen air mixtures were numerically investigated with respect to key issues which are vital for micro combustors. These issues are uniform temperature distribution, maximum temperature increase at the outer wall of the combustor, outer wall mean temperature value, conversion ratio of input chemical energy to total transferred heat and NO_xemissions.

Size limitation of micro combustors makes combustion process in such devices relatively less efficient because of the short flame residence time, destructive radical-wall interactions and intensified heat loss [7]. Even with low energy conversion efficiency, micro combustors can still provide higher energy than chemical batteries. So, combustion efficiency was excluded while deciding optimal operating condition.

Taking all of these issues into consideration, optimal working conditions for this micro combustor are 0.8 equivalence ratio and 1200 ml/min hydrogen flux.

Acknowledgement We would like to thank the Scientific and Technological Research Council of Turkey (TÜBİTAK-MAG-215 M821) for its financial support.

References

1. Yilmaz H, Cam O, Tangoz S, Yilmaz I (2017) Effect of different turbulence models on combustion and emission characteristics of hydrogen/air flames. Int J Hydrog Energy 42 (40):25744–25755
2. Tang A, Pan J, Yang W, Xu Y, Hou Z (2015) Numerical study of premixed hydrogen/air combustion in a micro planar combustor with parallel separating plates. Int J Hydrog Energy 40 (5):2396–2403
3. Zarvandi J, Tabejamaat S, Baigmohammadi M (2012) Numerical study of the effects of heat transfer methods on CH4/(CH_4+ H_2)-AIR pre-mixed flames in a micro-stepped tube. Energy 44 (1):396–409
4. Jiaqiang E, Peng Q, Zhao X, Zuo W, Zhang Z, Pham M (2017) Numerical investigation on the combustion characteristics of non-premixed hydrogen-air in a novel micro-combustor. Appl Therm Eng 110:665–677
5. Lei Y, Chen W, Lei J (2016) Combustion and direct energy conversion inside a micro-combustor. Appl Therm Eng 100:348–355
6. Fernandez-Pello AC (2002) Micropower generation using combustion: issues and approaches. Proc Combust Inst 29(1):883–899
7. Li J, Chou SK, Yang WM, Li ZW (2009) A numerical study on premixed micro-combustion of CH_4–air mixture: effects of combustor size, geometry and boundary conditions on flame temperature. Chem Eng J 150(1):213–222
8. Pan JF, Yang WM, Tang AK, Chou SK, Duan L, Li XC, Xue H (2010) Micro combustion in sub-millimeter channels for novel modular thermophotovoltaic power generators. J Micromech Microeng 20(12):125021
9. Su Y, Cheng Q, Song J, Si M (2016) Numerical study on a multiple-channel micro combustor for a micro-thermophotovoltaic system. Energy Convers Manag 120:197–205
10. Tang A, Xu Y, Shan C, Pan J, Liu Y (2015) A comparative study on combustion characteristics of methane, propane and hydrogen fuels in a micro-combustor. Int J Hydrog Energy 40 (46):16587–16596
11. Sakurai T, Yuasa S, Ono Y, Honda T (2013) Flame stability and emission characteristics of propane-fueled flat-flame miniature combustor for ultra-micro gas turbines. Combust Flame 160(11):2497–2506
12. Raimondeau S, Norton D, Vlachos DG, Masel RI (2002) Modeling of high-temperature microburners. Proc Combust Inst 29(1):901–907
13. Fluent Incorporated (2013) ANSYS fluent theory guide, version 15.0. Inc, Canonsburg, PA
14. Markatou P, Pfefferle LD, Smooke MD (1991) The influence of surface chemistry on the development of minor species profiles in the premixed boundary layer combustion of an H_2/air mixture. Combust Sci Technol 79(4–6):247–268
15. Norton DG, Vlachos DG (2003) Combustion characteristics and flame stability at the micro-scale: a CFD study of premixed methane/air mixtures. Chem Eng Sci 58(21):4871–4882
16. Jiaqiang E, Peng Q, Liu X, Zuo W, Zhao X, Liu H (2016) Numerical investigation on hydrogen/air non-premixed combustion in a three-dimensional micro combustor. Energy Convers Manag 124:427–438

17. Mazaheri K, Shakeri A (2016) Numerical optimization of laboratory combustor geometry for NO suppression. Appl Therm Eng 102:1328–1336
18. Habib MA, Mokheimer EM, Sanusi SY, Nemitallah MA (2014) Numerical investigations of combustion and emissions of syngas as compared to methane in a 200MW package boiler. Energy Convers Manag 83:296–305
19. Tang A, Xu Y, Pan J, Yang W, Jiang D, Lu Q (2015) Combustion characteristics and performance evaluation of premixed methane/air with hydrogen addition in a micro-planar combustor. Chem Eng Sci 131:235–242
20. Yang WM, Chou SK, Pan JF, Li J, Zhao X (2010) Comparison of cylindrical and modular micro combustor radiators for micro-TPV system application. J Micromech Microeng 20(8):085003

Chapter 4
Reducing Urban Heat Islands by Developing Cool Pavements

Muhammet Vefa Akpınar and Sedat Sevin

4.1 Introduction

The urban heat island (UHI) effect is commonly observed in urban environments, where the average temperature of cities is higher than that of surrounding rural areas [1–3]. One of the factors that lead to the development of a UHI is the higher thermal energy storage of paving materials [4]. In many city centers, pavements represent the largest percentage of a community's land cover, compared with roof and vegetated surfaces. Asphalt-paved areas, which can store much of the sun's energy contributing to the urban heat island effect, account for nearly 40% of land cover [5–7].

Pavements (roads, parking area, etc.) are one of the main factors contribute highly to the development of heat island [8, 9]. Paved surfaces (such as highways, roads, runways, parking areas, and driveways) typically constitute about 40% of developed urban areas. Conventional pavements are impervious and their surfaces can transfer heat downward to be stored in the pavement subsurface. This effect contributes to urban heat islands (especially at night time). The pavement surface temperature can reach peak summertime surface temperatures of 60 °C [10–12].

Albedo (solar reflectance) is the ratio of reflected solar radiation to the total amount that falls on that surface. Albedo values range from 0, for perfect absorbers, to 1, for perfect reflectors. In pavement structures, the surface is the only layer which affects albedo. Therefore, pavement type selection should also include a consideration of albedo where heat generation is a concern [13].

M. V. Akpınar (✉)
Karadeniz Teknik Üniversitesi, Civil Engineering Department, Trabzon 61080, Turkey
e-mail: mvakpinar@ktu.edu.tr

S. Sevin
Gümüşhane Üniversitesi, Civil Engineering, Gümüşhane, Turkey

S. Nižetić, A. Papadopoulos (eds.), *The Role of Exergy in Energy and the Environment*, Green Energy and Technology,
https://doi.org/10.1007/978-3-319-89845-2_4

Highly reflective materials can reduce the temperature of urban surfaces like roofs and pavements by reflecting solar radiation away from these surfaces [14–16]. Although the reduction in surface temperature of high-albedo roofs has been documented to reduce summertime building cooling energy requirements, no similar effect has been documented with regard to high-albedo pavements. Well-publicized simulations by Lawrence Berkeley National Laboratory and others infer that hundreds of billions of dollars in savings due to reduced cooling energy demands can be realized through the deployment of reflective pavements [17].

The objective of this study was to determine if the cool pavements can reduce the heat island's harmful environmental effects and ambient temperatures. High-reflectance material may show a positive effect on surface temperature and thermal gradient. The proposed study will help pavement to store less heat and may have lower surface temperatures compared with the conventional pavement. They can help address the problem of urban heat islands, which result in part from the increased temperatures of paved surfaces in a city or suburb.

4.2 Material and Method

For the albedo experimental measurements, three different pavement surface areas were selected for asphalt pavement (AP), concrete pavement (CP), and concrete painted with highly reflected pavement (HRP) as shown in Fig. 4.1. In order to obtain HRP, solvent-based and reflector-based gray spray paint used in automobile

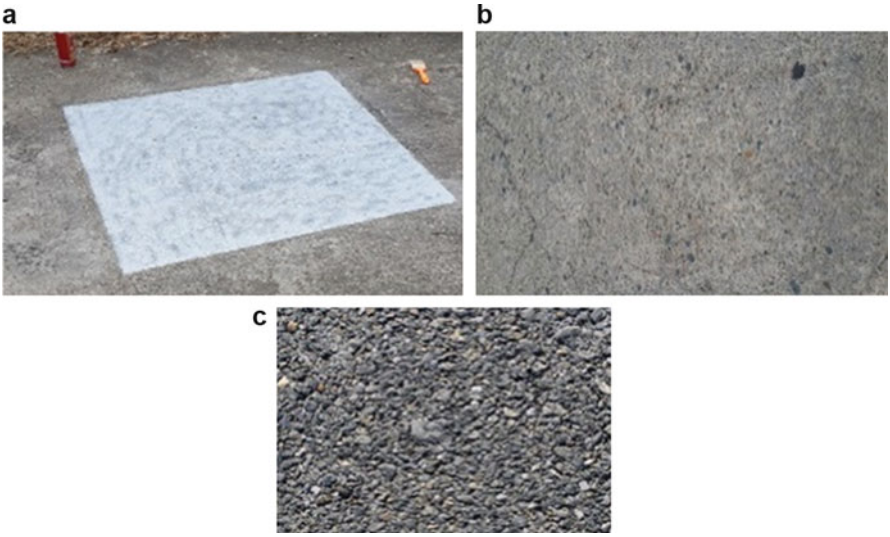

Fig. 4.1 (**a**) High-reflective paved concrete pavement, (**b**) concrete pavement, and (**c**) asphalt pavement

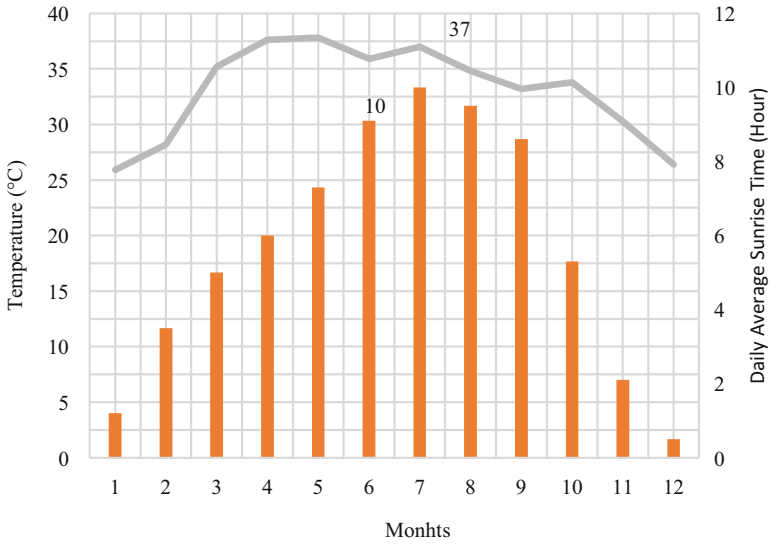

Fig. 4.2 Monthly maximum temperature and the average daily sunlight hours in Trabzon [18]

pavement industry was used. Since the concrete sample surface was painted, it was assumed that the paint will function as an impermeable layer. No further hydraulic permeability tests were conducted. Friction coefficient tests were not the main objective of this study.

In order to better understand the albedo effect on the surface temperature and the temperature distribution, it was decided to carry out the measurements in July, taking into consideration the average daily sunshine periods and the monthly maximum temperature values of the region from 1950 to 2015 belonging to the General Directorate of Meteorology. As shown in Fig. 4.2, the daily sunshine duration has reached its maximum annual value in 10 h in July.

This study was performed with a single-headed pyranometer in the form of albedo measurements in accordance with ASTM E1918 [19]. The CMA6 parameter provides solar reflectance (W/m^2) of the surfaces 50 cm above the area to be measured, as specified in the standard. For efficient albedo measurements, sunny weather was preferred.

In order to be able to measure the temperature through pavement thickness, a total of eight holes were drilled in the painted and unpainted areas at depths of 2.5–5–7.5–10 cm from the pavement surface. Temperature sensors were positioned inside the holes and later the holes were sealed with an insulating material. Measurements were taken between 15:00 and 16:00 in the afternoon, which was the hottest time of the day.

4.3 Result and Discussion

The 30-day albedo measurements taken on the pavements in Karadeniz Technical University campus are given in Table 4.1. According to the obtained results, the albedo (solar reflectance index) of HRP was measured higher than the other two pavement types. The measured mean 30-day albedo value of HRP, CP, and AP were 0.30, 0.15, and 0.06, respectively. Considering the albedo effects, HRP was two and five times higher than CP and AP, respectively. In the literature, the albedo value for concrete pavement varies between 0.25 and 0.35 [20]. However, since the concrete pavements in the campus area are old, they have lost their superficial characteristics over time. Therefore, lower values were obtained in experimental albedo

Table 4.1 Albedo values of pavements for 30 days

	Albedo values of pavement		
Day	HRP	CP	AP
1	0.24	0.13	0.05
2	0.25	0.14	0.06
3	0.25	0.14	0.05
4	0.24	0.13	0.06
5	0.23	0.13	0.06
6	0.28	0.17	0.07
7	0.28	0.17	0.09
8	0.29	0.16	0.09
9	0.29	0.17	0.09
10	0.29	0.16	0.09
11	0.27	0.15	0.06
12	0.22	0.14	0.05
13	0.23	0.16	0.05
14	0.25	0.15	0.07
15	0.25	0.14	0.05
16	0.30	0.20	0.06
17	0.33	0.21	0.08
18	0.30	0.20	0.08
19	0.32	0.15	0.09
20	0.30	0.16	0.09
21	0.26	0.13	0.05
22	0.29	0.14	0.07
23	0.28	0.14	0.05
24	0.29	0.13	0.05
25	0.26	0.13	0.07
26	0.30	0.17	0.07
27	0.34	0.22	0.09
28	0.34	0.16	0.09
29	0.33	0.17	0.07
30	0.30	0.16	0.06

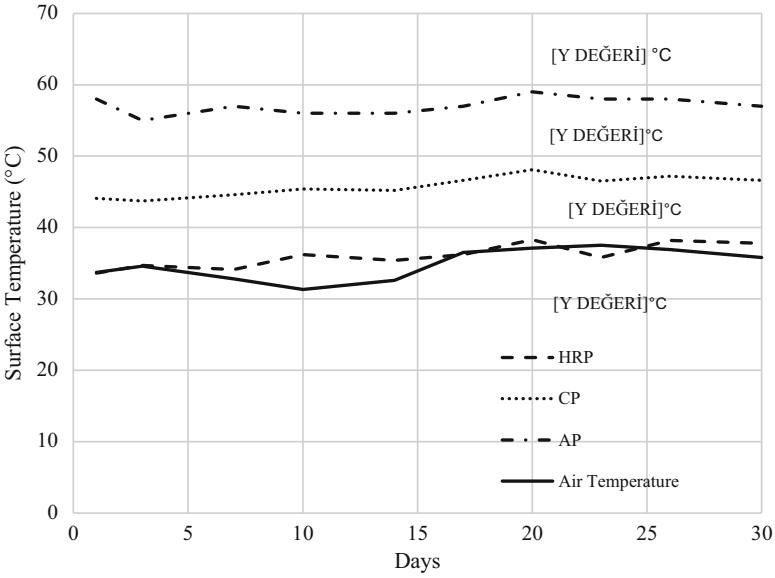

Fig. 4.3 The surface temperature of pavements

measurements than the standard. Similarly, 0.05–0.015 values were observed in the literature for albedo measurements on asphalt pavements [13]. In order to obtain HRP, solvent-based and reflector-based gray spray paint used in automobile pavement industry was used. The reflective nature of the paint increased the albedo values by 100%, compared to a concrete pavement with the same surface.

International environmental rating agency Leadership in Energy and Environmental Design (LEED) defines surface areas as "cool pavement" greater than 0.29 in albedo value. Accordingly, the CP (0.15) and the AP's (0.09) albedos fall into the nonreflective material group. The HRP pavement is in the reflective material group with a value of 0.30 albedo.

The average 30-day maximum air temperature during the experimental measurements was 34.8 °C. As can be seen, HRP and daily maximum temperature values were close to each other for 30 days. The surface temperature of HRP was the lowest due to its high surface reflectivity. As shown in Fig. 4.3, HRP surface temperature was 38.3 ° C on the 20th day which was lower than the other two pavement surface temperatures. Berg and Quinn [15] reported that in midsummer, white painted roads with an albedo close to 0.55 have almost the same temperature with the ambient environment, while unpainted roads with albedo close to 0.15 were approximately 11 °C warmer than the air. During the experimental run, the maximum surface temperature was observed at AP of 59 ° C. Santamouris [16] reported asphalt temperatures close to 63 °C and white topping pavements close to 45 °C. The main reason for this is that the asphaltic albedo is too low and the heat absorption capacity is high. Asaeda et al. [14] have reported the impact of various pavement materials used commonly in urban environments during the summer period. They

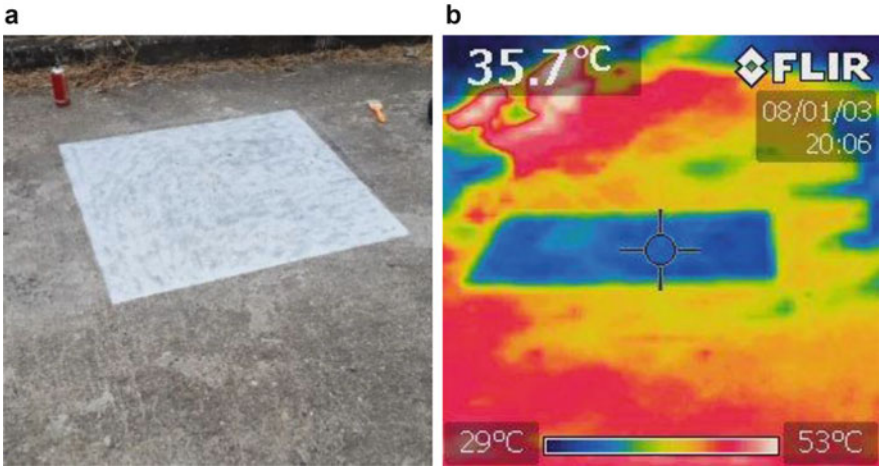

Fig. 4.4 (**a**) HRP view and (**b**) thermal camera view

found that the surface temperature, heat storage, and its subsequent emission to the atmosphere were significantly higher for asphalt than for concrete and soil.

In the observations made with the thermal camera, HRP and CP fields are shown in Fig. 4.4. As can be seen in Fig. 4.4b, the painted area appears at a lower temperature than the concrete coverage. As a result of the 30-day measurements, the maximum surface temperature of the CP and HRP surface were 43.7–48.1 ° C (average 45.8 °C) and 33–38.1 ° C (mean 36 °C), respectively.

Temperature variation through the thickness is shown in Fig. 4.5. Consequent 5-day measurements on CP are shown with A1, and consequent 5-day measurements on HRP are shown with A2. HRP and CP were the same concrete pavement with 10 cm thickness. The temperature difference between surface and bottom of the HRP layer was measured as 6 °C (ΔT2). For CP it was 12 °C (ΔT1). The temperature at the bottom (10 cm below) of CP and HRP were about 37 °C and 32 °C, respectively. The difference was due to the albedo effect.

4.4 Conclusion

In this study, surface temperatures and albedo values of three different pavement types were investigated. It was concluded that the lowest surface temperature and higher solar albedo values were measured in HRP pavement. Considering the albedo effects, HRP was two and five times higher than CP and AP, respectively. In conclusion, the street pavements should be painted with highly reflected paints which can prevent the solar reflection as a result the heat island effect significantly.

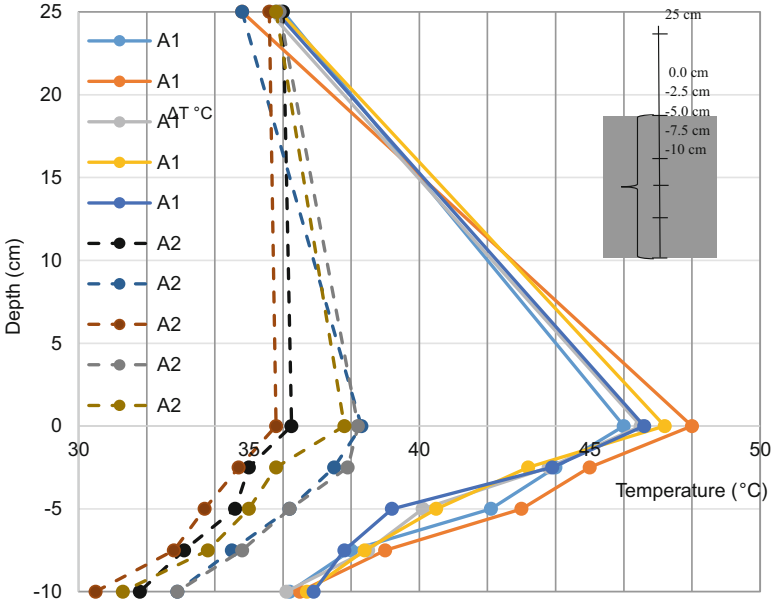

Fig. 4.5 Temperature variation through thickness

References

1. Kataoka K, Matsumoto F, Ichinose T, Taniguchi M (2009) Urban warming trends in several large Asian cities over the last 100? years. Sci Total Environ 407(9):3112–3119
2. Santamouris M (2007) Heat Island research in Europe: the state of the art. Adv Build Energy Res 1(1):123–150
3. Salleh SA, Latif ZA, Mohd WMNW, Chan A (2013) Factors contributing to the formation of an urban Heat Island in Putrajaya, Malaysia. Procedia Soc Behav Sci 105:840–850
4. Kleerekoper L, van Esch M, Salcedo TB (2012) How to make a city climate-proof, addressing the urban heat island effect. Resour Conserv Recycl 64:30–38. Aggarwal, R, USA
5. Guhathakurta S, Grossman-Clarke S, Lathey V (2012) How do variations in urban Heat Islands in space and time influence household water use? The case of Phoenix, Arizona. Water Resour Res 48(6):1–13
6. Sen S, Roesler J (2015) Assessment of concrete pavement structure on urban heat island. Department of Civil and Environmental Engineering, University of Illinois at Urbana-Champaign
7. Taha H, Akbari H, Rosenfeld A, Huang J (1988) Residential cooling loads and the urban Heat Island the effects of albedo. Build Environ 23:271–283
8. Synnefa A, Karlessi T, Gaitani N, Santamouris M, Assimakopoulos DN, Papakatsikas C (2011) Experimental testing of cool colored thin layer asphalt and estimation of its potential to improve the urban microclimate. Build Environ 46(1):38–44
9. Haselbach L, Boyer M, Kevern JT, Schaefer VR (2011) Cyclic Heat Island impacts on traditional versus pervious concrete pavement systems. Transp Res Rec J Transp Res Board 2240(1):107–115
10. Akbari H, Rose LS (2001) Characterizing the fabric of the urban environment: a case study of metropolitan Chicago, Illinois. Calif, Berkeley

11. Akbari H, Pomerantz M, Taha H (2001) Cool surfaces and shade trees to reduce energy use and improve air quality in urban areas. Sol Energy 70(3):295–310
12. Rose LS, Akbari H, Taha H (2003) Characterizing the fabric of the urban environment: a case study of greater Houston, Texas. Lawrence Berkeley National Laboratory, Berkeley
13. ACPA (2002, June) Concrete Pavement Research & Technology. Retrieved from Albedo: a measure of pavement surface reflectance
14. Asaeda T, Ca VT, Wake A (1996) Heat storage of pavement and its effect on the lower atmosphere. Atmos Environ 30(3):413–427
15. Berg R, Quinn W (1978) Use of light colored surface to reduce seasonal thaw penetration beneath embankments on permafrost
16. Santamouris M (ed) (2001) Energy and climate in the urban built environment. James and James Science Publishers, London
17. Li H (2012) Evaluation of cool pavement strategies for heat island mitigation. PhD dissertation, University of California, Davis
18. MGM (2016) https://www.mgm.gov.tr/veridegerlendirme/il-ve-ilceler-istatistik.aspx?m=TRABZON
19. ASTM (2006) ASTM E1918-06 standard test method for measuring the solar reflectance of horizontal and low-sloped surfaces in the field. American Society for Testing and Materials, USA
20. Akbari H, Levinson R (2007) Status of cool roofs standards in the United States. In: 2nd PALENC conference and 28th AIVC conference on building low energy cooling and advanced ventilation technologies in the 21st century, Crete island, Greece

Chapter 5
Urban Heat Island Effects of Concrete Road and Asphalt Pavement Roads

Muhammet Vefa Akpınar and Sedat Sevin

5.1 Introduction

In general, the asphalt pavement produces distinctly little noise, it is relatively low cost in comparison to different materials, and it is relatively easy to repair. However, asphalt is known to be significantly less long-lasting than most other choices and is not the best for the environment either. Concrete is another popular material choice for roadways. There are two essential kinds of concrete street surfaces, jointed reinforced concrete pavement (JRCP) and continuously reinforced concrete pavement (CRCP). Concrete is more long-lasting than asphalt and appreciably stronger built and quite highly priced to lay [1, 2].

The color of the pavement surfaces is open to choice and it affects the temperatures within the city. The effect of color is understandable because if a surface is dark, it means it has absorbed the visible light. This warms the surface, which eventually warms the air. The most practical means of mitigating the urban heat island, UHI, is to make urban surfaces brighter, by which we mean more reflective of the sunlight [3, 4].

The thermal performance of a pavement is defined as the change in its temperature (most often surface temperature) over time as influenced by properties of the paving materials (e.g., albedo, thermal emittance, thermal conductivity, specific heat, and surface convection) and by ambient environmental conditions (sunlight, wind, air temperature).

M. V. Akpınar (✉)
Karadeniz Teknik Üniversitesi, Civil Engineering Department, Trabzon 61080, Turkey
e-mail: mvakpinar@ktu.edu.tr

S. Sevin
Gümüşhane Üniversitesi, Civil Engineering, Gümüşhane, Turkey

S. Nižetić, A. Papadopoulos (eds.), *The Role of Exergy in Energy and the Environment*, Green Energy and Technology,
https://doi.org/10.1007/978-3-319-89845-2_5

Although urban heat islands (UHIs) are most often thought of as existing in the atmosphere above the city, they actually exist at many different levels, including at the ground/pavement surface, in the air just above the surface (near-surface), and in the ambient air temperatures well above street level, as well as in the atmosphere above the city. In many cases, it is convenient to consider near-surface heat islands, which are characterized by increased ambient air temperature just above the pavement surface, typically at 1–2 m where human outdoor activities occur [5]. Surface and near-surface heat islands can potentially affect human thermal comfort, air quality, and energy use of buildings and vehicles.

Atmospheric warmth islands can have an effect on groups through increasing summertime top electricity, air conditioning prices, air pollutants and GHG emissions, warmth-associated illness and demise, and water satisfactory [6–11].

The objective of this chapter is to evaluate the variation of heat flux from different road surface materials with contrasting thermal properties. Since the temperature of urban or regional-scale areas is directly dependent upon land use and material properties, this study would provide useful information for simulating urban and regional mixed layer dynamics in boundary layer models [12, 13].

5.2 Method

Paved surfaces contribute considerably to the temperature of cities because they cover a remarkably large fraction of urban surfaces. Detailed examination of Trabzon city shows that 45% of the area seen from above the tree canopy was paved (including roads, parking areas, sidewalks). Using the AutoCAD program, the road area within this built-up city is about 45%. There are considerable additional areas of paved driveways, sidewalks, and parking areas at homes and businesses. Our earlier work focused on asphalt pavement because it is the preponderant paving material for urban streets, by a ratio of about 20 to 1.

In order to better understand the variation of the heat flux on the surface temperature and the temperature distribution, it was decided to carry out the measurement in July, taking into consideration the average daily sunshine periods and the monthly maximum temperature values of the region from 1950 to 2015 belonging to the General Directorate of Meteorology. This is mainly due to the highest sunshine duration in July, and it is estimated that the albedo values and effect will be observed more efficiently and that the surface temperature will rise to the maximum level since the daily temperature value in the same month is 37 ° C and the second highest month in the year. As shown in Fig. 5.1, the daily sunshine duration has reached its maximum annual value in 10 h in July.

An intersection of concrete and asphalt pavement in Karadeniz Technical University campus was selected. The intersection had 7 m trees on one side of the intersection where the air temperature was lower (Fig. 5.2). With pavement albedo values around 0.10, extremely high pavement surface temperatures of 45–50 °C have been measured on hot summer days in mid-afternoon in the city of Trabzon,

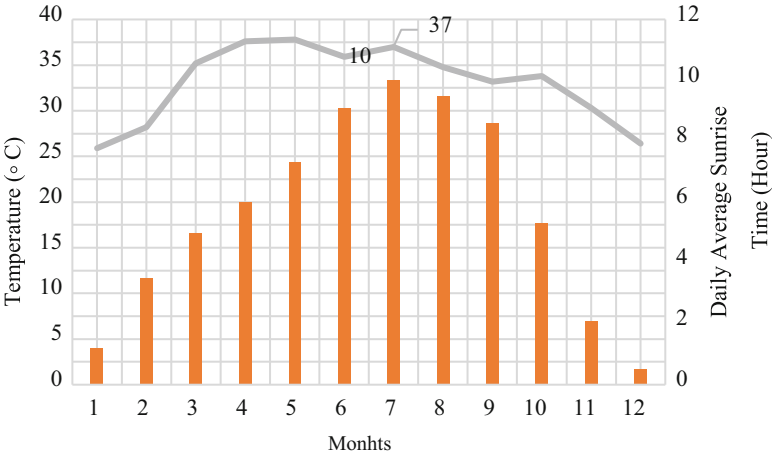

Fig. 5.1 Monthly maximum temperature values and daily average solar times during 1-year period in Trabzon

Turkey. Ambient air temperatures were collected at 1.5 m above the surface. Surface temperature sensors were placed directly on the asphalt or concrete surface and covered with a thin layer of asphalt or cement mortar to achieve a good contact.

5.3 Result and Discussion

Subsurface temperature measurements were obtained from a network of platinum thermocouple probes embedded in the pavement structure at various depths (Fig. 5.3). After the pavement was drilled, the thermocouples were inserted and later the holes were filled and closed with synthetic material to prevent air entering the whole. To assure good contact between temperature probes and pavement materials, probes were first placed at the required level of 0, 5, 10, 15, 20, and 25 cm and then repacked with silicon road materials. Subsurface temperature measurements were obtained to a depth of 25 cm beneath the concrete pavement and 0.25 cm beneath the asphalt pavement.

Figure 5.4 shows that the temperatures in the asphalt pavement exponentially drop through the thickness then becomes constant at 5 cm depth to the bottom. Figure 5.5 shows concrete pavement temperature variation with the street with no trees open to sunlight and with trees. Similar trends were observed as of asphalt pavement except that the drop in the temperature becomes stabilized at 2.5 cm depth. From Figs. 5.4 and 5.5, it can be said that increasing tree cover on both sides of the pavements lowers surface temperatures by providing shade and cooling through evapotranspiration. The standard deviation of the surface temperature was lower in

Fig. 5.2 Photo image of the university campus and asphalt concrete pavements where the works were taken

concrete pavement. It is clear that pavement covered with trees had much lower surface temperatures on both pavement types.

5.3.1 Comparison of Outgoing Radiation

The heat flux at the maximum surface temperatures of the asphalt and concrete coatings in the study was calculated with the aid of Eq. (5.1). The earth's surface is assumed to emit longwave radiation as a blackbody. Thus, the outgoing longwave radiation follows the Stefan-Boltzmann law [14].

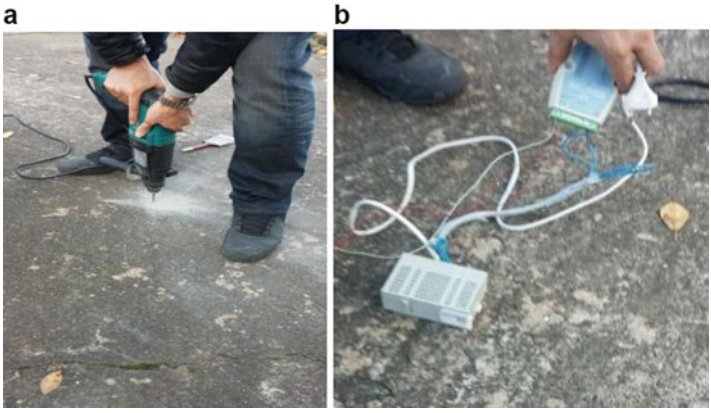

Fig. 5.3 Thermocouple installation on pavement. (**a**) Drilling whole, (**b**) thermocouple and data logger

$$q_r = \varepsilon\sigma(T_s)^4 \tag{5.1}$$

Where

q_r = outgoing radiation (W/m^2),
ε = emission coefficient (0.85 for concrete and 0.93 for asphalt),
σ = Stefan-Boltzmann constant, 5.68 × 10^{-8} W/(m^{2}K^4), and
T_s = temperature of surface (°K).

As can be seen in Fig. 5.6, the amount of radiation that the asphalt lays outdoors is greater. The q_r value for asphalt ranges from 500 to 580 W/m^2, while for concrete it ranges from 410–480 W/m^2, which is 10–15% lower. As the surface temperatures increase in both pavements, the amount of energy released to the external atmosphere will also increase. However, compared to the two pavements, asphalt can be expected to increase the temperature of the environment to a greater extent due to the high surface and external energy emitting capacity, especially in urban areas where asphalt coatings are present, so the difference between night and day temperatures may be low.

Several studies by Erhan P. [15], Erhan et al. [16], Tran et al. [4], and Boriboonsomsin and Reza [17] were conducted to reduce urban heat island by using innovative pavement materials. A study conducted by Erhan Pancar [15] showed that it was possible to reduce the slab surface temperature by using recycled glass as a fine aggregate and zeolite as cement in concrete. Recycled glass was used to replace fine aggregate in proportions of 10%, 20%, and 30% by total weight of aggregate. Zeolite replaced Portland cement in proportions of 10% and 30% for three different proportions of recycled glass concrete mixtures. Optimum proportions were determined by examining mechanical properties of concrete samples and alkali-silica reactions. It was noticed that using recycled glass and zeolite together in concrete reduces pavement surface temperature and temperature gradient in summer.

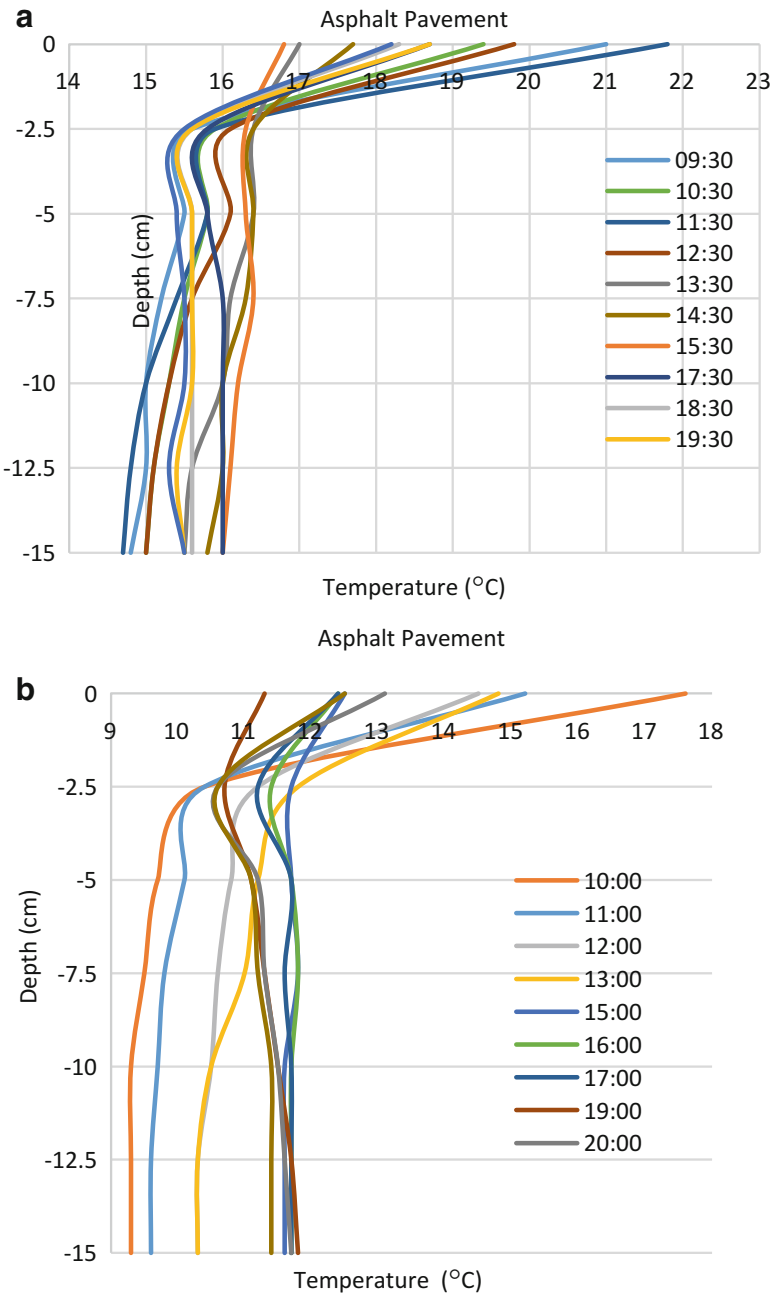

Fig. 5.4 Asphalt pavement temperature variation. (**a**) Open to sunlight, (**b**) shadowed by trees

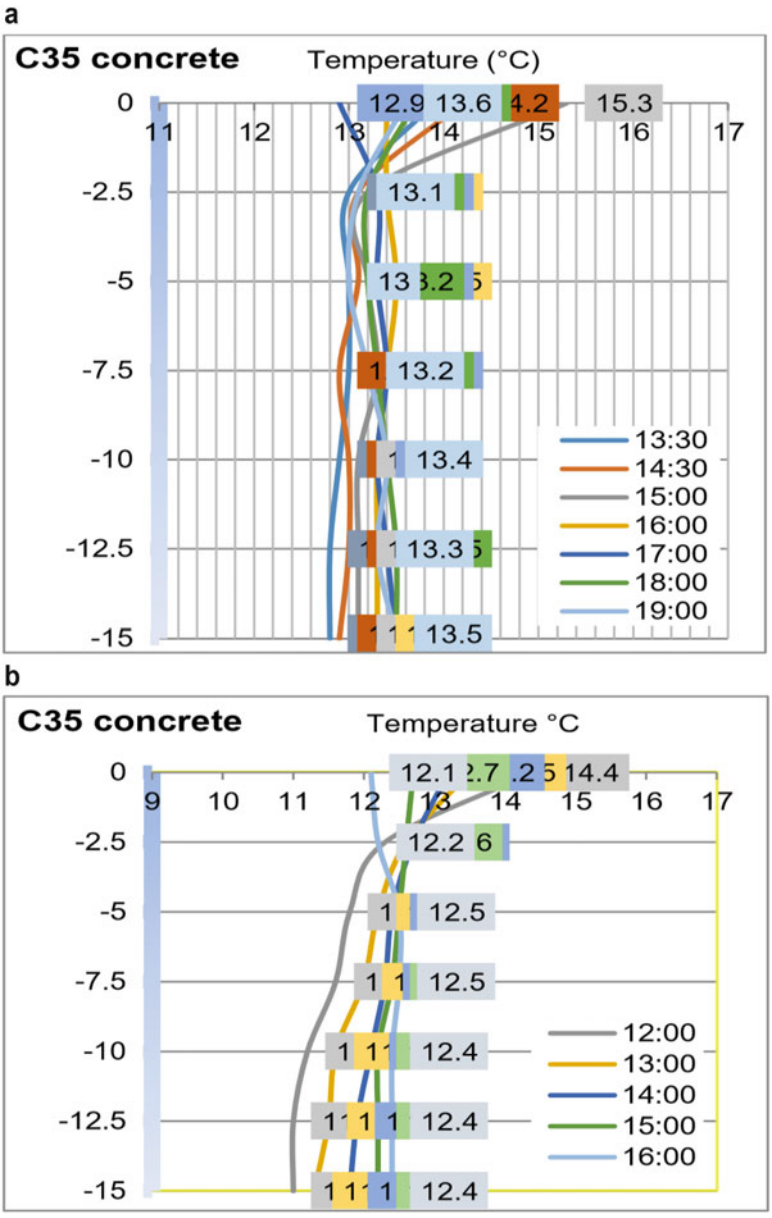

Fig. 5.5 Concrete pavement temperature variation. (**a**) Open to sunlight, (**b**) shadowed by trees

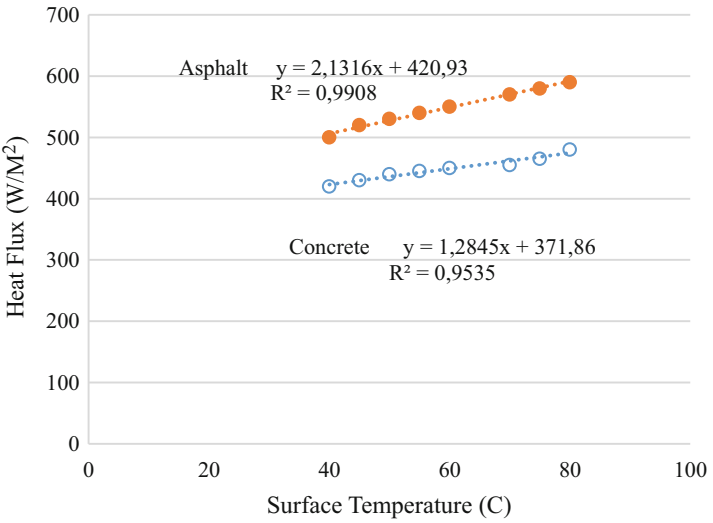

Fig. 5.6 Heat flux versus surface temperature

5.4 Conclusion

The purpose of this chapter was to research the warmth flux from asphalt and concrete pavements. Results showed that warmness flux of asphalt pavements is better than that of concrete pavements. Growing tree cover on both sides of the pavements lowers surface temperatures with the aid of imparting color and cooling through evapotranspiration. In the experimental study, the outgoing radiation value of asphalt pavement was observed to be 10–15% greater than the concrete pavement.

References

1. Asaeda T, Ca VT, Wake A (1996) Heat storage of pavement and its effect on the lower atmosphere. Atmos Environ 30(3):413–427
2. Yao ZK (2012) Methods research on asphalt pavement structure design based on multi-index. Final Report, Part 1, Shanghai, China
3. Doll D (1983) Diurnal variability of the surface energy budget fluxes for three contrasting land use surface materials. Master Thesis, North Carolina State University. Raleigh, p 132
4. Tran N, Powell B, Marks H, West R, Kvasnak A (2009) Strategies for design and construction of high reflectance asphalt pavements. Transportation Research Record: Journal of the Transportation Research Board, No. 2098, Washington, DC, pp 124–130
5. Li H, Qian X, Hu W, Wang Y, Gao H (2013) Chemical speciation and human health risk of trace metals in urban street dusts from a metropolitan city, Nanjing, SE China. Sci Total Environ 456–457(1):212–221

6. Huntingford C, Allen SJ, Harding RJ (1995) An intercomparison of single and dual-source vegetation atmosphere transfer models applied to transpiration from Sahelian Savannah. Bound-Layer Meteorol 74(4):397–418
7. Anting N, Din MFM, Iwao K, Ponraj M, Jungan K, Yong LY, Siang AJLM (2017) Experimental evaluation of thermal performance of cool pavement material using waste tiles in tropical climate. Energ Buildings 142:211–219
8. Zhang JR, Liu ZQ (2006) A study on the convective heat transfer coefficient of concrete in wind tunnel experiment. Chin Civil Eng J 39(09):39–42
9. Qin Y (2015) Urban canyon albedo and its implication on the use of reflective cool pavements. Energ Buildings 96:86–94
10. Qin Y (2016) Pavement surface maximum temperature increases linearly with solar absorption and reciprocal thermal inertial. Int J Heat Mass Transf 97:391–399
11. Qin Y, Liang J, Tan K, Li F (2017) The amplitude and maximum of daily pavement surface temperature increase linearly with solar absorption. Road Mater Pavement Des 18:440–452
12. ARA Inc., ERES Consultants Division (2004) Guide for mechanistic-empirical pavement design of new and rehabilitated pavement structures. National Cooperative Highway Research Program Transportation Research Board National Research Council. Final report, part 2, chapter 2, Champaign, pp 33–58
13. Tan ZM, Zou XL, Liu BY (2010) Numerical solution to pavement temperature fields and discussion on several key issues. J Tongji Univ Natl Sci 38(03):374–379
14. Gustafson GD, Larkins BA, Jackson AO (1981) Comparative analysis of polypeptides synthesized in vivo and in vitro by two strains of barley stripe mosaic virus. Virology 111:579–587
15. Pancar EB (2016) Using recycled glass and zeolite in concrete pavement to mitigate heat island and reduce thermal cracks. Adv Mater Sci Eng (1):1–8. https://doi.org/10.1155/2016/8526354
16. Pancar EB, Akpınar MV (2016) Temperature reduction of concrete pavement using glass bead materials. Int J Concrete Struct Mater 10(1):39–46
17. Boriboonsomsin K, Reza F (2007) Mix design and benefit evaluation of high solar reflectance concrete for pavements. Transportation Research Record: Journal of the Transportation Research Board, No. 2011, Washington, DC, pp 11–20

Chapter 6
Comparison of Asphalt and Concrete Pavement Solar Reflectance

Muhammet Vefa Akpınar and Sedat Sevin

6.1 Introduction

Research shows that on warm summer days, the air in large cities can be significantly hotter than the surrounding rural areas. The annual mean air temperature of a city with 1 million people or more can be 1–3 °C warmer than its surroundings [19] (Environmental Protection Agency (EPA) 2003). In the past few decades, the heat over the urban cities has been increased due to dark and heat-absorbing materials used in the construction of pavements and buildings. Elevated temperatures in urban heat islands can have detrimental effects on a community's environment and quality of life, including increased demand for energy, increased air pollution, greenhouse gas emissions, human health effects, and decreased water quality. Electricity demand, for example, for cooling increases 1.5–2.0% for every 0.6 °C increase in air temperatures, starting from 20 to 25 °C [3, 4, 8, 17, 18, 20, 21]. This means that 5–10% of the electricity demand for a city is used to compensate for the heat island effect [2]. In recent years, the use of low-thermal-absorbent materials in urban areas has become widespread to reduce heat island effect [11–13, 16].

Cool materials are characterized by high solar reflectance and high thermal emittance. The two properties could reduce the temperature of the surface. The term solar reflectance is the ability of a material to reflect solar energy from its surface back into the atmosphere [7]. Some previous studies are related to cool materials. In these studies, the albedo value of concrete is observed about 0.25–0.35 [1, 5, 14]. Because reflectivity limit adopted by Cool Roof Rating Council (CRCC)

M. V. Akpınar (✉)
Karadeniz Teknik Üniversitesi, Civil Engineering Department, Trabzon 61080, Turkey
e-mail: mvakpinar@ktu.edu.tr

S. Sevin
Gümüşhane Üniversitesi, Civil Engineering, Gümüşhane, Turkey

S. Nižetić, A. Papadopoulos (eds.), *The Role of Exergy in Energy and the Environment*, Green Energy and Technology,
https://doi.org/10.1007/978-3-319-89845-2_6

and Leadership in Energy and Environmental Design (LEED) as 0.29, using concrete in urban roads and parking spaces can increase solar reflectance as heat absorption decreases. In contrast, asphalt albedo ranges from 0.05 to 0.20, depending on the age and construction date of the asphalt pavement. Its albedo typically increases somewhat as its color fades with age. A typical concrete has an albedo of about 0.25–0.35 when constructed; these values can decrease to about 0.20–0.30 with normal usage. With the incorporation of slag or white cement, a concrete pavement can exhibit albedo readings as high as 0.70 [9]. Concrete has a significantly higher albedo than asphalt, either new or old. In fact, concrete usually has a higher albedo than almost every other material that is typical of urban areas, including grass, trees, colored paint, brick/stone, and most roofs [9].

In this study, the surface temperature and solar reflectance of concrete and asphalt paved roads were investigated during hot summer. The relationship between albedo values and pavement surface temperatures were developed.

6.2 Material and Method

The daily surface temperature and solar reflectance of concrete and asphalt paved areas on the university campus were investigated during July, August, and September months of 2016. Thermal camera and pyranometer were used to measure the surface temperature and albedo at 15:00 when the surface had the highest heat during the 3-month period.

This study was conducted with a single-headed pyranometer (Fig. 6.1) in accordance with ASTM E1918 [6]. The image shown in Fig. 6.1 was taken during the cloudy day. However, the albedo measurements were taken during the sunny days. The CMA6 parameter provides solar reflectance ($W.m^{-2}$) of the surfaces 50 cm above the area to be measured, as specified in the standard. The air temperature 25 cm just above the pavement surface was measured by the thermal camera and digital thermometer. Albedo measurements were started at 15:00 when the highest temperature was reached on the pavement surface during the day.

Measuring the albedo according to the ASTM E1918-06 leads to great measurement uncertainty. This single-pyranometer method has to invert the pyranometer to read this incoming solar radiation. During the inversion, the incoming solar radiation may differ from that at the time when the pyranometer faces down. The time interval between two measurements (facing up and down) was maintained for 30 s. By doing so, the uncertainty in the measurements was minimal.

Fig. 6.1 Single-headed pyranometer (**a**, **c**), data logger (**b**, **d**) (The value on the screen is based on $W.m^{-2}$)

6.3 Result and Discussion

6.3.1 Albedo Measurements

Albedo is the ratio of the amount of sunlight reflected from the pavement surface to the amount of sunlight coming from the pavement surface. As shown in Fig. 1, the albedo value of the surface is equal to 50 ($W.m^{-2}$)/256 ($W.m^{-2}$). The daily albedo

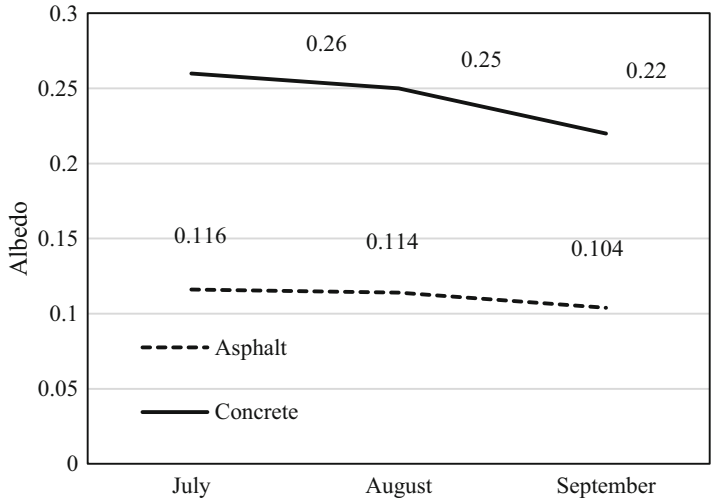

Fig. 6.2 Monthly mean albedo values

values of the pavements are calculated in this way. The average monthly albedo values of the asphalt and concrete overlays are shown in Fig. 6.2.

As can be seen in Fig. 6.2, the average albedo values of the concrete pavements for 3 months are two times that of the asphalt pavement. The average albedo value was 0.24, with a minimum of 0.18 and a maximum of 0.36 during the 3-month test on the concrete pavement. In the same way, the average albedo measurements for asphalt pavement was 0.11, with a maximum of 0.16 and a minimum of 0.06. Albedo measurements vary depending on the amount of incoming and reflected sunlight. The albedo values of this study are in the range found by Li [9] where typical concrete had an albedo of about 0.25–0.35.

As shown in Fig. 6.2, albedo values were very close to each other in July and August due to the same number of sunny days (27 day sunny). However, albedo values were 10% lower compared to July and August due to less sunny days (20 day sunny, 10 day cloudy).

LEED defines materials with an albedo greater than 0.29 as a reflective and low heat absorber. In this study, while the measured albedo values of the concrete pavement were 0.29, the albedo value of the asphalt pavement was 0.11. It can be said that the concrete pavement studied in this research can be classified as a reflective and low heat absorber in contrast to asphalt pavement. Similarly, Pometantz et al. [15] predicted that asphalt pavements stored a large part of the heat by reflecting a very small amount of sunlight due to its dark color and heat-absorbing property.

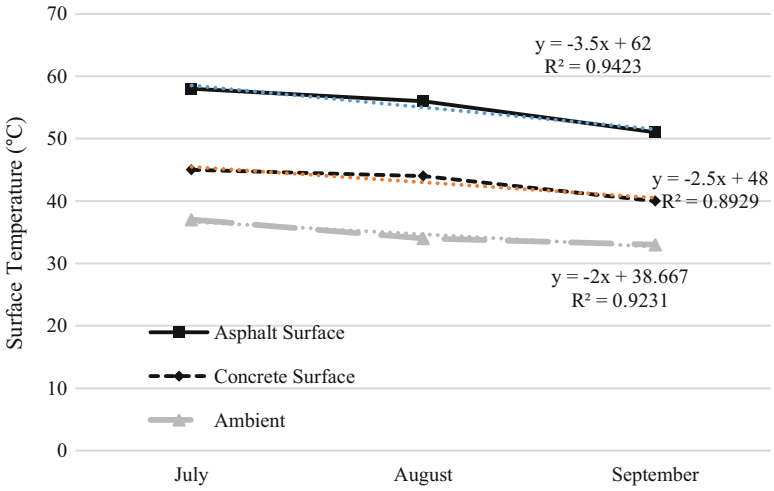

Fig. 6.3 Average monthly maximum surface temperatures of pavements

6.3.2 Maximum Surface Temperature Measurements

Similar to the albedo results, the monthly mean maximum pavement surface temperatures are shown in Fig. 6.3. According to these results, the maximum surface temperatures on concrete surfaces were 10–15° lower than the temperature values of asphalt surface. Asaeda and Vu (1993) reported that the surface temperature of asphalt pavements could exceed 55 °C and that the surfaces release more than 350 $W.m^{-2}$ and 600 $W.m^{-2}$ to the atmosphere in the form of sensible heat and longwave radiation, respectively. In this study, during the 3-month period, the measured maximum surface temperatures of the asphalt pavement and concrete pavement were 62 °C and 48 °C, respectively. Both values were obtained in July measurements. Likewise, air temperatures for 3 months were obtained in July at a maximum air temperature of 38 °C. This showed that both pavements stored more heat than the air. Due to the heat absorptive properties of both asphalt and concrete, the maximum pavement surface temperatures have exceeded air temperature. But especially in July, the surface temperatures of the asphalt pavements were 50% higher than the air temperature due to low albedo and high heat absorption properties. This ratio was observed to be about 20% in the concrete pavement. The main reason for this is the higher value of the albedo value of the concrete pavement, reflecting more of the sun's rays coming to the surface and storing less heat.

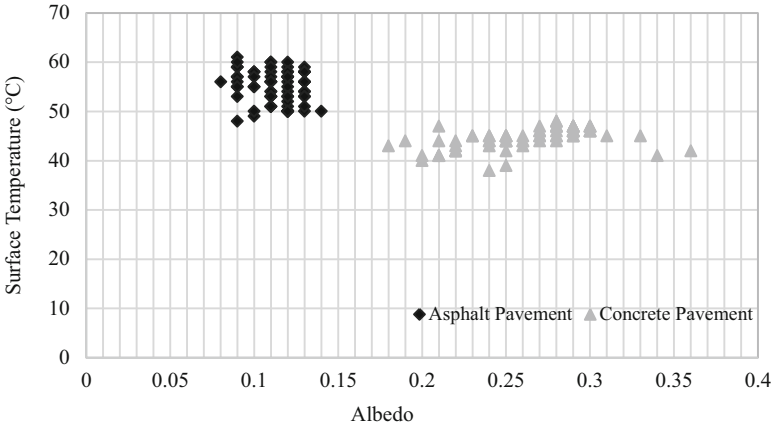

Fig. 6.4 The relationship between albedo values and pavement surface temperatures

6.3.3 Relationship Between Surface Temperature and Albedo

The relationship between albedo values and pavement surface temperatures for asphalt and concrete pavements are shown in Fig. 6.4. The albedo values do not change significantly with increasing pavement surface temperatures for both pavements.

6.3.4 Comparison of Outgoing Radiation of Pavements

Pavements absorb some of the sun's rays coming to the surface and heat up and then transfers heat to the external environment, causing them to heat up. The heat flux at the maximum surface temperatures of the asphalt and concrete pavements in the study was calculated with the aid of Eq. (6.1). The earth's surface is assumed to emit longwave radiation as a blackbody. Thus, the outgoing longwave radiation follows the Stefan-Boltzmann law (Solaimanian and Kennedy, Kreith, Sellers, and Gustafson (*8*)).

$$q_r = \varepsilon\sigma(T_s)^4 \tag{6.1}$$

Where,

q_r = outgoing radiation (W.m^{-2})
ε = emission coefficient (0.85 for concrete and 0.93 for asphalt)
σ = Stefan-Boltzmann constant, 5.68 $\times 10^{-8}$ W.m^{-2}K^{-4})
T_s = temperature of surface (°K)

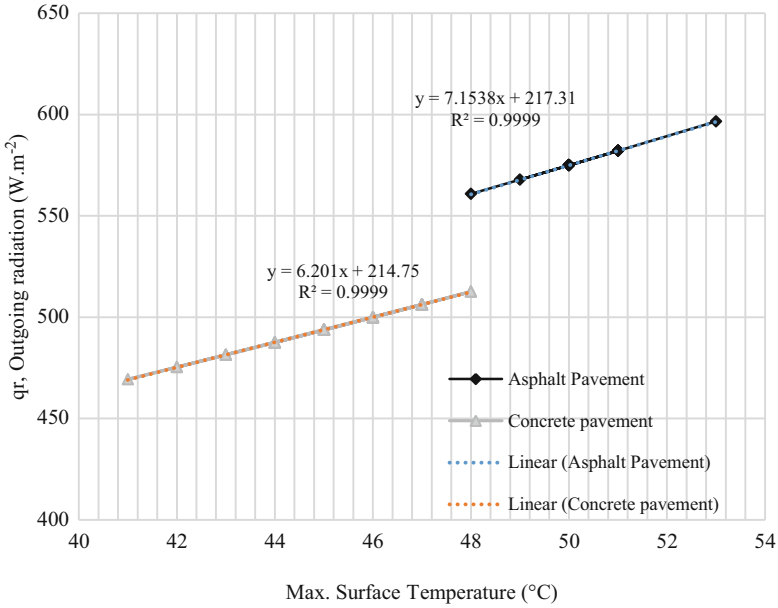

Fig. 6.5 The relationship between outgoing radiation and pavement surface temperatures

The relationship between outgoing radiation and surface temperature is shown in Fig. 6.5. As can be seen in Fig. 5, the amount of radiation that the asphalt pavement lays outdoors is greater. The q_r value for asphalt ranges from 560 to 600 W.m^{-2}, while for concrete it ranges from 470 to 510 W.m^{-2}, which is 10–15% lower. As the surface temperatures increase in both pavements, the amount of energy released to the external atmosphere will also increase.

Asphalt pavements can be expected to increase the temperature of the environment to a greater extent due to the high surface and external energy emit capacity, especially in urban areas where asphalt pavements are present, so the difference between night and day temperatures may be low.

6.4 Recommendations

Concrete pavement and asphalt pavements worn under traffic loads when aged. Their surfaces become gray finally, and the albedo of these surfaces depends on the aggregate wear resistance. The albedo measurements were taken on almost newly constructed 3-month old asphalt pavement and 10-year-old concrete pavement. Further readings will be taken on the same spot after 1 year, and they will be compared to the current study data. More attention will be given to the painted sections where the paint is subjected to fast wear. Further, similar studies are needed

on high-capacity highways. The current study albedo results are valid for university campus traffic.

6.5 Conclusion

This study investigated and compared the variation of maximum surface temperatures and albedo properties of asphalt and concrete pavements. The following conlusions are made according to the findings of this study:

(i) It can be said that the concrete pavement studied in this research can be classified as a reflective and low heat absorber in contrast to asphalt pavement.
(ii) The albedo values of concrete pavements are almost 100% higher than the albedo values of asphalt pavement. For this reason, the use of concrete pavements in urban areas can be extended, and a large amount of sunlight can be reflected back, reducing heat storage of cities.
(iii) The maximum surface temperatures of concrete pavements are 10–12 °C lower than the asphalt pavement surface temperatures at all 3-month measurements. By using concrete pavement in urban, environmental problems can be solved by reducing UHI influence.
(iv) The outgoing radiation value of asphalt pavement was observed to be 10–15% greater than the concrete pavement. Because of this, the asphalt pavements can have a negative effect on the thermal comfort that will keep the storage temperature hot during the night.

References

1. ACPA (2002) Concrete pavement research & technology. Retrieved from Albedo: a measure of pavement surface reflectance. American Concrete Pavement Association 5420 Old Orchard Road, Suite A100 Skokie, IL United States 60077. https://trid.trb.org/view/920184
2. Akbari H (2003) Measured energy savings from the application of reflective roofs in two small non-residential buildings. Energy 28(9):953–967. https://doi.org/10.1016/S0360-5442(03)00032-X
3. Akbari H, Garbesi E, Martien, P (1989) Controlling summer heat islands. Lawrence Berkeley Laboratory, Energy Analysis Program, Berkeley, CA trees and white surfaces. In: Proceedings of the 1992 ACEEE summer study on energy efficiency in buildings, America Council for an Energy-Efficient Economy, Washington DC
4. Akbari H, Bretz S, Hanford J, Sailor D, Taha H, Bos W (1992) Monitoring peak power and cooling energy savings of shade trees and white surfaces in the Sacramento Municipal Utility District (SMUD) service area: Project design and preliminary results, Final Report Prepared for California Institute of Energy Efficiency and SMUD Rep. No. LBL-33342, Lawrence Berkeley Laboratory, Berkeley, CA
5. Asaeda T, Ca VT, Wake A (1996) Heat storage of pavement and its effect on the lower atmosphere. Atmos Environ 30(3):413–427

6. ASTM (2006) ASTM E1918-06 standard test method for measuring solar reflectance of horizontal and low-sloped surfaces in the field. American Society for Testing and Materials, West Conshohocken
7. Bretz S, Akbari H, Rosenfeld A (1998) Practical issues for using solar-reflective materials to mitigate Urban Heat Islands. Atmospheric Environment 32(1):95–101
8. Gustafson K (1981) Road icing on different pavement structures. VTI Rapport 216A. Swedish National Road and Transport Research Institute, Linköping
9. Li H (2012) Evaluation of cool pavement strategies for heat island mitigation. PhD dissertation, University of California, Davis
10. Libbra A, Muscio A, Siligardi C, Tartarini P (2011) Assessment and improvement of the performance of antisolar surfaces and coatings. Process Org Coat 72:73–80
11. Lombard LP, Ortiz J, Pout C (2008) A review on buildings energy consumption information. Energy Build 40:394–398
12. Omer AB (2008) Energy, environment and sustainable development. Renew Sustain Energy Rev 12:2265–2300
13. Omer M (2008) Renewable building energy systems and passive human comfort solutions. Renew Sustain Energy Rev 12:1562–1587
14. Pearlmutter D, Berliner P, Shaviv E (2006) Physical modeling of pedestrian energy exchange within the urban canopy. Build Environ 41(6):783–795. https://doi.org/10.1016/j.buildenv.2005.03.017
15. Pometantz M, Pon B, Akbarians H, Chang S (2000) The effect of pavements' temperatures on air temperature in large cities (LBNL-3442). Lawrence Berkeley Laboratory, Energy Analysis Program, Berkeley, p 373
16. Sozer H (2010) Improving energy efficiency through the design of the building envelope. Build Environ 45:2581–2593
17. Synnefa A, Saliari A, Santamouris M (2012) Experimental and numerical assessment of the impact of increased roof reflectance on a school building in Athens. Energy Build 55:7–15
18. Synnefa A, Santamouris M (2012) Advances on technical, policy and market aspects of cool roof technology in Europe: The Cool Roofs project. Energy Build 55:35–41
19. Tran N, Powell B, Marks H, West R, Kvasnak A (2009) Strategies for design and construction of high-reflectance asphalt pavements. Transportation Research Record: Journal of the Transportation Research Board, No. 2098, Transportation Research Board of the National Academies, Washington, DC, pp 124–130
20. Vu TC, Asaeda T, Armfield S (1997) Study of the heating and evaporation processes in the urban canopy based on a LES model. In: editors, Leonardi E, Madhusudana CV Proceedings of sixth Australian heat and mass transfer conference, Dec 9–12, 1996, Sydney, Australia
21. Zinzi M, Agnoli S (2012) Cool and green roofs. An energy and comfort comparison between passive cooling and mitigation urban heat island techniques for residential buildings in the Mediterranean region. Energy Build 55:66–76

Chapter 7
Thermoeconomic Comparative Analyses of Different Approaches Used for Specific Carbon Dioxide Emission Reduction in Gas Turbine Power Plants

Mohammad Saghafifar and Mohamed Gadalla

7.1 Introduction

Climate change is one of the most discussed topics in recent years. Moreover, multiple reports indicate the considerable rate of growth in world's energy demand due to an increase in population. In particular, it is predicted that world's energy demand will experience a 35% growth from 2010 to 2035 [1]. Noting that about 80% of the world's required electricity is generated by fossil fuel and natural gases power plants [2], and activities associated with energy contribute to about 61% of greenhouse gases emission [3], it is necessary to reduce the rate of carbon dioxide emission from power generation, immediately. The aforementioned immediate reduction can be achieved through different approaches including renewable energy integration [4–8], carbon capture and storage/utilization [9–13], efficiency enhancement [14–18], and a combination of these methods [19–23].

One of the possible approaches of efficiency enhancement for simple gas turbine power plants is inlet air cooling. Gas turbine performance is considerably dependent on the inlet air temperature entering the compressor. As the air temperature rises, the required work input in the compressor increases which inversely affects the plant efficiency and accordingly its specific carbon dioxide emission [24, 25]. In a study by Saghafifar and Gadalla [26], different inlet air cooling technologies are investigated for integration in a simple gas turbine cycle. Results are in the favor of inlet air

M. Saghafifar (✉)
Department of Engineering, University of Cambridge, Cambridge, UK
e-mail: msaghafifar@alumni.aus.edu; ms2474@cam.ac.uk

M. Gadalla
Department of Mechanical Engineering, College of Engineering, American University of Sharjah, Sharjah, United Arab Emirates

S. Nižetić, A. Papadopoulos (eds.), *The Role of Exergy in Energy and the Environment*, Green Energy and Technology,
https://doi.org/10.1007/978-3-319-89845-2_7

cooling implementation, regardless of the technique utilized to cool down the air, both thermodynamically and economically.

Another possible method to reduce the rate of carbon dioxide emission by gas turbine efficiency enhancement is through bottoming cycle integration. Simple gas turbine power plant's exhaust gases contain substantial waste heat that can be recovered by a bottoming cycle and generate additional electricity. The most widely employed and arguably efficient bottoming cycle is Rankine (steam turbine) cycle [27]. Integrating a bottoming steam turbine cycle can significantly improve the plant's overall thermal efficiency. Therefore, plant's specific CO_2 emission is reduced either by increasing the amount of power generated or decreasing the required fuel mass flow rate in the combustion chamber.

The other possible method considered in this study is power plant hybridization. Solar hybridization can be considered to reduce the rate of carbon dioxide emission associated with power generation. Three different schemes are suggested for power plant hybridization comprising the solarized gas turbine, the hybrid combined cycle, and the solar reforming system [28, 29]. In the first two schemes, a solar thermal collector is coupled with a secondary source of energy (combustion chamber with fossil fuel). While in solar reforming systems, solar thermal energy is utilized to convert the fuel, mostly natural gases, into syngas which is used in the combustion chamber as the main source of thermal energy.

In a series of studies by Saghafifar and Gadalla [30–33], hybridization was accomplished using heliostat field collectors to provide a portion of the thermal energy required to operate a combined-cycle power plant. In all the investigated configurations, specific CO_2 emission was reduced when about 10% of annual thermal energy was provided by the integrated solar component. However, the plant levelized cost of electricity was increased because of high expenses associated with heliostat field collectors. In a study by Spelling et al. [34], a thermoeconomic optimization was conducted for hybrid gas turbine power plants. Furthermore, hybridization of combined-cycle power plants was investigated by Spelling et al. [35]. It should be noted that the abovementioned studies utilized heliostat field collector due to its high operating temperature and its suitability for integration in gas turbine cycles.

In this chapter, a comparative analysis between three different methods of specific carbon dioxide emission reduction for simple gas turbine power plants is presented including inlet air cooling, bottoming cycle integration, and solarized gas turbine hybridization using heliostat field collector. For inlet air cooling technique, a mechanical chiller is employed. For bottoming cycle integration, steam bottoming cycle presented by Saghafifar and Gadalla [30] is considered. Different methods are compared based on their effects on the plant-specific carbon dioxide emission and levelized cost of electricity for different capacities. Finally, a combination of all three studied methods is implemented to further minimize the specific carbon dioxide emission. It should be noted that Abu Dhabi is selected as an illustrative example for site location to signify the importance of the integrated technologies.

7.2 System Configurations

Figure 7.1 depicts the simple gas turbine cycle with the three proposed carbon dioxide reduction methods including inlet air cooling, hybridization, and bottoming cycle integration. In a simple gas turbine power plant, air is compressed adiabatically in the compressor from state 2 to 3. After the compression, air is heated in an isobaric process within the combustion chamber from state 4 to 5. Next, the heated stream of exhaust gases leaving the combustion chamber is expanded in the gas turbine from state 5 to 6. Finally, the exhaust gases leaving the gas turbine are released to the atmosphere. One of the recommended techniques is to employ a mechanical chiller to cool down the air stream entering the combustion chamber. From state 1 to 2, ambient air enters a mechanical chiller where it is cooled down to a predetermined temperature prior to the compressor. Alternatively, hybridization can be accomplished using heliostat field collectors. In this scheme, a portion of the required thermal energy is provided by concentrated solar power technologies which leads to

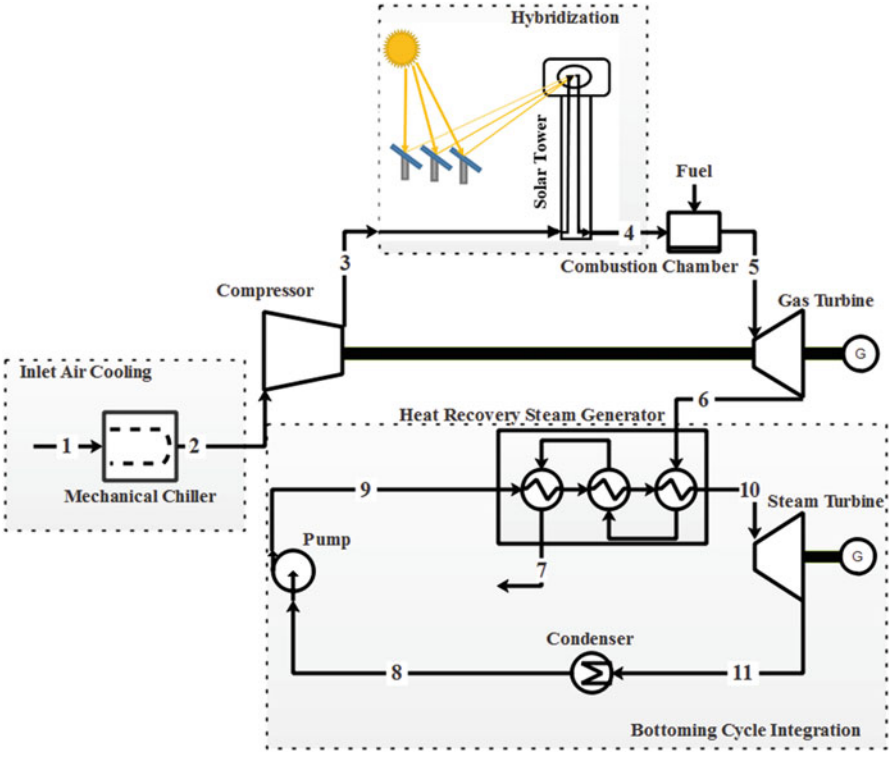

Fig. 7.1 Gas turbine power plant configuration with the proposed carbon dioxide emission reduction including inlet air cooling, hybridization, and bottoming cycle integration

a considerable reduction in the plant fuel consumption and accordingly the specific CO_2 emission. As it is shown in Fig. 1.1, the solar collector is placed between the compressor and combustion chamber. Thus, the compressed air leaving the compressor enters the central tower to be preheated by the available solar thermal energy flux at the receiver from state 3 to 4.

Another suggested method to decrease the rate of carbon dioxide emission is to integrate a bottoming cycle. For this study, steam turbine (Rankine) cycle is selected to employ the waste heat available in exhaust gases leaving the gas turbine at state 6. In the case of combined-cycle configuration, exhaust gases from the topping cycle turbine enter the heat recovery steam generator (HRSG) where a portion of the waste is utilized to generate steam and operate the steam bottoming cycle from state 6 to 7. In the bottoming cycle, saturated liquid water at state 8 is pumped in an adiabatic process to state 9. Afterward, water enters the HRSG which consists of three sections, economizer, evaporator, and superheater. In the HRSG, water is heated by exchanging heat with the topping cycle exhaust gases to generate steam from state 9 to 10. Next, the generated steam is expanded in the steam turbine from state 10 to 11. At the final stage of the steam bottoming cycle, the expanded steam leaving the turbine is condensed to saturated liquid water in the condenser from state 11 to 7 to complete the bottoming cycle.

7.3 Mathematical Formulation

7.3.1 Thermodynamic Model

In this study, air, exhaust gases, and steam heat capacities and entropies are evaluated based on NASA polynomial curve fits [36–38]. To conduct the thermodynamic analysis of the proposed configuration, the developed mathematical formulation is employed in a MATLAB code. Due to limitation in space, it is decided not to present commonly known thermodynamic formulas for compressor, combustion chamber, turbine, HRSG, pump, and condenser. Interested readers are advised to refer to Saghafifar and Gadalla [30] and Spelling [39, 40] for a comprehensive discussion on the employed mathematical formulations. Furthermore, all the thermodynamic assumptions and design parameters are listed in Table 7.1.

For heliostat field analysis, the developed model presented in Gadalla and Saghafifar [41] and Saghafifar and Gadalla [42, 43] is employed. It is strongly suggested to consult with the aforementioned studies for a detail presentation of the heliostat field analysis. It should be noted that the heliostat field instantaneous optical efficiency is calculated as follows [44, 45]:

$$\eta_{\mathrm{opt,f}} = \rho f_{\cos}(x,y,t) f_{\mathrm{at}}(x,y) f_{\mathrm{sp}}(x,y,t) f_{\mathrm{s\&b}}(x,y,t) \tag{7.1}$$

Table 7.1 Thermodynamic assumption, constraints, and design parameters

Parameter	Assigned value
Fuel lower heating value (kJ/kg)	50,142
Reference temperature (K)	298
Combustion chamber efficiency	98%
Combustion chamber pressure drop	4%
Net power output (MWe)	1, 5, 10, 50, 100, 500
Compressor isentropic efficiency	85%
Compressor mechanical efficiency	99%
Compressor pressure ratio	21
Turbine isentropic efficiency	85%
Turbine mechanical efficiency	99%
Gas turbine inlet temperature (K)	1500
Generator electrical efficiency	99%
Generator mechanical efficiency	98%
Pump isentropic efficiency	90%
Pump pressure ratio	1000
Solar tower maximum outlet temperature (K)	1223
HRSG superheater pinch temperature (K)	10
HRSG pinch temperature (K)	9
HRSG approach temperature (K)	9
HRSG pressure drop (both sides)	4%
HRSG degree of superheating (DOSH)	0.63
Mechanical chiller plant factor	1.2
Mechanical chiller coefficient of performance	2.9
Mechanical chiller pressure drop (kPa)	0.3
Mechanical chiller minimum allowable temperature (K)	278
Mechanical chiller outlet temperature (K)	288
Fan efficiency	80%
Condenser pressure (kPa)	10

Moreover, the heliostat field optimization approach named Campo recommended by Collado and Guallar [45–47] is employed. Heliostat field optimization is accomplished to maximize the field annual weighted efficiency as follows [48]:

$$\eta_{\text{ann,w}} = \frac{\sum_{i=1}^{365} \int_{\text{sunrise}}^{\text{sunset}} \text{DNI}(t)\, \eta_{\text{opt,f}}(t)\, dt}{\sum_{i=1}^{365} \int_{\text{sunrise}}^{\text{sunset}} \text{DNI}(t)\, dt} \tag{7.2}$$

Furthermore, all design parameters and assumptions associated with the heliostat field layout are tabulated in Table 7.2. Taking into account that direct normal radiation for Abu Dhabi with hourly time steps is considered for this research work [49].

Table 7.2 Initial assumption, constraints, and design variables for heliostat field design [40, 45–47, 50, 51]

Parameter	Assigned value
Tower height (m)	127.5
Air velocity in tower piping (m/s)	10
Receiver radius (m)	4
Receiver height (m)	9
Heliostat height (m)	12.30
Heliostat width (m)	9.75
Heliostat vertical elevation from the ground (m)	7.5
Standard deviation of surface error (mrad)	0.94
Standard deviation of tracking error (mrad)	0.63
Standard deviation of sun shape (mrad)	2.51
Effective reflectivity	0.836
Field number of zones	3
Number of heliostat in the first row	10, 15, 25, 35
Number of heliostat in the field	350, 840, 2350, 4550
Extra separation distance *dsep* (m)	0.3
Latitude location (^{o}N)	24.47
Field layout	Radial staggered
Field number of cells	100
Typical meteorological year (TMY)	Abu Dhabi [49]

It should be noted that the size of the analyzed heliostat field is selected based on the integrated power plant capacity. Next, the selected heliostat field is optimized, and a ranked array of mirror based on their annual thermal performance is generated. At the same time, an estimated required solar thermal input to achieve solar multiple of one during spring equinox noon is determined based on the power block's steady-state analysis. In this study, a specific case of maximum solar thermal energy penetration in power generation process without thermal energy storage through gas turbine hybridization using heliostat field collector is investigated. Due to lack of thermal energy storage, it is more economical to only select a subset of mirrors showing the highest annual potential and satisfying the specified thermal energy. This way, we can minimize the number of instances during the year when maximum allowable operating temperature in the receiver, i.e., $950^{\circ}C$ [40], is exceeded and reduce the amount of thermal energy loss due to the aforementioned restriction. To do so, the generated ranked array of mirrors is utilized to calculate the number of mirrors required to achieve the determined capacity during spring equinox noon. Afterward, annual performance assessment is conducted for the appropriately sized heliostat field and the integrated power block.

For the inlet air cooling technology, a mechanical chiller is chosen to be implemented before the compressor. Cooling load of the mechanical chiller is calculated based on the model presented by Farzaneh-Gord and Dashtebayaz [52]. It should be noted that the aforesaid model has been previously utilized by

the authors in [26]. Furthermore, 5 °C is considered as the minimum allowable temperature to cool down the air in the mechanical chiller in order to avoid icing at the compressor inlet. Moreover, the mechanical chiller coefficient of performance and the chiller plant factor are considered to be 2.9 and 1.2, respectively. It is noteworthy that the mechanical chiller coefficient of performance is assessed with respect to its relationship with the chiller plant factor to determine the amount of electricity consumption. Finally, electricity consumption associated with fans is evaluated by assuming fan efficiency of 0.8 [53] and pressure drop of 0.3 kPa [54]. In addition, it is decided to cool down air to 15 °C, based on the suggestion by Gareta et al. [54].

To properly evaluate the proposed bottoming cycle integration of a steam turbine cycle, HRSG degree of superheating (DOSH) is considered as follows [30]:

$$\mathrm{DOSH} = \frac{T_{\mathrm{s,sh}} - T_{\mathrm{s,sat}}}{\left(T_{\mathrm{g,ex}} - \Delta T_{\mathrm{pinch,sh}}\right) - T_{\mathrm{s,sat}}} \tag{7.3}$$

Furthermore, the plant net power output and efficiency are determined as follows:

$$\dot{W}_{\mathrm{net}} = \left[\eta_{\mathrm{M,G}}\left(\dot{m}_{\mathrm{g}}\, w_{\mathrm{Gt}} + \dot{m}_{\mathrm{s}}\, w_{\mathrm{St}}\right) - \frac{\left(\dot{m}_{\mathrm{a}}\, w_{\mathrm{c}} + \dot{m}_{\mathrm{s}}\, w_{\mathrm{p}}\right)}{\eta_{\mathrm{M,G}}} - \dot{W}_{\mathrm{IC}}\right]\eta_{\mathrm{ele,G}} \tag{7.4}$$

$$\eta = \frac{\dot{W}_{\mathrm{net}}}{\dot{m}_{\mathrm{f}}\,\mathrm{LHV} + \dot{Q}_{\mathrm{sol}}} \tag{7.5}$$

7.3.2 Economic Model

Economic analysis is conducted to investigate the economic advantages and disadvantages of the proposed carbon dioxide reduction approaches. Furthermore, chemical engineering plant cost index (CEPCI) is used to update the utilized cost functions. All the cost functions along with their respective sources and reference years are tabulated in Table 7.3. Additionally, each equipment installation cost is estimated as 20% of its initial capital investment [55].

Furthermore, the expenses associated with the decommissioning, construction planning and management, and unforeseen technical and regulatory problems are [40, 65, 66]:

$$Z_{\mathrm{if}} = 0.05\left[\sum Z_{\mathrm{eqp}} + Z_{\mathrm{ins}} + Z_{\mathrm{NGS}} + Z_{\mathrm{Civil}}\right] \tag{7.6}$$

$$Z_{\mathrm{cont}} = 0.1\left[\sum Z_{\mathrm{eqp}} + Z_{\mathrm{ins}} + Z_{\mathrm{NGS}} + Z_{\mathrm{Civil}}\right] \tag{7.7}$$

Table 7.3 Cost functions for the investigated power plant configurations' equipment

Component	Cost function	Reference year
Compressor	$Z_{\mathrm{c}} = \left(\frac{39.5 m_{\mathrm{a,c}} r_{\mathrm{c}}}{0.9-\eta_{\mathrm{c}}}\right) \ln\left(r_{\mathrm{c}}\right)$	1994 [56]
Gas turbine	$Z_{\mathrm{Gt}} = \left(\frac{266.3 \dot{m}_{\mathrm{Gt}}}{0.92-\eta_{\mathrm{Gt}}}\right) \ln\left(\frac{1}{r_{\mathrm{Gt}}}\right)[1+\exp(0.036 T_{\mathrm{Gt,i}} - 54.4)]$	1994 [56]
Steam turbine	$Z_{\mathrm{St}} = 150\left(\dot{m}_{\mathrm{s}}\, w_{\mathrm{St}}\right)(1+\exp(0.096(T_{\mathrm{St,i}} - 866)))\left(\frac{\dot{m}_{\mathrm{s}}\, w_{\mathrm{St}}}{50000}\right)^{0.67}$	1991 [57]
Combustion chamber	$Z_{\mathrm{cc}} = \left(\frac{25.6 \dot{m}_{\mathrm{a}}}{0.995 - \frac{P_{\mathrm{o,cc}}}{P_{\mathrm{i,cc}}}}\right)[1+\exp(0.018 T_{\mathrm{o,cc}} - 26.4)]$	1994 [56]
HRSG	$Z_{\mathrm{HRSG}} = 3650 F_{\mathrm{P}}\left[f_{\mathrm{g,ec}} f_{\mathrm{s,ec}}\left(\frac{\dot{Q}_{\mathrm{ec}}}{\mathrm{LMTD}_{\mathrm{ec}}}\right)^{0.8} + f_{\mathrm{g,ev}} f_{\mathrm{s,ev}}\left(\frac{\dot{Q}_{\mathrm{ev}}}{\mathrm{LMTD}_{\mathrm{ev}}}\right)^{0.8} + f_{\mathrm{g,sh}} f_{\mathrm{s,sh}}\left(\frac{\dot{Q}_{\mathrm{sh}}}{\mathrm{LMTD}_{\mathrm{sh}}}\right)^{0.8}\right] + 11820 f_{\mathrm{P}} \dot{m}_{\mathrm{s}} + 658 \dot{m}_{\mathrm{g}}^{1.2}$	1991 [58]
Pump	$Z_{\mathrm{p}} = 442\left[\dot{m}_{\mathrm{s}} w_{\mathrm{p}}\right]^{0.71} 1.41\left[1+\left(\frac{1-0.8}{1-\eta_{\mathrm{p}}}\right)\right]$	1991 [57]
Condenser	$Z_{\mathrm{con}} = 248\left(\frac{\dot{Q}_{\mathrm{con}}}{2.2\ \mathrm{LMTD}_{\mathrm{con}}}\right) + 659\left(\frac{\dot{Q}_{\mathrm{con}}}{4.185 \times 11.5}\right)$	1991 [57]
Air cooler	$Z_{\mathrm{AC}} = 1.53 + 1.27(3)(10)^{3.6418+0.4053 log\left(\frac{\dot{Q}_{\mathrm{AC}}}{0.3\ \mathrm{LMTD}_{\mathrm{AC}}}\right)}$	1998 [59]
Heliostat field (land)	$Z_{\mathrm{land}} = 0.62(1.5 A_{\mathrm{land}} + 1.8 \times 10^{5})$	1986 [60]
Heliostat field (mirror)	$Z_{\mathrm{mirror}} = 126 A_{\mathrm{hel}} N_{\mathrm{hel}}$	1986 [60]
Heliostat field (wire)	$Z_{\mathrm{wire}} = \sum_{i=1}^{N_{\mathrm{cell}}} N_{\mathrm{hel,cell},i}\left[0.031 r_{\mathrm{cell},i} + 24\sqrt{\frac{A_{\mathrm{hel}}}{\rho_{\mathrm{cell},i}}}\right]$	1986 [60]

Central tower (tower)	$Z_{\mathrm{Tw}} = \begin{cases} 1.09025 \times 10^6 \exp(0.00879 h_{\mathrm{Tw}}) & h_{\mathrm{Tw}} < 120 \\ 0.78232 \times 10^6 \exp(0.01130 h_{\mathrm{Tw}}) & h_{\mathrm{Tw}} \geq 120 \end{cases}$	1986 [61]
Central tower (piping)	$Z_{\mathrm{piping}} = \left[3600 \frac{r_{\mathrm{outer}}}{1.31} + 420 \frac{r_{\mathrm{int}}}{0.87}\right] h_{\mathrm{Tw}} + 90000 \frac{r_{\mathrm{int}}}{0.87}$	2010 [40]
Central receiver	$Z_{\mathrm{rec}} = A_{\mathrm{rec}}[79 T_{\mathrm{rec,\ o}} - 42000]$	1996 [62]
Mechanical chiller	$Z_{\mathrm{IC}} = 500(\dot{W}_{\mathrm{net,add}})$	2013 [63]
Water treatment	$Z_{\mathrm{wtr}} = 2.03 \times 10^6 \left(\frac{\dot{W}_{\mathrm{net}}}{110}\right)^{0.8}$	2010 [64]
Generator	$Z_{\mathrm{G}} = 4 \times 10^6 \left(\frac{\dot{W}_{\mathrm{net}}}{160}\right)^{0.7} + 10^7 \left(\frac{\dot{W}_{\mathrm{net}}}{120}\right)^{0.65}$	1991 [57]
Steam turbine auxiliary	$Z_{\mathrm{St,\ aux}} = 10^7 \left(\frac{\dot{W}_{\mathrm{net}}}{75}\right)^{0.7}$	1991 [57]
Gas turbine auxiliary	$Z_{\mathrm{Gt,\ aux}} = 4 \times 10^6 \left(\frac{\dot{W}_{\mathrm{net}}}{160}\right)^{0.7}$	1991 [57]
Civil engineering (CCC)	$Z_{\mathrm{Civil,CCC}} = 66.9 \times 10^6 \left(\frac{\dot{W}_{\mathrm{net}}}{144}\right)^{0.8}$	1995 [58]
Natural gas branching	$Z_{\mathrm{brs}} = 219000 \left(\frac{\dot{m}_{\mathrm{f}}}{14.4}\right)^{0.7} + 221000$	1995 [58]
Pressure reduction station	$Z_{\mathrm{prs}} = 1.27 \times 10^6 \left(\frac{\dot{m}_{\mathrm{f}}}{14.4}\right)^{0.7}$	1998 [58]

$$Z_{\text{dec}} = 0.05\left[\sum Z_{\text{eqp}} + Z_{\text{ins}} + Z_{\text{NGS}} + Z_{\text{Civil}}\right] \tag{7.8}$$

While, the plant operating cost is calculated by considering water and fuel consumption expenses as well as the penalty cost for carbon dioxide emission. The other important factors in economic analysis of the power plant and proposed methods annual operating and maintenance costs are listed in Table 7.4. It is strongly recommended to refer to the previously published papers by the authors about power plant thermoeconomic analysis [27, 67], hybridization [30–33, 68], heliostat field collector [41–43], and inlet air cooling technologies [26] for a more detailed presentation of the developed mathematical formulation.

The economic indicator selected for this investigation is the plant's levelized cost of electricity (LCOE) which is calculated as follows [40]:

$$\text{LCOE} = \frac{\alpha Z_{\text{inv}} + \beta Z_{\text{dec}} + Z_{\text{opt}} + Z_{\text{mai}} + Z_{\text{lab}}}{W_{\text{net}}} \tag{7.9}$$

where α and β are LCOE coefficients defined as follows [40]:

Table 7.4 Annual maintenance and repair costs, contract services annual financial requirements, and plant staffs' annual salaries [26, 40, 51]

Parameter	Assigned value
Maintenance:	
Civil engineering	1%
Turbomachinery components	2%
Heliostat field mirror	3%
Volumetric air receiver	4%
Central tower	4%
Mechanical chiller	6%
Contract service: (for heliostat field)	
Contract service for ground keeping	$10^5\left(\frac{A_{\text{hel}}N_{\text{hel}}}{854{,}000}\right)^{0.5}$
Contract service for mirror washing	$3.5 \times 10^5\left(\frac{A_{\text{hel}}N_{\text{hel}}}{854{,}000}\right)$
Contract service for control system	100,000 US$/year
Contract service for water treatment (conventional combined cycle only)	$1.45 \times 10^5\left(\frac{\dot{W}_{\text{net}}}{110}\right)$
Staff salary:	
Plant manager annual salary	$0.5 \times 95{,}000$
Plant engineer annual salary	$1 \times 92{,}000$
Maintenance supervisor annual salary	$2 \times 48{,}000$
Power block technician annual salary	$6 \times 40{,}000$
Solar field technician annual salary	$\left[1 + 3\left(\frac{A_{\text{hel}}N_{\text{hel}}}{100000}\right)\right] \times 40{,}000$
Operation manager annual salary	$2 \times 84{,}000$
Control room operator annual salary	$\left[3 + 2\left(\frac{A_{\text{hel}}N_{\text{hel}}}{100000}\right)\right] \times 40{,}000$

Table 7.5 Economic model design parameters and constraints [40, 51, 69–71]

Parameter	Assigned value
Interest rate	7%
Insurance rate	1%
Construction period (year)	2
Operation period (year)	25
Decommissioning period (year)	2
Demineralized water cost (US$/m^3)	1.15
Fuel cost (US$/GJ)	2.53
CO_2 emission penalty cost (US$/tonne$CO_2$)	40
Electricity price (US$/kWh)	0.07

$$\alpha = \left[\frac{[1+i]^{N_{con}}-1}{N_{con}i}\right]\left[\frac{i[1+i]^{N_{opt}}}{[1+i]^{N_{opt}}-1}\right] + r_{insur} \tag{7.10}$$

$$\beta = \left[\frac{[1+i]^{N_{dec}}-1}{N_{dec}i[1+i]^{N_{dec}-1}}\right]\left[\frac{i}{[1+i]^{N_{opt}}-1}\right] \tag{7.11}$$

All design variables for the thermoeconomic model are tabulated in Table 7.5. It should be noted that the thermoeconomic analysis of the proposed configurations consists of multiple stages. The first stage is to conduct a steady-state analysis of the plant in order to calculate the necessary air mass flow rate to achieve the design capacity at the ISO conditions. Afterward, transient analysis is performed to investigate the effect of variation in the ambient air temperature and humidity ratio as well as the available solar radiation during the year on the plant's thermoeconomic outputs. Noting that analysis is accomplished by having time steps of 1 h implying that 8760 instances were considered during a year. Nevertheless, plant capacity factor of 0.71 was selected to represent a more accurate and realistic scenario [40]. In consequence, the plant is only operational at full load from 6 am to 11 pm to fit well with demand curve's high-load periods.

7.4 Results and Discussion

7.4.1 Simple Gas Turbine

Initially, results concerning the simple gas turbine cycle are presented. The tabulated results in Table 1.6 must be taken as a reference to evaluate the proposed carbon dioxide emission reduction approaches effectiveness on different aspects of the plant. As it is presented in Table 7.6, the simple gas turbine plant annual energy efficiency and specific CO_2 emission, irrespective of its capacity, are 31.4% and 628.0 kgCO_2/MWh, respectively. Nevertheless, the plant annual fuel consumption,

Table 7.6 Simple gas turbine power plant's thermoeconomic results

Parameter	Capacity					
	1 MWe	5 MWe	10 MWe	50 MWe	100 MWe	500 MWe
Annual generated electricity (GWhe)	5.6	27.8	55.7	278.4	556.9	2784.5
Annual overall energy efficiency (%)	31.4	31.4	31.4	31.4	31.4	31.4
Specific CO_2 emission ($kgCO_2$/MWhe)	628.0	628.0	628.0	628.0	628.0	628.0
Annual fuel consumption (tonne)	1270	6360	12,720	63,580	127,170	635,830
Total capital cost (MUS$)	2.9	9.0	15.3	55.2	98.2	390.0
LCOE (US$/MWh)	128.1	93.6	86.5	76.7	74.1	69.9

electricity generation, and total capital investment are directly proportional to its design capacity. Moreover, the plants' LCOE values are abated as their capacity increases such that the costs of generating 1 MWh of electricity are 128.1 US$, 93.6 US$, 86.5 US$, 76.7 US$, 74.1 US$, and 69.9 US$ for plant capacities of 1MWe to 500 MWe, respectively.

7.4.2 Gas Turbine with Bottoming Cycle

In this section, a steam turbine bottoming cycle was integrated into the simple gas turbine power plant to study its impacts on the plant overall thermoeconomic performance indicators including its LCOE and specific CO_2 emission. Results concerning the effects of a steam turbine bottoming cycle integration on gas turbine power plant thermoeconomic performance indicators are listed in Table 7.7. It should be noted that the assigned capacity is the combined-cycle net power output at ISO conditions. Moreover, DOSH value is selected such that the plant LCOE is minimized. One can clearly notice that high ambient air temperature negative effect on the plant annual generated electricity is less significant. For instance, a 50 MWe power plant must generate 310.3 GWh (capacity factor of 0.71) at ISO conditions annually. For the simple gas turbine cycle, the annually generated electricity drops to 278.4 GWh due to high ambient air temperature of the Abu Dhabi. Nevertheless, high ambient air temperature reduces the combined-cycle annual power output to 285.4 GWh. In other words, the bottoming cycle implementation enhances the annually generated electricity by 2.5%.

Moreover, the combined-cycle energy efficiency is significantly greater than that of a simple gas turbine cycle. Approximately, bottoming cycle incorporation leads to 16–17% point improvement in the plant annual overall energy efficiency. Thus, the plant fuel consumption is abated considerably. It should be noted that fuel consumption reduction is more significant as the plant capacity increases. For a 1 MWe power plant, having a bottoming cycle reduces the plant's annual fuel consumption by 413 tonne of CH_4 (32.5%). While, annual fuel consumption is decreased by 205,290 tonne (32.3%) for a 500 MWe power plant. Overall, fuel consumption can be reduced by about one third of its initial value with integration of a steam bottoming

Table 7.7 Gas turbine with bottoming cycle integration power plant's thermoeconomic results

Parameter	Capacity					
	1 MWe	5 MWe	10 MWe	50 MWe	100 MWe	500 MWe
DOSH	0.40	0.45	0.45	0.25	0.25	0.7
Annual generated electricity (GWhe)	5.7	28.5	57.0	285.4	570.9	2845.3
Annual overall energy efficiency (%)	47.8	47.7	47.7	48.1	48.1	47.5
Specific CO_2 emission ($kgCO_2$/MWhe)	413.5	414.1	414.1	410.9	410.9	416.1
Annual fuel consumption (tonne)	857	4291	8582	42,652	85,304	430,540
Total capital cost (MUS$)	6.1	19.1	32.1	114.4	203.6	861.9
LCOE (US$/MWh)	325.3	144.5	115.5	83.5	76.9	70.1

cycle. In consequence of the reported fuel consumption reduction, the plant-specific CO_2 emission drops by about 212–217 $kgCO_2$/MWh (34–35%).

Unlike the thermodynamic aspect of the bottoming cycle integration, its economic aspect is not favorable. In general, the combined-cycle plant total capital cost is more than twice the required investment for a simple gas turbine power plant. Obviously, as the plant capacity rises, the required capital investment for the bottoming cycle integration increases. For instance, a 1 MWe combined-cycle power plant requires an additional 3.2 MUS$ (110.3%) as compared with a simple gas turbine power plant. While, a 50 MWe and 500 MWe combined cycles additional required capital costs are 59.2 MUS$ (107.2%) and 471.9 MUS$ (121.0%), respectively. Due to the significant rise in the plant's required capital investment, its LCOE, which is a combination of the plant thermodynamic and economic performance indicators, increases with the addition of a bottoming cycle. Increase in the LCOE is more significant for plants with lower capacities. For a 1 MWe power plant, having combined-cycle configuration increases the cost of generating electricity by 197.2 US$ (153.4%) from 128.1 US$ to 325.3 US$. Whereas, cost of electricity for a 500 MWe power plant only rises by 0.2 US$ (0.3%) if combined-cycle configuration is considered instead of a simple gas turbine cycle. Therefore, bottoming cycle integration (steam turbine cycle) is a more appropriate technique for large capacity power plants.

7.4.3 Gas Turbine with Inlet Air Cooling

In this section, another carbon dioxide reduction approach, i.e., inlet air cooling, is studied for a simple gas turbine power plant. In fact, inlet air cooling technology is mainly considered as a power augmentation approach for plants located in areas with hot climate. Thermoeconomic performance indicators for the plant with inlet air cooling are tabulated in Table 7.8. The main contribution of the inlet air cooling technique is the additional power generated by the plant. Nevertheless, part of the additionally produced electricity is utilized to operate the mechanical chiller. Overall, the plant annual generated electricity is improved by approximately 9%.

Table 7.8 Gas turbine with inlet air cooling power plant's thermoeconomic results

Parameter	Capacity					
	1 MWe	5 MWe	10 MWe	50 MWe	100 MWe	500 MWe
Annual generated electricity (GWhe)	6.1	30.4	60.7	303.7	607.4	3036.8
Annual overall energy efficiency (%)	31.7	31.7	31.7	31.7	31.7	31.7
Specific CO_2 emission ($kgCO_2$/MWhe)	623.2	623.2	623.2	623.2	623.2	623.2
Annual fuel consumption (tonne)	1380	6880	13,760	68,820	137,640	688,190
Total capital cost (MUS$)	3.0	9.3	15.8	58.0	103.8	418.1
LCOE (US$/MWh)	122.8	91.2	84.7	75.8	73.4	69.5

Consequently, plant annual overall energy efficiency and specific CO_2 emission are improved by 0.3% points and 0.8% from 31.4% and 628.0 kg/MWh to 31.7% and 623.2 kg/MWh, respectively.

In large scale, for instance, 500 MWe power plant, implementation of a simple inlet air cooling technique can significantly reduce the annual CO_2 emission by more than 14,500 tonne for generating the same amount of electricity (3036.8 GWh). Similarly, fuel consumption abatement is more notable for large capacity power plants. Nevertheless, one may argue that the plant annual fuel consumption is increased for the case of inlet air cooling addition. It should be noted that comparing the annual fuel consumption associated with the simple gas turbine cycle with and without inlet air cooling results in a false conclusion. Noting that inlet air cooling improves the plant annually produced power, while the plant fuel consumption rises as well. Hence, to generate the same amount of electricity with a simple gas turbine cycle without inlet air cooling, more fuel will be required. Specific fuel consumption can be considered as a more appropriate indicator of the investigated configurations environmental performance. To generate 1 MWh of electricity using a simple gas turbine power plant with and without inlet air cooling 226.6 $kgCH_4$ and 228.4 $kgCH_4$ are required.

Economic aspect of an inlet air cooling mechanical chiller implementation in a simple gas turbine power plant is also investigated. Obviously, the mechanical chiller addition necessitates additional initial investment which leads to a rise in the plant total capital cost. As the plant capacity increases, the additional initial investment associated with the integrated inlet air cooling technology rises. For instance, only 0.1 MUS$ (3.4%) is needed to integrate an inlet air cooling for a 1 MWe power plant, whereas the required additional investment increases to 28.1 MUS$ (7.2%) for a 500 MWe plant. Nonetheless, the reported LCOE for this case is the lowest among all the investigated configurations. Overall, the plant LCOE is improved by using an inlet air cooler for simple gas turbine power plant, while its specific CO_2 emission abatement is not as notable as a bottoming cycle integration. As a result, it can be concluded that bottoming cycle integration significantly reduces the plant-specific CO_2 emission, while inlet cooling technique manages to achieve improvement in both environmental and economic aspects of the plant though in a smaller scale. Plant LCOE is reduced by 5.3 US$/MWh (4.1%) and 0.4 US$/MWh (0.6%) for 1 MWe and 500 MWe power plants, respectively.

7.4.4 Gas Turbine with Heliostat Field

Another possible approach to reduce the rate of CO_2 emission associated with power generation. In this technique, part of the required thermal energy is provided by solar thermal collectors. Due to high operating temperature of gas turbine power plants, high temperature solar thermal collectors must be employed. Therefore, heliostat field collector is a viable candidate for integration in gas turbine power plants.

It must be mentioned that the number of mirror is selected such that the maximum solar thermal energy penetration without thermal energy storage implementation is assessed. To do so, spring equinox noon is considered as the design period to determine the number of mirrors required to achieve solar multiple close to one during the specified instance. For this section, 500 MWe power plant was not studied as the necessary heliostat field collector must contain more than 10,000 mirrors to achieve a similar annual solar share. Having 10,000 of mirrors is impractical and economically unjustified since mirrors must be situated considerably far from the tower and their thermal output will become insignificant. It is possible to consider multi-tower schemes for large capacity power plants which are beyond the scope of this research work.

Results concerning the thermoeconomic advantages and disadvantages of simple gas turbine hybridization using heliostat field collector are shown in Table 7.9. It is clear that the number of mirrors within the integrated solar field is directly proportional to the plant capacity. The reason behind the difference between the reported solar share for the 1 MWe and other power plants is that adding a single mirror to the field has a considerable thermal output as compared with the required thermal energy to operate the plant. Thus, it was more appropriate to integrate a field with smaller mirrors for the 1 MWe power plant to attain an approximately similar annual solar share. Moreover, the annual percentage of solar energy loss corresponds to losses in the receiver and instances of higher than allowable solar thermal input. In other words, it does not consider the field annual weighted efficiency into account. In fact, it is the ratio of solar energy utilized in the tower to heat the air stream over the overall solar thermal output provided by the field.

In regard to the thermodynamic performance of the plant, hybridization does not have any considerable impact on the plant annual generated electricity. Nevertheless, heliostat field implementation notably degraded the plant annual energy efficiency due to the aforementioned losses in the plant receiver. Noting that the energy efficiency is calculated by considering the amount of energy provided by the solar collector. Consequently, the field efficiency is not taken into consideration in determining the plant energy efficiency. The most important contribution of heliostat field integration is the decrease in the plant-specific CO_2 emission and annual fuel consumption. Overall, the plant-specific CO_2 emission can be reduced by more than 100 kg/MWh by providing about 20% of the required thermal energy by solar thermal collectors. In particular, the aforesaid reduction can significantly contribute toward a more environmentally friendly power generation for large capacity power plants. For instance, hybridization is capable of reducing the annual fuel

Table 7.9 Gas turbine power plant with heliostat field integration thermoeconomic results

	Capacity					
Parameter	1 MWe	5 MWe	10 MWe	50 MWe	100 MWe	500 MWe
Number of mirrors	35	179	366	2184	4550	*Not applicable*
Annual solar share (%)	17.9	19.4	19.8	20.4	19.6	
Solar field annual thermal output (GWh)	6.9	33.3	66.5	336.2	604.1	
Annual percentage of solar energy loss (%)	53.1	47.8	46.8	45.8	41.8	
Annual generated electricity (GWhe)	5.7	28.5	57.1	285.6	571.6	
Annual overall energy efficiency (%)	25.9	26.7	26.8	26.9	27.6	
Specific CO_2 emission ($kgCO_2$/MWhe)	523.5	510.1	507.4	503.1	507.5	
Annual fuel consumption (tonne)	1080	5290	10,531	52,250	105,490	
Total capital cost (MUS$)	16.8	29.0	43.0	158.2	300.0	
LCOE (US$/MWh)	541.8	195.8	150.1	115.2	110.8	

consumption and CO_2 emission of a 100 MWe power plant by about 22000 tonne of CH_4 and 69,000 tonne of CO_2, respectively.

Nevertheless, hybridization is the most expensive approach considered in this study. In particular, hybridization is economically unjustified for small capacity power plants. As compared with the initial investment of a 1 MWe power plant, hybridization increases its total capital investment by 13.9 MUS$ (479.3%). Hybridization is more acceptable for power plants with medium capacity. For example, total capital investment of 10 and 100 MWe power plants rises by 27.7 MUS$ (181.0%) and 201.8 MUS$ (205.5%), respectively. The reason is that the field annual weighted efficiency is extremely low for large capacities, thereof, a higher number of mirrors must be utilized which considerably affects the plant initial investment.

The plant LCOE experiences a substantial rise in result of the heliostat field integration. Heliostat field integration leads to a growth in the plant LCOE such that generating 1 MWh of electricity costs an additional 413.7 US$ (323.0%), 102.2 US$ (109.2%), 63.2 US$ (73.5%), 38.5 US$ (50.2%), and 36.7 US$ (49.5%) for 1 MWe, 5 MWe, 10 MWe, 50 MWe, and 100 MWe power plants, respectively. Clearly, reduction in the plant fuel consumption becomes a more significant factor in large capacity power plants which leads to more economically favorable results for large capacity power plants. Nevertheless, one should note that bottoming cycle integration is a more economical and environmental technique for simple gas turbine power plants as the plant-specific CO_2 emission and LCOE are lower for the bottoming cycle integration than heliostat field implementation regardless of the plant capacity.

7.4.5 *Gas Turbine with Heliostat Field, Inlet Air Cooling, and Bottoming Cycle*

In this section, all the proposed techniques investigated in this study are considered for integration in a simple gas turbine power plant to evaluate the maximum attainable carbon dioxide emission reduction by having an inlet air cooler in a hybrid combined-cycle power plant. Due to the higher annual overall efficiency of a combined cycle as compared with the gas turbine cycle, lower number of mirrors is necessary for plant hybridization. It can be concluded that power plant hybridization is more suitable for combined-cycle power plants as their energy efficiency leads to a more cost effective integrated solar field. It must be noted that DOSH value of 0.63 is considered in this section based on optimization results presented by Saghafifar and Gadalla [12].

It is clear that using all three approaches can have a considerable impact on the plant-specific CO_2 emission and annual fuel consumption as it is shown in Table 7.10. In particular, the amount of carbon dioxide emitted for generating 1 MWe of electricity reduces by about 285–300 kg (45–47.5%). Therefore, annual carbon dioxide emission abatement for 1 MWe, 5 MWe, 10 MWe, 50 MWe, and 100 MWe power plants are 1800 tonne, 9200 tonne, 18,700 tonne, 94,000 tonne, and

Table 7.10 Gas turbine power plant with heliostat field, bottoming cycle and inlet air cooling integrations thermoeconomic results

	Capacity					
Parameter	1 MWe	5 MWe	10 MWe	50 MWe	100 MWe	500 MWe
Number of mirrors	23	118	241	1346	3255	*Not applicable*
Annual solar share (%)	17.6	19.6	19.9	20.3	20.4	
Solar field annual thermal output (GWh)	4.5	22.4	44.7	222.1	446.5	
Annual percentage of solar energy loss (%)	49.4	43.4	42.2	40.7	40.8	
Annual generated electricity (GWhe)	6.3	31.5	63.0	315.2	630.5	
Annual overall energy efficiency (%)	40.8	41.7	41.9	42.1	42.1	
Specific CO_2 emission ($kgCO_2$/MWhe)	342.6	333.5	331.8	329.9	329.5	
Annual fuel consumption (tonne)	783	3819	7604	37,817	75,545	
Total capital cost (MUS$)	19.6	36.7	55.0	184.1	353.2	
LCOE (US$/MWh)	620.2	210.8	154.0	102.4	97.4	

188,200 tonne for the same amount of power generated, respectively. Nevertheless, the economic results are not very favorable. In particular, using all three methods requires the highest initial investment among all the investigated configurations. Consequently, the plant LCOE notably rises by 492.1 US$/MWh (384.2%), 117.2 US$/MWh (125.2%), 67.5 US$/MWh (78.0%), 25.7 US$/MWh (33.5%), and 23.3 US$/MWh (31.4%) for 1 MWe, 5 MWe, 10 MWe, 50 MWe, and 100 MWe power plants, respectively. In general, inlet air cooling must be considered for power plants located in hot climates, irrespective of their capacities, while bottoming cycle integration must be implemented for large capacity power generation only. Power plant hybridization without thermal energy storage must only be considered as the final approach to further improve the environmental aspect of a plant, in particular for medium to large-scale power generation. Otherwise, bottoming cycle integration can have a more favorable impact on simple gas turbine power plant's thermoeconomic performance indicators.

7.5 Conclusions

In this study, three different approaches for carbon dioxide emission reduction in a simple gas turbine power plant are investigated comprising of inlet air cooling using a mechanical chiller, bottoming cycle integration and solarized gas turbine hybridization using heliostat field collector. A thermoeconomic comparative assessment between the suggested methods is conducted based on their influences on the plant-specific carbon dioxide emission and LCOE for different capacities. In addition, all three studied methods are utilized simultaneously to evaluate the performance of the plant that benefits from all the recommended solutions to further decrease the specific carbon dioxide emission.

Steam bottoming cycle implementation reduces the plant-specific CO_2 emission by about 212–217 kgCO_2/MWh (34–35%). For a 1 MWe power plant, having combined-cycle configuration increases the cost of generating electricity by 197.2 US$ (153.4%); whereas, cost of electricity for a 500 MWe power plant only rises by 0.2 US$ (0.3%) if combined-cycle configuration is considered instead of a simple gas turbine cycle. Moreover, it is concluded that bottoming cycle integration significantly reduces the plant-specific CO_2 emission, while inlet cooling technique manages to achieve improvement in both environmental and economic aspects of the plant even in a smaller scale. In large scale, for instance 500 MWe power plant, implementation of a simple inlet air cooling technique can significantly reduce the annual CO_2 emission by more than 14,500 tonne for generating the same amount of electricity (3036.8 GWh).

Furthermore, hybridization is the most expensive approach considered in this study. Overall, the plant-specific CO_2 emission can be reduced by more than 100 kg/MWh by providing about 20% of the required thermal energy by solar thermal collectors. In addition, heliostat field integration leads to a rise in the plant LCOE

such that generating 1 MWh of electricity costs an additional 413.7 US$ (323.0%) and 36.7 US$ (49.5%) for 1 MWe and 100 MWe power plants, respectively. In general, inlet air cooling must be considered for power plants located in hot climates, irrespective of their capacities, while bottoming cycle integration must be implemented for large capacity power generation. Power plant hybridization without thermal energy storage must only be considered as the final approach to further improve the environmental aspect of a plant, in particular for medium to large-scale power generation. Otherwise, bottoming cycle integration can have a more favorable impact on simple gas turbine power plant's thermoeconomic performance indicators.

Nomenclature

A	Surface area [m^2]
f	Factor
h	Height [m]
i	Loan interest rate
LHV	Lower heating value [kJ/kg]
LMTD	Log mean temperature difference
$\dot{m}$	Mass flow rate [kg/s]
N	Number, number of years
P	Pressure [kPa]
$\dot{Q}$	Rate of thermal energy [kWth]
r	Pressure ratio, radius [m]
r_{insur}	Insurance rate
T	Temperature [K]
W	Generated electricity [MWh]
$\dot{W}$	Power [kWe]
w	Specific work [kJ/kg]
Z	Capital investment cost [US$]

Abbreviation

CCC	Combined-cycle configuration
CEPCI	Chemical engineering plant cost index
DNI	Direct normal radiation
DOSH	Degree of superheating
HRSG	Heat recovery steam generator
LCOE	Levelized cost of electricity

Greek Symbols

α, β	Thermoeconomic coefficients
ΔT	Temperature difference [K]
η	Efficiency
ρ	Mirror reflectivity, density [kg/m^3]

Subscript

AC	Air cooler
a	Air
add	Additional
ann	Annual
at	Attenuation
aux	Auxiliary
brs	Branching pipeline
c	Compressor
cc	Combustion chamber
cell	Cell
civil	Civil Engineering
con	Construction, condenser
cont	Contingency
cos	Cosine
dec	Decommissioning
ec	Economizer
ele	Electrical
eqp	Equipment
ev	Evaporator
ex	Exhaust
f	Fuel, field
G	Generator
g	Gas
Gt	Gas turbine
hel	Heliostat
HRSG	Heat recovery steam generator
i	Inlet
IC	Inlet cooling
if	Indirect factor
ins	Installation
int	Internal
inv	Investment
lab	Labor
land	Land
M	Mechanical
mai	Maintenance
mirror	Mirror
NGS	Natural gas branching
net	Net
o	Outlet
opt	Operation, optical
outer	Outer
p	Pump, pressure

pinch	Pinch
piping	Piping
prs	Pressure reduction station
rec	Receiver
s	Steam
sat	Saturated
sh	Superheater
sol	Solar
sp	Spillage
St	Steam turbine
s&b	Shading and blocking
Tw	Central tower
w	Weighted
wire	Wiring
wtr	Water treatment

References

1. Al-Alili A, Hwang Y, Radermacher R (2014) Review of solar thermal air conditioning technologies. Int J Refrig 39:4–22
2. Kaushik SC, Reddy VS, Tyagi SK (2011) Energy and exergy analyses of thermal power plants: a review. Renew Sust Energ Rev 15(4):1857–1872
3. Herzog B, Jonathan P, Baumert KA (2005) Navigating the numbers- greenhouse gas data and international climate policy. United States of America, Hyacinth Billings
4. Sheu EJ, Mokheimer EM, Ghoniem AF (2015) Dry redox reforming hybrid power cycle: performance analysis and comparison to steam redox reforming. Int J Hydrog Energy 40 (7):2939–2949
5. Sheu EJ, Ghoniem AF (2014) Redox reforming based, integrated solar-natural gas plants: reforming and thermodynamic cycle efficiency. Int J Hydrog Energy 39(27):14817–14833
6. Freeman J, Hellgardt K, Markides C (2015) An assessment of solar-powered organic Rankine cycle systems for combined heating and power in UK domestic applications. Appl Energy 138:605–620
7. Freeman J, Hellgardt K, Markides C (2017) Working fluid selection and electrical performance optimisation of a domestic solar-ORC combined heat and power system for year-round operation in the UK. Appl Energy 186:291–303
8. Zhai R, Li C, Chen Y, Yang Y, Patchigolla K, Oakey J (2016) Life cycle assessment of solar aided coal-fired power system with and without heat storage. Energy Convers Manag 111:453–465
9. Hanak D, Biliyok C, Manovic V (2015) Efficiency improvements for the coal-fired power plant retrofit with CO 2 capture plant using chilled ammonia process. Appl Energy 151:258–272
10. Gazzani M, Turi D, Ghoniem A, Macchi E, Manzolini G (2014) Techno-economic assessment of two novel feeding systems for a dry-feed gasifier in an IGCC plant with Pd-membranes for CO 2 capture. Int J Greenhouse Gas Control 25:62–78
11. Kang C, Brandt A, Durlofsky LJ (2014) Optimizing heat integration in a flexible coal–natural gas power station with CO 2 capture. Int J Greenhouse Gas Control 31:138–152
12. Lee U, Mitsos A, Han C (2016) Optimal retrofit of a CO2 capture pilot plant using superstructure and rate-based models. Int J Greenhouse Gas Control 50:57–69

13. Tola V, Pettinau A (2014) Power generation plants with carbon capture and storage: a techno-economic comparison between coal combustion and gasification technologies. Appl Energy 113:1461–1474
14. Singh OK (2016) Performance enhancement of combined cycle power plant using inlet air cooling by exhaust heat operated ammonia-water absorption refrigeration system. Appl Energy 180:867–879
15. Carapellucci R, Giordano L (2015) Upgrading existing coal-fired power plants through heavy-duty and aeroderivative gas turbines. Appl Energy 156:86–98
16. Meacock A, White A (2006) The effect of water injection on multispool gas turbine behavior. J Eng Gas Turbines Power 128(1):97–102
17. Zhang G, Zheng J, Yang Y, Liu W (2016) A novel LNG cryogenic energy utilization method for inlet air cooling to improve the performance of combined cycle. Appl Energy 179:638–649
18. Yang C, Yang Z, Cai R (2009) Analytical method for evaluation of gas turbine inlet air cooling in combined cycle power plant. Appl Energy 86(6):848–856
19. Brodrick PG, Kang CA, Brandt AR, Durlofsky LJ (2015) Optimization of carbon-capture-enabled coal-gas-solar power generation. Energy 79:149–162
20. Kang C, Brandt A, Durlofsky L (2011) Optimal operation of an integrated energy system including fossil fuel power generation, CO 2 capture and wind. Energy 36(12):6806–6820
21. Hu Y, Li H, Yan J (2012) Techno-economic evaluation of the evaporative gas turbine cycle with different CO2 capture options. Appl Energy 89(1):303–314
22. Wang F, Zhao J, Li H, Deng S, Yan J (2017) Preliminary experimental study of post-combustion carbon capture integrated with solar thermal collectors. Appl Energy 185:1471–1480
23. Gunasekaran S, Mancini N, El-Khaja R, Sheu E, Mitsos A (2014) Solar–thermal hybridization of advanced zero emissions power cycle. Energy 65:152–165
24. Poullikkas A (2005) An overview of current and future sustainable gas turbine technologies. Renew Sustain Energy Rev 9:409–443
25. Tsujikawa Y, Sawada T (1985) Characteristics of hydrogen-fueled gas turbine cycle with intercooler, hydrogen turbine and hydrogen heater. Int J Hydrog Energy 10(10):677–683
26. Saghafifar M, Gadalla M (2015) Innovative inlet air cooling technology for gas turbine power plants using integrated solid desiccant and Maisotsenko cooler. Energy 87:663–677
27. Saghafifar M, Poullikkas A (2015) Thermo-economic optimization of air bottoming cycles. J Power Technol 95(3):211–220
28. Beretta GP, Iora P, Ghoniem AF (2013) Allocating electricity production from a hybrid fossil-renewable power plant among its multi primary resources. Energy 60:344–360
29. Sheu E, Mitsos A, Eter A, Mokheimer E, Habib M, Al-Qutub A (2012) A review of hybrid solar–fossil fuel power generation systems and performance metrics. J Solar Energy Eng 134 (4):041006
30. Saghafifar M, Gadalla M (2016) Thermo-economic analysis of conventional combined cycle hybridization: United Arab Emirates case study. Energy Convers Manag 111:358–374
31. Saghafifar M, Gadalla M (2016) Thermo-economic analysis of air bottoming cycle hybridization using heliostat field collector: a comparative analysis. Energy 112:698–714
32. Saghafifar M, Gadalla M (2016) Thermo-economic evaluation of water-injected air bottoming cycles hybridization using heliostat field collector: comparative analyses. Energy 119:1230–1246
33. Saghafifar M, Gadalla M (2017) Thermo-economic optimization of hybrid solar Maisotsenko bottoming cycles using heliostat field collector: comparative analysis. Appl Energy 190:686–702
34. Spelling J, Laumert B, Fransson T (2014) A comparative thermoeconomic study of hybrid solar gas-turbine power plants. J Eng Gas Turbines Power 136(1):11801–11810
35. Spelling J, Favrat D, Martin A, Augsburger G (2012) Thermoeconomic optimization of a combined-cycle solar tower power plant. Energy 41(1):113–120
36. Turns SR (1996) An introduction to combustion, 2nd edn. McGraw-hill, New York

37. Kee RJ, Rupley FM, Miller JA (1990) The Chemkin thermodynamic data base. Sandia National Laboratories Report, San Diego
38. Burcat A (1984) Combustion chemistry. In: Thermochemical data for combustion calculations. Springer, New York, pp 455–473
39. Spelling J (2011) Solar gas-turbine power plants- a techno-economic evaluation. Internal Report, KTH, Stockholm
40. Spelling J (2013) Hybrid solar gas-turbine power plants: a thermoeconomic analysis. KTH Royal Institute of Technology, Stockholm
41. Gadalla M, Saghafifar M (2016) Thermo-economic and comparative analyses of two recently proposed optimization approaches for circular heliostat fields: campo radial-staggered and biomimetic spiral. Sol Energy 136:197–209
42. Saghafifar M, Gadalla M (2016) Improvement in spiral heliostat field layout thermo-economic performance by field zoning implementation. In: ASME 2016 power and energy conference and exhibition, Charlotte North Carolina
43. Saghafifar M, Gadalla M (2016) Selecting a proper design period for heliostat field layout optimization using Campo code. In: SPIE optics+ photonics for sustainable energy, San Diego
44. Pacheco JE, Reilly HE, Gregory J, Tyner CE (2000) Summary of the solar two: test and evaluation program, SAND2000-0372C. Distributed by the Office of Scientific and Technical Information, U.S. Department of Energy, Washington, DC
45. Collado FJ (2009) Preliminary design of surrounding heliostat fields. Renew Energy 34 (5):1359–1363
46. Collado FJ, Guallar J (2013) A review of optimized design layouts for solar power tower plants with campo code. Renew Sust Energ Rev 20:142–154
47. Collado FJ, Guallar J (2012) Campo: generation of regular heliostat fields. Renew Energy 46:49–59
48. Besarati SM, Goswami DY (2014) A computationally efficient method for the design of the heliostat field for solar power tower plant. Renew Energy 69:226–232
49. National renewable energy laboratory: typical meteorological year. [Online]. Available: http://apps1.eere.energy.gov/buildings/energyplus/weatherdata_about.cfm?CFID=856623&CFTOKEN=ee4c965b0935ba09-E3B5186A-9E62-5128-A32A2ED20A764672&jsessionid=08D708CC53F27721261D239F9C045DF8.eere. Accessed 10 5 2015
50. Noone CJ, Torrilhon M, Mitsos A (2012) Heliostat field optimization: a new computationally efficient model and biomimetic layout. Sol Energy 86(2):792–803
51. Sandoz R (2012) Thermoeconomic analysis and optimization of air based bottoming cycles for water free hybrid solar gas turbine power plant. Master, Department of Energy Technology, Ecole Polytechnique Federale de Lausanne, KTH, Stockholm
52. Farzaneh-Gord M, Deymi-Dashtebayaz M (2011) Effect of various inlet air cooling method on gas turbine performance. Energy 36:1196–1205
53. Goldsworthy M, White S (2011) Optimisation of a desiccant cooling system design with indirect evaporative cooler. Int J Refrig 34(1):148–158
54. Gareta R, Romeo LM, Gil A (2004) Methodology for the economic evaluation of gas turbine air cooling systems in combined cycle applications. Energy 29(11):1805–1818
55. Peters MS, Timmerhaus KD, West RE (1968) Plant design and economics for chemical engineers. New York, McGraw-Hill
56. Knopf FC (2012) Modeling, analysis and optimization of process and energy systems. Wiley, Hoboken
57. Frangopoulos CA (1991) Intelligent functional approach; a method for analysis and optimal synthesis-design-operation of complex systems. Int J Energy Environ Econ 1(4):267–274
58. Pelster S (1998) Environomic modeling and optimization of advanced combined cycle cogeneration power plants including CO2 separation options, PhD dissertation, Ecole Polytechnique Federale de Lausanne, Lausanne
59. Turton R, Bailie RC, Whiting WB, Shaeiwitz JA (1998) Analysis, synthesis and design of chemical processes. Pearson Education, Upper Saddle River

60. Kistler BL (1986) A user's manual for DELSOL3: a computer code for calculating the optical performance and optimal system design for solar thermal central receiver plants. Sandia National Labs, Livermore
61. Stine WB, Geyer M (1986) Solar energy systems design. Wiley, New Jersey
62. Schwarzbözl PBR, Sugarmen C, Ring A, Crespo MJM, Altwegg P, Enrile J (2006) Solar gas turbine systems: design, cost and perspectives. Sol Energy 80(10):1231–1240
63. Marzouk A, Hanafi A (2013) Thermo-economic analysis of inlet air cooling in gas turbine plants. J Power Technol 93(2):90–99
64. Turchi CS (2010) Parabolic trough reference plant for cost modeling with the solar advisor model (SAM). National Renewable Energy Laboratory, Golden
65. Pitz-Paal R, Dersch J, Milow B (2005) European concentrated solar thermal road-mapping (ECOSTAR). European Commission, Coordinated action sustainable energy systems SES6-CT-2003-502578, Cologne
66. Agency IE (2010) Projected costs of generating electricity. OECD, IEANEA, Paris
67. Saghafifar M, Poullikkas A (2017) Comparative analysis of power augmentation in ABC power plants. Int J Sustainable Energy 36(1):47–60
68. Saghafifar M (2016) Thermo-economic optimization of hybrid combined power cycles using heliostat field collector. American University of Sharjah, Sharjah
69. Infomine, price charts 1 year natural gas prices. [Online]. Available: http://www.infomine.com/investment/metal-prices/natural-gas/1-year/. Accessed 08 06 2015
70. Dubai GO (2015) Average dewa bills for water and electricity, Dubai electricity and water authority, 3 6 2015. [Online]. Available: http://www.dewa.gov.ae/tariff/tariffdetails.aspx. Accessed 11 6 2015
71. Maulbetsch JS, DiFilippo MN (2006) Cost and value of water use at combined cycle power plants. California Energy Commission, Sacramento

Part II
Energy Systems, Components and Applications

Chapter 8
Absorption Power Cycles with Various Working Fluids for Exergy-Efficient Low-Temperature Waste Heat Recovery

Vaclav Novotny, Monika Vitvarova, and Michal Kolovratnik

8.1 Introduction

There are a large number of low-temperature heat sources, holding relatively large potential for power production [1]. Utilization of them is limited due to high cost but also very low efficiency of the conversion systems, especially as the heat source temperature goes to 100 °C and below. At such low temperatures, commercially available technologies, typically ORC, are often too expensive with respect to efficiency and obtained power output. Highest irreversibility typically comes from isothermal boiling and condensation. Therefore researchers are trying to come up with novel power cycles which would effectively transform the low potential heat into power. The novel cycles then provide the potential of the significantly higher efficiency of heat source utilization and thus power production with all the economic and environmental benefits.

Figure 8.1 illustrates three different cases in waste heat recovery in T-S diagrams. First one (Fig. 8.1a) is an ideal trilateral cycle utilizing a maximum of the heat from the heat source (limited only by minimal temperature difference) and rejecting heat to the ambient. A Rankine cycle case is shown in Fig. 8.1b, where heat transfer to the cycle is limited by pinch point (the lower the evaporation pressure and temperature, the higher the heat transfer) and cycle efficiency is limited by heat addition temperature (the higher the evaporation temperature, the higher the cycle efficiency). Also, the heat rejection process needs a finite amount of cooling fluid. Its mass flow will be shown later to affect a parasitic load and the net power production. Lastly, Fig. 8.1c illustrates a case of non-isothermal boiling and condensation Rankine cycle,

V. Novotny (✉) · M. Vitvarova · M. Kolovratnik
Czech Technical University in Prague, Faculty of Mechanical Engineering, Technicka 4, Prague 6, Czech Republic
e-mail: Vaclav.novotny@fs.cvut.cz

S. Nižetić, A. Papadopoulos (eds.), *The Role of Exergy in Energy and the Environment*, Green Energy and Technology,
https://doi.org/10.1007/978-3-319-89845-2_8

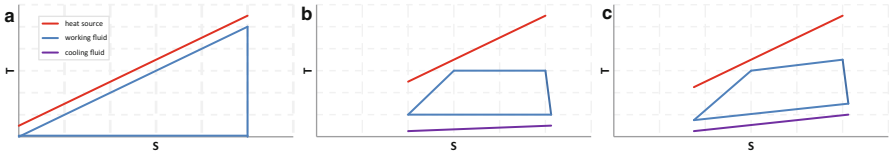

Fig. 8.1 Illustration of waste heat recovery by (**a**) ideal trilateral cycle, (**b**) Rankine cycle, (**c**) Rankine cycle with non-isothermal boiling and condensation fluids

improving the trade-off between the heat transfer and the cycle efficiency and also requiring less cooling fluid for the same mean temperature of heat rejection.

A range of perspective solutions for tapping low-temperature resources includes transcritical cycles [2], where the major problems are high pressures or fluid stability [3], and regardless theoretical advantages only little experimental data have been reported as from [4]. ORC with zeotropic mixtures appears perspective [5] but has issues of reported low heat transfer coefficients in mixtures [6, 7]. The trirlateral flash cycle has issues with inexistence of an efficient two phase expander; eventually, it has throttling loss and problems in system control [3]. Another option partly resulting from zeotropic mixture cycles are absorption power cycles, also referred to as Kalina cycles, which are in focus of this work.

Kalina cycles, or in general principle absorption power cycles (APC), were first proposed and most commonly considered using an ammonia-water mixture as a working fluid [8]. As so it has been partly commercialized, but technical problems from corrosion due to the working fluid or very high pressures [9, 10] limit further widespread. There is, however, a wide range of other mixtures of fluids that can be used in absorption cycles [11]. In a work of Novotny and Kolovratnik [12], it was shown that previous research using alternative working fluids had very limited attention to other fluids than water-ammonia mixture. In summary, there were in the past considered aqueous solutions of one or more inorganic salts or hydroxide (LiBr, LiCl, $CaCl_2$, $CaBr_2$, ZnBr, KOH) and organic fluids as amyl acetate-CO_2 mixture and mixture of hydrocarbons. The same work compared the performance of the LiBr, LiCl and $CaCl_2$ solutions with water-ammonia Kalina cycle and ORC with various pure working fluids. Accounting also for a parasitic load due to different means of heat rejection, it was shown that for a heat source below approximately 120 °C, absorption power cycles with salt solutions have superior performance to one with water-ammonia mixture as well as to single component ORC. For higher heat source temperatures, the situation becomes opposite. Recent work of Eller et al. [5] investigated alcohol mixtures as working fluids for Kalina cycle configuration KCS-34 with two recuperators: using sensible heat source and specified inlet and outlet temperatures of a heat sink. In comparison with pure component ORC and mixture ORC at both subcritical and supercritical pressures and for a heat source temperature range 200–400 °C, the best performance is provided by zeotropic mixtures, nearly identical for both sub- and supercritical pressures. Pure fluids ORC and alcohol mixtures APC have a relatively similar performance with slightly different results for different temperatures; pure fluids in supercritical state achieve

such performance only in selected temperatures fitting to a specific fluid. Ammonia-water APC performance is limited here due to adopted limitations on maximal system pressure.

Ionic liquids (IL) were proposed for many applications. According to Zheng et al. [13], imidazolium-based IL have the potential for various thermodynamic absorption cycles. Other work of Robbins and Garimella [14] suggests a combination of amyl acetate and CO_2 for waste heat recovery, but a comparison of performance with other standard power production systems was not made.

Here is presented a performance comparison of APC in waste heat recovery with working fluids selected from different representative groups proposed in the literature. Apart from that, it is compared with the performance of ORC with representative pure working fluids in sub- and supercritical pressures as well as zeotropic mixture ORC (only subcritical pressure).

8.2 Configurations and Models Description

8.2.1 Boundary Conditions

The heat source considered in this work is hot air at temperatures 100 °C and 200 °C, and the heat sink is assumed as air at 15 °C (288.15 K). Heat rejection takes place in an air cooled condenser for which there is specified design pressure drop that needs to be overcome by a fan. Values of the assumptions taken in the model are summarized in Table 8.1. Note that unlike in some other works, the pressure of working fluids is not limited by lower or upper bound. Rather there will be a discussion of an impact of resulting pressure on equipment design.

8.2.2 Cycle Evaluation

An important issue of many power systems is the parasitic load of auxiliary systems of the plant. Major parasitic load is the system for heat rejection (pumps, fans), especially for systems with low energy efficiency (as are the low-temperature systems). Literature often assumes certain ambient conditions, cooling water temperature, etc., but neglects the associated power consumption. To provide more realistic results, the power associated with heat rejection is included here.

Table 8.1 Common parameters of the models

T_0 [°C]	p_0 [kPa]	η_{exp} [%]	η_{pump} [%]	η_{fan} [%]	$\Delta T_{eva,\ min}$ [°C]	$\Delta T_{cond,\ min}$ [°C]	Δp_{air} [Pa]
15	101.325	80	70	70	20	10	150

Models are based on mass and energy balance in their nodes. Pinch-point analysis is adopted while the streams in all heat exchangers are assumed to be in a thermodynamic equilibrium. Major performance parameter is utilization efficiency calculated according to Eq. (8.1). For a better picture, there is also shown a gross efficiency of the cycles according to Eq. (8.2) and gross utilization efficiency demonstrating an effect of heat rejection fans power, defined by Eq. (8.3). In order to obtain information on how much of the heat source potential is utilized, exergy efficiency (also known as second law efficiency) is calculated with respect to gross and net output by Eq. (8.4) and (8.5), respectively. For further details of the calculation method, the reader is referred to the work of Novotny and Kolovratnik [12] from where the methodology is adopted. Parameters of the models (pressures, concentration) are for each case optimized to maximize utilization efficiency (the same point is for first law efficiency, second law efficiency and maximal net power production).

$$\eta_{\mathrm{u}} = \frac{W_{\mathrm{net}}}{Q_{\mathrm{hs}}} = \frac{W_{\mathrm{exp}} - W_{\mathrm{pump}} - W_{\mathrm{fan}}}{m_{\mathrm{hs}} \cdot (h_{\mathrm{in}} - h_0)} \tag{8.1}$$

$$\eta_{\mathrm{c,gross}} = \frac{W_{\mathrm{gros}}}{Q_{\mathrm{in}}} = \frac{W_{\mathrm{exp}} - W_{\mathrm{pump}}}{m_{\mathrm{hs}} \cdot (h_{\mathrm{in}} - h_{\mathrm{out}})} \tag{8.2}$$

$$\eta_{\mathrm{u,gross}} = \frac{W_{\mathrm{gross}}}{Q_{\mathrm{hs}}} = \frac{W_{\mathrm{exp}} - W_{\mathrm{pump}}}{m_{\mathrm{hs}} \cdot (h_{\mathrm{in}} - h_0)} \tag{8.3}$$

$$\eta_{\mathrm{ex,gross}} = \frac{W_{\mathrm{gross}}}{\mathrm{Ex}_{\mathrm{hs}}} = \frac{W_{\mathrm{exp}} - W_{\mathrm{pump}}}{m_{\mathrm{hs}} \cdot \{(h_{\mathrm{in}} - h_0) - T_0 \cdot (s_{\mathrm{in}} - s_0)\}} \tag{8.4}$$

$$\eta_{\mathrm{ex}} = \frac{W_{\mathrm{net}}}{\mathrm{Ex}_{\mathrm{hs}}} = \frac{W_{\mathrm{exp}} - W_{\mathrm{pump}} - W_{\mathrm{fan}}}{m_{\mathrm{hs}} \cdot \{(h_{\mathrm{in}} - h_0) - T_0 \cdot (s_{\mathrm{in}} - s_0)\}} \tag{8.5}$$

In the above mentioned equations, subscript exp stands for the expander, hs stands for a heat source, in/out refers to heat source inlet/outlet, and 0 stands for a dead state, i.e. temperature of the ambient environment and in case of temperature is in K.

8.2.3 *Absorption Power Cycles*

Absorption power cycles (APC) are based on a scheme presented in Fig. 8.2. The working fluid in the desorber evaporates only partially, and liquid and vapour phase are then split in the separator, from which only vapour phase stream goes to the turbine. Liquid stream is cooled in recuperator and throttled down to turbine outlet pressure, and the streams are adiabatically mixed at the beginning of absorber. The remaining part of the absorber needs cooling for heat rejection, to keep the absorption process in place. The liquid exiting the absorber is as in Rankine cycles pressurized by the pump and pushed through recuperator into the desorber.

In general, it is important to note that recuperation for ORC has minimal effect in waste heat recovery applications for sensible heat source without restrains on its

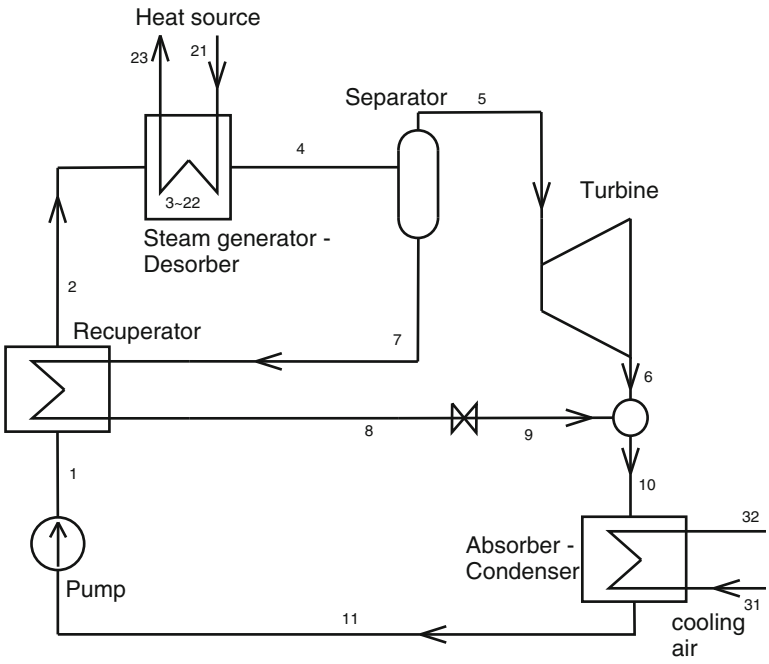

Fig. 8.2 Scheme of absorption power cycle configuration

outlet temperature. The reason is it does not increase gross power production [15, 16] but increases system complexity, in real devices it increases turbine backpressure, and there is minimal effect on net utilization efficiency [12]. In APC, however, the recuperator serves to lower the liquid absorbent temperature, improving the absorption process itself. Compared to ORC, the pressure loss also does not play a crucial role in this case as both fluids are liquid. Effect of recuperation on utilization efficiency is also a reason why more complex schemes are not considered.

Working fluids considered in this work are the traditional ammonia-water mixture, from salt solutions is chosen the water-LiBr solution as it has higher commercialization potential due to experience from absorption cooling [12], the amyl acetate-CO_2 mixture is chosen based on reference [14], methanol-heptanol is chosen as most perspective alcohol mixture [5]. Ionic liquids are included by 1-ethyl-3-methylimidazolium tetrafluoroborate with refrigerant R134a (R134a-[EMIM][BF4]) and with water (H2O-[EMIM][BF4]), as suggested by decent COP performance in absorption cooling regime [13].

For the Ammonia-water and water-LiBr mixtures are available empirical correlations of their properties, and the cycles are modelled in Engineering Equation Solver. Remaining APC are modelled in Aspen Plus, where for amyl acetate-CO_2 is used Peng-Robinson equation of state and alcohol mixture uses NRTL model. Ionic liquid mixtures are based on Peng-Robinson equation of state. Parameters for ionic liquids that are not in Aspen Plus databases are obtained from references [17, 18].

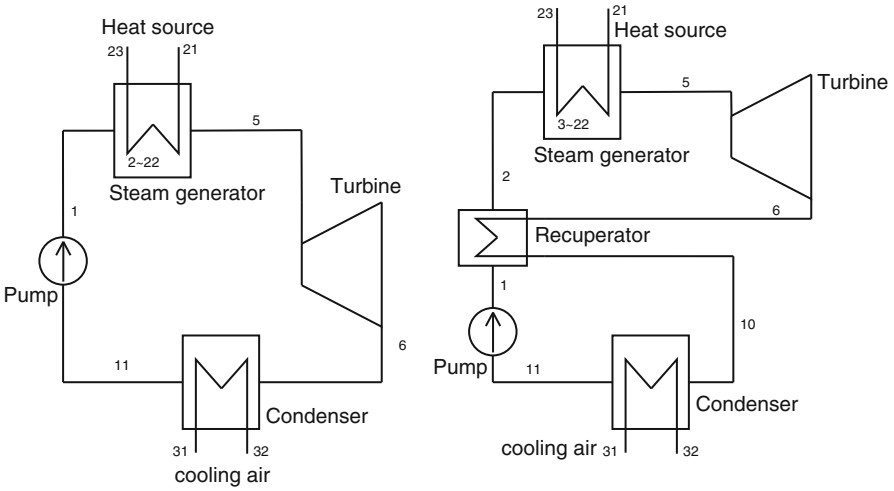

Fig. 8.3 Scheme of (left) simple and (right) recuperated ORC

8.2.4 Pure Component ORC

ORC is considered both subcritical (denoted just as ORC) and supercritical (SC-ORC). All pure component ORC is modelled in Engineering Equation Solver using empirical correlations for the fluid properties. Components for subcritical ORC are chosen as perspective ones from Novotny and Kolovratnik [12], particularly isobutane, hexamethyldisiloxane (MM), R245fa, R134a and for reference also water.

The maximal pressure in subcritical operation is limited to 90% of critical pressure and expansion takes place from the saturated vapour state (superheating does not bring thermodynamic benefit). Subcritical ORC is demonstrated as both non-recuperated and recuperated (R-ORC) in order to show the minimal benefit, supercritical only as non-recuperated (see both configurations in Fig. 8.3). Supercritical fluids are chosen specifically for each temperature. For 100 °C are the considered fluids R143a, and R41 (azeotropic mixture), for 200 °C R143a, R245fa and isobutane.

Except for pinch-point specification, the endpoint of heat addition in the supercritical state is constrained by the requirement that the expansion does not pass through the saturated vapour line more than once and outlet steam quality is more than 95%.

8.2.5 Zeotropic Mixture ORC

ORC with zeotropic mixtures are represented by a mixture of n-pentane-cyclohexane based on Eller et al. [5]. A non-recuperated scheme according to the Fig. 8.3 is adopted. At the same time, a zeotropic mixture ORC is a limiting case for several

APC fluids. Within APC performance optimization, it is allowed for the mixture quality to reach 100% and thus behave as an ORC. Expansion same as for regular ORC takes place from the saturated vapour state. Superheating does not bring any thermodynamic benefit as is also supported by our optimization results.

8.3 Results and Discussions

Performance of the cycles after optimization is summarized in Table 8.2 for 100 °C heat source and in Table 8.3 for 200 °C heat source. The results clearly show that a simple Rankine cycle is a better choice at higher temperatures, while lower temperatures are a domain of cycles using mixed working fluids. Best performance at low temperature has the water-LiBr APC, closely followed by the zeotropic ORC and methanol-heptanol APC. Traditional water-ammonia Kalina APC has performance behind these, but it is still better than a single fluid ORC.

Performance of the selected ionic liquids is rather disappointing, performing worse than all ORC. On the other hand, this should not be generalized to all ionic liquids as a number of possible fluids, and even absorbent-absorbate pairs, are enormous. Similarly, the performance of amyl acetate in comparison with other cycles is poor. Supercritical cycles do not bring any advantage for the higher temperatures and only a very small improvement against other cycles for an R41 refrigerant for lower temperatures.

Table 8.2 Results of thermodynamic analysis for 100 °C heat source

Cycle, fluid	η_u [%]	$\eta_{c,\ gross}$ [%]	$\eta_{u,\ gross}$ [%]	$\eta_{ex,\ gross}$ [%]	η_{ex} [%]	Note
APC NH_3-H_2O	1.4	5.5	1.7	13.8	11.3	$c_{NH_3} = 89\%$
APC H_2O-LiBr	1.6	6.1	2.0	15.8	13.2	$c_{H_2O} = 41\%$
APC amyl-acetate-CO_2	1.0	3.6	1.8	14.6	7.8	$c_{AA} = 11\%$
APC imidazolium-R134a	0.9	8.7	1.5	11.8	7.3	$c_{R134a} = 77\%$
APC imidazolium–H2O	1.0	6.8	1.4	11.7	8.1	$c_{H_2O} = 8\%$
APC MeOH–HepOH	1.5	6.5	2.0	15.8	12.2	$c_{MeOH} = 60\%$
ORC pentane-cyclohexane	1.6	7.1	2.0	16.5	12.9	$c_{n-Pentane} = 60\%$
RC H2O	1.0	6.4	1.5	12.4	8.4	
ORC isobutane	1.1	5.9	1.6	13.0	8.6	
ORC MM	1.0	5.5	1.5	12.1	8.0	
ORC R245fa	1.1	6.0	1.6	13.1	8.7	
R-ORC isobutane	–	–	–	–	–	Optimum at $Q_{rec} = 0$
R-ORC MM	1.0	5.9	1.5	12.2	8.2	
R-ORC R245fa	–	–	–	–	–	Optimum at $Q_{rec} = 0$
SC-ORC R143a	0.8	6.2	1.1	8.7	6.2	
SC-ORC R41	1.2	4.6	2.0	16.0	9.6	

Table 8.3 Results of thermodynamic analysis for 200 °C heat source

Cycle, fluid	η_u [%]	$\eta_{c,gross}$ [%]	$\eta_{u,gross}$ [%]	$\eta_{ex,gross}$ [%]	η_{ex} [%]	Note
APC NH_3-H_2O	7.1	14.3	7.8	34.4	30.9	$c_{NH_3} = 97\%$, RC mode
APC H_2O-LiBr	6.3	17.8	6.9	30.2	27.8	$c_{H_2O} = 80\%$
APC amyl-acetate-CO_2	5.8	9.3	6.7	29.2	25.4	$c_{NH_3} = 13\%$, RC mode
APC imidazolium-R134a	5.7	15.7	6.1	26.7	25.1	$c_{R134a} = 50\%$
APC imidazolium–H_2O	5.0	12.3	5.6	24.7	21.9	$c_{H_2O} = 9\%$
APC MeOH–HepOH	6.5	17.6	7.1	31.0	28.4	$c_{MeOH} = 65\%$, RC mode
ORC pentane-cyclohexane	7.2	13.1	7.9	34.5	31.6	$c_{n-Pentane} = 60\%$
RC H2O	5.8	14.7	6.6	28.9	25.3	
ORC isobutane	8.5	12.6	10.0	43.8	37.4	
ORC MM	6.7	11.8	7.8	34.3	29.4	
ORC R245fa	9.3	14.6	10.6	46.4	40.7	
R-ORC isobutane	8.8	13.0	10.3	45.2	38.4	
R-ORC MM	7.0	14.9	8.0	34.9	30.6	
R-ORC R245fa	9.3	15.2	10.6	46.6	40.9	
SC-ORC R143a	6.3	9.7	7.4	32.6	27.6	
SC-ORC isobutane	8.8	13.6	10.1	44.2	38.5	
SC-ORC R245fa	7.2	15.2	8.0	34.9	31.7	

Results of gross cycle efficiency demonstrate that in waste heat recovery, applications cycles with high efficiency do not necessarily provide high utilization efficiency of the heat source (and thus absolute power output). Also, a difference between gross and net efficiency shows how important it is at the low temperature, using even more than 30% of gross power output. Most obvious is a case of SC-ORC with R41 where gross 2.0% efficiency shrinks to only 1.2% net efficiency. Exergy efficiency further shows the share of the parasitic load on the whole work potential by the differences between gross and net values. Absolute values of exergy efficiency then point at the impact of pinch-point values relative to available temperature differences between the heat source and the heat sink, where at the 200 °C heat source the values are above 40% while for the 100 °C the best value exceeds 13%. Thus it points the issue the low-temperature heat utilization poses in general.

Temperature glide effect is illustrated by *Q-T* curves of heat addition and heat rejection of selected fluids in Fig. 8.4 for the 100 °C heat source and Fig. 8.5 for the 200 °C heat source. Note that cooling air for heat rejection has different mass flow for each case, and for lucidity it is not shown in the figures. The fluids with zeotropic mixtures or with a fluid in the supercritical state can well follow the heat source as it cools down. Amyl acetate-CO_2 and ORC with supercritical or near-supercritical fluids have excellent pinch match at the heat source side. Net power production is, however, affected by other parameters. In this case, lower enthalpy difference to be utilized by expander causes low power production. An excessive amount of the heat

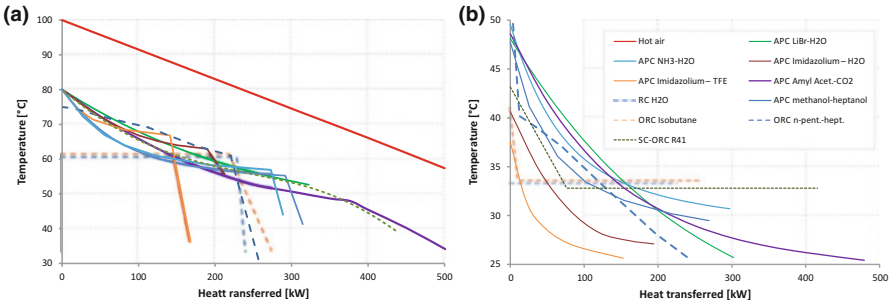

Fig. 8.4 *Q-T* curves for (**a**) heat addition and (**b**) heat rejection of cycles with mixture fluids, selected ORC and SC-ORC for 100 °C heat source (cooling air curves not shown as they would be different for each case)

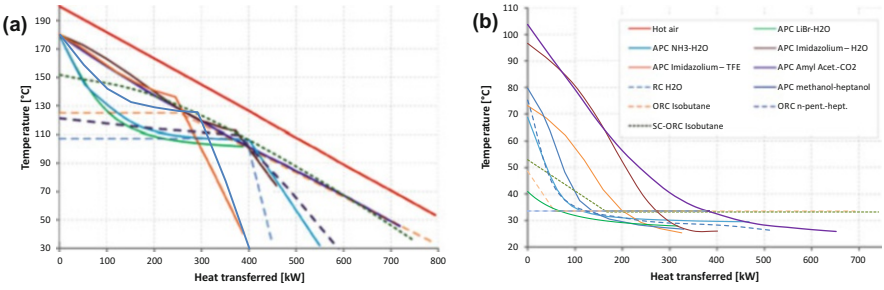

Fig. 8.5 *Q-T* curves for (**a**) heat addition and (**b**) heat rejection of cycles with mixture fluids, selected ORC and SC-ORC for 200 °C heat source (cooling air curves not shown as they would be different for each case)

transferred to the working fluid then gets rejected which can further increase the parasitic load. On the other hand, APC with imidazolium-R134a achieves high cycle efficiency, but limited heat transferred to the cycle allows only a limited power production.

For practical application of the power cycles are important another aspects as the pressures in the system or the vapour quality for expander design and reliable operation. These parameters are presented in Table 8.4. The highest pressures are in amyl acetate-CO_2 APC and are in order of 10 MPa, which can mean small device as many authors claim. However, the necessity of thick walls and safety measures for high pressure vessels increases the cost and thus limits actual applicability. Smaller-sized units in a distributed generation would also suggest the low efficiency of expanders due to relatively large leakages through necessary design clearances. Similar is the case of NH_3-H_2O APC, SC-ORC and some subcritical ORC with still very high pressures in the order of MPa.

On the other hand, especially for the low-temperature applications, some perspective APC operate entirely in a vacuum. Deepest vacuum is in H_2O-LiBr APC with absolute pressures in the order of kPa. The vacuum might pose design issues

Table 8.4 Pressure levels and expander outlet quality for the investigated cycles

	p_{high}	p_{low}	x_e	p_{high}	p_{low}	x_e
	[bar]	[bar]	[%]	[bar]	[bar]	[%]
Cycle, fluid	100 °C heat source			200 °C heat source		
APC NH3-H2O	20.70	10.67	98	68.80	11.13	96
APC H2O-LiBr	0.06	0.01	98	0.94	0.03	95
APC amyl-acetate-CO2	92.50	60.00	97	200.00	60.00	93
APC imidazolium-R134a	0.60	0.10	99	4.90	0.08	100
APC imidazolium–H2O	0.90	0.33	94	4.70	0.31	100
APC MeOH–HepOH	0.63	0.18	95	6.50	0.16	97
ORC pentane-cyclohexane	1.40	0.43	100	5.50	0.52	100
RC H2O	0.20	0.05	95	1.31	0.05	90
ORC isobutane	8.97	4.46	100	30.91	4.46	100
ORC MM	0.28	0.09	100	1.56	0.09	100
ORC R245fa	4.79	2.00	100	32.86	2.00	100
R-ORC MM	0.28	0.09	100	1.57	0.09	100
SC-ORC R143a	39.00	16.25	100	–	–	–
SC-ORC R41	75.20	45.70	100	–	–	–
R-ORC isobutane	–	–	–	30.91	4.41	100
R-ORC R245fa	–	–	–	32.86	1.99	100
SC-ORC R143a	–	–	–	50.00	14.97	100
SC-ORC isobutane	–	–	–	45.00	4.41	100
SC-ORC R245fa	–	–	–	37.00	2.05	100

especially related to sealing, similarly as it is in LiBr absorption cooling machines. APC using the alcohol mixture (methanol-heptanol) or ionic liquids have their vacuum much more moderate. From this point comes interesting, the zeotropic ORC with n-pentane- cyclohexane as the high pressure is slightly above ambient, while the low pressure is at moderate vacuum. High corrosivity of the LiBr solution is another aspect negatively affecting a design. Interesting aspect further affecting the design is volumetric flow of vapour, where large volumetric flow results in a bulky device but allows the design of a highly efficient turbine [12, 19].

Application of cycles with mixed working fluids might come across further issues from actual kinetics and heat transfer coefficients. Current literature does not successfully report actual temperature glide in Kalina cycles even though demonstration units have been built and other works report only cases of very small temperature glide designs for LiBr absorption systems [20]. Actual phase change behaviour and performance of the perspective APC mixtures water-LiBr and methanol-heptanol, as well as ORC mixture n-pentane-cyclohexane, should be investigated in greater detail. Environmental impact and toxicity of working fluids are recently getting also much more attention. LiBr perfectly fulfils these requirements. Ammonia and methanol do have some, though still limited toxicity, and imidazolium ionic liquids and amyl acetate have their toxicity higher.

8.4 Conclusions

This work explores a theoretical performance of different types of working fluids for absorption power cycles in waste heat recovery regime, presented with a heat source of 100 °C and 200 °C, where the effect of heat rejection power requirement (fans of air cooling) is taken into account. Comparison with other waste heat recovery cycles shows that simple ORC has better performance at higher temperatures, but super-critical or regenerative ORC gives very small further improvement.

For lower heat source temperature, the best performance is obtained for absorption power cycles with a water-LiBr solution, alcohol mixture (methanol-heptanol) and ORC with a zeotropic mixture of n-pentane-cyclohexane. Performance of Kalina cycle with the traditional ammonia-water mixture is behind these, but still is better than ORC, both in sub- and super-critical operation. On the other hand, amyl acetate-CO_2 and selected mixtures with ionic liquids have their performance rather poor.

Pressures, volumetric flows and fluid properties as corrosivity will play a major role in more detailed design. The actual temperature profile of mixed working fluids has not been, however, satisfactorily verified according to the literature. Together with the change in heat transfer kinetics, these issues should be addressed in greater detail in further investigations.

Nomenclature

0	Ambient conditions
APC	Absorption power cycle
c	Cycle
Ex	Exergy flow (kW)
exp	Expander
fan	Air cooled condenser fan
h	Enthalpy (kJ kg^{-1})
hs	Heat source
in	Heat source inlet
is	Isentropic
m	Mass flow ($kg.s^{-1}$)
out	Heat source outlet
ORC	Organic Rankine cycle
p	Pressure (Pa/bar)
pump	Feed pump
Q	Heat transfer (kW)
R-ORC	recuperated organic Rankine cycle
s	Entropy (kJ kg^{-1} K^{-1})
SC-ORC	Supercritical organic Rankine cycle
T	Temperature (°C, K in exergy calculations)
u	Heat source utilization
W	Work (kW)
η	Efficiency (%)

References

1. Johnson I, William T, Choate WT, Amber Davidson A (2008) Waste heat recovery: technology and opportunities in US industry. US Department of Energy, Washington, DC
2. Chen H, Goswami DY, Stefanakos EK (2010) A review of thermodynamic cycles and working fluids for the conversion of low-grade heat. Renew Sust Energ Rev 14:3059–3067. https://doi.org/10.1016/j.rser.2010.07.006
3. Lecompte S, Huisseune H, van den Broek M et al (2015) Review of organic Rankine cycle (ORC) architectures for waste heat recovery. Renew Sust Energ Rev 47:448–461
4. Rossi N (2013) Testing of a new supercritical ORC technology for efficient power generation from geothermal low temperature resources. In: ASME ORC 2013 Conference, Rotterdam, Netherlands
5. Eller T, Heberle F, Brüggemann D (2017) Second law analysis of novel working fluid pairs for waste heat recovery by the Kalina cycle. Energy 119:188–198. https://doi.org/10.1016/j.energy.2016.12.081
6. Ragazzi F, Pedersen CO (1995) Thermodynamic optimization of evaporators with zeotropic refrigerant mixtures. No. CONF-960606. Am. Soc. Heating, Refrig. Air-Conditioning Eng. Inc., Atlanta, GA (United States)
7. Mulroy WJJ, Domanski PAPA, Didion DAA (1994) Glide matching with binary and ternary zeotropic refrigerant mixtures part 1. An experimental study. Int J Refrig 17:220–225. https://doi.org/10.1016/0140-7007(94)90037-X
8. Kalina AI (1982) Generation of energy by means of a working fluid, and regeneration of a working fluid, U.S. Patent No. 4,346,561
9. Maack R, Valdimarsson P (2002) Operating experience with Kalina power plants. VDI Ber 1703:107–116
10. Whittaker P (2009) Corrosion in the Kalina cycle: An investigation into corrosion problems at the Kalina cycle geothermal power plant in Húsavik, Iceland. Diss. 2010. (University of Iceland & the University of Akureyri, 2009).
11. Sun J, Fu L, Zhang S (2012) A review of working fluids of absorption cycles. Renew Sust Energ Rev 16:1899–1906
12. Novotny V, Kolovratnik M (2017) Absorption power cycles for low-temperature heat sources using aqueous salt solutions as working fluids. Int J Energy Res 41:952–975. https://doi.org/10.1002/er.3671
13. Zheng D, Dong L, Huang W et al (2014) A review of imidazolium ionic liquids research and development towards working pair of absorption cycle. Renew Sust Energ Rev 37:47–68
14. Robbins T, Garimella S (2010) Low-grade waste heat recovery for power production using an absorption-Rankine cycle. In: International refrigeration and air conditioning conference, Purdue, USA
15. DiPippo R (2012) Geothermal power plants: principles, applications, case studies, and environmental impact. Butterworth-Heinemann, Oxford, UK
16. An Q, Lemort V, Zhai H et al (2016) Categorization and analysis of heat sources for organic Rankine cycle systems. Renew Sust Energ Rev 64:790–805. https://doi.org/10.1016/j.rser.2016.06.076
17. Valderrama JO, Robles PA (2007) Critical properties, normal boiling temperatures, and acentric factors of fifty ionic liquids. Ind Eng Chem Res 46:1338–1344. https://doi.org/10.1021/ie0603058
18. Seiler M, Jork C, Schneider W, Arlt W (2002) Ionic liquids and hyperbranched polymers–promising new classes of selective entrainers for extractive distillation. In: International conference on distillation and absorption, Düsseldorf, Germany

19. Novotny V, Vitvarova M, Jakobsen PJ, Kolovratnik M (2016) Analysis and design of novel absorption power cycle plants. In: ASME 2016 10th international conference energy sustainability collocated with ASME 2016 power conference ASME 2016 14th international conference on fuel cell science, engineering and technology. ASME, Charlotte, pp V001T13A005–V001T13A005
20. Miller WA (1998) The experimental analysis of aqueous lithium bromide vertical film absorption. The University of Tennessee, Knoxville

Chapter 9
Thermodynamic Analysis of a Refrigeration System Operating with R1234yf Refrigerant

Vedat Oruç and Atilla G. Devecioğlu

9.1 Introduction

According to European Union regulations on fluorine gases (i.e., F-Gas Regulation), it is mandatory to use refrigerants having a global warming potential (GWP) value lower than 150 in mobile air conditioners since 2011 (Regulation No:517/2014) [1]. It is expected in the near future that these restrictions should also be applied for both refrigeration and domestic air-conditioning systems. Therefore, it is necessary to investigate the thermodynamic performances of low-GWP refrigerants which have been recently started to use for different applications [2].

There are some papers in the available literature related to utilization of low-GWP refrigerants in refrigeration and air-conditioning systems operating with R134a. Some studies were only theoretically carried out. Furthermore, most of the investigations have been conducted in the last few years which points out that the topic is current and worthy to study.

It can be seen in available literature that an extensive investigation was performed by Navarro-Esbri et al. [3]. They have experimentally compared R134a and R1234yf refrigerants in a chiller. The results demonstrated that cooling capacity was reduced by 9% as a result of using R1234yf. Consequently, they found that COP of R1234yf was lower than that of R134a by 5–30% depending on superheat value, condenser temperature, and rotational speed of the compressor.

Navarro-Esbri et al. [4] also experimentally investigated the effect of IHX in a vapor-compression refrigeration system using R1234yf as a substitute for R134a. They determined that cooling capacity was enhanced by 5% and 9% for R134a and R1234yf, respectively, when IHX was present in the system. They have also

V. Oruç (✉) · A. G. Devecioğlu
Dicle University, Department of Mechanical Engineering, Diyarbakır, Turkey
e-mail: voruc@dicle.edu.tr

S. Nižetić, A. Papadopoulos (eds.), *The Role of Exergy in Energy and the Environment*, Green Energy and Technology,
https://doi.org/10.1007/978-3-319-89845-2_9

expressed that COP was increased by 6% and 10% for R134a and R1234yf refrigerants, respectively.

Fukuda et al. [5] studied both numerically and experimentally (in part) the high-temperature heat-pump application using low-GWP refrigerants of R1234ze(E) and R1234ze(Z). It was suggested in their paper that R1234ze(Z) was suitable for the high-temperature heat-pump applications. Navarro-Esbri et al. [6] modeled a shell-and-tube-type evaporator. The performance comparison was implemented through heat transfer correlations for two-phase flow. The experiments were done with R134a and R1234yf for testing the model. The simulations in the literature were compared with their data. As a result, they stated that their modeling could be used for the aim of design and analysis processes.

Zilio et al. [7] studied using of R1234yf as an alternative to R134a in automobile air-conditioning systems. The variable parameters were compressor rotational speed (900, 2500, and 4000 rpm) and ambient temperature. The results suggested that R1234yf, which is a potential candidate refrigerant instead of R134a, could be suitable for the systems they considered.

Yana Motta et al. [8] studied R134a, R1234yf, and R1234ze gases for vending machines. The results indicated that the cooling capacity and COP parameters of R1234yf were lower by 2% and 1%, respectively, compared to R134a. Similarly, cooling capacity and COP of R1234ze were also smaller by 9% and 7%, respectively, than that of R134a.

Endoh et al. [9] investigated the possibility of using R1234yf in a split-type air conditioner with a capacity of 4 kW operating with R410A. When the system was operated using R1234yf without making a constructional modification, COP was substantially lower in comparison with R410A. On the other hand, COP values of R1234yf and R410A were nearly the same when performing some modifications in the system.

Aprea et al. [10] investigated R134a and R1234yf gases in a domestic-type refrigerator for different amounts of refrigerants. The electrical power consumption was reduced with decreasing charging amount of R1234yf. It was similarly obtained in many studies considering utilization of low-GWP refrigerants in refrigeration systems that both cooling capacity and COP values of R1234yf were smaller compared to those of R134a [6, 11–14].

Although alternative refrigerants, which do not deplete ozone layer, are widely utilized in recent years, there is a continuing effort to develop new refrigerants due to their reduced effects on global warming and lower energy consumption potential. R1234yf is a refrigerant with low GWP; hence, it may be used as a substitute for R134a. Additionally, the thermodynamic properties of these refrigerants are similar. In the present investigation, the energy and exergy analyses for a refrigeration system originally operating with R134a were experimentally carried out at an evaporation temperature of 0 °C using R1234yf which has a low GWP.

Table 9.1 Characteristics of the studied refrigerants

	Boiling temperature at 100 kPa (°C)	Critical temperature (°C)	Critical pressure (kPa)	Temperature glide (°C)	Flammable rating	GWP
R134a	−26.07	101	20	40	40	40
R1234yf	−29.45	94.7	72	97	97	97

9.2 Tested Refrigerants

R1234yf and R134a which were studied in the test facility are HFO-based refrigerants with GWP values of 4 and 1430, respectively. Both of these gases are pure substances; consequently, their temperature glide magnitudes are zero. These refrigerants can be suitably used with polyolester (POE) oils available in the compressor. It is remarked that both refrigerants are nontoxic; R1234yf is mildly flammable, while R134a is non-flammable as classified by ASHRAE. Some other specifications of the tested refrigerants are given in Table 9.1 [15, 16].

9.3 Experimental Setup

The experimental setup was constructed as schematically shown in Fig. 9.1. There was a piston-type compressor with 1 HP designed for R134a, thermostatic expansion valve, air-to-air evaporator, and air-to-air condenser in the system.

The evaporator was inside an insulated cooled space in which temperature and heat loads were adjusted. The electrical resistances were available in the cooled space in order to provide a heat load equal to the cooling load of control volume (i.e., cooled space).The electrical resistances were controlled through a Variac, and, hence, the evaporation temperature was continuously kept at 0 °C. The condenser was placed inside an insulated channel to obtain required ambient conditions. The electrical resistances at air-inlet side of the insulated channel provided constant temperature of airflow over the condenser. Another Variac was present in the system for regulating the ambient temperature (T_a) by the electrical resistances at the condenser inlet. Two different T_a values were considered as 20 and 40 °C in the experimental work. The mass flow rate and electrical consumption of the compressor were measured with a Coriolis mass flow meter and wattmeter, respectively. The thermocouples and pressure sensors were installed at both inlet and exit sides of basic components of the system which were condenser, thermostatic expansion valve (TEV) evaporator, and compressor as shown in Figs. 9.1 and 9.2.

Before charging of the refrigerant, the system was purged by means of a vacuum pump. Subsequently, refrigerant charging was accomplished using a digital scale. The amounts of R134a and R1234yf charged into the system were 1700 g and 1650 g, respectively. The uncertainties of measuring instruments utilized in experiments were presented in the paper by Devecioğlu and Oruç [17].

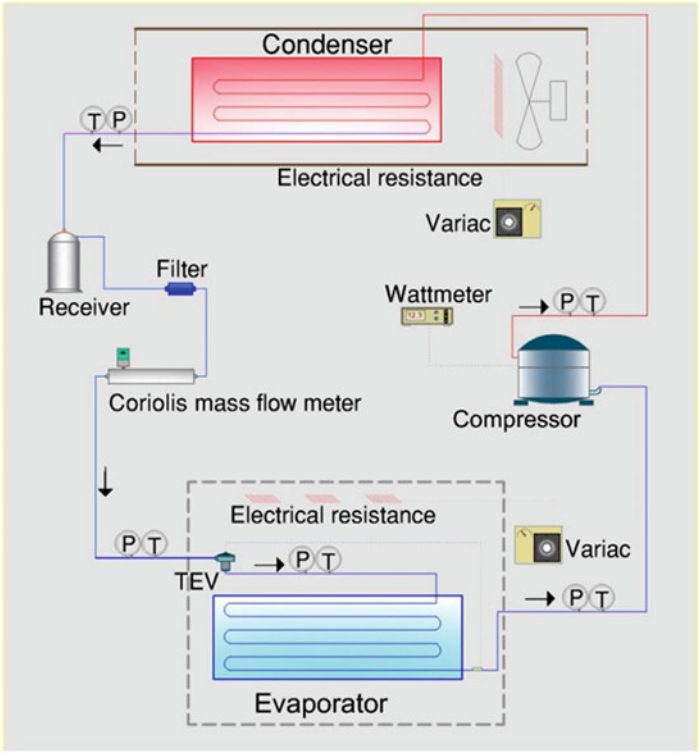

Fig. 9.1 Schematic representation of experimental setup

9.4 Energy and Exergy Analysis

The cooling capacity, Q_e, was evaluated as

$$Q_e = \dot{m}\left(h_{ev,out} - h_{ev,in}\right) \tag{9.1}$$

where $\dot{m}$ is the mass flow rate and $h_{ev,out}$ and $h_{ev,in}$ are enthalpies at the exit and inlet of evaporator, respectively. REFPROP [18] was referred to obtain enthalpy values corresponding to the measured temperature and pressure data.

The system attained a steady-state regime when the temperature of air flowing over condenser was reached to a specified value. This case was checked and confirmed by a digital manifold. The coefficient of performance (COP) of the system was determined as [19]

$$\mathrm{COP} = \frac{Q_e}{W_{comp}} \tag{9.2}$$

Fig. 9.2 A view of the experimental setup

where Q_e is computed by Eq. (9.1) and W_{comp} is the power consumed by compressor which was digitally measured using a wattmeter. The temperature and pressure data was obtained by means of a data acquisition card, and it was recorded by a software installed to the computer.

Exergy is a significant and useful thermodynamic parameter for having knowledge on the total irreversibility amount regarding the basic components of refrigeration cycle. The exergy destruction in each system component can be calculated as

$$\mathrm{Ex}_{\mathrm{des,comp}} = \dot{m}\, T_0 \left(s_{\mathrm{out,comp}} - s_{\mathrm{in,comp}}\right) \tag{9.3}$$

$$\mathrm{Ex}_{\mathrm{des,ev}} = T_0 \left[\dot{m}\left(s_{\mathrm{out,ev}} - s_{\mathrm{in,ev}}\right) - \frac{Q_e}{T_L}\right] \tag{9.4}$$

$$\mathrm{Ex}_{\mathrm{des,con}} = T_0\left[\dot{m}\left(s_{\mathrm{out,con}} - s_{\mathrm{in,con}}\right) + \frac{Q_{\mathrm{con}}}{T_{\mathrm{H}}}\right] \tag{9.5}$$

$$\mathrm{Ex}_{\mathrm{des,TEV}} = \dot{m}\,T_0\left(s_{\mathrm{out,TEV}} - s_{\mathrm{in,TEV}}\right) \tag{9.6}$$

$$\mathrm{Ex}_{\mathrm{total}} = \mathrm{Ex}_{\mathrm{des,comp}} + \mathrm{Ex}_{\mathrm{des,ev}} + \mathrm{Ex}_{\mathrm{des,con}} + \mathrm{Ex}_{\mathrm{des,TEV}} \tag{9.7}$$

where $\mathrm{Ex}_{\mathrm{des,comp}}$, $\mathrm{Ex}_{\mathrm{des,ev}}$, $\mathrm{Ex}_{\mathrm{des,con}}$, and $\mathrm{Ex}_{\mathrm{des,TEV}}$ are the exergy destructions in compressor, evaporator, condenser, and TEV, respectively, while $\mathrm{Ex}_{\mathrm{total}}$is the total exergy destruction in kW that developed through the mentioned components. T_{H} is high temperature assumed to be equal to $T_0 = 298$ K which is the reference temperature, and T_{L} is temperature of the refrigerated medium (i.e., low temperature) in Kelvin. Q_{con} is heat rejection by condenser in kW. In Eqs. (9.3–9.7), s_{out} and s_{in} are the entropy magnitudes in kJ/kg·K at the exit and inlet of the system components, respectively. Furthermore, the overall exergetic efficiency of the system, η_{ex}, can be computed as [20]

$$\eta_{\mathrm{ex}} = 1 - \frac{\mathrm{Ex}_{\mathrm{total}}}{W_{\mathrm{comp}}} \tag{9.8}$$

9.5 Results and Discussion

The cooling capacity, Q_{e}, determined by Eq. (9.1) is a significant parameter in refrigeration and air-conditioning systems. The dependence of Q_{e} on ambient temperature, T_{a}, is shown in Fig. 9.3 for the investigated refrigerants. It is obvious that Q_{e} decreases for both refrigerants with T_{a}. Additionally, R134a has a greater amount

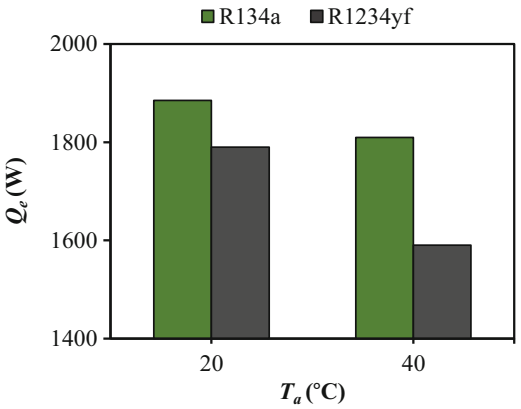

Fig. 9.3 The distribution of cooling capacity depending on T_{a}

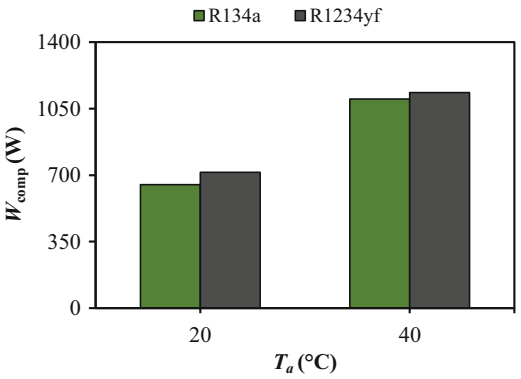

Fig. 9.4 The power consumption of the system depending on T_a

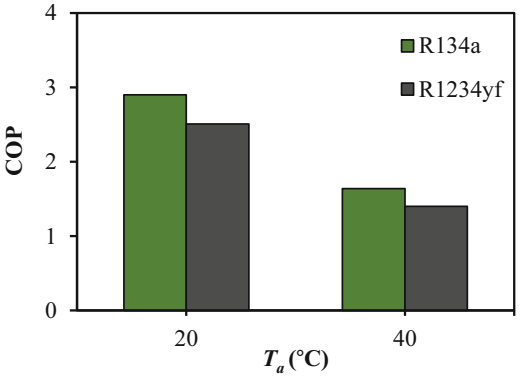

Fig. 9.5 The variation of COP with T_a for R134a and R1234yf

of Q_e regardless of T_a. Since Q_e is not enough parameter for making general discussion on the system, the electricity consumption should also be referred.

The power consumption of compressor, W_{comp}, at studied T_a cases is considered in Fig. 9.4. It can be clearly said that higher T_a causes the system to consume much power. Furthermore, R1234yf seems to have higher W_{comp} compared to R134a at both T_a cases; however, the difference between W_{comp} amounts for the tested refrigerants is not too high. Note that the difference between W_{comp} values for R1234yf and R134a is decreasing as T_a increases. Presumably, W_{comp} may be almost the same for both refrigerants at higher ambient temperatures.

It is well known that neither Q_e nor W_{comp} is not a sufficient parameter in order to evaluate a refrigeration system. The most important reference is the coefficient of performance, COP, as found by Eq. (9.2). The measured Q_e and W_{comp} as indicated in Figs. 9.3 and 9.4, respectively, are utilized for calculating COP. Hence, the obtained results are presented in Fig. 9.5 which may be evaluated as a combination of Figs. 9.3 and 9.4. First of all, COP of R134a is greater than that of R1234yf about by 14.0% and 12.5% at T_a values of 20 and 40°C, respectively. Nevertheless, R1234yf could be accepted as a reasonable alternative for the refrigeration systems since COP difference between two studied refrigerants is not too high as discussed.

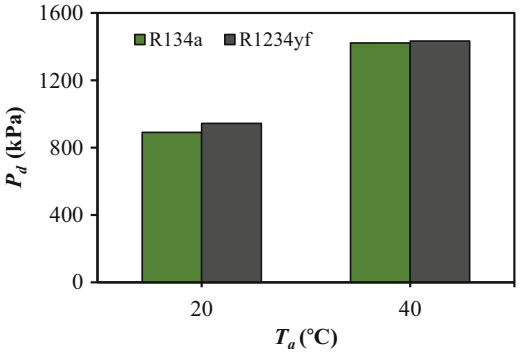

Fig. 9.6 The distribution of discharge pressure of compressor with respect to ambient temperature

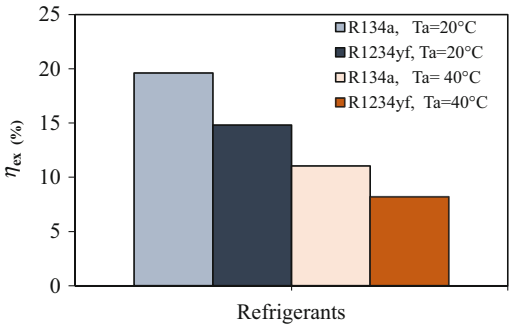

Fig. 9.7 The variation of exergetic efficiency of the system for studied refrigerants at different ambient temperatures

Meanwhile, COP is substantially affected by T_a which causes an evident decrease in system's performance such that increasing T_a from 20 to 40°C, a reduction in COP about by 45% occurs for both refrigerants.

The compressor discharge pressure, P_d, is a useful indication for the suitability of using a new refrigerant in a refrigeration system. The relationship between P_d and T_a is demonstrated in Fig. 9.6. The greater T_a causes P_d to increase considerably for the refrigerants. Although P_d is slightly greater for R1234yf case, it can be seen in Fig. 9.6 that P_d values are nearly the same independent of refrigerant type. Since P_d magnitudes are very similar for both refrigerants, R1234yf can be safely used in the refrigeration systems designed and manufactured for R134a without implementing any constructional modification.

The variation of exergetic efficiency computed by Eq. (9.8), η_{ex}, with studied refrigerants at different T_a cases is plotted in Fig. 9.7. Obviously η_{ex} is bigger for R134a at a given T_a which means that higher total exergy destruction develops for R1234yf case. For instance, η_{ex} is reduced about by 25% as a result of using R1234yf instead of R134a at 20°C. Furthermore, the increase in T_a (i.e., from 20°C to 40°C) leads to substantial reduction in η_{ex} nearly by 44% for both refrigerants.

The mass flow rate of refrigerants $\dot{m}$ and discharge temperature of compressor T_d have been varied in the experiments depending on ambient temperature, T_a, as given in Table 9.2. Obviously, higher T_a causes $\dot{m}$ and T_d to increase for both refrigerants.

Table 9.2 The data on ambient temperature, mass flow rate of refrigerants, and compressor discharge temperature

Parameter	R134a		R1234yf	
T_a (°C)	20	40	20	40
$\dot{m}$ (g/s)	11.5	13.4	14	16
T_d (°C)	82	110	72	97

Table 9.3 Thermodynamic properties corresponding to the points in refrigeration cycle shown in Fig. 9.8

Refrigerant	T_a (°C)	Point	P (kPa)	T (°C)	h (kJ/kg)	s (kJ/kg·K)
R134a	20	1	292	0	398.63	1.727
		2	890	35	466.98	1.863
		3	890	32	244.62	1.153
		4	292		244.62	1.163
	40	1	292	0	398.63	1.727
		2	1422	53	489.12	1.889
		3	1422	50.7	272.68	1.240
		4	292		272.68	1.266
R1234yf	20	1	315	0	363.31	1.598
		2	945	37	425.17	1.728
		3	945	33.6	245.62	1.155
		4	315		245.62	1.167
	40	1	315	0	363.31	1.598
		2	1434	54	446.47	1.761
		3	1434	51.9	272.71	1.240
		4	315		272.71	1.266

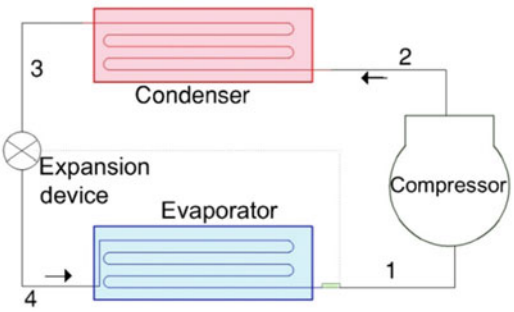

Fig. 9.8 The schematic representation of refrigeration cycle

The experimental information for some thermodynamic properties of the refrigeration cycle is presented in Table 9.3. Note that points 1–4 in Table 9.3 can be seen in Fig. 9.8.

9.6 Conclusions

The results of this study indicated that COP values are close to each other for R134a and R1234yf refrigerants. Therefore, R1234yf, which yields with a diminished COP, may be utilized for the refrigerating systems operating with R134a without carrying out any constructional modification. However, it may be suggested that increasing surfaces of evaporator and condenser as well as selecting a compressor with higher capacity should compensate the decrease of COP. It is important also to note that P_d values for both refrigerants were nearly the same. This points out that R1234yf is a suitable refrigerant as a substitute for R134a and it can be safely used in the systems operating with R134a. The behavior of η_{ex} was found to be similar to that of COP, namely, η_{ex} is reduced when R1234yf was used. Thereby, the exergetic efficiency of R134a was determined to be higher in comparison with R1234yf for the same experimental conditions.

Nomenclature

COP	Coefficient of performance
Ex	Exergy, W
Ex_{total}	Total destroyed exergy in system, W
GWP	Global warming potential
h	Enthalpy, kJ/kg
$\dot{m}$	Mass flow rate of refrigerant, kg/s
P_d	Pressure at compressor exit, kPa
Q_e	Cooling capacity, W
Q_{con}	Heat rejection of condenser, W
s	Entropy, kJ/kg·K
T_a	Ambient temperature, °C
T_0	Reference temperature, K
T_H	High temperature, K
T_L	Low temperature, K
W_{comp}	Power consumption of system, W
η_{Ex}	Exergetic efficiency

Subscripts

comp	Compressor
con	Condenser
des	Destruction
ev	Evaporator
in	Inlet
out	Exit
TEV	Thermostatic expansion valve

Acknowledgments The authors are indebted to Scientific Research Projects Coordination Unit of Dicle University for the financial support under research project no. MÜHENDİSLİK 15-004.

References

1. Regulation (EU) No 517/2014 of the European Parliament and the Council of 16 April 2014 on fluorinated greenhouse gases and repealing Regulation (EC) No 842/2006. Off J Euro Union. Link: http://eur-lex.europa.eu/legal-content/EN/TXT/PDF/?uri=CELEX:32014R0517&from=EN. Last accessed date: 14 Dec 2015
2. Akasaka R (2010) An application of the extended corresponding states model to thermodynamic property calculations for trans-1,3,3,3-tetrafluoropropene (HFO-1234ze(E)). Int J Refrig 33:907–914
3. Navarro-Esbri J, Mendoza-Miranda JM, Mota-Babiloni A, Barragan-Cervera A, Belman-Flores JM (2013) Experimental analysis of R1234yf as a drop-in replacement for R134a in a vapor compression system. Int J Refrig 36:870–880
4. Navarro-Esbri J, Moles F, Barragan-Cervera A (2013) Experimental analysis of the internal heat exchanger influence on a vapour compression system performance working with R1234yf as a drop-in replacement for R134a. Appl Therm Eng 59:153–161
5. Fukuda S, Kondou C, Takata N, Koyama S (2014) Low GWP refrigerants R1234ze(E) and R1234ze(Z) for high temperature heat pumps. Int J Refrig 40:161–173. 298–306
6. Navarro-Esbrí J, Molés F, Peris B, Barragán-Cervera A, Mendoza-Miranda JM, Mota-Babiloni-A, Belman JM (2014) Shell-and-tube evaporator model performance with different two-phase flow heat transfer correlations. Experimental analysis using R134a and R1234yf. Appl Therm Eng 62:80–89
7. Zilio C, Brown JS, Schiochet G, Cavallini A (2011) The refrigerant R1234yf in air conditioning systems. Energy 36:6110–6120
8. Yana Motta S, Spatz M, Vera Becerra E (2010) Analysis of LGWP alternatives for small refrigeration (plug-in) applications. International refrigeration and air conditioning conference at Purdue. Link: http://docs.lib.purdue.edu/iracc/1149. Last accessed date: 09.06.2014
9. Endoh K, Matsushima H, Takaku S (2010) Evaluation of cycle performance of room air conditioner using HFO-1234yf as refrigerant. International refrigeration and air conditioning conference at Purdue. Link: http://docs.lib.purdue.edu/iracc/1050. Last accessed date: 09.06.2014
10. Aprea C, Greco A, Maiorino A (2016) An experimental investigation on the substitution of HFC134a with HFO1234YF in a domestic refrigerator. Appl Therm Eng 106:959–967
11. Pottker G, Hrnjak P (2015) Experimental investigation of the effect of condenser subcooling in R134a and R1234yf air conditioning systems with and without internal heat exchanger. Int J Refrig 50:104–113
12. Mota-Babiloni A, Navarro-Esbri J, Barragan-Cervera MF, Peris B (2014) Drop-in energy performance evaluation of R1234yf and R1234ze(E) in a vapor compression system as R134a replacements. Appl Therm Eng 71:259–265
13. Jankovic Z, Atienza JS, Suarez JAM (2015) Thermodynamic and heat transfer analyses for R1234yf and R1234ze(E) as drop-in replacements for R134a in a small power refrigerating system. Appl Therm Eng 80:42–54
14. Illan-Gomez F, Lopez-Belchi A, Garcia-Cascales JR, Vera-Garcia F (2015) Experimental two-phase heat transfer coefficient and frictional pressure drop inside mini-channels during condensation with R1234yf and R134a. Int J Refrig 51:12–23
15. DuPont HFC-134a properties, uses, storage, and handling (2004) Link: https://www.chemours.com/Refrigerants/en_US/assets/downloads/h45945_hfc134a_push.pdf. Last accessed date: 11.01.2017

16. Honeywell Solstice® yf (2015) Link: http://www.honeywell-refrigerants.com/europe/wp-content/uploads/2015/06/Solstice-yf-Properties-and-Materials-Capatibility-060115.pdf. Last accessed date: 25 Jan 2015
17. Devecioğlu AG, Oruç V (2017) The influence of plate-type heat exchanger on energy efficiency and environmental effects of the air-conditioners using R453A as a substitute for R22. Appl Therm Eng 112:1364–1372
18. Lemmon EW, Huber ML, McLinden MO (2013) NIST standard reference database 23 reference fluid thermodynamic and transport properties-REFPROP, version 9.1. National Institute of Standards and Technology, Standard Reference Data Program, Gaithersburg
19. Stoecker WF, Jones JW (1982) Refrigeration and air conditioning. McGraw-Hill, Singapore
20. Dinçer İ, Kanoğlu M (2010) Refrigeration systems and applications. Wiley, New York

Chapter 10
A Design Approach for Cooling Gas Turbine Intake Air with Solar-Assisted Absorption Cooling Cycle

Umit Unver, Gokçen Ozkara, and Elif Merve Bahar

10.1 Introduction

The main reason for and the biggest actor in Turkey's current account deficit is its importing of energy. For this reason, all imported power should be consumed with maximum benefit. Increasing the benefit ratio both in industry and in households can be made possible by utilizing energy-saving alternatives. In terms of energy production, the production per unit energy source should be increased. In this chapter, an alternative for decreasing the fuel source per unit energy production by increasing the thermal efficiency was studied. Thus, the aim was to contribute to decrease the importing of energy, as well as to avoid the negative effects of power production on both the environment and the economy.

There are satisfactory amount of studies in the literature about increasing the efficiencies of gas turbine power plants [1–3]. An aircraft gas turbine splitted into parts and performed an exergy analysis for each part of the cycle. The unavoidable exergy destruction rate was given as 93.55% and concluded that the system has low potential of improvement. It was stated that 81.83% of the exergy destruction is endogenous and that causes a weak relationship between the cycle components [4]. Another study performed an exergy analysis on a gas turbine cycle and indicated that the exergy destruction costs more than capital investment costs. It is said that the pressure ratio, isentropic efficiency of the compressor and gas turbine, may augment the performance of the cycle [5]. However, to change the pressure ratio of an existing gas turbine compressor requires a redesign in the compressor construction, which means replacing the gas turbine with a new one. Ahmadi and Dincer analyzed large-scale gas turbine cycle. They have developed software to investigate the effect of gas

U. Unver (✉) · G. Ozkara · E. M. Bahar
Energy Systems Engineering, University of Yalova, Yalova, Turkey
e-mail: umit.unver@yalova.edu.tr

S. Nižetić, A. Papadopoulos (eds.), *The Role of Exergy in Energy and the Environment*, Green Energy and Technology,
https://doi.org/10.1007/978-3-319-89845-2_10

turbine parameters like isentropic efficiency of the compressor and gas turbine, turbine inlet temperature, and air preheater temperature on the cycle performance [6]. Similarly, the gas turbine parameters to achieve more effective and efficient cycle were investigated in [7]. The study mainly focuses onto the effect of compression ratio on the performance of the cycle, and this paper also provides insight into the design stage of the gas turbine like in [5]. Energy and exergy analyses were performed to evaluate the effect of supplementary firing of a gas turbine performance considering economical and environmental aspects [8]. The assessment of the energy efficiency of the combined-cycle gas turbines at various modes was studied in [9]. The effect of the raised inlet temperature on the performances of a gas turbine cogeneration system was investigated in [10]. Some researchers focused on the various methods to improve the efficiency of cogeneration systems, namely, conducted eight different ways of boosting the system performance [11–14].

Gas turbines are constant volumetric flow machines, and their performance is highly affected by the environmental conditions [15–18]. This leads researches to the inlet air cooling of gas turbine cycles. Over the past few decades, different inlet air cooling systems for gas turbine cycles have been proposed [19, 20]. The previous studies concluded that the spray coolers are useful for hot and dry climates and the coil cooling negatively affects the overall system performance [21]. Another cooling system that is thermal energy storage system was investigated but not proposed for intake air cooling of gas turbines by Zurigat et al. [22] for the climate of the considered location. Years later Saghafifar and Gadalla introduced an innovative cooling system that is Maisotsenko to be utilized instead of evaporative coolers [20]. The authors compared seven different cooling techniques and stated that the most economic was the direct evaporative cooling. Another comparison considered wetted-media evaporative cooling, high-pressure fogging, absorption chiller cooling, refrigerative cooling, and thermal energy storage. The conclusion of the study was the best way for gas turbine inlet air cooling is refrigerative cooling with chilled water of ice thermal storage [23].

Some researches are focused on the absorption cooling systems because of their low operating costs [24]. In 1996 Najjar studied on a NH3-H2O absorption cooling system for gas turbine inlet air cooling and reported that the intake air cooling with absorption cooling system boosted the power output by 21% and thermal efficiency by 38% [25]. Nineteen years later, 9–15% efficiency augmentation by utilizing an inlet air cooling system composed of a humidifier and absorption cooling system was reported [26]. An applicability method for gas-steam combined cycles introduced and advised to utilize the absorption cooling systems for To > 25 °C and RH > 0.4 zones [27]. A study about LiBr-H2O absorption cooling system was conducted, and each 10 °C decrease of inlet air increases the power production between 6% and 12% [28].

This chapter is aimed at designing an absorption cooling system for a gas turbine cycle located in Bursa, Turkey, and contributing to the present literature both in terms of investigation of increasing the gas turbine cycle efficiency by the absorption cooling system and by utilizing renewable resources in the absorption cooling system. The ground source heat exchangers were designed within the absorption

cooling system, and the soil was assumed to be the cold reservoir. It was assumed that the exchanger cycles of the condenser and absorber redirect the heat to the cold reservoir through a small circulation pump.

The COP of the cooling system was calculated to be 0.75, which coincides with the findings given in the previous studies [29]. However, in experimental studies the COP of the absorption cooling systems is given to be about 0.35 [30]. Another finding of this chapter is the boosted energy (BE) amount. COP is a powerful comparison tool that is widely used in the literature. It comprises of $\dot{Q}_{\text{evap}}$ and $\dot{Q}_{\text{gen}}$ as well as pump powers. However, the heat sources used in the generator, condenser, and absorber of absorption cycle are renewable. Because of this, comparing the cooling systems with these thermal powers is not explanatory. The target function is to achieve an approximation to the enhanced useful work ($\Delta \dot{W}_{\text{u}}$) of the gas turbine. Thus, the utilization factor (UF number) is introduced as an evaluation parameter which takes both $\Delta \dot{W}_{\text{u}}$ and total consumed power ($\sum P$) into account. The utilization of UF in order to evaluate the absorption cooling system is proposed in order to achieve more convenient results.

10.2 Material and Method

10.2.1 Bursa Ovaakça Power Plant

The Bursa Ovaakça power plant was set up by TEAS (the Turkish Electricity Production Company) in 1999. Its overall capacity in terms of electric output is 1400 MW (@iso conditions). There are 700-MW-powered twin blocks within the plant. Each block has its own heat recovery steam generator (HRSG). Two sets of gas turbines are assembled to one HRSG as part of a triple-pressure steam turbine cycle. There are a total of four gas turbine cycles as well as two steam turbine cycles in the plant. In the scope of this chapter, the gas turbines have been taken into consideration, with the rest of the plant being excluded from the scope.

10.2.2 Absorption Cooling System

There are many fluid pairs used in the absorption cooling cycles. The most frequently used coolants are LiBr-H_2O and NH_3-H_2O [31]. In the study, a NH_3-H_2O coolant pair was preferred because of its ease of production, high latent heat, low condenser pressure/temperature, and low cost [32, 33].

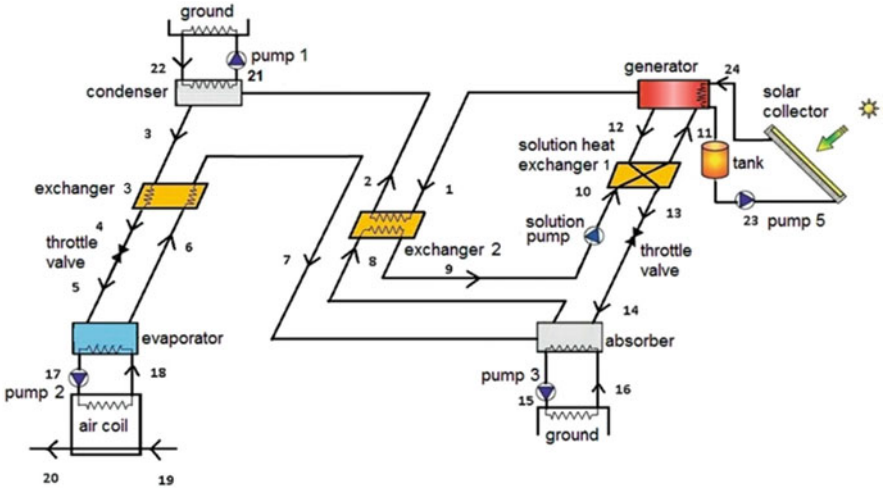

Fig. 10.1 Schematic illustration of an absorption cooling system for gas turbine inlet air cooling

10.2.3 Thermal Analysis

There are numerous studies that are mentioning the principles of absorption cooling systems. The procedure used in this chapter is detailed in [34]. An air coil was added in front of the air inlet in order to cool the inlet air of the gas turbine cycle (Fig. 10.1). The total cooling load of the coil can be calculated by

$$\dot{Q}_{\text{ac}} = \dot{m}_{\text{air}}.\dot{C}_{\text{p,air}}(T_{20} - T_{19}) \tag{10.1a}$$

or with constant C_{p} approach

$$\dot{Q}_{\text{ac}} = \dot{m}_{\text{w,ac}}(h_{18} - h_{17}) \tag{10.1b}$$

The mass flow rate of the coolant in the closed loop of the air coil can be calculated by:

$$\dot{m}_{\text{w,ac}} = \frac{\dot{m}_{\text{air}}.\ C_{\text{p,air}}\ (T_{20} - T_{19})}{(h_{18} - h_{17})} \tag{10.2}$$

The mass flow rate of the coolant in the closed loop of the condenser can be calculated by:

$$\dot{m}_{\text{w,con}} = \frac{\dot{Q}_{\text{con}}}{C_{\text{p,w}}(T_{21} - T_{22})} \tag{10.3}$$

The mass flow rate of the coolant in the closed loop of the absorber can be calculated by:

$$\dot{m}_{\mathrm{w,abs}} = \frac{\dot{Q}_{\mathrm{abs}}}{C_{\mathrm{p,w}}(T_{15} - T_{16})} \tag{10.4}$$

The circulating pump power used in the condenser, absorber, and air coil can be calculated by:

$$W_{\mathrm{p}} = \rho.g.Q.H_{\mathrm{m}} \tag{10.5}$$

whereby ρ is the density of the fluid in (kg/m^3), g is the gravitational force in (m/s^2), Q is the volumetric flow rate in (m^3/s), and H_{m} is the manometric head in (m). The useful power that can be obtained from a solar collector can be calculated by:

$$\frac{\dot{Q}_{\mathrm{u}}}{\mathrm{n_{sc}}} = A_{\mathrm{sc}}.I.\eta_{\mathrm{sc}} \tag{10.6}$$

whereby η_{sc} is the number of solar collector, I is the collected thermal solar power, A_{sc} is the area of the solar collector in (m^2), and η_{sc} is the efficiency of the solar collector that is given by the manufacturer. The useful power (T_{i}), alongside the inlet temperature ($\dot{W}_{\mathrm{u@i}}$), can be calculated by:

$$\dot{W}_{\mathrm{u@i}} = \mathrm{PR}.\dot{W}_{\mathrm{iso}} \tag{10.7}$$

whereby $\dot{W}_{\mathrm{iso}}$ is the 237 MWe electric power produced by one gas turbine in the power plant. $\dot{W}_{\mathrm{u@i}}$ accounts for the power production in MWs vs. inlet air temperature, and PR is the power ratio introduced in [18] according to the following equation:

$$\mathrm{PR} = 6.897622928.10^{-6}.T_0^2 - 2.3465207.10^{-3}.T_0 + 0.48593 \tag{10.8}$$

whereby T_0 is the atmospheric temperature that can be accepted as the actual gas turbine inlet air temperature. Now, the boosted energy production done by cooling the intake air from 36 °C to 26 °C can be calculated by:

$$\Delta\dot{W}_{\mathrm{u}} = \dot{W}_{\mathrm{u@26}} - \dot{W}_{\mathrm{u@36}} \tag{10.9}$$

And the utilization factor can be calculated by:

$$\mathrm{UF} = \frac{\Delta\dot{W}_{\mathrm{u}}}{\sum P} \tag{10.10}$$

whereby $\sum P$ is the total pumping power of the absorption system including the closed loops at the air coil, condenser, generator, absorber, and exchangers.

Table 10.1 Operating temperatures

Op. no	Operating point	Unit	Magnitude
1	Generator temperature	(°C)	90
5	Water temperature at the collector inlet	(°C)	60
24	Water temperature at the collector exit	(°C)	110
8	Absorber temperature	(°C)	20
15	Water temperature at the absorber exit	(°C)	25
16	Water temperature at the absorber inlet	(°C)	15
3	Condenser temperature	(°C)	20
22	Water temperature at the condenser exit	(°C)	25
21	Water temperature at the condenser inlet	(°C)	15
6	Evaporator temperature	(°C)	10
17	Water temperature at the evaporator exit	(°C)	12
18	Water temperature at the evaporator inlet	(°C)	17
19	Air temperature at air coil inlet	(°C)	36
20	Air temperature at air coil exit	(°C)	26
	Solution heat exchanger 1 effectiveness	(%)	90
	Exchanger 2 effectiveness	(%)	90
	Exchanger 3 effectiveness	(%)	90
	Pump	(%)	85

10.3 Results and Discussion

In this chapter, a NH_3-H_2O absorption cooling system was designed in order to cool the inlet air of Bursa-Ovaakça combined-cycle power plants' gas turbine at 10 °C increments. Thermodynamic analysis had been performed via basic mass and energy balance equations in order to evaluate the cooling performance of the system. The enthalpy, mass flow rate, concentration of each flow, heat capacities, and the coefficient of the performance of the system were calculated. The operating conditions of the system are given in Table 10.1.

The thermodynamic properties of ammonium and ammonium-water solution for each flow, including the operating conditions of the system, are detailed in Table 10.2. The temperature of the ammonium that leaves the generator had decreased to 63.8 °C in exchanger 1. The temperature of the solution leaving the absorber at flow no 8 had increased to 22.63 °C. The temperature of the ammonium leaving the condenser at flow no 3 had increased to 5.21 °C, while at flow no 6, the temperature of the ammonium had increased to 8.9 °C. In the exchanger 1, it was seen that the temperature of the rich solution had increased to 14.7 °C, while the temperature of the poor solution had decreased to 42.4 °C. At flow no 1, the mass flow rate of the ammonium is less than the rich solution. Thus, the temperature of the ammonium had increased more than the temperature of the rich solution.

The temperature difference between the solution and cooling water affects the heat transfer area [32]. The evaporator, condenser, and absorber were selected as the plate-type heat exchanger. The reasons behind selecting these include high

Table 10.2 Results of the thermodynamic analysis of the absorption cooling system

Flow no	Material	T (°C)	P (kPa)	X (%)	h (kJ/kg)	m (kg/s)
1	A	90.00	857.22	100.00	1650.09	5.11
2	A	26.17	857.22	100.00	1480.36	5.11
3	A	20.00	857.22	100.00	274.1	5.11
4	A	14.79	857.22	100.00	249.13	5.11
5	A	10.00	614.95	100.00	249.13	5.11
6	A V	10.00	614.95	100.00	1453.3	5.11
7	A V	18.87	614.95	100.00	1478.27	5.11
8	RS	20.00	614.95	75.13	−78.85	8.07
9	RS	42.63	614.95	75.13	28.44	8.07
10	RS	42.71	857.22	75.13	28.85	8.07
11	RS	57.39	857.22	75.13	100.65	8.07
12	PS	90.00	857.22	32.40	178.93	2.96
13	PS	47.56	857.22	32.40	−16.24	2.96
14	PS	47.56	614.95	32.40	−16.24	2.96
15	Water	25	1.7057	–	62.982	10
16	Water	15	3.1698	–	104.83	10
17	Water	12	1.42	–	50.41	179.95
18	Water	20	2.34	–	83.92	179.95
19	Air	36	101.5	–	309.25	650
20	Air	26	98	–	298.20	650
21	Water	25	3.1698	–	104.83	5
22	Water	15	1.7057	–	62.982	5
23	Water	60	19.947	–	251.18	8.45
24	Water	110	143.38	–	461.42	8.45

A ammonium, *AV* ammonium vapor, *RS* rich solution, *PS* poor solution

efficiency, low cost, and the special designs of these exchangers that facilitate split and turbulent flow [35]. Some other characteristics of the cooling system are as follows:

The hot flow through the condenser is the high-pressure ammonium vapor in the coolant side, whereas the cold flow is water that redirects the heat from condenser to the ground in a closed loop. The cooling water leaves the condenser at 25 °C and enters at 15 °C. Water is also used for cooling the absorber with a similar closed-loop system. The exchangers of the closed loops of both the condenser and the absorber cooling cycles are buried underground. The head (H_m) is designed at 5 m for the closed condenser and absorber loops.

The solvent in the absorber is cooled with serpentines that are also buried beneath the ground. In order to maintain 20 °C at the absorber, the cooling water leaves the absorber at 25 °C outside of the cooling system, discharges the heat to the soil, and then reenters the absorber at 15 °C.

The evaporator temperature is selected as 10 °C at the coolant side because of problems relating to iciness. The working fluid that cools the water of the air coil in

Table 10.3 Thermal capacities of the system components and the coefficient of performance

Thermal capacity (kW)	
$\dot{Q}_{gen}$	12877.19
$\dot{Q}_{abs}$	12865.49
$\dot{Q}_{cond}$	6163.74
$\dot{Q}_{evap}$	6153.06
$\dot{Q}_{exc1}$	917.07
$\dot{Q}_{exc2}$	127.59
$\dot{Q}_{exc3}$	867.29
COP	0.76

the coolant side (flow no 18 and 19) leaves the evaporator at 12 °C and reenters at 20 °C.

The system performance and the thermal capacities of the system components, as calculated through the analysis, are presented in Table 10.3. The highest thermal capacity belongs to generator and absorber, followed by condenser and evaporator. Between the heat exchangers, the highest thermal capacity belongs to the first exchanger, followed by the third and the second exchanges. The heat transfer in the first exchanger occurs between the rich and poor solutions. In the second exchanger, the solution temperature is heated by superheated vapor leaving the absorber. In the third exchanger, the working fluid cools by itself after leaving the evaporator. The reduction of the NH3 temperature decreases the enthalpy and increases the enthalpy difference at both the inlet and outlet of the first exchanger. Hence, the cooling capacity of the system increases. The heat transfer in the first exchanger is high because the mass flow rate of the rich solution is greater than the ammonium mass flow rate.

The COP is the rate of cooling performance to the energy consumption. The COP of the system was calculated as 0.755, meaning that the system consumed more energy than the cooling. The effectiveness of the exchangers and generator affects the COP directly, as mentioned by [36]. The COP result is nearly twice as the experimental studies and more than 0.42 that is given in the literature [37] for a solar-assisted absorption chiller and close with the COP given in [2] that is between 0.6 and 0.7.

Noting that the solar energy reaches peak capacity during the summer season, obtaining the required energy from solar energy for cooling is a suitable option for reducing the negative effects of greenhouse gases as well as for reducing costs by boosting the efficiency of the electricity production. The solar collector selected was the Baymak Apollo XL for obtaining the required energy for the generator. The temperature of the water was calculated to be 60 °C at the inlet and 110 °C at the outlet of the collectors. In order to obtain the required heat for the 12,877-kW-powered absorption cooling system, the following configurations were considered:

(i) All collectors were parallel assembled.
(ii) Two collectors were grouped with serial assembly, with the groups being assembled.

Table 10.4 Solar system results with respect to serial group numbers

	Mass flow rate (kg/s)	Total collector number	Collector cost ($)	Required area for collectors (m^2)	Pump power (kW)
All parallel	2.04	13,457	2,663,558	74,282	68
2-serial	5.41	11,008	2,178,824	60,764	280
3-serial	8.45	10,562	2,090,547	58,302	645
4-serial	11.03	10,788	2,135,378	59,552	1184

Table 10.5 Power of pumps, BE, and UF (kW)

Pumps	Power
Wp1	0.735
Wp2	26.48
Wp3	1.47
Wp4	5.22
Wp5	645
Total power of pumps	678.90
Boosted energy	19,420
Utilization factor	28.61

(iii) Three collectors were grouped with serial assembly, with the groups being parallel assembled.
(iv) Four collectors were grouped with serial assembly, with the groups being parallel assembled.

The mass flow rates, the total collector amount, the investment cost, the required area for the collectors, and the pump power were given in Table 10.4 according to each assumption.

For the first (all parallel) assumption, the pump power is lower, whereas the collector number, area, and collector cost are higher among other assumptions. For the third assumption, the mass flow rate is four times higher than that of the first assumption. The higher mass flow rate results at pumping power that is nine times higher but involves a lower area requirement. For the 2-serial in one group assumption, the number of collectors and the required area are greater than the third assumption. Therefore, the most appropriate assumption is the third one according to the number of collectors as well as the required area.

The useful power of this particular plant is 198 MW, when the atmospheric temperature is 36 °C, and 217 MW when it is 26 °C [18]. That means the boosted energy (BE) will approximately be 19.42 MW when the inlet air temperature of the system is cooled down to 10 °C. The 10% of power augmentation agrees with [38]. In Table 10.5, the power augmentations alongside the power consumption of the system are given.

10.4 Conclusion

In this chapter, the ground source heat exchangers and solar-assisted absorption cooling system were designed for the gas turbines of Bursa's Ovaakça power plant. The cooling capacity of the absorption cooling system was calculated to be 6.15 MW, while the corresponding solar thermal power generator power was calculated to be 12.9 MW. With the purposed system, a power augmentation of up to 1.94 MW/°C was calculated. In order to achieve this power augmentation, a pump power consumption of 0.68 MW was calculated. The utilization factor of the proposed absorption cooling system was calculated to be 28.61 MWs, and net power benefit was calculated to be 18.74 MWs. We recommend that future studies be done that further investigate the utilization of heat pumps in place of heat exchangers.

Nomenclature

A	Area (m^2)
ARS	Absorption refrigerator system
BE	Boosted energy
COP	Coefficient of performance
C _p	Specific heat capacity (kJ/kgK)
f	Circulation ratio
g	Gravity (m/s^2)
GT	Gas turbine
h	Enthalpy (kJ/kg)
I	Incident beam on solar collector
$\dot{m}$	Mass flow rate (kg/s)
N	Collector number
P	Pressure (kPa)
P_t	Total power of collectors
$\dot{Q}$	Heat transfer (kW)
$\dot{q}$	Heat transfer (kJ/kg)
$\dot{Q}$ _v	Capacity (m^3/s)
T	Temperature ()
UF	Utilization factor
X	Ammonium-water concentration (%)
W _useful	Useful energy (MW)
W _iso	Total useful power at ISO condition
Wp	Pump power (kW)

Greek Symbols

ρ	Density (kg/m^3)
?	Efficiency
ν	Specific volume (m^3/kg)

Subscripts

Abs	Absorber
Ac	Air coil
Col	Collector
Con	Condenser
Evap	Evaporator
Gen	Generator
P	Pump
Sc	Solar collector

Acknowledgment This chapter is the extended version of the earlier work of Unver et al. published in the 9th International Exergy, Energy and Environment Symposium (IEEES-9) Proceedings book with the title "The design of a renewable assisted absorption cooling system for gas turbine intake air cooling" [39].

References

1. Barigozzi G, Perdichizzi A, Gritti C, Guaiatelli I (2015) Techno-economic analysis of gas turbine inlet air cooling for combined cycle power plant for different climatic conditions. Appl Therm Eng 82:57–67. https://doi.org/10.1016/j.applthermaleng.02.049
2. Moya M, Bruno JC, Eguia P, Torres E, Zamora I, Coronas A (2011) Performance analysis of a trigeneration system based on a micro gas türbine and an air-cooled, indirect fired, ammonia-water absorption chiller. Appl Energy 88:4424–4440. https://doi.org/10.1016/j.apenergy.2011.05.021
3. Noroozian A, Bidi M (2016) An applicable method for gas turbine efficiency improvement. Case study: Montazar Ghaem power plant, Iran. J Nat Gas Sci Eng 28:95–105. https://doi.org/10.1016/j.jngse.2015.11.032
4. Şöhret Y, Açıkkalp E, Hepbasli A, Karakoc TH (2015) Advanced exergy analysis of an aircraft gas turbine engine: splitting exergy destructions into parts. Energy 90:1219–1228
5. Khaljani M, Khoshbakhti Saray R, Bahlouli K (2015) Comprehensive analysis of energy, exergy and exergo-economic of cogeneration of heat and power in a combined gas turbine and organic Rankine cycle. Energy Convers Manag 97:154–165
6. Ahmadi P, Dincer I, Rosen MA (2011) Exergy, exergoeconomic and environmental analyses and evolutionary algorithm based multi-objective optimization of combined cycle power plants. Energy 36:5886–5898
7. Kotowicz J, Job M, Brzeczek M (2015) The characteristics of ultramodern combined cycle power plants. Energy 92:197–211
8. Ahmadi P, Dincer I (2011) Thermodynamic and exergoenvironmental analyses, and multi-objective optimization of a gas turbine power plant. Appl Therm Eng 31:2529–2540
9. Aminov Z, Nakagoshi N, Xuan TD, Higashi O, Alikulov K (2016) Evaluation of the energy efficiency of combined cycle gas turbine. Case study of Tashkent thermal power plant, Uzbekistan. Appl Therm Eng 103:501–509. https://doi.org/10.1016/j.applthermaleng.2016.03.158
10. Al-Fahed SF, Alasfour FN, Abdulrahim HK (2009) The effect of elevated inlet air temperature and relative humidity on cogeneration system. Int J Energy Res 33(15):1384–1394. https://doi.org/10.1002/er.1552
11. Karaali R, Öztürk IT (2017) Efficiency improvement of gas turbine cogeneration systems. Tech Gaz 24(Suppl. 1):21–27

12. Karaali R, Öztürk IT (2017) Performance analyses of gas turbine cogeneration plants. J Therm Sci Technol 37(1):25–33
13. Karaali R, Öztürk IT (2015) Thermoeconomic optimization of gas turbine cogeneration plants. Energy 80:474–485. https://doi.org/10.1016/j.energy.2014.12.004
14. Karaali R, Öztürk IT (2015) Thermoeconomic analyses of steam injected gas turbine cogeneration cycles. Acta Phys Pol A 128(2B):B279–B281
15. De S, Al Zubaidy A (2011) Gas turbine performance at varying ambient temperature. Appl Therm Eng 31:2735–2739
16. Unver U, Kılıç M (2007) Second law based Thermoeconomıc Analysıs of Combıned cycle power plants Consıderıng the effects of Envıronmental temperature and load Varıatıons. Int J of Energy Res. (doi: 10.1002/er.1239) 31(2):148–157
17. Unver U, Kılıç M (2014) Performance estimation of gasturbine system via degree-day method. SPRINGER, progress in exergy, energy, and the environment. Part II: Energy:553–558. https://doi.org/10.1007/978-3-319-04681-5_51
18. Unver U, Kılıç M (2017) Influence of environmental temperature on exergetic parameters of a combined cycle power plant. Int J Exergy 22(1):73–88
19. Najjar YSH, Abubaker AM, El-Khalil AFS (2015) Novel inlet air cooling with gas turbine engines using cascaded waste-heat recovery for green sustainable energy. Energy 93:770–785. https://doi.org/10.1016/j.energy.2015.09.033
20. Saghafifar M, Gadalla M (2015) Innovative inlet air cooling technology for gas turbine power plants using integrated solid desiccant and Maisotsenko cooler. Energy 87:663–677
21. Alhazmy MM, Najjar YSH (2004) Augmentation of gas turbine performance using air coolers. Appl Therm Eng 24:415–429
22. Zurigat YH, Dawoud B, Bortmany J (2006) On the technical feasibility of gas turbine inlet air cooling utilizing thermal energy storage. Int J Energy Res 30:291–305
23. Al-Ibrahim AM, Varnham A (2010) A review of inlet air-cooling technologies for enhancing the performance of combustion turbines in Saudi Arabia. Appl Therm Eng 30:1879–1888
24. Bruno JC, Miquel J, Castells F (1999) Modeling of ammonia absorption chillers integration in energy systems of process plants. Appl Therm Eng 19:1297–1328. https://doi.org/10.1016/s1359-4311(99)00004-6
25. Najjar YSH (1996) Enhancement of performance of gas turbine engines by inlet air cooling and cogeneration system. Appl Therm Eng 16(2):163–173
26. Najjar YSH, Abubaker AM (2015) Indirect evaporative combined inlet air cooling with gas turbines for green power technology. Int J Refrig 59:235–250. https://doi.org/10.1016/j.ijrefrig.2015.07.001
27. Yang C, Yang Z, Cai R (2009) Analytical method for evaluation of gas turbine inlet air cooling in combined cycle power plant. Appl Energy 86:848–856
28. Mahmoudi SMS, Zare V, Rnajbar F, Farshi LG (2009) Energy and exergy analysis of simple and regenerative gas turbines inlet air cooling using absorption refrigeration. J Appl Sci 9 (13):2399–2407
29. Kaynakli O, Kilic M (2007) Theoretical study on the effect of operating conditions on performance of absorption refrigeration system. Energy Convers Manag 48:599–607. https://doi.org/10.1016/j.enconman.2006.06.005
30. Eicker U, Pietruschka D (2009) Design and performance of solar powered absorption cooling systems in office buildings. Energ Buildings 41:81–91
31. Kaynaklı Ö, Yamankaradeniz R (2003) Absorpsiyonlu Soğutma Sistemlerinde Kullanılan Eşanjörlerin Sistemin Performansına Etkisi. Uludag Univ J Eng Facul 8(1):111–120
32. Atmaca İ, Yiğit A, Kilic M (2002) The effect of input temperatures on the absorber parameters. Int Comn Heat Mass Transf 29(8):1177–1186
33. Atmaca İ, Yiğit A (2003) Simulation of solar – powered absorption cooling system. Renew Energy 28:1277–1293
34. Karamangil MI, Coskun S, Kaynakli O, Yamankaradeniz N (2010) A simulation study of performance evaluation of single-stage absorption refrigeration system using conventional

working fluids and alternatives. Renew Sust Energ Rev 14(7):1969–1978. https://doi.org/10.1016/j.rser.2010.04.008
35. Palm B, Claesson J (2006) Plate heat exchangers: calculation methods for Singleand two-phase flow. Heat Transf Eng 27(4):88–98. https://doi.org/10.1080/01457630500523949
36. Colonna P, Gabrielli S (2003) Industrial trigeneration using ammonia–water absorption refrigeration systems (AAR). Appl Therm Eng 23:381–396. https://doi.org/10.1016/s1359-4311(02)00212-0
37. Calise F, Libertini L, Vicidomini M (2017) Design and optimization of a novel solar cooling system for combined cycle power plants. J Clean Prod 161:1385–1403
38. Bassily AM (2004) Performance improvements of the intercooled reheat recuperated gas-turbine cycle using absorption inlet-cooling and evaporative after-cooling. Appl Energy 77(3):249–272
39. Unver U, Ozkara G, Kalyoncu EM (2017) Design of a renewable assisted absorption cooling system for gas turbine intake air cooling. 9th International Exergy, Energy and Environment Symposium (IEEES-9), May 14–17, 2017, Split, Croatia. Proceeding Book in Sandro Nizetic Eds. pp 811–816

Chapter 11
Assessment of Energy and Environmental Performance of Low-Charge Multiplex Refrigeration System

Enver Yalcin, M. Ziya Sogut, and T. Hikmet Karakoc

11.1 Introduction

One of the domains having intensive energy demand in supermarkets is refrigeration applications. Primarily, example of these refrigeration applications is preserving of perishable foods (e.g., dairy, deli, meat, fish, and vegetables) stored as frozen or cooled in display or storage units. Energy consumption for refrigeration in supermarket is almost half of total store energy consumption. In refrigeration processes, compressors defined as one of the main core components consume approximately 30–35% of energy, and the other users of energy are fans and lighting. Approximately 15–20% of total energy consumption of the supermarket is consumed to prevent sweating in display cases [1].

In general, R-404a is preferred as refrigerant in supermarket refrigeration systems used in direct expansion (D4) valve. Several parameters such as high energy consumption and excess refrigerant charge because of long liquid line and height refrigerant leakage rate affect adversely on environmental impact assessment. Nowadays, several new systems such as distributed, secondary loop, multiplex direct expansion (D4) system, low-charge multi-compressor (LCMRS), and advanced self-contained refrigeration systems (WLSC) are used. LCMRS and WLSC refrigeration plants stand out among these systems [2]. A traditional multi-compressor supermarket refrigeration system with thermostatic expansion valve (T4V) operates in a static

E. Yalcin
Engineering Faculty of Balikesir University, Mechanical Engineering, Balikesir, Turkey

M. Z. Sogut (✉)
Piri Reis University, Maritime Faculty, Istanbul, Turkey
e-mail: mzsogut@gmail.com

T. H. Karakoc
Anadolu University, Faculty of Aeronautics and Astronautics, Eskisehir, Turkey

S. Nižetić, A. Papadopoulos (eds.), *The Role of Exergy in Energy and the Environment*, Green Energy and Technology,
https://doi.org/10.1007/978-3-319-89845-2_11

suction pressure. An electronic expansion valve (EEV) can be used in order to operate at lower condensation pressures and increase the liquid line efficiency. For the refrigerant control in supermarket, if a control valve is preferred in LCMRSs considering bypass, the refrigerant liquid charge in display case evaporators can be limited. In this application, bypassed liquid refrigerant is expanded and then evaporated by means of heat exchange with vapor refrigerant in the other side of exchanger. Vapor is piped to the suction collector and returns to the condenser for recompression. Thus, the charging need for considered conventional multiplex systems can be reduced approximately 30% [1]. Thanks to this application, the refrigerant charge need of traditional multiplex system reduces severely. In the cabinets, the circulating water usage instead of refrigerant is an effective application in terms of reducing refrigerant charge amount [3]. On the other hand, TEWI of WLSC is 3% less than LCMRS, whereas its annual energy consumption is about 20% more than LCMRS [1].

Evaluation of energy efficiency for a refrigeration system is carried out based on coefficient of performance (COP). This parameter provides a quantitative assessment on energy usage. However, it is not sufficient for evaluation of environmental impacts caused by systems and ineffectiveness caused by irreversibility. The exergy analysis stands out as a measure of irreversibility related with energy flow rate in thermodynamic processes. Exergy, defined as maximum work that can be obtained in environment conditions taken as reference, is a measure of quality of mass and energy rates for thermodynamic processes [4, 5]. It is important to understand exergy and information that may be related to productivity for scientists and engineers who are working on environmental impact and sustainable energy systems. It is observed that similar studies for cooling systems and applications [6–8]. Today, cooling systems are produced by about 60–70 million and hundreds of millions of coolers, and air conditioning units are working. This demand and accordingly their effects on climate change will be increased continuously. Since the early 1990s, the factors such as the increase of ozone depletion in the stratosphere, reduction of energy consumption in refrigeration, and air conditioning technology due to effects of greenhouse gas emissions stand out the choice of more environmentally friendly refrigerants [9]. In recent years, TEWI is the most effective method used to determine the effects of refrigerant emissions. TEWI that described both the direct emissions of refrigerants and the indirect emissions resulting from energy consumption by refrigeration system is very important criteria [10].

As different from literature, in this study, environmental impacts of LCMRSs in supermarkets were examined according to different refrigerants by exergetic approach. COP and exergetic performance of LCMRS investigated separately according to refrigerants R-404A, R-507, R-407C, and R-152a are taken as reference. Then, effects of CO_2 emissions are calculated separately for each refrigerant by TEWI taken as reference. For this purpose, firstly, refrigeration systems used in supermarkets were described briefly, and LCMRSs were detailed. The exergy concept in section three, methodology of TEWI concept and formulas in fourth section, findings and analysis of the results obtained in the system were given in section five. Then, the specific results and recommendations were given in conclusion.

11.2 Refrigeration Systems for Supermarkets

Various cooling systems with many subsystems working in different temperature ranges are used for food storage in supermarkets. In these systems, especially product type, storage volumes, type of refrigerant, and refrigerant cooling capacity should be considered as preference parameters. The energy-consuming activities for a supermarket are refrigeration, air conditioning, heating and lighting, etc. While annual energy consumption of a supermarket is approximately 2 million kWh, this value of gross market or hypermarket is around 3 million kWh. Energy consumption of refrigeration applications is approximately 45–60% of total energy consumption in a supermarket [11]. As the top of preferred traditional supermarket refrigeration applications, refrigeration system with multi-compressors and direct expansion (D4) is observed. In these systems working based on principle of traditional vapor-compressed refrigeration cycle in which refrigerant absorbs heat from the cold reservoir by evaporation in the evaporator and rejects it to the hot reservoir by condensation in condenser, refrigeration of 3–4 kW/kW energy consumption can be obtained based on COP. In supermarket, display cases with evaporators and storage areas are located generally close to each other. There is a machine room at which main core elements like compressor, condenser, and a large amount of pipelines needed to connect components of each other. In the multiplex D4 systems, refrigerant charge amount is about 4–5 kg per kW of refrigeration capacity. The use of long pipeline and numerous fittings reveals tremendous refrigerant leakage in refrigerating systems. While this annual leak rate is about 30% of the total amount in the old system, it is about 15% for new systems [12]. Because of the reasons such as effect of refrigerants on global warming potential (GWP), leak rates up to 30% for these systems applied in large areas and complex structures, and problems that occur in the control systems, more effective systems have begun to develop instead of low-efficient D4 refrigeration systems. These systems are:

- Secondary loop systems, separate from primary circuit, that operate between the central chiller and cabinets are secondary circuit. The secondary fluid is chilled by chillers, and refrigeration of cabinet occurs depending on refrigeration effect. In these systems, two separate circuits are used for low and medium temperatures. While brine at low temperature is used for frozen foods, chilled brine at medium temperature is used for cold storage. Two volumes can be controlled by this application; on the other hand, the investment costs are affected adversely due to controlling of each volume by different compressor groups. Another approach developed in secondary loop systems is cascade refrigeration. While propane is used in the high-temperature stages of these systems, CO_2 is used in the low-temperature ranges. In multistage applications, CO_2 is especially preferred to remove heat from the frozen food cabinets by means of direct expansion evaporators.
- Distributed systems include many cabinets which are distributed to many places in the shop and have small compressor racks for each unit. Thus, the long pipeline

used to connect each cabinet and the main compressor located in a machine room are eliminated via this application [1].

- Advanced self-contained systems have been developed as low-refrigerant charge systems. In these systems, display case units contain the compressors and water-cooled condensers. Heat released from display units is removed out of the supermarket by a propylene glycol-assisted water loop (for medium-temperature storage) and potassium format (for low-temperature storages). Airflow used to cool each display case is cooled by this brine loop without an evaporator [1, 13].
- CO_2 secondary loop/cascade system. A couple of propane and CO_2 are used as refrigerant. Because the critical point temperature is low, the CO_2 refrigeration systems must operate at higher temperatures than their critical point values. Therefore, instead of the condenser in conventional systems, a heat exchanger called a gas cooler is used in CO_2 refrigeration systems. In the system gas cooler, higher pressure values than the critical point pressure occur (80–120 bar) [14]. A gas cooler with increased wall thickness due to high pressure is needed. It can be said that this system is no suitable for warm climate zone yet.

11.2.1 Low-Charge Multi-compressor Refrigeration Systems

Low-charge multi-compressor refrigeration systems operate with low refrigerant controlled by means of valves by maintaining the critical values of refrigerant mass flow. Less energy consumption is also provided depending on the level of refrigerant charge. Another feature of this system is reducing effect of long connecting lines between the display cases and compressor racks. In these systems, the pipe length is not a problem [15].

A portion of the bypassed liquid refrigerant from liquid line is evaporated in discharge manifold connected to compressor outlet, and then it is supplied to the compressor suction line. So, both the compressor suction temperature and the condensing pressure of superheated refrigerant vapor in the compressor outlet are also reduced. In this way, a floating condensation is obtained. By acting together temperature sensor and control valve, a constant temperature difference between ambient air and subcooled refrigerant at condenser outlet is maintained as shown in Fig. 11.1 [16].

Thus, both condenser capacity and cooling effect of evaporator will be increased. The amount of refrigerant required in the refrigeration system is decreased about 30% in accordance with a traditional multi-compressor refrigeration system. In these systems, saturated refrigerant temperatures in condensers are decreased about 5 °C and 15 °C for low-temperature racks and medium-temperature racks, respectively [1].

In this study, a new approach is recommended which replaces traditional low-charge multi-compressor refrigeration system. After a portion of the liquid refrigerant bypassed from liquid line is evaporated in discharge manifold connected to compressor outlet, a floating evaporation can be obtained by repetitive expanding.

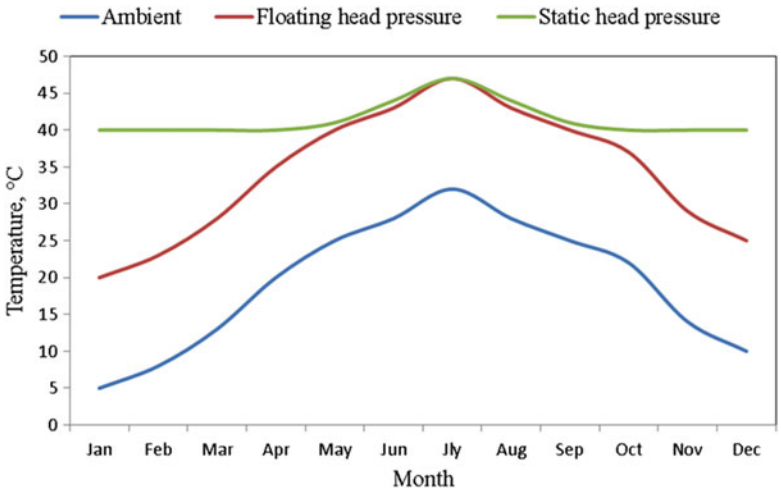

Fig. 11.1 Floating condensing temperature. (Modified from [16])

The temperature and pressure of refrigerant at the compressor outlet can be controlled depending on the mass flow of refrigerant from the bypass line. Based on the ambient temperature, the floating condensation application also decreases energy consumption by reducing the condenser fan speed. By controlling refrigerant flow in the evaporator, pipe diameters that are used in the liquid lines can be minimized. Thus, the amount of refrigerant charge is reduced. System operating schema is given in Fig. 11.2.

Another approach for low-charge system which is operated depending on a needed minimum charge for evaporator is a secondary charge control approach, and schematic diagram is given in Fig. 11.3.

By reducing refrigerant charge, the mixture of saturated liquid and vapor is sent into the evaporator placed in display cases and the storage volumes. Meanwhile, refrigerant flow into compressor is controlled by balance and control valves. This situation, if compared with D4 system, creates a saving of up to 30%. Using of bypass control valve in the system allows operation of compressor at low pressure, which would provide energy-saving. Condenser fans consume energy so close to the compressor consumption. Thus, the development of the fan control strategy is also important. For this purpose, the use of variable speed fans stands out. In addition, hot water which is obtained by a heat exchanger can be used for different purposes such as air conditioning systems [15].

The analytical performance of this new approach is examined based on the first and second law analysis of the thermodynamics analysis, and exergy concept is given below.

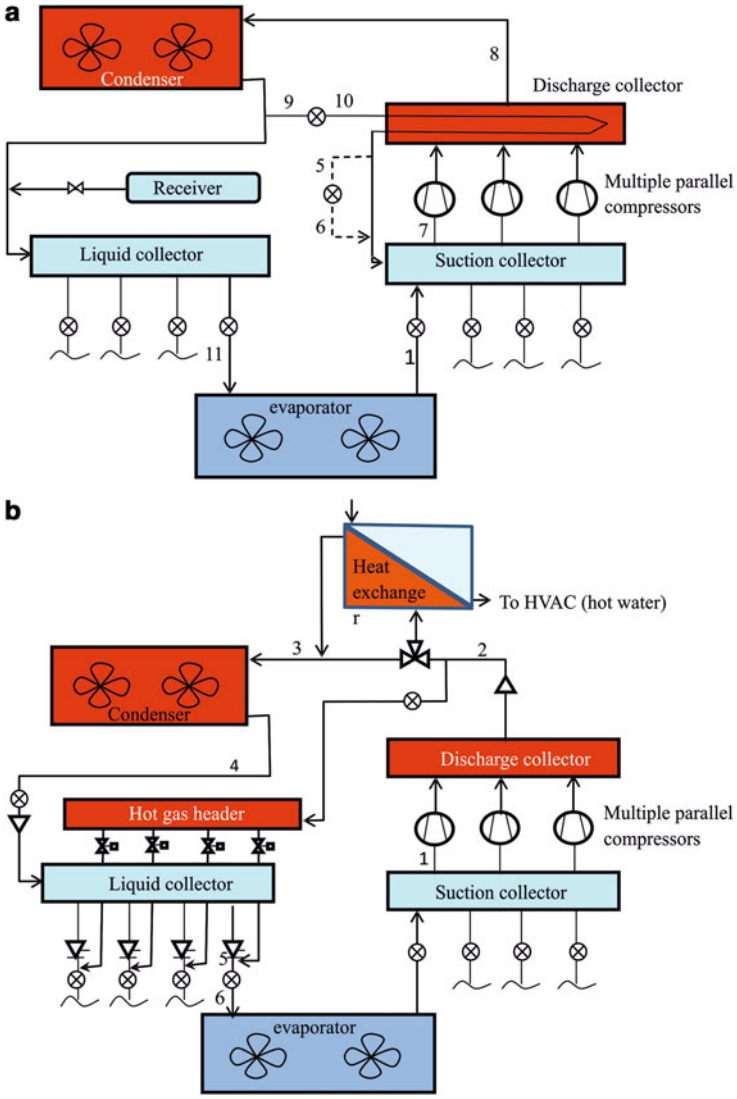

Fig. 11.2 Modified low-charge multi-compressor refrigeration system. (**a**) Operating schema. (**b**) Second approach. (Modified from Baxter [1])

11.3 Exergy Concept

As a measure of equipment's working efficiencies in refrigeration systems, coefficient of performance (COP) is defined as the heat of absorbing from the cooled environment is divided by compressor's work. This definition is expressed as efficiency for the first law of thermodynamics. COP is

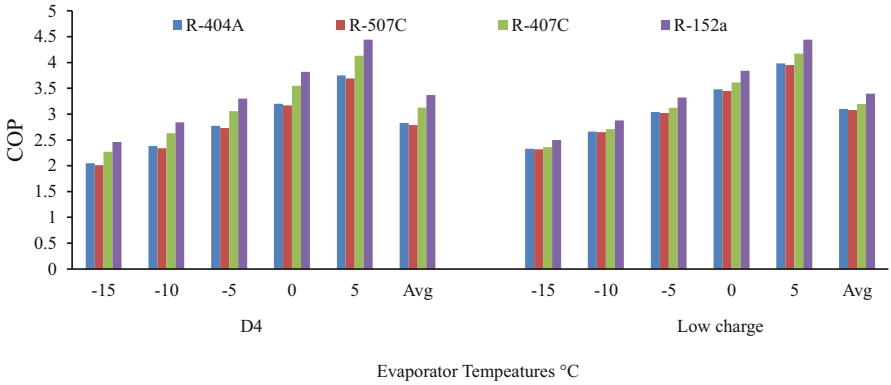

Fig. 11.3 COP distributions of refrigerants

$$\mathrm{COP} = \frac{\dot{Q}_{\mathrm{evap}}}{\dot{W}_{\mathrm{comp}}} \tag{11.1}$$

[17]. $\dot{Q}_{\mathrm{evap}}$ and $\dot{W}_{\mathrm{comp}}$ indicate the heat absorbed from the cooled area and the compressor power input, respectively. Cooling machines are one of the thermodynamics machines, and vapor-compression refrigeration cycle is working system used commonly. The compressor power input for this cycle is expressed as follows:

$$\dot{W}_{\mathrm{comp}} = \dot{Q}_{\mathrm{cond}} - \dot{Q}_{\mathrm{evap}} \tag{11.2}$$

$\dot{Q}_{\mathrm{cond}}$ is heat rejection to environment by means of condenser. A basic vapor-compression refrigeration system has four major thermal processes. These are (1–2) compression, (2–3) desuperheating-condensation-subcooling, (3–4) expansion, and (4–1) evaporation-superheating. Accordingly, the energy balances for each equipment of the system are as follows (theoretically). For compressor:

$$\dot{W}_{\mathrm{comp}} = \dot{m}.(h_2 - h_1) \tag{11.3}$$

where $\dot{m}$ is mass flow rate of refrigerant; h is enthalpy; and $\dot{W}_{\mathrm{comp}}$ is compressor power input.

For condenser and evaporator:

$$\dot{Q}_{\mathrm{cond}} = \dot{m}.(h_2 - h_3) \tag{11.4a}$$
$$\dot{Q}_{\mathrm{evap}} = \dot{m}.(h_1 - h_4) \tag{11.4b}$$

For expansion valve, inlet and outlet enthalpies aren't changed. Therefore, energy balance equation is

$$h_3 = h_4 \tag{11.5}$$

The ability of the real work of a refrigeration machine is defined by the concept of exergy according to the second law of thermodynamics. Exergy efficiency is defined as actual COP divided by reversible COP_{rev}. The COP_{rev} of a refrigeration cycle operating between temperature limits of TL and TH is based on the Carnot refrigeration cycle. COP_{rev} is

$$COP_{rev} = \frac{1}{\frac{T_H}{T_L}} - 1 \tag{11.6}$$

[18]. T_H is outdoor temperature (high temperature), and T_L is temperature of cold environment where heat is absorbed. Exergy efficiency is

$$\eta_{II} = \frac{COP}{COP_{rev}} \tag{11.7}$$

If Eqs. (11.1) and (11.3) are combined,

$$\eta_{II} = \frac{Q_{evap}\frac{T_H}{T_L} - Q_{evap}}{\dot{W}_{comp}} \tag{11.8}$$

[17, 19].

11.4 TEWI Concept

Effects of emissions caused by refrigerants have been discussed in many ways, especially with the increasing environmental threats. Montreal Protocol process including the initial evaluation, effect of greenhouse gas emissions, and global warming potential of synthetic refrigerants on the atmosphere is discussed in many ways. Later, in 1990 the London Conference, to reduce the global warming impact of refrigerants depending on the effect of COPs in the system, a process that aimed usage of the low global warming potential refrigerants instead of ozone depletion potential refrigerants, was discussed. Meanwhile, the global warming potential of the refrigerants in the cooling system was also questioned. In the Copenhagen Meeting that followed this meeting, a concept for evaluating the total global warming potential caused by the cooling system was presented. In this concept, CO_2 emission effects depending on the global warming potential of refrigerant and CO_2 emission effects caused by energy supplied from power plant that burns fossil fuel for cooling system were evaluated. Then, this assessment was defined as total equivalent warming impact (TEWI) developed by Oak Ridge National Laboratory [2].

TEWI concept has been developed as sum of global warming effects of CO_2 emissions that resulted from refrigerant emissions (direct effect) and emitted into the atmosphere depending on energy used by a system during its life cycle (indirect

effect). In contrast to the life cycle climate performance (LCCP), including emissions from production processes of cooling systems and greenhouse gas emissions emitted depending on energy consumption for its production, TEWI includes emissions from system during its working process [10]. The TEWI value as defined in EN 378:2000 is a suitable method of evaluating for refrigerants. This parameter is an international method that can be used to directly compare the relative effect of different systems. The height of the TEWI indicates the weakness of the system with environmental aspects. TEWI is

$$\begin{aligned} \mathrm{TEWI} = [\mathrm{GWP}.L.n] + \left[1 - \alpha_{\mathrm{recovery}}\right] + \\ + [n.E_{\mathrm{annul}}.\beta] \quad (\mathrm{kgCO_2}) \end{aligned} \tag{11.9}$$

where GWP is total global warming potential; L is leakage rate; n is system operating life (year); m is refrigerant charge (kg); α-recovery is recovery/recycling factor from 0 to 1; E_{annual} is energy consumption per year (kWh); and β is indirect emission factor (kg CO_2/kWh) [20].The global warming effects of different substances are compared with an index used for CO_2 emission known as the GWP. The GWP of a substance is defined as the global warming impact due to the emission of 1 kg of that substance is divided by the global warming impact of 1 kg of CO_2. The GWP values applied relate to a time horizon of 100 or 500 years [21]. Whole of the climatic effects caused by cooling processes is the sum of direct and indirect greenhouse gas emissions. Direct effect includes emissions of refrigerant due to maintenance, repair, and leakage effects (losses during its life cycle). Indirect effect includes CO_2 emissions, which are emitted depending on the electrical energy supplied from a power plant to operate the system [22]. In the TEWI analysis, the emission per unit produced energy is a parameter taken into account in the calculation of the indirect effects of TEWI. In calculation of the indirect effects, the effect values of CO_2 emissions per unit of energy are considered different in the world. In this study, 0.47 kg CO_2/kWh that is adopted in North America, Europe, and Japan has been recognized as the CO_2 emission.

11.5 Results and Discussion

When examples of low-charge application are examined, a cooling capacity of up to about 100 kW and a refrigerant charge of almost 40 kg are observed. In this system, 2.77 kg refrigerant charge per kW cooling load is used. In study, this value has been an accepted reference, and direct expansion (D4) systems have been made a comparative analysis for per unit cooling capacity. Besides, COP and exergetic analyses were examined using Eqs. (11.1–11.8) for R-404A and R-507 refrigerants and R-152a and R-407C refrigerants investigated as alternative in the adiabatic conditions at −15/46 °C temperature limits. In evaporating temperature ranges between −15 °C and 5 °C, the COP and exergetic performance are calculated separately. COP distributions of the refrigerants are given in Fig. 11.3.

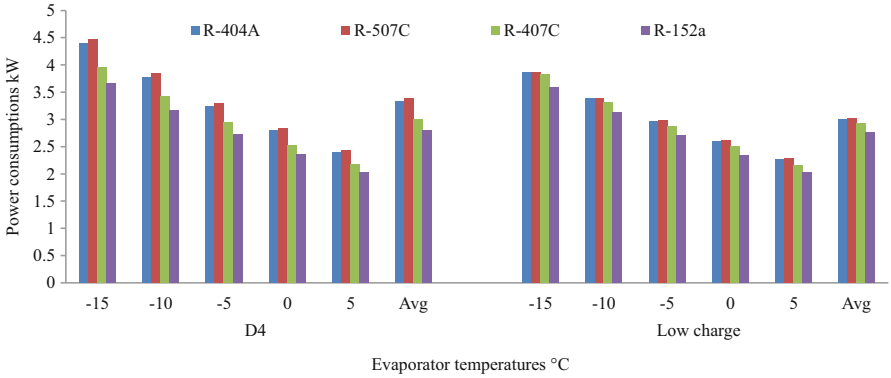

Fig. 11.4 Power consumption based on refrigerants

COP advantages of R-404A and R-507 refrigerants, which are intensively used in the cooling sector, have been determined 10.4% and 9.47%, respectively. Characteristics of the alternative refrigerants showed close feature for both systems. For R-407C and R-152A refrigerants, advantages of low-charge system were calculated 11.2% and 0.7%, respectively. In low-charge system, average COPs for R-404A, R-507, R-407C, and R-152a were found 3.098, 3.078, 3.194, and 3.396, respectively. In the analysis, the effects of alternative gases have been seen to be highly effective compared to current gases. Similar analyses are studied according to the compressor power consumption, and results of analysis are shown in Fig. 11.4.

The compressor energy consumption shows similar characteristics to the COP distribution. Accordingly, compressor power consumption advantages of the low-charge system for R-404A, R507, R-152a, and R-407C are 10.43%, 11.63%, 1.08%, and 2.38%, respectively. Compressor power consumption in low-charge applications is range of 2.76 kW to 3026 kW per kW of cooling. The advantages of R-407C and R-152a among these refrigerants in comparison with R-404A are 8.31% and 2.46%, respectively. Identification of real irreversibility of the system at low-charge applications is expressed with exergy analysis. With this perspective, comparative exergy analysis of low-charge and D4 systems has been shown in Fig. 11.5.

Exergy efficiency for such thermal processes is important for identification of irreversibility and determination of potential improvements in systems. Exergy efficiency of low-charge system is found in the range of 0.8% and 9.90% to be better than D4 systems based on refrigerant types. In this analysis, it is seen that refrigerant choice is also the effect on the system performance in comparison with other systems. Indeed, while exergy efficiency of R-404A is 56.23%, average exergy efficiencies of refrigerants R-407C and R-152a, proposed as an alternative, are 57.85% and 61.50%. When these refrigerants are compared with the current refrigerants, while refrigerants R407C and R-152a have better performance 3.53% and 10.05% in comparison with R-507, they have better performances 2.88% and 9.37% in comparison with R-404A, respectively.

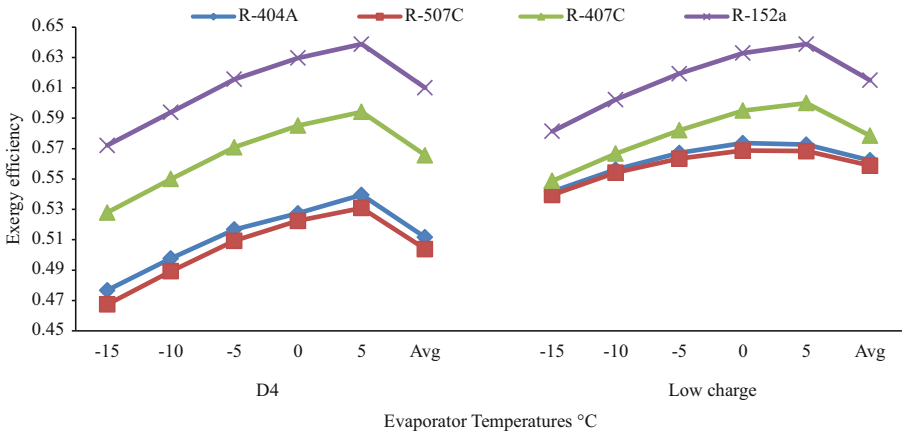

Fig. 11.5 Exergy efficiencies based on refrigerants

Table 11.1 Environmental features of refrigerants

Refrigerant	R-404A	R-507	R-407C	R-152a
ODP	0	0	0	0
GWP	3900	4000	1530	140
Atmospheric life (year)	16	–	29	29

In the early 1990s, the effects of global warming of refrigerants used in air conditioning and refrigeration applications have been found to be quite high due to their ozone depletion and global warming potentials. Firstly, for decreasing of this effect and usage and sale of hydrochlorofluorocarbons (HCFCs) and chlorofluorocarbons (CFCs) instead of the commonly used refrigerants, e.g., ammonia, in the 1930s, the cooling systems are limited by the Montreal Protocol and the European Council Directive (3093/94) (Horst, 2000). Hydrofluorocarbons (HFCs) and R-134a, R-404A, R-507, R-407C, and R-410A which are mixtures of HFCs began to be used widely as alternatives for HCFCs and CFCs in the supermarket refrigeration applications. Although these refrigerants have low ODP, a high GWP stands out as a significant problem in terms of the environmental impact [4]. The environmental features of the proposed alternative refrigerants and the refrigerants used in the low-charge system are given in Table 11.1.

Recycling factor for environmental parameters assumed the lowest value is 0.5, and the highest is 0.95. The leakage rate for low-charge system seems as the lowest 15% and the highest 30% in literature. Analysis was performed considering minimum and maximum leakage rate. 8600 operating hours per year for emissions is taken as reference. CO_2 equivalent emission potentials of low-charge system are evaluated separately, and the results are given in Table 11.2.

In TEWI analysis, the lowest and the highest emission potentials of R-404A are 202.3 tonCO_2/year and 226.5 tonCO_2/year, respectively. The emission potential of

Table 11.2 TEWI values of refrigerants

	System				
	Low charge		D4 system		Advantage of CO_2
	kg/CO_2 year		kg/CO_2 year		kg/CO_2 year
Refrigerant	Min	Max	Min	Max	
R-404A	202300.8	226506.3	221338.6	245544.1	19037.82
R-507	203513.9	228016.4	224855.6	249358.1	21341.76
R-407C	187304.4	198664.7	191548.5	202908.8	4244.1
R-152a	168189.3	169228.8	170008.2	171047.7	1818.9

R-507 is higher than from R-404. However, emissions of R-407C and R-152a as an alternative refrigerant are the lowest 187.3 tonCO_2/year and 168.2 tonCO_2/year and the highest 198.7 tonCO_2/year and 169.2 tonCO_2/year, respectively.

11.6 Conclusions

In this study, COPs and exergy efficiencies for low-charge cooling systems and D4 systems were comparatively examined considering an analytic study. Besides, these analyses were repeated for each different refrigerant. Then, the potentials of environmental effect for each refrigerant are calculated according to the TEWI values. The results obtained from these analyses are shown as follows:

(a) While COP of R-404A is 3.098, R-407C and R-152a were found 3.194 and 3.396, respectively.
(b) While irreversibility rate for R-404A was 57.85%, they were found 56.23% and 61.50% for R-407C and R-152a, respectively.
(c) Compressor power inputs for R-407C and R-152a are lower 8.31% and 2.46% in comparison with R-404A.
(d) When equivalent emission potential of CO2 is examined, the emission potentials of proposed refrigerants as an alternative are lowest. When R-404A is taken as reference, emissions of R-407C and R-152a as an alternative refrigerant are the lowest 187.3 tonCO2/year and 168.2 tonCO2/year and the highest 198.7 tonCO2/year and 169.2 tonCO2/year, respectively.

Results from investigations regarding low-charge multiplex refrigeration systems and the others provide crucial information about energy demand and amount of refrigerant charge supermarkets in the future. These results can be guide about the size of TEWI values of refrigerants used in cooling systems based on this energy demand.

This study revealed that low-charge system has the lower energy consumption. Besides such potential impacts, the refrigerant selection based on exergetic approach is very important parameter in terms of energy consumption. In other words, not

only insufficient of the COP concept but also the requirement of exergy analysis to determine irreversibility rate is revealed. New-generation refrigerants can be evaluated further.

Nomenclature

E_{annual}	Energy consumption (kWh/year)
GWP	Total global warming potential
L	Leakage rate
h	Enthalpy (kJ/kg)
$\dot{m}$	Mass flow rate of refrigerant/refrigerant charge (kg/s)
n	System operating life (year)
T_{H}	Outdoor temperature (K)
T_{L}	Temperature of cold environment where heat is absorbed (K)
$\dot{Q}_{\text{evap}}$	Heat absorbed from the cooled area (kW)
$\dot{Q}_{\text{cond}}$	Heat rejection to environment by means of condenser (kW)
$\dot{W}_{\text{comp}}$	Compressor power input (kW)
α	Recovery/recycling factor
β	Indirect emission factor (kg CO_2/kWh)

References

1. Baxter VD (2003) IEA Anne4 26: advanced supermarket refrigeration/heat recovery systems final report volume 1 – E4ecutive summary. Oak Ridge National Laboratory, Oak Ridge
2. Horst K (2000) Refrigerant use in Europe. ASHRAE J. www.ashraejournal.org
3. Bagarella G, Lazzarin R, Noro M (2014) Annual energy analysis of a water-loop self-contained refrigeration plant and comparison with multiple4 systems in supermarkets. Int J Refrig 45:55–63
4. Schijnel PPAJV, Kasteren JMN, Janssen FJJG (1998) Exergy analysis–a tool for sustainable technology – in engineering education. Eindhoven University of Technology, The Netherlands
5. Dincer I, Rosen MA (2005) Thermodynamic aspects of renewable and sustainable development. Renew Sust Energ Rev 9:169–189
6. Stegou-Sagia A, Paignigiannis N (2005) Evaluation of mi4tures efficiency in refrigerating systems. Energy Convers Manag 46:2787–2802
7. Otaibi DA, Dincer I, Kalyon M (2004) Thermoeconomic optimization of vapor-compression refrigeration systems. Int Commun Heat Mass Transfer 31(1):95–107
8. Schwiegel M, Meurer C (1998) Refrigerants concepts for commercial refrigeration, Solvay Fluor und Derivate GmbH Technical Service-Refrigerants-Product Bulletin no. C/0302/16/E, 3–4
9. Hellmann J, Barthelemy PA (1997) TEWI III study: results and evaluation of alternative refrigerants, Solvay Fluor und Derivate GmbH Technical Service-product Refrigerants, no: C/11.97/06/E
10. Rhiemeier JM, Kauffeld M, Leisewitz A (2009) Comparative assessment of the climate relevance of supermarket refrigeration systems and equipment, Environmental Research of the Federal Ministry of Environment Nature Conservation and Nuclear Safety Research Report 206 44 300, UBA-FB 001180/e, Federal Environmental Agency

11. Brian F, Bryan B (2010) Energy use of doored and open vertical refrigerated display cases In: 13th international refrigeration and air conditioning conference at Purdue, July 12–15, West Lafayette, IN, USA
12. ICF Consulting for U.S. EPA's Stratospheric Protection Division (2005) Revised draft analysis of U.S. commercial supermarket refrigeration systems, November 30, 2005
13. Zhang M (2006) Energy analysis of various supermarket refrigeration systems. In: international refrigeration and air conditioning conference, Purdue University, Indiana-United States
14. Özay A, Ali G (2010) Maximum performance analysis for CO2 refrigeration cycles. J Therm Sci Technol 30(2):37–43
15. Gungor A (2011) Comparison of technologies used in supermarket refrigeration systems in terms of energy efficiency, 4. National Installation Engineering Congress –/İzmir, pp 1185–1199
16. Scott D (2007) Refrigeration control for operating cost reduction, ASHRAE 2007 annual meeting, Long Beach, California
17. Dincer I, Kanoglu M (2010) Refrigeration systems and applications, 2nd edn. Wiley, Chichester
18. Cengel Y, Boles MA (2001) Thermodynamics: an engineering approach, 4th edn. McGraw-Hill, New York
19. Hepbasli A (2010) A review on energetic, energetic and energoeconomic aspects of geothermal district heating systems(GDHSs). Energy Convers Manag 51(10):2041–2061
20. Moore D (2005) A comparative method for evaluating industrial refrigerant systems, Sabroe Ltd. (revA). www.sabroe.org
21. Dupont (2005) Dupont refrigerants the science of cool, Du Pont de Nemours (Germany) GmbH, Germany. www.refrigerants.dupont.com
22. Eurammon (1996) Evaluation of the environmentally friendly refrigerant ammonia according to the TEWI Concept. NH3 for ecologically friendly future, Frankfurt, Germany. www.eurammon.com

Chapter 12
Aerodynamic Design of a Twin-Entry Radial-Inflow Turbine Impeller: A Numerical and Experimental Investigation

Siavash Vaezi, Misagh Irandoost Shahrestani, and Farshad Ravosh

12.1 Introduction

Radial-inflow turbines have a specific role in the industry. Their applications are mostly considered when the need for power generation in a small space matters. Radial turbine is one of the main components of turbochargers which increases the power-to-weight ratio and efficiency of engines. Utilization of the twin-entry radial-inflow turbine in a turbocharger allows the use of pulse energy of the output exhaust gas of an engine's cylinders. Therefore, the design knowledge and analysis of these turbines are an essential need for the industry.

The design of a radial turbine's impeller can generally be carried out in two different ways, direct and indirect method. In direct method the designer obtains the geometry of the impeller by using parameters like inlet total pressure and temperature and other geometrical constraints. Afterwards, the geometry is analyzed and modified until the desired performance is achieved. The possibility to control the geometrical constraints is one of the advantages of this method. In indirect method, the designer starts with preliminary geometry, and some modifications are applied by analysis of the flow field and this process is repeated until the optimum geometry is obtained. The radial turbine studies include 1D modeling as well as 2D and 3D numerical simulations. One-dimensional modeling is the most appropriate method for performance prediction in the primary steps of designing due to high computational cost of 2D and 3D methods. Futral and Wasserbauer [1] studied a radial turbine which was used as powers generation in NASA's spatial system.

S. Vaezi (✉) · F. Ravosh
Sharif University of Technology, Mechanical Engineering, Tehran, Iran
e-mail: vaezi_siavash@alum.sharif.edu

M. Irandoost Shahrestani
University of Tehran, Mechanical Engineering, Tehran, Iran

S. Nižetić, A. Papadopoulos (eds.), *The Role of Exergy in Energy and the Environment*, Green Energy and Technology,
https://doi.org/10.1007/978-3-319-89845-2_12

Wasserbauer and Glassman [2] estimated the off-design performance of radial-inflow turbine by FORTRAN program. Wallace et al. [3] used one-dimensional modeling to predict the performance of radial turbine. The design of radial turbine has been described by Rohlik [4] and Benson [5]. Whitfield [6] considered the non-dimensional design of radial turbine. The goal of his method was to reduce the inlet and outlet Mach number of impeller in order to minimize the loss. Zangeneh [7] performed three-dimensional design of a radial turbine by using indirect method. He achieved the three-dimensional shape of the blade by determining the average tangential component of velocity and solving three-dimensional equations of subsonic compressible flow. Studies on 1D design of radial turbines was also conducted by Ebaid et al. [8]. Moustapha et al. [9] presented an integrated method for a radial turbine's design. In this method the designer chooses the flow coefficient and stage-loading coefficient in the desired range, and the design point for optimum efficiency will be achieved by changing these parameters successively. Xuwen Qiu et al. [10] presented a mean line method for modeling a radial turbine with variable area nozzle.

The purpose of this research is aerodynamic design of the main part of the radial turbine, i.e., the impeller. In this chapter, three targets are followed. The first is to initially present a method for designing twin-entry radial turbine impeller based on the direct method. The second goal is to conduct an experimental study on radial turbine in Sharif University of Technology turbocharger lab to obtain the performance curves of the turbine. The third goal is to use 1D modeling method to predict the performance of turbine with designed and the existing impeller.

12.2 Preliminary Design

Preliminary design which is called mean line design is based on the assumption that there is a mean streamline running through the machine, and the conditions on this streamline are representative of the stations being considered [11]. The objective of mean line analysis is not to reveal the full details of the flow state and velocity through the machine [9]. In most of the 1D design methods, a lot of assumptions are considered. It is obvious that the lesser the assumptions are, the more accurate the properties of flow field are predicted and can affect the final geometry of the blade. In this research, it has been tried to use less assumptions and primary data. The design primary data include $T_{0_i}, \dot{m}, P_{0_i}, \frac{P_{o_i}}{P_{s_o}}, \eta_{t-s}, n_S$. Furthermore, the designer needs some geometrical constrains such as $\frac{r_h}{r_s}$, or blade angle at inlet or outlet.

In this research two primary assumptions are considered: (1) at impeller's inlet, the blade is radial which means that the blade angle at inlet is equal to zero; therefore, the incidence angle is equal to flow relative angle. (2) At outlet there is no swirl. This assumption prevents efficiency decrement due to the swirl at the outlet [12]. It is worth noting that these assumptions are considered at design point and might not be established in off-design points. Impeller is the most important part of a radial-inflow

turbine, and most of the losses are related to impellers. In the following, the impeller's losses and the experimental model for them will be considered.

12.2.1 Incidence

Flow usually enters the impeller with nonzero incidence angle, but experimental results show that in short distances from the impeller's entrance, the flow obey the impeller's geometry as well [13]. If the incidence angle differs from the optimum incidence angle, significant loss happens in a small area which is called incidence area. The target of incidence model is to determine the optimum incidence angle and entropy increment due to the incidence loss. For achieving the incidence loss, the NASA incidence model, which was presented by [14], was used. In this model it is assumed that kinetic energy related to the relative tangential component velocity is converted to the internal energy of the fluid. According to the Eq. (12.1), the incidence loss is obtained by:

$$\Delta q_{\text{in}} = 0.5\left[\frac{w_{\text{i}} \sin\left(\left|\beta_{\text{i}} - \beta_{\text{i,opt}}\right|\right)}{U_{\text{i}}}\right]^2 \tag{12.1}$$

It is suggested that if the $|\beta_{\text{i,opt}} - \beta_{\text{i}}|$ is greater than $\frac{\pi}{4}$; Eq. (12.2) can be used for incidence loss [15]:

$$\Delta q_{\text{in}} = 0.5 W_{\text{i}}^2 \left(0.5 + \left|\beta_{\text{i}} - \beta_{\text{i,opt}}\right| - \frac{\pi}{4}\right) \tag{12.2}$$

12.2.2 Friction

These kinds of losses are due to the fiction between flow and walls. Furthermore, secondary flows are made due to the curved pass, and they cause loss through the impeller. Friction loss and loss due to the curved pass are considered together, and they are achieved with one correlation [13].

$$\Delta q_{\text{f}} = \frac{4C_{\text{f}}\left[\left(\frac{W_{\text{i}}}{a_{01}}\right)^2 + \left(\frac{W_{\text{o}}}{a_{01}}\right)^2\right]}{4\left(\frac{D_{\text{H}}}{L_{\text{H}}}\right)\left(\frac{U_{\text{i}}}{a_{0\text{i}}}\right)^2} \tag{12.3}$$

12.2.3 Blade Loading

Loading loss is one of the most important losses in impellers and is representative of the ability of the blade in obtaining energy from the flow. This kind of loss is due to the difference between loading force of the fluid on the blade and the force related to the distribution of the static pressure [16].

$$\Delta q_{\mathrm{bl}} = \frac{2\left(\frac{C_{\theta i}}{U_{\mathrm{i}}}\right)^2}{Z_{\mathrm{b}} L_{\mathrm{R}}} \tag{12.4}$$

12.2.4 Clearance

Because of the clearance between blade and shroud, flow moves from pressure side to suction side and causes some loss which is called tip-leakage loss, and it is accounted by this correlation [13].

$$\Delta q_{\mathrm{cl}} = 0.4\left(\frac{e_{\mathrm{cl}}}{b_2}\right)\left(\frac{C_{\theta i}}{u_{\mathrm{i}}}\right)^2 \tag{12.5}$$

$$e_{\mathrm{cl}} = \frac{0.008}{\frac{b_{\mathrm{i}}}{r_{\mathrm{i}}}} \tag{12.6}$$

12.2.5 Exit Loss

This loss is due to the nonexistence of diffuser in outlet [17].

$$\Delta q_{\mathrm{ex}} = 0.5\left(\frac{C_{\mathrm{o}}}{U_{\mathrm{i}}}\right)^2 \tag{12.7}$$

Finally, with regard to relations (12.1), (12.2), (12.3), (12.4), (12.5), (12.6), and (12.7), the sum of the impeller's losses (Δq_{th}) is carried out, and impeller's efficiency can be accounted by relation (12.8):

$$\eta_{\mathrm{RC}} = \frac{\Delta q_{\mathrm{th}}}{\Delta q_{\mathrm{th}} + \Delta q_{\mathrm{tot}}} \tag{12.8}$$

$$\Delta q_{\mathrm{tot}} = \frac{C_{\theta i}}{U_{\mathrm{i}}} \tag{12.9}$$

12.2.6 Preliminary Design Algorithm

The target of this design is to achieve the geometry of a blade which has the same dimension with the blade used in experimental studies. The process of the design is in such a way that at first, the designer chooses the inlet data such as inlet total pressure and temperature, mass flow rate, and outlet static pressure and then the outlet hub radius to inlet radius ratio, and outlet shroud radius to inlet radius are chosen according to proportions used in existing blade. In design, the ratio r_{h5}/r_4 and r_{s5}/r_4 $^{r_{s5}}/_{r_4}$ are considered 0.38 and 0.89, respectively. Then the amount of total efficiency to static efficiency is estimated. The amounts of absolute and relative flow angle as well as the optimum number of the blades are determined with regard to the relation (12.10), (12.11), and (12.12) which were presented by Rohlik [12] and Glassman [13] to minimize the incidence loss. According to these values and gas dynamic relations, the properties of the flow as well as velocity triangle in inlet and outlet are carried out. In this step the designer can obtain the impeller's losses, and the efficiency of the impeller and turbine can be calculated according to the losses, and it can be compared with estimated efficiency. If these two efficiencies are equal, then the process of design is stopped, and the results are written; otherwise, estimated efficiency is corrected according to the calculated efficiency, and the process is repeated until the value of efficiency with considering losses gets close to the ideal efficiency. In this method, it has been tried to use the lowest possible inlet data; therefore, the method used has high flexibility. The algorithm used for preliminary design can be seen in Fig. 12.1.

$$\alpha_i = 90 - \left(10.8 + 14.2 n_S^2\right) \tag{12.10}$$

$$\cos^2(\alpha_i) = \frac{0.63\pi}{2Z_b} \tag{12.11}$$

$$\cos(\beta_i) = 1 - \frac{0.63\pi}{Z_b} \tag{12.12}$$

12.3 Experimental Facility

The test facility of Sharif University turbocharger lab is shown in Fig. 12.2. In this laboratory, compressed air is used in order to investigate and simulate the turbine's performance. Compressed air is supplied by five screw compressors and then stored in reservoirs. The pressure of the reservoirs changes from 6 to 7 bar. Then a control valve (number 1) adjusts its pressure and mass flow rate, and an orifice plate is used to measure the flow rate of the fluid. Air enters the turbine by two adjustable ducts and control valve numbers 3 and 4. In the entrance of the turbine, total temperature and pressure as well as static pressure are measured by J-type thermocouple and a pitot tube, respectively.

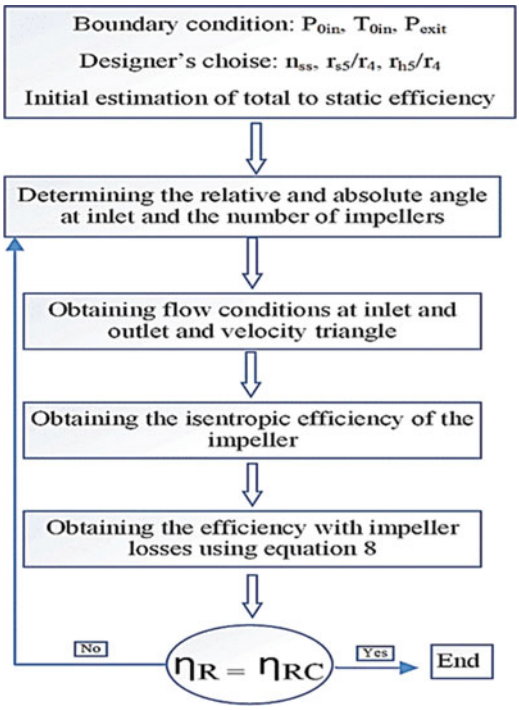

Fig. 12.1 Algorithm for preliminary design

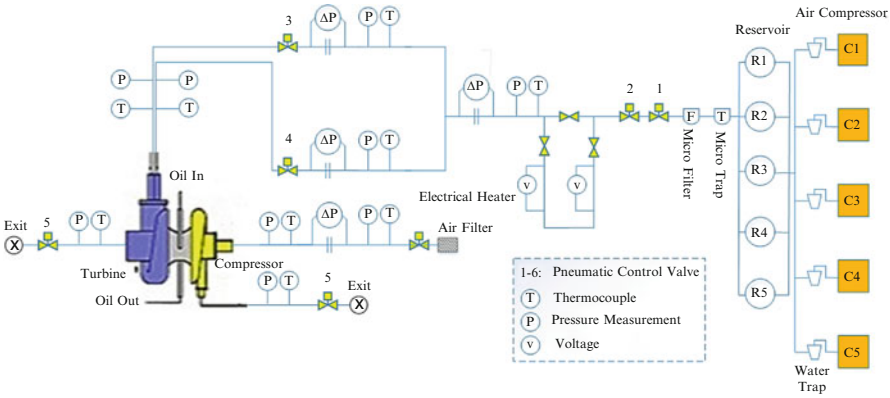

Fig. 12.2 Experimental installation of turbocharger lab

Pressure- and temperature-measuring devices are embedded in outlet as well. Air is expanded after passing through the turbine and drives its blades and the shaft as well. It should be noted that the optical tachometer is used for measuring the rotational speed of the shaft.

12.4 1D Modeling in Full Admission Condition

There are two different operating conditions in twin-entry radial turbine, full and partial admission. In full admission the total pressure is equal on both two turbine's entrance, but in partial admission, the total pressure is not equal. In this research the full admission is just considered, so it can be concluded that the inlet flow rate is equal on both turbine's entrance.

In step by step analyzing for 1D modeling, turbine is considered as separated channels. In this method as the inlet flow conditions in each section's entrance and the geometry of flow path are specified, the flow condition can be carried out in the outlet by using experimental relations for energy losses. Then these outlet conditions are used as inlet conditions for the next part. This process is repeated until the flow is solved in the whole turbine. These paths include entrance channel (0–1), volute including hub-side channel and shroud-side channel (1–2), interspace (2–3), incidence area (3–4), and the impeller (4–5). General Eq. (12.13) for twin entry turbine is a dimensionless mass flow rate equation which must be solved for each channel that combines the continuity equation, energy equation, and entropy [13]. In Eq. (12.13), σ is the energy loss coefficient which is achieved from Eq. (12.14):

$$\begin{aligned}
&\frac{\dot{m}\sqrt{\frac{R}{\gamma}}}{A_e}\left(\sqrt{\frac{T'_{0i_s}}{P'_{0i_s}}}\right)^{Mr_s}\left(\sqrt{\frac{T'_{0i_h}}{P'_{0i_h}}}\right)^{Mr_h} = \sigma\cos(\beta_e)M'_e \\
&\times\left(1+\tfrac{\gamma-1}{2}M'_e 2\right)^{\frac{\gamma+1}{2(1-\gamma)}}\times\left[\left(1-\frac{U_i^2-U_e^2}{2C_pT'_{0i_2}}\right)^{Mr_s}\left(1-\frac{U_i^2-U_e^2}{2C_pT'_{0i_2}}\right)^{Mr_h}\right]^{\frac{\gamma+1}{2(1-\gamma)}}, \\
&Mr_s=\frac{\dot{m}_s}{\dot{m}_s+\dot{m}_h},\quad Mr_h=\frac{\dot{m}_h}{\dot{m}_s+\dot{m}_h}
\end{aligned} \tag{12.13}$$

$$\sigma = e^{-\frac{\Delta s}{R}} = \left(1-\frac{\gamma-1}{\gamma RT'_{0e}}U_t^2\frac{1}{2}\Delta q\right)^{\frac{\gamma}{\gamma-1}} \tag{12.14}$$

$$\Delta q = \frac{h'_{0e}-h'_{0es}}{U_t^2} \tag{12.15}$$

12.4.1 Stationary Channel

In turbine, stationary channel includes entrance, volute, and interspace. In stationary channel loss coefficient is equal to outlet-to-inlet total pressure ratio. In entrance section loss coefficient and outlet angle are 1 and 0, respectively, due to short distances. For the volute, the method presented by [18] is used. In the volute and entrance sections, Eq. (12.13) is solved for both shroud side and hub side separately,

but in the interspace section, due to mixing of two flows, the impact of two streams on each other must be considered. In this section, the friction loss and the effect of wake made by the separator wall are considered separately. For friction loss numerical method presented by [19] is used. In this method continuity and momentum equation in both radial and tangential direction, energy equation, and gas equation of state are solved, and then loss coefficient and outlet angle are obtained. To take the losses of the separator wall into account, a sequence is used. By considering the average of the inlet conditions and solving continuity, momentum, and energy equation, the outlet condition is achieved [20]. Then wake loss coefficient is obtained, and the total loss coefficient is calculated with regarding to the relation (12.16).

$$\sigma_{2-3} = \sigma_{\text{friction}} \sqrt{\sigma_{\text{wake}}} \tag{12.16}$$

12.4.2 Moving Channel

Moving channel includes incidence area and impeller. The incidence area is considered as hypothetical duct that is placed immediately upstream of the impeller and downstream of the interspace. The target of modeling of this section is to achieve the optimum incidence angle and its losses. Equation (12.13) must be solved separately for shroud side and hub side in this area. For the impeller, the dimensionless flow rate equation is solved with regard to the relations presented in part (II). In the impeller section, the only unknown parameters are loss coefficient and Mach number since the outlet angle is the known geometrical parameter.

12.4.3 1D Modeling Algorithm

The algorithm used in this case is as follows: at first the geometry data of turbine, inlet total pressure and temperature of each entrance, and outlet static pressure are entered in the 1D code, and a value for the mass flow is guessed. Then the Eq. (12.13) is solved for each channel, and the outlet calculated conditions are considered as the inlet condition for next channel. The method of solving Eq. (12.13) is that if the loss coefficient and outlet angle are unknown, an initial guess is considered for them, and the equations for Mach number and outlet flow conditions are solved, and then the guessed parameters are corrected if needed till achieving Mach number convergence. The solution of this equation is kept on till the end of the turbine. Then the calculated static pressure is compared with the pressure used as the input data. If the difference between these two values is less than the considered error, the results are written; otherwise the above process is repeated until the static pressure is converged. 1D modeling algorithm is seen in Fig. 12.3.

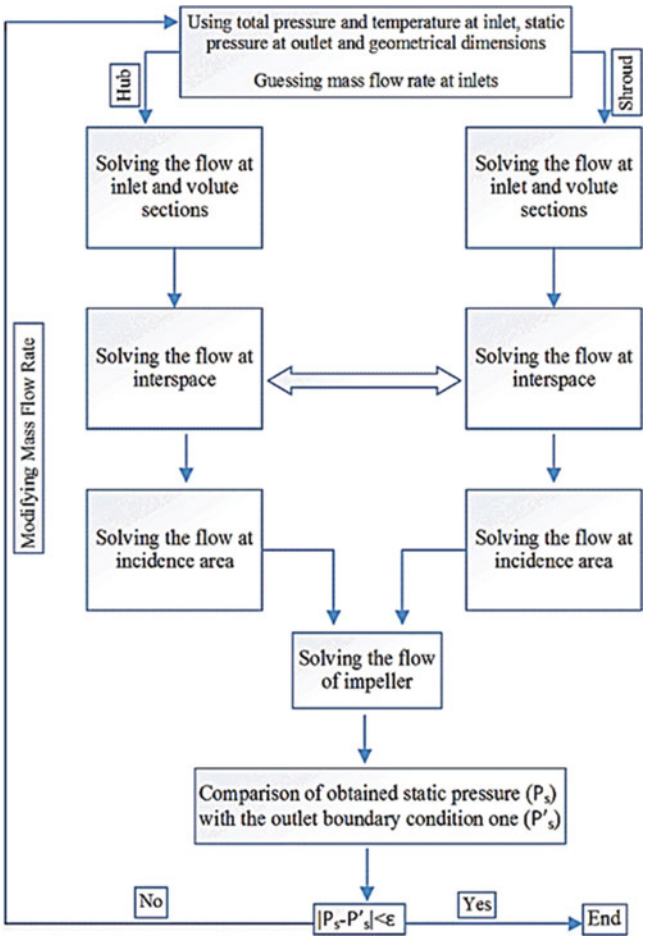

Fig. 12.3 1D modeling algorithm

12.5 Detailed Design

After achieving the primary dimensions of the blade in preliminary design, it is needed to determine the profiles of hub and shroud that is done in detailed design. The detailed design includes two stages. First, the primary curves of the hub and shroud are shaped, and then with the use of Bezier polynomial curve, profiles will be shaped accurately.

There are several methods for drawing of curves; one of these methods is Bezier polynomial. The reason for choosing this method is having high accuracy and high flexibility in drawing of curves. In this research for plotting curves, seven reference points were used; therefore, the accuracy is equal to six orders. For choosing reference points, at first the primary curves of hub and shroud and the blade angle

distribution are achieved, and then reference points are chosen on each curve, and the final shape of the blade is carried out.

12.5.1 The Primary Curve of Hub and Shroud

The impeller hub contour is constructed to minimize passage curvature effects by using the largest circular arc that is compatible with the rotor dimensions obtained from the rotor sizing. The radius of this arc depends *on the blade's dimension that is* carried out with regard to the below relations [12]:

$$R_c = L_R \quad \text{if } L_R + r_{h5} < r_4 \tag{12.17}$$

$$R_C = r_4 - r_{h5} \quad \text{if } L_R + r_{h5} > r_4 \tag{12.18}$$

Figure 12.4 shows the primary hub when the inlet radius is bigger than the sum of the hub radius in outlet and the length of the blade. For primary contour of the shroud curve, the power profiles are used according to Eq. (12.19). The order of this curve can be from 2 to 9, but the fact that which power must be chosen depends on which n the A_m area is made of connecting the middle point of tow contours, is equal the average of the inlet and outlet area.

$$r = r_{s5} + (r_4 - r_{s5})\xi^n, \qquad \xi = \frac{z - z_5}{L_R - b_4} \tag{12.19}$$

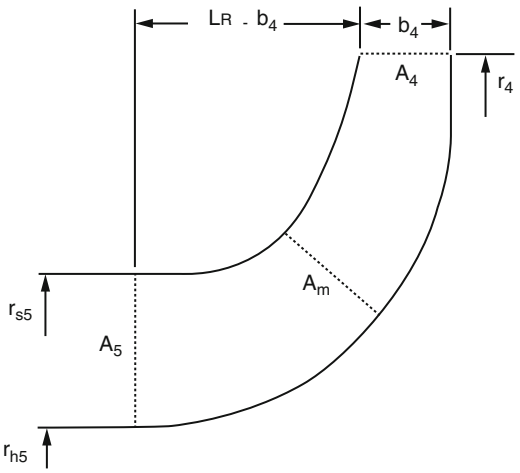

Fig. 12.4 Primary curve of hub and shroud

12.5.2 Camber Line Along Hub and Shroud

In radial-inflow turbine which works in high-rotational speeds, using of radial blade for removing bending tension that is made of centrifugal forces is common [12]. The radial blade is defined by the following equation:

$$\frac{\partial \theta}{\partial r} = 0 \tag{12.20}$$

According to the Eq. (12.20), the θ distribution can be applied only on one of the profiles. Furthermore, θ is constant for each value of z from Z_s to Z_h. In this case the shroud profile is chosen, and since the blade angle is considered zero in inlet, the Eqs. (12.21), (12.22), (12.23), and (12.24) are used [12].

$$\theta(\mathrm{m}) = A\mathrm{m} + B\mathrm{m}^2 + C\mathrm{m}^3 \tag{12.21}$$

$$A = \frac{\cot \beta_{5s}}{r_{53}} \tag{12.22}$$

$$B = \frac{1}{m_4^2}\left[-\frac{\cot \beta_{5s}}{r_{5s}}\right] \tag{12.23}$$

$$C = -\frac{B}{2m_4} \tag{12.24}$$

In the above equations, m_4 is the total meriodional length of shroud profile. In order to obtain cot β_{3s} in above equations, it is assumed that there is no swirl in outlet. Therefore, C_θ is equal to zero and c_m is constant from hub to shroud.

$$r_m \tan \beta_m = r_{5s} \tan \beta_{5s} = r_{5h} \tan \beta_{5h} \tag{12.25}$$

In Eq. (12.25) r_m and β_m are average radius and blade angle, respectively, which are calculated from the preliminary design. To plot the camber line of the hub side, Eq. (12.21) is used and since θ is constant from Z_s to Z_h, numerical interpolation of θ can be used as a function of z. With known values of θ, the blade angle is calculated according to the following equation [12]:

$$\cot \beta = r\frac{\partial \theta}{\partial m} \tag{12.26}$$

Now by using seven reference points on each curve, the final hub and shroud profiles and blade angle distribution are calculated.

Table 12.1 Input data for design code

Parameter	Value
$\dot{m}$	0.13
P_{OIN}	1.57
T_{OIN}	1000
P_{exit}	0.94
η_{t-s}	0.8
r_{s3}/r_2	0.89
r_{h3}/r_2	0.38
n_s	0.57

Table 12.2 Dimensions of designed impeller and comparison with existing impeller

	Designed	Existing
r_2	37	37
r_{s3}	32.9	32.9
r_{h3}	14	14
b_2	14.2	14
L_R	28.3	28.5
Z	14	10

12.6 Results

In Table 12.1 the input data for the design code is shown. Some of data are obtained from test results of Sharif University Gas turbine lab. The value for efficiency is the initial estimation modified in code procedure, and the chosen value for specific velocity is considered based on the reference [12]. In Table 12.2 the geometrical dimensions of the designed turbine impeller and the comparison with the existing impeller can be seen. According to this table there is good agreement between the dimensions of two impellers, and there is only a slight difference between the width of the blade at the entrance and the length of the blade. Another difference is the number of the blades. According to [13] the optimum incidence, the angle depends on the number of the blades, and because of this, to minimize the incidence loss in design point, the Glassman's method is used in this research, and this causes difference in the number of blades. In the following sections, the effect of blade number increment is investigated. In Table 12.3 the performance of the turbine in design point is shown. It is obvious that most of the parameters are in the ideal range. In Table 12.4 the components of velocity triangle at inlet and outlet are shown. According to this table, the incidence angle at inlet is about -30° which is ideal. Furthermore, the outlet absolute angle is equal to zero which means there is no swirl in exit.

The diagram of efficiency and mass parameter in terms of pressure ratio based on the modeling and experimental results for 40,000, 50,000, and 60,000 rpm are seen in Figs. 12.5 and 12.6. According to Fig. 12.5, for a constant rotational speed, the efficiency increases by enhancing the pressure ratio and decreases after reaching to its maximum value. In low-pressure ratios, the incidence loss is great, but as it gets close to the optimum value, a decrement in the loss is seen. Over the optimum area,

Table 12.3 Turbine's performance in design point

Parameter	Value	Ideal range
ψ	0.86	0.9–1
$\varnothing$	0.27	0.2–0.3
U_2/C_s	0.67	0.6–0.7
R_n	0.58	0.45–0.65
η_R	0.81	
η_t	0.78	
$\dot{W}$ (KW)	13.85	

Table 12.4 Velocity triangle at inlet and outlet

Parameter	Inlet	Outlet
Blade angle	352.235 (m/s)	223.67
Absolute velocity	313.738 (m/s)	94.09
Relative velocity	97.11(m/s)	242.62
Absolute flow angle	74.58 (deg)	0
Relative flow angle	−30.83 (deg)	−62.65

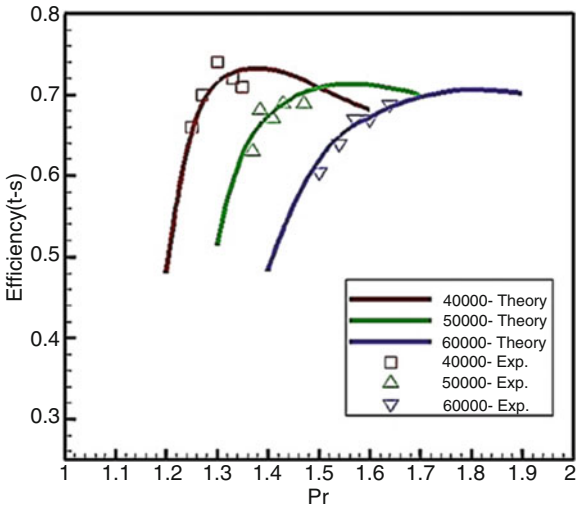

Fig. 12.5 Variation of efficiency versus pressure ratio

the incidence loss increases once again. Another point which is seen in this figure is a decrement of maximum value of efficiency by increasing the rotational speed. This can be due to the increment of incidence, friction, and blade-loading losses in higher rotational speed. According to Fig. 12.6, mass parameter increases by pressure ratio increment, and the curve tends to the constant mass parameter condition asymptotically. The mass parameter increment due to the pressure ratio increment in a constant rotational speed indicates that the absorbed energy from the fluid is enhanced.

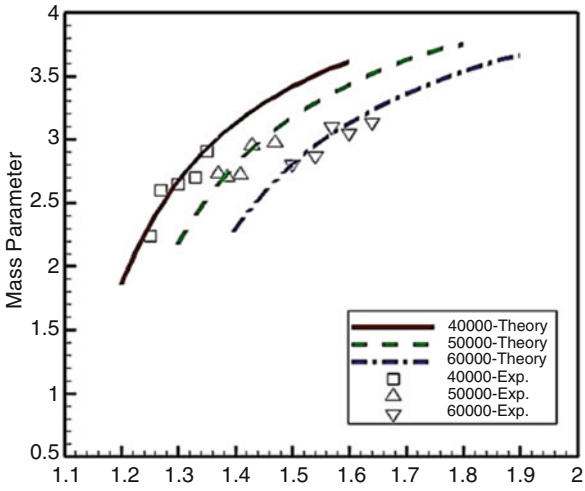

Fig. 12.6 Variation of mass parameter versus pressure ratio

At the other side, the mass parameter decreases in higher rotational speeds in a constant pressure ratio. This can be attributed to the increment of centrifugal forces due to the rotational speed increment which is a counterpoise against the inlet mass flow. The comparison between experimental and modeling results shows that by increasing the rotational speed, the discrepancy decreases. The maximum difference in efficiency and mass parameter is in 40,000 rpm and equals to 4% and 5%, respectively. This can be due to the fact that the flow field is three-dimensional, viscous, and complicated. Therefore, the 1D modeling method cannot present the perfect and exact solution. In Figs. 12.7 and 12.8, the performance comparison between turbine with existing impeller and turbine with designed impeller is performed. As can be seen, the turbine with designed impeller has higher efficiency compared to the turbine with existing impeller. The reason for efficiency increment in turbine compared to the existing impeller can be due to the increment in number of blades, which leads to lower blade loading according to Chen et al. [20]. However, the increment in number of blades can decrease mass flow rate in a constant pressure ratio. The maximum difference for efficiency is 3.6% in 40,000 rpm, and this difference decreases to 1.8% in 60,000 rpm that can be due to friction and blade-loading losses that are under the influence of blade number and rotational speed. The designed impeller with more blade number is more affected by mentioned losses that can decrease efficiency difference in higher rotational speeds. In mass parameter diagram, the turbine with designed impeller has lower mass parameter values, which can be due to more blade number, and therefore, blockage is more in this turbine. The maximum difference is 0.36 in 60,000 rpm.

In Figs. 12.9 and 12.10, the results of impeller design with hub and shroud curves, the blade distribution, and their comparison with existing impeller are illustrated. According to Fig. 12.9, it is seen that the final curves which are made of Bezier polynomial just pass the first and end points. There are slight differences between

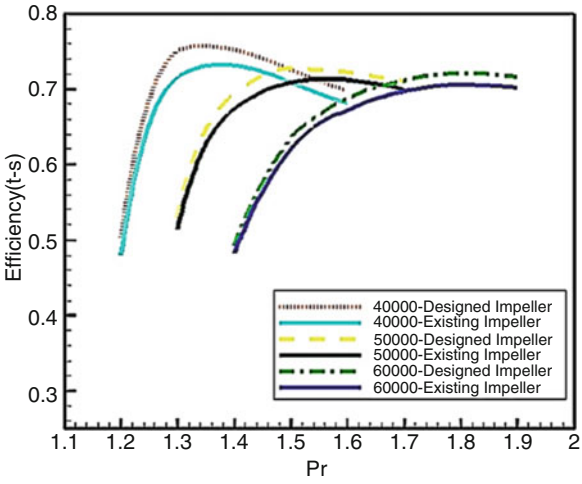

Fig. 12.7 Efficiency comparison between turbine with an existing impeller and turbine with a designed impeller

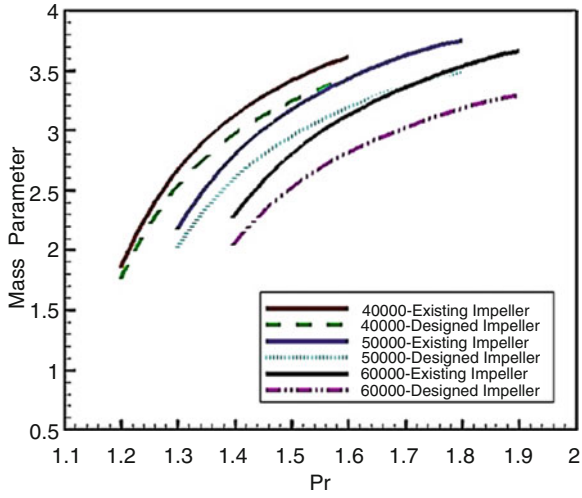

Fig. 12.8 Mass parameter comparison between turbine with an existing impeller and turbine with a designed impeller

existing and designed curves. The maximum difference is related to the entrance area, so that unlike the designed impeller in the existing one, the hub profile has tangency to the vertical axis. In Fig. 12.10 the blade angle distribution in terms of non-dimensional meridional distance is depicted. According to this figure, the blade angle at the entrance is equal to zero, and it is clear that the two impellers are slightly different.

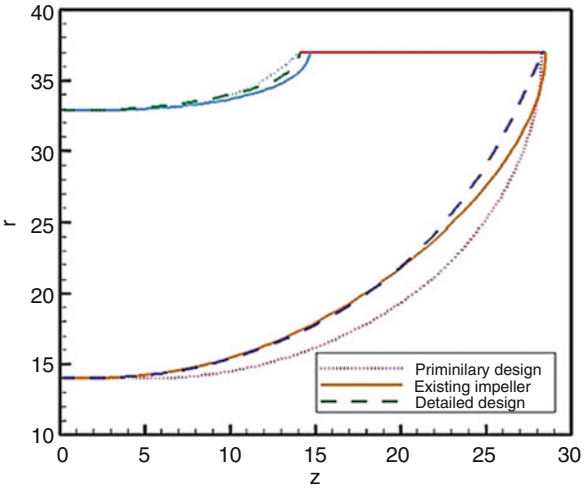

Fig. 12.9 Blade profiles for designed and existing impellers

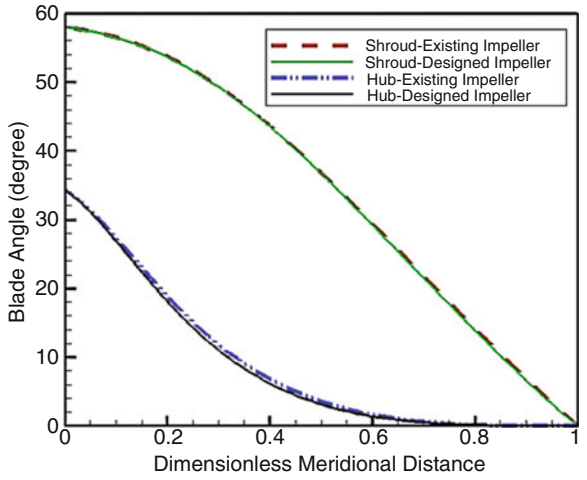

Fig. 12.10 Blade angle distribution for designed and existing impeller

12.7 Conclusion

In this research, one- and three-dimensional aerodynamic design of radial-inflow turbine are conducted based on the direct method and design codes. The main conclusions are:

- The main target of this research is to present a method for twin-entry radial turbine impeller design in a way that the performance parameters of turbine at design point be ideal.
- The only shortcoming of design code is the prediction of blade numbers inaccurately. It is worth noting that this weakness is due to the utilization of conventional relations for minimizing the incidence loss.

- Using 1D and 3D design code with minimum inlet data for aerodynamic design of turbine in a way that it has the ability to design the existing impeller effectively.
- Utilization of one-dimensional code in order to predict the performance of turbine with both designed and existing impeller that has been validated with experimental test results of Garrett turbocharger model GT-4082.

Nomenclature

a	Speed of sound (m/s)
b	Inlet width of blade (mm)
c	Absolute velocity (m/s)
D	Diameter (mm)
h	Enthalpy (kJ/Kg)
L	Length of blade (mm)
m	Meridional distance (mm)
n	Specific speed
p	Pressure (bar)
q	Enthalpy (KJ/Kg-K)
T	Temperature (K)
R, r	Radius (mm)
s	Entropy
u	Blade speed (m/s)
w	Relative speed (m/s)
Z	Axial coordinate (mm)
z	Number of blade

Greek Letters

η	Efficiency
α	Absolute angle
β	Relative flow angle, blade angle
θ	Camber angle
σ	Loss coefficient
ψ	Blade-loading coefficient
$\varnothing$	Flow coefficient

Superscripts

.	Rate of a parameter

Subscripts

b	Blade
cl	Clearance
H	Hydraulic
h	Hub
I, in	Inlet
m	Meridional component

o	Outlet
R	Rotor
S	Specific (specific speed)
s	Shroud and isentropic process
θ	Tangentional component
0	Stagnation parameter

References

1. Futral SM, Wasserbauer AC (1965) Off-design performance prediction with experimental verification for a radial-inflow turbine, NASA TN D-262
2. Wasserbauer CA, Glassman AJ (1975) Fortran program for predicting off-design performance of radialinflow turbines, NASA TN D-8063
3. Wallace FJ, Baines NC, Whitfield A (1976) A unified approach to the one dimensional analysis and design of radial and mixed flow turbines, ASME Paper 76-GT-100
4. Rohlik HE (1968) Analytical determination of radial inflow turbine design geometry for maximum efficiency, NASA TN-D 4384
5. Benson RS (1977) Computer aided design of radial gas turbine: a method for determining the overall rotor dimensions. J Comput Fluids 5:219–240
6. Whitfield A (1990) The preliminary design of radial-inflow turbines. J Turbomach 112:50–57
7. Zanganeh M (1991) A compressible three-dimensional method for radial and mixed flow turbomachinery blades. Int J Numer Methods Fluids 13:599–624
8. Ebaid MSY, Bhinde FS, Khadiri GH (2002) A unified approach for designing a radial-inflow gas turbine, ASME Paper, 2002-GT-30578
9. Moustapha H, Zelesky M, Baines NC, Japikse D (2003) Axial and radial turbines. Concepts NREC, White River Junction, pp 265–300
10. Qiu X, Andeson MR, Baines NC (2009) Mean line modeling of radial inflow turbines with variable area nozzle. In: ASME Turbo Expo Conference 2009: Power for Land, Sea, and Air, Vol 7. USA, pp 1185–1191.
11. Qiu X, Baines NC (2007) Performance prediction for high pressure-ratio radial inflow turbines. In: ASME Turbo Expo Conference 2007: Power for Land, Sea, and Air, Vol 6. Canada, pp 945–956.
12. Aungier RH (2006) Turbine aerodynamics: Axial Flow and radial-inflow turbine design and analysis. ASME Press, New York, pp 235–290
13. Whitfield A, Baines NC (1990) Design of radial turbomachines. Longman Scientific & Technical Publishing Company, New York, pp 137–217
14. Futral SM, Wasserbauer CA (1970) Experimental performance evaluation of a 4.59-inch radial inflow turbine with and without splitter blades, NASA TN D-7015
15. Chen H, Winterbone DE (1990) A method to predict performance of vaneless radial turbines under steady and unsteady flow conditions. IMechE Turbocharging Turbochargers C405/008:13–22
16. Glassman AJ (1994) Turbine design and application: Volume 1, NASA SP.290
17. Rodgers C (1987) Main line performance prediction of radial inflow turbines, VKI Lecture series 1987-07
18. Shahhosseini MR (2009) Theoretical and experimental investigation of losses in twin-entry radial inflow gas turbine under full and partial admission conditions, Ph.D. Thesis, Sharif University of Technology, Iran
19. Ghasemi S, Shirani E, Hajilouy A (2002) Performance prediction of twin entry turbocharger turbines. In: ASME Turbo Expo Conference 2002, Vol 1. The Netherlands, pp 1087–1095.
20. Chen H, Abidat M, Bains NC, Firth MR (1992) The effect of blade loading in radial and mixed flow turbines, ASME Paper 92-GT-92

Chapter 13
Combustion and Emission Characteristics of Wood Pyrolysis Oil and N-Butanol-Blended Fuel in a Diesel Engine

Seokhwan Lee, Yongrae Kim, and Kernyong Kang

13.1 Introduction

In recent years, replacement of petroleum-based fuels has attracted due to global warming, depletion of natural sources, and environmental pollution. A viable method of overcoming these global problems is the use of alternative fuels, in particular those derived from biomass. There are many technologies that convert biomasses to gaseous or liquid fuels. Among them, fast pyrolysis processing is a promising technology that converts wood to a liquid fuel called wood pyrolysis oil (WPO) or bio-oil (BO) [1, 2]. In countries with abundant sources of wood, there has been considerable research into the power generation application of WPO in cogeneration power plants or gas turbines [3, 4]. Furthermore, some research groups are trying to assess the feasibility of WPO as a fuel for stationary diesel engines, and the combustion and emission characteristics of WPO and diesel have been compared [5–9]. It has been reported that WPO mixed with a cetane enhancement showed a comparable combustion performance to that of diesel, while a 30% WPO-diesel emulsified fuel showed decreased emission of NOx in a diesel engine [7, 8]. However, the application of WPO to conventional diesel engines is highly constrained because of its poor fuel properties and the negative impact it has on the fuel supply system in a short period of time [8–10].

The fuel properties of WPO are highly dependent on the process and the type of biomass used in its production. However, WPO usually contains 18–30% water and has higher oxygen content than fossil fuel. Due to these different properties, diesel and WPO have different fuel spray atomization levels, ignition temperatures, combustion characteristics, and exhaust emission characteristics. WPO does not usually

S. Lee (✉) · Y. Kim · K. Kang
Korea Institute of Machinery and Materials, Engine Research, Daejeon, Republic of Korea
e-mail: shlee@kimm.re.kr

S. Nižetić, A. Papadopoulos (eds.), *The Role of Exergy in Energy and the Environment*, Green Energy and Technology,
https://doi.org/10.1007/978-3-319-89845-2_13

produce self-ignition in conventional diesel engines due to a lower cetane number (~5–25). Since the oxygen content of WPO is between 42–50%, it has a calorific value approximately 1/3 to that of fossil fuels. The viscosity of WPO, which depends on the source material and production process, is between that of heavy fuel oil (HFO) and conventional light diesel fuel. Due to the high acidity (pH of 2–3) and the high water content of WPO, long-term operation could lead to corrosion of the injection system, if the system is made from conventional materials. The tar in WPO becomes a gum-like material through polymerization, which occurs at room temperature over time. Polymer, tar, solid particles, and other substances can therefore accumulate in the injection system [1, 2, 10, 11].

The most widely used approach to improve the fuel qualities of WPO for stable combustion within a conventional diesel is to blend the WPO with other hydrocarbon fuels that have a higher cetane number [7, 8, 12]. However, WPO and fossil fuels are not usually blended because of their different polarities, which results in phase separation. Therefore, a cumbersome emulsification process is needed to mix the WPO and fossil fuels with appropriate surfactants. The emulsification process has additional time and financial costs, and clogging of the fuel supply system can still occur due to the polymer, tar, and solid particles in WPO-fossil fuel emulsions [7, 13, 14]. Polymerization of WPO can be prevented by diluting WPO in alcohol fuels like ethanol, methanol, or butanol. Mixing with alcohol fuels confers the added benefit of significantly improving the storage and handling properties of WPO [15, 16]. However, WPO-alcohol-blended fuel still does not result in self-ignition; hence, additional cetane enhancements or an additional flame source are required to initiate combustion in the blended fuel [17–19].

In this study, we use WPO mixed with an alcohol fuel and cetane enhancements. The WPO-alcohol-blended fuel has auto-ignitability, which can be produced by simple mixing of the WPO, alcohol fuel, and cetane enhancements. Among the alcohol fuels, n-butanol was selected as the main component of the blended fuel in this study. N-butanol has a viscosity of 3.6 cSt and can effectively lower the viscosity of the blended fuel to a suitable level for direct application in a conventional diesel engine. Furthermore, as an organic solvent, n-butanol dissolves solid particles present in the WPO and suppresses the polymerization of tar. Additionally, WPO can be blended easily with n-butanol, with no phase separation. The higher cetane number (17–25) of n-butanol compared to other alcohol fuels such as ethanol and methanol results in better auto-ignitability in diesel engines. It has also been reported that n-butanol can simultaneously lower soot and NOx emissions in diesel engines by lowering the in-cylinder equivalence ratio due to the fuel-bound oxygen and the in-cylinder temperature due to the higher heat of vaporization [20, 21]. Polyethylene glycol 400 (PEG 400) and 2-ethylhexyl nitrate (2-EHN) were used as cetane enhancements to improve the auto-ignitability of the blended fuel. Available commercial ignition improvers are expensive and are normally mixed directly into alcohol fuels. Due to the high price of 2-EHN, other cetane enhancements are required. Dissolved polyethylene glycol has been used in Scania and Volvo engines [22]. Therefore, in this study PEG 400 was selected as the main cetane enhancement and 2-EHN as a supplementary enhancement.

When using WPO diluted with n-butanol, it was found that clogging and polymerization still occurred in the fuel supply system in a diesel engine equipped with an electronically controlled common rail fuel injection system. Therefore, all engine experiments were performed on an indirect injection (IDI) diesel generator equipped with a mechanical fuel injection system that was less sensitive to sediments. The blending strategy enabled the use of WPO in a WPO-butanol blended fuel, with a maximum WPO content of 40 wt%, to supply an electrical load range of 0–7.7 kW_e. The combustion and emission characteristics of an IDI diesel generator operated with diesel and WPO-butanol blended fuel were experimentally investigated. Additionally, on-road tractor tests were carried out to investigate the feasibility of using a WPO in a real-world driving situation.

13.2 Experimental Facility

13.2.1 Test Fuel

A tilted slide reactor with a 15.5 kg/h pyrolysis capacity was developed at our institute; using this reactor, fast pyrolysis of lignocellulosic biomass was carried out to obtain WPO [23]. The maximum yield was calculated as the ratio between the collected WPO and supplied biomass weights and was almost 65%. The fuel properties of diesel, WPO, and n-butanol, as determined by the Korea Petroleum Quality & Distribution Authority, are provided in Table 13.1. According to the data acquired, it can be seen that WPO possesses a lower heating value (LHV), corresponding to 1/3 that of diesel, in turn signifying that the energy density of WPO is only 1/3 that of diesel. Additionally, due to the 33% water content of WPO, it is unsuitable for independent use as a fuel for conventional engines.

To prevent polymerization and lower the viscosity of WPO, n-butanol and two cetane enhancements (PEG 400 and 2-EHN) were blended to ensure stable autoignitability in a diesel engine. The base fuel was produced by blending n-butanol,

Table 13.1 Fuel properties of WPO (wood pyrolysis oil), n-butanol, cetane enhancements, and diesel

	WPO	n-butanol	PEG400	2-EHN	Diesel
Viscosity (cSt at 40 °C)	9.5	3.6	40.4	1.3	2.7
LHV (MJ/kg)	15.9	33.1	23.2	27.6	42.6
Water content (%)	33.6	–	0.3	<0.1	–
C (wt%)	41.0	64.8	52.2	54.9	86.1
H (wt%)	10.1	13.6	9.2	9.7	13.9
O (wt%)	48.8	21.6	38.6	27.4	–
Density (kg/m^3)	1193.5	810.0	1128.0	960.0	821.0
Cetane number	5–25	17	N/A	N/A	52.6

N/A : not available

PEG 400, and 2-EHN at a ratio of 70:25:5 by weight. Additionally, 500 ppm of lubricant (Lubrizol Corp.) was added to the blended fuel to avoid mechanical wear in the fuel supply system. The WPO was added to the base fuel in ratios of 10–40 wt% at intervals of 10 wt%. As the proportion of WPO increased, that of n-butanol decreased. The combustion and emission results from diesel fuel were used as a comparison.

13.2.2 Engine Test Procedure

All engine bench experiments were performed on a four-stroke IDI diesel generator equipped with a mechanical fuel supply system. Because the char from WPO can accumulate in the fuel injection system, a mechanical fuel supply system was adopted instead of a common-rail injection system, which is sensitive to sediment. A schematic diagram of the experimental setup and summary of the generator engine features are provided in Fig. 13.1a and Table 13.2, respectively. To analyze the combustion characteristics, a pressure transducer (6052C; Kistler) and an adapter (6542Q27; Kistler) were installed at the cylinder glow plug and set to measure the cylinder pressure at every 1 degree of crank angle by synchronizing to the signal from the encoder. A flow meter (Meriam Inst. Co.) was installed on the upper side of the intake reservoir to measure the mass flow of intake air. The air/fuel ratio was measured using a lambda meter (LA4; ETAS) connected to a wide-band O_2 sensor. The amount of fuel was gauged with a balance. For the analysis of gaseous emission, an exhaust gas analyzer (AMA i-60; AVL) was used to measure the total hydrocarbon (THC; detection limit: 5000 ppm), carbon monoxide (CO; detection limit: 50,000 ppm), and nitrogen oxides (NOx; detection limit: 5000 ppm) emissions; an aerosol monitor (Dusttrak DRX 8533; TSI) and opacimeter (AVL) were used to measure the particulate matter (PM) mass. The particle number concentrations and number size distributions of engine particle emissions were measured using a Fast Mobility Particle Sizer (FMPS; TSI). The FMPS is based on an electric aerosol spectrometer and measures particle sizes from 5.6 to 560 nm with a sizing resolution of 32 channels. The FMPS can measure particle size distributions at a frequency of 1 Hz.

The experiments were conducted at an engine speed of 3600 rpm with different generator output powers (0–7.7 kW_e). To protect the fuel supply system from damage, the engine was first started using diesel for 10 min; after the experiment, the blended fuel without WPO was introduced, in order to dissolve and rinse out solidified materials left inside the fuel supply system.

The vehicle test was conducted in actual on-road driving conditions using a diesel tractor equipped with a mechanical fuel supply system to investigate the applicability of WPO to a vehicle. The on-road tractor tests presented more severe experimental conditions than the engine bench test; therefore, less WPO was added to the base fuel in ratios of 5–15 wt% at intervals of 5 wt%. The experiments were carried out at engine speeds of 2300 and 3000 rpm while traveling on the same 5 km route. A photo of the on-road tractor test setup and summary of tractor engine features are

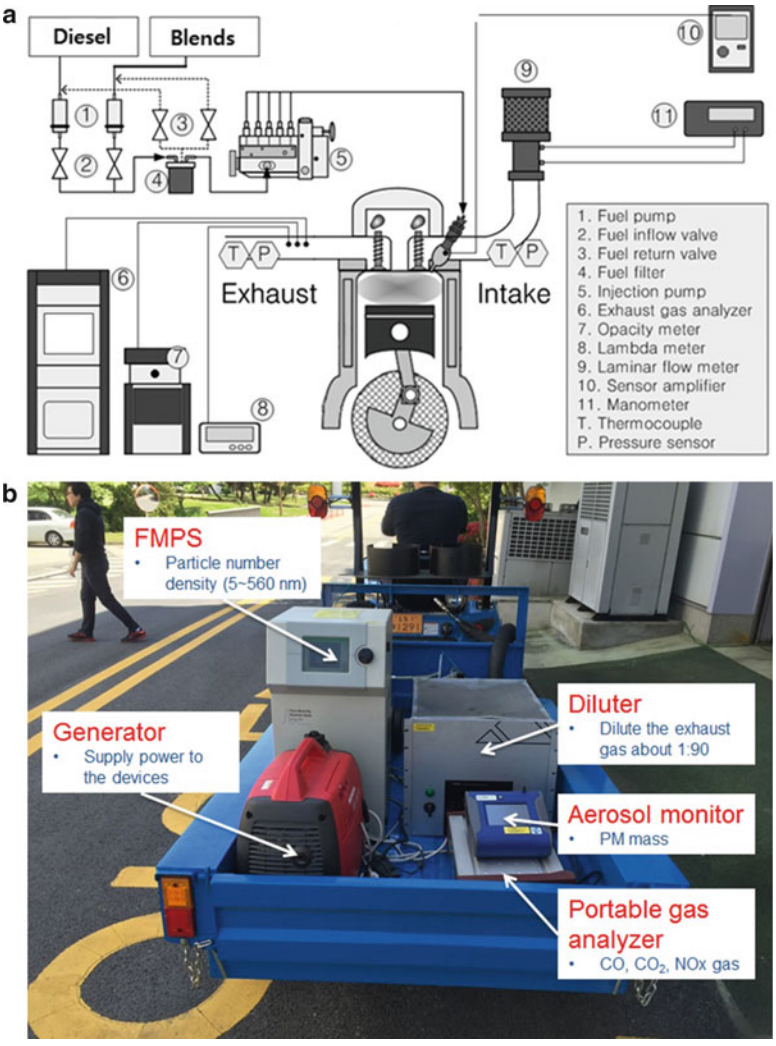

Fig. 13.1 (**a**) Schematic diagram of engine bench setup (left), (**b**) photo of on-road tractor test setup (right)

provided in Fig. 13.1b and Table 13.2, respectively. For the analysis of gaseous emissions, a portable exhaust gas analyzer (DELTA 1600-V; MRU) was used to measure the THC (detection limit: 2000 ppm), CO (detection limit: 4000 ppm or 10%), carbon dioxide (CO_2; detection limit: 20%), and NOx (detection limit: NO = 4000 ppm, NO_2 = 1000 ppm) emissions; an aerosol monitor (Dusttrak DRX 8533; TSI) was used to measure the PM mass. The particle number

Table 13.2 Test engine specifications

Parameters	Test engine	
	Diesel generator	Tractor
Cylinders	2	3
Displacement	794 cm^3	761 cm^3
Bore stroke	80 mm × 79 mm	67 mm × 71 mm
Compression ratio	23	23.5
Engine rated output	12.5 kW/3000 rpm	13.4 kW/3200 rpm
Generator rated output	8.5 kW_e/3600 rpm	–

concentrations of engine particle emissions were measured using the FMPS (TSI). Since THC, CO, and CO_2 were measured using an NDIR bench, and NOx was measured using an electrochemical cell, the measuring accuracy of the MRU instrument cannot be guaranteed. Therefore, the portable exhaust gas analyzer was calibrated with a high-precision gas analyzer (AMA i-60; AVL). The values of CO, CO_2, and NOx from the MRU instrument were highly correlated with those of the AVL instrument; however, for THC the correlation between the MRU and AVL was very poor. In this study, we only monitored the CO, CO_2, and NOx values from the MRU gas analyzer.

13.3 Results and Discussion

13.3.1 Combustion Stability and Efficiency

Figure 13.2a shows the combustion stability of each fuel in terms of the coefficient of variation in the indicated mean effective pressure (COV_{IMEP}). Generally, 5% COV_{IMEP} is considered the threshold for determining combustion stability. The COV_{IMEP} was less than 5% for all of the fuels tested under the whole range of generator outputs, which indicates highly stable combustion. As the generator output increases, the combustion stability also increases, while the COV_{IMEP} value decreases and the COV_{IMEP} of the blended fuels becomes comparable to that of diesel.

The indicated fuel conversion efficiency (IFCE) results are shown in Fig. 13.2b. The IFCE can be calculated from the ratio of work done in a cycle to the total energy input. It was found that the IFCE of the 10 wt% WPO-blended fuel was comparable to that of diesel. However, the blended fuels with more than 20 wt% WPO content showed lower efficiency than diesel. As the WPO content increased, the injection period was lengthened, and the ignition delay became longer due to the lower cetane number; consequently, the efficiency was lowered. In the case of the blended fuel with 50 wt% WPO, we found that the combustion was very unstable due to the severe ignition delay.

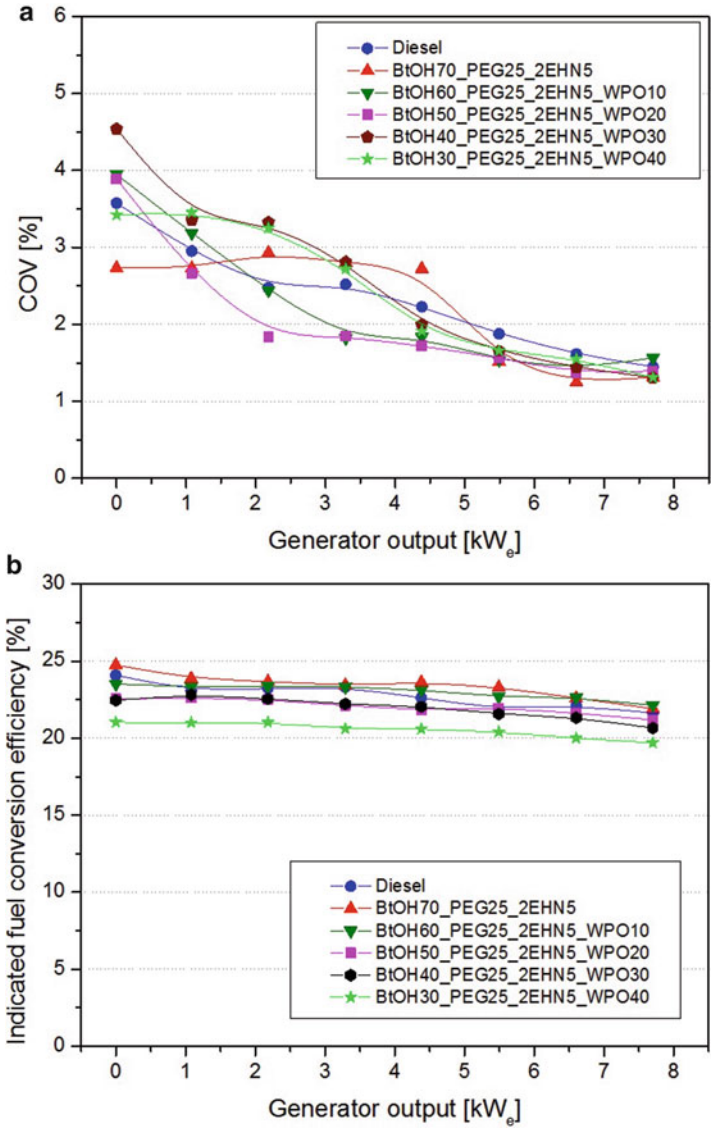

Fig. 13.2 (**a**) Combustion stability in terms of COV_{IMEP} with various test fuels as a function of generator output (left), (**b**) indicated fuel conversion efficiency with various test fuels as a function of generator output (right)

13.3.2 Engine-Out Exhaust Gas Emission

Engine-out exhaust indicating specific THC, CO, and NOx were measured at all generator output loads as shown in Fig. 13.3. It was observed that the ISHC decreased as the generator output increased for all test fuels. At low-engine loads, the pressure and temperature in the combustion chamber were suboptimal; therefore, the ignition delay and amount of unburned fuel increased due to the low auto-ignitibility. The THC levels of the blended fuel, with the exception of 40 wt% WPO fuel, were comparable to those of diesel. A lower-energy density than diesel leads to a higher input blended fuel mass, which in turn leads to increased wall wetting on the piston surface compared to diesel fuel. This is compensated for by the higher oxygen content in the blended fuels, which help to combust the unburned fuel in the combustion chamber and consequently shows comparable ISHC levels to that of diesel. The blended fuel with 40 wt% WPO content had a significantly longer ignition delay, which contributed to its higher ISHC emissions.

ISCO emissions are strongly affected by fuel atomization characteristics. The fuel components of WPO-blended fuels (except 2-EHN) have higher viscosities than that of diesel and show higher ISCO emissions due to poor fuel atomization. For WPO-blended fuels, as the WPO with a high viscosity replaces n-butanol with a relatively low viscosity, the ISCO emissions increase according to WPO content under low load. The ISCO of diesel and the blended fuels tended to drastically increase under low-load conditions of less than 2 kW_e output. This is because under low-load conditions, the in-cylinder pressures and temperatures are low, and thus, incomplete combustion occurred due to the low auto-ignitibility, which consequently increased the ISCO.

Generally, the formation mechanisms of NOx are strongly dependent on the peak combustion temperature, local oxygen concentrations (thermal NOx), oxidation of intermediate combustion products (such as hydrogen cyanide (HCN), nitrogen (N), and nitrogen oxide (NO)) (prompt NOx), and fuel-bound nitrogen (FBN) in the fuel (fuel NOx) [24]. The NOx emissions of the blended fuels were higher than diesel and increased with WPO content. The formation of NOx emissions was strongly dependent on the in-cylinder peak temperature and oxygen concentration. It is known that the additional fuel-bound oxygen from the oxygenated fuels brings more zones near to stoichiometric conditions and little to the lean; these conditions favor NOx formation [24]. Additional oxygen availability results in a more complete combustion of the fuel air mixture and increases the amount of burned gas, which tends to be converted into more NOx in the high-temperature regions during combustion. Although the high water content of WPO suppresses NOx formation by both lowering the in-cylinder temperature and increasing the specific heat capacity of the fuel-air mixture, fuel-bound oxygen is believed to have a greater influence on NOx formation than the water content in the WPO.

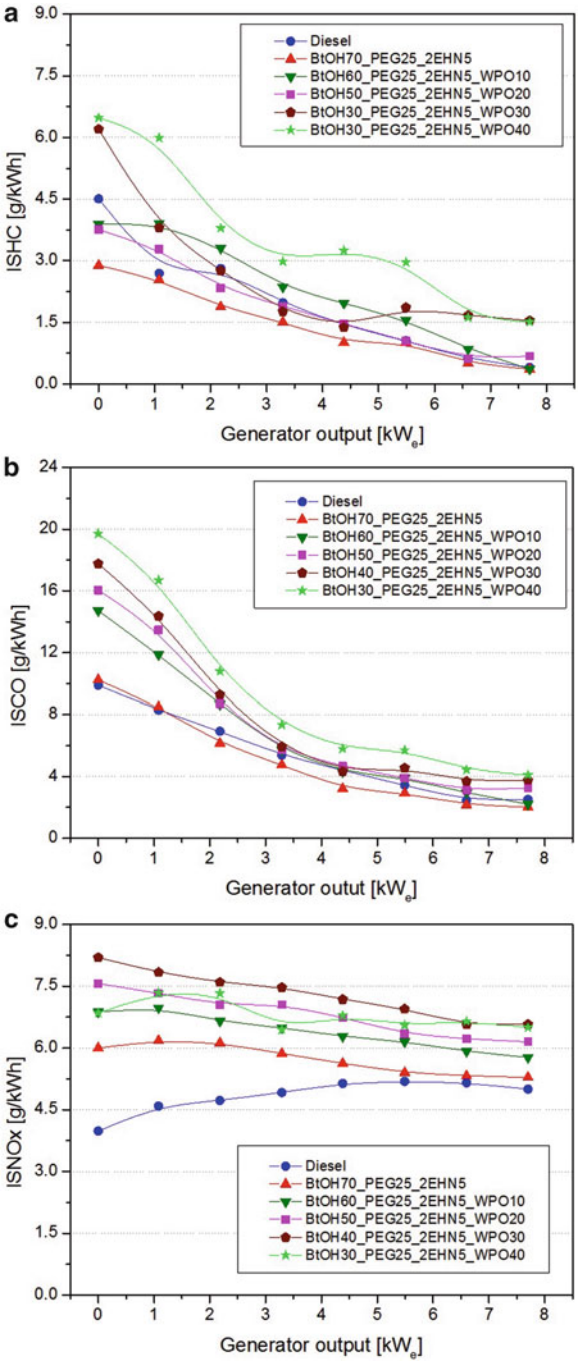

Fig. 13.3 (**a**) Indicated specific THC emissions with various test fuels (upper left), (**b**) indicated specific CO emissions with various test fuels (upper right), (**c**) indicated specific NOx emissions with various test fuels (bottom left)

13.3.3 Particulate Matter (PM) Emissions

Figure 13.4a shows the PM mass concentrations measured by the aerosol monitor. Diesel particulate matter (DPM) consists principally of combustion-generated carbonaceous material (soot) in which some organic compounds have been absorbed. Unsaturated hydrocarbons, such as polycyclic aromatic hydrocarbons (PAHs) and

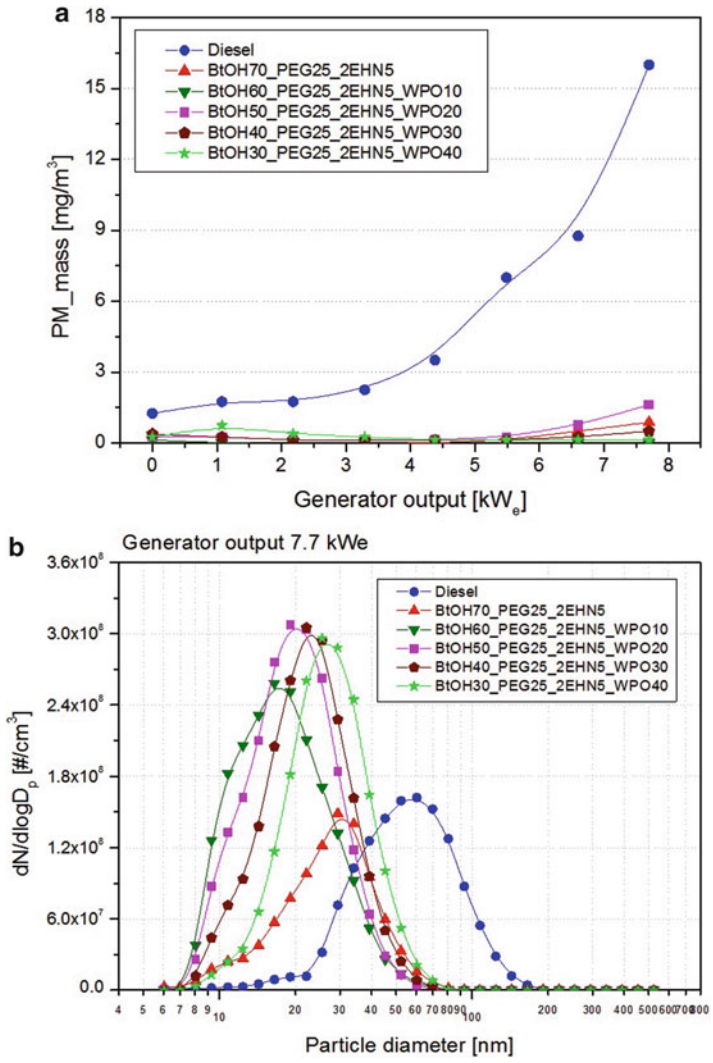

Fig. 13.4 (**a**) Particulate matter (PM) mass with various test fuels according to generator outputs (left), (**b**) particle number size distributions with various test fuels at generator output 7.7 kW_e (right)

acetylene, are the most likely precursors of soot particles [24]. In the case of diesel, PM mass tends to increase with generator output because the volume for fuel-rich regions increases with the amount of fuel injected, which increases with engine load. This results in high PM mass emissions due to worsening air-fuel mixing in the combustion chamber. However, for blended fuels, the PM mass observed was almost zero for the entire generator output range. This may be attributed to the high oxygen content species in the n-butanol and WPO. As stated above, PAHs and acetylene are the most likely precursors of soot particles. Thus, the presence of oxygen atoms in the fuel creates a locally lean fuel-air mixture environment and helps the hydrocarbons to oxidize during the combustion process. It has also been reported that carbon atoms bonded to oxygen atoms in oxygenated fuels do not take part in soot formation [25].

Figure 13.4b shows particle number-size distributions obtained at a generator output of 7.7 kW_e for an engine speed of 3600 rpm. For blended fuels, most particles were concentrated in nuclei mode with a particle diameter below 50 nm; particles in this nuclei mode showed higher concentrations than in diesel. However, diesel showed higher concentrations in the accumulation mode (50–1000 nm) where most of the particle mass was concentrated due to agglomerated large soot particles; therefore, a significantly higher PM mass was observed as shown in Fig. 13.2. The existence of WPO in the blended fuel significantly increased the particle concentrations in nuclei mode due to the abundant oxygen content in the WPO.

Diesel fuel consists of macromolecular carbon-to-carbon or carbon-to-hydrogen bonds that are likely to form large-scale soot particles during the combustion process. In blended fuels, some oxygen atoms exist between the carbon-to-carbon or carbon-to-hydrogen bonds because the WPO and the n-butanol have high oxygen content. Due to the presence of these oxygen atoms, carbon atoms in the blended fuels are easier to oxidize into gas phase CO or CO_2 compared to diesel, or they are transformed into smaller soot particles. Tan et al. (2009) reported that oxygen atoms break the carbonaceous fine-size particles (<2.5 μm) into ultrafine (<0.1 μm) or nanoscale particles, thereby increasing the number of nuclei mode particles [26]. Lapuerta et al. (2002) reported that fuel-bound oxygen in oxygenated fuels improved combustion in fuel-rich diffusion flame regions in the combustion chamber and promoted oxidation of the already formed soot [27].

13.3.4 On-Road Tractor Test

The base fuel for the on-road tractor test was produced by blending n-butanol, PEG 400, and 2-EHN at a ratio of 65:30:5 by weight, which was different from the engine bench test to ensure stable combustion. The n-butanol was substituted with WPO in ratios of 5–15 wt% at intervals of 5 wt%. The experiments were carried out at engine speeds of 2300 and 3000 rpm while traveling on the same route (approximately 5 km in distance). Although all experiments were conducted on the same route, the test time, average speed, and actual traveling distance were slightly different in each test due to traffic. Table 13.3 shows a summary of the on-road tractor test results. At

Table 13.3 Summary of the on-road tractor test results

Engine speed	Fuel	Time [s]	Distance [km]	Avg. speed [km/h]	Avg. exh. temp.	NOx [g/km]	CO [g/km]	CO_2 [g/km]	PN [#/km]	PM [mg/km]
2300 rpm	Diesel	2269	4.89	7.77	154.23	4.21	0.98	491.44	1.14E13	1.12
	WPO 0	2270	4.96	7.75	156.30	3.71	0.83	488.67	1.68E13	0.46
	WPO 5	2274	4.98	7.74	157.92	3.61	0.84	482.72	1.94E13	0.47
	WPO 10	2272	5.02	7.77	153.26	3.71	1.18	472.59	1.92E13	0.62
	WPO 15	2221	4.95	8.02	154.22	3.68	1.34	485.27	2.02E13	0.65
3000 rpm	Diesel	2076	5.25	5.25	189.01	3.16	1.87	572.08	1.30E13	0.82
	WPO 0	2065	5.22	5.22	188.80	3.43	1.40	559.71	7.40E12	0.33
	WPO 10	1902	5.13	5.13	191.93	3.10	1.37	546.92	5.58E12	0.36
	WPO 10	1901	5.29	5.29	189.19	3.16	1.82	547.07	5.84E12	0.67
	WPO 15	1860	5.06	5.06	189.13	3.21	1.76	563.78	5.17E12	0.60

engine speeds of 2300 and 3000 rpm, the average speeds of each test were recorded at about 7.7–8.0 and 9.1–10.0 km/h.

Figure 13.5 shows the CO, CO_2, NOx, PN, and PM emissions with various test fuels at an engine speed of 2300 rpm. The CO emissions of the blended fuels were comparable or slightly increased compared to diesel, as the WPO content was increased. These results are consistent with the engine bench test results, as shown in Fig. 13.3. The blended fuel showed slightly less CO_2 emission than the diesel due

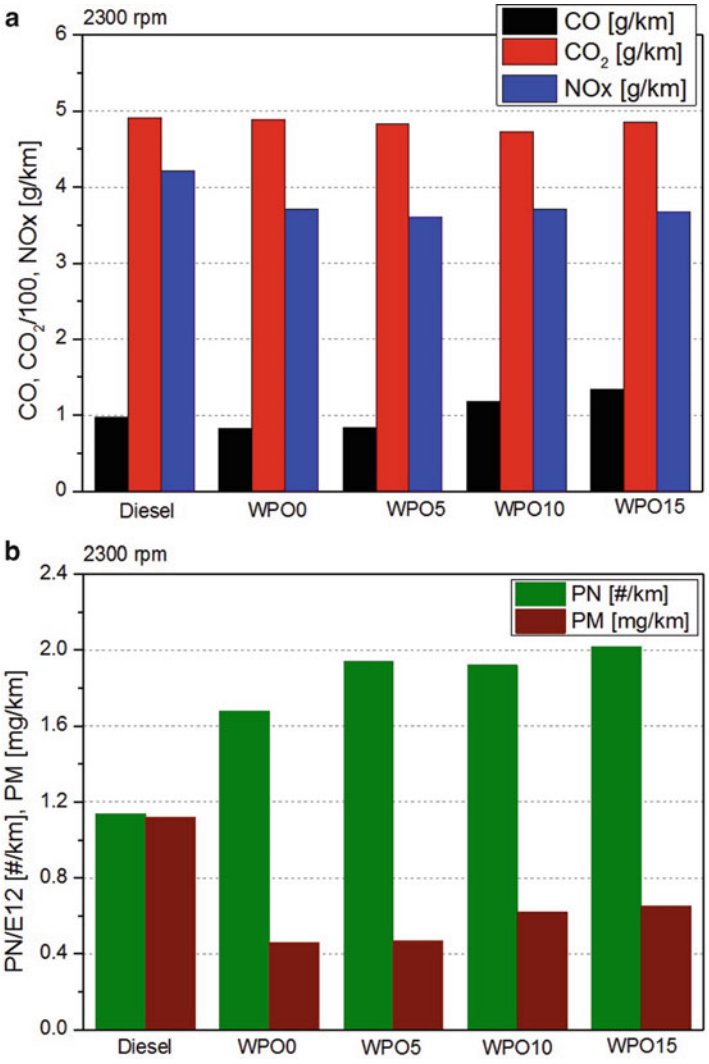

Fig. 13.5 CO, CO_2, NOx, PN, and PM emissions with various test fuels at an engine speed of 2300 rpm

to lower carbon content in the fuel. However, the NOx level of the blended fuel was lower than that of diesel; this result was inconsistent with the engine bench test result. The blended fuel showed higher particle number and lower PM mass compared to diesel due to the high oxygen content of the WPO and n-butanol, which was consistent with the engine bench test results.

Figure 13.6 shows CO, CO_2, NOx, PN, and PM emissions with various test fuels at an engine speed of 3000 rpm. The blended fuels showed comparable or slightly

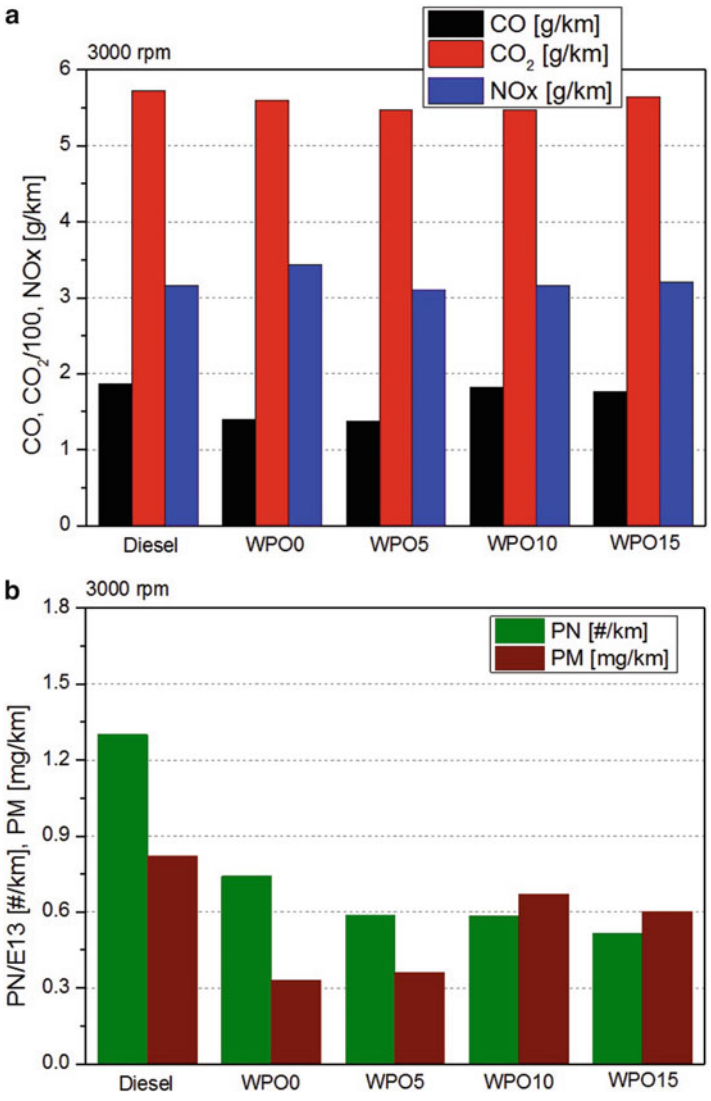

Fig. 13.6 CO, CO_2, NOx, PN, and PM emissions with various test fuels at an engine speed of 3000 rpm

lower CO emission than diesel, which was inconsistent with the previous test results of 2300 rpm. The blended fuels also showed slightly lower CO_2 emission than diesel for an engine speed of 3000 rpm. The NOx level of the blended fuels was comparable to that of diesel. The blended fuel also showed a slightly lower PM mass compared to diesel; however the PN also decreased according to WPO content, which was inconsistent with the test results of 2300 rpm. During the on-road test, the engine ran quite smoothly, and no significant change in performance or emissions was observed. Therefore, we conclude that the diesel tractor equipped with the mechanical fuel supply system can operate on the road without any malfunction when operated with a blended fuel with 15 wt% WPO content. However, a long-term operation on-road test, such as a few hundred hours, should be conducted to guarantee the stable usage of WPO-butanol-blended fuels in a diesel tractor.

13.4 Conclusion

A WPO-butanol-blended fuel was examined as an alternative fuel to conventional diesel. By selecting correct portions of WPO-butanol-cetane enhancements, the fuel properties were improved, particularly the energy density, viscosity, and auto-ignitability. In an IDI diesel generator, the performance and emission characteristics were measured and the following conclusions were reached:

- The combustion stability in terms of COV_{IMEP} was less than 5% for diesel and the blended fuels for a range of generator outputs, which indicates highly stable combustion.
- The IFCE of the blended fuel with a WPO content of less than 10 wt% was comparable to that of diesel. However, the blended fuel with a WPO content of more than 20 wt% showed lower efficiency than diesel.
- Higher levels of THC and CO were observed for the blended fuels compared to those of diesel. Although the blended fuels have higher oxygen content, the longer ignition delay and high viscosity of the blended fuels contributes to larger THC and CO emissions.
- Although the high water content of the WPO suppresses the NOx formation by both lowering the in-cylinder temperature and increasing the specific heat capacity of the fuel-air mixture, fuel-bound oxygen is believed to have a greater influence on NOx formation than the water content in the WPO.
- For the blended fuel, the PM mass observed was almost zero over the entire generator output range. This may be attributed to the high oxygen content species in the n-butanol and WPO.
- At higher engine loads, most particles produced by the blended fuels were concentrated in nuclei mode; the particles in nuclei mode showed higher concentrations than in diesel. However, diesel produced higher concentrations in the accumulation mode where most of the particle mass was concentrated due to large agglomerated soot particles.

- The on-road tractor test showed that a diesel tractor equipped with a mechanical fuel supply system can operate on the road without any malfunction in the engine system, even when operated with a blended fuel containing 15 wt% WPO.

References

1. Bridgwater AV, Meier D, Radlein D (1999) An overview of fast pyrolysis of biomass. Org Geochem 30:1479–1493
2. Mohan D, Pittman CU, Steele PH (2006) Pyrolysis of wood/biomass for bio-oils: a critical review. Energy Fuel 20:848–889
3. Boucher ME, Chaala A, Roy C (2000) Bio-oils obtained by vacuum pyrolysis of softwood bark as a liquid fuel for gas turbines. Part I: properties of bio-oil and its blends with methanol and a pyrolytic aqueous phase. Biomass Bioenergy 19:337–350
4. Chiaramonti D, Oasmaa A, Solantausta Y (2007) Power generation using fast pyrolysis liquids from biomass. Renew Sustain Energy Rev 11:1056–1086
5. Bertoli C, D'Alessio J, Giacomo N, Lazzaro M, Massoli P, Moccia V (2000) Running light-duty DI diesel engines with wood pyrolysis oil. SAE Paper no. 2000-01-2975
6. Shihadeh A, Hochgreb S (2000) Diesel engine combustion of biomass pyrolysis oils. Energy Fuel 14:260–274
7. Chiaramonti D, Bonini M, Fratini E, Tondi G, Gartner K, Bridgwater AV, Grimm HP, Soldaini I, Webster A, Baglioni P (2003) Development of emulsions from biomass pyrolysis liquid and diesel and their use in engines-Part 2: tests in diesel engines. Biomass Bioenergy 25:101–111
8. Lee S, Kim T, Kang K (2014) Performance and emission characteristics of a diesel engine operated with wood pyrolysis oil. Proc ImechE Part D J Automob Eng 228:180–189
9. Beld BV, Holle E, Florijn J (2013) The use of pyrolysis oil and pyrolysis oil derived fuels in diesel engines for CHP applications. Appl Energy 102:190–197
10. Oasmaa A, Peacocke C, Gust S, Meier D, McLellan R (2005) Norms and standards for pyrolysis liquids. End-user requirements and specifications. Energy Fuel 19:2155–2163
11. Qi Z, Jie C, Tiejun W, Ying X (2007) Review of biomass pyrolysis oil properties and upgrading research. Energy Convers Manag 48:87–92
12. Laesecke J, Ellis N, Kirchen P (2017) Production, analysis and combustion characterization of biomass fast pyrolysis oil – Biodiesel blends for use in diesel engines. Fuel 199:346–357
13. Ikura M, Stanciulescu M, Hogan E (2003) Emulsification of pyrolysis derived bio-oil in diesel fuel. Biomass Bioenergy 24:221–232
14. Jiang X, Ellis N (2010) Upgrading bio-oil through emulsification with biodiesel: mixture production. Energy Fuel 24:1358–1364
15. Acala A, Bridgwater AV (2011) Upgrading fast pyrolysis liquids: blending bio-oil, biodiesel and (bio)alcohols. TCbiomass, Chicago
16. Nguyen D, Honnery D (2008) Combustion of bio-oil ethanol blends at elevated pressure. Fuel 87:232–243
17. KIM TY, LEE SH (2015) Combustion and emission characteristics of wood pyrolysis oil-butanol blended fuels in a DI diesel engine. Int J Automot Technol 16:903–912
18. Kim TY, Lee S, Kang K (2015) Performance and emission characteristics of a high-compression-ratio diesel engine fueled with wood pyrolysis oil-butanol blended fuels. Energy 93:2241–2250
19. Lee S, Kim TY (2015) Feasibility study of using wood pyrolysis oil-ethanol blended fuel with diesel pilot injection in a diesel engine. Fuel 162:65–73

20. Chen Z, Liu J, Wu Z, Lee CF (2013) Effects of Port Fuel Injection (PFI) on n-butanol and EGR on combustion and emissions of a direct injection diesel engine. Energy Convers Manag 76:725–731
21. Jin C, Yao M, Liu H, Lee CF, Ji J (2011) Progress in the production and application of n-butanol as a biofuel. Renew Sust Energ Rev 15:4080–4106
22. Olsson E, Hiljemark S, Gjirja S (2003) Use of alternative fuels in heavy duty engines. In: Proceedings 26th joint meeting of the Scandinavian-Nordic and Italian sections of The Combustion Institute, Ischia
23. Choi Y, Choi S, Jeong Y (2014) Development of a tilted-slide reactor for the fast pyrolysis of biomass. Environ Prog Sustain Energy 33:1405–1410
24. Heywood JB (1988) Internal combustion engine fundamentals. McGraw Hill, New York
25. Westbrook CK, Pitz WJ, Curran HJ (2006) Chemical kinetic modelling study of the effects of oxygenated hydrocarbons on soot emissions for diesel engines. J Phys Chem A 110:6912–6922
26. Tan P, Hu Z, Lou D, Li B (2009) Particle number and size distribution from a diesel engine with Jatropha biodiesel fuel. SAE Paper no. 2009-01-2726
27. Lapuerta M, Armas O, Ballesteros R (2002) Diesel particulate emissions from biofuels derived from Spanish vegetable oils. SAE Paper no. 2002-01-1657

Chapter 14
Thermal Modelling of a Plate-Type Heat Exchanger-Based Biomass-Fired Regenerative Organic Rankine Cycle

Ozum Calli, Can Ozgur Colpan, and Huseyin Gunerhan

14.1 Introduction

Organic Rankine cycle (ORC) technology, which is similar to steam Rankine cycle technology, provides converting heat into electricity. The organic Rankine cycle (ORC) applies the principle of the steam Rankine cycle but uses organic working fluids having a lower boiling point and a higher vapour pressure (e.g. R134a, R245fa, R123, and hydrocarbons such as isopentane and isooctane), instead of steam. Thus this kind of fluids enables using low-temperature heat sources to produce electricity [1]. There are various types of energy sources that can be used as a heat source in an ORC system such as geothermal, solar, waste heat from industry, and biomass.

Organic Rankine cycle was investigated in terms of many parameters in the studies found in the literature. The most investigated parameter is the working fluid, and the most preferred fluid is R134a [2–5]. On the other hand, the selection of the most suitable working fluid depends on the operating conditions of the cycle. Lakew et. al. investigated different working fluids for power production at different operating conditions and heat sources with different temperatures for a subcritical Rankine cycle [6]. Their studies showed that R227ea gives the highest power for a

O. Calli (✉)
Ege University, The Graduate School of Natural and Applied Sciences, Izmir, Turkey
e-mail: ozum.calli@ieu.edu.tr

C. O. Colpan
Dokuz Eylul University, Faculty of Engineering, Mechanical Engineering Department, Izmir, Turkey

H. Gunerhan
Ege University, Faculty of Engineering, Mechanical Engineering Department, Izmir, Turkey

S. Nižetić, A. Papadopoulos (eds.), *The Role of Exergy in Energy and the Environment*, Green Energy and Technology,
https://doi.org/10.1007/978-3-319-89845-2_14

heat source temperature range of 80–160 °C and R245fa produces the highest power in the range of 160–200 °C.

Biomass-fired ORC systems can efficiently convert the chemical energy of biomass into electricity. Biomass is an important renewable energy source, available nearly everywhere, and has advantages in terms of continuity, while solar and wind are intermittent. There are a few studies on the biomass-fired ORC in the literature. Huang et al. [7] investigated regenerative and non-regenerative biomass-fired ORC with dry and wet working fluids and found that the highest electric power was obtained for the regenerative system with methylcyclohexane applied as the "dry" working fluid.

Assessment of different configurations of ORC and system components is another research area. There are few studies on the performance or design analysis of the heat exchangers in ORC systems. In general, plate or shell and tube heat exchanger is investigated in different ORC systems in the literature [8–12]. For instance [13] modelled an ORC system to compare plate heat exchanger and shell and tube heat exchanger using Python Software. The results show that ORC with plate heat exchangers performs better than ORCs with shell and tube heat exchangers. But the disadvantage of plate heat exchangers is that the geometry of both sides is the same, which can result in an inefficient heat exchange when the two fluid streams require different channel geometries [14]. Walvaren et. al. has also a study on the optimum configuration of the shell and tube heat exchangers for ORC and found that 30° tube configuration is optimal for single-phase heat exchangers and 60° tube configuration is optimal for two-phase heat exchangers.

The aim of this paper is to analyse the energetic and exergetic performances of a regenerative biomass-fired ORC.

14.2 System Description

14.2.1 Plate Heat Exchanger Modelling

A detailed geometry of the brazed plate is shown in Fig. 14.1. Plate heat exchanger consists many plates joining to each other.

To design a plate heat exchanger, calculations for the total heat transfer area of the plate heat exchanger must be applied. Some parameters used in these calculations are important.

Surface enlargement factor is defined as [15]:

$$\Phi = \frac{A_1}{A_{1p}} \tag{14.1}$$

where A_1 is the developed area of the plate and A_{1p} is the projected plate area. A_{1p} is calculated from Eqs. (14.2), (14.3), and (14.4):

$$A_{1p} = L_p \cdot L_w \tag{14.2}$$

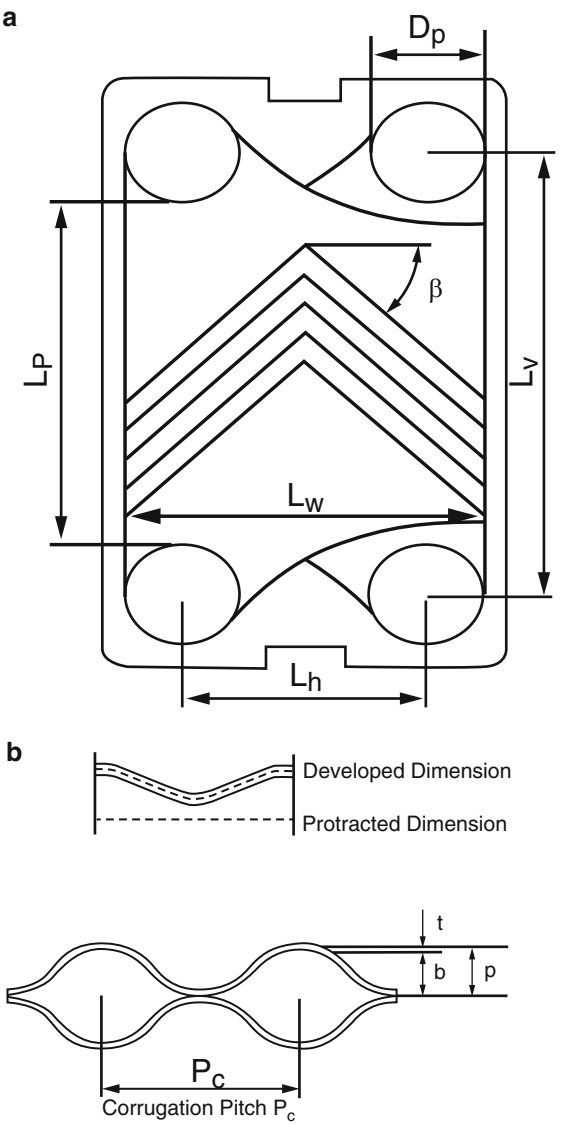

Fig. 14.1 (**a**) Plate geometry in a heat exchanger and (**b**) corrugation dimensions

$$L_{\mathrm{p}} = L_{\mathrm{v}} - D_{\mathrm{p}} \tag{14.3}$$

$$L_{\mathrm{w}} = L_{\mathrm{h}} + D_{\mathrm{p}} \tag{14.4}$$

Mean channel spacing can be defined as:

$$b = p - t \tag{14.5}$$

$$p = L_{\mathrm{C}} - N_{\mathrm{t}} \tag{14.6}$$

where p is the plate pitch or outside depth of the corrugated plate and t is the plate thickness.

The number of efficient plate means the number of the total plates except the end plates of the plate heat exchanger which are located on the front side and back side:

$$N_e = N_t - 2 \tag{14.7}$$

Channel flow area is defined as:

$$A_c = b \cdot L_w \tag{14.8}$$

- *Single-phase heat transfer and pressure drop*

It may be possible that some of these correlations could be used for plates of different manufacturers as long as the geometric parameters are incorporated as defined in the specific correlation; for quick calculations, the correlations are recommended; and for more elaborate calculations:

$$\mathrm{Nu} = \mathrm{Ch} \cdot Re^n \cdot \mathrm{Pr}^{1/3} \tag{14.9}$$

Friction factor is defined as:

$$f = K_p / Re^m \tag{14.10}$$

Kp, m, and n values are selected with respect to β for determining Nusselt number.

- *Two-phase heat transfer and pressure drop*

For the two-phase evaporation, the convective heat transfer correlations of Han et al. are implemented:

$$\mathrm{Nu} = G_{1,e} \cdot \left(Re_{\mathrm{eq}}\right)^{G_{2,e}} \cdot \left(\mathrm{Bo}_{\mathrm{eq}}\right)^{0.3} \cdot \mathrm{Pr}^{0.4} \tag{14.11}$$

Coefficients Re_{eq} and $\mathrm{Bo}_{\mathrm{eq}}$ can be defined as:

$$Re_{\mathrm{eq}} = \frac{G_{\mathrm{eq}} \cdot \mathrm{Dh}}{\mu_1} \tag{14.12}$$

$$B_{\mathrm{eq}} = \frac{\dot{q}}{G_{\mathrm{eq}} \cdot h_{fg}} \tag{14.13}$$

Reynolds number can be defined as:

$$Re_h = (Gc_h \cdot D_{h,h}) / \mu_h \tag{14.14}$$

Channel mass velocity is shown in Eq. (14.15):

$$Gc = \dot{m}_{\mathrm{ch}}/A_{\mathrm{c}} \tag{14.15}$$

where $\dot{m}_{\mathrm{ch}}$ is channel mass flow rate and A_{c} is flow channel area.

Port mass velocity is shown in Eq. (14.16):

$$Gp = \dot{m}/\left(\pi \cdot \left({D_{\mathrm{p}}}^2/4\right)\right) \tag{14.16}$$

Pressure drop in the port ducts is shown in Eq. (14.17):

$$\Delta Pp = 1.4 \cdot N_{\mathrm{p}} \cdot \left(\frac{Gp^2}{2 \cdot \rho}\right) \tag{14.17}$$

Frictional pressure drop is shown in Eq. (14.18):

$$\Delta Pc = 4 \cdot f \cdot \left(\left(L_{\mathrm{eff}} \cdot N_{\mathrm{p}}\right)/D_h\right) \cdot \left(\frac{Gc^2}{2 \cdot \rho}\right) \tag{14.18}$$

$$L_{\mathrm{eff}} = L_{\mathrm{v}}$$

Total pressure drop is defined as:

$$\Delta P_{\mathrm{total}} = \Delta Pc + \Delta Pp \tag{14.19}$$

14.2.2 ε-NTU Method

In the ε-NTU method, the heat transfer rate from the hot fluid to the cold fluid in the exchanger is expressed as:

$$\dot{Q} = \varepsilon \cdot C_{\min} \cdot \left(T_{\mathrm{h,in}} - T_{\mathrm{c,in}}\right) = \varepsilon \cdot C_{\min} \cdot \Delta T_{\max} \tag{14.20}$$

where ε is the heat exchanger effectiveness, $C_{\min}$ is the minimum of Cp_h and Cp_c, and $T_{\max} = (T_{\mathrm{h,\ in}} - T_{\mathrm{c,\ in}})$ is the fluid inlet temperature difference. The heat exchanger effectiveness ε is nondimensional, and it can be shown that in general it is dependent on the number of transfer units NTU, the heat capacity rate ratio C^*, and the flow arrangement for a direct transfer type heat exchanger [15].

Effectiveness ε is a measure of thermal performance of a heat exchanger. It is defined for a given heat exchanger of any flow arrangement as a ratio of the actual heat transfer rate from the hot fluid to the cold fluid to the maximum possible heat transfer rate:

$$\varepsilon = \frac{\dot{Q}}{\dot{Q}_{\max}} \tag{14.21}$$

$$\varepsilon = \frac{1 - \exp(-\mathrm{NTU}) \cdot (1 - C^*)}{1 - C^* \cdot \exp(-\mathrm{NTU} \cdot (1 - C^*))} \tag{14.22}$$

where $C^*$is the rate of the fluid flowing in the heat exchanger which has the minimum specific heat capacity to the maximum one:

$$C^* = Cp_{\min}/Cp_{\max} \tag{14.23}$$

The number of transfer units NTU is defined as a ratio of the overall thermal conductance to the smaller heat capacity rate:

$$\varepsilon = (U \cdot A)/C_{\min} \tag{14.24}$$

NTU designates the nondimensional heat transfer size or thermal size of the exchanger, and therefore it is a design parameter. NTU provides a compound measure of the heat exchanger size through the product of heat transfer surface area A and the overall heat transfer coefficient U.

In this study, plate heat exchanger is investigated in detail. Those plate heat exchangers are used as an evaporator in regenerative biomass-fired ORC system which is shown in Fig. 14.2. Energy and exergy analyses are applied to this system, and some parameters are investigated.

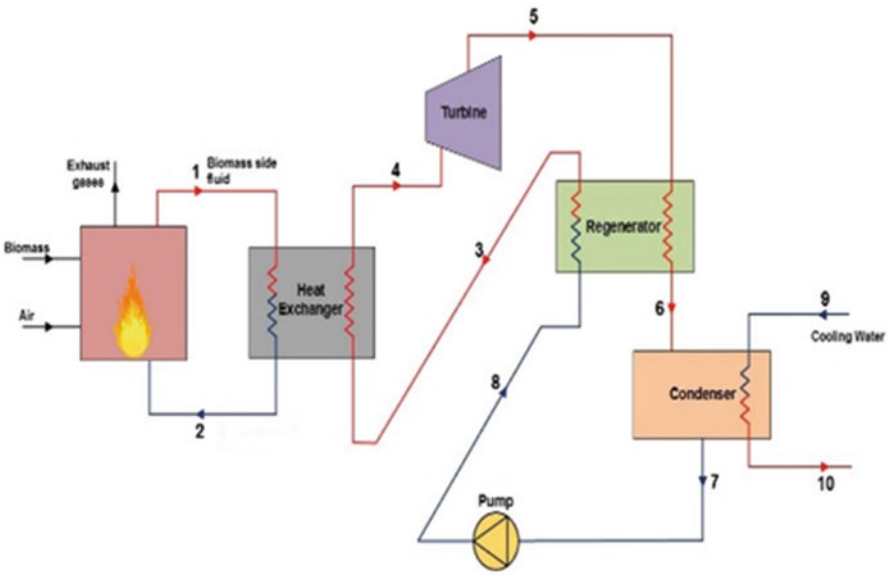

Fig. 14.2 Schematic diagram of a regenerative biomass-fired ORC system

14.3 Mathematical Model

Energy and exergy analyses, which are discussed in the following subsections, are composed of the mathematical model of the biomass-fired ORC system. For solving these equations, a commercially available software Engineering Equation Solver (EES) is used.

14.3.1 Energy Analysis

Energy balance for steady-state control volumes can be defined as follows:

$$\dot{Q}_{\mathrm{cv}} - \dot{W}_{\mathrm{cv}} = \sum \dot{n}_{\mathrm{o}} \cdot \left(\bar{h} + \frac{v^2}{2} + g.z\right)_{\mathrm{o}} - \sum \dot{n}_{\mathrm{i}} \cdot \left(\bar{h} + \frac{v^2}{2} + g.z\right)_{\mathrm{i}} \tag{14.25}$$

where $\dot{Q}_{\mathrm{cv}}$ and $\dot{W}_{\mathrm{cv}}$ are the net heat transfer input and the net power output of the control volume, respectively, and $\dot{n}_{\mathrm{i}}$ and $\dot{n}_{\mathrm{o}}$ are the molar flow rate of the working fluid at the inlet and outlet of the control volume, respectively. In this study molar unit system is selected for convenience as some of the modelling equations are written as a function of the molar compositions of the chemical species. v, g, and z denote the velocity, gravitational acceleration, and elevation according to a reference point, respectively.

In the burner, biomass combustion process occurs. Air and biomass fuel react, and combustion gases are released to atmosphere. The chemical reaction for the combustion of biomass, which mainly consists of C, H, and O atoms, can be shown as follows:

$$\begin{aligned} \mathrm{C}_x\mathrm{H}_y\mathrm{O}_z + (\lambda \cdot \gamma)(\mathrm{O}_2 + 3.76\,\mathrm{N}_2) \rightarrow x\,\mathrm{CO}_2 + (y/2)\ \mathrm{H}_2\mathrm{O} + (\alpha \cdot \gamma)\mathrm{O}_2 \\ + (3.76 \cdot \lambda \cdot \gamma)\mathrm{N}_2 \end{aligned} \tag{14.26}$$

In this equation, λ and α denote the theoretical air and excess air coefficient, respectively. γ is the stoichiometric air coefficient for the complete burning reaction of $\mathrm{C}_x\mathrm{H}_y\mathrm{O}_z$ when there is no excess air. The relation between the excess air coefficient and the theoretical air can be shown as:

$$\alpha = \lambda - 1 = \lambda + \frac{2z - 4x - y}{4\gamma} \tag{14.27}$$

Energy balance for the burner can be shown as:

$$\begin{aligned} \dot{n}_{\mathrm{air}} \cdot \bar{h}_{\mathrm{air}} + \dot{n}_{\mathrm{biomass}} \cdot \bar{h}_{\mathrm{biomass}} = \dot{n}_{\mathrm{excessgases}} \cdot \bar{h}_{\mathrm{excessgases}} + \dot{n}_{\mathrm{biomassfluid}} \\ \cdot \left(\bar{h}_{\mathrm{outlet}} - \bar{h}_{\mathrm{inlet}}\right) \end{aligned} \tag{14.28}$$

Energy balance around the control volume enclosing the heat exchanger that connects the biomass side with the ORC is:

$$\dot{n}_{\text{biomassfluid}} \cdot \left(\bar{h}_1 - \bar{h}_2\right) = \dot{n}_{\text{ORCfluid}} \cdot \left(\bar{h}_4 - \bar{h}_3\right) \tag{14.29}$$

Energy balance for the regenerator can be written in a similar way using Eq. (14.30). Using the energy balance for the condenser, heat transfer rate from the condenser to the cooling water can be shown as follows:

$$\dot{Q}_{\text{condenser}} = \dot{n}_{\text{ORCfluid}} \cdot \left(\bar{h}_6 - \bar{h}_7\right) = \dot{n}_{\text{cw}} \cdot \left(\bar{h}_{10} - \bar{h}_9\right) \tag{14.30}$$

$$\dot{W}_{\text{turbine}} = \eta_{s,t}\left(\bar{h}_4 - \bar{h}_{5,s}\right) \tag{14.31}$$

$$\dot{W}_{\text{pump}} = \frac{\left(\bar{h}_{8,s} - \bar{h}_7\right)}{\eta_{s,p}} = \frac{v_7(P_8 - P_7)}{\eta_{s,p}} \tag{14.32}$$

14.3.2 Exergy Analysis

Exergy analysis is a helpful tool in the assessment of performance of thermal energy systems. The exergy method can help in using energy resources more efficiently. Exergy analysis is generally used to quantify the magnitudes of the irreversibilities in the thermal energy systems. Exergy balance, which is derived combining the energy and entropy balances, is applied to the components of the system to find the exergy flow rates at each state and the exergy destruction of each component. Exergy destruction can also be regarded the potential work lost due to irreversibilities. At the steady-state conditions, the exergy destruction rate of a control volume can be found applying the exergy balance for a control volume, as follows:

$$\dot{\text{Ex}}_{\text{d}} = \sum\left(1 - \frac{T_0}{T_j}\right) \cdot \dot{Q}_j - \dot{W}_{\text{cv}} + \sum\left(\dot{n} \cdot \overline{\text{ex}}\right)_{\text{i}} - \sum\left(\dot{n} \cdot \overline{\text{ex}}\right)_{\text{o}} \tag{14.33}$$

where $\dot{n}$, T_j, T_0, $\dot{Q}$, $\dot{\text{Ex}}$, and $\dot{\text{Ex}}_{\text{d}}$ are the molar flow rate, temperature of the boundary where heat transfer occurs, temperature of the environment, heat transfer rate between control volume and the environment, exergy flow rate, and rate of exergy destruction.

The summation of the exergy destruction rate of the each component is called the total exergy destruction of the system. The contribution of the exergy destruction of each component in the total exergy destruction rate can be found by calculating the exergy destruction ratio as follows:

$$y_{1,i} = \frac{\dot{\text{Ex}}_{\text{d},i}}{\dot{\text{Ex}}_{\text{d,total}}} \tag{14.34}$$

where $\dot{\text{Ex}}_{\text{d},i}$ and $\dot{\text{Ex}}_{\text{d,total}}$ denote the exergy destruction rate of the component i and the total exergy destruction of the system.

Alternatively, the exergy destruction rate of a component can be compared to the chemical exergy rate of the fuel [16], which is taken as biomass for this study:

$$y_{2,i} = \frac{\dot{\mathrm{Ex}}_{\mathrm{d},i}}{\dot{\mathrm{Ex}}_{\mathrm{biomass}}} \tag{14.35}$$

where $\dot{\mathrm{Ex}}_{\mathrm{biomass}}$ and $\dot{\mathrm{Ex}}_{\mathrm{d},i}$ denote the exergy flow rate of the fuel and exergy destruction rate of the component i, respectively.

The exergy includes the physical and chemical exergy, if the kinetic and potential exergies are neglected:

$$\overline{\mathrm{ex}} = \overline{\mathrm{ex}}^{\mathrm{ch}} + \overline{\mathrm{ex}}^{\mathrm{ph}} \tag{14.36}$$

where $\overline{\mathrm{ex}}^{\mathrm{ph}}$ is the specific physical exergy and $\overline{\mathrm{ex}}^{\mathrm{ch}}$ is the specific chemical exergy at a given state. In general, if the chemical composition of a substance does not change at the inlets or exits of a control volume, the chemical exergy is not needed to be calculated to find the exergy destruction in that control volume. For the system studied, chemical exergy is included in the calculations only in the burner because chemical reaction takes place in the combustion process.

Physical flow exergy rate at a given state is defined as:

$$\overline{\mathrm{ex}}^{\mathrm{ph}} = \left(\bar{h} - \bar{h}_0\right) - T_0\left(\bar{s} - \bar{s}_0\right) \tag{14.37}$$

where $\bar{h}$ and $\bar{s}$ denote specific enthalpy in molar basis and specific entropy in molar basis. $\bar{s}_0$ and $\bar{h}_0$ denote specific enthalpy and specific entropy in molar basis for the dead state which defines conditions of the reference environment.

The specific chemical exergy of an ideal gas mixture is defined as:

$$\overline{\mathrm{ex}}^{\mathrm{ch}} = \sum \overline{\mathrm{ex}}_o{}^{\mathrm{ch}} + \sum \bar{R} \cdot T_o \cdot \ln x_i \tag{14.38}$$

Here, x_i is the mole fraction of species i, and $\overline{\mathrm{ex}}_o{}^{\mathrm{ch}}$ is the standard specific chemical exergy (in molar basis) at the reference temperature and pressure.

The chemical exergy of biomass can be defined as [17]:

$$\dot{\mathrm{Ex}}_{\mathrm{biomass}} = \beta \cdot \left(\dot{n}_{\mathrm{biomass}} \cdot \left(\overline{\mathrm{LHV}}_{\mathrm{biomass}} + w \cdot \bar{h}_{fg}\right)\right. \tag{14.39}$$

$$\beta = \frac{\left[1.044 + 0.016 \cdot \left(\frac{H}{C}\right) - 0.3493 \cdot \left(\frac{O}{C}\right) \cdot \left(1 + 0.0531 \cdot \left(\frac{H}{C}\right)\right)\right]}{\left(1 - 0.4124 \cdot \left(\frac{O}{C}\right)\right)} \tag{14.40}$$

where $\dot{n}_{\mathrm{biomass}}$ is the molar flow rate of the biomass, w is the percentage of the moisture in the biomass, $\bar{h}_{fg}$ is the molar-specific enthalpy of vaporization of water, and $\overline{\mathrm{LHV}}_{\mathrm{biomass}}$ is the molar lower heating value of the biomass. C, H, O, and S denote the dry-biomass weight percentages of carbon, oxygen, hydrogen, and sulphur.

14.3.3 Performance Assessment Parameters

As a result of the energy analysis of the integrated system, the heat input to the burner and ORC, the net power output of the system, the heat transferred to ORC, and the electrical efficiency of the ORC and the entire system can be found using Eqs. (14.41), (14.42), (14.43), and (14.44), respectively:

$$\dot{Q}_{\text{burner}} = \dot{n}_{\text{biomass}} \cdot \overline{\text{LHV}}_{\text{biomass}} \tag{14.41}$$

$$\dot{W}_{\text{net}} = \dot{W}_{\text{turbine}} - \dot{W}_{\text{pump}} \tag{14.42}$$

$$\dot{Q}_{\text{ORC,in}} = \dot{n}_{\text{ORC,fluid}} \cdot \left(\bar{h}_4 - \bar{h}_3\right) = \dot{n}_{\text{bio,fluid}} \cdot \left(\bar{h}_1 - \bar{h}_2\right) \tag{14.43}$$

$$\eta_{\text{el,ORC}} = \frac{\dot{W}_{\text{net}}}{\dot{Q}_{\text{ORC,in}}} \tag{14.44}$$

where $\dot{n}_{\text{ORC,fluid}}$ and $\dot{n}_{\text{bio,fluid}}$ denote working fluid circulating throughout the ORC and the fluid providing the heat transfer from biomass side to ORC.

The lower heating value of the biomass can be calculated knowing the higher heating value of the biomass, as shown in Eq. (14.45):

$$\overline{\text{LHV}}_{\text{biomass}} = \overline{\text{HHV}}_{\text{biomass}} - \bar{h}_{fg} \tag{14.45}$$

According to Dulong's formula (Cho et al., 1995), the higher heating value of the biomass is a function of the dry-biomass weight percentages of carbon, oxygen, hydrogen, and sulphur, as shown in Eq. (14.46):

$$\overline{\text{HHV}}_{\text{biomass}} = 338.3 \cdot C + 1442 \cdot \left(H - \frac{O}{8}\right) + 94.2 \tag{14.46}$$

The exergy efficiency is defined as the ratio of the ratio of desired exergy outputs to exergy inputs expended to generate these outputs.

An exergy efficiency is defined differently in each component due to having different working principles.

For pump:

$$\eta_{\text{ex,pump}} = \frac{\overline{\text{ex}}_8 - \overline{\text{ex}}_7}{w_{in}} \tag{14.47}$$

For turbine:

$$\eta_{\text{ex,tur}} = \frac{w_{\text{out}}}{\overline{\text{ex}}_4 - \overline{\text{ex}}_5} \tag{14.48}$$

For heat exchanger:

$$\eta_{\text{ex,HX}} = \frac{\dot{n}_{\text{ORC,fluid}} \cdot \left(\overline{\text{ex}}_4 - \overline{\text{ex}}_3\right)}{\dot{n}_{\text{bio,fluid}} \cdot \left(\overline{\text{ex}}_1 - \overline{\text{ex}}_2\right)} \tag{14.49}$$

For regenerator:

$$\eta_{\text{ex,reg}} = \frac{\left(\overline{\text{ex}}_3 - \overline{\text{ex}}_8\right)}{\left(\overline{\text{ex}}_5 - \overline{\text{ex}}_6\right)} \tag{14.50}$$

For the ORC and entire system, exergy efficiencies can be found using Eqs. (14.51) and (14.52), respectively:

$$\eta_{\text{ex,system}} = \frac{\dot{W}_{\text{net}}}{\dot{\text{Ex}}_{\text{biomass}}} \tag{14.51}$$

$$\eta_{\text{ex,ORC}} = \frac{\dot{W}_{\text{net}}}{\dot{n}_{\text{ORC,fluid}} \cdot \left(\overline{\text{ex}}_1 - \overline{\text{ex}}_2\right)} \tag{14.52}$$

14.4 Results and Discussion

14.4.1 Effect of the Number of Plates

The number of plates is an important parameter of a heat exchanger. As shown in Fig. 14.3, plate number is associated directly with heat transfer rate, so it affects directly many variables such as electrical efficiency and exergy efficiency of both the system and the heat exchanger. For instance, an increase of number of plates provides an increase of the heat transfer rate. This causes electrical efficiency of the ORC to drop. Because in this case, the net output power does not change with respect to the number of plates. Also exergy efficiency does not change because of the fact that fuel exergy does not change. However heat exchanger exergy efficiency increases because specific exergy of the state 3 (inlet of the working fluid stream) and state 1 (outlet of the fluid stream transferring heat) decreases. While a number of the plates change from 11 to 19, temperature drop of the state 3 and 1 causes specific enthalpy drop of these states, so the heat transfer to ORC increases. Change of the number of the plates does not affect turbine power generation or pump power consumption, so net output power rate does not change.

14.4.2 Effect of Working Fluid Type

In this ORC system, four different working fluids are investigated in terms of both energy and exergy analyses. In Fig. 14.4, it's clearly seen that most amount of net power is gained when R134a is used as a working fluid in system and also most amount of heat transferred to the cycle occurs with this type working fluid. Also shown in Fig. 14.4a, ORC electrical efficiency is the highest when R134a is used.

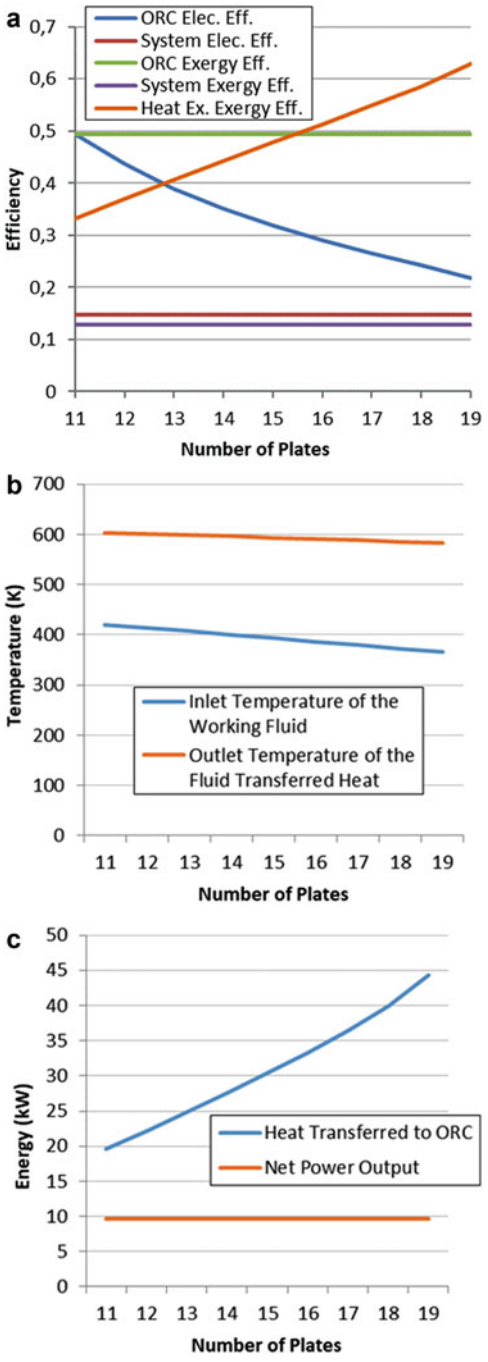

Fig. 14.3 Change of the (**a**) efficiency, (**b**) temperature, and (**c**) efficiency by the number of plates

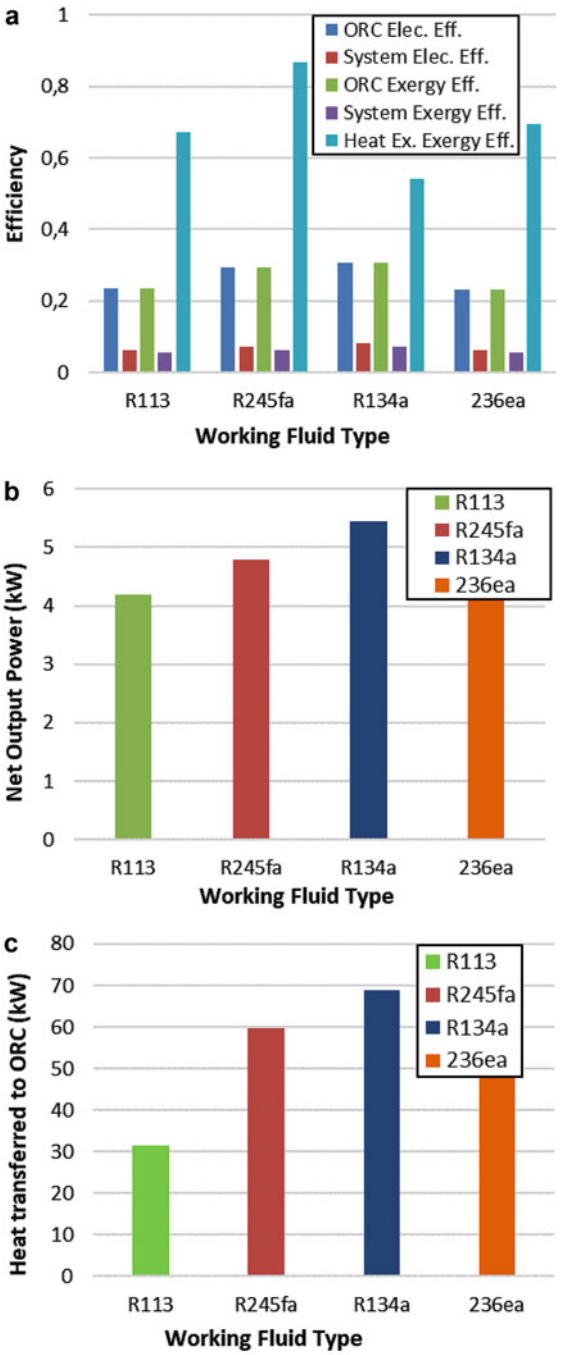

Fig. 14.4 Change of the (**a**) efficiency, (**b**) temperature, and (**c**) efficiency by the number of plates

Despite the most amount of heat and power produced, the ratio between these two parameter is highest for R134a. However, R134a performs lower heat exchanger exergy efficiency. Because of the high amount of heat transfer occurring, the most irreversibility occurs; thus the exergy efficiency decreases. When R245fa is used as the working fluid, the heat exchanger performs the highest exergy efficiency.

14.5 Conclusions

In this study plate, heat exchanger is investigated in detail in terms of heat transfer rate with respect to plate geometry. Then, this plate heat exchanger is used as an evaporator of the biomass-fired ORC system and energy and exergy analysis applied to the entire system. The main conclusions derived from this study are:

- R134a yields the highest electrical and exergy efficiency although the most amount of heat is transferred to the ORC occurs with this case. More net power output is acquired with using this working fluid.
- A number of plates increase the heat transfer but decrease the ORC electrical efficiency.
- Heat exchanger exergy efficiency is the highest performance with R245fa beacuse of the spesific enthalpy difference between state 3 and 4 increase dramatically while between the state 1 and 2 does not change.
- With increase of the number of plates, decrease of the outlet temperature of the working fluid is more than inlet temperature of the fluid transferred heat because spesific of the fluid transferred heat is higer than the working fluid's.

References

1. Qiu G, Liu H, Riffat S (2011) Expanders for micro-CHP systems with organic Rankine cycle. Appl Therm Eng 31:3301–3307
2. Guo T, Wang HX, Zhang SJ (2011) Selection of working fluids for a novel low-temperature geothermally-powered ORC based cogeneration system. Energy Conversation Management 52:2384–2391
3. Chen H, Goswami DY, Stefanakos EK (2011) A review of thermodynamic cycles and working fluids for the conversion of low-grade heat. Renew Sust Energ Rev 14:3059–3067
4. Maizza V, Maizza A (1996) Working fluids in non-steady flows for waste energy recovery systems. Appl Therm Eng 16:579–590
5. Marion M, Voicu I, Tiffonnet AL (2012) Study and optimization of a solar subcritical organic Rankine cycle. Renew Energy 48:100–109
6. Lakew AA, Bolland O, Bolland O (2010) Working fluids for low-temperature heat source. Appl Therm Eng 30:1262–1268
7. Huang Y, Wang YD, Rezvani S, McIlveen-Wright DR, Anderson M, Mondol J, Zacharopolousa A, Hewitta NJ (2013) A techno-economic assessment of biomass fuelled trigeneration system integrated with organic Rankine cycle. Appl Therm Eng 53:325–331

8. Karellas S, Schuster A, Leontaritis AD (2012) Influence of supercritical ORC parameters on plate heat exchanger design. Appl Therm Eng 33-34:70–76
9. Harris C, Despa M, Kelly K (2000) Design and fabrication of a cross flow micro heat exchanger. J Microelectromech Syst 9:502–508
10. Baumann T, Zunft S (2012) Moving bed heat exchanger for solar central receiver power plants: a multi-phase model and parameter variations. Solar PACES 2012, 11–14 September, Marrakech
11. Lee S, Bae C (2008) Design of a heat exchanger to reduce the exhaust temperature in a spark-ignition engine. Int J Therm Sci 47:468–478
12. Zipf V, Neuhäuser A, Willert D, Nitz P, Gschwander S, Platzer W (2013) High temperature latent heat storage with a screw heat exchanger: design of prototype. Appl Energy 109:462–469
13. Walraven D, Laenen B, D'Haeseleer W (2014) Comparison of shell-and-tube with plate heat exchangers for the use in low-temperature organic Rankine cycles. Energy Convers Manag 87:227–237
14. Walraven D, Laenen B, D'Haeseleer W (2014) Optimum configuration of shell-and-tube heat exchangers for the use in low-temperature organic Rankine cycles. Energy Convers Manag 83:177–187
15. Kakac S, Liu H, Pramuanjaroenkij A (2012) Heat Exchangers: Selection, Rating, and Thermal Design, 3rd edn. CRC Press, Boca Raton
16. Colpan CO (2005) Exergy analysis of combined cycle cogeneration systems, Ms.C. Thesis, Middle East Technical University
17. Szargut J (2005) Exergy Method: Technical and Ecological Applications. WIT Press, Billerica

Chapter 15
Development of Cooling Performance of Clinker Cooler Process Based on Energy Audit

Mohammadreza Emami, Kevser Dincer, M. Ziya Söğüt, and T. Hikmet Karakoç

15.1 Introduction

Cement production is fundamentally an energy-intensive and extreme heat-demanding process which is a significant contributor to climate change and environmental imbalances. Furthermore, it requires vast amount of nonrenewable resources like raw materials and fossil fuels. Approximately 5–6% of total global carbon dioxide emissions and greenhouse gases originate from cement production [16]. Cement production will always cause carbon dioxide and other pollutant emissions as its chemistry of the process cannot be changed; but many scientific studies and researches are being carried out to develop sustainability of cement.

Up to now, many possible ways to reduce energy consumption and correspondingly emissions have been investigated which are the key constituents of sustainability. In this regard, clinker cooling department which is one of the most important parts of cement production line plays a significant role. Consequently, cooler performance necessitates comprehensive studies, analyses, and controls to contribute to saving energy.

Clinker nodules are formed at the entrance to the hottest part of the kiln and subsequently fall into the cooler with approximately 1400–1450 °C temperature. To maintain a required phase composition, the clinker should be introduced to rapid

M. Emami (✉) · K. Dincer
Selcuk University, Faculty of Engineering, Department of Mechanical Engineering, Konya, Turkey

M. Z. Söğüt
Piri Reis University, Maritime Faculty, Istanbul, Turkey

T. H. Karakoç
Anadolu University, Faculty of Aeronautics and Astronautics, Department of Airframe and Power plant Maintenance, Eskisehir, Turkey

S. Nižetić, A. Papadopoulos (eds.), *The Role of Exergy in Energy and the Environment*, Green Energy and Technology,
https://doi.org/10.1007/978-3-319-89845-2_15

quenching effects for improving clinker quality. Therefore, for proper cooling (below 200 °C), there should be an efficient heat exchange between clinker and air which is produced by cooler fans. This is, in addition, maintaining high rate recovery of heat to secondary air, tertiary air, and the related process requirement. All these functions must be accomplished efficiently and simultaneously in modern clinker coolers which are designed by different cooler manufacturers. Today any design project would include some of the following provisions which conducts the design and selection of a clinker cooler: low capital cost, optimum cooling rate for good quality of clinker, low clinker outlet temperature, minimum possible impact upon the environment, high heat recovery, low power consumption, low wear and maintenance cost, and reliable to operate. Having maintained these requirements causes minimal downtime and easiness of control and provides a steady flow of combustion air at an unchanging temperature to the kiln and calciner accordingly. For having a desirable performance of a clinker cooler, any designer looks at these criteria and tries to optimize the design. Also some activities can be considered to develop cooler performance while it is already installed and operating. Based on energy audit and performance tests of clinker cooler, any plant can make necessary decisions to optimize its own clinker cooler performance.

From the viewpoint of energy-/fuel-saving and maintenance issues, the cement manufacturers always desire to get their cooling system checked and evaluated based on the measurements through an audit operation. The development of clinker cooler performance by energy audit which is the topic of this study comprises comprehensive measurements and analyses, taking into account the plant's previous regular records of some important values. After getting evaluated of the measurements, the bottlenecks of cooling can be easily recognized from aspects of process or mechanical issues.

With regard to energy consumption in cement plants, some important studies have been carried out based on energy and efficiency analyses which were mainly about the kiln system. Shaleen et al. [17] carried out a research on energy balance in a cement plant located in India with a production capacity of 1MT per year. The study had shown about 35% of the input energy loss through waste heat streams. By using a waste heat recovery system, it was estimated that about 4.4 MW of electricity could be regenerated. Camdali et al. [4] performed an energy and exergy analysis for a rotary burner with precalciner in a cement plant located in Turkey using actual operational data. In this case study, it is found that the energy and exergy efficiency values were 85% and 64%, respectively, for rotary burner. Engin and Ari [7] carried out an energy audit analysis for a 600 TPD rotary kiln system of a cement plant located in Turkey. They concluded that about 40% of the total input energy was lost through hot flue gas (19.15%), through cooler exhaust (5.61%), and by kiln shell (15.11%). For partially recovering these lost energies, a waste heat recovery system was recommended to be established which could recover 1 MW energy. Sogut et al. [18] studied heat recovery from rotary kiln for a cement plant in Turkey. Approximately, 5% of the waste heat could be reused by this system which was used in the neighboring installations; so the local coal and natural gas consumption could be decreased by 51.55% and 62.62%, respectively.

This study includes a methodology pertaining to energy saving in cooling process. The main objective of this study is to emphasize the importance of clinker cooler regarding the energy consumption and recovery. This paper evaluates the system gains and losses to estimate overall efficiency. Furthermore, it submits a reusable template for routine auditing of all cooling systems and the feasible optimizations in the cooler system to save energy and power.

15.2 Cement Production and Cooling Progress

Cement is an inorganic material with hydraulic behavior properties which has made it one of the most usable construction ingredients. In the cement manufacturing process, basically a mixture of calcareous and siliceous with some other oxides like alumina (Al2O3) and iron oxide (Fe2O3) is heated and burned to their clinkering temperature. The resulting material is a hard nodule called clinker which is subsequently ground to find the desired fineness and mixed with some additives to form cement powder. Cement manufacturing process comprises the main stages as mining and quarrying of raw materials, preparation of raw materials which includes raw material homogenizing and grinding, clinkering or burning of raw material to form clinker, and finally grinding of clinker and mixing with additives [11].

At the first step, a combination of raw ingredients must be selected to maintain desired chemical composition in the clinker to be produced. The most common raw materials required for an appropriate chemical composition are limestone, chalk, and clay [7]. Limestone as a sedimentary rock composes mainly the minerals which are different crystal forms of calcium carbonate ($CaCO_3$). As a calcareous source, limestone provides the necessary calcium oxide for clinker making, while some of the other materials, like clay, chalk, shale, etc., furnish the siliceous ingredients, aluminum and iron oxides, which are required for the production process [8]. The calcareous and siliceous constituents ensure the main strength of the cement, while the iron compounds reduce the reaction temperature and determine the cement characteristic gray color. The ingredients are quarried, crushed, and transported to a wide area to be blended and homogenized. For getting a uniform kiln feed, the homogenized mixed material must be ground into fine particles. The amount of resulting clinker cannot be at the same quantity of raw mix. For production of 1 tone clinker, an amount of 1.5–1.7 tons of raw mix shall be burned which indicates the clinker factor. The electricity consumption for raw mix grinding varies between 25 and 30 kWh/tone of cement depending on the type of mill [8].

Once the raw materials have been ground and homogenized, they are fed into kiln to be subjected to a desired heat under which the clinkering reactions are taken place. The kiln feed is burned at high temperature (typically 1450 °C). Prior to this, the kiln feed enters the preheater from the top cyclone to be preheated and precalcined. At a temperature between 900 and 1000 °C, the calcination of the materials starts as the following reaction [8]:

$$CaCO_3 + \text{heat} \rightarrow CaO + CO_2 \quad (15.1)$$

The raw mix comes downward through the cyclones by swirling motions until entering the kiln. On the reverse direction, the kiln hot gases get drawn by ID fan upward to the top cyclones of preheater. Consequently, the raw mix is preheated by having an intimate contact with kiln hot gases. As a result of cyclonic motions of hot gases and raw mix, preheater acts as a heat exchanger. A modern pyroprocessing system normally has a special-designed vessel called precalciner in the bottom stages of preheater building to substantially calcinate the kiln feed before getting fed into the kiln. This crucial phase relieves kiln remarkably since the main part of calcination is already fulfilled and the kiln feed needs only a partial calcination and then sintering for completing the clinkering process. The combustion air for burning fuel in the precalciner is provided by hot gases from clinker cooler region which pass through the tertiary air duct. Typically, 60% of the total fuel is burnt in the calciner, and over 90% of the raw meal is calcined before it reaches the rotary kiln section. The efficiency of calciner depends on uniform airflow and uniform diffusion of fuel and raw meal in the air [12]. Inside the rotary kiln, the clinkerization process is accomplished while the temperature rises. Clinkerization is carried out at 1300–1450 °C, where the material is partially in liquid phase and sticky so that clinker nodules can be developed. Formation of alite takes place at this step. Alite is one of the most important fractions of the clinker as this determines the hardening property of the cement. Along with alite, the Portland cement clinker can mainly contain the following mineral phases (Table 15.1).

The above components can be derived from the chemical analysis denoted by Bogue [3] as a potential composition. The most commonly used cement in general construction is nominally containing 50% C_3S, 25% C_2S, 12% C_3A, 8% C_4AF, and 5% gypsum. This is the typical composition of ASTM Type I cement. There are also other types of cement such as Type II, III, IV, and V cements with remarkable differences in composition and special utilization fields [2]. In addition to these, Portland cement clinker contains approximately the following chemical constituents [6] (Table 15.2).

Once the clinker is formed in the rotary kiln, the melted material must be cooled rapidly to maintain product quality. After getting cooled, the clinker now can be safely handled to be stocked in clinker silos. At the final stage, the cooled clinker is ground to find acceptable Blaine. Here the ground clinker is mixed with a minor quantity of gypsum to accomplish the final product cement. Gypsum as an additive reacts with the C_3A (tricalcium aluminate) phase in the clinker and performs as a set

Table 15.1 Main compounds of Portland cement [6]

Compound	Chemical formula	Common formula
Tricalcium silicate (alite)	3 CaO. SiO_2	C_3S
Dicalcium silicate	2 CaO. SiO_2	C_2S
Tricalcium aluminate	3 CaO. Al_2O_3	C_3A
Tetracalcium aluminoferrite	4 CaO. Al_2O_3. Fe_2O_3	C_4AF

Table 15.2 Approx. percentage of chemical constituents in Portland cement [6]

Constituent	Percentage (%)
SiO_2	16–26
Al_2O_3	4–8
Fe_2O_3	2–5
Mn_2O_3	0–3
TiO_2	0–0.5
CaO	58–67
MgO	1–5
$K_2O + Na_2O$	0–1
SO_3	0.1–2.5
P_2O_5	0–1.5

controller. Furthermore, it can ensure the desirable strength in concrete in case of getting used in a correct dosage [19]. The clinker cooler can perform as a heat exchanger. A modern cooler must maintain the process internal recuperation by heat transfer from hot clinker to the cooling air. It is extremely important to pay attention to controlling the clinker cooler functions owing to the fact that the cooler affects burning process functions in the kiln system and consequently the quality of the clinker. For this reason, all controls should be applied in order to ensure low temperature in discharge clinker, low temperature at exhaust air, high secondary and tertiary air temperatures, slightly negative pressure at kiln hood, desirable cooling air distribution, and proper bed height for free passage of air in each location of the bed [14].

15.3 Theoretical Analyses

As explained above, the cooler efficiency plays a key role in reduction of energy consumption in a cement plant providing that an optimization on the values of cooler operating parameters is accomplished. The major aim of energy audit is to provide a detailed analysis of energy consumption by variant components and to submit the useful information required for determining the possible opportunities of energy conservation. This study describes an audit operation of clinker cooler in a cement plant located in Turkey which is executed by the first author. The plant nominal production capacity was 2500 TPD (maximum 2900 TPD) having a five-stage cyclone preheater kiln with precalciner.

During the audit, the kiln was running in a stable state. A mixture of 90% petcock and 10% steam coal (with the net calorific values of 35,161 kJ/kg and 31,100 kJ/kg, respectively) was used in the kiln main burner and calciner burners as heat source. Sixty-one percent of the mixed fuel was getting used in the calciner, and the rest (39%) was burnt in the kiln main burner.

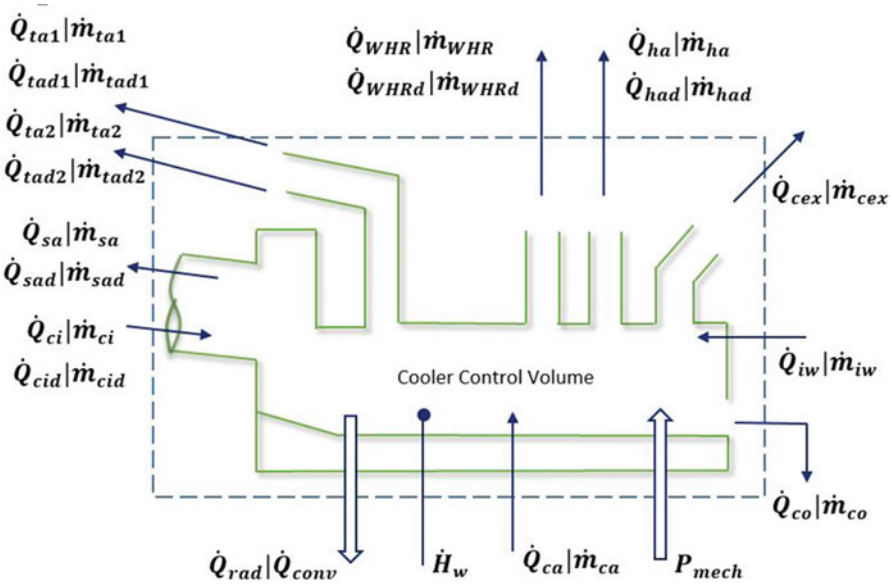

Fig. 15.1 Energy and mass flows going into and leaving cooler control volume

Table 15.3 Cooling fan flow rates

Fan no.	Flow rate (m^3/min)	Flow rate (kg/kg.cl)
Fan-1	574	0.281
Fan-2	936	0.458
Fan-3	762	0.372
Fan-4	904	0.442
Fan-5	881	0.431
Total	4057	1.984

In this study, the mass and energy flows are analyzed considering the instantaneous specific heat capacity of any material going into and leaving the control volume which is defined for the candidate cooler [5]. The complete energy losses are calculated using the first law of thermodynamics. To get a better picture of the analysis, the cooler system considered for the energy audit is schematically shown in Fig. 15.1 as a control volume.

To provide a baseline for evaluating the losses, all process item measurements were performed at site including flows, temperatures, pressures, and gas analyses as shown in the tables below. In the first step, the cooling fan parameters were measured (Tables 15.3 and 15.4). The total cooling air impelled into the cooler by five fans was found as 4057 m^3/min. For calculating total fan efficiencies (Eq. 15.2), the actual power consumption of each fan was measured directly from the related electrical panel:

$$\eta_{\text{fan}} = \frac{\dot{V}\,(\text{m}^3/\text{s}) \cdot \Delta P_{\text{t}}(\text{mmWG})}{P_{\text{w}}(\text{kW}) \times 1000} \tag{15.2}$$

Table 15.4 Cooling fan power consumption and efficiency

Fan no.	Power consumption (kW)	Total efficiency
Fan-1	160.0	0.64
Fan-2	224.0	0.80
Fan-3	149.4	0.86
Fan-4	128.7	0.91
Fan-5	149.3	0.66
Total	811.3	

The fan results were inserted into the balance table (Table 15.5) together with the other collected or measured data.

All fans were running on more than 90% of their full capacities. Indeed, there is no possibility to measure secondary airflow rate; so it should be calculated theoretically. For this purpose, all required components must have been measured like primary airflow rate and temperature, the stoichiometric combustion air required to burn the fuel inside kiln, the relative humidity of air and fuel, stoichiometric flue gases that resulted from combustion, the residual hot meal decarbonation, the calcination degree, and oxygen and carbon monoxide quantities at the kiln inlet. Besides, an important amount of false air was detected by making an inspection over the kiln outlet sealing. It was calculated as 0.007 Nm^3/kg.cl which could adversely affect the secondary air temperature and flow rate (about 12.14 kJ/kg.cl heat loss). The secondary air flow rate was typically defined as 0.385 kg/kg.cl using the below function:

$$\dot{V}_{\text{sa}} = \dot{V}_{\text{comb\_air}} + \dot{V}_{\text{kex}} - \dot{V}_{\text{pr\_tr}} - \dot{V}_{\text{false\_air}} \tag{15.3}$$

The input and output energies were calculated using the equations mentioned in Table 15.5 based on 0 °C and ambient temperature. In addition, a Sankey diagram was prepared using the calculated data which is illustrated in Fig. 15.2. The mathematical formulation for energy analysis is shown below [5, 6].

$$\sum \dot{E}_{\text{in}} = \sum \dot{E}_{\text{out}} \tag{15.4}$$

where;

$$\sum \dot{E}_{\text{in}} = \dot{Q}_{\text{ci}} + \dot{Q}_{\text{cd}} + \dot{Q}_{\text{ca}} + P_{\text{mech}} + \dot{Q}_{iw} \tag{15.5}$$

$$\sum \dot{E}_{\text{out}} = \dot{Q}_{\text{sa}} + \dot{Q}_{\text{sad}} + \dot{Q}_{\text{tad1}} + \dot{Q}_{\text{ta2}} + \dot{Q}_{\text{ta1}} + \dot{Q}_{\text{tad2}} + \dot{Q}_{\text{ha}} + \dot{Q}_{\text{had}} + \dot{Q}_{\text{WHR}} + \dot{Q}_{\text{WHRd}} + \dot{Q}_{\text{cex}} + \dot{Q}_{\text{co}} + \dot{Q}_{\text{rad-conv.}} + \dot{H}_{\text{w}} \tag{15.6}$$

The total input energy based on 0°C and ambient temperature references were 1746.4 kJ/kg.cl and 1692.6 kJ/kg.cl, respectively. The same quantities were balanced for output as well in this method by balancing one of the items which might be difficult or impossible to be measured. Here, the temperature of secondary air was balanced since it was impossible to be measured individually or the measurement could be imprecise.

Table 15.5 Cooler system energy and mass balance

Input energy	**Formula [13]**	**Flow kg/kg.cl**	**Flow Nm3/kg.cl**	**Temperature (°C)**	**Heat kJ/kg.cl**	
					Ref. 0 °C	**Ref. ambient**
Inlet clinker	$\dot{Q}_{ci} = \dot{m}_{ci} C_{P.cl}(T_{cl} - T_{amb})$	1.000		1450	1603.7	1589.3
Inlet clinker dust	$\dot{Q}_{cid} = \dot{m}_{cid} C_{P.cl}(T_{cl} - T_{amb})$	0.050		1450	80.2	79.5
Cooling air	$\dot{Q}_{ca} = \dot{m}_{ca} C_{P.air}(T_{ca} - T_{amb})$	1.984	1.540	19	38.7	0.0
Fan energy (kWh/t.cl)	$P_{mech} = 0.9 P_{mech\_Fan}$	6.61			23.8	23.8
Injected water	$\dot{Q}_{iw} = \dot{m}_{iw} C_{P.w}(T_{iw} - T_{amb})$	0.000		19	0.0	0.0
Total heat, input					**1746.4**	**1692.6**
Output energy	**Formula [13]**	**Flow kg/kg.cl**	**Flow Nm3/kg.cl**	**Temperature (°C)**	**Heat kJ/kg.cl**	
					Ref. 0 °C	**Ref. ambient**
Secondary air	$\dot{Q}_{sa} = \dot{m}_{sa} C_{P.air}(T_{sa} - T_{amb})$	0.385	0.299	998	422.2	414.7
Secondary air dust	$\dot{Q}_{sad} = \dot{m}_{sad} C_{P.cl}(T_{sa} - T_{amb})$	0.019	(=12.0 g/m^3)	998	18.8	18.5
Tertiary air-1	$\dot{Q}_{ta1} = \dot{m}_{ta1} C_{P.air}(T_{ta1} - T_{amb})$	0.635	0.493	934	647.8	635.4
Tertiary air-1 dust	$\dot{Q}_{tad1} = \dot{m}_{tad1} C_{P.cl}(T_{ta1} - T_{amb})$	0.031	(=12.6 g/m^3)	934	28.7	28.2
Tertiary air-2	$\dot{Q}_{ta2} = \dot{m}_{ta2} C_{P.air}(T_{ta2} - T_{amb})$	0.000	0.000	0	0.0	0.0
Tertiary air-2 dust	$\dot{Q}_{tad2} = \dot{m}_{tad2} C_{P.cl}(T_{ta2} - T_{amb})$	0.000		0	0.0	0.0
Hot air for coal mill	$\dot{Q}_{ha} = \dot{m}_{ha} C_{P.air}(T_{ha} - T_{amb})$	0.000	0.000	0	0.0	0.0
Hot air dust coal mill	$\dot{Q}_{had} = \dot{m}_{had} C_{P.cl}(T_{ha} - T_{amb})$	0.000		0	0.0	0.0
Hot air for WHR	$\dot{Q}_{WHR} = \dot{m}_{WHR} C_{P.air}(T_{WHR} - T_{amb})$	0.000	0.000	0	0.0	0.0
Hot air dust WHR	$\dot{Q}_{WHRd} = \dot{m}_{WHRd} C_{P.cl}(T_{WHR} - T_{amb})$	0.000		0	0.0	0.0
Cooler excess air	$\dot{Q}_{cex} = \dot{m}_{cex} C_{P.air}(T_{cex} - T_{amb})$	0.964	0.748	470	473.9	455.0
Discharge clinker	$\dot{Q}_{co} = \dot{m}_{co} C_{P.cl}(T_{co} - T_{amb})$	1.000		165	134.2	119.8
Radiation/convection	$\dot{Q}_{rad\_conv} = h_{comb} A_c (T_s - T_\infty)$ $h_{comb} = h_{conv} + \varepsilon\sigma(T_s + T_\infty)(T_s^2 + T_\infty^2)$				20.9	20.9
Heating and evaporation of water	$H_{evap} = \dot{m}_{iw}[C_{P.w}(100 - T_{amb}) + 2260]$	0.000			0.0	0.0
Total heat, output					**1746.4**	**1692.6**

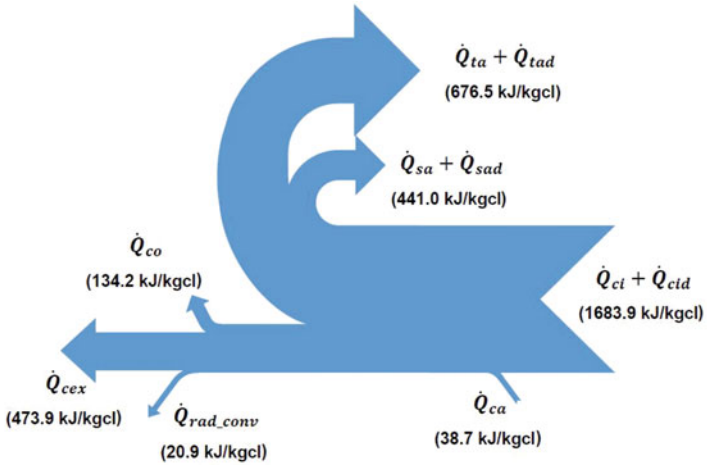

Fig. 15.2 Cooler input/output energies (Sankey diagram)

The same procedure was applied for mass balance [5]:

$$\sum \dot{m}_{\text{in}} = \sum \dot{m}_{\text{out}} \tag{15.7}$$

where

$$\sum \dot{m}_{\text{in}} = \dot{m}_{\text{ci}} + \dot{m}_{\text{cd}} + \dot{m}_{\text{ca}} + \dot{m}_{\text{iw}} \tag{15.8}$$

$$\sum \dot{E}_{\text{out}} = \dot{m}_{\text{sa}} + \dot{m}_{\text{sad}} + \dot{m}_{\text{ta1}} + \dot{m}_{\text{tad1}} + \dot{m}_{\text{ta2}} + \dot{m}_{\text{tad2}} + \dot{m}_{\text{ha}} + \dot{m}_{\text{had}} + \dot{m}_{\text{WHR}} + \dot{m}_{\text{WHRd}} + \dot{m}_{\text{cex}} + \dot{m}_{\text{co}} + \dot{m}_{\text{w}} \tag{15.9}$$

The plant didn't have water injection and WHR system. Moreover, there were no more than one tertiary air duct, and the damper on the coal mill hot air duct was closed as was often the case before. The equation can be split to gas and solid phase mass balances as below:

$$\dot{m}_{\text{ci}} + \dot{m}_{\text{cd}} = \dot{m}_{\text{sad}} + \dot{m}_{\text{tad1}} + \dot{m}_{\text{co}} \tag{15.10}$$

$$\dot{m}_{\text{ca}} = \dot{m}_{\text{sa}} + \dot{m}_{\text{ta1}} + \dot{m}_{\text{cex}} \tag{15.11}$$

The last two equations are equal to 1.050 kg/kg.cl and 1.984 kg/kg.cl, respectively.

It should be paid more attention that the cooler excess air measurement cannot be performed precisely because of the serious false air arising from crusher side and expansion joints. Hence, it was preferred to find out the excess air by calculating secondary air and measuring the other components. The total loss of cooler is the sum of the heat and enthalpy flows that are released by the cooler into the atmosphere. In this context, the total loss can be defined as below (reference temperature is 0 °C):

$$\dot{E}_{\text{loss}} = \dot{Q}_{\text{co}} + \dot{Q}_{\text{cex}} + \dot{Q}_{\text{ha}} + \dot{Q}_{\text{had}} + \dot{Q}_{\text{rad\_conv}} \tag{15.12}$$

The quantity of total loss was found as 629.0 kJ/kg.cl.

Cooler losses are usually calculated according to the rules specified by the German makers association VDZ, which use ambient temperature as the reference. For calculating the recuperation efficiency, VDZ assumes a clinker temperature of 1450 °C and inconsiderable dust circulation between kiln and cooler which can have a huge influence on the actual cooler loss. The VDZ cooler loss (known as Actual Loss) was calculated as 595.86 kJ/kg.cl by the following formula:

$$\dot{E}_{\text{loss\_VDZ}} = \dot{Q}_{\text{co}} + \dot{Q}_{\text{cex}} + \dot{Q}_{\text{WHR}} + \dot{Q}_{\text{WHRd}} + \dot{Q}_{\text{ha}} + \dot{Q}_{\text{had}} + \dot{Q}_{\text{rad\_conv}} + \dot{H}_{\text{w}} - \dot{Q}_{\text{iw}} \tag{15.13}$$

The cooler efficiency according to the definition of VDZ was calculated as 62.5% using the following general formula [6]:

$$\eta_{\text{VDZ}} = \frac{\dot{Q}_{\text{ci}} - \dot{E}_{\text{loss\_VDZ}}}{\dot{Q}_{\text{ci}}} \tag{15.14}$$

To estimate the recovered energy efficiency (secondary and tertiary airs including dust), the following equation is used which gives 64.9% and 65.7% recovered energy based on reference temperature of 0 °C and ambient temperature, respectively [1]:

$$\eta_{\text{recovery}} = \frac{\dot{Q}_R}{\dot{Q}_{\text{ci}} + \dot{Q}_{cid} + \dot{Q}_{\text{ca}}} \tag{15.15}$$

Both recuperation and actual efficiencies are directly affected by the amount of cooler losses. As it is evident, the lower the heat loss in the clinker, exhaust air, radiation, and convection, the higher the amount of heat recuperation in the secondary air and tertiary air and, accordingly, the higher the thermal efficiency of the cooler.

The actual loss was actually being taken place in the cooler candidate to audit. But there are some factors in pyro system which could affect this, like primary air, including fuel transport air, kiln excess air, and false air entering at the kiln through the outlet seal between the kiln tube and kiln hood and through the gaps on the kiln hood. These factors are not related to cooler but increase the actual loss of cooler and reduce the recuperation efficiency. Considering these, we can define a new value to characterize the heat recuperation ability of a cooler and find a way to compare coolers in different kiln systems. This is realized by ignoring the abovementioned factors, meanwhile maintaining a standard rate of combustion air by recuperated air from cooler which is 1.15 kg.air/kg.cl [9]. This value comes from the empirical value for minimum combustion air per 1000 kcal lower (net) heat value of a fuel (1.41 for petcock), fuel NCV, and fuel to clinker ratio. The actual loss at this recuperation air indicates the standard cooler loss which is independent of kiln system. The standard loss of the candidate cooler has been calculated as 519.16 kJ/kg.cl.

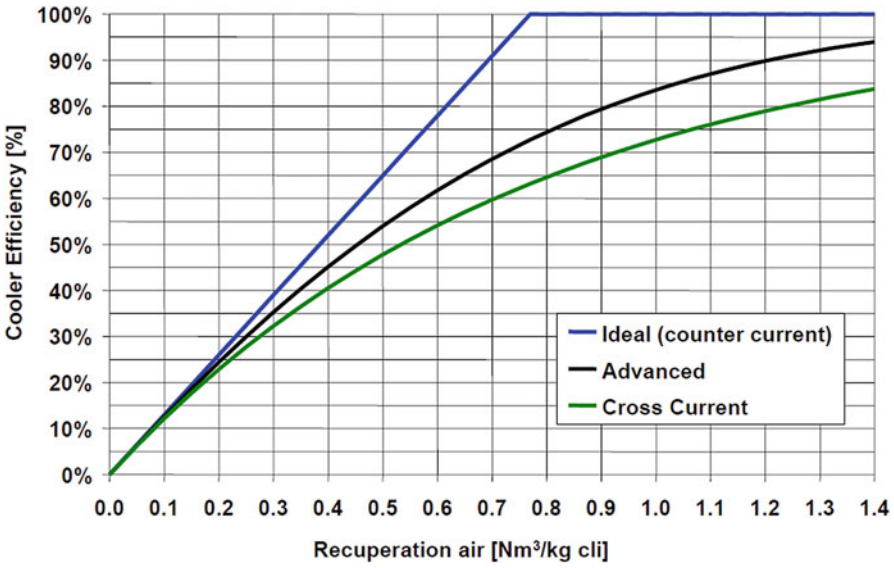

Fig. 15.3 Cooler efficiency versus recuperation air [15]

15.4 Results and Discussions

The detailed analyses in this study define the characteristics of the cooler which help us to judge the cooler and make the necessary decisions to conserve energy and increase the production. The total recuperation air, entering the kiln for getting used in better combustion, is found as 0.792 Nm^3/kg.cl. By applying the total amount of recuperation air together with cooler efficiency as 62.5% in the following assessment diagram shown in Fig. 15.3, it can be estimated that the existing cooler is not an advanced cooler [10]. To establish a desirable cooler, it's essential that the new cooler must have at least 73% efficiency to produce the same recuperation air. Furthermore, in a modern cooler the cooling air produced by cooling fans should be more than 2 Nm^3/kg.cl which is defined as installed specific cooling air [10]. The total cooling air volume, however, was 1.540 Nm^3/kg.cl despite all fans were running on more than 90% of their full capacities having no margin to meet the probable overloads. On discharge side of the cooler, the clinker outlet temperature was very higher than the standard amount published by modern cooler manufacturers as 65 °C + ambient temperature. In addition to this, a huge amount of energy was being lost by the exhaust air with 470 °C temperature.

In conclusion, the standard loss of cooler should be dropped to about 418.68 kJ/kg.cl, and the total power consumption of cooling fans is recommended to decrease from 6.61 kWh/kg.cl to maximum rate of 5.5 kWh/kg.cl. These figures are recommended by the manufacturers in order to make big profit.

15.5 Conclusions

The performance test of cooler is normally executed in the plants having a cooler with old technology. This kind of coolers normally doesn't meet the state-of-the-art technology requirements especially in the regions having serious energy issues. In this regard, a proper analysis from technical and financial point of view can be accomplished to meet the manufacturers' satisfactions, in order to conserve the energy and maintain sustainability of cement industry. By establishing a modern cooler, 100.48 kJ/kg.cl will be saved according to the following equation. This amount comes from subtraction of the candidate cooler standard loss from that of a modern one:

$$\dot{E}_{\text{saved}} = \dot{E}_{\text{st.loss}-1} - \dot{E}_{\text{st.loss}-2} \qquad \left(\frac{\text{kJ}}{\text{kg.cl}}\right) \tag{15.16}$$

where

$\dot{E}_{\text{saved}}$: energy saved
$\dot{E}_{\text{st.loss}-1}$: standard loss of existing cooler
$\dot{E}_{\text{st.loss}-2}$: standard loss of modern cooler

Also, as per the experiences, by renewing the fans approximately 1 kWh/t.cl can be saved. By taking into account the daily rate of production as 2900 TPD, the approximate amount of annual savable energy and power consumption shall be 9.6×10^{10} kJ and 957,000 kW, respectively. By estimating a new cooler price and fuel and power prices as 1,250,000€, 98 €/t, and 0.05 €/kWh, respectively, the total annual profit amount shall be about 320,000 € with 4 years payback time. This is not including the kiln halt intervals which lead to huge financial losses.

Nomenclature

A_c	Cooler surface area (m^2)
$C_{P.\ cl}$	Specific heat of clinker (kJ/kg. °C)
$C_{P.\ air}$	Specific heat of air (kJ/kg. °C)
$C_{P.\ w}$	Specific heat of water (kJ/kg. °C)
$\dot{m}_{ci}$	Inlet clinker mass flow (kg/s)
$\dot{m}_{cd}$	Inlet clinker dust mass flow (kg/s)
$\dot{m}_{ca}$	Cooling air mass flow (kg/s)
$\dot{m}_{iw}$	Injected water mass flow (kg/s)
$\dot{m}_{sa}$	Secondary air mass flow (kg/s)
$\dot{m}_{sad}$	Mass flow secondary air dust (kg/s)
$\dot{m}_{ta1}/\dot{m}_{ta2}$	Tertiary air 1 and 2 mass flow (kg/s)
$\dot{m}_{tad1}/\dot{m}_{tad2}$	Mass flow of tertiary air 1 and 2 dust (kg/s)
$\dot{m}_{ha}$	Mass flow of hot air going to coal mill (kg/s)
$\dot{m}_{had}$	Mass flow of hot air dust going to coal mill (kg/s)
$\dot{m}_{WHR}$	Mass flow of air going to WHR (kg/s)

$\dot{m}_{\text{WHRd}}$	Mass flow of air dust going to WHR (kg/s)
$\dot{m}_{\text{cex}}$	Mass flow of cooler excess air (kg/s)
$\dot{m}_{\text{co}}$	Mass flow of outlet clinker (kg/s)
P_{mech}	Mechanical performance (kW)
$\dot{Q}_{\text{ci}}$	Inlet clinker heat transfer rate (kJ/s)
$\dot{Q}_{\text{cd}}$	Inlet clinker dust heat transfer rate (kJ/s)
$\dot{Q}_{\text{ca}}$	Cooling air sensible heat transfer rate (kJ/s)
$\dot{Q}_{\text{iw}}$	Injected water heat transfer rate (kJ/s)
$\dot{Q}_{\text{sa}}$	Secondary air heat transfer rate (kJ/s)
$\dot{Q}_{\text{sad}}$	Heat transfer rate of secondary air dust (kJ/s)
$\dot{Q}_{\text{ta1}}/\dot{Q}_{\text{ta2}}$	Tertiary 1 and 2 air heat transfer rate (kJ/s)
$\dot{Q}_{\text{tad1}}/\dot{Q}_{\text{tad2}}$	Heat transfer rate of tertiary 1 and 2 air dust (kJ/s)
$\dot{Q}_{\text{ha}}$	Heat transfer rate of hot air going to coal mill (kJ/s)
$\dot{Q}_{\text{had}}$	Heat transfer rate of hot air dust going to coal mill (kJ/s)
$\dot{Q}_{\text{WHR}}$	Heat transfer rate of air going to WHR (kJ/s)
$\dot{Q}_{\text{WHRd}}$	Heat transfer rate of air dust going WHR (kJ/s)
$\dot{Q}_{\text{cex}}$	Heat loss rate by cooler excess air (kJ/s)
$\dot{Q}_{\text{co}}$	Heat loss rate by outlet clinker (kJ/s)
$\dot{Q}_{\text{R}}$	Recuperation air energy flow (kJ/s)
$\dot{Q}_{\text{rad\_conv}}$	Combined radiation and convection heat transfer rate (kJ/s)
T_{amb}	Ambient temperature (°C or K)
T_{cl}	Inlet clinker temperature (°C or K)
T_{ca}	Cooling air temperature (°C or K)
T_{sa}	Secondary air temperature (°C or K)
$T_{\text{ta1}}/T_{\text{ta2}}$	Tertiary air 1 and 2 temperature (°C or K)
T_{ha}	Temperature of hot air going to coal mill (°C or K)
T_{WHR}	Temperature of hot air going to WHR (°C or K)
T_{cex}	Temperature of cooler excess air (°C or K)
T_{co}	Outlet clinker temperature (°C or K)
T_{s}	Cooler surface temperature (°C or K)
T_{∞}	Surrounding temperature (°C or K)
$\dot{V}_{\text{sa}}$	Secondary air volume flow (m^3/s)
$\dot{V}_{\text{comb\_air}}$	Combustion air volume flow (m^3/s)
$\dot{V}_{\text{kex}}$	Kiln excess air volume flow (m^3/s)
$\dot{V}_{\text{prtr}}$	Primary air and fuel transport air volume flow (m^3/s)
$\dot{V}_{\text{false\_air}}$	False air volume flow (m^3/s)
h_{comb}	Combined heat transfer coefficient
ε	Emissivity
σ	Stefan-Boltzmann constant $= 5.670 \times 10^{-8}$ ($W/m^2.K^4$)

References

1. Ahamed JU, Madlool NA, Saidur R, Shahinuddin MI, Kamyar A, Masjuki HH (2012) Assessment of energy and exergy efficiencies of a grate clinker cooling system through the optimization of its operational parameters. Energy 46:664–674
2. Bhatty JI (2002) Role of trace element on cement manufacture and use – a laboratory study. Portland Cement Association, Skokie
3. Bogue RH (1955) The chemistry of Portland cement, 2nd edn. Reinhold Publishing Corp, New York
4. Camdali U, Erisen A, Celen F (2004) Energy and exergy analyses in a rotary burner with pre-calcinations in cement production. Energy Convers Manag 45:3017–3031
5. Cengel YA (2013) Heat and mass transfer, fundamentals and applications, fourth edition in SI Units, New York, McGraw-Hill
6. Duda WH (1984) Cement databook, Volume 1, International Process Engineering in the Cement Industry, 3rd Edition
7. Engin T, Ari V (2005) Energy auditing and recovery for dry type cement rotary kiln systems: a case study. Energy Convers Manag 46:551–562
8. Execution and evaluation of kiln performance tests, German Association of Cement Works (VDZ) (1992) Specification Vt 10, Tannenstrasse 2, 4 Düsseldorf
9. Smidth FL (2003) Comminution Manuel, Vigerslev Alle 77 DK-2500 Valby, Copenhagen, Denmark
10. Hendriks CA, Worrell E, Jager D, Blok K, Reimer P (2000) Emission reduction of greenhouse gases from the cement industry. In: greenhouse gas control technologies conference paper. California
11. Innovations in Portland Cement Manufacturing (2004). Portland Cement Association
12. Manias CG (2004) Kiln Burning Systems. In: Bhatty JI, Miller FM, Kosmatka SH (eds) Innovations in Portland cement manufacturing, SP400. Portland Cement Association (PCA), Skokie
13. Peray KE (1979) Cement manufacture's Handbook. Chemical Publishing Co., Inc., New York
14. Peray KE (1986) The rotary cement kiln, second edition, Chemical Publishing Co., Inc., New York
15. Reference Guide for Process Performance Engineers (2004) 1st ed. Holcim Group Support Ltd
16. Rodrigues FA, Joekes I (2010) Cement industry: sustainability, challenges and perspectives, environmental chemistry letters. https://doi.org/10.1007/s10311-010-0302-2
17. Shaleen K, Rangan B, Uday G (2002) Energy balance and cogeneration of cement plant. Appl Therm Eng 22:485–494
18. Sogut MZ, Oktay Z, Hepbasli A (2009) Energetic and exergetic assessment of a trass mill process in a cement plant. Energy Convers Manag 50:2316–2323
19. Taylor HFW (1997) Cement chemistry. Thomas Telford Publishers, London

Chapter 16
Energy Efficiency of a Special Squirrel Cage Induction Motor

Mine Sertsöz and Mehmet Kurban

16.1 Introduction

Preventing losses from electric motors as much as possible is a significant importance in terms of energy efficiency. Even if energy is produced efficiently, if this is wasted in preventable losses, you have not gained any efficiency.

Two productivity analyses come to mind in terms of productivity. These are analyses of energy and exergy. According to the first law of thermodynamics, the amount of energy entering a system is equal to the amount of total energy which results as work or loss from the system. The analysis based on the first law of thermodynamics to see how the energy entering a system is distributed is called "energy analysis."

In this analysis, the input of 100 units of input energy is calculated, and it is possible to make a comment about whether the system works efficiently. Based on the results of these analyzes, further comments can be made as to where improvements can be made in the system [1].

The second law of thermodynamics is used to explain the concepts of entropy and exergy. Entropy is defined as the irregularity of a system. The more irregularity in a system, the higher the entropy of the system. Heat is a phenomenon that increases the entropy of the system, that is, as the heat increases, entropy increases. It would not be incorrect to say that entropy increases in parallel with the increasing global warming in the world [2].

M. Sertsöz (✉)
Anadolu University, Vocational School of Transportation, Eskişehir, Turkey
e-mail: msertsoz@anadolu.edu.tr

M. Kurban
Bilecik Şeyh Edebali University, Electric and Electronic Engineering Faculty, Bilecik, Turkey

S. Nižetić, A. Papadopoulos (eds.), *The Role of Exergy in Energy and the Environment*, Green Energy and Technology,
https://doi.org/10.1007/978-3-319-89845-2_16

The second law of thermodynamics is used to explain "exergy analysis." Exergy is defined as the usability and how usable the energy is [3]. Since the energy efficiency of electric motors is equal to the exergy analysis, also the exergy analysis calculation is also not performed.

Within this scope, in this article, firstly the losses of electric motors will be mentioned, then the efficiency analysis tests will be explained, then the experiments which are made in this study will be presented, and the results will be interpreted. Lastly, some solutions will be proposed concerning how induction motor efficiency can be improved in the future.

16.2 Motor Losses

It is possible to divide losses in asynchronous motors into three groups.

16.2.1 Iron Losses

This refers to the hysteresis and eddy losses occurring in the stator and rotor sheets. These losses are directly proportionate to the magnetic induction and frequency. While stator iron losses do not change, as the stator frequency is constant, the rotor iron losses change by rotor frequency. However, in empty and loaded operation, the rotor frequency is low enough to be negligible. For this reason, rotor iron losses are very low and may be ignored. Therefore it can be said that the iron losses of an asynchronous motor are equal to the stator iron losses. As the stator frequency is constant, iron losses are constant for all loads.

16.2.2 Friction and Wind Losses

Though normally it changes by the rated speed, this change generally is ignored. Friction and wind losses are found from the open-circuit heat which run alongside iron losses. Iron losses and wind and friction losses are the constant losses.

16.2.3 Copper Losses

These are the losses caused by the ohmic resistance of the stator and rotor in asynchronous motors. Given that these losses change by the square of the current, we can understand that they are parallel with the charge. We can obtain this information from the short-circuit test of the motor.

16.3 Motor Efficiency Tests

The efficiency of electric motors can be measured directly or indirectly. Experimental methods are generally more precise; however, they are not widely used due to the establishment and operation costs of test laboratories.

16.3.1 Direct Methods

(IEEE 112-B, CSA-390) The efficiency of electric motors can be measured by using directly the following equation:

$$\text{Efficiency}\% = \frac{\text{Mechanical Output Power}}{\text{Electrical Input Power}} \times 100 \tag{16.1}$$

For this reason, both mechanical output power and electrical input power need to be measured. Electric input power can be measured precisely with medium price equipment that is easy to set up. Mechanical output power can be defined as the multiplication of the torque and angular velocity. While it is possible to obtain an accurate result with a relatively easy procedure that requires cheap equipment for the speed measurement (± 1 RPM), the torque measurement requires a more detailed setting up and more expensive equipment. The torque measurement generally requires a connection to a dynamometer which is equipped with an accurate torque converter that allows the generation of a variable charge that can control the motor. In North America, test methods depending on the direct measurement of efficiency are commonly used. The Institute of Electrical and Electronic Engineers (IEEE) Standard 112 is a standard adopted both by the National Electric Manufacturers Association (NEMA Standard MG-1) and the US Ministry of Energy. In Canada, the Canadian Standards Association (CSA) Standard 390 follows a procedure that is very similar to the IEEE Standard 112.

This tool is thought to be expensive, as maintenance and calibration are needed, and then the need to interrupt the operation of the motor in order to be able to take measurements increases the accuracy of the prognosis of the estimation method.

16.3.2 Indirect Methods

In order to avoid the complexity and expensive costs of the (IEC 34-2, JEC 37) torque measurements, a motor's efficiency can be calculated by the following equation:

Table 16.1 A comparison between IEC34-2 and IEEE112-B

	IEC 34-2	IEEE 112-B
Measurement type	Sum of losses	Direct
Core loss with voltage drop measurement	No	Yes
Leakage load loss by regression analysis	No	Yes
Corrected winding losses temperature for stator and rotor	No	Yes
A thermal balance in certain load	No	Yes
Balance of no-load losses	No	Yes
Dynamometer torque correction	No	Yes

$$\text{Efficiency}\% = \frac{(\text{Electrical Inp.Power} - \text{Losses})}{\text{Electrical Input Power}} \times 100 \tag{16.2}$$

This calculation requires the measurements of the motor's losses. Most of the motor's losses (copper, iron, mechanical) can be measured quite precisely. However, the remaining losses (stray charge losses) cannot be measured exactly. In indirect efficiency test methods, the stray charge losses at full charge are considered as equal to 0.5% of the input power at full charge, as recommended by the International Electrotechnical Commission (IEC) 34-2 standard. These hypotheses do not take into account the stray charge losses particularly in small motors. Not to take into account the stray charge losses is a failure in energy efficiency calculations. The failure in 60 Hz systems is more than in 50 Hz systems. The failure is much more in Japanese Standard JEC 37, because the stray charge losses are completely ignored in the indirect measurement.

In a comparison between IEC 34-2 and IEEE 112-B, from the direct and indirect methods, the result is as follows: (Table 16.1)

Because IEEE 112 is a direct method, the efficiency results can be measured with greater precision. IEEE 112 includes 11 different efficiency tests, namely, Methods A, B, B1, C, E, E1, F, F1, C/F, E/F, and E1/F1. These methods are briefly given below (IEEE-112: test procedure for polyphase induction motors and generators (2015)):

1st Method A: By using input-output
2nd Method B: By using input-output and the indirect measurements of the stray loss and by separating losses
3rd Method B1: By using input-output and the indirect measurements of the stray loss and a default temperature by separating losses
4th Method C: By using input-output and the indirect measurements of the stray loss by separating losses of the equivalent machines
5th Method E: By separating the losses and using the electric power measurement under the charge and direct measurement of the stray loss
6th Method E1: By separating the losses and using the electric power measurement under the charge and supposed measurement of the stray loss

7th Method F: By using the direct measurement of the stray loss and using the equivalent circuit
8th Method F1: By using the supposed measurement of the stray loss and using the equivalent circuit
9th Method C/F: By using an equivalent circuit that is calibrated to the C charge point of each method and using the indirect measurement of the stray loss
10th Method E/F: By using an equivalent circuit that is calibrated to the E charge point of each method and using the direct measurement of the stray loss
11th Method E1/F1: By using an equivalent circuit that is calibrated to the E charge point of each method and using the assumption of the stray loss

However, while the electrical measurement is a simple procedure, the torque measurement required for measuring the mechanical power at output is costly and has a complicated structure. Therefore, the efficiency calculation is made according to IEC60349-2 rotating electrical machines for rail and road vehicles in Tülomsaş. In IEC60349-2 the efficiency measurement is based on the same principle as IEC 34-2.

16.3.3 Estimation Methods

In addition to the direct and indirect energy efficiency test methods described above, there are also predictive energy efficiency calculations. The underlying reason for the development of estimation methods is to be able to calculate efficiency without stopping the work. However, especially in IEEE-B, if the process is to be done experimentally, there is a need for speed and torque to be measured. There are many efficiency estimates for motors that are currently operating in business. These are slip [4, 5], current [6], equivalent circuit [7–10], and air gap torque [11–16].

Another classification is as follows:

1. Slip method
2. Current method
3. Circuit equation method [17]
4. Separation of losses method [18]
5. Air gap torque (AGT) (NAGT) method [7]
6. Optimization-based methods [5, 19–28]

These are based on direct and indirect methods except for the optimization-based methods. Optimization-based methods for estimating efficiency under real industrial conditions are a good alternative, because there is no need for the experiment.

Table 16.2 Motor plate values

Type	Three-phase four-pole squirrel cage asynchronous motor
Continuous nominal power	200 kW, 1370 V, 106A, 75 Hz, 2200 rpm
One hour nominal power	220 kW, 1370 V, 117A, 75 Hz, 2200 rpm
Insulation class	Class 200
Cooling	Self-cooled
Dielectric test voltage	4600 V
Maximum service speed	3822 rpm
Weight	640 kg ± 5%
Gear ratio	7.0

16.4 Experimental Facility

A squirrel cage induction motor, which is being used in the Marmaray project, is utilized in the experiments. (Marmaray project is one of the biggest projects to solve the public transportation in Istanbul. With this project, an uninterrupted above-ground metro line of 76.3 km (47.4 mil) will be constructed from Halkali on the European side to Gebze on the Asian side that will be modern, high capacity, fast, and integrated with the other transportation systems)

The plate values of the motor used in this test are as follows (Table 16.2):

If we assume that the rotor and stator copper and core losses are negligible as a result of this test [30], it is possible to find the losses as a result of turning.

If we assume that core losses are negligible as a result of this test [30], it is possible to find the losses as a result of stator and rotor copper.

$$\text{Leakage Load Losses} = 0,05 \times \text{Input power in full load} \tag{16.3}$$

$$\text{Efficiency}\% = \frac{(\text{Input power in full load} - (\text{Copper Losses} + \text{Friction/Wind Losses} + \text{Leakage Load Losses}))}{\text{Input power in full load}} \tag{16.4}$$

$$\text{Efficiency}\% = \frac{(\text{Input power in full load} - (\text{Copper Losses} + \text{Friction/Wind Losses}))}{\text{Input power in full load}} \tag{16.5}$$

Core losses are negligible in both equations. Equation 16.2 is an energy efficiency calculation according to IEC 34-2, and Eq. 16.3 is an energy efficiency calculation according to TS EN 60349-2.

Leakage Load Losses $= 200 \times 0,05 = 10$ kW (Eq. 16.3).
Input power in full load $= 200$ kW.
Efficiency% $= \frac{(200-25.4)}{200} \times 100 = 87.3\%$(IEC $34-2$) (Eq. 16.4).
Losses % $= 100\ \% - 87.3\ \% = 12.7\ \%$ (IEC $34-2$).
Efficiency% $= \frac{(200-15.4)}{200} \times 100 = 92.3\%$(TS EN $60349-2$) (Eq. 16.5)
Losses % $= 100\ \% - 92.3\ \% = 7.7\ \%$ (TS EN $60349-2$)

In order to be able to accept the motor, the company Rotem stated that the efficiency test was successful according to the specification. It is stated in this specification the efficiency test [31] should be made according to TS EN 60349-2, and the maximum loss value should be 9.2%. Lost value was found to be 7.7% according to TS EN 60349-2 in the experiment. This means that the engine being tested can be used in the Marmaray project. However, the efficiency was calculated according to IEC 34-2, another productivity standard, and the loss was found to be 12.7%.

The test units which were used for this study are shown in Figs. 16.1, 16.2, and 16.3. The results shown in Tables 16.3 and 16.4 above were obtained from experiments on these test units.

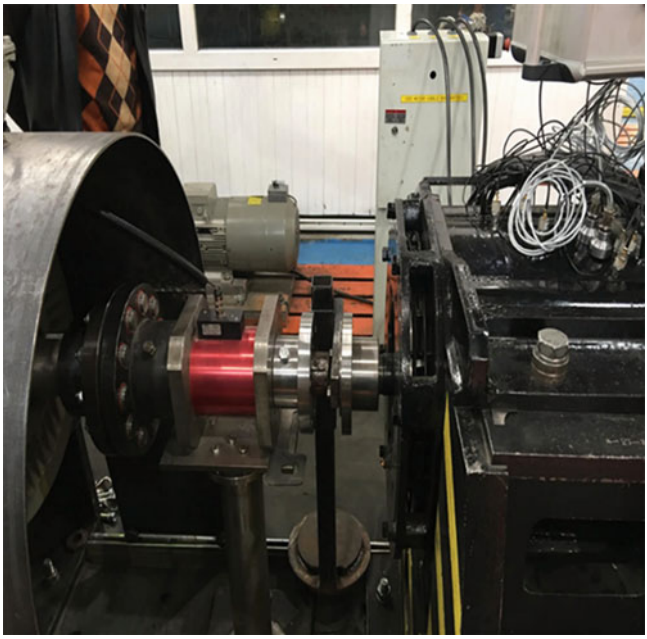

Fig. 16.1 Load and test motor

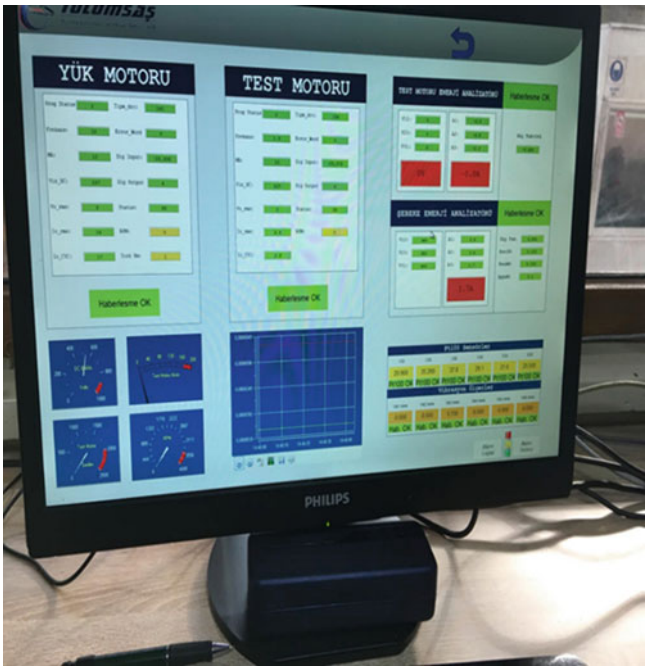

Fig. 16.2 Motor control unit

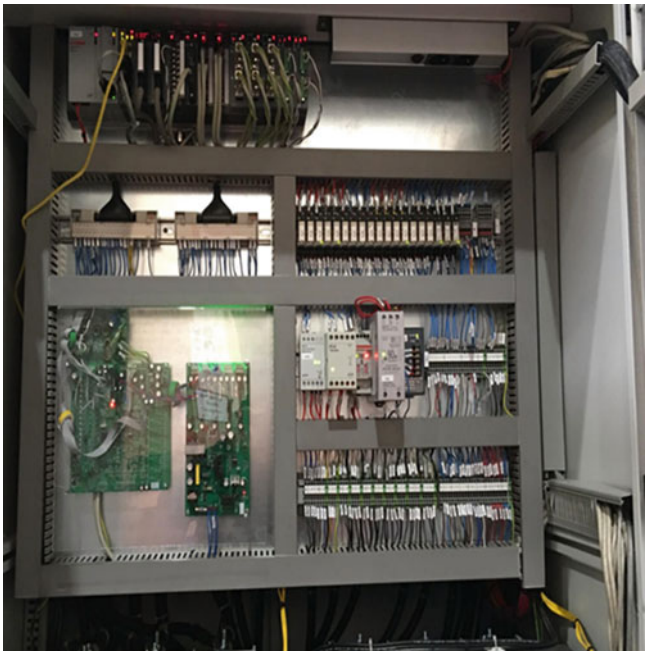

Fig. 16.3 Control panel

Table 16.3 No-load characteristic test [29]

Test condition: 1370 V, 66 Hz			
Voltage (V)	Frequency (Hz)	Current (A)	Power (kW)
1376	66	54.7	7

Table 16.4 Locked rotor characteristic test [29]

Test condition: 106 A, 66 Hz			
Rated current (A)	Frequency (Hz)	Voltage (A)	Power (kW)
106	66	106	8.4

16.5 Conclusions

In order to measure the efficiency experimentally, the motor must be stopped. When the cost and difficulty aspects of this are considered, the easiest approach is to determine the efficiency by estimation methods rather than experimental methods. There are many efficiency estimation methods for the motors that are already being used in the industry. These are shift, current, equivalent circuit, and air space torque.

In this experiment the efficiency was found to be 92% according to standard IEC60349-2. The experiment indicated that stator and rotor impedance causes 8.4 kW loss and turning losses were 7 kW. As can be understood from the results for this machine, the copper loss is more than the loss from turning. We also know that copper losses are directly related to temperature, if it is not considered in the design phase of the machine. For this reason, the operating temperature of the motor is quite important when losses occur. In order to prevent this loss, avoiding the overloading of the engine and preventing the copper losses due to the temperature contribute to productivity. However, in the standard TSE 60349-2, since the dc test is not performed, the stator resistance and also the stator loss are not known. If the quantities of these two (stator and rotor) losses were known, productivity studies could be improved. For a more detailed study, in future work, the IEEE 112-B1 standard will be applied to this motor. All the losses can be known in the IEEE-112B standard. A comparison can then be made between an indirect and direct method according to efficiency value and losses.

Acknowledgments The Tülomsaş Company supported this research. This support is gratefully acknowledged. Special thanks to Aylin Tören.

References

1. Dincer I, Rosen MA (2013) Exergy: energy, environment and sustainable development, 2nd edn. Elsevier, Oxford, UK
2. Romero JC, Linares P (2014) Exergy as a global energy sustainability indicator: a review of the state of the art. Renew Sust Energ Rev 33:427–442

3. Çengel YA, Boles MA (2008) Termodinamik, Güven Bilimsel, 5.Baskı
4. Lima-Filho AC, Gomes RD, Adissi MO, Borges da Silva TA, Belo FA, Spohn MA (2012) Embedded system integrated into a wireless sensor network for online dynamic torque and efficiency monitoring in induction motors. IEEE/ASME Trans Mechatronics 17(3):404–414
5. Siraki A, Pillay P (2012) An in situ efficiency estimation technique for induction machines working with unbalanced supplies. IEEE Trans Energy Convers 27(1):85–95
6. Herndler B, Barendse P, Khan MA (2011) Considerations for improving the non-intrusive efficiency estimation of induction machines using the air gap torque method. In: Proceedings IEEE IEMDC, May 2011, pp 1516–1521
7. Lu B, Habetler TG, Harley RG (2008) A nonintrusive and in-service motor efficiency estimation method using air-gap torque with considerations of condition monitoring. IEEE Trans Ind Appl 44(6):1666–1674
8. Sebastian D, Manjusha VA, Anto R (2013) Energy management of induction motors using non-intrusive methods. In: Proceedings ICPEC, Feb. 2013, pp 767–772
9. Zhang H, Zanchetta P, Bradley KJ, Gerada C (2010) A low-intrusion load and efficiency evaluation method for in-service motors using vibration tests with an accelerometer. IEEE Trans Ind Appl 46(4):1341–1349
10. Hydraulics & pneumatics: rightsize your electric motors. [Online]. Available: http://hydraulicspneumatics.com/200/TechZone/HydraulicPumpsM/Article/False/21602/TechZone-HydraulicPumpsM. Accessed 5 Sept 2014
11. IEEE-112: Test Procedure for Polyphase Induction Motors and Generators, Silva WL, AMN L, Oliveira A (2015) A method for measuring torque of squirrel-cage induction motors without any mechanical sensor. IEEE Trans Instrum Meas 64(5):1223–1231
12. Hsu JS, Scoggins BP (1995) Field test of motor efficiency and load changes through air-gap torque. IEEE Trans Energy Convers 10(3):477–483
13. Szychta L, Figura R (2012) Analysis of efficiency characteristics of squirrel-cage induction motor for pump applications. In: Proceedings ICEM, Sep. 2012, pp 73–78
14. Al-Badri M, Pillay P, Angers P (2015) A novel algorithm for estimating refurbished three-phase induction motors efficiency using only no-load tests. IEEE Trans Energy Convers 30 (2):615–625
15. Sakthivel VP, Bhuvaneswari R, Subramanian S (2010) Non-intrusive efficiency estimation method for energy auditing and management of in-service induction motor using bacterial foraging algorithm. IET Electr Power Appl 4(8):579–590
16. Silva WL, Lima AMN, Oliveira A (2015) A method for measuring torque of squirrel-cage induction motors without any mechanical sensor. IEEE Trans Instrum Meas 64(5):1223–1231
17. Kueck JD, Olszewski M, Casada DA, Hsu J, Otaduy PJ, Tolbert LM (1996) Assessment of methods for estimating motor efficiency, load under field conditions. Oak Ridge Nat. Lab., Oak Ridge, TN, Rep. ORNL/ TM-13165
18. In-plant electric motor loading and efficiency techniques. (1990) Ontario hydro, Toronto, ON, Canada, Rep. TSDD-90-043
19. Charette A, Xu J, Ba-Razzouk A, Pillay P, Rajagopalan V (2000) The use of the genetic algorithm for in situ efficiency measurement of an induction motor. In: Proceedings IEEE power engineering society winter meeting, 2000, pp 392–397
20. Phumiphak P, Chat-uthai C (2008) Nonintrusive method for estimating field efficiency of inverter-fed induction motor using measured values. In: Proceedings IEEE international conference sustainable energy technology, Signapore, pp 580–583
21. Aspalli MS, Shetagar SB, Kodad SF (2008) Estimation of induction motor field efficiency for energy audit and management using genetic algorithm. In: Proceedings international conference sensing technology, Venice, Italy, pp 440–445
22. Lu B, Wenping C, French I, Bradley KJ, Habetler TG (2007) Nonintrusive efficiency determination of in-service induction motors using genetic algorithm and air-gap torque methods. In: Conference record of IEEE 42nd IAS annual meeting, New Orleans, Louisiana, pp 1186–1192

23. Phumiphak T, Chat-uthai C (2002) Estimation of induction motor parameters based on field test coupled with genetic algorithm. In: Proceedings international conference power system technology, Kunming, China, pp 1199–1120
24. Pillay P, Levin V, Otaduy P, Kueck J (1998) In-situ induction motor efficiency determination using the genetic algorithm. IEEE Trans Energy Convers 13(4):326–333
25. Phumiphak T, Chat-uthai C (2004) An economical method for induction motor field efficiency estimation for use in on-field energy audit and management. In: Proceedings international conference power system technology, Taipei, Taiwan, pp 1250–1254
26. Gomez JR, Quispe EC, de Armas MA, Viego PR (2008) Estimation of induction motor efficiency in-situ under unbalanced voltages using genetic algorithms. In: Proceedings international conference electrical machines, Wuhan, China, pp 1–4
27. Cunkas M, Sag T (2010) Efficiency determination of induction motors using multi-objective evolutionary algorithms. Adv Eng Softw 41(2):255–261
28. Sakthivel VP, Bhuvaneswari R, Subramanian S (2010) Non-intrusive efficiency estimation method for energy auditing and management of inservice induction motor using bacterial foraging algorithm. IET Elect Power Appl 4(8):579–590
29. Tülomsaş, October 2012
30. Fitzgerald AE, Kingsley C Jr, Umans SD (2014) Elektrik makinalari. In: Palme yayincilik, 6th edn. McGraw-Hill, New York, pp 330–340
31. https://www.tulomsas.com.tr/

Chapter 17
Multi-criteria Method and Its Application for Compressed Air Energy Storage in Salt Domes

M. Cruz Castañeda, Carlos Laín, Juan Pous, and Bernardo Llamas

17.1 Introduction

The fight against climate change requires harnessing novel technologies to decrease CO_2 emissions. Renewable energy must be among the main strategies for complying with the COP-21 agreements. Energy storage technologies will play a crucial role in increasing both the efficiency, as well as the availability, of this kind of energy source [1]. Moreover, energy storage technologies will help reduce the supply risk of the electric power system, by overcoming the uncertainty of renewable energy generation.

There are only two alternatives of energy storage technologies with an installed capacity of over 100 MW: compressed air energy storage (CAES) and pumped hydroelectric storage (PHS). The investment cost (CAPEX) according to energy capacity and the maintenance and operating cost (OPEX) are higher than pumped hydroelectric technology. Moreover, compressed air energy storage (hereinafter "CAES") enables the efficient and cost-effective storage of large amounts of energy [2]. Consequently, CAES is the only possibility.

There are several geological structures that can be used as CAES; however, the development of CAES in salt domes is one of the intermediate solutions, given that it reduces the exploration risk, while the cost associated with its development is not high and it is cheaper than making a cavity in a rock formation. Moreover, it is the geological structure most suited to make a cavity; in addition, it offers a reasonable geographical distribution and a nearby site with wind farms [3].

Nevertheless, the cost associated with underground exploration, as the risk inherent to mining exploration, means that it is advisable to establish a detailed

M. Cruz Castañeda · C. Laín · J. Pous · B. Llamas (✉)
Universidad Politécnica de Madrid, Ingeniería Geológica y Minera, Madrid, Spain
e-mail: bernardo.llamas@upm.es

S. Nižetić, A. Papadopoulos (eds.), *The Role of Exergy in Energy and the Environment*, Green Energy and Technology,
https://doi.org/10.1007/978-3-319-89845-2_17

schedule to select and characterize structures to minimize the aforementioned risk [4]. In accordance with the purpose of selecting the best geological structure for a CAES from among the alternatives considered, multi-criteria algorithms make it possible to establish a hierarchy of the alternatives to be studied and to objectively identify those structures with the greatest potential.

Notable among the procedures and mathematical algorithms is the analytical hierarchy process (hereinafter "AHP") method, devised by Thomas L. Saaty in the 1970s. This methodology has the advantage of being simple and clear [5]. The AHP breaks down the main problem into a hierarchical structure, enabling a detailed and thorough analysis to be carried out of the criteria levels considered, in such a way as to construct a breakdown structure to select salt domes.

Accordingly, a structure hierarchization method that makes possible to objectively establish the areas with the greatest potential for CAES is presented, not only taking technical aspects into account, but socio-economic ones also [6]. The specifying of the selection algorithm for structures in saline formations makes possible to establish a selection and classification of these structures for a particular purpose: reducing the exploration risk related to underground structures and applying this methodology in potential CAES locations in Europe or any other region around the world. In this case, the study was focused on the Basque-Cantabrian basin (Spain).

In the Basque-Cantabrian basin, it is possible to identify up to 11 diapiric structures, surfacing and with sufficient depth to develop a CAES. These peculiar characteristics allow to consider new research topics (Fig. 17.1): establish a new definition of energy storage capacity, considering not only the storage of compressed air at great depth, but also the definition of mini-CAES with storage capacity power in the range 10–100 MW, shallow structure and less expensive than the conventional CAES. Moreover, the mini-CAES will be defined in accordance with the renewable capacity of the surrounding area.

This research will contribute to implement CAES technology, which would be a milestone in the field of renewable energies. The communication will include

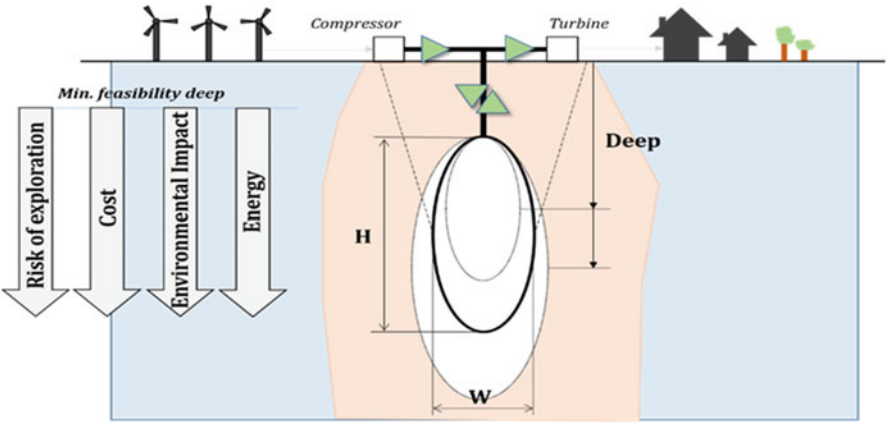

Fig. 17.1 The schematics of mini-CAES concept

technical description of the novel mini-CAES concept and its application to a specific region in Spain.

17.2 Materials and Methods

17.2.1 Favourable Site in Which to Develop CAES

The Basque-Cantabrian basin [7] is located in the northern edge of the Iberian Peninsula, at the western end of the Pyrenees mountain range, and covers a surface area of 25,000 km^2 (Fig. 17.2). Diapiric structures of Triassic saline materials (Keuper) in the Basque-Cantabrian basin are characteristics of the evolution of a basin with deep saline levels, affected first by a tensional period and later by a compressional period [8]. Some of these diapiric characteristics have surfaced, and others are recognized through geophysics. In the north of the Basque-Cantabrian

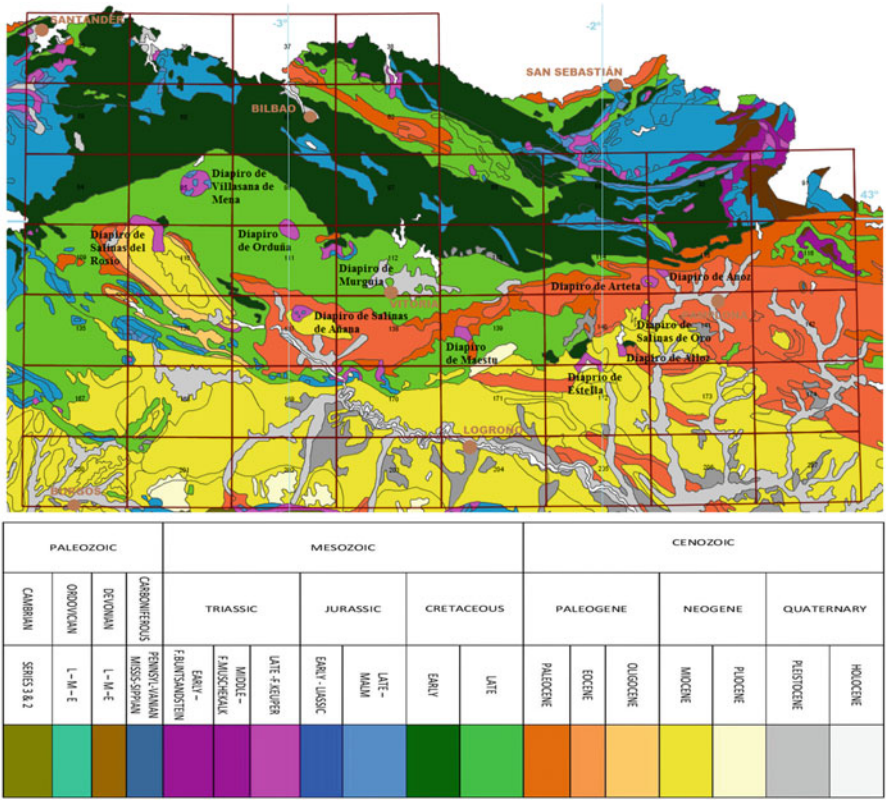

Fig. 17.2 The Basque-Cantabrian basin (11 structures)

basin, diapirs tend to present highly evolved chimney shapes, which narrow at depth due to the lack of salinity and greater sedimentary load [9].

The 11 subsurface structures are shown in Fig. 17.2. These possibilities are located in the Basque-Cantabrian basin (Spain), and the most distinguishing feature is that they are shallower and with sufficient depth to develop a CAES technology: Rosio, Villasana de Mena, Orduña, Murguía, Añana, Maestu, Estella, Alloz, Oro, Arteta and Anoz salt domes.

17.2.2 Hierarchy and Selection Methodology

In this section, the evaluation and multi-criteria decision methods are described according to a set of possibilities with various simultaneous target functions, a decision agent and consistent and rational evaluation procedures [10]. Notable among the procedures and mathematical algorithms is the AHP method, devised by Thomas L. Saaty, 1977. The AHP breaks down the main problem into a hierarchical structure, enabling a detailed and thorough analysis to be carried out of the criteria levels considered. The breakdown in Fig. 17.3 was made considering

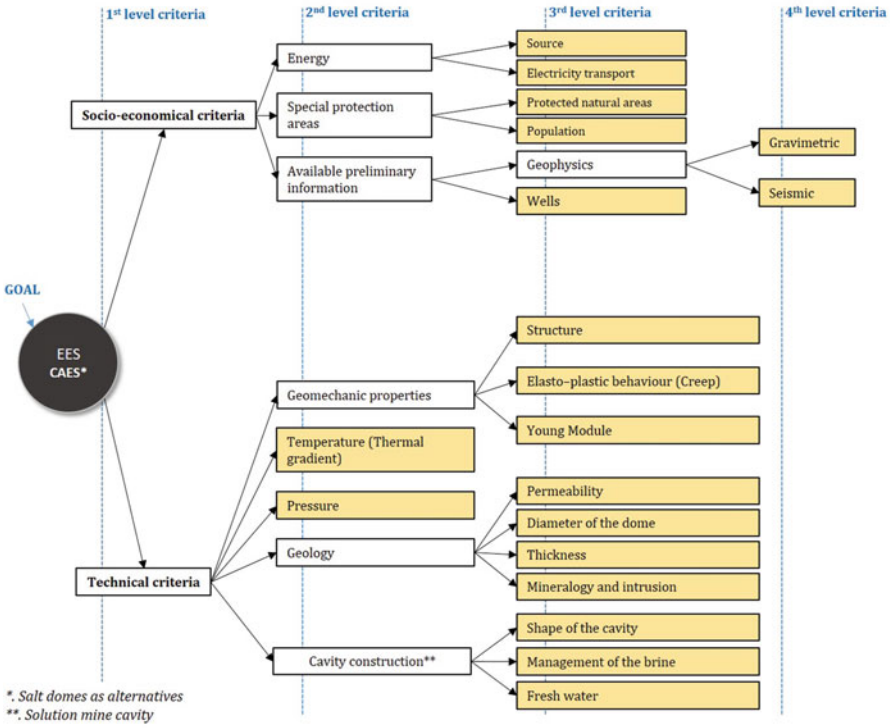

Fig. 17.3 Structure developed. Highlighted are the criteria with a scientific and mathematical scale

only one topic: selecting salt domes to develop an energy storage facility (CAES). It shows various criteria levels. For example, the first level is considered to describe technical and socio-economic criteria.

This structure was made considering various criteria levels. Each criterion converges into a node that it is measurable and quantifiable. According to the figure, the criteria that have an assessment value are highlighted. This structure allows developing a scientific scale and their transformation into a mathematical scale. The assessment of each alternative is based on the AHP methodology:

$$A_1 = \sum_{i=1}^{n} W_i \cdot V_i \tag{17.1}$$

where the hierarchy of alternatives (A) is established by allocating weightings (W) to each criterion and the values (V) for each criterion in each alternative under evaluation by using Eq. (17.1).

17.2.3 Geographic Information System

Geographic information systems (GIS) have become a basic tool for managing geotagged information [11]. A GIS project called GIS-CAES was developed to demonstrate all the information described in the breakdown structure (previous section). The choice of a GIS software package was based on the preferences, functional requirements or training of this research. The open-source gvSIG® programme was used, whose integration into the underground research flow is in line with the requirements. Indeed, as it is open source, it allows the code to be developed, and the functionalities of the original package to be customized [12].

17.3 Results and Discussion

The solution to the problem posed in the selection of structures for underground energy storage, following AHP methodology, allows the problem to be broken down into a series of criteria (Fig. 17.3), of which many are geotagged.

17.3.1 Socio-Economic Criteria

According to the structure developed to select and rank the most favourable structure, the next sub-criteria respond with the second level in the socio-economic criteria: the energy criterion (Fig. 17.4) considered wind farms and their installation capacity as well as the transmission grid. Two areas were established around each of the 11 structures: the first with 5 km radius and the second with a 10 km radius.

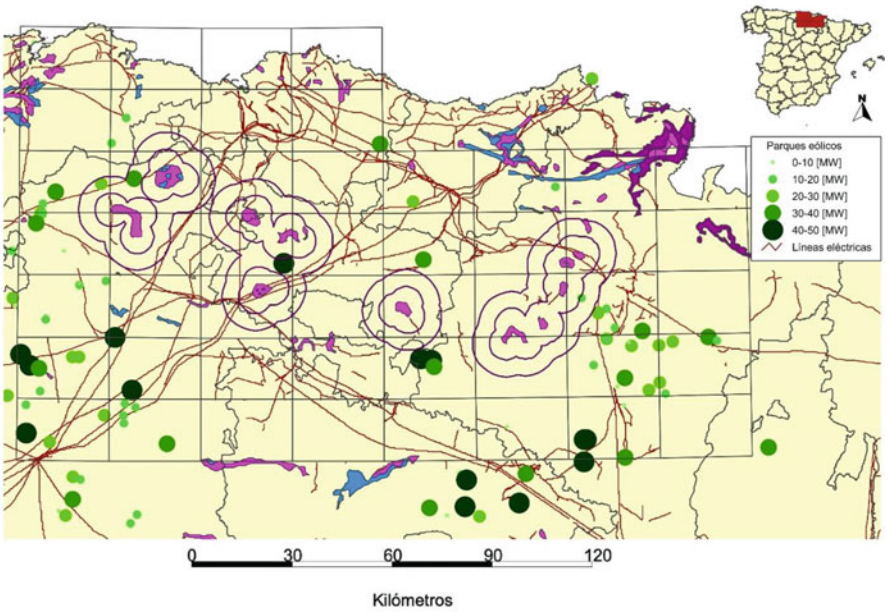

Fig. 17.4 Application of the "energy" section criterion

The special protection area criterion (Fig. 17.5) is broken down into populated areas and environmental protection areas. Studing the population criterion, we considered a protection area with a radius of 10 and 20 km. In this area the possibility of developing a CAES technology is potentially dangerous. Considering environmental protection areas, it has been considered SAC (Special Areas of Conservation) and special areas of conservation for birds, both included in the NATURA 2000 NETWORK. In addition, natural parks are included based in the Law 30/2014. All of the subsurface structures around these environmental protection areas will be more difficult to explore and operate.

The available preliminary information criterion (Fig. 17.6) is described as the availability of information on the undersoil which is considered to be particularly relevant:

(i) Geophysics, as an indirect measurement and structural definition tool. Specifically, the existence of refraction seismic data and gravimetry.
(ii) Surveys performing direct measurements of the target formations (Keuper formation).

According to criteria description [13–15], a summary has been included in Table 17.1. The scientific scale has been described and their translation into the mathematical scale (1–9 values). Most suitable values in each criterion were assigned as the highest mathematical value.

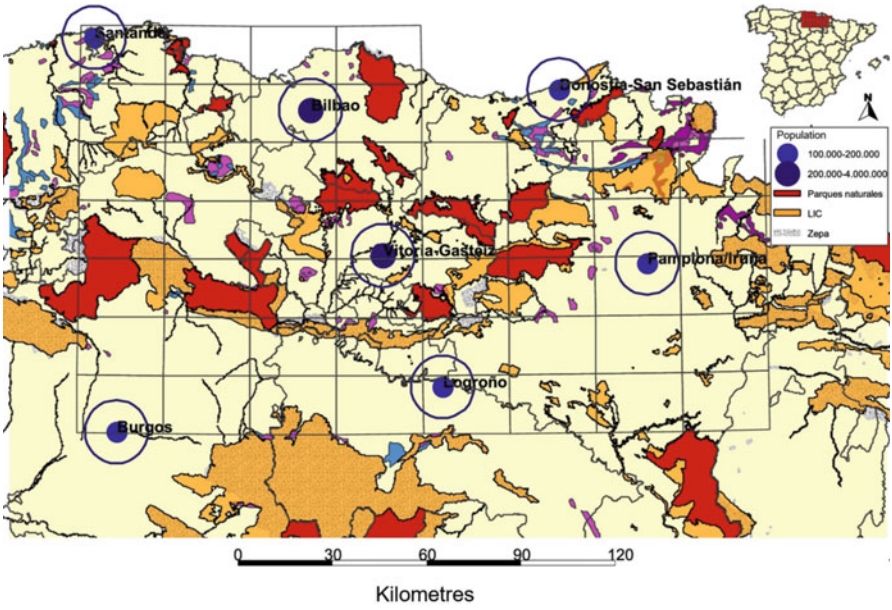

Fig. 17.5 Application of the "special protection areas" criterion

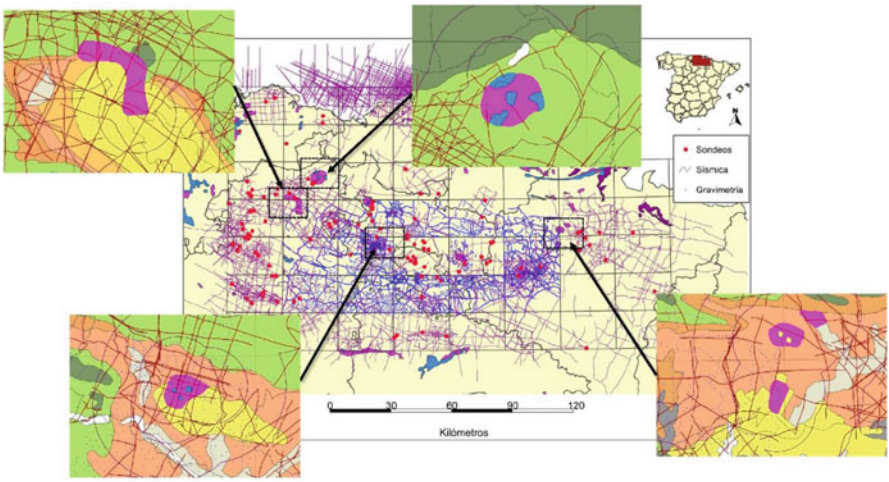

Fig. 17.6 Application of the "available preliminary information" criterion

Table 17.1 Evaluation of the quantifiable criteria within the first level "socio-economic" criterion

Criteria and sub-criteria	Mathematical scale (AHP) → Values				
	1	3	5	7	9
Energy					
Power generation/source (km)	>10	<10	<5 <50 MW	<5 >50 MW	0
Transmission lines/ electricity transport	>10	5–10	0–5 Distribution grid	0–5 Transport grid	0
Special protection areas					
Protected natural areas	Natural park		LIC/ZEPA		None
Population (km)/ inhabitant	<20 >200,000	<20 100,000–200,000	20–30 >200,000	20–30 100,000–200,000	>30
Available information					
Wells	None	Few data related to the saline formation (shallow wells)	Few data related to the saline formations (shallow wells)	Digital and enough data related to the saline formation (shallow wells)	Digital and enough data related to the saline formation(deep wells)
Geophysics					
Gravimetry Seismic	None	Few surveys. It is possible to make an interpretation based on adjacent regions	Detail data and enough deep. General or shallow data	Digital regional data (GIS). Considering outcrop and gravimetry analysis	Digital regional data (GIS). Considering seismic and outcrop analysis

17.3.2 Technical Criteria

According to the structure developed to select and rank the most favourable structure, Table 17.2 summarized the sub-criteria respond with the second level in the technical criteria. Also, the evaluation of both scientific and mathematical scales is developed.

17.3.3 Weight Assessment

The assignment of weights begins with a pairwise comparison of the criteria and sub-criteria Eq. (17.2). The eigenvalues are used as determination of the value of prioritization of each of the criteria.

Table 17.2 Evaluation of the quantifiable criteria within the first level "technical" criterion

	Mathematical scale (AHP) → Values		
Criteria and sub-criteria	1	3	5
Geomechanical			
Structure	Abandoned mines	Deep aquifer	Saline formation
Elastoplastic behaviour creep test (h)	<10	10–60	>60
Young module	18	22	21
Temperature gradient (°C)	Warm basin >35	25–35	Cold basin <25
Deep (m)	<400 and > 1200	800–1000	400–800
Geology			
Permeability (m^2)	<10–24	10–22	10–18
Diameter of the cavity (m)	<30	30–80	>80
Diameter cavity/thickness dome	<3	3–5	>5
Mineralogy and impurity content	>30%	20–30%	<20%
Cavity construction			
Cavity shape	Other	Spherical	Ellipsoidal
Brine management	Sea disposal	Injection in shallow formations	Use in local industries
Fresh water (m^3)	0.4×10^6	0.7×10^6	10^6

$$A = \begin{bmatrix} 1 & a_{12} & \dots a_{1n} \\ \frac{1}{a_{12}} & 1 & \dots a_{2n} \\ \frac{1}{a_{13}} & \frac{1}{a_{23}} & \dots 1 \end{bmatrix} \tag{17.2}$$

The calculation of the weight for each criterion will be obtained by Eq. (17.3), where the judgement of value and hierarchy is assigned to the maximum eigenvalue of matrix A (Eq. 17.2).

$$W_i = \sqrt[n]{\prod_{j=1}^{n} a_{ij}} \tag{17.3}$$

Considering AHP methodology, different matrixes were used to calculate each criterion (Table 17.3).

Table 17.3 Weights for each criterion: (**a**) socio-economical and (**b**) technical criterion

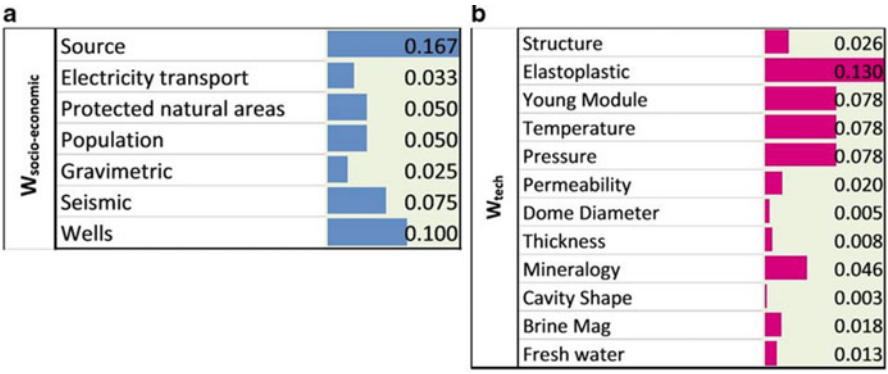

Table 17.4 Site selection and classification of the 11 alternatives under consideration

Alternatives	Añana	Mena	Rosio	Murguia	Orduña	Estella	Oro	Anoz	Arteta	Maestu	Alloz
Total	7.11	6.88	6.58	6.24	6.09	6.06	6.01	5.81	5.79	5.64	5.63

17.3.4 Alternatives

Once the weights and values have been defined, it is possible to establish a calculation and assessment of the 11 alternatives described in the previous section. AHP methodology helps decision-makers to hierarchy the alternatives under investigation (preliminary phase in any subsurface exploration).

In this study, 11 domes saline in Basque-Cantabrian basin was studied (Table 17.4). As it is shown, Añana is the most promising structure to develop next research studies (outcrop analysis and geophysics and wells reinterpretation).

The Añana salt dome is located in the southern part of the Basque-Cantabrian basin (Spain) (Fig. 17.6). As reservoir this study evaluated an outcrop diapiric structure belonging to Triassic Muschelkalk and Keuper facies. The evolution of the saline structure was greater in the Basque-Cantabrian basin, where the sedimentary load and rotational slippage of listric faults were greater.

As a result, diapirs tend to present highly evolved chimney shapes, which narrow at depth due to lack of salinity and greater sedimentary load. Due to the presence of two wells and seismic profile, the ascent of Triassic materials can be confirmed through more than 5000 metres. Their lithostratigraphic characteristics allow different levels to be distinguished, comprising different coloured shales, insertions of evaporates (halite, gypsum) and basic igneous rocks (ophites) which are frequently included, and, in the upper part of the unit, dolomites.

Tables 17.5 and 17.6 summarized the socio-economic and technical criteria description and their evaluation. The scientific scale has been described and their

Table 17.5 Añana salt dome: evaluation of socio-economic parameters, using AHP algorithm

Criteria and subcrieria	Mathematical scale (AHP) → Values				
	1	3	5	7	9
Energy					
Power generation/ source (km)	>10	<10	<5 <50MW	<5 >50MW	0
Transmis-sion lines/ Electricity transport	>10	5–10	0–5 Distribution grid	0–5 Transport grid	0
Special protection areas					
Protected natural areas	Natural park		LIC/ZEPA		None
Population (km)/ inhabitant	<20 >200.000	<20 100.000–200.000	20–30 >200.000	20–30 100.000–200.000	>30
Available information					
Wells	None	Few data related to the saline formation (shallow wells)	Few data related to the saline formations (shallow wells)	Digital and enough data related to the saline forma-tion (shallow wells)	Digital and enough data related to the saline forma-tion (deep wells)
Geophysics					
Gravimetry	None	Few surveys. It is possible to make an interpretation based on adjacent regions	Detail data and enough deep. General or shallow data	Digital regional data (GIS). Considering outcrop and gravimetry analysis	Digital regional data (GIS). Considering seismic and outcrop analysis
Seismic					

translation into the mathematical scale. Most suitable values in each criterion were assigned as the highest mathematical value.

As a result, Añana salt dome was evaluated, and its characteristics are suitable for the original goal (CAES facility) [6]. The structure examined in this chapter presents a distinguishing feature compared with the CAES plants currently in operation: there is a surfacing diapiritic structure, which makes technical research easier, and offers excellent usability potential.

Indeed, the study and development of a CAES facility in surfacing structures, such as this considered here, will enable the target depth of the structure to be modulated, which will be directly related to the maximum working pressure and, therefore, with energy storage; conversely, smaller depth will reduce the costs linked to building the cavern. These peculiar characteristics allow considering a new definition of CAES: mini-CAES technology with storage capacity power in the range 10–100 MW, shallow structure and less expensive than the conventional CAES.

Table 17.6 Añana salt dome: evaluation of technical parameters, using AHP algorithm

	Mathematical scale (AHP) → Values		
Criteria and subcrieria	1	3	5
Geomechanical			
Structure	Abandoned mines	Deep aquifer	Saline formation
Elastoplastic behaviour Creep test (h)	<10	10–60	>60
Young Module	18	22	21
Temperature gradient (ºC)	Warm basin >35	25–35	Cold basin <25
Deep (m)	<400 and >1200	800–1000	400–800
Geology			
Permeability (m^2)	<10–24	10–22	10–18
Diameter of the cavity (m)	<30	30–80	>80
Diameter cavity/thickness dome	<3	3–5	>5
Mineralogy and impurity content	>30%	20–30%	<20%
Cavity construction			
Cavity shape	Other	Spherical	Ellipsoidal
Brine managment	Sea disposal	Injection in shallow formations	Use in local industries
Fresh water (m^3)	0.4×10^6	0.7×10^6	10^6

17.4 Conclusions

The development of renewable energies will increase interest in energy storage, in order to boost the availability factor, management of surplus energy and peak demand. In this case, to store large amounts of energy, CAES technology is considered to be the most suitable option, along with the related developments that might be implemented, such as the joint use of heat storage systems for usage in the subsequent preheating phase, so as to achieve an isothermal process and therefore enhance the efficiency of the process. However, the cost associated with underground exploration, as the risk inherent to mining exploration, means that it is advisable to establish a detailed schedule to select and characterize structures to minimize the aforementioned risk. In accordance with the purpose of selecting the best geological structure for a CAES from among the alternatives considered, multicriteria algorithms make it possible to establish a hierarchy of the alternatives to be studied and to objectively identify those structures with the greatest potential.

Accordingly, a structure hierarchization method that makes possible to objectively establish the areas with the greatest potential for CAES is presented, not only taking technical aspects into account, but socio-economic ones also. The specifying of the selection algorithm for structures in saline formations makes possible to

establish a selection and classification of these structures for a particular purpose: reducing the exploration risk related to underground structures and applying this methodology in potential CAES locations in Europe or any other region around the world. In this case, the study was focused on the Basque-Cantabrian basin (Spain). This research will contribute to implement CAES technology, which would be a milestone in the field of renewable energies. The communication will include technical description of the novel mini-CAES concept and its application to a specific region in Spain.

References

1. Madlener R, Latz J (2013) Economics of centralized and decentralized compressed air energy storage for enhanced grid integration of wind power. Appl Energy 101:299–309
2. Lund H, Salgi G (2009) The role of compressed air energy storage (CAES) in future sustainable energy systems. Energy Convers Manag 50:1172–1179
3. Luo X, Wang J (2013) Overview of current development on compressed air energy storage. EERA Technical Report. Warwick University
4. Llamas B, Cienfuegos P (2012) Multicriteria decision methodology to select suitable areas for storing CO2. Energy Environ 23(2–3):249–264
5. Saaty T (1977) A scaling method for priorities in hierarchical structures. J Math Psychol 5:234–281
6. Llamas B, Castañeda M, Laín C, Pous J (2017) Study of the Basque-Cantabrian basin as a suitable region for the implementation of an energy storage system based on compressed air underground storage (CAES). Environ Earth Sci. https://doi.org/10.1007/s12665-017-6515-y
7. Lanaja J, Navarro A (1987) Contribución de la exploración petrolífera al conocimiento de la geología de España. IGME, p 465
8. Hernaiz PP, Serrano A, Malagón J, Cañas CR (1994) Evolución estructural del margen SO de la cuenca Vasco-Cantábrica. Geogaceta 15:143–146
9. Vera J (2010) Geología de España, Instituto Geológico y Minero de España
10. Martínez E (1998) Evaluación y decisión multicriterio: una perspectiva. Universidad de Santiago
11. Madden M (2009) Manual of geographic information systems. The American Society for Photogrammetry and Remote Sensing, New York, ASPRS
12. Chen D, Shams S, César C, Andrea L (2010) Assessment of open source GIS software for water resources management in developing countries. J Hydro Environ Res 4:253264
13. Zhang G, Li Y, Daemen J, Yang C, Wu Y, Zhang K, Chen Y (2015) Geotechnical feasibility analysis of compressed air energy storage (CAES) in bedded salt formations: a case study in Huai'an City, China. Rock Mech Rock Eng 48:2111–2127
14. Crotogino F, Mohmeyer K, Scharf R (2001) Huntorf CAES: more than 20 years of successful operation. In: Spring 2001 meeting, Orlando
15. Rodríguez L (2014) Evaluación de la tecnología CAES como sistema de almacenamiento de energía eólica. Caso de estudio en España. Escuela Técnica Superior de Ingenieros de Minas. Proyecto fin de Carrera

Chapter 18
4-E Analysis and Optimization of a 660 MW Supercritical Combined Rankine-Kalina Cycle Coal-Fired Thermal Power Plant for Condenser Waste Heat Recovery

Goutam Khankari and Sujit Karmakar

18.1 Introduction

To meet the growing energy demand, use of fossil fuels, more specifically coal for power generation, is increased day by day, and about 70% of the total power is generated from coal-fired thermal power plants in India [1]. Depletion of natural resources and its detrimental effect on environment put the energy researchers to a great challenge at present. Migrating to higher steam parameters to supercritical (SupC)-based and ultra-supercritical (USC)-based thermal power plants are under either in operation or in the state of development to cope with the huge energy demand. The steam parameters for a 660 MW SupC thermal power plants are 242.20 bar/537 °C/565 °C and the same for a 430 MW USC power plants are 350 bar/700 °C/720 °C [2]. About 50–60% of total input energy is lost in condenser and carried away by the cooling water system [3]. Utilization of waste energy from such plants can be used for additional power generation. Turbo-generator (TG) cycle efficiency of steam power plant improves by reducing the heat rejection temperature at the condenser resulting in the reduction of condenser heat. Modern coal-fired steam power plant is designed to run the plant efficiently at an optimum condenser back pressure of 0.103 bar (absolute) and the corresponding saturation temperature is about 46.39 °C. Plant cannot be run below this operating condition due to increase in exit loss and poor dryness fraction at later stages of LP turbine. By considering this matter in view, the latent heat of steam exhausted from steam turbines can be utilized for additional electric power generation by integrating Kalina cycle system 11 (KCS11) at condenser side where ammonia-water mixture is used as a working fluid for the bottoming cycle.

G. Khankari · S. Karmakar (✉)
National Institute of Technology Durgapur, Durgapur, West Bengal, India

S. Nižetić, A. Papadopoulos (eds.), *The Role of Exergy in Energy and the Environment*, Green Energy and Technology,
https://doi.org/10.1007/978-3-319-89845-2_18

Last few decades, various combined cycle systems have been proposed by several researchers to improve the system performance by using different thermodynamic cycles [4–7]. Ozdil et al. [8] have shown the performance variation of evaporator by varying water phase quality and drawn a relation in between pinch point and its exergy efficiency. As Organic Rankine Cycle (ORC) has poor overall efficiency than the Kalina cycle [9], Kalina cycle can be used for efficient power generation from low-graded waste heat [10]. El-Sayed et al. [11] have shown that the Kalina cycle can attain higher thermal efficiency over Rankine cycle based on energy and exergy analysis under same thermal boundary conditions. In literature, several researchers have analysed the thermodynamic performance of thermal power plants based on energy and exergy analysis [12–14]. Khankari and Karmakar [13] have shown an approach for additional power generation from mill rejection using Kalina cycle.

To the best of authors' knowledge, there is hardly any research work carried out towards reducing the heat rejection temperature at condenser directly or indirectly for efficiency improvement of coal-fired steam power plants. In the present study, an effort has been made by replacing the main plant condenser by the evaporator of KCS11 and its shell side design value (TTD: 6 °C) is maintained same as the main plant condenser. The KCS11 is used as a bottoming power cycle for condensing the exhausted steam of the main steam power plant and the heat is utilized to produce ammonia-water vapour mixture resulting in additional electric power generation. Thermodynamic performance analysis based on 4-E (Energy, Exergy, Environment and Economic) of a standalone 660 MW SupC coal-fired steam power plant and KCS11 integrated combined cycle thermal power plant is carried out at different operating conditions. Both the plants are modelled by using a flow sheet computer program 'Cycle-Tempo' [15].

18.2 System Description

Figure 18.1 shows the process flow path of a standalone 660 MW SupC coal-fired steam power plant which is operated at drum pressure and steam temperature of about 242.20 bar and 537 °C, respectively. It comprises of coal-fired boiler, one high-pressure turbine (HPT), one double-flow intermediate pressure turbine (IPT), two double-flow low-pressure turbines (LPTs), water-cooled condenser, condensate extraction pump (CEP), four low-pressure heaters (LPHs), deaerator, turbine-driven boiler feed pump (TDBFP), three high-pressure heaters (HPHs), forced draft (FD) fan and induced draft (ID) fan. Figure 18.2 also shows the flow diagram of 660 MW combined Rankine-Kalina cycle coal-fired thermal power plant. The conventional water-cooled condenser is replaced by KCS11 for condensing the steam exiting from steam turbine and resulting in additional power generation [12]. The KCS11 consists of various components like evaporator, separator, binary mixture vapour turbine, condenser, feed pump and feed heater. Evaporator is a shell and tube type heat exchanger where phase change of the working fluid occurs at different quality at its outlet by exchanging heat with the low-quality steam

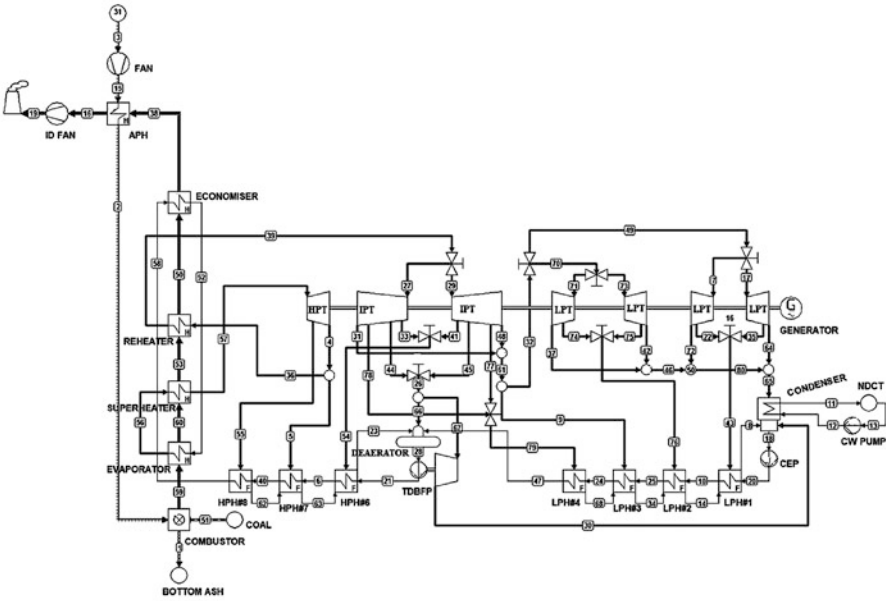

Fig. 18.1 Schematic diagram of 660MW SupC coal-fired thermal power plant

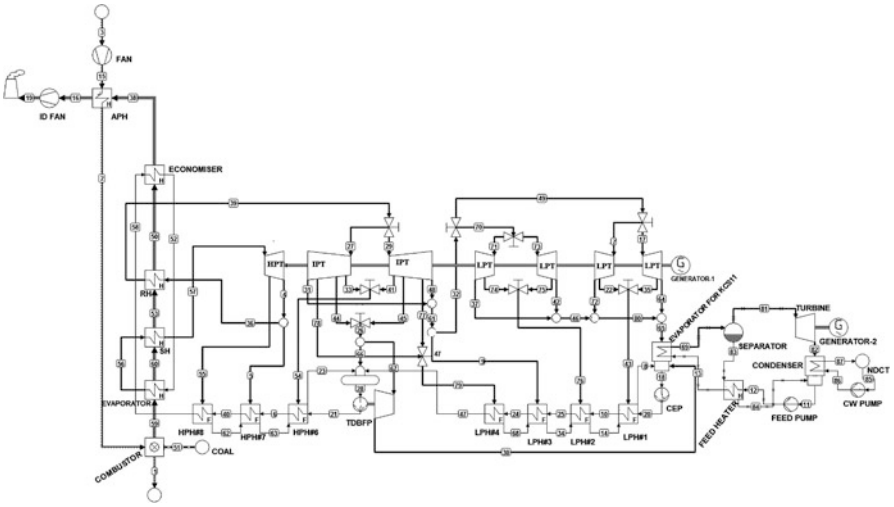

Fig. 18.2 Schematic diagram of 660MW SupC combined Rankine-Kalina cycle thermal power plant

exhausted from low-pressure steam turbines. Saturated vapour binary mixture from the separator is supplied to the binary mixture turbine for expansion and it is condensed in the condenser of KCS11 by cooling water flow. Saturated hot liquid binary mixture from separator is used as extraction fluid for NH_3-H_2O mixture heating and its drip is discharged into the condenser. Liquid ammonia-water binary mixture is again fed to the evaporator by running feed pump after heating in the feed heater. The generator is directly coupled with the turbine shaft of KCS11 for electric power generation.

18.3 Methodology

Thermodynamic performance analysis of 660 MW SupC coal-fired steam power plant and KCS11 integrated 660 MW combined cycle SupC thermal power plant are done based on energy and exergy analysis under steady-state condition by thermodynamic modelling using a computer flow sheet computer program 'Cycle-Tempo' [15]. The required input parameters at different plant-operating conditions of equipments and process path are specified like pressure, temperature, fuel quality and the efficiencies of the pumps, fans and turbines. Steady flow equation for open system based on conservation of mass and energy can be written as follows:

Mass balance:

$$\sum \dot{m}_{\text{in}} = \sum \dot{m}_{\text{out}} \tag{18.1}$$

Energy balance:

$$\sum \dot{m}_{\text{in}}\, h_{\text{in}} + \dot{Q}_k = \sum \dot{m}_{\text{out}} h_{\text{out}} + \dot{W} \tag{18.2}$$

where $\dot{m}$ is mass flow rate, h is specific enthalpy and $\dot{Q}_k$ is heat transfer rate to the system at temperature T_{k}.

Exergy balance:

$$\sum \dot{m}_{\text{in}}\, \varepsilon_{x\,\text{in}} + \dot{Q}_k \left(1 - \frac{T_0}{T_{\text{K}}}\right) = \sum \dot{m}_{\text{out}}\, \varepsilon_{x\,\text{out}} + \dot{W} + \dot{\text{Ex}}_{\text{D}} \tag{18.3}$$

where $\dot{\text{Ex}}_{\text{D}} = T_0 \dot{S}_{\text{gen}}$ and $\varepsilon_{\text{x}} = \varepsilon_{\text{ph}} + \varepsilon_{\text{ch.}}$

$\dot{\text{Ex}}_{\text{D}}$ indicates the exergy destruction in the system and subscript '0' indicates the environment condition of the system. ε_x indicates the specific exergy of energy carrier. For steam cycle analysis, only physical exergy (ε_{ph}) is considered, but for KCS11 analysis, physical and chemical exergy (ε_{ch}) are both considered [16]. These are calculated as follows:

$$\varepsilon_{\text{ph}} = [(h - h_0) - T_0(s - s_0)] \tag{18.4}$$

$$\varepsilon_{ch} = [\, y\, \varepsilon_{ch,NH3} + (1-y)\varepsilon_{ch,H2O}] \tag{18.5}$$

where y indicates the ammonia mass fraction in ammonia-water binary mixture. Fluid properties are calculated based on different thermodynamic relations and empirical correlations [13]. Thermodynamic relations are based on Gibbs free energy concept of pure substance.

Specific exergy of coal is calculated on the basis of the following formula [17].

$$\varepsilon_{coal} = (0.9775\mathrm{LHV}_{coal} + 2.416) \pm (0.0065\mathrm{LHV}_{coal} + 0.054) \tag{18.6}$$

18.3.1 Assumptions

The following assumptions have been made for the thermodynamic study of both plants:

(i) Ambient pressure (P_0) and temperature (T_0) of environment are 1.013 bar and 25 °C, respectively.
(ii) The chemical compositions of atmospheric air (in mole %) are Ar 0.90%, CO_2 0.03%, H_2O 1.88%, O_2 20.56 % and N_2 76.61%, and the relative humidity (RH) of the ambient air is 60%.
(iii) Lower heating value (LHV) of coal is 15,234 kJ/kg.
(iv) Excess air of 20% is supplied for complete combustion.
(v) Isentropic efficiencies of both fans and pumps are considered as 85%.
(vi) CW pressure and temperature at condenser inlet are taken as 2 bar and 25 °C, respectively.
(vii) TTD of the KCS11 evaporator is considered as 6 °C which is same as standalone plant condenser for maintaining the design parameters in the steam power cycle ($T_{0.103bar}^{sat.condensate} = 46$ °C and $T_{cwi/l} = 30$ °C with temperature rise of 10 °C [17]).
(viii) The terminal temperature difference of all low-pressure heaters (LPH) and high-pressure heaters (HPH) in steam power cycle are considered as 3 °C [17].
(ix) Generator efficiency is taken as 98.7% [17].
(x) Dry saturated vapour at turbine inlet and saturated liquid for feed heating are considered.
(xi) Suitable LMTD value for the condenser and feed heater of the KCS11 are assumed based on optimum heat transfer area of the equipments and kept constant throughout the analysis.

Table 18.1 Ultimate analysis of coal as per as-received basis (% of weight)

	Ultimate analysis of coal						Unburnt carbon	
C (%)	H_2 (%)	O_2 (%)	N_2 (%)	S (%)	TM (%)	Ash (%)	BA (%)	FA (%)
34.46	2.43	6.97	0.69	0.45	12.00	43.00	2.50	1.50

18.3.2 Performance Analysis of the Plant

Net combined cycle power plant energy efficiency:

$$\eta_{\text{plant}}^{\text{comb.}} = \frac{\dot{W}_{\text{mp}}^{\text{TG}} + \dot{W}_{\text{KCS11}}^{\text{TG}} - \dot{p}_{\text{aux.}}^{\text{comb.}}}{\text{Energy supplied by coal}} \tag{18.7}$$

$\dot{p}_{\text{aux.}}^{\text{comb.}}$ indicates the auxiliary power consumption for combined power plant (2.93% of rated load).

$$\text{Energy supplied by coal} = \dot{m}_{\text{coal}} \text{LHV} \tag{18.8}$$

Net combined power plant exergy efficiency:

$$\Psi_{\text{plant}}^{\text{comb.}} = \frac{\dot{W}_{\text{mp}}^{\text{TG}} + \dot{W}_{\text{KCS11}}^{\text{TG}} - \dot{p}_{\text{aux.}}^{\text{comb.}}}{\text{Exergy supplied by coal}} \tag{18.9}$$

$$\text{Energy supplied by coal} = \dot{m}_{\text{coal}}\, \varepsilon_{\text{coal}} \tag{18.10}$$

The CO_2 emission is calculated by the following equation on the basis of used coal analysis which is given in Table 18.1.

$$\text{CO}_2^{\text{emission}} = \frac{\dot{m}_{\text{coal}}^{\text{consumption}} \left[\%\text{C} - \%\text{Ash}\left(0.80 \frac{\%\text{UC}_{\text{FA}}}{100} + 0.20 \frac{\%\text{UC}_{\text{BA}}}{100}\right)\right]}{100} \tag{18.11}$$

18.3.3 Performance Analysis of Combined Rankine-Kalina Cycle System

Net energy efficiency of combined Rankine-Kalina cycle system

$$\eta_{\text{comb.cycle}}^{\text{net}} = \frac{\dot{W}_{\text{net}}^{\text{comb.}}}{\dot{E}_{\text{int.}}^{\text{comb.}}} \tag{18.12}$$

$$\dot{W}_{\text{comb.cycle}}^{\text{net}} = \dot{W}_{\text{mp}}^{\text{TG}} + \dot{W}_{\text{kcs11}}^{\text{TG}} - \dot{W}_{\text{CEP}} - \dot{W}_{\text{kcs11}}^{\text{FP}} \tag{18.13}$$

$$\dot{E}_{\text{int.}}^{\text{comb.}} = \dot{m}_{\text{s}} h_{\text{s}} - \dot{m}_{\text{f}}^{\text{e}} h_{\text{f}}^{\text{e}} + \dot{m}_{\text{r}}(h_{\text{h}} - h_{\text{c}}) \tag{18.14}$$

where $\dot{W}_{\text{kcs11}}^{\text{FP}}$ indicates power consumed by feed pump of KCS11 and $\dot{E}_{\text{int.}}^{\text{comb.}}$ indicates energy input rate to combined plant TG cycle.

$$E_{\text{comb.}}^{\text{rej}} = \dot{m}_{\text{kcs11}}^{\text{cw}}\left(h_{\text{kcs11}}^{\text{cwout}} - h_{\text{kcs11}}^{\text{cw in}}\right) \tag{18.15}$$

Net exergy efficiency of combined cycle system:

$$\Psi_{\text{comb.cycle}}^{\text{net}} = \frac{\dot{W}_{\text{net}}^{\text{comb.}}}{\dot{\text{Ex}}_{\text{int.}}^{\text{comb.}}} \tag{18.16}$$

$$\dot{\text{Ex}}_{\text{int.}}^{\text{comb.}} = \dot{m}_{\text{s}}\varepsilon_{\text{s}} - \dot{m}_{\text{f}}^{\text{e}}\varepsilon_{\text{f}}^{\text{e}} + \dot{m}_{\text{r}}(\varepsilon_{\text{h}} - \varepsilon_{\text{c}}) \tag{18.17}$$

$$\dot{\text{Ex}}_{\text{comb.}}^{\text{rej}} = \dot{m}_{\text{kcs11}}^{\text{cw}}\left(\varepsilon_{\text{kcs11}}^{\text{cwout}} - \varepsilon_{\text{kcs11}}^{\text{cw in}}\right) \tag{18.18}$$

18.3.3.1 Relative Energy/Exergy (R_{en} / R_{ex}) Index

The performance of the power cycle based on all equipments used or on individual equipment basis with respect to the TG output can be assessed for comparative purpose at different plant-operating conditions by formulating a relative energy/exergy index which is defined as

$$R_{\text{en}}^{\text{rej.}} = \frac{\dot{E}_{\text{rej}}}{\dot{W}_{\text{plant}}^{\text{TG}}}; R_{\text{ex}}^{\text{rej.}} = \frac{\dot{\text{Ex}}_{\text{rej}}}{\dot{W}_{\text{plant}}^{\text{TG}}}$$

This is very much important for taking crucial decision for the CW pump in or out of operation during seasonal variation for getting significant efficiency improvement with marginal increase in auxiliary power consumption [18].

18.3.4 Performance Analysis of KCS11

Net energy efficiency of KCS11:

$$\eta_{\text{kcs11}}^{\text{net}} = \frac{\left(\dot{W}_{\text{kcs11}}^{\text{TG}} - \dot{W}_{\text{kcs11}}^{\text{FP}} - \dot{W}_{\text{kcs11}}^{\text{CWP}}\right)}{\dot{E}_{\text{kcs11}}^{\text{in}}} \tag{18.19}$$

$\dot{W}_{\text{kcs11}}^{\text{TG}}$ indicates TG output of KCS11.
$\dot{W}_{\text{kcs11}}^{\text{CWP}}$ indicates power consumed by condenser cooling water pump of KCS11.

Energy input rate into the Kalina cycle system is calculated by Eq. (18.20).

$$\dot{E}^{\text{in}}_{\text{kcs11}} = \dot{m}^{\text{LPT exhaust}}_{\text{s}}\, h^{\text{LPT exhaust}}_{\text{s}} + \dot{m}^{\text{TDBFP exhaust}}_{\text{s}}\, h^{\text{TDBFP exhaust}}_{\text{s}} + \dot{m}^{\text{LPH}}_{\text{drip}}\, h^{\text{LPH}}_{\text{drip}} - \dot{m}^{\text{CEP suction}}_{\text{condensate}}\, h^{\text{CEP suction}}_{\text{condensate}} \tag{18.20}$$

Energy rejection rate from the Kalina cycle system is calculated by Eq. (18.21).

$$E^{\text{rej}}_{\text{kcs11}} = \dot{m}^{\text{cw}}_{\text{kcs11}}\left(h^{\text{cwout}}_{\text{kcs11}} - h^{\text{cw in}}_{\text{kcs11}}\right) \tag{18.21}$$

Net exergy efficiency of Kalina cycle system 11 (KCS11):

$$\Psi^{\text{net}}_{\text{kcs11}} = \frac{\dot{W}^{\text{net}}_{\text{kcs11}}}{\dot{\text{Ex}}^{\text{in}}_{\text{kcs11}}} \tag{18.22}$$

Exergy input rate to the Kalina cycle is calculated by Eq. (18.23).

$$\dot{\text{Ex}}^{\text{in}}_{\text{kcs11}} = \dot{m}^{\text{LPT exhaust}}_{\text{s}}\, \varepsilon^{\text{LPT exhaust}}_{\text{s}} + \dot{m}^{\text{TDBFP exhaust}}_{\text{s}}\, \varepsilon^{\text{TDBFP exhaust}}_{\text{s}} + \dot{m}^{\text{LPH}}_{\text{drip}}\, \varepsilon^{\text{LPH}}_{\text{drip}} - \dot{m}^{\text{CEP suction}}_{\text{condensate}}\, \varepsilon^{\text{CEP suction}}_{\text{condensate}} \tag{18.23}$$

Exergy rejection rate from the Kalina cycle is calculated by the following equation:

$$\text{Ex}^{\text{rej}}_{\text{kcs11}} = \dot{m}^{\text{cw}}_{\text{kcs11}}\left(\mathcal{E}^{\text{cwout}}_{\text{kcs11}} - \mathcal{E}^{\text{cw in}}_{\text{kcs11}}\right) \tag{18.24}$$

The vapour fraction (DF) after the evaporator of the ammonia-water mixture or separator inlet is determined as follows [19]:

$$\text{DF} = \frac{\dot{m}^{\text{sep.o/l}}_{\text{sat.v}}}{\dot{m}^{\text{sep.i/l}}_{\text{mix.}}} = \frac{y^{\text{sep.i/l}}_{\text{mix.}} - y^{\text{sep.o/l}}_{\text{sat.l}}}{y^{\text{sep.o/l}}_{\text{sat.v}} - y^{\text{sep.o/l}}_{\text{sat.l}}} \tag{18.25}$$

18.4 Results and Discussion

18.4.1 Energetic and Exergetic Performance Analysis of the Plants

Thermodynamic performance analysis and comparison of both the standalone and combined cycle plants are done by using simulated operating data as shown in Table 18.2, based on energy and exergy analysis at full load. From Tables 18.3 and 18.4, it is observed that maximum energy and exergy losses take place in the condenser and boiler for the standalone SupC thermal power plant accounting about 50.055% and 53.692% of total input, respectively. Similar results are also observed for the combined cycle SupC power plant. By integrating KCS11 as a bottoming cycle with main steam power plant at condenser side, condenser energy

Table 18.2 Operating parameter of 660 MW standalone and combined cycle power plant at full load

660MW Stand-alone coal-fired steam power plant						660MW Combined Rankine-Kalina cycle power plant				
Pipe no.	Pressure [bar]	Temperature [°C]	Mass flow [kg/s]	Enthalpy [kJ/kg]	Entropy [kJ/kg.K]	Pressure [bar]	Temperature [°C]	Mass flow [kg/s]	Enthalpy [kJ/kg]	Entropy [kJ/kg.K]
1	1.013	1050.000	10.193	–14346.030	2.361	1.013	1050.000	10.013	–14346.030	2.361
2	1.030	244.320	612.145	62.950	7.490	1.030	244.320	601.369	62.950	7.490
3	1.013	25.000	612.145	–162.180	6.930	1.013	25.000	601.369	–162.180	6.930
4	45.500	291.910	516.465	2917.130	6.233	45.500	291.930	507.021	2917.190	6.233
5	44.310	290.420	48.330	2917.130	6.244	44.310	290.440	47.445	2917.190	6.244
6	308.700	211.950	552.846	917.920	2.397	308.700	211.950	542.735	917.920	2.397
7	2.980	215.630	86.875	2897.760	7.382	2.980	215.640	85.287	2897.790	7.382
8	0.270	66.720	78.562	279.240	0.915	0.270	66.720	77.125	279.240	0.915
9	2.980	215.630	31.524	2897.760	7.382	2.980	215.640	30.947	2897.790	7.382
10	11.940	63.720	431.227	267.640	0.877	11.940	63.720	423.343	267.640	0.877
11	2.030	35.010	19030.076	146.770	0.505	9.800	27.390	1068.620	55.040	0.421
12	2.030	25.010	19030.076	104.990	0.367	11.700	27.450	1068.620	55.390	0.421
13	1.013	25.000	19030.076	104.860	0.367	11.700	30.010	1068.620	67.500	0.461
14	0.640	68.720	64.982	287.650	0.939	0.640	68.720	63.793	287.650	0.939
15	1.040	27.800	612.145	–159.330	6.932	1.040	27.800	601.369	–159.330	6.932
16	1.000	140.420	706.219	–3300.990	6.748	1.000	140.420	693.786	–3301.020	6.748
17	2.980	215.630	86.875	2897.760	7.382	2.980	215.640	85.287	2897.790	7.382
18	0.103	46.410	431.227	194.250	0.657	0.103	46.410	423.343	194.250	0.657
19	1.060	148.000	706.219	–3293.030	6.751	1.060	148.000	693.786	–3293.060	6.751
20	11.940	46.520	431.227	195.750	0.658	11.940	46.520	423.343	195.750	0.658
21	308.700	193.930	552.846	839.280	2.232	308.700	193.930	542.735	839.280	2.232
23	21.040	198.930	99.135	847.810	2.320	21.040	198.930	97.319	847.810	2.320
24	11.940	130.310	431.227	548.260	1.637	11.940	130.310	423.343	548.260	1.637
25	11.940	84.620	431.227	355.200	1.129	11.940	84.620	423.343	355.200	1.129

(continued)

Table 18.2 (continued)

660MW Stand-alone coal-fired steam power plant						660MW Combined Rankine-Kalina cycle power plant				
Pipe no.	Pressure [bar]	Temperature [°C]	Mass flow [kg/s]	Enthalpy [kJ/kg]	Entropy [kJ/kg.K]	Pressure [bar]	Temperature [°C]	Mass flow [kg/s]	Enthalpy [kJ/kg]	Entropy [kJ/kg.K]
26	11.940	381.060	55.376	3221.010	7.321	11.940	381.060	54.363	3221.030	7.321
27	42.000	565.000	234.067	3590.920	7.250	42.000	565.000	229.788	3590.920	7.250
28	11.940	187.740	552.846	797.420	2.214	11.940	187.740	542.735	797.420	2.214
29	42.000	565.000	234.067	3590.920	7.250	42.000	565.000	229.788	3590.920	7.250
30	0.103	46.410	32.892	2503.190	7.882	0.103	46.410	32.290	2503.200	7.882
31	2.980	215.630	189.512	2897.760	7.382	2.980	215.640	186.048	2897.790	7.382
32	2.980	215.630	347.501	2897.760	7.382	2.980	215.640	341.148	2897.790	7.382
34	2.98	89.62	50.834	375.51	1.1879	2.980	89.620	49.905	375.510	1.188
36	45.5	291.91	468.135	2917.13	6.2332	45.500	291.930	459.576	2917.190	6.233
37	0.103	46.41	79.801	2422.48	7.6296	0.103	46.410	78.343	2422.900	7.631
38	1	319	706.219	–3108.32	7.1341	1.000	319.000	693.786	–3108.360	7.134
39	42	565	468.135	3590.92	7.2503	42.000	565.000	459.576	3590.920	7.250
40	308.7	253.47	552.846	1104.57	2.7661	308.700	253.470	542.735	1104.570	2.766
41	21.04	459.85	7.212	3378.02	7.2908	21.040	459.850	7.080	3378.030	7.291
42	0.103	46.410	79.801	2422.480	7.630	0.103	46.410	78.343	2422.900	7.631
43	0.270	66.720	13.580	2521.940	7.513	0.270	66.720	13.332	2521.960	7.513
46	0.103	46.410	159.603	2422.480	7.630	0.103	46.410	156.685	2422.900	7.631
47	11.940	156.230	431.227	659.470	1.904	11.940	156.230	423.343	659.470	1.904
48	2.980	215.630	189.512	2897.760	7.382	2.980	215.640	186.048	2897.790	7.382
49	2.980	215.630	173.750	2897.760	7.382	2.980	215.640	170.574	2897.790	7.382
51	1.030	33.000	104.266	–8542.640	1.209	1.030	25.000	102.431	–8548.560	1.179
52	294.700	341.000	552.846	1554.800	3.558	294.7	341	542.735	1554.8	3.5575
54	21.04	459.85	14.42	3378.02	7.29	21.04	459.85	14.16	3378.03	7.29
55	66.75	339.98	36.38	2996.75	6.22	66.75	340.00	35.71	2996.81	6.22

56	263.20	480.00	552.85	3064.41	5.81	263.20	480.00	542.74	3064.41	5.81
57	242.20	537.00	552.85	3304.54	6.15	242.20	537.00	542.74	3304.54	6.15
58	308.70	279.59	552.85	1227.60	2.99	308.70	279.59	542.74	1227.60	2.99
61	2.98	215.63	379.02	2897.76	7.38	2.98	215.64	372.10	2897.79	7.38
62	66.75	258.47	36.38	1127.08	2.87	66.75	258.47	35.71	1127.08	2.87
63	44.31	216.95	84.71	930.28	2.49	44.31	216.95	83.16	930.28	2.49
64	0.10	46.41	80.09	2422.40	7.63	0.10	46.41	78.62	2422.82	7.63
65	0.10	46.41	319.77	2422.44	7.63	0.10	46.41	313.93	2422.86	7.63
66	11.94	381.06	22.49	3221.01	7.32	11.94	381.06	22.07	3221.03	7.32
67	11.94	381.06	32.89	3221.01	7.32	11.94	381.06	32.29	3221.03	7.32
68	6.06	135.31	19.31	569.20	1.69	6.06	135.31	18.96	569.20	1.69
69	–	–	–	–	–	11.70	40.41	1068.62	798.10	2.83
70	2.98	215.63	173.75	2897.76	7.38	2.98	215.64	170.57	2897.79	7.38
71	2.98	215.63	86.88	2897.76	7.38	2.98	215.64	85.29	2897.79	7.38
72	0.10	46.41	80.09	2422.40	7.63	0.10	46.41	78.62	2422.82	7.63
73	2.98	215.63	86.88	2897.76	7.38	2.98	215.64	85.29	2897.79	7.38
74	0.64	87.62	7.07	2640.83	7.47	0.64	87.62	6.94	2640.85	7.47
75	0.64	87.62	7.07	2640.83	7.47	0.64	87.62	6.94	2640.85	7.47
76	0.64	87.62	14.15	2640.83	7.47	0.64	87.62	13.89	2640.85	7.47
79	6.06	295.44	19.31	3052.62	7.35	6.06	295.45	18.96	3052.65	7.35
80	0.10	46.41	239.69	2422.45	7.63	0.10	46.41	235.31	2422.88	7.63
81	–	–	–	–	–	11.70	40.38	624.17	1318.35	4.38
82	–	–	–	–	–	9.80	30.27	624.17	1298.49	4.39
83	–	–	–	–	–	11.70	34.48	444.45	67.46	0.51
84	–	–	–	–	–	11.70	28.45	444.45	38.91	0.41
85	–	–	–	–	–	1.13	25.00	42207.10	104.87	0.37
86	–	–	–	–	–	2.00	25.01	42207.10	104.97	0.37
87	–	–	–	–	–	2.00	29.37	42207.10	123.19	0.43

Table 18.3 Energy balance at 100% of rated load

Energy balance at 100% of rated load		
Components	Standalone steam power plant	Combined cycle power plant
Power plant gross efficiency (%)	41.550	42.296
Condenser loss (%)	50.055	49.282
Heat rejected through stack (%)	6.125	6.125
Heat rejected in bottom ash (%)	0.857	0.857
Other losses (by difference) (%)	1.412	1.440

Table 18.4 Exergy balance at 100% of rated load

Exergy balance at 100% of rated load		
Components	Standalone steam power plant	Combined cycle power plant
Power plant gross efficiency (%)	36.590	37.242
Condenser loss (%)	0.728	0.310
Turbine losses (%)	3.722	3.867
Heaters losses (%)	0.884	0.892
Boiler loss (%)	53.692	53.732
Others losses (by difference) (%)	4.384	3.958

Table 18.5 Energetic and exergetic analysis at full load

	100% of rated						
Power plant	$R^{int}{}_{en}$	$R^{rej}{}_{en}$	$R^{int}{}_{ex}$	$R^{rej}{}_{ex}$	$R^{dest}{}_{ex}$	η_{TG} (%)	Ψ_{TG} (%)
Combined cycle power plant	2.363	1.265	1.293	0.009	0.284	42.313	77.310
Standalone steam power plant	2.398	1.303	1.313	0.022	0.291	41.693	76.177

and exergy losses are decreased by 0.773% point and 0.418% point, respectively. As a result, plant net energy and exergy efficiencies are increased by 0.543% point and 0.472% point, respectively. From Table 18.5, it is also studied that energy and exergy efficiencies of power cycle (TG) of combined Rankine-Kalina cycle power plant are improved over standalone power plant due to less relative energy rejection and exergy destruction in TG cycle compared to standalone power plant. This is caused due to reduction in specific steam consumption for generating same power as additional electric power comes from condenser waste heat.

18.4.2 Effect of Part-Load Operation on the Plant Performance

Plant performance analyses are studied at different part-load conditions (60%, 80% and 100% of rated load condition) at constant pressure control mode of operation. From Fig. 18.3, it is observed that combined plant energy and exergy efficiencies are higher than the main standalone power plant at all part-load conditions. It is also

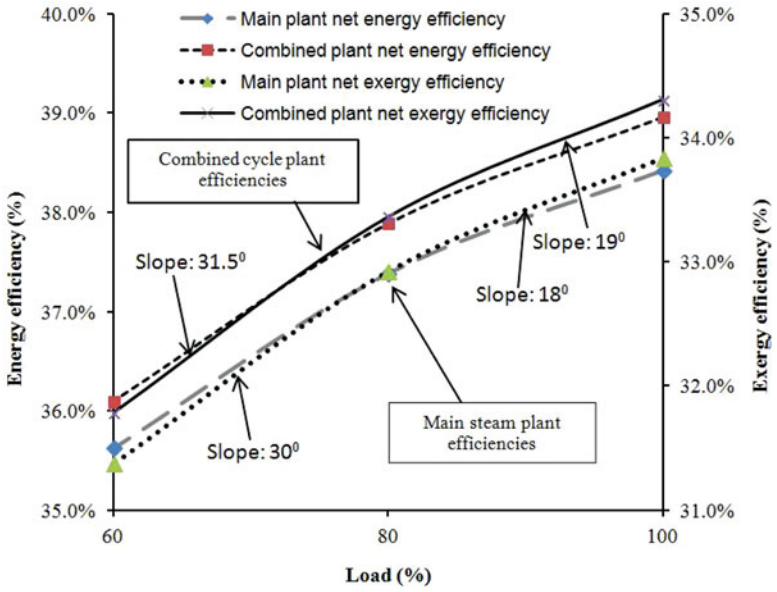

Fig. 18.3 Effect of load variation on plant performance

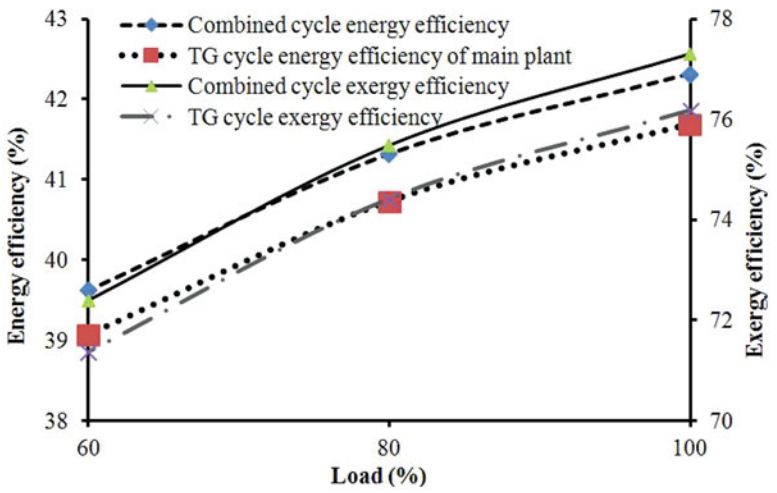

Fig. 18.4 Effect of load variation on cycle efficiencies

observed that the rate of improvement of energy and exergy efficiencies is more at low load (below the 80% of rated load) due to higher rate of efficiency improvement in TG cycle or power cycle (Fig. 18.4). Moreover, at a lower part-load operation, the

Table 18.6 Thermodynamic analysis at different part load

% of load	660MW main steam power plant					660MW combined cycle power plant				
	R^{int}_{en}	R^{rej}_{en}	R^{int}_{ex}	R^{rej}_{ex}	R^{dest}_{ex}	R^{int}_{en}	R^{rej}_{en}	R^{int}_{ex}	R^{rej}_{ex}	R^{dest}_{ex}
100	2.398	1.303	1.313	0.022	0.291	2.363	1.265	1.293	0.009	0.284
80	2.455	1.342	1.344	0.022	0.322	2.420	1.304	1.325	0.009	0.315
60	2.560	1.415	1.401	0.023	0.378	2.524	1.375	1.381	0.010	0.372

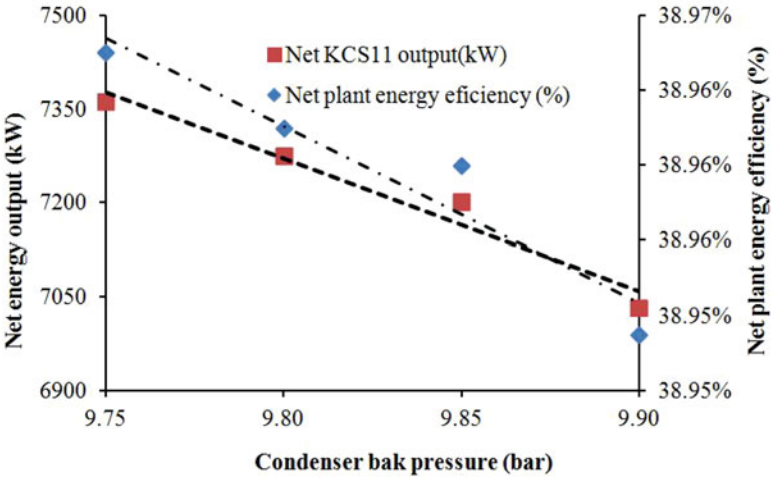

Fig. 18.5 Effect of condenser back pressure on KCS11 and combined cycle plant performances

effect of throttling in control valves is more, which reduces towards higher part-load operation. As a result, relative exergy destruction and relative energy rejection are more at lower part load and decrease at higher part load and the same is shown in Table 18.6. Figures 18.3 and 18.4 also show that the rate of change of exergy efficiency of combined cycle power plant is more than the rate of change of energy efficiency and the rate of change of both the efficiencies reduces with increase in load condition. However, the rate of decrease in the improvement of energy efficiency is more than the exergy efficiency for both the plants at higher load condition.

18.4.3 Effect of Condenser Back Pressure on the Combined Cycle Power Plant Performance

From Fig. 18.5 and Table 18.7, it is concluded that energy and exergy efficiencies of power cycle (TG) increase with the decrease in condenser back pressure, resulting in an increase in the plant efficiency. Decreasing condenser back pressure increases the KCS11 output, resulting in an improvement of the cycle efficiencies. Table 18.7 shows that the relative energy and exergy input increase with the decrease in

Table 18.7 Effect of condenser back pressure on cycle performance

660MW combined cycle Supc thermal power plant							
Condenser back pressure (bar)	R^{int}_{en}	R^{rej}_{en}	R^{int}_{ex}	R^{rej}_{ex}	R^{dest}_{ex}	Ψ_{TG} (%)	η_{TG} (%)
9.75	2.365	1.266	1.294	0.009	0.285	77.317	42.318
9.80	2.363	1.265	1.293	0.009	0.284	77.310	42.313
9.85	2.362	1.264	1.293	0.009	0.284	77.303	42.310
9.90	2.361	1.264	1.292	0.009	0.284	77.285	42.300

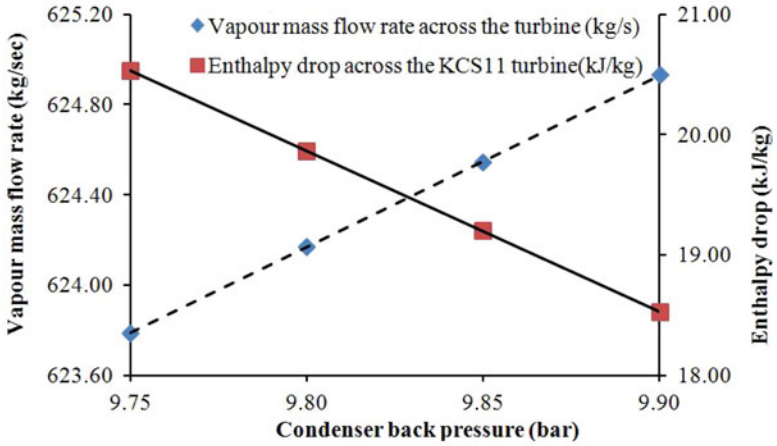

Fig. 18.6 Effect of condenser back pressure on the performance of KCS11turbine

condenser back pressure causing higher energy output from power cycle as there is no such significant change in relative energy rejection and relative exergy destruction at all condenser back pressure. From Fig. 18.6, it is also observed that the change in the increasing slope of enthalpy drop is higher than the decreasing slope of vapour mass flow rate at lower condenser back pressure, resulting in an increase of the KCS11 output. Gain in net output by lowering the condenser pressure also decreases due to an increase in CW flow rate at condenser. To avoid high cost and robust condenser design for getting marginal efficiency improvement, the optimum condenser pressure of 9.75 bar is considered for the present study.

18.4.4 Effect of Ammonia Mass Fraction Variation on KCS11 and Model Validation

The effect of ammonia mass fraction (0.80, 0.85 and 0.90) variation in KCS11 is shown in Table 18.8 and Fig. 18.7. Table 18.8 shows that the energy and exergy efficiencies of KCS11 decrease with a decrease in ammonia mass fraction. Lower

Table 18.8 Thermodynamic analysis of KCS11 at different ammonia mass fraction

Ammonia mas fraction	$R^{int}{}_{en}$	$R^{rej}{}_{en}$	$R^{int}{}_{ex}$	$R^{rej}{}_{ex}$	$R^{dest}{}_{ex}$	η_{KCS11} (%)	Ψ_{KCS11} (%)
0.90	76.309	105.525	3.636	0.753	1.883	1.310	27.506
0.85	179.096	110.221	4.390	0.786	2.604	0.558	22.779
0.80	259.218	112.456	4.700	0.802	2.898	0.386	21.275

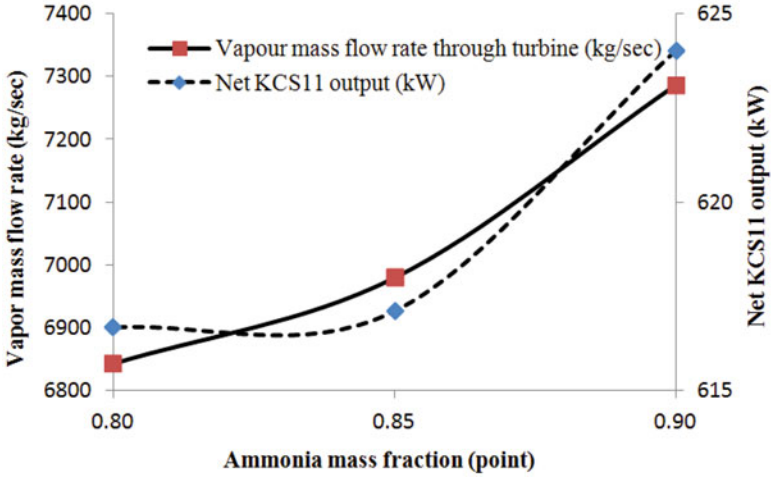

Fig. 18.7 Effect of ammonia mass fraction variation on KCS 11 performance

ammonia mass fraction has higher saturation temperature of the binary mixture for a particular operating pressure, resulting in the decrease of vapour mass flow rate through the binary mixture turbine, and the same is shown in Fig. 18.7. Moreover, the KCS11 output decreases with a decrease in ammonia mass fraction. Both the relative energy rejection and relative exergy destruction increase with the decrease in ammonia mass fraction. Simulation results are validated with existing literature at full load with ammonia mass fraction of 0.90 and the result is well matched with the published paper [12]. Trend of the thermal efficiency curve at different ammonia mass fraction (at 0.80, 0.85 and 0.90) is closely matched with the published research paper at higher operating pressure (above 40 bar).

18.4.5 Effect of Evaporator Shell Pressure (Steam Turbine Back Pressure) on the Combined Cycle Power Plant Performance

The effect of evaporator shell pressure (absolute) variations is studied for optimizing the combined cycle plant performance. The results are given in Fig. 18.8 and

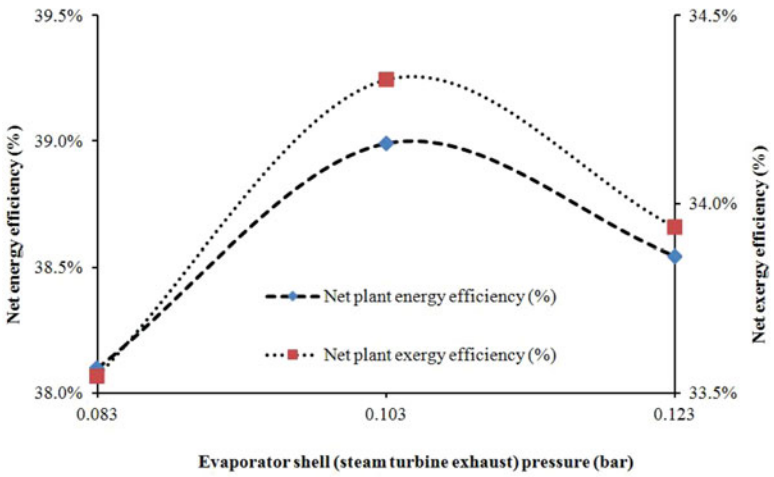

Fig. 18.8 Evaporator shell pressure vs. plant efficiencies

Table 18.9 Energy and exergy analysis at different evaporator shell pressure of the combined cycle power plant

660MW combined Rankine-Kalina Cycle Power Plant	100% of rated						
Evaporator shell (steam turbine exhaust) Pressure (bar)	R^{int}_{en}	R^{rej}_{en}	R^{int}_{ex}	R^{rej}_{ex}	R^{dest}_{ex}	Ψ_{TG}	η_{TG}
0.083	2.416	2.848	1.322	0.006	0.316	75.636	41.397
0.103	2.362	1.247	1.293	0.008	0.285	77.363	42.343
0.123	2.390	1.254	1.308	0.013	0.295	76.461	41.849

Table 18.9. From Fig. 18.8, it is observed that net plant energy and exergy efficiencies increase with the decrease in evaporator shell pressure, and below the shell pressure of 0.103 bar (absolute), efficiency starts decreasing. The variation in net plant efficiencies are found due to variations in net cycle energy and exergy efficiencies at different shell pressure as shown in Table 18.9. Moreover, from Table 18.9, it is observed that the less relative energy rejection and relative exergy destruction of the combined power cycle are found at a shell pressure of 0.103 bar compared to other shell pressures. Higher specific steam consumption causes higher relative energy and exergy input into the power cycle at a shell pressure above or below 0.103 bar. At very low shell pressure (i.e. steam turbine exhaust pressure), the exit loss of the steam turbine found more. On the other hand, at very high shell pressure, the enthalpy drop of the steam power cycle reduces. As a result, the specific steam consumption for both the cases are increased. As the efficiency of the steam power cycle is higher than the KCS11 in the combined cycle power plant, the maximum energy conversion takes place in the steam power cycle rather than Kalina cycle to maximize the combined cycle performance. Hence, the evaporator shell pressure of 0.103 bar is considered to be the optimum one for the performance improvement.

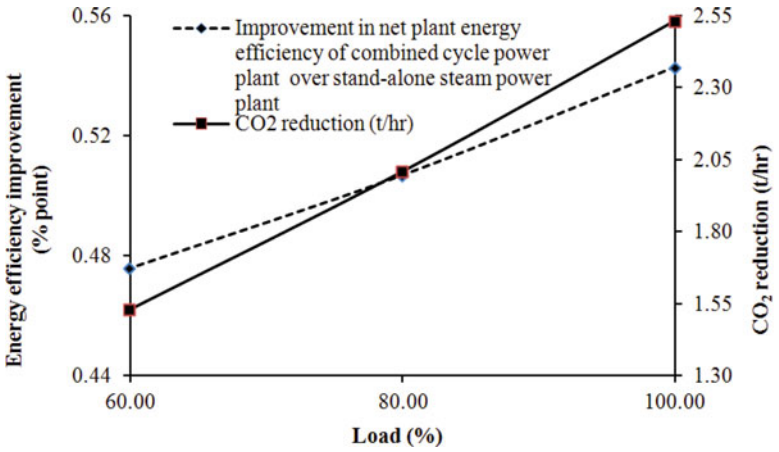

Fig. 18.9 Effect of KCS11 integration for condenser waste heat recovery on CO_2 emission

18.4.6 Environmental Impact of 660 MW Combined Cycle SupC Coal-Fired Thermal Power Plant

Coal-fired thermal power plant is the major emitter of different pollutants like CO_2, SO_x, NO_x and other suspended particulate matter (SPM), out of which CO_2 is the major greenhouse gas responsible for global warming. Figure 18.9 shows that the net energy efficiency improvement of combined cycle plant over standalone power plant increases with higher part load and the maximum improvement is observed as 0.543% point at full-load condition. This improvement reduces the specific coal consumption rate and about 2.53 tons of CO_2 emission can be reduced per hour at full load.

18.4.7 Economic Analysis

Techno-commercial feasibility study of the proposed combined cycle power plant is done through economic comparison based on levelized cost of electricity (LCoE) generation and cost of saved fuel [17]. Capital costs of the standalone steam power plant and KCS11 are assumed as INR 50,000/− per kW [17] and INR 62,000/− per kWh [20], respectively. Economic analyses of the plants are made by considering the plant capacity factor of 90%, discount rate of 12%, fixed O&M cost of 15% of total capital cost and fuel cost (i.e. coal) of INR 0.75 per kg, and the values of different economic parameters are shown in Table 18.10. The LCoE generation and simple payback period (SPP) of the 660 MW combined cycle SupC power plant are, respectively, about INR 1.919/− per kWh and 4.021 years which are marginally

Table 18.10 Economic comparison of standalone power plant and combined cycle power plant

Description	Unit	660MW Main steam power plant	660MW Combined cycle power plant
Capital cost (C_C)	INR/kW	50000.000	50222.000
Life of the power plant (n)	Year	20.000	20.000
Discount rate (d)	fraction	0.120	0.120
Capital recovery factor (RF_C)	fraction	0.134	0.134
Annualized capital cost (CC_A)	INR/kW	6693.939	6723.660
Plant capacity factor (PCF)	fraction	0.900	0.900
Auxiliary power consumption (P_{aux})	fraction	0.075	0.079
Net energy generated annualy (P_{net})	kWh/kW	7290.335	7262.741
Fixed capital cost per unit (FCc)	INR/kWh	0.918	0.926
Fixed O&M cost (FOM)	INR/kW	1004.091	1008.549
Fixed O&M cost per unit($FC_{O\&M}$)	INR/kWh	0.138	0.139
Fuel Cost (C_{fuel})	INR/kg	0.750	0.750
Lower heating value of fuel (LHV)	kJ/kg	17162.600	17162.600
Net heat rate(NHR)	kJ/kWh	10555.614	10409.852
Fuel cost per unit (FC_{fuel})	INR/kWh	0.461	0.455
variable O&M cost per unit (FC_{VOM})	INR/kWh	0.200	0.200
Total variable cost per unit (C_V)	INR/kWh	0.661	0.655
Annualized cost of electricity generation (AC_OE)	INR/kWh	1.717	1.720
Excalation rate (fuel/O&M- fixed and variable) (e)	fraction	0.031	0.031
Equiavalent discount rate with escalation (d')	fraction	0.087	0.087
Levelizing factor (L_F)	fraction	1.251	1.251
Levelized fuel and O&M cost(C_L)	INR/kWh	1.000	0.993
Levelized cost of electricity generation (LC_OE)	INR/kWh	1.918	1.919
Simple payback period (SPP)	Year	3.994	4.021
Additional cost for KCS11 integration	INR/kWh	–	0.001
Energy saved for KCSI 1 integration	kJ/kWh	–	145.762
Cost of saved energy	INR/kJ	–	0.00001
Cost of Saved fuel	INR/kg	–	0.122

higher than the standalone 660 MW SupC coal-fired steam power plant. The cost of implementation of KCS11 technology is about INR 0.122/− per kg of fuel saved which is about 6.15 times lower than the fuel cost. Hence, this may be one of the power generation technologies for energy efficient, environment friendly, and economically viable power generation.

18.4.8 Conclusions

The following are some of the major conclusions that could be drawn from the present study:

- Maximum energy and exergy losses take place in the condenser and boiler of the standalone 660 MW SupC thermal power plant which is about 50.055% and 53.692% of total input, respectively. Integration of KCS11 at condenser side decreases the condenser energy and exergy losses by about 0.773 and 0.418% points, respectively, resulting in the improvement of plant energy and exergy efficiency by about 0.543 and 0.472% points, respectively. The CO_2 emission can be reduced by 2.53 tons per hour by this novel approach at full load.
- More relative energy rejection and relative exergy destruction cause less plant efficiency at part-load condition.
- The optimum condenser back pressure and evaporator shell pressure of the combined cycle power plant are about 9.75 bar and 0.103 bar (absolute), respectively, for maximizing the plant performance.
- The levelized cost of electricity (LCoE) generation and simple payback period (SPP) of the proposed combined cycle plant are about INR 1.919 per kWh and 4.021 years, respectively.
- The cost of saved fuel for KCS11 integration of the combined cycle power plant is about INR 0.122 per kg of fuel, which is about 6.15 times lower than the fuel cost.

Nomenclature

$\dot{E}$	Energy rate (kW)
$\dot{\mathrm{E}}\mathrm{x}_{\mathrm{D}}$	Exergy destruction rate (kW)
ε	Specific exergy (kJ/kg K)
h	Specific enthalpy (kJ/kg)
LHV	Lower heating value (kJ/kg)
LP	Low pressure
$\dot{m}$	Mass flow rate (kg/s)
P	Pressure (bar)
$\dot{P}$	Power consumption rate (kW)
R	Relative energy/exergy ratio
S	Specific entropy (kJ/kg K)
T	Absolute temperature (K)
$\dot{W}$	Rate of work (kW)
η	Energy efficiency (%)
ψ	Exergy efficiency (%)

Superscript

Comb.	Combined power plant
evp	Evaporator

e	Economizer inlet
FP	Feed pump
i/o	Inlet/outlet
sat. l	Saturated liquid state

Subscript

c	Cold reheat
en	Energy
ex	Exergy
f	Feed water flow
h	Hot reheat
int.	Input of TG cycle
kct	Kalina cycle turbine
mix.	Ammonia-water binary mixture
mpcw	Cooling water of main plant condenser
mp	Main plant
s	Main steam

References

1. Energy Statistic Report-2016 (2016) India http://www.mospi.gov.in
2. Suresh MVJJ, Reddy KS, Kolar A (2010) 3-E analysis of advanced power plants based on high ash coal. Int J Energy Res 34:716–735
3. Khankari G, Biswas M, Pramanick A, Karmakar S (2013) Thermodynamic analysis of a 500MW coal-fired Indian power plant. In: ESMOC conference, NIT Durgapur, India
4. Kim KH, Blanco HP (2015) Performance analysis of a combined organic Rankine cycle and vapour compression cycle for power and refrigeration cogeneration. J Appl Therm Eng 91:964–974
5. Camporeale PSM, Cilibert PD, Fortunato B, Torresi M, Marce A (2016) Externally fired micro-gas-turbine and ORC bottoming cycle: Optimal biomass/natural gas combined heat and power generation configurations for residential energy demand, Int J Eng Gas Turbines Power (ASME), 139(4), paper no. GTP-16-1127, https://doi.org/10.1115/1.4034721
6. Vidhi R, Kuravi S, Goswami DY, Stefanakos E, Sabau AS (2013) Organic fluids in a supercritical Rankine cycle for low temperature power generation, J Energy Res Technol (ASME), paper no. JERT-12-1253, 135(4):042002(1–9)
7. Jubeh NM, Najjar YSH (2014) Cascaded waste-heat recovery as a green technology for energy sustainability in power generation. Int J Energy Res 38:1361–1365
8. Ozdil NFT, Segmen MR, Tantekin A (2015) Thermodynamic analysis of an organic rankine cycle based on industrial data. J Appl Therm Eng 91:43–52
9. Hettiarachchi HBM, Mihajlo G, Woreck WM, Lkegami Y (2007) The performance of the KCS11 with low-temperature heat sources. J Energy Resour Technol 129:243–248
10. Kalina AI (1983) Combined cycle and waste-heat recovery power systems based on a novel thermodynamic energy cycle utilising low-temperatures heat for power generation, ASME paper: 83-JPGC-GT-3
11. El-Sayed YM, Tribus MA (1985) A theoretical comparison of the Rankine and Kalina cycles. ASME 1:97–102

12. Singh OK, Kaushik SC (2013) Energy and exergy analysis and optimization of Kalina cycle coupled with coal fired steam power plant. J Appl Therm Eng 51:787–800
13. Khankari G, Karmakar S (2016) Power generation from coal mill rejection using Kalina cycle. ASME J Energy Resour Technol 138:052004. (1–11)
14. Nag PK, Gupta AVSSKS (1998) Exergy analysis of Kalina cycle. J Appl Therm Eng 18:427–439
15. Delft University of Technology (2008) Cycle-tempo release 5.0, http://www.tudelft.nl
16. Kotas TJ (1985) The exergy method of thermal plant analysis. Butterworth, London
17. Suresh MVJJ, Reddy KS, Kolar AK (2010) 4-E (energy, exergy, environment, and economic) analysis of solar thermal aided coal-fired power plants. Energy Sustain Dev 14:267–279
18. Ray TK, Datta A, Gupta A, Ganguly R (2010) Exergy-based performance analysis for proper O&M decision in a steam power plant. J Energy Convers Manag 51:1333–1344
19. Srinivas T, Reddy BV (2014) Thermal optimization of a solar thermal cooling cogeneration plant at low temperature heat recovery. ASME J Energy Resour Technol 136:021204. (1–10)
20. Mirolli MD (2005) The Kalina Cycle for cement kiln waste heat recovery power plants. In: Record cement industry technical conference, Kansas City, pp 330–336

Chapter 19
Computational Study on the Design for Fluid Flow in High Angular Velocity Screw Pumps

Jaison Philip, Abhilash Suryan, T. V. Sanand, and P. Unnikrishnan Nair

19.1 Introduction

A screw pump is a typical rotary pump which pumps the fluid in axial direction. Screw pumps are widely used for various applications including pumping lubricating oil, petroleum products, dilute acids and alkalis in chemical engineering. It is very simple to construct, thus making it ideal for applications where a lot of complexities are involved. The screw pump has two parts, a hub (rotor with helical channels) and a shroud (stator) which covers the hub so as to contain the flow driven by the hub. The shroud can be profiled, thereby creating cavities which adds to pumping efficiency. Likewise, different types of screw pumps with different profiles can be used such as labyrinth screw pumps, twin-screw pumps, etc. These pumps can work at a very wide range of angular velocities, especially at higher angular velocities which have not been pondered much. But working at higher angular velocities may increase cavitation risks. Cavitation can cause several negative effects such as vibrations, performance losses, erosion and structural damage. These effects make cavitation an important issue in turbomachinery design and operation, which should be controlled or at least well understood.

J. Philip
Department of Mechanical Engineering, John Cox Memorial C.S.I Institute of Technology, Trivandrum, Kerala, India

A. Suryan (✉)
Department of Mechanical Engineering, College of Engineering Trivandrum, Trivandrum, Kerala, India
e-mail: suryan@cet.ac.in

T. V. Sanand · P. Unnikrishnan Nair
Turbopump Division, Liquid Propulsion System Centre, ISRO, Trivandrum, Kerala, India

S. Nižetić, A. Papadopoulos (eds.), *The Role of Exergy in Energy and the Environment*, Green Energy and Technology,
https://doi.org/10.1007/978-3-319-89845-2_19

Cavitation is the phenomena by which vapour or gas cavities form within a given liquid, which is driven by pressure change alone. Cavitation occurs at a given temperature T whenever the pressure p in the liquid becomes lower than the saturated vapour pressure $P_v(T)$, namely, $P(T) \leq P_v(T)$. This phenomenon can be observed in various engineering systems, ranging from hydraulic machinery to turbo pumps for space applications.

Numerous studies have been conducted on cavitating behaviour of pumps. Works have been done as early as 1917 when Lord Rayleigh [1] studied the collapse of bubbles and derived an expression for the pressure in the interior of the fluid during tile collapse. In 1949, Plesset [2] studied the dynamics of cavitation bubbles and used the equation derived by Rayleigh to derive an expression explaining the behaviour of cavitation bubbles. Chen et al. [3] developed a non-linear numerical model to explain the non-equilibrium effects in cavitation flows. They modified the Rayleigh-Plesset equation to incorporate non-equilibrium effects. Ahuja et al. [4] simulated cavitation behaviour over a cylindrical head form and a NACA66 hydrofoil using CFD. They included a source term in order to indicate phase change when liquid pressure drops below its saturation value. Athavale et al. [5] using CFD solved Rayleigh-Plesset equation on three different turbomachines and found out that the presence of non-condensible gases reduced the pump head as well as the extent of cavitation. Bakir et al. [6] and Coutier-Delgosha et al. [7] did a detailed numerical study on the cavitating behaviour on turbo-pump inducers having similar geometry to a screw pump. They observed that for high flow rate where the blockage occurs, the model underpredicts the head drop location. Thus, the cavitation model itself requires careful testing for the determination of empirical constants relevant to the flow conditions. Their model is useful in the design of hydraulic machines operating under conditions where large vapour cavities are present.

Numerous works have been done on the field of screw pump numerical modelling and analysis as well. Campbell et al. [8] studied the drag flow in the screw pump at low RPM experimentally by rotating the barrel and screw separately. They proposed an expression connecting the flow rate, rotational velocity and a constant based on the screw helix geometry. Li and Hsieh [9] developed an analytical model for a screw pump which pumps highly viscous fluids and provided a more detailed prediction. Main assumption was that all inertial terms can be neglected since they are inconsequential compared to the viscous terms. Alves et al. [10] further developed this analytical model by studying the flow inside the screw pump with a low viscous fluid. They used this analytical model to predict the flow for a screw pump supplying oil into reciprocating compressors [11]. Numerous studies are conducted on labyrinth screw pumps. In 2010 a CFD analysis on triangular thread labyrinth screw pumps was done by Ma and Wang [12] explaining how the screw pump behaves under varying diametric clearances. They concluded that fitting clearances have no effect on drag on the rotor and hence have no effect on the pump. Based on Prandtl's mixing length theory, they also developed a mathematical model for modelling two-dimensional Reynolds stress equations for screw pump applications [13].

Though cavitation studies have been done in the case of inducers, the case of a screw pump was not discussed much as most screw pumps on literature had a working angular velocity less than 3000. Jaison et al. has reported numerical studies on screw pumps with high angular velocities [14, 15]. Present study is an extension of that work; a cavitation study is done in order to predict the behaviour of cavitation of screw pumps under high angular velocities.

19.2 CFD Modelling

Three screw pumps were modelled in order to study cavitation and the NPSH required for each pump. Case 1 has a plain shroud and a 12TS (thread start) hub, Case 2 is the combination of 12TS shroud with 6TS hub, and Case 3 is the combination of a 12TS shroud with 12TS hub (Fig. 19.1). Internal threads are given in order to guide the fluid more efficiently.

Threads used in all these pumps are all trapezoidal threads. All the threads are right-handed threads with a lead of 72 mm. Diameter of hub shaft is 69 mm with threads on top of it. Internal diameter of the shroud is taken as 73 mm as no diametrical clearance is modelled. As for the shroud with internal threads, maximum diameter is taken as 77 mm. In all these cases, the thread shape is kept constant with a height of 2 mm and cross-sectional base width of 2.5 mm. Included angle of the thread is taken as 30°. Cross-sectional view of the thread is illustrated in Fig. 19.2.

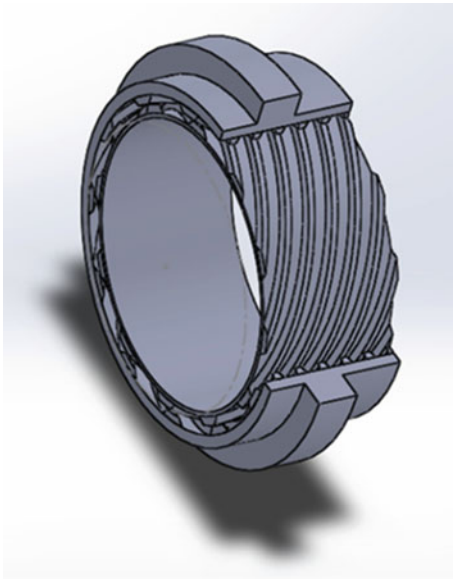

Fig. 19.1 Cut section of screw pump with 12TS shroud and 12TS hub

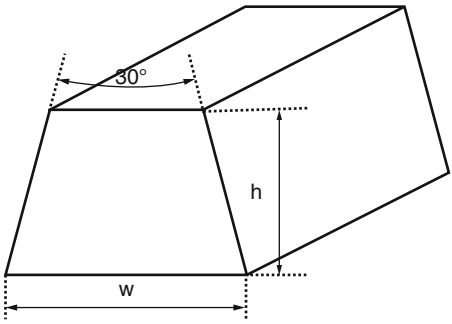

Fig. 19.2 Cross-sectional view of screw thread

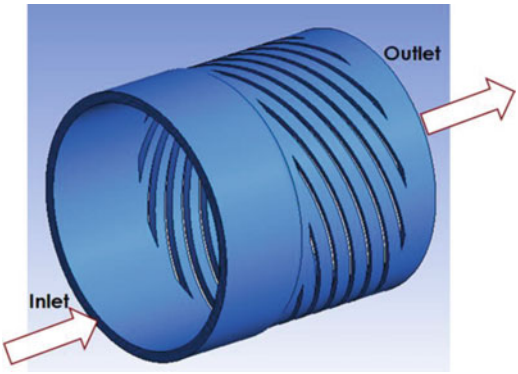

Fig. 19.3 Fluid section modelled including inlet and exit buffer zones for screw pump with plain shroud and a 12 TS hub

Total axial length of the pump is 34 mm. Fluid domain of the pump according to the above geometry was made with buffer zones to capture entry and exit phenomena (Fig. 19.3). Water at 25 °C is used as simulating fluid for this analysis.

19.3 Numerical Scheme

Because of the complexity of the geometry, unstructured tetrahedral elements are used to mesh the groove of the hub and shroud with number of prism layers not less than 28. Local y + on the walls of hub and shroud is less than 2 for SST k-ω turbulence model. The resulting grid size was 14 million elements to 20 million elements depending on the geometry which are independent. Inlet pressure is specified at the inlet boundary, and mass flow rate is specified at the outlet. The screws of the hub are maintained in rotating frame, and the shroud wall is maintained as stationary wall. Screw is rotated about the z-axis at a constant rotating speed of 19,000 RPM in such a way that it pushes the fluid in the positive z-axis direction. Working fluid is water with constant properties. The model selected is MRF model, and the continuity and momentum equations are discretized by the higher-order discretization and solved by the pressure-velocity coupled algorithm. Since the fluid

flow in screw pump is turbulent with high Reynolds number, of the order of 105, SST k-ω turbulence model is used. The model can capture the flow under adverse pressure gradient and has given better results for similar problems [5]. For modelling cavitation, Rayleigh-Plesset equation was used. Homogeneous mixture model was used in the present analysis. Inlet pressure was gradually decreased keeping the rotational speed and mass flow rate constant, in order to plot the drop curve and to calculate NPSH required for each screw pump. Saturation pressure of the working fluid is taken as 3169 Pa.

19.4 Governing Equations

Governing equations used in present study [16] are:

Continuity equation

$$\frac{\partial u}{\partial x}+\frac{\partial v}{\partial y}+\frac{\partial w}{\partial z}=0 \tag{19.1}$$

Momentum equations

$$\rho\left(u\frac{\partial u}{\partial x}+v\frac{\partial u}{\partial y}+w\frac{\partial u}{\partial z}\right)= -\frac{\partial P}{\partial x}+\frac{\partial}{\partial x}\left(\mu\left(2\frac{\partial u}{\partial x}-\frac{2}{3}\nabla.\underset{v}{\rightarrow}\right)\right) +\frac{\partial}{\partial y}\left(\mu\left(\frac{\partial v}{\partial x}+\frac{\partial u}{\partial y}\right)\right)+\frac{\partial}{\partial z}\left(\mu\left(\frac{\partial w}{\partial x}+\frac{\partial u}{\partial z}\right)\right) \tag{19.2}$$

$$\rho\left(u\frac{\partial v}{\partial x}+v\frac{\partial v}{\partial y}+w\frac{\partial v}{\partial z}\right)= -\frac{\partial P}{\partial y}+\frac{\partial}{\partial x}\left(\mu\left(\frac{\partial v}{\partial x}+\frac{\partial u}{\partial y}\right)\right) +\mu\frac{\partial}{\partial y}\left(\mu\left(2\frac{\partial v}{\partial y}-\frac{2}{3}\nabla.\underset{v}{\rightarrow}\right)\right)+\frac{\partial}{\partial z}\left(\mu\left(\frac{\partial w}{\partial y}+\frac{\partial v}{\partial z}\right)\right) \tag{19.3}$$

$$\rho\left(u\frac{\partial w}{\partial x}+v\frac{\partial w}{\partial y}+w\frac{\partial w}{\partial z}\right)= -\frac{\partial P}{\partial z}+\frac{\partial}{\partial x}\left(\mu\left(\frac{\partial w}{\partial x}+\frac{\partial u}{\partial z}\right)\right) +\frac{\partial}{\partial y}\left(\mu\left(\frac{\partial w}{\partial y}+\frac{\partial v}{\partial z}\right)\right)+\mu\frac{\partial}{\partial z}\left(\mu\left(2\frac{\partial w}{\partial z}-\frac{2}{3}\nabla.\underset{V}{\rightarrow}\right)\right) \tag{19.4}$$

The two equations of the turbulence model [17] are

$$\rho.\frac{\partial\left(u_j k\right)}{\partial x_j}=\tau_{ij}\frac{\partial u_i}{\partial x_j}-\beta^*\rho\omega k+\frac{\partial}{\partial x_j}\left[\left(\mu+\sigma_k\mu_t\right)\frac{\partial k}{\partial x_j}\right] \tag{19.5}$$

$$\rho.\frac{\partial\left(u_j\omega\right)}{\partial x_j}=\frac{\gamma}{\nu_t}\tau_{ij}\frac{\partial u_i}{\partial x_j}-\beta\rho\omega^2+\frac{\partial}{\partial x_j}\left[\left(\mu+\sigma_\omega\mu_t\right)\frac{\partial\omega}{\partial x_j}\right]+2\rho(1-F_1)\sigma_{\omega2}\frac{1}{\omega}\frac{\partial k}{\partial x_j}\frac{\partial\omega}{\partial x_j} \tag{19.6}$$

A cavitation model has been implemented based on the first-order approximation of Rayleigh-Plesset equation (RPE) [16] to estimate the rate of vapour production in order to make the calculation faster. For a vapour bubble nucleated in a surrounding liquid, the dynamic growth of bubble can be described as

$$\frac{dR_B}{dt}=\sqrt{\frac{2}{3}\frac{p_v-p}{\rho_f}} \tag{19.7}$$

The interphase mass transfer rate per unit volume is considered as a source term and is plugged into the continuity equation, where

$$\rho=\alpha_f\rho_f+\alpha_g\rho_g \tag{19.8}$$

and the source term can be derived [18] as;

$$m_{fg}=F\frac{3r_{nuc}\left(1-r_g\right)\rho_g}{R_{nuc}}\sqrt{\frac{2}{3}\frac{|p_v-p|}{\rho_f}sgn(p_v-p)} \tag{19.9}$$

19.5 Results and Discussion

Cavitation study was carried out for three screw pumps (Cases 1, 2, 3). The results are discussed below.

Drop curve is plotted in order to find the NPSH required for a pump. Drop curve is plotted by varying the inlet pressure and plotting the pressure rise in the y-axis. The drop curve of case 1 is shown in Fig. 19.4. We can observe that when the inlet pressure is reduced, the pressure rise remains constant for up to a point, and then it suddenly falls. This is due to the formation of cavitation bubbles at the inlet of the pump blades. Vapour bubbles are formed when the local pressure at the pump inlet blades is less than the saturation pressure of the working fluid (water). Figures 19.5 and 19.6 show the vapour fraction when the inlet pressure is 0.75 MPa and 0.45 MPa, respectively.

When the inlet pressure is 0.75 MPa, small bubbles are created at the trailing edge of the rotor blades. At 0.45 MPa, a large quantity of bubbles are formed, thus blocking the inlet. This is why we see a head drop. Here to find of the NPSH required, the pressure rise and inlet pressure is plotted as head rather than pressure. We can observe that the head rise drops when NPSH at inlet is at 90 m. NPSH required is taken as the NPSH at inlet corresponding to 3% drop in pump head rise.

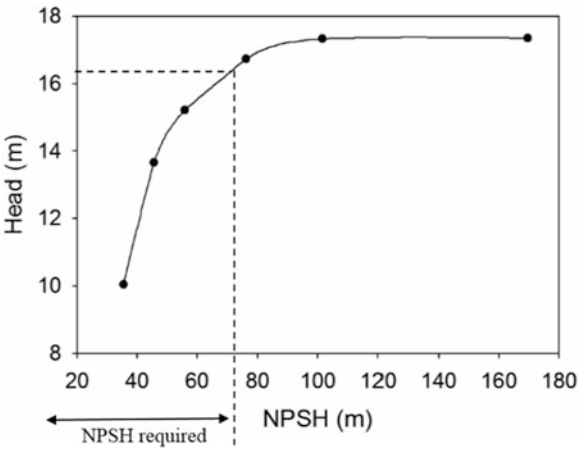

Fig. 19.4 Drop curve for the Case 1

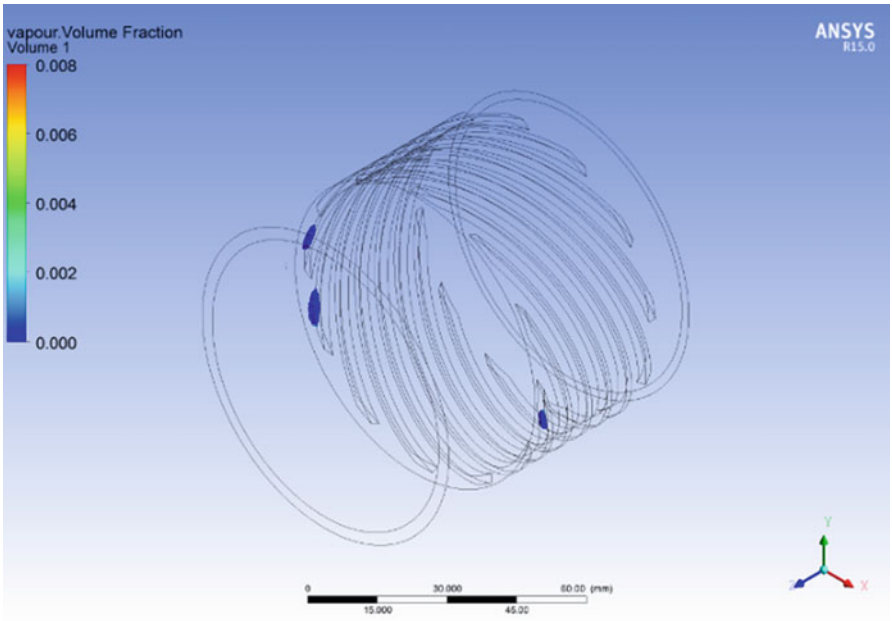

Fig. 19.5 Vapour fraction contour of Case 1 at inlet pressure 0.75 MPa

Here the 3% drop of head rise corresponds to a NPSH of 73 m. Therefore 73 m is the NPSH required of the Case 1.

Figure 19.7 shows the drop curve plotted for the Case 2. In this case, the NPSH corresponding to 3% of head rise occurs at the inlet NPSH of 24 m. Figures 19.8 and 19.9 show the vapour fraction at inlet pressure 0.5 MPa and 0.2 MPa.

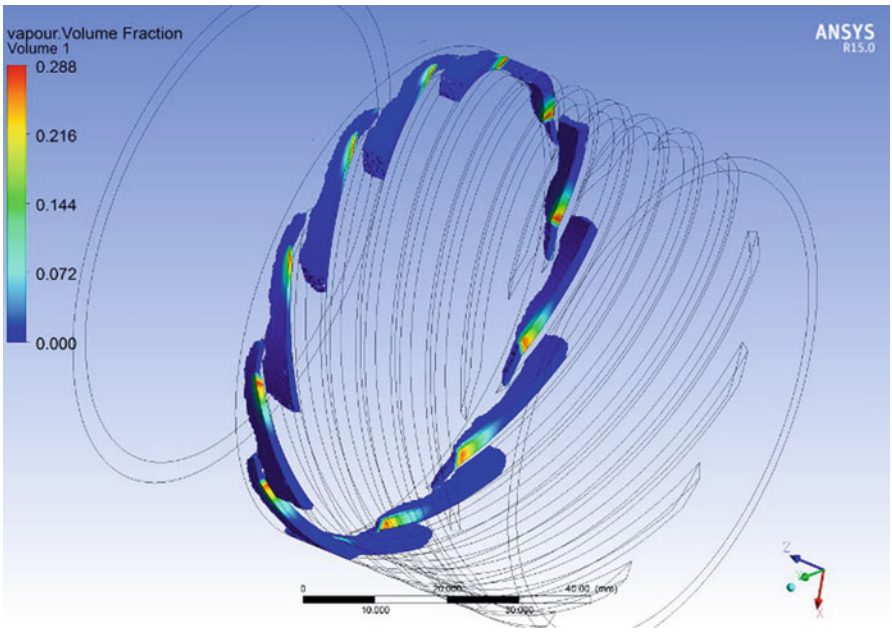

Fig. 19.6 Vapour fraction contour of Case 1 at inlet pressure 0.45 MPa

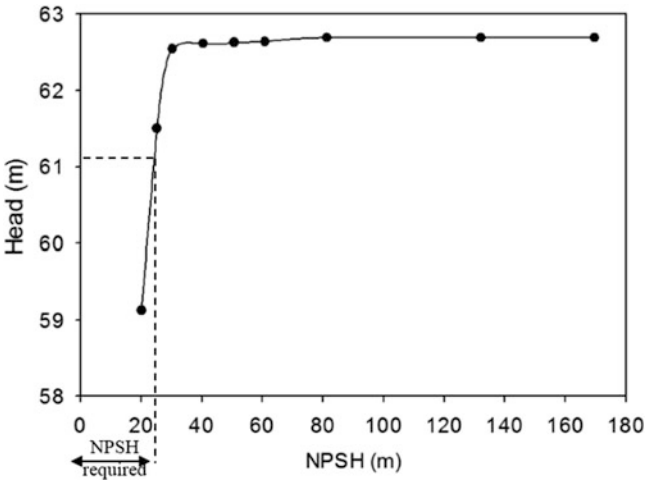

Fig. 19.7 Drop curve for the Case 2

Figure 19.10 shows the drop curve plotted for the Case 3. In this case, the NPSH corresponding to 3% of head rise occurs at the inlet NPSH of 63 m. Figures 19.11 and 19.12 show the vapour fraction contour of Case 3 at 0.6 MPa and 0.3 MPa. This difference of NPSH required Cases 2 and 3 compared to case 1 even though the

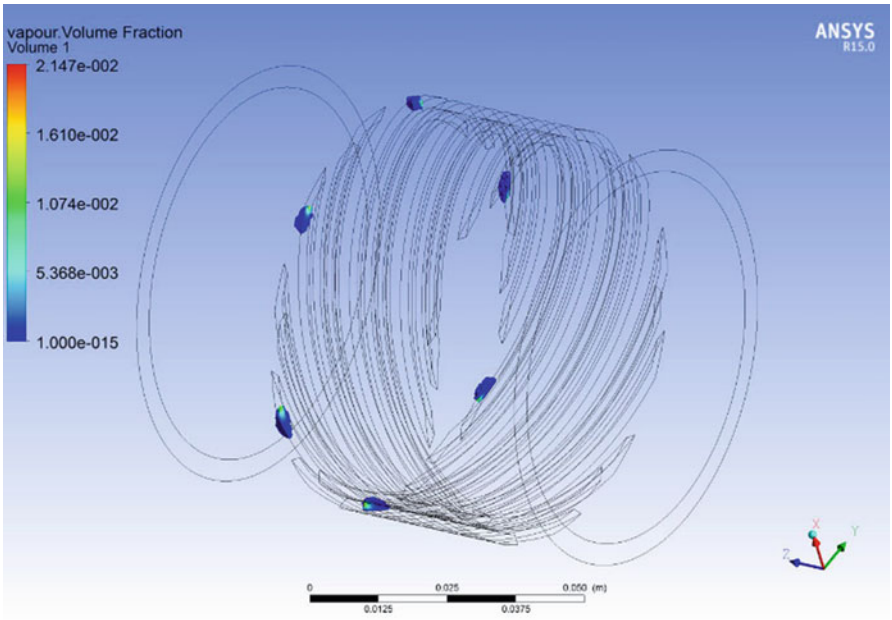

Fig. 19.8 Vapour fraction contour of Case 2 at inlet pressure 0.5 MPa

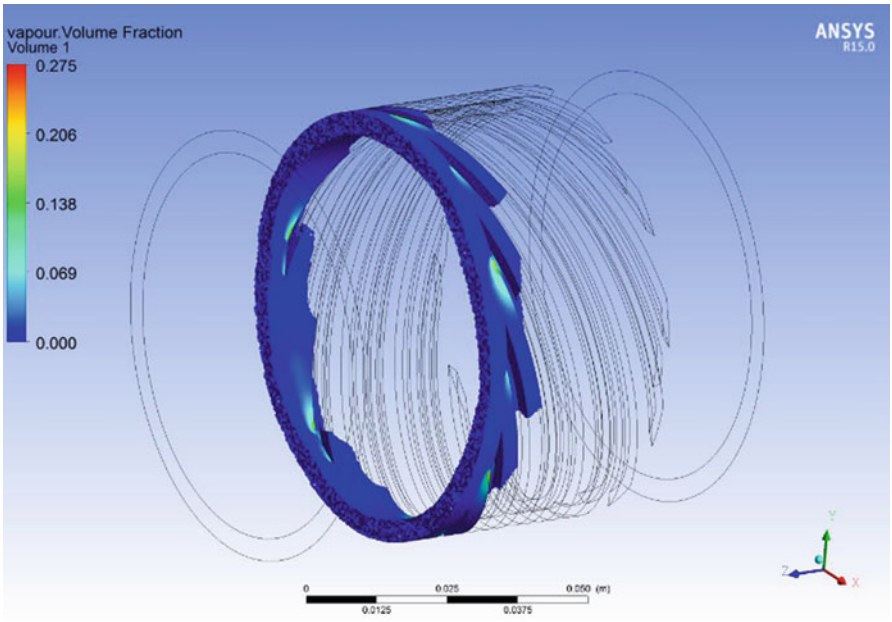

Fig. 19.9 Vapour fraction contour of Case 2 at inlet pressure 0.2 MPa

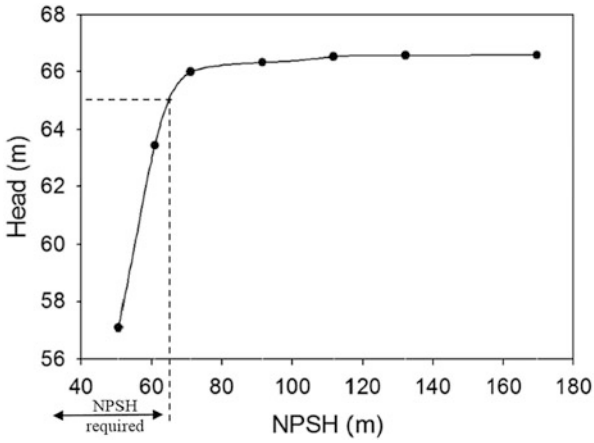

Fig. 19.10 Drop curve for the Case 3

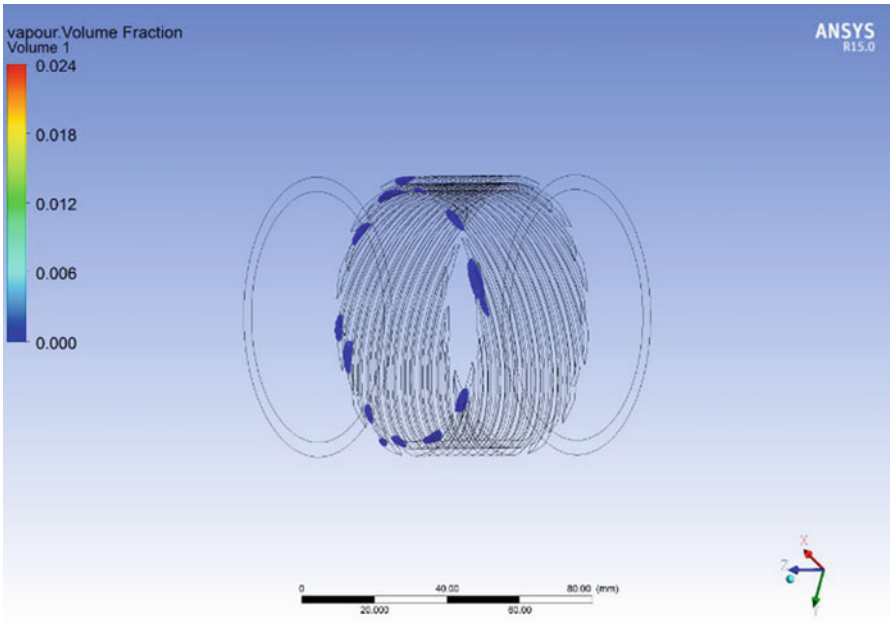

Fig. 19.11 Vapour fraction contour of Case 3 at inlet pressure 0.6 MPa

number of threads associated with the pump increased can be attributed to the increase in pump cross-sectional area.

Figure 19.13 shows the cross-sectional areas of the three cases under consideration. Since Case 2 has the largest cross-sectional area, even though the inlet area gets blocked, there is enough space left for the flow to flow. This may be the reason so as to why the Case 2 has such low NPSH required. The effect of increase in

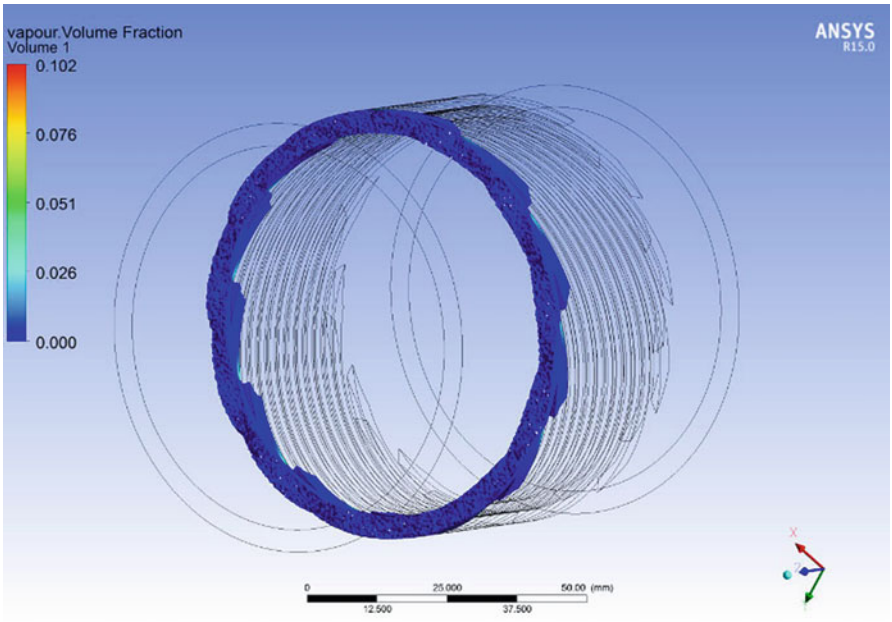

Fig. 19.12 Vapour fraction contour of Case 3 at inlet pressure 0.3 MPa

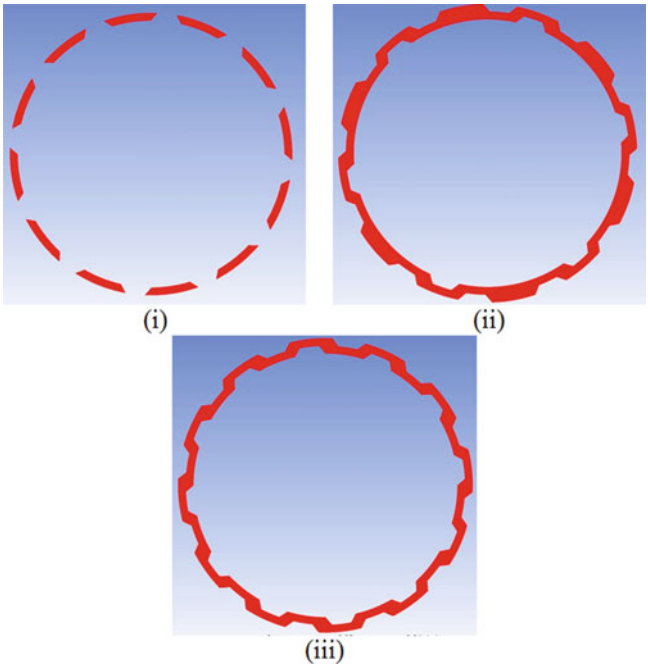

Fig. 19.13 Cross-sectional areas of Cases 1, 2 and 3. (i) Case 1 cross-sectional area 2.9 × 10-4 m^2, (ii) Case 2 cross-sectional area 6.7 × 10^{-4} m^2 and (iii) Case 3 cross-sectional area 5.9 × 10^{-4} m^2

number of blades associated with the pump is counteracted by the increase in area. Thus NPSH required goes down. Which means this pump can perform at low head requirement applications compared to the other cases.

The cross-sectional area of the Case 3 is approximately twice that of the Case 1. But Case 3 also has twice the number of threads associated with it than Case 1. This can be the reason why the NPSH required of Cases 1 and 3 are comparable. But still the NPSH required of Case 3 is less. This can be due to the fact that half the threads associated with the Case 3 are stationary but in the case of Case 1, all threads are rotating.

19.6 Conclusions

In the present analysis, three screw pumps at high angular velocity were analysed for cavitation, and NPSH required was found out for each pump. Results were obtained for models with no diametrical clearance which is a hypothetical situation. When diametrical clearance is added, the NPSH required will get reduced in proportion to the clearance.

The following are the conclusions obtained in the present analysis:

(i) Cavitation depends on the number of blades associated with pump and the cross-sectional area of the pump.
(ii) If the pump has relatively low cross-sectional area, when bubbles are formed at the inlet of the pump, it will cause blockage in the flow through the pump, and the pump will fail to generate the required head rise.
(iii) This blocking at the inlet due to bubble formation increases NPSH required.

Nomenclature

De	Hydraulic diameter of the screw channel (m)
F	Empirical constant
h	Height of the screw thread (m)
k	Turbulent kinetic energy
m_{fg}	Interphase mass transfer rate per unit volume
p,p_v	Pressure and saturation vapour pressure of the fluid (Pa)
r	Average radius of the fluid domain (m)
r_g	Volume fraction
R_B	Bubble radius (m)
Re	Reynolds number, $(\rho \times V_{avg} \times D_e)/\mu$
u	Velocity in x direction (m/s)
v	Velocity in y direction (m/s)
V_{avg}	Average velocity of the fluid in the screw channel
$\vec{v}$	Velocity vector
v	

w	Velocity in z direction (m/s)
W	Cross-sectional base width of the screw thread

Greek Letters

α_f, α_g	Volume fraction of fluid and vapour
β, β^*	Turbulence model constants
ε	Turbulence dissipation rate
μ	Dynamic viscosity of the simulating fluid (kg/m/s)
ρ_f, ρ_g, ρ	Density of the simulating fluid, vapour and average density (kg/m3)
σ	Turbulence model constants
ω	Specific dissipation rate

References

1. Rayleigh L (1917) On the pressure developed in a liquid during the collapse of a spherical cavity. The London, Edinburgh, and Dublin Philosophical Magazine and Journal of Science. 34:94–98
2. Plesset M, Prosperetti A (1977) Bubble dynamics and cavitation. Annu Rev Fluid Mech 9:145–185
3. Chen Y, Heister SD (1996) Modeling hydrodynamic nonequilibrium in cavitating flows. ASME J Fluids Eng 118(1):172–178
4. Ahuja V, Hosangadi A, Arunajatesan S (2001) Simulations of cavitating flows using hybrid unstructured meshes. ASME J Fluids Eng 123(2):331–340
5. Athavale MM, Li HY, Jiang Y, Singhal AK (2002) Application of the full cavitation model to pumps and inducers. Int J Rotating Mach 8(1):45–56
6. Coutier-Delgosha O, Morel P, Fortes-Patella R, Reboud JL (2005) Numerical simulation of turbopump inducer cavitating behavior. Int J Rotating Mach 2005(2):135–142
7. Bakir F, Rey R, Gerber AG, Belamri T, Hutchinson B (2004) Numerical and experimental investigations of the cavitating behavior of an inducer. Int J Rotating Mach 10(1):15–25
8. Campbell GA, Sweeney PA, Felton JN (1992) Analysis of an alternative extruder screw pump design. J Int Polym Process 7(4):320–326
9. Li Y, Hsieh F (1996) Modeling of flow in a single screw extruder. J Food Eng 27:353–375
10. Alves MVC, Barbosa JR Jr, Prata AT (2009) Analytical solution of single screw extrusion applicable to intermediate values of screw channel aspect ratio. J Food Eng 92:152–156
11. Alves MVC, Barbosa JR Jr, Prata AT, Ribas FA Jr (2011) Fluid flow in a screw pump oil supply system for reciprocating compressors. Int J Refrig 34(1):74–83
12. Ma R, Wang K (2010) CFD numerical simulation and experimental study of effects of screw-sleeve fitting clearance upon triangular thread labyrinth screw pump (LSP) performance. J Appl Fluid Mech 3(1):75–81
13. Ma R, Wang K (2009) Modeling of pumping performance of labyrinth screw pump (LSP) by 2D Reynolds stress equations. ASME J Fluids Eng 131(8):085001
14. Philip J, Suryan A, Sanand TV, Unnikrishnan Nair P (2016) Flow analysis of a screw pump in the turbo pump of a semi-cryogenic engine. In: Proceedings of LAMSYS 2016, Sriharikota
15. Philip J, Suryan A, Sanand TV, Unnikrishnan Nair P (2017) Computational study on the influence of number of threads on the performance of single screw pump at high angular velocities. J Therm Sci 26(1):54–59
16. ANSYS CFX-Solver, Theory Guide
17. Menter FR (1994) Two-equation eddy-viscosity turbulence models for engineering applications. AIAA J 32(8):1598–1605
18. Liuzzi D (2012) Two-phase cavitation modelling, PhD Dissertation, University of Rome – LA SAPIENZA

Part III
Sustainable Energy and the Environment

Chapter 20
An Integrated Fuzzy Multi-criteria Approach for Evaluation of Energy Resources: A Case Study of Turkey

Hasan Hüseyin Turan, Umit Unver, and Hikmet Erbıyık

20.1 Introduction

The new energy technologies are far from maturity to meet increasing energy demand, which feeds worries over energy supply security. The International Energy Agency (IEA) (2008) reported that the primary energy demand of the world will increase by 47.5% between 2009 and 2035, and it will reach to 16.8 billion tons of equivalent petroleum (TEP) in 2035, compared to 2009, which is about 12 billion TEP [1]. Evidently, developing conventional and nonconventional energy sources and conversion technologies is inevitable [2].

Selection of the appropriate type through numerous energy alternatives is a laborious job with multi-scenarios. Thus, a systematic approach is needed in energy investment planning. The goal of this chapter is to help decision-makers for managing energy sources effectively by evaluating energy investment policies. The rest of the chapter is organized as follows. In Sect. 20.2, multi-criteria decision-making applications in literature related to energy investment planning are discussed. The proposed solution methodology and the case study are presented in Sect. 20.3. Section 20.4 includes the post-optimality analysis, and recommendations for future studies are summarized in Sect. 20.5.

H. H. Turan (✉)
Capability Systems Centre, School of Engineering and Information Technology, University of New South Wales, Canberra, Australia
e-mail: h.turan@adfa.edu.au

U. Unver
Department of Energy Systems Engineering, University of Yalova, Yalova, Turkiye

H. Erbıyık
Department of Industrial Engineering, University of Yalova, Yalova, Turkiye

S. Nižetić, A. Papadopoulos (eds.), *The Role of Exergy in Energy and the Environment*, Green Energy and Technology,
https://doi.org/10.1007/978-3-319-89845-2_20

20.2 Literature Review

Energy planning by utilizing multi-criteria analysis has attracted the attention of decision-makers and researchers. Multi-criteria decision-making (MCDM) is a robust operational decision-making approach under high uncertainty, intersecting objective functions, multiple interests, and multiple perspective conditions. Due to this capability of MCDM, there exist several MCDM applications related to energy investment planning and management of energy sources. The remainder of this section presents a brief review of existing literature about energy planning in which various MCDM techniques are employed.

Becali et al. [3] apply ELECTRE III for allocation of renewable resources for different regions. Another renewable focused application via MCDM for local purposes in Kirklees in Yorkshire, UK, was presented in [4]. The application of participatory multi-criteria evaluation (MCE) to UK energy policy as a tool for structuring the deliberative process was analyzed by Stagl [5]. The prospects for the exploitation of the Kyoto Protocol's Clean Development Mechanism (CDM) in Greece by PROMETHEE method was investigated in [6].

Kowalski [7] performed a participatory multi-criteria analysis (PMCA) of renewable energy for Austria. In the paper, 17 sustainability criterions were examined for five renewable scenarios until 2020. Begic and Afgan [8] evaluated energy power systems for Bosnia and Herzegovina via a multi-criteria sustainability assessment framework. Aragones et al. [9] applied analytic network process (ANP) to the selection of photovoltaic (PV) solar power projects. San [10] used VIKOR method for selection of appropriate energy project for Spain. Cavallaro and Ciraolo [11] proposed a multi-criteria method to support the feasibility analysis of installing alternative wind energy turbine configurations in a site in Italy. An applicable group decision-making framework with the multi-criteria analysis in renewable energy projects, utilizing the PROMETHEE II outranking method described in [12]. A MCDM technique with modified fuzzy TOPSIS methodology for the selection of the best energy technology alternatives was applied in [13]. Kaya and Kahraman [14] considered the determination of the best renewable energy alternative as well as selection among alternative energy production sites for Istanbul by using an integrated VIKOR-AHP methodology. Fuzzy analytic hierarchy process (AHP) and fuzzy axiomatic design are used to make a decision to select the best renewable energy for Turkey [15].

20.3 Proposed Method and Application

In this chapter, fuzzy set theory, which is first introduced by [16], is used and adapted to overcome the difficulty of inexplicit information for multi-criteria decision-making methods. In this direction, AHP is used as a MCDM technique together with fuzzy logic for decision formulation. One of the methods that is used to fuzzify AHP

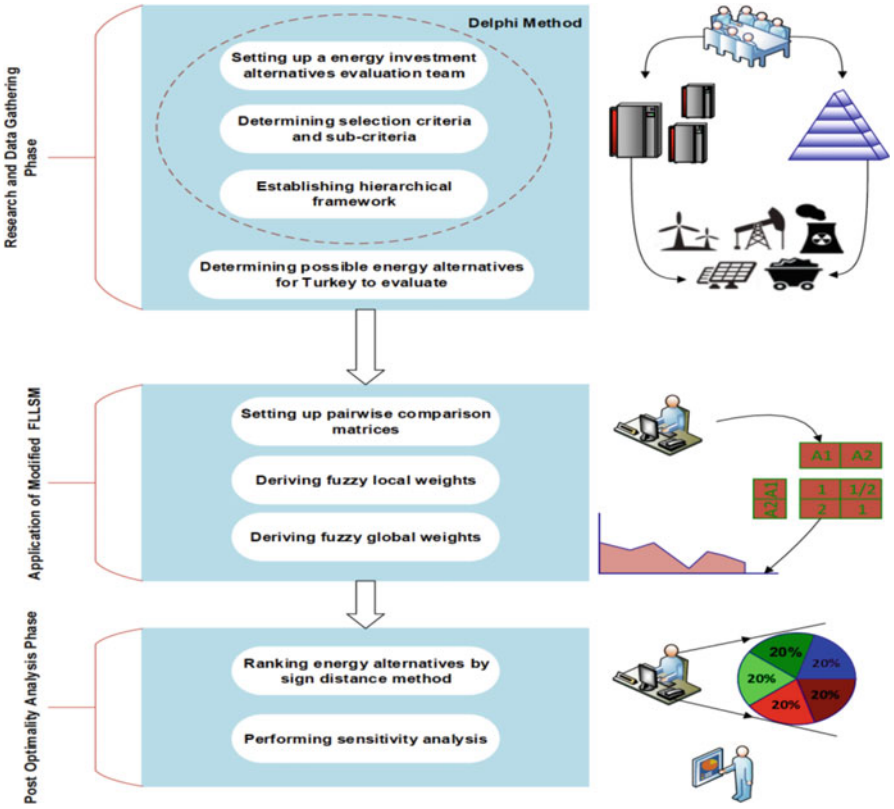

Fig. 20.1 Application flow for energy investment alternative selection

is fuzzy logarithmic least squares method (FLLSM). It is a constrained nonlinear optimization model which has been developed to solve the triangular fuzzy comparison matrix [17]. A modified fuzzy LLSM to eliminate the drawbacks in deriving fuzzy weights by adjusting the normalization of local fuzzy weights and the model's constraints was proposed in [18]. For this reason, in the paper, modified fuzzy logarithmic least squares method (FLLSM), which is proposed by Wang [18], is used to develop a fuzzy-based system for energy investment selection.

The flow of the proposed methodology is presented in Fig. 20.1. The first step of the algorithm is to define evaluation attributes and to establish a hierarchical framework. In the second step, the pair-wise comparison matrices are set up for each factor. Next, the priority vectors are obtained. The local and global fuzzy weights are calculated by employing modified FLLSM in step 4. At the final step, alternatives are ranked by using the sign distance method.

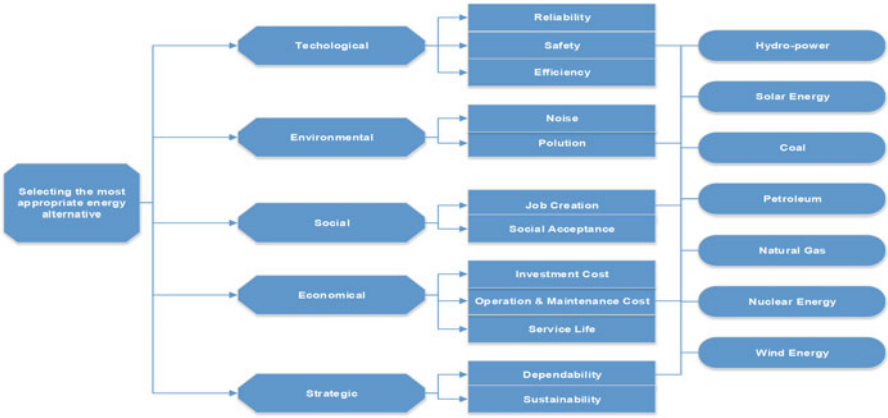

Fig. 20.2 Hierarchical structure to select the most appropriate energy investment alternative

20.3.1 Step 1: Define the Evaluation Attributes Used to Select and Evaluate the Most Appropriate Energy Alternative for Turkey, and Establish a Hierarchical Framework

This chapter employs the Delphi method to determine selection criteria and sub-criteria through anonymous experts with interviews and surveys. The Delphi method that we used gathers and analyzes the relevant findings of various experts of relevant study and provides written communication and discussions to the concerned parties. By this way, various experts on the subject will be able to exchange their experience, skills, and competencies until they come together on an expected consensus [19]. The Delphi method has five main procedures: (1) selection of anonymous experts, (2) conduction of the first step survey, (3) conduction of the second step survey with a questionnaire, (4) conduction of the third step survey with a questionnaire, and (5) integration of the anonymous experts' opinions to find a consensus. In most cases, steps 3 and 4 are repeated until the consensus is achieved on a particular subject. For this reason, several decision-makers are selected from different areas and backgrounds. Finally, results of the literature review and expert interviews are used to identify and synthesize all common views expressed in the surveys. The energy investment selection attributes and hierarchical framework which reveals from Delphi method are presented in Fig. 20.2.

20.3.2 Step 2: Define Energy Alternatives to Select and Establish Pair-Wise Comparison Matrixes

The proposed main investment selection procedure is demonstrated with seven alternatives such as hydropower, solar, wind, coal (fossil), petroleum, natural gas, and nuclear energy for Turkey. The fuzzy set theory is presented first by [16] to investigate and solve the uncertainty cases since they have the ambiguity and vagueness.

A unique advantage of the fuzzy set theory is its capability of handling imprecise data. At the same time, the theory allows the mathematical operations to be conveyed into the fuzzy domain. A fuzzy set consists of a cluster of objects in continual grades of membership. That kind of a set is defined by a membership function, which assigns to each object a degree of membership valuating between zero and one. In Fig. 20.3, a triangular fuzzy number (TFN) is depicted and a triangular fuzzy number usually defined as (l, m, u). The parameters of l, m, u in the definition define the smallest possible value, the most promising value, and the largest possible value in sequential order that describe an event of fuzzy where $l_{ij} \leq m_{ij} \leq u_{ij}$ and l_{ij}, m_{ij}, $u_{ij} \in [1/10, 1] \cup [1, 10]$. Since each number in the pair-wise comparison matrix represents the subjective opinion of decision-makers and is an ambiguous concept, fuzzy numbers work best to consolidate fragmented expert opinions [20]. A set of group triangular fuzzy pair-wise comparison matrixes are set up to compare each alternative with respect to each sub-criteria, each sub-criteria with respect to corresponding upper level criteria, and each decision factor with respect to the main goal, namely, selecting most appropriate energy alternative. To set up group triangular fuzzy pair-wise comparison matrixes, three anonymous experts who joined interviews for Delphi method are chosen among previously mentioned decision-makers in step 1. A group triangular fuzzy comparison matrix is expressed as follows:

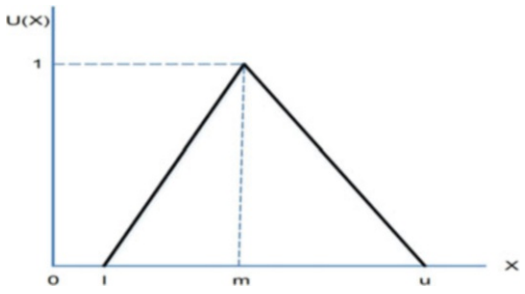

Fig. 20.3 Triangular fuzzy membership function

Table 20.1 Pair-wise comparison matrix for social factors

	Creating job opportunities	Social acceptance
Creating job opportunities	(1, 1, 1)	$\left\{\begin{matrix}(6,8,10)\\(4,6,8)\\(4,6,8)\end{matrix}\right\}$
Social acceptance	$\left\{\begin{matrix}\left(\frac{1}{10},\frac{1}{8},\frac{1}{6}\right)\\\left(\frac{1}{8},\frac{1}{6},\frac{1}{4}\right)\\\left(\frac{1}{8},\frac{1}{6},\frac{1}{4}\right)\end{matrix}\right\}$	(1, 1, 1)

$$\tilde{A} = \begin{bmatrix} (1,1,1) & \left\{\begin{matrix}(l_{121},m_{121},u_{121})\\ \vdots \\ l_{12\delta_{12}},m_{12\delta_{12}},u_{12\delta_{12}}\end{matrix}\right\} & \cdots & \left\{\begin{matrix}(l_{1n1},m_{1n1},u_{1n1})\\ \vdots \\ l_{1n\delta_{1n}},m_{1n\delta_{1n}},u_{1n\delta_{1n}}\end{matrix}\right\} \\ \left\{\begin{matrix}(l_{211},m_{211},u_{211})\\ \vdots \\ l_{21\delta_{21}},m_{21\delta_{21}},u_{21\delta_{21}}\end{matrix}\right\} & (1,1,1) & \cdots & \left\{\begin{matrix}(l_{2n1},m_{2n1},u_{2n1})\\ \vdots \\ l_{2n\delta_{2n}},m_{2n\delta_{2n}},u_{2n\delta_{2n}}\end{matrix}\right\} \\ \vdots & \vdots & \ddots & \vdots \\ \left\{\begin{matrix}(l_{n11},m_{n11},u_{n11})\\ \vdots \\ l_{n1\delta_{n1}},m_{n1\delta_{n1}},u_{n1\delta_{n1}}\end{matrix}\right\} & \left\{\begin{matrix}(l_{n21},m_{n21},u_{n21})\\ \vdots \\ l_{n2\delta_{n2}},m_{n2\delta_{n2}},u_{n2\delta_{n2}}\end{matrix}\right\} & \cdots & (1,1,1) \end{bmatrix}$$

where $\tilde{a}_{ijk} = (l_{ijk}, m_{ijk}, u_{ijk})$ are triangular fuzzy judgments with $\tilde{a}_{ijk} = \tilde{a}_{ijk}^{-1}\left({}^{1}/_{u_{ijk}}, {}^{1}/_{m_{ijk}}, {}^{1}/_{l_{ijk}}\right)$ for $i, j = 1, \ldots, n$, $i \neq j$, $k = 1, \ldots, \delta_{ij}$ and $\delta_{ij} = \delta_{ji}$. If $\delta_{ij} = 0$, then there is no judgment that has been made about $\tilde{a}_{ij}$, which is denoted as "–."

Table 20.1 represents pair-wise comparison matrix for social factors via interviewing with energy experts.

20.3.3 Step 3: Derive Priorities of Group Triangular Fuzzy Comparison Matrixes via Modified FLLSM

In this subsection, previously formed fuzzy group triangular comparison matrixes are used as input for modified FLLSM to calculate priorities. Modified FLLSM is a constrained nonlinear optimization model with linear constraints and can be solved without difficulty by professional optimization software packages such as MATLAB. In this research, algebraic modeling language AMPL is used; and as a solver option, open-source code IPOPT is chosen to solve all given nonlinear models. The optimum solution to the model directly forms normalized fuzzy weights

$\tilde{w}_i = \left(w_i^L, w_i^M, w_i^U\right)$, $i = 1,\ldots, n$. Furthermore, detailed discussion of this methodology can be found in [18]. Modified FLLSM is formulated as follows:

$$\text{Min } J = \sum_{i=1}^{n} \sum_{j=1\ j\neq 1}^{n} \sum_{k=1}^{\delta_{ij}} \left(\left(lnw_i^L - lnw_j^U - lna_{ijk}^L \right)^2 + \left(lnw_i^M - lnw_j^M - lna_{ijk}^M \right)^2 + \left(lnw_i^U - lnw_j^L - lna_{ijk}^U \right)^2 \right) \tag{20.1}$$

$$\begin{aligned} \text{subject to}: & w_i^L + \sum_{j=1\ j\neq 1}^{n} w_j^U \geq 1, \quad i = 1, \ldots, n \\ & w_i^U + \sum_{j=1\ j\neq 1}^{n} w_j^L \leq 1, \quad i = 1, \ldots, n \\ & \sum_{i=1}^{n} w_i^M = 1 \\ & \sum_{i=1}^{n} \left(w_i^L + w_j^U \right) = 2 \\ & w_i^U \geq w_i^M \geq w_i^L, \qquad i = 1, \ldots, n \\ & w_i^L \geq 0, \qquad i = 1, \ldots, n \end{aligned} \tag{20.2}$$

Priority vectors, which are obtained by employing modified FLLSM, for seven energy alternatives with respect to sustainability criteria, are given in Table 20.2.

20.3.4 Step 4: Calculate Local and Global Fuzzy Weights by Employing Modified FLLSM

Global fuzzy weights can be obtained by solving two linear programming models and an equation for each decision alternative $A_k (k = 1,\ldots, K)$:

Table 20.2 Priority vectors for energy alternatives with respect to sustainability

Energy alternatives	Priority vector modified FLLSM
Hydropower energy	(0.1226, 0.1448, 0.1726)
Solar energy	(0.0901, 0.1034, 0.1195)
Wind energy	(0.0861, 0.0989, 0.1156)
Fossil (coal) energy	(0.0889, 0.1072, 0.1289)
Natural gas energy	(0.0949, 0.1149, 0.1381)
Nuclear energy	(0.2416, 0.3069, 0.3653)
Petroleum energy	(0.1040, 0.1234, 0.1452)

Table 20.3 Local weights with respect to social factors

	Job opportunities	Social acceptance	Local weights
Weight	(0.6125, 0.5360, 0.4639)	(0.5360, 0.4640, 0.3874)	
Hydropower energy	(0.0672, 0.0565, 0.0497)	(0.2070, 0.1784, 0.1498)	(0.0885, 0.1131, 0.1422)
Solar energy	(0.0303, 0.0255, 0.0235)	(0.2198, 0.1951, 0.1714)	(0.0808, 0.1042, 0.1319)
Wind energy	(0.0388, 0.0334, 0.0311)	(0.2751, 0.2520, 0.2246)	(0.1061, 0.1348, 0.1655)
Fossil (coal) energy	(0.2307, 0.2024, 0.1747)	(0.0935, 0.0802, 0.0687)	(0.1179, 0.1457, 0.1775)
Natural gas energy	(0.3147, 0.2788, 0.2369)	(0.1644, 0.1434, 0.1221)	(0.1754, 0.2160, 0.2565)
Nuclear energy	(0.1140, 0.0955, 0.0813)	(0.0423, 0.0357, 0.0315)	(0.0546, 0.0678, 0.0862)
Petroleum energy	(0.3431, 0.3079, 0.2640)	(0.1281, 0.1152, 0.1015)	(0.1769, 0.2185, 0.2598)

$$w_{A_k}^L = \underset{W \in \Omega w}{\text{Min}} \sum_{j=1}^{m} w_{kj}^L w_j \quad k = 1, \ldots, K \tag{20.3}$$

$$w_{A_k}^U = \underset{W \in \Omega w}{\text{Max}} \sum_{j=1}^{m} w_{kj}^U w_j \; k = 1, \ldots, K \tag{20.4}$$

$$w_{A_k}^M = \sum_{j=1}^{m} w_{kj}^M w_j^M, k = 1, \ldots, K \tag{20.5}$$

where $\Omega_W = \left\{ W = (w_1, \ldots, w_m)^T | w_j^L \le w_j \le w_j^U, \; \sum_{j=1}^{m} w_j^m, j = 1, \ldots, m \right\}$ is the space of weights, $\left(w_j^L, w_j^M, w_j^U\right)$ is the normalized triangular fuzzy weight of criterion j ($j = 1, \ldots, m$), and $\left(w_{kj}^L, w_{kj}^M, w_{kj}^U\right)$ is the normalized triangular fuzzy weight of alternative A_k with respect to criterion j ($k = 1, \ldots, K$; $j = 1, \ldots, m$). Computed local weights of seven energy alternatives with respect to social factors are illustrated in Table 20.3. Furthermore, calculated global weights are also presented in Table 20.4.

20.3.5 Step 5: Rank Energy Alternatives by Using Sign Distance Method

In this step global weights, which are fuzzy triangular numbers, of each energy investment alternative are ordered by using sign distance method. To rank fuzzy

Table 20.4 Global weights of energy alternatives with respect to the goal

	Technological	Environmental	Social	Economical	Strategic	Global weights
Weight	(0.110,0.096,0.087)	(0.540,0.499,0.438)	(0.121,0.104,0.092)	(0.110,0.096,0.087)	(0.218,0.204,0.192)	
Hydropower	(0.151,0.180,0.21)	(0.088,0.099,0.114)	(0.088,0.113,0.142)	(0.186,0.217,0.248)	(0.191,0.221,0.249)	(0.122,0.144,0.172)
Solar	(0.156,0.184,0.21)	(0.081,0.089,0.098)	(0.080,0.104,0.131)	(0.078,0.087,0.098)	(0.094,0.107,0.126)	(0.090,0.103,0.119)
Wind	(0.164,0.184,0.2)	(0.072,0.078,0.084)	(0.106,0.134,0.165)	(0.077,0.088,0.101)	(0.083,0.096,0.114)	(0.086,0.099,0.115)
Coal	(0.069,0.078,0.089)	(0.101,0.118,0.137)	(0.117,0.145,0.177)	(0.069,0.082,0.096)	(0.070,0.085,0.108)	(0.089,0.107,0.129)
Natural gas	(0.094,0.108,0.124)	(0.091,0.109,0.128)	(0.175,0.216,0.256)	(0.138,0.161,0.182)	(0.051,0.058,0.067)	(0.095,0.115,0.138)
Nuclear	(0.147,0.177,0.211)	(0.299,0.37, 0.435)	(0.054,0.067,0.086)	(0.205,0.234,0.259)	(0.296,0.368,0.419)	(0.241,0.307,0.365)
Petroleum	(0.077,0.086,0.096)	(0.118,0.134,0.152)	(0.176,0.218,0.259)	(0.111,0.128,0.146)	(0.053,0.062,0.075)	(0.104,0.123,0.145)

numbers, several different strategies were used. Each of these techniques has been shown to produce nonintuitive results in some instances.

In this chapter, to cope with the weaknesses of the previous techniques, sign distance approach was used [21]. This method is based on a modification of the distance. The trapezoidal fuzzy number $u = (x_0, y_0, \sigma, \beta)$ with two defuzzifiers x_0 and y_0, left fuzziness $\sigma > 0$, and the right fuzziness $\beta > 0$ is a fuzzy set where the membership function is as:

$$u(x) = \begin{cases} \frac{1}{\sigma}(x - x_0 + \sigma) & if\ x_0 - \sigma \le x \le x_0 \\ 1 & if\ x \in [x_0, y_0] \\ \frac{1}{\beta}(y_0 - x + \beta) & if\ y_0 - \sigma \le x \le y_0 + \beta \\ 0 & \text{otherwise} \end{cases} \tag{20.6}$$

and its parametric for

$$\underline{u}(r) = x_0 - \sigma + \sigma r, \bar{u}(r) = y_0 + \beta - \beta_r \tag{20.7}$$

For arbitrary fuzzy numbers $u = (\underline{u}, \bar{u})$ and $v = (\underline{v}, \bar{v})$, the function

$$D_p(u, v) = \left[\int_0^1 \left| \underline{u}(r) - \underline{v}(r) \right|^P dr + \int_0^1 \left| \bar{u}(r) - \bar{v}(r) \right|^P dr \right]^{1/P}, (p \ge 1) \tag{20.8}$$

is the distance between u and v. If u_0 is considered as fuzzy origin, then left fuzziness σ and right fuzziness β become 0. As a consequence:

$$D_p(u, u_0) = \int_0^1 \left| \underline{u}(r) \right|^P dr + \int_0^1 \left| \bar{u}(r) \right|^P dr \tag{20.9}$$

Finally, sign distance is defined as follows:

$$d_p(u, u_0) = \gamma(u)\ D_p(u, u_0) \tag{20.10}$$

where

$$\gamma(u) = \begin{cases} 1 & \text{if sign } \int_0^1 \left(\underline{u} + \bar{u} \right)(r) dr \ge 0 \\ -1 & \text{if sign } \int_0^1 \left(\underline{u} + \bar{u} \right)(r) dr < 0 \end{cases} \tag{20.11}$$

As a conclusion, for any two trapezoidal fuzzy numbers u and $v \in E$ (E stands the set of fuzzy numbers), it is defined the ranking of u and v by the d_p on E as follows:

$$\begin{aligned} &d_p(u, u_0) > d_p(v, u_0) \text{ if and only if } u \succ v, \\ &d_p(u, u_0) < d_p(v, u_0) \text{ if and only if } u \prec v, \\ &d_p(u, u_0) = d_p(v, u_0) \text{ if and only if } u \sim v \end{aligned} \tag{20.12}$$

Table 20.5 Sign distance values and rankings of energy alternatives

Alternative	Sign distance value	Rank
Hydropower energy	0.1875	2
Solar energy	0.1361	6
Wind energy	0.1297	7
Fossil (coal) energy	0.1378	5
Natural gas energy	0.1476	4
Nuclear energy	0.3913	1
Petroleum energy	0.1603	3

Table 20.5 summarizes calculated sign distances ($p = 2$) for each energy alternatives and presents their ranking. Based on Table 20.5, the "nuclear energy," which $dp\ (u, u_0)$ value is the greatest, is determined as the best investment alternative for Turkey. The ranking of energy investment alternative is evaluated as follows: nuclear energy, hydropower energy, petroleum energy, natural gas energy, fossil (coal) energy, solar energy, and wind energy.

20.4 Sensitivity Analysis

Due to dynamic nature of the decision environment in the real-life situation, it is essential to equip the proposed model with the capability to distinguish changes in the problem parameters. Therefore, an essential step in many applications of FMCDM is to perform a sensitivity analysis on the weight of the decision factors. In this section of the proposed methodology, different scenarios are tested by changing the weights of five primary factors and calculating global weights of alternatives to analyze the performance of each energy alternatives in non-static settings.

The idea of sensitivity analysis is to exchange each criterion's weight with another criterion's weight, so ten different calculations are formed. Sign distance values (d_p) are calculated for each exchange and different names are given for each exchange. For example, d^{12} means criterion 1 (technological)'s and criterion 2 (environmental)'s weights have changed, and d^{34} means criterion 3 (social)'s and criterion 4 (economical)'s weights have changed. Figure 20.4 summarizes new d_p values of the alternatives on the graph. Also, Table 20.6 presents new d_p values. Fig. 20.4 and Table 20.6 show that nuclear energy is the best alternative in all of the cases considered. In the scenario d^{23}, when weights of environmental and social factors change, hydropower, natural gas, and petroleum investment options become very competitive rivals for nuclear energy.

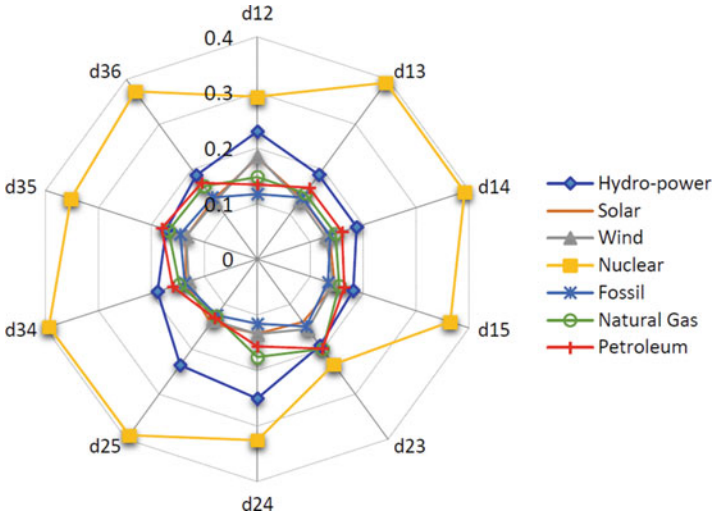

Fig. 20.4 Ranking of alternatives under different scenarios

Table 20.6 New sign distance values after sensitivity analysis

	Hydropower	Solar	Wind	Fossil	Natural gas	Nuclear	Petroleum
d^{12}	0.2299	0.1828	0.1856	0.1174	0.1481	0.2920	0.1345
d^{13}	0.1881	0.1362	0.1302	0.1371	0.1467	0.3926	0.1590
d^{14}	0.1875	0.1361	0.1297	0.1378	0.1476	0.3913	0.1603
d^{15}	0.1812	0.1463	0.1429	0.1337	0.1548	0.3642	0.1641
d^{23}	0.1918	0.1395	0.1550	0.1493	0.1995	0.2339	0.1987
d^{24}	0.2504	0.1341	0.1343	0.1161	0.1760	0.3256	0.1568
d^{25}	0.2354	0.1418	0.1356	0.1242	0.1270	0.3916	0.1305
d^{34}	0.1885	0.1354	0.1293	0.1371	0.1472	0.3934	0.1596
d^{35}	0.1722	0.1344	0.1343	0.1455	0.1678	0.3522	0.1803
d^{36}	0.1868	0.1329	0.1288	0.1376	0.1624	0.3731	0.1700

20.5 Conclusions

Today, increase in the population and dependency on depleting fossil fuels necessitates the utilization of alternative sources carefully and wisely. Therefore, to investigate the best energy investment alternative for countries becomes a difficult task for policy- and decision-makers. Selecting the best from various energy investment alternatives requires that different groups of decision-makers become involved in the process. In that sense, taking into consideration social, economic, technological, and environmental factors in decision-making makes the process somewhat complicating.

In this chapter, for evaluation of energy alternatives and selecting the best case, Delphi integrated fuzzy multi-criteria decision-making methodology is utilized. Following this approach, the chapter is finalized with sensitivity analysis. Analysis results indicated that among the suggested energy alternatives, nuclear energy appeared as the most feasible and appropriate solution. The results also showed that hydropower is the second best alternative after nuclear power. Having a higher rank through other renewables agrees with Atilgan and Azapagic [22]. Hydropower is a domestic energy resource and existing hydropower potential has not been fully exploited. Unexpectedly, wind energy and solar power have received lower ranks compared to other alternatives. There is still a long way to go because the existing infrastructures, legal arrangements, and incentive schemes are not yet sufficient enough to support the massive quantities of solar and wind energy investments.

Acknowledgments This article is the extended version of the earlier work of Turan et al. published in the 9th International Exergy, Energy and Environment Symposium (IEEES-9) Proceedings book with title the *Utilisation of Fuzzy Multicriteria Method for Selection of Energy Alternatives for Turkey* [23].

References

1. International Energy Agency, Key world energy statistics (2007) website http://892www.iea.org/textbase/nppdf/free/2007/key_stats_2007.pdf, (2008)
2. Kahraman C, Kaya I (2010) A fuzzy multi criteria methodology for selection among energy alternatives. Expert Syst Appl 37(9):6270–6281
3. Beccali M, Cellura M, Mistretta M (2003) Decision making in energy planning: application of the ELECTRE method at regional level for the diffusion of renewable energy technology. Renew Energy 28:2063–2087
4. Burton J, Hubacek K (2007) Is small beautiful? A multicriteria assessment of small-scale energy technology applications in local governments. Energy Policy 35(12):6402–6412
5. Stagl S (2006) Multicriteria evaluation and public participation: the case of UK energy policy. Land Use Policy 23(1):53–62
6. Diakoulaki D, Georgiou P, Tourkolias C, Georgopoulou E, Lalas D, Mirasgedis S, Sarafidis Y (2007) A multicriteria approach to identify investment opportunities for the exploitation of the clean development mechanism. Energy Policy 35(2):1088–1099
7. Kowalski K, Stagl S, Madlener R, Omann I (2009) Sustainable energy futures: methodological challenges in combining scenarios and participatory multi-criteria analysis. Eur J Oper Res 197 (3):1063–1074
8. Begic F, Afgan NH (2007) Sustainability assessment tool for the decision making in selection of energy system – Bosnian case. Energy 32:1979–1985
9. Aragones BP, Chaparro GF, Pastor FJP, Rodriguez PF (2010) An ANP-based approach for the selection of photovoltaic solar power plant investment projects. Renew Sust Energy Rev 14 (1):249–264
10. San CJR (2011) Multi-criteria decision-making in the selection of a renewable energy project in Spain: the Vikor method. Renew Energy 36(2):498–502
11. Cavallaro F, Ciraolo L (2005) A multicriteria approach to evaluate wind energy plants on an Italian Island. Energy Policy 33:235–244
12. Haralambopoulos DA, Polatidis H (2003) Renewable energy projects: structuring a multicriteria group decision-making framework. Renew Energy 28(6):961–973

13. Kaya T, Kahraman C (2011) Multicriteria decision making in energy planning using a modified fuzzy TOPSIS methodology. Expert Syst Appl 38(6):6577–6585
14. Kaya T, Kahraman C (2010) Multicriteria renewable energy planning using an integrated fuzzy VIKOR & AHP methodology: the case of Istanbul. Energy 35(6):2517–2527
15. Kahraman C, Kaya ˙I, Cebi S (2009) A comparative analysis for multiattribute selection among renewable energy alternatives using fuzzy axiomatic design and fuzzy analytic hierarchy process. Energy 34(10):1603–1616
16. Zadeh L (1965) Fuzzy sets. Inf Control 8(3):338–353
17. Kwiesielewicz M (1996) The logarithmic least squares and the generalized pseudoinverse in estimating ratios. Eur J Oper Res 93(3):611–619
18. Wang YM, Elhag TMS, Hua Z (2006) A modified fuzzy logarithmic least squares method for fuzzy analytic hierarchy process. Fuzzy Sets Syst 157(23):3055–3071
19. Sung WC (2001) Application of Delphi method, a qualitative and quantitative analysis, to the health care management. J Healthc Manag 2(2):11–19
20. Changa CW, Wub CR, Linc HL (2009) Applying fuzzy hierarchy multiple attributes to construct an expert decision making process. Expert Syst Appl 36(4):7363–7368
21. Abbasbandy S, Asady B (2006) Ranking of fuzzy numbers by sign distance. Inf Sci 176 (16):2405–2416
22. Atilgan B, Azapagic A (2016) Renewable electricity in Turkey: life cycle environmental impacts. Renew Energy 89:649–657
23. Turan HH, Erbiyik H, Unver U (2017) Utilisation of fuzzy multicriteria method for selection of energy alternatives for Turkey, The 9th international exergy, energy and environment symposium (IEEES-9), pp 407–414

Chapter 21
Impact Assessment of Sustainable Mobility in Touristic Cities of Europe: The CIVITAS DESTINATIONS Approach on Energy, Environment and Economy

Stavroula Tournaki, Eleni Farmaki, and Theocharis Tsoutsos

21.1 Introduction

The International Energy Agency estimates that 28% of global primary energy consumption and around 25% of CO_2 emissions can be attributed exclusively to the transport sector [1]. Meanwhile, the European transport sector contributes to nearly one-third of the CO_2 emissions, and despite the economic downturn, the ongoing vehicle technology and the promotion of clean fuels, transport is the only major sector with an increased rate of emissions over the last decade [2]. Road transport accounts for approximately 73% of the total transport greenhouse gas (GHG) emissions in the EU and nearly two-thirds of road transport emissions originate from light-duty vehicles, while the remaining one-third originates from heavy-duty vehicles [3]. Besides the extensive GHG emissions and impact on climate change, transport is also responsible for the emissions of noxious air pollutants which are proven to have serious implications for human health [4]. Thousands of deaths annually can be attributed to road transport-related air pollution, almost equivalent to the deaths from road accidents [5], highlighting further the need for action.

According to the European Commission [6], the EU needs to reduce the GHG emissions by 40% below 1990 levels by 2030 and by 80–95% by 2050. Transport will contribute to the goals by reducing its GHG emissions below 1990 levels by 60% by 2050 [7]. In order to achieve these goals, the European Commission has set as a priority pillar the reduction of energy consumption in the transportation sector,

S. Tournaki · E. Farmaki · T. Tsoutsos (✉)
Technical University of Crete, School of Environmental Engineering, Renewable and Sustainable Energy Systems Laboratory, Chania, Greece
e-mail: theocharis.tsoutsos@enveng.tuc.gr

S. Nižetić, A. Papadopoulos (eds.), *The Role of Exergy in Energy and the Environment*, Green Energy and Technology,
https://doi.org/10.1007/978-3-319-89845-2_21

which is set in national/regional and European environmental policies and is reflected in the Paris Agreement on climate change commitments [8].

Cities hold a key part in achieving these goals since they attract the biggest part of the population and drive economic growth, but they can also drive the change towards sustainability. Many metropolitan or fast-growing cities are focusing on more green spaces, better environmental quality, innovative energy-efficient technologies, clean transportation and increased quality of life [9]. While embracing the vision towards sustainable urban development, urban planners and public authorities realise the key role of the transportation sector and acknowledge the potential for significant social, environmental and economic benefits towards sustainability [10].

The CIVITAS DESTINATIONS is one of the CIVITAS demonstration projects funded by the European Commission within the framework of the Horizon 2020 programme. It is the first one to take into account the connection of mobility and tourism, aiming to provide mutually reinforcing innovative mobility solutions for residents and tourists and to improve the urban environment at six demonstration areas. It will now provide a refined assessment framework in order to evaluate the impacts of the mobility measures in touristic island cities.

The scope of this study is to present an environmental assessment framework, which is developed to evaluate the impacts of proposed measures at city, region and project level. More specifically, it outlines the case of the Rethymno, one of the project demonstration areas which will adopt a set of innovative mobility solutions. Rethymno's case is used to demonstrate the environmental assessment framework by indicating the suitable evaluation indicators according to the specific measures under implementation, in terms of energy and sustainability.

21.2 Demonstration Area

21.2.1 Description of Rethymno Municipality

Rethymno municipality is located in Southern Greece, in the island of Crete (Fig. 21.1). It was established in 2011 by the unification of four pre-existing municipalities, covering an area of 397,48 km^2. The city of Rethymno is the municipality's seat and the 3rd largest city of Crete. During the last decade, the population increased by 17% and currently reached a total of 55.525 inhabitants, while 32.468 inhabitants live in Rethymno city. The rest of the population lives in surrounding settlements, daily commuting from and to the city. Tourism contributes significantly to the growth of the local economy. Rethymno's central location, numerous archaeological sites, historic monuments, spectacular beaches, traditional villages, cultural events and famous gastronomy construct a very appealing touristic destination, which attracts more than 1 million visitors and accommodates more than half a million tourists annually.

Rethymno has a strong vision towards sustainability and is a member of the Covenant of Mayors' initiative since 2011. Sustainable mobility is one of the main

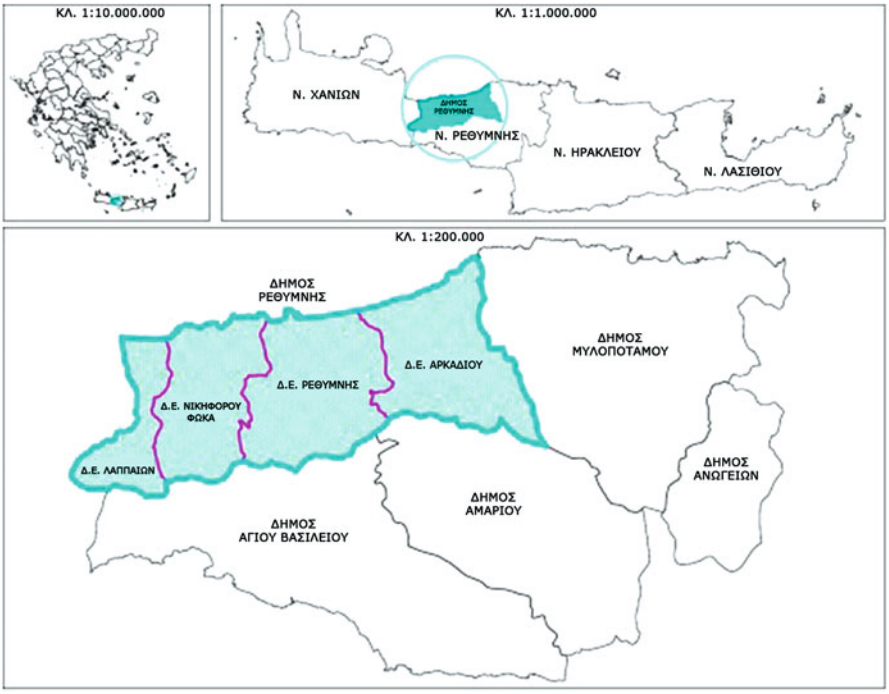

Fig. 21.1 The location of the municipality of Rethymno within Greece

Table 21.1 Fuel, energy use and CO_2 emissions of the municipal fleet (2012)

Type of vehicle	Main type of fuel	Energy use (MWh)	CO2 emissions (tons)
Vehicles	Diesel gasoline (unleaded)	3.134,09	810,73
Motor wheeled	Diesel	276,63	71,65
Non-motor wheeled	Diesel	9,02	2,34
Total	–	3.419,74	884,82

priorities of the municipal Sustainable Energy Action Plan (SEAP), which has been approved by the EU and is currently in the implementation phase.

The Rethymno's SEAP included the most recent data regarding the city's energy profile. To provide an overview of the transport sector, the energy consumption and the corresponding CO_2 emissions per vehicle type of the municipal transportation system are presented in Table 21.1. According to SEAP, the annual energy consumption and CO_2 emissions of the municipal vehicle fleet correspond to 3,4 GWh and 884 tons CO_2, respectively [11]. However, the energy use of the SEAP transport sector does not take into account the private vehicle fleet due to the unavailability of data; thus, the consumption appears to be lower than the actual.

The public transport and mobility services of the municipality have to cope with a significant additional load of commuters during the 7-month touristic period. From

April to October, the municipality population is dramatically enlarged, while almost a million visitors stay or pass through the municipality annually. The identified mobility patterns of residents and tourists are very similar since both groups strongly prefer private vehicles over alternative mobility modes for their daily trips. Public buses are mostly preferred by specific population groups, while bicycle use is slightly increasing lately, due to the enlargement of the existing city's bicycle path network. During the peak season, the public buses are not able to cover the extended transportation needs, while the insufficient links between public transport services with the main attractions and the cycling and walking networks make alternative transport modes less appealing for tourists and citizens. Under these circumstances, private vehicles became the dominant option for convenient transportation.

The intense use of cars and the significant tourist influx result in many problems in the city's traffic. Especially in the peak season, the city's transportation is characterised by heavy congestion, lack of parking spaces, noise pollution, increased energy consumption and air pollution. Rethymno aims to address the local needs and mobility-related problems and to upgrade specific transportation services. The city's priorities also include the enhancement of citizen involvement, behavioural change, environmental and economic development, energy use, social cohesion, health and safety and land use.

21.2.2 Sustainable Mobility Measures in the City of Rethymno

In the frame of the CIVITAS DESTINATIONS, Rethymno municipality has planned to upgrade its SUMP integrating the interregional mobility and the tourist needs, including the implementation of a set of tailored mobility measures.

The demonstration measures are briefly presented below:

- M1: Sustainable Urban Mobility Plan (SUMP) Integrating Tourist Mobility. Rethymno will revise the existing SUMP in order to combine the needs of visitors and residents alike and to address the transportation problems and the impact of tourist inflow on the transport infrastructure within the prefecture area. To successfully set a strong strategy for the demonstration measures and future planning, a SUMP observatory will be operated to monitor the social, economic and environmental aspects of local mobility.
- M2: Smart systems for urban planners, PT operators and users. This measure involves the operation of IT systems/smart applications and an online platform to monitor the mobility services and analyses mobility patterns, traffic load, PT use, the user's feedback and environmental indicators. The analysis of data will be used for the improvement of transportation services.
- M3: Active, healthy and inclusive mobility for all. This action will expand the city's cycling networks, reallocate road space, efficiently link PT transportation with cycling and walking and promote the "car-free life" lifestyle. To further

increase accessibility, Rethymno will improve the infrastructure, equipment and transport services for disabled people.

- M4: Mobility plan for schools/University. This measure will address the traffic congestion surrounding schools and increase safety by creating efficient mobility plans for schools and the University and improved PT routes and infrastructure. Awareness campaigns targeting younger citizens will reinforce the modal shift towards alternative mobility.
- M5: Uptake of electric vehicles by fleet operators. Rethymno plans to install the first EV charging points to introduce infrastructure for electric mobility. The measure will give incentives to fleet operators in order to propel demand for EVs and reduce pollution.
- M6: Building a sharing mobility culture. It consists of actions to drive behavioural change of citizens towards sharing mobility modes, aiming to take unnecessary car journeys off the road by reducing single occupancy vehicles. The development of a web-based platform to facilitate sharing of means and the optimisation of the existing bike-sharing system and infrastructure are foreseen.
- M7: Sustainable Urban Logistics Plan (SULP). This measure will establish a unified freight delivery system in the historic centre and will develop a Freight Logistics Plan with an emphasis on logistics management in key areas. The optimised freight distribution will decrease traffic congestion, noise and air pollution.
- M8: Cooperative mobility on a UCO-to-biodiesel transformation chain. This measure aims to set up a business model to operate locally the UCO-to-biodiesel chain. It includes expansion of the existing UCO collection network with smart containers, a demonstration project with an urban waste collection truck running on UCO biodiesel and the engagement of the HORECA industry and citizens to increase UCO collection.
- M9: New products and services combining tourism and mobility. Rethymno will develop an online platform for promoting sustainable mobility plans and launch a sustainable mobility information hub to promote alternative mobility modes to visitors, aiming to achieve a modal shift towards cycling, walking and PT.
- M10: Introducing electric vehicles for PT. Rethymno will introduce clean vehicles in the municipal fleet, through the launch of the first electric car in the public fleet and the first electric mini bus to serve a new route of high touristic interest. This measure will decrease private car circulation and reduce pollutant emissions and noise.
- M11: Improved PT for tourists and citizens. The measure includes the upgrade of PT services with rescheduled PT plans, the operation of new PT routes, “smart” bus stops and attractive info packages. By improving the PT services, Rethymno aims to increase PT users, avoid increased circulation of rental cars during the peak months and reduce air pollution

21.3 Environmental Assessment of CIVITAS Projects

Many urban areas hesitate to implement innovative solutions because of the limited information available on their effectiveness and due to insufficient expertise and guidance for a successful implementation. As a result, transport-related problems are conserved, while new technologies and emerging solutions are not taken up at the necessary scale. Acknowledging this challenge, the CIVITAS initiative incorporated the impact evaluation of the demonstrated measures during the implementation process into the core of CIVITAS objectives. One of the key priorities is to establish and to apply an efficient methodological framework to assess the impacts and processes of all CIVITAS demonstration actions.

Over the years, the evaluation framework is constantly improved, in order to correspond efficiently to the different needs and objectives of the demonstration projects and to be applicable in all involved cities. The first project to compile the evaluation framework was CIVITAS METEOR in 2002, and since then, the projects GUARD, POINTER and WIKI undertook the further elaboration of the framework. This work continues in the frame of the CIVITAS SATELLITE, which is currently developing the CIVITAS impact and process evaluation framework aiming to provide an optimised evaluation framework to be applied to future CIVITAS2020 projects. The framework aspires for the efficient and consistent evaluation of economic, societal and environmental impacts of different mobility demonstration measures. Thus, SATELLITE works for the definition of appropriate monitoring indicators and scenarios and the development of practical guidelines to be adjusted accordingly by the demonstration projects.

An important element of the framework in terms of environment, energy and economy is the identification of the appropriate indicators to clearly monitor the impact of the implemented measures and to provide significant insights regarding the effectiveness of the measures under the various implementation conditions. Within this scope, TUC introduced also new indicators to properly evaluate the demonstration measures, taking into account the new technologies involved and the tourism-related approach.

The framework is formulated with simplicity, in order to provide an extensive set of indicators to the sites, but also to allow the Local Evaluation Managers to select the most suitable indicators for their case, according to the local strategy. These indicators are not uniquely connected to a specific measure, but they reflect the overall DESTINATIONS project implementation, and they help to get the baseline and the environmental implications of the various measures in the city. The broader list of indicators is provided along with structured guidelines for data collection and calculation tools, so common measurement and monitoring methods are adopted by all demonstration sites. This approach will allow a valid comparison not only between measures but also between cities and finally provide a consistent analysis in project level. Figure 21.2 presents the steps taken for the environmental assessment framework development.

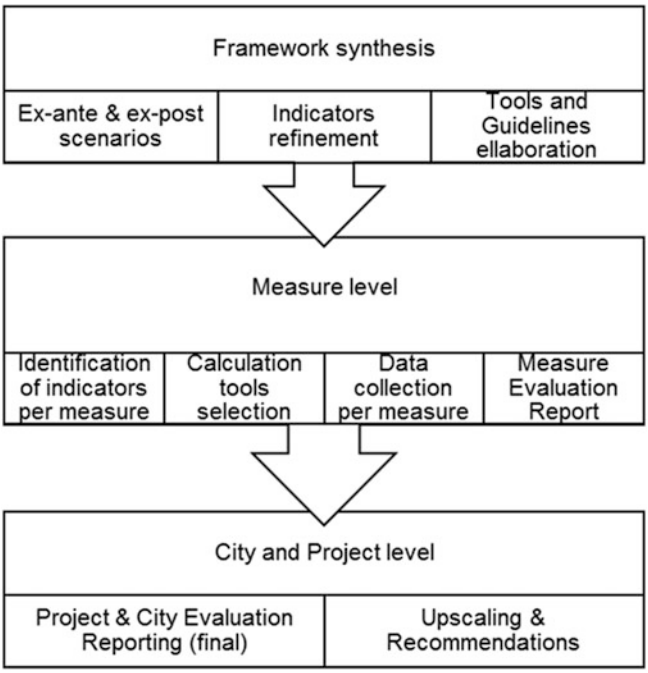

Fig. 21.2 Development steps of the environmental assessment framework

21.4 Refined Environmental Assessment Framework

The CIVITAS DESTINATIONS assessment methodology integrates the approach of CIVITAS SATELLITE and forms a measure based evaluation process, in order to evaluate the individual impact of each measure.

All the measures are going to be evaluated within the project. The methodology is formulated with simplicity to allow local managers without a technical background to apply the framework to their city's measures and to facilitate the future dissemination of outcomes and lessons learned to other European cities with urban mobility challenges.

The first step of the framework process is to define examined scenarios. The ex ante and ex post evaluations are essential for the assessment of the indicators before and after the implementation of measures in order to track the progress. In addition, a business as usual scenario will be estimated to identify the actual impact of the measure, by excluding the possible effects of external factors. Calculating and assessing the evolution of the impacts will define the elements that affect the environmental outcome of the measures. The second step is the refinement of indicators and the development of a framework that corresponds completely to the specific DESTINATIONS measures.

Table 21.2 DESTINATIONS environmental assessment indicators

Environmental indicator	Units	Source
CO_2 emissions	t/a saved emissions of CO_2 g/vkm	SATELLITE
CO emissions	t/a saved emissions of CO g/vkm	SATELLITE
NO_x emissions	t/a saved emissions of NO_x g/vkm	SATELLITE
VOC emissions	t/a saved emissions of HC g/vkm	TUC
Particulate matter emissions	t/a saved emissions of air particulates g/vkm	SATELLITE
CO_2 levels	g/m^3, total and per resident % drop compared to 1990 level	TUC
CO levels	g/m^3, total and per resident	SATELLITE
NO_x levels	g/m^3, total and per resident	SATELLITE
VOC levels	g/m^3, total and per resident	TUC
Particulate matter levels	$\mu g/m^3$, total and per resident	SATELLITE
Noise perception	% of people troubled by transport noise	SATELLITE
Vehicle fuel efficiency	MJ/km, fuel used per vkm, per vehicle type (annual average)	SATELLITE
Fuel mix	% of fuel used by vehicle type	SATELLITE
Used cooking oil collection	UCO litres collected per capita annually	TUC

The indicators forming the environmental assessment framework are presented in Table 21.2, by source.

21.4.1 Calculation Tools and Guidelines

The following section provides the calculation tools and data collection guidelines for the indicators.

Vehicle fuel efficiency is defined as the energy consumption per unit of transport activity, and, thus, every mode of transport has specific energy efficiency, according to vehicle type and fuel type. The formula to calculate measure-related vehicle fuel efficiency is presented below.

$$\mathrm{FE} = \frac{\sum_{j=1}^{j}\left(\sum_{m=1}^{m}\left(B_{jm}\cdot C_{ijm}\cdot D_{m}\right)\right)}{\sum_{j=1}^{j}\left(\sum_{m=1}^{m}\left(B_{jm}\right)\right)} \tag{21.1}$$

where:

FE: Vehicle fuel efficiency (MJ/km)
B: Total vehicle-kilometres driven by vehicle category *j* using fuel *m* (km)
C: Fuel consumption rate of vehicle category *j* using fuel *m* (g/km)
D: Energy density of fuel *m* (MJ/g)

Vehicle fuel efficiency calculation involves a variety of vehicles and fuel types and that can be challenging. Data should be obtained from fleet operators.

Fuel mix per vehicle type represents the share (%) of transport fuel for each type of fuel for every vehicle during the examined period. The calculation can be made per vehicle type. The calculation will be made for the PT, but it can also extend to private vehicles. In the case of PT, the PT operator should be advised to keep a record of fuel volume consumed and vkm.

Emissions of CO_2, CO, NO_x, VOC and PM indicators correspond to emissions saved (avoided) in tonnes and will be derived according to each measure separately. Saved emissions are calculated by the following formula:

$$A_i = \sum_{j=0}^{j} \left(\sum_{m=0}^{m} \left(B_{jm} \cdot C_{ijm} \cdot D_{jm} \cdot 10^{-9} \right) \right) \tag{21.2}$$

where

A: Total emissions of pollutant i saved (tonnes)
B: Total vehicle-kilometres avoided of vehicle category j using fuel m (km)
C: Pollutant i emission factor for vehicle category j using fuel m (g/kg fuel)
D: Fuel consumption rate of vehicle category j using fuel m (g/km)

Pollutant i correspond to CO_2 or CO or NO_x or particulate matter (PM) or volatile organic compounds (VOC). The factor 10^{-9} is used to convert grams of fuel consumption to kg and grams of pollutant emissions saved to tons. The calculation requires the exact vkm avoided by the implementation of the measure and the appropriate emission factors for each vehicle category. The framework provides a set of the required emission factors per vehicle category [12], but the local manager can also use alternative emission factors if considered more appropriate.

Additionally, in each city, monitoring stations with integrated sensors will be used for the measurements of CO_2, CO, NO_x, VOC and PM levels. The measurements will be continual and will correspond to real-time values for one or multiple air pollutants.

The noise perception indicator will be monitored by questionnaire surveys that will follow a certain structure. The assessment will be based on levels of satisfaction and will include both daytime and night-time conditions. In addition to the surveys, the local manager can also install an inexpensive sound sensor in the monitoring stations that will monitor the noise levels.

The "used cooking oil (UCO) collection" indicator presents the progress of the collected UCO in litres per resident annually in the measure demonstration area. A UCO collection system was already demonstrated by TUC and Rethymno municipality during the RecOil initiative [13], and now the existing infrastructure will be expanded to increase further the UCO collection.

21.4.2 Implementation in Measure, City and Project Level

In order to properly present the impact evaluation per measure, the city of Rethymno is demonstrated as an example. For each one of the measures described in the previous section, a set of environmental indicators has been attributed. Tables 21.3 and 21.4 present each measure with the selected indicators, in terms of energy and environmental pollution.

To achieve a full evaluation of the measures involving the UCO-to-biodiesel chain (M8) and the operation of the electric bus (M11), TUC plans to perform a life cycle assessment (LCA) analysis following a "from-cradle-to-grave" life cycle approach [14].

According to the environmental assessment framework, in each demonstration site, a local evaluation manager is designated and responsible for guiding the rest of the project members of the site for the environmental assessment. The local evaluation manager will collect the environmental indicator data every month manually.

Table 21.3 Environment related indicators per measure for Rethymno

Measures	CO_2	CO	NOx	HC	PM
M1	✓	✓	✓	✓	✓
M2					
M3[a]	✓	✓	✓	✓	✓
M4[a]					
M5[a]	✓	✓	✓	✓	✓
M6[a]	✓	✓	✓	✓	✓
M7	✓	✓	✓	✓	✓
M8[a]	✓	✓	✓	✓	✓
M9[a]	✓	✓	✓	✓	✓
M10[a]	✓	✓	✓	✓	✓
M11[a]	✓	✓	✓	✓	✓

[a]These measures use only emission indicators

Table 21.4 Noise and energy related indicators per measure for Rethymno

Measures	Noise level	Vehicle fuel efficiency	Fuel mix	UCO collection
M1	✓			
M2				
M3				
M4				
M5		✓	✓	
M6				
M7	✓	✓		
M8		✓	✓	✓
M9				
M10		✓	✓	
M11				

Although CIVITAS SATELLITE suggests data collection to be conducted once per year, DESTINATIONS requires, when possible, a more consistent data collection in a monthly base, in order to present the differences between the peak and off-peak season and provide a clear insight into mobility and environmental problems caused to the city of Rethymno.

The framework can be implemented in city or project level by some indicators that provide an overview of the progress of the measures in the area. A city and project level report, including the measure and project related data, will be compiled to present the progress of the measures and the overall impact assessment at the end of the project. The evaluation reports are substantial for the dissemination of results and lessons learned at European and at international level. By the completion of impact evaluation for each measure, the most effective and viable measures implemented will emerge. The city can request for measure upscaling, including further recommendations for the full implementation throughout the city and estimations regarding the potential impacts. The insights of such estimation will be essential, not only for the demonstration area, in our case Rethymno, but also for similar European cities that could exploit these findings when they prepare or implement similar measures.

21.4.3 Barriers and Drivers

The implementation of the proposed environmental assessment framework is developed to provide a comprehensive and thorough method for the evaluation of targeted mobility measures within the CIVITAS DESTINATIONS project. However, this approach encloses barriers that may discourage the cities during the evaluation process, but also strong drivers that result in multiple benefits.

One of the main barriers concerns the availability of the required data. Lack of data can result to a deficient baseline and undermine the comparison between the examined scenarios and the evaluation of the actual impacts. The solution, in this case, would be the preparation of the site in advance, through the installation of appropriate monitoring systems to collect data, not only as proposed by the guidelines but also for data that are essential for later calculations and currently are not recorded. As a result, the city will start building a more consistent database.

Another potential barrier that could also lead to insufficient data would be the lack of cooperation with external parties, such as the fleet operators. It is crucial for cities to engage the specific stakeholders at an early stage, by sharing their vision and goals and facilitating further cooperation.

Lack of expertise or experience of the local managers could be another possible barrier. The detailed guidelines that will be distributed before the implementation of the measures aim to prevent any difficulties during the calculations and data collection process and also increase the capacity of the local managers.

In certain cases, the impact assessment per measure may prove more challenging; however, if the cities engage completely, they will gain a high-value database,

engagement of relevant stakeholders and increased expertise and capacity. Obviously, all these elements are a great advantage in shaping future policies.

21.5 Conclusions

The DESTINATIONS project demonstrates a set of mobility solutions, combining newly emerging technologies and policy-based and soft measures with a strong replication potential to address the needs of citizens and visitors in six urban tourist areas. The evaluation of the measures' effectiveness is strongly integrated into the core of the project. Under this scope, a common impact assessment framework is developed based on the CIVITAS SATELLITE approach and adapted accordingly to the DESTINATIONS measures. In this study, the refined framework is presented with the addition of new monitoring indicators, along with practical guidance on calculation tools and data collection. The proposed framework provides the grounds to create a comprehensive assessment process that accounts for the mobility solutions that are common to all the demonstration areas. The impact evaluation is based on "before-and-after" scenarios to conduct comparisons and a common structure for surveys and other measurements required for data collection.

Amongst the identified barriers for the implementation of the framework, data unavailability appears to be the dominant one and restrict the cities from compiling a comparable baseline, but it can be overcome by installing the appropriate equipment and engaging in the process stakeholders that are essential for data collection.

In this study, Rethymno is used as an example for the implementation of the proposed framework, demonstrating the selection of the appropriate indicators per measure. The evaluation framework provides a flexible approach to cities in order to select and assess impact indicators and evaluate single actions that could define future policies. Through CIVITAS DESTINATIONS, Rethymno is expecting very promising outcomes after the implementation of the measures, in terms of air pollution and energy consumption, while in addition to the environmental goals, the overall ambition of Rethymno is to achieve a behavioural change of citizens and involved stakeholders, to improve the municipality image and functionality, to demonstrate innovative mobility solutions and to become a lighthouse example for other cities in Greece and Europe.

Nomenclature

CO_2	Carbon dioxide
CO	Carbon monoxide
EPRS	European Parliamentary Research Service
EU	European Union
GHGs	Greenhouse gas emissions
LCA	Life cycle assessment
NO_x	Nitrogen oxides
PM	Particulate matter
PT	Public transport

SEAP	Sustainable Energy Action Plan
SULP	Sustainable Urban Logistics Plan
SUMP	Sustainable Urban Mobility Plan
TUC	Technical University of Crete
UCO	Used cooking oil
VOC	Volatile organic compounds

Acknowledgements This publication is supported by the European Commission by the European Union's Horizon 2020 research and innovation programme, within the framework of the project CIVITAS DESTINATIONS. The sole responsibility for the content of this paper lies with the authors. It does not necessarily reflect the opinion of the European Union. Neither the INEA nor the European Commission is responsible for any use that may be made of the information contained therein.

References

1. IEA (International Energy Agency) (2016) Key world energy trends. Retrieved on Jan 2016, https://www.iea.org/publications/freepublications/publication/KeyWorldEnergyTrends.pdf
2. EPRS (European Parliamentary Research Service) (2016) Reducing CO_2 emissions from transport. Retrieved on Feb 2016, http://www.europarl.europa.eu/RegData/etudes/BRIE/2015/569031/EPRS_BRI(2015)569031_EN.pdf
3. European Commission (2016) EU transport in figures: statistical pocketbook. Publications Office of the European Union, Luxembourg
4. Zhang K, Batterman S (2013) Air pollution and health risks due to vehicle traffic. Sci Total Environ 450–451:307–316
5. World Health Organization (2005) Health effects of transport-related air pollution. Retrieved on Feb 2016, http://www.euro.who.int/__data/assets/pdf_file/0006/74715/E86650.pdf
6. European Commission (2013) GREEN PAPER: A 2030 framework for climate and energy policies
7. European Commission (2011) White paper: roadmap to a single european transport area – towards a competitive and resource efficient transport system. COM (2011) 144
8. European Commission (2016) Communication from the commission to the European Parliament, the Council, the European Economic and Social Committee and the Committee of the Regions, A European strategy for low-emission mobility. COM/2016/0501 final
9. Martos A, Pacheco-Torres R, Ordóñez J, Jadraque-Gago E (2016) Towards successful environmental performance of sustainable cities: intervening sectors. A review. Renew Sust Energ Rev 57:479–495
10. Barkenbus JN (2010) Eco-driving: an overlooked climate change initiative. Energy Policy 38 (2):762–769
11. Municipality of Rethymno (2012) Sustainable energy action plan. Internal document
12. EMEP/EEA (European Monitoring and Evaluation Programme/European Environment Agency) (2016) Air pollutant emission inventory guidebook 2016, Technical guidance to prepare national emission inventories. Retrieved on Jan 2016, http://www.eea.europa.eu/publications/emep-eea-guidebook-2016
13. Tsoutsos T, Tournaki S, Paraíba O, Kaminaris S (2016) The used cooking oil-to-biodiesel chain in Europe assessment of best practices and environmental performance. Renew Sust Energ Rev 54:74–83
14. Tsoutsos T, Kouloumpis V, Zafiris T, Foteinis S (2010) Life cycle assessment for biodiesel production under Greek climate conditions. J Clean Prod 18(4):328–335

Chapter 22
The Impact of Developed Energy Efficiency Model on Vessel Valuation

Murat Koray, M. Ziya Sogut, Murat Pasa Uysal, and T. Hikmet Karakoc

22.1 Introduction

The total GDP (gross domestic product) of the world in 2017 is about 77.988 trillion dollars [1]. Under normal conditions, 90% of these goods are transported by maritime trade [2]. Compared to other transportation practices, it can be said that the sector has an environmentalist structure with the emission effects per tonnage, according to environmental criteria. Within these effects, ships are also required to be examined in terms of environmental factors due to effective pollutants such as pollutants from physical wastes, chemicals, cleaning and lubrication functions. In this respect, it has developed studies for taking national and international measures based on the efficient use of energy in the sector and providing of environmental awareness [3]. For example, the International Maritime Organization (IMO) has highlighted a global approach based on the industry as a whole, for efficient use of energy and reduction of emissions. In this context, it has been planned to develop the applications of carbon footprint in the sector. However, national or international limitations, especially in global assessment and planning, have put a lot of strain on practice. Despite all these problems, the IMO continued to work on sustainable energy efficiency policies for this sector. The Energy Efficiency Design Index

M. Koray (✉)
Piri Reis University, MHVS, Istanbul, Turkey
e-mail: nmkoray@pirireis.edu.tr

M. Z. Sogut
Piri Reis University, Maritime Faculty, Istanbul, Turkey

M. P. Uysal
Baskent University, Faculty of Commercial Sciences, Ankara, Turkey

T. H. Karakoc
Anadolu University, Faculty of Aeronautic and Astronautics, Eskisehir, Turkey

S. Nižetić, A. Papadopoulos (eds.), *The Role of Exergy in Energy and the Environment*, Green Energy and Technology,
https://doi.org/10.1007/978-3-319-89845-2_22

(EEDI), the Energy Efficiency Operational Index (EEOI) and the Ship Energy Efficiency Management Plan (SEEMP) have been developed within the scope of standard works [4].

In addition to these studies, IMO has also improved in recent years on market-based measures (MBMs) based on the marine industry. In these studies, EEDI has defined a technical regulation aimed at reducing CO_2 emissions in the sector, taking into account the limitations set by the Marine Environmental Protection Committee (MEPC). Despite that, SEEMP is a plan based on the specifically improved definitions for shipowners. However, the most important point of this plan is to be mandatory of institutional energy management. In addition, SEEMP is compliant with the environmental management system (EMS) under ISO 14001 and is also directly associated with the ship's safety management system (SMS), which is implemented in ships. In this respect, it is aimed at the creation of an effective management chain of the energy system in ships with a rather complex structure [5]. However, all these developed indexes and plans should be regarded as results in a structural integrity. The important question is how the compatibility and management of these structures should be done. In other words, how these structures, especially those described in energy consumption or energy business plans, will be controlled by a sustainable model or programme [6] has developed a framework for energy-saving solutions. In this context, Energy Efficiency Design Index (EEDI) not only supports motor technologies but also supports alternative fuel usage and puts forward speed factor in design. Especially, dual fuel engine technologies have been evaluated instead of alternative fuel engine technologies in motor technologies. Along with these, many studies based on energy efficiency, low emission and sustainability can be seen in the literature [7]. However, all these studies do not provide enough information on an energy manageable architecture, especially for container ships. However, in ship management with many entrances, the entire process is directly related to energy and its management. One of the most important solutions for possible problems in decision-making process is to have an efficient and applicable energy management infrastructure. In this regard, this study presents an improved model for efficient sustainable energy management using information technologies in ships.

22.2 Modelling and Methods of Sustainable Energy Management of Ships

22.2.1 Information Systems for Sustainable Energy Management

Modern IS applications are basically shaped through an information system, and the application area allows for modelling for all structures from small to large. ISs are basically based on a process and have five components: data, hardware, software,

human and process. The structural features of information technology (IT) include hardware, software and telecommunications directly (Watson 2007; David 2014). The concepts of IT and IS are very confusing. IT stores and processes information for a process. IS is the formation of a holistic, collaborative system in which ITs, based on defined organizational or individual goals, are managed by a software. In other words, IS uses IT when it performs its functions [8].

A sustainable information system is expected to (i) comply with the environment and be capable of managing, (ii) be compatible with layers related to the data stream and (iii) be able to process data and take the implementation of the process management and efficiency into account [9]. Nowadays, ship transportation, which is developing rapidly, is a sector that uses technology effectively. In this context, although the vessels have different functions according to their intended use, the ISs have achieved a versatile use structure. ISs are basically composed of sensor network, communication network and display network. The ships need efficient energy management for their operational needs. For this reason, the modelling of energy management in ships is under the influence of sustainable ISs.

Ships are defined as complex constructions designed for different purposes. Energy systems of vessels are composed of many components and subsystems. In general, systems that require power and heat-source energy consume different energy sources to meet their needs. Energy requirements are determined in accordance with the environmental factors and legal arrangements on the routes of the ships. In this context, energy consumption of vessels is a dynamic rather than a static one. In demand management, it can be said that it requires a very complex and dynamic system structure within the scope of energy control and management. Basic components in a complex system analysis include the formation of multiple sections or units, connections and relationships, linearities or differences and occurrences [10]. Two approaches to complex structures are evaluated. One of these approaches is the local processing of each unit or part, and the other is the whole processing of all components or connections. In ships, energy systems can be assessed by a centralized management structure related to one another.

In this context, the management of the ship's energy systems can be achieved through the holistic control of all components or structures. In this case, the main components and related concepts in ship operations should be examined. In the literature, these constructions, which are defined as conceptual maps, describe system components, concepts and relations with each other [11]. Conceptual maps can be seen as an effective method in the research process. It provides a graphical presentation of all the components that are particularly interested in the problem or process being examined. It shows how these relationships and concepts have a network structure or how relations and concepts can be managed. Energy components of ships provide identification of the focus processes. When the energy system components of ships are examined, they can be defined by many components or relationships. In the energy management system, their structural relations and effects should be shaped as a structural model. In this study, conceptual models related to the energy systems of vessels and their operational relations are defined as given in Fig. 22.1.

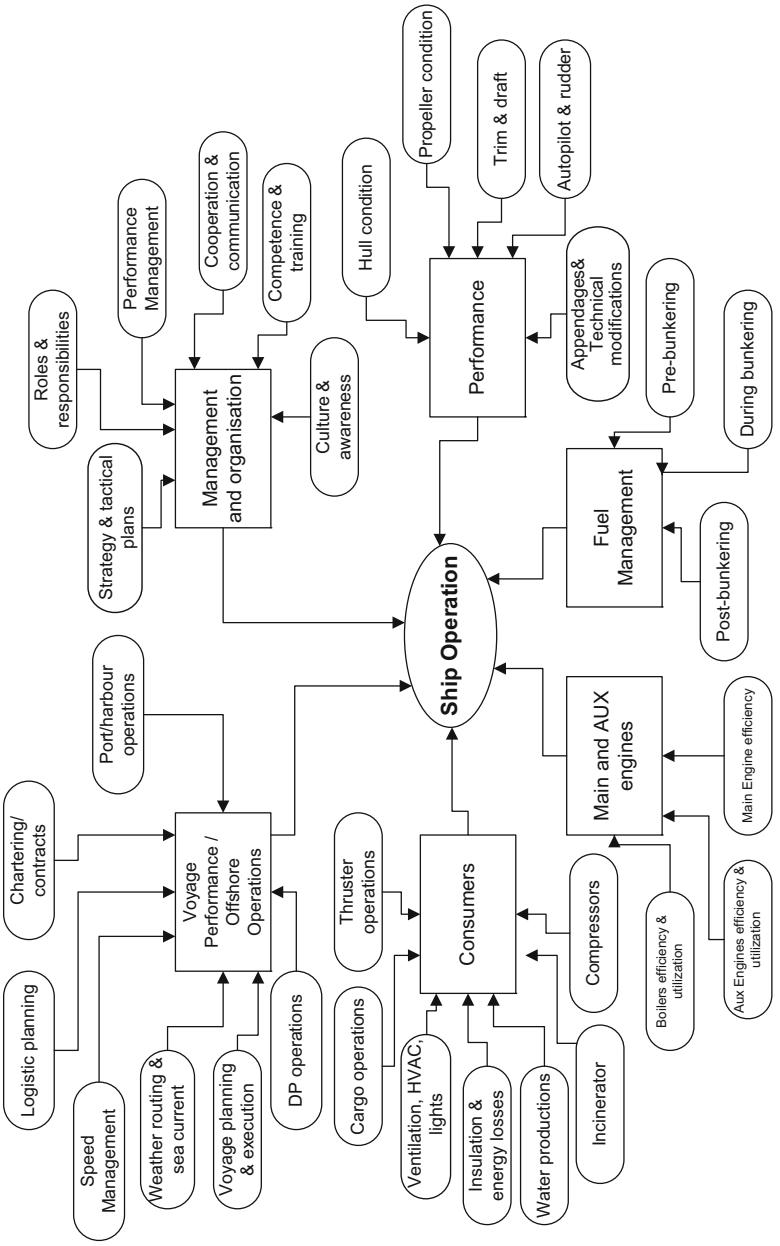

Fig. 22.1 Development of concept map for ship operation

The vessels are depending on multiple input and very complex energy systems. Effective energy management in such dispersed and complex structures requires a methodological approach. This method will ensure that all components that use energy for integrated control of the energy in ships and energy flow forms are handled in a process [12]. The energy management information system (EMIS) as a structural feature must be available for all relevant elements and be able to instantly assess performance, to manage it and to provide decision support for processes. In this study, the development of a sustainable energy information management model for container vessels engaged in international transport is primarily planned, although energy-related system components vary according to the ship's model. However, they are assessed by the provisions of the territorial waters of the country where they have passed or are in accordance with international ship operating legislation at sea. For this reason, process management can be considered as quite complex systems [13]. The first step in creating a system model for ships is the creation of the energy system components to be managed and to prepare the flow charts.

Vessels are power cycling machines as energy systems. They are systems that operate with diesel or gas turbine engines, working with petroleum-derived fuels such as diesel, gas or fuel oil. In addition to propelling power to move the ship, the electricity and heat energy consumed on board are also managed together with this system. Energy conversion systems are very varied depending on the needs of the energy plant. The cost of primary fossil-based energy consumption can also be seen as the basic energy cost of the ship [14]. In container ships, the energy system flow starts with the engine. In ships, many energy conversion processes such as power, drive, manoeuvre, heat generation, cooling, cargo transportation and storage, which define energy consumption, are the elements to be managed.

EMIS defines a holistic approach to management of complex energy consumption networks for multi-source and multi-consumption facilities such as ships. Energy management and information systems (EMIS) are software tools that store, analyse and display energy use or ship data. This is the EMIS activity; it depends on the characteristics of the building components in ships, the types of energy and usage, the definition of the criteria and consumption capacities, the effectiveness of the systems to monitor and control these consumptions, the storage volumes to which the data of the systems and analyses are collected and the operators and experts that can govern this integrity. As an administrative organization, an EMP is a collection of training and awareness, policy and strategy, EMIS, audits and analyses, project development and implementation phases [15].

22.3 Method

The creation of architectural infrastructure in information technologies for ships has been considered as a scientific research topic. This focuses on research methodologies, action research (AR) and design science research (DSR). These research

approaches are mainly based on an innovative approach to real problems [16]. These two approaches proposed in complex system solutions have a structure complementing and reinforcing each other. The operation can be basically defined by two loops. These are Cycle 1, where the architectural model is defined, and Cycle 2, where the energy performance is defined by sampling. Each cycle refers to the DSR activities defined in the design/build, evaluation and reflection processes. The theoretical process required to extract the information infrastructure and architectural template of the ship will be evaluated directly on the basis of ontological structure, energy management and information technologies and information systems. Indirectly, all these structures can be expressed in the AR and DSR paradigms, including a known solution directly in energy management processes or shaping solutions with a new problem [17].

22.3.1 Formulation of the Problem

The current business conditions of the ships, integrated modelling in energy systems, technological analysis, architecture-based integrated management programme and sustainable productivity evaluations in energy processes are not sufficient and widespread. In addition, energy management and productivity have not been used as a factor in ship valuation processes, which have gained value in the sector in recent years. In this context, this study, which we have considered as a sectoral benefit, has been defined as follows in order to shape a sustainable energy management architecture:

- The business processes, valuation criteria, applications, system components, substructures and optimizations for efficient energy management system and system efficiency in ships.
- It is defined as the realization of continuous system of control and analytical knowledge system for sustainable management processes.

22.3.2 Formulation of the Problem

Based on AR and DSR activities, a methodological infrastructure has been evaluated for the architectural structure targeted to be developed. In this context, the system design steps are given in Fig. 22.2.

Fig. 22.2 Research methodology for information architecture

22.3.3 Architectural Knowledge Base and Theory

The research structure is related to many repetitive processes. In this case, Open Group Architecture Framework (TOGAF) will be used as an effective tool for topic and repetitive processes [18]. Architectural development method (ADM), which is used as a general method in the development of architectural infrastructure, which is prominent in the study, is adapted to the needs in a structure compatible with DSR.

22.3.4 Describing Architecture Policy and Vision

In the formation of the ADM in particular, it is necessary to consider this as a process. In this context, we first assessed the feasibility of an energy management system and the suitability of these system components in ship systems.

22.3.5 Defining Basic and Target Architectural Definitions

The definition of target architecture defines the navigation processes of vessels, climatic data, policies, targets, legislation and limitations, scope and limits, energy flow patterns and transformations, system components, usage and requirement capacities, operation programmes, maintenance plans and personnel information and competences. In addition, productivity, cost-efficiency and environmental boundary conditions have also been evaluated in terms of system or business. The programme is structured as a process that evaluates the data flow in an integrated manner with all components.

22.3.6 Architectural Creation and Conclusion

In an information system architecture based on ship energy systems, priorities, scope and limits are important inputs. Greenhouse gas emission control, as defined by IMO's energy management systems, can be seen as an important target for combating climate change [19]. Based on this criterion, ship management architecture has been shaped.

In this respect, the basic architectural process is described as follows: infrastructure layer, legislation, protocols and limits, EMIS applications, analyses and data layer, EMIS process and control layer, uses and roles. In this study, the architectural structure of the enterprise is defined by considering the energy flow process of a container ship system. A sustainable management model is based on the defined architectural structure. Open Group Architecture Framework (TOGAF v.9.1) has

been combined with ontological design, development and evaluation principles to provide guidance and principles. Furthermore, EA development steps that are compatible with the ADM, AR and DSR methods are described. As shown in Fig. 22.3, the process, application and data layers of the infrastructure layers constitute the main components of the EA.

22.4 Value Effect of Green Ship

There are different kinds of value approaches to estimate the real or personal value of properties including vessels. These are generally named such as cost, comparative sales and income approaches. Appraisers or valuers consider market value, dividend value, expectation value, replacement value, utility value, liquidation value or value in respect of ships.

Time element has also remarkable importance to estimate the values of ships for credit purposes, hull insurance, collision recovery, salvage and general average, limitation and liability and other aspects on them. However, no one is applicable for vessel's value completely by oneself. All of these approaches should be considered all together. In that reason, individual appraisal companies' estimations will be relative and variable.

Relative valuations can be misleading for strategic decisions of companies, credit approvals of banks, risk assessments of insurance companies, buyers or sellers, etc. if it cannot be admitted under a certain discipline. Additionally, companies or institutions spend much time, money and resource to collect data related with shipping market and compare the market value of ships within limited data. However, exponential growth in data volume and variety has important impact on financial services firms in order to make accurate predictions on long-term asset value of ships, big data should be aggregated to unified platforms, and then decision support tools should be improved. There are a lot of industrial innovations to meet the needs of marine environment protection. However, new technologies do not provide cost-effective solutions to meet the requirements. For example, the International Convention for the Control and Management of Ships' Ballast Water and Sediments (the Convention) will enter into force on 08 September 2017. Therefore, making a modernization to current ships is very expensive. It is expressed by experts in various symposia that the cost of modernization can be about $ 1 million for a ship. For this reason, the shipowners will have to choose one of the options to get out of service, laid up or operate without profit.

In this study, it is aimed to use information technology in order to reduce the misuse of the ship by the ship's personnel. Thus, it is evaluated that operational support in port, inland waters, passageways and open seas can be provided in different operational modes of ships without making modifications, modernizations or major expenses. It is possible to say that the operational expenditures can be reduced naturally if the unnecessary energy consumption on the ships is reduced to a minimum using IT systems. A commonly accepted calculation model for

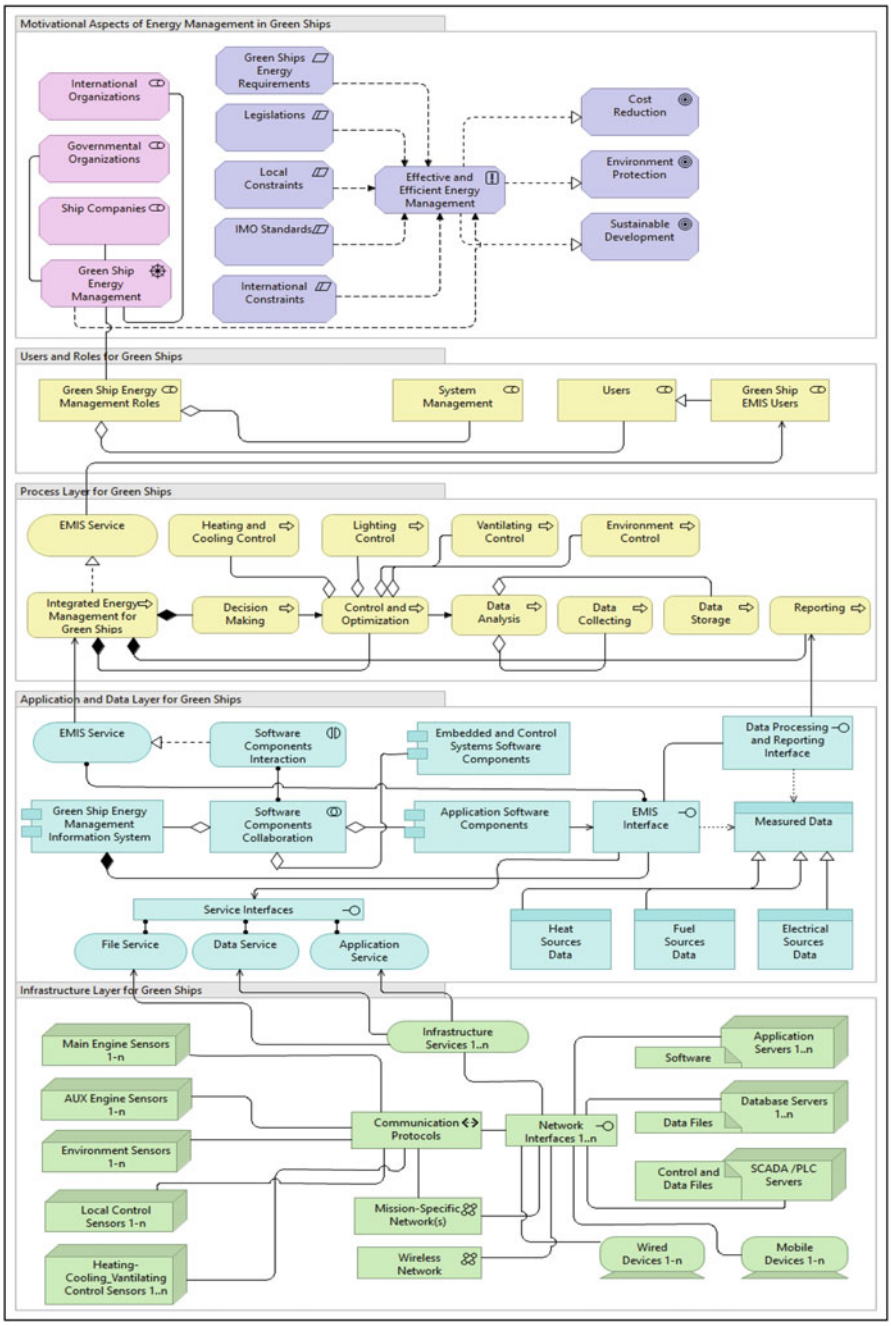

Fig. 22.3 An enterprise architecture for cargo ship

determining the value of vessels is the Hamburg Ship Evaluation Standards (HSESs). HSESs have been set as a practical approach to assessing vessel. In the view of Hamburg Shipbrokers' Association, through long-term asset value (LTAV) formula, the LTAV of a vessel is determined on the grounds of its long-term earning potential, using a present value and discounted cash flow (DCF) method, respectively, customized to account for the requirements of vessel valuation. Long-term asset formula (22.1) retrieved from Hamburg Shipbrokers' Association –VHSS, 2009 [20], is as follows:

$$\mathrm{LTAV} = \sum\nolimits_{t=1}^{T} \left(\frac{(Ct - Bt)}{(1+i)^{t}} + \frac{\mathrm{RW}t}{(1+i)^{T}} \right) \tag{22.1}$$

where Ct is the charter income; $C1$, current Net-TC rate in running year; C2-T, average Net-TC rate of the past 8–10 years (if possible, otherwise shorter); Bt, average OPEX of the last 8–10 years (if possible, otherwise shorter) (OPEX: operating costs); i, discount rate; t, period; $t1$, current year; $t2$-T, period end, average 10-year charter rate); T, remaining period until age 20/25; and RWT, residual value (based on LDT, average USD scrap price/ldt and multiple) (ldt in long tons; 1 t = 0.9842 lt). When LTAV formula is examined, it is seen that operational expenditures are one of the most important factors affecting ship evaluation. According to the TC rate equivalent of the vessels, the relationship between the freight charge and OPEX determines the profit or loss situation of the vessels. For example, if the operating cost of the ship is $ 6000 per day and that ship earns $ 8000 a day, it means the day is profitable. However, if it stays below $ 6000, it means that the ship is operating at a loss. Because of the frequent changes in the ship's personnel who come from different nations and the different technical characteristics of each ship, it is not always possible to use ships taking into consideration energy efficiency. For example, it may not always be possible to determine the most suitable route to the currents and winds in bad weather conditions. Factors such as high-speed usage for ship's arrival to ports on time and to avoid damaging the burden increase the energy consumption. However, altering route 2 degrees can provide significant savings for a ship that will pass 1000 nautical miles. In that reason, average OPEX of the last 8–10 years can be minimized using IT systems.

22.5 Results and Discussions

This study includes an operational architecture to provide efficient and manageable energy, especially for cargo ships. In this context, the architectural infrastructure given above includes a green ship feature and the management layers and components of the ship. The five layers described above work in a hierarchical structure. The process management of information technology involves a multi-faceted and multilayered structure. In these structures, the process management of the combinations that will occur on each different input is difficult due to the manual conditions.

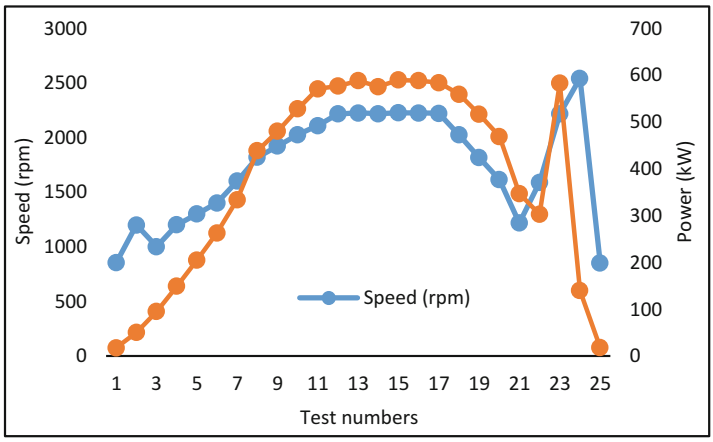

Fig. 22.4 Speed and power changes of diesel

Ships are not structures that can be interfered with in the course of navigation. For this reason, manual processes can lead to control problems and significant energy losses in processes. In this way, the architectural infrastructure will allow each defined energy system component to be operated at the desired load values or depending on the defined scenario. Cargo vessels are mostly systems in which the main engines are diesel engines. In these systems, the efficiency loads depend on the operating conditions, but the thermal efficiency is 20–60%, depending on the first law of thermodynamics. This change may vary according to the operating conditions, load, environment and marine conditions. In all these inputs, the optimization of the engine speed and the generated power can only be controlled by an operating programme. This can be seen by a diesel engine analysis. In the study, power, speed and fuel relations of a diesel engine load distribution were investigated. In Fig. 22.4 the motor speed and power relation is investigated.

The engine produces a minimum power of 17.2 kW and a maximum power of 589.6 kW at speeds ranging from 850 rpm to 2225 rpm. It is certain that power generation directly affects fuel consumption in engines. The motor fuel consumption for these load distributions is examined, and the distributions are given in Fig. 22.5.

Considering the limit conditions of the engine, minimum 153,5 gr/min and maximum 2457,2 gr/min have been realized. There is a similarity between engine power consumption and fuel consumption. However, when this similarity is evaluated over speed, significant differences in fuel consumption are noticeable. This was evaluated at a range of 1601 rpm with 1000 rpm and is given in Fig. 22.6. Engine speed changes directly affect fuel consumption with generated power. In this consumption, there are significant changes in the intervention of the decision-makers in speed change.

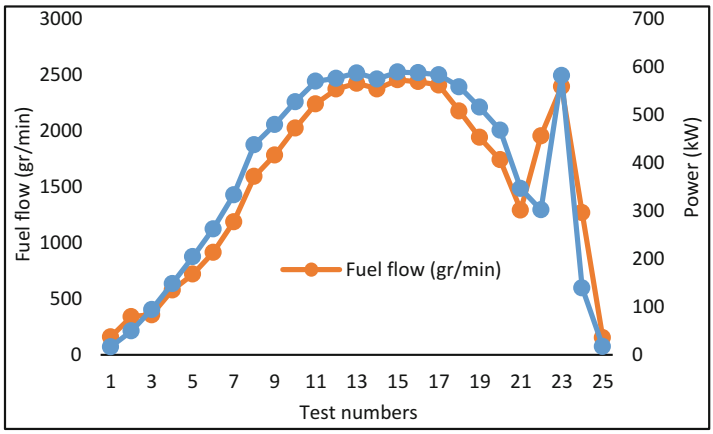

Fig. 22.5 Power and fuel flow rate change of diesel engine

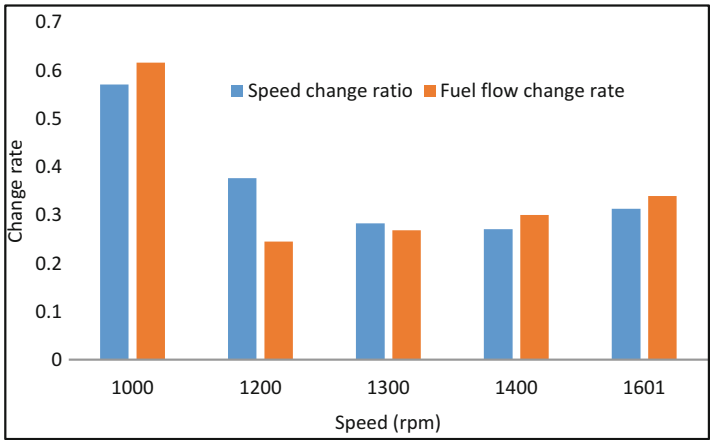

Fig. 22.6 Change rate of diesel engine

As a matter of fact, it seems that fuel change is not equal in every 100 unit change. Also, energy efficiency in the speed preference shows a 25% change in optimization.

In this way, the process must be evaluated for each speed change. The power and speed relationship of the fuel can be seen in Fig. 22.7.

There is only one cost effect of fuel consumption. At the same time, environmental impact is also important. For this reason, it is ensured that all parameters together with the data flow in this architecture can be checked together in a continuous manner. Continuous decision support will be provided especially in process management.

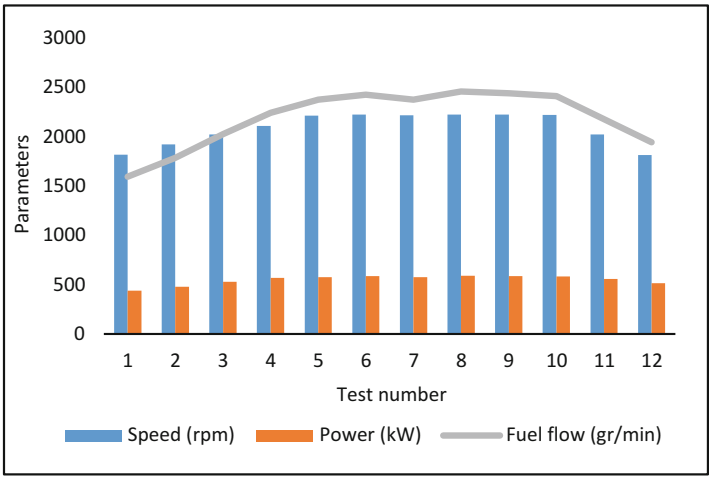

Fig. 22.7 Parametric change of diesel engine

22.6 Conclusions

The maritime industry is a sector that has made important decisions in the fight against global warming and climate change in recent years. The main actor of energy consumption in this sector is the ships, and the energy systems of the ships have a very complex structure. As aforementioned before in this study, in these systems where many entrances are present, efficient energy management is provided by an integrated information technology. The management of such information technologies is provided by an architectural structure. The energy management information system defined in the study will directly contribute to the provision of IMO standards defined for the green ship. This study is based on a scientifically based study of the energy systems of a cargo ship. The study is also exemplified for speed, power and fuel relations for a diesel engine. Vessels are a platform that is influenced by many international legislation and standards. Along with this information management, an integrated management infrastructure and decision support elements are presented in this direction. OPEX costs will be reduced because the ships with information systems will provide decision support to reduce energy consumption to a minimum, which will contribute positively to the increase in long-term ship values.

References

1. Global GDP (gross domestic product) at current prices from 2010 to 2020 (in billion U.S. dollars). https://www.statista.com/statistics/268750/global-gross-domestic-product-gdp/. Last Accessed Day: 17.10.2017

2. UNCDAT (2017) Review of maritime transport 2016. United Nations Conference on Trade and Development. http://unctad.org/en/PublicationsLibrary/rmt2016_en.pdf. Last Accessed Day: 25.02.2017
3. Pike K, Butt N, Johnson D, Walmsley S. Global sustainable shipping initiatives: audit and overview 2011 A report for WWF, Southampton Solent University, School of Maritime and Technology, East Park Terrace, Southampton SO14 0YN
4. Kirk T, Ferreira JC (2012) Shipboard energy efficiency: regulations, standards & opportunities, Intertanko Latın Amerıca Panel, Rio de Janeiro, http://www.intertanko.com/upload/93963/LAPEnergyEfficiencyOct12.pdf. Last Accessed Day: 17.10.2017
5. Arslan O, Besikci EB, Olcer AI (2014) Improving energy efficiency of ships through optimisation of ship operations, theme: sustainable modern shipping technologies, International Association Maritime Universities, http://iamu-edu.org/wp-content/uploads/2015/06/Final-report-RP2014-20140301-ITUMF.pdf. Last Accessed Day: 17.10.2017
6. Stevens L, Sys C, Vanelslander T, van Hassel E (2015) Is new emission legislation stimulating the implementation of sustainable and energy-efficient maritime technologies? Res Transport Business Manag 17:14–25
7. Lindstad H, Eskeland GS (2015) Low carbon maritime transport: how speed, size and slenderness amounts to substantial capital energy substitution. Transportation Research Part D: Transport and Environment 41:244–256
8. Watson RT Information Systems, University of Georgia, Copyright in 2007 by the Global Text Project, http://www.uky.edu/~gmswan3/777/IS_Book.pdf. Last Accessed Day: 17.10.2017
9. Maruşster L, Faber NR, Peters K (2008) Sustainable information systems: a knowledge perspective, advanced information systems engineering, 20th international conference, CAiSE 2008, Montpellier, June 16–20, http://ceur-ws.org/Vol-344/paper15.pdf. Last Accessed Day: 17.10.2017
10. Yates F (1978) Complexity and the limits to knowledge. Am J Physiol 4:R201–R204. https://doi.org/10.1152/ajpregu.1978.235.5.R201
11. Humbolt Unv (2017) Concept mapping, Humbolt University's research road map series, http://library.appstate.edu/sites/all/files/video/handouts/conceptmap_0.pdf. Last Accessed Day: 17.10.2017
12. Flood RL, Carson ER (1993) Dealing with complexity – an introduction to the theory and application of systems science. The language of science, 2nd edn. Plenum Press, New York. 9, 10, 17, 27, 28
13. Baldi F (2013) Improving ship energy efficiency through a systems perspective, Department of Shipping and Marine Technology, Chalmers Unıversıty of Technology, Gothenburg
14. Sekimuzu K. Reducing emissions and improving energy efficiency in international shipping. http://www.climateactionprogramme.org/climate-leader-papers/reducing_emissions_and_improving_energy_efficiency_in_international_shippin. Last Accessed Day: 17.10.2017
15. Hooke JH, Landry BJ, David Hart MA (2004) Energy management information systems, Office of Energy Efficiency of Natural Resources Canada. http://www.nrcan.gc.ca/energy/publications/efficiency/industrial/emis/6035. Last Accessed Day: 17.10.2017
16. Vaishnavi VK, Kuechler WJ (2008) Design science research methods and patterns: innovating information and communication technology. Auerbach Publications, Taylor & Francis Group, New York
17. Gregor S, Hevner AR (2013) Positioning and presenting design science research for maximum impact. MIS Q 37(2):337–355
18. Lankhorst M (2009) Enterprise architecture at work: modelling, communication, and analysis. Springer, Berlin/Heidelberg
19. Irclass (2012) Ship Energy Efficiency Management Plan (SEEMP), Guidance Notes for Ship Owners and Ship Operators, Indian Register of Shipping, 52-A, Adi Shankaracharya Marg, Opp. Powai Lake Powai, Mumbai – 400 072. http://www.irclass.org/media/1397/ship-energy-efficiency-management-plan.pdf. Last Accessed Day: 17.10.2017
20. Hamburg Shipbrokers' Association (VHSS) (2009) Hamburg ship evaluation standart. http://addressitalydownload.it/asamar/fed09/circolare0152009hamburgshipevaluationstandard.pdf. Last Accessed Day: 17.10.2017

Chapter 23
Criteria and Indicators for the Development of Sustainable Tourist Sites

Silvia Arias

23.1 Introduction

It is public knowledge that in Mexico there is a growth of energy consumption for environmental conditioning (climate and light) of homes, which has a very important impact on the economy of the users. This impact of the energy sector drives away new investment and emphasizes the dependence on the use of nonrenewable fossil fuels, as well as the environmental impact that this entails.

One of the most important elements that determine the levels of comfort and energy consumption in dwellings is available to natural climatic factors and its surround. Rules in our country, the housing for the most unprotected sector, are designed and built according to the cost of construction and not based on operating costs. This is evident in the majority of new buildings, which reflect high energy consumption and serious environmental comfort issues, problems that can be solved through proper application of a methodology adequate bioclimatic design, unless this generates a significant impact on the cost of the building.

Under this theme, research proposed has its antecedents in the work of linking the University of Guadalajara that has been carrying the guild of construction through the college of architects in the state of Jalisco. Since 1998 different approaches have been applied for municipalities related to the metropolita area of Guadalajara, being muncipalitiy of Zapopan. Interest related to the retool of the construction regulations was expressed on the first working meetings, concludding that to carry out the relevant environmental recommendations it is necessary to analyze both the conditions physical, as social study area.

S. Arias (✉)
University of Guadalajara Mexico, Department of Urbanism, Guadalajara, Jalisco, Mexico

S. Nižetić, A. Papadopoulos (eds.), *The Role of Exergy in Energy and the Environment*, Green Energy and Technology,
https://doi.org/10.1007/978-3-319-89845-2_23

Although the regulation that controls the activities of building remains in force today, variations of which has undergone have been diverse, although it should be noted that such changes are more administrative aspects, as well as the expert functions of the construction.

23.2 Justification

For the demographic transition in the year 2030, the population of Mexico will be nearly 130 million inhabitants, for which Mexico must reach 100% of sewage treatment rate and promote their reuse for agriculture and industry and even for consumption.

Between 2007 and 2030, the number of cities will grow 40% by what not it can continue facing a loss of more than a third of the water in the public networks or not follow without retrieving it and reusing it. By the year 2030, for example, they should build as many homes as that have been built throughout the twentieth century in the country, if you want truly to meet the population growth and the demand for Mexicans.

The long-term vision announced by the Presidency of the Republic in the program Mexico 2030 will be built through the formulation of proposals on five axes: respect for the rule of law and public safety, competitive economy and creation of jobs, equal opportunities, sustainable development, and being democratic.

The ten most important developers in Mexico built 25–45% of the housing market. Larger developers built more than 15,000 annual housing units. Due to the limited availability of reserves, developers have their own reservation to be used in 2–5 years.

The new housing developments are adapted to styles of living of its residents, as well as new family structures and forms of work. Owning one's own space is increasingly important, and cities are faced with the challenge of providing the opportunity for such demands.

So far, the full response was not provided to these demands, and as a result have cities that grow without control, badly used land and avenues and congested streets.

The construction of a million average homes per year will require:

- A net density of 50 homes per hectare, without services
- An approximate area of 40,000 hectares of land
- Wastewater treatment = 1343 million pesos
- Hydraulic infrastructure = 10,000 million pesos
- Drainage infrastructure = 9000 million pesos
- Electrical infrastructure = 3500 million pesos
- 28 billion pesos annually to provide infrastructure services to housing that is built from 2007 [1]

23.3 Objective

Promote the implementation of the concepts and criteria of sustainability in activities related to the construction of housing at the regional level, seeking to adapt the technical and administrative processes in response to the different physical and environmental requirements in the area west of Mexico. Similarly, reference indexes of quality and approval to the standards laid down in international standards, engaging for this purpose both academics and students, as well as other actors related to the construction industry.

23.3.1 Scientific Impact

Housing and sustainable development in Mexico. Buildings and dwellings have an important impact on the environment and on the health of the people.

Environmental quality associated with the comfort of humans to the sustainable development of natural resources; applied to architecture, this concept implies the incorporation of new demands on all of the constructive process of a dwelling, changing customs of developers and users.

To support the above which is required to make reference to the "scope and challenges in housing," the Presidency of the Republic has established five aspects which are planned to guide national housing policy:

- Eminently social nature of homeownership programs.
- Promote quality housing.
- Make efforts with the different actors and institutions of housing.
- Provide greater opportunities for families.
- Creation of infrastructure throughout the country.

The Presidency of the Republic has established as a goal the creation of a wider infrastructure of housing in the country, which requires the construction of a million average homes per year. To give recommendations to develop sustainable housing, it is necessary to formulate the following criteria as instruments of environmental policy, in accordance to state environmental laws:

Approaches to urban development. The care that must exist between green areas and buildings intended for room, services, and general activities. The conservation of forested areas, fertile, avoiding their urban neighborhood. Limitations to create residential areas around industrial centers.

Criteria in the field of housing. The use of devices and systems for saving water, uptake, storage, and utilization of rainwater, as well as the treatment and recycling of these. The optimum utilization of solar energy, both for heating and lighting.

The incorporation in the planning, design, and construction elements and architectural and aesthetic criteria that harmonize with the environment, giving priority to the use of local materials and respect for cultural traditions. Designs that facilitate

natural ventilation. The use of construction materials that cause the lowest environmental impact.

As a result, it is possible to carry out some future actions that would be feasible to consider as a continuation of this project:

- Recommended technology alternatives for sustainable housing.
- Carry out measurements and monitoring designs and technologies incorporated into the housing.
- Analyze a study cost-benefit of alternative products and technologies.
- Promote the regulation and evaluation of sustainable housing.
- Make references to the draft of NOM-020-ENER, energy efficiency in buildings, envelope of residential buildings.
- Generate indicators functioning as baseline to generate policies, standards, and regulations to be included in the regulations.
- Establish a system of analysis to evaluate and qualify the technical aspects of sustainable projects.
- Encourage financial mechanisms that allow you to solve the above cost, which today involves the incorporation of ecological technologies in sustainable housing, in reference to the applied in other countries with the addition of calls "green mortgages."
- Promote the dissemination and training for the implementation of environmental technologies in sustainable housing.
- Establish programs related to sustainability at the national level.

23.3.2 Technological Impact

To influence both community of academics and professionals aims to use and disseminate computer programs and utilities existing which serve as a tool for the builders, which contain processed environmental data that serve as parameters to achieve sustainable designs.

Through technical recommendations the lead developers and homebuilders could ensure energy saving measures, i.e. rational use of water and solid waste treatment. Test mechanisms that encourage the different agents involved in this issue, especially the builders and users to ensure that dwellings contain sustainability criteria that promote a better quality of life and the natural environment.

Also, take advantage of existing programs of the government sector, to incorporate technological elements of energy saving in housing [2].

23.3.3 Social Impact

It is necessary to have an impact on users through the adaptation of existing building regulations to the characteristics and focal points demanded by the architectural spaces in terms of savings and energy efficiency and solid waste management, as well as of the rational use of water, in the process of achieving sustainable social and economic development. This is through greater involvement of users themselves, academics involved, as well as the building professionals, developing guidelines and criteria for the use of environmental technologies as an alternative to traditional systems of housing and the elements.

The results of the research project aimed to promote the participation of public and private institutions such as:

CONAVI, FIDE, INFONAVIT, FOVISSSTE, federal mortgage society, FONHAPO, banks, suppliers and equipment manufacturers, agencies and national chambers (CMIC and the CANADEVI), colleges of architects, engineers, institutions of higher education, developers, and homebuilders.

23.3.4 Economic Impact

Through the proposed regulations, there arises the feasibility of achieving environmental conditions in the initial stage of architectural projects developing lower cost of the habitability of these looking for savings in electric power and water supply. These regulations are intended to establish the appropriate parameters to achieve environmentally appropriate designs which generate quality for the users of the same spaces seeking to influence at the same time economic and social conditions in the region.

Similarly, it intends, through the conduct of the research project, to analyze the feasibility of carrying out programs on a large scale and identify sources of funding for their development.

Analyze the possibility of certifying so-called carbon credits (reduction of emissions of CO_2 in the atmosphere) as a result of the saving of electricity to run a program on a large scale in this area. For example, the feasibility of which could be considered the rightful claimant (for public financing) that you purchase a house with ecological criteria in which larger financing amounts are available. The increase in funding that families would have for purchasing homes with efficient systems would get financing, which in practical terms can be translated into a greater area of the housing.

23.3.5 Environmental Impact

Development of the reseach project proposal was focused to regulate actions in different stages of constructions to be able to reduce as much as possible enviromental impact related to the construction activities.

This comes as a result of analyzing the urgent need that is in Mexico to develop low-income housing but at the same time produce such housing to improve the quality of life of the population. Therefore, these proposals intended to promote the environmental conditions in the architectural spaces, ways of improving the housing and working conditions of the users at three specific points: energy efficiency (reduction of CO_2 emissions), recycling of water, and solid waste treatment.

23.4 Methodology

23.4.1 Exam Obtaining Technical Information

The methodological strategy that will determine the follow-up of the project is part of essential considerations such as analyzing the qualitative and quantitative aspects of the rules and regulations of existing buildings. On the other hand physical, social data as well as consideration of the existing infrastructure should be taken as the key parameters related to the possible levels of the sustainability in housing. General basic information are population-based data, the physical and social environment, and the existing infrastructure.

A. Existing rules and regulations. Consult and analyze the rules and/or regulations affecting the levels of sustainability of dwellings. In the same way, analyze the "building of housing code" and the "criteria and indicators for sustainable development" proposed by the National Housing Commission [3].
B. Demographic data to analyze the energy consumption of the users of dwellings.
C. Physical data of the study site, to analyze the temperature, relative humidity, winds, rainfall, and solar radiation, in order to determine the climate behavior of the region.
D. The urban landscape. Aspects of the existing natural resources as a type of vegetation, the urban image.
E. Solid waste, sewage, and gray water.
F. Bioclimatic design. Analyze the factors for thermal comfort. Light and sound dwellings.
G. Levels of energy consumption. Energy audit of the consumption averages.

23.4.2 Interpretation of Data: Description of Concepts of Sustainability

A. Determining the levels of sustainability of dwellings.
   2.2 Establish statistics of energy consumption of the population in the study area.
B. Establish physical and social parameters to develop criteria and indicators of sustainability.
C. Develop urban sustainability levels and identify the impacts on the natural environment.
D. The capacity of reinstatement of waste through separation of garbage, compost, etc. In addition to the transfer to the immediate environment and in surrounding areas to the region.
E. Determination of bioclimatic architectural space; aimed at obtaining sustainable housing design-specific indicators and criteria.
F. Develop energy audit model, based on the obtaining of the aspects of energy saving, in the development of sustainable housing, the study area.

23.4.3 Synthesis: Measurement of Levels of Sustainability

The levels of sustainability are developed through the proposed three categories of use as a control's appearance in each standard or regulation of existing buildings, related either to urban or architectural, level as a proposal of quantitative aspects:

A. By means of the accomplishment of a calculation
B. Making measurements in the same project
C. By default (maximum or minimum) values

This is also valid for the other proposals for regulations, although, depending on the complexity of the architectural element, the levels could be combined.

Proposal of Criteria of Sustainability for Housing

Estimations of the aspects quantitative rules and regulations of construction will take place through the opening of spaces for reflection and participation for the various actors involved, designers and builders, researchers, municipalities, and end users, and are intended to the stages of analysis, data processing, and policy proposals that are grouped into five major aspects:

A. Location, densification of the soil, verticality, and services

   I. Integrity and proximity to urban sprawl
   II. Connectivity and mobility
   III. Infrastructure
   IV. The land use and housing density

B. Efficient use of energy

I. Gas
II. Electric power
III. Thermal envelope
IV. Passive systems
IV. a. Urban design
IV. b. Architectural design

C. Efficient use of water

I. Availability of water in the whole
II. Water supply in the housing
III. Wastewater
IV. Rainwater
V. Post sale service

D. Adequate management of solid waste

I. In the process of construction
II. Housing
III. Assembly
IV. Green areas

23.5 Strategies for Action

To suit each one of the aspects, technical, legal, and administrative processes in response to the different requirements of the main climates of the region required the application of the proposed methodology, through the following progress:

A. The participation of local actors (public and private) construction guild representatives, representatives of municipal institutions, as well as the users of the buildings in the analysis of current regulatory processes, as well as its possible environmental adaptation
B. The formulation of recommendations of environmental readjustment to the relevant authorities and to encourage the participation of actors involved in the building process
C. Processing of data. Development of reports, databases, indexes of quality, and mental maps of synthesis

Development of Evaluation
Weighting of the qualitative and quantitative aspects:

A. Development of policy proposals
B. Strategies and recommendations for adaptation of the physical and social processes in response to the different requirements of the main climates of the region

Expected Results

- Training of human resources. Training and dissemination among construction professionals, real estate promoters, and community in general
- Catalogue of criteria and indicators for livability for the development of sustainable housing in the area center-west of Mexico
- Document of diagnosis of the current state of regulation of existing construction.
- Energy audits and water consumption format

5. Comparative matrix of greenhouse gas (GHG) emissions, between a conventional housing and buildings with the implementation of alternative technologies toward sustainability

- Evaluation of proposals for sustainability, through the establishment of procedures and tools to conduct environmental surveys [4]

Technical Application

Criterion: (A) location, densification of the soil, verticality, and services

Location of the house on the lot.

The buildings of five levels or more above sidewalk level shall conduct a study of shadows in which to show projections resulting in new construction on grounds and buildings during various periods of the year.

Indicators

Restrictions regulations, concenring the artificial obstructions (between the buildings) should contemplate the sunpaths different seasonal climatic seasons, as well as adequate conditions of natural lighting, visual and natural ventilation. This section is directly linked to those relating to separation and the adjacent buildings (Fig. 23.1).

Required Documentation

Architectural project with the study of shadows

Technical documentation: descriptive report, physical schedule

Construction details necessary for the analysis

Proposed Regulations A

Restriction of calculation of which rules you should refer must be directly based on a study of shadows that determines the separation and the height of the buildings. Although this is treated in greater detail in the following paragraph, here it intends to establish guidelines for such a study.

The information required for the elaboration of the mentioned calculation are shown in the tables of solar tours. The angle of orientation of the buildings with respect to the angle of azimuth (Z) and the angle of solar height (H) is first selected and will then continue with the following steps (Fig. 23.2):

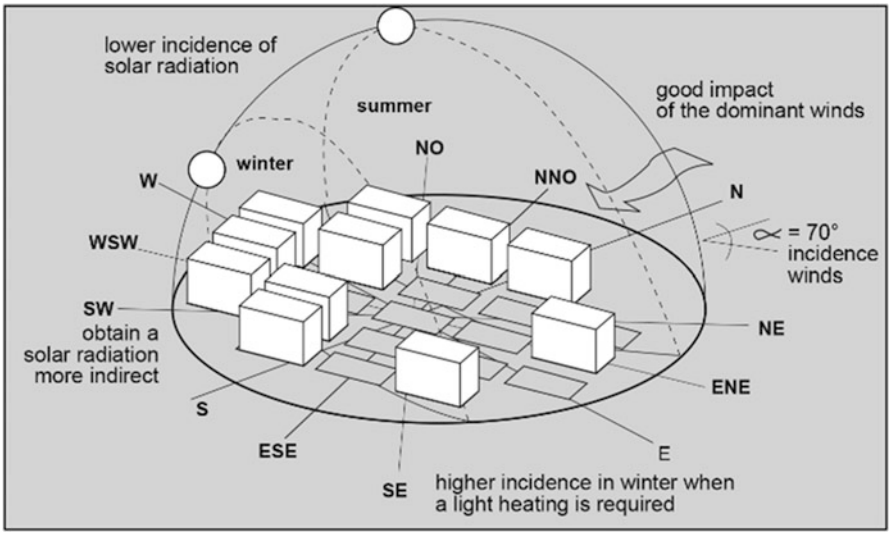

Fig. 23.1 Orientation of the urban shape

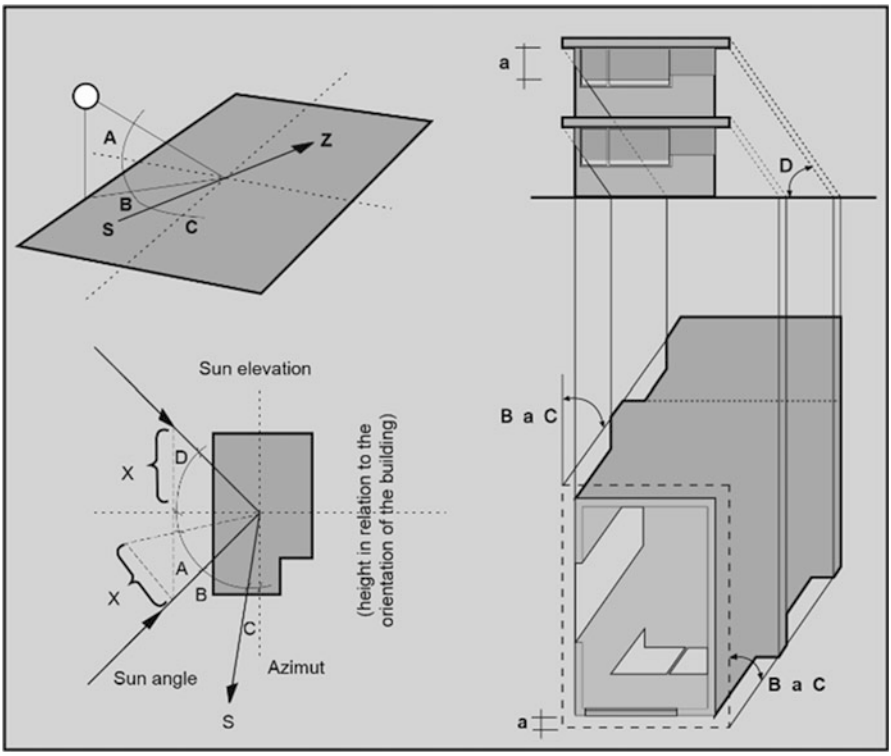

Fig. 23.2 Analysis of shadows

1. Draw the east-west axis (in this case) and the angle of azimuth *Z*.
2. Draw the solar height *H* with a perpendicular to *Z* in any part of the line to cut the line of the angle *H*, *X* from which has been mapped the perpendicular, made a reference to the upper surface with the same distance *X* and resulting in the *D* line which is an elevation of the Sun in relation to the orientation of the building.
3. For the direction of the Sun on the ground, the angle *Z*+*C* is used and *D* to the elevations, and the shadows are drawn conventionally.

As it is known, this is applicable elsewhere with temperate climate through the application of the solar tour in hours, days, and months (including climate data) and which is set in the following manner:

$$\text{Sen to} = (\cos \times \text{sen}\, W - L)/\cos\ \text{h}$$

where:

L = latitude of the site in degrees
d = solar declination for the day in question, in degrees
W = angle clockwise

For the layout of the diagram of the solar, it is necessary to have the following:

- Latitude of the site (L). It should always indicate whether concerned latitude is North or South, and with results measured in degrees.
- Solar declination (d). Preferably as data from the 21st day of each month. Included angle between the Tropic (either Cancer or Capricorn) define its obliquity and on the dates of the solstices of winter (December 21) and summer (June 21). On other days the declination value is by using the following expression:

$$d = 2345 \times \text{sen}\,(360 \times (284 + n)/365)$$

where n is the number of the day ordinal, i.e., the i for the number 1st. January is one and the i on December 31 is 365 (Fig. 23.1).

Proposed Regulations B

A proposal of rules for artificial and natural obstructions would be the request of a study of shadows, and more appropriate even if you develop according to the requirements of air conditioning of the different orientations. Since solar obstruction level will be different in the W or SO directions the requirement of direct solar incidence is necessary to be considered. For a latitude close to the Tropic of Cancer and a semi-tempered climate, air conditioning requirements vary considerably, since in temperate months, heating requirements can reach the 490w per m2, and in the hot months, required ventilation amounts to 2.0 m/sec.

This proposal considering climatic requirements in the different apparent positions of the Sun (altitude and azimuth) is numerically set in the following tables; the indicated values assist in the elaboration of the study of shadows to be measured in the architectural project (Fig. 23.3).

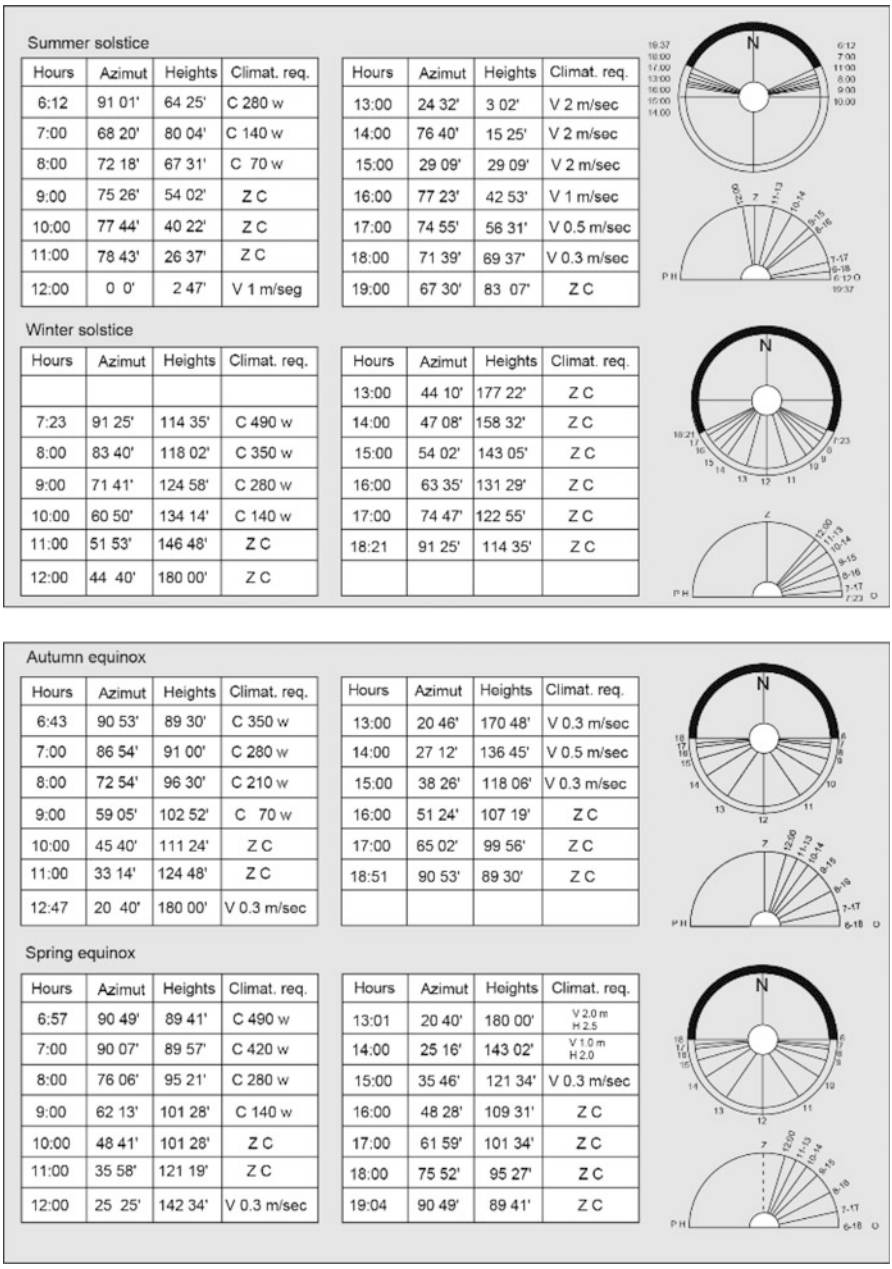

Summer solstice

Hours	Azimut	Heights	Climat. req.
6:12	91 01'	64 25'	C 280 w
7:00	68 20'	80 04'	C 140 w
8:00	72 18'	67 31'	C 70 w
9:00	75 26'	54 02'	Z C
10:00	77 44'	40 22'	Z C
11:00	78 43'	26 37'	Z C
12:00	0 0'	2 47'	V 1 m/seg

Hours	Azimut	Heights	Climat. req.
13:00	24 32'	3 02'	V 2 m/sec
14:00	76 40'	15 25'	V 2 m/sec
15:00	29 09'	29 09'	V 2 m/sec
16:00	77 23'	42 53'	V 1 m/sec
17:00	74 55'	56 31'	V 0.5 m/sec
18:00	71 39'	69 37'	V 0.3 m/sec
19:00	67 30'	83 07'	Z C

Winter solstice

Hours	Azimut	Heights	Climat. req.
7:23	91 25'	114 35'	C 490 w
8:00	83 40'	118 02'	C 350 w
9:00	71 41'	124 58'	C 280 w
10:00	60 50'	134 14'	C 140 w
11:00	51 53'	146 48'	Z C
12:00	44 40'	180 00'	Z C

Hours	Azimut	Heights	Climat. req.
13:00	44 10'	177 22'	Z C
14:00	47 08'	158 32'	Z C
15:00	54 02'	143 05'	Z C
16:00	63 35'	131 29'	Z C
17:00	74 47'	122 55'	Z C
18:21	91 25'	114 35'	Z C

Autumn equinox

Hours	Azimut	Heights	Climat. req.
6:43	90 53'	89 30'	C 350 w
7:00	86 54'	91 00'	C 280 w
8:00	72 54'	96 30'	C 210 w
9:00	59 05'	102 52'	C 70 w
10:00	45 40'	111 24'	Z C
11:00	33 14'	124 48'	Z C
12:47	20 40'	180 00'	V 0.3 m/sec

Hours	Azimut	Heights	Climat. req.
13:00	20 46'	170 48'	V 0.3 m/sec
14:00	27 12'	136 45'	V 0.5 m/sec
15:00	38 26'	118 06'	V 0.3 m/sec
16:00	51 24'	107 19'	Z C
17:00	65 02'	99 56'	Z C
18:51	90 53'	89 30'	Z C

Spring equinox

Hours	Azimut	Heights	Climat. req.
6:57	90 49'	89 41'	C 490 w
7:00	90 07'	89 57'	C 420 w
8:00	76 06'	95 21'	C 280 w
9:00	62 13'	101 28'	C 140 w
10:00	48 41'	101 28'	Z C
11:00	35 58'	121 19'	Z C
12:00	25 25'	142 34'	V 0.3 m/sec

Hours	Azimut	Heights	Climat. req.
13:01	20 40'	180 00'	V 2.0 m H 2.5
14:00	25 16'	143 02'	V 1.0 m H 2.0
15:00	35 46'	121 34'	V 0.3 m/sec
16:00	48 28'	109 31'	Z C
17:00	61 59'	101 34'	Z C
18:00	75 52'	95 27'	Z C
19:04	90 49'	89 41'	Z C

Fig. 23.3 Solar positions

The study of the apparent motion of the Sun (altitude and azimuth) sets the angles of protection necessary to prevent the direct incidence, as well as promote it in hours and months which may be required to heat. The study of shadows would be applied in reference to the data shown here, where if you have a building oriented North-South, it will have its angles of height and azimuth angles, respectively.

Proposed Regulations C

In buildings of four or more levels above the ground level, you must present a study of shadows where it shows its annual and time impact on adjacent buildings. If these neighboring buildings affected their "rights to the Sun," it may restrict the location or the height of the new building.

I. The percentages of angles of solar projection may not be obstructed in different axis with respect to the neighboring constructions that are:
   Azimuth 48 ° 40′ North-South axis (12:00 h winter)
   East-West axis azimuth 44 ° 41′ (12:00 h spring)
II. Other guidelines will have to be governed by the average value of the two basic axes that delimit them.
III. In special circumstances to ensure optimal conditions (weather and lighet) the architectual features should be applied: patios, fireplaces of Sun, exterior finishes with indices of reflection for lighting and all passive system that help environmental comfort.

23.6 Conclusions

In a warm climate, external devices for sun control and incorporated to the building architectonic design are needed to be installed. The main objective of these elements is sun penetration restraining. Even if visual penetration is reduced from the interior (visual opening), admitting just a natural light portion. Undoubtedly horizontal sun control devices are more effective for South facades in warm climates of latitudes close to the Tropic of Cancer. Other control device advantages are that it may be designed to protect and, at the same time, to diffuse sun incidence and introduced into the building interior. The efficiency of these control devices had been analyzed in scale models at simulated environment.

Acknowledgments We are grateful to the organizing committee of the 9th International Exergy, Energy and Environment Symposium (IEEES-9), of Split (Croatia, EU), and the Faculty of Electrical Engineering, Mechanical Engineering and Naval Architecture (FESB), University of Split, for sending in time and satisfactorily the necessary information. We are also grateful to the National Council of Science and Technology, of Mexico, for the support offered to the research projects realized under their support, in previous stages, for which it was possible to obtain the summary for the present document.

References

1. Conavi (2005) Hacia un código de edificación de vivienda. Ed. Comisión Nacional de la Vivienda. México
2. Ashrae (1993) Fundamentals handbook. American Society of Heating, Refrigerating and Air-Conditioning Engineers USA, Atlanta
3. Conavi (2006) Uso eficiente de energía en la vivienda. ED. Comisión Nacional de Fomento a la Vivienda. México
4. Avouac P (1990) Bien voir, bien apprendre. ED. ENTEP-LASH. Francia. L'École nationale des travaux publics de l'État

Chapter 24
Energy and Environmental Analysis of Multi-effect Active Vertical Solar Desalination Unit for Indian Conditions

K. S. Reddy and H. Sharon

24.1 Introduction

Water plays a major role in industrial and domestic activities. Non-availability of potable water is a major problem in many parts of the globe, and it could be tackled by desalination of saline water. Large-scale centralised desalination units consume large amount of fossil fuel for their operation [1]. Desalination industry also accounts for pollution and environmental degradation [2]. In remote and arid regions, small-scale desalination using renewable energy is more viable to tackle water scarcity. Renewable energy that is much suited for water desalination and detoxification is solar energy. Solar energy is directly utilised to produce distilled water in basin-type desalination units, which has been widely studied. The average distillate yield from simple solar still is around 2–3 L/m^2-d [3]. One of the most interesting types of still considered for desalination of saline water is vertical solar still, and studies associated with this type of still are found to be scarce in literature. This type of still receives solar radiation from either east-west or north-south direction depending on orientation and occupies minimum ground space. Vertical solar still tested in Bangkok and Egypt produced an distillate yield of 1.0 kg/m^2-d and 3.99 kg/m^2-d, respectively [4, 5]. Experiments conducted by Boukar and Harmim [6] and Boukar and Harmim [7] depict their suitability for desalination. Multiple effects and evacuation can enhance productivity of vertical solar still. Under Chennai condition, active multi-effect vertical evacuated solar still produced a distillate yield of 21.29 kg/m^2-d [8]. In this article, environmental benefits and

K. S. Reddy (✉) · H. Sharon
Heat Transfer and Thermal Power Laboratory, Department of Mechnaical Engineering, Indian Institute of Technology Madras, Chennai 600 036, Tamilnadu, India
e-mail: ksreddy@iitm.ac.in

S. Nižetić, A. Papadopoulos (eds.), *The Role of Exergy in Energy and the Environment*, Green Energy and Technology,
https://doi.org/10.1007/978-3-319-89845-2_24

economic feasibility of evacuated multiple effect vertical solar still for different coastal regions of India have been estimated and discussed.

24.2 Evacuated Active Multi-effect Vertical Solar Still: System Description

The system consists of a number of vertical trays stacked against one another to form distillation chamber and is shown schematically in Fig. 24.1. The interior surface of each vertical metallic tray acts as evaporating surface where preheated water from solar flat plate collector will be uniformly distributed as thin film by lining the

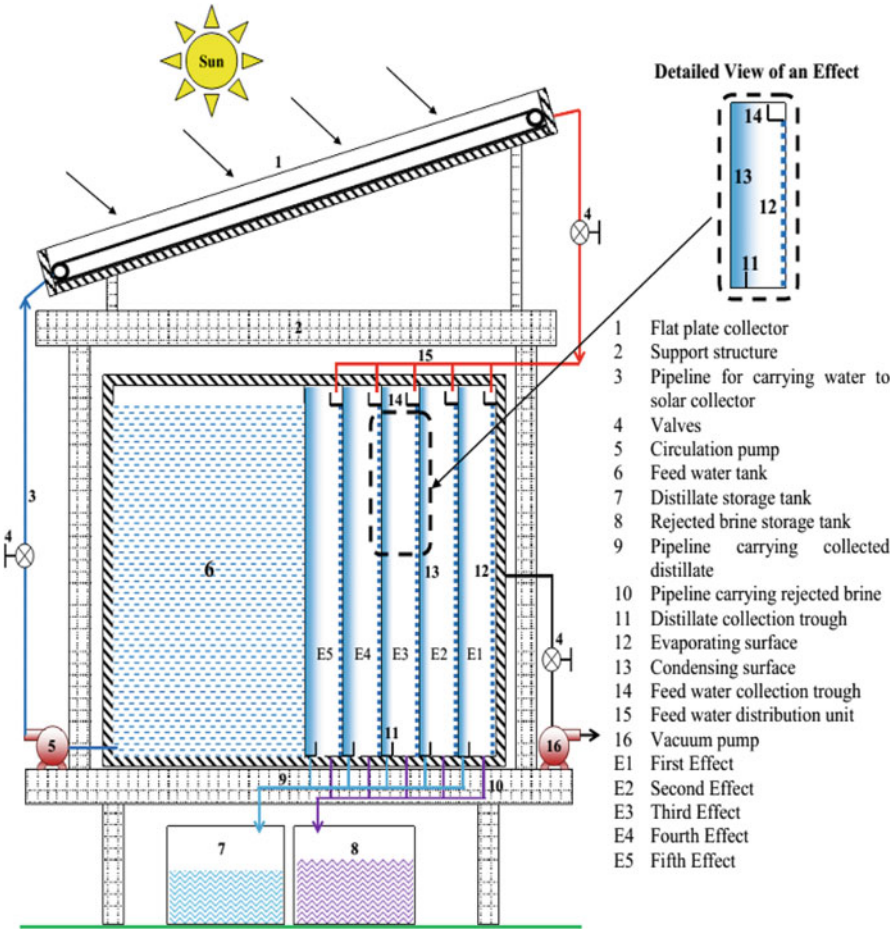

Fig. 24.1 Evacuated active multi-effect vertical solar still [8]

surface with capillary cloth whose one end is dipped inside feed water distribution trough. The exterior surface of each metallic tray stacked next to the previous tray acts as condensing surface where vapours from evaporating surface will be condensing and is collected using suitable distillation trough, which are kept at the bottom of each condensing surface. Each such stacked metallic tray with evaporating and condensing surface is called as an effect. Feed water storage tank kept integrated with the last effect acts as the condensing surface for the last effect. Evaporation of preheated water takes place due to difference in partial pressure of evaporator and condenser surface. In this setup, latent heat released from each effect is reused in next effects leading to enhanced evaporation in remaining effects.

24.3 Enviro-Economic Analysis

Enviro-economic analysis plays an important role is assessing the impact of each technology on environment and financial capability. It paves the way for selection of suitable technology among available options for the betterment of any nation by improving its sustainability. Enviro-economic analysis is carried out based on the literatures [9–11].

24.3.1 Impact of Solar Desalination Unit on Environment

In general, fossil fuel-based energy sources are used for manufacturing and fabrication of each component of solar desalination unit. Hence, during this process lot of CO_2, SO_2 and NO are rejected into atmosphere. Nearly, 1.58 kg of CO_2, 0.0114 kg of SO_2 and 0.00464 kg of NO are emitted for every 1.0 kWh of electricity produced from Indian coal-based power plants [12]. SO_2 and NO have huge health impacts and are responsible for nearly 500 and 120 deaths per year in India [13]. Solar energy-powered desalination unit can cut off these harmful emissions during their operation, and it can be quantified by environmental analysis. Energy utilised for production of solar distillation unit is termed as embodied energy and is estimated by summation of energy content, obtained by multiplying mass and energy density of each component associated with the unit [11].

Distillate yield of the unit, converted in terms of energy, is considered as energy output of the distillation unit, which can be given by:

$$E_{\text{out}} = \frac{M_{\text{y}} \times \text{LH}}{3600} \tag{24.1}$$

Energy spent on the unit can be recovered during its operation, and the time taken to recover the spent energy could be assessed by calculating energy payback time.

$$\text{EPBT} = \frac{E_{\text{in}}}{E_{\text{out}}} \tag{24.2}$$

CO_2 emission mitigated can be calculated by:

$$\mathrm{NCM} = \frac{((E_{\mathrm{out}} \times \mathrm{LT}) - E_{\mathrm{in}}) \times 1.58}{1000} \tag{24.3}$$

SO_2 emission mitigated can be calculated by:

$$\mathrm{NSM} = ((E_{\mathrm{out}} \times \mathrm{LT}) - E_{\mathrm{in}}) \times 0.0114 \tag{24.4}$$

NO emission mitigated can be calculated by:

$$\mathrm{NNM} = ((E_{\mathrm{out}} \times \mathrm{LT}) - E_{\mathrm{in}}) \times 0.00464 \tag{24.5}$$

24.3.2 Economic Analysis of Solar Desalination Unit

From economic analysis, cost of distillate production, production rate per rupee invested and impact of selling price on payback time can be estimated. Since the unit is operated under partial vacuum condition, annual operation and maintenance cost is taken as 20% of the fixed annual cost; salvage value is taken as 20% of capital cost.

Total annualised cost is given by:

$$\mathrm{TAC} = \left(\mathrm{CC} \times \left[\frac{\mathrm{IR}(\mathrm{IR}+1)^{\mathrm{LT}}}{(1+\mathrm{IR})^{\mathrm{LT}}-1}\right]\right) + \left(0.15 \times \left(\mathrm{CC} \times \left[\frac{\mathrm{IR}(\mathrm{IR}+1)^{\mathrm{LT}}}{(1+\mathrm{IR})^{\mathrm{LT}}-1}\right]\right)\right) - \left(0.2 \times \mathrm{CC} \times \left[\frac{\mathrm{IR}}{(1+\mathrm{IR})^{\mathrm{LT}}-1}\right]\right) \tag{24.6}$$

Distillate production cost per litre is given by:

$$\mathrm{CPL} = \frac{\mathrm{TAC}}{M_{\mathrm{y}}} \tag{24.7}$$

Production rate per rupee invested:

$$\mathrm{PRR} = \frac{M_{\mathrm{y}}}{\mathrm{TAC}} \tag{24.8}$$

Time taken to regain the invested on the unit based on selling price is given by:

$$n_{\mathrm{p}} = \frac{\ln\left(\frac{M_{\mathrm{y}} \times S_{\mathrm{p}}}{(M_{\mathrm{y}} \times S_{\mathrm{p}}) - (\mathrm{CC} \times \mathrm{IR})}\right)}{\ln(1+\mathrm{IR})} \tag{24.9}$$

Interest rate of 5% based on government banks [9] and lifetime of 20 yr are considered during the analysis.

Performance ratio of the distillation unit is estimated by [8]:

$$\mathrm{PR} = \frac{\Sigma M_{\mathrm{d}} \times \mathrm{LH}}{Q_{\mathrm{u}}} \tag{24.10}$$

24.4 Results and Discussions

In this section, distillate productivity, performance, environmental benefits and economic feasibility of evacuated multi-effect vertical solar desalination unit for different coastal regions of India are estimated and reported. The coastal regions considered for assessing the environmental benefits and economic feasibility of evacuated multi-effect vertical solar desalination unit are tabulated in Table 24.1, along with its location and daily average solar radiation intensity.

24.4.1 Distillate Yield and Performance Ratio

Distillate yield and performance ratio of evacuated active multi-effect vertical solar still for some coastal regions of India are graphically represented in Fig. 24.2. For east coastal regions, maximum distillate yield was noticed during March to May, and minimum distillate yield was recorded during December. Distillate yield of Rameshwaram and Tuticorin was found to be nearly closer to each other due to

Table 24.1 Indian coastal regions – location and daily average solar radiation intensity

Name of the Site	Latitude	Longitude	Average solar radiation intensity (kWh/m^2-d)
Port Blair (POB)	11.62° N	92.72° E	4.33
Minicoy (MCY)	8.27° N	73.04° E	5.70
Rameshwaram (RAM)	9.28° N	79.31° E	5.48
Tuticorin (TUT)	8.76° N	78.13° E	5.56
Vizag (VIZ)	17.68° N	83.21° E	5.30
Puri (PUR)	19.81° N	85.83° E	4.97
Kolkata (KOK)	22.57° N	88.36° E	5.12
Mumbai (MUM)	19.07° N	72.87° E	5.42
Karwar (KAR)	14.81° N	74.14° E	5.42
Kochi (KOC)	9.93° N	76.26° E	5.24
Trivandrum (TVM)	8.52° N	76.93° E	5.42
Mandvi (MAN)	22.84° N	69.32° E	4.86
Panaji (PAN)	15.49° N	73.82° E	5.79

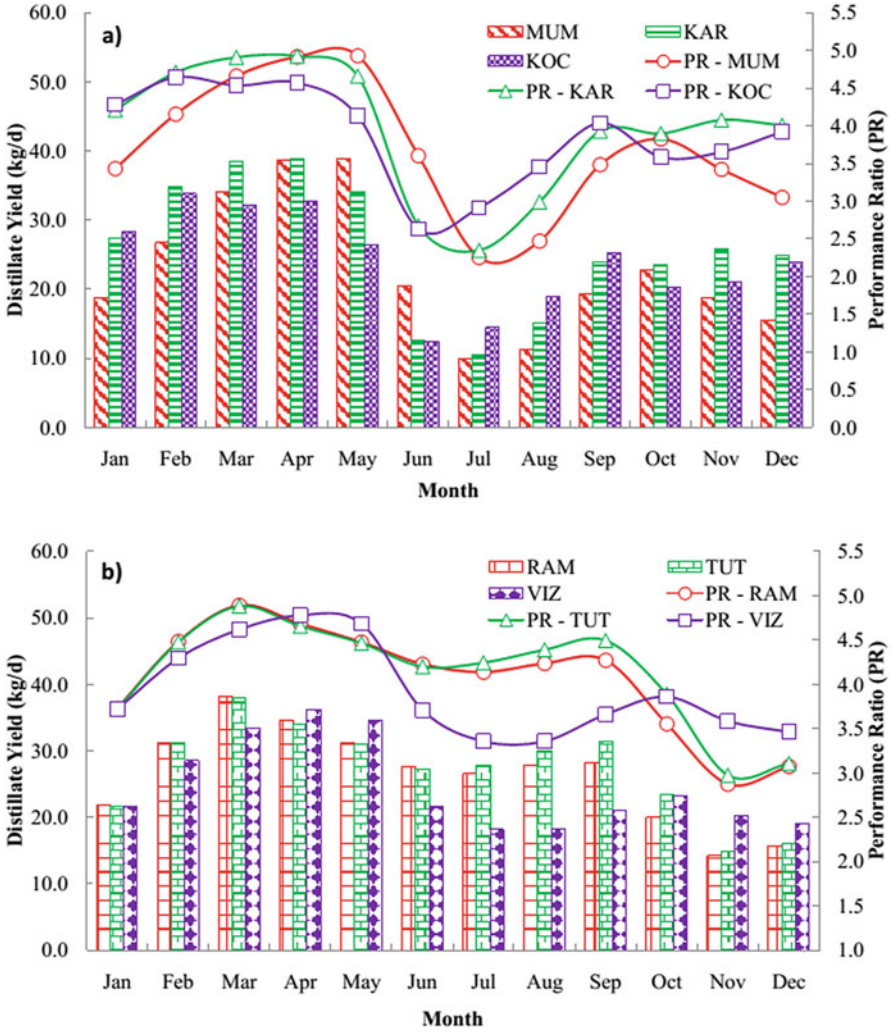

Fig. 24.2 Distillate yield and performance ratio for selected (**a**) west coast and (**b**) east coast regions of India

their closer geographical location. Annual average distillate yield of 26.40 and 27.22 kg/m^2-d was noticed for Rameshwaram and Tuticorin, respectively. Among the considered locations in east coast, Kolkata recorded the minimum annual average distillate yield of 20.39 kg/m^2-d. Highest annual average distillate yield of 29.44 kg/m^2-d was noticed for Panaji in west coast of India. Distillate yield of 42.45 kg/d was noticed during April for Panaji. Minimum distillate yield was noticed during July for regions along the west coast of India. Distillate yield and performance ratio of the unit for islands is shown in Fig. 24.3. Maximum distillate yield of

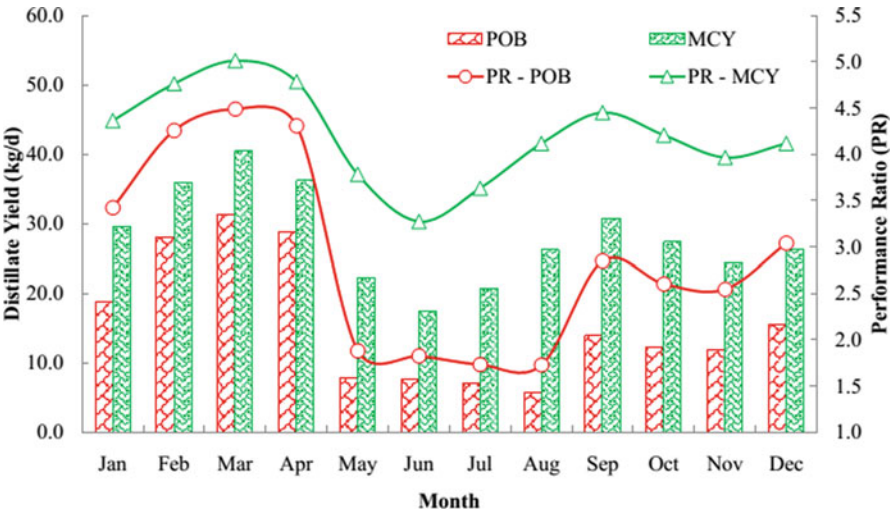

Fig. 24.3 Distillate yield and performance ratio for major islands of India

31.36 and 40.50 kg/m^2-d was noticed during the month of March for Port Blair and Minicoy. Yearly average distillate yield was around 15.70 and 28.12 kg/m^2-d for Port Blair and Minicoy.

Performance ratio of the solar desalination unit was in the range from 2.25 to 5.10, 2.57 to 4.89 and 1.73 to 5.01 for west coast and east coast regions and islands, respectively. Annual average performance ratio of solar desalination unit in west coast regions Mumbai, Karwar, Kochi, Trivandrum, Mandvi and Panaji was 3.68, 3.94, 3.86, 4.04, 4.07 and 4.29, respectively. Annual average performance ratio of solar desalination unit in east coast regions Rameshwaram, Tuticorin, Vizagapatnam, Puri and Kolkata was 4.05, 4.12, 3.92, 3.56 and 3.48, respectively. For Port Blair and Minicoy, annual average performance ratio was 2.89 and 4.20, respectively.

24.4.2 Energy Payback Time and Emission Mitigation Potential

The energy payback time of proposed solar desalination unit under Indian conditions is shown in Table. 24.2 Except Port Blair the energy payback time of the desalination unit for other considered locations was 1.0 yr or below.

Net CO_2, SO_2 and NO emission mitigated by evacuated active multi-effect vertical desalination unit for different coastal regions of India is graphically shown in Fig. 24.4. Net emission mitigated was estimated for a lifetime of 20 yrs and annual distillate yield for 5 wt% saline feed water. The unit was found to be capable of mitigating CO_2, SO_2 and NO emissions in the range of 74.74–137.65 tons, 730.53–989.70 kg and 225.75–404.27 kg, respectively, for considered coastal

Table 24.2 Energy payback time of solar desalination for Indian conditions

East coast regions	Energy payback time (Yr)	West coast regions	Energy payback time (Yr)
Rameshwaram	0.8	Trivandrum	0.9
Tuticorin	0.8	Kochi	0.9
Vizagapatnam	0.9	Karwar	0.9
Puri	1.0	Panaji	0.8
Kolkata	1.1	Mumbai	1.0
Port Blair	1.4	Mandvi	0.9
		Minicoy	0.8

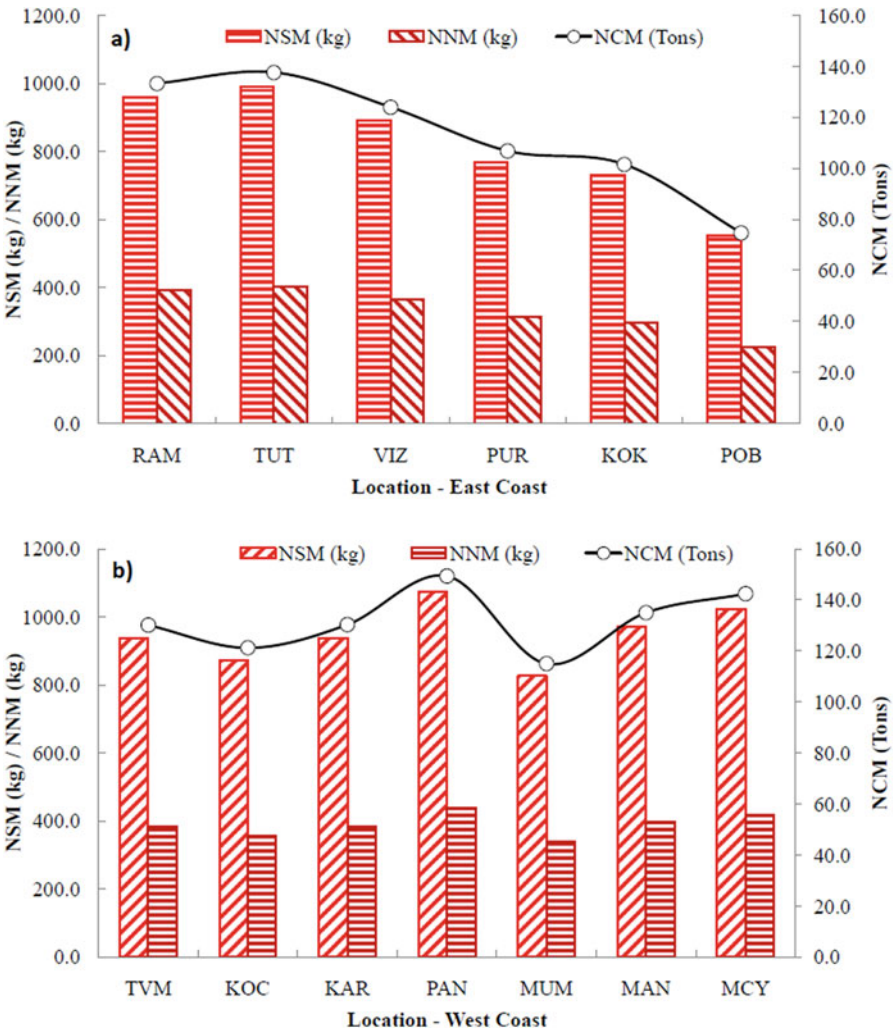

Fig. 24.4 Net CO_2, SO_2 and NO emission mitigated by solar distillation unit for (**a**) east coast and (**b**) west coast regions of India

locations in eastern part of India. Similarly, CO_2, SO_2 and NO emission mitigation in the range of 115.01–149.36 tons, 872.07–1073.94 kg and 337.75–438.65 kg, respectively, was noticed for coastal regions in western part of India.

24.4.3 Distillate Production Cost

Cost per litre of distilled water production and production rate per rupee invested for different locations in east and west coast regions of India are shown in Fig. 24.5.

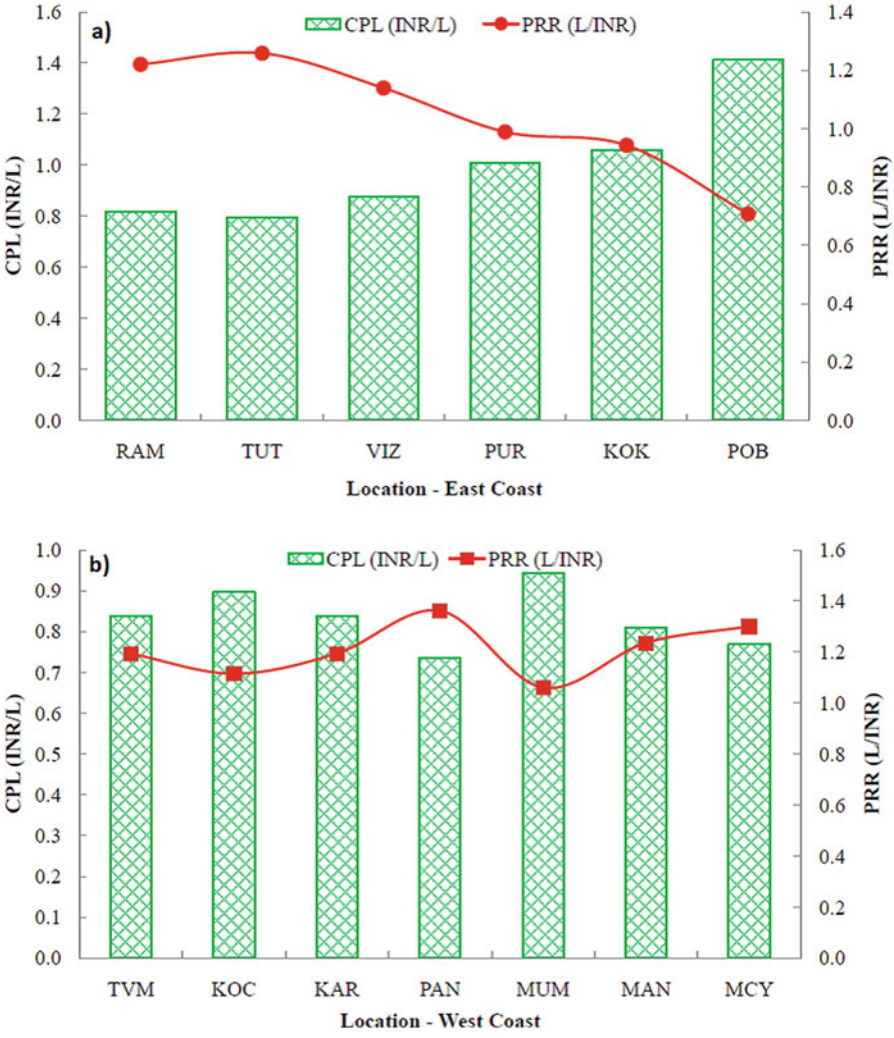

Fig. 24.5 Cost per litre of distilled water production and production rate per rupee invested on the unit for (**a**) east coast and (**b**) west coast regions of India

Table 24.3 Comparison of distillate production cost of different desalination units [14]

Desalination unit	Cost of distillate production (INR/m^3)
Evacuated active multi-effect vertical solar desalination unit (minimum yield)	1060.46
Evacuated active multi-effect vertical solar desalination unit (maximum yield)	734.47
Cascaded vertical double slope still	1205.00
Solar operated MD unit (0.10 m^3/d)	1033.00
Conventional RO (few m^3/d)	894.00
Conventional MED (<100 m^3/d)	482.00
Solar operated MSF unit (1.0 m^3/d)	196.00
Conventional MSF unit (528,000 m^3/d)	121.00
Conventional RO (60,000 m^3/d)	112.00

The distillate production cost of the unit under the climatic conditions in east coast was below INR1.5/L. Minimum production cost of INR 0.79/L was noticed for Tuticorin. Similarly, for west coast regions, production cost of distilled water was below INR1.0/L, and minimum production cost of INR 0.73/L was noticed for Panaji. Distillate production cost per litre was within INR 1.0/L for all the considered locations in west coast of India. For each rupee invested in the unit, distillate quantity of around 1.26 L and 1.36 L can be produced for climatic conditions of Tuticorin and Panaji in east and west coast regions, respectively. Distillate production cost of different desalination units is shown in Table 24.3. Minimum production cost was recorded for conventional reverse osmosis (RO) plant because of its huge capacity and matured technology. Evacuated active multi-effect vertical solar desalination unit has distillate production cost in the range of INR 734.47/m^3 (minimum) to INR 1060.46/m^3 (maximum).

24.4.4 Finance Payback Period

The role of selling price on finance payback period of solar desalination unit for different coastal locations in India is tabulated in Table 24.4. For a selling price of INR1.0/L, payback time was well below the lifetime of the unit for most of the sites except Port Blair. Payback period was nearly same for most of the sites on east coast for a selling price of INR 6.0/L or above. In case of west coast, for selling price of Rs.5.0/L or above payback period remains nearly same. Payback period is below 2.0 yrs for a selling price of INR 6.0/L and INR 7.0/L for west and east coast regions. Selling price of government-funded commercial RO-based bottled mineral water is around INR 10.0/L in India. Hence, this system is more viable for all locations on the coastal regions of India if proper selling price is fixed and marketed. Moreover, it can be utilised for meeting family freshwater demands in these coastal regions.

Table 24.4 Finance payback period based on selling price of distillate

Finance payback period (Yr)											
Selling price (INR/L)		1.0	2.0	3.0	4.0	5.0	6.0	7.0	8.0	9.0	10.0
East coast regions	RAM	12.4	5.3	3.4	2.5	2.0	1.6	1.4	1.2	1.1	1.0
	TUT	11.8	5.0	3.3	2.4	1.9	1.6	1.3	1.2	1.0	0.9
	VIZ	13.6	5.7	3.6	2.7	2.0	1.7	1.5	1.3	1.1	1.0
	PUR	16.8	6.7	4.2	3.0	2.4	2.0	1.7	1.5	1.3	1.2
	KOK	18.2	7.1	4.5	3.3	2.6	2.1	1.8	1.6	1.4	1.2
	POB	31.3	10.2	6.2	4.5	3.5	2.9	2.4	2.1	1.9	1.7
West coast regions	TVM	12.8	5.4	3.4	2.5	2.0	1.7	1.4	1.2	1.1	1.0
	KOC	14.1	5.9	3.7	2.7	2.1	1.8	1.5	1.3	1.2	1.0
	KAR	12.8	5.4	3.4	2.5	2.0	1.6	1.4	1.2	1.1	1.0
	PAN	10.7	4.7	3.0	2.2	1.7	1.4	1.2	1.1	0.9	0.9
	MUM	15.1	6.2	3.9	2.9	2.3	1.9	1.6	1.4	1.2	1.1
	MAN	12.1	5.2	3.3	2.4	1.9	1.6	1.4	1.2	1.0	0.9
	MCY	11.4	4.9	3.1	2.3	1.8	1.5	1.3	1.1	0.9	0.9
1 INR = 0.015 USD (2017)											

24.5 Conclusions

Evacuated active multi-effect vertical solar desalination unit was found to be more beneficial in terms of yield, emission mitigation and distillate production cost. The maximum annual average daily distillate yield of 29.43 kg/m^2-d was recorded for Panaji in west coast of India and 27.22 kg/m^2-d for Tuticorin in east coast of India. Annual average performance ratio of 2.89 and 4.29 was noticed under climatic conditions of Port Blair and Panaji, respectively. In east coast and west coast of India, the unit can mitigate large quantities of CO_2, SO_2 and NO emissions for 20-yr lifetime. Energy payback time of the unit was well below 1.5 yr for all considered locations. Lowest distillate production cost of 0.79 INR/L and 0.73 INR/L was noticed for east and west coast region of India. Payback period is below 2.0 yrs for a selling price of INR 6.0/L and INR 7.0/L for west and east coast regions, respectively.

Nomenclature

CC	Capital cost (INR)
CPL	Cost per litre (INR)
E_{in}	Embodied energy (kWh)
E_{out}	Energy content of distillate (kWh)
EPBT	Energy payback time (Yr)
IR	Interest rate
LH	Latent heat (kJ/kg)
LT	Lifetime (Yr)

M_y	Annual average yield (kg/d)
n_P	Payback period (Yr)
PRR	Production rate per rupee invested (L/INR)
Q_u	Useful heat energy supplied by solar collector (J)
S_p	Selling price (INR)
TAC	Total annualised cost (INR)

Acknowledgements The financial support provided by the Department of Science and Technology (DST, Government of India), New Delhi, through the research project (Grant no: DST/TM/SERI/2 k12/16(G)) is duly acknowledged.

References

1. Al-Mutaz IS, Wazeer I (2014) Comparative performance evaluation of conventional multi-effect evaporation desalination processes. Appl Therm Eng 73:1194–1203
2. Hong-Jin J, Kwak H-Y (2013) Performance evaluation of multi-effect distiller for optimized solar thermal desalination. Appl Therm Eng 61:491–499
3. Sharon H, Reddy KS (2015) A review of solar energy driven desalination technologies. Renew Sust Energ Rev 41:1080–1118
4. Kiatsiriroat T, Bhattacharya SC, Wibulswas P (1987) Transient simulation of vertical solar still. Energy Convers Manag 27(2):247–252
5. El-Sebaii AA (1998) Parametric study of a vertical solar still. Energy Convers Manag 39 (13):1303–1315
6. Boukar M, Harmim A (2004) Parametric study of a vertical solar still under desert climatic conditions. Desalination 168:21–28
7. Boukar M, Harmim A (2005) Performance evaluation of a one-sided vertical solar still tested in the desert of Algeria. Desalination 183:113–126
8. Reddy KS, Sharon H (2016) Active multi-effect vertical solar still: Mathematical modeling, performance investigation and enviro-economic analyses. Desalination 395:99–120
9. Kumar S, Tiwari GN (2009) Life cycle cost analysis of single slope hybrid (PVT) active solar still. Appl Energy 86:1995–2004
10. Kumar S, Kurmaji KT (2013) Carbon credit earned by some designs of solar stills. Desalin Water Treat 51:1–10
11. Dwivedi VK, Tiwari GN (2010) Thermal modeling and carbon credit earned of a double slope passive solar still. Desalin Water Treat 13:400–410
12. Mittal ML, Sharma C, Singh R (2014) Decadal emission estimates of carbon dioxide, sulphur dioxide and nitric oxide emissions from coal burning in electric power generation plants in India. Environ Monit Assess 186:6857–6866
13. Kanchan S, Kumarankandath A (2015) The Indian power sector: need of sustainable energy access. Socio-Ecol Narratives:126–141
14. Al-Karaghouli A, Kazmerski LL (2013) Energy consumption and water production cost of conventional and renewable energy powered desalination processes. Renew Sust Energ Rev 24:343–356

Chapter 25
Integration of Solar Power Plant to Existing Network with Adaptive Relay Protection in the Concept of Smart Grid

Mehmet Tan Turan, Yavuz Ates, and Erdin Gokalp

25.1 Introduction

Nowadays, the popularity of conventional power plants that produce electrical energy is being replaced by renewable energy power plants which use renewable energy as the power source. The number of renewable power plants such as wind turbine plants and solar power plants are being increased as a result of environmental concerns [1]. Conventional power plants and outdated technology of existing transmission and distribution systems do not meet the requirements of new complex infrastructure where the complexity is caused by integration of renewable power plants and their unpredictable energy production values. At this point, realization of integration of conventional power plants and renewable power plants should be the first step in order to eliminate this complexity problem. The sequence of integration studies should include realization of necessary improvements on the grid that becomes inadequate for the requirements of new-generation power plants, and improved grid control and protection solutions should be furnished. One of the major drawbacks for grid control systems is the power production estimation and power supply continuity of renewable power plants [2]. The wind speed and the solar radiation estimations are the major criteria for the net and gross power output of the renewable power plants. For that reason, conventional and renewable power plants are being operated as parallel, and renewable power plants are coordinated with conventional power plants through the grid for safe and reliable operation. This methodology is used for ensuring consumers fed from the grid will be energized in case of power output decrement from the renewable power plants. The methodology considers conventional and renewable power plants as the integrated parts of grid [3].

M. T. Turan (✉) · Y. Ates · E. Gokalp
Yildiz Technical University, Electrical Engineering Department, Istanbul, Turkey

S. Nižetić, A. Papadopoulos (eds.), *The Role of Exergy in Energy and the Environment*, Green Energy and Technology,
https://doi.org/10.1007/978-3-319-89845-2_25

The first criterion for integration of a solar power plant to the grid is the determination of power plant effects on the grid. The existing grid network shall be examined for necessary connection requirements of solar power plants. The examination shall include current carrying capacity of connection bus, short circuit power limitation, voltage level of the bus and system stability studies. The relay coordination analysis shall be realized before integration of power plant. The coordination analysis shall cover existing relays and integrated relays of solar power plant considering different operating conditions and all possible scenarios. The existing relays of the grid and connection bus shall be considered before implementation of power plant relay settings along with an extended relay coordination study including selectivity factor.

The reduction of CO_2 emission which is caused by thermal power plants is one of the major advantages of renewable energy power plants. Pulverized coal power plants are considered as the reference point for the CO_2 emission ratio which varies between 850 kg/MWh and 950 kg/MWh [4, 5]. In this study, average yearly production of solar power plant is calculated, and total CO_2 emission reduction is presented along with relevant calculations and protection system design.

One of the major aims of the solar power plant integration is to increase efficiency of the plant and optimize the power generation of the plant. For that reason, solar radiation and daylight duration values contain an important effect on plant location and integration point to the grid. The integration criteria and effects of the integration were inspected and analysed [6–9]. The solar power plant integration shall include an optimized production capacity, efficiency and wide operation range for different scenarios [10]. The short circuit power capacity of the existing system and the effect of integrated solar power plant which are the major factors for integration shall be analysed for all possible scenarios. Integrated power plants cause an increment on the short circuit current during a possible fault event whereas recently added relays with plant may decrease the fault clearing time [11]. For that reason, all positive and negative effects of integrated new power plant shall be analysed [12].

In this chapter, the IEEE 9 bus test system is used as the grid model where ETAP is used as the simulation environment [13]. As the first step, IEEE 9 bus system model is built and relevant load flow short circuit analysis is realized in order to observe behaviour of the system. After the first stage, the integration bus for solar power plant is decided in accordance with optimal connection parameters. The evaluated structure contains load models designated as critical consumers and non-critical consumers. A 600 kVA rated solar power plant model is designed for the purpose of solar power integration and analysis. The solar radiation data of Yildiz Technical University Davutpasa Campus is implemented to the designed plant model (latitude = 41.02, longitude = 28.89). The proposed operation philosophy contains parallel operation of the grid and plant along with the island operation mode. The grid and plant operate in parallel mode during normal operation where the solar power plant operates in island mode if any fault occurs in relevant buses. The solar power plant continues to feed isolated critical loads during a possible fault with the sequentially coordinated relays for different operation scenarios. Different scenarios are designed and simulated in ETAP in order to ensure reliability and stability of the network.

25.2 System Methodology

In this section, IEEE 9 bus test system is built, and necessary configuration requirements are applied to the system in ETAP environment as indicated in Fig. 25.1. The existing load models, line parameters and connection configurations are not changed.

The solar power plant is connected to bus 8 of the network through relevant medium voltage (MV) and low voltage (LV) transformers as indicated in Fig. 25.2. The integrated section includes solar power plant, MV consumers which are designated as local consumers for island mode operation of the plant, transformers and relevant protection equipment.

All necessary protection equipment for plant and 9 bus system are adopted to network model along with protection methodology since the 9 bus system did not equipped with any protection equipment at the first stage. The required parameters for current transformers, relays and circuit breakers are obtained from the necessary load flow and short circuit calculations.

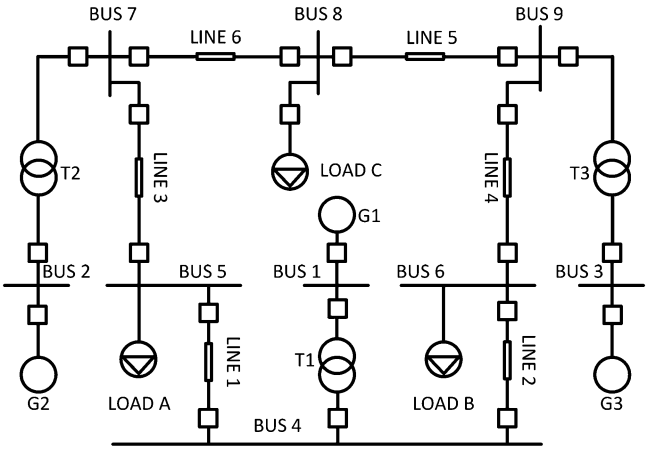

Fig. 25.1 IEEE 9 bus test system scheme

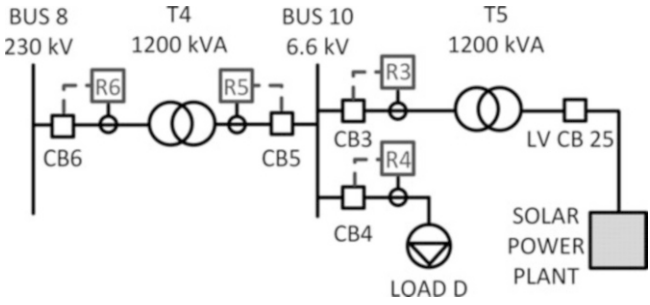

Fig. 25.2 Solar power plant – grid integration scheme

The load flow study is realized as the first stage of the study which presents the maximum and minimum current levels for various scenarios during normal operation. The obtained values are used to determine minimum operating current of the relays for coordination and selectivity studies. The minimum and maximum short circuit current values are calculated to determine pickup current of the relays and withstand current of protection equipment.

25.2.1 Simulation Parameters

The network and plant models are designed with the combination of transformers, transmission lines, load models, circuit breakers, generators, relays and photovoltaic (PV) modules in ETAP environment. The data and parameters of the generators are indicated in Table 25.1.

The consumers of the grid are modelled as stack loads which are indicated in Table 25.2.

The simulation test environment is designed in accordance with IEC standards with 50 Hz frequency and metric system. The circuit breakers and relays of the network and the plant model are presented in Table 25.3.

The relays and circuit breakers for LV system are chosen as ABB where the MV system components are chosen Siemens and SEL models. The current transformers (CTs) are used to generate input signals for relays and circuit breakers. CT ratings are indicated in Table 25.4.

The set values of relays are chosen in accordance with IEC normal inverse curve formula. The formula for protection curve selection is given by Eq. (25.1).

$$t = 0.14/\left(\left(I/I_{\mathrm{P}}\right)^{0.02} - 1\right) \times T_{\mathrm{P}} \tag{25.1}$$

Table 25.1 Generator model parameters

	Rating		% Impedance	
ID	MVA	kV	Xd″	*R*
G1	247.5	16.5	8.5	0.1
G2	192.0	18.0	10.2	0.1
G3	128.0	13.8	15.4	0.2

Table 25.2 Load model parameters

	Connection	Consumption	Island mode
ID	Bus ID	(MVA)	(Y/N)
Load A	5	135.5	N
Load B	6	92.5	N
Load C	8	102.6	N
Load D	10	0.5	Y

Table 25.3 Circuit breaker and relay model parameters [14–19]

CB ID	Current rating (A)	Model	Trip unit of CB	Relay ID	Model
CB 3	400	12-3AF-20	–	Relay 3	SEL 311 L
CB 4	400	12-3AF-20	–	Relay 4	SEL 311 L
CB 5	400	12-3AF-20	–	Relay 5	SEL 311 L
CB 6	400	245-3AP1–50	–	Relay 6	SEL 311 L
CB 7	400	245-3AP1–50	–	Relay 7	SEL 311 L
CB 8	400	245-3AP1–50	–	Relay 8	SEL 311 L
CB 2	400	245-3AP1–50	–	Relay 9	SEL 311 L
CB LV 1...24	63	XT2-L	Thermal magnetic	–	–
CB LV 25	1600	E2B	ABB SACE PR112	–	–

Table 25.4 Current transformer parameters

Current transformer ID	Circuit breaker ID	Relay ID	Conversion ratio
CT 2	CB 2	R 2	400/1 A
CT 3	CB 3	R 3	100/1 A
CT 4	CB 4	R 4	100/1 A
CT 5	CB 5	R 5	100/1 A
CT 6	CB 6	R 6	50/1 A
CT 7	CB 7	R 7	150/1 A
CT 8	CB 8	R 8	400/1 A

25.2.2 Solar Power Plant Model

The solar power plant model consists of PV panels, PV module and inverter models. As the first stage of the study, the PV panel shall be modelled. In this study, Kyocera KD205GX-LPU PV panel is modelled with the parameters indicated in Table 25.5.

The panels shall be connected in parallel and series in order to obtain the PV module with required power and voltage values. For that reason 153 PV panels are connected as 9 in series and 17 in parallel, and the PV module is obtained as indicated in Table 25.6.

The inverters are modelled with the data indicated in Table 25.7 after the PV module design stage.

The combination of PV module and inverter is used to gain 600 kVA power output from the solar power plant with the integration of 24 units to plant main bus. The voltage level of the plant main bus is designed as 400 V. The protection system of power plant consists of 63 A circuit breakers for main bus connection and 1600 A

Table 25.5 PV panel parameters [20]

Panel ID	Power (W)	Isc (A)	Vdc max (V)	Power tolerance (%)
KD205GX-LPU	205	8.33	600	5

Table 25.6 PV module parameters

Number of panels	Vdc (V)	Pdc (kW)	Idc (A)
$9 \times 11 = 99$	244,71	21,238	86,79

Table 25.7 Inverter design parameters

DC power (kW)	**Voltage (V)**	**Vmax/Vmin**	**FLA (A)**	**Efficiency (%)**	**Imax (%)**
23.611	220	%120/%80	107.3	90	150
AC power (kVA)	**Voltage (V)**	**Pfmax/ Pfmin**	**FLA (A)**	**PF (%)**	**K factor (%)**
25	480	100/80	30.07	85	150

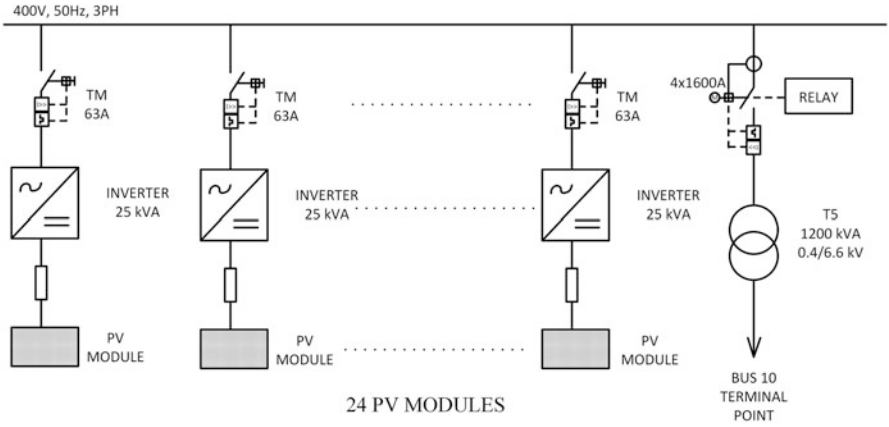

Fig. 25.3 Solar power plant model

main circuit breaker for main transformer connection. The solar power plant model is indicated in Fig. 25.3.

The indicated solar power plant model in Fig. 4.3 is connected to 9 bus network through bus 8 which is shown in Fig. 25.4.

The operation philosophy for solar power plant and the network is defined for three different conditions. The conditions and operation sequence are indicated in Fig. 25.5.

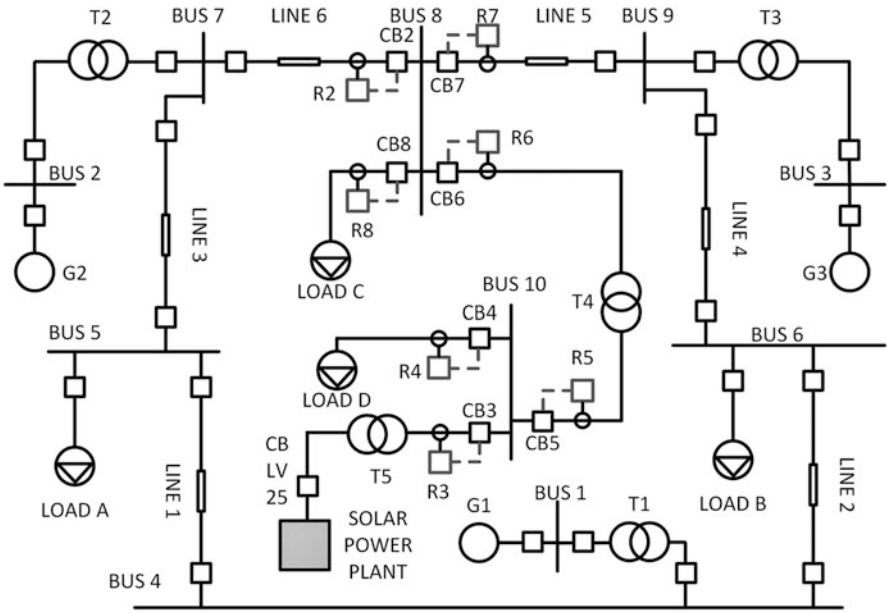

Fig. 25.4 Bus system and solar power plant integration scheme

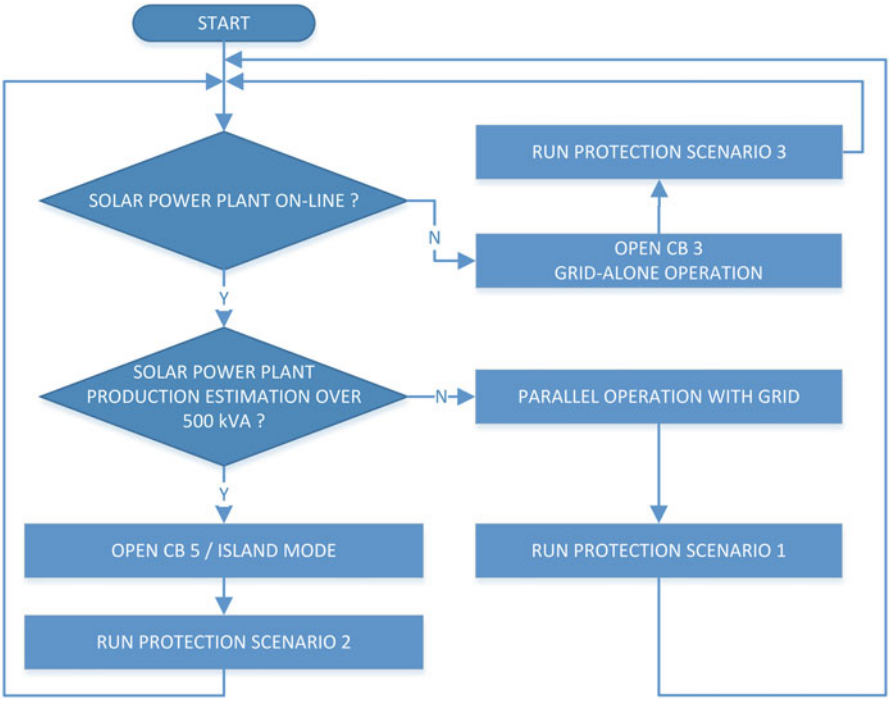

Fig. 25.5 Network – power plant operation flowchart

25.3 Test and Results

As the first step of the study, load flow calculations are realized to determine ratings of circuit breakers, relays, CTs and operating currents of relays for the purpose of solar power plant integration and selective relay coordination. After the determination of circuit breaker, relay and CT ratings, the minimum short circuit current values for whole network is calculated in order to decide minimum trip signal generation point for relays. The maximum short circuit current is calculated for the worst-case scenario which is the generators and solar system operating in parallel at full load with peak solar radiation data. IEC 60909 standards are used as the reference standard for the short circuit calculations. After the determination of maximum short circuit currents, the calculations for minimum short circuit current values are realized. The voltage c factor, reactance tolerance factors and temperature correction factors were applied as per IEC 60909 standard. The short circuit values used for relay setting studies are indicated in Table 25.8.

IEC normal inverse curve is not applied to LV CB 1–24 since the LV CBs of the inverter protection units are rated as 63 A of thermal magnetic type. The pickup current value for relays is decided in accordance with operating current of the lines which is calculated with relevant load flow studies. The pickup current values are indicated in Table 25.9.

The coordination studies are performed in the sequence of relay pickup current calculation, determination of time interval and time dial setting calculations including selective operation criteria. The relay time interval is set as 200 ms to ensure safe operation of relays in the concept of selectivity. The necessary sequential coordination functions are determined and applied to relays to avoid any possible power outage during a possible fault event. The sequential coordination functions are designed in a way that realizes the self-healing grid concept for the network. The relay time dial settings are presented in Table 25.10.

The simulation studies are performed as the fault insertions to all buses for all scenarios on ETAP environment. Short circuit fault simulations are applied and

Table 25.8 Maximum and minimum short circuit values for plant and network

Bus ID	Voltage level (kV)	Isc max (kA)	Isc min (kA)
1	16.5	209.4	190.4
2	18	159.1	144.6
3	13.8	155	140.9
4	230	9.19	8.33
5	230	9.17	8.36
6	230	9.17	8.34
7	230	9.18	8.33
8	230	9.17	8.34
9	230	9.18	8.35
10	6.6	2.62	1.99
PV BUS	0.4	19.41	13.88

Table 25.9 Relay pickup current (I_p) values

	Scenario 1		Scenario 2		Scenario 3	
Trip unit	Nominal current (A)	Pickup current (A)	Nominal current (A)	Pickup current (A)	Nominal current (A)	Pickup current (A)
R2	173	208	173	208	173.6	208
R3	44.9	54	43.6	52	0	0
R4	43.7	52	43.6	52	43.6	52
R5	24.4	30	0	0	43.6	52
R6	0.7	2.5	0	0	1.3	3
R7	93	111	92.9	110	93.5	112
R8	259	312	259	312	259	312
LV CB 25	740.2	880	719	864	0	0
LV CB 1...0.24	30.84	44.1	29.96	44.1	0	44.1

Table 25.10 Relay time dial (*T*p) settings

	Scenario 1	Scenario 2	Scenario 3
Trip unit	Time dial setting (*T*p)	Time dial setting (*T*p)	Time dial setting (*T*p)
R2	0.08	0.08	0.21
R3	0.12	0.08	0.05
R4	0.08	0.05	0.05
R5	0.08	0.05	0.08
R6	0.05	0.08	0.12
R7	0.08	0.08	0.21
R8	0.05	0.05	0.12
LV CB 25	*FIXED*	*FIXED*	*FIXED*
LV CB 1...0.24	*FIXED*	*FIXED*	*FIXED*

transient response of the system is observed. The predefined sequential coordination functions are tested to ensure consumers are being fed during a possible fault event via another possible transmission line. The operation sequence is set to be executed as indicated in Fig. 25.6.

The short circuit fault location, relay setting and sequential coordination functions are combined in ETAP environment and simulated. The results of the system response are presented in Table 25.11.

Three different scenarios are applied to the system to simulate worst-case situations to test stability and reliability of the system. As the first scenario, solar power plant and the grid is modelled in parallel operation mode. During a fault at transformer side and bus side, system response is observed as indicated in Table 25.11. The relays which are coordinated with adaptive set values responded to the fault in 259 ms as the maximum fault clearing time.

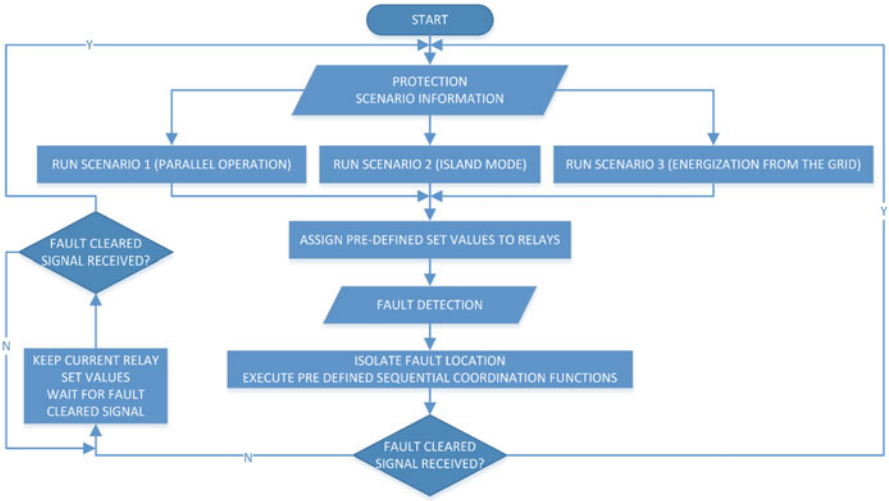

Fig. 25.6 Protection system flowchart

Table 25.11 System response for short circuit fault

Scen.	Fault location	Coordinated relays	Action	Time (ms)
1	T5 transformer MV side	R - 3/4/5	CB-3 OPENCB-LV-25 OPEN	219255
1	Bus 8	R - 2/7/6	CB-6 OPENCB-2 OPENCB-7 OPEN	159174259
3	T4 transformer HV side	R - 3/4/5/6	CB-6 OPENCB-5 OPENCB-3 CLOSE	99.4159400
2	T5 transformer MV side	R - 3/4/5	CB-3 OPENCB-LV-25 OPENCB-5 CLOSE	161255671

The second scenario consists of the transfer of the loads from solar power plant to grid during a possible fault event on the solar power plant. The system response is calculated as 671 ms including isolation of fault location and transfer of the loads. The implemented algorithm realizes the transfer of loads to another source in 671 ms in a reliable way which includes isolation of fault location, checking of possible feeders for re-energizing the consumers.

The last scenario examines the transfer of load from grid to solar power plant during a fault on the grid side. System response for the load transfer took 400 ms including fault location isolation and energization of consumer from the solar power plant in accordance with network operation and protection flowcharts.

25.4 Conclusions

In this chapter, IEEE 9 bus test system is combined with a solar power plant including necessary protection functions in self-healing grid concept. The study is based on adaptive and selective coordination of protection relays considering solar power plant operation schedule. Necessary algorithms are designed and applied to the network model in order to handle all possible scenarios as the combination of solar power plant control and protection system.

The major aim of the study is to obtain reliable protection system that isolates fault location and uses other possible sources to feed consumers along with integration of solar power plant. The solar radiation criterion and unexpected power decrements at solar power plant factors are implemented to protection philosophy.

After the integration of solar power plant to grid, worst-case scenarios are simulated and system response is observed. According to test results, protection system operates properly for all scenarios including load transfer from plant to grid and vice versa. The load transfer system lets the consumers being fed during any possible fault event from another power source in limitations of solar power plant generation.

The solar power plant generates 3,06 MWh/day and with the average CO_2 emission data total CO_2 emission is reduced by 2754 kg/day in normal operation which is the parallel operation of grid and the solar power plant. The normal operation philosophy of the network presents advantages of cost reduction and CO_2 emission reduction for the aim of green cities combined with smart protection systems.

Nomenclature

MV	Medium voltage
LV	Low voltage
HV	High voltage
ms	Milliseconds
PV	Photovoltaic
CB	Circuit breaker
R	Protection relay
CT	Current transformer

References

1. Arrinda J, Barrena JA, Rodriguez MA, Guerrero A (2014) Analysis of massive integration of renewable power plants under new regulatory frameworks, In: 3rd international conference on renewable energy research and applications, Milwakuee, USA, 19–22 Oct 2014
2. Chua KH (2012) Energy storage system for mitigating voltage unbalance on low-voltage networks with photovoltaic systems. IEEE Trans Power Delivery 27:1783–1790

3. Bilal HM, Khan AZ (2015) Economic planning of network for integration of renewable: a review. Power Gener Syst Renew Energy Technol (PGSRET) 10–11:1–3
4. Marion J, Nsakala N, Griffin T, Bill A (2001) Controlling power plant CO2 emissions: a long range view. In: first national conference on carbon sequestration. NETL Publications, Washington DC
5. Narula RG, Wen H, Himes K (2002) Incremental cost of CO2 reduction in power plants. In: Proceedings of IGTI ASME turbo expo, The Netherlands, June 3–6 2002
6. Mahela OP, Shaik AG (2015) Detection of power quality events associated with grid integration of 100kW solar PV plant. In: 2015 International conference on energy economics and environment (ICEEE), Greater Noida Uttar Pradesh, India, 27–28 March 2015, pp 1–6
7. Shah J, Narimani M, Mochopoulos G (2013) Solar power plant installation and integration: case study for Oshawa Power and Utilities Corporatio. In: 2013 26th IEEE canadian conference on electrical and computer engineering (CCECE), Regina, Canada, 5–8 May 2013, pp 1–4
8. Gomes JPR, Boaventura WC, Cardoso EN, Lopes BM (2015) Impact of integrating a solar power plant in a distribution feeder considering short circuit events. In: 2015 I.E. 13th Brazilian power electronics conference and 1st southern power electronics conference (COBEP/SPEC), Fortaleza, Ceara, Brazil, 28 Nov–2 Dec 2015, pp 1–5
9. Tripathi A, Sahay KB (2016) Modeling and simulation of proposed grid connected 10 MW solar PV array power plant at Lucknow. In: 2016 I.E. 1st international conference on power electronics, intelligent control and energy systems (ICPEICES), New Delhi, Delhi, India, 4–6 July 2016, pp 1–6
10. Deane JP, Drayton G, Gallachoir BPO (2014) The impact of sub-hourly modelling in power systems with significant levels of renweable generation. Appl Energy 113:152–158
11. Afifi SN, Darwish MK (2014) Impact of hybrid renewable energy systems on short circuit levels in distribution networks. In: Power engineering conference (UPEC), 49th international universities, Cluj-Napoca, Romania, pp 1–5
12. Safty El S, Abd El Geliel BM, Ammar CM (2010) Distributed generation stability during fault conditions. In: International conference on renewable energies and power quality, Granada, Spain, Mar 23–25 2010
13. IEEE 9 bus test system. http://icseg.iti.illinois.edu/wscc-9-bus-system/
14. Siemens_12-3AF-20 MV Circuit Breaker Catalogue. https://w5.siemens.com/italy/web/MediaTensione/interruttoriecomponenti
15. SEL 311 L Relay Catalogue. https://selinc.com/products/311L
16. ABB E2N Circuit Breaker Catalogue. http://new.abb.com/products/1SDA055889R1
17. ABB XT2-L Circuit Breaker Catalogue. http://new.abb.com/products/1SDA067644R1
18. ABB E2B Circuit Breaker Catalogue. http://new.abb.com/products/1SDA055792R1
19. ABB SACE PR122 Trip Unit Catalogue. http://www02.abb.com/global/abbzh/abbzh251
20. Kyocera PV Panel Catalogue. http://www.kyocerasolar.eu/index/products.html

Chapter 26
Comparison of Acid and Alkaline Pretreatment Methods for the Bioethanol Production from Kitchen Waste

Mine Nazan Kerimak Öner

26.1 Introduction

Pretreatment methods can be categorized as mechanical, thermal, chemical, biological, or a combination of these methods. Among the widely reported pretreatment methods tested at the lab scale, only a few mechanical, thermal, and thermochemical methods have been successfully applied at full scale [4].

Biomass is a renewable resource, which causes problems when it is not used. The challenge, therefore, is to convert biomass into a resource for energy and other productive uses. There are advantages in the use of biomass. Biomass is a renewable resource and has a steady and abundant supply, especially those biomass resources that are by-products of agricultural activity. Biomass use is carbon neutral, can displace fossil fuels, and helps reduce greenhouse gas (GHG) emissions, while closing the carbon cycle loop. As the debate on food versus fuel intensifies, biomass can provide added income for farmers without compromising the production of main food and even nonfood crops [9].

Kitchen waste, which is a renewable biomass, is one of the major components of municipal solid waste, which mainly includes leftover food and vegetable residue waste generated from the kitchens at various places of food preparation such as restaurants, cafes, hospitals, hotels, canteens, jails, and picnic spots, as well as from different food-processing industries. It is highly biodegradable, which has been found to pose pollution problems during its disposal and treatment. Its biodegradation is the main source of decay/odor and leachate during collection and transportation. It is not suitable for landfilling and incineration, because of its rapid

M. N. Kerimak Öner (✉)
Kocaeli University, Köseköy Vocational School, Department of Food Technology, Kocaeli, Türkiye
e-mail: mine@kocaeli.edu.tr

S. Nižetić, A. Papadopoulos (eds.), *The Role of Exergy in Energy and the Environment*, Green Energy and Technology,
https://doi.org/10.1007/978-3-319-89845-2_26

putrescibility, moisture content, and low heat value. Moreover, these processes do not accomplish the dual goals of waste reduction and energy production. Furthermore, the valuable energy contained in organic waste is lost to the energy cycle [9].

Many technologies have been developed recently—including physical, chemical, and biological pretreatments—in order to treat biomass stock. Every treatment has different effects on the subsequent processing and the yield of the products. Pretreatment with acid such as sulfuric acid (H_2SO_4) has been commercially used to treat biomass such as switchgrass, corn stover, and spruce (softwood). Other acids such as hydrochloric acid (HCl), phosphoric acid (H_3PO_4), and nitric acid (HNO_3) can also be applied in a pretreatment process to remove hemicelluloses [7].

This study reviews pretreatment techniques that are thermal, chemical, or a combination of the two, to enhance the production of fermentable sugars. The effects of acid and alkaline pretreatment methods are discussed independently and in thermal combinations. Pretreatment methods are compared in terms of their efficiency in production of reducing sugars. On the basis of the comparison, thermal pretreatment at low temperatures (<110 °C) and HCl and sodium hydroxide (NaOH) methods result in a more cost-effective process performance than other pretreatment methods.

26.2 Materials and Methods

26.2.1 Kitchen Waste Sample Preparation

The kitchen waste (KW) sample was collected from the students' cafeteria at the Köseköy Vocational School, Kocaeli University. Plastics, glasses, tissues, and other inorganic materials were separated out. The remaining organic fractions (consisting of rice, meats, and vegetables) were ground with water at a 1:1 volume ratio, using a commercial blender (Waring, Torrington, CT, USA) to ensure liquidity of the sample. The samples were stored at −20 °C for a maximum of a month prior to hydrolysis to prevent the degradation of organic matter and formation of organic acids. The ground sample was dried at 55 °C until it was a fixed mass. Then, the waste sample was screened to obtain a particle size of <2 mm to be used for the prehydrolysis treatment. The flow diagram for saccharification of kitchen waste is shown in Fig. 26.1.

Various methods of prehydrolysis pretreatment were investigated, including different chemical pretreatments combined with steam and enzyme treatment, and various combinations of chemicals coupled with microwave treatment. Additionally, the effects of H_2SO_4, HCl, and NaOH combined with enzyme/steam treatment (in an autoclave) were investigated in this research project [13]. However, only the results of pretreatment with HCl and NaOH at different concentrations, at different temperatures, and for different durations are described in this chapter.

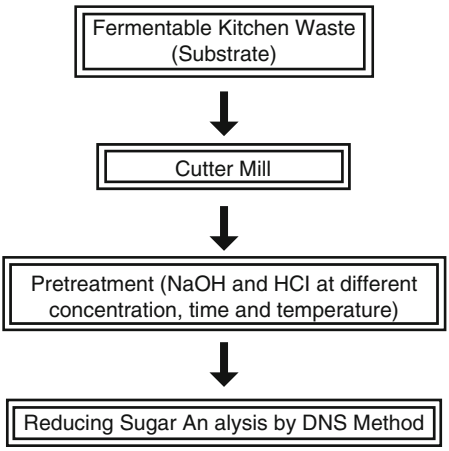

Fig. 26.1 Pretreatment of fermentable kitchen waste

26.2.2 Acid and Alkaline Pretreatments

26.2.2.1 Acid Hydrolysis

The kitchen waste sample was soaked in HCl at different concentrations of 0–5% at a solid-to-liquid ratio of 10 g in 100 mL. After pretreatment for increasing durations and at increasing temperatures, both raw and treated kitchen waste were analyzed. The reducing sugar concentration was assayed by the dinitrosalicylic acid (DNS) method [8]. The maximized parameter in this study was set to be the amount of soluble sugars. Three replicates were done for each experiment.

26.2.2.2 Alkaline Hydrolysis

The kitchen waste sample was soaked in NaOH at different concentrations of 0–5% at a solid-to-liquid ratio of 10 g in 100 mL. After pretreatment for increasing durations and at increasing temperatures, both raw and treated kitchen waste were analyzed. The reducing sugar concentration was assayed by the DNS method [8]. The maximized parameter in this study was set to be the amount of soluble sugars. Three replicates were done for each experiment.

26.2.3 Analytic Methods

The physicochemical analysis of kitchen waste included determination of pH, total solids (TS) and total volatile solids (TVS), moisture, ash, and total carbohydrates. The analyses were based on the standard method [3]. Moisture and ash were

determined on the basis of the standard method [1, 2]. The remaining percentage was assumed to be the total carbohydrate content [10]. The total carbohydrate amount was determined according to the method described by Dubois et al. [5].

26.2.4 Effect of Solid Loading on Hydrolysis Performance

In order to test the effect of solid loading on hydrolysis performance, the best conditions of the pretreatment hydrolysis method in this work were tested with different KW loadings: 0.5%, 1%, and 2%. The reducing sugar concentration was assayed by the DNS method after each experiment [8]. Three replicates were done for each experiment.

26.3 Results and Discussion

Prior to pretreatment of kitchen waste, a detailed physicochemical characterization was performed. The main characteristics of the kitchen waste are listed in Table 26.1.

The main characteristic of the sample was its high content of carbohydrates (>50% of the total composition of the sample) because the kitchen waste was taken from cafeterias. Thus, this waste was suitable for production of ethanol and other biofuels. Comparable compositional analyses have previously been reported by Vavouraki et al. [12] and Thembehurkar and Mhaisalkar [9]. In particular, their analyses of volatile solids (VS) were in agreement with our measurements, whereas our total solid value was quite a lot higher than their values. A similar total KW solid value was also reported by Uncu and Çekmecelioğlu [10]. The chemical pretreatment of the substrate was aimed at increasing the content of soluble sugars in the sample in order to facilitate its subsequent biochemical conversion into

Table 26.1 Characteristics of fermentable food waste used in this study

Parameter	Value[a] (%) [w/w]
Total solids	35.02
Total volatile solids[b]	97.00
Moisture	58.18
pH	6.50
Ash	5.20
Total sugars[c]	67.20
Soluble sugars[c]	32.35

[a]Results for three replicates
[b]Composition of food waste per gram of dry mass. The percentages of total and soluble sugars correspond to the equivalent grams of glucose per 100 g of kitchen waste dry mass
[c]The percentages of total and soluble sugars correspond to the equivalent grams of glucose per 100 g of kitchen waste dry mass

Table 26.2 Total soluble sugar yields after pretreatment of kitchen wastes with increasing NaOH concentrations, temperatures, and durations

	Soluble sugar yield (mg glucose/g dry sample)					
	30 °C			60 °C		
NaOH concentration	30 min	60 min	90 min	30 min	60 min	90 min
0%	153.16	–	145.04	36.01	–	153.05
1%	205.20	218.02	244.12	115.30	48.62	154.85
2%	180.16	162.14	360.32	72.06	68.43	165.65
3%	216.19	261.23	414.35	61.26	61.26	174.66
4%	126.11	234.21	288.25	57.62	42.31	151.25
5%	144.13	162.14	284.65	46.82	39.61	169.25

ethanol. Different concentrations of chemical solutions (HCl and NaOH) were tested at different temperatures and for different durations of contact.

In this study the best results were obtained with HCl pretreatment methods. Acid pretreatment at 90 °C resulted in high concentrations of soluble sugars. In particular, chemical pretreatment with 1% HCl for 90 min at 60 °C resulted in a yield of 638.24 mg of carbohydrates per gram of dry sample, which was very close to the total sample content of carbohydrates (672 mg of carbohydrates per gram of dry KW). When pretreatment is conducted with a higher percentage of acids at an elevated temperature (>100 °C), it may lead to negative effects on the sugar content of samples. This is due to the formation of sugar degradation compounds such as furfural and 5-hydroxymethyl furfural (5-HMF) [7, 11]. Undesirable formation of sugar degradation compounds such as furfural, 5-HMF, and other compounds was avoided by applying mild acid hydrolysis conditions (<100 °C); therefore, measurement of those by-products was omitted in this study [6, 11]. When the glucose recovery from the dry kitchen wastes was evaluated, the best pretreatment method to obtain maximum glucose generation was the HCl pretreatment method, but those findings are not detailed in this chapter; they have been submitted for publication elsewhere as an original research article.

Besides the HCl pretreatment, which yielded 672 mg of carbohydrates per gram of dry KW, the second best results were obtained with 3% NaOH pretreatment, yielding 414.35 mg of carbohydrates per gram of dry sample) (Table 26.2, Figs. 26.2 and 26.3). The effect of the NaOH concentration on the glucose yield in terms of milligrams of glucose per gram of dry kitchen waste sample is shown in Table 26.2. The highest glucose yield of 414.35 mg of carbohydrates per gram of dry sample was achieved after treatment with 3% NaOH at 30 °C for 90 min (Fig. 26.2). This is much more glucose than that released by 3% NaOH treatment at 60 °C for 90 min (174.66 mg of carbohydrates per gram of dry sample (Fig. 26.3).

Additionally, detailed information on the soluble sugars obtained, in terms of glucose recovery percentages, from NaOH pretreatments for 30-, 60-, and 90-min durations are presented in Table 26.3 and Fig. 26.4.

On the other hand, kitchen waste subjected to pretreatment with 2% H_2SO_4 was found to have the lowest glucose recovery, with a value of 14.89% (data not shown).

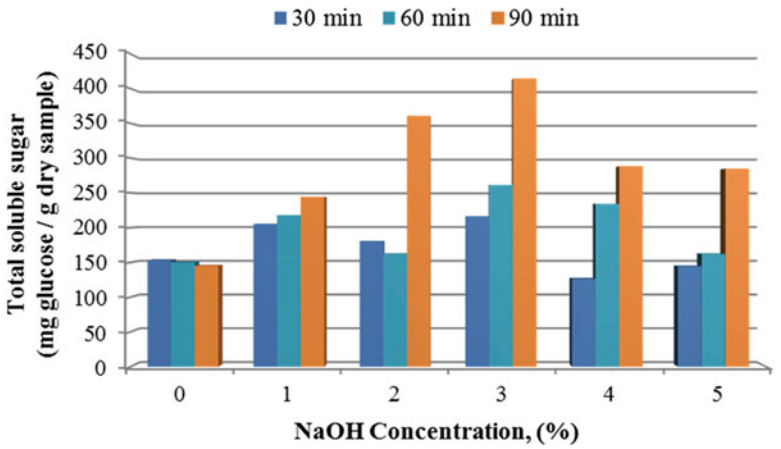

Fig. 26.2 Glucose yield from kitchen waste after NaOH pretreatment at 30 °C

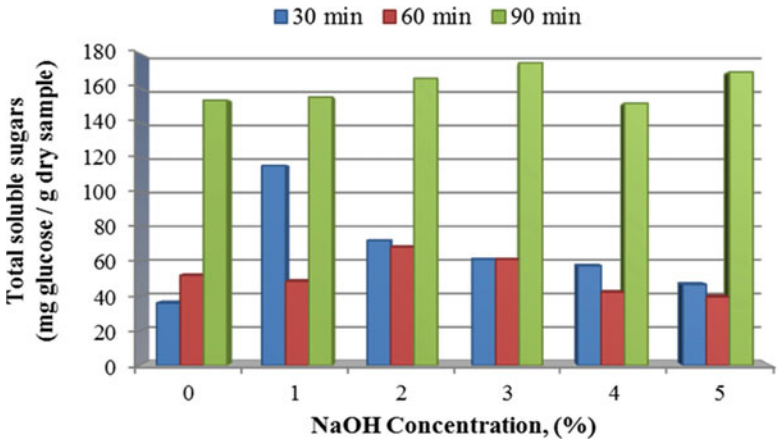

Fig. 26.3 Glucose yield from kitchen waste after NaOH pretreatment at 60 °C

Table 26.3 Glucose recovery from kitchen waste after pretreatment with increasing NaOH concentrations and durations

	Glucose recovery (%)		
NaOH concentration	30 min	60 min	90 min
0%	22.79	22.75	21.58
1%	30.53	32.43	36.33
2%	26.80	24.12	53.62
3%	32.16	38.86	61.66
4%	18.76	34.84	42.89
5%	21.42	24.12	42.35

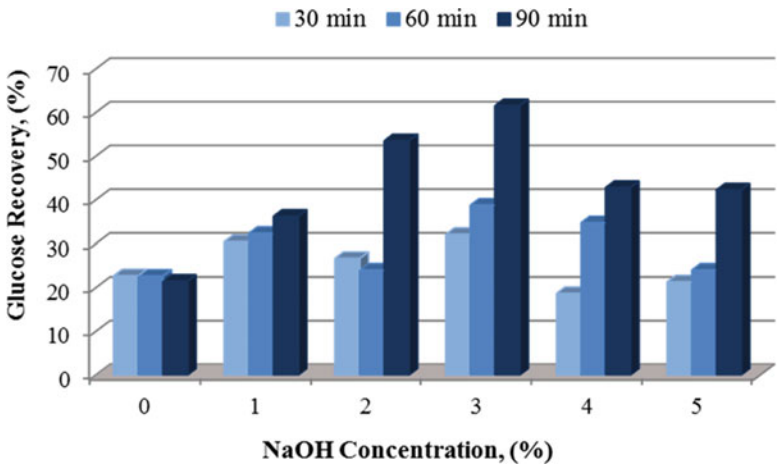

Fig. 26.4 Glucose recovery (%) from kitchen waste after pretreatment at 30 °C with increasing NaOH concentrations and durations

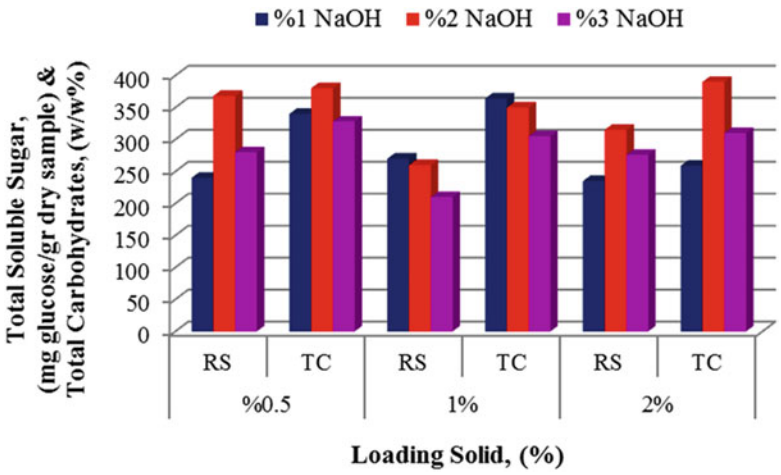

Fig. 26.5 Effects of solid material loading (0.5%, 1%, and 2%) on hydrolysis performance of kitchen waste at 100 °C with 120-min incubation and pretreatment with increasing NaOH concentrations. RS reducing sugars, TC total carbohydrates

In order to test the effect of solid loading on hydrolysis performance, the conditions of the pretreatment hydrolysis methods in this work were tested with different KW loadings: 0.5%, 1%, and 2%. The best result was achieved with a 2% solid loading at 100 °C after 120-min incubation in the presence of 2% NaOH. The effect of solid loading on hydrolysis performance of kitchen waste in the presence of NaOH at 100 °C after 120-min incubation is shown in Fig. 26.5 and that in the presence of HCl at 100 °C after 120-min incubation is shown in Fig. 26.6.

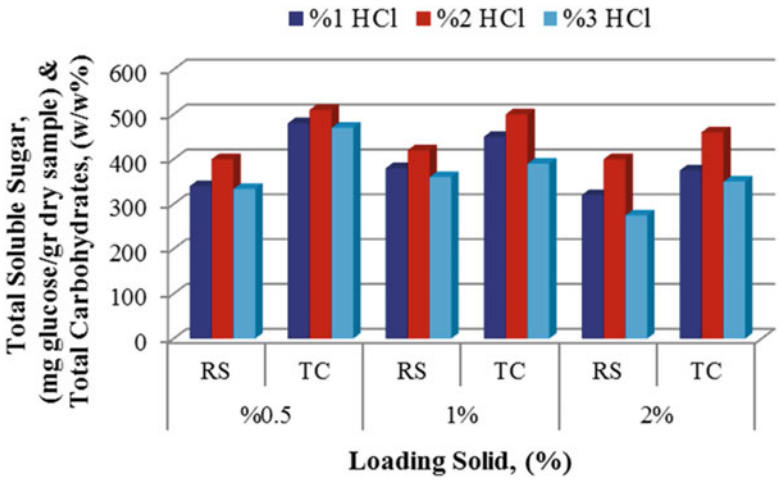

Fig. 26.6 Effects of solid material loading (0.5%, 1%, and 2%) on hydrolysis performance of kitchen waste at 100 °C with 120-min incubation and pretreatment with increasing HCl concentrations. RS reducing sugars, TC total carbohydrates

Table 26.4 Effects of solid loading on reducing sugar (RS) and total carbohydrate (TC) content

	RS and TC content (%)					
	0.5% solid loading		1.0% solid loading		2.0% solid loading	
NaOH concentration	RS	TC	RS	TC	RS	TC
1%	240	340	270	364	235	259
2%	368	380	260	350	315	390
3%	280	328	210	305	276	310

The effect of solid loading on total carbohydrate solubilization into fermentable sugars was observed using the acid and alkaline conditions described in this chapter. When half of the solid loading was tested (i.e., 0.5%), no significant increase was observed, whereas the total carbohydrate and soluble sugar yields remained unaffected (Table 26.4).

26.4 Conclusions

Different pretreatment methods for kitchen waste have been described and widely studied to improve ethanol production processes. Among the different methods, chemical, thermochemical, and enzymatic methods, and combinations of them, are currently the most effective methods and the most promising technologies for industrial applications. Combinations of different pretreatments have been also considered and might be interesting to obtain optimal fractionation of the different components and achieve very high yields.

This study investigated the influence of single and combined pretreatments by acid and alkaline hydrolysis of kitchen waste on fermentable sugar production. The optimum experimental conditions for single pretreatment were 1% HCl incubation for 90 min at 60 °C, which produced 638.24 mg of carbohydrates per gram of dry sample fermentable sugars, and 3% NaOH pretreatment for 90 min at 30 °C, which produced 414.35 mg of carbohydrates per gram of dry sample fermentable sugars and 61.66% glucose recovery. The worst pretreatment method was H_2SO_4 pretreatment, which had the lowest glucose recovery (14.89%). These results indicated that the NaOH pretreatment method can be used for glucose generation in a saccharification process.

All pretreatment and hydrolysis techniques used for KW are of great importance for bioconversion of KW to bioproducts. Thus, optimization of hydrolysis techniques may result in both environmental and economic benefits. Hence, this study investigated the impact of acid and alkaline chemical pretreatment methods on the hydrolysis of KW to glucose and other fermentable sugars used in bioethanol production.

Acknowledgements The author is thankful to the Scientific Research Support Fund of the University of Kocaeli for supporting this work under research grant no. 2016/062.

Nomenclature

5-HMF	5-Hydroxymethyl furfural
AACC	American Association of Clinical Chemistry
DNS	Dinitrosalicylic acid
GHG	Greenhouse gas
H_3PO_4	Phosphoric acid
HCl	Hydrochloric acid
HNO_3	Nitric acid
H_2SO_4	Sulfuric acid
KW	Kitchen waste
NaOH	Sodium hydroxide
RS	Reducing sugars
TC	Total carbohydrates
TS	Total solids
TVS	Total volatile solids
VS	Volatile solids

References

1. American Association of Clinical Chemistry (1999a) Moisture-air-oven methods (44-15.02), International Approved Methods (1999)
2. American Association of Clinical Chemistry (1999b) Ash-basic method (08-01.01), International Approved Methods (1999)
3. American Public Health Association (1995) Standard methods for the examination of water and waste water, 19th edn. American Water Works Association, Water Environment Federation, USA

4. Ariunbaatar J, Panico A, Esposito G, Pirozzi F, Lens PNL (2014) Pretreatment methods to enhance anaerobic digestion of organic solid waste. Appl Energy 123:143–156
5. Dubois M, Gilles KA, Hamilton JK, Rebers PA, Smith F (1956) Colorimetric method for determination of sugars and related substances. Anal Chem 28(3):350–356
6. Hafid HS, Rahman NA, Shah UKM, Baharudin AS (2015) Enhanced fermentable sugar production from kitchen waste using various pretreatments. J Environ Manag 156:290–298
7. Jamaludin SIS, Abd Kadir SAS, Safri NHM, Aba ND, Krishnan J (2012) Comparison of pretreatment methods for the enhancement of fermentable sugar production from kitchen waste. IEEE Colloquium on Humanities, Science and Engineering Research, (CHUSER 2012), Dec 3–4
8. Miller GL (1959) Use of dinitrosalysilic acid for determining reducing sugars. Anal Chem 31:426–428
9. Thembehurkar AR, Mhaisalkar VA (2007) Studies on hydrolysis and acidogenesis of kitchen waste in two phase anaerobic digestion. J Inst Public Health Eng 08:2
10. Uncu ON, Çekmecelioğlu D (2011) Cost-effective approach to ethanol production and optimization by response surface methodology. Waste Manag 31:636–643
11. Vavouraki AI, Angelis EMV, Kornaros M (2013) Optimization of thermo-chemical hydrolysis of kitchen wastes. Waste Manag 33:740–745
12. Vavouraki AI, Volioti V, Kornaros ME (2014) Optimization of thermo-chemical pretreatment and enzymatic hydrolysis of kitchen wastes. Waste Manag 34:167–173
13. Yoswathana N, Phuriphipat P, Treyawutthiwat P, Eshtiaghi MN (2010) Bioethanol production from rice straw. Energy Res J 1(1):26–31

Chapter 27
Investigation of Cultivation and Wastewater Treatment Potential of Microalgae and Cyanobacteria in Controlled Environment Minkery Wastewater

Yuchen Ji and Ilhami Yildiz

27.1 Introduction

The mink industry in Nova Scotia began in the 1930s and had grown at a high rate over the past 20 years. Today, there are around 100 mink farms, employing more than 1000 workers in Nova Scotia. According to the 2012 Statistics Canada census, Nova Scotian mink farming accounted for 54.3% of Canada's total mink production. Even further, the estimated value of the mink industry in Nova Scotia in 2012 was $140 million [1]. This number has dropped since then, due to weak demand and a problematic virus called Aleutian mink disease (AMD) virus. Mink products still consistently form the largest agricultural export in Nova Scotia. Amid the success of Nova Scotian mink industry, there are some concerns about the environmental impact of mink production. The main concerns are feces and urine produced by the mink. Rough estimates suggest that there are at least 18,000 tons of mink manure and 16 million liters of urine generated by mink farms in Nova Scotia each year [2]. Many concerned citizens, academics, and journalists suspect that the impacts of mink production on adjacent surface waters are detrimental. One report concluded that multiple instances of eutrophication and algae blooms were related to discharges from mink farms [3]. As with most agricultural wastewaters, mink discharges have high concentrations of pollutants, such as ammonium and phosphorus [4]. The composition of minkery wastewater will invariably have impacts on the local aquatic ecosystems, thereby damaging vital Nova Scotian resource.

As mentioned above, along with solid wastes, Nova Scotia minkery farms generate huge amounts of wastewater and continuously ignored the public outcry

Y. Ji · I. Yildiz (✉)
Dalhousie University, Faculty of Agriculture, Department of Engineering, Truro-Bible Hill, NS, Canada
e-mail: iyildiz@dal.ca

S. Nižetić, A. Papadopoulos (eds.), *The Role of Exergy in Energy and the Environment*, Green Energy and Technology,
https://doi.org/10.1007/978-3-319-89845-2_27

for their environmental impacts. As a consequence of the Fur Industry Act, approved on January 11, 2013, the industry is now forced to employ different bioenvironmental technologies for reducing the environmental impacts of its operations. With the new regulations from this act, mink producers are required to identify means to reduce pollutants in effluent waters [5]. This new government regulation of fur industry will have further implications for operational practices in the future. Minkery wastewater integrated into microalgae and cyanobacteria production as a means to reduce effluent water pollutants may provide a service to the mink industry as it tries to adapt to new regulations. Many studies reported microalgae and cyanobacteria assimilate multiple nutrients present in waste streams, which include ammonium, nitrate, nitrite, and phosphorus, and it has even been found to remove heavy metals along with some toxic organic compounds as well [6, 7]. It is the characteristic of microalgae and cyanobacteria that make them obvious candidates for wastewater treatment. Studies on using the microalgae and cyanobacteria cultivation as a tertiary wastewater treatment process started in the early 1970s [8]. The initial purpose was to treat the secondary wastewater even further to mitigate the potential eutrophication of surface water bodies following discharge [9]. One study even concluded that freshwater microalga *Chlorella pyrenoidosa* removed nutrients from settled domestic sewage more efficiently than activated sludge process did, suggesting that it would be more economical and desirable to employ microalgae cultivation as the secondary rather than tertiary treatment process [10].

At present, the large-scale microalgae and cyanobacteria production faces a number of cost-related bottlenecks [11, 12]. The energy and fertilizer costs of the large-scale microalgae and cyanobacteria production have been too high to be economically feasible. Despite the tremendous opportunity and value of the large-scale microalgae and cyanobacteria production, it is still hampered by the nagging impediment of reaching economic viability [13]. One study analyzing resource implications of microalgae and cyanobacteria cultivation concluded that nutrients, water, carbon, land, and energy were five main factors of reaching microalgae and cyanobacteria cultivation success [14]. Extensive research has been conducted exploring using a variety of agricultural wastewaters to offset the financial burden of nutrient, water, and even carbon supplies. Many researchers have demonstrated that a number of agricultural wastewaters have potential to be a viable substrate for microalgae and cyanobacteria cultivation with even improved yields when compared to other substrates [15–17].

As with most agricultural wastewaters, minkery wastewater has extremely high concentrations of nutrients including ammonium, phosphorus, and even organic carbon [4]. While posing some serious environmental problems, minkery wastewater could potentially be an ideal substrate for the large-scale microalgae and cyanobacteria production, especially under heterotrophic and mixotrophic conditions. At present, the most common organic carbon source for the large-scale microalgae and cyanobacteria production is glucose, and it comes at an enormous expense. Minkery wastewater is extremely rich in organic compounds that could potentially be an excellent organic carbon alternative for heterotrophic and

mixotrophic cultivation. Further research is essential because many questions remain unanswered regarding the suitability of using minkery wastewater as a substrate for microalgae and cyanobacteria cultivation. Such concerns include investigating the challenge of introducing a biologically diverse substrate into a pure culture, exploring potential sterilization techniques, quantifying biomass and bioproduct productivities, identifying nutrient deficiencies (if any) in wastewaters, and quantifying remediation efficiencies. Effectively answering these questions will provide invaluable technical information to microalgae and cyanobacteria industry.

In building upon existing research, this study aimed to assess the viability of using minkery wastewaters for microalgae and cyanobacteria cultivation, identify the effect of different cultivation techniques on microalgae and cyanobacteria cultivation, and quantify remediation efficiencies of wastewater treatment using microalgae and cyanobacteria. Our findings will provide the framework for future investigation of using minkery wastewater as a potential resource in Nova Scotia.

27.2 Materials and Methods

27.2.1 Strain and Culture Maintenance

Two strains used in this study, namely, *Chlorella vulgaris* and *Anabaena* sp., were purified and inoculated in 1-L Erlenmeyer flasks at approximately 20 °C and illuminated with a cool-white fluorescent light (32 W, 6500 K) with a light cycle of 16-h light and 8-h dark. Both flasks were sealed with a plug, allowing for aseptic gas exchange, and placed on a mechanical stirrer (HI 190, Hanna Instruments, USA) with 150-rpm rotation.

Both strains and mediums were purchased from the Canadian Phycological Culture Centre (CPCC), Department of Biology, University of Waterloo, Ontario, Canada. *Chlorella vulgaris* was cultured in a modified Bold's basal medium, and *Anabaena* sp. was cultured in BG-11_o medium (modified by J. Acreman). Table 27.1 summarizes the nutrient content of these two mediums.

27.2.2 Pretreatment of Minkery Wastewater

Minkery wastewater (cage-washing wastewater) was collected from the Dalhousie University's Fur Animal Research Centre in Bible Hill, Nova Scotia, and all samples were taken on the same day to ensure homogeneity among samples. Samples were frozen and then thawed as needed in order to discourage biological activity.

Prior to experiments, the raw minkery wastewater was thoroughly homogenized and filtered with filter cloth in order to remove all large solid particles. And then, the minkery wastewater was filtered one more time using 1.5-μm glass microfiber filters (691, VWR, UK). In this way, all side effects of solid particles and indigenous

Table 27.1 Nutrient concentrations of two traditional mediums

Nutrients	Concentration (mg/L)	
	Bold's basal medium	BG-11$_o$ Medium
$NaNO_3$	250	0
$MgSO_4 \cdot 7H_2O$	75	75
$CaCl_2 \cdot 2H_2O$	25	36
K_2HPO_4	75	30
$Na_2EDTA \cdot 2H_2O$	10	1
H_3BO_3	10.91	2.86
$MnCl_2 \cdot 4H_2O$	1.81	1.81
$ZnSO_4 \cdot 7H_2O$	0.222	0.222
$Na_2MoO_4 \cdot 2H_2O$	0.390	0.390
$CuSO_4 \cdot 5H_2O$	0.079	0.079
$Co(NO_3)_2 \cdot 6H_2O$	0.0494	0.0494
KH_2PO_4	175	0
KOH	6.2	0
$FeSO_4 \cdot 7H_2O$	4.98	0
NaCl	25	0
Na_2CO_3	0	20
Ferric ammonium citrate	0	6
Citric acid	0	6

bacteria in minkery wastewater on the cultivation of microalgae and cyanobacteria were eliminated. After filtration, the minkery wastewater was autoclaved at a sustained temperature and pressure of 121°C and 15 psi, respectively, for 20 min; after which, the minkery wastewater was stored at 4°C and prepared for the experiment.

27.2.3 Experimental Equipment

For each experimental unit, cultures were transferred from the flasks to three transparent plastic cylinders, which were 2.25-L vertical column controlled environment photobioreactors (Aqua Medic GmbH, Plankton Reactor, Bissendorf, Germany) (Fig. 27.1). These three photobioreactors essentially served as a holding tank, allowing microalgae or cyanobacteria cultivation and wastewater treatment. Three photobioreactors were employed under three independent cool-white fluorescent lights (8 W, 6700 K) at 20°C. Each fluorescent light can provide enough light for photosynthesis to occur. Three independent ambient air pumps (Fusion Quiet Power, 400, Taiwan) were used to continuously agitate the culture in each photobioreactor in order to keep the microalgae or cyanobacteria culture homogeneous. Moreover, three independent pH meters (Milwaukee, SMS 122, Romania) controlled and continuously monitored the pH of microalgae or cyanobacteria cultures.

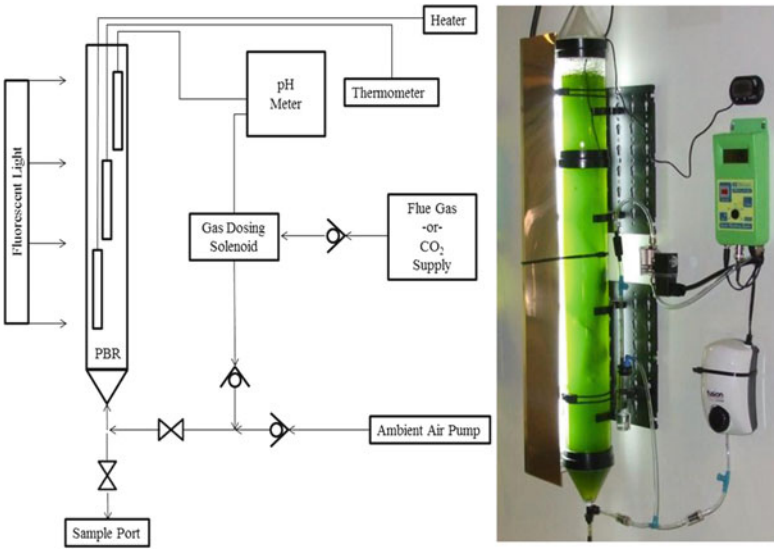

Fig. 27.1 Schematic diagram of the photobioreactor. (Adapted from [18], Fig. 30.7)

Once all three photobioreactors were inoculated, the growth period commenced. Upon analyzing the samples at the end of the growth period, all three photobioreactors were taken apart and sanitized carefully and put back together for the proceeding experimental units.

27.2.4 Experimental Design

In this study, for each photobioreactor, exactly 400-mL purified *Chlorella vulgaris* or *Anabaena* sp. inoculum (0.3–0.4 g/L) (20%) and 1600 mL of certain medium (80%) were inoculated. Each experimental unit was limited to 6 days of cultivation. A split-split-plot experimental design was used to arrange each experimental unit accordingly (Table 27.2). The whole plots were strains, the subplots were light cycles, and the sub-subplots were mediums. In total, the design had 24 different treatments, and three replications for each treatment were used to ensure effective integrity of findings. All statistical analyses were performed using a combination of the *Minitab 17* and *SAS* softwares. As mentioned earlier, strains were *Chlorella vulgaris* and *Anabaena* sp.; light cycles were (1) 6-day continuous light, (2) 48-h light and 24-h dark, (3) 24-h light and 48-h dark, and (4) 6-day continuous dark; and mediums were (a) minkery wastewater, (b) traditional mediums (modified Bold's basal medium and BG-11_o medium) (first control), and (c) distilled water (second control).

Table 27.2 Split-split-plot experimental design employed in the study

	Strains							
	Chlorella vulgaris				*Anabaena* sp.			
Light cycles:	1	2	3	4	1	2	3	4
Mediums	a	a	a	a	a	a	a	a
	b	b	b	b	b	b	b	b
	c	c	c	c	c	c	c	c
Mediums	a	a	a	a	a	a	a	a
	b	b	b	b	b	b	b	b
	c	c	c	c	c	c	c	c
Mediums	a	a	a	a	a	a	a	a
	b	b	b	b	b	b	b	b
	c	c	c	c	c	c	c	c

Whole plots were strains *Chlorella vulgaris* and *Anabaena* sp.; subplots (light cycles) were all light (1), 48-h light +24-h dark (2), 24-h light +48-h dark (3), and all dark (4); sub-subplots (mediums) were minkery wastewater (a), traditional mediums (b), and distilled water (c). Note that the table does not show any randomization used in the study

27.2.5 Quantification of Growth Kinetics

Four biomass estimation methods are commonly used to determine biomass generated in microalgae and cyanobacteria cultivation, including dry weight, optical density, cell count, and chlorophyll *a* content. Each method has an ideal sampling condition with regard to strain selection, culture size, growth medium, and desired output accuracy and precision.

Dry weight is a simple and intuitive method for biomass estimation. The major advantages of this method are the useful mass-based units, the simplicity of execution, and the inclusion of constituents based upon minimum particle size. The limiting assumption is that all material collected will be the target organism, which is only applicable in a pure culture. Dry weight of the samples was measured from the triplicate averages of volatile suspended solids (VSS) obtained by means of membrane filtration according to the *Standard Methods for the Examination of Water and Wastewater*, Method 2540 [19].

Optical density, also known as absorbance or turbidity, is frequently used as a rapid measurement of biomass in cultures. Using absorbance as an indicator offers perhaps the simplest and quickest means for quantifying culture productivity. This method has enormous value because it provides effective noninvasive approximation of biomass. There are however some major disadvantages of this method, including not being able to distinguish dead and live cells, and cellular conglomerates can give faulty readings. The optical density of *Chlorella vulgaris* was measured by a UV-Vis spectrophotometer (Cole-Parmer, USA) at 684 nm wavelength [20], with a light path of 10 mm, and the optical density of *Anabaena* sp. was measured with a light path of 10 mm at 683 nm [21], using the same UV-Vis spectrophotometer.

Cell count is another widely used method for estimating biomass through direct enumeration of the cells in the solution. The manual cell count method offers specific advantages in observer control and identification of contaminants. It requires an extensive time commitment and is potentially subjected to observer bias. The Bright-Line™ hemocytometer was used to count the number of cells under the microscope (Motic, BA310). The counting method was taken from *Standard Methods for the Examination of Water and Wastewater*, Methods 10200E and 10200F [19].

Chlorophyll *a* is regularly used as an estimator of microalgae and cyanobacteria biomass. The greatest advantage of this method is that it directly targets plant biomass. A substantial margin of error exists in the underlying assumption about the chlorophyll *a* concentration, because this concentration is highly variable in microalgae and cyanobacteria cells. Chlorophyll *a* content of the samples was measured according to the *Standard Methods for the Examination of Water and Wastewater*, Method 150.1 [19].

Overall, methods of optical density and cell count were performed every 12 h, while dry weight and chlorophyll a content methods were carried out at the beginning and end of each growth period. Once these measurements were taken, biomass increase in percentage of each growth period was calculated using Eq. 27.1.

$$\text{Biomass increase} = \left(\frac{x_6 - x_0}{x_0}\right) \times 100\% \tag{27.1}$$

where x_0 was the measurement at the beginning of each growth period (day 0) and x_6 was the measurement at the end (day 6).

27.2.6 Evaluation of Wastewater Treatment

The efficiency of wastewater treatment was evaluated by comparing the selected nutrients' contents of wastewater samples before and after microalgae and cyanobacteria cultivation. All samples were filtered using a Millipore 47 mm vacuum filter assembly with a 0.4-μm glass microfiber filter (GB-140, ADVANTEC, Japan) to remove all microalgae or cyanobacteria cells and other large suspended solids before analysis. Nutrient removal analysis was performed using Hanna Multiparameter Photometer (HI 83200, Hanna Instruments) and corresponding reagents, according to the instruction manual. The tested nutrients were ammonium, nitrate, nitrite, and phosphorus. Once these measurements were taken, efficiencies of wastewater treatment were calculated using Eq. 27.2 below:

$$\text{Nutrient removal} = \left(\frac{y_0 - y_6}{y_0}\right) \times 100\% \tag{27.2}$$

where y_0 was the nutrient content at the beginning of each growth period (day 0) and y_6 was the content at the end of each growth period (day 6).

27.3 Results and Discussion

When combined with biofuel production, microalgae species from the genus of *Chlorella* were most commonly used due to its high productivity of fatty acids relevant to transesterification reaction [22]. *Anabaena* is a genus of filamentous cyanobacteria known for nitrogen-fixing abilities. They are also one of four genera of cyanobacteria that produce neurotoxins, which are harmful to local wildlife. Both *Chlorella vulgaris* and *Anabaena* sp. showed potential to simultaneously accumulate biomass and treat minkery wastewater. Thereby, *Chlorella vulgaris* and *Anabaena* sp. were selected representing highly valuable and viable microalgae and cyanobacteria, respectively.

27.3.1 Minkery Wastewater Characteristics

The raw minkery wastewater collected from the Dalhousie Fur Animal Research Centre had an extremely high concentration of some major plant nutrients, such as nitrogen and phosphorus. These nutrient concentrations were much higher than what would normally be needed for microalgae and cyanobacteria cultivation. Therefore, the dilution of raw minkery wastewater should be employed to provide optimum nutrient content for microalgae and cyanobacteria cultivation. In our pre-experimental tests, *Chlorella vulgaris* and *Anabaena* sp. were cultivated in various concentrations of diluted minkery wastewaters, and it demonstrated that the most advantageous minkery wastewater concentration for microalgae cultivation ranged from 1% to 3% and the most favorable concentration for cyanobacteria cultivation was between 0.5% and 1%. As a consequence, all pretreated minkery wastewaters in this study were diluted with 99% autoclaved distilled water prior to actual experiment.

The nutrient content of the 1% pretreated minkery wastewater is provided in Table 27.3. Compared to the traditional mediums mentioned earlier, the characteristic of the minkery wastewater is different in terms of nitrogen form. In minkery

Table 27.3 Nutrient concentration of 1% minkery wastewater

Nutrient	Concentration (mg/L)
Alkalinity ($CaCO_3$)	160
Ammonium (NH_4^+)	73.27
Calcium (Ca^{2+})	0
Chemical oxygen demand (COD)	126
Dissolved oxygen (DO)	8.9
Magnesium (Mg^{2+})	0
Nitrate (NO_3^-)	0.1
Nitrite (NO_2^-)	0.18
Phosphorus (P)	13.6
Sulfate (SO_4^{2-})	10.0

wastewater, about 99% of total nitrogen was in the form of ammonium, which makes it an excellent growth medium for strains with a high ammonium demand, such as *Chlorella vulgaris* and *Chlorella* sp. [23, 24]. It may however not be an ideal growth medium for strains with a high demand in nitrate and nitrite, such as cyanobacteria *Anabaena* sp. and *Anabaena cylindrica* [25, 26].

With emerging government regulations [5], the surface and groundwater monitoring are required following recommendations from the designated professionals, and the mink farm owner must sample for total phosphorus, nitrate, and ammonia concentrations of the surface water and groundwater at the farm. If the water sample results come back higher than any of the concentrations listed, the owner of that mink farm may be required to take measures to reduce concentration levels.

Compared to the concentration limits of the surface water and groundwater for mink farms, the 1% pretreated minkery wastewater used in this study already had a much lower nitrate concentration. However, the ammonium and total phosphorus concentrations of the 1% pretreated minkery wastewater were much higher than those concentration limits. It means that a further wastewater treatment would be required to reduce ammonium and total phosphorus concentrations of even 1% pretreated minkery wastewater.

27.3.2 Biomass Accumulation Comparisons

The means of biomass increase in dry weight of *Chlorella vulgaris* and *Anabaena* sp. in various mediums under different light cycles were provided in Table 27.4.

Table 27.4 Means of biomass increase (%) in dry weight of *Chlorella vulgaris* and *Anabaena* sp. in minkery wastewater, traditional mediums, and distilled water under light cycles of 6-day continuous light, 48-h light and 24-h dark, 24-h light and 48-h dark, and 6-day continuous dark

			Chlorella vulgaris	*Anabaena* sp.
No.	Light cycle	Medium	Mean (%)	Mean (%)
1	All light	MW	834 a	108 hi
2	All light	TM	695 b	427 cd
3	All light	DW	677 b	201 gh
4	48-h L/24-h D	MW	831 a	117 hi
5	48-h L/24-h D	TM	529 c	449 cd
6	48-h L/24-h D	DW	475 c	201 gh
7	24-h L/48-h D	MW	418 cde	86 hi
8	24-h L/48-h D	TM	341 def	283 fg
9	24-h L/48-h D	DW	301 efg	99 hi
10	All dark	MW	83 hi	53 i
11	All dark	TM	3 i	13 i
12	All dark	DW	4 i	9 i

Means that do not share the same letter are significantly different

Based on the findings, *Chlorella vulgaris* achieved the highest biomass increase in minkery wastewater under the light cycle of 6-day continuous light. This particular treatment yielded a biomass increase of 834% over the 6-day period, which was significantly higher than those under any treatment associated with traditional medium and distilled water.

While *Chlorella vulgaris* did experience the largest biomass accumulation in minkery wastewater under light cycle of 6-day continuous light, the Tukey's test (with a confidence coefficient of 95%) determined that there was no significant difference between the mean biomass increase under the light cycles of 6-day continuous light and 48-h light and 24-h dark. This leads to the conclusion that both light cycles, 6-day continuous light and 48-h light and 24-h dark cycles, could be employed for achieving highest biomass cultivation of *Chlorella vulgaris* in minkery wastewater; and using 48-h light and 24-h dark instead of 6-day continuous light has a potential to reduce energy costs of microalgae and cyanobacteria cultivation.

In contrast, the biomass accumulation of *Chlorella vulgaris* cultivated in traditional medium and distilled water was observed to be highly dependent on the light cycles. Li et al. [27] reported similar finding in the biomass accumulations of microalgae *Chlorella protothecoide* and *Chlorella kessleri* cultured in highly concentrated municipal wastewater correlated to the light cycles.

In comparing these experimental results to the minkery wastewater characteristics, these findings could be easily explained. Both traditional mediums and distilled water used in this study were short of organic carbon (less than 30 mg/L); however, minkery wastewater contained a certain amount of organic carbon (126 mg/L), which makes it a better organic carbon substrate for the heterotrophic cultivation of *Chlorella vulgaris*. The only deficiency of minkery wastewater used in this study was that its content of organic carbon was too low to support a 6-day heterotrophic cultivation due to the dilution of minkery wastewater before the experiment. As a consequence, although mean biomass increase of *Chlorella vulgaris* under the light cycle of 6-day continuous dark in minkery wastewater was higher than those in traditional medium and distilled water under the same heterotrophic condition, the Tukey's test did not determine that there was a statistically significant difference between these findings.

In comparing the mean biomass increase in minkery wastewater between *Chlorella vulgaris* and *Anabaena* sp. across each of the light cycles, it was found that there was no significant difference for the 6-day continuous dark. There was, however, a significant difference for the rest of light cycles. *Chlorella vulgaris* showed a much better adaptation than *Anabaena* sp. in minkery wastewater because the mean biomass increase of *Anabaena* sp. was significantly lower than those of *Chlorella vulgaris*. The growth characteristics of *Anabaena* sp. in BG-11_o medium were significantly better than those in minkery wastewater. Oliveira et al. [25] reported that *Anabaena* sp. has a high demand in nitrate. Insufficient nitrate of minkery wastewater made the minkery wastewater an inappropriate substrate for *Anabaena* sp. cultivation.

Table 27.5 Means of total nitrogen removal (%) from minkery wastewater, traditional mediums, and distilled water by culturing *Chlorella vulgaris* and *Anabaena* sp. under light cycles of 6-day continuous light, 48-h light and 24-h dark, 24-h light and 48-h dark, and 6-day continuous dark, and means that do not share the same letter are significantly different

			Chlorella vulgaris	*Anabaena* sp.
No.	Light cycle	Medium	Mean (%)	Mean (%)
1	All light	MW	96.2 a	29.2 f
2	All light	TM	82.8 b	94.8 a
3	All light	DW	85.2 b	92.6 a
4	48-h L/24-h D	MW	94.8 a	30.9 f
5	48-h L/24-h D	TM	52.4 e	95.0 a
6	48-h L/24-h D	DW	51.6 e	91.9 a
7	24-h L/48-h D	MW	57.4 d	28.5 f
8	24-h L/48-h D	TM	22.9 g	65.2 c
9	24-h L/48-h D	DW	20.3 gh	61.2 cd
10	All dark	MW	21.4 gh	18.4 h
11	All dark	TM	1.6 i	4.5 i
12	All dark	DW	1.6 i	3.6 i

27.3.3 Nutrient Removal Comparisons

The means of total nitrogen removal from various mediums via cultivation of *Chlorella vulgaris* and *Anabaena* sp. under different light cycles were provided in Table 27.5.

In comparing the total nitrogen removal from minkery wastewater between *Chlorella vulgaris* and *Anabaena* sp. across each of the light cycles, it was found that *Chlorella vulgaris* has higher potential than *Anabaena* sp. to treat minkery wastewater and accumulate highly valuable biomass simultaneously. The total nitrogen removal from minkery wastewater via cultivation of *Chlorella vulgaris* was significantly higher than that of *Anabaena* sp. under three of the four light cycles, including 6-day continuous light, 48-h light and 24-h dark, and 24-h light and 48-h dark.

The highest total nitrogen removal from minkery wastewater in this study was achieved through the cultivation of *Chlorella vulgaris* under light cycle of 6-day continuous light. This particular treatment achieved a nitrogen removal of 96.2% over the 6-day growth period, and the Tukey's test (with a confidence coefficient of 95%) determined that there were no significant differences between this and the total nitrogen removal from minkery wastewater by cultivating *Chlorella vulgaris* under the light cycle of 48-h light and 24-h dark. This leads to the conclusion that *Chlorella vulgaris* showed the highest total nitrogen removal from minkery wastewater under the light cycle of 6-day continuous light and 48-h light and 24-h dark, and using light cycle of 48-h light and 24-h dark instead of 6-day continuous light reduced energy costs.

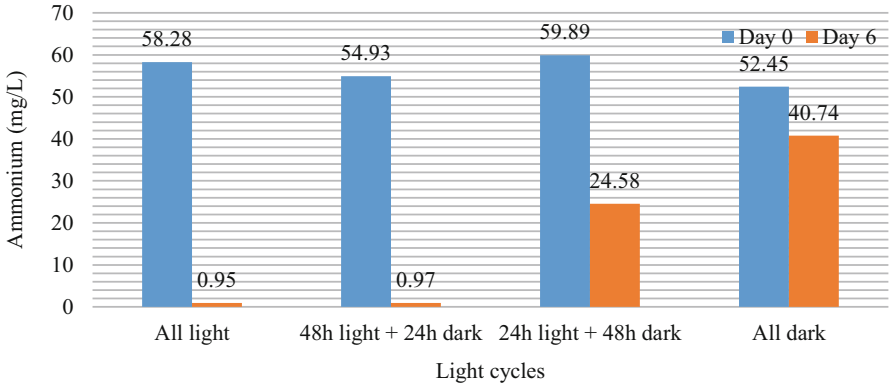

Fig. 27.2 Ammonium concentrations of minkery wastewater before and after 6-day treatment by *Chlorella vulgaris* under light cycles of 6-day continuous light, 48-h light and 24-h dark, 24-h light and 48-h dark, and 6-day continuous dark

In comparison, Li et al. [27] reported that mixotrophic microalgae *Chlorella kessleri* and *Chlorella protothecoide* cultivated in highly concentrated municipal wastewater achieved 62.2% and 64.5% total nitrogen removal in only 4 days, respectively. Wang et al. [25] reported that microalgae *Chlorella* sp. cultivated in municipal wastewater from sludge centrifuge achieved 82.8% total nitrogen removal in 9 days. It should be noted that minkery wastewater used in our study had a higher initial nitrogen concentration than those of municipal wastewaters used in those studies, which makes these numbers even more impressive.

Figure 27.2 provided the ammonium concentrations of minkery wastewater before and after 6-day treatment by *Chlorella vulgaris* under four light cycles employed. It demonstrates that the minkery wastewater after 6-day treatment by *Chlorella vulgaris* under light cycles of 6-day continuous light and 48-h light and 24-h dark had a lower ammonium concentration than both surface water and groundwater concentration limits. Ammonium concentration limits of the surface water and groundwater for mink farms are 1 mg/L and 4 mg/L, respectively.

The means of total phosphorus removal from various mediums by culturing *Chlorella vulgaris* and *Anabaena* sp. under different light cycles are shown in Table 27.6.

In comparing the total phosphorus removal from minkery wastewater between *Chlorella vulgaris* and *Anabaena* sp. across each of the light cycles, it was observed that the total phosphorus removal from minkery wastewater through cultivation of *Chlorella vulgaris* was significantly higher than that of *Anabaena* sp. under all four light cycles.

The highest total phosphorus removal from minkery wastewater was performed by cultivating *Chlorella vulgaris* under 6-day continuous light, and the Tukey's test (with a confidence coefficient of 95%) did not determine that there was a statistically significant difference between this and the total phosphorus removal from minkery wastewater via culturing *Chlorella vulgaris* under 48-h light and 24-h dark. This

Table 27.6 Means of total phosphorus removal (%) from minkery wastewater, traditional mediums, and distilled water through the cultivation of *Chlorella vulgaris* and *Anabaena* sp. under light cycles of 6-day continuous light, 48-h light and 24-h dark, 24-h light and 48-h dark, and 6-day continuous dark, and means that do not share the same letter are significantly different

			Chlorella vulgaris	*Anabaena* sp.
No.	Light cycle	Medium	Mean (%)	Mean (%)
1	All light	MW	29.7 a	5.9 j
2	All light	TM	23.4 b	12.1 ef
3	All light	DW	23.5 b	12.5 ef
4	48-h L/24-h D	MW	28.8 a	6.1 ij
5	48-h L/24-h D	TM	17.4 cd	12.5 ef
6	48-h L/24-h D	DW	17.7 c	11.8 fg
7	24-h L/48-h D	MW	14.8 de	5.8 j
8	24-h L/48-h D	TM	9.2 gh	8.4 hij
9	24-h L/48-h D	DW	8.8 hi	8.6 hij
10	All dark	MW	7.7 hij	3.1 k
11	All dark	TM	1.6 k	1.4 k
12	All dark	DW	1.5 k	1.5 k

leads to the conclusion that *Chlorella vulgaris* showed the highest total phosphorus removal from minkery wastewater under the light cycles of 6-day continuous light and 48-h light and 24-h dark, and using light cycle of 48-h light and 24-h dark instead of 6-day continuous light reduced energy costs of the cultivation. These two particular treatments achieved phosphorus removals of 29.7% and 28.8% over the 6-day growth period, respectively.

In comparison with other studies, the phosphorus removal rates observed in this study were relatively low. Li et al. [27] observed that mixotrophic microalgae *Chlorella kessleri* and *Chlorella protothecoide* cultivated in highly concentrated municipal wastewater achieved 87.4% and 86.1% total phosphorus removal in only 4 days. Wang et al. [25] reported that microalga *Chlorella* sp. cultivated in municipal wastewater from sludge centrifuge achieved 85.6% total phosphorus removal in 9 days. It should be noted that minkery wastewater used in our study had a much higher initial phosphorus concentration than those of the municipal wastewaters used in those studies. When it comes to the amount of phosphorus removal (mg/L), the findings were much closer.

The total phosphorus concentrations of minkery wastewater before and after 6-day treatment by *Chlorella vulgaris* under different light cycles are provided in Fig. 27.3. And total phosphorus concentration limits of the surface water and groundwater for mink farms are 20 μg/L and 0.1 mg/L, respectively. Unfortunately, even after 6-day treatment by *Chlorella vulgaris*, the total phosphorus concentration of minkery wastewater was still much higher than the required concentration limits for the surface water and groundwater, which means that further treatment would be required to reduce the concentration levels of total phosphorus in minkery wastewater.

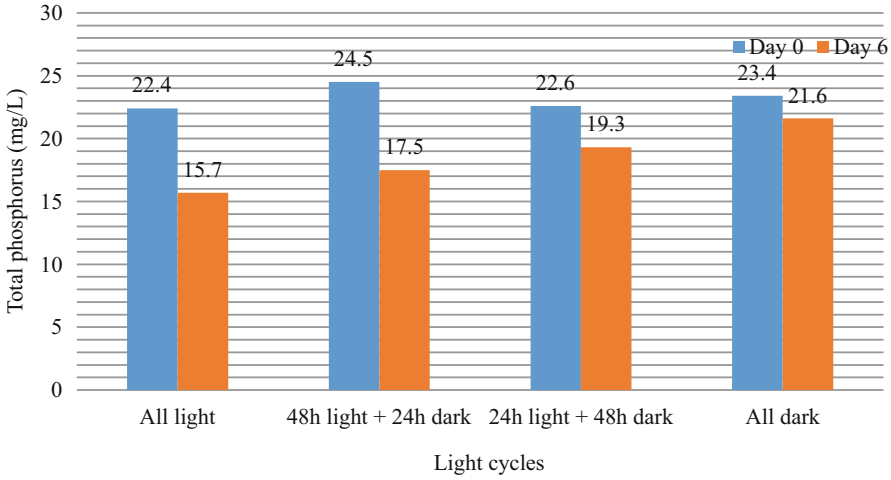

Fig. 27.3 Total phosphorus concentrations of minkery wastewater before and after 6-day treatment by *Chlorella vulgaris* under light cycles of 6-day continuous light, 48-h light and 24-h dark, 24-h light and 48-h dark, and 6-day continuous dark

27.4 Conclusions

According to the experimental data, the minkery wastewater was proved to be a superior medium than modified Bold's basal medium for *Chlorella vulgaris* cultivation under most of the light cycles, and the growth characteristics of *Anabaena* sp. in BG-11_0 were significantly better than those in minkery wastewater under most of the light cycles. Based on the findings, this study proved the potential of using minkery wastewater as an alternative growth medium, even though the cultivation of *Anabaena* sp. in minkery wastewater remains a challenge due to the insufficient nitrate levels of minkery wastewater. Furthermore, this study also demonstrated the wastewater treatment potential of *Chlorella vulgaris* in controlled environment minkery wastewater. It is concluded that the best treatment potential for minkery wastewater was achieved using *Chlorella vulgaris* under the light cycle of 48-h light and 24-h dark. This particular treatment yielded the highest biomass increase, the highest total nitrogen removal, and the highest total phosphorus removal along with a reduced demand in light energy.

Nomenclature

D	Dark
DW	Distilled water
L	Light
MW	Minkery wastewater
TM	Traditional growth medium
x	Algae biomass measurement
y	Nutrient content measurement

Subscripts

0 Day 0
6 Day 6

References

1. Statistics Canada (2011) Fur Statistics 2010, Catalogue no. 23-013-X, vol. 8, ISSN 1705-4273, Ottawa, pp. 1–20
2. Boon J (2014) Poop problems: mink stink leads to formal complaints, The Coast: Halifax's Website. https://www.thecoast.ca/RealityBites/archives/2014/11/13/poop-problemsLast accessed 10 Oct 2017
3. Taylor DA (2009) A water quality survey of nine lakes in the Carleton river watershed area Yarmouth county, Nova Scotia. Nova Scotia Environment, pp.1–48, https://novascotia.ca/nse/surface.water/docs/Yarmouth.Area.Lakes.Report.with.Appendices.pdf Last accessed 10 Oct 2017
4. Ferguson JL (2001) Characterizing the process of composting mink manure and pelted mink carcasses. Master's Thesis, Nova Scotia. Agricultural College. Truro, NS, Canada
5. Fur Industry Act. (2010). Fur Industry Act, Chapter 4 of the Acts of 2010 as amended by 2012, c. 58: An act respecting the fur industry. House of Assembly, Halifax, Nova Scotia, pp. 1–18, https://nslegislature.ca/sites/default/files/legc/statutes/fur%20industry.pdf Last accessed 10 Oct 2017
6. Rai L, Gaur J, Kumar H (1981) Phycology and heavy metal pollution. Biol Rev 56(2):99–151
7. Redalje DG, Duerr EO, de la Noiie J, Mayzaud P, Nonomura AM, Cassin R (1989) Algae as ideal waste removers: biochemical. In: Biotreatment of agricultural wastewater. CRC press, Boca Raton, p 91
8. McGriff EC, McKenney RE (1971) Activated algae: a nutrient process. Water Sewage Works 118:377
9. McGriff EC, McKinney RC (1972) The removal of nutrients and organics by activated algae. Water Res 6(10):1155
10. Tam NFY, Wong YS (1989) Wastewater nutrient removal by *Chlorella pyrenoidosa* and *Scenedesmus sp*. Environ Pollut 58:19–34
11. Campbell PK, Beer T, Batten D (2011) Life cycle assessment of biodiesel production from microalgae in ponds. Bioresour Technol 102:50–56
12. Lee YK (2001) Microalgal mass culture systems and methods: their limitation and potential. J Appl Phycol 13:307–315
13. Lardon L, Helias A, Sialve B, Steyer JP, Bernard O (2009) Life-cycle assessment of biodiesel production from microalgae. Environ Sci Technol 43:6475–6481
14. Pate R, Klise G, Wu B (2011) Resource demand implications for US algae biofuels production scale-up. Appl Energy 88:3377–3388
15. Shi J, Podola B, Melkonian M (2007) Removal of nitrogen and phosphorus from wastewater using microalgae immobilized on twin layers: an experimental study. J Appl Phycol 19:417–423
16. Hammouda O, Gaber A, Abdelraouf N (1995) Microalgae and wastewater treatment. Ecotoxicol Environ Saf 31:205–210
17. Lowrey J, Yildiz I (2011) Seawater/wastewater production of microalgae-based biofuels in closed loop tubular photobioreactors. Masters Theses Proj. Reports
18. Yildiz I, Nguyen-Quang T, Mehlitz T, Brooker B (2013) Algae, Biofuels, and Modeling. In: Dincer, I, Colpan, CO, and Kadioglu, F (Eds), Causes, Impacts, and Solutions to Global Warming. Springer, New York, NY, 30:525–607
19. American Public Health Association (ed) (1998) Standard methods for the examination of water and wastewater, 20th edn. American Public Health Association, Washington, DC

20. Griffiths MJ, Garcin C, van Hille RP, Harrison ST (2011) Interference by pigment in the estimation of microalgal biomass concentration by optical density. J Microbiol Methods 85 (2):119–123
21. Yoon J, Sim S, Kim M, Park T (2002) High cell density culture of Anabaena variabilis using repeated injections of carbon dioxide for the production of hydrogen. Int J Hydrog Energy 27:1265–1270
22. Hempel N, Petrick I, Behrendt F (2012) Biomass productivity and productivity of fatty acids and amino acids of microalgae strains as key characteristics of suitability for biodiesel production. J Appl Phycol 24:1407–1418
23. Šoštarič M, Golob J, Bricelj M, Klinar D, Pivec A (2009) Studies on the growth of *Chlorella vulgaris* in culture media with different carbon sources. Chem Biochem Eng Q 23(4):471–477
24. Wang L, Min M, Li Y, Chen P, Chen Y, Liu Y, Wang Y, Ruan R (2009) Cultivation of green algae *Chlorella sp.* in different wastewaters from municipal wastewater treatment plant. Appl Biochem Biotechnol 162:1174–1186
25. Oliveira P, Martins NM, Santos M, Couto NAS, Wright PC, Tamagnini P (2015) The *Anabaena sp.* PCC 7120 exoproteome: taking a peek outside the box. Life 5:130–163
26. Weare NM, Benemann JR (1972) Nitrogen fixation by *Anabaena cylindrica*: localization of nitrogen fixation in the heterocysts. Arch Mikrobiol 90:323–332
27. Li Y, Zhou W, Hu B, Min M, Chen P, Ruan RR (2012) Effect of light intensity on algal biomass accumulation and biodiesel production for mixotrophic strains *Chlorella kessleri* and *Chlorella protothecoide* cultivated in highly concentrated municipal wastewater. Biotechnol Bioeng 109:2222–2229

Chapter 28
Comparative Analysis of Four Analytical Methods for Measuring Microalgae and Cyanobacteria Biomass Growth in Controlled Environment Minkery Wastewater

Yuchen Ji and Ilhami Yildiz

28.1 Introduction

Both developed and developing economies and growing world population highly rely on the natural resources of our planet. According to the 2017 Revision of World Population Prospects, which is released every 2 years, the world population is expected to reach 8.6 billion in 2030, 9.8 billion in 2050, and 11.2 billion in 2100 [1]. For the human race, the demand for energy sources is greater than ever before, and sustainable techniques and sources are necessary for energy production. The cultivation of microalgae and cyanobacteria has potential to make a significant contribution to the transition to a more sustainable production of energy. Microalgae and cyanobacteria cells contain many useful substances, such as oil, proteins, and pigments (e.g., beta-carotene). Applications of these products are numerous, ranging from energy to pharmaceuticals, to fertilizers, to cosmetics, and to food. Moreover, microalgae and cyanobacteria are not only suitable for the bioproduct production but also for the use of waste streams and closing the loop. Many researchers have demonstrated that a number of waste streams have potential to be a viable culture medium for microalgae and cyanobacteria production and sometimes with even improved yields when compared to the traditional medium [2–4].

With the increased demand of microalgae and cyanobacteria comes an equivalent increase in production and production practices. Microalgae or cyanobacteria cultivation ends up with a dilute aqueous suspension including microalgae or cyanobacteria cells and culture medium. Depending on the employed cultivation technology, the maximum concentration is commonly reported ranging from 0.1 to

Y. Ji · I. Yildiz (✉)
Dalhousie University, Faculty of Agriculture, Department of Engineering, Truro-Bible Hill, NS, Canada
e-mail: iyildiz@dal.ca

S. Nižetić, A. Papadopoulos (eds.), *The Role of Exergy in Energy and the Environment*, Green Energy and Technology,
https://doi.org/10.1007/978-3-319-89845-2_28

4 g of dried microalgae or cyanobacteria biomass per liter growth medium [5]. Quantifying microalgae and cyanobacteria biomass, however, remains one of the most important and challenging practices of production, because of the low density of microalgae and cyanobacteria cells. A successful microalgae or cyanobacteria production will demand commercially viable biomass determination methods that are both economically and logistically acceptable. That means such methods should be accurate and reliable and could be seamlessly incorporated into a large-scale biomass production system.

Four methods are commonly used to determine the biomass generated in the microalgae and cyanobacteria culture, including dry weight, optical density, cell count, and chlorophyll *a* content. This chapter looks at the basis of these methods, their required equipment, function, and total biomass measurement. This study aimed to investigate the effectiveness of four different conventional methods for microalgae and cyanobacteria biomass determination on the basis of their time and cost requirements, as well as their accuracy and precision in multiple culture conditions (growth medium and light cycle).

28.1.1 Gravimetric (Dry Weight) Method

The gravimetric method of dry weight is considered as one of the most accurate measurements of microalgae or cyanobacteria biomass. This technique measures the biomass directly because we assume that microalgae or cyanobacteria biomass is in the proportion of volatile suspended solids (VSS). Dry weight analysis involves a multistage process, which yields an end measurement of biomass in the unit of g/L. The major advantages of this method are the useful mass-based units, the simplicity of execution, and the inclusion of constituents based upon minimum particle size.

Samples can be concentrated in a multitude of ways with the most popular being centrifugation. While there is some risk of cell destruction with this method, it is generally species specific and often insignificant. Alternatively, one can pass a known volume of microalgae or cyanobacteria solution through a glass fiber filter, with the aid of a vacuum pump. It is important to rinse, dry, and tare the filter prior to use, in order to remove and volatilize any unwanted contaminants. In addition to this, it should be noted that a small sample volume could introduce a significant amount of error into the measurement. As such, larger volumes are preferred when possible. Generally speaking, at least 25 mL should be used, though with a larger sample volume comes less chance for error [6]. Once completed, the concentrated wet sample will be placed in an oven at 105 °C. This has the effect of evaporating all of the remaining water from the concentrated sample so that only suspended particles remain (including microalgae, suspended organic material, suspended inorganic material). Once removed from the oven, the sample should be cooled in a desiccator to room temperature. The sample should then be weighed in order to attain the dry weight. After this, samples are placed into a furnace at 550 °C. Eventually,

depending on the nature of the culture medium, samples may simply be weighed to attain the ash weight, and the difference between this ash weight and the dry weight will account for the total amount of organic material (primarily microalgae or cyanobacteria biomass) present in the sample. However, in the case where the culture medium has high amounts of clay or other minerals, then the samples may need to be rewetted and brought to a constant weight at a temperature of 105 °C. This is done in order to return water of hydration to these minerals. This is a major step as the water of hydration can account for as much as 10% of the weight difference following incineration [7]. Once again, the samples can be weighed, and the difference between the ash and dry weights will be the total amount of organic material present in the sample [6].

Within microalgae and cyanobacteria research, it is an unfortunate reality that the terms dry weight and ash weight are used interchangeably to mean both the same and different things. Some published papers use the term dry weight when in reality they should be saying ash weight or will perform an analysis and only utilize dry weight when ash weight would be more appropriate [8, 9]. Ash weight is a more appropriate method than simply using dry weight as inorganic substances in the solution can account for as much as 50% of the sample depending on nature. In phytoplankton such as diatoms, which have inorganic structures, this is of increasing importance [10, 11].

Another unique challenge for gravimetric methods is that of performing dry weight analysis on marine microalgae and cyanobacteria species. As one would imagine, the presence of salt in marine cultures can have a drastic effect on measurements of dry weight [12]. This serves to strengthen the argument for the use of ash weight further. With that being said, there are some ways, which the presence of salt can be circumvented if dry weight is the only available option. The most popular choice for performing dry weight of marine species is to rinse the microalgae or cyanobacteria solutions prior to concentration or filtration. This is generally performed through the use of an isotonic solution such as ammonium formate [13, 14], sodium chloride [15], N HCl, and distilled water [16] or simply distilled water on its own [17]. Despite this, relevant literature has some major gaps, in that rinsing procedures are not often reported or discussed in detail in the determination of dry and ash weight [18–21]. As discussed, this is a concerning issue as the presence of salt can significantly hinder the measurement of dry weight. For these reasons, samples should be either rinsed or ashed to account for the salt content; however, this is not the case in many published studies.

28.1.2 Spectrophotometric (Optical Density) Method

Optical density, also known as absorbance or turbidity, is frequently used as a rapid measurement of biomass in cultures of microalgae or cyanobacteria. Using absorbance as an indicator offers perhaps the simplest and quickest means for quantifying culture productivity. Absorbance measurements have the added benefit of being

nondestructive and can easily be implemented into bioreactor systems as a means of providing constant monitoring for microalgae or cyanobacteria cultures [22–24]. Absorbance is generally measured through the use of a spectrophotometer, and while there are different types of spectrophotometers, those employed in phycology generally operate in the UV-visible (UV-Vis) or near-infrared (NIR) range. Typically, utilized wavelengths range from 400 to 460 nm and 650 to 680 nm for the measurement of microalgae or cyanobacteria biomass [22]. Taking perhaps the most studied microalgae, *Chlorella vulgaris*, as an example, maxima in the absorbance were found at wavelengths of 443, 487, and 684 nm [22].

A spectrophotometer consists of five primary components, including a light source, wavelength selector, sample compartment, detector, and readout [25]. The light source, generally provided by a tungsten filament bulb for the visible region, directs light toward the sample. The wavelength selector then screens out all the light except for the specific wavelength desired by the analyst. This is done through the use of a dispersing element, which disperses the emitted light into individual wavelengths. This is generally accomplished through the utilization of a prism of the diffraction grating. The next step in the light's path is the passage through a small, repositionable slit, which allows for the passage of a single wavelength of the dispersed light to make its way toward the sample compartment. In some designs, the position of the slit may be static, and the dispersing element may move or turn to select specific wavelengths. As the specified wavelength makes its way into the light tight sample compartment, it irradiates the sample and attempts to pass through. The sample is held in a cuvette, and as the light attempts to pass through the cuvette, a certain amount of the light is absorbed by the absorbing species so that the light that does make its way through the sample and on to the detector is less intense than if there were no sample at all. By properly blanking the sample, the analyst can compare the difference between a sample with and without the absorbing species. The function of the detector is quite similar to that of a solar cell. It converts the transmitted electromagnetic energy into electrical energy by giving off electrons. This is known as the photoelectric effect. This electrical output is read and relayed via the readout as a measure of absorbance [25]. Most spectrophotometers also provide a reading of percent transmittance. It should be noted that percent transmittance is not often used in research, as it does not vary linearly with concentration. This makes the development and implementation of standard curves impossible for comparing known values [25, 26]. While standard curves may not be employed for biomass monitoring of microalgae and cyanobacteria, the reading of absorbance remains the primarily utilized output and the only true reading of interest. This is because it allows for easy model development and comparisons across multiple biomass quantification techniques, which also vary linearly with concentration. Measurements of absorbance can be used to estimate biomass under certain conditions. The most important of these conditions is that there is an already developed standard curve linking measured absorbance values to a more exact technique, which normally is dry weight [22]. In this way, one can convert the measured absorbance units (AU) into more appropriate dry weight units, which is g/L.

With all this being said, it should be noted that there are some issues with the spectrophotometric approach as well. The main issue is that even if the incident wavelength is held constant, that is not to say that the nature of the microalgae or cyanobacteria is staying the same, especially when it comes to its absorbing characteristics. This can create a certain amount of bias when it comes to the absorbance readings. The most pertinent of this absorbing characteristic is the pigment concentration of microalgae or cyanobacteria cells. As the growth cycle and culture conditions change, so does the pigment concentration within the cell. For example, the pigment content of the *Chlorella vulgaris* cells varies between 0.5% and 5.5% of dry weight depending on culture conditions and age [22]. This is an aspect, which must be properly accounted for should the spectrophotometric approach become a fully accurate predictor of microalgae or cyanobacteria biomass.

28.1.3 Microscopic (Cell Count) Method

For microalgae and cyanobacteria, the most basic approach for biomass estimation comes in the form of cell count. Cell count makes use of microscopy as a means of directly counting the number of cells within a known volume of the culture. This is generally done through the utilization of a hemocytometer. A hemocytometer is a specialized counting device used to help in counting microscopic cells [27]. It was originally developed to aid in the counting of red blood cells and has since evolved to be applicable in a variety of fields including phycology [28–32].

There are a number of advantages of using a hemocytometer as opposed to other counting mechanisms. The first is the ease, in which a known volume can be counted. Provided the proper methods are followed, then this volume is specified by the particular hemocytometer that is employed. Following a thorough homogenization of the suspended cells within the culture, a Pasteur pipette can be used to transfer the solution to the hemocytometer. Once the solution is taken into the pipette, the pipette must be touched to the cover slip, and the solution must be allowed to fill the chambers by capillary action [33]. In this way, any potential errors associated with under- or overfilling of the chambers can be minimized. Hemocytometers aim to avoid bias by dividing their countable area into squares of known dimension. In this way, specific counting patterns can be used to reduce any bias, which may come in the form of cell clumping or counting errors.

The most commonly employed hemocytometer is the improved Neubauer. The improved Neubauer's central square is divided into 25 smaller squares, which are further divided into 25 smaller squares. The generally accepted counting pattern is to count the four corner squares within the large square along with the middle square and multiply the result by five [33]. Figure 28.1 shows a schematic view of the improved Neubauer's counting chamber. Squares outlined in red are the squares, which are generally counted in samples where the cell counts exceed 100. The resulting count is then multiplied by five in order to give an indication of the larger

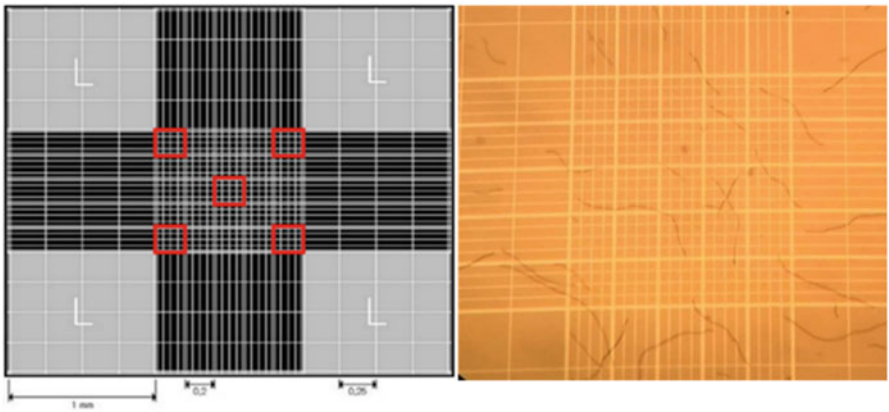

Fig. 28.1 Schematic view of the improved Neubauer's counting chamber (edited to show general counting pattern in samples of more than 100 cells) (left) and counting *Anabaena* sp. (right)

square. Should the cell count be fewer than 100, then all squares can be counted for the most accurate measurement [33].

What is important to note is that hemocytometers actually hold a three-dimensional volume despite the fact that they appear two dimensional under the microscope. In this way, the number of cells per mL can easily be determined based on a quick calculation [27]. For example, with the improved Neubauer, each large square holds 10^{-4} cm^3 or 10^{-4} mL of culture solution. Therefore, based on the cell count, the number of cells per liter can quickly be determined and compared with other measurements [33, 34].

For microalgae or cyanobacteria applications, proper use of a hemocytometer generally requires a microscope with a minimum of 100 times magnification. In this way, dead cells and any potential contaminants or excipients can easily be spotted and discounted.

28.1.4 Chlorophyll (Chlorophyll a *Content) Method*

As a result of the ever-changing pigment concentration of the microalgae and cyanobacteria cells, another employable technique, which aims to combat this, is that of chlorophyll *a* content. Chlorophyll *a* is the predominant pigment, and there are a number of different methods for utilizing it to quantify the biomass of microalgae or cyanobacteria cultures. The greatest advantage of this approach is that it directly targets the biomass. However, a substantial margin of error exists in the underlying assumption about the chlorophyll *a* concentration, because it is highly variable in microalgae and cyanobacteria cells.

The first step in analyzing chlorophyll *a* is pigment extraction. This process begins with filtering the microalgae or cyanobacteria solution through glass fiber

filter. Glass fiber filters are preferable as the nature of the filters causes ruptures, which will help in releasing the targeted pigments. Filtered samples are then placed in a tissue grinder, covered in 2–3 mL of mixed solution with 90% of acetone and 10% of magnesium carbonate, and then macerated for at least 1 min at 500 rpm. The magnesium carbonate solution is comprised of 1 g magnesium carbonate in 100 mL distilled water. The grinder is then rinsed with the acetone solution with the rinse solution being added to the extraction slurry. The extraction slurry is then added to a screw cap centrifuge tube. Samples should then be steeped for at least 2 h at 4 °C in complete darkness. Depending on how the samples will be analyzed, they may need to be appropriately clarified by either filtration or centrifugation [6]. It is imperative that throughout the extraction process the samples are kept in the dark. Light levels during this process should be kept at a minimum as exposure to electromagnetic radiation would cause a deterioration and loss of chlorophyll pigments in the sample [6]. While the above-listed method is generally considered the standard method, there exist some variations that are commonly used in pigment extraction from microalgae or cyanobacteria cells.

Once the pigment is extracted, there are a few different techniques that can be used to determine the chlorophyll profile. The first of these methods is spectrophotometry, which measures the absorbance of light being passed through the sample. A detailed explanation of spectrophotometry is described in the previous section. Fluorometric approach for chlorophyll *a* determination can also be used and in fact often yield more sensitive results than spectrophotometric determinations [6]. Before used, the fluorometer should be calibrated with a chlorophyll solution with a known concentration. Once the concentration is known, the solution can be diluted to concentrations of 2, 6, 20, and 60 μg/L. From this point, each solution is analyzed fluorometrically at sensitivity settings of 1×, 3×, 10×, and 30×. Once these readings have been taken, calibration factors can be calculated using Eq. (28.1) [35]:

$$F = \frac{C_a}{R} \tag{28.1}$$

where F is the calibration factor for sensitivity setting, C_a is the concentration of chlorophyll *a*, and R is the fluorometer reading for particular sensitivity.

From this point, samples can be read and multiplied by the appropriate calibration factors in order to attain concentrations of chlorophyll *a*. Sensitivity setting of 1× should be avoided for measurements of chlorophyll *a* in order to mitigate any quenching effects, which may limit fluorescence [36, 37].

Last, but not least, the high-performance liquid chromatography (HPLC) is perhaps the most effective tool in the accurate determination of chlorophyll concentrations. With that being said, with greater accuracy comes a more complex analytical process along with a greater time and economic cost. As such, HPLC is generally only used when one wishes to determine the complete pigment profile and not for biomass determination. A brief description of this technique is discussed below [38, 39]. Following the appropriate steps for the calibration, equilibration,

injection, separation, and generation of chromatograms, the pigment concentrations can be calculated. These pigment concentrations can be calculated using Eq. (28.2) [6]:

$$C = \frac{A\,F\,V_{\mathrm{E}}}{V_{\mathrm{I}}\,V_{\mathrm{S}}} \tag{28.2}$$

where V_{I} is the injection volume, V_{E} is the extraction volume, V_{S} is the sample volume, C is the pigment concentration (mg L^{-1}), A is the area under pigment peak, and F is the standard response factor, which is equal to [(mg pigment/0.1 mL standard)/peak area].

Regardless of the employed technique, the resulting measurement is a chlorophyll concentration; therefore, to determine biomass, a conversion must be performed. The standard method uses the assumption that chlorophyll *a* makes up 1.5% of the total dry biomass within the microalgae or cyanobacteria cell. Once the content of chlorophyll *a* has been determined, one needs simply to multiply the value by 67 to estimate the total biomass [6]. The obvious issue with this analysis is that not all microalgae or cyanobacteria are comprised of 1.5% chlorophyll *a* by dry weight; and therefore, the estimate may be rough or entirely false in some cases. Therefore, the model must be adapted to the particular strain being studied along with the specific set of growth conditions. This would involve determining the individual chlorophyll *a* content as well as the biomass using a different method in order to determine the percentage of chlorophyll *a* of studied microalgae or cyanobacteria strains. From this point, the method of chlorophyll *a* content could be used for estimation of microalgae or cyanobacteria biomass.

28.2 Materials and Methods

28.2.1 Strain Selection and Culture Conditions

Two strains selected in this study were *Chlorella vulgaris* and *Anabaena* sp. due to their prevalence representing highly valuable and viable microalgae and cyanobacteria, respectively. Both strains and growth mediums (modified Bold's Basal medium for *Chlorella vulgaris*; BG-11_{o} medium for *Anabaena* sp.) were obtained from the Canadian Phycological Culture Centre, Department of Biology, University of Waterloo, Ontario, Canada. The enclosed cultures were stored in 1 L Erlenmeyer flasks at approximately 20 °C and illuminated with a cool-white fluorescent light (32 W, 6500 K) with light/dark photoperiod of 16 h:8 h. Also, both culturing flasks were sealed with a plug, allowing for aseptic gas exchange, and placed on a mechanical stirrer (HI 190, Hanna Instruments, USA) with 150 rpm rotation. Additionally, microscopic inspections of both strains were performed daily, in order to verify culture purity.

28.2.2 Mediums and Minkery Wastewater

During the experimental phase, nutrition was provided to both strains by three different mediums, including distilled water, traditional culture mediums (Modified Bold's Basal or BG-11_o), and minkery wastewater medium. The raw minkery wastewater was obtained from the Dalhousie University's Fur Animal Research Centre in Bible Hill, Nova Scotia, Canada, and the minkery wastewater medium was a mixture of 1% raw minkery wastewater and 99% distilled water.

28.2.3 Experimental Equipment

Cultures were transferred from the flasks to the transparent plastic cylinders, which were 2.25 L vertical column photobioreactors (Aqua Medic GmbH, Plankton Reactor, Bissendorf, Germany). Each photobioreactor was inoculated with 400 mL purified microalgae or cyanobacteria culture (0.3–0.4 g/L) (20%) and 1600 ml of certain medium (80%). All trials were conducted under independent cool-white fluorescent light (8 W, 6700 K) at 20 °C in an effort to provide optimal growth conditions. Moreover, for each photobioreactor, an independent ambient air pump (Fusion Quiet Power, 400, Taiwan) was used to allow for gas exchange and keep the culture homogeneous.

28.2.4 Experimental Design

The approach employed in this study is illustrated in Fig. 28.2. The experiment commenced with the cultivation of microalgae and cyanobacteria. For each experimental unit, the growth period was 6 days, and a split-split-plot design was used to arrange each experimental unit. The whole plots were strains, the subplots were light cycles, and the sub-subplots were growth mediums. In total, the cultivation process had 24 different treatments with triplicate observations for each treatment. The strains were *Chlorella vulgaris* and *Anabaena* sp.; the light cycles were (1) 6-day continuous light, (2) 48-h light and 24-h dark, (3) 24-h light and 48-h dark, and (4) 6-day continuous dark; and the growth mediums were (1) minkery wastewater, (2) traditional culture mediums (modified Bold's Basal medium and BG-11_o medium), and (3) distilled water. All statistical analyses were performed using a combination of the *Minitab 17* and *SAS* software.

During the cultivation process, four different methods were employed at the beginning and end of each growth period to determine the biomass generated in

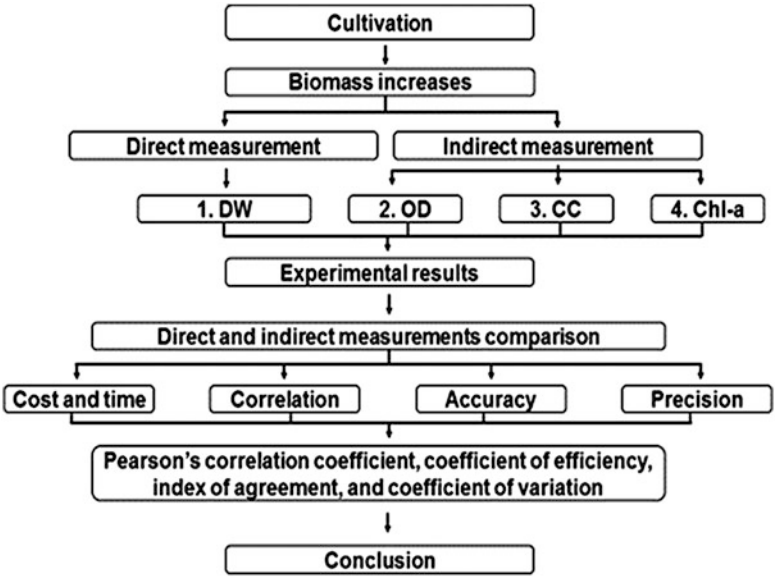

Fig. 28.2 A flowchart of the approach used (1) dry weight; (2) optical density; (3) cell count; (4) chlorophyll *a* content

the same microalgae or cyanobacteria culture. Once these measurements were taken, biomass increase of each 6-day culture was calculated using Eq. (28.3):

$$\text{Biomass increase} = \left(\frac{x_6 - x_0}{x_0}\right) \times 100\% \tag{28.3}$$

where x_0 was the measurement at the beginning of each growth period (day 0) and x_6 was the measurement at the end (day 6).

In all four methods for measurement of microalgae or cyanobacteria biomass increase, the gravimetric method of dry weight was the only method that directly measured the biomass; therefore, it was considered as the only direct measurement. Then, the other three methods employed were considered as the indirect measurements.

Subsequently, the results of four different methods were compared in the category of cost and time, correlation, accuracy, and precision. This experiment formed four different statistical analysis techniques, namely, Pearson's correlation coefficient, the coefficient of efficiency, index of agreement, and coefficient of variation; and it also recorded the cost and time consumed when performing four different methods.

28.2.5 Statistical Techniques

28.2.5.1 Pearson's Correlation Coefficient

Pearson's correlation coefficient (r), developed by Pearson (1895), is a measure of the linear dependence (correlation) between two quantitative variables, and it does not matter what units are used. It is given in Eq. (28.4) as follows:

$$r = \frac{\sum_{i=1}^{n} \left(x_i - \bar{x}\right)\left(y_i - \bar{y}\right)}{\sqrt{\sum_{i=1}^{n} \left(x_i - \bar{x}\right)^2} \sqrt{\sum_{i=1}^{n} \left(y_i - \bar{y}\right)^2}} \tag{28.4}$$

where n values of one method for biomass measurement were denoted by x_i and the corresponding values of another method were denoted by y_i. The $\bar{x}$ is the mean of the values of the first method, and $\bar{y}$ is the mean of the values of the second method.

The value of r ranges from -1 to 1, and 1 is a perfect positive linear correlation, 0 is no linear correlation, and $-$ 1 is a perfect negative linear correlation.

28.2.5.2 Coefficient of Efficiency

Nash and Sutcliffe (1970) proposed an efficiency (E) criterion for objective assessment of measurement performance presented in Eq. (28.5) as:

$$E = 1 - \frac{\sum_{i=1}^{n} \left(x_i - y_i\right)^2}{\sum_{i=1}^{n} \left(x_i - \bar{x}\right)^2} \tag{28.5}$$

where n values of direct measurement (dry weight) were denoted by x_i and the corresponding values of one indirect measurement (optical density, cell count, or chlorophyll a) were denoted by y_i. The $\bar{x}$ is the mean of the values of direct measurement.

The value of E ranges from minus infinity to 1, with higher values indicating better performance of the indirect method employed. If $E > 0$, then the indirect measurement gives better results than representing all values by the mean ($\bar{x}$); $E =$ 0 means that there is no difference between the indirect measurement and the mean; and if $E < 0$, then it means that the indirect measurement is worse than representing all values by the mean.

28.2.5.3 Index of Agreement

The index of agreement (d), developed by Willmott (1981), is another relative performance measure, which is given in Eq. (28.6) as:

$$d = 1 - \frac{\sum_{i=1}^{n} (x_i - y_i)^2}{\sum_{i=1}^{n} \left(|x_i - \bar{x}| + |y_i - \bar{x}|\right)^2} \tag{28.6}$$

where $\bar{x}$ is the mean of the values of direct measurement, n values of direct measurement were denoted by x_i, and the corresponding values of one indirect measurement were denoted by y_i.

The value of d ranges from 0 to 1, and values closer to one are desirable. One problem with d is that its values are usually very high.

28.2.5.4 Coefficient of Variation

The coefficient of variation (C_v) is a standardized measure of dispersion of a probability distribution or frequency distribution. In this study, the coefficient of variation was calculated as an indicator of within method precision for biomass measurement. It is defined in Eq. (28.7) as:

$$C_v = \frac{\sigma}{\mu} \tag{28.7}$$

where σ is the standard deviation of the values of each method and μ is the mean of the values of each method.

28.2.6 Biomass Measurements

28.2.6.1 Dry Weight

The dry weight of the samples was measured from the triplicate averages of volatile suspended solids (VSS) obtained by means of membrane filtration according to the *Standard Methods for the Examination of Water and Wastewater*, Method 2540 [40]. These methods are commonly used for wastewater examination. The detailed procedure is as follows:

1. Prepare three 0.4 μm glass microfiber filters (GB-140, ADVANTEC, Japan) by rinsing with distilled water under Millipore 47 mm vacuum filter assembly.
2. Place three filters in three aluminum foil containers, and bake in the furnace (550 °C) for approximately 15 min.
3. Remove three filters with the container from furnace, and place in a bell jar desiccator until the sample reaches room temperature.
4. Weigh three filters with their containers and record weight (A).
5. Filter uniform aqueous sample of known volume (V) through the filter under vacuum filter assembly.
6. Return three filters to the corresponding container.
7. Bake them in the oven at 103–105 °C for 1 h.

8. After baking, remove them from the oven and allow cooling in a desiccator.
9. Reweigh three filters with dry residue and container and record weight (*B*).
10. TSS is then calculated using Eq. (28.8):

$$\text{TSS} = \frac{B - A}{V} \tag{28.8}$$

11. Place three filters with dry residue and container in a furnace at 550 °C and leave there for 5 min.
12. After ignition, remove them from the furnace and allow cooling in a desiccator.
13. Reweigh three filters with ash residue and container and record weight (*C*).
14. Calculate then VSS using Eq. (28.9):

$$\text{VSS} = \frac{B - C}{V} \tag{28.9}$$

28.2.6.2 Optical Density

The optical density of *Chlorella vulgaris* was measured by a UV-Vis spectrophotometer (Cole-Parmer, USA) at 684 nm wavelength [22], with a light path of 10 mm, and the optical density of *Anabaena* sp. was measured with a light path of 10 mm at 683 nm [41], using the UV-Vis spectrophotometer. Before each measurement, the readings of the UV-Vis spectrophotometer were blanked by a purpose-made sample. As an example, blanks for measuring minkery wastewater samples contained the same 80% minkery wastewater and 20% traditional mediums instead of microalgae and cyanobacteria cultures.

28.2.6.3 Cell Count

A Bright-Line™ hemocytometer was used to count the number of cells under the microscope (Motic, BA310). The counting method was taken from *Standard Methods for the Examination of Water and Wastewater*, Method 10200E and 10200F [40]. Before each sample was loaded for counting the hemocytometer, the cover slip was rinsed with distilled water and dried via lens paper. Ensuring the hemocytometer and the cover slip were clean, the sample was ready to be loaded. After mixing the sample well, a sterile Pasteur pipette was used to dispense the sample into the counting chamber. Caution was taken upon injecting the sample into the counting chamber because if the sample spills over the grid surface, the chamber volume becomes compromised and the process must be repeated.

28.2.6.4 Chlorophyll *a* Content

Chlorophyll *a* content of the samples was measured according to the *Standard Methods for the Examination of Water and Wastewater*, Method 150.1 [40]. The detailed procedure is as follows:

1. Place the filter containing the concentrated cyanobacteria or microalgae residue in a centrifuge tube.
   (a) Add about 10 mL of aqueous acetone solution and cap tightly, and place in the dark box.
2. Repeat Step (1) until the desired number of samples has been processed.
3. Remove the cap from the centrifuge tube, insert the microtip, and sonify for 20 s at the 5 setting.
   (a) Rinse the microtip into the centrifuge tube with approximately 1 mL of an aqueous acetone solution.
   (b) Bring the extract to a volume of 13.0 mL with the acetone solution, cap, mix, and return to the dark box.
   (c) Repeat the steps outlined in Step (3) until all of the samples have been sonified.
4. Place the dark box in the 4 °C cold room and allow the extract to steep overnight.
5. Clarify the extract by centrifuging the extract for 20 min at 4000 rpm.
6. Carefully transfer the clear extract to a 5.0 cm cell, and using the multiwavelength mode on the spectrophotometer, measure the absorbance at 750, 663, 645, and 630 nm.
   (a) Use a shorter or longer cell as necessary to maintain absorbance between approx. 0.1 and 1.0 at 663 nm.
   (b) Note: Operate the spectrophotometer at a slit width no wider than 2 nm for maximum resolution.
7. For corrected samples: Immediately after measuring the absorbance, add 0.1 mL of 0.1 N HCl to the spectrophotometer cell, mix, wait for 90 s, and measure the absorbance specified in Step (6).
8. Discard the sample; rinse the cell twice with 5 mL portions of an aqueous acetone solution.
9. Repeat Steps (6) through (8) until all of the samples have been measured.
10. Determine the absorbance at 750, 663, 645, and 630 nm directly from the printout.
11. Subtract the absorbance at 750 nm from the 630, 645, and 663 nm values (turbidity correction).
12. Calculate the uncorrected chlorophyll *a* concentration by inserting the corrected absorbance values in the following Eq. (28.10):

$$\text{Uncorrected chlorophyll } a\ (\mu/L) = \frac{[11.64\ (\text{Abs663}) - 2.16\ (\text{Abs645}) + 0.10\ (\text{Abs630})]\ E(F)}{V(L)} \quad (28.10)$$

where F is the dilution factor, E is the volume of acetone used for the extraction (mL), V is the volume of water filtered (L), and L is the cell path length (cm).

13. For corrected samples, determine the absorbance at 665 nm and 750 nm after acidification.
14. Subtract the absorbance at 750 nm from the absorbance at 665 nm (turbidity correction).
15. Calculate the corrected chlorophyll a concentration by inserting the turbidity corrected absorbance readings in the following Eq. (28.11):

$$\text{Corrected chlorophyll } a\ \left(\mu\frac{g}{l}\right) = \frac{26.73(663b - 665a)E(F)}{V(L)} \quad (28.11)$$

where F is the dilution factor (if the extract requires dilution), E is the volume of acetone used for the extraction (mL), V is the volume of water filtered (L), L is the cell path length (cm), 665_a is the turbidity corrected absorbance at 665 nm after acidification, and 663_b is the turbidity corrected absorptivity at 663 nm before acidification.

28.3 Results and Discussion

28.3.1 Cost and Time Comparisons

Cost and time requirements reported below were recorded during execution of each method in the laboratory. The only direct method, dry weight, was limited by the spatial capacity of the furnace to only three samples per measurement. Therefore, the time required to measure three samples was also recorded for other methods as a comparison. In this way, the most reliable and reasonable time required per sample can be obtained by all four methods. In addition, the "warming-up" time of each equipment used during the measurement was also included. In detail, the time required per sample for each of the biomass estimation methods was shown in Table 28.1.

Table 28.1 The time required per sample for each of the biomass estimation methods

Method	Time required (per sample)	
Dry weight	3.0 h – 3 samples	1.00 h
Optical density	0.4 h – 3 samples	0.13 h
Cell count	0.5 h – 3 samples	0.17 h
Chlorophyll *a*	1.5 h – 3 samples	0.50 h

Table 28.2 Estimated cost per sample for each of the biomass estimation methods

Method	Labor	Material	Total
Dry weight	$15.00	$3.00	$18.00
Optical density	$2.00	$1.00	$3.00
Cell count	$2.50	$0.30	$2.80
Chlorophyll *a*	$7.50	$3.00	$10.50

Table 28.3 Pearson's correlation (*r*) matrix comparing the methods for measuring both microalgae and cyanobacteria biomass growth in various growth mediums under different light cycles. Methods were cell count (CC), dry weight (DW), chlorophyll *a* (Chl-*a*), and optical density (OD)

Method	OD	CC	DW
Cell count	0.990	–	–
Dry weight	0.971	0.974	–
Chlorophyll *a*	0.965	0.978	0.969

Table 28.4 Pearson's correlation (*r*) matrix comparing the methods for measuring microalgae biomass growth in various mediums under different light cycles. Methods were cell count (CC), dry weight (DW), chlorophyll *a* (Chl-*a*), and optical density (OD)

Method	OD	CC	DW
Cell count	0.990	–	–
Dry weight	0.972	0.982	–
Chlorophyll *a*	0.938	0.965	0.961

Selection of the methods was not only based upon minimizing the time requirement but also the total cost for each measurement. In this case, it was assumed that the labor rate was $15.00 per hour and the total cost for each sample was the combination of labor and material costs. The materials consumed during execution of measurement included glass microfiber filters, aluminum foil containers, disposable Pasteur pipettes, and pipette tips. Overall, estimated cost per sample for each of the biomass estimation methods was provided in Table 28.2.

28.3.2 Correlation Between Methods

The values of *r* comparing biomass estimation methods for measuring the biomass growth of *Chlorella vulgaris* and *Anabaena* sp. are provided in Table 28.3. It demonstrates that values of *r* were all very close to one, suggesting that regardless of strains, culture mediums, and light cycles, experimental results of four different biomass estimation methods were all highly correlated.

Table 28.4 provides values of *r* comparing biomass estimation methods for only measuring the biomass growth of *Chlorella vulgaris*. Methods of dry weight, optical density, and cell count demonstrated excellent correlations between one another. This finding supports the common practice of relying solely on these three methods to monitor *Chlorella vulgaris* cultivation [42].

Table 28.5 Coefficient of efficiency (E) and index of agreement (d) for optical density, cell count, and chlorophyll *a* methods for measuring the biomass growth of *Chlorella vulgaris* and *Anabaena* sp. in various mediums under different light cycles

Method	E	d
Optical density	0.879	0.972
Cell count	0.850	0.966
Chlorophyll *a*	0.878	0.970

In conclusion, the resulting matrices proved the excellent correlations between the methods for measuring the biomass growth of *Chlorella vulgaris* and *Anabaena* sp. in various growth mediums under different light cycles. This finding was supported by another study [43].

28.3.3 Assessment of Method Accuracy

The methods of optical density, cell count, and chlorophyll *a* were measurements that indirectly measured the *Chlorella vulgaris* and *Anabaena* sp. biomass. One should consider relative measures to determine the accuracy of those three indirect measurements using the only direct measurement, dry weight, as a reference. One such relative performance measure was an index of agreement (d); however, a potential problem with d is usually that its values are high and might give a false impression of good performance. Therefore, another relative performance measure, coefficient of efficiency (E), was also performed. Both E and d were calculated as an indicator of the accuracy of indirect methods.

Table 28.5 demonstrates that including all strains, growth mediums, and light cycles, values of E in the second column are all above zero, suggesting that all three methods gave better results than representing all values by the mean of dry weight method. The values of E identified the method of optical density as the most accurate indirect measurement for determining the biomass growth of *Chlorella vulgaris* and *Anabaena* sp. in various growth mediums under different light cycles. On the other hand, according to d shown in the third column of Table 28.5, the method of optical density also gave better performance than did the other methods. In short, the results proved that all three indirect measurements were quite accurate for measuring the biomass growth of *Chlorella vulgaris* and *Anabaena* sp. in various growth mediums under different light cycles; however, the method of optical density was more accurate than the methods of cell count and chlorophyll *a*.

In addition, values of E and d of these three methods for only measuring the biomass growth of *Anabaena* sp. were provided in Table 28.6. Obviously, values of E in the second column were quite different from each other in magnitude. The values of E of optical density and chlorophyll *a* methods were around 0.5 and 0.6, respectively, whereas the value of E of cell count method was only around 0.2, which means that the method of cell count was not as accurate as the other two

Table 28.6 Coefficient of efficiency (E) and index of agreement (d) for optical density, cell count, and chlorophyll *a* methods for only measuring the biomass growth of *Anabaena* sp. in various mediums under different light cycles

Methods	E	d
Optical density	0.522	0.911
Cell count	0.206	0.853
Chlorophyll *a*	0.581	0.913

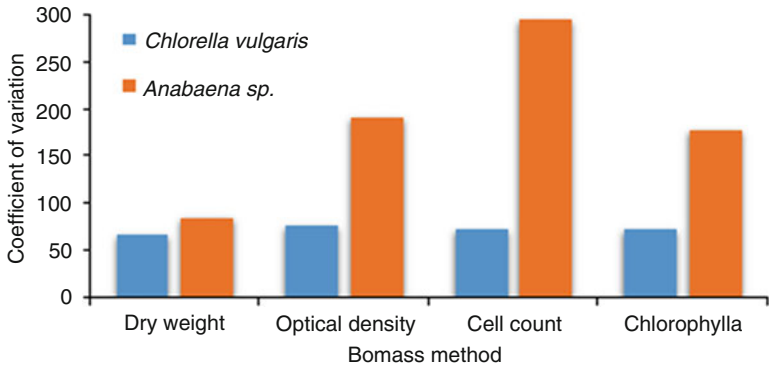

Fig. 28.3 Coefficient of variation (C_v) for dry weight, optical density, cell count, and chlorophyll *a* methods for measuring the biomass of *Chlorella vulgaris* and *Anabaena* sp. in various mediums under different light cycles

methods for measuring the biomass growth of *Anabaena* sp. Based on the experience, the reason was related to the filamentous structure of *Anabaena* sp. The filaments could be straight, circinate, or even irregular, which makes the execution of cell count extremely difficult. As a result, the method of cell count should be avoided for measuring the biomass of microalgae or cyanobacteria with a filamentous structure.

28.3.4 Assessment of Within-Method Precision

In this study, the coefficient of variation (C_v) was performed as a technique for determining the precision of the biomass estimation methods. Each C_v was compared to those of other strains and mediums to assess the potential impacts of different strains and mediums upon the precision of the biomass estimation methods. Figure 28.3 shows that values of C_v of the method of dry weight were smaller than any other methods used in both strains, which means that dry weight was the most precise method for measuring the biomass of *Chlorella vulgaris* and *Anabaena* sp. in various mediums under different light cycles.

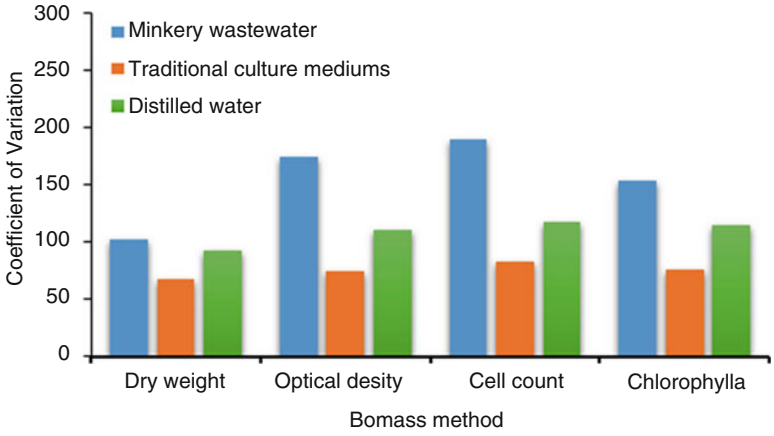

Fig. 28.4 Coefficient of variation (Cv) for dry weight, optical density, cell count, and chlorophyll *a* methods for measuring the biomass of *Chlorella vulgaris* and *Anabaena* sp. in minkery wastewater, traditional culture mediums, and distilled water under different light cycles

A much higher value of C_v in *Anabaena* sp. for cell count method can be observed in Fig. 28.3. As mentioned earlier, it can be explained by potential influence of the filamentous structure of *Anabaena* sp. The execution of cell count method for microalgae or cyanobacteria with a filamentous structure is much more difficult than of that for unicellular microalgae or cyanobacteria. Because of that, the method of cell count was more precise for measuring the biomass of *Chlorella vulgaris* rather than for measuring the biomass of *Anabaena* sp. in this study.

Although contradicting, the expected interferences associated with chromophoric dissolved organic matter in minkery wastewater, Fig. 28.4, reinforce the utility of the method of dry weight for measuring biomass in minkery wastewater. There was no evidence that organic matter in minkery wastewater increased the variability of this method.

The chlorophyll *a* method for measuring the biomass growth of *Chlorella vulgaris* and *Anabaena* sp. appears to be not as practical as the other three biomass estimation methods employed, because of the low precision and high cost. Ramaraj et al. [44] reported similar finding that chlorophyll *a* is not an appropriate measurement for microalgae or cyanobacteria biomass.

28.4 Conclusions

The cost and time analyses suggested that cell count was the most cost-effective method with a total cost of $2.80 per sample, and the most time-effective method was optical density with an average required time of 0.13 h per sample. The resulting correlation matrix demonstrated excellent correlations between each biomass

estimation methods. The coefficient of efficiency and index of agreement suggested that optical density was the most accurate indirect method for measuring the biomass growth of *Chlorella vulgaris* or *Anabaena* sp. In contrast, the method of cell count demonstrated a lack of accuracy compared to the other two indirect methods for the measurement of *Anabaena* sp. with a filamentous structure. The method of dry weight was identified as the most precise method for measuring the biomass growth of *Chlorella vulgaris* or *Anabaena* sp. Overall, this study suggests the practice of performing dry weight measurements at the beginning and end of the growth period partnered with more frequently optical density measures and cell counts (daily), as a means of monitoring microalgae or cyanobacteria biomass growth in minkery wastewater.

Nomenclature

A	Area under pigment peak
AU	Absorbance units
C	Pigment concentration (mg L^{-1}); coefficient
CC	Cell count
Chl-*a*	Chlorophyll *a*
DW	Dry weight
d	Index of agreement
E	Coefficient of efficiency; volume of acetone used (mL)
F	Calibration factor for sensitivity setting; standard response factor; dilution factor
L	The cell path length (cm)
NIR	Near infrared
OD	Optical density
r	Pearson's correlation coefficient
R	Fluorometer reading for specific sensitivity
TSS	Total suspended solids
UV	Ultraviolet
V	Volume; the volume of water filtered (L)
VSS	Volatile suspended solids
x	Growth measurement made on a day
$\bar{x}$	Mean of the values of the 1st method
$\bar{y}$	Mean of the values of the 2nd method
665	Absorptivity at 665 nm
663	Absorptivity at 663 nm

Greek Letters

σ	Standard deviation
μ	Mean

Subscripts

a	Chlorophyll *a*; after
b	Before
E	Extraction
I	Injection
i	*i*th value
n	*n*th value
S	Sample
v	Variation
0	Day 0
6	Day 6

References

1. United Nations Population Division (2017) World population prospects the 2017 revision: key findings and advance tables. Department of Economic and Social Affairs, New York
2. Shi J, Podola B, Melkonian M (2007) Removal of nitrogen and phosphorus from wastewater using microalgae immobilized on twin layers: an experimental study. J Appl Phycol 19:417–423
3. Hammouda O, Gaber A, Abdelraouf N (1995) Microalgae and wastewater treatment. Ecotoxicol Environ Saf 31:205–210
4. Lowrey J, Yildiz I (2011) Seawater/wastewater production of microalgae-based biofuels in closed loop tubular photobioreactors, Masters Theses Proj. Reports
5. Bhatnagar A, Chinnasamy S, Singh M, Das KC (2011) Renewable biomass production by Mixotrophic algae in the presence of various carbon sources and wastewaters. Appl Energy 88:3425–3431
6. American Public Health Association (ed) (2005) Standard methods for the examination of water and wastewater, 21st edn. American Public Health Association, Washington, DC
7. Yoo C, Jun SY, Lee JY, Ahn CY, Oh HM (2010) Selection of microalgae for lipid production under high levels carbon dioxide. Bioresour Technol 101(1):S71–S74
8. Chevalier P, De la Noüe J (1985) Efficiency of immobilized hyperconcentrated algae for ammonium and orthophosphate removal from wastewaters. Biotechnol Lett 7(6):395–400
9. Atta M, Idris A, Bukhari A, Wahidin S (2013) Intensity of blue LED light: a potential stimulus for biomass and lipid content in fresh water microalgae Chlorella vulgaris. Bioresour Technol 148:373–378
10. Round FE, Crawford RM, Mann DG (1990) Diatoms: biology and morphology of the genera. Cambridge University Press, Cambridge, UK
11. Davis SC, Sheppard VC, Begum G, Cai Y, Fang Y, Berrigan JD, Kröger N, Sandhage KH (2013) Rapid flow through biocatalysis with high surface area, enzyme loaded carbon and gold bearing diatom frustule replicas. Adv Funct Mater 23(36):4611–4620
12. Zhu CJ, Lee YK (1997) Determination of biomass dry weight of marine microalgae. J Appl Phycol 9(2):189–194
13. Brown MR, Farmer CL (1994) Riboflavin content of six species of microalgae used in mariculture. J Appl Phycol 6(1):61–65
14. Wikfors GH, Ferris GE, Smith BC (1992) The relationship between gross biochemical composition of cultured algal foods and growth of the hard clam, Mercenaria mercenaria (L.). Aquaculture 108(1–2):135–154
15. Qiang H, Richmond A (1994) Optimizing the population density in Isochrysis galbana grown outdoors in a glass column photobioreactor. J Appl Phycol 6(4):391–396

16. Grima EM, Pérez JS, Camacho FG, Sánchez JG, Fernández FA, Alonso DL (1994) Outdoor culture of Isochrysis galbana ALII-4 in a closed tubular photobioreactor. J Biotechnol 37 (2):159–166
17. Craigie JS, Correa JA, Gordon ME (1992) Cuticles from chondrus crispus (rhodophyta) 1. J Phycol 28(6):777–786
18. Ben-Amotz A, Tornabene TG, Thomas WH (1985) Chemical profile of selected species of microalgae with emphasis on lipids. J Phycol 21(1):72–81
19. Chu WL, Phang SM, Goh SH (1994) Studies on the production of useful chemicals, especially fatty acids in the marine diatom Nitzschia conspicua. Springer, Dordrecht, pp 33–40
20. Reitan KI, Rainuzzo JR, Olsen Y (1994) Effect of nutrient limitation on fatty acid and lipid content of marine microalgae. J Phycol 30(6):972–979
21. Roleda MY, Slocombe SP, Leakey RJ, Day JG, Bell EM, Stanley MS (2013) Effects of temperature and nutrient regimes on biomass and lipid production by six oleaginous microalgae in batch culture employing a two-phase cultivation strategy. Bioresour Technol 129:439–449
22. Griffiths MJ, Garcin C, van Hille RP, Harrison ST (2011) Interference by pigment in the estimation of microalgal biomass concentration by optical density. J Microbiol Methods 85 (2):119–123
23. Sandnes JM, Ringstad T, Wenner D, Heyerdahl PH, Källqvist T, Gislerød HR (2006) Real-time monitoring and automatic density control of large-scale microalgal cultures using near infrared (NIR) optical density sensors. J Biotechnol 122(2):209–215
24. Meireles LA, Azevedo JL, Cunha JP, Malcata FX (2002) On-line determination of biomass in a microalga bioreactor using a novel computerized flow injection analysis system. Biotechnol Prog 18(6):1387–1391
25. Kenkel J (1988) Analytical chemistry for technicians, 1st edn. Lewis Publishers Inc, Chelsea
26. Pitts, N (2016) CHMA3010 Bio-Analytical Chemistry (Unpublished Lecture Notes), Dalhousie University, Faculty of Agriculture, Truro, NS, Canada
27. Salm S, Goodwyn L, van Loon N, Lind G (2010) Throwing the dice: teaching the Hemocytometer. J Coll Sci Teach 39(6):64
28. Berkson J, Magath TB, Hurn M (1939) The error of estimate of the blood cell count as made with the hemocytometer. Am J Physiol Legacy Content 128(2):309–323
29. Dragone G, Fernandes BD, Abreu AP, Vicente AA, Teixeira JA (2011) Nutrient limitation as a strategy for increasing starch accumulation in microalgae. Appl Energy 88(10):3331–3335
30. Aruoja V, Dubourguier HC, Kasemets K, Kahru A (2009) Toxicity of nanoparticles of CuO, ZnO and TiO_2 to microalgae Pseudokirchneriella subcapitata. Sci Total Environ 407 (4):1461–1468
31. Tao DG, Salihon J, Meng L (2009) Modelling of microalgae growth and oil production by using sewage and carbon dioxide for biodiesel. In: The Proceedings of National Conference on Postgraduate Research (Eds. MM Noor; MM Rahman and K Kadirgama), Universiti Malaysia Pahang, Malaysia. Paper no. 011, pp. 59–66
32. Heilmann SM, Davis HT, Jader LR, Lefebvre PA, Sadowsky MJ, Schendel FJ, Von Keitz MG, Valentas KJ (2010) Hydrothermal carbonization of microalgae. Biomass Bioenergy 34 (6):875–882
33. SimuLab Testing Laborator (2001) Methods Manual, SOP: Haemocytometer. Controlled Document MTH 51, Ver 4, June 6, 2001 http://simulab.ltt.com.au/4/laboratory/methodsman/MMSOPHaemocytometer.htm Last accesses 10 Oct 2017
34. Sigma-Aldrich (2016) BRAND ® counting chamber BLAUBRAND Neubauer improved. https://www.sigmaaldrich.com/catalog/product/aldrich/br717820?lang=en®ion=CA Last accesses 10 Oct 2017
35. Holm-Hansen O, Lorenzen CJ, Holmes RW, Strickland JD (1965) Fluorometric determination of chlorophyll. J Conseil 30(1):3–15
36. Lakowicz JR, Johnson ML, Gryczynski I, Joshi N, Laczko G (1987) Transient effects in fluorescence quenching measured by 2-GHz frequency-domain fluorometry. J Phys Chem 12:3277–3285

37. Schreiber U, Schliwa U, Bilger W (1986) Continuous recording of photochemical and non-photochemical chlorophyll fluorescence quenching with a new type of modulation fluorometer. Photosynth Res 10(1–2):51–62
38. Wright SW (1991) Improved HPLC method for the analysis of chlorophylls and carotenoids from marine phytoplankton. Mar Ecol Prog Ser 77:183–196
39. Abrahamsson V, Rodriguez-Meizoso I, Turner C (2012) Determination of carotenoids in microalgae using supercritical fluid extraction and chromatography. J Chromatogr A 1250:63–68
40. American Public Health Association (ed) (1998) Standard methods for the examination of water and wastewater, 20th edn. American Public Health Association, Washington, DC
41. Yoon J, Sim S, Kim M, Park T (2002) High cell density culture of Anabaena variabilis using repeated injections of carbon dioxide for the production of hydrogen. Int J Hydrog Energy 27:1265–1270
42. Safi C, Zebib B, Merah O, Pontalier PY, Vaca-Garcia C (2014) Morphology, composition, production, processing and applications of *Chlorella vulgaris*: a review. Renew Sust Energ Rev 35:265–278
43. Lowrey J, Yildiz I (2011) Comparative analysis of four cost effective laboratory methods for quantification of microalgae biomass in controlled environment wastewater and nutrient media. Masters Theses Project Reports
44. Ramaraj R, Tsai DDW, Chen PH (2013) Chlorophyll is not accurate measurement for algal biomass. Chiang Mai J Sci 40(4):547–555

Chapter 29
Energy Recovery, Raw Material Conservation and Pollutant Emission Reductions Through the Coprocessing of Wastes in Cement Rotary Kilns

Ilyes Ghedjatti, Mohamed Tebbal, Khadidja Safer, Philippe Martin, and Boudjelal Kadi Hanifi

29.1 Introduction

The Sustainable Development Goals (SDGs), officially known as Transforming Our World: the 2030 Agenda for Sustainable Development, is a set of 17 Global Goals with 169 targets amongst them. Spearheaded by the United Nations through a deliberative process involving its 193 member states, the goals are contained in paragraph 54 United Nations Resolution A/RES/70/1 of 25 September 2015. This set of goals covers a broad range of sustainable development issues, including making cities more sustainable, combating climate change and protecting oceans and forests. Sustainable development focuses more on economic development, social development and environmental protection for future generations [1]. The social and economic development of a country can cause an increase in pressures on its environment and increases the need for a reduction in environmentally damaging activities. Some of these damaging activities involve the production and disposal of waste.

Waste management and waste disposal are all the activities and actions required to manage waste from its inception to its final disposal. This includes amongst other things collection, transport, treatment and disposal of wastes together with monitoring and regulation. Waste management practices are not uniform amongst countries (developed and developing nations), regions (urban and rural area) and sectors

I. Ghedjatti (✉) · M. Tebbal · K. Safer
Laboratoire des Carburants Gazeux et de l'Environnement, Département de Génie Mécanique, Institut de Génie Civil et Mécanique d'Oran, Université des Sciences et de la Technologie d'Oran Mohamed Boudiaf, Oran, Algeria
e-mail: ilyes.ghedjatti@univ-usto.dz

P. Martin · B. Kadi Hanifi
Lafarge Ciment Oggaz, Lafarge Algeria, A Member of LafargeHolcim, Mascara, Algeria

S. Nižetić, A. Papadopoulos (eds.), *The Role of Exergy in Energy and the Environment*, Green Energy and Technology,
https://doi.org/10.1007/978-3-319-89845-2_29

(residential and industrial). During these years, many countries have been engaged in this alternative to provide positive ways to be involved in the cycle of production, consumption and waste [2]. This research work fits into a national project of coprocessing of wastes in Algeria, conducted by Lafarge Group, with the collaboration of the Ministry of Water Resources and Environment and the Laboratory of Gaseous Fuels and Environment. This project is to be launched by 2018. One of the most important goals of industrial ecology is to make one industry's waste another's raw material [3]. Within the cement industry, the use of wastes as fuel and raw materials is a positive, forward-thinking example.

Researches related to this field [4] conclude that as long as the different waste streams having large variation in the chemical characteristics can be managed in an environmentally sound manner in the cement kilns, the cement kiln emissions and the product quality are not influenced by the variation in the chemical constituents present in the waste streams. However, releases of dioxins and dioxin-like compounds from cement kilns coprocessing solid wastes remain an issue; dioxins could be released from cement kilns coprocessing solid wastes. Actually, dioxin-like compounds, such as polychlorinated biphenyls (PCBs) and polychlorinated naphthalenes (PCNs), could also be produced and released along with dioxins as reported in previous publications [5–7]. Other findings [8] revealed that coprocessing of waste can be one of the most effective industrial waste disposal techniques in developing countries considering other practices of waste disposal methodology in terms of zero ash generation, emission, less auxiliary technology requirements and less set-up cost. The effectiveness of the coprocessing in cement plants is regarded as a way for an effective utilization of energy and recoverable raw materials locked in the industrial waste. In this paper, we explored the alternative of waste coprocessing in cement rotary kilns which will lead, if input and process control are properly conducted, to pollutant emission reductions, energy recovery and raw material conservation. First, a list of admissible wastes and Lafarge experience feedback are presented. Next, the methodology is described and the initial conditions are illustrated. Then, results of substitution rate variations are discussed. Finally, the benefit and the efficiency of this alternative are summarized.

29.2 Cement Manufacture, Coprocessing of Waste and Experience Feedback

Cement is made from a mixture of clinker and gypsum and active ingredients. Typically, the clinker, which is a semi-finished product of cement manufacture, has a composition of about 67% CaO, 22% SiO_2, 5% Al_2O_3, 3% Fe_2O_3 and 3% of other components [5]. Clinker burning is the most important phase of the production process in terms of the environmental impact associated with cement manufacture [9–11]. The key pollutants released to air are particulates, nitrogen oxides and

Table 29.1 Admissible wastes [10, 18]

Type of mineral wastes used in cement industry	Hazardous wastes used in cement industry for energy recovery	Non-hazardous wastes used in cement industry for energy recovery
Wastes containing lime Industrial sewage sludge Dried wastewater treatment plants sludge Calcic wastes *Wastes containing silica* Wastes from casting Bottom sediment sludge Slag from the steel industry *Wastes containing iron* Shot-blasting *Wastes containing alumina* Hydroxide sludge	*Liquid and pasty wastes* Solvents Emulsions Used oils Fuels and hydrocarbon vessel bottom Oily wastes Contaminated soils *Solid wastes* Soiled/contaminated packaging Sawdust impregnated with paint wastes, adhesives, varnish, vessels' bottom, organic powdered wastes, organic sludge	Used tires Dried sludges Animal bone meal

sulphur dioxide. Other emissions include carbon oxides, polychlorinated dibenzo-p-dioxins and dibenzofurans, volatile organic compounds, metals and their compounds, hydrogen chloride and hydrogen fluoride. Determining minimum and maximum quantities of waste to be introduced into cement kilns is not always obvious, because of the compositional complexity and the physicochemical properties of these alternative materials and substitutes. This complexity appears especially during combustion and atmospheric emissions processes and through the obtained quality of the produced clinker as well [4] (Table 29.1).

For all the industrial sites of Lafarge Group across the world, and that are employing the coprocessing of wastes, substitution rates varied from 0 to 80%. In 2010, the average of substitution rate has reached 50%, which means that Lafarge Group has met half of its energetic needs by using various range of wastes [17] (Figs. 29.2, 29.3, 29.4 and 29.5).

According to Figs. 29.2, 29.3, 29.4 and 29.5, it is noticeable that there is an inverse proportion between pollutant concentrations (at the chimney exit of Lafarge plants) and substitution rates [17].

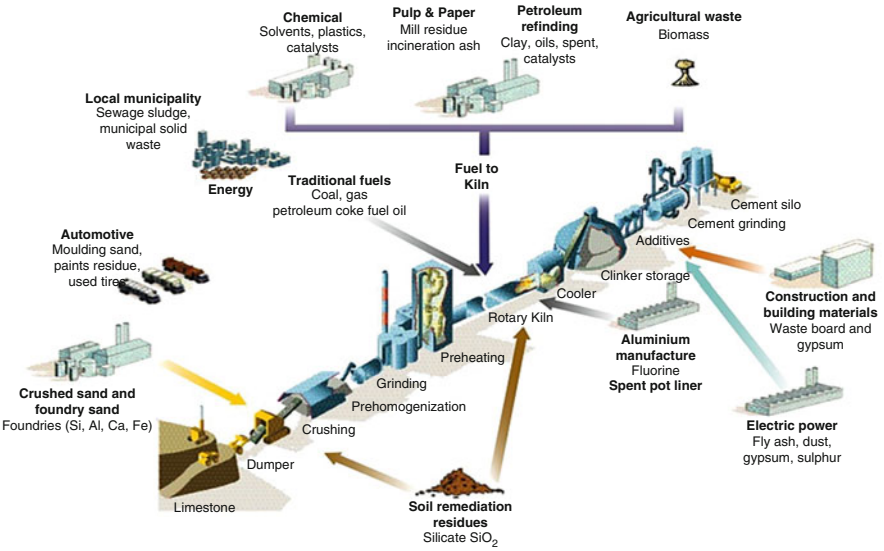

Fig. 29.1 Coprocessing of different types of wastes through the cement manufacturing system [16]

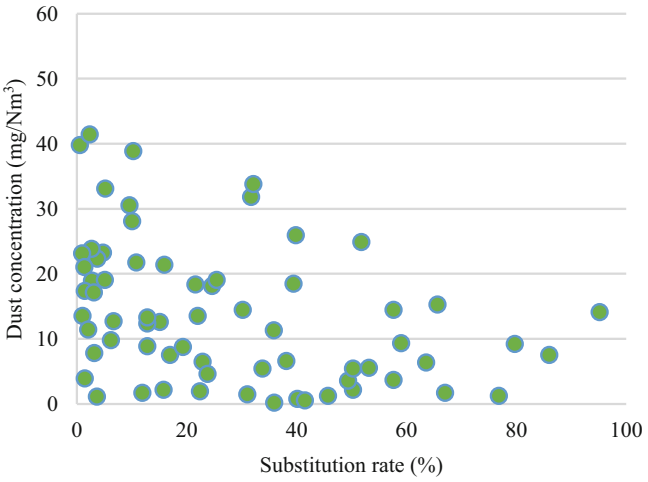

Fig. 29.2 Dust concentration

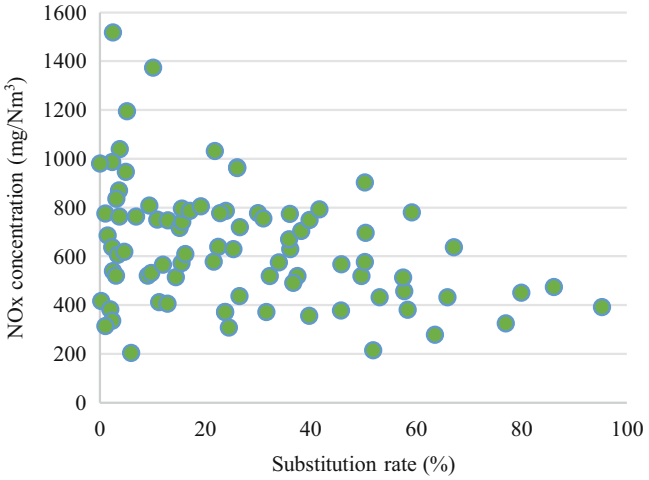

Fig. 29.3 NOx concentration

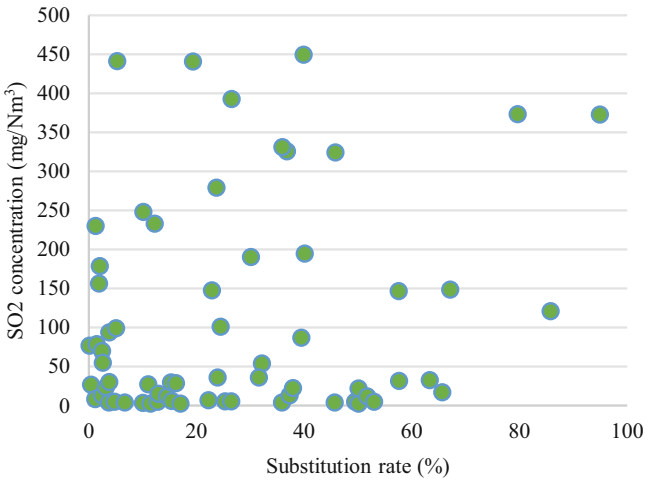

Fig. 29.4 SO_2 concentration

29.3 Methodology

Quantifying raw meal composition allows to determine the clinker characteristics and to enhance the burning phase. The only way to obtain a high-quality clinker is to have a well-dosed and perfectly burnt raw meal. For this reason, the following indicators [12] are usually considered as basis:

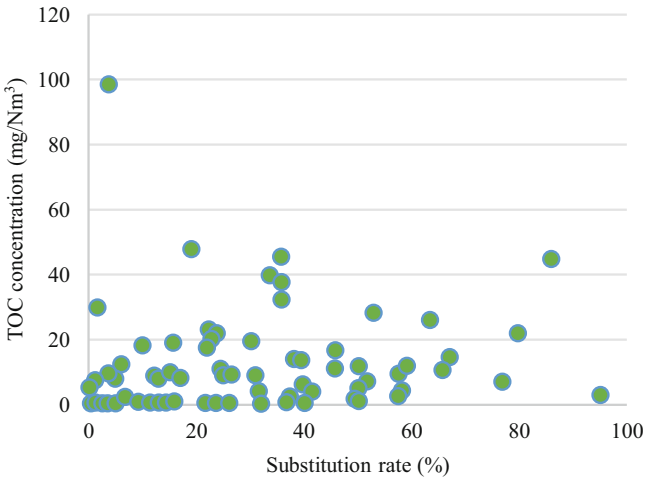

Fig. 29.5 Total organic compound concentration

- LSF: Lime saturation factor
- KST: Kalkstandard
- Delta: Lime deficiency

In this paper, only LSF is used, Eq. (29.1):

$$\mathrm{LSF} = \frac{\mathrm{Cr}}{2.8 \times S + 1.18 \times A + 0.65 \times F} \times 100 \tag{29.1}$$

Cr, lime-real; S, silicon dioxide; A, aluminium oxide; F: ferric oxide

When using a combustible that does not contain ashes (i.e. natural gas), LSF values are as follows:

- Regular cement: LSF = 90–95
- Premium priced cement: LSF = 95–98

MAF and MS modulus are calculated through the following equations, Eqs. (29.2) and (29.3):

$$\mathrm{MS} = \frac{S}{A + F} \tag{29.2}$$

S, silicon dioxide; *A*, aluminium oxide; *F*, ferric oxide

When the MS modulus decreases, the burning phase is enhaced, thus, the sum of (*A*+*F*) increases and the liquid phase proportion as well. All of this will lead to residence time reduction, and the reaction between lime and silicon dioxide will be improved. As a consequence, more of the lime will react and less free lime will be obtained. The ideal value of MS is between 2.2 and 3.2.

Table 29.2 Production capacity and premium priced clinker proportions (tonne/day)

Capacity	Tonne/year	Tonne/day	Proportions of a premium priced clinker (tonne/day)		
			Elements	Proportions (%)	Quantity (T)
Clinker production	2,225,000.00	6164.384	*C* (lime)	68.5	4222.603
Raw meal	3,600,775.00	9865.137	*S* (silicon dioxide)	22	1356.164
			A (aluminium oxide)	5	308.220
			F (ferric oxide)	4.5	277.390

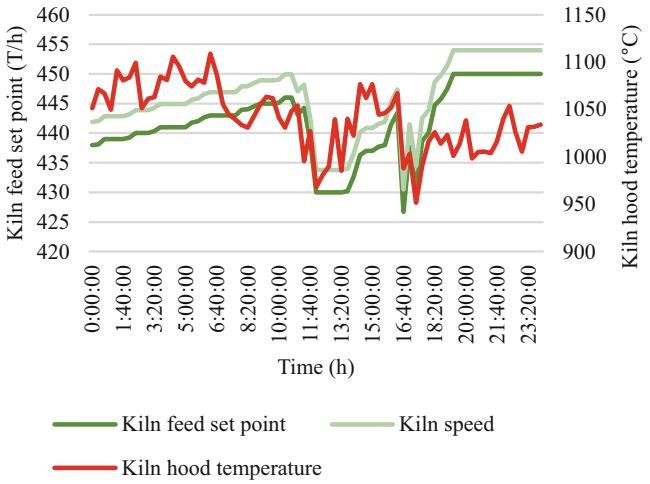

Fig. 29.6 Kiln feed set point, kiln speed and kiln hood temperature variations

$$\mathrm{MAF} = \frac{A}{F} \tag{29.3}$$

A, aluminium oxide; *F*, ferric oxide

The aluminium oxide reacts to proprietarily form tetracalcium aluminoferrite (C_4AF). The tricalcium aluminate (C_3A) is provided by the remaining aluminium oxide (Al_2O_3). The ideal value of MAF is between 1 and 2.5. In this paper, the considered cement plant is Lafarge Ciment d'Oggaz, Lafarge cement plant located in Mascara, Algeria. The clinker/raw meal ratio is equal to 0.625; the production capacity and proportions (premium priced clinker) are as follows (Table 29.2):

The following operating parameters have been recorded during April 2016 and mainly concern a 24-h on-site recording, with a time-based interval of 20 min between each recorded data.

The operating parameters such as kiln feed set point, kiln speed, kiln hood temperature, kiln burner gas flow and calciner burner gas flow are illustrated in Figs. 29.6 and 29.7 as follows:

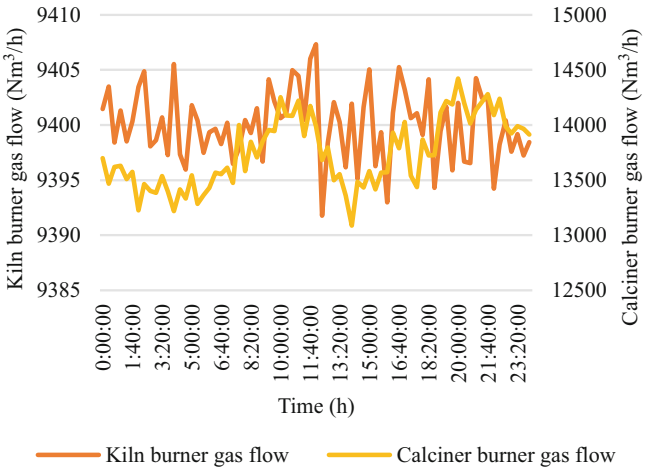

Fig. 29.7 Kiln burner gas flow and calciner burner gas flow variations

First, LSF is calculated from Eq. (29.1) considering the case of a premium priced cement. For this reason, a reference mineral proportion of raw materials is established, in order to reach an LSF equal to 97.26. Then, another factor, similar to the previous one, is set up to consider waste mineral constituents and which must be equal to the first one, 97.26.

However, waste organic and mineral contents with different proportions have been considered, with a variation of the minerals in wastes from 50 to 100%. A third indicator is established, called total LSF, calculated from the addition of both previous indicators involving waste and raw material contents, in order to obtain a total LSF value of 97.26.

Next, a reference of waste proportion equal to the premium priced clinker proportion is set up to determine the value range that mineral proportions in waste should not exceed, in order to keep the same mineral proportions in the blend (raw meal-wastes) and the same LSF value (97.26), which means keeping the same clinker quality (premium priced).

As soon as the proportions exceed the reference values established for wastes, the gap between them is calculated in order to compensate it by removing the quantity expressed by this gap from the raw meal, to keep the same requested quantity and quality. Using this method, it becomes possible to obtain an LSF equal to 97.26, no matter how waste proportions or substitution rates are changed. In case that another LSF value is desired (e.g. between 90 and 95 for a standard clinker quality), only the reference proportions (in %) need to be changed (Tables 29.3, 29.4, and 29.5).

Table 29.3 A case of clinker production without waste input

	Clinker (T/day)	Waste input (T/day)	Waste input (%)	Total quantity (T/day)	Waste ref. (T)	Waste ref. (%)	Gaps (T)
C (68.5%)	4222.603	–	–	4222.603	–	–	–
S (22%)	1356.164	–	–	1356.164	–	–	–
A (5%)	308.2192	–	–	308.2192	–	–	–
F (4.5%)	277.3973	–	–	277.3973	–	–	–
Total (100%)	6164.384	–	–	6164.384	–	–	–
Total prod.	6164.384		Minerals in wastes (%, T)	–			
Substitution rate (%)	–	–	Organics in wastes (%, T)	–		LSF	97.26

29.4 Results and Discussion

By varying both the substitution rates and organic and mineral proportions in waste, the maximum values to not exceed for each case is deduced, and coefficients related to the maximum values of the four principal components (C, S, A, F) have been set for each case by calculating the ratio of each component proportion out of the mineral content substitution rate and then making the sum of the four component coefficients for each case by varying the minerals' substitution rate. The results are illustrated in Fig. 29.8.

Coefficient variations proportionally decrease with substitution rates; meanwhile, their values proportionally increase with organic proportions in waste.

These coefficients represent reference values for maximum proportions of raw meal that must be considered in order to obtain the requested value of LSF (between 95 and 98 for the premium priced clinker), because as soon as the organic proportion in waste decreases, the input of minerals through waste will not meet the need of the manufacture process to obtain the clinker quality sought after. In this case, the only asset is the contribution of some wastes in a very high energy potential intake [8, 13] (high lower calorific values) to improve the combustion process. Minimum and maximum values of theoretical emissions are calculated based on minimum and maximum values of pollutant emission limit reference (kg per tonnes of the clinker daily production). The results are gathered in Table 29.6 that illustrates the minimum and maximum values of emissions according to substitution rates and waste composition variations. These quantities are reported to the clinker daily production.

The pollutant emissions noticeably decrease as soon as the substitution rates increase (Fig. 29.9); the condition is that the reference values of waste content proportions must always be considered. The pollutant emission values represent the average amounts (T/day) of cement kiln emissions resulting from the clinker daily production, which is in our case about 6164.384 T/day. When operating in compliance with the reference limit values of the introduced waste streams, high

Table 29.4 A case of a substitution rate of 10% (with reference waste input proportions)

	Clinker (T/day)	Waste input (T/day)	Waste input (%)	Total quantity (T/day)		Waste ref. (T)	Waste ref. (%)	Gaps (T)
C (68.5%)	3800.342	422.2603	68.5	4222.603		422.2603	68.5	0
S (22%)	1220.548	135.6164	22	1356.164		135.6164	22	0
A (5%)	277.3973	30.82192	5	308.2192		30.82192	5	0
F (4.5%)	249.6575	27.73973	4.5	277.3973		27.73973	4.5	0
Total (100%)	5547.945	616.4384	100	6164.384		616.4384	100	0
Total prod.	6164.384		Minerals in wastes (%, T)	100%	616.4384 T			
Substitution rate (%)	10	616.4384	Organics in wastes (%, T)	0%	0 T		LSF	97.26

Table 29.5 A case of a substitution rate of 20% (80:20) (with random waste input proportions)

	Clinker (T/day)	Waste input (T/day)	Waste input (%)	Total quantity (T/day)		Waste ref. (T)	Waste ref. (%)	Gaps (T)
C (68.5%)	3511.233	542.4658	55	4053.699		675.6164	68.5	133.1507
S (22%)	1094.795	207.1233	21	1301.918		216.9863	22	9.863014
A (5%)	269.2603	26.63014	2.7	295.8904		49.31507	5	22.68493
F (4.5%)	253.4795	12.82192	1.3	266.3014		44.38356	4.5	31.56164
Total (100%)	5128.767	789.0411	80	5917.808		986.3014	100	197.2603
Total prod.	6164.384		Minerals in wastes (%, T)	80%	986.3014 T			
Substitution rate (%)	20	1232.877	Organics in wastes (%, T)	20%	246.5753 T		LSF	97.26

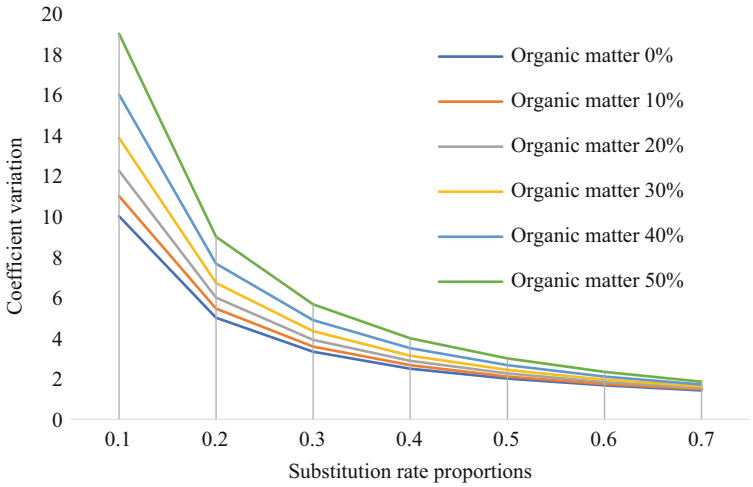

Fig. 29.8 Coefficient variation with substitution rate variation

substitution rates can be reached without affecting the proper functioning of the production process nor the kiln emissions.

Although the waste streams have large variation in their chemical characteristics, if proper input and process control are exercised, the large variation in the chemical characteristics will not have any negative impact on the product quality nor the pollutant emissions from the cement kiln stack [10].

CO emissions are related to the organic content and the running conditions of the manufacture process, but it is also the consequence of an incomplete combustion, especially when the control of solid alternative fuel feeding is not optimal [8]. Depending on the characteristics of the quarry, between 1.5 and 6.0 g of organic carbon per kilogram of clinker originating from the raw materials is fed into the process. Tests carried out with raw materials from various origins have shown that between 85 and 95% of the organic compounds present in raw materials oxidize completely to CO_2 in the presence of a 3% oxygen excess [12–14], while between 5 and 15% oxidize partially to CO. With certain raw materials, the CO concentration may, in certain cases, exceed 2000 mg/Nm^3.

Finally, the CO concentration reduction indicates a better combustion, while CO_2 concentration reduction represents less carbon loading to the atmosphere [12–14]. Figure 29.10 shows the inverse proportion between the kiln hood temperature and CO from the preheater outlet.

Other factors related to the fuels' characteristics like viscosity and caloric value can affect atomization and combustion characteristics, through which they dominate the temperature distribution and NO concentration. When O_2 concentration, temperature and non-uniformity of the temperature distribution increase, NO formation largely increases as well, especially when the temperature is higher than 1500 °C [12, 14], as shown in Figs. 29.12 and 29.13.

Table 29.6 Pollutant emission variation with substitution rate

Substitution rate (%)	0		10 (organics 0%)		10 (organics 50%)		30 (organics 50%)		50 (organics 50%)	
Emissions (T/day)	Min	Max	Min	Max	Min	Max	Min	Max	Min	Max
NOx	2.465753	36.9863	2.219178	33.28767	2.342466	35.13699	2.09589	31.43836	1.849315	27.73973
SO_2	0.123288	43.15068	0.110959	38.83562	0.117123	40.99315	0.104795	36.67808	0.092466	32.36301
PM	0.061644	2.465753	0.055479	2.219178	0.058562	2.342466	0.052397	2.09589	0.046233	1.849315
TOC	0.061644	6.164384	0.055479	5.547945	0.058562	5.856164	0.052397	5.239726	0.046233	4.623288
CO	6.164384	24.65753	5.547945	22.19178	5.856164	23.42466	5.239726	20.9589	4.623288	18.49315
PCDD/F	1.232877	6.164384	1.109589	5.547945	1.171233	5.856164	1.047945	5.239726	0.924658	4.623288
HCl	0.012329	0.308219	0.011096	0.277397	0.011712	0.292808	0.010479	0.261986	0.009247	0.231164
HF	0.004932	0.061644	0.004438	0.055479	0.004685	0.058562	0.004192	0.052397	0.003699	0.046233
CO_2	4931.507	6410.959	4438.356	5769.863	4684.932	6090.411	4191.781	5449.315	3698.63	4808.219

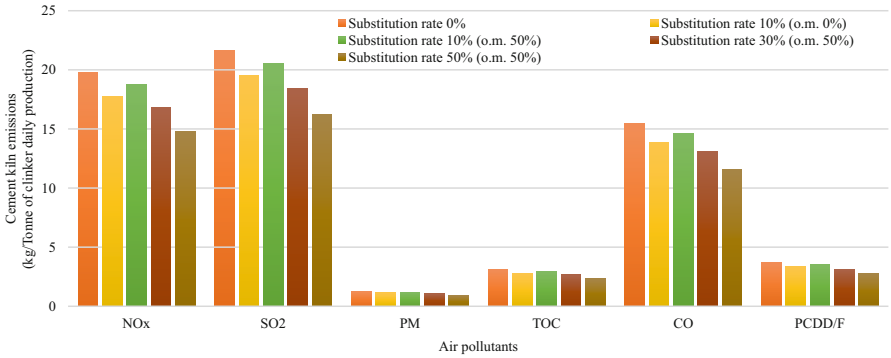

Fig. 29.9 Pollutant emission variation based on substitution rates and organic contents

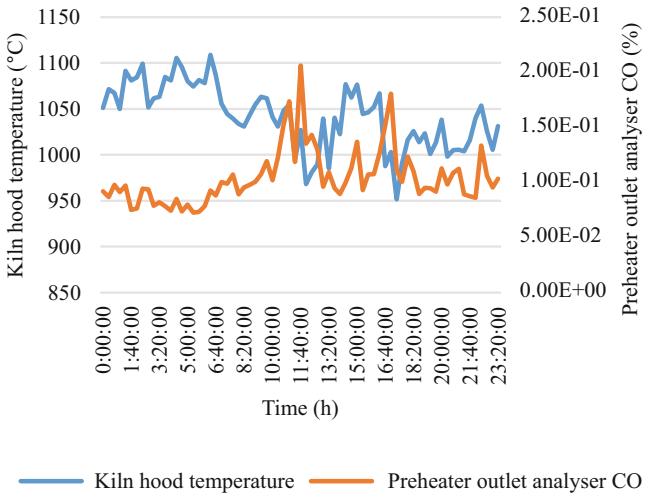

Fig. 29.10 Kiln hood temperature and preheater outlet CO

On the one hand, if the flame temperature increases, NO formation increases as well; variation of NO is faster than other parameters. Also, the combustion air temperature, or the zone temperature, varies with NO variation. NO is considered as an anticipator of the zone temperature. Indeed, when NO increases, it means that the zone temperature has increased as well. To limit NO formations and emissions, air excess must be limited, on the one hand. On the other hand, it is noticeable from Fig. 29.11 that the NO decrease is related to CO increase [12, 14].

Basically, it would be logical to locally create CO and unburned gases to narrow down NO, for instance, by using some alternative combustibles such as tires, oils and other wastes. The lower carbon/hydrogen ratio leads to a decrease in carbon compounds. Volatile particulate emissions are the consequence of lower combustion efficiency resulting in increased HC emissions which condenses onto particulates. When the latter decrease, volatile particulates also decrease.

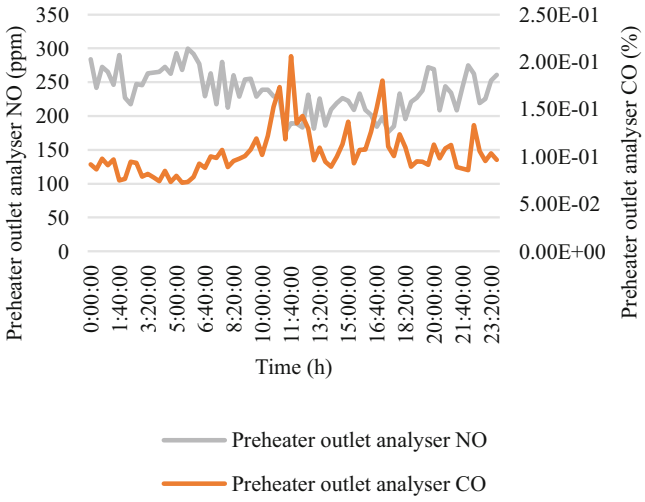

Fig. 29.11 Preheater outlet NO and preheater outlet analyser CO

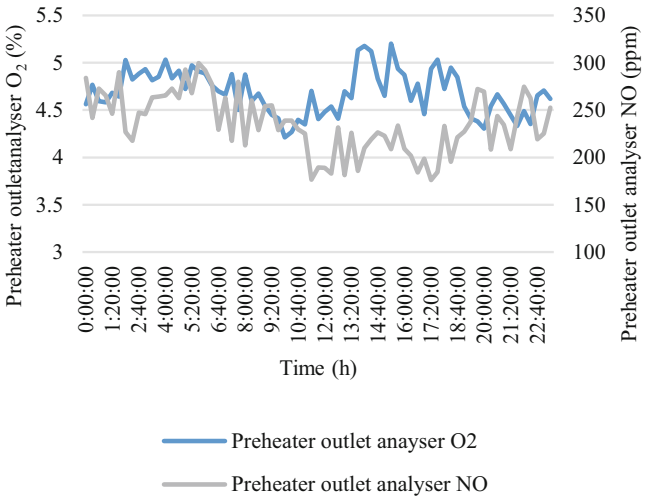

Fig. 29.12 Preheater outlet NO and preheater outlet O_2

Another remaining risk is the SO_2 increase. Indeed, SO_2 emissions from cement plants are directly related to the volatile sulphur compounds in the raw materials. Kilns that use raw materials with low contents of volatile sulphur compounds have much lower SO_2 emissions, in some cases below detection limits. To limit SO_2 emissions, volatilization phenomena must be limited. It is well known that the increase of such phenomena is proportional to the temperature increase [12, 14]. Thus, the burning

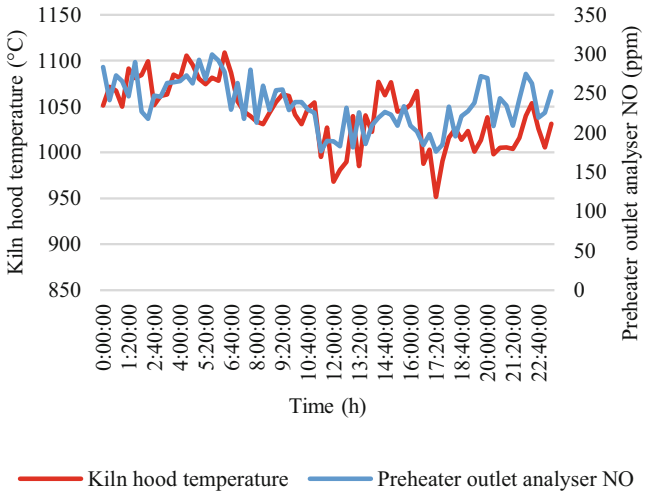

Fig. 29.13 Kiln hood temperature and preheater outlet NO

phase should occur at lower temperatures, which requires a good ability for burning. To achieve this, a fine grinding of the raw meal is highly recommended. To avoid any variation or disturbance, the raw meal must be regular in tonnes and quantities.

29.5 Conclusion

Wastes have been coprocessed in cement kilns for more than 20 years, and this practice is prevalent in some developed countries such as the United States and Japan, as well as in a number of countries in the European Union. Many developing countries are initiating programmes to promote coprocessing of wastes in the cement industry. The main environmental aspects associated with the production of cement are energy consumption and emissions into the atmosphere of NOx, SO_2 and CO_2 particles. These particles are due to diffusive sources and specific foci, and the gases come from the main focus which is the clinker kiln [15]. Coprocessing in resource-intensive industries involves the use of waste in manufacture processes for the purpose of energy recovery and raw material conservation and reducing the use of conventional fuels through substitution.

Organic constituents act as fuel and get totally destroyed due to the high temperatures, long residence time and oxidizing conditions in the kiln. Chlorine or sulphur (acid gases, HCL and SO_2) are produced and neutralized by the freshly formed lime and absorbed in product phase. Inorganic constituents including heavy metals react as raw materials in the cement process. The high temperatures and sufficiently long residence time in cement kilns and other characteristics of cement manufacture make

the coprocessing of waste materials a viable strategy. In summary, the benefits of coprocessing are:

- To provide a permanent solution to waste problems by saving landfill space and reducing the pollution caused by the disposal of these wastes
- To provide a new source for material/natural (non-renewable) resources recovery
- Energy recovery (by providing organic-based wastes)
- Lessens reliance on fossil fuels and primary resource markets
- To narrow down the total emissions and GHGs in order to slow global warming and demonstrate a positive impact on integrated environmental indicators, such as the ecological footprint
- High temperatures (1500–2000 °C) and residence time > 2 s, i.e. a complete destruction of organics

Nomenclature

A	Aluminium oxide
AFR	Alternative fuels and raw materials
C	Lime
C_2S	Belite
C_3A	Aluminate or celite
C_3S	Alite
C_4AF	Ferrite
Delta	Lime deficiency
F	Ferric oxide
KST	Kalkstandard
LSF	Lime saturation factor
MAF	Alumino ferric modulus
M.M.	Minerals in waste
MS	Silicium modulus
O.M.	Organics in waste
S	Silicon dioxide
SDGs	Sustainable Development Goals

References

1. Sustainable Development Goals: 17 goals to transform our world, United Nation, online: http://www.un.org/sustainabledevelopment/
2. Waste and the Sustainable Development Goals, WasteAidUk, online: https://wasteaid.org.uk/waste-sustainable-development-goals/
3. An initial view on methodologies for emission baselines: cement case study, the Organisation for Economic Co-operation and Development and the International Energy Agency (OECD), Reference: COM/ENV/EPOC/IEA/SLT(2001)2, online: https://www.oecd.org/env/cc/2390789.pdf

4. Parlikara U, Bundelab PS, Baidyac R, Ghoshd SK, Ghoshe SK (2016) Effect of variation in the chemical constituents of wastes on the co-processing, performance of the cement kilns. Procedia Environ Sci 35:506–512
5. Liu G, Zhan J, Zheng M, Li L, Li C, Jiang X, Wang M (2016) Distributions, profiles and formation mechanisms of polychlorinated naphthalenes in cement kilns co-processing municipal waste incinerator fly ash. Chemosphere 155:348–357
6. Jin R, Zhan J, Liu G, Zhao Y, Zheng M, Yang L, Wang M (2017) Profiles of polychlorinated biphenyls (PCBs) in cement kilns co-processing solid waste. Chemosphere 174:165–172
7. Zhao Y, Zhan J, Liu G, Ren Z, Zheng M, Jin R, Yang L, Wang M, Jiang X, Zhang X (2016) Field study and theoretical evidence for the profiles and underlying mechanisms of PCDD/F formation in cement kilns co-incinerating municipal solid waste and sewage sludge. Waste Manage https://doi.org/10.1016/j.wasman.2016.12.008
8. Baidya R, Ghosh SK, Parlikar UV (2016) Co-processing of industrial waste in cement kiln – a robust system for material and energy recovery. Procedia Environ Sci 31:309–317
9. Technical guidelines on the environmentally sound co-processing of hazardous wastes in cement kilns, Conference of the parties to the basel convention on the control of transboundary movements of hazardous wastes and their disposal, Tenth meeting, Basel Convention, United Nation, Cartagena, Colombia, 17–21 October 2011, Designed and printed by the Publishing Service, United Nations, Geneva — GE.12-01570 — October 2012 — 300 — UNEP/SBC/2012/6, online: http://www.basel.int/Portals/4/download.aspx?d=UNEP-CHW-WAST-GUID-CementKilns.English.pdf
10. Elimination des déchets dans les cimenteries (Directive), Office fédéral de l'environnement, des forêts et du paysage (OFEFP), L'environnement pratique, 2ème édition actualisée, Octobre 2005, Référence: VU-3002-F
11. Manual of Pollution Prevention in the Cement Industry, Regional Activity Centre for Cleaner Production (CP/RAC), Mediterranean Action Plan. Published in May 2008, online: www.cprac.org/docs/cemento_ang.pdf
12. "CECIL", An 80 hour training program (courseware) conceived by Mourad Zellouf, Patrick Prevot and Régis Aubry, Designed for Cement Kiln Control (LAFARGE-COPPEE Company), Accessed in 2016, Lafarge Ciment Oggaz, Mascara, Algeria.
13. Mikulčić H, Jaromír Klemeš J, Vujanović M, Urbaniec K, Duić N (2016) Reducing greenhouse gasses emissions by fostering the deployment of alternative raw materials and energy sources in the cleaner cement manufacturing process. J Clean Prod 136., Part B:119–132
14. Tsiliyannis CA (2016) Cement manufacturing using alternative fuels: enhanced productivity and environmental compliance via oxygen enrichment. Energy 113(15):1202–1218
15. Van Oss HG (2005) Background facts and issues concerning cement and cement data, U.S. Geological Survey Open File 2005–1152. Accessed 18 Jan 2006. Online: http://minerals.usgs.gov/minerals/pubs/commodity/cement
16. Guidelines for Co-Processing Fuels and Raw Materials in Cement Manufacturing, World Business Council for Sustainable Development (WBCSD), Cement Sustainability Initiative (CSI), Version 2.0 (2014), ISBN: 978-2-940521-19-7
17. Rapport complémentaire à l'étude d'impact sur l'environnement de la coincinération de déchets au sein du four de la cimenterie Lafarge, Centre National des Technologies de Production plus Propre (CNTPP), Site: Oggaz, Mascara, Septembre 2014, Référence projet client: 17/CE/2014, Référence projet CNTPP: 0342
18. Environmental Impact Assessment and Hazard Study for the Coprocessing of wastes for the Lafarge Cement Plant (Lafarge Ciment Oggaz), Studies realized by: Business Relations and Consulting Company (B.R.C.C), June 2016

Chapter 30
PPI4Waste Project: Current Practice and New Trends in Waste Management Sector

Bojan Ribić, Robert Kostić, Anne Dominique Furphy, and Lorenzo Chacon Ladron de Guevara

30.1 Introduction

The PPI4Waste (Public Procurement of Innovation for Waste) project aims to achieve resource efficiency, sustainable waste management and sustainable consumption throughout Europe by increasing innovative public procurement through networking, capacity building and dissemination. The project covers the complete cycle of preparation activities to implementation of PPI in urban waste management. The project is based on an integrated approach which defines needs, goals and improvement opportunities of functional performances. This project will complete the cycle of preparation activities and will test the feasibility and implementation of PPI processes in urban waste management. It will also make procedural knowledge of innovation procurement widely available. This can be accomplished through the establishment of a purchasing community, accessibility of state-of-the-art solutions to a considerable number of procurers, capacity building and a feasibility assessment for the uptake of PPI in the waste sector.

The state-of-the-art in waste management will facilitate the identification of innovative solutions with high potential for PPI process. It acts as a complementary step after the definition of common needs which was previously identified from the waste public sector in Europe. The project will set the ground for PPI preparation in the urban waste management field. This analysis is the main objective of this paper, where emerged common needs are described in the EU context. It will also help in determining potentially available solutions to be shared and discussed through

B. Ribić (✉) · R. Kostić
Zagreb City Holding, Department of Projects and International Cooperation, Zagreb, Croatia
e-mail: bojan.ribic@zgh.hr

A. D. Furphy · L. C. L. de Guevara
Andalusian Institute of Technology, Sevilla, Spain

S. Nižetić, A. Papadopoulos (eds.), *The Role of Exergy in Energy and the Environment*, Green Energy and Technology,
https://doi.org/10.1007/978-3-319-89845-2_30

market dialogue with the offer side. The purpose of this paper is to give an overall picture of the state of waste management in the European Union, in line with common needs identified. In this case it is biowaste and plastic waste management. Although geographically close to each other, the countries in the EU differ significantly from each other regarding the waste management and the implementation of innovative solution in this sector. The amount of municipal waste generated varies significantly across member states, and applied waste management models vary substantially among member states. One of the main consequences of this is that waste management innovation can be understood in different ways among member states and even among regions; while one solution can be innovative in one region, it may be non-innovative in another region.

In this project, a broader definition of innovation has been used, as adopted by the OECD. There is a clear recognition that innovation encompasses a wide range of activities in addition to research and development. As stated, innovation is defined as the implementation of a new or significantly improved product (good or service) or process, a new marketing method or a new organizational method in business practices, workplace organization or external relations. Innovation, thus defined, is clearly a much broader notion and is therefore influenced by a wide range of factors, some of which can be influenced by policy drivers, for example, and can occur in any step of the waste management chain. The PPI4Waste approach in the project implies that innovation performance differs from one country to another and includes not only transformative innovation but also incremental innovation to existing practices. This is so that it considers a wide spectrum of options and is as comprehensive as possible.

30.1.1 Municipal Waste Management in Europe

As mentioned before, the current situation in municipal waste management in Europe varies significantly between member states [10]. In fact there are broad differences regarding waste production, collection models and treatment techniques applied as well as regarding the implementation of European directives on waste. The waste hierarchy set by Waste Framework Directive constitutes the general European's approach for waste management by member states in order to boost recycling and reduce the use of resources. According to Eurostat in 2013, 43% of municipal solid waste was recycled, while 31% of waste was landfilled, and the rest (26%) was incinerated.

Even though recycling practices have been increasing each year, as shown in Fig. 30.1, and in general terms recycling is preferred over other practices, landfilling is still a widely used choice in waste management. Figure 30.2 gives an insight into the different situation of European countries regarding the evolution in the implementation of the waste hierarchy.

In Europe, municipal waste management can be performed through different models, depending on if the responsibility of the waste management is public,

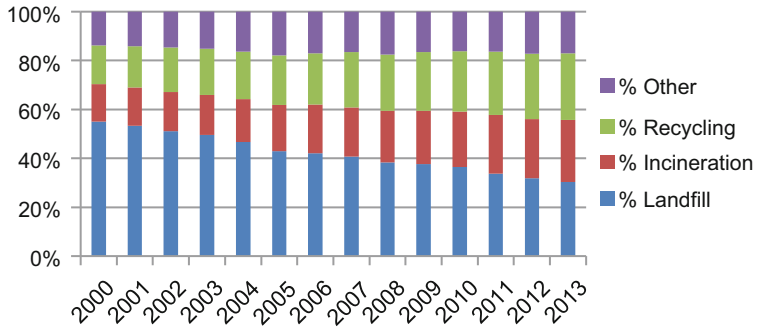

Fig. 30.1 Development of municipal waste management in 27 European countries, 2000–2013 [16–19]

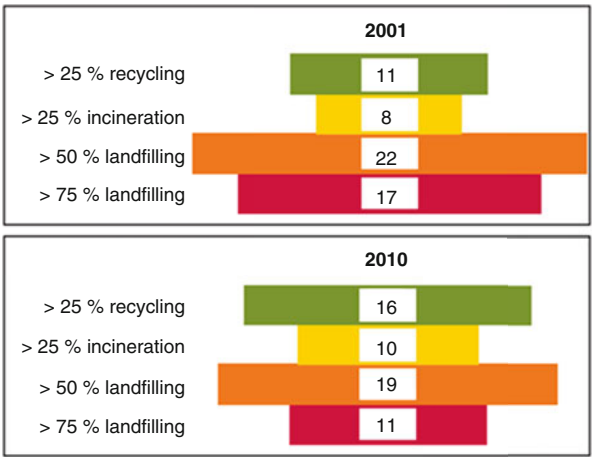

Fig. 30.2 Number of countries at different levels of the municipal waste management hierarchy, 2001 and 2010 [14]

private or shared in some cases. Public service is often responsible for the municipal waste management. In this case municipalities must create and maintain an effective system for managing their waste, including collection, transport, treatment and disposal, which can be carried out either by themselves or through contracts with the private sector. Normally, the treatment is granted to a private waste manager, while collection and transport are carried out by Swedish Environment Research Institute [2]. In the majority of member states, waste management is public, although some tasks are shared with private companies, as presented in Table 30.1.

30.1.2 Waste Collection Schemes

In Europe, there are different collection schemes depending on the degree of source separation of recyclable fraction. For instance, dry recyclables can be collected

Table 30.1 Overview of the waste management sector in EU

Country	Treatment responsibility	Collection and transport responsibility
Austria	Public	Public
Belgium	Public	Public
Denmark	Public/private	Public/private
Finland	Public	Public
Germany	Public	Public/private
Hungary	Public/private	Public
Ireland	Private	Private
Italy	Public	Public
Lithuania	Public	Public
Norway	Public	Public
Poland	Public	Public
Portugal	Public	Public
Spain	Public	Public
Sweden	Public	Public
Netherlands	Public/private	Public/private

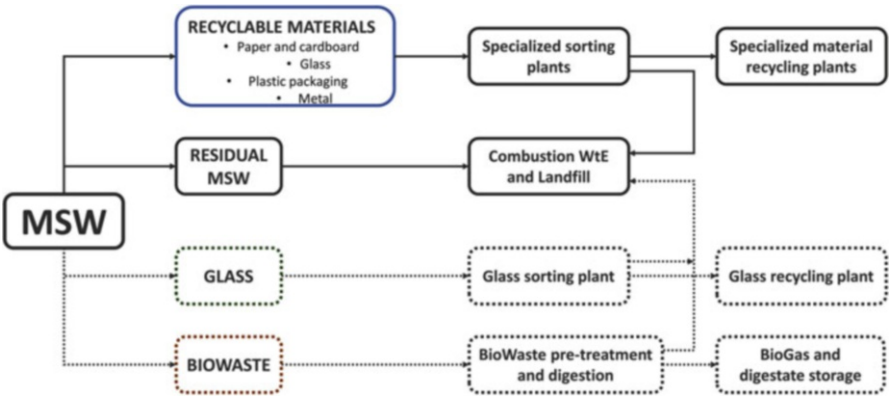

Fig. 30.3 Multi-material collection scheme. Single-stream

together and separate from residual waste, or completely separated in mono-material streams, or even mixed in the residual waste stream. On the other hand, biowaste can also be collected separately from dry recyclables and residual waste. But in general terms, there are four systems for recyclables mainly applied in member states [3]. Bulky waste usually is not collected through conventional systems due to their size. In some parts of Europe like Spain, these wastes are collected separately by local services several times a year, but in other cases, the only way of collecting is in civic amenity sites. For this reason, bulky waste is not included in these systems [4]. Below, a brief description and outline of each system is presented (Fig. 30.3).

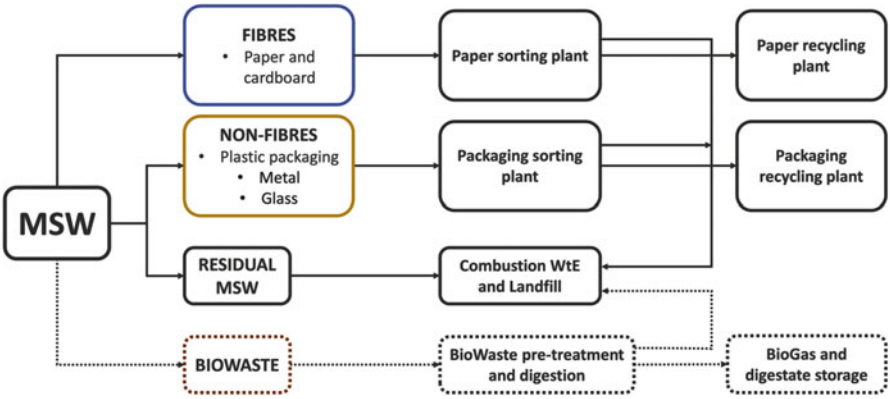

Fig. 30.4 Multi-material collection scheme (dual-stream)

- Single-stream collection system: all dry recyclables (plastic, metal, glass and paper and cardboard) are collected together into a single stream. Some alternatives can include glass and/or biowaste collected separately. At national level, this is the primary applied collection system in Greece, while in Ireland, the system includes the separate collection of biowaste, and in Malta and Romania, glass is collected separately.
- Dual-stream collection system: dry recyclables are collected in two different streams; paper and cardboard are collected separately, and the other recyclables, plastic, metal and glass, are collected commingled in one stream. Other options which include separate collection for biowaste are possible.

  Dual-stream is the collection mainly applied in the United Kingdom, where plastic and cardboard are collected in one bin and glass, plastic and metal are collected commingled in a different bin, apart from the residual waste stream. In this case, separate collection of biowaste is also applied (Figs. 30.4, 30.5, and 30.6).
- Mixed packaging waste collection system: a source separation is carried out in order to normally obtain a separate stream for each recyclable fraction, one stream for paper and cardboard, one for glass and one for lightweight packaging which includes plastic and metal packaging waste. Biowaste fraction can also be collected separately. After collection, each stream is treated in material recovery facilities, and the residual waste is usually treated in mechanical biological treatment plants. This collection system is applied in most member states, either with separately collected biowaste (Belgium, Germany, Luxemburg, Hungary, Italy and Slovenia) or together with residual waste stream (Bulgaria, Croatia, Cyprus, France, Lithuania, Poland, Portugal and Spain).
- Recovery from residual/mixed stream system: all or some of the recyclable fractions have no separate collection and are collected commingled with the residual fraction, which means that recyclable materials may be present in

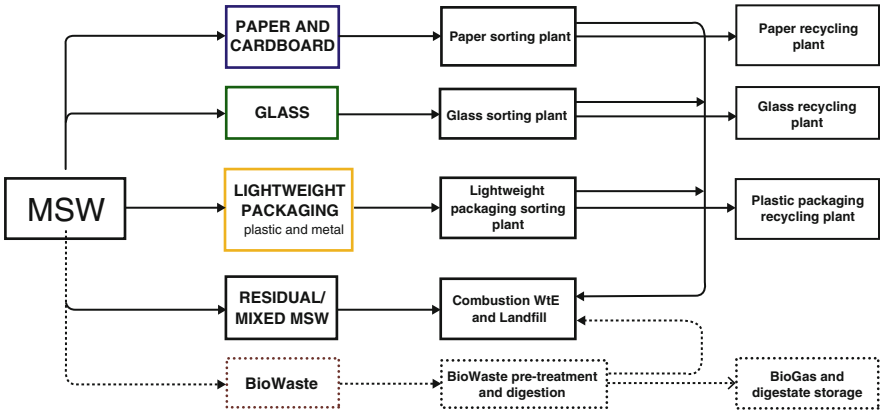

Fig. 30.5 Mono-stream collection system

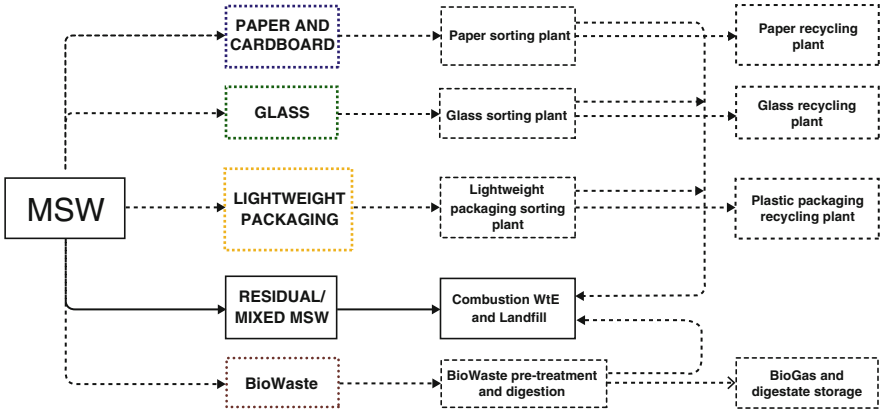

Fig. 30.6 Mixed MSW collection scheme

significant quantities in residual or mixed waste stream. This presence of recyclable materials may be due to the poor performance of selective collection system employees or simply due to the lack of a separate collection system. This collection scheme allows material recovery to be carried out in a relatively inexpensive way, although these materials are highly contaminated and need intensive further treatment in the material recovery facilities, as presented by Plastic ZERO [28].

Apart from these four systems, another way for separately collecting municipal solid waste is a completely segregated collection of dry recyclables and biowaste, in which each recyclable fraction, paper and cardboard, glass, plastic, metal and biowaste, is collected in separate streams.

The primary collection system applied in each member state is the collection system with which most inhabitants are connected to, but this is not necessarily the only system implemented in one country, and not all regions of a member state has to be connected to that system. In fact, the collection systems vary widely, not only between countries but also between municipalities, because normally, local authorities are responsible for the choice and implementation of waste collection system [12, 13]. In this sense, EC has carried out an analysis about collection systems applied by both countries and capitals [12, 13]. In some cases, the system applied in the capital has little differences with the primary system applied at national level, but in other, the system is completely different. In some member states such as Bulgaria and Croatia, where the mixed packaging waste collection is the primary system applied, there are little differences in the system applied in their capitals. Mixed packaging waste collection also is the primary system in France, Lithuania and Poland; however, the systems applied in their capitals are completely different. In Paris, dry recyclables are collected commingled except glass, through the single-stream collection system, and although there is not a separate collection for biowaste, in some regions there are composters where citizens can bring their biowaste. In the capital of Poland, Warsaw, dry recyclables and biowaste are also collected by the single-stream collection system, and in Vilnius, dry recyclables are collected completely segregated.

30.1.3 Separate Collection Systems

The implementation of these three models is carried out through different collection systems: curb side collection, door-to-door collection or bring systems [6].

- Curb side collection system. In this system, bins are placed on the sidewalk, outside buildings, so residents can deposit their waste in them. In countries such as Austria, France, Germany or the United Kingdom, among others, curb side system is the most common collection system, and specifically there are several European municipalities where selective collection is done exclusively through that system, such as Capannori (IT), Limerick (IE), Lisbon (PT) or Verdu (Spain) [32].
- In door-to-door collection, the waste is also deposited by residents into bins located on the sidewalk. This system is almost identical to curb side system with the difference that for apartments, door-to-door means that residents put their waste bags outside their door and a collection service is responsible for depositing them in containers on the sidewalk.
- Bring systems are a common way to collect municipal solid waste in some countries such as Norway or Denmark, for instance [3]. This system permits that citizens bring their segregated waste in drop off collection points placed at the neighbourhood level or at household waste and recycling centres [31] (Fig. 30.7).

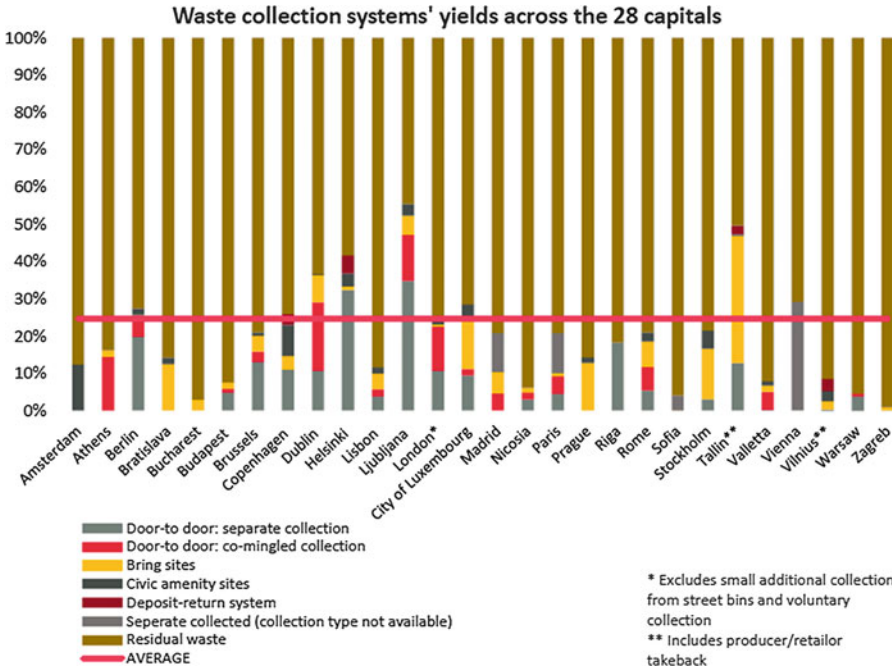

Fig. 30.7 Implementation percentage of collection systems [12, 13]

30.2 Biowaste and Plastic Waste Management

This paper addressed the main needs of public bodies in charge of municipal waste management identified within PPI4Waste project. Two of these needs are related with specific waste streams, biowaste management and plastic separation. In order to contextualize these needs in the framework of European policies on waste, this paper has been structured to focus on the specific waste streams while transversal needs are generally addressed within them. In essence, this structure is expected to provide a practical overview of how innovation can support public bodies to face challenges in municipal waste management.

30.2.1 Biowaste

According to the Waste Framework Directive, biowaste include biodegradable garden and park waste, food and kitchen waste from households, restaurants, caterers and retail premises and comparable waste from food processing plants. That doesn't include other biodegradable wastes such as paper, cardboard, wood or sewage sludge. Within biowaste two main streams of waste are identified [10]:

- Green waste: waste from parks, gardens, etc. That waste content is usually 50–60% of water and has high composition of lignocellulose materials.
- The so-called kitchen waste. That waste content is up to 80% of water and has a low quantity of lignocellulose materials.

Biowaste collection and treatment was identified in the PPI4Waste project as of the main areas of needs for public buyers in charge of municipal waste management. Biowaste collection was identified as an area where public buyers expect to invest funding in short and medium terms focused mainly on to set up separate collection systems. Biowaste treatment was identified as needs area for several reasons:

- Increase biowaste treatment capacity in current facilities.
- Improve the performance of current solutions applied, as anaerobic digester.
- Set up new facilities for appropriate treatment of biowaste coming from expected separate biowaste collection systems.

According to these needs, PPI4Waste project put the focus in biowaste management for the so-called kitchen waste, which according to European Commission is more often collected and treated as part of the mixed municipal solid waste [10].

30.2.2 Plastics

Sorting and plastic separation is one of the common needs identified within the PPI4Waste project in order to increase the material recovery rate and to obtain good quality products. Certain purity is necessary to use plastic waste as a recyclable material and optimize the result of recycling (COM (2013) 123 final); hence, it is not only necessary to separate plastics from other waste streams but also to sort different types of plastic. Due to these needs, source separation and separate collection systems, as well as waste management systems which involve separation techniques in material recovery facilities (MRFs), are essential to improve material recovery.

The need to improve plastic waste separation is increased because of the large amount of plastic waste generated each year by different consumer plastic sectors in the European Union [5, 8]. It is estimated that in 2014 almost 26 Mt of plastic waste were generated [27].

The construction sector is the second largest consumer of plastic in Europe, but, although its consumption is around 21% per year, it only generates 6% of the total plastic waste per year, because the durability of the plastic products used in construction causes them to last between 30 and 40 years. In other plastic-consuming sectors, the degree of plastic waste generation is similar. In particular, agriculture, waste electrical and electronic equipment (WEEE) and the automotive industry in Europe generate, respectively, around 3%, 7% and 5% of the total plastic waste generated each year [21]. However, plastic waste generation from these areas is increasing at a slower rate than plastic packaging waste, which represents the majority of the total plastic waste generated in Europe [1], with share of 63%.

This is because a significant amount of plastics packaging are single-use products with a short lifespan. In essence, the packaging sector contributes 73% to the generation of plastics wastes from households [7].

30.3 General Trends in Innovation Solutions

30.3.1 Trends in Separate Collection of Biowaste

Some member states have already implemented biowaste separate collection, but the countries that collect commingled biowaste are carrying out pilot experiences and pilot projects to implement a separate collection and to develop and establish a biowaste collection policy. The separate collection of biowaste is necessary to increase the rate of recovered material as well as the quality of recovered material, which will determine subsequent recycling and the use of the obtained products [15]. One of the main aspects that mark the management of biowaste is that the establishment of management models that are economically, socially and environmentally sustainable strongly depends on various local conditions, such as the distribution of production, the composition, the climate and the potential use of products obtained from biowaste treatment: methane, compost, electricity, heat, etc. Because of this, innovative solutions have been developed for the treatment of biowaste adapted to local conditions, and tools have been developed to support decision-making, allowing for the implementation of adequate management systems. To coincide with this, in 2011, the European Commission published the guide [22] that aims to support decision-making in the management of biowaste under the approach of life-cycle thinking and life-cycle assessment. In terms of management models, there is a tendency towards the development of centralized or decentralized models according to local characteristics, such as the distribution of producers, the existence of infrastructure or the availability of other organic wastes that can be jointly treated.

30.3.2 Trends in Plastic Waste Management

The Circular Economy Package [12, 13] proposes to modify the European directives related to waste management, in particular regarding the recycling targets. The future discussion and possible approval of new targets and other measures by the European Parliament and the Council of the EU will have an influence on national and local policies in terms of plastic separation and collection. The circular economy package proposes to amend the Directive 1994/62/EC on packaging and packaging waste, by tightening some of the quantitative targets.

- In Article 6, it is proposed that the minimum recycling target is raised to 65% of total packaging waste, to be reached by the end of 2025, with a minimum of 55% for plastic packaging waste in particular.
- The same article proposes that the total packaging waste recycling reaches a minimum of 75% by 2030.

On the other hand, the circular economy package proposes to amend the Directive 2008/98/EC by establishing new incentives and introducing new recycling targets.

- In Article 11, it is proposed that the minimum target for preparing for reuse and recycling is increased to 60% of the weight of municipal waste by 2025 and to 65% by 2030.

In the current directive on packaging and packaging waste, under Article 6, energy recovery was encouraged as preferable option to waste management when it is a more profitable option, both economically and environmentally than the material recycling. This article sets minimum percentages for energy recovery higher than that of recycling, which member states must comply by the end of 2008. However, energy recovery is no longer the focus on the new proposed directive. The proposed directive only sets new targets for recycling and adds a new article, Article 6a, paragraph 2 (b). According to this article, a percentage of packaging waste that has not been subjected to a recycling process and that is subject to energy recovery or landfilled can be included as recycled on the calculation of the attainment of targets laid down, provided that the percentage is below 10%. Plastic materials continuously cause environmental problems throughout their life cycle, not only during the production phase, in which greenhouse gases are generated, but also during the waste management phase. In 2015, although part of plastic waste was recycled or incinerated with energy recovery, it is estimated that 50% of plastic waste was still landfilled [30] causing a considerable accumulation of plastic waste in the environment.

On the other hand, improved separation and sorting systems paired with the recycling rate would reduce the consumption of renewable and non-renewable natural resources for industrial production. Furthermore, greenhouse gas emissions are also reduced, since the energy consumption involved in the production of virgin materials is much greater than consumption derived from the production of raw materials from recycled materials ([14](2)). Furthermore, recycling is considered one of the best waste management systems in reducing CO_2 emissions. Approximately 1.45 tonnes of CO_2 can be saved per each tonne of recycled plastic [21]. Additionally, it is necessary to take into account the relatively recent emergence of bioplastics. In EU, for instance, bioplastics are mainly used in the packaging industry and waste collection bags [7]. Furthermore, the bioplastics market increased by about 10% in 2009 in Europe, and it is estimated that their consumption will increase annually by 20% [7]. Although biodegradable plastics can be a potential solution to the problem of managing packaging waste, they also can complicate the management of waste because currently waste treatment systems are not able to separate effectively enough bioplastics from petroleum-based plastics (COM (2013) 123 final).

The economic success of plastic waste recycling depends heavily on an effective separation of waste streams [23] as well as the classification of different types of waste. At the same time, this separation should be done quickly and affordably, meaning the benefits of the recycled product should exceed the costs of the recycling process. Many plastic wastes are recoverable and recyclable in the majority of cases, which means their life cycle can be extended and they would become raw materials, allowing them to return to the industrial and commercial cycle [24, 25]. If the different types of polymers are clean and well separated, this would reduce consumption and therefore reduce costs not only of raw materials but also of energy and water resources that are necessary for the production of any product [29]. As recycling produces economic benefits such as reduced production costs [9, 11], it is particularly important to improve waste management systems as well as waste separation and sorting techniques as tools for increasing the recycling rate. Another important benefit of improving collection and separation systems is the increased efficiency of both processes that reduce their costs [20]. Also, the innovation in plastic separation reduces the amount of plastic waste landfilled and incinerated, thus decreasing the landfill taxes and the incineration fees [9, 11].

In order to comply with policy targets, different industrial organizations have been created in all member states to manage the municipal packaging waste, although in Austria, Finland, Ireland, the Netherlands and Italy, these organizations are responsible for packaging waste management both municipally and industrially. The Green Dot System was the first packaging waste management system implemented in Europe whose aim was developing schemes to coordinate the collection, sorting and recycling of plastic packaging waste. However, the licence of the Green Dot System was ceded to a European organization, allowing member states to transfer the responsibility for waste management to this organization [33].

Different strategies for the management of plastic packaging waste are used that depend on varying degrees of the source separation of different recyclables, but all systems have a common point which is the effort and collaboration of citizens to sort their waste in some way. Plastic packaging waste can be completely source-sorted or can be separated of MSW into a fraction which contains other mixed recyclable waste. Specifically, the household plastic packaging waste can be collected in three different ways [9, 11]:

- Mono-material collection, where plastic waste is collected alone in a separate stream from other recyclables
- Multi-material collection, where plastic waste is collected as part of a recyclable stream which contains other types of recyclables, normally commingled with metal in a lightweight packaging stream
- Mixed municipal solid waste collection, where plastic waste is collected commingled with MSW

The current status regarding collection systems as well as collection and sorting responsibility of a group of member states is presented in Table 30.2.

Table 30.2 Packaging waste collection by country

Country	Collection and sorting	Collection system	Collection scheme
Austria	ARA	Door-to-door	Mono-material
Belgium	Fost Plus	Door-to-door	Multi-material (with metal)
Denmark	Private operator	Door-to-door	Mono-material
Finland	PYR	–	–
France	Eco-Emballages	Door-to-door	Multi-material (with metal)
Germany	Duales System Deutschland, GmbH	–	–
Ireland	Repak	Door-to-door	Multi-material (with metal)
Italy	CONAI	Door-to-door	Multi-material (with metal)
Luxembourg	Valorlux	Door-to-door	Multi-material (with metal)
Netherlands	Nedvang	Door-to-door	Mono-material
Portugal	Ponto Verde	Bring points	Mono-material
Spain	Ecoembes	Bring points	Multi-material (with metal)
Sweden	FTI	Bring points	Mono-material
United Kingdom	Valpak	Door-to-door	Multi-material (with metal)

Sources: www.pro-e.org; [12, 13]

After collection, the plastic packaging waste stream or lightweight packaging waste stream is sorted in material recovery facilities, where plastic packaging waste is separated from other waste and then sorted further by polymer type.

The typical sorting process in Europe is comprised of three sorting steps, although there is no general way of designing the sorting process [26, 28]. The first step is an initial material sorting in which different types of materials such as metals are removed from the plastic packaging waste stream. In this stage, a manual sorting is carried out first to remove elements that may damage the process. After the manual sorting, an NIR sorter separates plastic waste which is then treated in a ballistic separator, a magnetic separator then removes metal waste. In the second step, plastic is washed and dried in order to clean and remove any impurities before a polymer sorting takes place by optical or density separators. Finally, different types of polymers are purified and subjected to quality control in the post-sorting stage.

30.4 Conclusions

Different EU legislations address the issue of sustainable biowaste and plastic waste management, with a priority to have high human and environmental protection standards during the whole waste management process.

Separate collection will divert waste streams from landfill and have positive impact also on overall employment. This is a step towards more sustainable waste management as it allows waste recovery and recycling, as well as the preservation of the natural resources. Many member states have already implemented waste management models that involve separate collection for different recyclable fractions in order to improve the quality of recycling. Although there are several ways to collect biowaste and plastic waste, the costs associated with this type of collection are usually higher.

For the collection of biowaste and plastic waste, separate bin is the most common option, although some member states use coloured bags for separating packaging waste or multi-compartment bins for the separation of different fractions of recyclables, including packaging waste. As an alternative, in some member states, there is a tendency towards a collection of plastic mixed with metal, mainly through door-to-door systems. This collection system is a good way to achieve a balance between the costs associated with management and the quality of the separated fractions, therefore improving the subsequent recycling.

Another important stage in a waste management system is the separation and sorting in material recovery facilities, which strives to achieve a high degree of separation. Therefore, many of the technological advances in the field of waste management have focused on improving the process as well as the techniques and equipment involved in this stage, developing it into an increasingly automated process.

Having all this in mind, an efficient management system as innovative solution is required in order to achieve new goals set by current and upcoming EU directives, especially for biowaste and plastic waste. This has to be developed as a waste collection service in order to optimize current waste management. Collaboration and interaction between citizens, municipalities and municipal waste management services will permit a well-organized waste management system that increases separate collection and recycling efficiency.

Acknowledgements The authors would like to acknowledge the PPI4Waste project for its financial support. This project has received funding from the European Union's Horizon 2020 research and innovation programme under grant agreement No 642451.

Any communication activity related to the action must indicate that it reflects only the author's view and that the Commission is not responsible for any use that may be made of the information it contains.

References

1. Al-Salem S, Lettieri P, Baeyens J (2009) Recycling and recovery routes of plastic solid waste (PSW): a review. Waste Manag 29:2625–2643
2. Avfall Sverige (2015) Swedish waste management. [Online] Available at: http://www.avfallsverige.se/fileadmin/uploads/Rapporter/SWM_2015.pdf

3. Cimpan C et al (2015) Central sorting and recovery of MSW recyclable materials: a review of technological state-of-the-art, cases, practice and implications for materials recycling. J Environ Manag 156:181–199
4. Clarke E, Bridgwater E (2012) Composition of kerbside and HWRC bulky waste. [Online] Available at: http://www.wrap.org.uk/content/study-re-use-potential-household-bulky-waste
5. CORDIS (European Commission) (2013) BURBA report summary. [Online] Available at: http://cordis.europa.eu/result/rcn/54291_en.html
6. Dahlén L, Lagerkvist A (2010) Pay as toy throw. Strengths and weaknesses of weight-based billing in household waste collection systems in Sweden. Waste Manag 30:23–31
7. DG Environment (2011) Plastic waste in the environment. [Online] Available at: http://ec.europa.eu/environment/waste/studies/pdf/plastics.pdf
8. European Commission (2013) Green paper: on a European strategy on plastic waste in the environment. [Online] Available at: http://eur-lex.europa.eu/legal-content/EN/TXT/?uri=CELEX:52013DC0123
9. European Commission (2014) End-of-waste criteria for waste plastic for conversion. [Online] Available at: http://susproc.jrc.ec.europa.eu/activities/waste/documents/2014-JRC91637_ed2015.pdf
10. European Commission, Directive 2008/98/EC of the European Parliament and of the Council of 19 November 2008 on waste and repealing certain Directives
11. European Commission (2014) Waste as a resource. [Online] Available at: http://bookshop.europa.eu/en/eu-research-pbKI0313591/
12. European Commission (2015) Assessment of separate collection schemes in the 28 capitals of the EU [Online] Avaliable at: http://bookshop.europa.eu/en/assessment-of-separate-collection-schemes-in-the-28-capitals-of-the-eu-pbKH0215939/
13. European Commission (2015) Circular economy package. [Online] Avaliable at: https://ec.europa.eu/commission/priorities/jobs-growth-and-investment/towards-circular-economy_en
14. European Environmental Agency (2013) Managing municipal solid waste – a review of achievements in 32 European countries. [Online] Available at: http://www.eea.europa.eu/publications/managing-municipal-solid-waste
15. Eurostat (2012) Guidance on municipal waste data collection. [Online] Available at: http://ec.europa.eu/eurostat/documents/342366/351811/Municipal-waste-statistics-guidance.pdf
16. Eurostat (2015) Packaging waste statistics. [Online] Available at: http://ec.europa.eu/eurostat/statistics-explained/index.php/Packaging_waste_statistics
17. Eurostat (2015) Waste statistics – electrical and electronic equipment. [Online] Available at: http://ec.europa.eu/eurostat/statistics-explained/index.php/Waste_statistics_-_electrical_and_electronic_equipment
18. Eurostat (2015) Municipal waste statistics. [Online] Available at: http://ec.europa.eu/eurostat/statistics-explained/index.php/Municipal_waste_statistics
19. Eurostat (2015) Waste statistics. [Online] Available at: http://ec.europa.eu/eurostat/statistics-explained/index.php/Waste_statistics
20. Hestin M, Faninger T, Milios L (2015) Increased EU plastics recycling targets: environmental, economic and social impact assessment. [Online] Available at: http://www.plasticsrecyclers.eu/environmental-economic-social-impact-assessment-increased-plastic-recycling
21. Hopewell J, Dvorak R, Kosior E (2009) Plastic recycling: challenges and opportunities. Philos Trans R Soc 364:2115–2126
22. EC, JRC (2011) Supporting environmentally sound decisions for biowaste management
23. Luijsterburg B, Goossens H (2014) Assessment of plastic packaging waste: material origin, methods, properties. Resour Conserv Recycl 85:88–97
24. OECD report: innovation in firms: a microeconomic perspective. [Online] Avaliable at: http://www.oecd.org/berlin/44120491.pdf
25. OECD (2014) Waste management services. [Online] Available at: http://www.oecd.org/daf/competition/Waste-management-services-2013.pdf

26. Plastic Zero (2014) Survey on existing technologies and methods for plastic waste sorting and collection. [Online] Available at: http://www.plastic-zero.com/media/20355/action_3.1_collection_and_sorting_technologies_-_final_july_2012.pdf
27. Plastics Recyclers Europe (2013) Plastics Recyclers Europe. [Online] Available at: http://plasticsrecyclers.eu/enstudy-increased-mechanical-recycling-target-plasticspdf
28. Plastic Zero (2013) Report on initial assessment of relevant recycling technologies. [Online] Available at: http://www.plastic-zero.com/media/39275/Plastic%20technologies%20catalouge%202.1%20-%20130902%20-%20rev.pdf
29. Sevigné-Itoiz E, Gasol CM, Rieradevall J, Gabarrell X (2015) Contribution of plastic waste recovery to greenhouse gas (GHG) savings in Spain. Waste Manag 46:557–567
30. Wong S, Ngadi N, Abdullah T, Inuwa I (2015) Current state and future prospects of plastic waste as source of fuel: a review. Renew Sust Energ Rev 50:1167–1180
31. WRAP (2009) Choosing the right recycling collection system. [Online] Available at: http://www.wrap.org.uk/sites/files/wrap/Choosing%20the%20right%20recycling%20collection%20system.pdf
32. Xevgenos D et al (2015) Success stories for recycling of MSW at municipal level: a review. Waste Biomass Valor 6:657–687
33. Zero Waste (n.d.) Handbook: on alternative waste management schemes. [Online] Available at: http://www.med-zerowaste.eu/deliverables/handbook.pdf

Chapter 31
Kinetic Model Development and Bi-objective Optimization of Levulinic Acid Production from Sugarcane Bagasse

Aramide Adesina and David Lokhat

31.1 Introduction

The emergence of lignocellulosic biomass as the best replacement feedstock for production of fuels and chemical products from fossil has continuously attracted interest because they are renewable, they do not impact on the supply of food for humans and they are environmentally friendly. Consequently, researchers [3–5, 10] have proposed different processes for producing target chemicals and fuels. One of such target chemicals is levulinic acid. Levulinic acid, LA (4-oxopentanoic acid), is an important intermediate molecule and a precursor to the production of several chemicals such as gamma-valerolactone [1], butenes and pentanoic acid [8], furfural [9], butanone [14] and methyltetrahydrofuran [17].

Levulinic acid is produced by the acid-catalysed hydrolysis of biomass. An example of a sustainable biomass used is lignocellulosic biomass. When lignocellulosic biomass is catalytically hydrolysed, its cellulose, hemicellulose and lignin constituents are degraded. The cellulose fraction is degraded to glucose oligomers and monomers and further hydrolysed to 5-hydroxymethylfurfural (5-HMF) and then further to LA and formic acid (FA). The hemicellulose fraction is degraded to pentose (C5) and hexose (C6) sugars. The hexose sugars in the hemicellulose fraction are hydrolysed to levulinic and formic acids, while the pentose oligomers and monomers are further degraded to furfural. Depending on the target products, furfural formed from the pentose monomer can also be converted to LA [13]. However, the furfural needs to be separated out of the aqueous solution because reaction conditions that favour the rehydration of 5-HMF to LA and FA also favour the formation of insoluble humins.

A. Adesina (✉) · D. Lokhat
School of Engineering, University of Kwazulu-Natal, Durban, South Africa
e-mail: 214584716@stu.ukzn.ac.za

S. Nižetić, A. Papadopoulos (eds.), *The Role of Exergy in Energy and the Environment*, Green Energy and Technology,
https://doi.org/10.1007/978-3-319-89845-2_31

The conversion process of biomass to renewable fuels and chemicals is faced with challenges which are different from that of petroleum refining [16]. This is as a result of the selective increase in the energy density of biomass feedstock when fuels are the target product and the decrease in the energy density when chemicals are the target product [18]. These challenges include the formation of reactive intermediates which could be the target product or a precursor to other products and the co-formation of unwanted reaction products from competing side reactions. Hence, controlling the yield and selectivity of the reaction becomes a challenge. Specifically, for the production of LA from lignocellulosic biomass, process challenges include the selective production of LA at high yield as well as the formation of unwanted degradation products called humins.

Humins, at times referred to as humic [6], are soluble or insoluble degradation products formed during the acid-catalysed hydrolysis of lignocellulosic biomass. Humins are formed from the condensation reaction of 5-HMF with itself or polyoxygenates [15]. They impact on the subsequent biorefinery processes and they need to be separated from the hydrolysis products before the next downstream stage. These additional purification steps increase the overall cost of production. Hence, there is the need to maximize the selectivity towards LA during the transformation of lignocellulosic biomass.

The interwoven relationship between the operating conditions for optimum production of LA further explains the importance of selectively converting lignocellulosic biomass to LA. While long reaction time is needed for complete degradation, high temperature reactions at extended reaction times lead to degradation to unwanted inhibitory products [15]. At too low temperatures and acid concentrations, yield of LA becomes low due to degradation proceeding at a slow rate. Also, if the concentration is too high, degradation proceeds too quickly, and inherent metal leaching and future corrosion of reactor vessels take place [15].

Therefore, a thorough understanding of the reactions involved in the production of LA, the side reactions to the formation of unwanted humins and the dependence of these rate reactions on important reaction conditions (temperature and acid concentration) are vital to the choice of process conditions and successful design of the hydrolysis process. This study, therefore, aims to simultaneously determine process conditions for optimal yield and selectivity to LA. This involves the development of a more rigorous kinetic model describing the acid-catalysed hydrolysis of lignocellulosic biomass, the determination of kinetic parameters using already published data of Girisuta et al. [12], the development of models for yield and selectivity using the determined kinetic parameters and the final determination of reaction conditions required for optimum yield and selectivity to LA using the desirability function approach for multi-response optimization.

31.1.1 State of the Art

Although, several researches have focused on the kinetic model development and optimization of the acid-catalysed hydrolysis of biomass feeds to different platform molecules, little kinetic studies have been carried out on the acid-catalysed hydrolysis of biomass to LA (Table 31.1). The first kinetic study on biomass hydrolysis to LA was carried out by Girisuta et al. [11], who studied the acid-catalysed hydrolysis of water hyacinth to LA at varying temperatures of 150–175 °C, sulphuric acid concentration of 0.1–1.0 M and initial water hyacinth intake of 1–5 wt%. Kinetic models were developed by the application of a correction factor to the initial results obtained from the kinetic studies of the hydrolysis of pure feeds of cellulose, glucose and HMF to LA. The kinetic parameters of the adopted pure feeds were given by the modified Arrhenius relationship:

Table 31.1 Overview of kinetic studies of acid-catalysed hydrolysis of lignocellulosic biomass

Biomass source (conc.)	Kinetic parameters	Temperature	Acid (conc.)	Ref.
Miscanthus × *giganteus*	K_1 ($A_0 = 4.25e12$, $E_1 = 107.9$, $m_1 = 1.22$) K_3 ($A_0 = 1.32e19$, $E_3 = 167.9$, $m_3 = 1.23$) K_4 ($A_0 = 3.31e20$, $E_4 = 179.3$, $m_4 = 0.75$) K_5 ($A_0 = 3.33e11$, $E_5 = 105.7$, $m_5 = 1.54$)	(150–200) °C	(0.1–0.53) M H_2SO_4	[9]
Sugarcane bagasse	K_1 ($A_0 = 1.59e18$, $E_1 = 144.85$, $m_1 = 1.57$) K_3 (A0 = 6.56e18, $E_3 = 152$, $m_3 = 1.14$) K_4 (A0 = 6.94e19, $E_4 = 161.41$, $m_4 = 1.08$) K_5 (A0 = 2.71e14, $E_5 = 101.63$, $m_5 = 1.32$)	(150–200) °C	(0.11–0.55) M H_2SO_4	[12]
Wheat straw (16:1 solid-to-liquid ratio)	K_1 (A0 = 1.488e10, $E_1 = 78.66$, $m = 1.434$) K_3 (A0 = 1.502e5, $E_3 = 54.51$, $m = 0.268$) K_4 (A0 = 1.430e7, $E_4 = 61.06$, $m = 0.679$ K_5 (A0 = 1.425e7, $E_5 = 56.47$, $m = 0.804$) K_6 (A0 = 2.425e6, $E_6 = 51.37$, $m = 0.620$)	(190–230) °C	1–5% by mass H_2SO_4	[6]
Water hyacinth (1–5 wt %)	$R_1 = 0.410R_{cel\text{-}Glc}$ $R_2 = 0.714R_{cel\text{-}Hum}$ $R_3 = R_{Glc\text{-}HMF}$ $R_4 = R_{Glc\text{-}Hum}$ $R_5 = R_{HMF\text{-}LA}$	(150–175) °C	(0.1–1.0) M H_2SO_4	[11]

$$k_i = k_{Ri}(C_{H^+})^{\propto_i} \exp\left[\frac{E_i}{R}\left(\frac{T-T_R}{T_R T}\right)\right] \tag{31.1}$$

where k_i is the rate constant, k_{Ri} is the frequency factor, $\propto_i$ is the acid reaction order, C_{H^+} is the concentration of the acid, E_i is the activation energy, T is the temperature and T_R is the reference temperature. However, a full understanding of the temperature dependence of the hydrolysis reaction of water hyacinth is unclear as the exact values of the kinetic parameters (acid reaction order, Arrhenius constant and activation energy) for water hyacinth are still unknown.

Further kinetic studies have been carried out on the acid-catalysed hydrolysis of biomass to LA using wheat straw [6], sugar cane bagasse [12] and *Miscanthus* × *giganteus* [9]. Chang et al. [6] developed kinetic models using simple first-order rate equations to describe the sulphuric acid-catalysed hydrolysis of wheat straw in a batch reactor at an acid concentration of 1–5%, over a temperature range of 190–230 °C and pressure of 10 MPa. However, the determination of the rate of formation of humins and information on the optimum process conditions are lacking. Hence, the kinetics given cannot adequately describe conditions for optimum selectivity for the design of the process.

Girisuta et al. [12] also developed kinetic models using pseudo-first-order equations and determined process conditions required for optimum yield of LA by hydrolysing sugarcane bagasse to LA over a temperature range of 150–200 °C and acid concentration of 0.11–0.55 M in a batch reactor. At temperature 150 °C and 0.55 M sulphuric acid concentration, high LA yield (63%) was obtained. However, detailed rate expression on the formation of humins is lacking as a result of assumptions taken during kinetic model development. This might explain the great disparity in the optimum yield obtained from the kinetic model (53%) and that obtained from the experiments (63%). Furthermore, the determined optimum reaction conditions at high LA yield are not optimum conditions that will selectively produce LA from sugarcane bagasse.

Dussan et al. [9] also applied the kinetic models developed by Girisuta et al. [12] to determine the kinetic parameters for the sulphuric acid hydrolysis of *Miscanthus* × *giganteus* at 150–200 °C and acid concentration of 0.1–0.5 M in a batch reactor. The highest yield of LA (80%) was obtained at 150 °C and 0.5 M H_2SO_4 in a plug flow reactor configuration. However, a single-response optimization is not efficient to determine reaction conditions for simultaneous optimum responses of yield and selectivity towards LA because the responses are related.

31.2 Kinetic Modelling

Figure 31.1 shows the mechanism for the hydrolysis of sugarcane bagasse to levulinic acid and formic acid based on the following assumptions:

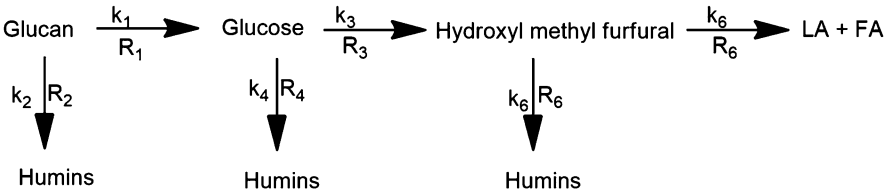

Fig. 31.1 Simplified schematic of the kinetic reaction

1. The reaction rates were assumed to be pseudo-first-order reactions. This is because the concentration of sulphuric acid is in excess of the concentration of sugarcane bagasse.
2. Only the glucan component of biomass is converted to LA. This is because the composition of galactan and arabinose in the sugarcane bagasse is negligible. Hence, the kinetic parameters of the model will have its wide application to pretreated lignocellulosic biomass since the hemicellulose fraction is dissolved in solution during pretreatment making glucan the only rich source of LA production. The reaction proceeds by:

   - The cleavage of the 1-4 glycosidic bonds linking the glucan units to glucose
   - Side decomposition of glucan to humins in a parallel way
   - Dehydration of glucose to HMF
   - Parallel decomposition of glucose to humins
   - Hydrolysis of HMF to LA and formic acid
   - Parallel decomposition of HMF to humins

The temperature dependence of the rate constants K_i is expressed using the modified Arrhenius equation as

$$K_i = k_{0i}[C_{H^+}]_0^{q_i} e^{-\frac{E_i}{RT}} \tag{31.2}$$

The change in concentration of glucan in biomass cellulose with time is given as

$$\frac{d[C]}{dt} = -k_1[C] - \ k_2[C] \tag{31.3}$$

For an initial concentration of cellulose$[C]_0$, the final concentration at time t is given as

$$[C] = [C]_0 e^{-(k_1 + \ k_2)t} \tag{31.4}$$

The change in concentration of glucose with time is given as

$$\frac{d[G]}{dt} = K_1[C] - K_3[G] - K_4[G] \tag{31.5}$$

$$[G] = \frac{k_1 C_0}{(k_3 + k_4) - (k_1 + k_2)} \left(e^{-(k_1 + k_2 t)} - e^{-(k_3 + k_4 t)} \right) \tag{31.6}$$

The change in concentration of HMF with time is given as

$$\frac{d[HMF]}{dt} = K_3[G] - K_5[HMF] - K_6[HMF] \tag{31.7}$$

$$\begin{aligned}[HMF] = {} & \frac{k_1 k_3 C_0}{\{(k_3 + k_4) - (k_1 + k_2)\}\{(k_5 + k_6) - (k_1 + k_2)\}} e^{-(k_1 + k_2)t} \\ & + \frac{k_1 k_3 C_0}{\{(k_1 + k_2) - (k_3 + k_4)\}\{(k_5 + k_6) - (k_3 + k_4)\}} e^{-(k_3 + k_4)t} \\ & + \frac{k_1 k_3 C_0}{\{(k_1 + k_2) - (k_5 + k_6)\}\{(k_3 + k_4) - (k_5 + k_6)\}} e^{-(k_5 + k_6)t}\end{aligned} \tag{31.8}$$

The rate of formation of LA and FA is given as

$$\frac{d[L]}{dt} = \frac{d[F]}{dt} = k_5[HMF] \tag{31.9}$$

$$\begin{aligned}r_1 = {} & \frac{k_5 k_1 k_3 C_0}{\{(k_3 + k_4) - (k_1 + k_2)\}\{(k_5 + k_6) - (k_1 + k_2)\}} e^{-(k_1 + k_2)t} \\ & + \frac{k_5 k_1 k_3 C_0}{\{(k_1 + k_2) - (k_3 + k_4)\}\{(k_5 + k_6) - (k_3 + k_4)\}} e^{-(k_3 + k_4)t} \\ & + \frac{k_5 k_1 k_3 C_0}{\{(k_1 + k_2) - (k_5 + k_6)\}\{(k_3 + k_4) - (k_5 + k_6)\}} e^{-(k_5 + k_6)t}\end{aligned} \tag{31.10}$$

The concentration of levulinic acid at time t is give as

$$\begin{aligned}[LA] = {} & {}^{1}/_{(k_1 + k_2)} \left[\frac{k_5 k_1 k_3 C_0}{\{(k_3 + k_4) - (k_1 + k_2)\}\{(k_5 + k_6) - (k_1 + k_2)\}} \right. \\ & \left. - \frac{k_5 k_1 k_3 C_0}{\{(k_3 + k_4) - (k_1 + k_2)\}\{(k_5 + k_6) - (k_1 + k_2)\}} e^{-(k_1 + k_2)t} \right] \\ & + {}^{1}/_{(k_3 + k_4)} \left[\frac{k_5 k_1 k_3 C_0}{\{(k_1 + k_2) - (k_3 + k_4)\}\{(k_5 + k_6) - (k_3 + k_4)\}} \right. \\ & \left. - \frac{k_5 k_1 k_3 C_0}{\{(k_1 + k_2) - (k_3 + k_4)\}\{(k_5 + k_6) - (k_3 + k_4)\}} e^{-(k_3 + k_4)t} \right] \\ & + {}^{1}/_{(k_5 + k_6)} \left[\frac{k_5 k_1 k_3 C_0}{\{(k_1 + k_2) - (k_5 + k_6)\}\{(k_3 + k_4) - (k_5 + k_6)\}} \right. \\ & \left. - \frac{k_5 k_1 k_3 C_0}{\{(k_1 + k_2) - (k_5 + k_6)\}\{(k_3 + k_4) - (k_5 + k_6)\}} e^{-(k_5 + k_6)t} \right]\end{aligned} \tag{31.11}$$

The rate of formation of humins from the side reactions is given as

$$\frac{d[HU]}{dt} = k_2[C] + k_4[G] + k_6[HMF] \tag{31.12}$$

$$\begin{aligned} r_2 = \quad & k_2 C_0 e^{-(k_1+k_2t)} + \left[\frac{k_4 k_1 C_0}{(k_1+k_2)-(k_3+k_4)} e^{-(k_3+k_4t)}\right. \\ & \left. + \frac{k_4 k_1 C_0}{(k_3+k_4)-(k_1+k_2)} e^{-(k_1+k_2t)}\right] \\ & + \left[\frac{k_6 k_1 k_3 C_0}{\{(k_3+k_4)-(k_1+k_2)\}\{(k_5+k_6)-(k_1+k_2)\}} e^{-(k_1+k_2)t}\right. \\ & + \frac{k_6 k_1 k_3 C_0}{\{(k_1+k_2)-(k_3+k_4)\}\{(k_5+k_6)-(k_3+k_4)\}} e^{-(k_3+k_4)t} \\ & \left. + \frac{k_6 k_1 k_3 C_0}{\{(k_1+k_2)-(k_5+k_6)\}\{(k_3+k_4)-(k_5+k_6)\}} e^{-(k_5+k_6)t}\right] \end{aligned} \tag{31.13}$$

The rate constants for each of the six reactions were expressed in the form of the modified Arrhenius relationship) (Eq. 31.2), making a total of 18 kinetic parameters to be determined from 120 literature data sets. The kinetic parameters were determined by non-linear least squares minimization of errors between the predicted concentration of products and experimental data from literature using solver tool in excel.

$$\sum_{i=1}^{k}\sum_{j=1}^{n}\left[\left(C_{i,j}\right)_{\text{cal}} - \left(C_{i,j}\right)_{lit}\right]^2 \quad i = \text{Glucose, LA, HMF}$$
$$j = \text{no of experimetal data points} \tag{31.14}$$

31.2.1 Application of the Models

The kinetic models developed can be used to gain insight into the effect of process variables on the yield, conversion and selectivity of the process and hence optimize the yield and selectivity. Process conditions from the simultaneous optimization of yield and selectivity can also be determined through multi-objective optimization. For this purpose, the yield is defined as:

$$Y_i = \frac{C_i}{[C]_0} \tag{31.15}$$

where

$$[C]_0 = \frac{\text{mass of sugarcane bagasse} \times \text{wt\%of glucan in biomass}}{\textit{molecular weight of glucan} \times \textit{volume of reaction mixture}} \tag{31.16}$$

and the molecular weight of glucan = 116.117 g/ml.

For a batch reactor setup, combining Eqs. 31.11 and 31.16 gives the yield of LA.

The selectivity S, towards LA production, is

$$S = \frac{r_1}{r_1 + r_2} \tag{31.17}$$

and the reactor conversion as

$$X = \frac{[C]}{C_0} \tag{31.18}$$

31.3 Approach for Single-Response Optimization

It is essential to carry out single-response optimization of the yield and selectivity in order to determine boundary conditions required for the multi-response optimization. It is supposed that the simultaneous responses as well as the variables will lie within this region. The Nelder-Mead simplex algorithm is used to carry out the independent optimization of each of the objective functions. This is given as

$$\begin{aligned} &\text{maximize}_{X \in \Omega} F1(\boldsymbol{X}) = {F_1}^{\mathrm{U}}(X^*), \text{at this optimum point } F_2(X^*) = {F_1}^{\mathrm{L}}(X^*) \\ &\text{maximize}_{X \in \Omega} F2(\boldsymbol{X}) = {F_2}^{\mathrm{U}}(X^*), \text{at this optimum point } F_2(X^*) = {F_2}^{\mathrm{L}}(X^*) \end{aligned} \tag{31.19}$$

31.4 Technique for Multi-response Optimization

In this paper, multi-response optimization was performed to determine the optimal acid concentration, temperature and time required for simultaneous maximum yield of LA and selectivity to LA. The approach is different from the single-response optimization because both of the single-objective functions are merged into a single-objective function f(X) so that conditions that maximizes yield will equally maximize the selectivity. The desirability approach of multi-response optimization is the technique proposed to be used for solving this problem. The desirability approach was developed by Derringer and Suich [7] and involves converting each response y_i into an individual desirability function d_i which ranges between 0 and 1. For $d_i = 0$, this implies the response is outside the acceptable region, and for $d_i = 1$, the response

is at its target T. The design variable which fits into these acceptable ranges is then used to maximize the overall desirability D where there are m responses. It also follows that the overall desirability will be equal to zero if both or any of the individual responses is undesirable. The structure of the desirability function is as follows:

If the objective function is to be maximized or larger-the-best response,

$$d = \begin{cases} 0 & y < L \\ \left(\frac{y-L}{y-T}\right)^w & L \leq y \leq T \\ 1 & y > T \end{cases}$$

where L and U are the lower and upper boundaries and w is the weight assigned to each desirability function to show the relative importance of the individual objective functions. If the objective function is to be minimized or smaller-the-best response,

$$d = \begin{cases} 0 & y < T \\ \left(\frac{U-y}{U-T}\right)^w & T \leq y \leq U \\ 1 & y > U \end{cases}$$

If the target lie within the lower and upper boundaries or nominal-the-best response,

$$d = \begin{cases} 0 & y < L \\ \left(\frac{y-L}{y-T}\right)^w & L \leq y \leq T \\ \left(\frac{U-y}{U-T}\right)^w & T \leq y \leq U \\ 0 & y > T \end{cases} \tag{31.20}$$

The design variables are then used to maximize the overall desirability, D, given as

$$D = (d_1 * d_2 * \ldots d_m)^{1/m} \tag{31.21}$$

31.4.1 Algorithm for Desirability Approach

Step 1 Develop independent response models for the yield (Eq. 31.15) and selectivity (Eq. 31.17) from the developed kinetic models.

Step 2 Determine values of the maximum and minimum responses of each objective functions using the Nelder-Mead simplex method of optimization. This was used to determine the boundary conditions (Eq. 31.19) and also to determine the target goal for the multi-response optimization. For this study there are two objective functions and hence termed a bi-objective optimization problem.

Step 3 Convert each response function to a desirability function using Eq. 31.20. For this study, the structure of the desirability function used is that of nominal-the-best (NTB) because the optimal values for yield and selectivity lie within the upper and lower boundaries.

Step 4 Maximize the overall desirability (Eq. 31.21) by maximizing the geometric mean of the two desirability functions obtained from the two objective functions. Steps 2–4 were carried out using fminsearch in MATLAB tool box.

31.5 Results and Discussion

31.5.1 Kinetic Modelling

Table 31.2 shows that the activation energy for the conversion of HMF to LA is the lowest (106.88 kJ/mol). This shows that the conversion of HMF to LA is more temperature sensitive than other reactions. Consequently, the rate constant for the reaction of HMF to LA is far higher than that of other reactions by about 30–5000 times. This is in good agreement with the work of Girisuta et al. [12], who stated that the rate of reaction of HMF to LA is 6–49-fold higher than other reactions. The rate of reaction of glucan to humins and HMF to humins are much lower than the rate of formation of glucose from glucan. This is also in agreement with earlier research [9] who neglected this reaction rate in the overall kinetics. However, the concentration of humins produced from R_2, R_4 and R_6 is about 5000 times more than when R_4 is considered as the only rate step to the formation of humins. This becomes necessary to be included in the design of the hydrolysis reaction so as not to negatively impact the next catalytic reaction in the biorefinery. This therefore shows the importance of this work in incorporating these side reactions to determine the optimum selectivity and yield.

The kinetic models were simulated using literature data [12] and showed a good fit with data (Fig. 31.2). The model was validated by carrying out residual plots (Figs. 31.3 and 31.4) of predicted concentration of levulinic acid, glucose and HMF against observed data. The model showed a good fit with data with a correlation

Table 31.2 Kinetic parameters for the acid-catalysed hydrolysis of sugarcane bagasse

K	$K_0(s^{-1})$	q_i	E_i (KJ/mol)
K_1	2.28E + 17	1.5	167.59
K_2	9.10E + 14	1.5	157.72
K_3	4.51E + 15	1.23	154.63
K_4	5.36E + 16	1.13	165.66
K_5	2.10E + 11	1.5	106.88
K_6	6.27E + 9	1.29	126.59

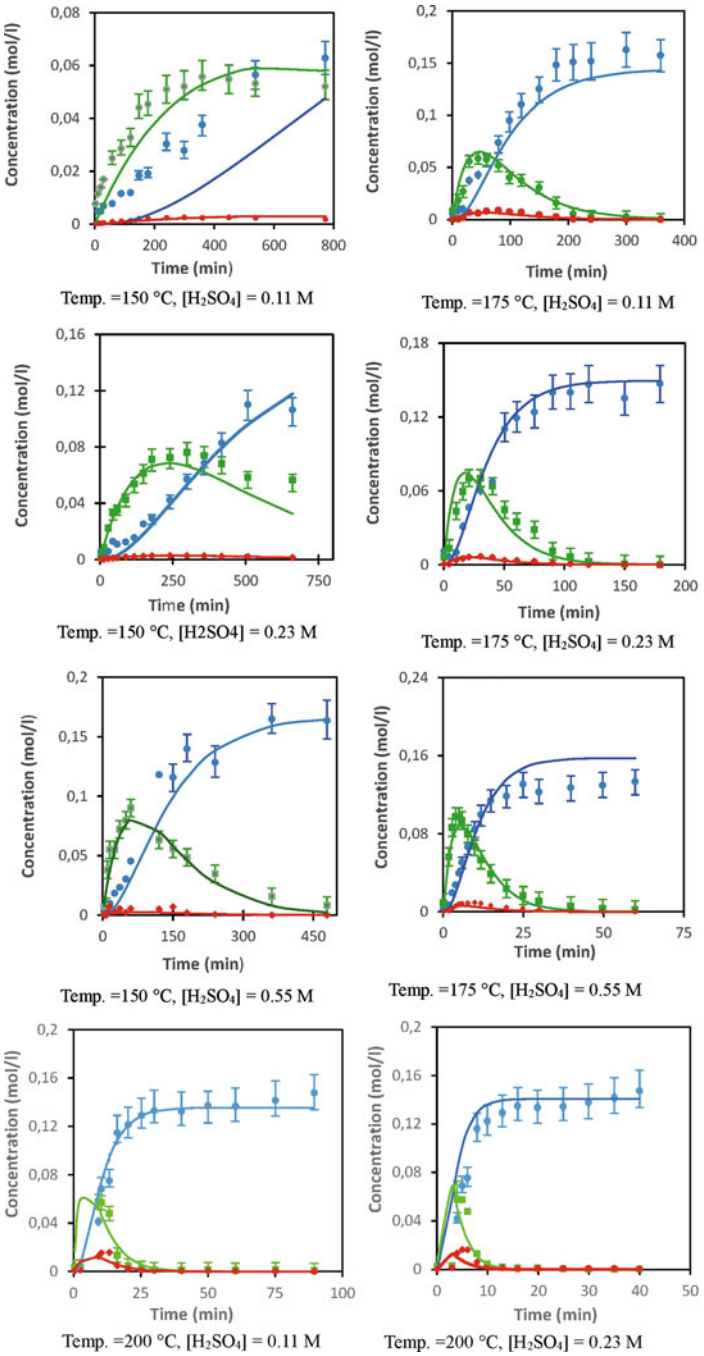

Fig. 31.2 Acid-catalysed hydrolysis of sugarcane bagasse to levulinic acid kinetic simulation results. Simulated kinetic models (lines) and literature data (markers); LA (blue dots), Glucose (green dots), HMF (red dots)

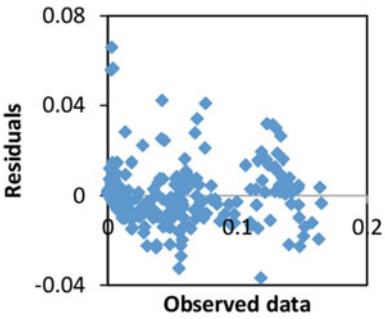

Fig. 31.3 Predicted concentration data residual plot

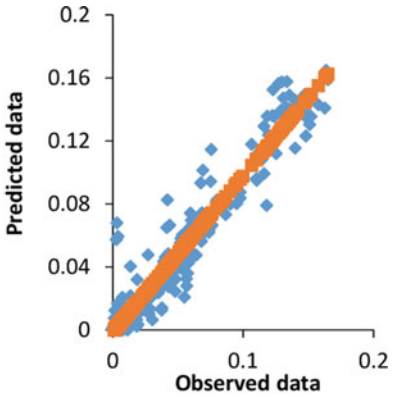

Fig. 31.4 Parity plot of simulated concentration of LA against literature data

coefficient of 0.944. The resulting kinetic parameters also show a correlation with existing results from literature (Table 31.1).

The models were used to optimize the yield and selectivity of LA independently by varying the acid concentration, temperature and reaction time. The optimum yield of LA obtained was 60.5634% (Fig. 31.5) at H_2SO_4 concentration of 0.54 mol/l over a reaction time of 771 min. This shows the model gave a good prediction of the experimental data in which the highest yield of LA obtained from experiment was 63%. This shows a better prediction than the initial work of Girisuta et al. [12] who obtained an optimum LA yield of 53% using their models. For single-objective optimization of selectivity, the selectivity was 64.3% (Fig. 31.6). However, at conditions that favoured the optimum selectivity, the yield of LA dropped to 60.56%. Although the drop in the value of the yield was low at optimum selectivity, a bi-objective optimization is necessary to determine the best compromise between the resulting Pareto points. This is in line with the work of Amin [2] who stated that a single-objective function is not sufficient to describe chemical processes because the variables that optimize the yield and selectivity are interwoven.

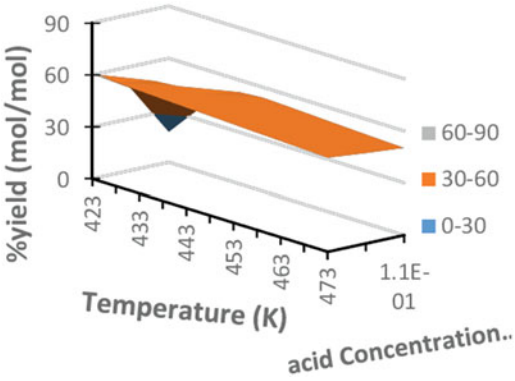

Fig. 31.5 Dependence of the LA yield on temperature and acid cone concentration

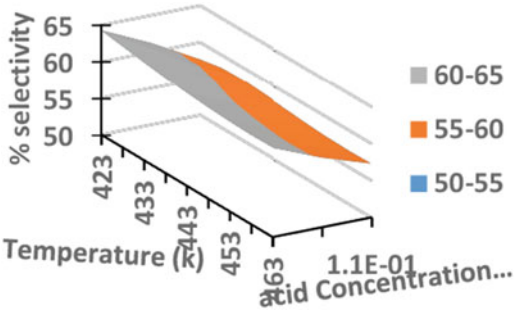

Fig. 31.6 Dependence of selectivity on temperature and acid cone concentration

Table 31.3 Results of the bi-objective optimization

D	Yield (%)	S (%)	Weight (w_1, w_2)	Process variables [conc. (mol/l), temp(K) and time (min)]
0	26.877	61.160	1,1	0.48, 422, 717
1	60.2	64	1,1	0.50, 423, 655
1	60.3	64	1,1	0.50, 423, 755

31.5.2 Bi-objective Optimization

The results from the bi-objective optimization (Table 31.3) show that taking a weight of 1 for both yield and selectivity to show their relative importance, the reaction conditions favoured both the yield (60.3%) and selectivity (64%) at time 655 mins. Although, the desirability D was the same for optimum point 2 (Table 31.3) at concentration 0.50 mol/l and temperature 423 K, the optimum responses were slightly different. There was an increase in reaction time, but the yield increased slightly for result 3 as against result 2. This further establishes the fact that acid concentration, reaction time and temperature have an interwoven relationship with

the yield and selectivity and, hence, must be controlled to prevent the formation of unwanted humin product. The result 1 in Table 31.3 was rejected because the desirability is 0.

31.6 Conclusions

A widely applicable rigorous kinetic model has been developed for the acid-catalysed hydrolysis of sugarcane bagasse to LA. Its application also involves pretreated biomass since glucan is the source of sugar producing LA. All possible pathways to humins were incorporated to gain insight into the selectivity of the reaction and also determine the process conditions that favour yield and selectivity towards the desired product using literature data carried out within the range of acid concentration 0.11–0.55 M and temperature 150–200 °C. Complex kinetic models were successfully used for the bi-objective optimization of biomass to levulinic acid. The highest yield and selectivity obtained from the bi-objective optimization were 60.3% and 64%, respectively. Hence, the models gave a good description of the process at specified operating conditions.

Nomenclature

C_0	Concentration of component i (mol/l)
$[C]_0$	Concentration of glucan in cellulose (mol/l)
$[G]$	Concentration of glucose (mol/l)
$[HMF]$	Concentration of HMF (mol/l)
$[Hu]$	Concentration of humins (mol/l)
$[C]_0$	Initial concentration of cellulose (mol/l)
$[H]_0$	Initial concentration of acid (mol/l)
$[t]$	Time (s)
$C_H{}^+$	Acid concentration (mol/l)
K_i	Rate constant of reaction i (reaction dependent)
K_1	Rate constant of reaction 1
K_2	Rate constant of reaction 2
K_3	Rate constant of reaction 3
K_4	Rate constant of reaction 4
K_5	Rate constant of reaction 5
K_6	Rate constant of reaction 6
k_{0i}	Arrhenius constant of reaction i
D	Desirability
E_i	Activation energy of reaction i (KJ/mol)
R	Universal gas constant
T	Reaction temperature (°C, K)
r_1	Rate of the main reaction ($moll^{-1}\ s^{-1}$)
r_2	Rate of formation of humins
S	Selectivity (dimensionless)

Y_i	Yield of product i (dimensionless)
C_i	Concentration of product i (mol/l)
q_i	Order of reaction of the acid (reaction dependent)
$F_1^U(X^*)$	Upper bound for response 1 (dimensionless)
$F_2^U(X^*)$	Upper bound for response 2 (dimensionless)
$F_1^L(X^*)$	Lower bound for response 1 (dimensionless)
$F_2^L(X^*)$	Lower bound for response 2 (dimensionless)
$F1(X)$	Response of function 1 (dimensionless)
$F2(X)$	Response of function 2 (dimensionless)
Ref	Reference

Acknowledgement This work was supported by the National Research Funding (NRF). Opinions expressed and conclusions arrived at are those of the authors and are not necessarily to be attributed to the NRF.

References

1. Alonso DM, Wettstein SG, Mellmer MA, Gurbuz EI, Dumesic JA (2013) Integrated conversion of hemicellulose and cellulose from lignocellulosic biomass. Energy Environ Sci 6:76–80
2. Amin NAS (2005) A hybrid numerical approach for multi-responses optimization of process parameters and catalyst compositions in CO 2 OCM process over CaO-MnO/CeO 2 catalyst. Chem Eng J 106:213–227
3. Antunes MM, Lima S, Neves P, Magalhães AL, Fazio E, Fernandes A, Neri F, Silva CM, Rocha SM, Ribeiro MF (2015) One-pot conversion of furfural to useful bio-products in the presence of a Sn, Al-containing zeolite beta catalyst prepared via post-synthesis routes. J Catal 329:522–537
4. Canilha L, Chandel AK, Suzane Dos Santos Milessi T, Antunes FAF, Luiz Da Costa Freitas W, Das Graças Almeida Felipe M, Da Silva SS (2012) Bioconversion of sugarcane biomass into ethanol: an overview about composition, pretreatment methods, detoxification of hydrolysates, enzymatic saccharification, and ethanol fermentation. J Biomed Biotechnol 2012:989572 doi: 10.1155/2012/989572
5. Chang C, Cen P, Ma X (2007) Levulinic acid production from wheat straw. Bioresour Technol 98:1448–1453
6. Chang C, Ma X, Cen P (2009) Kinetic studies on wheat straw hydrolysis to Levulinic acid. Chin J Chem Eng 17:835–839
7. Derringer G, Suich R (1980) Simultaneous optimization of several response variables. J Qual Technol 12:214–219
8. Dumesic, J. A., Alonso, D. M., Bond, J. Q., Wang, D. & West, R. M. (2013). Integrated process and apparatus to produce hydrocarbons from aqueous solutions of lactones, hydroxy-carboxylic acids, alkene-carboxylic acids, and/or alcohols. United States patent application 12/687,471,
9. Dussan K, Girisuta B, Haverty D, Leahy J, Hayes M (2013) Kinetics of levulinic acid and furfural production from Miscanthus× giganteus. Bioresour Technol 149:216–224
10. Gallo JMR, Alonso DM, Mellmer MA, Yeap JH, Wong HC, Dumesic JA (2013) Production of furfural from lignocellulosic biomass using beta zeolite and biomass-derived solvent. Top Catal 56:1775–1781
11. Girisuta B, Danon B, Manurung R, Janssen LPBM, Heeres HJ (2008) Experimental and kinetic modelling studies on the acid-catalysed hydrolysis of the water hyacinth plant to levulinic acid. Bioresour Technol 99:8367–8375

12. Girisuta B, Dussan K, Haverty D, Leahy J, Hayes M (2013) A kinetic study of acid catalysed hydrolysis of sugar cane bagasse to levulinic acid. Chem Eng J 217:61–70
13. Lange J-P, Van De Graaf WD, Haan RJ (2009) Conversion of Furfuryl alcohol into ethyl Levulinate using solid acid catalysts. ChemSusChem 2:437–441
14. Min K, Kim S, Yum T, Kim Y, Sang B-I, Um Y (2013) Conversion of levulinic acid to 2-butanone by acetoacetate decarboxylase from Clostridium acetobutylicum. Appl Microbiol Biotechnol 97:5627–5634
15. Raspolli Galletti AM, Antonetti C, Ribechini E, Colombini MP, Nassi O, Di Nasso N, Bonari E (2013) From giant reed to levulinic acid and gamma-valerolactone: A high yield catalytic route to valeric biofuels. Appl Energy 102:157–162
16. Tukacs JM, Novak M, Dibo G, Mika LT (2014) An improved catalytic system for the reduction of levulinic acid to [gamma]-valerolactone. Cat Sci Technol 4:2908–2912
17. Upare PP, Lee JM, Hwang YK, Hwang DW, Lee JH, Halligudi SB, Hwang JS, Chang JS (2011) Direct hydrocyclization of biomass-derived levulinic acid to 2-methyltetrahydrofuran over nanocomposite copper/silica catalysts. ChemSusChem 4:1749–1752
18. Vlachos DG, Chen JG, Gorte RJ, Huber GW, Tsapatsis M (2010) Catalysis Center for Energy Innovation for biomass processing: research strategies and goals. Catal Lett 140:77–84

Chapter 32
Biodiesel Production from Nonedible Oil Using Heterogeneous Solid Base Catalysts

Karim Khiari, Zakaria Bekkar Djelloul Sayah, Lyes Tarabet, Khaled Loubar, Rachid Mahmoud, and Mohand Tazerout

32.1 Introduction

The world economic and industrial growth, as well as the demographic rapid expansion, has led to an increase of the demand for energy. Currently, this request is satisfied mainly by resources with fossil origin [1, 2]. The production and the use of fossil energies generate the emission and the accumulation of gases with greenhouse effect (CO_2, SO_2, and NO_X), which are the principal causes of environmental pollution and climatic changes [3, 4]. To overcome these risks, it is imperative to direct the world power consumption toward new clean resources such as bioethanol and biofuels [5, 6]. The production of biofuels from food sources, biofuels of first generation, favors the rise in the foodstuffs prices. This contrariety and the interest to replace the fuels of fossil origin made it possible to reconsider the source of production of these biofuels and to focus the research toward a nonedible biomass [7]. Previous researches have shown that the most suitable technique to adapt the vegetable oil properties for diesel engine fuelling is the transesterification conversion process [7]. The use of biofuel prepared from nonedible vegetable oils is becoming a promising source to produce a fuel for diesel engine, commonly referred to as "biodiesel." Considering the high oil extraction yield (around 40%) and the great quantity of *Pistacia lentiscus* (PL) trees available in arid and semiarid areas of Mediterranean countries, it is selected in the present work to study the biodiesel prepared from PL oil.

In the present work, the vegetable oil of *Pistacia lentiscus* fruit is extracted, and the heterogeneous base-catalyzed transesterification is applied for producing a

K. Khiari (✉) · Z. Bekkar Djelloul Sayah · L. Tarabet · R. Mahmoud
Ecole Militaire Polytechnique, LGP, Algiers, Algeria

K. Loubar · M. Tazerout
IMT Atlantique, Systèmes Energétiques et Environnement, Nantes, France

S. Nižetić, A. Papadopoulos (eds.), *The Role of Exergy in Energy and the Environment*, Green Energy and Technology,
https://doi.org/10.1007/978-3-319-89845-2_32

biodiesel starting from a nonedible and abundant vegetable source in the Mediterranean Basin such as *Pistacia lentiscus* (PL). The catalysts are compared in terms of activities in the transesterification process under suitable conditions (reaction temperature of 50 °C, methanol to oil molar ratio of 12:1, catalyst loading of 1 wt.%, and reaction time of 2 h). For the two catalysts, a higher than 90% conversion is found. The most important physical and chemical properties of the obtained biodiesel are determined.

32.2 Experimental Facility

32.2.1 Raw Materials

The mature PL fruits are collected in mountains situated in the north of Algeria, in January. The oil is extracted with n-hexane in Soxhlet apparatus and 42% of yield is achieved. The KOH and ethanol are purchased from Sigma-Aldrich with a purity of 85% and 98%, respectively. The KF, CaO, and MgO are purchased from Proanalysis-Merck with a purity superior to 99%.

32.2.2 Analyses and Characterizations

The catalysts are characterized by using several techniques. The XRD measurements were performed on an XRD PANalytical X'Pert Pro powder diffraction using Cu-Kα radiation over a 2θ range of 0–61° with a step size of 0.06° at a scanning speed of 4°/min. The BET surface area and pore volume of the prepared catalysts were measured by using Quantachrome Nova 3200.

The fatty acid composition of PL biodiesel is determined using a gas chromatography GC Clarus 600 coupled to a PerkinElmer TurboMass Gold Mass Spectrometer and Flame Ionization Detect or using a PE-5MS column (30 m*0.25 mm*0.25 μm) with a split ratio of 1:100 and an injection volume of 1 μl. Column temperature is programmed from 160 to 220 °C at 1 °C/min. Helium is the carrier gas, and the injection and detector temperatures are 230 and 250 °C, respectively. Elemental composition analysis is performed using a CHNS-O Analyzer FLASH 1112 series E. The heating value is measured using a PARR 6200CLEF calorimeter. Viscosity and density are measured at different temperatures using a vibro viscometer SVM 3000/G2 and a densimeter DMA 4500, respectively. Pensky Martens NPM 440 apparatus with a precision of 2 °C is used to determine the flash point. Cetane number is determined using Era flash apparatus. Water content is measured using the Karl Fisher apparatus. Acid values are determined by titrimetry. Cloud and congelation points are measured by 70Xi analysis.

32.2.3 Methods of Catalysts Preparation

Concerning the adopted procedure, we chose the mechanical mixture where, we mixed 5 g each oxide (CaO and MgO) with a precise quantity of doping agent KF. It is advisable to notice that this quantity of the doping agent added during the preparation of catalysts is given starting from the orientations reported in the literature [8] chose a rate of loading of 50%, average of these two molar reports/ratios. In the same way for KF/MgO blend, where MgO is added up to 70% due to its highest catalytic activity as it is reported in Liang et al. work.

32.2.4 Biodiesel Preparation

To produce *Pistacia lentiscus* biodiesel for this study, a transesterification reaction has been carried out. Transesterification reaction is performed in a 250 ml batch reactor equipped with a reflux condenser and a magnetic stirrer.

PL oil is then added to the reaction tank in order to start the transesterification reaction. The reaction mixture (containing absolute ethanol of 96% purity, PL oil, and the catalyst (KOH)), with a molar ratio alcohol/oil of 6:1 and catalyst loading of 1 wt.%, is allowed to reflux at the alcohol boiling point. The mixture is agitated throughout 2 h at 50 °C. The stirring process is characterized by the mixture color modification from clear yellow to reddish yellow. At the end of the transesterification process, the mixture is poured into a separator funnel. Once the separation is operated, the glycerol is removed as a dark-brown-colored liquid from the bottom of the flask. Then, the PL biodiesel is washed to remove the remaining alcohol and catalyst in the biodiesel phase. The experimental setup for transesterification reaction is shown in Fig. 32.1.

32.3 Results and Discussions

The results obtained make it possible to release from the interesting conclusions; they are shown in Fig. 32.2 by diffractograms X-ray of the calcined/not calcined samples for both KF/CaO and KF/MgO systems.

Starting from the KF/CaO catalyst not calcined, it was observed the appearance of typical peaks allotted on the one hand to KF to $2\theta = 28.96$, 33.66, 48.30, and 57.75° (ICDD 00–04-0726) and on the other hand in CaO with $2\theta = 36.07$ and 54.46° (ICDD 00–001-1160), compound prevailing of catalyst. The sample contains other peaks allotted to various mineral phases, considered as impurities.

Fig. 32.1 Experimental setup for transesterification reaction

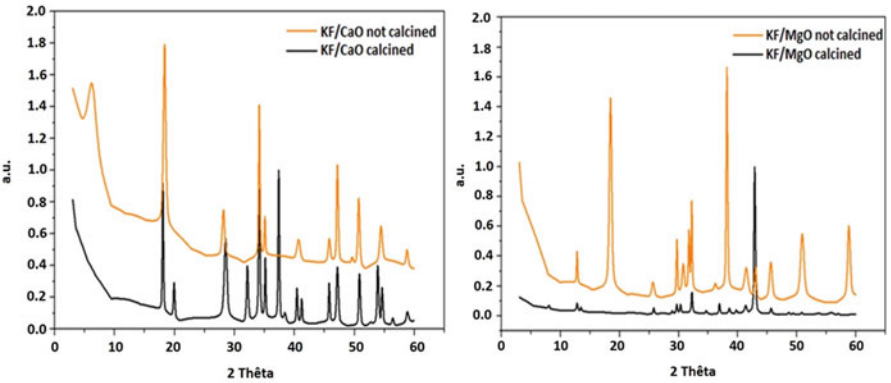

Fig. 32.2 XRD patterns of KF/CaO and KF/MgO not calcined and calcined

The comparison of the diffractograms obtained for calcined and not calcined catalysts shows the appearance of new peaks characteristic of $KCaF_3$ to $2\theta = 19.97$, 31.14, 36.9, 38.45, 41.27, and 56.37° (ICDD 00-003-0567).

After calcination, we observe a clear reduction in peaks characteristic of the elements considered as impurities, as it is the case with $2\theta = 18.20°$. It is interesting to also notice an intensification of peaks relating to KF and to CaO. In this context,

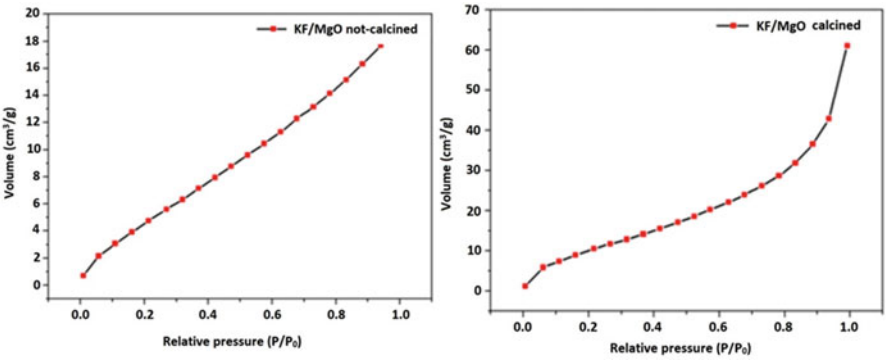

Fig. 32.3 Adsorption isotherm of KF/MgO not calcined and calcined

Liu et al. [9] report that $KCaF_3$ is probably formed at the time of the calcination according to the reaction (Eq. 32.1):

$$CaO + 3KF \rightarrow KCaF_3 + K_2O \tag{32.1}$$

In the case of the KF/MgO couple, the diffractogram resulting from the characterization of the KF/MgO catalyst not calcined shows the appearance of typical peaks allotted to KF with $2\theta = 29.06$, 33.32, and 58.15° (ICDD 00-04-0726) and in MgO with $2\theta = 37.10$ and 43.00° (ICDD 00-004-0829), major compound of catalyst. In the same way, the analyzed sample makes us distinguish from other peaks of various mineral phases being able to be impurities.

The intensity of the peaks obtained after calcination of the KF/MgO catalyst is less significant relative with the results obtained in the case of the KF/CaO system. This may be attributed to the rate of relatively high loading of KF/MgO; it is probable that the surface of the KF/MgO catalyst is covered with an excess of KF, making difficult the detection of the phases formed after calcination.

The exploitation of the isotherms obtained (Figs. 32.3 and 32.4) enabled us to estimate BET surface of the two studied samples. We also released a BET surface of 23.809 m^2/g in the case of KF/MgO not calcined and 43.69 m^2/g for calcined KF/MgO. The effect of the calcination is obvious and the heat treatment led to the increase in porous volume.

The adsorption isotherms obtained for KF/CaO, calcined and not calcined, are not identifiable with any types stated by the IUPAC (International Union of Pure and Applied Chemistry). They present negative values for the relative pressures and return of this impossible fact, the exploitation of these isotherms for a possible estimate of BET surface.

In order to supplement the analyses, structural and textural, of two catalysts considered, a topographic examination of the two catalysts, KF/MgO and KF/CaO, is carried out.

The pictures obtained by SEM (Figs. 32.5 and 32.6) for the two studied catalysts present, in an obvious way, rough reliefs and an absence of cavities.

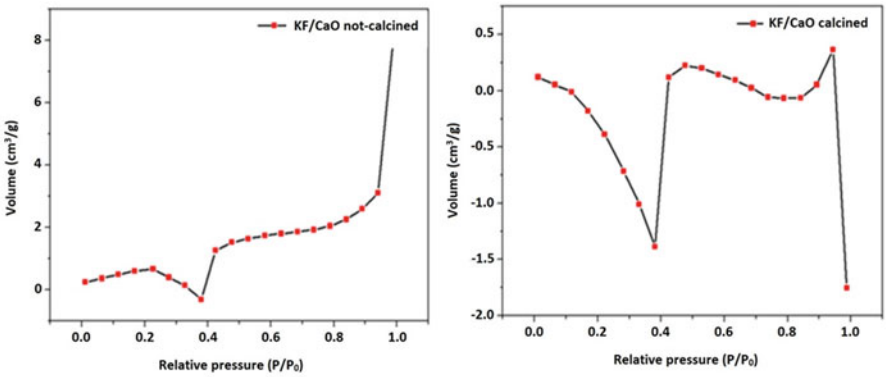

Fig. 32.4 Adsorption isotherm of KF/CaO not calcined and calcined

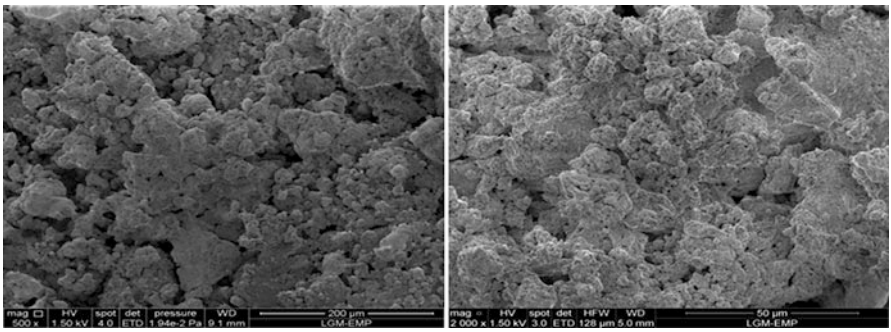

Fig. 32.5 SEM image of KF/MgO calcined: the scale bar corresponds to (**a**) 200 μm and (**b**) 50 μm

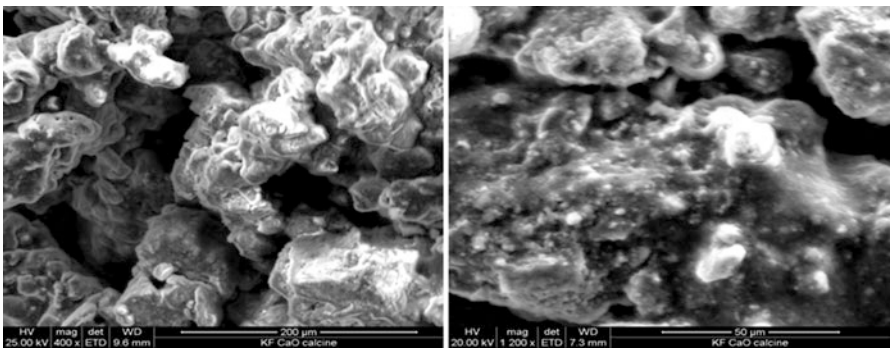

Fig. 32.6 SEM image of KF/CaO calcined: the scale bar corresponds to (**a**) 200 μm and (**b**) 50 μm

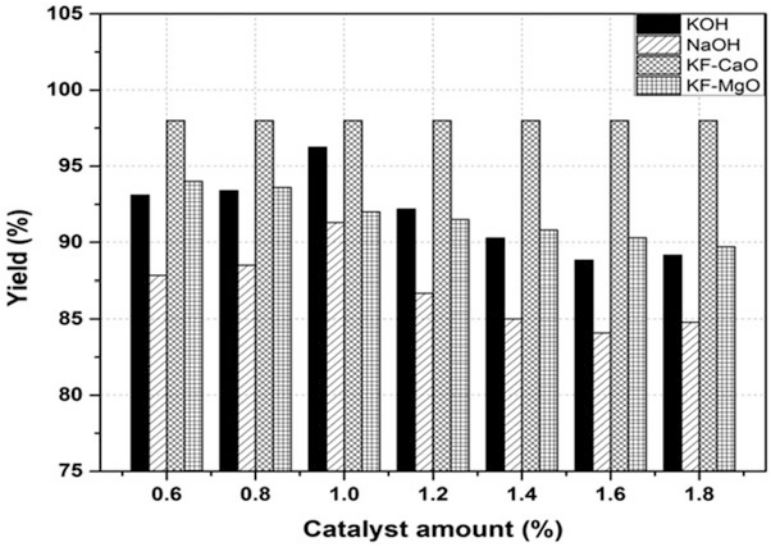

Fig. 32.7 Effect of the nature of the catalysts on the reaction yield

The KF/MgO system shows aggregates which tend to have a spherical form distributed, in an inhomogeneous way, on the whole of its surface. On the other hand, the KF/CaO system has a more compact surface quality with very irregular forms.

In order to compare between the efficiency of the prepared heterogeneous catalysts (KF/MgO, KF/CaO) and that of the commercialized homogeneous catalysts (KOH and NaOH), the four catalysts are used in the methanoic transesterification reaction with proportions ranging from 0.6% to 1.8% of the initial mass of the *Pistacia lentiscus* oil under the optimum operating conditions determined previously, i.e., a reaction temperature of 50 ° C, a molar ratio (oil/methanol) of (1:6), and a stirring speed of 300 rpm for 60 minutes.

Figure 32.7 shows the homogeneous and heterogeneous base catalysts effect on the conversion rate of *Pistacia lentiscus* oil to methyl esters.

For the two catalysts, a higher than 90% conversion is found (95.38% for KF/CaO and 90.75% for KF/MgO). These experimental results prove that the yield of methyl esters, in homogeneous catalysis, is higher using the KOH catalyst than NaOH. The optimum amount of catalyst for obtaining the highest biodiesel yield is 1% of the initial mass of the *Pistacia lentiscus* oil. This difference is due to the better reactivity of KOH compared to that of NaOH and its solubility in methanol.

For heterogeneous catalysis, it is noticed that the yield of the methanoic transesterification reaction catalyzed by KF/CaO is greater than that using KF/MgO. This result may be due to the catalytic nature which shows a difference in the loading rate of the two catalysts, 50% loaded CaO and 70% loaded MgO.

Table 32.1 Properties of diesel fuel and PL biodiesel

Properties	Units	Diesel	PL biodiesel	EN 14214
Density at 15 °C	kg/m^3	840	860	860–900
Kinematic viscosity at 40 °C	mm^2/s	3.2	3.44	3.5–5.0
Gross heating value	kJ/kg	45.00	40.00	–
Cetane number		49	53.94	51 min
Flash point	°C	55	168	101 min
Acid value	mg_{KOH}/g	–	0.187	0.5 max
Elementary composition				
Carbon content	(wt.%)	86	76.17	–
Hydrogen content	(wt.%)	14	13.93	–
Oxygen content	(wt.%)	0	9.90	–
Fatty acid composition				
Palmitic acid	(wt.%)	–	13.93	–
Oleic acid	(wt.%)	–	47.02	–
Linoleic acid	(wt.%)	–	29.56	–
Linolenic acid	(wt.%)	–	4.85	–

A low loading rate does not allow enough active sites to be created. On the other hand, if the alkaline earth oxide is loaded in excess, KF will be poorly dispersed on the surface of the oxide, and this may lead to active sites saturation as well as the compromise of reactive-catalyst interaction.

This result is consistent with the results already obtained in this field, such as in the case of Wan's work [10].

The principal properties of PL biodiesel determined according to the standard method (EN14214) are presented in Table 32.1 and compared to those of petroleum diesel fuel. The PL ethyl esters property values show an agreement with European standard method which is relatively closer to those of regular diesel. Also, PL biodiesel's physicochemical properties are similar to those of sunflower and eucalyptus biodiesels [11, 12]. It can be seen the formation of fatty acids ethyl esters from PL oil. The PL biodiesel has a low acid value of 0.187 mg KOH/g fat and a lower viscosity than the usual animal fats and vegetable oils. A high cetane number (53.94) generates a short ignition delay and thereafter allows good ignition ability in the engine. However, the gross heating value obtained is lower than that of the conventional diesel whose value is 45.4 MJ/kg because, certainly, of excesses of oxygen in the biodiesel. The value of flash point obtained during this characterization is higher than the minimal temperature recommended by the European standard, what ensures a safety during storage and handling of the PL biodiesel. The mass composition in carbon, nitrogen, hydrogen, oxygen, and sulfur is comparable of the values reported in the literature by Zeng et al. [13].

32.4 Conclusions

- For the two catalysts, a higher than 90% conversion is found.
- The study of the effect of the catalyst nature on transesterification also enabled us to better evaluate the catalytic activity of two studied catalysts; thus the KF/CaO catalyst is more acting than the KF/MgO system, because probably of the difference in existing alkalinity between two oxides.
- The nonedible nature of the PL oil and the easy access to this resource in the Mediterranean area make this biomass an interesting raw material for the local production of biodiesel.
- PL biodiesel characterization, according to the standard methods, shows that the physicochemical properties are comparable to those of conventional diesel fuel.
- PL biodiesel's physical-chemical properties are similar to those of sunflower and eucalyptus biodiesels.

Nomenclature

P	Pressure ($N.m^{-2}$)

Subscripts

a. u.	Arbitrary unit
BET	Brunauer-Emmett-Teller
CaM	Calcium oxide
IUPAC	International Union of Pure and Applied Chemistry
KF	Potassium fluoride
KOH	Potassium hydroxide
MgO	Magnesium oxide
PL	*Pistacia lentiscus*
SEM	Scanning electron microscopy
XRD	X-ray diffraction

References

1. Varuvel EG, Mrad N, Tazerout M, Aloui F (2012) Experimental analysis of biofuel as an alternative fuel for diesel engines. Appl Energy 94:224–231
2. Awad S, Loubar K, Tazerout M (2014) Experimental investigation on the combustion, performance and pollutant emissions of biodiesel from animal fat residues on a direct injection diesel engine. Energy 69:826–836
3. Yoon SH, Lee CS (2012) Effect of undiluted bioethanol on combustion and emissions reduction in a SI engine at various charge air conditions. Fuel 97:887–890
4. Roy MM, Tomita E, Kawahara N, Harada Y, Sakane A (2011) Comparison of performance and emissions of a supercharged dual-fuel engine fueled by hydrogen and hydrogen-containing gaseous fuels. Int J Hydrog Energy 36:7339–7352
5. Mc Taggart-Cowan GP, Rogak SN, Munshi SR, Hill PG, Bushe WK (2010) The influence of fuel composition on a heavy-duty, natural-gas direct-injection engine. Fuel 89:752–759

6. Xin Z, Jian X, Shizhuo Z, Xiaosen H, Jianhua L (2013) The experimental study on cyclic variation in a spark ignited engine fueled with biogas and hydrogen blends. Int J Hydrog Energy 38:11164–11168
7. Singh SP, Singh D (2010) Biodiesel production through the use of different sources and characterization of oils and their esters as the substitute of diesel: a review. Renew Sust Energ Rev 14:200–216
8. Liang X, Gao S, Yang J (2009) Highly efficient procedure for the transesterification of vegetable oil. J Renewable Energy 34:2215–2217
9. Liu H, Lingyan S, Yong S, Lubin Z (2012) Biodiesel production catalyzed by cinder supported CaO/KF particle catalyst. J Fuel 97:651–657
10. Wan T, Yu P, Gong S (2008) Application of KF/MgO as a heterogeneous catalyst in the production of biodiesel from rapeseed oil. Korean J Chem Eng 25(5):998–1003
11. Saydut A, Erdogan S, Kafadar AB, Kaya C, Aydin F, Hamamci C (2016) Process optimization for production of biodiesel from hazelnut oil, sunflower oil and their hybrid feedstock. Fuel 183:512–517
12. Tarabet L, Loubar K, Lounici MS, Tazerout M (2012) Eucalyptus biodiesel as an alternative to diesel fuel: preparation and tests on DI diesel engine. Biomed Res Int 7243–7251
13. Zeng J, Wang X, Zhao B, Sun J, Wang Y (2009) Rapid in situ transesterification of sunflower oil. Ind Eng Chem Res 48:850–856

Chapter 33
Chemometric Exploration of the Data Concerning Gases Emitted from Burning Mine Waste Dump

Adam Smoliński, Natalia Howaniec, and Patrycja Kuna-Gwoździewicz

33.1 Introduction

In recent years, the process of mine waste dump reclamation has gained an increased attention [1–6]. In many cases, such areas are of high investment potential in terms of location, provided that their ecological safety is ensured. A large amount of gangue has been extracted with coal and deposited on the surface for several decades. This waste material contains also coal, interlayers, or carbonaceous shale, as well as other combustible materials. It is estimated that on average, about 0.4−0.5 Mg of waste material is produced for each 1 Mg of coal extracted, and some part of it is deposited in dumps [7, 8]. The attempts of the fire risk assessment for mine waste dumps are based mainly on the expertise of a particular research or consultancy unit. Frequently, the methods and procedures applied in the assessment of spontaneous ignition of hard coal are used in the evaluation of waste self-ignition tendency, which is disputable, since the content of carbon in waste is relatively low in comparison with the carbon content of coal. Coal mine waste dumps are often thermally active objects. They are the source of exhaust gas emission including both inorganic compounds, such as carbon monoxide, sulfur dioxide, and hydrogen sulfide, and organic compounds, such as polycyclic aromatic hydrocarbons (PAHs), phenols, or BTEX (benzene, toluene, ethylbenzene, and xylenes) [9]. The objective of the study was the determination of PAH concentrations in gases emitted in the process of mine waste dump combustion simulated in a laboratory installation with a fixed-bed reactor.

A. Smoliński (✉) · N. Howaniec · P. Kuna-Gwoździewicz
Central Mining Institute, Katowice, Poland
e-mail: smolin@gig.katowice.pl

S. Nižetić, A. Papadopoulos (eds.), *The Role of Exergy in Energy and the Environment*, Green Energy and Technology,
https://doi.org/10.1007/978-3-319-89845-2_33

33.2 Materials and Methods

33.2.1 Materials

The samples were collected in accordance with the PN-EN 14899:2006 standard from the areas where mining waste from various coal mines is deposited (three samples), from mine waste dumps where waste from one colliery is deposited (seven samples, including three samples from the area of the currently created objects and four samples from heaps that are several decades old and had been created by defunct mines), and from slime separators, where fine-grained mine waste from water and mud circuits of collieries was deposited (two samples). The samples were collected from sites thermally active in the past as well as from the objects where such phenomena have never been observed. The physical and chemical parameters of the samples tested were determined in the Laboratory of Solid Wastes Analyses of the Department of Environmental Monitoring of the Central Mining Institute (see Table 33.1).

33.2.2 Methods

The research was conducted with the use of the laboratory installation with a fixed-bed reactor, shown in Fig. 33.1. The installation is composed of gaseous reagent supply system – inlets, valves, and reaction gas flow controllers (1), reactor of a capacity of 0.8 L heated with a resistance furnace (2), system of process gas cooling (3), water trap, gas treatment system and gas dehumidifier (4), solid particle filter (5), gas chromatograph (6), gas flow meter (7), and product gas sampling kit (8).

A sample of mining waste of 150 g in an analytical state, of a grain size of <0.2 mm, was placed inside the reactor between two layers of quartz wool applied to ensure a better temperature distribution, to prevent the sample grains of being captured by the gas stream supplied to the reactor, and also to avoid clogging of the outlet connection of the reactor. Once the sample was placed in the reactor, it was heated to a temperature of 180 °C at a heating rate of 1.33 °C/s in an atmosphere of inert gas (nitrogen). The temperature to which the sample was heated was determined at the initial stage of the research based on observations of intensification of the self-heating of a model mining waste containing 20%w/w of carbon at temperatures between 100 °C and 200 °C. The temperature inside the reactor was measured with a thermocouple. When the temperature stabilized, air was supplied to the reactor with the flow rate of 5 mL/s. The exhaust gases were directed to the system of separators in which the separation of moisture took place. The amount of cooled and dried product gas was measured with a mass flow meter, and its composition was analyzed with a gas chromatograph Agilent 3000A. In order to collect the samples for quantification of PAH compounds in the gas phase, samplers with a solid PUF sorbent (polyurethane foam) with a quartz fiber filter and an aspirator were used. Gas

Table 33.1 Characteristics of the examined mine waste samples

	Sample											
Parameter, %w/w	1	2	3	4	5	6	7	8	9	10	11	12
C	14.86	35.31	7.93	13.8	9.04	21.66	23.08	7.24	5.39	17.78	23.42	46.74
H	1.32	2.81	0.87	1.41	0.98	1.68	1.85	0.89	1.00	1.14	1.61	30.20
S	0.16	0.76	0.14	0.14	0.08	0.82	1.52	0.41	0.26	0.62	0.66	1.11
SiO_2	49.77	21.54	57.8	48.06	48.35	37.81	35.36	50.86	54.31	42.47	35.2	20.80
Al_2O_3	16.79	12.38	18.21	20.4	18.54	15.19	14.51	20.89	23.38	19.66	17.12	6.45
Fe_2O_3	3.83	7.95	4.04	3.68	6.81	3.94	5.75	5.51	3.05	6.39	2.82	4.06
CaO	1.03	0.98	0.38	0.28	1.32	0.86	1.00	0.59	0.03	1.01	0.45	1.00
MgO	1.33	0.92	1.12	1.15	2.15	1.34	0.70	1.27	0.80	1.39	1.03	0.79
Na_2O	0.18	0.07	0.14	0.19	0.76	0.30	0.26	0.33	0.22	0.32	0.13	0.18
K_2O	1.69	1.06	2.66	2.43	2.74	1.82	1.77	2.59	2.95	2.38	1.95	0.66
SO_3	0.29	0.62	0.25	0.23	0.29	0.64	1.24	0.74	0.14	0.58	0.54	1.14
TiO_2	0.98	0.52	0.78	1.09	0.78	0.61	0.54	0.99	1.06	0.72	0.72	0.26
P_2O_5	0.15	0.20	0.04	0.05	0.13	0.05	0.17	0.08	0.03	0.18	0.07	0.03
Ignition losses	23.49	53.43	14.04	22.28	17.38	36.97	38.21	15.48	13.30	26.25	39.55	65.06

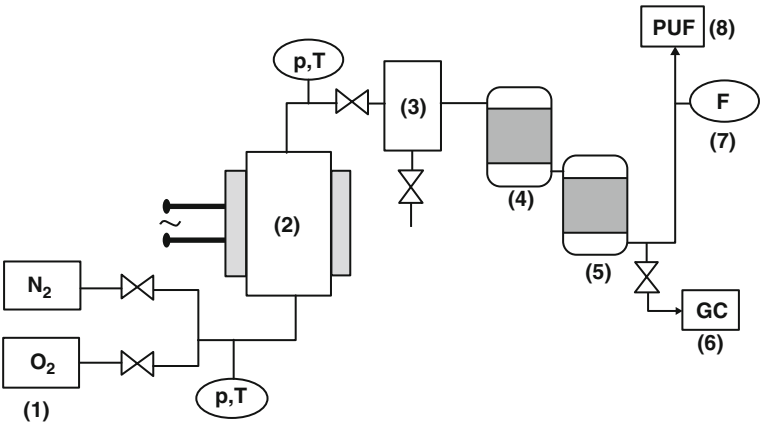

Fig. 33.1 Layout of the laboratory installation with a fixed-bed reactor for testing the self-ignition of mine waste

samples were collected for 20 minutes with the use of SKC AirChek 2000 aspirator under a flow rate of 3 L/min. The components adsorbed on the sampler were extracted using the ASE (accelerated solvent extraction) technique with the DIONEX ASE 200 extractor with hexane. The extraction of samplers consisted of a series of preheat for 5 min and static extraction lasting also 5 min at 100 °C and under the pressure of 1.5 MPa. The extract was purified using SPE (solid phase extraction) technique and next concentrated by evaporation under a stream of nitrogen and dissolved in 1 mL of acetonitrile. All tested samples were analyzed with the application of high-performance liquid chromatography (HPLC) with a FLD detector (fluorescence detection). A HPLC 1200 Series liquid chromatograph of Agilent Technologies with ZORBAX Eclipse PAH column (4.6 mm × 150 mm, 3.5 μm) was applied at a flow rate of 1200 mL/min and acetonitrile-water gradient.

33.2.3 Organization of Experimental Data and Methods of their Visualization and Interpretation

The experimental data resulting from measurements of PAH concentration in gases emitted from the mine waste dump combustion process, simulated under laboratory conditions in the fixed-bed reactor, were organized in a matrix $\mathbf{X}(12 \times 5)$. The rows of the matrix describe waste samples from various dumps, and the columns represent the examined aromatic hydrocarbons (see Table 33.2). The analysis of average profiles and standard deviations for data of a matrix $\mathbf{X}(12 \times 5)$ showed the need for data standardization.

Table 33.2 PAHs determined in exhaust gas from a fixed-bed reactor during a simulated mine waste dump combustion

No.	Parameter, μg/m^3
1	Naphthalene (NAP)
2	Acenaphthene (AcP)
3	Fluorene (Flu)
4	Phenanthrene (PA)
5	Anthracene (Ant)

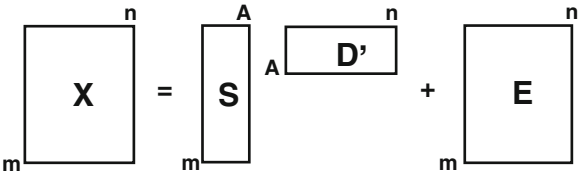

Fig. 33.2 Graphical representation of the principal component analysis

The principal component analysis, PCA [10–14], is one of the most commonly applied methods of data compression. This method allows, if compression is effective, visualization and interpretation of the results.

The PCA result is decomposition of a data matrix, $\mathbf{X}(m \times n)$ to a matrix $\mathbf{S}(m \times A)$ and $\mathbf{D'}(A \times n)$, where m, n reflects the number of objects and variables, respectively, A is the number of significant principal components, the matrix **S** is a matrix of objects including (in the case of experimental data considered) information on the waste samples examined, and the matrix **D'**, called the weigh matrix, describes measured parameters (see Fig. 33.2).

The columns of the matrix **S** and rows of the matrix **D'** are called the principal components (PCs) or eigenvectors, and they are designed to maximize the description of the data variance. Due to the fact that the principal components include information not only about the data structure but also about the error (noise), it is necessary to select the optimal number of components (A), enabling efficient modeling of the data and elimination of experimental error. Matrix **E** contains the part of the data that has not been modeled by the constructed model with A principal components. The effective data compression with the application of PCA is the one that allows this data to be visualized.

33.3 Results and Discussion

Based on the research results, it was found that the self-ignition occurred in case of samples 1, 2, 3, 5, 6, 9, 10, and 11. In case of samples 4, 7, 8, and 12, the process of self-ignition of waste was not observed. Figures 33.3 and 33.4 show the change in the content of oxygen, carbon dioxide, and carbon monoxide in the gaseous samples from the laboratory tests of waste for which the self-ignition was and was not observed, respectively. The differences in the course of the process in the laboratory research on self-ignition of mine waste samples included various concentrations of

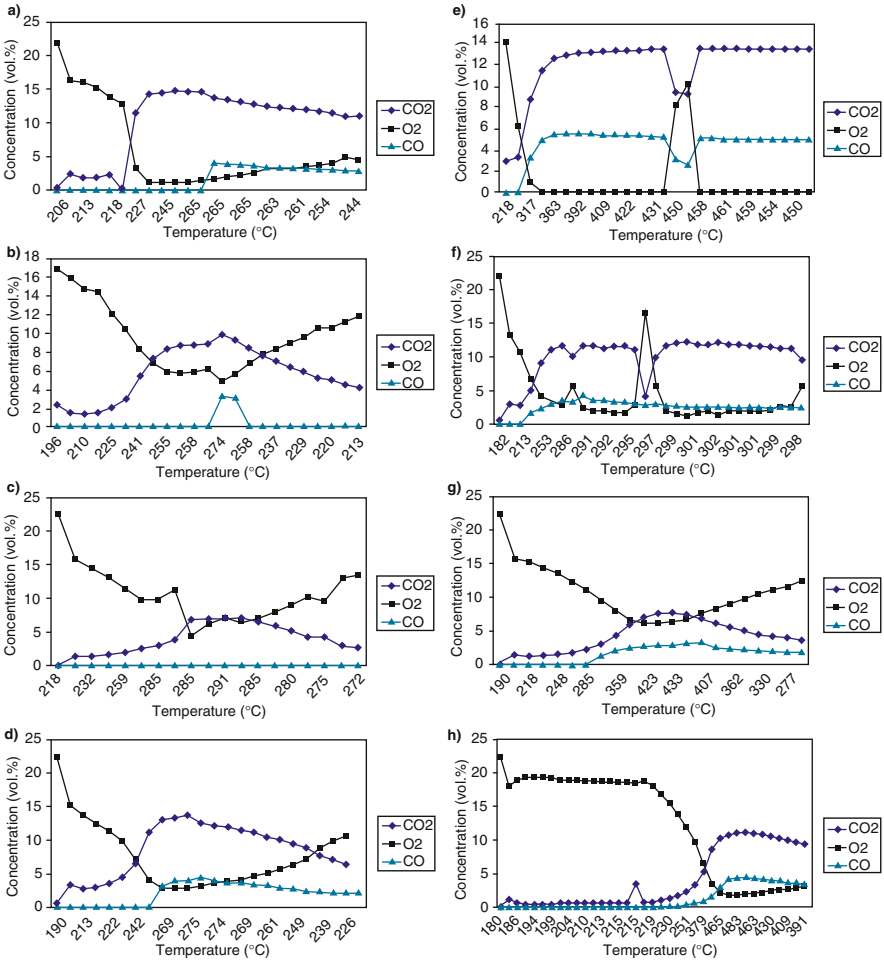

Fig. 33.3 Content of O_2, CO_2, and CO (vol. %), in exhaust gases from the reactor in tests of PAH emission under laboratory conditions, (**a**) sample 1, (**b**) sample 2, (**c**) sample 3, (**d**) sample 5, (**e**) sample 6, (**f**) sample 9, (**g**) sample 10, (**h**) sample 11

the measured gases as well as the temperature of self-ignition. It was assumed that the point of initiation of the self-ignition is the moment when in addition to carbon dioxide also carbon monoxide appears in exhaust gases, which indicates a temporary deficiency of oxygen for the complete oxidation of carbon in waste.

In the examined 12 gas samples collected during the laboratory tests, the compounds of the so-called "lighter PAH" group, two- and three-cyclic, such as naphthalene, acenaphthene, fluorene, phenanthrene, and anthracene, were quantified. In all collected samples, also fluoranthene was quantified as the only compound of the PAH group with a higher number of rings, which includes, for example, pyrene (Pyr) or benzo(a)pyrene (BaP). This is due to their tendency to an increased sorption on

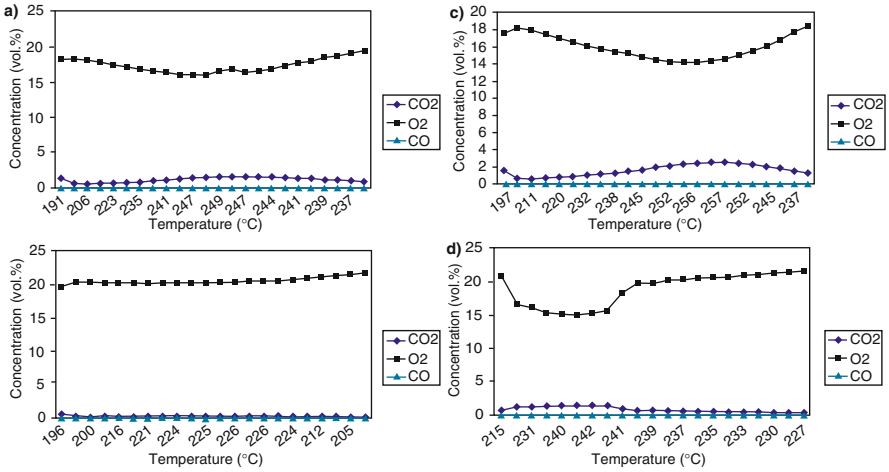

Fig. 33.4 Content of O_2, CO_2, and CO (vol. %), in exhaust gases from the reactor in tests of PAH emission under laboratory conditions, (**a**) sample 4, (**b**) sample 7, (**c**) sample 8, (**d**) sample 12

the dust particles and decreased tendency to evaporate with increasing molecular weight of particular PAHs [15]. Distribution of PAH compounds in the solid and gas phase depends mainly on the vapor pressure of a given PAH compound and its affinity for particulate matter particles defined by the adsorption coefficient Koc [16]. Therefore, the hydrocarbons quantified in the tested samples included the hydrocarbons of the highest volatility. Other PAH compounds were not detected in the samples of gases emitted during the laboratory research, and it may be related to their lower volatility.

The highest concentration in all tested samples was reported for NAP, and it amounted to 507.76 μg/m^3. Very high NAP concentration in the gas phase is associated with its highest volatility among all PAH group compounds. The lowest concentration was observed for Ant and AcP. Flu and PA were quantified in all eight tested gas samples. FluT was quantified only in samples 1 and 2. The differences in the contents of the particular PAHs for the samples for which the self-ignition was observed are shown in Table 33.3.

The results of the study on self-ignition of mine waste allowed describing the process of formation of PAH compounds during the mine waste dump combustion in real conditions. The above data showed that PAHs are formed not only in the process of combustion of carbon material contained in waste but also during the heating of waste material preceding the self-ignition. However, in this case, the amounts of PAHs in emitted gases are significantly lower, about 10−20 times less than during combustion. Different dynamics of the self-ignition process in the laboratory studies resulted in the differences in PAH concentrations. Moreover, during the process of combustion of waste sample, under conditions of rapid consumption of available oxygen/oxygen deficiency, a greater amount of examined analytes were formed than in the same process with higher availability of oxygen.

Table 33.3 PAH contents in gaseous samples from laboratory research on self-ignition of mine waste

PAH, μg/m^3	Carcinogenicity[a]	Number of rings	Sample							
			1	2	3	5	6	9	10	11
NAP	0.001	2	625.17	663.40	50.01	507.76	463.42	270.03	7.79	6.77
AcP	0.001	3	6.47	5.54	nd	2.75	nd	0.51	0.77	0.86
Flu	0.001	3	11.59	10.50	2.56	2.88	1.21	4.29	1.37	1.60
PA	0.001	3	19.56	6.33	7.33	5.63	3.44	10.80	4.50	4.49
Ant	0.010	3	2.32	0.37	0.83	0.44	0.13	nd	nd	nd
FluT	0.001	4	3.66	0.84	nd	nd	nd	nd	nd	nd
Total			668.77	686.98	60.82	519.46	468.20	285.63	14.43	13.72

nd – not determined, the value below the limit of quantification

[a]Relative carcinogenicity of particular PAH [17]

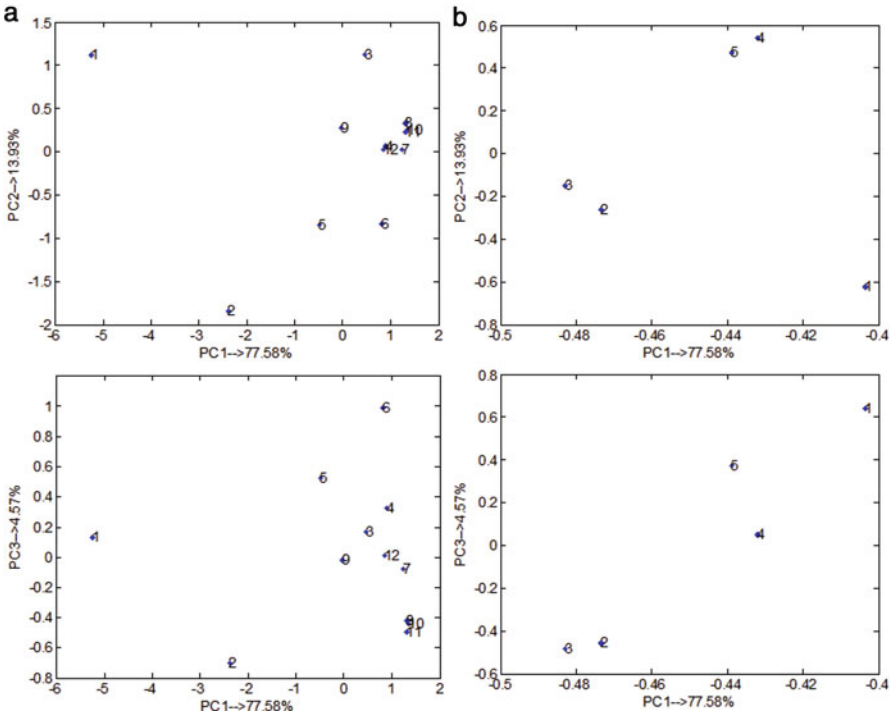

Fig. 33.5 The results of PCA analysis for data arranged in a matrix $\mathbf{X}(12 \times 5)$; (**a**) projections of objects and (**b**) projections of parameters on the plane defined by particular pairs of principal components

The purpose of the analysis of standardized experimental data arranged in a matrix $\mathbf{X}(12 \times 5)$ was to show the differences in the PAH concentrations in exhaust gas from the combustion of mine waste from various dumps, simulated in the fixed-bed reactor, and to indicate the dumps of the greatest PAH concentrations during the fire. For this purpose, the PCA method was applied. It allows tracing the relationships between the analyzed waste samples from various dumps and the parameters measured. To determine the correct complexity of the PCA model for data $\mathbf{X}(12 \times 5)$, the percentage of the data variance described by the subsequent principal components was used. Data compression was effective, and three principal components were required to describe 96.08% of the total data variance. Based on the projection of objects and parameters on the planes defined by particular pairs of principal components (see Fig. 33.5), the relationships between the examined samples were traced and conclusions were drawn on the correlation between the studied parameters.

The first two principal components described 91.51% of the total data variance. PC1 clearly indicated the difference between the samples 1 and 2 and all other examined waste samples. By applying also the projection of parameters on the plane defined by PC1 and PC2, it was proved that the waste samples 1 and 2 had relatively

higher concentration values of all tested parameters, compared to other tested waste samples. The greatest differences along PC1 were observed between the sample 1 and samples 8, 10, and 11. The lowest concentration values of naphthalene (parameter 1) among all examined samples were determined for samples 8, 10, and 11, while the highest concentration values of acenaphthene, fluorene, phenanthrene, and anthracene (parameters 2, 3, 4, and 5) among all examined samples were characteristic for the sample 1.

The second principal component, PC2, described 13.93% of the total data variance. It described the variance being the result of the significant difference between the sample 1 and the sample 2, resulting mainly from different concentrations of naphthalene, phenanthrene, and anthracene (parameters 1, 4, and 5). The sample 2 had the highest concentration of naphthalene (parameter 1) and low concentrations of phenanthrene and anthracene (parameters 4 and 5), comparable with all the other samples tested. Additionally, PC2 showed that the sample was very specific due to high concentration of anthracene (parameter 5).

The principal component PC3, which described 4.57% of the total data variance, showed the difference between the sample 6 and all other examined waste samples: the most significant between the samples 6 and 2. The specific nature of the sample 6 was associated with relatively high concentration of naphthalene (parameter 1). PC3 indicated again that the sample 2 was specific due to high concentrations of acenaphthene and fluorene (parameters 2 and 3). The compression of analyzed data organized in the matrix $\mathbf{X}(12 \times 5)$ was effective, and thus, the conclusions about the correlation between the examined parameters could be drawn. The correlated parameters describing the concentrations of acenaphthene and fluorene (parameters 2 and 3) brought the largest contribution to the first axis PC1. Additionally, the axis PC2 showed a positive correlation between the concentrations of phenanthrene and anthracene (parameters 4 and 5). It was also observed that the parameter describing the concentration of naphthalene (parameter 1) was not correlated with any other parameter.

33.4 Conclusions

In the exploration of the experimental data from measurements of PAH concentrations in gases emitted during the combustion of the mining waste dump simulated under laboratory conditions in the fixed-bed reactor, the principal component analysis was applied. The application of the PCA to data containing only the results of the measurements of PAH concentrations in gas products of the combustion process simulated in a laboratory installation did not allow dividing the waste samples into groups, for which the combustion was and was not observed. Nevertheless, the PCA analysis showed clear differences between the sample 1 and samples 8, 10, and 11 in terms of concentrations of naphthalene, acenaphthene, fluorene, phenanthrene, and anthracene. It was found that the samples 8, 10, and 11 were characterized by low concentrations of naphthalene, and the sample 1 had the highest concentrations of acenaphthene, fluorene, phenanthrene, and anthracene.

Acknowledgments This research was supported by the Ministry of Science and Higher Education, Poland, under the grant no. 10020217.

References

1. Ciesielczuk J, Misz-Kennan M, Hower JC, Fabiańska JM (2014) Mineralogy and geochemistry of coal wastes from the Starzykowiec coal-waste dump (Upper Silesia, Poland). Int J Coal Geol 127:42–55
2. Kosior G, Steinnes E, Samecka-Cymerman A, Lierhagen S, Kolon K, Dołhańczuk-Śródka A, Ziembik Z (2017) Trace elements in native and transplanted Fontinalis antipyretica and Platyhypnidium riparioides from rivers polluted by uranium mining. Chemosphere 171:735–740
3. Kosmaty J (2011) Wałbrzyskie tereny pogórnicze po 15 latach od zakończenia eksploatacji węgla [Wałbrzych post-mining land 15 years after coal extraction was terminated]. Górnictwo i Geologia 6:134–148
4. Misz-Kennan M, Gardocki M, Tabor A (2014) Fire prevention in coal waste dumps: exemplified by the Rymer cones, upper Silesian Coal Basin, Poland. In: Coal and peat fires: a global perspective, vol 3. Elsevier, Amsterdam, The Netherlands, pp 350–385
5. Ravindra K, Sokhi R, Van Grieken R (2008) Atmospheric polycyclic aromatic hydrocarbons: source attribution, emission factors and regulation. Atmos Environ 42:2895–2921
6. Smoliński A, Drobek L, Dombek V, Bąk A (2016) Modeling of experimental data on trace elements and organic compounds content in industrial waste dumps. Chemosphere 162:189–198
7. Jabłońska-Czapla M, Szopa S, Rosik-Dulewska C (2014) Impact of mining dump on the accumulation and mobility of metals in the bytomka river sediments. Arch Environ Prot 40:3–9
8. Korban Z (2011) Problem odpadów wydobywczych i oddziaływania ich na środowisko, na przykładzie zwałowiska nr 5A/W-1 KWK "X". [Problem of mining waste and their impact on environment in the case of burrow no. 5A/W-1 of "X" colliery] Górnictwo i Geologia 6:109–120
9. Smolinski A, Kuna-Gwozdziewicz P, Łaczny MJ, Bak A (2015) Study of the polycyclic aromatic hydrocarbons content in gas released from burning mine waste dump. Acta Chromatogr 27:239–254
10. Joliffe T (1986) Principal components analysis. Springer, New York
11. Wold S (1987) Principal components analysis. Chemom Intell Lab Syst 2:37–52
12. Howaniec N, Smolinski A (2014) Influence of fuel blend ash components on steam co-gasification of coal and biomass – chemometric study. Energy 78:814–825
13. Smolinski A, Walczak B, Einax JW (2002) Exploratory analysis of data sets with missing elements and outliers. Chemosphere 49:233–245
14. Smolinski A, Howaniec N, Stanczyk K (2011) A comparative experimental study of biomass, lignite and hard coal steam gasification. Renew Energy 3:1836–1842
15. Howsam M, Jones KC (1998) Sources of PAHs in the environment. In: Neilson AH (ed) Part 1. PAHs and related compounds. The handbook of environmental chemistry, vol 3. Springer–Verlag, Berlin/Heidelberg, pp 139–141
16. Ramirez N, Cuadras A, Rovira E, Marcé RM, Borrull F (2011) Risk assessment related to atmospheric polycyclic aromatic hydrocarbons in gas and particle phases near industrial sites. Environ Health Perspect 119:1110–1116
17. Petryl T, Schmidz P, Schlatter C (1996) The use of toxic equivalency factors in assessing occupational and environmental health risk associated with exposure to airborne mixtures of polycyclic aromatic hydrocarbons (PAHs). Chemosphere 32:639–648

Chapter 34
Biomass as a Renewable Energy Option in Electricity Generation: "Trakya Region" Case Study

Betül Özer and Sinem Bayar

34.1 Introduction

The adverse effects of human activities on the environment and extremes in the consumption of natural resources have caused major environmental problems, especially global warming. The most important reason for these ecological crises is historically the great usage of fossil fuels in energy production. Although energy is a vital necessity for the continuity of life, the energy production and consumption cause negative effects on both the environment and the human health.

In the world, approximately 80% of the energy production is provided by fossil fuels, which causes climate change by disrupting the ecosystem [1]. Renewable energy sources, which can be obtained from the earth and nature mostly without the requirement of any production process, are described as non-fossil-derived (coal, oil, and carbon type), having low level of CO_2 emission during electricity generation, causing much lower damage and impact on the environment than traditional energy sources, and being renewed in a continuous movement and available in nature, such as hydropower, wind, solar, geothermal, biomass, wave, tidal, and hydrogen energy [2]. Biomass is one of the earliest used energy sources especially in rural areas [3].

Globally, biomass ranks fourth among all the energy sources coming after oil, coal, and natural gas, which corresponds the first in the other renewable energy sources by supplying the primary energy [1]. Biogas is a type of biomass that is produced by the anaerobic digestion of organic matter, in the presence of various groups of microorganism, and is colorless, flammable, and comprised mainly of methane and carbon dioxide, with a small amount of hydrogen, nitrogen, oxygen,

B. Özer (✉) · S. Bayar
Energy Systems Engineering Department, Technology Faculty, Kırklareli University, Kırklareli, Turkey
e-mail: betulozer@klu.edu.tr

S. Nižetić, A. Papadopoulos (eds.), *The Role of Exergy in Energy and the Environment*, Green Energy and Technology,
https://doi.org/10.1007/978-3-319-89845-2_34

Table 34.1 Turkey's gross electricity generation by shares of primary energy resources by years [8]

Year	Total, GWh	Coal	Liquid fuels	Natural gas	Hydraulic	Renewable energy and wastes
		%				
1970	8623	32.8	30.2	–	35.2	1.9
1980	23,275	25.6	25.1	–	48.8	0.6
1990	57,543	35.1	6.8	17.7	40.2	0.2
2000	124,922	30.6	6.8	37.0	24.7	0.3
2006	176,300	26.5	2.5	45.8	25.1	0.3
2007	191,558	27.9	3.4	49.6	18.7	0.4
2008	198,418	29.1	3.8	49.7	16.8	0.6
2009	194,813	28.6	2.5	49.3	18.5	1.2
2010	211,208	26.1	1.0	46.5	24.5	1.9
2011	229,395	28.8	0.4	45.4	22.8	2.6
2012	239,497	28.4	0.7	43.6	24.2	3.1
2013	240,154	26.6	0.7	43.8	24.7	4.2
2014	251,963	30.2	0.9	47.9	16.1	4.9
2015	261,783	29.1	0.9	37.9	25.6	6.5

and carbon monoxide. Biomass has the greatest technical potential among all the renewable energy sources and, with biofuels technology, its sources can be evaluated directly or through conversion products. Animal waste, agricultural residue, forest residue, industrial and domestic wastes, urban waste, wastewater, and algae can be used as sources of biogas. Biogas production technology is an inexpensive system that repays the initial investment cost within a reasonable period of time (e.g., a few couple of years) [4]. The uses of biogas can be summarized as heat, steam and electricity production (via a gas turbine and generator, cogeneration, and fuel cells), vehicle fuel, etc. [5]. The determined advantages of using biogas as an energy source include prevention of uncontrolled greenhouse gas emissions, reduction of manure odor problem, protection of water resources, waste recycling, destruction of pathogens and wild plant seeds, production of fly and insect repellent and high-quality fertilizer, savings for farmers, etc. [6].

Especially, after the 1970s, the energy issue has had a critical prescription for countries which obtain their requirements substantially with import, due to the external dependency. This issue is still valid for Turkey today; at present, around 75% of the total energy demand is being provided from imports [7]. Annual development of Turkey's gross electricity generation by shares of the primary energy resources is given in Table 34.1 [8]. The share of renewable energy sources is approximately 25% since 2000, and it is on a rising trend during the last decade. On the other hand, it is important to assess the current policies and trends of Turkey in terms of clean and renewable energy. The Tenth Development Plan that is in force between 2014 and 2018 is pointed out to increase the share of renewable resources in energy production to 29% by 2018 [9]. Besides, according to the National

Renewable Energy Action Plan for Turkey, the share of renewable energy is aimed to increase to 37.6% in total electricity generation in 2023 [10]. In addition to the positive effects of the current Turkish energy policies including increasing the share of renewable energy, correspondingly reducing carbon dioxide (CO_2) emissions, and decreasing environmental pollution, perhaps strategically the most important one would be to reduce Turkey's dependency on foreign energy resources.

There are several studies in the literature about regional biogas potential of Turkey. In the study of Ilgar [11], the biogas potential in Çanakkale, one of the districts of the city named Gallipoli, which is in Trakya Region, was assessed, and it was determined that approximately 97 million m^3 of annual biogas potential can be obtained from approximately 1.76 million tons of cattle, small ruminant, and poultry manure. The calculations were based on the animal wealth of the city, and the average manure generation values are also used in this study. Akyol et al. [12] have determined the biomass potential of Trakya Region stating that approximately 89 million m^3 of annual biogas potential can be obtained from approximately 2 million tons of cattle, small ruminant, and poultry manure. In both studies, availability factor of dried manure was not taken into consideration which is a significant factor for the evaluation of the biogas potential.

The aim of this study is to determine the biogas potential of Trakya Region of Turkey including Tekirdağ, Kırklareli, and Edirne cities based on the animal wealth considering the available dried animal manure.

34.2 Materials and Methods

The biogas energy potential of animal waste in Trakya Region is calculated according to the numbers and the types of the animals in the country's data taken from the Turkish Statistical Institute (TURKSTAT) [13].

34.2.1 Data

Trakya Region including Tekirdağ, Edirne, and Kırklareli cities has 18,665 km^2 surface area which corresponds to 2.4% of Turkey's area. The populations of the cities Tekirdağ, Edirne, and Kırklareli are 937,910, 402,537, and 346,973, respectively. The region is bordered by the Black, the Marmara, and the Aegean Seas and the countries of Bulgaria and Greece. Agriculture and husbandry are the most important income sources for the region. Approximately 77.4% of the agricultural production value of the region is derived from plant production and 22.6% from animal production. Farming in this region is rather a small scale and is a form of family business [14]. The animal wealth including cattle, small ruminants, poultry, and Equidae of the cities in 2015 is given in Tables 34.2, 34.3, and 34.4, respectively [13].

Table 34.2 The animal numbers in Kırklareli, thousands [13]

Districts	Cattle	Small ruminant	Poultry	Equidae	Total
Center	41	201	24	1	267
Babaeski	23	27	57	0.19	107
Demirköy	7	2	31	0.052	40
Kofçaz	5	26	5	0.049	36
L.Burgaz	48	54	146	0.27	248
P.Köy	3	6	7	0.017	16
P.Hisar	9	35	24	0.211	68
Vize	13	33	8	0.085	55
Total	149	384	302	1.8	837

Table 34.3 The animal numbers in Edirne, thousands [13]

Districts	Cattle	Small ruminant	Poultry	Equidae	Total
Center	20	39	48	0.236	107
Enez	15	43	6	0.082	64
Havsa	23	26	84	0.074	128
İpsala	22	31	15	0.34	69
Keşan	23	71	39	0.33	134
Lalapaşa	16	24	15	0.082	55
Meriç	7.5	33	25	0.2	66
Süloğlu	10	19	15	0.083	45
U.Köprü	5	65	52	0.191	122
Total	141	347	299	1.6	788

Table 34.4 The animal numbers in Tekirdağ, thousands [13]

Districts	Cattle	Small ruminant	Poultry	Equidae	Total
Çerkezköy	3.85	13.6	2.2	0.11	19
Çorlu	3	12	86	0.098	101
Hayrabolu	21	29	76	0.099	125
Malkara	52	75	45	0.019	172
Marmara Ereğlisi	3	7	12	0.062	22
Muratlı	0.6	17	132	0.042	150
Saray	11	4	38	0.174	53
Şarköy	7	40	7	0.511	55
Ergene	9	21	396	0.033	426
Kapaklı	5	9	10	0.294	24
S.Paşa	16	34	42	0.132	92
Total	132	262	844	1.5	1240

Table 34.5 Biogas energy potential of Kırklareli

	Cattle	Small ruminant	Poultry	Equidae	Total
Wet manure, ton/year $\times 10^3$	535	279	6.7	6.9	828
Dry manure rate	0.15	0.3	0.35	0.3	
Dry manure, ton/year $\times 10^3$	80	84	2.3	2	168
Manure availability	0.65	0.13	0.99	0.13	
Available dry manure, ton/year $\times 10^3$	52	11	2.3	0.27	66
Biogas, m^3/year $\times 10^3$	10,427	2178	461	54	13,120
Methane, m^3/year $\times 10^3$	5787	1209	256	30	7282

Table 34.6 Biogas energy potential of Edirne

	Cattle	Small ruminant	Poultry	Equidae	Total
Wet manure ton/year $\times 10^3$	507	243	6.6	5.9	762
Dry matter rate	0.15	0.3	0.35	0.3	
Dry manure, ton/year $\times 10^3$	76	73	2.3	1.7	153
Manure availability	0.65	0.13	0.99	0.13	
Available dry manure, ton/year $\times 10^3$	49	9,5	2.3	0.23	61.4
Biogas, m^3/year $\times 10^3$	9889	1893	455	46	12,283
Methane, m^3/year $\times 10^3$	5489	1050	253	25.6	6817

34.2.2 Biogas Potential Calculations

The assumptions used in the calculation of the biogas potential of the region are given below:

- 3.6 ton wet manure/year from a cattle.
- 0.7 ton wet manure/year from a small ruminant.
- 0.022 ton wet manure/year from a poultry [15–17].
- 3.65 ton wet manure/year from an equidae [18].
- Biogas is assumed containing about 55.5% methane (CH_4) [19].
- Biogas yield is accepted to be 200 m^3/ton dry manure [20].
- 1 m^3 methane gas is equivalent to 10 kWh electric energy [21, 22].
- The electricity generation efficiency is 38.5% [23, 24].

According to these values, the methane potentials of the cities are calculated and given in Tables 34.5, 34.6, and 34.7 separately.

The total energy equivalents of biogas are 72,817 MWh/year, 68,173 MWh/year, and 66,767 MWh/year in Kırklareli, Edirne, and Tekirdağ, respectively.

Table 34.7 Biogas energy potential of Tekirdağ

	Cattle	Small ruminant	Poultry	Equidae	Total
Wet manure, ton/year $\times 10^3$	475	183	18.6	5.7	683
Dry matter Rate	0.15	0.3	0.35	0.3	
Dry manure, ton/year $\times 10^3$	71	55	6.5	1.7	135
Manure availability	0.65	0.13	0.99	0.13	
Available dry manure, ton/year $\times 10^3$	46	7	6.4	0.224	60
Biogas, m^3/year $\times 10^3$	9268	1430	1287	45	12,030
Methane, m^3/year $\times 10^3$	5144	793	714	24.9	6677

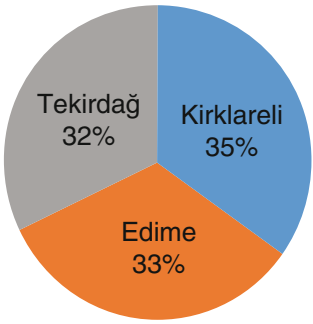

Fig. 34.1 Total biogas capacity distribution in Trakya Region

34.3 Results and Conclusions

Total biogas capacity distribution of Trakya Region by cities is given in Fig. 34.1. Although Kırklareli has the largest share, the three cities have approximately the close biogas energy potential. This study was prepared to reveal biogas potential of animal manure from Trakya Region including Kırklareli, Edirne, and Tekirdağ cities. Animal waste amounts are calculated according to the numbers and the types of animals by using 2015 data. According to the results, about 187,168 tons of available dried animal manure can be collected per year, through which 37.4 million m^3 of biogas potential and 21 million m^3 of methane (CH_4) can be obtained. It has also been determined that methane gas has an electricity generation potential of approximately 80,000 MWh/year. The annual electricity consumption of Trakya Region is about 6 million MWh [25]. The determined biogas potential of animal manure in this study corresponds to 1.33% of the region's demand. This energy contributes to the strengthening of a decentralized but reliable energy infrastructure through the use of the regional potential.

As a clean and sustainable energy source, biomass has additional environmental advantage of disposing animal husbandry waste. Biogas energy is recommended mostly because it helps in reducing environmental problems and Turkey's energy

dependency and also provides the economic contribution of animal husbandry waste management. Since Turkey has very high biomass potential, investments in biomass energy, as well as all the other renewable energy resources, should be increased corresponding with the long-term Turkish energy policy strategies. Using all the biomass potential in Turkey is an important factor in reducing dependency on foreign energy sources.

In this study, only the animal waste is evaluated as biogas source. The other organic resources such as the agricultural and municipal solid wastes and the economic benefits of biomass use for reduction of greenhouse gas emissions may be the subject of a possible future work for Trakya Region.

References

1. IEA (2014) Key world energy statistics. International Energy Agency, Paris
2. SERKA (2015) Green Energy Sources Sector Report in Turkish, T.C. Serhat Development Agency, Kars, January, 2015
3. Keche AJ, Rao GAP, Tated RG (2011) Efficient Utilization of Biomass By Gasification – A Case Study, International J Adv Therm Sci Eng, V. 2 • N.1 • January–June 2011, p 1–7
4. NKU, Namık Kemal University, Faculty of Agriculture (2015) Feasibility Study on Electricity Generation Facility from Biogas in Tekirdağ City, Trakya Development Agency No.TR21/14/DFD/003 No.lu Project Result Report in Turkish
5. Çallı B (2012) Biogas Generation from Wastes in Turkish, Turkish Chemical Association, Young Chemists Platform, Marmara University Environmental Engineering Department, February, 2012
6. Kızılaslan N, Kızılaslan H (2007) Turkey's biogas energy potential. Energy Sources, Part B 2:277–286
7. Url-1: http://www.mfa.gov.tr/turkeys-energy-strategy.en.mfa). Accessed 01 Mar 2017
8. Url-2:TEİAŞ. http://www.teias.gov.tr/ TurkiyeElektrikistatistikleri/ istatistik2015/ istatistik. Accessed 27 Feb 2017
9. MD;Republic of Turkey, The Ministry of Development, (2013) Tenth Development Plan, 201–2018, Ankara
10. MENR, Republic of Turkey The Ministry of Energy and Natural Resources (ETKB in Turkish), 2014. National Renewable Energy Action Plan, Ankara
11. Ilgar R (2016) A study for determination of biogas potential in Çanakkale. Assets by Animals, Eastern Geographical Review 35:89–106
12. Akyol E, Yaka İF, Koçer A, Güngör A (2016) Hacıhafızoğlu, O. 2016. In terms of the potential of biomass fixed bed vaporiser Trakya region, in Turkish. J Glob Eng Stud 3(2):155–162. e-ISSN: 2149-2735
13. Url-3: Turkstat (2016) https://biruni.tuik.gov.tr/hayvancilikapp/hayvancilik.zul, accessed on: 22.11.2016
14. Trakyaka, Trakya Development Agency (2013) Agriculture and Food in Trakya Region, Edirne Investment Support Office
15. Akbulut A, Dikici A (2004) Biogas potential and cost analysis of Elazığ City, in Turkish. Res East Anatolia Region:36–41
16. Bayramoğlu T, Yapraklı S (2014) Biomass energy potential and its economic effects in Turkish, a field research in TRA1 region, Atatürk University. J Soc Sci Inst 18(2):319–336
17. Url-4: http://www.eie.gov.tr/yenilenebilir/biyogaz.aspx, Accessed on 13/03/2017
18. Sabuncu ÖC (2010) Technical, Economical and Environmental Analysis of Biogas Production. In Turkish, MSc. Thesis, Hacettepe University, Ankara, Turkey

19. Bilgili V, Yaldız O, Bilgili A (2011) Compost and biogas facility feasibility report, in Turkish. Harran University, Şanlıurfa
20. WEC, World Energy Council (2007) Hydraulic and renewable energy working group biomass energy sub-working group report, in Turkish, Ankara, Turkey
21. DBFZ (2011) Resource Efficient and Climate Friendly Use of Animal Waste through Biogas Production in Turkey - Turkish-German Biogas Project Republic of Turkey The Ministry of Environment and Urbanization, Ankara
22. Gümüşçü M. ve Uyanık S (2010) South-East Anatolian Region Obtaining Biogas and Biofertilizer from Animal Waste, The Chamber of Mechanical Engineers, (TMMOB) Installation Engineering Journal, in Turkish, July–August 20120, p 59–65
23. Özer B (2013) Biogas Potential of Animal Wastes for Electricity Generation in Ardahan City of Turkey. In: Dincer I, Colpan CO, Kadioglu F (ed) Causes, Impacts and Solutions to Global Warming, XVIII, 1183 p, pp 697–707. Springer, New York, DOI: https://doi.org/10.1007/978-1-4614-7588-0_36, Online ISBN:978-1-4614-7588-0, Springer Science Business Media, New York
24. Tolay M, Yamankaradeniz H, Yardımcı S, Reiter R (2008) Biogas production from animal wastes in Turkish, VIIth National Clean Energy Symposium, UTES 2008, s:259–264, December 17–19, ˙Istanbul, Turkey
25. Url-5: http://www.tredas.com.tr/Faaliyetlerimiz/Enerji-Bilgileri/Sayfalar/Aylik-Bazda-Bilgiler-2012.aspx. Accessed 21 Apr 2017

Part IV
Solar Energy Technologies

Chapter 35
A Framework of Economic and Environmental Assessment of Solar Energy Water Heating System for Public Buildings

M. Ziya Sogut, Süleyman Ozkaynak, and T. Hikmet Karakoc

35.1 Introduction

Nowadays, the social pressure in parallel to the fight against global warming and climate change has affected especially all applications that use fossil fuels directly. In this context, in all countries, the works on reducing the effects of fossil fuel consumption made significant progress with the corresponding change in the national strategy plans. Considering related sectors, particularly the public sector which will particularly be deemed to be a significant energy user, has been at the top of them. Taking the work processes and service qualities into consideration, the public sector is a sector that heavily uses many types of energy. For these structures that consume more than 20% of the national energy consumption, the sustainable energy approach will be possible by the popularization of the total energy management systems. The public energy management and its job descriptions acquired a legal framework with the Energy Efficiency Law adopted in 2008 in Turkey. The energy management with a corporate identity in this structure contains a practical management system with ISO 50001 [1].

The system preference in public administrations is usually based on traditional project choices. However, in the heat-based energy solutions, the preference of clean energy and particularly the solar technologies as the renewable energy systems must be considered to be a priority application. In such structures, the service periodicality or economic use of public finance is essential in such structures rather than the efficient use of energy. In this aspect, the present developments in energy technologies created an alternative approach for the energy management system

M. Z. Sogut (✉) · S. Ozkaynak
Maritime Faculty, Piri Reis University, Istanbul, Turkey

T. H. Karakoc
Faculty of Aeronautic and Astronautic, Anadolu University, Eskisehir, Turkey

S. Nižetić, A. Papadopoulos (eds.), *The Role of Exergy in Energy and the Environment*, Green Energy and Technology,
https://doi.org/10.1007/978-3-319-89845-2_35

applications in public choices. The present study examined the solar energy-aided solution of the energy need for hot water for a public gym. The study covers the system optimization and the evaluation of the emission potential with the thermo-economic analyses based on the real direct process requirements.

35.2 A Framework About Strategy of Energy Management in Public Sector

The public sector is one of the most important actors in national strategies and policies. The public sector is an important user in energy consumption, and its processes need attention with regard to all energy-consuming sectors. However, there are four basic criteria for the public sector to keep pace with the current changes, to develop the energy efficiency in particular and to play a leading role in the fight against climate change.

Public Administrators or Personnel The public sector is considered to be structures combining many different administrative components and different disciplines. The service priority of public administration causes problems in other management tools. Particularly the technical inadequacy in energy efficiency and management as well as the lack of information about technology can be considered to be the problems of the public sector. The shortcomings of public administrations include the definition of energy use density in many public structures, monitoring and control of the energy, and system administration based on energy efficiency.

Financial Hardships The most important problem faced by the energy management is the cost-effectiveness of the projects based on energy efficiency. Such project applications can be considered to create savings when dealt together with the current structural changes. Energy costs are a standard payment item particularly in public finance. However, these conditions are not figures to be taken into consideration within the current expenditures. Savings that may be achieved in the annual energy consumptions in public buildings that are considered to be integrated structures will create savings also in the energy costs that have a significant potential in budget items.

Budgetary Hardships The financial hardships within the investment in the public sector are the most common problems. The public sector has difficulty to execute many short-term, medium-term, and long-term projects in this aspect. Particularly, the works based on energy efficiency for many countries can be saved with respect to public financing. Particularly the budget administration hardships for the less developed or developing countries create financial resource problems in the energy efficiency or renewable energy projects. However, this is just the reverse in developed countries where all investments based on energy efficiency directly find a place in public financing programs. This is also related with the pushing role of social

awareness. This effect defines energy efficiency as an effective parameter in public budgets.

Legal and Institutional Hardships The energy efficiency of public administrations is a priority problem faced by these administrations with renewable energy systems and applications, low- or zero-carbon technology applications. Particularly the limitations required by the legislation, lack of support by the tender requirements to energy technologies, and related applications can be considered to be important problems faced by energy administrations. Lack of legislation or regulations on energy efficiency and management in the public sector in many countries impairs effective behavior of users and administrators.

All these parameters prevent sustainability in the energy management process with respect to public administration. Particularly considering the state organizations, sectoral effectiveness, infrastructure, components, and services of the public administration, energy management is an element that will provide important advantages in public. One needs to define the share of the public sector in energy consumption or the share of consumption in the economy to be able to evaluate the effects of these activities. Several countries defined the consumption data of the public sector in their energy projections. For example, the share of the public sector among the total number of houses in the USA is around 21%. The consumption ratio of these institutions is 25% of the total consumption. This public ratio is approximately 22% in China [2]. Energy management is an administrative organization process in the direct or indirect energy consumption of all instruments in service and production.

The basic aim of the energy management is to reduce the energy consumptions, energy costs, and emissions [3]. In this scope, reducing the fossil-based energy consumptions and increasing the potential of clean energy sources are an important gain. The clean energy concept which has been recently developed aims to cover the energy demand with renewable energy technologies, technologies that reduce emissions, and energy storage technologies instead of the fossil-based primary energy consumption that causes an emission threat. The basic aim in these technologies is to cover the demand for the energy that is consumed by traditional technologies with the above clean energy sources. Clean energy technologies reduce fossil fuel consumption as well as emissions [4].

Solar energy is one of the most important sources in clean energy technologies. The solar technologies in heat resources are very popular. However, despite such development of clean energy technologies, it is not to say that it gained priority in project processes of public applications. In this, especially, legislation and a methodological deficiency stand out. In this context, Fig. 35.1 includes the flow chart of

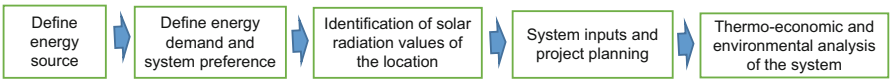

Fig. 35.1 Methodology of the clean energy application

the methodology that was developed for the choice of a clean energy system in buildings.

Solar energy systems are the most popular applications in clean energy systems. Particularly the evaluation of clean energy systems in public buildings includes the study of the solar energy choice as a reference.

35.3 Building Features and Solar Potential

For this study, an application was modelled in Turkey. Turkey is fortunate compared to many countries with regard to its solar energy potential due to its geographical location. The measured sunshine duration and radiation magnitude data of Turkey were used, and the annual average of total sunshine duration of Turkey was determined to be 2640 h (average daily total 7.2 h) and the average total radiation magnitude to be 1311 kWh/m^2-year (average daily total 3.6 kWh/m^2) [5]. The public building taken as a sample is a gymnasium, which has a high-intensity usage. Thermo-economic and environmental analyses were conducted for this building based on the above flow process.

35.3.1 Definition of the Energy Type

The hot water demand in the gymnasium is covered by an exchange system related to the central system. Fuel oil is used as the fuel source for the central system. But, the corporate governance has planned the choice of natural gas instead of fuel oil consumption in the central system. Considering both the energy costs and the environmental effects caused by the energy, the fuel oil choice should be changed although it is required by the public administration. In this study, comparative analyses were evaluated for two fuel types, and this study intends to cover the demand of the solar energy system based on regional data.

35.3.2 Definition of Energy Demand and System choice

The use of hot water in the gymnasium becomes intensified at certain hours depending on the user conditions. Accordingly, around 10 tons of hot water is necessary for a total of 200 people including 50 people on average between 12:00 and 14:00 h and 150 people on average between 16:00 and 19:00 h depending on the team activities. The solar energy system is integrated into the existing mechanical system with the goal to operate the system with storage.

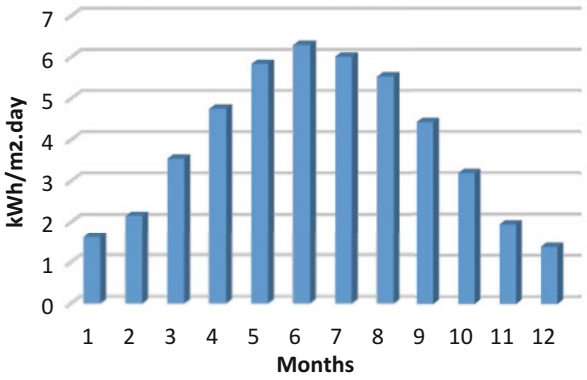

Fig. 35.2 Solar radiation potential of the location

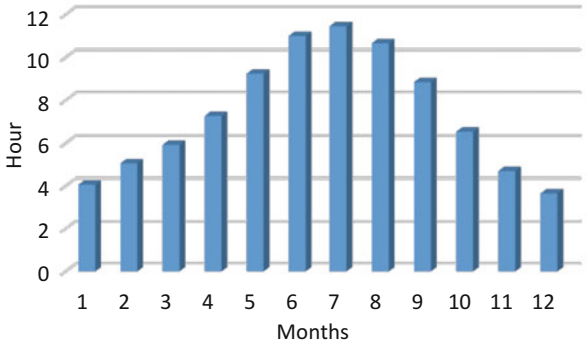

Fig. 35.3 Sunshine duration of the location [5]

35.3.3 Definition of Solar Radiation Values of the Location

The solar radiation values of the location need to be known. Solar radiation values of the location were studied, and the month-based distribution is given in Fig. 35.2.

Taking the location data into account, the annual average radiation value of the region is 1450 kWh/m^2-year. The daily average radiation value of the location per month has been determined between 1.39 kWh/m^2-day and 6.29 kWh/m^2-day (5). The average sunshine durations of the location per month were studied, and the relevant distribution was given in Fig. 35.3. The annual average sunshine period of the region is 7.36 h. With these data, the solar energy potential has a very important potential (5).

35.3.4 System Inputs and Project Planning

Management of and meeting the energy demand in the public sector and development of effective solutions in project processes are considered to be a project

management process. An engineering study is required for the energy effective solutions in clean energy applications. Within this scope, first the energy effective solutions should be considered in project planning processes.

In recent years, energy efficiency methodologies were developed in this kind of planning processes. The energy efficiency design methodology designed in Denmark and Ireland can be given as an example. It was observed that the energy efficiency design process can have a saving potential of up to 30% even in the project processes through such project methodologies. For this purpose, creating the energy efficiency-based project processes, it is essential to develop products with high efficiency and a design based on energy efficiency. According to the project scope, this design process goes through planning, design, tendering, contract, and installation processes [6]. In this scope, the energy efficiency is a multidisciplinary process. There are two ways to use the solar energy systems in energy demand: heat production or electricity production. In this scope, when we consider the usage hours of hot water in the gymnasium, we chose a hybrid system with a flat collector. For situations not using solar energy, hot water needs will be taken from the exchanger circuit in the conventional mechanic system of the campus. Accordingly, the solar collector analyses will be used in projecting the system. This study will include a project work based on the collector capacity in projecting a solar energy application. The required hot water in hot water preparation systems with solar energy is calculated depending on the number of people $(\dot{\forall})$:

$$\dot{\forall} = \dot{\alpha} .\dot{m} .n \tag{35.1}$$

Here, $\boldsymbol{\alpha}$ defines the correction factor, $\boldsymbol{m}$ defines the water consumption per person, and $\boldsymbol{n}$ defines the number of people. To find the energy obtained from the total solar radiation coming to the collector surface, the following equation was used [7, 8]:

$$\dot{Q}_{\mathrm{k}} = \dot{Q}_{\mathrm{Y}} R \Delta_{\mathrm{I}} \tag{35.2}$$

Here, $\dot{Q}_{\mathrm{k}}$ is the total radiation average coming to the surface of the inclined collector, $\dot{Q}_{\mathrm{Y}}$ is the total solar radiation average coming to the horizontal surface, R is the conversion factor for the inclined collector, and Δ_{I} is the correction factor of the collector's azimuth angle. The useful energy to be obtained from the total solar beam coming to the collector surface depends on the collector efficiency and system efficiency. Useful energy can be calculated from the following equation:

$$\dot{Q}_{\mathrm{n}} = \dot{Q}_{\mathrm{n}} N_{\mathrm{k}} N_{\mathrm{m}} \tag{35.3}$$

Here, Q_{n} is the useful energy to be obtained, N_{k} is the collector efficiency, and N_{m} is the system efficiency. The energy amount necessary to meet the hot water need depends on the water amount and the specific heat capacity according to the Kirchhoff law. The necessary energy amount is found with the following equation [8]:

$$\dot{Q}_{\mathrm{d}} = m_{\mathrm{w}} C_{\mathrm{p}} (T_{\mathrm{w}} - T_{\mathrm{f}}) \tag{35.4}$$

Here, $\dot{Q}_{\mathrm{d}}$ is the heat amount necessary to prepare hot water, $\dot{m}_{\mathrm{w}}$ is the amount of water to be heated, T_{w} is the amount of the requested hot water, and T_{f} is the average temperature of supply water. The collector surface area necessary to meet the current heat need is evaluated as the ratio of the required amount of energy to the useful energy. This equation is defined as follows [7]:

$$F_{\mathrm{k}} = Q_{\mathrm{d}}/Q_{\mathrm{n}} \tag{35.5}$$

CO_2 emission and the fight against it are handled multidimensionally for the fight against global warming and climate change. In this concept, this conceptual process is defined from two dimensions. Particularly as a result of the burning processes in the consumption of fossil resources, CO_2 is used as an emerging product. The second one is the equivalent CO_2 based on primary consumption for the energy-consuming processes. The first one is a measurable value, while the second one is used to define the effect of the greenhouse gases. Generally the second method is used to define the CO_2 emission potential caused by sectoral differences. A correlation was defined for this first parameter in the engineering analyses or comparable evaluations [9] (1 ppm CO_2 ~ around 7.78 equivalent $GtCO_2$).

Within the scope of the fight against climate change or in sectoral works, different prediction analyses are used for the CO_2 emission evaluations. Relevant examples are given in Table 35.1.

The IPPC approach is remarkable particularly in fossil fuel-based predictions. The emission equivalent in this approach which is accepted by official agencies in Turkey is:

$$M_{\mathrm{CO_2}} = m_{\mathrm{fuel}}.\alpha_{\mathrm{CO_2}}.(\mathrm{FOC} \times \mathrm{EF}) \times (M_{\mathrm{CO_2}}/M_{\mathrm{C}}) \times 10^{-3} \tag{35.6}$$

Building performance based on the emission according to the building energy performance regulation is:

$$E_{\mathrm{P,SEG}} = 100 \times (\mathrm{SEG_a}/\mathrm{SEG_r}) \tag{35.7}$$

SEG (kg-CO_2/m^2-year) defines the amount of annual CO_2 emission of the building per m^2; a and r define the real and reference buildings.

$$\mathrm{SEG} = m_{\mathrm{fuel}}.F_{\mathrm{SEG}} \tag{35.8}$$

Table 35.1 Approaches in CO_2 emission prediction analyses [9]

Country	Method
USA	Vintanging model developed by the energy environment agency using the data collected from sectors
European Union	Gross domestic product cost of every country is found by dividing European Union member countries to individual consumption
Other countries	Ozone consumption value estimation of the countries supplied from the United Nations Environment Programme (UNEP)

Here, F_{SEG} is the CO_2 conversion coefficients (kg.CO_2/kWh), and the value of 0.234 is taken for the natural gas, 0.433 for the lignite coal, 0.33 for fuel oil, and 0.320 for the other fossil fuels (diesel) [10]

35.4 Results and Discussions

The use of hot water in the gymnasium becomes intensified at certain hours depending on the student and personnel conditions. Around 10 tons of hot water is necessary for a total of 200 people including 50 people on average between 12:00 and 14:00 h and 150 people on average between 16:00 and 19:00 h depending on the team activities. In units with internal hot water, the hot water consumption amount is related with the life standards of the people in the consumption unit, habits, culture, and education levels, and their financial income level is the most important indicator. Hot water consumptions are given in various ranges in various resources depending on many factors. Table 35.2 includes some data on hot water consumption per person.

An approximation account is taken into consideration according to the usage density in integrated buildings. The classification of water consumption per person includes as low (30–50 l/day), medium (50–80 l/day), normal (80–100 l/day), and high density (100–200 l/day) [7].

Table 35.2 includes the potential calculation over the data in consumption taking the existing building usage densities into consideration. The change in the supply water temperature was studied for the capacity calculations before analyses, and the changes of the water temperature are given in Fig. 35.4.

The annual average temperature of the supply is 15.08 °C. The annual temperature change of the supply water is from 9.6 to 22.4 °C. Heat capacity for the water temperature of 45 °C in the system based on the current supply reference and monthly distribution were studied. Figure 35.5 includes the requested heat change.

There is a linear relationship between the changes in the supply temperature and the heat demand. This demand is high particularly for the winter months and low for

Table 35.2 Amounts of water consumption l/day/person [7]

Place of use	Consumption (l/day)	Temperature (°C)
Student residence	50	45
Hospital	35–55	55
Gymnasium	30–50	40
Hotel 2 star	50–75	45
Hotel 5 star	150–200	45
Restaurant	20–30	55
Swimming pool	30–50	50
Pension	35–50	40

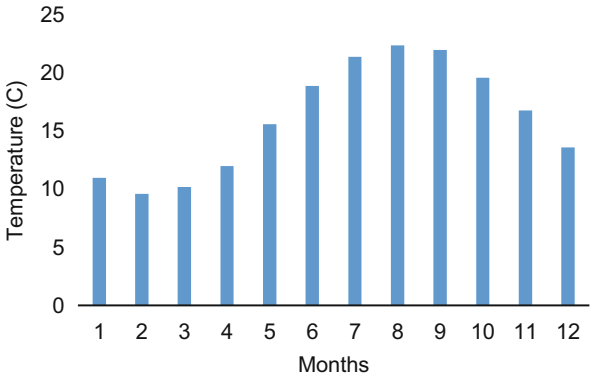

Fig. 35.4 Supply water temperature changes

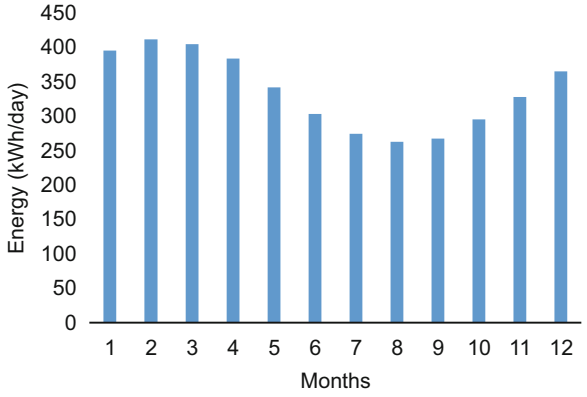

Fig. 35.5 Heat demand for hot water

the summer months. The peak and lowest points of the heat demand were 411.7 kWh for February and 262.8 kWh for August, respectively.

In such solar energy applications, the need for water storage emerges when we consider the usage density and hours. In such project applications, the storage potential of water should be defined. Storage temperature was taken as 60 °C in this project study. The most important criterion in the storage potential is the usage ratio. This ratio was taken as 80% within the scope of this project when we take the usage time and needs into consideration. In such buildings, storage time and usage efficiency are important. The determination of the storage capacity and capacity selection in line with the project should be taken in a holistic manner per month. Figure 35.6 includes the monthly storage requirement per month.

The storage capacity required in the system reaches to 8.78 m^3. A minimum of 7.51 m^3 per month was found in the project. It was decided to use a storage area of 5 tons for the hot water storage capacity within this scope. The heat requirement for the hot water should be calculated together with the storage requirement in the system. The heat amount needed for stored hot water and the distribution were evaluated again, and the results were given in Fig. 35.7.

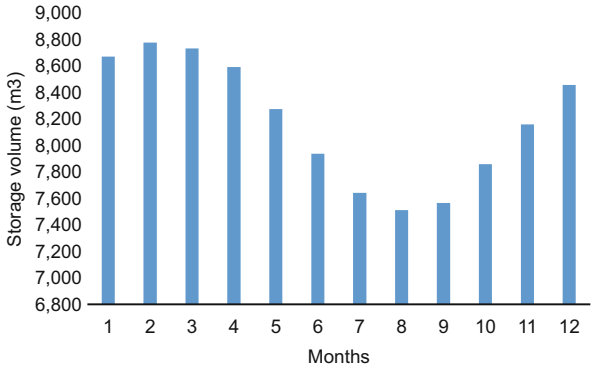

Fig. 35.6 Storage volume of hot water

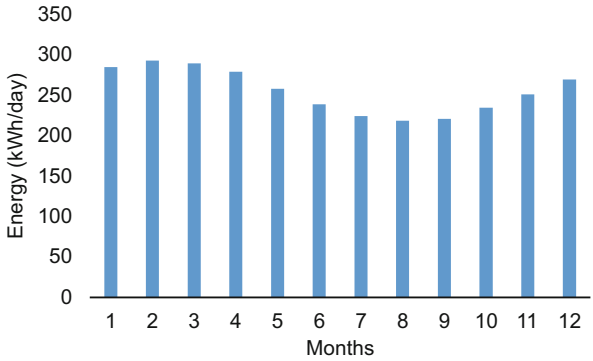

Fig. 35.7 Heat energy demand of hot water storage

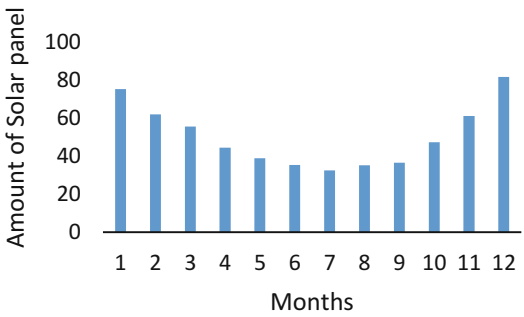

Fig. 35.8 Amounts of solar collector

Collector distributions according to the solar radiation loads were evaluated by taking the maximum coverage ratio of 100% at summer conditions into consideration in Fig. 35.8. Accordingly, a total of 55 collectors were found to conform to the heat demand of the heat process. For the collector calculations of the system, collector yield was taken to be 68% considering the annual average. A maximum of 82 collectors was calculated for December, and a minimum of 32 collectors was calculated for July. The annual average in the number of collectors was increased to 51, also including the passage months of the system. An 8% improvement was

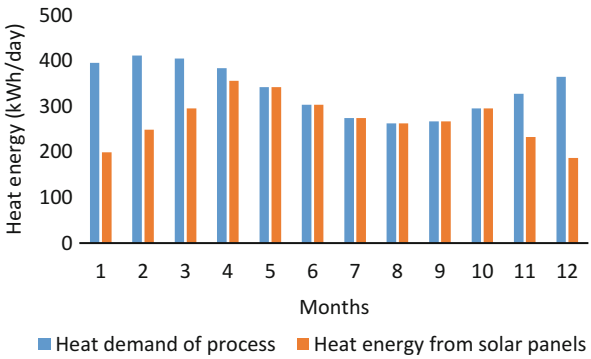

Fig. 35.9 Demand and supply of heat energy

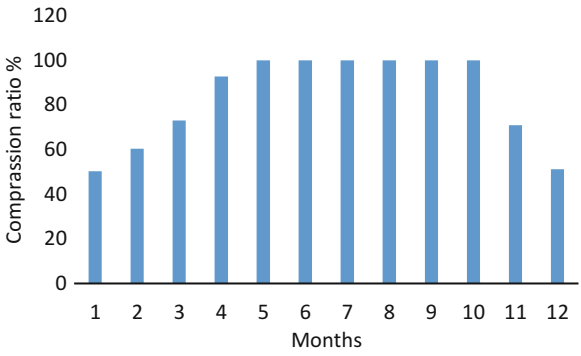

Fig. 35.10 Coverage ratio of solar energy

realized for the total number of collectors in the system paying attention to the losses in the passage months. Accordingly, the heat demand of the system and heat amount that can be covered by the collector were studied, and monthly distributions are given in Fig. 35.9.

When taking the coverage ratio of the system in the solar energy optimization, selection of excessive collectors causes greater problems in the system to be established. Particularly in some applications, maximum collector choices will be far too many, and it will cause evaporation of the fluid in the system especially under summer conditions as well as uncontrollable explosions in the system. Therefore, it is a must to carry out comparable analyses in the system according to the properties of the selected collector. This study fully covers the heat demand based on the number of collectors selected between May and October and allows steam control of the system. Figure 35.10 includes the system coverage ratio of the solar collector according to the analysis values and the concerned distributions.

The coverage ratio of the solar system for the current energy demand was found to be 83% in annual average. Accordingly, the peak points of the system to cover the current demand are a minimum 50% for January and 100% for the months of May and October. This way, the heat demand in the system was more than 50% for the general distribution and created a savings of up to 83% in the annual energy

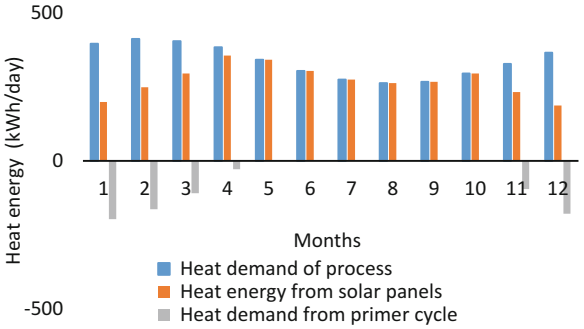

Fig. 35.11 Comparative analysis of heat energy

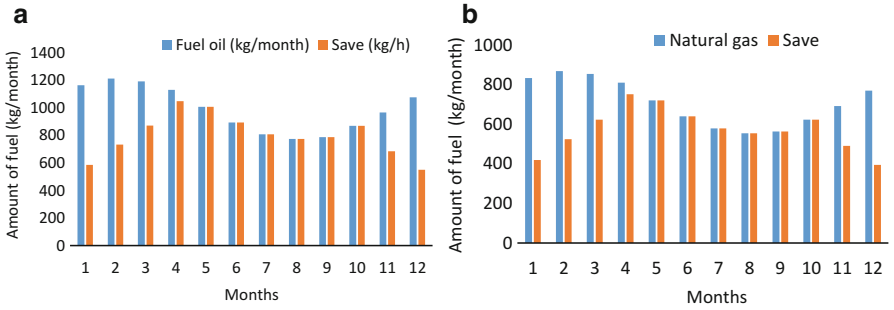

Fig. 35.12 Fuel consumptions. (**a**) Fuel oil. (**b**) Natural gas

consumption. The study location is actually consuming fuel oil. However, a decision to convert the system was made, and natural gas will be used as the primary fuel. Therefore, fuel saving, thermo-economic analyses, and environmental impact analyses were done separately for both fuels. Figure 35.11 includes the comparable energy demand saved with consideration of the energy coverage ratios of the process.

The annual total energy demand of the system is around 4034.45 kWh, and 3265.26 kWh of it is covered by the designed solar system, and a total energy of −769.85 kWh is demanded from the current primary circuit. This corresponds to only 19.07% of the total heat demand in the annual total. The total fuel savings of the system were evaluated based on these distributions. Figure 35.12 includes the total demand and saving distributions with reference to natural gas and fuel oil.

The annual total of fuel amount consumed by the system for the current heat demand is 11907.94 kg/year for fuel and nearly 8560.6 m^3/year for natural gas. An annual total saving of 6264.47 kg/year for fuel and 6889.03 m^3/year for natural gas was ensured corresponding to nearly 83.24% of both consumptions. Thermo-economic evaluations of this consumption were done over the fuel costs. Total cost was found to be USD 18460.65 considering the current cost evaluations. Figure 35.13 includes the fuel consumption and saving cost distributions.

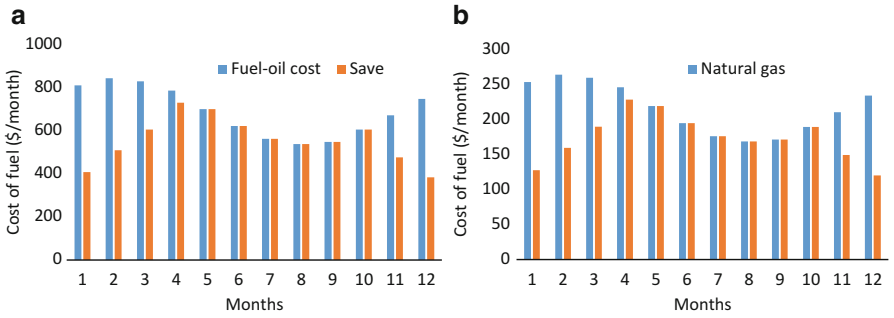

Fig. 35.13 Fuel costs. (**a**) Fuel oil. (**b**) Natural gas

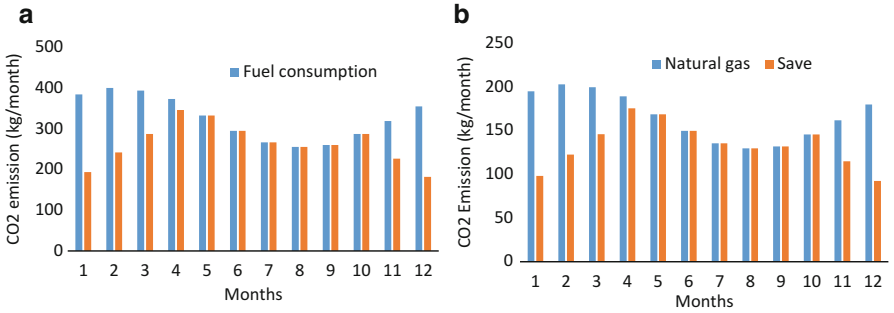

Fig. 35.14 CO_2 emission saving. (**a**) Fuel oil. (**b**) Natural gas

The annual cost of the fuel oil consumption is 8269.4 $/year, while the fuel cost saving of the solar system is 4350.32 $/year. A similar evaluation was also done for natural gas. Cost of annual natural gas consumption is 2585.95 $/year, while the saving is 4350.32 $/year. There is an effective saving for the consumption costs of both fuels. In addition to all of these cost effects, the environmental evaluations are also remarkable. The emission savings of such a system choice with respect to CO_2 equivalent were also evaluated. Figure 35.14 provides separate examinations of the saving ratios based on natural gas and fuel consumptions.

One of the most important gains of this type of system choice is the CO_2 emission saving based on actual fuel saving. According to this project data, there is a saving of 2067.27 kg/CO_2/year in the potential of 3929.6 kg/CO_2/year in fuel oil consumption. For natural gas consumption, a saving of 1611.8 kg/CO_2/year will be possible in a potential of 1991.49 kg/CO_2/year. The most important evaluation in this type of system installations is the cost evaluation. Recovery period based on system installation is important for such choices. According to the present value analyses, the recovery costs of the system are 4.24 years for the fuel oil consumption and 8.82 years for the natural gas consumption.

35.5 Conclusions

This study covers the thermo-economic and environmental analyses of a solar energy system by the clean energy system approach in a public building. The study includes the application process via a methodology. Depending on the demanded energy, the coverage ratio and the corresponding saving ratios are evaluated separately. Alternative solutions like solar energy provide very useful results in energy management which is an important problem in the public sector. Likewise, despite the coverage ratio of 83.27%, the system recover cost is 4.24 years for fuel oil. This value may be lower if the efficiency ratio is increased in system choices. The public institutions provide the least reaction in energy management. This study showed the public sector the advantage of the renewable energy choices with respect to energy management. The study presents a methodological approach particularly for the energy administrators.

Nomenclature

F_{SEG}	CO_2 conversion coefficients ($kgCO_2/kWh$)
$\dot{m}$	Water consumption per person (kg/day)
$\dot{m}_w$	Amount of water to be heated (kg/s)
n	Number of people
N_k	Collector efficiency
N_m	System efficiency
R	Conversion factor
SEG	Amount of annual CO_2 emission ($(kg\text{-}CO_2/m^2\text{-}yıl)$
T_w	Amount of the requested hot water
T_f	Average temperature of supply water
$\dot{Q}_k$	Total radiation average coming to the surface of the inclined collector (kW)
$\dot{Q}_Y$	Total solar radiation average coming to the horizontal surface (kW)
$\dot{Q}_n$	Useful energy to be obtained (kW)
$\dot{Q}_d$	Heat amount necessary to prepare hot water (kW)
α	Correction factor
Δ_I	Correction factor of the collector's azimuth angle

References

1. Enve (2017) Why energy efficiency? Enve energy, Resitpasa Neigh. Tuncay Artun street, Nu:6 34467 Emirgan/Istanbul. http://enve.com.tr/enerji-verimliligi-bilgi.pdf
2. Harris J, Johnson F (2000) Potential energy, cost, and CO2 savings from energy-efficient government purchasing. ACEEE summer study on energy efficiency in buildings, commercial buildings: program design, implementation, and evaluation
3. SEI (2006) Building energy manager's resource guide. Sustainable Energy Ireland, Glasnevin, Dublin 9, Ireland

4. WBG (2011) Promotion of new clean energy, technologies and the World Bank Group, background paper for the World Bank Group energy sector strategy, World Bank Group energy sector strategy. http://siteresources.worldbank.org/INTESC/Resources/Clean_tech_background_paper.pdf
5. Yegem (2017) Solar energy potential of Turkey. Ankara, Turkey. http://www.eie.gov.tr/MyCalculator/pages/10.asp4
6. Petersen PM, O'Sullivan J (2012) Energy efficient design – a methodology applied in major international projects, ECEEE 2012 Summer study on energy efficiency in industry
7. Altuntop N (2008) Renewable in construction technology energy and alternative systems, solar energy, TTMD workshop 2008, Turkey. http://www.ttmd.org.tr/userfiles/file/TTMD%20Calistayi-NALTUNTOP.1.pdf
8. Acar K, ve Turan B (2005) Energy analysis of solar systems. Energy 42(9):12–16
9. Algedik Ö (2013) Role of local government in the fight against climate change, civil climate summit report, the organization of civil climate summit, November. www.iklimzirvesi.org/wp.../11/Yerel-Yonetimlerin-ID-Mucadelede-Rolu.pdf
10. Bayram M (2011) The reference building concepts and energy classification in calculation Method of Bep-TR, 4. National Installation Engineering Congress – April 13/16 /İzmir, page 755–762

Chapter 36
Framework for Calculating the Rooftop Solar Photovoltaic (PV) Footprint Considering Building Electricity Supply and Demand from the Urban Level

Taehoon Hong and Minhyun Lee

36.1 Introduction

Ever since the industrial revolution, electricity supply always has been a great issue for energy security and economic growth in all over the world [1]. However, conventional energy sources for supplying electricity, fossil fuels such as coal, oil, and gas, are the biggest contributors to climate change and global warming which threaten human healths and environments [2]. Recent concerns on climate change and environmental pollution had led to the emergence of renewable energy, and various efforts for promoting these technologies are made over the past few decades [3].

This new energy paradigm shift from fossil fuels to renewable energy brought a concept of energy "prosumer" through distributed solar generation (DSG). An energy "prosumer," who can both produce and consume energy, makes it possible to increase the market penetration through DSG, on-site electricity generation from solar energy (i.e., rooftop solar photovoltaic (PV) system). They can also sell the surplus electricity back to the grid for supplying electricity to their neighborhoods to meet the urban-level electricity demand [4]. In this regard, to successfully implement DSG and ultimately achieve nearly zero-energy building (nZEB) from the urban level, it is crucial to analyze and determine how much electricity from DSG is required to offset the urban-level electricity demand. This can be done by analyzing and investigating the electricity supply (i.e., electricity generated from DSG) and demand (i.e., electricity consumed in buildings) of each individual building in the neighborhood [5].

T. Hong · M. Lee (✉)
Department of Architecture and Architectural Engineering, Yonsei University, Seoul, Republic of Korea
e-mail: mignon@yonsei.ac.kr

S. Nižetić, A. Papadopoulos (eds.), *The Role of Exergy in Energy and the Environment*, Green Energy and Technology,
https://doi.org/10.1007/978-3-319-89845-2_36

To analyze the relationship of the electricity supply and demand effectively and strategically, this study applied the "ecological footprint" approach to DSG by introducing the rooftop solar PV footprint, the total rooftop area required for DSG to meet building electricity demand [5]. From the energy usage aspect, the relationship of the electricity supply and demand can be analyzed by using the self-sufficiency rate of electricity. This self-sufficiency rate indicates the proportion of locally produced electricity from DSG to consumed electricity in buildings [6]. However, as mentioned above, the self-sufficiency rate can only provide some information on how the electricity from DSG has been used locally. Instead, the rooftop solar PV footprint can provide some plans and strategies on how the rooftops could be utilized for installing DSG from the rooftop usage aspect. Therefore, the rooftop solar PV footprint could be very useful for planning future energy policies and strategies from the urban level.

Regarding this issue, several previous studies were conducted to investigate the relationship of the building electricity supply and demand [5–8]. However, most of the previous studies mainly focused on analyzing the building electricity supply and demand by the self-sufficiency. There was almost no study dealing with the concept of solar PV footprint.

Therefore, this study aims to propose a framework for calculating the rooftop solar PV footprint by considering building electricity supply and demand from the urban level. Toward this end, the methods for calculating the available rooftop area, rooftop solar PV potential, and rooftop solar PV footprint were suggested in stages using building information, solar radiation, and energy consumption data based on geographical information system (GIS). The proposed framework was applied to Yeoksam-dong and Samseong-dong in the Gangnam District, Seoul, South Korea, a popular metropolitan area where high-rise office buildings abound, to show and compare the analysis results.

36.2 Materials and Methods

This study proposed a framework for calculating the rooftop solar PV footprint in four steps (refer to Fig. 36.1): (i) step 1, establishment of the database; (ii) step 2, calculation of the available rooftop area; (iii) step 3, calculation of the rooftop solar PV potential; and (iv) step 4, calculation of the rooftop solar PV footprint.

36.2.1 Step 1: Establishment of the Database

In step 1, the database on the building information, solar radiation, and energy consumption should be established to ultimately calculate the rooftop solar PV footprint. First, the building information data should be collected to calculate the available rooftop area using the Hillshade analysis. Building information data such

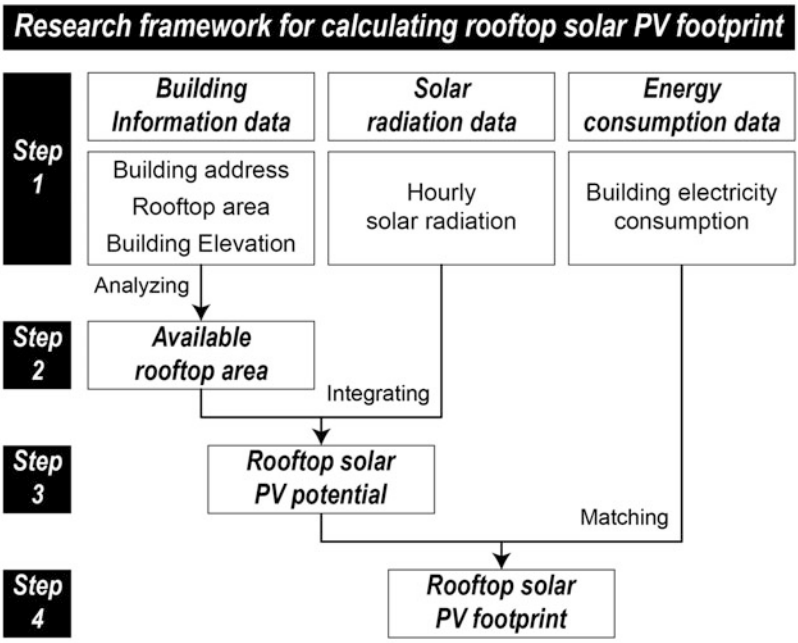

Fig. 36.1 Research framework

as building address and rooftop area and building elevation in South Korea can be collected from a foundation corporation called Spatial Information Industry Promotion Institute (SPACEN) under the Ministry of Land, Infrastructure, and Transport (MOLIT) of the Korean government [9]. These building information data, particularly the building elevation data, are used to calculate the available rooftop area for solar PV installation by excluding the shaded rooftop area.

Second, the solar radiation data should be collected to calculate the rooftop solar PV potential. Since this study proposed a calculation method of the rooftop solar PV potential on an hourly basis, this study needed the hourly solar radiation data. The hourly solar radiation data in Seoul can be collected from the World Radiation Data Centre (WRDC), sponsored by the World Meteorological Organization [10].

36.2.2 Step 2: Calculation of the Available Rooftop Area

In step 2, the available rooftop area for solar PV installation should be calculated to analyze the practical and realistic rooftop solar PV potential. First, the shaded rooftop area should be calculated based on the altitude and azimuth of the sun using the Hillshade analysis. To calculate the shaded area using the Hillshade analysis, it requires two types of input data. First, the building spatial data with

elevation information, which can be collected in step 1, is needed. Second, the location data of the sun, specifically the altitude and azimuth of the sun at the time of the analysis, is needed. The altitude and azimuth of the sun at any time in South Korea can be calculated using the Sun Altitude and Azimuth Calculation tool from Korea Astronomy and Space Science Institute (KASI) [11]. By using these input data, Hillshade analysis can be conducted using the ArcGIS, a GIS software by the Environmental Systems Research Institute (ESRI) [12].

Second, the available rooftop area should be calculated by excluding the shaded and small rooftop area. First, the shaded rooftop area should be excluded from the total rooftop area based on the Hillshade analysis results. By excluding the shaded rooftop area, it is possible to quantify the rooftop area where DSG can perform at the optimal level without any disturbance of the building shadow. Second, the small rooftop area where it is hard to install DSG should be additionally excluded. The rooftop area below 33 m^2 should be excluded from the available rooftop area, since the Korea New and Renewable Energy Center (KNREC) requires at least 33 m^2 in rooftop area for installing a 1-kW DSG [13].

36.2.3 Step 3: Calculation of the Rooftop Solar PV Potential

In step 3, the rooftop solar PV potential considering the available rooftop area should be calculated to analyze the practical and realistic rooftop solar PV potential. First, the solar PV module efficiency should be defined to analyze the rooftop solar PV potential. Although the solar PV module efficiency varies depending on the different types and manufacturers of solar panels [14], the efficiency of the commercial solar PV modules usually ranges from 15% to 18% [15]. By using the solar PV module efficiency between this range for calculating the technical potential of the rooftop solar PV system, it is possible to reflect the current technology level of the solar PV market and industry.

Second, the installed condition of DSG should be also determined to analyze the rooftop solar PV potential. Since this study proposed a calculation method of the rooftop solar PV potential on an hourly basis, the available rooftop area where DSG can perform at the optimal level without any disturbance of the building shadow changes by time. Accordingly, to fully consider the difference in the available rooftop area by time and calculate the rooftop solar PV potential on an hourly basis, this study assumed that the solar PV panels are installed horizontally with no tilt on the entire rooftops [3].

36.2.4 Step 4: Calculation of the Rooftop Solar PV Footprint

In step 4, the rooftop solar PV footprint should be calculated by matching and integrating the rooftop solar PV potential and energy consumption data of the

individual building. To match these two data from the different data source, it is necessary to define the identification reference to be based on for combining the two different data of the same building together. Since the building is managed based on its official address in South Korea, this study used the official building address for matching the rooftop solar PV potential and energy consumption data of a building.

36.3 Numerical Scheme

The rooftop solar PV potential and footprint explained in steps 3 and 4 can be calculated using Eqs. (36.1) and (36.2). By integrating the available rooftop area estimated through the process in step 2 with the hourly solar radiation data, it is possible to calculate the rooftop solar PV potential on an hourly basis [3]. By matching the rooftop solar PV potential per unit rooftop area with the energy consumption data of each individual building, it is possible to calculate the rooftop solar PV footprint of a building.

$$\mathrm{RSPP} = e_{\mathrm{PV}} \times \sum_{i=1}^{12} \left(\sum_{j=6}^{18} \left(\mathrm{ARA}_{ij} \times \mathrm{SR}_{ij} \right) \right) \tag{36.1}$$

$$\mathrm{RSPF} = \frac{\mathrm{EC}}{\mathrm{RSPP}/\mathrm{RA}} \tag{36.2}$$

where RSPP stands for the rooftop solar PV potential of a given building for a year (kWh), e_{PV} stands for the solar PV module efficiency, ARA_{ij} stands for the available rooftop area of a given building on the fifteenth of month i at time j to $j + 1$ (m^2), SR_{ij} stands for the total solar radiation on month i at time j to $j + 1$ ($\mathrm{kWh/m}^2$), i stands for the month ($i = 1, 2, 3, \ldots, 12$), j stands for the time in 24-h format ($j = 6, 7, 8, \ldots, 18$), *RSPF* stands for the rooftop solar PV footprint of a given building (m^2), *EC* stands for the total electricity consumption of a given building (kWh), and RA stands for the total rooftop area of a given building (m^2).

By multiplying (i) the total solar radiation at a certain time frame (e.g., 6 a.m. to 7 a.m.) for an entire month, (ii) the available rooftop area at a certain time frame in month i, and (iii) the solar PV module efficiency, it is possible to calculate the rooftop solar PV potential of month i at a certain time frame. This process can be continued for every time frame and every month for calculating the rooftop solar PV potential of a year.

By dividing (i) the total electricity consumption by (ii) the rooftop solar PV potential per unit rooftop area of a given building, it is possible to calculate the total rooftop area required for a given building to meet its electricity demand. This process can be done for the entire buildings in the neighborhood for calculating the rooftop solar PV footprint of that geographical boundary.

36.4 Results and Discussions

To actually calculate and analyze the rooftop solar PV footprint by applying the proposed framework, this study conducted a case study for buildings in Yeoksam-dong and Samseong-dong in the Gangnam District, Seoul, South Korea. Yeoksam-dong and Samseong-dong are wards of the Gangnam District with 4933 and 2500 buildings, respectively. Teheranno, a street in the Gangnam district, runs through Yeoksam-dong and Samseong-dong, which holds most of the tallest buildings in Seoul [16].

First, to calculate the available rooftop area solar PV footprint in Yeoksam-dong and Samseong-dong, this study conducted the Hillshade analysis for 12 days (on the fifteenth of each month from January to December) at hourly intervals (from 6 a.m. to 6 p.m.), resulting in a total of 156 times. Second, to calculate the rooftop solar PV potential in Yeoksam-dong and Samseong-dong, this study used 15% and 18% for the minimum and maximum solar PV module efficiency, respectively. Third, to calculate the rooftop solar PV footprint in Yeoksam-dong and Samseong-dong, this study conducted data matching between the calculated rooftop solar PV potential and collected energy consumption data of each building using the official building address. As a result, the rooftop solar PV footprint in Yeoksam-dong and Samseong-dong was calculated for 2531 and 1255 buildings from a total of 4933 and 2500 buildings, respectively.

As shown in Table 36.1, the rooftop solar PV potential and footprint in Yeoksam-dong were calculated and compared with the building electricity consumption and total rooftop area, respectively. First, the rooftop solar PV potential was examined to consider the building electricity supply and demand separately and to analyze the energy usage aspect. From the perspective of building electricity supply, the rooftop solar PV potential was examined. When the solar PV module efficiency is 15%, the total rooftop solar PV potential in Yeoksam-dong came out to be 105,956 MWh, whereas it came out to be 127,147 MWh when the solar PV module efficiency is 18%. From the perspective of building electricity demand, the building electricity consumption was examined. The total electricity consumption of 2531 buildings in Yeoksam-dong was found to be 815,955 MWh. According to aforementioned building electricity supply and demand in Yeoksam-dong, it was shown that the

Table 36.1 The rooftop solar PV potential and footprint results in Yeoksam-dong by solar PV module efficiency

Solar PV module efficiency	15%	18%
No. of buildings	2531	
Total electricity consumption (MWh)	815,955	
Rooftop solar PV potential (MWh)	105,956	127,147
Self-sufficiency rate (%)	12.99	15.58
Total rooftop area (m^2)	757,703	
Rooftop solar PV footprint (m^2)	5,561,714	4,634,762
Solar PV occupancy rate (%)	734.02	611.69

self-sufficiency rate could reach 12.99% and 15.58% when the solar PV module efficiency is 15% and 18%, respectively.

Second, the rooftop solar PV footprint was examined to consider and analyze both building electricity supply and demand at the same time and to analyze the rooftop usage aspect. When the solar PV module efficiency is 15%, the total rooftop solar PV footprint in Yeoksam-dong came out to be 5,561,714 m^2, whereas it came out to be 4,634,762 m^2 when the solar PV module efficiency is 18%. That is, 5,561,714 m^2 and 4,634,762 m^2 of rooftop area is required for installing DSG to supply the amount of electricity consumed in 2531 buildings in Yeoksam-dong, when the solar PV module efficiency is 15% and 18%, respectively. This information on the rooftop solar PV footprint can be used to directly plan how much rooftops should be utilized for installing DSG from the urban level. However, the total rooftop area of 2531 buildings in Yeoksam-dong was found to be 757,703 m^2, which is far less than its rooftop solar PV footprint. This indicates that it is not enough to offset the total electricity consumption even if all the rooftops of 2531 buildings in Yeoksam-dong are used for installing DSG. To be 100% self-sufficient in electricity, 734.02% and 611.69% of the total rooftop area are required for the 2531 buildings in Yeoksam-dong, when the solar PV module efficiency is 15% and 18%, respectively.

Figures 36.2 and 36.3 show the solar PV occupancy rate of the individual building in Yeoksam-dong when the solar PV module efficiency is 15% and 18%, respectively. As shown in Fig. 36.2, among a total of 2531 buildings, 247 buildings (i.e., colored in red in Fig. 36.2) and 120 buildings (i.e., colored in orange in Fig. 36.2), respectively, require less than 50% and 100% of their own rooftop areas to offset the electricity consumption with DSG, when the solar PV module efficiency is 15%. That is, only 367 buildings (i.e., 14.5% of total buildings) are eligible for being 100% self-sufficient in electricity in Yeoksam-dong when DSG is installed on their rooftop with 15% module efficiency.

Meanwhile, as shown in Fig. 36.3, among a total of 2531 buildings, 272 buildings (i.e., colored in red in Fig. 36.3) and 129 buildings (i.e., colored in orange in Fig. 36.3), respectively, require less than 50% and 100% of their rooftop areas to offset the electricity consumption with DSG, when the solar PV module efficiency is 18%. That is, still only 401 buildings (i.e., 15.8% of total buildings) are eligible for being 100% self-sufficient in electricity in Yeoksam-dong when DSG is installed on their rooftop with 18% module efficiency.

As shown in Table 36.2, the rooftop solar PV potential and footprint in Samseong-dong was calculated and compared with the building electricity consumption and total rooftop area, respectively. First, the rooftop solar PV potential was examined to consider the building electricity supply and demand separately and to analyze the energy usage aspect. From the perspective of building electricity supply, the rooftop solar PV potential was examined. When the solar PV module efficiency is 15%, the total rooftop solar PV potential in Samseong-dong came out to be 75,590 MWh, whereas it came out to be 90,709 MWh when the solar PV module efficiency is 18%. From the perspective of building electricity demand, the building electricity consumption was examined. The total electricity consumption of 1255

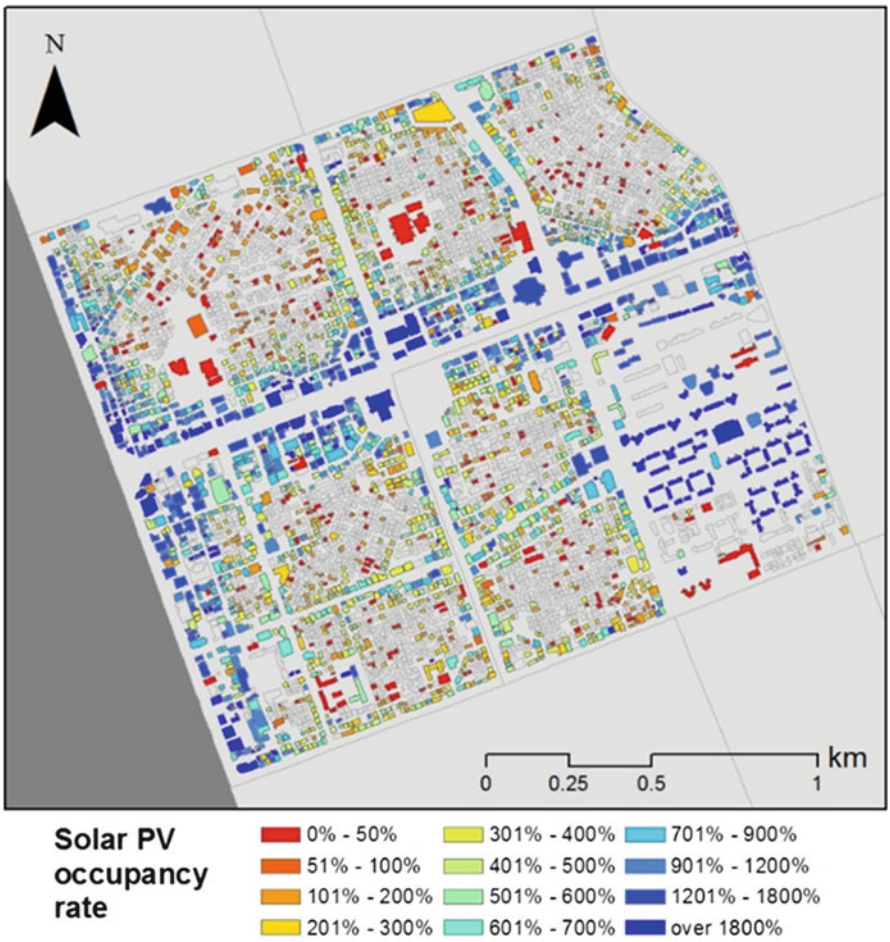

Fig. 36.2 The solar PV occupancy rate of the individual building in Yeoksam-dong (module efficiency: 15%)

buildings in Samseong-dong was found to be 531,887 MWh. According to aforementioned building electricity supply and demand in Samseong-dong, it was shown that the self-sufficiency rate could reach 14.21% and 17.05% when the solar PV module efficiency is 15% and 18%, respectively.

Second, the rooftop solar PV footprint was examined to consider and analyze both building electricity supply and demand at the same time and to analyze the rooftop usage aspect. When the solar PV module efficiency is 15%, the total rooftop solar PV footprint in Samseong-dong came out to be 4,568,403 m^2, whereas it came out to be 3,807,003 m^2 when the solar PV module efficiency is 18%. That is, 4,568,403 m^2 and 3,807,003 m^2 of rooftop area is required for installing DSG to supply the amount of electricity consumed in 1255 buildings in Samseong-dong,

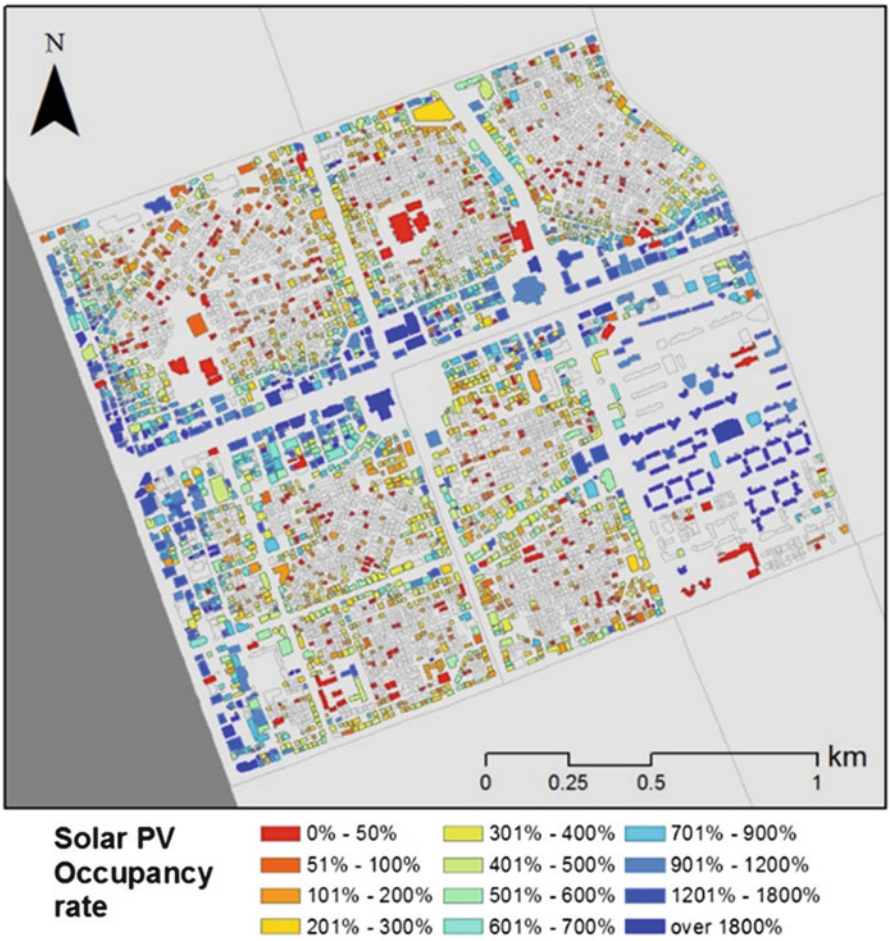

Fig. 36.3 The solar PV occupancy rate of the individual building in Yeoksam-dong (module efficiency: 18%)

Table 36.2 The rooftop solar PV potential and footprint results in Samseong-dong by solar PV module efficiency

Solar PV module efficiency	15%	18%
No. of buildings	1255	
Total electricity consumption (MWh)	531,887	
Rooftop solar PV potential (MWh)	75,590	90,709
Self-sufficiency rate (%)	14.21	17.05
Total rooftop area (m^2)	522,802	
Rooftop solar PV footprint (m^2)	4,568,403	3,807,003
Solar PV occupancy rate (%)	873.83	728.19

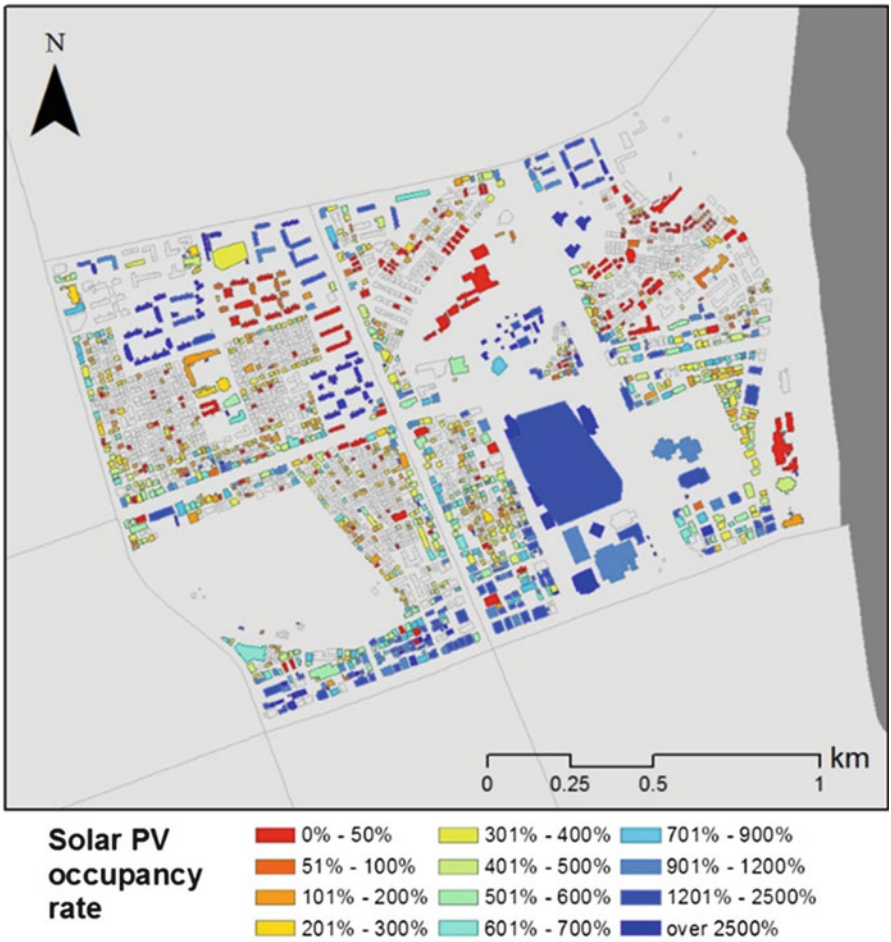

Fig. 36.4 The solar PV occupancy rate of the individual building in Samseong-dong (module efficiency: 15%)

when the solar PV module efficiency is 15% and 18%, respectively. However, the total rooftop area of 1255 buildings in Samseong-dong was found to be 522,802 m^2, which is far less than its rooftop solar PV footprint. This indicates that it is not enough to offset the total electricity consumption even if all the rooftops of 1255 buildings in Samseong-dong are used for installing DSG. To be 100% self-sufficient in electricity, 873.83% and 728.19% of the total rooftop area are required for the 1255 buildings in Samseong-dong, when the solar PV module efficiency is 15% and 18%, respectively.

Figures 36.4 and 36.5 show the solar PV occupancy rate of the individual building in Samseong-dong when the solar PV module efficiency is 15% and 18%, respectively. As shown in Fig. 36.4, among a total of 1255 buildings,

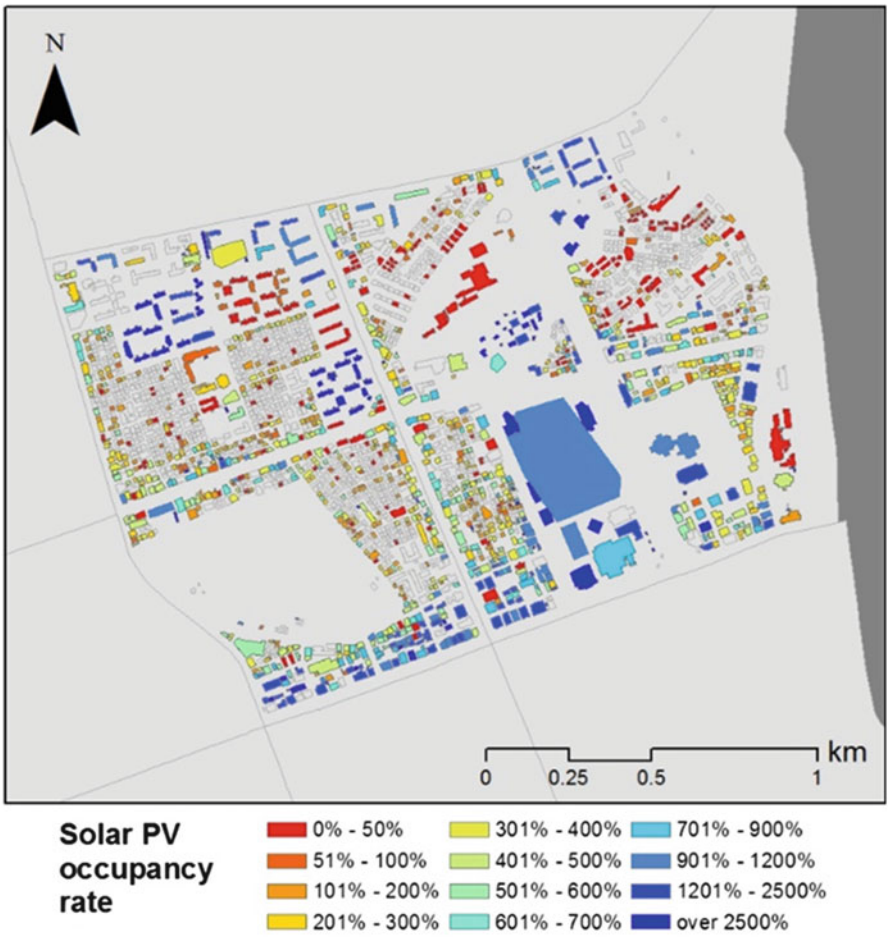

Fig. 36.5 The solar PV occupancy rate of the individual building in Samseong-dong (module efficiency: 18%)

172 buildings (i.e., colored in red in Fig. 36.4) and 50 buildings (i.e., colored in orange in Fig. 36.4), respectively, require less than 50% and 100% of their own rooftop areas to offset the electricity consumption with DSG, when the solar PV module efficiency is 15%. That is, only 222 buildings (i.e., 17.7% of total buildings) are eligible for being 100% self-sufficient in electricity in Samseong-dong when DSG is installed on their rooftop with 15% module efficiency.

Meanwhile, as shown in Fig. 36.5, among a total of 1255 buildings, 176 buildings (i.e., colored in red in Fig. 36.5) and 69 buildings (i.e., colored in orange in Fig. 36.5), respectively, require less than 50% and 100% of their rooftop areas to offset the electricity consumption with DSG, when the solar PV module efficiency is 18%. That is, still only 245 buildings (i.e., 19.5% of total buildings) are eligible for

being 100% self-sufficient in electricity in Samseong-dong when DSG is installed on their rooftop with 18% module efficiency.

36.5 Conclusions

This study proposed a framework for calculating the rooftop solar PV footprint considering building electricity supply and demand from the urban level. Toward this end, this study suggested a novel method for calculating the available rooftop area, rooftop solar PV potential, and rooftop solar PV footprint using data on building information, solar radiation, and energy consumption. To apply the proposed framework to a real example, a case study was conducted for buildings in Yeoksam-dong and Samseong-dong in the Gangnam District, Seoul, South Korea. As a result, the rooftop solar PV potential and footprint in Yeoksam-dong and Samseong-dong was calculated and compared.

In terms of the energy usage aspect, the self-sufficiency rate of 1255 buildings in Samseong-dong (i.e., up to 17.05% with 18% module efficiency) was superior to that of 2531 buildings in Yeoksam-dong (i.e., up to 15.58% with 18% module efficiency).

In terms of the rooftop usage aspect, the solar PV occupancy rate of 2531 buildings in Yeoksam-dong (i.e., at least 611.69% with 18% module efficiency) was superior to that of 1255 buildings in Samseong-dong (i.e., at least 728.19% with 18% module efficiency). That is, Yeoksam-dong requires less rooftop area than Samseong-dong for installing DSG to become 100% self-sufficient in electricity, which indicates that Yeoksam-dong could be more effective in utilizing the rooftop area for installing DSG.

The results of this study show that the energy and rooftop usage performance could differ from each other. Thus, it is important to consider both the self-sufficiency rate and rooftop solar PV footprint when evaluating the building energy performance considering electricity supply and demand from the urban-level.

Nomenclature

DSG	Distributed solar generation
E-AIS	Electronic Architectural administration Information System
ESRI	Environmental Systems Research Institute
GIS	Geographical information system
KASI	Korea Astronomy and Space Science Institute
KNREC	Korea New and Renewable Energy Center
MOLIT	Ministry of Land, Infrastructure, and Transport
nZEB	Nearly zero-energy building
PV	Photovoltaic
SPACEN	Spatial Information Industry Promotion Institute
WRDC	World Radiation Data Centre

Acknowledgments This research was supported by a grant (16CTAP-C117226-01) from the Technology Advancement Research Program (TARP) funded by the Ministry of Land, Infrastructure, and Transport of Korean government.

References

1. Camilo HF, Udaeta MEM, Veiga Gimenes AL, Grimoni JAB (2017) Assessment of photovoltaic distributed generation – issues of grid connected systems through the consumer side applied to a case study of Brazil. Renew Sust Energ Rev 71:712–719. https://doi.org/10.1016/j.rser.2016.12.099
2. Lee M, Koo C, Hong T, Park HS (2014) Framework for the mapping of the monthly average daily solar radiation using an advanced case-based reasoning and a geostatistical technique. Environ Sci Technol. https://doi.org/10.1021/es405293u
3. Hong T, Lee M, Koo C, Jeong K, Kim J (2017) Development of a method for estimating the rooftop solar photovoltaic (PV) potential by analyzing the available rooftop area using Hillshade analysis. Appl Energy 194:320–332. https://doi.org/10.1016/j.apenergy.2016.07.001
4. Gauntlett D, Asmus P (2011) Distributed solar energy generation. Pike Research LCC, Colorado
5. Denholm P, Margolis RM (2008) Land-use requirements and the per-capita solar footprint for photovoltaic generation in the United States. Energy Policy 36:3531–3543. https://doi.org/10.1016/j.enpol.2008.05.035
6. Koo C, Hong T, Park HS, Yun G (2014) Framework for the analysis of the potential of the rooftop photovoltaic system to achieve the net-zero energy solar buildings. Prog Photovolt Res Appl 22:462–478. https://doi.org/10.1002/pip.2448
7. Balcombe P, Rigby D, Azapagic A (2015) Energy self-sufficiency, grid demand variability and consumer costs: integrating solar PV, Stirling engine CHP and battery storage. Appl Energy 155:393–408. https://doi.org/10.1016/j.apenergy.2015.06.017
8. Quoilin S, Kavvadias K, Mercier A, Pappone I, Zucker A (2016) Quantifying self-consumption linked to solar home battery systems: statistical analysis and economic assessment. Appl Energy 182:58–67. https://doi.org/10.1016/j.apenergy.2016.08.077
9. Spatial Information Industry Promotion Institute (SPACEN). http://www.spacen.or.kr/main.do. Accessed 5 Oct 2017
10. World Radiation Data Centre (WRDC). http://wrdc.mgo.rssi.ru/. Accessed 5 Oct 2017
11. Korea Astronomy & Space science Institute (KASI). https://astro.kasi.re.kr:444/index. Accessed 5 Oct 2017
12. Environmental Systems Research Institute (ESRI). https://www.esri.com/en-us/home. Accessed 5 Oct 2017
13. Korea New & Renewable Energy Center (KNREC). http://www.knrec.or.kr/knrec/13/KNREC130110.asp?idx=554. Accessed 5 Oct 2017
14. Green MA (2014) Developments in crystalline silicon solar cells. In: Sol. Cell Mater. Wiley, West Sussex, United Kingdom, pp 65–84
15. Green MA, Hishikawa Y, Warta W, Dunlop ED, Levi DH, Hohl-Ebinger J, Ho-Baillie AWH (2017) Solar cell efficiency tables (version 50). Prog Photovolt Res Appl 25:668–676. https://doi.org/10.1002/pip.2909
16. Gangnamgu. http://www.gangnam.go.kr/main.do. Accessed 5 Oct 2017

Chapter 37
Parametric Optimization of Concentrated Photovoltaic-Thermoelectric Hybrid System

Ravita Lamba and S. C. Kaushik

37.1 Introduction

In light of the overgrowing energy demand together with green energy resources, the sun is considered as a feasible future energy resource. The main route for conversion of solar energy directly into electricity without emitting pollutants to the atmosphere is by using photovoltaic (PV) technology. However, in PV cell, a significant portion of solar spectrum is wasted as heat due to thermalization process and absorption of low-energy photons. In PV conversion process, only photons having energy equal to semiconductor bandgap are converted into electricity effectively. The photons having energy lesser than the bandgap and in excess of bandgap are dissipated as heat which increases the temperature of the PV cell [1]. Further, the efficiency of PV cell has inverse relation with the cell temperature and thus, the efficiency decreases with increasing cell temperature. Therefore, the cooling of PV cells is very important for their efficient working. The cooling of PV cells can be done by various techniques. Thermoelectric generator (TEG) can be an alternative green technology option for cooling of PV cells which exploit the residual heat for additional electricity generation [2]. The TEG can be attached to the backside of PV cell to harvest the excess heat of the PV cell which mostly comes from infrared portion of solar spectrum. Thus, combining the PV and TEG can effectively harvest the solar spectrum. Much attention has been paid towards the novel hybrid PV-TE systems in recent years by many researchers [3, 4]. In hybrid systems, the full solar spectrum can be utilized either by beam splitting method or by integrating TEG to the backside of PV system. Ju et al. used a spectral beam splitter to split the solar spectrum into two parts, one of which is directed to the PV cell and other is directed to the TEG

R. Lamba (✉) · S. C. Kaushik
Centre for Energy Studies, Indian Institute of Technology Delhi, New Delhi, India
e-mail: kaushik@ces.iitd.ac.in

S. Nižetić, A. Papadopoulos (eds.), *The Role of Exergy in Energy and the Environment*, Green Energy and Technology,
https://doi.org/10.1007/978-3-319-89845-2_37

[5]. Van Sark proposed the idea of PV-TEG hybrid system in which the wasted thermal energy of concentrated photovoltaic (CPV) system can be utilized in TEG [6]. Wu et al. developed and analysed the performance of glazed and unglazed PV-TE hybrid system theoretically [7]. They have taken nano-fluid as heat sink for TE module to decrease the temperature of cold junction of TE module which results in enhanced temperature difference between hot and cold junctions of TE module. Lin et al. established the thermodynamic model of the PV-TE hybrid system and analysed the performance and load matching of hybrid system [8]. Although, in TEG systems, the performance has been evaluated by considering a constant temperature difference across the TEG [9, 10]. However, in case of PV-TEG system, the thermal input is nearly constant and temperature difference varies because the TEG is connected between the backside of PV module and heat sink for heat transfer between TEG and reservoirs. When no load is connected to the terminals of TEG, heat transfer takes place only by conduction between hot and cold junctions due to temperature difference. However, when electrical load is connected across the terminals of TEG, electrical current flows through the device depending on load resistance and thus, Peltier heating, Joule heating and Thomson heating occur through the device which change the temperature difference across the device. Gomex et al. numerically determined the actual temperature of TEG and the effect of thermal resistance on optimum working conditions has been presented [11].

In this chapter, a numerical model based on first and second laws of thermodynamics has been developed for a hybrid CPV-TEG system and solved in MATLAB using an iterative method. The temperatures of PV cell and both junctions of TEG have been calculated, and the optimum working conditions have been determined for the hybrid system.

37.2 Thermodynamic Model

The schematic diagram of proposed hybrid CPV-TEG system is shown in Fig. 37.1. It consists of, from top to bottom, a concentrator, a PV module and a TEG module. The TEG is attached to the backside of the PV module, and a heat sink is attached to the cold side of the TEG. The PV module consists of series-connected crystalline silicon PV cells, and the TEG consists of electrically series- and thermally parallel-connected thermoelements. In this hybrid CPV-TEG system, the residual heat generated in the PV module acts as a heat source for TEG and thus can be utilized effectively in TEG to generate additional electricity. Therefore, the performance of the hybrid system can be improved. In the combined CPV-TEG system, the CPV and TEG modules are thermally connected and electrically isolated. The electrical equivalent circuit of hybrid system is shown in Fig. 37.2.

In order to study the overall performance of combined system, the two subsystems are analysed one by one. To develop the theoretical model of combined system, the following simplifying assumptions have been taken:

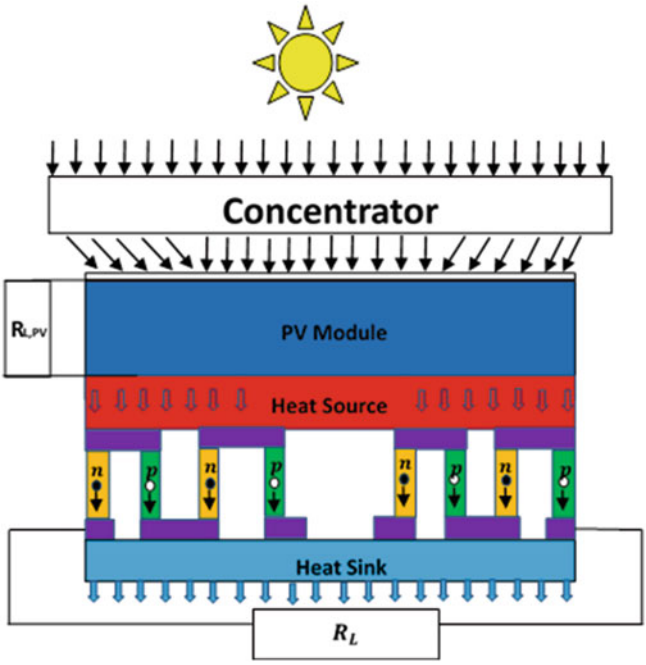

Fig. 37.1 Schematic diagram of hybrid CPV-TEG system

Fig. 37.2 The electrical equivalent circuit of hybrid CPV-TEG system

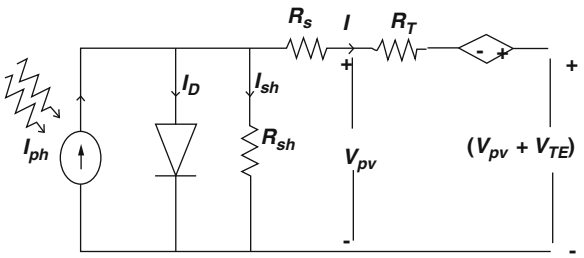

1. For simplifying the analysis, steady-state conditions have been considered.
2. The temperature gradient along the thickness of glass cover has been considered negligible due to very less thickness of glass cover.
3. The system is insulated from two sides, and therefore, one-dimensional heat transfer has been considered for the analysis.
4. Convective and radiative heat transfer from the sides of thermoelectric couples are neglected.

37.2.1 PV Module

The solar irradiation incident on the concentrator is concentrated on PV module. After absorption, a part of irradiation is converted into electricity by PV module, some part is lost from the upper surface of PV module to ambient via convection and radiation, and rest is conducted to the TEG from the backside of the PV module. The TEG converts a portion of thermal energy absorbed by it from PV module into the electricity using Seebeck effect, and a major part of it is rejected to the heat sink. Thus, the energy balance equation for PV module can be given as [12]:

$$CGA_{\mathrm{PV}}\tau_{\mathrm{g}}[\alpha_{\mathrm{c}}\beta_{\mathrm{c}} + \alpha_{\mathrm{T}}(1-\beta_{\mathrm{c}})] = \varepsilon\sigma A_{\mathrm{PV}}\left(T_{\mathrm{PV}}^4 - T_{\mathrm{sky}}^4\right) + U_{\mathrm{t}}A_{\mathrm{PV}}(T_{\mathrm{PV}} - T_{\mathrm{a}}) + U_{\mathrm{b}}A_{\mathrm{PV}}(T_{\mathrm{PV}} - T_{\mathrm{h}}) + \eta_{\mathrm{PV}}\beta_{\mathrm{c}}\tau_{\mathrm{g}}CGA_{\mathrm{PV}} \quad (37.1)$$

where $U_{\mathrm{t}} = ((L_{\mathrm{g}}/k_{\mathrm{g}}) + (1/h_{\mathrm{conv}}))^{-1}$and $U_{\mathrm{b}} = ((L_{\mathrm{PV}}/k_{\mathrm{PV}}) + (L_{\mathrm{T}}/k_{\mathrm{T}}))^{-1}$ are the heat transfer coefficients from the top surface of PV module to ambient through conduction and convection and from the bottom surface of PV module to the TE module by conduction, respectively [12], and h_{conv} is the convective heat transfer coefficient from top surface of PV module to ambient.

The temperature-dependent efficiency and power output of PV module are given, respectively, by [13]:

$$\eta_{\mathrm{PV}} = \eta_{\mathrm{ref}}[1 - \beta_0(T_{\mathrm{PV}} - T_{\mathrm{ref}})] \quad (37.2)$$

$$P_{\mathrm{PV}} = \eta_{\mathrm{PV}}A_{\mathrm{PV}}CG \quad (37.3)$$

37.2.2 TE Module

The heat conducted from the backside of PV module to the hot side of TE module can be utilized partly to generate electricity, and rest is rejected to the heat sink from the cold side of TE module. The basic unit of a TEG consists of p-type and n-type semiconductor elements. The conversion of heat into electricity is based on Seebeck and Peltier effects. Along with these effects, there exists Fourier's heat conduction due to temperature gradient between the junctions, Joule's heat due to electrical current flowing through TEG module and Thomson's heat due to temperature gradient and electrical current both. Based on these effects, the rate of heat flow from the backside of PV module to hot side of TE module and from the cold side of TEG module to the cold reservoir can be written, respectively, as follows [14, 15]:

$$Q_{\mathrm{h}} = N\left(\alpha_{\mathrm{h}}T_{\mathrm{h}}I_{\mathrm{TE}} + K(T_{\mathrm{h}} - T_{\mathrm{c}}) - \frac{1}{2}I_{\mathrm{TE}}^2R - \frac{1}{2}\mu(T_{\mathrm{h}} - T_{\mathrm{c}})I_{\mathrm{TE}}\right) \quad (37.4)$$

$$Q_c = N\left(\alpha_c T_c I_{TE} + K(T_h - T_c) + \frac{1}{2}I_{TE}^2 R + \frac{1}{2}\mu(T_h - T_c)I_{TE}\right) \tag{37.5}$$

where $R = ((\rho_p L_p/A_p) + (\rho_n L_n/A_n) + (4R_{ec}/A_{TE}))$ and $K = ((k_p A_p/L_p) + (k_n A_n/A_L))$ are the electrical resistance and thermal conductance of one thermoelement pair of the TEG and R_{ec} is the electrical contact resistance. The electrical resistance and thermal conductance of the TE module are given as $R_{TE} = NR = \frac{2N(\rho L + 2R_{ec})}{A_{TE}}$ and $K_{TE} = NK$. The fill factor, $FF = \frac{2NA_{TE}}{A}$, is the ratio of area covered by thermoelements in the TE module to that of the entire TE module. The heat flowing inside the hot and cold junctions of TE module via heat conduction, Peltier heating, Joule heating and Thomson heating as given by Eq. (37.4) and (37.5), respectively, should be matched with the amount of heat transfer from the PV module to the hot side of TE module through contact pads and amount of heat transfer from the cold side of TE module through the heat sink which are given as, respectively:

$$Q_h = \frac{(T_{PV} - T_h)}{\psi_h} \tag{37.6}$$

$$Q_c = \frac{(T_c - T_a)}{\psi_c} \tag{37.7}$$

where ψ_h and ψ_c are the thermal resistance between PV module and hot side of TE module and between cold side of TE module and heat sink, respectively, which are equal to the inverse of the product of heat transfer coefficient and surface area. Therefore, Eq. (37.4) should be matched with Eqs. (37.6), and (37.5) should be matched with Eq. (37.7).

$$N\left(\alpha_h T_h I_{TE} + K(T_h - T_c) - \frac{1}{2}I_{TE}^2 R - \frac{1}{2}\mu(T_h - T_c)I_{TE}\right) = \frac{(T_{PV} - T_h)}{\psi_h} \tag{37.8}$$

$$N\left(\alpha_c T_c I_{TE} + K(T_h - T_c) + \frac{1}{2}I_{TE}^2 R + \frac{1}{2}\mu(T_h - T_c)I_{TE}\right) = \frac{(T_c - T_a)}{\psi_c} \tag{37.9}$$

The power output of TEG system can be written as follows:

$$\begin{aligned} P_{TE} &= Q_h - Q_c = I_{TE}^2 R_L \\ &= N\left[(s_h T_h - s_c T_c)I_{TE} - I_{TE}^2 R - \mu I_{TE}(T_h - T_c)\right] \end{aligned} \tag{37.10}$$

The electric current flowing through TEG can be written as:

$$I_{TE} = \frac{N[(s_h T_h - s_c T_c) - \mu(T_h - T_c)]}{R_{TE}(1 + m)} \tag{37.11}$$

where $m = \frac{R_L}{R_{TE}} = \frac{R_L A(FF)}{4N^2(\rho L + 2R_c)}$ is the ratio of electrical load resistance connected to TE module to the internal electrical resistance of TE module. By using expression of R_{TE}, K_{TE} and FF, Eqs. (37.8) and (37.9) can be written as follows:

$$P_1 T_h^2 + P_2 T_c^2 + P_3 T_h T_c + P_4 T_h + P_5 T_c + P_6 = 0 \tag{37.12}$$

$$Q_1 T_h^2 + Q_2 T_c^2 + Q_3 T_h T_c + Q_4 T_h + Q_5 T_c + Q_6 = 0 \tag{37.13}$$

where the expressions for P_1 through P_6 and Q_1 through Q_6 and the temperature-dependent material properties of Bi_2Te_3 are given in Appendix A [16].

Equations (37.1), (37.12) and (37.13) are non-linear equations and cannot be solved analytically. Therefore, iterative methods have been used to solve these equations numerically.

After calculating the temperature of PV module, hot side and cold side of the TE module, the voltage, power output and efficiency of TE module can be given as:

$$V_{TE} = I_{TE} R_L = \frac{N[(s_h T_h - s_c T_c) - \mu(T_h - T_c)]m}{(1+m)} \tag{37.14}$$

$$P_{TE} = I_{TE}^2 R_L = \frac{mA(FF)[(s_h T_h - s_c T_c) - \mu(T_h - T_c)]^2}{4(\rho L + 2R_c)(1+m)^2} \tag{37.15}$$

$$\eta_{TE} = \frac{P_{TE}}{Q_h} \tag{37.16}$$

The overall power output and efficiency of hybrid CPV-TEG system can be given as:

$$P = P_{PV} + P_{TE} \tag{37.17}$$

$$\eta = \frac{P}{CGA_{PV}} \tag{37.18}$$

37.3 Results and Discussion

The performance of the hybrid CPV-TEG system depends on various parameters such as solar irradiation, concentration ratio, electrical resistance ratio and fill factor of TE module, height and cross section of TE module, temperature of hot and cold side of TE module and thermal resistance between TE module and reservoirs. The various parameters used in modeling of PV-TEG hybrid system are given in Table 37.1. In this study, the fill factor, height and cross section of TE module have been fixed, and the effect of remaining parameters have been studied. Since the expressions for temperatures of PV module, hot and cold side of TE module cannot be found out explicitly, therefore, a MATLAB Simulink model has been designed to calculate the various temperatures by solving Eqs. (37.1), (37.12) and (37.13) iteratively based on a numerical method. In this Simulink model, by defining various optical, design, geometric and operating parameters, the various temperatures have been calculated for different resistance and concentration ratios by providing the

Table 37.1 Values of parameters used in modelling of hybrid CPV-TEG system [11, 14]

Parameter	Symbol	Value
Thermal conductivity of PV cell	k_{PV}	148 W/mK
Thermal conductivity of glass cover	k_g	1.1 W/mK
Thermal conductivity of Tedlar	k_T	0.2 W/mK
Absorptivity of PV module	α_c	0.9
Absorptivity of Tedlar	α_T	0.5
Packing factor of PV module	β_c	0.85
Temperature coefficient of PV module	β_0	0.005 K^{-1}
Thickness of PV cell	L_{PV}	0.0003 m
Thickness of glass cover	L_g	0.003 m
Thickness of Tedlar	L_T	0.000175 m
PV module efficiency at standard test conditions (STC)	η_{ref}	13%
Transmissivity of glass cover	τ_g	0.95
Ambient temperature	T_a	300 K
Electrical contact resistance	R_{ec}	3.41×10^{-10} Ωm^2
Number of pairs	N	127
Module surface area	A	9.0×10^{-4} m^2
Thermoelectric area	A_{TE}	8.7×10^{-7} m^2
Length of TE module leg	L_{TE}	1.6×10^{-3} m

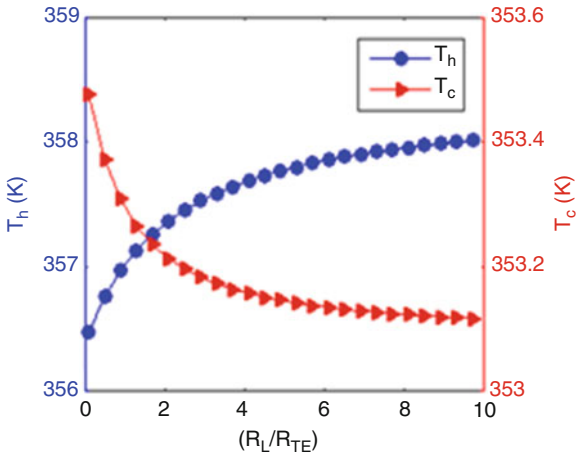

Fig. 37.3 Variation of hot side and cold side temperature of TEG with resistance ratio

initial guess values of temperatures to solve Eqs. (37.1), (37.12) and (37.13) iteratively. Once these temperatures are known, the voltage, current, power output and efficiency of PV module, TE module and hybrid CPV-TEG system can be determined.

Figure 37.3 shows the actual hot side and cold side temperatures varying with resistance ratio of TE module. Both hot side and cold side temperatures change rapidly at lower resistance ratios. At higher resistance ratios, the change becomes

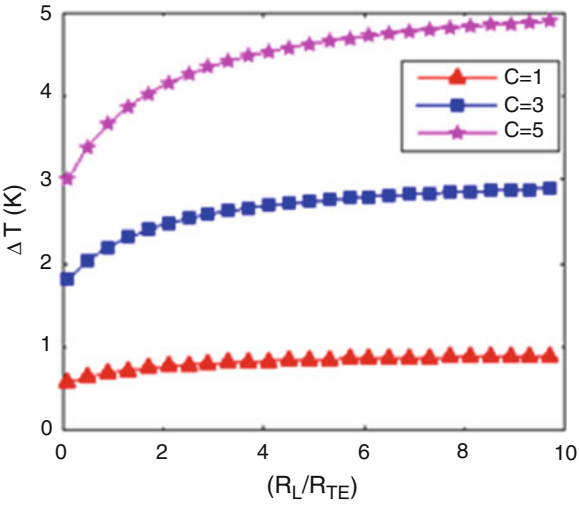

Fig. 37.4 Effect of concentration ratio on variation of hot side and cold side temperature difference (ΔT) with resistance ratio

lesser. The magnitude of change in hot side temperature is large as compared to cold side temperature because the hot side temperature depends on PV module temperature which is varying continuously with solar irradiation. Further, the thermal resistance between PV module and hot side of TE module and between cold side of TE module and heat sink is not same which results in different magnitudes of variation. The effect of concentration ratio on temperature difference between hot and cold side of TE module has been plotted in Fig. 37.4. It shows that the magnitude of temperature difference is higher for higher values of concentration ratio due to increased temperature of PV module at higher concentration ratio which further results in increased hot side temperature of TE module. The magnitude of change in temperature difference is higher at lower resistance ratios. As the resistance ratio increases to higher values where the TE module acts as an open circuit due to very large load resistance and no current flows through the device, thus, Peltier heating, Joule heating and Thomson heating diminish, causing almost constant temperature resistance.

The effect of concentration ratio on TE module voltage and electric current has been shown in Figs. 37.5 and 37.6, respectively. Both voltage and current are higher at higher concentration ratios due to increased temperature difference between hot and cold junctions at higher concentration ratios. The TE voltage increases and TE current decreases with increase in resistance ratio which is obvious because higher load resistance causes higher voltage and lower current. However, the rate of increment in TE voltage and rate of decrement in TE current are higher at lower resistance ratios.

The effect of concentration ratio on power output of TE module has been shown in Fig. 37.7. The power output increases with increase in concentration ratio because the PV module temperature and thus hot side temperature of TE module increases at higher concentration ratio, which results in increased temperature difference

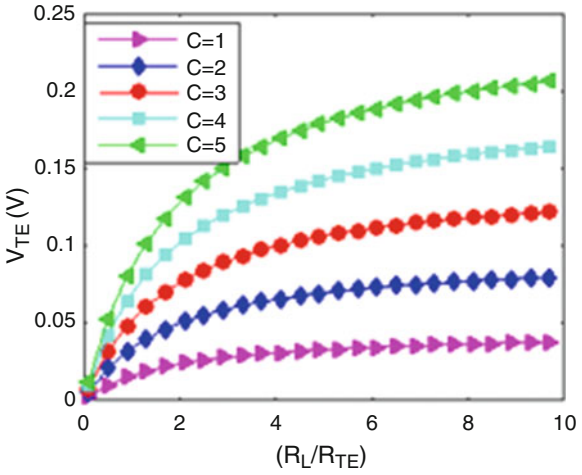

Fig. 37.5 Effect of concentration ratio on variation of TEG voltage with resistance ratio

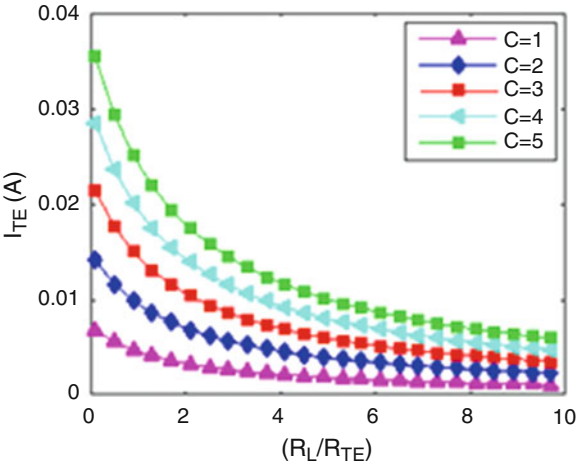

Fig. 37.6 Effect of concentration ratio on variation of TEG current with resistance ratio

between hot side and cold side of TE module. The increased temperature difference increases the Seebeck voltage, and thus power output increases. The power output first increases and becomes maximum at a particular value of resistance ratio and then further increase in resistance ratio decreases the power output. It is clear that the power output is not maximum when the load resistance is matched with the internal resistance of TE module which is the case for conventional thermoelectric devices to get maximum power output. Since the temperature difference between hot and cold side of TE module has been considered constant in the conventional TE devices. However, it should not be considered constant for real TE devices and should be determined by solving energy balance equations at hot and cold side of TE device based on first law of thermodynamics. The maximum power output occurs when load resistance is equal to $\sqrt{1+Z\bar{T}_m}$ times the internal resistance of TE module. The

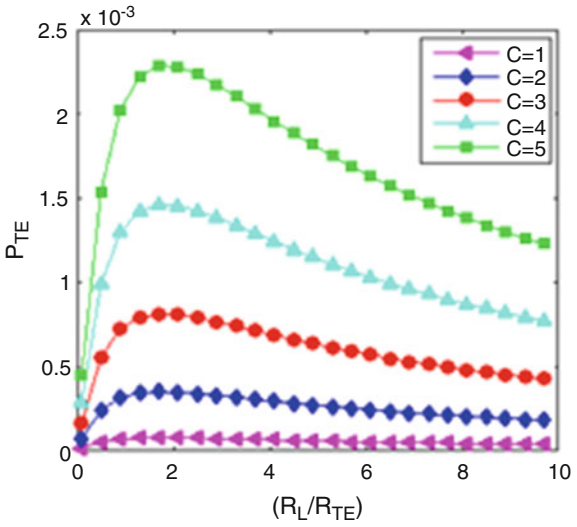

Fig. 37.7 Effect of concentration ratio TEG power output

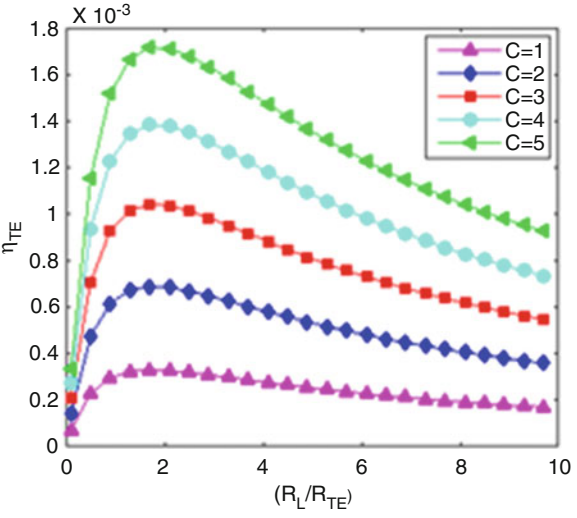

Fig. 37.8 Effect of concentration ratio on TEG efficiency

optimum value of resistance ratio is 1.7 for maximum power output and it is same for all concentration ratios. The effect of concentration ratio on TE module efficiency has been plotted in Fig. 37.8. The efficiency increases with increase in concentration ratio similar to the reason being explained earlier for TE module power output. The trend of efficiency variation with the resistance ratio is similar to that of power output with the resistance ratio. The optimum value of resistance ratio is 1.7 for maximum efficiency and it is same for all concentration ratio values. It is interesting to note that the optimum value of resistance ratio is same for both maximum power output and maximum efficiency similar to solar thermoelectric generator where the optimum

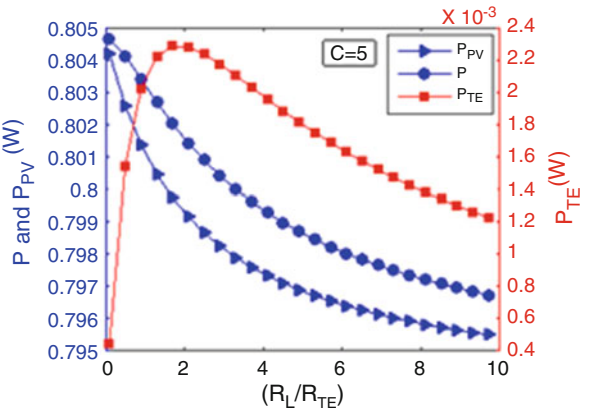

Fig. 37.9 Variation of power output of CPV, TEG and CPV-TEG with resistance ratio

resistance ratio is same for both maximum power output and maximum efficiency conditions which is desired. However, for conventional thermoelectric devices, the optimum conditions are not same for maximum power output and maximum efficiency and therefore, either maximum power output or maximum efficiency can be achieved at an optimum resistance ratio.

The variation of power output of PV module, TE module and CPV-TEG system has been indicated in Fig. 37.9 for concentration ratio of 5. It is clear that both the PV module and hybrid CPV-TEG system power output decrease continuously with increasing resistance ratio. The TE module power output first increases and then decreases with increase in resistance ratio after attaining maximum value at a particular value of resistance ratio. The power output of hybrid system varying with resistance ratio follows the similar trend of PV module power output varying with resistance ratio because contribution of PV power is very high as compared to that of TE module. However, the power of hybrid system is higher than that of PV due to added contribution from TE module power output. Further, the contribution of TE module power output decreases rapidly at higher resistance ratios. The efficiencies of PV module, TE module and hybrid CPV-TEG system varying with resistance ratio have been shown in Fig. 37.10 for concentration ratio of 5. The efficiency of TE module first increases and then decreases after attaining maximum value with increase in resistance ratio similar to power output trend of TE module. The PV module and hybrid CPV-TEG system efficiencies also decrease with increase in resistance ratio. However, the rate of decrement is different for PV module, TE module and hybrid system. Further, the efficiency of TE module is very less as compared to that of PV module.

The variation of power output and efficiency of TE module with CG product for three different values of resistance ratio have been shown in Figs. 37.11 and 37.12 respectively. The power output and efficiency both are highest at optimum resistance ratio value of 1.7 which was determined earlier. The other two resistance ratio values are the maximum and minimum values of the chosen range of resistance ratio and the TE power output and efficiency corresponding to these values of resistance ratio are

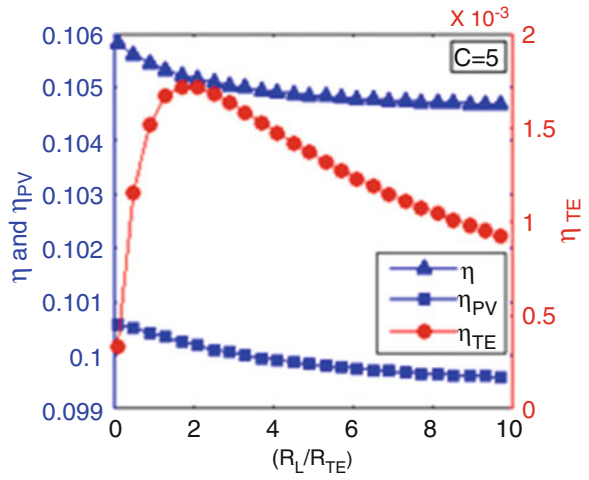

Fig. 37.10 Variation of efficiency of CPV, TEG and CPV-TEG with resistance ratio

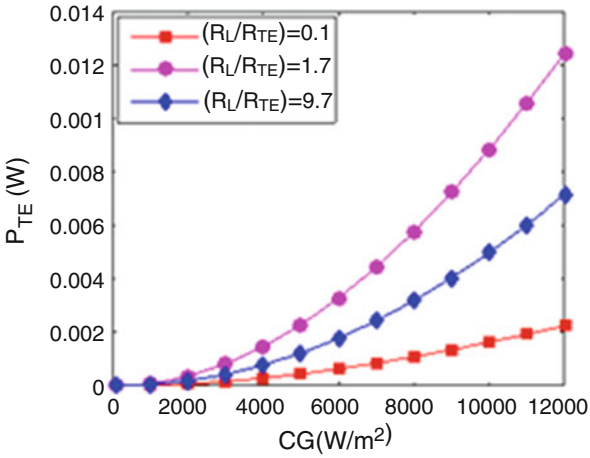

Fig. 37.11 Effect of resistance ratio on variation of TEG power output with product of solar irradiance and concentration ratio

small compared to that of at optimum resistance ratio value for all CG product values. The TE module power output and efficiency both increase with increase in *CG* product due to increased temperature of PV module and thus, increased temperature difference between the hot and cold junctions of TE module.

The variation of power output of PV module, TE module and hybrid CPV-TEG system have been plotted in Fig. 37.13 for optimum resistance ratio value of 1.7. The power output of PV module and hybrid CPV-TEG system first increase with increase in product of solar irradiance and concentration ratio (CG) and gets maximum value at a particular value of CG product and then decreases with further increase in CG product value. Thus, there exists an optimum value of CG product for maximum power output of PV or hybrid CPV-TEG system. The contribution of TE module power output to the hybrid CPV-TEG system power output increases continuously

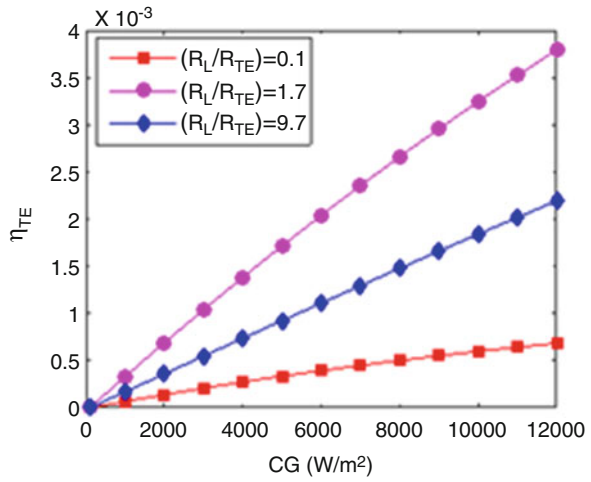

Fig. 37.12 Effect of resistance ratio on variation of TEG efficiency with product of solar irradiance and concentration ratio

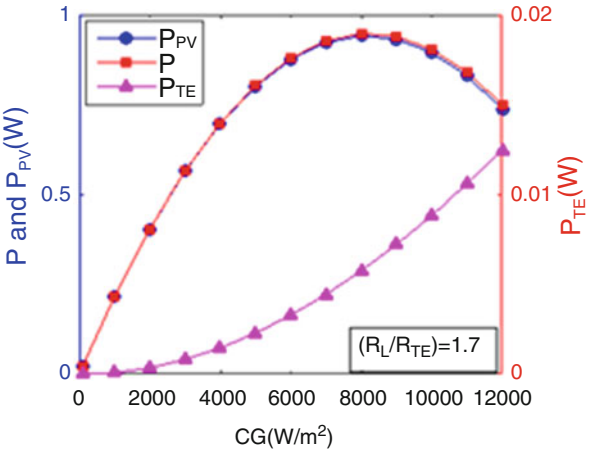

Fig. 37.13 Variation of power output of CPV, TEG and CPV-TEG with CG product

with increase in CG product value due to increased temperature difference between hot and cold junction of TE module at higher concentration ratio. However, at smaller values of CG product, the contribution of TE module power output is very less as compared to that of PV module. The variation of efficiency of PV module, TE module and hybrid CPV-TEG system with product of solar irradiance and concentration ratio (CG) has been plotted in Fig. 37.14 for optimum resistance ratio value of 1.7. The efficiency of PV module and hybrid CPV-TEG system decrease with increase in CG product due to increased temperature of PV module at higher CG values. However, the efficiency of TE module increases with increase in CG value due to increased temperature of hot side of TE module. It is clear that the efficiency of hybrid system is higher than that of PV system alone.

Figure 37.15 shows the variation of maximum power output of CPV and TEG modules with cold side thermal resistance of TE module and hot side thermal

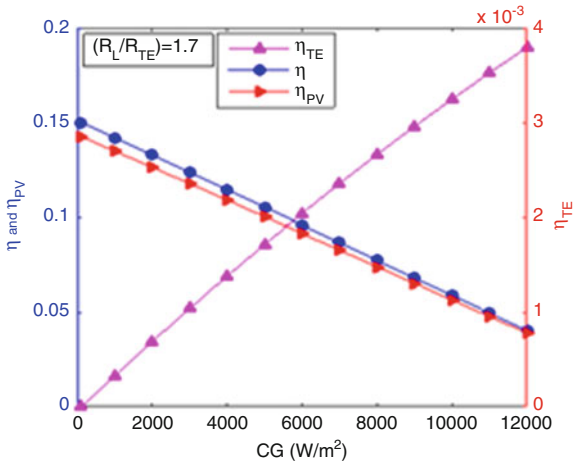

Fig. 37.14 Variation of efficiency of CPV, TEG and CPV-TEG with CG product

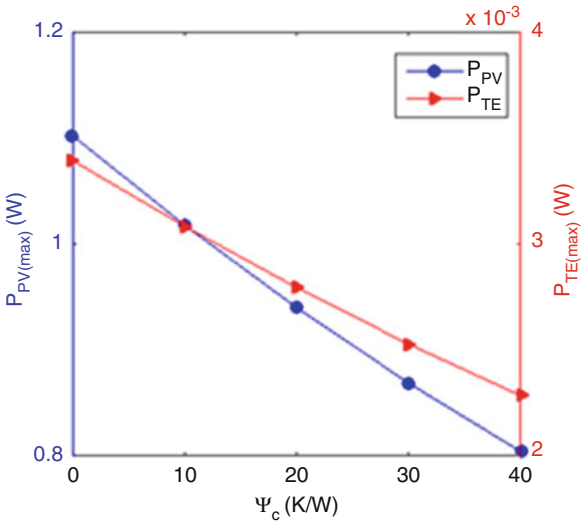

Fig. 37.15 Variation of maximum power output of CPV and TEG with thermal resistance at cold side of TEG

resistance is kept constant. It is clear that the power output of CPV and TEG modules system decreases with increase in cold side thermal resistance and become almost zero at very high values of thermal resistance. Since, at higher cold side thermal resistance, the heat transfer from cold junction to heat sink becomes very less and thus, the cold side temperature does not decrease which causes very small temperature difference between hot side and cold side of TE module which replace in very low power output. Similar to power output trend of PV module and TE module, the variation of maximum efficiency of PV module and TE module with cold side thermal resistance has been plotted in Fig. 37.16. The maximum efficiencies of both PV module and TE module decrease with increase in thermal resistance;

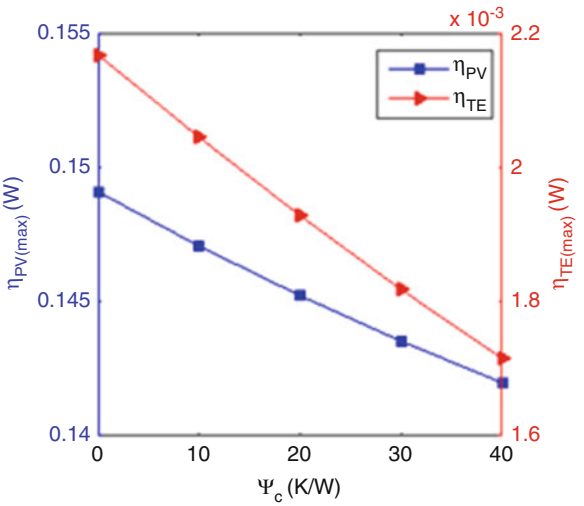

Fig. 37.16 Variation of maximum efficiency of CPV and TEG with thermal resistance at cold side of TEG

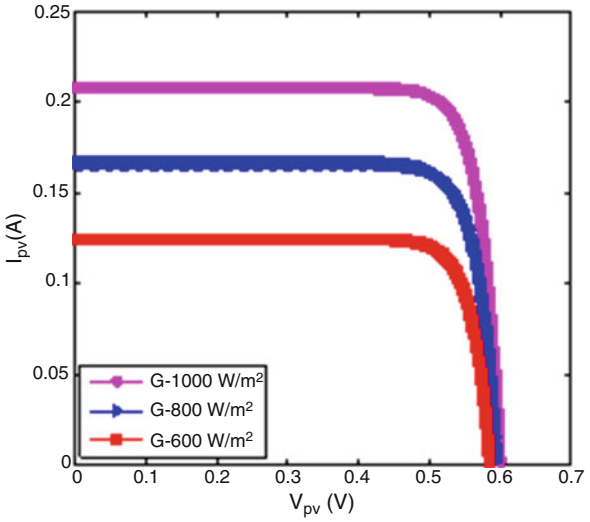

Fig. 37.17 Effect of solar irradiance on variation of PV current with PV voltage

the reason being similar to that of power output variation. The effect of solar irradiance on PV current and power output with $C = 1$ has been shown in Figs. 37.17 and 37.18, respectively. It is clear that both the current and power output increase with increase in solar irradiance. The power output and current of hybrid CPV-TEG system for CG = 1 W/m^2 are almost same to that of PV system because at lower CG values, the contribution of TE system is negligible.

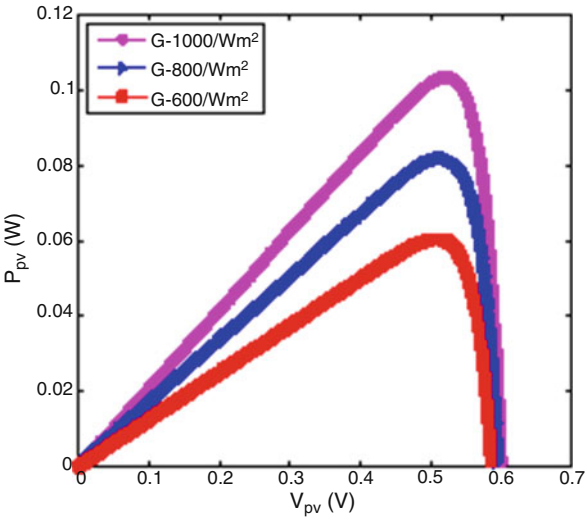

Fig. 37.18 Effect of solar irradiance on variation of PV power with PV voltage

37.4 Conclusions

In this paper, a thermodynamic model based on first and second laws of thermodynamics has been investigated for a hybrid CPV-TEG system to analyse its performance. The temperatures of PV cell and hot and cold junction temperatures of TEG have been calculated by solving energy balance equations for PV and TE modules in MATLAB using an iterative method. The optimum working conditions have been determined for the hybrid system. The results show that the power output and efficiency of hybrid CPV-TEG system are higher than that of PV system alone by attaching the TE module to the back side of PV module to harvest the residual heat from PV module. The concentration ratio and resistance ratio have been optimized for maximum power output and efficiency of the hybrid system. Both the power output and efficiency of TE module are highest at optimum resistance ratio value of 1.7 which are 2.285 mW and 0.172%, respectively, at a fixed GC = 5000 W/m^2. The optimum CG value at which the power output of PV system and CPV-TEG system is maximum is 8000 W/m^2 for optimum resistance ratio value of 1.7. The increase in power output and efficiency of hybrid CPV-TEG system are almost 1% and 5%, respectively, as compared to PV system alone for the given system. The power output of PV system and TE module increases by 16.87% and 22.28%, respectively, and the efficiency of PV system and TE module increases by 2.25% and 12.5%, respectively, as the cold side thermal resistance decreases from 40 K/W to 20 K/W.

Nomenclature

A	Area (m^2)
C	Concentration ratio
FF	Fill factor
G	Solar irradiation (W/m^2)
H	Heat transfer coefficient (W/m^2K)
I	Electric current (A)
k	Thermal conductivity (W/mK)
L	Length of thermocouple element
m	Resistance ratio
N	Number of p-n thermocouple elements
P	Electrical power (W)
Q	Heat (W)
R	Electrical resistance (Ω)
s	Seebeck coefficient (V/K)
T	Temperature (K)
U	Overall heat transfer coefficient (W/m^2K)
V	Voltage (V)
Z	Figure of merit (1/K)

Greek letters

α	Absorptivity
β_c	Packing factor of PV module
β_0	PV cell temperature coefficient (1/K)
ε	Surface emissivity of PV module
μ	Thomson coefficient (V/K)
σ	Stefan Boltzmann coefficient (W/m^2K^4)
ρ	Electrical resistivity (Ω-m)
τ	Transmissivity
η	Efficiency
ψ	Thermal resistance (K/W)

Subscripts

a	Ambient
b	Bottom
c	Cold side of TEG
ec	Electrical contact
g	Glass cover
h	Hot side of TEG
L	Load
max	Maximum
n	n-type semiconductor material
p	p-type semiconductor material
PV	Photovoltaic module
ref	Reference

sky	Sky
TE	Thermoelectric module
T	Tedlar
t	Top

Appendix-A

The temperature-dependent material properties of Bi_2Te_3 and the expressions for P_1 through P_6 and Q_1 through Q_6 are defined as:

$s = [s_p - (-s_n)] = (44448.0 + 1861.2T_m - 1.9810T_m^2) \times 10^{-9}$	$\rho_n = \rho_p = (5112.0 + 163.4T_m + 0.6279T_m^2) \times 10^{-10}$
$k_n = k_p = (62605.0 - 277.7T_m + 0.4131T_m^2) \times 10^{-4}$	$\mu = [\mu_p - (-\mu_n)] = (1861.2T_m - 3.962T_m^2) \times 10^{-9}$
$P_1 = \dfrac{\alpha_h A(\mathrm{FF})[\mu(m+1) - \alpha_h(2m+1)]\psi_h}{8(\rho L + 2R_{ec})(m+1)^2}$	$Q_1 = \dfrac{\alpha_h A(\mathrm{FF})[\mu(m+1) - \alpha_h]\psi_c}{8(\rho L + 2R_c)(m+1)^2}$
$P_2 = \dfrac{\alpha_c A(\mathrm{FF})[\mu(m+1) + \alpha_c]\psi_h}{8(\rho L + 2R_{ec})(m+1)^2}$	$Q_2 = \dfrac{\alpha_c A(\mathrm{FF})[\mu(m+1) + \alpha_c(2m+1)]\psi_c}{8(\rho L + 2R_c)(m+1)^2}$
$P_3 = \dfrac{-A(\mathrm{FF})[\mu(m+1)(\alpha_h + \alpha_c) - 2m\alpha_h\alpha_c]\psi_h}{8(\rho L + 2R_{ec})(m+1)^2}$	$Q_3 = \dfrac{-A(\mathrm{FF})[\mu(m+1)(\alpha_h + \alpha_c) + 2m\alpha_h\alpha_c]\psi_c}{8(\rho L + 2R_c)(m+1)^2}$
$P_4 = \dfrac{-(kA(\mathrm{FF})\psi_h + L)}{L}$	$Q_4 = \dfrac{-kA(\mathrm{FF})\psi_c}{L}$
$P_5 = \dfrac{kA(\mathrm{FF})\psi_h}{L}$	$Q_5 = \dfrac{kA(\mathrm{FF})\psi_h + L}{L}$
$P_6 = T_{PV}$	$Q_6 = -T_a$

References

1. Makki A, Omer S, Sabir H (2015) Advancements in hybrid photovoltaic systems for enhanced solar cells performance. Renew Sust Energ Rev 41:658–684
2. Yang D, Yin H (2011) Energy conversion efficiency of a novel hybrid solar system for photovoltaic, thermoelectric, and heat utilization. IEEE Trans Energy Convers 26(2):662–670
3. Deng Y, Zhu W, Wang Y, Shi Y (2013) Enhanced performance of solar-driven photovoltaic–thermoelectric hybrid system in an integrated design. Sol Energy 88:182–191
4. Zhang J, Huan Y, Yuang L (2014) Performance estimation of photovoltaic thermoelectric hybrid systems. Energy 78:895–903
5. Ju X, Wang Z, Flamant G, Zhao W (2012) Numerical analysis and optimization of a spectrum splitting concentration photovoltaic–thermoelectric hybrid system. Sol Energy 86 (6):1941–1954
6. VanSark WGJHM (2011) Feasibility of photovoltaic–thermoelectric hybrid modules. Appl Energy 88:2785–2790
7. Wu G, Yu X (2014) A holistic 3D finite element simulation model for thermoelectric power generator element. Energy Convers Manag 86:99–110

8. Lin J, Liao T, Lin B (2015) Performance analysis and load matching of a photovoltaic–thermoelectric hybrid system. Energy Convers Manag 105:891–899
9. Tian H, Sun X, Jia Q, Liang X, Shu G, Wang X (2015) Comparison and parameter optimization of a segmented thermoelectric generator by using the high temperature exhaust of a diesel engine. Energy 84:121–130
10. Wu YY, Wu SY, Xiao L (2015) Performance analysis of photovoltaic–thermoelectric hybrid system with and without glass cover. Energy Convers Manag 93:151–159
11. Gomez M, Reid R, Ohara B, Lee H (2013) Influence of electrical current variance and thermal resistances on optimum working conditions and geometry for thermoelectric energy harvesting. J Appl Phys 113(17):174908
12. Najafi H, Woodbury KA (2013) Modeling and analysis of a combined photovoltaic–thermoelectric power generation system. J Sol Energy Eng 135(3):031013
13. Evans D (1981) Simplified method for predicting photovoltaic array output. Sol Energy 27:555–560
14. Lamba R, Kaushik SC (2016) Modeling and performance analysis of a concentrated photovoltaic–thermoelectric hybrid power generation system. Energy Convers Manag 115:288–298
15. Lamba R, Kaushik SC (2017) Thermodynamic analysis of thermoelectric generator including influence of Thomson effect and leg geometry configuration. Energy Convers Manag 144:388–398
16. Xuan XC, Ng KC, Yap C, Chua HT (2002) The maximum temperature difference and polar characteristic of two-stage thermoelectric coolers. Cryogenics 42(5):273–278

Chapter 38
Solar-Powered Drip Irrigation System

M. W. Akram, Yi Jin, Guiqiang Li, Zhu Changan, and J. Aiman

38.1 Introduction

Water and energy are the key drivers of agriculture sector. It consumes 85% of fresh water. Consumption of water, especially by agriculture sector, has reached a very high level which causes water scarcity and affects food security, due to high population growth rate [1]. The continuous increase in population and the increasing water and energy demand by agriculture, domestic, and industrial sectors have caused great stress on the world's water and energy resources. The annual water withdrawal from different sectors increases from 580 km^3 to 3500 km^3 during the years 1900–2010 showing enormous stress over water resources [2]. On the other hand, world primary energy supply increases from 6101 Mtoe to 13,699 Mtoe resulting in a continuous increase in CO_2 emission from 15,458 Mt to 32,381 Mt during the years 1973–2014 [3]. This causes an increase in environmental degradation. Present global surface temperature is 0.6 degree Celsius higher than average for the period between the years 1900 and 2010 [2]. The world is using fossil fuels as energy resources, which are nonrenewable and environment unfriendly. The prices

M. W. Akram · Y. Jin (✉) · Z. Changan · J. Aiman
University of Science and Technology of China, Department of Precision Machinery and Precision Instrumentation, Hefei, Anhui, People's Republic of China
e-mail: jinyi08@ustc.edu.cn

G. Li (✉)
University of Science and Technology of China, Department of Thermal Science and Energy Engineering, Hefei, Anhui, People's Republic of China
e-mail: ligq@mail.ustc.edu.cn

S. Nižetić, A. Papadopoulos (eds.), *The Role of Exergy in Energy and the Environment*, Green Energy and Technology,
https://doi.org/10.1007/978-3-319-89845-2_38

of fossil fuels are increasing as well. On the other hand, most of the farmers in the world are using conventional methods of irrigation which cause a huge loss of precious resource of water and reduce yield as well. The farmers in the developing countries are also facing unreliable availability of electricity. The farmers need an independent and alternative energy system. Thus, the need of the time is to use sustainable approaches in every field to use our resources judiciously. It has become necessary to replace the conventional sources of energy with green renewable energy and conventional methods of irrigation with high-efficiency irrigation systems to ensure global energy, food, and environmental security.

Solar energy is one of the best renewable energy resources which can be combined with mechanical systems to pump irrigation water as solar irradiation coincides with crop water requirement. The crop requires more water as solar irradiation increases and therefore more water can be pumped [4, 5]. Furthermore, it is a long-term cost-saving and environment-friendly resource. Chandel [6] and Posorski [7] stated that this resource is more attractive in remote areas having no electricity grid connection. They found that PV pumps are promising alternative to conventional diesel and electricity-based pumps for irrigation purpose especially in developing countries considering huge solar potential. The future goal of agriculture is to produce more with less by increasing crop production per unit drop of water. This goal can be accomplished using high-efficiency irrigation systems like drip irrigation. It is a pressurized irrigation method which uses a pump to provide the required system pressure. Therefore, it is a sound option to combine solar pumping system with drip irrigation. The use of solar-powered drip irrigation system reduces the energy and water consumption in the agriculture sector as well as increases the yield and enhances the environment. Burney et al. [5] stated that solar-operated drip irrigation system is a cost-effective approach in comparison to alternative approaches. Use of drip irrigation offers very high water use efficiency and crop productivity [8]. Different research studies conducted in India showed that drip irrigation saves 40–80% water and increases yield up to 100% for different crops. This approach is feasible for both small- and large-sized farms [9]. Burney et al. [5] stated that it is an environment-friendly approach.

In the context of circumstances stated above, it is a sound option to combine high-efficiency irrigation systems with renewable energy resources. The present research is a step toward it. This study was conducted to design, develop, and evaluate techno-economic performance of solar-powered drip irrigation system in an agricultural farm located in Pakistan. The main objectives of the present study are to (1) design a sustainable irrigation system (solar-powered drip irrigation) for citrus, olives, and grapes according to climatological characteristics of the subject region, (2) determine optimum water requirements and propose a drip irrigation schedule for these crops according to available solar energy and water requirements, and (3) evaluate the hydraulic performance, water saving, fertilizer saving, and yield optimization potential of the system.

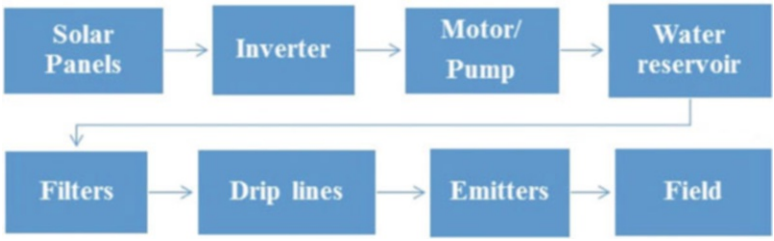

Fig. 38.1 Block diagram of the system

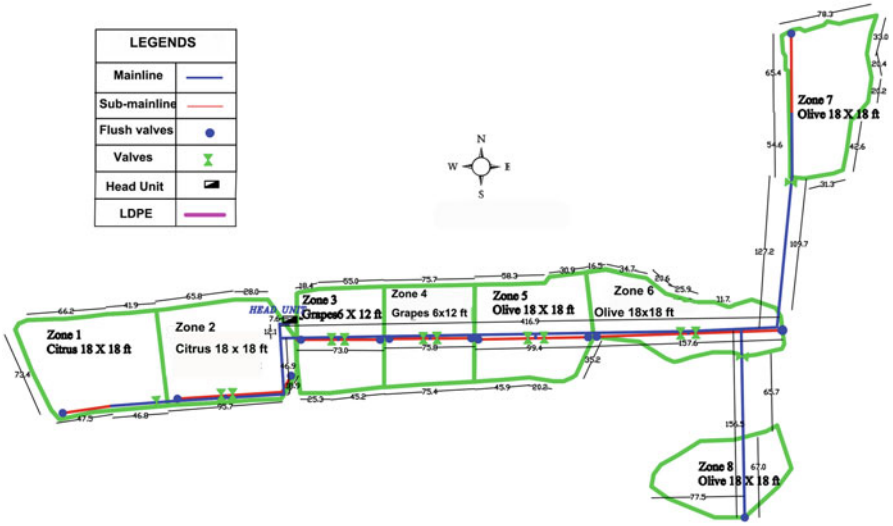

Fig. 38.2 Zone-wise distribution of crops in the study area

38.2 System Design

This section includes the complete design process. The information required for the design of the complete system includes solar insolation, water requirement, proposed layout, hydraulic characteristics, and total dynamic head of the system. The block diagram of system is shown in Fig. 38.1.

38.2.1 Site Description and Climatological Characteristics

The study was conducted at a farm in Town Tamman, District Chakwal, Potohar region, Pakistan. The study area is divided into eight zones as shown in Fig. 38.2. Three different types of crops are grown in these zones. The zone-wise distribution

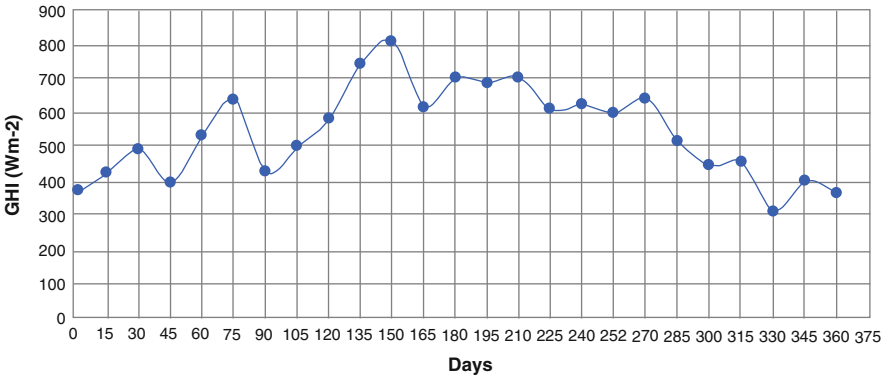

Fig. 38.3 Global horizontal irradiance (daily average) during different days of the year 2015 in Potohar

of crops is also shown in Fig. 38.2. Citrus is grown at an area of 2.25 acres, grapes at an area of 1.5 acres, and olive at an area of 3.5 acres. Chakwal lies in subtropical zone. The average rainfall in the region is 22–25 inches [10]. Based on the classification by FAO [11], according to annual rainfall, this area falls in semiarid climatic zone. A good sunshine is present for more than average 6 h throughout the whole year in this region [12]. The global horizontal irradiance (daily average) during different days of the year 2015 in Potohar region is shown in Fig. 38.3 which shows that, in summer days, the daily average GHI goes above 800 Wm^{-2}.

38.2.2 Crop Water Requirement

Crop water requirements can be determined by estimation of crop evapotranspiration (ET). ET depends upon meteorological parameters and management and environmental conditions [13]. Allen et al. [13] recommended to use FAO Penman-Monteith method for computation of crop evapotranspiration. Rasul and Mahmood [14] said that FAO Penman-Monteith method is best for estimation of evapotranspiration in Pakistan's climate. Firstly, reference evapotranspiration (ET_o) was calculated for different months of the year. This refers to standard growing conditions of grass. The FAO Penman-Monteith expression is shown in Eq. 38.1:

$$ET_o = \frac{0.408\Delta(R_n - G) + \gamma\frac{900}{T+273}U_2(e_s - e_a)}{\Delta + \gamma(1 + 0.34U_2)} \tag{38.1}$$

where ET_o is reference evapotranspiration ($mmday^{-1}$), R_n is net radiation at the crop surface (MJ m^{-2} day^{-1}), G is soil heat flux density (MJ m^{-2} day^{-1}), T is mean daily air temperature at 2 m height (°C), U_2 is wind speed at 2 m height (m s^{-1}), e_s is saturation vapor pressure (kPa), e_a is actual vapor pressure (kPa), (e_s - e_a) is

Table 38.1 ET_o, K_c, and CWR of the subject crops during different months of the year

Month	J	F	M	A	M	J	J	A	S	O	N	D
ET_o (mm/day)	1.8	2.8	3.8	5.9	7.8	8.5	6.7	5.8	5.2	4.1	2.8	1.8
K_c (olive/citrus)	0.7	0.7	0.7	0.7	0.7	0.7	0.7	0.7	0.7	0.7	0.7	0.7
K_c (grapes)	0.95	0.95	0.95	0.95	0.95	0.95	0.95	0.95	0.95	0.95	0.95	0.95
CWR (olive/citrus)	1.26	1.96	2.66	4.13	5.46	5.95	4.69	4.06	3.64	2.87	1.96	1.26
CWR (grapes)	1.71	2.66	3.61	5.6	7.41	8.07	6.36	5.51	4.94	3.89	2.66	1.71

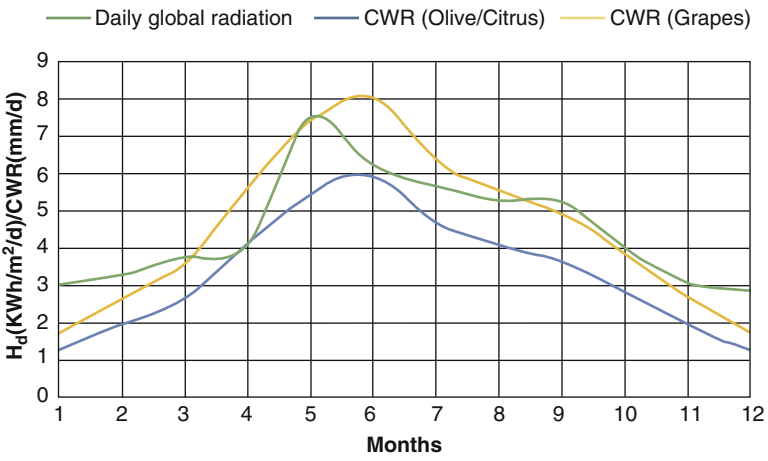

Fig. 38.4 Daily global radiation and water requirement of the subject crops in Potohar region

saturation vapor pressure deficit (kPa), Δ is slope of vapor pressure curve (kPa°C^{-1}), and γ is psychrometric constant (kPa°C^{-1}). However, the original growing conditions of a crop differ significantly. The effect of those differences in conditions is accounted in final estimation using crop coefficient (K_c). The crop coefficient considers crop type, climate, soil evaporation, and growth stage. Finally, crop evapotranspiration (ET) is determined by multiplying ET_o by K_c [15]. The calculated water requirements of the subject crops and the other parameters during different months of the year are given in Table 38.1. Those ET_o and K_c values are considered for final design of the system for which crop water requirement (CWR) is maximum. Solar irradiation in the region coincides with crop water requirement. The coincidence between water requirements of grapes, olive, and citrus and daily global radiation (H_d) throughout the year 2015 is shown in Fig. 38.4.

Table 38.2 Design calculations for drip layout

Sr. No.	Parameters	Unit	Zone (1–2) Citrus	Zone (3–4) Grapes	Zone (5–7) Olive	Zone (8) Olive
1.	Total area	Acres	2.25	1.5	2.0	1.5
2.	Canopy area	m^2	12.01	2.67	12.01	12.01
3.	No. of dripper per plant	Nos.	6	2	6	6
4.	Emitter spacing along plant canopy	m	1	1	1	1
5.	No. of drip lines per row	Nos.	2	1	2	2
6.	Irrigation cycle (assume 1 day)	Days	1	1	1	1
7.	Peak daily consumptive use per day	mm/day	2.64	3.58	2.64	2.64
8.	Total no. of plants	Nos.	303	909	270	202
9.	Total drip line length	m	3323	1663	2954	2216
10.	Total no. of emitters	Nos.	1818	1818	1620	1212
11.	Average emitter spacing along lateral	m	1.82	0.92	1.82	1.82
12.	Total flow rate	LPH	14,544	14,544	12,960	9696
13.	Application rate	mm/h	1.60	2.40	1.60	1.60
14.	Operation time	Hours	1.65	1.49	1.65	1.65

38.2.3 Drip Layout Design

From Table 38.1, it is clear that values of reference evapotranspiration and crop water requirements are highest in the month of June. So, the values of ET^o and K_c for the month of June are considered as reference for the design of drip system. Furthermore, plant and row spacing for citrus are 5.48 m and 5.48 m, respectively; for grapes are 1.83 m and 3.65 m, respectively; and for olive are 5.48 m and 5.48 m, respectively. Canopy area can be simply found by multiplying plant spacing, row spacing, and maturity factor as shown in Table 38.2. The assumed irrigation system efficiency for drip irrigation is 90%. The emitter flow rate and optimal wetted width of each emitter are 8 LPH and 1 m, respectively. The peak daily consumptive use per day (mm/day) is found by using Eq. 38.2. The other design calculations are shown in Table 38.2:

$$\text{Peak daily consumptive use per day (mm/day)} = \frac{\text{CWR}\left(\frac{\text{mm}}{\text{day}}\right) \times \text{Maturity factor}}{\text{Irrigation system efficiency}} \tag{38.2}$$

Variation in pressure and discharge of the emitters should be in permissible limits to ensure uniform water distribution. This can be ensured using appropriate lateral lengths [16]. Pande [17] designed solar-powered drip irrigation system for orchards.

Table 38.3 Calculated head losses

Head loss in lateral	1.19 m
Sub-mainline: head loss	1.11 m
Mainline: head loss	7.97 m
Suction line: head loss	0.088 m
Delivery line: head loss	0.088 m
Total head loss: pipe network	10.446 m
Elevation difference	0 m
Emitter operating pressure	10 m
Fitting loss (lateral, mainline, sub-mainline, and head unit)	1 m
Head loss in filter	6 m
Head loss in fertigation system	4 m
Head loss in flow meter	3 m
Field fitting losses	2 m
Miscellaneous head loss	2 m
Pumping lift	3 m
Total dynamic head	41.446 m (42)

He recommended to consider factors like variation in pressure of pump with respect to solar irradiance during different hours of the day. Asif et al. [18] recommended to install pressure-compensating emitters in orchards to create uniform pressure. Considering these studies, importance of uniform water distribution was kept in mind, and accordingly pressure-compensating emitters are used.

38.2.4 Pumping System Design

For calculation of head losses in the pipe network, Hazen-Williams equation, suggested by Miller [19], is used. The expression is shown in Eq. 38.3, and the calculated head losses for different components of the system are given in Table 38.3:

$$H_L = \frac{10.67 Q^{1.852} L}{C^{1.852} d^{4.8704}} \tag{38.3}$$

where H_L is head loss (m), L is length of pipe (m), Q is volumetric flow rate (m^3/s), C is pipe roughness coefficient, and d is pipe inside diameter (m). Pande [17] said that pump size for solar-powered drip irrigation system depends upon energy needed to operate the drip system at specific pressure for a specific area. The volume of water to be pumped, required pressure, pressure losses at all components, and efficiencies

of all subcomponents like motor-pump were taken into account to choose an appropriate pump.

The required horsepower for the motor-pump is calculated by the formula given in Eq. 38.4 [19]. The efficiency of motor and pump was 70% and 65%, respectively. The estimated required horsepower was 4.9 HP. 5 HP was taken into account for further calculation:

$$\mathrm{HP} = \frac{Q \times H}{3960 \times \text{motor\&pump efficiency}} \tag{38.4}$$

where HP is motor horsepower, Q is discharge (GPM), and H is pumping head (feet).

38.2.5 PV Design

The high initial cost of the PV system is a problem, so it should be designed and installed perfectly to make it cost-effective [4, 20]. Yahyaoui I. et al. [21] proposed and evaluated an optimum PV sizing approach to ensure an uninterrupted power supply to the pump. The proposed approaches help to determine suitable PV configuration. Cuadros F. et al. [20] designed PV system to power drip irrigation system for olive orchard. Considering these studies, the PV system was designed. The size of PV array is given by Eq. 38.5 [22]:

$$A_{\mathrm{PV}} = \frac{E_{\mathrm{H}}}{H_{\mathrm{avg}} \eta_{\mathrm{pv}} \eta_I T_{\mathrm{CF}}} \tag{38.5}$$

where A_{PV} is the required area of PV array in m^2, E_{H} is the required hydraulic energy including pumping system losses (KWhday^{-1}), H_{avg} is the average daily global irradiation ($\mathrm{KWhm}^{-2}\ \mathrm{day}^{-1}$), η_{PV} is the efficiency of PV panel (%), η_{I} is the efficiency of inverter (%), and T_{CF} is the temperature correction factor. Equation 38.6 gives the peak power of PV generator [22]:

$$P_{\mathrm{PV}} = A_{\mathrm{pv}} I_{\mathrm{p}} \eta_{\mathrm{pv}} \tag{38.6}$$

where P_{PV} is PV peak power (W) and I_{P} is peak solar irradiance (taken as 1000 Wm^{-2}). The computed power for the present PV system was 5.5 KW (5500 watts). The array of photovoltaic panels was selected according to the power requirement. As multiple PV panels were used to generate required power, so they were connected in combination of series-parallel to match the voltage and current requirement of the inverter.

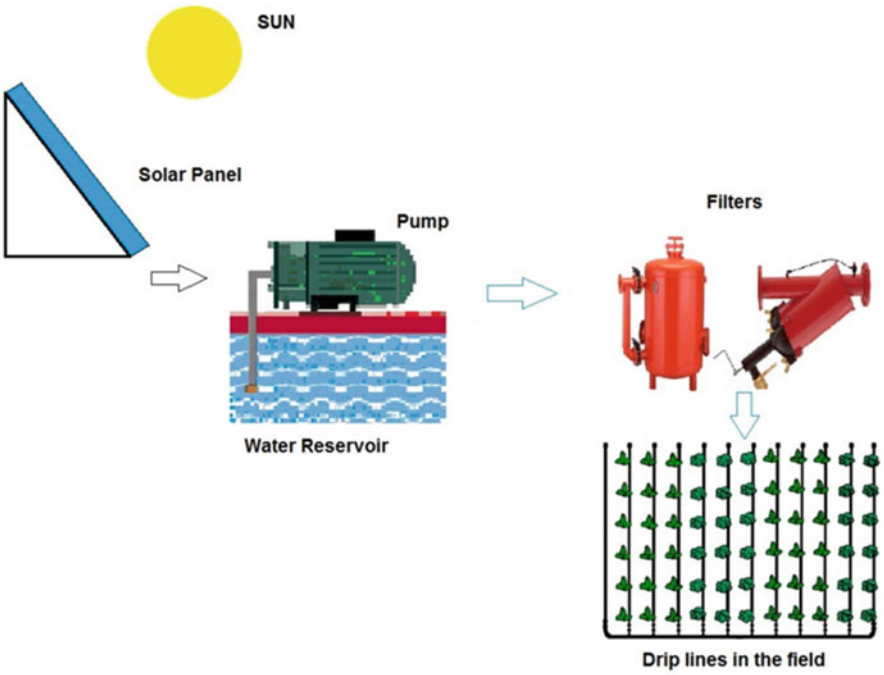

Fig. 38.5 Complete system diagram

38.3 Results and Discussion

The complete system diagram is shown in Fig. 38.5.

The system was designed in a way that it can irrigate as more area as possible within least investment. The total area was divided into different blocks and each block is irrigated separately. The system has the capacity to irrigate all the blocks, one by one, within 6.44 h during peak demand days, while available sunshine hours are also sufficient. The graph between actual required operational time for the whole system and sunshine hours throughout the year is given in Fig. 38.6 and clearly shows that the designed system can fulfill the water demands of the subject crop

It is mentioned earlier that the system was designed according to peak demand. Thus, in actual, the required operational time varies during different months. Considering the yearly variability of climate data, the daily required operational time for the system throughout the whole year is given in Table 38.4.

The hydraulic performance of the system was evaluated during effective sun hours to check water application uniformity. The design discharge of the emitter was 8 LPH. The average discharge from these emitters on different laterals was in acceptable range. According to performance evaluation methods, suggested by Smajstrla A. G. et al. [23], coefficient of variation and water application uniformity

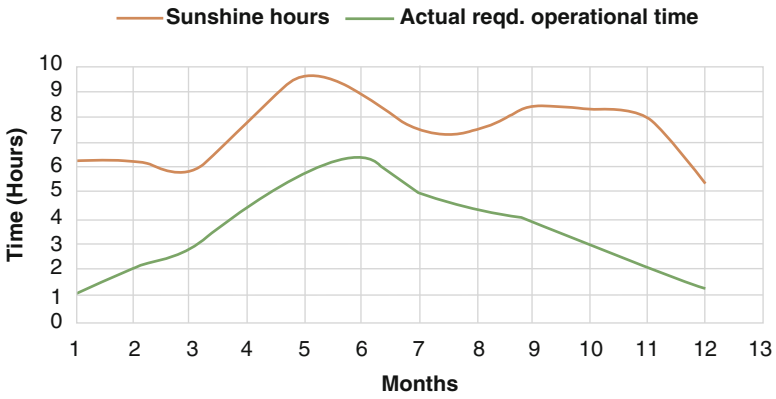

Fig. 38.6 Operational time and sunshine hours

were determined. The coefficient of variation for overall system was observed as 0.15. The calculated water application uniformity of the system was 85%, which is considered as very good according to uniformity classifications by ASAE [24]. It shows that the system was properly designed which ensures evenness in water and fertilizer distribution. Moreover, the clogging in emitters, choking in filters, and accumulation of dust on PV panels were observed during performance evaluation of the system. These all factors reduce the efficiency of system. Thus, these factors should be monitored regularly, after drip installation for proper working of the system. In addition to this, water saving by use of drip irrigation was also studied and observed as 50%, 55%, and 60% for grapes, olive, and citrus, respectively, as compared to traditional irrigation method adopted in the region. The fertilizer saving was also observed for the subject crops. The fertilizer saving was observed as 45%, 40%, and 42% for grapes, olive, and citrus, respectively. The reduction in use of fertilizer decreases the input cost as well as reduces groundwater and soil contamination due to excessive use of chemical fertilizers. In addition to conservation of natural resources, a high increase in the yield and quality is expected for these crops. The cost of complete system is 1,420,110 PKR. The percentage share in total cost by different components of the system is shown in Fig. 38.7.

38.4 Conclusions

In this chapter, a research-based study combining drip irrigation and PV system is presented. Solar-powered drip irrigation is found suitable for point application of irrigation water for orchards and high-value crops. The system has the potential to enhance yield, water productivity, water use efficiency, reduced input cost, and reduced energy requirements and ensure energy and environment security. It contributes toward long-term reduction of water and energy consumption in irrigation

Table 38.4 Daily required operational time during different months

Month	Jan	Feb	March	April	May	Jun	July	Aug	Sep	Oct	Nov	Dec
Required operational time (hours)	1.15	2.12	2.88	4.47	5.92	6.45	5.08	4.40	3.94	3.11	2.12	1.36

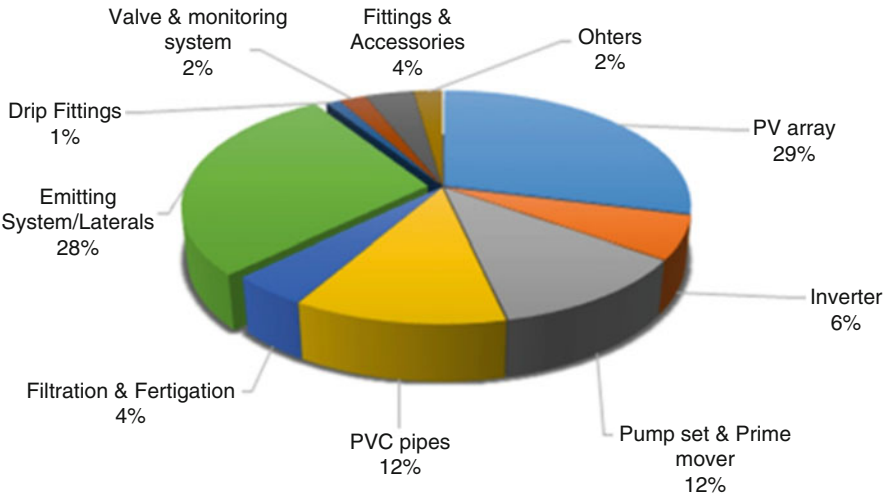

Fig. 38.7 Percentage share in total cost by different components

sector. Furthermore, this system allows farming in areas with water shortage and absence of electricity or electricity shortfall (in developing countries), thereby enhancing sustainability. The system design is based on peak water requirements and applicable for all subject crops. The system was evaluated and satisfactory results were found in every aspect. The coefficient of variation and water application uniformity were found in good ranges. It was concluded from the evaluation of pumping system that cleaning of filter, emitters, and PV panels enhances the efficiency of system. Furthermore, the use of pressure-compensating drippers is found necessary for solar-powered drip irrigation system.

A natural coincidence exists between the crop water requirement and available solar energy. The designed system can fulfill the water demands of the subject crops throughout the year within available sunshine hours. Water saving and fertilizer saving were greater than 50% and 40%, respectively, as compared to traditional methods adopted in the region. PV system and the laterals have the greatest share in total cost, and with the expected reduction in prices of PV panels in the future and use of indigenized materials, the system will become more and more viable. This chapter may provide technical guidance for design and installation of solar-powered drip irrigation system.

Nomenclature

A_{PV}	Required area of PV array in m^2
C	Pipe roughness coefficient
γ	Psychrometric constant ($kPa^{\circ}C^{-1}$)
D	Pipe inside diameter (m)
Δ	Slope of vapor pressure curve ($kPa^{\circ}C^{-1}$)
e_a	Actual vapor pressure (kPa)

e_s	Saturation vapor pressure (kPa)
$(e_s - e_a)$	Saturation vapor pressure deficit (kPa)
E_H	Required hydraulic energy ($KWhday^{-1}$)
ET	Crop evapotranspiration
ET_o	Reference evapotranspiration ($mmday^{-1}$)
G	Soil heat flux density ($MJ\ m^{-2}\ day^{-1}$)
H	Pumping head (feet)
H_d	Daily global radiation
H_L	Head loss (m)
H_{avg}	Avg daily global irradiation ($KWhm^{-2}\ day^{-1}$)
HP	Motor horsepower
η_{PV}	Efficiency of PV panel (%)
η_I	Efficiency of inverter (%)
I_P	Peak solar irradiance (Wm^{-2})
K_c	Crop coefficient
L	length of pipe (m)
P_{PV}	PV peak power (W)
Q	Volumetric flow rate (m^3/s)
R_n	Net radiation at the crop surface ($MJ\ m^{-2}\ day^{-1}$)
T	Mean daily air temperature at 2 m height (°C)
T_{CF}	Temperature correction factor
U_2	Wind speed at 2 m height ($m\ s^{-1}$)

Acknowledgment The study was sponsored by the National Natural Science Foundation of China (Grant Nos. 51408578, 51611130195, 51605464) and Anhui Provincial Natural Science Foundation (1508085QE96, 1508085QE83). The authors would also like to acknowledge the Chinese Academy of Sciences and The World Academy of Sciences for awarding CAS-TWAS President's fellowship to PhD scholars. The authors would also like to thank Mr. M. Muzammil, Mr. Irfan, and Mr. Naeem-Ur-Rehman for their assistance in experimental facility.

References

1. Jury WA, Vaux HJ (2007) The emerging global water crisis: managing scarcity and conflict between water users. Adv Agron 95:1–76
2. Food and Agriculture Organization of the United Nations (FAO). FAO statistical pocketbook 2015. https://doi.org/978-92-5-108802-9
3. International Energy Agency (IEA). Energy statistics 2016. http://www.iea.org/statistics/statisticssearch/
4. Gajic B, Tomic Z, Sredojevic Z (2013) A simple method estimates and economic indicators of photovoltaic systems for drip irrigation. Econ Agric 60(2):223–236
5. Burney J, Woltering L, Burke M, Naylor R, Pasternak D (2010) Solar-powered drip irrigation enhances food security in the Sudano-Sahel. Proc Natl Acad Sci (PNAS) 107(5):1848–1853
6. Chandel SS, Naik MN, Chandel R (2015) Review of solar photovoltaic water pumping system technology for irrigation and community drinking water supplies. Renew Sust Energ Rev 49:1084–1099

7. Posorski R (1996) Photovoltaic water pumps, an attractive tool for rural drinking water supply. Sol Energy 58(4–6):155–163
8. Maisiri N, Senzanje A, Rockstrom J, Twomlow SJ (2005) On farm evaluation of the effect of low cost drip irrigation on water and crop productivity compared to conventional surface irrigation system. Phys Chem Earth Parts A/B/C 30(11):783–791
9. Sivanappan RK (1994) Prospects of micro-irrigation in India. Irrig Drain Syst 8(1):49–58
10. Ahmad SS, Sherazi A, Shah MTA (2010) A preliminary study on climate change causing decline in forest cover area in district Chakwal, Pakistan. Pak J Bot 42(6):3967–3970
11. Brouwer C, Heibloem M (1986) Irrigation water management training manual No. 3: irrigation water needs, food and agriculture organization (FAO) of the United Nations, Rome, Italy
12. Chaudhry QZ, Rasul G (2004) Agro-climatic classification of Pakistan. Sci Vis 9:59–66
13. Allen RG, Pereira LS, Raes D, Smith M (1998) Crop evapotranspiration-guidelines for computing crop water requirements, FAO irrigation and drainage paper 56, Rome, Italy
14. Rasul G, Mahmood A (2009) Performance evaluation of different methods for estimation of evapotranspiration in Pakistan's climate. Pak J Meteorol 5(10):25–36
15. Doorenbos J, Pruitt WO (1997) Guideline for predicting crop water requirements, FAO irrigation and drainage paper 24, Rome, Italy
16. Yurdem H, Demir V, Mancuhan A (2015) Development of a simplified model for predicting the optimum lengths of drip irrigation laterals with coextruded cylindrical in-line emitters. Biosyst Eng 137:22–35
17. Pande PC, Singh AK, Ansari S, Vyas SK, Dave BK (2003) Design development and testing of a solar PV pump based drip system for orchards. Renew Energy 28:385–396
18. Asif M, Ahmad M, Mangrio AG, Akbar G, Wahab A (2015) Design, evaluation and irrigation scheduling of drip irrigation system on citrus orchard. Pak J Meteorol 12(23):37–48
19. Miller DS (1990) Internal flow systems, 2nd edn. Bhra Information Service Publishers, Cranfield, Bedford, UK
20. Cuadros F, López-Rodríguez F, Marcos A, Coello J (2004) A procedure to solar powered irrigation (photo-irrigation) schemes. Sol Energy 76(4):465–473
21. Yahyaoui I, Atieh A, Tadeo F, Tina GM (2017) Energetic and economic sensitivity analysis for photovoltaic water pumping systems. Sol Energy 144:376–391
22. Alamsyah TMI, Sopian K, Shahrir A (2003) Technoeconomic analysis of a photovoltaic system to provide electricity for a household in Malaysia. In: Proceedings of the international symposium on renewable energy: environment protection & energy solution for sustainable development, Kuala Lumpur, Malaysia, pp 387–396
23. Smajstrla AG, Boman BJ, Haman DZ, Pitts DJ, Zazueta FS (2012) Field evaluation of micro irrigation water application uniformity. University of Florida IFAS Extension, BUL265, pp 1–8. Retrieved from http://edis.ifas.ufl.edu/ae094
24. ASAE (1996) Field evaluation of micro irrigation systems. ASAE Standards, American Society of Agricultural Engineers, St. Joseph, EP405.1, pp 756–759

Chapter 39
Energetic Optimization of the Flat Plate Solar Collector

Mohamed Hany Abokersh, Abdelghani A. Elimam, and Mohamed El-Morsi

Abbreviations

ANOVA	The analysis of variance
DOE	Design of experiment
OA	Orthogonal array
S/N	The signal-to-noise ratio
SQP	Sequential quadratic programming
POE	Propagation of error
PRESS	The predicted residual error of sum square
RSM	Response surface methodology

39.1 Introduction

The solar collector is the core component of the solar water heating system [1] where the flat plate collector type is the most economical and popular solar collector type since it's simple in construction and requires less maintenance [2]. Typically the flat plate solar collector consists of an absorber plate painted with a selective coating material to enhance its absorptivity, transparent glass cover (glazing), insulation material in order reduce the losses to the environment, flow tubes welded to the absorber plate, and galvanized steel frame to hold the mentioned components [3] as shown in Fig. 39.1.

M. H. Abokersh (✉) · A. A. Elimam · M. El-Morsi
The American University in Cairo, Mechanical Engineering Department, New Cairo, Egypt
e-mail: m.hany@aucegypt.edu

S. Nižetić, A. Papadopoulos (eds.), *The Role of Exergy in Energy and the Environment*, Green Energy and Technology,
https://doi.org/10.1007/978-3-319-89845-2_39

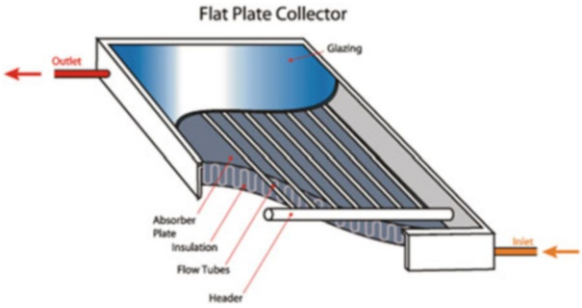

Fig. 39.1 The main structure of the flat plate collector [3]

Over the last decades, the researchers have been working on the analysis and development of the flat plate collector. Alvarez et al. [4] conducted an experimental and numerical analysis based on the finite element method for a newly designed flat plate solar collector with a corrugated channel. Besides, Hobbi and Siddiqui [5] performed an experimental study to investigate the impact of various passive heat enhancement devices based on shear-produced turbulence on the thermal performance of a flat plate solar collector. Moghadam et al. [6] investigated the effect of utilizing a mixture of CuO/water nanofluid as heat transfer fluid on the efficiency of the flat plate solar collector. The results illustrated that the usage of this mixture could increase the flat plate collector efficiency by about 21.8%. Furthermore, Zambolin and Del Col [7] presented a comparative study between the glazed standard flat plate solar collector and the evacuated tube solar collector based on EN 12975-2 standard. The daily results showed that the flat plate solar collector was more sensitive to environmental conditions.

Several design parameters affect the thermal performance of the flat plate solar collector. Therefore, in this context, many researchers [8, 9] have strived to obtain the optimum levels of these factors that maximize the thermal performance of the flat plate solar collector. Most of the above researchers utilized the traditional experimental strategy (one factor at time (OFAT)) approach [10] in order to evaluate the effect of the flat plate solar collector design parameters. This method has a failure in discussing the optimum conditions for a combination of design parameters based on multi-responses. Therefore, Jeffrey Kuo et al. [3] attempted to introduce the Taguchi method combined with the Grey relation analysis to overcome the disadvantage of OFAT in optimizing multi-responses of the flat plate solar collector. Even though this method solves the problem of obtaining the optimum values for the design parameters based on the multi-responses, it evaluates the optimum conditions only based on the main factor analysis without consideration for the interaction between design parameters which leads to different optimum conditions. Therefore, the present study intends to combine the response surface methodology (RSM) from the design of experiment (DOE) approach with the Taguchi method to optimize multi-responses of the flat plate solar collector with consideration for the interaction between the design parameters.

39.2 Basic Equations Performance

Beckman and Duffie [11] defined the total useful energy output from the flat plate solar collector as given by Eq. 39.1.

$$Q_{\text{net}} = F_{\text{R}} A \left[(\tau\alpha)_{\text{e}} . I_{\text{T}} - U_{\text{s}} (T_{\text{i}} - T_{\text{a}}) \right] \tag{39.1}$$

where F_{R} is the heat removal factor which represents the actual useful energy gain of the collector to the useful gain if the whole collector surface were at the fluid inlet temperature, $(\tau\alpha)_{\text{e}}$ is the effective transmittance-absorptance product, and I_{T} is the hourly solar radiation. U_{s} represents the total heat loss coefficient of the flat plate solar collector, T_{i} is the inlet water temperature, and T_{a} is the ambient temperature. The instantaneous efficiency can be expressed as expressed by Eq. 39.2:

$$\eta = \frac{Q_{\text{net}}}{I_{\text{T}} . A} = F_{\text{R}} (\tau\alpha)_{\text{e}} - U_{\text{s}} . \frac{(T_{\text{i}} - T_{\text{a}})}{I_{\text{T}}} \tag{39.2}$$

where the value of $F_{\text{R}}(\tau\alpha)_{\text{e}}$, the optical efficiency, and $F_{\text{R}}U_{\text{s}}$, the total heat loss coefficient, can be calculated using the least square method to get the instantaneous efficiency. Therefore, the performance of the solar collector can be represented by the $F_{\text{R}}(\tau\alpha)_{\text{e}}$ and $F_{\text{R}}U_{\text{s}}$.

Based on the instantaneous efficiency model developed by Duffie and Beckman [11], a numerical software called CoDePro is developed to evaluate the performance of the flat plate collector. This software is established according to the test standard [12].

39.3 Optimization Methodology

The main purpose of the current study is to find out the optimum configuration of the flat plate solar collector design parameters with independency on the environmental factors (Robust design).

For this purpose, the cross array Taguchi method [10] is presented to investigate the design parameters that optimize the flat plate solar collector responses. This optimization includes maximizing the optical efficiency and minimizing the heat loss coefficient of the solar collector.

39.3.1 The Design Parameters Levels and the Characteristic Responses

Several controlled factors which include air gap between glass and absorber plate, absorber plate material, absorber plate thickness, absorption film type, insulation

Table 39.1 The controlled factors levels

Factor, unit	Symbol	Levels		
		1	2	3
Air gap between glass and plate (cm)	*A*	0.5	4.75	9
Air gap between cover glass 1 and cover glass 2 (cm)	*B*	0.3	0.8	1.3
Absorber plate material	*C*	Aluminium	Copper	Steel
Absorption film type	*D*	Black chrome	Thermalox 250	Tinox
Absorber plate thickness (cm)	*E*	0.05	0.1	0.2
Back insulation thickness (cm)	*F*	1	3	5
Side insulation thickness (cm)	*G*	1	3	5
Number of collector flow tubes	*K*	5	10	15
Inner diameter of collector flow tubes (cm)	*L*	0.6	1.3	2
Absorber length (m)	*M*	0.5	1.5	2.5

Table 39.2 Uncontrolled factors levels

Factor, unit	Symbol	Levels	
		1	2
Solar radiation	I_t	800	1000
Ambient temperature	T_a	20	35
Wind speed	u_s	2	4

thickness, number of collector flow tubes, and inner and outer diameters of the collector tubes might affect the thermal performance of the flat plate solar collector as shown in Fig. 39.1. Furthermore, the performance of the flat plate solar collector is sensitive to the environmental factors Therefore, the effect of these parameters must be also considered in the current problem. The levels of the controlled and uncontrolled factors are summarized in Tables 39.1 and 39.2, respectively. For the characteristic responses of the flat plate solar collector performance, the optical efficiency$F_R(\tau\alpha)_e$ and the heat loss coefficient F_RU_s are selected.

39.3.2 Taguchi Method

The Taguchi method is employed to obtain a robust design with a limited number of runs based on the orthogonal array (OA). The cross-array design approach L27 for the inner array and L8 for the outer array is utilized to obtain the robust design where the inner array is advocated for the controlled factors, whereas the outer array is advocated for the uncontrolled factors (noise factors). The combination of the inner and outer arrays provides information about the interaction between the controlled factors and uncontrolled factors [10].

39.3.3 The Signal-to-Noise Ratio (S/N Ratio)

The experimental data are then analysed through the "signal-to-noise ratio." There are several types of the *S/N* ratio depending on the desired response. However, there are two primary types. The *S/N* ratio for the maximum and minimum outputs is estimated by [13] as shown in Eqs. 39.3 and 39.4.

Smaller is better:

$$S/N = 10\log\left(\frac{1}{n}\sum_{i=1}^{n}\frac{1}{y_i^2}\right) \tag{39.3}$$

Larger is better:

$$S/N = 10\log\left(\frac{1}{n}\sum_{i=1}^{n}y_i^2\right) \tag{39.4}$$

where y_i is the observed run and n is the total number of the experimental runs.

Since the characteristic responses of the flat plate solar collector at the current study are the optical efficiency and heat loss coefficient. Therefore, the optimum configuration can be found at higher optical efficiency and lower heat loss coefficient where Eq. 39.3 satisfies the goal of achieving a higher optical efficiency, whereas Eq. 39.4 meets the goal of achieving a lower heat loss coefficient.

39.3.4 Analysis of Variance (ANOVA)

The *S/N* ratio is utilized to evaluate the experimental responses without obtaining information about the significance of each factor. The ANOVA [14] evaluates the significance of each factor through estimating the experimental error associated with the responses. The ANOVA calculation includes an estimation for several parameters which include (i) degree of freedom, (ii) correction factor, (iii) the sum square, (iv) mean square, and (v) F-ratio, as given by [3].

39.3.5 Taguchi Method Limitations

Even though the Taguchi method presents a useful manner to obtain a robust design with independency on the noise factors, it has several limitations which include the following:

I. The cross array design does not present an economical design for investigating a large number of factors [14]; since it crosses the noise factors matrix with the

controlled factors matrix, this crossing produces a large number of experimental trials.

II. The cross array design does not estimate the effect of the interaction between the controlled factors and the noise factors [10].
III. The cross array design discards the effect of the quadratic terms in the controlled and noise factors [10].
IV. The cross array design fails to obtain the optimum design parameters based on multi-responses.
V. The response model approach is combined with the cross array design to overcome these limitations.

39.3.6 Response Method Approach

The key issue of obtaining a robust design is to consider the interaction between the controlled and noise factors. Therefore, the response model approach tends to develop a correlation model that involves the main effect, the interaction between the controlled and noise factors, and their quadratic terms with a small number of experimental trials relative to the number of experimental trials required by the cross array design.

39.3.6.1 Governing Equations

For considering a first-order model including the controlled and noise factors, the model formula is mentioned by Montgomery [10] as shown in Eq. 39.5.

$$y = \beta_o + \beta_1 x_1 + \beta_2 x_2 + \beta_{12} x_1 x_2 + \gamma z_1 + \delta_{11} x_1 z_1 + \delta_{21} x_2 z_1 + \varepsilon \tag{39.5}$$

where x_1, x_2 are the controlled factors, z_1 is the noise factor, β_o is the constant coefficient of the response model, β_1, β_2 are the intercept coefficient of controlled factors, β_{12} is the intercept coefficient of the interaction between the controlled factors, γ is the intercept coefficient of the noise factor, and δ_{11}, δ_{12} are the intercept coefficients of the interaction between the controlled factors and the noise factor.

According to the assumptions given in [10], the noise factors are random variable even though they are controlled for the experimentation purpose. Moreover, the expected value of noise factors is zero, and its variance is σ_z^2. Based on these assumptions, the mean response can be estimated as shown in Eq. 39.6.

$$E_z(y) = \beta_o + \beta_1 x_1 + \beta_2 x_2 + \beta_{12} x_1 x_2 \tag{39.6}$$

For the variance model, Montgomery [10] expanded the response model shown in Eq. 39.7 using the Taylor series, and the result becomes

$$V_z(y) = \sigma_z^2(\gamma_1 + \delta_{11}x_1 + \delta_{12}x_2)^2 + \sigma^2 \tag{39.7}$$

From the mean and variance models mentioned above, it is noticed that only the controlled factors appear in the response models. This mean provides the ability to achieve the design target with a small variation due to the noise factors. Even through the noise factor doesn't appear in the responses model, the intercept coefficient between the controlled factors and the noise factor appear in the variance model. This appearance shows the influence of the noise factors in the model response. Also, σ^2 presents the mean square of the residuals estimated from the response model.

39.3.6.2 Choice of the Experimental Design

The selection of the experimental design is vital in the response model approach. In the current problem, we are interested in obtaining a second-order model that includes the interaction between the controlled factors and their quadratic terms. Therefore, the standard response surface designs, such as the central composite design and Box-Behnken design [14], might be applicable especially when the design domain is cube or sphere even though in the current problem the design domain is not a standard one.

The optimal design is a computer-aided design that involves the best subset of all possible experiments based on a certain criterion and a certain algorithm [10]. The optimal design offers an ability to develop a response model based on a nonstandard design domain with a limited number of experimental trials. There are several types of the optimal design such as D-optimal design, G-optimal design, V-optimal design, and I-optimal design. The selection of the appropriate design depends on the order of the required model. The I-optimal design mentioned by Montgomery [14] can satisfy the current problem requirement since it has the ability to form a second-order response model with a limited number of experimental trials. Design matrix can be considered as an I-optimal design when the smallest prediction variance shown in Eq. 39.8 is obtained.

$$I = \frac{1}{A^*} \int V[\widehat{y}(x)].dx \tag{39.8}$$

where A^* tends to represent the volume of the design domain and $V[\widehat{y}(x)]$ is the prediction variance of the design matrix. The minimum prediction variance is calculated based on the coordinate exchange algorithm [10].

39.3.6.3 Statistical Analysis of the Data

Several statistical criteria are utilized to analysis the experimental results. The statistical analysis includes (i) analysis of variance, (ii) model adequacy checking, and (iii) goodness of fit.

39.3.6.4 The Optimization in the Response Model Approach

Since the objective of the response model approach is to determine the optimum design parameters levels that maximize the optical efficiency and minimizes the heat loss coefficient, the current experiment can be formulated using the desirability function as:

Maximum	$F_R(\tau\alpha)_e$
Minimum	$F_R U_s$, POE
Subjected to	
	5 mm $\leq A \leq$ 90 mm
	3 mm $\leq B \leq$ 13 mm
	C: Steel, copper, and aluminium
	D: Tinox, black chrome, and Thermalox 250
	0.5 mm $\leq E \leq$ 2 mm
	10 mm $\leq F \leq$ 50 mm
	10 mm $\leq G \leq$ 50 mm
	$5 \leq K \leq 15$
	6 mm $\leq L \leq$ 20 mm
	0.5 m $\leq M \leq$ 2.5 m

where POE is the propagation of error, and it tends to present the standard deviation associated with the responses a function of the controlled factors [10]. Once the optimum design parameters that maximize the optical efficiency and minimize the heat loss coefficient are obtained, a confirmation run is required to verify the optimum configuration.

39.4 Results and Discussion

39.4.1 Taguchi Method Results

Based on the cross array design L27-L8, 216 runs of experimental trails are implemented using CoDePro software. The response graph of *S/N* ratio for the optical efficiency response based on the controlled factors levels is shown in Fig. 39.2.

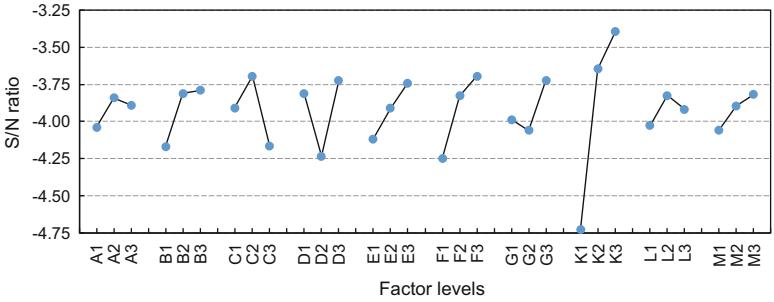

Fig. 39.2 Response graph for the optical efficiency response

Table 39.3 Response graph for the optical efficiency response

Factor	Sum of squares	Mean square	*P*-value	Contribution percentage (%)
A	0.19	0.09	0.6306	1.13
B	0.81	0.41	0.1977	4.88
C	1.00	0.50	0.151	5.98
D	1.33	0.67	0.0976	7.98
E	0.64	0.32	0.2616	3.84
F	1.50	0.75	0.0802	8.98
G	0.57	0.29	0.2943	3.43
K	9.04	4.52	0.0014	54.25
L	0.18	0.09	0.6401	1.09
M	0.27	0.13	0.5289	1.61

The response graph for the optical efficiency shows that the optimum factor levels that maximize the optical efficiency are *A*2, *B*3, *C*2, *D*3, *E*3, *F*3, *G*3, *K*3, *L*2, and *M*3. This means that the maximum optical efficiency is found when the absorber plate of the collector is made from copper, with a thickness of 0.2 cm and a length of 2.5 m, and painted with Tinox as an absorption film. For both the side and back insulation, a layer of 5 cm is selected. The distance between the glass and the absorber plate is 4.75 cm, and the distance between the upper and the lower glass layer is 1.3 cm. In terms of the flow tubes, 15 tubes with an inner diameter of 1.3 cm are selected.

To obtain the effect of the controlled factors on the optical efficiency response, the ANOVA is calculated. The results shown in Table 39.3 illustrate that the number of the flow tubes has the most significant effect on the optical efficiency response followed by the back insulation thickness and then the absorption film type, while the remaining factors seem to be insignificant since *P*-value of these factors is larger than 0.1.

In terms of the heat loss coefficient response, the response graph of *S*/*N* ratio based on the controlled factors levels, shown in Fig. 39.3, illustrates that the optimum configuration levels that minimize the heat loss coefficient are *A*3, *B*3, *C*3, *D*1, *E*1, *F*3, *G*2, *K*1, *L*1, and *M*3.

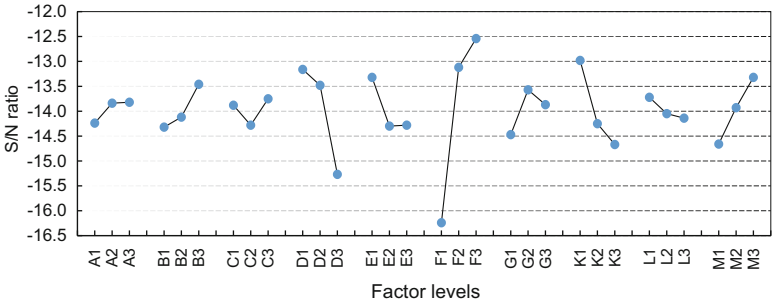

Fig. 39.3 Response graph for the heat loss coefficient response

Table 39.4 Analysis of variance of the heat loss coefficient output based on the cross array design

Factor	Sum of squares	Mean square	*P*-value	Contribution percentage (%)
A	1.01	0.51	0.58	0.732
B	3.63	1.81	0.20	2.622
C	1.35	0.68	0.50	0.978
D	23.28	11.64	0.01	16.823
E	5.73	2.87	0.11	4.143
F	71.36	35.68	0.0003	51.567
G	3.76	1.88	0.19	2.716
K	14.07	7.04	0.02	10.170
L	0.89	0.45	0.62	0.645
M	8.13	4.07	0.06	5.878

This means that the minimum heat loss coefficient is achieved when the absorber plate of the collector is made from steel, with a thickness of 0.05 cm and a length of 2.5 m, and painted with black chrome as an absorption film. A layer of 5 cm is selected for the back insulation, and a layer with a thickness of 3 cm is chosen for the side insulation. The distance between the glass and the absorber plate is 9 cm, and the distance between the upper and the lower glass layer is 1.3 cm. In terms of the flow tubes, five tubes with an inner diameter of 0.6 cm are selected.

The ANOVA for the heat loss coefficient responses illustrates that the back insulation thickness is the most significant factor, followed by the absorption film type, then the number of the flow tubes, and finally the absorber length, whereas the remaining factors seem to be insignificant since *P*-value of these factors is larger than 0.1 as shown in Table 39.4.

39.4.2 Results of the Response Model Approach

The obtained results using the cross array Taguchi method show that the optimum optical efficiency response is found at *A*2, *B*3, *C*2, *D*3, *E*3, *F*3, *G*3, *K*3, *L*2, and *M*3,

whereas the optimum heat loss coefficient is found at *A*3, *B*3, *C*3, *D*1, *E*1, *F*3, *G*2, *K*1, *L*1, and *M*3. Since the optimum combination between the optical efficiency response and the heat loss coefficient is different from the optimum of each single response, the response model approach based on I-optimal design is presented.

A total of 140 numerical trails are implemented based on I-optimal design matrix to investigate the effect of the main controlled factors, their interaction, and quadratic terms on the selected responses.

39.4.2.1 Regression Models Analysis

Based on the I-optimal design matrix and ANOVA, nonlinear regression models including the main effect, the interaction, and the quadratic terms are developed for both the optical efficiency and heat loss coefficient.

For the optical efficiency model, *R*-squared is 98.3%, adjusted *R*-squared is 96.7%, and PRESS criteria is 0.04, while for the heat loss coefficient response, the *R*-squared is 97.3%, adjusted *R*-squared is 96.09%, and PRESS criterion is 0.77. These results show the high ability of the proposed regression models in estimating the optical efficiency and the heat loss coefficient within the limits of the design parameters.

39.4.2.2 Multiple Responses Optimization Using Desirability Function

Based on the desirability function formulation mentioned previously in Sect. 39.3.6.4, the maximum optical efficiency of 71.8% with POE of 0.012 and the minimum heat loss coefficient of 2.76 W/m^2-C with POE of 0.059 can be obtained when the distance between the glass and absorber plate is 8.88 cm, the distance between the upper and lower glass cover is 1.29 cm, and the absorber plate is made from aluminium with dimensions of 2.47 m and 0.117 cm for length and thickness, respectively. Furthermore, the absorber plate is painted with Tinox. Regarding the insulation, 4.2 cm and 3.65 cm of thickness are selected for the back and side insulation, respectively. Finally, for the collector flow tubes, 14 tubes with an inner diameter of 1.6 cm are selected. Furthermore, the low value of the POE shows the robustness based on the response model approach can yield to a satisfactory solution.

39.4.2.3 Validation Run

To confirm the obtained results based on the response model approach, the design parameters at the optimum configuration that maximizes the optical efficiency and minimizes the heat loss coefficient are used to run a validation numerical experiment using CoDePro. The confirmation run shows an offset of 0.5% in predicting the

optical efficiency response and about 12.38% in predicting the heat loss coefficient response. These results show the ability of the obtained response models in successfully predicting the characteristics of the flat plate solar collector.

39.5 Conclusions and Recommendations

The current study attempts to find the design parameters configuration that optimizes the characteristic responses of the flat plate solar collector namely the optical efficiency and the heat loss coefficient, with independency on the environmental factors through using the Taguchi method, and the response model approaches. The results of the study can be summarized as follows:

Based on the analysis of the main factors effect, the Taguchi method shows that the number of collector flow tubes is the most significant factor in the optical efficiency response, while the back insulation thickness is the most significant one for the heat loss coefficient. Furthermore, the optimum design parameters of the optical efficiency are different from the optimum design parameter for the heat loss coefficient. This shows the failure of Taguchi method in optimizing multiple responses.

Based on the analysis of the factors effect and their interaction, the response model approach succeeds in optimizing the multiple responses which include the optical efficiency and the heat loss coefficient with a drop in the POE where it is 0.012 for the optical efficiency and 0.05 for the heat loss coefficient.

The validation run shows the ability of the response models in predicting the optical efficiency and the heat loss coefficient precisely.

As a recommendation for the current study, an experimental test rig based on the optimum design parameters needs to be built in order to validate the optimization results. Furthermore, the same technique of investigation can be extended to various components of the solar water heating system in special and renewable energy systems in general with consideration for the life cycle cost effect in obtaining the optimum configuration for the design parameters.

Nomenclature

A	The air gap between glass and plate (cm)
A·	The solar collector area (m^2)
B	Air gap between cover glass 1 and cover glass 2
C	Absorber plate material
D	Absorption film type
E	Absorber plate thickness (cm)
F	Back insulation thickness (cm)
F_R	The heat removal factor
G	Side insulation thickness (cm)
I_t	The hourly solar radiation (W/m^2)
K	Number of collector flow tubes

L	Inner diameter of collector flow tube (cm)
M	Absorber length (m)
T_a	Ambient temperature (°C)
T_i	Initial solar collector temperature (°C)
U_s	The heat loss coefficient (W/m °C)
u_s	Wind speed (m/s)
Q_{net}	The total useful energy output from flat plate solar collector (W)

References

1. Chen G, Doroshenko A, Koltun P, Shestopalov K (2015) Comparative field experimental investigations of different flat plate solar collectors. Sol Energy 115:577–588
2. Rao SS, Hu Y (2010) Multi-objective optimal design of stationary flat-plate solar collectors under probabilistic uncertainty. J Mech Des 132(September 2010):094501
3. Jeffrey Kuo CF, Su TL, Jhang PR, Huang CY, Chiu CH (2011) Using the Taguchi method and grey relational analysis to optimize the flat-plate collector process with multiple quality characteristics in solar energy collector manufacturing. Energy 36(5):3554–3562
4. Alvarez A, Cabeza O, Muñiz MC, Varela LM (2010) Experimental and numerical investigation of a flat-plate solar collector. Energy 35(9):3707–3716
5. Hobbi A, Siddiqui K (2009) Experimental study on the effect of heat transfer enhancement devices in flat-plate solar collectors. Int J Heat Mass Transf 52(19–20):4435–4448
6. Moghadam AJ, Farzane-Gord M, Sajadi M, Hoseyn-Zadeh M (2014) Effects of CuO/water nanofluid on the efficiency of a flat-plate solar collector. Exp Thermal Fluid Sci 58:9–14
7. Zambolin E, Del Col D (2010) Experimental analysis of thermal performance of flat plate and evacuated tube solar collectors in stationary standard and daily conditions. Sol Energy 84 (8):1382–1396
8. Khademi M, Jafarkazemi F, Ahmadifard E, Younesnejad S (2012) Optimizing exergy efficiency of flat plate solar collectors using SQP and genetic algorithm. Appl Mech Mater 253–255:760–765
9. Mintsa Do Ango AC, Medale M, Abid C (2013) Optimization of the design of a polymer flat plate solar collector. Sol Energy 87(1):64–75
10. Montgomery DC (2013) Design and analysis of experiments, 8th edn. Wiley, New Jersey, United States
11. Beckman WA, Duffie JA (2006) Solar engineering of thermal processes, 3rd edn. Wiley, New Jersey, United States
12. ASHRAE Standard 93-2003 (2003) Methods of testing to determine the thermal performance of solar collectors, American Society of Heating, Refrigerating and Air-Conditioning Engineers Atlanta
13. Roy R (1990) A primer on the Taguchi method, 1st edn. Society of Manufacturing Engineers, Dearborn
14. Myers R, Montgomery D, Anderson C (2009) Response surface methodolgy: process optimization using designed experiments, 3rd edn. Wiley, Hoboken

Chapter 40
Solar Water Heating for Aquaculture Applications in Cold Climates: A Case Study of Finland

Michael Anees, Maresa Bussa, Cristina Dominguez, Marco Duran, Mandar Kadam, and Luis Rojas-Solórzano

40.1 Introduction

Aquaculture has been the fastest-growing food production sector globally during the last two decades. Conversely, in Europe, especially in the Baltic Sea Region, it has stagnated or shrunk in certain cases [1]. For this reason, the European Union's Baltic Sea Region Programme developed the Aquabest Project to promote the growth of aquaculture production with sustainable practices and technologies.

The aim of this paper is to analyze the feasibility of using solar water heating (SWH) systems for aquaculture in cold climates, challenging conventional technologies (e.g., pure electric heating) with a low-carbon intensive alternative. A case study of the implementation of the Danish model fish farm in Tampere, Finland, is considered [2], where solar water heating systems are not commonly applied at large scale. The Danish fish farm model adopts the recirculating aquaculture system (RAS), which is an economic and eco-friendly solution for freshwater farming [3]. In the original case study, [2] electric heating are used to reach the optimum temperature for fast growth of fish. In this paper, the techno-economic viability of using thermal solar heating to supply a fraction of the energy required for raising the water temperature to the optimum temperature for fish growth is examined. Next, the potential CO_2 savings that will result from reducing the dependence on electrical energy, according to the energy mix in the Finish electrical grids, are presented. Further, national policies that would increase the project's NPV and attractiveness for investors are proposed.

M. Anees · M. Bussa · C. Dominguez · M. Duran · M. Kadam
IMT Atlantique, Department of Energy Systems and Environment, Nantes, France

L. Rojas-Solórzano (✉)
Nazarbayev University, School of Engineering, Astana, Republic of Kazakhstan
e-mail: luis.rojas@nu.edu.kz

S. Nižetić, A. Papadopoulos (eds.), *The Role of Exergy in Energy and the Environment*, Green Energy and Technology,
https://doi.org/10.1007/978-3-319-89845-2_40

40.2 Energy Model

An energy model was developed using RETScreen [4]. Under a conservative analysis (assuming the highest possible energy consumption), we assume that the fish farm operates on a capacity factor of 100%. The daily hot-water supply reported for this farm is 200,000 L/d [1]. The required water temperature depends on the type of fish produced. In this case, the farm produces rainbow trout, which requires a temperature from 6 to 12 °C [5]. Thus, 12 °C was selected to accelerate fish growth and biological development.

RETscreen calculates the annual minimum and maximum supplied water temperature based on the local ambient temperature found in RETscreen's meteorological databases. Thus, the calculated minimum and maximum temperature of the water supplied in Tampere are 1 and 8.8 °C, respectively. RETscreen then calculates the temperature profile of the rest of the year based on an annual sinusoidal temperature profile. Accordingly, RETscreen calculates the overall annual heating demand required to keep the water temperature at 12 °C. The heating demand was found to be almost 750 MWh/year.

Tampere has a latitude of approximately 61°; thus the collectors are installed with a slope of 46° to take advantage of the summer conditions, since the daily global horizontal solar radiation during the fall and winter months is lower than that of the spring and summer months. See Table 40.1.

Iterations were run, and accordingly, 138 glazed solar collectors with 2.33 m^2 of aperture area per collector were found to yield the highest NPV as explained in Sect. 40.5. The area 2.33 m^2 was chosen as it corresponds to the largest area/unit of the high-efficiency collectors available in the market. The technical details of the chosen collectors are summarized in Table 40.2.

Table 40.1 Average daily global horizontal solar radiation per month

Month	Daily global horizontal solar radiation kWh/m^2/d
January	0.28
February	1.00
March	2.37
April	3.92
May	5.43
June	5.60
July	5.25
August	4.02
September	2.52
October	1.11
November	0.44
December	0.14

Source: RETscreen database

Table 40.2 Specifications of solar collectors

Type of SWH	Glazed
Manufacturer, model	Viessmann, Vitosol 200-F SH2
Gross area/solar collector	2.52 m^2
Aperture area/solar collector	2.33 m^2
Fr (tau alpha) coeff.	0.72
Fr UL coeff.	3.5 (W/m^2)/°C
Number of collectors	138
Solar collector area	348.17 m^2
Capacity	225.46 kW
Miscellaneous losses	3%
Slope (tilt angle)	46°

Although the collector angle was designed to maximize summer operating conditions, the proposed solar water heating system works throughout the whole year.

The average electricity price in Finland is 0.1 US$/kWh [6]. Thus, the annual cost of electricity required for heating in the base case (only electric heating) is US$ 75,000, based on the heating demand of 750 MWh/year. On the other hand, the annual cost of electricity required for heating in the proposed case (electric + solar heating) is almost US$ 52,000.

40.3 Cost Analysis

The project total cost includes capital cost and operation and maintenance costs. Capital cost includes the cost of preliminary studies, the solar collectors, pipes, pumps, accessories, labor, spare parts, and contingencies, as well as salvage value. See Table 40.3. The operation and maintenance cost includes labor and electricity cost. See Table 40.4.

40.3.1 Preliminary Study

The initial studies include the feasibility, development, and engineering studies. Each of which is expected to cost an average of 2.5% of the total equipment and construction cost [7].

Table 40.3 Summary of capital cost

Item	Cost
Studies	
Feasibility study	US$ 6,157
Development	US$ 6,157
Engineering	US$ 6,157
Subtotal	**US$ 18,471**
Heating system	
Solar water heater	US$ 232,116
Piping, pumps, installation	US$ 14,152
Subtotal	**US$ 246,268**
Balance of system and miscellaneous	
Spare parts	US$ 24,627
Transportation	US$ 3,200
Training and commissioning	US$ 800
Contingencies	US$ 29,336
Interest during construction	US$ 1,210
Subtotal	**US$ 59,173**
Total initial costs	**US$ 323,912**

Subtotals and total initial costs are in bold

Table 40.4 Summary of operation and maintenance cost

Item	Cost per month
Parts and labor	US$ 4900
Electricity cost	US$ 52,000

40.3.2 Collector and Transportation

The price of solar collectors was obtained from the Californian vendor: SunEarth. The model selected as a price reference is the AE32/66D model. Further, transportation cost was calculated in three stages: ground freight from manufacturer's site at Fontana to Fort Lauderdale, maritime shipping to Helsinki, and ground freight from Helsinki to Tampere [8].

40.3.3 Pipes, Pumps, and Accessories

The solar heating technology used is an indirect active technology, which consists of a cold-water circuit (fish water) that is heated up by a closed hot-water circuit within a heat exchanger (indirect system). The hot-water circuit is heated in the solar collectors. The model also uses electrically driven pumps to control the circulation

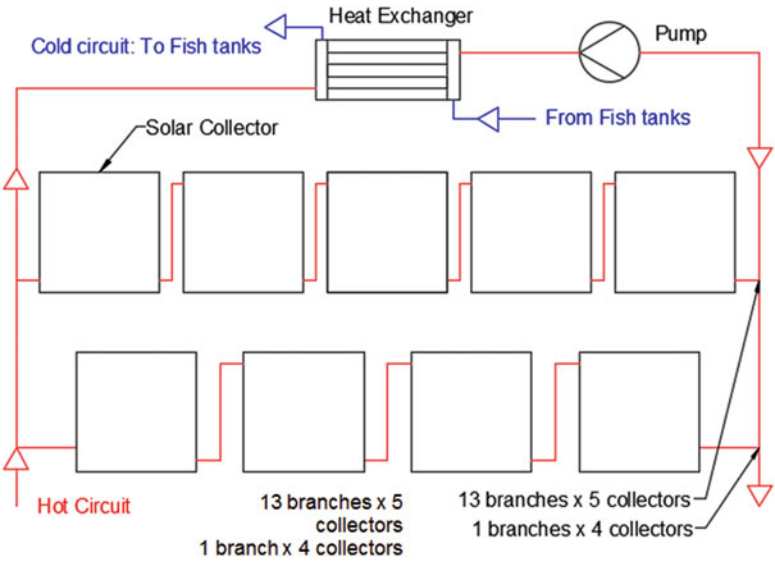

Fig. 40.1 Heating circuit schematic

of the water (active system) and an auxiliary heating system to make up for the rest of the needed thermal energy.

It is assumed that the cold-water circuit and the heating storage tanks along with a heat exchanger with 80% of efficiency already exist since these appliances are needed for the electric heating system of the base case as well. Thus, we base he calculation of the cost of parts and labor on a simple design of the hot-water circuit and the solar collectors.

The flow rate in each collector was set as recommended (1.9 L/min to 4.5 L/min), according to the manufacturer's technical specification. To better manage the total flowrate and reduce the piping size, an arrangement of two equal circuits was chosen. Each circuit has 14 branches in parallel. Thirteen branches of which have five collectors in series, while the last branch has four, as shown in Fig. 40.1.

Furthermore, the recommended water velocity inside the pipes per [9] is 1.0 m/s. Accordingly, the main pipe diameter is calculated to be 1 ¾ inches and the branch pipe diameter to be ½ inches. Each circuit has one pumping unit. Both pipes and pumps are priced according to [10]. The main pipes are established to have a length of 40 meters, while the branches have a length of 160 meters, constructed with copper pipe (p/n: 8967 K141 [10]), with insulation (MMC p/n: 4463 K139 [10]), and copper pipe (p/n: 8967 K69 [10]) with insulation (p/n: 4734 K132 [10]), respectively. The installation accessories are assumed to be 20% of the piping cost; hence a total investment of US$5400 is accounted. In addition, the pump units (p/n: 8249 K81) [10] accrue a cost of US$944.

40.3.4 Labor

Installation is assumed to be done by qualified technicians. Therefore, based on the construction hour rate of 50 meters of piping per 78 h [11], 312 h is needed to complete the installation. The average wage in Finland for construction and installation is US$22/h [12]. Accordingly, the construction labor cost is calculated as US $6864.

40.3.5 Training

We consider an 8-h training session to be given to the farm staff by an expert in solar thermal systems. The cost considers the average hourly salary of a solar thermal systems expert in Finland: US$25/h in 2016 [12]. Travel and meal expenses are assumed to be US$400. Therefore, the total training cost will be US$800 approximately.

40.3.6 Spare Parts and Contingencies

The spare parts cost during the construction is estimated to be 10% of the total facility cost [13, 14]. Contingency costs are considered for unexpected events during the construction phase and are set to 10% of the total facility cost [15].

40.3.7 Salvage Value

A salvage value of 5% of the heating system cost was assumed; the latter includes collectors, pipes, pumps, and accessories.

40.3.8 Operation and Maintenance

The parts and labor cost during operation and maintenance can be approximated to 2% of the total heating system cost [16]. In addition to labor cost, the annual electricity cost is near US$52,000 based on an average price of 100 US$/MWh [17, 18]. See Table 40.4.

40.4 Financial Parameters

The economic comparison of the base and proposed case is based on the Net Present Value. Therefore, the considered financial parameters include the electricity escalation rate, inflation rate, project discount rate, government incentives, debt and equity interest rates, debt term, debt/equity ratio, and project lifetime.

40.4.1 Fuel Escalation and Inflation Rates

The escalation rate of electricity prices depends on many factors, and its prediction is usually a source of uncertainty. It must be estimated based on the past trend. In this project, based on Meyer's work [19], a 2% escalation rate of electricity prices was assumed.

The inflation rate in Finland's economy was set to almost 1% based on the arithmetic mean value for the past 5 years [20].

40.4.2 Discount Rate

The German research society Fraunhofer-Gesellschaft set the default discount rate for renewable energy projects to 7.5% [21]. However, the rate can be adapted to specific projects, technologies, and countries by using three different multiplier factors, as seen in Eq. 40.1.

$$\begin{aligned}\text{Discount rate} = {} & \text{default discount rate} \times \text{country risk factor} \\ & \times \text{policy risk factor} \times \text{technology risk factor}\end{aligned} \tag{40.1}$$

According to Fraunhofer, Finland's country risk factor is 1. In addition, since Finland's political stability and regulatory quality are higher than the average of the high-income OECD countries, Finland is considered to have a low policy-risk factor of 1.18 [21].

There is no technology risk factor given for solar heating in Finland. Thus, the risk factor of large PV plants is used instead [21]. Accordingly, the calculated overall discount rate for a solar heating project in Finland is 8%.

40.4.3 Government Incentives

The Finnish government provides capital grants for projects that invest in measures which improve environmental conditions. For solar water heating projects, the grant

Table 40.5 Summary of financial parameters

Parameter	Value
Electricity price escalation rate	2%
Inflation rate	1%
Discount rate	8%
Government incentives on capital cost	20%
Equity/debt ratio	15/85
Debt term	15 years
Debt interest rate	3%

covers in general 20% of eligible costs, which includes investment costs as well as energy audit and energy analyses [22].

40.4.4 Debt Characteristics and Project Lifetime

As for the debt ratio, per Finnvera, a state-owned financing company, a minimum equity of 15% is required to be eligible for borrowing the rest of the investment cost [23]. Thus, a debt ratio of 85% is set. The debt interest rate amounts to 3% based on values obtained from the Bank of Finland. Finally, the calculations were based on a debt term of 15 years and a project lifetime of 20 years. The project's financial parameters are summarized in Table 40.5.

40.5 Choosing the Optimum Number of Collectors

To determine the optimum number of collectors, iterations of different number of collectors were run, and the corresponding NPV and simple payback time were graphed (Fig. 40.2).

Thus, the evolution of NPV is characterized as a function of number of collectors by the following equation:

$$y = -3.2152\,x^2 + 889.25x - 18382 \tag{40.2}$$

where y is the NPV and x is the number of collectors. Hence, to calculate the number of collectors that achieves the highest NPV, the polynomial equation (Eq. 40.2) is differentiated with respect to x:

$$\frac{dy}{dx} = -6.4304x + 889.25 \tag{40.3}$$

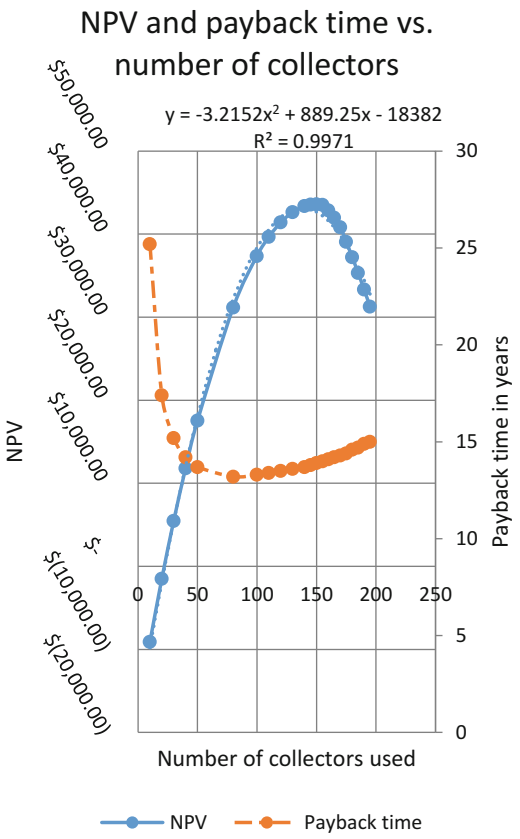

Fig. 40.2 NPV and simple payback time vs. number of collectors with a trend line fit on the NPV series

By setting $dy/dx = 0$ and solving for x, the number of collectors that achieves the highest NPV is 138, which corresponds to an NPV of almost US$42,200, a benefit/cost ratio of 1.95, a simple payback time of almost 13.5 years, and a solar fraction of 30.5%.

40.6 Risk Analysis

To test the effect of the change of prices and other uncertainties on the whole project, the parameters initial cost, operation and maintenance cost, and electricity cost were increased and decreased by 10%, while the parameters debt ratio, interest rate, and debt term were increased and decreased by 5% since the latter set of parameters is more stable than the first set. See Table 40.6.

The effect of the changes is calculated and presented in Fig. 40.3. The highest parameter that positively affects NPV is the electricity cost; i.e., the higher the electricity cost, the higher the NPV would be. On the contrary, adverse effects

Table 40.6 Parameter range investigated for risk analysis

Parameter	Range (+/−)
Initial costs	10%
O&M	10%
Fuel cost – base case	10%
Debt ratio	5%
Debt interest rate	5%
Debt term	5%

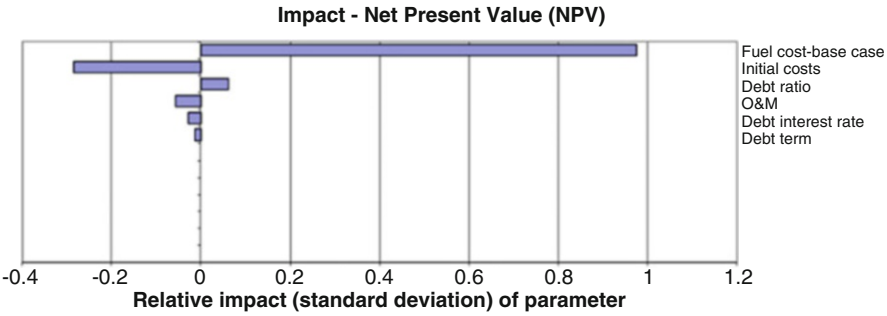

Fig. 40.3 Impact of the change of different parameters on NPV (as extracted from RETScreen)

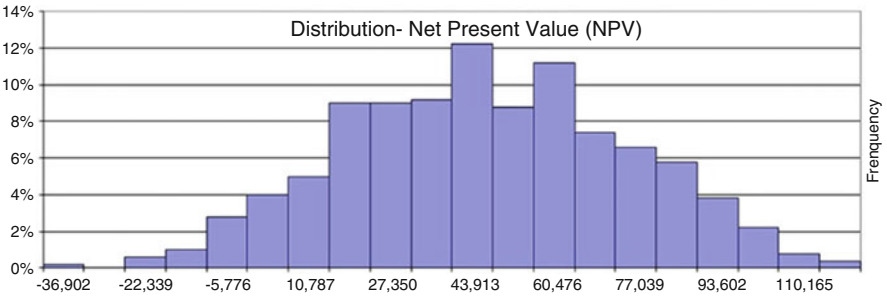

Fig. 40.4 Distribution of NPV based on the standard deviation of the parameters specified (as extracted from RETScreen)

would be due to increasing the initial cost, followed by operation and maintenance cost, debt interest rate, and debt term.

Figure 40.4 shows the probability distribution of NPVs based on the uncertainty introduced in Table 40.6 after running a Monte Carlo analysis with 500 samples. The recorded median is almost US$46,000. It is worth mentioning that up to a risk of 22.2%, negative NPV might occur (see Table 40.7). In addition, the probability distribution is wide, indicating a medium risk. Further focus on thermal solar heating policies and subsidies could help increase NPV or reduce risk and subsequently attract investors to implement this technology in cold climates. We investigate different policies that may achieve this goal in Section VIII.

Table 40.7 Min. and max. NPV versus risk

Risk	Min. NPV within level of confidence	Max. NPV within level of confidence
10%	−14,000 US$	106,800 US$
20%	−1373 US$	88,200 US$
30%	7800 US$	81,900 US$
40%	15,300 US$	77,600 US$

Table 40.8 CO_2 emissions in the base and proposed case and the corresponding savings of CO_2

Base case	Proposed case	Total reduction
Fuel: Electricity (100%) *Consumption:* 751 MWh	*Fuel:* Electricity (69.5%) + Solar (30.5%) *Consumption:* 492 MWh	*GHG base case – emissions:* 172.4 tCO2 *GHG proposed case – emissions:* 115.1 tCO2
GHG emission factor: 0.229 tCO2/MWh	*GHG emission factor:* 0.160 tCO2/MWh	*Net annual GHG emission reduction:* 57 tCO2

40.7 Emission-Reduction Analysis

Greenhouse gases (GHG) include water vapor, carbon dioxide (CO_2), methane (CH_4), nitrous oxide (N_2O), ozone (O_3), and several classes of halo carbons (i.e., chemicals that contain carbon together with fluorine, chlorine, and bromine) [24]. GHG allow solar radiation to enter the Earth's atmosphere but prevent the infrared radiation emitted by the Earth's surface from escaping. Instead, this outgoing radiation is absorbed by the greenhouse gases; and then partially reemitted as thermal radiation back to Earth, warming its surface.

RETscreen has a built-in database that includes the current energy mix in Finland. Accordingly, the RETscreen model can calculate the CO_2 emissions due to electricity consumption in tCO_2-eq./MWh. While the base case consumes 751 MWh electricity per year and emits 172.4 tCO_2-eq./year with a GHG emission factor of 0.229 tCO_2-eq./MWh, the proposed case consumes 561 MWh of electricity, and the rest of the heating demand is supplied by solar heating (solar energy, 30.5% – electricity, 69.5%) with an equivalent GHG emission factor of 0.160 tCO_2-eq./MWh (due to substituting a fraction of electric energy consumption by solar energy). As a result, GHG emission is reduced to 115.1 tCO_2/year. Thus, annual CO_2 savings are 57.3 tCO_2-eq./year. If the project's lifetime is 20 years, the total savings of CO_2 emissions are 1146 tonnes (Table 40.8).

40.8 Policy Recommendation

As seen in the risk analysis section, the distribution of NPV probabilities is skewed to the right, i.e., toward high NPV. However, the NPV distribution is quite wide, which suggests a relatively high project risk. Thus, we studied the effect of

Table 40.9 Percentage of capital grant and the corresponding NPV, B/C ratio, and payback time

Capital grant % of CAPEX	NPV	Benefit/cost ratio	Payback (year)
20%	US$ 42,200	1.95	13.5
25%	US$ 53,500	2.2	12.9
30%	US$ 67,888	2.45	12.3
35%	US$ 76,000	2.7	11.7
40%	US$ 87,400	2.96	11.2

Table 40.10 Interest rate and the corresponding NPV, B/C ratio, and payback time

Interest rate	NPV	Benefit/cost ratio	Payback (year)
3.0%	US$ 42,200	1.95	13.5
2.9%	US$ 43,400	1.97	13.5
2.8%	US$ 44,800	2.00	13.5
2.7%	US$ 46,000	2.03	13.5
2.6%	US$ 47,400	2.06	13.5
2.5%	US$ 48,700	2.09	13.5

Table 40.11 Scenario analyses of changing the percentage of capital grants and interest rate and the corresponding NPV, B/C ratio, and payback time

Capital grant	Debt interest rate	NPV	Benefit/cost ratio	Payback
25%	2.80%	$ 56,100	2.26	12.9
25%	2.70%	$ 57,400	2.29	12.9

increasing the government incentives on NPV, benefit/cost ratio, and payback time. Government incentives were increased in terms of (1) increasing grants on capital costs (Table 40.9), (2) reducing the interest rate (Table 40.10), and (3) a combination of both (Table 40.11).

Based on the results, we propose a possible and a realistic change in policy that would increase the NPV. The change includes increasing the capital grant from 20% to 25% and reducing the interest rate from 3% to 2.8%. This change in policy increases the NPV from US$42,200 to US$57,400 (an increase of 36%). Furthermore, Fig. 40.5 shows the NPV probability distribution with the new policy in place compared to the NPV distribution with the old policy in place. The comparison shows that the NPV probability distribution does not change much in terms of skewness or width which is explainable by the fact that the project risk depends mainly on the capital cost and changes in electricity price, as explained earlier. As a result, the only noticeable change between the old and the new policy is the scale of abscissa which shifts toward higher NPV values in the new policy, compared to the lower NPV values in the old policy. See Fig. 40.5.

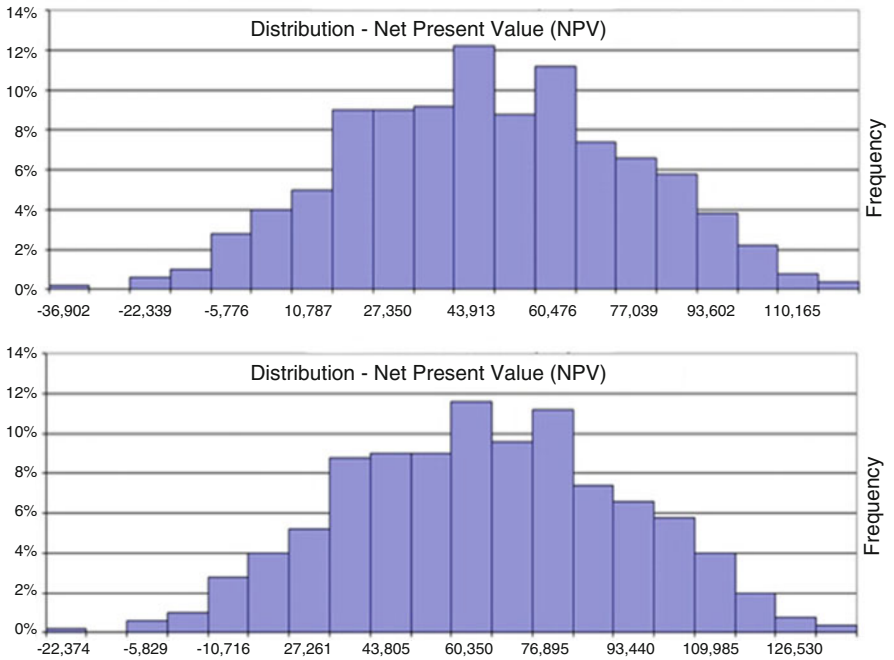

Fig. 40.5 NPV distribution as a result of existing government policy (top) vs. proposed governmental policy (bottom) (as extracted from RETScreen)

40.9 Conclusions

Economic feasibility calculations are routinely used to assess new technologies. This report serves as an example of the use of solar energy to produce hot water for a fish farm located in a cold climate region by coupling a hot loop (where the water is heated in glazed solar collectors) to a cold loop (where the fish lives) using heat exchangers. A case study is presented based on a fish farm that would be located in Finland to assess the techno-economic viability of the technology to complement the electric heating system. The project saves about 31% of electricity consumption. This saving would result in an NPV of almost US$42,200, a benefit/cost ratio of 1.95, a simple payback time of almost 13.5 years, and a reduction of CO_2 emissions by almost 57 tCO_2 eq./year.

Even though the risk of uncertain initial cost, from what is estimated in this study, has a high impact on the project feasibility, further state subsidies in terms of capital grant and lower interest rate could be implemented to shift the risky NPV distribution toward a higher range of NPV. By increasing the capital grants from 20% to 25% and reducing the debt interest rate from 3% to 2.8%, the NPV for this project increases from US$42,200 to US$57,400, which represents an increase of about 36%. Thus, if cold climate countries (such as the Nordic countries) offer a slightly

higher incentive package, solar thermal projects will become more attractive economically, and their penetration rate into the local market may increase, which, by turn, will reduce GHG emissions.

Nomenclature

dy/dx	First-order differential equation
Y	Variable
X	Variable
RAS	Recirculation aquaculture system
NPV	Net present value
SWH	Solar water heating
GHG	Greenhouse gases
L/min	Liters/minute
MWh	Megawatt*hour
CO_2	Carbon dioxide
OECD	Organisation for Economic Co-operation and Development

References

1. Aquabest (2016) Aquabest project. Retrieved from http://www.aquabestproject.eu/
2. Kankainen M, Nielsen P, Vielma J (2014) Economic feasibility tool for fish farming – case study on the Danish model fish farm in Finnish production environment. Aquabest, Helsinki
3. FAO (2016) (Food and Agriculture Organization of the United Nations), Cultured Aquatic Species Information Programme. Retrieved 10 04, 2016, from http://www.fao.org/fishery/culturedspecies/Oncorhynchus_mykiss/en
4. Government of Canada – Natural Resources (2016) RETScreen, Clean energy management software. Retrieved from http://www.nrcan.gc.ca/energy/software-tools/7465
5. FAO (2016) (Food and Agriculture Organization of the United Nations), Fisheries and Aquaculture Department. Retrieved 10 04, 2016, from http://www.fao.org/fishery/statistics/en
6. Eurostat (2016) Energy price statistics. Retrieved 10 10, 2016, from http://ec.europa.eu/eurostat/statistics-explained/index.php/Energy_price_statistics
7. Gautama A, Chamolib S, Kumara A, Singh S (2017) A review on technical improvements, economic feasibility and world scenario of solar water heating system. Renew Sust Energ Rev 68(1):541–562
8. World Freight Rates (2016) "Freight Calculator," World Freight Rates, [Online]. Available: http://www.worldfreightrates.com/freight. [Accessed 11 2016]
9. Campbell M, Barnard P, Curtis R, Davies R, Day T, Hughes D, Woods P (2016) GVB1/16 CIBSE Guide B1: Heating. Retrieved from http://www.cibse.org/getmedia/76229a96-c37e-4d2f-b4f9-7d62ba62bab4/Guide-B1-appendix.pdf.aspx
10. McMaster-Carr (2016) Online catalogue. Retrieved from McMaster-Carr Supply Company https://www.mcmaster.com/
11. Ogershok D (2005) 2005 national construction estimator. Craftsman Book Company, Carlsbad
12. Salary Explorer (2015) Hourly wage. Retrieved from http://www.salaryexplorer.com
13. Jubran B, Ahmed M, Ismail A, Abakar Y (2000) Numerical modelling of a multi-stage solar still. Energy Convers Manag 41(11):1107–1121
14. Al-Hinai H, Al-Nassri M, Jubran B (2002) Effect of climatic, design and operational parameters on the yield of a simple solar still. Energy Convers Manag 43(13):1639–1650
15. Ruster J (1996) Public policy for the private sector. The WorldBank, Washington, DC

16. Kulkarni GN, Kedare SB, Bandyopadhyay S (2007) Determination of design space and optimization of solar water heating systems. Sol Energy 81(8):958–968
17. Energy Authority (2016) "National Report 2016 to the Agency for the Cooperation of Energy Regulators and to the European Commission," Council of European Energy Regulators (CEER), Helsinki, Finland, 2016
18. Invest in Finland (2010) "Finland's electricity prices among the cheapest in the EU," Invest in Finland, Helsinki, 2010
19. Meyer J (2015) Solar electricity utilization in Finland. Bachelor of Engineering Thesis, Helsinki Metropolia University of Applied Sciences, Helsinki
20. Triami Media BV (2016) Inflation.eu. Retrieved 11 05, 2016, from Historic Inflation Finland http://www.inflation.eu/inflation-rates/finland/historic-inflation/cpi-inflation-finland.aspx
21. Held A, Ragwitz M, Eichhammer W, Sensfuss F, Pudlik M, Pfluger B, Resch G, Olmos L, Ramos A, Rivier M, Kost C, Senkpiel C, Peter F, Veum K, Slobbe J, Joode J d (2014) Estimating energy system costs of sectoral RES and EE targets in the context of energy and climate targets for 2030. Fraunhofer ISI, Karlsruhe
22. Ministry of Economic Affaires and Employment (n.a.) Retrieved 11 04, 2016, from Energy Aid: http://tem.fi/en/energy-aid
23. Finnvera (n.a.) When setting up a business. Retrieved 11 28, 2016, from Financial Planning. https://www.finnvera.fi/eng/Start/Financial-planning/When-setting-up-a-business?source=3165#_financial_planning
24. U.S. Climate Action Report (2002) University of Minnesota, Minneapolis, MN, 2002

Chapter 41
On-Grid PV Opportunities in University Campuses: A Case Study at Nazarbayev University in Astana, Kazakhstan

Daniyar Aitkulov, Zhuldyz Assylova, Elnara Suanbekova, and Luis Rojas-Solórzano

41.1 Introduction

The Republic of Kazakhstan is very rich in fossil fuel resources such as oil, coal, and natural gas. Most of Kazakhstan's power and heating grid is supported by coal-fired power plants. Nevertheless, the country has the firm aim to turn into an emission-free nation in the near future. For this purpose, the nation has to exploit its vast renewable resources, such as wind, solar, and biomass. In particular, there is a large potential for solar energy harvesting throughout the vast territory of the country. The number of sunny hours is 2200–3000 per year, and the energy of solar irradiation is 1300–1800 kW/m^2/year. By the end of 2016, six photovoltaic plants of total of 50 MWp are expected to be built in the southern region, namely, in Zhambyl oblast [2].

Nowadays, there are numerous ongoing laws and programs, which support renewable energy resources development throughout the country. In 2009, Kazakhstan's Parliament passed the final amendments to the Law on the Use of Renewable Energy Sources, which obliges all electricity transmission companies to allow the renewable sector to connect to the grid. The law also provides a number of incentives including Feed-in-Tariff adopted by the end of August 2013 with rates for solar electric stations to be 34.61 KZT/kWh [3]. In addition, the legislation states that 5% of Kazakhstan's total energy balance must be renewable by 2024. Kazakhstan

D. Aitkulov · Z. Assylova · E. Suanbekova
Nazarbayev University, School of Engineering and Graduate School of Business, Astana, Kazakhstan

L. Rojas-Solórzano (✉)
Nazarbayev University, School of Engineering, Department of Mechanical Engineering, Astana, Kazakhstan
e-mail: luis.rojas@nu.edu.kz

S. Nižetić, A. Papadopoulos (eds.), *The Role of Exergy in Energy and the Environment*, Green Energy and Technology,
https://doi.org/10.1007/978-3-319-89845-2_41

also adopted the Energy Efficiency 2020 Program that would reduce 10% of greenhouse gas emissions every year until 2020 [3]. With these supporting legislation frameworks, there is a huge potential for energy companies and other organizations to start exploiting renewable energy sources and contribute to fulfill this "green" commitment. Universities are no exception, and like any other organization, these ones want to become more proactive on green issues and contribute to continuous development of the country.

According to the mission statement of Nazarbayev University, it is fully committed "to be a model for higher education reform and modern research in Kazakhstan and to contribute to the establishment of Astana as an international innovation and knowledge hub," and it is clear that Nazarbayev University is devoted to sustainable development process through innovation. Thus, in order to be the leading and world-class educational system in Central Asia, the university has started considering the environmental issues locally, from the university context, to create favorable conditions for construction and operation of clean energy technologies in-campus.

Consequently, the key problem considered in this investigation was how to reduce the CO_2 equiv. emissions associated to the consumption of grid-electricity by Nazarbayev University using solar in-campus photovoltaic (PV) technology. To answer this question, it is proposed to examine at pre-feasibility level, the viability of installing rooftop arrays of PV panels in the campus. It was decided to analyze the project using Feed-in-Tariff (FIT) schemes and potential use of incentive or grants.

In next sections it is presented:

- Life Cycle Cost Analysis of the proposed installation of PV systems at Nazarbayev University supported on the platform RETScreen to determine the feasibility of the project under current FIT scenario. Alternative scenarios II and III, with inclusion of incentive and improved FIT, respectively, were also analyzed.
- In the concluding remarks, the emphasis was given to compare the options and recommendations.

41.2 Related Work

There are extensive numbers of projects carried out in the field of installing PV panels at universities worldwide. According to the ranking of top 10 campuses by total installed capacity, the University of Arizona, Arizona State University, and State University of New Jersey are the top three with the total capacity of 28,095 kW, 23,567 kW, and 17,417 kW, respectively [4]. Another PV panel installations are found in Washington DC universities for a total of 52 MW. Washington University in St. Louis is committed to pursuing renewable energy projects to show and test new technologies. The 2014 Solar Photovoltaic Projects event was carried out at Washington University with an estimated output of 545,000 kWh each year [5]. It is

expected that the arrays will save the university about $190,000 over 10 years. Most of the solar arrays had been installed on flat roofs on several buildings, such as the School of Medicine (50kWp), West Campus (75kWp), the University City Children's Center (50kWp), and other spaces. The contributors of the project were the seniors of the University, the treasurer's office, the General Counsel's office, and some facility teams at the Danforth and School of Medicine campuses, financial planning, and others.

All these institutional facilities have a comprehensive solar system that is used either for campus everyday needs or for their extensive research and development. There is indeed, a substantial encouragement coming from the government (The Association for the Advancement of Sustainability in Higher Education, 2015). For example, there are extensive financial incentives from the US Renewable Energy Incentive Program that helps to cut up to half the cost of the solar system. Future installation plan includes various PV technologies such as high concentration, low concentration, monocrystalline, polycrystalline, and thin film [1]. It also incorporates single- and dual-axis tracking systems along with technologically advanced inverter and controller designs.

The objective of another on-campus project [6] was to implement a midsize photovoltaic plant integrated into the main university building. The project consisted of four photovoltaic sub-generators connected to the grid at Jaen University Campus in Spain. The system was supposed to subsequently generate the 10% of the total campus energy requirements; the energy output by the on-grid PV system is estimated as 240 MWh per year. PV panels were integrated into three main facilities: parking covers, façade, and a pergola. Safety was one of the major concerns since Jaen University is visited by 14,000 students daily. The main outcome of this project was the possibility to utilize research findings in other areas of Spain.

Another case study is concerned with the complete design of a photovoltaic installation at the University of Malaya that was supposed to be either used for university's electric consumption or for sale using the renewable energy incentive program initiated by the government of Malaysia. In this program renewable energy sources were benefited by additional incentives in the form of tax relief and cost waivers [7]. The installation of PV panels was evaluated in terms of sellback price, IRR, subsidy rate, and project lifetime.

In summary, there are a number of completed case studies that are concerned with economic and social aspects of PV panel installations on university campuses. Their experience can be analyzed and utilized in terms of further feasibility evaluation around the world.

41.3 Life Cycle Cost Analysis

Kazakhstan is entering a new era in terms of solar power. Technological improvements of today, affordable solar costs, and search for the alternatives of traditional energy sources have all contributed to solar energy finally entering the premises of Kazakhstani Unified Power System [8].

In order to analyze the installation of PV panels at NU campus, the Life Cycle Cost Analysis and the evaluation of technical and GHG emissions were performed using RETScreen software tool.

41.3.1 Energy Model

The various aspects that affect the performance of a solar PV system in the current model are presented in Table 41.1.

It is assumed that the array of panels has a fixed slope.

Electricity export rate was obtained from FIT in Kazakhstan [4]. It is estimated at 36,410 KZT/MWh and will be used in the Case Scenario I. The tariffs are supposed to be valid for 15 years; there are measures taken for annual indexation of tariffs adjusted to inflation.

In order to identify what type of PV panels can be utilized, "Astana Solar" LLP was contacted, and the main technical specifications of panels were withdrawn. Thus, 100 pv panels, model KZ PV 230 M60, efficiency: 12.4%, conformed the 24 kWp system under consideration.

Inverter was chosen according to the required capacity with proposed efficiency of 93%, according to technical specification kindly provided by Astana Solar. The input data for the energy model and the estimated yearly energy production are presented in Table 41.2. An annual income will be used in the Life Cycle Cost Analysis according to the Feed-in-Tariff (FIT) in place for the expected 31 MWh of electricity exported to the University grid per year.

41.3.2 Cost Analysis

41.3.2.1 Initial Costs

Feasibility study Feasibility study is provided free by manufacturer "Astana Solar" LLP which is the provider of the PV panels chosen in this project. The company offers to carry site investigation, resource assessment, environmental assessment, and preliminary design as part of the sales agreement.

Development Project development activities will include cost for such items as contract negotiations, permits and approvals, site survey and land rights, GHG

Table 41.1 Parameters for energy model

Solar tracking mode	Fixed
Slope	30 deg
Azimuth	0 deg
Electricity export rate (KZT/MWh)	36,410

Table 41.2 Technical specifications of PV panels (as extracted from RETScreen)

Photovoltaic			
Type		mono-Si	
Power capacity	kW	24,00	
Manufacturer		Astana Solar	
Model		KZ PV 230M60	100 unit(s)
Efficiency	%	12,4%	
Nominal operating cell temperature	°C	45	
Temperature coefficient	% / °C	0,40%	
Solar collector area	m²	194	
Miscellaneous losses	%	10,0%	
Inverter			
Efficiency	%	93,0%	
Capacity	kW	24,0	
Miscellaneous losses	%	0,0%	
Summary			
Capacity factor	%	14,7%	
Electricity exported to grid	MWh	30,889	

validation and registration, project financing, legal and accounting, and project development management. It is assumed to have no cost for the development phase as the University's Central Research Office, Technopark, and PI "NURIS" will provide consulting, organizational and other support to the project members in the process of preparation, submission, and evaluation of research proposals and purchasing of goods (PV panels, software, etc), works, and services necessary for the research project.

Engineering The engineering phase includes costs for the proposed case project site and building design, mechanical design, electrical design, civil design, tenders and contracting, and construction supervision. These costs are assumed to be covered by the supporting University's organizations such as PI "NURIS" and Center for Commercialization. Some additional expenses are assumed to be of 200,000 KZT.

Power System Photovoltaic panels will be procured from "Astana Solar" LLP. "Astana Solar" LLP is a subsidiary of "Kazatomprom" company implementing a project on production of photovoltaic modules using Kazakhstani silicon "KazPV" [4]. The price for PV panel with capacity of 1 kWp is 315,000 KZT; therefore the total amount for the expected 24 kWp is 7,560,000 KZT. Road construction and transmission lines are not necessary since the panels will be located on the roof on the university blocks (School of Engineering). The cost for inverter is 145,000 KZT per 1 kW, thus 3,480,000 KZT for 24 kW.

Balance of System and Miscellaneous The cost allocated to spare parts is assumed as a 30% of the total equipment cost, which is 3,312,000 KZT. According to "Astana Solar" LLP marketing representatives, the costs for transportation and training and commissioning are 300,000 KZT and 120,000 KZT, respectively. The allowance for contingencies is calculated as 1,497,200 KZT. The interest during construction is assumed as 15% of the project costs in 6 months. Therefore, total initial costs are 16,469,200 KZT.

41.3.2.2 Annual Costs

The parts and labor costs are the costs of spare parts and annual labor required for routine and emergency maintenance and operation of the proposed project. PV systems typically require little maintenance. The PV modules of "Astana Solar" LLP will last for 25 years and will need minimal maintenance (only cleaning from snow, ice, and dirt). An annual visual inspection is recommended to check for loose wires, structure solidity, and inverter, and it is assumed that the cost for annual maintenance inspection of a PV system is 150,000 KZT.

41.3.2.3 Periodic Costs

Inverter lifecycle is reported to be 10 years by "Astana Solar" LLP, and therefore, it is assumed that this equipment will be replaced every 10 years.

41.4 Feasibility Analysis

A preliminary study was performed to check if the estimated covering area for PV panels and location is economically feasible. For the installation of the panels, it was chosen the adjacent territory of the engineering building, named Block 6, shown in Fig. 41.1, indicating also in shadowed area the convenient location of the panels on the roof. However, there could be problems with post-installation on the roof such as operation and maintenance. For instance, if PV panels were installed on the roof, it would be harder to perform maintenance work. Thus, the roof shall be reached easily. After investigating the entire building, it was found that the Engineering School has flat and easily accessible roof. It was also found out that according to university rules, there are no specific regulations on the use of the roof. Obviously, there are some issues such as if installation of PV panel on the roof could break fire safety rules or endanger life of pedestrians passing by the building. For sensitivity purposes of the project, the current scenario is considered as an alternative to ground installation, which should be considered up front to mitigate safety risks.

As it was previously mentioned, the ground mount was one of the alternatives, but as the nearby territory of the building is already developed for other purposes, land prices are high; in addition, it may provide uncontrolled shadow and possibly pose other difficulties; therefore, the roof was finally selected as the most suitable location.

The area of solar panels is 194 m^2, which will be installed on the roof of the building Block 6, as shown in Fig. 41.2.

The following three different policy scenarios were considered: (a) Feed-in-Tariff (FIT), which is implemented according to current policy in Kazakhstan (scenario I); (b) FIT plus a government grant of 30% of capital cost (scenario II); and (c) FIT

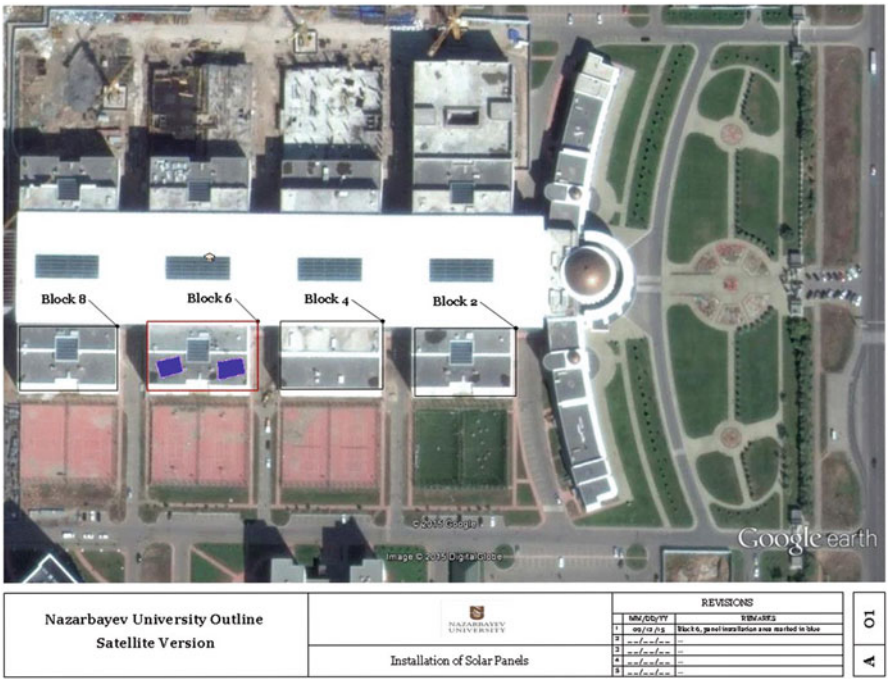

Fig. 41.1 Nazarbayev University area. Top view. Highlight of Blocks. (Source: Google Earth)

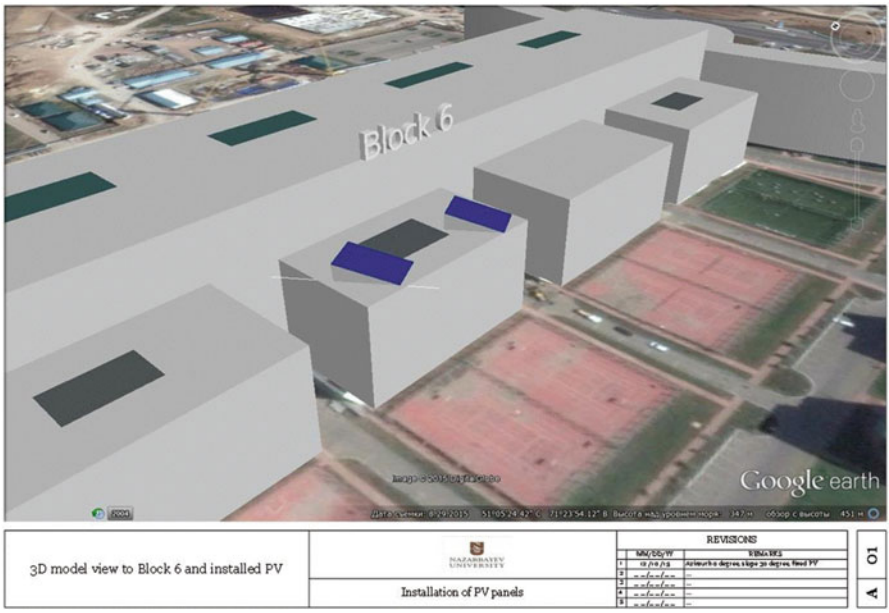

Fig. 41.2 Potential placement of PV panels on the roof of Block 6 at NU. (Source: Google Earth)

Table 41.3 Potential scenarios

Scenario	I	II	III
Brief description	No incentives, actual FIT of 36,410 KZT/MWh	30% incentives from government with actual FIT	New proposed FIT of 70,000 KZT/MWh and no incentives

Table 41.4 Financial parameters and viability indexes for scenario I (as extracted from RETScreen v4.0)

Financial parameters		
Electricity export escalation rate	%	9.7
Inflation rate [11]	%	9.7
Discount rate	%	12.0
Project life	yr	20
Finance		
Incentives and grants	KZT	
Debt ratio	%	25.0
Debt	KZT	4,117,300
Equity	KZT	12,351,900
Debt interest rate	%	15.0
Debt term	yr	20
Debt payments	KZT/yr	657,786
Financial viability		
After-tax IRR – equity	%	15.1
Simple payback	yr	17.6
Equity payback	yr	8.8
Net present value (NPV)	KZT	4,587,237
Annual life cycle savings	KZT/yr	614,134
Benefit-cost (B-C) ratio		1.37

without government grant, but with a substantial increase of the FIT rate offered (scenario III). These three proposed policy options or scenarios are summarized in Table 41.3.

Scenario I

In this scenario the current situation was taken into consideration, so the current FIT for electricity is 36,410 KZT/MWh, and there are no additional incentives from the government for renewable energy source projects. Inflation rate was taken as 9.72% as of October 2015 [9]. It is assumed that the loan for the project is taken from Asia Credit Bank at a rate of 15% [10]. Electricity export escalation rate is assumed to be 9.72% (all financial parameters are summarized in Table 41.4). These financial indexes are also used in scenarios II and III. It is observed that under scenario I the NPV is 4,587,237 KZT, and the payback period shows the project breaks even in year 9 (i.e., equity payback), despite a year later the cumulative cash flow becomes negative due to acquisition of the new inverter (as shown in Fig. 41.3). Hence, in overall, scenario I demonstrates to be just marginally feasible.

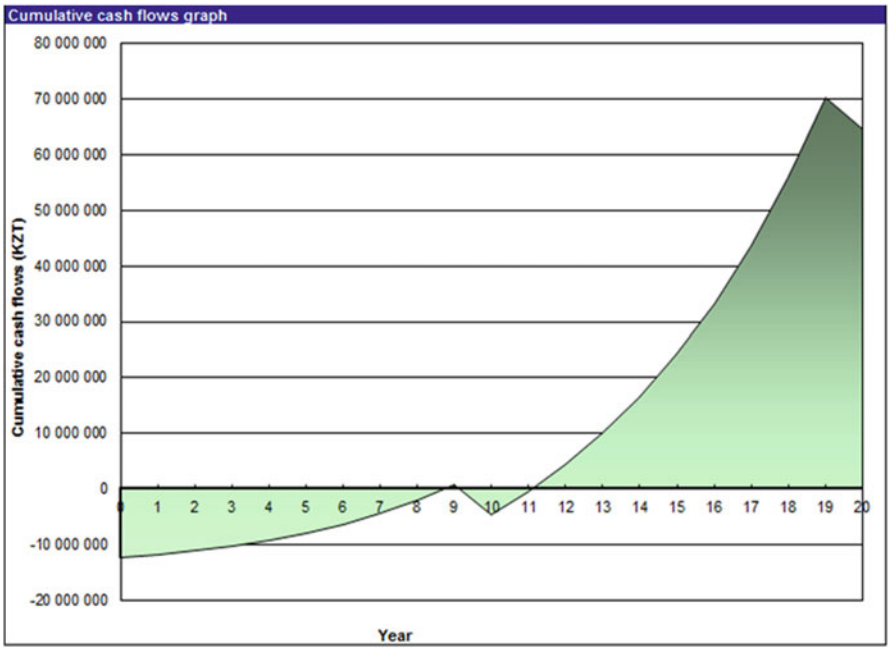

Fig. 41.3 Cumulative cash flows graph, scenario I (as extracted from RETScreen)

Scenario II

In this scenario, incentives and grants from the government are assumed to be given to educational establishments which use renewable energy sources for their academic purposes. It is assumed that 30% of the total project cost (16,469,200 KZT) is funded by the government, which in current case represents 4,940,760 KZT. The summary of financial parameters for scenario II is presented in Table 41.5, with the corresponding cumulative cash flow presented in Fig. 41.4. As for the financial indexes, scenario II increases the IRR on equity from 15.1% to 20.9% and the benefit-cost ratio from 1.37 to 1.47, compared to scenario I. These improvements, despite being consistent with expectations, might still be interpreted as modest.

Therefore, under this scenario, the project becomes more attractive than scenario I, demonstrating the potential positive impact that a subsidy from the government may have on the viability of the project.

Scenario III

In this option it is assumed that the government will change the rules and legislations for FIT. It is assumed that FIT becomes in 70,000 KZT/MWh. All other financial parameters remain constant as in scenarios I and II. Table 41.6 shows the financial parameters and indexes for this scenario.

In this scenario it is assumed that the government will change the rules and legislations for FIT. It is assumed a new FIT of 70,000 KZT/MWh. All other parameters remain constant as in previous scenarios. Table 41.7 presents the

Table 41.5 Financial parameters for scenario II (as extracted from RETScreen)

Financial parameters		
General		
Fuel cost escalation rate	%	3.0
Inflation rate	%	9.7
Discount rate	%	12.0
Project life	yr	20

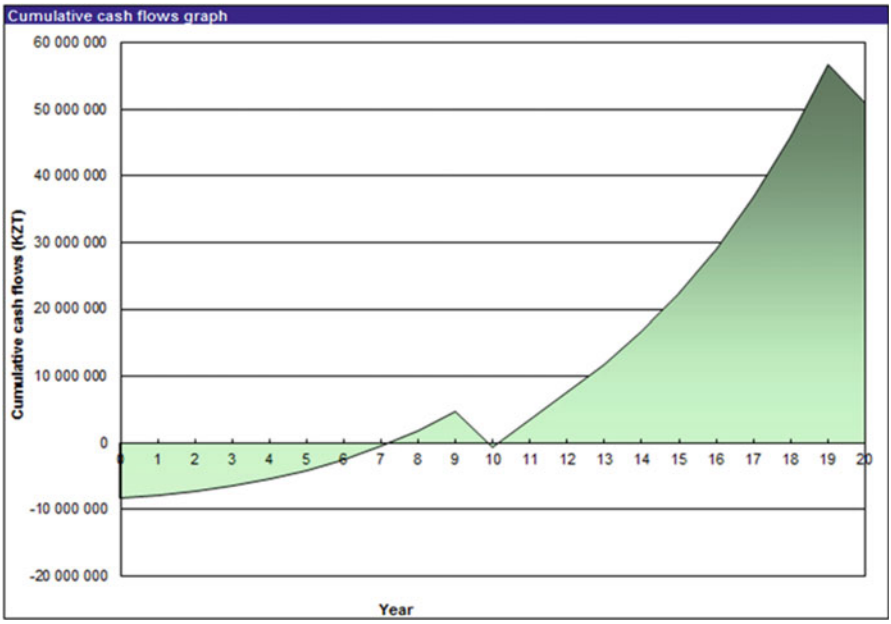

Fig. 41.4 Cumulative cash flows, scenario II (as extracted from RETScreen)

summary of the financial outcomes for each scenario. Figure 41.5 shows the cumulative cash flow for this scenario.

41.5 Conclusions

The assessment of on-grid PV system installed on the roof of Nazarbayev University is presented. Three scenarios were explored: (I) current FIT of 34,610 KZT/MWh for on-grid PV systems without subsidies, (II) adding an incentive equivalent to 30% of CAPEX, and (III) withdrawing the incentive and raising FIT to 70,000 KZT/MWh.

Results demonstrate that current scenario of FIT is marginally favorable (IRR on equity, 15.1%; benefit-cost ratio, 1.37; equity payback, 8.8 years), while the 30% of

Table 41.6 Financial parameters and indexes for scenario III

Financial parameters		
Electricity export escalation rate	%	9.7
Inflation rate	%	9.7
Discount rate	%	12.0
Project life	yr	20
Incentives and grants	KZT	
Debt ratio	%	25.0
Debt	KZT	4,117,300
Equity	KZT	12,351,900
Debt interest rate	%	15.0
Debt term	yr	20
Debt payments	KZT/yr	657,786
Financial viability		
After-tax IRR – equity	%	28.3
Simple payback	yr	8.3
Equity payback	yr	5.0
Net present value (NPV)	KZT	32,298,837
Annual life cycle savings	KZT/yr	4,323,727
Benefit-cost (B-C) ratio		3.61

Table 41.7 Summary of results per scenario

	Scenario I	Scenario II	Scenario III
Scenario brief description	No incentives, actual Feed-in-Tariff 36,410 KZT/MWt	30% incentives from government with actual Feed-in-Tariff	New proposed Feed-in-Tariff 70,000 KZT/MWt
Pretax IRR on equity (%)	15.1	20.9	28.3
Pretax IRR on assets (%)	12.3	15.8	23.7
Simple payback (years)	17.6	12.3	8.3
Equity payback (years)	8.8	7.2	5
Net present value (NPV) (KZT)	4,587,237	5,849,558	32,298,837
Benefit-cost ratio	1.37	1.47	3.61

incentives on top of current FIT moderately improve the benefits of the project (IRR on equity, 20.9%; benefit-cost ratio, 1.47; equity payback, 7.2 years).

Furthermore, upgrading current FIT to 70,000 KZT/MWh, even without incentives, proved to be enormously positive in improving the outcome of the project for

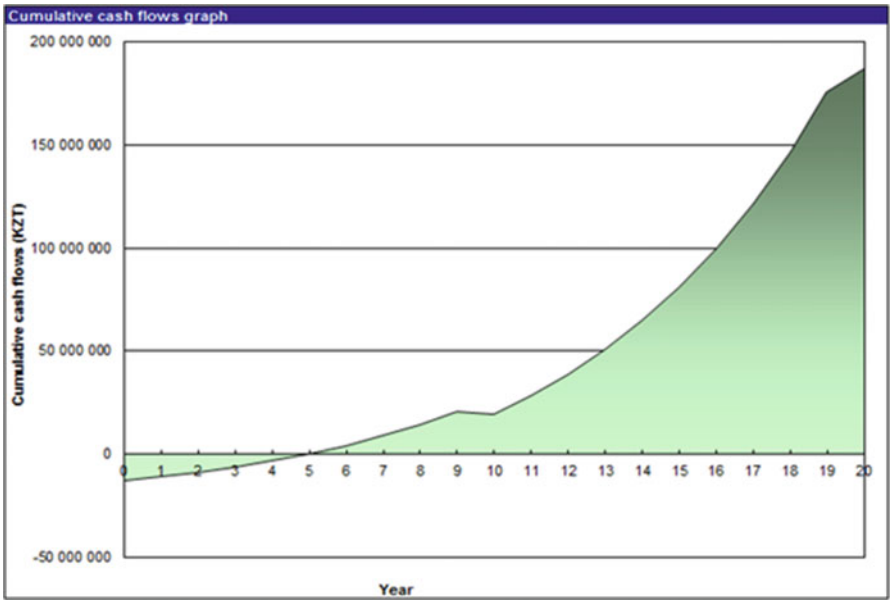

Fig. 41.5 Cumulative cash flow, scenario III (as extracted from RETScreen)

investors (IRR-equity >28%, equity payback of 5 years, and benefit-cost ratio > 3.6), demonstrating that with a subtle change in policies, Nazarbayev University, like many other campuses in the country, may easily justify the investment in their on-grid PV systems.

Acknowledgments We would like to express our deepest appreciation to all those who provided us with the possibility to complete this work.

Furthermore, we would like to acknowledge with much appreciation the crucial role of our colleagues from the Laboratory of Intellectual Systems and Energy Efficiency, Victor Ten, Albina Khakimova, and Farkhat Muratov; Office of the Registrar, Aigerim Baikenova; and Astana Solar marketing office manager and teaching assistant Soudabeh Gorjinezhad for providing us with necessary information.

Nomenclature

IRR	Internal rate of Return
kWh	Kilowatt hour
MW	Megawatts
NPV	Net present value PV – Photovoltaic
RES	Renewable energy sources

References

1. The Association for the Advancement of Sustainability in Higher Education (2015) Available from: http://www.aashe.org/resources/campus-solar-photovoltaic-installations/top10/#top-capacity
2. REEEP Policy Database (2015) Available from: http://www.reegle.info/policy-and-regulatory-overviews/KZ
3. Kazinform, Kazakh Government adopts Energy Efficiency 2020 Program (2016) Available at: http://www.inform.kz/en/kazakh-government-adopts-energy-efficiency-2020-program_a2584998
4. Astana Solar official website (2001) Feed-in Tariffs for renewable energy sources ratified. Available online at: http://www.astanasolar.kz/en/news/tariffs-renewable-energy-sources-approved
5. University of Washington in St.Louis (2017) Renewable energy. Available at: https://sustainability.wustl.edu/vision-progress/energy-emissions/renewable-energy/
6. Perez P, Aguilera J (2003) Project Univer (Universidad Verde). 200 kwp grid connected pv system at Jaen university campus. Final conclusion after four operation years. Available online at: http://ieeexplore.ieee.org/stamp/stamp.jsp?tp=&arnumber=1305050&tag=1
7. Kamali S (2015) Evaluation Study on grid-connected PV System at University of Malaya. Available online at: http://ieeexplore.ieee.org/stamp/stamp.jsp?tp=&arnumber=5412043
8. National power system of Kazakhstan (2017) Kegoc. Available at: http://www.kegoc.kz/en/company/national-power-system
9. Solar Electricity Handbook, Solar Angle Calculator (2015) Available online at: http://solarelectricityhandbook.com/solar-angle-calculator.html
10. Asia Credit Bank (2017) Available at: http://www.asiacreditbank.kz/p/Businesscredits.html
11. Trading Economics (2015) Kazakhstan core inflation rate. Available from: http://www.tradingeconomics.com/kazakhstan/core-inflation-rate

Chapter 42
Effectiveness and Prospects of Implementing a Solar Water Heating System in Astana, Kazakhstan

Askar Absemetov, Medet Mukushev, Alibek Yerubayev, Zarina Zhumanalina, and Luis Rojas-Solórzano

42.1 Introduction

Astana is a fast-growing city located in a region where winter lasts on average 6 months. Due to this fast growth, not all of its houses are connected to the central heating system. There are about 22,000 private houses that use coal for heating [1], and every day in the atmosphere of the city, about 100 tonnes of harmful substances are emitted [1]. Currently, many people install electrical heaters for water and use coal for heating their homes. There are two problems for people using these heating methods: Firstly, price for electricity has increased twofold in the last 6 years and continues growing [2]. Secondly, burning coal either for space heating or for centralized power generation (according to the [3] 80% of power source in the country in 2014) produces a big amount of CO_2 and pollutes the air. Furthermore, electrical heaters for water and autonomous coal heating systems are not connected between each other and are not very efficient.

Kazakhstan is planning to focus more on renewable energy usage, and its Ministry of Environment and Water Resources plans to attract about 2 billion US dollars of investment into renewable energy sector until 2020 within the strategy "Kazakhstan-2050." It is expected to have 1850 MW of installed power projects by 2020, divided as 1300 MW in wind power, 500 MW in solar plants, and 50 MW in biogas plants [4]. Most of the expected investments are considered as pilot projects

A. Absemetov · M. Mukushev · A. Yerubayev · Z. Zhumanalina
Nazarbayev University, School of Engineering and Graduate School of Business, Astana, Kazakhstan

L. Rojas-Solórzano (✉)
Nazarbayev University, School of Engineering, Department of Mechanical Engineering, Astana, Kazakhstan
e-mail: luis.rojas@nu.edu.kz

S. Nižetić, A. Papadopoulos (eds.), *The Role of Exergy in Energy and the Environment*, Green Energy and Technology,
https://doi.org/10.1007/978-3-319-89845-2_42

which will be used to test technologies and their overall feasibility. Implementation of national projects requires big investments and takes a long period of deployment until results can be appreciated. However, it is important to solve existing problems in a short period of time, and therefore, this becomes an interesting challenge to be faced and solved.

The project presented in this work is the assessment of a solar water heating (SWH) system. The key elements preliminarily considered as favorable to the project are the availability of good insolation in most regions of Kazakhstan, technology efficiency, and its low installation and maintenance expenses. The SWH system economic and environmental advantages will be analyzed in detail in the next sections.

42.2 Related Works

Most of the power generated today in Kazakhstan is produced using coal [3]. This fuel emits tonnes of carbon dioxide and other pollutants to the atmosphere. Nowadays, people start to focus more on new sources of energy, which are renewable and cause less harm to environment, being solar energy technologies one of the fastest growing industries.

Non-concentrated photovoltaic solar panels (PV) and concentrated solar power (CSP) are the two most commercialized and mature technologies, with PV panels as the most common technology used for electricity generation [5].

Frid et al. [6] in their work analyzed effectiveness and prospects of using different solar water heating systems. According to their analysis, integrated SWHs are most efficient for use in summer period. But for systems that need to be operated all over the year, the separated accumulation scheme should be considered. The scheme with separate accumulation corresponds to SWH systems in which solar collector and storage tank of specified volume are placed separately. Additionally, it is well known that evacuated collectors (ECs) have higher overall performance compared to flat-plate surface collectors, and furthermore, the disparity in costs between both sub-technologies is dropping down as manufacturers are reducing costs due to mass-scale production and improved design of ECs [6].

Drakoulaki et al. [7] analyzed the use of SWH systems instead of electricity, diesel, and natural gas. According to their analysis, the highest benefit-cost (B-C) ratio is achieved when SWH replaces electricity. Substitution of fuel diesel with SWH also gave ratio higher than one. The only negative B-C ratio came up when natural gas fuel was substituted by SWH system. They also found social benefits of using SWH systems. These benefits were distinguished in three categories: energy saving, decrease in environmental burdens, and generation of new jobs [7].

42.3 Model Set-Up

The main problem that is tackled in this paper is the excessive usage of electricity for water heating by private houses in Astana that results in large bills as well as negative environmental impact. Therefore, this investigation analyzes how environmentally and economically feasible are SWH systems for private households in Astana to replace or complement existing widely used water heating systems that are based on boilers operated with electricity.

Moreover, the goal of this paper is to make analysis based on the Kazakhstani solar collectors developed by Nazarbayev University Research Innovation System (NURIS) spin-off company KunTech.

The scope of analysis includes the usage of solar water heating system only for water heating purposes. The analysis will be conducted on data provided by NURIS researchers regarding the solar technology and from open sources and statistical data provided by governmental agencies for energy and water usage, as well as, consumption habits of the population. In this research only private houses in Astana are taken into account.

42.4 Methodology

Life cycle cost analysis (LCCA) on the proposed case cash flows (SWH complementing electric heaters) vs. the base case (100% electric heaters) to evaluate the financial viability of the project is performed using the decision-making tool platform RETScreen V4, Clean Energy Management Software system provided by the Department of Natural Resources of Canada (Natural Resources Canada, 2014). In the next subsections, the following aspects are provided: (a) practical issues on the economic-technical evaluation of the project, (b) assessment of natural resources, (c) justification of appropriate technology, and (d) LCCA with its financial outcomes and complementary risk and sensitivity analyses. Thus, a brief theoretical description of these aspects and their implementation in the study is firstly presented for better understanding of the project.

42.4.1 Issues on Project Evaluation

The economic-technical assessment of a given project includes technical specifications and requirements, determination of project cost-effectiveness and benefits, and assessment of its environmental impact.

In particular, the following issues need to be answered in the assessment of this project:

- Existence of a need for this project on the market
- Availability of sufficient technical data in order to determine the equipment type needed
- Availability of technical options and their properties
- The costs associated with clean energy option compared to the costs of the base case
- Emissions produced by both base and proposed cases

If all these issues are addressed in the evaluation stage, the analysis of project feasibility will be conducted thoroughly and it will give accurate results.

42.4.2 Natural Resources Assessment

Since the subject of study is a SWH technology, which transforms solar radiation into heat, then solar energy is the natural resource that is assessed in the study. RETScreen platform provides access to uploaded data from ground station on solar irradiance and climate conditions in Astana. However, as an audit exercise, solar irradiance data was also accessed from the local ground station offered by the developer of the solar collector (NURIS, a research entity based in Astana) to provide further assurance of accuracy of the data.

42.4.3 Technology

The SWH technology is based on solar collectors, which absorb solar irradiance and convert it into heat to produce hot water. Solar water heating systems are classified into active/passive and direct/indirect. Whether a SWH system is active or passive depends on the presence of electric pumps and controls to manage the circulation of the water; active system requires pumps and controls, whereas passive system relies on buoyancy to circulate water. In direct SWH system, water is heated directly in the collector. Indirect SWH system heats nontoxic heat transfer fluid-like propylene glycol in the collector, and then it transfers heat to water via heat exchanger [9]. There are several types of solar collectors available on the market:

- *Unglazed solar collector:* it has relatively low cost and low temperature operation. Usually it is used for heating water in pools. It performs poorly in cold and windy weather.
- *Glazed flat-plate solar collector:* it is protected from external factors and operates well in cold and windy weather. This collector has moderate cost and high temperature of operation.

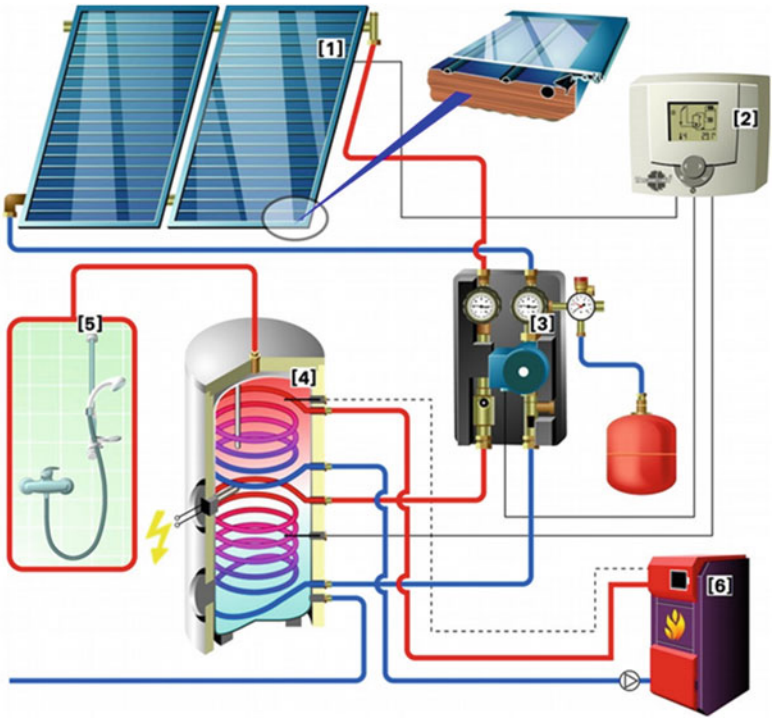

Fig. 42.1 Scheme of tested system: (1) collector, (2) controller, (3) pump, (4) heating storage cylinder, (5) hot water, (6) boiler [8]

- *Evacuated tube collector:* it has high cost and high temperature of operation. This collector provides almost no convection losses and operates well in cold and windy climate. However, its installation process is more complex than for previous two types of collectors.

In this study, SWH system utilizing glazed flat-plate solar collectors is considered for implementation because it fits better for local weather conditions of Astana than system with unglazed solar collectors, and it is less expensive and easier to install than evacuated tube collectors. The scheme of assessed system is shown in Fig. 42.1.

42.4.4 Cost Analysis

The main objective of the cost analysis is to determine the cash flow generated by the implementation of the proposed technology. The analysis takes into consideration all the costs required for implementation (CAPEX, capital expenditures) and usage of the system (OPEX, operational expenditures) and also denominated as initial and annual costs, annual savings, and periodic costs. Therefore, the cost analysis includes the following parameters:

- *Debt interest rate:* it defines the effective rate that a person (house owner) pays on his/her debt if any loan is taken in order to acquire the proposed technology.
- *Energy escalation rate*: it defines the rate at which the energy prices increase annually.
- *Discount rate:* it defines the interest rate used to determine the present value of future cash flows.
- *Life of the project*: it refers to the time the proposed technology is going to be used from its installation to decommissioning.
- *Operations and maintenance costs*: it refers to annual costs that are required to keep running the system without any major breakages.
- *Taxes*: it refers to the taxes a person (house owner) needs to pay if he/she makes any income on the implementation of the system.

42.4.5 Financial Analysis

The following indicators are used to determine the economic feasibility of the project:

- *Net present value (NPV)*: a difference between present values of cash inflows and outflows over the project life. The positive NPV indicates that the investment into this project will be profitable.
- *Internal rate of return (IRR)*: a discount rate that makes NPV of the project equal to zero. Higher IRR indicates a more attractive project.
- *Benefit-cost (B-C) ratio*: a ratio to identify the relationship between discounted benefits and costs of the project.

42.4.6 Risk and Sensitivity Analyses

As in any other study, the risk and sensitivity analyses should be performed for the project. Risk analysis is performed to determine the potential risks of the project, i.e., an event with negative impact on the project, and how to prevent or mitigate it. Sensitivity analysis is used to determine how particular independent variables affect a particular financial outcome variable of the project.

42.5 Feasibility Analysis

42.5.1 Assessment of Natural Resources

The climate data of Astana was downloaded from RETScreen software database and verified with local ground measurements by NURIS as previously indicated.

Table 42.1 Astana yearly-average ambient conditions (as extracted from RETScreen)

	Air temperature	Relative humidity	Atmospheric pressure
	°C	%	kPa
Annual	3.4	67.2	97.8

Table 42.2 Prices of proposed SWH system and components

#	Component	Amount	Unit Price, KZ	Total, KZ
1	KT 300 collector	3	170,000	510,000
2	Water storage tank	1	325,000	325,000
3	Solar pump TW, 25–65W	1	110,000	110,000
4	Foam rubber for pipe insulation, 19mm	30m	900	27,000
5	Stainless corrugated pipe, 20mm	30m	1200	36,000
6	Membranous expansion tank, 191	1	9500	9500
7	Temperature controller with sensors	1	103,000	103,000
8	Frame for mounting solar collectors	1	115,000	115,000
9	Heat transfer fluid (propylene glycol)	20	1100	22,000
10	Total			1,257,500
11	Installation			200,000
	Total cost			1,457,500

For reference purposes, the yearly-average ambient conditions are presented in Table 42.1.

42.5.2 Equipment and Component Costs

For the purpose of heating water, active indirect solar flat glazed collectors of LLP KunTech were chosen. The company offers three types of solar collectors, and depending on the number of collectors, there are various typical systems. For a house with four occupants in Astana, 100% occupancy rate, the proposed system consists of three collectors for water heating from catalogue [8]. Table 42.2 describes the chosen system and gives the prices for the components of the system for October 2015.

Since the project is oriented to providing only hot water, then daily hot water usage was estimated based on the average daily consumption of 100 L per person [10]. The technical specifications of the selected collector, a KT 330, are presented in Table 42.3.

One important point to consider is the orientation of the house in terms of how it faces the sun. According to the manufacturer, if the roof is not oriented to south, then extra equipment will be required to make collectors be oriented to south at a slope of 45° and azimuth 0°. The manufacturer ranges the delivery and installation costs from 60,000 to 250,000 KZT depending on the type of the system, the orientation of the building, and the complexities inherent to specific places. Thus, in this case the

Table 42.3 KT 330, flat-plate solar collector specifications [8]

Gross area, m^2	2.03
Aperture area, m^2	1.78
Fr (tau alpha) coefficient	0.81
Fr UL coefficient, $(W/m^2)/°C$	3.59
Storage capacity, L	100
Pump power, W	50

delivery and installation cost was estimated to be 200,000 KZT to include some provisions for support structure in case the house was not facing south roof.

Therefore, total capital cost of the SWH system is 1,457,500 KZT including the delivery and installation costs. Annual operations and maintenance costs of 4430 KZT were considered. Additionally, periodic (every 7 years) costs derived from a requirement of changing the heat transfer fluid of 20 L, costing 22,000 KZT today, were included. Cost of electricity was considered since it is required to run the system for the base case and proposed case scenarios. In the proposed case, electricity is still needed to complete the load not provided by the SWH system and to run the pump of the heat transfer fluid throughout the collector. The electric utility company "Astanaenergosbyt" is currently offering an average rate of 11.15 KZT/kWh + VAT for private users, since August 1, 2015 (Astanaenergosbyt, 2015). This gives the final average price of 12.49 KZT/kWh with VAT. The model predicted annual electricity consumptions of 13.5 MWh and 5.9 MWh for the base case and proposed case with KunTech LLP SWH system, respectively (i.e., a reduction of 56.3%).

42.5.3 Financial Indexes: Sensitivity and Risk Analysis

In the past years, the cost of 1 kWh of electricity has increased from 6.04 KZT in 2008 to 12.67 KZT in 2014 [11]. This gives a 13.14% increase per year. This value is required to escalate the cost of the electricity in the model. The annual inflation rate was 9.4% [11].

The deposit rate of 10% for the national currency in Kazakhstan was effective since July 1, 2015 [12]. Taking this into account, the minimum discount rate that was required was chosen as 12% for the model.

The manufacturer estimates the life of the equipment to be 35 years, and therefore, the project life was limited to 30 years with no salvage value. There were no incentives or grants included in the model as there are no such programs for consumers provided by the governmental bodies at present moment.

High attention should be paid to the financing part of the project. Two scenarios were reviewed. The first one is financing the project with 10% equity and taking 90% or 1311750 KZT as a consumer loan. The interest rate was chosen as 15% due to (a) the absence of a deposit or security and (b) the debt term and the maximum amount that can be taken. The debt term was stated as 5 years [12]. The second

Table 42.4 Loan scenarios for the project

	Scenario 1	Scenario 2
Bank	Other banks	HCSBK
Debt ratio	90%	50%
Debt	1,311,750 KZT	728,750 KZT
Debt interest rate	15%	5%
Debt term	5 years	5 years
Debt payment per year	391,315 KZT	168,323 KZT

Table 42.5 Scenario 1: Financial viability and GHG reduction (case with 15% interest rate) (as extracted from RETScreen)

	Unit	Value
After-tax IRR-equity	%	19.2
Simple payback	yr	16.3
Equity payback	yr	10.6
Net present value (NPV)	KZT	1,656,487
Annual life cycle savings	KZT/yr	205,642
Benefit-cost (B-C) ratio		12.37
GHG emission reductions	tCO_2	3.3

Table 42.6 Scenario 2: Financial viability and GHG reduction (case with 5% interest rate) (as extracted from RETScreen)

	Unit	Value
After-tax IRR-equity	%	20.1
Simple payback	yr	16.3
Equity payback	yr	9
Net present value (NPV)	KZT	1,877,325
Annual life cycle savings	KZT/yr	233,058
Benefit-cost (B-C) ratio		3.58
GHG emission reductions	tCO_2	3.3

scenario considered using the House Construction and Savings Bank of Kazakhstan (HCSBK). The differences with other banks are that in order to get low interest rates from 3.5% to 5%, fewer requirements have to be met. HCSBK offers 50% of the needed capital, and this has to be achieved by making savings within minimum of 3-year time frame by depositing into savings account regularly, at least once a month. The information for these two scenarios is summarized in Table 42.4.

Financial viability and greenhouse gas emissions reduction (GHG) can be summarized in Tables 42.5 and 42.6.

After-tax and pretax IRR are the same for the equity and assets as the model assumes the use of the system for a private or individual purpose only with no taxes.

Firstly, it is evident from Tables 42.5 to 42.6 the significant amount of GHG emissions reduction by 3.3 tonnes per year.

Attention has to be paid to NPV 1656487 KZT and 1877325 KZT, which look attractive enough and payback periods of 9 and 10.6 years, which are normal for such a new technology. The B-C ratios for both scenarios are 12.37 and 3.58, accordingly, and are good enough to be profitable. Annual savings of 205,642

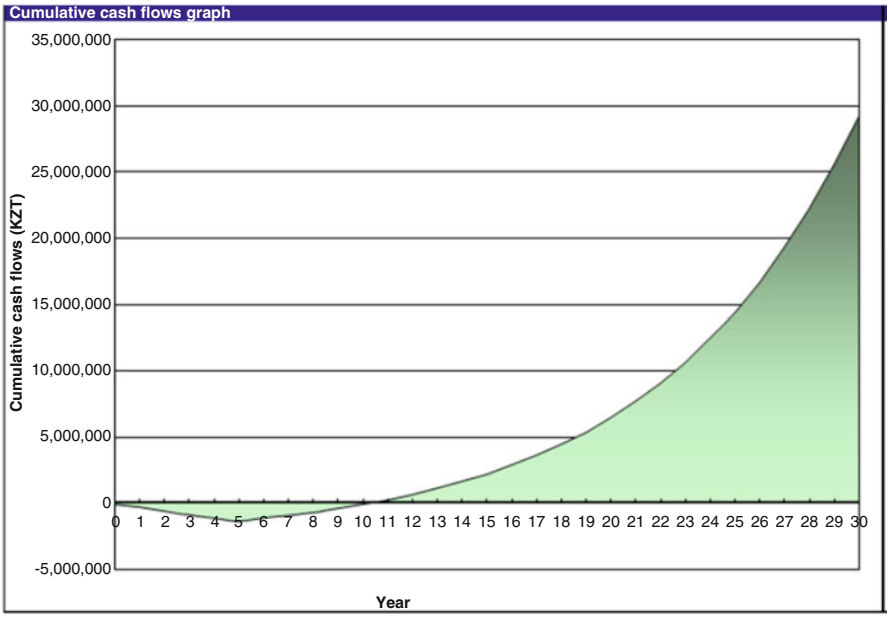

Fig. 42.2 Cash flow diagram (Scenario 1: 15% interest rate) (as extracted from RETScreen)

KZT for Scenario 1 and 233058 KZT for Scenario 2 show positive monetary benefits that bring the proposed system every year in either case.

The yearly and cumulative expected cash flows are shown in Figs. 42.2 and 42.3 for both scenarios previously discussed. These figures display the plots of the cumulative cash flow depicting clearly the strong benefits of the project. It is evident that the negative cash flow is staying relatively the same for the Scenario 2 for the first 5 years, whereas for the Scenario 1, it is getting more and more negative up to year 5 due to the debt term being set as 5 years. Afterward, both scenarios show signs of positive growth and relatively similar year-to-zero cash flow. After reaching break-even point, cash flows are growing exponentially and bring long-term benefits to the user.

The sensitivity and risk analysis for a risk of 10% (confidence of 90%) for both scenarios showed the following results for NPV range for both cases in Table 42.7.

42.6 Conclusions

The technical and economic assessment of a solar water heating system manufactured by a local firm in the city of Astana used for local water heating in a family house is presented under two scenarios of capital loans. Scenario 1 corresponds to capital loan based on debt ratio of 90% and interest rate of 15% for 5 years,

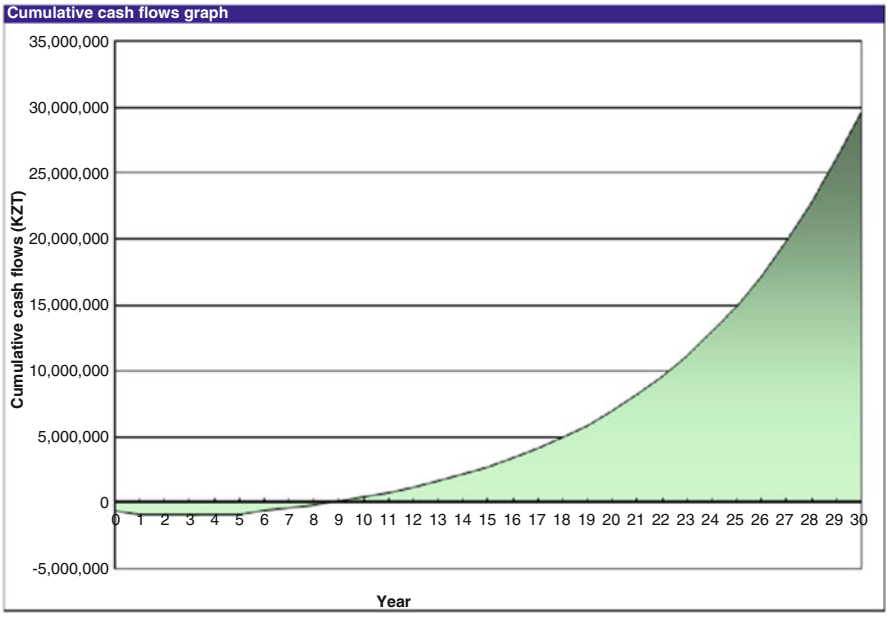

Fig. 42.3 Cash flow diagram (Scenario 2: 5% interest rate) (as extracted from RETScreen)

Table 42.7 Risk and sensitivity analysis for NPV

	Unit	Case with 15% interest rate	Case with 5% interest rate
Median	KZT	1,681,286	1,905,549
Level of risk	%	10.0	10.0
Minimum within level of confidence	KZT	1,340,661	1,557,918
Maximum within level of confidence	KZT	2,039,521	2262,779

while Scenario 2 corresponds to a loan with debt ratio of 50%, debt term of 5 years, and interest rate of 5%.

Results of the feasibility analysis show that the proposed system in the climatic conditions of Astana is cost-efficient and beneficial when Scenario 2 is implemented. This second scenario leads to a payback period of 9 years, resulting in 1.6 years shorter than obtained in Scenario 1. Also, it can be observed that the proposed system has solar fraction of 52% producing 4.5 MWh of heating demand per year. The electricity consumption due to water heating decreases from 13.5 MWh to 5.9 MWh, which saves 95,515 KZT annually. Regarding environmental impact of the proposed system, it can be observed that CO_2 equivalent emissions caused by water heating are reduced from 5.9 tCO_2 equiv. to 2.6 tCO_2 equiv., which is equivalent to 0.6 cars and light trucks not used annually. Therefore, it can be stated that the

proposed system is efficient and beneficial for household with four occupants in Astana.

Nomenclature

CAPEX	Capital expenditures
CSP	Concentrated solar power
GHG	Gas emissions reduction
HCSBK	House Construction and Savings Bank of Kazakhstan
IRR	Internal rate of return
LCCA	Life cycle cost analysis
NPV	Net present value
NURIS	Nazarbayev University Research and Innovation System
OPEX	Operational expenditures
PV	Solar panels
SWH	Solar water heating

Acknowledgments We thank faculty of the School of Engineering and Graduate School of Business of Nazarbayev University, who provided insight and expertise that greatly assisted this investigation.

We would also like to show our gratitude to Diaz Baiseitov, director of Technopark NURIS, for providing us with all required information about the SWH system from KunTech LLP.

References

1. Baimanov D (2016) More than 22 thousand of private sector houses of Astana will move to gas heating. KazInform News Agency. [Online] Available from: http://www.kazinform.kz/rus/article/2874279. Accessed 26 Feb 2016
2. Pchelyanskaya I (2016) Utility rates increased in Kazakhstan. Krisha.kz. [Online] Available from: https://krisha.kz/content/news/2016/v-rk-vyrosli tarify-na-uslugi-zhkh
3. Breakdown of Electricity Generation by Energy Source (2016) The Shift Project. [Online] Available from: http://www.tsp-data-portal.org/Breakdown-ofElectricity-Generation-by-Energy-Source#tspQvChart. Accessed 26 Feb 2016
4. Kazakhstan will attract about 2 bln dollars of investment into renewable energy sector until 2020: Ministry of Environment and Water Resources, Strategy 2050.Kz News Agency, 2016. [Online] Available from: http://strategy2050.kz/en/news/6502/?sf23366391=1. Accessed: 26 Feb 2016
5. Chu Y, Meisen P (2011) Review and comparison of different solar energy technologies. Global Energy Network Institute. [Online] Available from: http://www.geni.org/globalenergy/research/reviewand-comparison-of-solar-technologies/Reviewand-Comparison-of-Different-SolarTechnologies.pdf. Accessed 9 Dec 2015
6. Frid SE, Kolomiets YuG, Sushnikova EV, Yamuder VF (2011) Effectiveness and prospects of using different solar water heating systems under the climatic conditions of the Russian Federation. Therm Eng 58–11: 910–916. [Online] Available from: http://link.springer.com/article/10.1134/S0040601511110061# Accessed 10 Dec 2015. Analytical review of the market of private houses in the Kazakhstani capital for the 3rd quarter of 2014. Forbes, 2014. [Online] Available from: http://forbes.kz/process/property/tsenyi_na_chastnyie_doma_v_astane_budut_snijatsya_na_10_v_god/. Accessed 2 June 2016

7. Drakoulaki D, Zervos A, Sarafidis J, Mirasgedis S (2001) Cost benefit analysis for solar water heating systems, Laboratory of Industrial and Energy Economics. Energy Convers Manag 42–14: 1727–1739. [Online] Available from: http://www.sciencedirect.com/science/article/pii/S0196890400001539 2015. Accessed 10 Dec
8. KunTech LLP (2016) Solar collectors. [Online] Available from: http://kuntech.kz/products/#solar-collectors. Loans, House Construction Savings Bank of Kazakhstan, 2015. [Online] Available from: http://www.hcsbk.kz/ru/credits/zhilishchnyi-zaem Accessed 10 Dec 2015
9. Rojas-Solórzano LR (2015) Solar water heating project analysis, using RETScreen, workshop: case studies
10. Tariffs (2015) AstanaEnergoSbyt LLP [Online] Available from: http://www.astanaenergosbyt.kz/tarif. Accessed 9 Dec 2015
11. Urazova I (2015) Kazakhstan revises 2015 inflation rate forecast. Tengrinews. [Online] Available from: http://en.tengrinews.kz/finance/Kazakhstanrevises-2015-inflation-rate-forecast-263004/. Accessed 10 Dec 2015
12. Recommended deposits interest rates, Kazakhstan Deposit Insurance Fund, 2015 [Online] Availablefrom: http://kdif.kz/en/recommended_rates. Accessed 10 Dec 2015. "Consumer loans". All Banks, 2015. [Online] Available from: http://allbanks.kz/credits/. Accessed 10 Dec 2015

Chapter 43
Analysis of Solar Collectors Application and the Influence of Domestic Hot Water Consumption on Energy Demand in Multifamily Buildings with Implementation of LCA Methodology

Justyna Gołębiowska and Agnieszka Żelazna

43.1 Introduction

One of the main direction of European Union action related to the principle of sustainable development is to develop technologies based on renewable energy sources. Thanks to their application, it is possible to slow down consumption of traditional energy sources and to reduce the environmental burden associated with the combustion of fossil fuels [1].

Statistics show that the use of renewable energy continues to grow. In the EU, the share of renewable energy sources in gross final energy consumption in 2004 and 2013 increased from 8.3% to 15%. Forecasts of use of renewable energy sources also show that the majority of EU member states achieve their individual goals established in the Europe 2020 strategy [2].

Thermal systems with solar collectors are one of the most popular environmentally friendly technologies. The use of this type of installation contributes to the reduction of operational costs and emissions of pollutants. Finally, it can affect positively energy efficiency of buildings [3].

By the end of 2014, 586 million square meters of collector area have been installed worldwide. It corresponds to 410.2 GWth of installed capacity. The majority of the total capacity in operation was installed in China (289.5 GWth), Europe (47.5 GWth), and the United States and Canada (18.0 GWth).The annual collector yield of all water-based solar thermal systems in operation by the end of 2014 was 335 TWh. This is connected with final energy savings on the level of 36.1 million tons of oil equivalent and 116.4 million tons of CO_2 equivalent. The number of solar thermal systems of different kinds is estimated at 101 million. In 2014, 94%

J. Gołębiowska (✉) · A. Żelazna
Faculty of Environmental Engineering, Lublin University of Technology, Lublin, Poland
e-mail: j.golebiowska@wis.pol.lublin.pl

S. Nižetić, A. Papadopoulos (eds.), *The Role of Exergy in Energy and the Environment*, Green Energy and Technology,
https://doi.org/10.1007/978-3-319-89845-2_43

of the energy provided by solar thermal systems worldwide was used for heating domestic hot water, 68% of which was used in small-scale systems in single-family houses. In larger applications, installed, for example, in multifamily houses, the share of energy provided by solar thermal systems was 27% [4]. While in the case of single-family houses, solar collector installations may be the solution depending on individual user preferences; in the case of multifamily buildings, it is necessary to examine the actual results of solar system operation.

Some research has been published about the use of large-scale solar domestic hot water installations [5–8]. However, installations integrating district heating substation with solar collectors, often implemented in multi-familiar buildings, are relatively new solutions. Based on the literature review, it can be observed that there are still not enough long-term studies to present cooperation results of domestic hot water installations with solar collectors in multifamily buildings.

Therefore, the purpose of this work is to present results of long-term field tests in four apartment buildings, which are equipped with solar collectors.

43.2 Experimental Facility

Operational tests were conducted over 3 years (2012–2014) in four multi-family buildings located in the Lublin region (Poland) and were performed to determine the influence of solar collectors use and domestic hot water consumption on the conventional energy demand.

The analyzed buildings are equipped with individual, dual-function (space heating and preparation of DHW) heating substations, fully automated. Substations are supplied with the heat from district heating network. Installations of solar collectors, whose characteristics are shown in Table 43.1, support only preparation of DHW. In the analyzed systems, flat plate collectors were used. An area of a single collector is at the level of 2.11 m^2.

Installations were equipped properly with calibrated sensors. Thanks to them it was possible to record the consumption of district heat used for heating domestic water [GJ], the consumption of water from supply network for the preparation of hot water [m^3], and the average solar radiation [W/m^2] in 2-week periods. Based on obtained results from monitored buildings, the unit heat consumption required for the preparation of hot water [GJ/m^3] was calculated.

Table 43.1 Value range for parameters

Building	Number of solar collectors	Total water volume in tanks [dm^3]	Number of residents	Ordered power DHW [kW]
B1	42	2000	98	50
B2	16	1000	28	30
B3	60	2000	104	50
B4	52	2000	104	60

43.3 Results and Discussion

Figure 43.1 shows the consumption of district heat for the preparation of 1 m^3 of domestic hot water in four multifamily buildings (B1, B2, B3, and B4) in selected year: 2014. It can be easily seen that in all buildings the energy needed for DHW preparation is lower in spring and summer, when DWH system is supported by solar collectors. In all buildings, the highest heat demand was noted for December while the lowest in July and August.

In the Fig. 43.2, the average unit heat consumption in all buildings, in 2012 and 2013, is presented for two seasons: winter (from October to April) and summer (from May to September, a season of higher level of solar radiation).

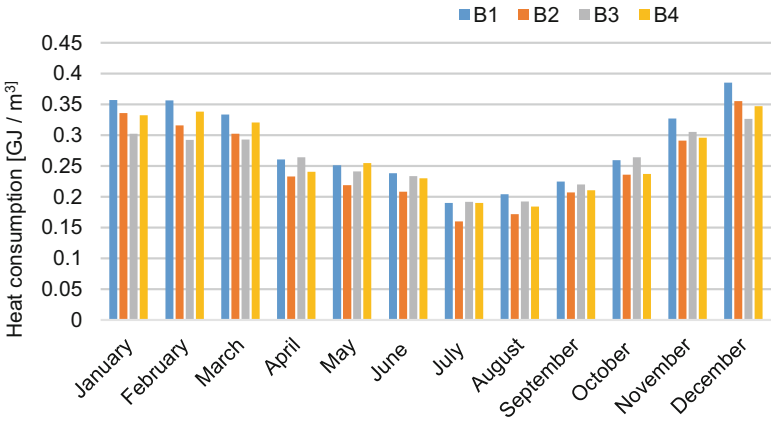

Fig. 43.1 Unit consumption of district heat for the DHW in buildings B1, B2, B3, and B4 (presented in GJ/m^3)

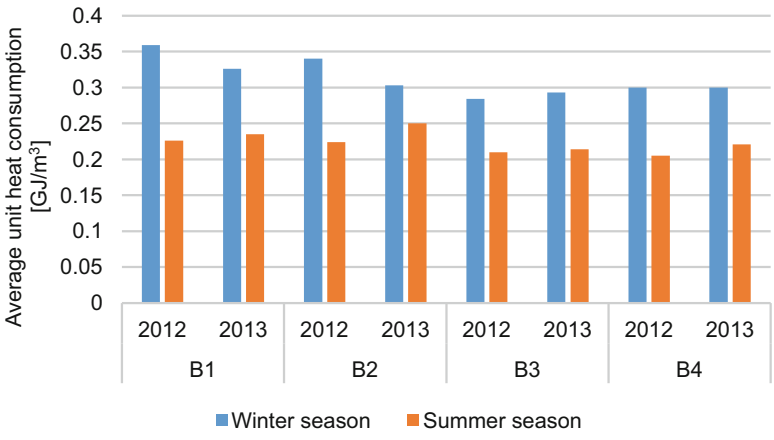

Fig. 43.2 Average unit consumption of district heat for the DHW preparation in summer and winter seasons (presented in GJ/m^3)

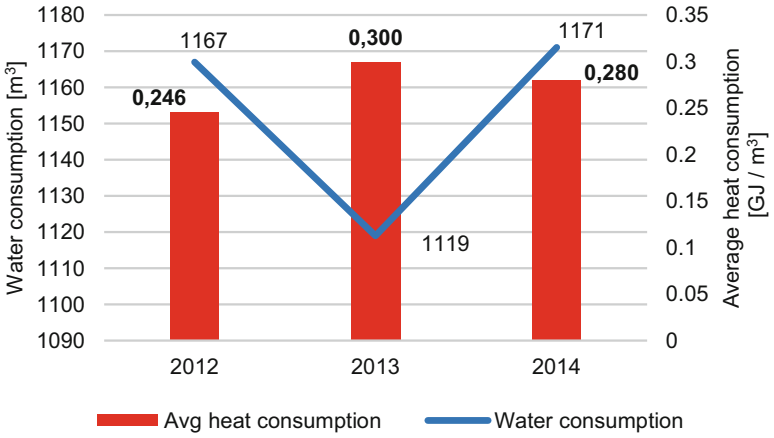

Fig. 43.3 Average unit consumption of district heat and water in building B1

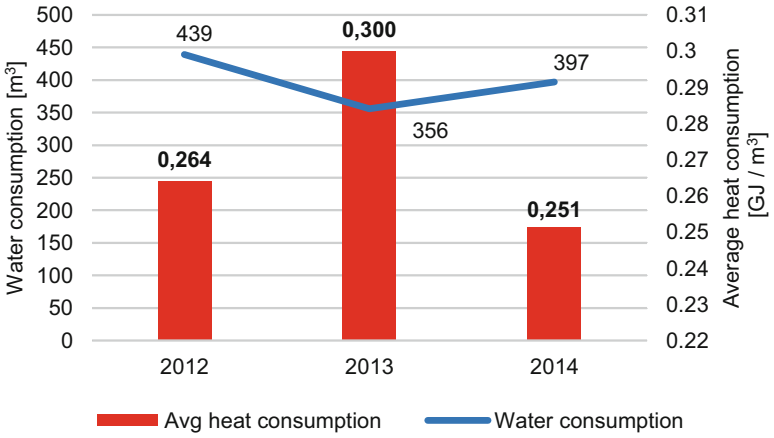

Fig. 43.4 Average unit consumption of district heat and water in building B2

It can be noticed that the use of solar collectors for supporting preparation of DHW enabled a reduction of district heat consumption in presented buildings by 33%, 26%, 27%, and 29%, respectively.

In the Figs. 43.3, 43.4, 43.5, and 43.6, unit heat consumption in individual buildings and the hot water demand during the 3 years of operation of the monitored systems are presented.

In all buildings, the average heat consumption decreased with increasing consumption of hot water. This is due to the fact that multifamily buildings are equipped with hot water circulation. When the water consumption is higher, the heat loss (related to hot water transport from the water tank to residential premises) is lower. Therefore, using larger amount of hot water (m^3) decreases heat loses and, eventually, the amount of heat needed for the preparation of DHW (GJ/m^3).

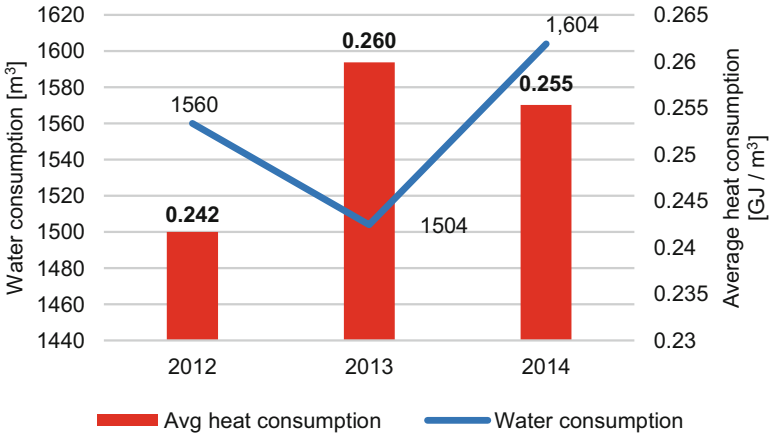

Fig. 43.5 Average unit consumption of district heat and water in building B3

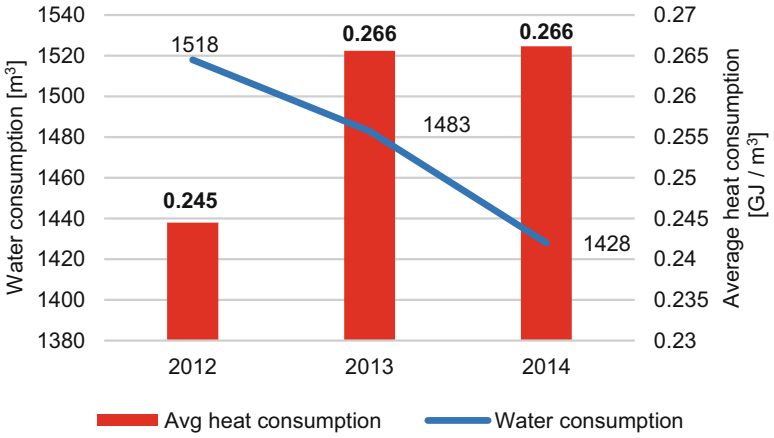

Fig. 43.6 Average unit consumption of district heat and water in building B4

This correlation can be also notice by a compression of water consumption and energy demand between building B2 (the lowest number of residents) and the rest of buildings. Even though this building is characterized by the lowest water consumption, the heat needed for water heating is significant.

In the Fig. 43.7, the level of water consumption in winter and summer seasons is presented. In all cases water consumption is lower in the summer season. This situation appears because months like June, July, August, and September are also a vacation time for many of residents. Taking into the consideration all presented data connected with heat and water consumption, we can assume that the reduction of district heat demand could be even more significant if water consumption in the summer season was higher.

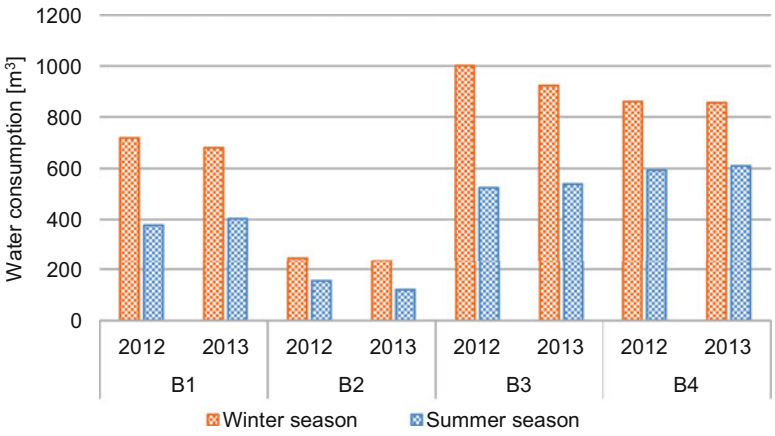

Fig. 43.7 Seasonal water consumption in buildings

43.4 Life Cycle Assessment

Life cycle assessment is a tool that can be used to evaluate the potential environmental impacts of a product in its full life cycle, encompassing the following main phases: production, operation, and end of life. Several studies have been published in the literature about the evaluation of solar domestic hot water systems [9–12].

In this paper, for life cycle impact assessment the global warming potential (GWP) method was used. In Fig. 43.8 results of GWP 100a analysis for winter and summer seasons are presented in the form of carbon dioxide equivalent emissions (kg CO_{2eq}). Results are presented for the years 2012 and 2013. In global warming potential method, greenhouse gasses are converted into carbon dioxide equivalents based upon their global warming potential. For example, 1 kg of methane is equivalent to 25 kg of carbon dioxide.

According to the ecoinvent database, the main emissions resulting from the heat generation in thermal power plants are associated with airborne emissions. In the analyzed system, the main substances responsible for the global warming potential, with respect to 1 kWh of thermal energy obtained from the system, are carbon dioxide (86.4 kg CO_{2eq}), methane (7.53 kg CO_{2eq}), and dinitrogen monoxide (0.217 kg CO_{2eq}). This relates to the extraction and processing of raw materials.

Analyzing the results presented in Fig. 43.8, we can notice how the solar energy gained from collectors can contribute to decreasing environmental burdens.

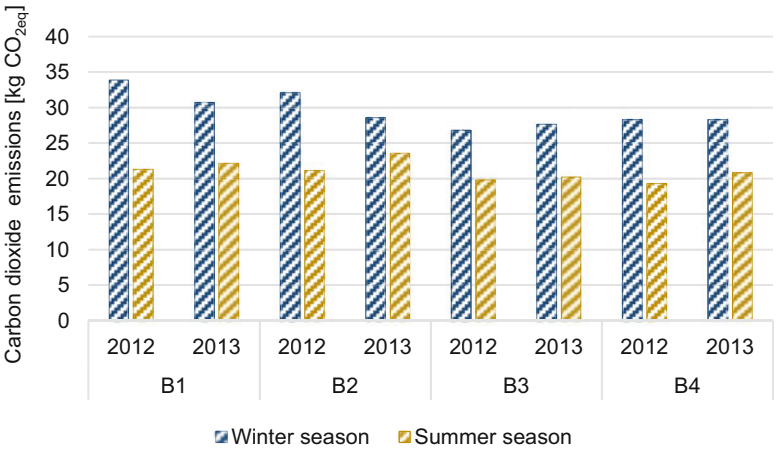

Fig. 43.8 Carbon dioxide equivalent emissions in winter and summer seasons (presented in kg CO_{2eq})

43.5 Conclusions

In this chapter the long-term (3 years) operational results of solar domestic hot water systems in multifamily buildings were presented. On the basis of presented results, the following conclusions can be drawn:

- The use of solar collectors in multifamily buildings contributes to the reduction of district heat consumption and thereby to the reduction of the costs of hot water preparation.
- Average heat consumption [GJ] for the DHW preparation (in amount of 1 m^3) decreases with increasing consumption of hot water [m^3]. Therefore, in case of the comparative analysis, regarding the DWH systems, it is necessary to pay attention to this correlation.
- Solar collectors contribute to the reduction of greenhouse gasses emission, connected mainly with the combustion of fossil fuels, which can be noticed easily by comparison GWP results for the summer (season of higher solar gains) and winter season.

According to the results of conducted research presented in this work, it can be concluded that the use of solar collectors for hot water heating assistance is important in terms of congenital energy savings and reduction of greenhouse gasses emissions.

Acknowledgments This research was supported by the Polish Ministry of Science and Higher Education. Project no. UMO-2015/17/N/ST8/02824.

References

1. Pawłowski A (2009) Sustainable energy as a sine qua non condition for the achievement of sustainable development. Probl Sustain Dev 4(2):3–7
2. Żelazna A, Gołębiowska J (2015) The measures of sustainable development–a study based on the European monitoring of energy-related indicators. Probl Sustain Dev 10(2):169–177
3. Ziembicki P, Bernasiński J (2015) Porównanie układów technologicznych dużych instalacji kolektorów słonecznych współpracujących z węzłami ciepłowniczymi. Zeszyty Naukowe. Inżynieria Środowiska/Uniwersytet Zielonogórski 157:94–104
4. Mauthner, F, Weiss, W, Spörk-Dür, M (2016) Solar heat worldwide: markets and contribution to the energy supply 2014. International Energy Agency-Solar Heating and Cooling Program
5. Branco G, Lachal B, Gallinelli P, Weber W (2004) Predicted versus observed heat consumption of a low energy multifamily complex in Switzerland based on long-term experimental data. Energ Buildings 36(6):543–555
6. Gołębiowska J (2015) Wpływ zastosowania kolektorów słonecznych na ekonomikę przygotowania ciepłej wody użytkowej. Informatyka, Automatyka, Pomiary w Gospodarce i Ochronie Środowiska 3:71–78
7. Thygesen R (2017) An analysis of different solar-assisted heating systems and their effect on the energy performance of multifamily buildings—a Swedish case. Energies 10(1):88
8. Yoo JH (2015) Evaluation of solar hot water heating system applications to high-rise multi-family housing complex based on three years of system operation. Energ Buildings 101:54–63
9. Cabeza LF, Rincón L, Vilariño V, Pérez G, Castell A (2014) Life cycle assessment (LCA) and life cycle energy analysis (LCEA) of buildings and the building sector: a review. Renew Sust Energ Rev 29:394–416
10. Carnevale E, Lombardi L, Zanchi L (2014) Life cycle assessment of solar energy systems: comparison of photovoltaic and water thermal heater at domestic scale. Energy 77:434–446
11. Zambrana-Vasquez D, Aranda-Usón A, Zabalza-Bribián I, Janez A, Llera-Sastresa E, Hernandez P, Arrizabalaga E (2015) Environmental assessment of domestic solar hot water systems: a case study in residential and hotel buildings. J Clean Prod 88:29–42
12. Żelazna A, Pawłowski A (2013) Life cycle assessment of solar hot water system for multifamily house. Environ Eng IV:479

Chapter 44
Thermoelectric Cooling of a Photovoltaic Panel

Hossein Moshfegh, Mohammad Eslami, and Arian Hosseini

44.1 Introduction

Energy consumption is a grand controversial matter in the world today. Clean energy production using alternative sources such as solar energy is growing in attention amongst researchers due to its promises of lesser pollution contribution, negligible waste production and ease of implementation. Photovoltaic cells are commonly used today to transform the solar energy to electricity. However, the low efficiency of these cells and their high capital costs have had negative impacts on their popularity. Therefore, possible improvements to these cells' performance are widely appealing.

The performance of these cells is highly dependent on cell temperature. Furthermore, it is clear that the cell temperature has a close tie with the ambient temperature. Accordingly, an innovative approach towards increasing these cells' efficiency is to utilize thermoelectric cooling in order to reduce the cells' temperature. Thermoelectric cooling can be described by the Peltier effect. This effect which occurs by heating or cooling one end of a circuit requires no operating fluids and therefore demands less maintenance and offers more reliability when compared to other cooling methods. Therefore, a combined TEC and PV design will be the subject of analyses in this paper.

The combined TEC and PV system operates as a unit by converting the solar energy to electrical energy. The TEC module can either be supplied energy from an external source or utilize the energy converted by the PV module. In either case, the net power output remains the same. For this research, the latter was considered. An

H. Moshfegh (✉) · M. Eslami
School of Mechanical Engineering, Shiraz University, Shiraz, Fars, Iran

A. Hosseini
Industrial Engineering & Management, KTH Royal Institute of Technology, Stockholm, Sweden

S. Nižetić, A. Papadopoulos (eds.), *The Role of Exergy in Energy and the Environment*, Green Energy and Technology,
https://doi.org/10.1007/978-3-319-89845-2_44

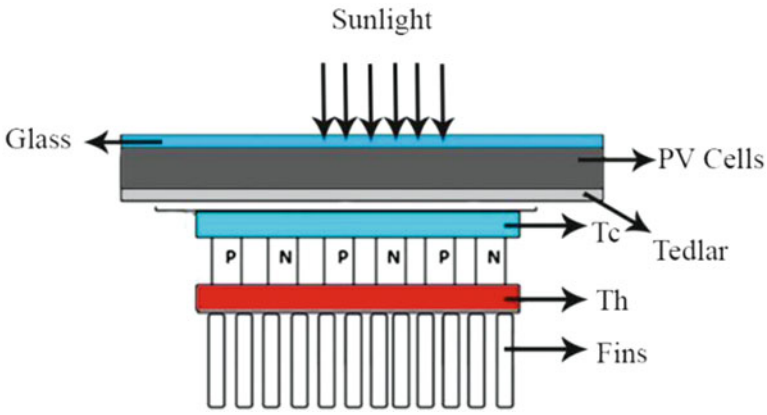

Fig. 44.1 A schematic of hybrid PV cells combined with TEC modules

overall schematic of this system is presented in Fig. 44.1. Numerical analyses will be conducted based on this system to assess whether the proposed method will result in improvements to the performance of the PV cells.

The efficiency of the combined system can be influenced by various design and operation parameters. An operation parameter which can affect the performance of these systems is the wind speed. This effect can demonstrate negative or positive feedbacks on the system based on the operating conditions. Furthermore, design parameters such as the fin area can play a role in these combined systems' output. Moreover, the TEC current can change the efficiency of the system based on the operating conditions, and an optimized amount can be calculated under certain circumstances.

Xi et al. [1] first discussed the development and applications of two solar-driven thermoelectric technologies. Van Sark [2] proposed to use the thermal waste by attaching thermoelectric modules to the back of PV cells to form a hybrid module. Their work focuses on generating power from the TE module in order to increase the efficiency.

Thermoelectric cooling is utilized today as a novel approach to increase the efficiency of PV cells. Previous studies by Najafi and Woodbury [3] have analysed the possibility of using thermoelectric cooling on PV cells by controlling the cell temperature in a desired range and optimizing the cell output power in several ambient temperatures. Their approach focuses on optimizing the PV cells using a genetic algorithm and does not cover parameters such as wind speed, ambient temperature and fin area.

Benghanem et al. [4] have analysed the effects of the ambient temperature on these cells in the presence of thermoelectric cooling experimentally in hot sites. Their work proposes that TEC cooling has a desirable performance in high ambient temperatures.

Through this paper, the output power will be optimized respective to design and operating parameters such as wind speed, fin area, irradiation and ambient

temperature. The PV cell model will be introduced next. The governing equations will follow the cell model, and the results will be designated after simulating the module in MATLAB.

44.2 Photovoltaic Cell Model

The PV cell model implemented in the calculations has a schematic as shown below. In this work, a thermoelectric module with a heat sink is considered to be attached to the back side of photovoltaic panel. The incoming irradiation from the top side crosses the glass and is absorbed by the PV cells. A percentage of the sunlight's energy is converted to electrical energy by the PV cells, and the remainder is given back to the surroundings through convection and radiation.

A TEC module is installed in the back of the model to reduce the cell temperature and increase the efficiency. As the TEC current increases, the cooling effect and, also, the TEC's hot side temperature increase. In order to reach an adequate cooling for the TEC module, fins were installed as heat sinks in the back of the module to enhance the heat transfer to the ambient air.

The following equation can be presented to estimate the efficiency of PV cells with temperature variation (Sarhaddi et al. [5]):

$$\eta = \eta_0[1 - 0.0045(T_{\text{cell}} - T_{\text{cell,ref}})] \tag{44.1}$$

where η_0 is the PV efficiency at reference conditions and T(cell,ref) is commonly assumed as 298 K. It is assumed that the power required to run the thermoelectric cooling module is provided by the photovoltaic panel itself. A TEC module can be defined by four characteristic parameters, namely, $I_{\max}$, $V_{\max}$, $Q_{\max}$ and $\Delta T_{\max}$ (Zhang [6]). The module parameters can be calculated by the following equations:

$$S_{\text{m}} = \frac{V_{\max}}{T_{\text{a}}} \tag{44.2}$$

$$R_{\text{m}} = \frac{(T_{\text{a}} - \Delta T_{\max})V_{\max}}{T_{\text{a}} I_{\max}} \tag{44.3}$$

$$K_{\text{m}} = \frac{(T_{\text{a}} - \Delta T_{\max})V_{\max} I_{\max}}{2T_{\text{a}}\Delta T_{\max}} \tag{44.4}$$

where S_{m}, R_{m} and K_{m} represent the TEC module's Seebeck coefficient, electrical resistance and thermal conductance, respectively.

Q_{c} which is the total absorbed power at the TEC's cold side can be calculated by:

$$Q_{\text{c}} = S_{\text{m}} I_{\text{c}} T_{\text{c}} - \frac{I^2 R_{\text{m}}}{2} - K_{\text{m}}\Delta T \tag{44.5}$$

Similarly, Q_{h} is the total amount of heat generated at the hot side:

$$Q_h = S_m I_c T_h + \frac{I^2 R_m}{2} - K_m \Delta T \tag{44.6}$$

ΔT represents the temperature difference between the hot and cold sides of the TEC module:

$$\Delta T = T_h - T_c \tag{44.7}$$

U_T is the heat conduction coefficient from the PV cell to ambient through Tedlar and can be calculated by:

$$U_T = \left[\frac{L_{si}}{K_{si}} + \frac{L_T}{K_T}\right]^{-1} \tag{44.8}$$

The combined module can be described by assuming control volumes about the components of the system. The following equations can be achieved in order to calculate the properties of the module in steady-state operation:

$$\begin{aligned} &\tau_{glass}[\alpha_{cell}\beta_{cell}G + \alpha_T(1-\beta_{cell})G]A_{PV} \\ &= U_t(T_{cell} - T_{amb})A_{PV} \\ &+\varepsilon_{glass}\sigma A_{PV}(T^4{}_{cell} - T^4{}_{sky}) \\ &+U_T(T_{cell} - T_{Tedlar})A_{PV} \\ &+\tau_{glass}\beta_{cell}\eta_{el}G.A_{PV} \end{aligned} \tag{44.9}$$

where T_{sky} can be calculated as follows (Wong and Chow [7]):

$$T_{sky} = 0.0552 \times T_a{}^{1.5} \tag{44.10}$$

β_{cell} which is the packing factor demonstrates the percentage of cell area to the panel area. α_{cell} is the absorptivity factor which accounts the amount of absorbed irradiation by the cell. The left-hand side of Eq. 44.8 represents the total incoming irradiation. $U_t(T_{cell} - T_{amb})A_{PV}$ is the amount of heat convection from the cell to the ambient air from the top side. $\varepsilon_{glass}\sigma A_{PV}(T^4{}_{cell} - T^4{}_{sky})$ represents the emitted heat from the cell to the sky. $U_T(T_{cell} - T_{Tedlar})A_{PV}$ is the heat transferred from the cell to the Tedlar. Finally, $\tau_{glass}\,\beta_{cell}\eta_{el}G.\,A_{PV}$ is the power output of the PV cell.

$$U_t(T_{cell} - T_{amb})A_{PV} = N_{TEC}Q_c + h_a(T_{Tedlar} - T_{amb})(A_{PV} - A_{TEC}) \tag{44.11}$$

$N_{TEC}Q_c$ calculates the amount of heat removed by the TEC modules. $h_a(T_{Tedlar} - T_{amb})(A_{PV} - A_{TEC})$ is the transferred heat due to convection between the Tedlar and the flowing air from ambient.

In order to calculate the temperature at the junction between the Tedlar and the PV cells, the following equation is presented:

$$T_{Tedlar} = T_c + Q_c R_{jc} \tag{44.12}$$

Furthermore, the temperature at the hot side of the cells can be calculated by:

$$T_h = T_a + Q_h R_{ha} \tag{44.13}$$

It is clear that the net power output of the combined system can be calculated by extracting the TEC power consumption from the PV cells' power output:

$$\text{Net output power} = \text{PV}'\text{s generated power} - \text{TEC}'\text{s power consumption} \tag{44.14}$$

In the next section, a MATLAB code will be implemented based on the above equations in order to calculate the net power output of the combined TEC-PV cell system under various circumstances.

44.3 Simulation and TEC Model

The simulations were performed in MATLAB in order to assess the effects of the following parameters on the performance of the system:

Ambient temperature variation
Fin area variation
Radiation variation
Wind velocity variation

The differences between the net power outputs for each case were calculated in order to reach an accurate analysis. Moreover, the TEC modelling and design parameters were based on the Kryotherm TB-4-(83-18-4-1)-1.3. Table 44.1 lists the values and units for the model used.

Next, the results will be presented, and a comparison between cases with and without thermoelectric cooling will be conducted.

44.4 Results and Discussion

This section focuses on the analysis of TEC cooling of PV cells and its consequences while affected by the parameters mentioned earlier. For the research purposes in this article, ideal amounts of optimized currents were calculated in MATLAB for the Kryotherm TB-4-(83-18-4-1)-1.3 in each case, and the rest of the results were based

Table 44.1 TEC design characteristic parameters

Parameter	Value	Unit
Imax	3.70	Amps
Qmax	0.80	Watts
Umax	0.80	Volts
ΔTmax	138.00	K
Area	494.40	mm2

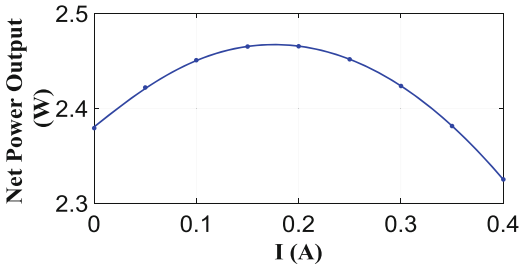

Fig. 44.2 Net generated power reaches a maximum amount at an optimized current

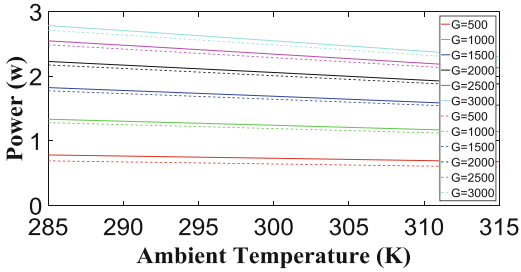

Fig. 44.3 Net output power is decreased with ambient temperature's rise

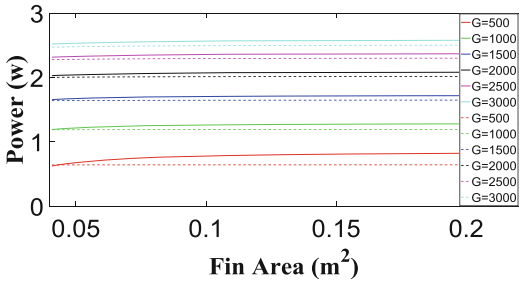

Fig. 44.4 Net output power is increased as the fin area becomes larger

on the respective amounts. In the presented figures, the dashed and connected lines represent cases without and with thermoelectric cooling, respectively.

Obviously, the TEC consumes power from the PV cell in order to operate and cool the panel. However, this power consumption reduces the net power output. In order to optimize the net power output based on the efficiency increase and power consumption, in this research, the maximum net output power from the PV cell while under the effect of TEC has been calculated, and its respective current was used for the rest of calculations. Figure 44.2 plots the net power output respective to the supplied current.

Clearly, the performance of PV cells is gradually reduced as the cell temperature rises. Furthermore, the ambient temperature affects the cell temperature greatly. This can also be seen in the simulations. Figure 44.3 illustrates this fact and confirms the modelling performed.

Figure 44.4 presents the net output power respective to fin area variation. As demonstrated, as the fin area increases, the heat transfer to the ambient air is also escalated which leads to a lower cell temperature and higher performance.

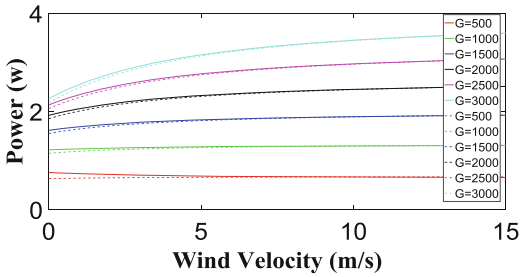

Fig. 44.5 Effects of wind velocity variation on net power output

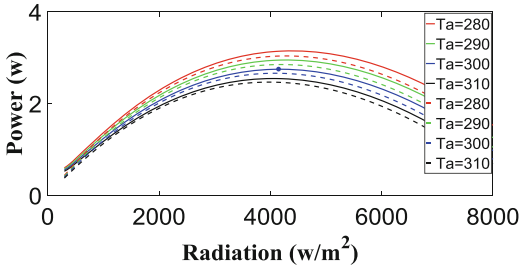

Fig. 44.6 Net generated power plot for the PV cell in the presence and absence of thermoelectric cooling

Wind velocity has a complicated effect on the net power output of the combined PV-TEC system as its effects are based on the ambient temperature and incoming radiation. In low amounts of irradiation, the effect on wind velocity tends to decrease the efficiency of the PV cells by transferring heat from the ambient air to the system as these cells tend to be cooler than the ambient air at low irradiations. On the other hand, wind has a favourable effect in high irradiations as it cools the system by transferring heat from the hot side of the TEC module to the ambient temperature to reduce the cell temperature and achieve higher efficiencies. Moreover, as the wind velocity increases, the favourable effect of thermoelectric cooling is decreased as the cooling from wind takes place. This effect can even expand to reduce the net power output at very high wind velocities as the TEC only consumes power in these cases (Fig. 44.5).

PV cells have the ability of concentrating the incoming radiation to reach higher amounts. In order to reach a comparison for the effects of thermoelectric cooling and irradiation, Fig. 44.6 is provided. It is observed that optimum thermoelectric cooling increases the efficiency and the effect of cooling is more realizable at higher irradiations. Furthermore, as the irradiation increases, the power generation is also increased, while the efficiency of the PV cells is reduced due to excessive heating. This issue leads to a maximum net power output at an optimum irradiation amount which is marked by a dot in Fig. 44.6.

Table 44.2 presents the net output powers at different ambient temperatures.

Table 44.3 assesses the net output powers under the effects of various fin areas at 300 K temperature.

Table 44.2 Selected power outputs at different ambient temperatures and irradiations

Irradiation (W/m2)	Temperature (K)	Power output with cooling (W)	Power output without cooling (W)	Percent increase
4100	300	2.75	2.66	3.26
4100	310	2.55	2.46	3.24

Table 44.3 Selected power outputs at various fin areas and irradiations at 300 K

Irradiation (W/m2)	Fin area (m2)	Power output with cooling (W)	Power output without cooling (W)	Percent increase
3000	0.07	2.55	2.49	2.63
3000	0.2	2.58	2.50	3.05
500	0.07	0.74	0.64	15.35
500	0.2	0.82	0.64	27.87

Table 44.4 Selected power outputs at various wind velocities and irradiations at 300 K

Irradiation (W/m^2)	Wind velocity (m/s)	Power output with cooling (W)	Power output without cooling (W)	Percent increase
3000	1	2.55	2.48	2.57
3000	5	3.16	3.13	0.77
500	1	0.73	0.64	13.66
500	5	0.69	0.66	3.24

Table 44.4 compares the net output powers at different wind velocities at 300 K temperature.

44.5 Conclusion

In this paper, a combined PV-TEC model was modelled and analysed numerically under different operating conditions. The results demonstrate possibilities for the optimization of these modules. An algorithm was implemented to optimize the TEC current in each case which resulted in detecting the maximum net power output. Moreover, the effects of parameters such as fin area, ambient temperature, irradiation and wind velocity on the net output power of the model were assessed. While higher ambient temperature results in the reduction of the performance of these cells, larger fin areas can result in higher power outputs. Wind velocity acts as a cooling factor for the cells which reduces the effect of TEC cooling but increases the net power output at certain irradiations. However, this effect might result in a negative feedback under other circumstances. Further analyses demonstrate that these modules have a peak net power output at an optimum irradiation. The increase is due to the higher available power as the irradiation increases; on the other hand, higher irradiation results in the warming of these cells which in turn reduces the performance of the

system. These results promise a great potential for conducting further research to utilize combined forced air and thermoelectric cooling to reach more effective measures for increasing the efficiency of these cells.

Nomenclature

T	Temperature (K)
S	Seebeck coefficient (V/K)
R	Electrical resistance (Ω)
K	Thermal conductance (W/K)
I	Current (A)
V	Voltage (V)
Q	Transferred heat (W)
U	Overall heat transfer coefficient (V)
L	Thickness (m)
A	Area (m^2)
G	Solar irradiance (W/m^2)
ΔT	Temperature difference (K)
N	Number of TECs
h	Convection coefficient (W/m^2)

Greek Letters

η	PV efficiency
α	Absorptivity
τ	Transmissivity
β	Packing factor
ε	Emissivity
σ	Stefan–Boltzmann constant (W/m^2K^4)

Subscripts

m, TEC	TEC module
a, amb	Ambient
glass	Glass
PV, cell	PV cell
T, Tedlar	Tedlar
max	Maximum
h	TEC's hot side
c	TEC's cold side
t	Overall
si	Silicon
sky	Sky
jc	Cold-side junction
ha	Heat sink

References

1. Xi H, Luo L, Fraisse G (2007) Development and applications of solar-based thermoelectric technologies. Renew Sust Energ Rev 11(5):923–936
2. Van Sark WGJHM (2011) Feasibility of photovoltaic–thermoelectric hybrid modules. Appl Energy 88(8):2785–2790
3. Najafi H, Woodbury KA (2013) Optimization of a cooling system based on Peltier effect for photovoltaic cells. Sol Energy 91:152–160
4. Benghanem M, Al-Mashraqi AA, Daffallah KO (2016) Performance of solar cells using thermoelectric module in hot sites. Renew Energy 89:51–59
5. Sarhaddi F et al (2010) Exergetic performance assessment of a solar photovoltaic thermal (PV/T) air collector. Energ Buildings 42(11):2184–2199
6. Zhang HY (2010) A general approach in evaluating and optimizing thermoelectric coolers. Int J Refrig 33(6):1187–1196
7. Wong LT, Chow WK (2001) Solar radiation model. Appl Energy 69(3):191–224

Chapter 45
Life Cycle Analysis of Solar Thermal Systems in Hotel Buildings

Effrosyni Giama, Elli Kyriaki, and Agis M. Papadopoulos

45.1 Introduction

Europe faces challenges in the energy and financial sector. The unstable economic circumstances are an intense source of disturbance and a brake on the continued growth of the European countries. The ongoing increase of energy demands, observed in the past years, led to the gradual depletion of fossil fuels. Furthermore, the significant increase of gas pollutants (CO2, ?Ox) has had major impacts on climate and environmental quality (e.g. global warming). The need for renewable energy in conjunction with the demand for higher quality of life and reduction of environmental impact is becoming a major aim of developing and integrating technologies that promote the application of renewable energy sources and adopt best practices of rational energy use. Towards this effort, the European Union has a leading role through a series of actions and initiatives (target 20-20-20), in order to ensure a development on solid economic, social and environmental bases. Towards the promotion of renewable energy sources, a variety of solar energy systems mainly for the production of domestic hot water (DHW) and the space heating have been developed. Furthermore, several solar systems for solar cooling have been developed, but they are not very widespread in Europe.

Energy management is undoubtedly a complex issue especially for large commercial buildings with strongly varying heat/cold and/or electricity loads, such as big urban hotels, and requires a holistic optimization approach in order to ensure economic, environmental and operational efficiency as well as natural resource conservation. In general, buildings contribute approximately 30% to total global GHG emissions. In efforts to reduce global warming, GHG reductions in this area

E. Giama (✉) · E. Kyriaki · A. M. Papadopoulos
Mechanical Engineering, Aristotle University of Thessaloniki, Thessaloniki, Greece
e-mail: fgiama@auth.gr

S. Nižetić, A. Papadopoulos (eds.), *The Role of Exergy in Energy and the Environment*, Green Energy and Technology,
https://doi.org/10.1007/978-3-319-89845-2_45

would make a significant contribution [1]. According to the Intergovernmental Panel on Climate Change (IPCC), there are three areas to focus on in reducing emissions from buildings: reducing energy consumption and building embodied energy, switching to renewable energy and controlling non-CO2 emissions [2].

Hotels are typically purpose-dedicated pieces of infrastructure handling facilities, installations and equipment to serve the overall variety of tasks required by contemporary logistics services but also quite extensive retail and leisure services. In that sense, they have to satisfy commercial as well as entrainment services for visitors. For these reasons, hotels, especially the bigger one, show significant demand for energy. The energy demand is composed mainly of electricity, space cooling and heating and hot water provision. Given this high energy requirements, but also it's quite significant variation on a daily and seasonal basis depending especially on the local climatic conditions, energy conservation measures as well as the implementation of renewables and state-of-the-art energy management can contribute to reduce the energy demand by increasing energy efficiency, by optimizing the overall environmental performance, by lowering operational cost and by improving the level of services provided. Moreover, hotels are demanding energy consumers due to their 24-h-based operation and the variety of facilities and functions provided [3].

This paper evaluates the environmental impact of solar thermal systems in hotel buildings using LCA approach. The energy and the environmental performances of one of the most common renewable technologies have been studied: the solar thermal systems for space heating and domestic hot water production (solar combi systems). A life cycle assessment has been performed following the international standards of ISO 14040 series, supported by GaBi software. The aim is to trace the energy system's environmental impact related to its life cycle. Life cycle thinking in environmental impact assessment has been for over 40 years now prevalent in the industrial and the service sector, with some early life cycle analysis (LCA)-type practitioners bringing a multi-attribute quantitative approach to decisions related to beverage packaging as far back as the1960s.

This approach evolved into LCA, with well-established international standards for guidance [4]. LCA is therefore a science-based, quantitative and integrative methodology that measures the material and energy flows to and from nature over the lifetime of a product or service and assesses the potential impact of those flows on resources, ecosystems and human health. These impacts occur in various segments of the manufacturing value chain and throughout the life of the product. Often the assessment is referred to as a cradle to grave evaluation. Commonly reported impact metrics include global warming ("carbon footprint"), acidification ("acid rain"), eutrophication ("algal bloom"), photochemical oxidant creation ("summer smog") and ozone depletion ("ozone hole").

A comprehensive review of similar analysis for energy systems is presented, and the results are compared with the ones derived from conventional systems as well as other renewable energy technologies. The results presented in this paper include the analysis of the production, disposal and transportation of the materials and energy used for the manufacturing processes of the building's energy systems, which

include an oil- and a gas-fired boiler as auxiliary sources and the solar combi system (solar collectors and all the other components).

The goal is the integrated environmental evaluation of solar thermal energy systems as well as the comparison of the system analysed with other conventional ones in order to add the environmental criteria and the energy consumption to the selection of energy systems in hotel buildings.

45.2 Life Cycle Analysis Methodology

LCA is a science-based, quantitative and integrative methodology that measures the material and energy flows to and from nature over the lifetime of a product or service and assesses the potential impact of those flows on resources, ecosystems and human health. These impacts occur in various segments of the manufacturing value chain and throughout the life of the product. Often the assessment is referred to as a cradle to grave evaluation. Commonly reported impact metrics include global warming ("carbon footprint"), acidification ("acid rain"), eutrophication ("algal bloom"), photochemical oxidant creation ("summer smog") and ozone depletion ("ozone hole") [5].

The main purposes of LCA are to identify hot spots in the value chain, identify and quantify alternatives and disclose environmental information. The following phases have been evaluated: production and transportation of energy and raw materials, production process, installation, maintenance, disposal and transports occurring during each step. The LCA approach used is best termed as "streamlined" LCA (SLCA), as it does not take into account the recycling of building materials or their disposal into landfill, while it is more focused on two impact categories: global warming impact, or carbon footprint, and embodied energy [6].

LCA is a popular environmental tool that has been applied since the early 1980s to a plethora of products and processes, examining the environmental performance of the selected reference systems from "cradle to grave". In brief, the concept of LCA is based on (a) the consideration of the entire life cycle which includes raw material extraction and processing, the production, the use of the product, up to the recycling and/or disposal, (b) the coverage of all environmental impacts connected with the products' life cycle, such as emissions to air, water and soil, waste, raw material consumption or land use and (c) the aggregation of the environmental effects in consideration of possible impacts and their evaluation in order to give oriented environmental decision support.

LCA therefore offers a comprehensive analysis which links actions with environmental impacts. At the same time, it provides quantitative and qualitative results, and taking into consideration the link between system's functions and environmental impacts, it is easy to identify the issues that need improvement. There are four main stages for the implementation of LCA: (a) planning, (b) inventory analysis, (c) impact assessment and (d) improvement analysis. The main purpose of planning is to define the scope and goal as well as the boundaries of the system studied.

During the planning, the objective should be clear and the data collection sources defined. The inventory analysis is the stage where the inputs and outputs are quantified. Energy, raw materials, water consumption, air emissions and solid waste are quantified either through measurements or database searches, surveys and software calculations.

During impact assessment, the environmental impact is calculated as a result from the inventory analysis. The input and output data are translated to environmental impacts like climate change, acidification, eutrophication and photochemical oxidation. Finally, the stage of improvement analysis involves discussion and improvement suggestions. For implementing LCA at the inventory phase, software tool was used for the results' reliability control: the GaBi LCA software, which is a life cycle analysis model with embodied EcoInvent LCA. At the environmental impact assessment phase (normalization and weighting), a set of specialized indicators were used, derived from CML 2. The analysis was used as a tool to define the energy-consuming processes taking into consideration the most significant energy consumption and improve the present situation of the system studied. Energy and environmental goals were set to improve the environmental and consequently the energy efficiency processes. The results produced were compared with other similar case studies reported in the literature [7, 8].

45.3 Solar Combi Systems Technology

The analysis and description of these systems will be based on their scope of application. Firstly, solar combi systems for DHW production as well as heating will be presented. Then, solar combi+ systems for DHW, heating and cooling will be presented in detail. In these systems, the solar collector is responsible for collecting the incident solar radiation, converting it into thermal energy and transferring this energy to a fluid flowing through the collector. The main component in a solar collector is the absorber where collection of the radiation takes place. The heat is then partly transferred to the heat medium (usually water or water-glycol mixture), with the rest lost to the environment. The collector is connected to a piping network, through which the heat medium is transferred either directly to the heating/cooling equipment or to the heat storage from where it can be drawn for later use. The solar collector is placed usually on the roof of the buildings.

In solar combi systems, the installed collector surface which now has to ensure two energy supplies (both DHW preparation and heating) is significantly higher than that in the case of only DHW preparation. Usually, a combi system contains two thermal sources. Solar collectors produce thermal energy depending on the available solar radiation, and an auxiliary source (usually natural gas, electricity or oil) is used, either when excessive demand needs to be covered and solar radiation is not available or when it is not cost-efficient to cover 100% of the demand with a solar system. DHW and space heating should always have thermal energy available in two different temperature fields. In order to achieve this, two different hot water tanks

can be used in combination with a smart control unit, acting on the pumps and valves of the hydraulic system. Tanks will contain water in different temperatures, making it available whenever needed. However, another configuration can also be implemented, with the use of a single storage tank if this is carefully designed; attention should be paid to avoid water mixing in order to attain different water temperature levels in the same tank. The different temperatures are achieved due to the property of water to have different densities depending on its temperature. The necessary subsystems will be described below.

As mentioned earlier, the solar combi technology has the ability to cover both thermal needs and provide DHW. The necessary subsystems for these functions are the absorber and heat storage system, as well as the distribution system. Specifically, the absorber and heat storage system consists of:

45.3.1 Solar Collector

Solar energy is collected through the absorber, while the basic operating principle is the transmission of this energy in a fluid medium (water or mixture of water-glycerol) through a piping system. The geometry of the solar collectors varies, taking into consideration the efficiency, the available space and the purpose of each application (e.g. flat or parabolic collectors). It should be noted here that the dimensioning of the collector is always based on the needs for space heating and DHW production. There are many different types of solar collectors: unglazed water, evacuated tube (EVC), flat plate (FPC), compound parabolic (CPC), glazed and unglazed air and concentrating ones are only some of them. The distribution of the different collectors' types used around the world is presented in Fig. 45.1.

FPC are usually permanently fixed in position and require no tracking of the sun. They should be oriented directly towards the equator, facing south in the northern hemisphere and north in the southern. These energy systems are most commonly used in Europe for water heating, while EVC are most commonly used in Asia, particularly in China. The latter achieve higher solar gains in colder weather and in

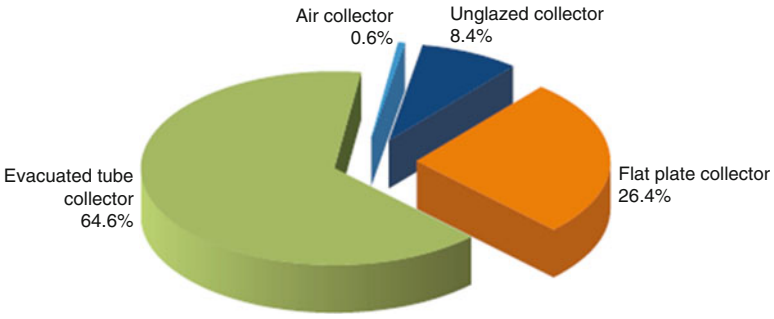

Fig. 45.1 Distribution based on the collector type—World

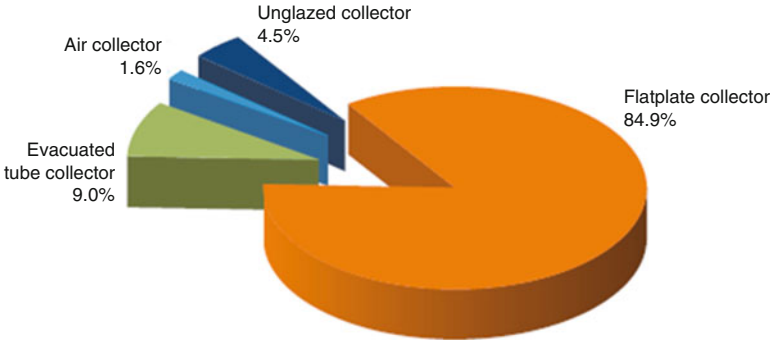

Fig. 45.2 Distribution based on the collector type—Europe [4]

less favourable conditions and can also produce water at higher temperatures than FPC. EVC achieve higher efficiency at lower incidence angles; hence, they are more appropriate for a day-long performance. Unglazed water collectors are used to heat seasonal running swimming pools. As they have no insulation and no cover, they are susceptible to weather conditions and demonstrate high heat losses. Air collectors are used for supplementary heating or agriculture applications (drying).

It is obvious that the evacuated tube collectors are the predominant solar thermal collector technology worldwide, followed by the flat-plate collectors and then the unglazed ones. Air collectors only play a minor role in total numbers. However, in Europe the situation is different, where the flat-plate collectors are the most widespread technology, as it is shown in Fig. 45.2.

45.3.2 Heat Storage Tank

This subsystem extends the capabilities of a solar combi system for continuously efficient operation during periods with low solar radiation. Furthermore, it ensures the efficient operation of the auxiliary systems during periods with medium loads, guaranteeing the overall efficient operation of the system. Finally, heat storage tanks are an important research and development field in order to achieve continuous energy autonomy, using solar systems (high combi systems) [9].

There are two main types of heat storage:

(a) Short-term storage: the solar energy is captured for several days to make up for rainy weather. In this case, it is obligatory to have good temperature stratification inside the tank. For this reason, units have to be tall and slender, so a large temperature range can be built up over the height. With short-term storage, solar thermal energy can be made to cover up to 30% of the total heat demand.
(b) Seasonal storage: the solar energy is captured for several weeks. This system is mostly used for district heating networks. However, it is also used in large residential buildings, with many apartments, but latterly as well as in separate

apartment buildings. Seasonal storage allows solar energy to meet up to 100% of total heat demand.

Moving from the design and construction of solar collectors and the heat storage system, the heat distribution system is described. Based on the heat medium that is used, there are two main categories for the heat distribution systems, namely, the air and water distribution systems.

- Air Distribution System: In these systems, air is transmitted through air ducts to the conditioned space and is delivered to them through air outlets (diffusers and grilles) or mixing boxes. The return air is driven back to the heat/cool production system where energy is recovered or exhausted to the environment. Air systems are often used in big buildings like hotels, office buildings, hospitals and schools. Their biggest advantages are that they allow for individual control of every zone and that they have the potential to use external air for natural cooling.
- Water Distribution System: Unlike air systems, water transmission systems provide or extract heat to/from a space by heat transfer between the indoor air and the heat medium (usually water). These systems are able to cover both heating and cooling demands, but in order to satisfy the minimum required ventilation rate, fresh air must be provided to the building. This can be done by infiltration, by natural ventilation or even by an additional mechanical ventilation system.

Solar combi + systems are the evolution of solar combi systems as they incorporate a cooling system in order to cover the space's cooling loads. They have been the centre of intense study in the past years, with 600 pilot applications, 87% of which have been implemented in Europe. As an evolution of solar combi systems, the operating principle and their structure are quite similar. The additional element worth to describe is the cooling subsystem. For the sake of brevity, at this point, only the cooling subsystem will be presented. Cooling System-Operation Principle: A thermally driven heat pump consumes energy in order to extract heat from a low-temperature source and transfer it to a sink with higher temperature (intermediate level). While in the case of a conventional vapour compression heat pump the energy is consumed in the form of electricity, in a thermally driven chiller, the necessary energy comes from a high-temperature fluid (in our case from the solar collector or the hot storage) and is called driving heat. The low-temperature source represents the conditioned space, and the heat obtained is essentially producing the cooling effect. The heat is finally rejected in the intermediate heat source, which is usually the external environment. The same principle also applies for desiccant cooling systems (open cycle). Like heating system, there is always an auxiliary source (usually electricity) in order to cover the demand when solar radiation is not available.

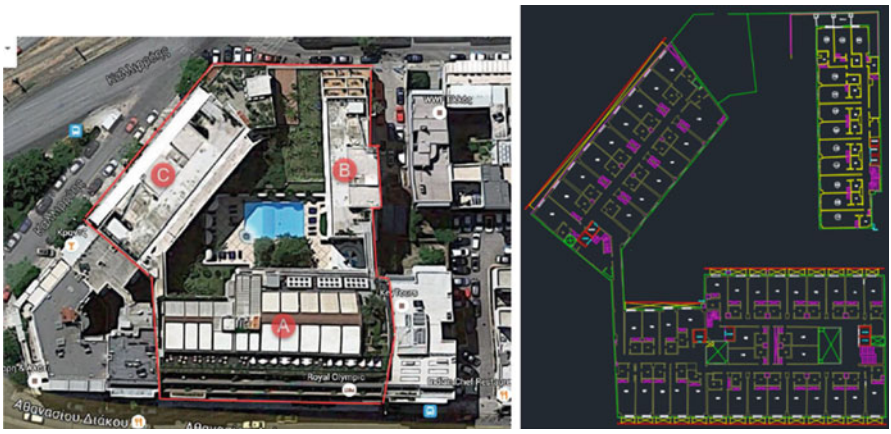

Fig. 45.3 Royal Olympic Hotel Athens

Table 45.1 Distribution of floors and rooms in the hotel

Building	Floors	Rooms
Building A	6	186
Building B	6	60
Building C	5	65
Total	–	311

45.4 A Hotel Building in Greece

The hotel building studied in the framework of this paper is "Royal Olympic Hotel Athens", and it is located in the centre of Athens (Fig. 45.3).

The hotel consists of three different buildings (A, B, C) with a total surface area of 12,058 m2. The distribution of floors and rooms in the three buildings is presented in Table 45.1.

45.5 Energy Analysis

The studied solar combi system and its components are presented in Fig. 45.4 and in Table 45.2.

Boilers are used as an auxiliary source when solar radiation is not available or is not enough to cover the hotel's needs. Boilers' total power is 840 kW. Also, the total collectors' installed area is 900 m2. The calculated total solar fraction when vacuum tube collectors are used is 60%, whereas when flat-plate collectors are installed, the solar fraction is 52%.

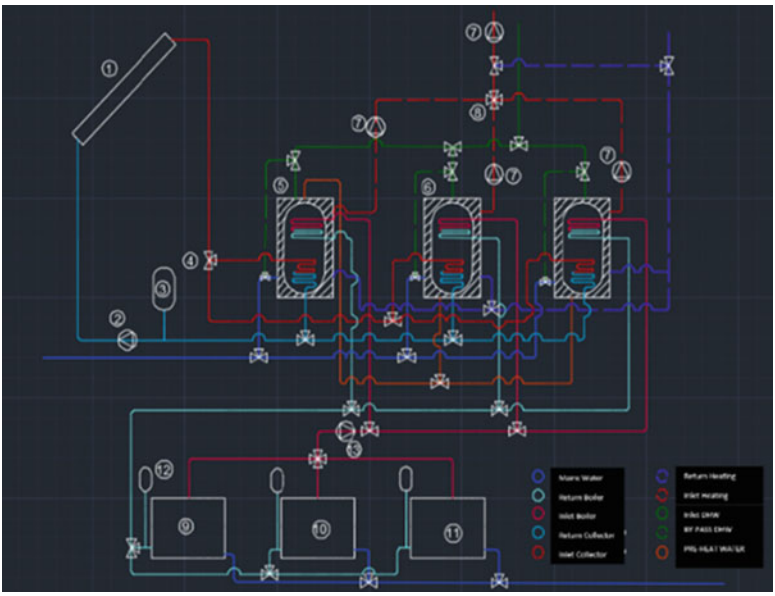

Fig. 45.4 Diagram of solar combi system

Table 45.2 Components of solar combi system

Number	Name
1	Solar collector
2	Circulator of solar loop
3	Expansion tank of solar loop
4	Valve
5	Water storage tank
6	Water storage tank
7	Circulator of heating loop
8	Valve
9	Boiler 1
10	Boiler 2
11	Boiler 3
12	Expansion tank of boiler
13	Circulator of boiler loop

45.6 Environmental Analysis

The environmental analysis is based on LCA methodology supported by GaBi software [10]. The system studied included raw materials production and use, transportation, installation and use. For these processes, the input data concerned the hotel studied. For the disposal phase, the data derived from the ecoinvent database.

The components studied for the environmental analysis of the solar thermal system are:

- Buffers
- Gas low-temperature boiler
- Solar collector
- Pipelines
- Circulating pump
- Radiators

The flat-plate collector consists of single copper pipes, mounted in aluminium casing, that pass through a dark painted surface (absorber) in order to heat directly the water that circulates into them. There is also a glazing in order to increase the efficiency of the heat transfer and insulation in the back and edge to reduce thermal losses. On the other hand, the evacuated tube collector features a heat pipe placed inside a vacuum-sealed tube. The pipe, which is sealed copper pipe, is then attached to a black copper fin that fills the tube. Protruding from the top of each tube is a metal tip attached to the pipe (condenser). The heat pipe contains a small amount of fluid (e.g. methanol) that undergoes a repeating evaporating condensing (using solar heat) cycle and indirectly heats the water [11, 12].

Both systems require a hot water storage tank. This tank is either mounted in the upper part of the collector or it is located somewhere in the building studied. The inventory analysis is the stage where the inputs and outputs are quantified. Energy, raw materials, water consumption, air emissions and solid waste are quantified either through measurements or in situ survey at the hotel studied. During impact assessment, the environmental impact is calculated as a result from the inventory analysis. The input and output data are translated to environmental impacts like climate change, acidification, eutrophication and photochemical oxidation. Focused mainly on climate change impact, the kg CO2-equiv. for the two different solar systems was registered as total for the entire energy system studied and separately for the different system's components.

The climate change impact does not differ significantly to the two different systems studied, as it is presented in Tables 45.3 and 45.4. The solar thermal system with vacuum solar collector has 204,000 kg CO2-equiv. and the solar thermal system with flat solar collector 197,000 kg CO2-equiv. From the other components, the solar collectors cause significant CO2 emissions and the radiators. Finally, the CO2 emissions for electricity and natural gas use are also worth noticing compared to the emissions form the other system's components.

CML 2001 is an impact assessment method which restricts quantitative modelling to early stages in the cause-effect chain to limit uncertainties. Results are grouped in midpoint categories according to common mechanisms (e.g. climate change) or commonly accepted groupings (e.g. ecotoxicity). CML 2001 is developed by the Institute of Environmental Sciences, Leiden University, The Netherlands, and is published in a handbook with several different authors, see literature below. The main principles behind the methodology are not being further developed. A Microsoft Excel spreadsheet with characterization factors for more than 1700

Table 45.3 Environmental performance per impact category of solar thermal system with flat-plate solar collector and vacuum tube collector

Environmental impact (CML 2001)	Solar thermal system with flat-plate collector	Solar thermal system with vacuum plate collector
Global warming potential (kg CO2-eq)	197000	204000
Acidification (kg SO2-eq)	978	1380
Eutrophication (kg phosphate-eq)	46,9	54,3
Abiotic depletion elements (kg Sb-eq)	6,95	17,3
Abiotic depletion fossil (MJ)	2370000	2440000
Freshwater aquatic ecotoxicity potential (kg DCB-eq)	822	1180
Human toxicity potential (kg DCB-eq)	238000	126000
Marine aquatic potential ecotoxicity (kg DCB-eq)	11800000	6200000
Terrestrial ecotoxicity potential	525	676
Photochemic ozone creation potential (kg ethene-eq)	72,3	89,6

Table 45.4 Environmental performance of solar thermal system with vacuum solar collector based on CML emission factors

Environmental impact (CML 2001)	Flat-plate collector	Vacuum plate collector
Global warming potential (kg CO2-eq)	76300	83300
Acidification (kg SO2-eq)	715	1120
Eutrophication (kg phosphate-eq)	26,3	33,7
Abiotic depletion elements (kg Sb-eq)	5,78	16,2
Abiotic depletion fossil (MJ)	822000	886000
Freshwater aquatic ecotoxicity potential (kg DCB-eq)	608	968
Human toxicity potential (kg DCB-eq)	299000	175000
Marine aquatic potential ecotoxicity (kg DCB-eq)	11100000	54900000
Terrestrial ecotoxicity potential	202	353
Photochemical ozone creation potential (kg ethene-eq)	35,7	53

different flows can be downloaded from the CML website. The characterization factors are updated when new knowledge on substance level is available. Several additional characterization factors are calculated by PE and LBP-GaBi following the principles described in the CML 2001 methodology documents. Normalization factors for CML 2001 are available for the Netherlands, Western Europe, EU and the World. The normalization factors are calculated via total substance emissions and characterization factors per substance and are hence following the substance level updates as described above. Normalization data for other countries (e.g. Germany, USA and Japan) and geographical units (e.g. North America or OECD) is available in GaBi5. This data is scaled from the original CML 2001 normalization via gross domestic product.

It is obvious from Table 45.4 that vacuum tube collector and correspondingly the solar thermal system with vacuum tube collector has increased environmental impacts in comparison to flat-plate collector and correspondingly to solar thermal system with flat-plate collector. This is due to the more complex construction of vacuum tube collectors compared to flat-plate ones.

45.7 Conclusions

Europe faces multiple socio-economic challenges, which have a direct impact on the energy and the financial sector. The increase in energy demand, observed in the past years, led to the gradual depletion of fossil fuels. Furthermore, the significant increase in gas pollutants (e.g. CO2 and ?Ox) has had major impacts on climate and environmental quality (e.g. global warming). Therefore, and also because of the strict European legislation framework, global climate change and carbon emissions as indicative environmental factors have been a top priority in the decision-making process for governments and companies.

Environmental sustainability has emerged as a key issue amongst governments, policymakers, researchers and public. Increasing efforts and resources have been devoted to research and environmental policies in order to identify, evaluate and assess harmful environment impacts. Tourism and the leisure market in general are significant energy consumers and have a respectively high environmental impact. This paper evaluates the environmental impact of solar thermal systems in hotel buildings using LCA approach. The energy and the environmental performances of one of the most common renewable technologies have been studied: the solar thermal systems for space heating and domestic hot water production (solar combi systems). The LCA approach used is best termed as "streamlined" LCA (SLCA), as it does not take into account the recycling of building materials or their disposal into landfill, while it is more focused on two impact categories: global warming impact, or carbon footprint, and embodied energy.

A comprehensive review of similar analysis for energy systems is presented, and the results are compared with the ones derived from conventional systems as well as other renewable energy technologies. The results presented in this paper include the analysis of the production, disposal and transportation of the materials and energy used for the manufacturing processes of the building's energy systems, which include an oil- and a gas-fired boiler as auxiliary sources and the solar combi system (solar collectors and all the other components).

References

1. UNEP (2009) Buildings and climate change – summary for decision makers. UNEP DTIE, Sustainable Consumption & Production Branch, Paris
2. Biswas WK (2014) Carbon footprint and embodied energy consumption assessment of building construction works in Western Australia. Int J Sustain Built Environ 3:179–186
3. Filimonau V, Dickinson J, Robbins D, Huijbregts MAJ (2011) Reviewing the carbon footprint analysis of hotels: Life Cycle Energy Analysis (LCEA) as a holistic method for carbon impact appraisal of tourist accommodation. J Clean Prod 19:1917–1930
4. Bare JC, Norris GA, Pennington DW, McKone T (2003) TRACI: the tool for the reduction and assessment of chemical and other environmental impacts. J Ind Ecol 6(3):49–78
5. Guinée JB, Gorrée M, Heijungs R, Huppes G, Kleijn R, de Koning A, van Oers L, Wegener Sleeswijk A, Suh S, Udo de Haes HA, Bruijn H de, van Duin R, Huijbregts MAJ (2002) Handbook on life cycle assessment. Operational guide to the ISO standards. I: LCA in perspective. IIa: Guide. IIb: Operational annex. III: Scientific background. Kluwer Academic Publishers, Dordrecht, ISBN 1-4020-0228-9, 692pp. cml.leiden.edu/research/industrialecology/researchprojects/finished/new-dutch-lca-guide.html
6. ISO 14040 (1997) Environmental management: life cycle assessment, principles and framework. International Standard Organization, Geneva, Switzerland
7. ISO 14041 (1998) Environmental management: life cycle assessment, principles and framework. International Standard Organization, Geneva, Switzerland
8. ISO 14043 (2000) Environmental management: life cycle assessment, life cycle interpretation. International Standard Organization, Geneva, Switzerland
9. Kyriaki E, Drosou V, Papadopoulos AM (2015) Solar thermal systems for low energy hotel buildings: state of the art, perspectives and challenges. Energy Procedia 78C:1968–1973. https://doi.org/10.1016/j.egypro.2015.11.385
10. Gabi Software (2016) Life cycle analysis software. http://www.gabi-software.com/international/index/
11. Anastaselos D, Oxizidis S, Manoudis A, Papadopoulos AM (2016) Environmental performance of energy systems of residential buildings: towards sustainable communities. J Sustain Cities Soc 20:96–108
12. Giama E (2016) Energy performance of buildings – energy efficiency and built environment in temperate climates. In Chap. 6, Life cycle vs carbon footprint analysis for construction materials, edited by M. Santamouris. New York, Springer Science & Business Media, pp 95–106. ISBN 978-3-319-20830-5, ISBN 978-3319-20831-2 (eBook). https://doi.org/10.1007/978-3-319-20831-2

Chapter 46
A Symmetric and an Asymmetric mini Compound Parabolic Collector Under Optical Investigation

Dimitrios N. Korres and Christos Tzivanidis

46.1 Introduction

Solar energy utilization has as a main representative the solar thermal collectors. The simplest of them is the flat plate collector which has been widely examined. For instance, Korres and Tzivanidis [1] conducted a CFD analysis in order to analyze the operation of a flat plate collector with a serpentine flow system.

The revolution in the solar energy utilization field is getting into practice by a specific kind of solar systems which is none other than the concentrating solar collectors. There are many different types of such systems, the most well-known of which are the parabolic trough and the compound parabolic collector (PTC, CPC). The last one is of considerable interest since it can give great efficiency without the need of using tracking.

There are a few analyses that have been conducted in how such configurations perform. For example, the optical and the thermal performance of two mini compound parabolic collectors with a circular and a flat absorber was analyzed by Korres and Tzivanidis [2, 3] and Korres et al. [4], respectively, while a compound parabolic collector was tested and optically optimized by Bellos et al. [5]. Also, Tzivanidis et al. [6] investigated the thermal and the optical performance of a parabolic trough collector for several different operating conditions, while Tsai and Lin [7] optimized a variable focus parabolic trough concentrator and compared it to the classical PTC and the semicylindrical configuration. Moreover, Cheng et al. analyzed a PTC optically [8] and developed a new method for concentrating systems [9] by using the Monte Carlo ray-tracing method.

D. N. Korres (✉) · C. Tzivanidis
Mechanical Engineering, National Technical University of Athens, Athens, Greece

S. Nižetić, A. Papadopoulos (eds.), *The Role of Exergy in Energy and the Environment*, Green Energy and Technology,
https://doi.org/10.1007/978-3-319-89845-2_46

The asymmetric setup has also been barely examined by Souliotis et al. [10] who analyzed asymmetric CPC for integrated solar systems with one tank inside the collector as well as by Kessentini and Bouden [11] who studied numerically the thermal performance of a double-tank integrated collector storage system (ICS) accompanied by asymmetric CPC reflectors. Moreover, Adsten et al. [12] examined six different setups with special asymmetric reflectors so as to determine the optimum case that provides the highest optical efficiency.

A quite different configuration has also been examined by Bellos et al. [13]. In this study, the optical performance of a typical CPC was compared with the respective of a complex CPC geometry which consisted of two different sloped concentrators connected to each other.

46.2 Examined Models

In this analysis, the optical performances of two different compound parabolic collectors, a symmetric and an asymmetric one, were investigated under the same operating conditions. The design and the main dimensions of the two collectors are depicted on Fig. 46.1. The length of the collectors is 1000 mm.

It is essential to explain in a deeper manner how the reflectors' profiles were designed. For this reason, we have to define two different parabolas A and B as well as their symmetrical A' and B'. The symmetric configuration comes from parabolas A and A', while the asymmetric one is a combination among B, B', and A' parabolas as Fig. 46.2 suggests. We should mention that *K* point in Fig. 46.2 belongs to the central axis of the cylindrical absorber, while the focal distances of B and B' parabolas form an angle $\theta = 39.2^{\circ}$ between each other. The A and A' parabolas' focal distances are both perpendicular to the horizontal plane.

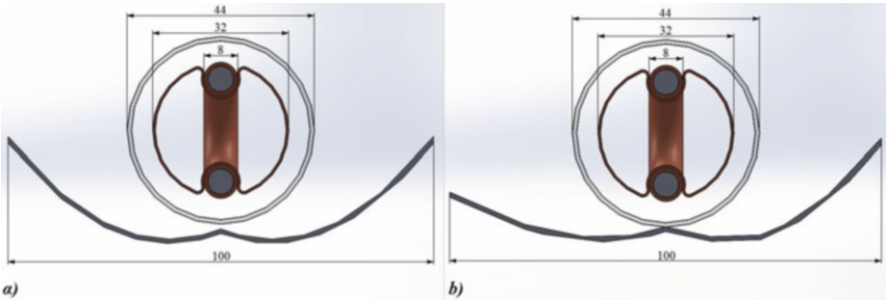

Fig. 46.1 (**a**) Symmetric and (**b**) asymmetric mini-CPC

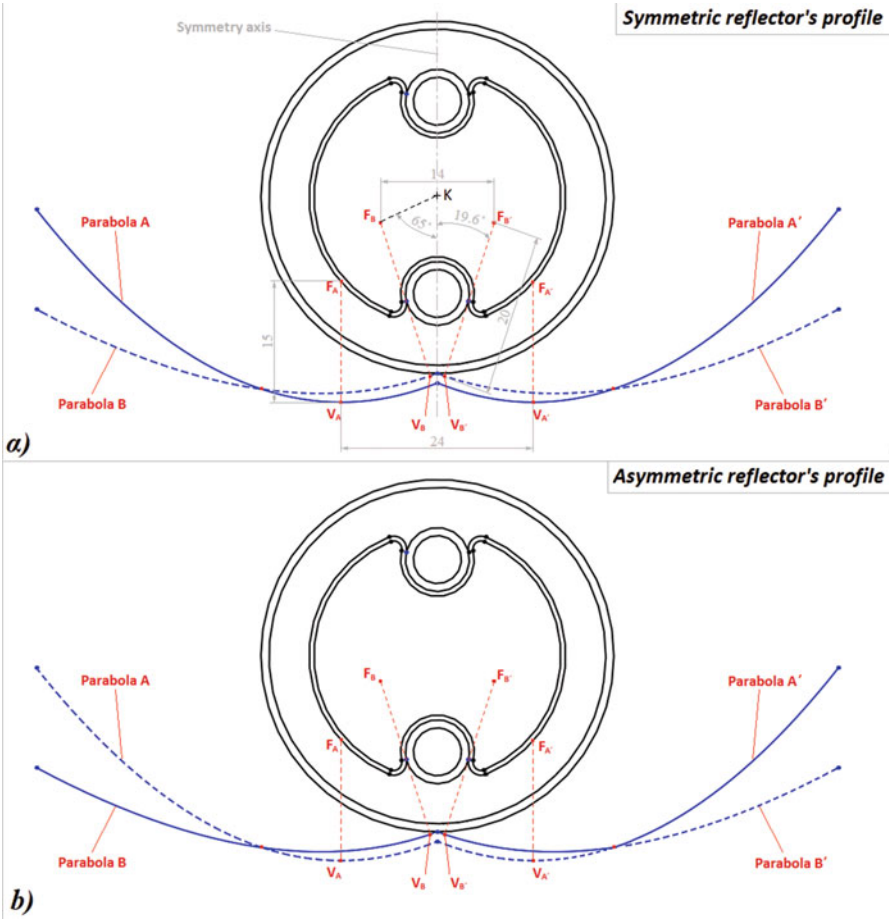

Fig. 46.2 Design of the (**a**) symmetric and (**b**) the asymmetric reflector

46.3 Methodology

The main aspect of this study was to determine the best, among the examined, reflector's configuration as well as the best orientation of the collectors. The two configurations were studied for an entire year in Athens at the typical day of each month. We have to mention that the typical day is the mean day[1] of the month adjusted on the typical year's conditions. Especially, the collectors' optical performances were examined at 9 h of each mean day from 8:00 to 16:00 considering

[1] At the mean day, the extraterrestrial solar irradiation is about the same with the respective mean daily solar irradiation of the month [14].

different clearness indexes (k_t) for each examined hour depended on the total hourly horizontal plane solar irradiation for the typical year (I_{ty}). The symmetric configuration was examined not only at horizontal position but also by setting its aperture plane parallel to this of the asymmetric configuration, while the collectors' orientation was first considered as E-W and then as N-S.

The design of the collectors was done in Solidworks, while the simulation of each setup was conducted in Solidworks Flow Simulation environment. The latitude for the area of Athens was set equal to 37.98°, while the solar angles for each hour of the examined days were provided from the Flow Simulation libraries.

At this point, it is important to mention that Solidworks Flow Simulation provides the extraterrestrial solar irradiation field which is obviously beam. Hence, the amount of the hourly incident solar radiation on the absorber arising from the simulation (I_o^p) is much greater than the real one. In order to convert that incident field into the beam one[2] we would have inside the atmosphere at the typical conditions ($I_{b,ty}^p$), we should multiply it with the $k_t \cdot I_{b,ty}^h / I_{ty}^h$ product where $I_{b,ty}^h$ is the hourly solar beam radiation on a horizontal plane for the typical conditions. The procedure we followed in order to calculate this product is presented via the next equations (Duffie and Beckman [14], Kouremenos et al. [15]).

Hourly clearness index

$$k_t = \frac{I_{ty}^h}{I_o^h} \tag{46.1}$$

Total hourly and daily horizontal plane extraterrestrial solar irradiation

$$\left.\frac{I_o^h}{H_o^h}\right\} = \frac{12 \cdot 10^{-3}}{\pi} \cdot G_{sc} \cdot A_1 \cdot (A_2 + A_3) \tag{46.2}$$

where:

$$G_{sc} = 1367 W/m^2$$

$$A_1 = 1 + 0.033 \cdot \cos\left(\frac{360 \cdot n}{365}\right) \quad A_2 = \cos(\varphi) \cdot \cos(\delta) \cdot \Big(\sin(\omega_2) - \sin(\omega_1)\Big)$$

$$A_3 = \frac{2 \cdot \pi \cdot (\omega_2 - \omega_1)}{360} \cdot \sin(\varphi) \cdot \sin(\delta)$$

Here $\omega_2 - \omega_1$ difference is the time duration we want to examine expressed in degrees. Hence, in the hourly irradiation case, ω_1 and ω_2 represent the hour angle 30 min before and after the examined hour, respectively, while in the daily one they express ω_s and $-\omega_s$, respectively, since ω_s represents the duration of the day

[2]The diffusive radiation contribution was not examined in this study because it would not affect the comparison process, since the compared configurations utilize it with the same way.

from the solar noon to the sunset. Consequently, in the daily irradiation case, $\omega_2 - \omega_1$ is equal to $2\omega_s$ which corresponds to the time duration from the sunrise to the sunset.

Total daily horizontal plane solar irradiation for the typical year in Athens

$$H_{ty}^{h} = 4.348 + 2.676 \cdot \sin\left(\frac{360 \cdot n}{365} - 86.410\right) \tag{46.3}$$

Total hourly horizontal plane solar irradiation for the typical year

$$I_{ty}^{h} = H_{ty}^{h} \cdot B_1 \cdot B_2 \tag{46.4}$$

where:

$$B_1 = \alpha + b \cdot \cos(\omega)$$
$$\alpha = 0.4090 + 0.5016 \cdot \sin(\omega_s - 60)$$
$$b = 0.6609 - 0.4767 \cdot \sin(\omega_s - 60)$$
$$B_2 = \frac{\pi}{24} \cdot \frac{\cos(\omega) - \cos(\omega_s)}{\sin(\omega_s) - \frac{2 \cdot \pi \cdot \omega_s}{360} \cdot \cos(\omega_s)}$$

Daily clearness index

$$K_T = \frac{H_{ty}^{h}}{H_{o}^{h}} \tag{46.5}$$

Diffusive daily horizontal plane solar irradiation for the typical year

$$H_{d,ty}^{h} = (1.188 - 2.272 \cdot K_T + 9.473 \cdot {K_T}^2 - 21.865 \cdot {K_T}^3 + 14.648 \cdot {K_T}^4) \cdot H_{ty}^{h} \tag{46.6}$$

Holds for: $0.17 \leq K_T \leq 0.75$
In the present study, K_T is in the range of 0.4–0.61.

Diffusive hourly horizontal plane solar irradiation for the typical year

$$I_{d,ty}^{h} = H_{d,ty}^{h} \cdot B_2 \tag{46.7}$$

Hence, by dividing Eq. (46.7) with Eq. (46.4), Eq. (46.8) that expresses the amount of the diffusive hourly radiation relatively to the total one for the typical conditions is created.

$$\frac{I_{d,ty}^{h}}{I_{ty}^{h}} = \frac{H_{d,ty}^{h}}{H_{ty}^{h}} \cdot \frac{1}{B_1} \tag{46.8}$$

Given this amount, we are able to calculate the respective beam radiation according to Eq. (46.9) that follows.

$$\frac{I_{\mathrm{b,ty}}^{\mathrm{h}}}{I_{\mathrm{ty}}^{\mathrm{h}}} = 1 - \frac{I_{\mathrm{d,ty}}^{\mathrm{h}}}{I_{\mathrm{ty}}^{\mathrm{h}}} \tag{46.9}$$

So, we have calculated the two parameters the required product consists of, and we could, finally, determine the amount of beam hourly solar radiation that reaches the absorber's surface at the typical conditions.

$$I_{\mathrm{b,ty}}^{\mathrm{p}} = k_{\mathrm{t}} \cdot \frac{I_{\mathrm{b,ty}}^{\mathrm{h}}}{I_{\mathrm{ty}}^{\mathrm{h}}} \cdot I_{\mathrm{o}}^{\mathrm{p}} = \frac{I_{\mathrm{b,ty}}^{\mathrm{h}}}{I_{\mathrm{o}}^{\mathrm{h}}} \cdot I_{\mathrm{o}}^{\mathrm{p}} \tag{46.10}$$

The specific conversion was conducted with this particular product because the reduction in the beam horizontal plane solar irradiation switching from the extraterrestrial to the atmosphere conditions is the same in percentage with the respective reduction in the beam solar radiation that goes on the absorber, given that the reflector's operation is not affected by this change. The third part of Eq. (46.10) declares clearly that fact.

46.4 East-West Axis Orientation

In this paragraph, the operation of the collectors was examined for the E-W axis orientation case as this is depicted on Fig. 46.3.

In Fig. 46.4, the power per square meter that reaches the absorber's surface is given for the three examined systems in the mean day of each month of the year for 8:00–16:00 time range. Table 46.1 gives the mean daily beam radiation for all months ($H_{\mathrm{b,ty}}^{\mathrm{p}}$) as well as the yearly one ($Y_{\mathrm{b,ty}}^{\mathrm{p}}$) that reaches the receiver's surface in each setup.

It is obvious from Fig. 46.4 that the asymmetric configuration performs better in most cases. More specifically, when the symmetric reflector has its aperture plane in horizontal position, it always delivers the lowest of all cases power to the receiver, while when its aperture is parallel to the respective of the asymmetric reflector (symmetric in slope), it beats the last one in March, partially in September from 10:00 to 14:00 and in June before 9:00 and after 15:00. Hence, the most suitable

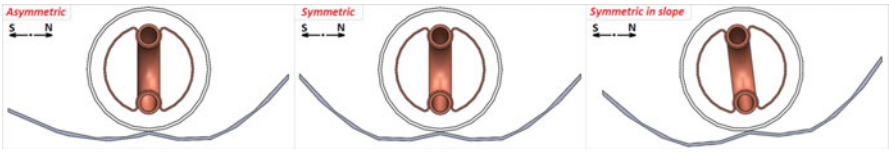

Fig. 46.3 E-W axis orientation

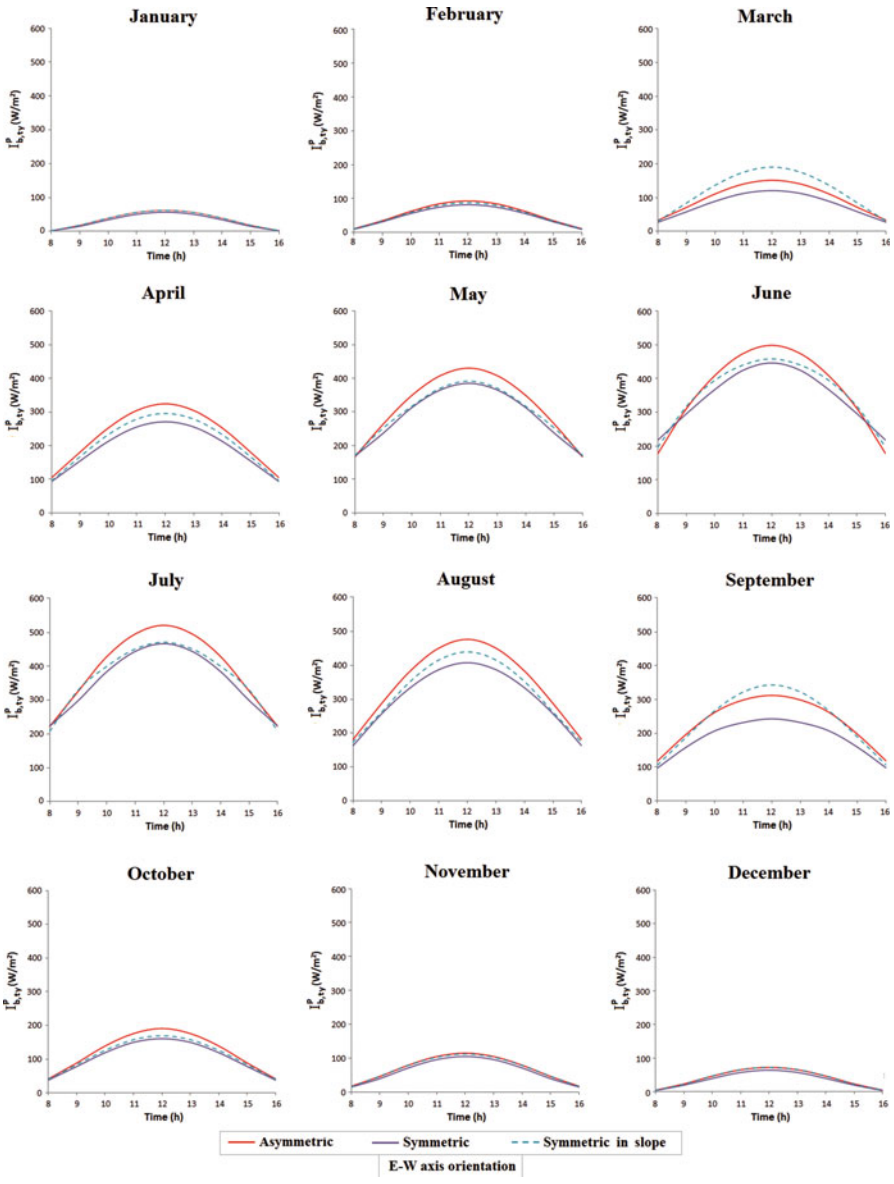

Fig. 46.4 Beam solar irradiation delivered on the absorber in each setup for the E-W axis orientation

concentrator for the whole year is the asymmetric one since it delivers the highest amounts of power on the absorber.

As we can see from Table 46.1, the maximum yearly beam radiation on the receiver's surface appears on the asymmetric configuration, while the inclined

Table 46.1 Daily and yearly beam solar irradiation delivered on the receiver for the E-W axis orientation

	$H^{p}_{b,ty}$(kWh/m^2/day)		
	East-west axis orientation		
Month	Asymmetric	Symmetric	Symmetric in slope
January	0.30	0.26	0.29
February	0.47	0.42	0.44
March	0.83	0.67	1.01
April	1.91	1.61	1.74
May	2.64	2.38	2.44
June	3.07	2.84	2.96
July	3.25	2.95	3.04
August	2.91	2.53	2.67
September	1.95	1.54	2.00
October	1.04	0.89	0.94
November	0.59	0.53	0.58
December	0.35	0.30	0.34
$Y^{p}_{b,ty}$ **(kWh/m^2/year)**	589.68	516.74	563.35

symmetric follows. Particularly, the asymmetric concentrator delivers 14.1% and 4.7% more yearly beam radiation on the receiver compared to the symmetric and the inclined symmetric, respectively, while slope increases by 9.1% the optical performance of the symmetric reflector.

Also, this configuration exceeds the rest systems in daily performance for the whole year except March and September where the inclined symmetric concentrator prevails as this is depicted on Fig. 46.5, where the mean daily beam radiation that reaches the absorber is presented for the mean day of each month of the year.

46.5 North-South Axis Orientation

Here we are going to investigate how the asymmetric and the horizontal symmetric configurations react under the N-S axis orientation (Fig. 46.6) and finally to determine the best position of the collectors opposite to the sun.

In Fig. 46.7, the respective diagrams for the specific case are given.

As we can see from Fig. 46.7, the asymmetric configuration exceeds the symmetric one for the whole year before 12:00. This happens because B parabola's focal distance is inclined to the east considering the specific orientation. Hence, the asymmetric reflector reserves the solar rays more gently at the morning hours compared to the symmetric one, leading the majority of them on the tubular receiver. Instead, the symmetric reflector provides totally 2% more yearly power delivered on the absorber as Table 46.2 suggests.

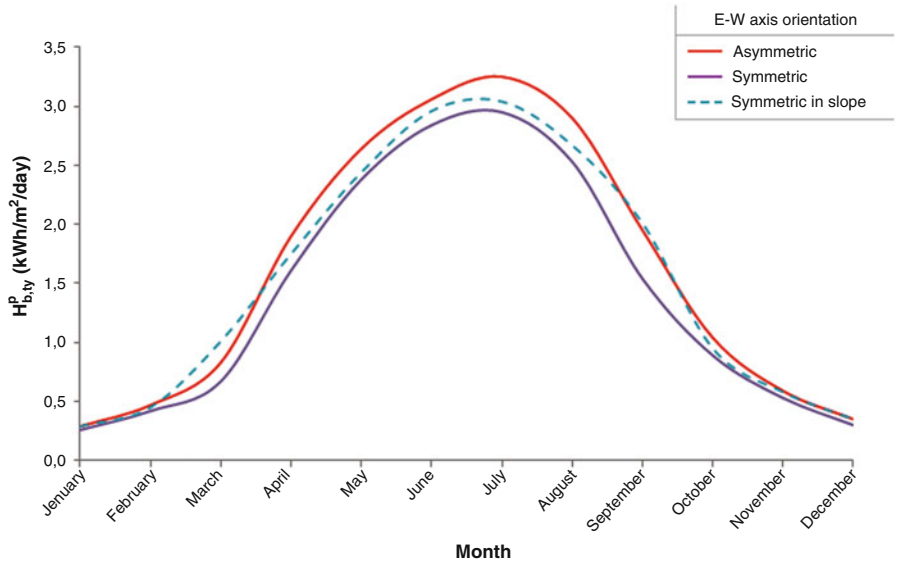

Fig. 46.5 Mean daily beam solar irradiation reaches the absorber in each examined month for the E-W axis orientation

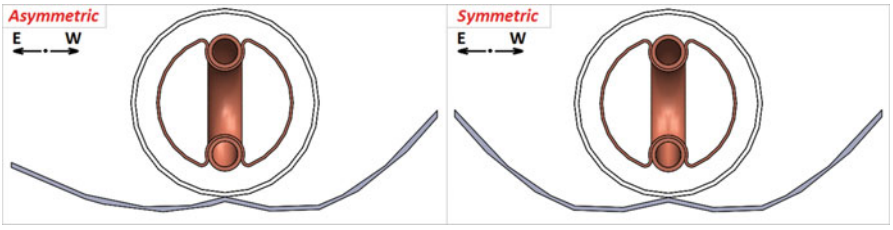

Fig. 46.6 N-S axis orientation

Generally, according to Table 46.2, the maximum yearly beam radiation delivered on the receiver is obtained through the combination between the asymmetric setup and the E-W axis orientation. However, if we take into consideration the daily energy that is delivered on the absorber, the N-S axis orientation beats the E-W one in February, March, and October as regards the asymmetric setup as well as at the periods from January to March and from September to December considering the symmetric configuration. Last but not least, the orientation seems that it does not diversify the yearly operation of the symmetric setup significantly.

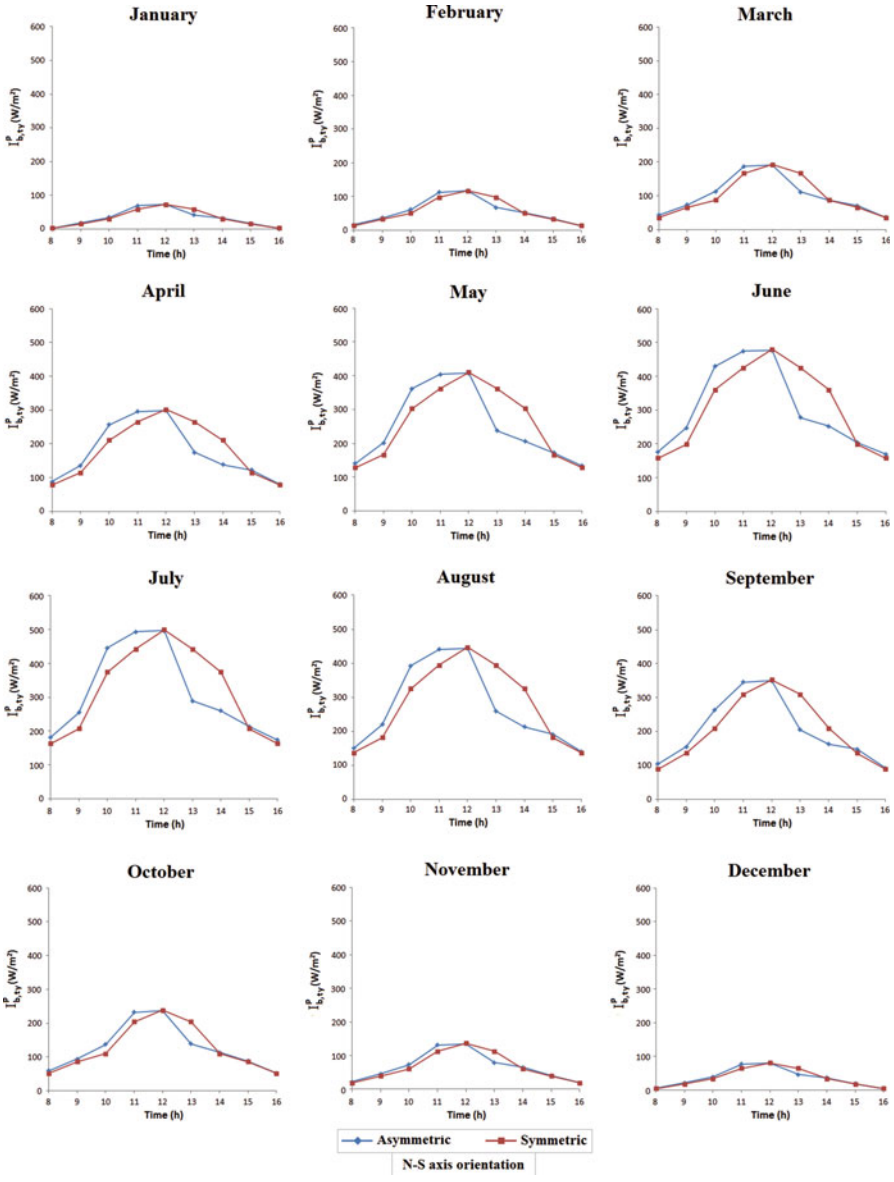

Fig. 46.7 Beam solar irradiation delivered on the absorber in each setup for the N-S axis orientation

Table 46.2 Daily and yearly beam solar irradiation delivered on the receiver for the E-W and the N-S axis orientation

	$H^{p}_{b,ty}$ (kWh/m^2/day)				
	East-west axis orientation			North-south axis orientation	
Month	Asymmetric	Symmetric	Symmetric in slope	Asymmetric	Symmetric
January	0.30	0.26	0.29	0.28	0.28
February	0.47	0.42	0.44	0.49	0.49
March	0.83	0.67	1.01	0.87	0.87
April	1.91	1.61	1.74	1.51	1.56
May	2.64	2.38	2.44	2.13	2.2
June	3.07	2.84	2.96	2.53	2.6
July	3.25	2.95	3.04	2.63	2.71
August	2.91	2.53	2.67	2.31	2.39
September	1.95	1.54	2.00	1.73	1.75
October	1.04	0.89	0.94	1.1	1.09
November	0.59	0.53	0.58	0.59	0.58
December	0.35	0.30	0.34	0.33	0.32
$Y^{p}_{b,ty}$ **(kWh/m^2/year)**	589.68	516.74	563.35	503.67	514.08

46.6 Conclusions

In this paper, three different reflector's scenarios, one asymmetric and two symmetric, were investigated through CFD analysis, under the same operating conditions in the city of Athens, in order to find the optimum among them. Also, except the reflector's design, the position of it opposite to the sun was examined too.

Firstly, the asymmetric reflector was compared with the horizontal and the inclined symmetric configurations for the E-W axis orientation. The results showed a clear prevalence of the first which was found to exceed the other two about 14.1% and 4.7%, respectively, while the inclined symmetric beats the horizontal one by 9.1%.

Secondly, the N-S axis orientation case where the horizontal symmetric concentrator antagonizes the asymmetric one was examined. The outcome of the specific case indicated the symmetric reflector as the best choice since it appeared 2% better optical performance compared to the asymmetric one.

Thirdly, considering the daily energy is delivered on the absorber, the N-S axis orientation exceeds the E-W one at 3 and 7 months regarding the asymmetric and the symmetric reflector, respectively, while the yearly operation of the symmetric setup seems to be independent from the orientation.

Generally, the yearly beam radiation delivered on the absorber appears its minimum values in the case of the N-S axis orientation while maximizes itself in

the asymmetric configuration for the E-W orientation. Hence, the asymmetric reflector is, finally, determined as the best choice among the three examined configurations as far as the optical performance is concerned, while the collectors' optimum orientation is the E-W one.

Nomenclature

General Parameters

G_{sc}	Solar constant (W/m^2)
H	Daily solar irradiation (kWh/m^2/day)
I	Hourly solar irradiation (kWh/m^2/h)
k_t	Hourly clearness index (−)
K_T	Daily clearness index (−)
n	Day of the year (−)
Y	Yearly solar irradiation (kWh/m^2/year)

Greek Letters

δ	Declination (^{o})
φ	Latitude (^{o})
ω	Hour angle (^{o})
ω_s	Sunset hour angle (^{o})

Superscripts

h	Horizontal surface
p	Absorber surface

Subscripts

b	Beam
d	Diffusive
o	Extraterrestrial
ty	Typical conditions

References

1. Korres D, Tzivanidis C (2016) Thermal analysis of an entire flat plate collector with a serpentine flow system and determination of the water and air flow and convection regime, ECOS 2016: proceedings of 29th international conference on efficiency, cost, optimization, simulation, and environmental impact of energy systems, Portoroz, Slovenia
2. Korres D, Tzivanidis C (2017) A new mini-CPC under thermal and optical investigation, Renewable Energy, article in press, https://doi.org/10.1016/j.renene.2017.06.054
3. Korres D, Tzivanidis C (2016) Optical and thermal analysis of a new U-type evacuated tube collector with a mini-compound parabolic concentrator and a cylindrical absorber, ECOS 2016: proceedings of 29th international conference on efficiency, cost, optimization, simulation, and environmental impact of energy systems, Portoroz, Slovenia
4. Korres D, Tzivanidis C, Alexopoulos J, Mitsopoulos G (2016) Thermal and optical investigation of a U-type evacuated tube collector with a mini-compound parabolic concentrator and a

flat absorber, IC-SCCE 2016: proceedings of 7th international conference from scientific computing to computational engineering, Athens, Greece
5. Bellos E, Korres D, Tzivanidis C, Antonopoulos KA (2016) Design, simulation and optimization of a compound parabolic collector. Sustainable Energy Technologies and Assessments 20:53–63
6. Tzivanidis C, Bellos E, Korres D, Antonopoulos KA, Mitsopoulos G (2015) Thermal and optical efficiency investigation of a parabolic trough collector. Case Studies in Thermal Engineering 6:226–237
7. Tsai C-Y, Lin PD (2012) Optimized variable focus parabolic trough reflector for solar thermal concentrator system. Solar Energy 86:1164–1172
8. Cheng ZD, He YL, Cui FQ, Du BC, Zheng ZJ, Xu Y (2014) Comparative and sensitive analysis for parabolic trough solar collectors with a detailed Monte Carlo ray-tracing optical model. Applied Energy 115:559–572
9. Cheng ZD, He YL, Cui FQ (2013) A new modelling method and unified code with MCRT for concentrating solar collectors and its applications. Applied Energy 101:686–698
10. Souliotis M, Quinlan P, Smyth M, Tripanagnostopoulos Y, Zacharopoulos A, Ramirez M, Yianoullis P (2011) Heat retaining integrated collector storage solar water heater with asymmetric CPC reflector. Solar Energy 85:2474–2487
11. Kessentini H, Bouden C (2013) Numerical and experimental study of an integrated solar collector with CPC reflectors. Renewable Energy 57:577–586
12. Adsten M, Helgesson A, Karlsson B (2005) Evaluation of CPC-collector designs for stand-alone, roof or wall installation. Solar Energy 79:638–647
13. Bellos E, Tzivanidis C, Antonopoulos KA (2016) Optical performance and optimization of two stationary compound parabolic collectors (CPC), MHMT'16: proceedings of the world congress on momentum, heat and mass transfer, Prague, Czech Republic
14. Duffie J, Beckmann W (2013) Solar engineering of thermal processes, 4th edn. Wiley, New York
15. Kouremenos DA, Antonopoulos KA, Domazakis ES (1985) Solar radiation correlations for the Athens. Solar Energy 35(3):259–269

Chapter 47
Simulation and Optimization of a Mini Compound Parabolic Collector with a Coaxial Flow System

Dimitrios N. Korres and Christos Tzivanidis

47.1 Introduction

The increasing need for renewable energy sources brinks solar thermal systems at the global foreground by setting them as the main representative of such energy sources. Many different kinds of solar thermal collectors have been set under investigation most of which are the flat plate, the parabolic trough, the compound parabolic, and the evacuated tube collectors (FPCs, PTCs, CPCs, and ETCs).

Korres and Tzivanidis [1] investigated the operation of a flat plate collector with a serpentine flow system through CFD analysis, and they found how the slope of the collector affects the convection inside the gap and as a consequence the thermal performance of the collector. The effects of the plate to cover spacing and the inclination angle at the efficiency of a flat plate collector have been studied from Cooper [2] while an innovative method for calculating the air function inside the gap space of an FPC was applied by Bellos et al. [3]. Subiantoro and Tiow [4] presented analytical models for the top heat losses of an FPC and compared them to CFD analysis conducted with ANSYS.

There are, also, few studies in the subject of compound parabolic and parabolic trough technology. For instance, a mini-compound parabolic collector with a circular absorber and an optically optimized reflector was examined by Korres and Tzivanidis [5, 6], while Korres et al. [7] studied the thermal and the optical performance of a similar collector with a flat receiver. Li et al. [8] compared the thermal efficiency of two different CPCs and concluded that the collector with the lower concentration ratio performs better at high efficiency range while a new flat stationary evacuated CPC was developed and analyzed by Buttinger et al. [9]. Moreover, Antonelli et al. [10] examined the performance of two different CPCs with a

D. N. Korres (✉) · C. Tzivanidis
Mechanical Engineering Department, National Technical University of Athens, Athens, Greece

S. Nižetić, A. Papadopoulos (eds.), *The Role of Exergy in Energy and the Environment*, Green Energy and Technology,
https://doi.org/10.1007/978-3-319-89845-2_47

circular and a flat absorber and found that the first configuration gives greater thermal efficiency in a wide operating range especially at high temperatures. PTCs have, also, been tested by many researchers as far as their thermal and optical performance as well as the heat transfer fluid effect is concerned (Wang et al. [11], Tzivanidis et al. [12]).

The ETC technology is of particular interest since it provides negligible thermal losses, and hence, we can achieve greater thermal performances. There are various different piping systems which could be applied on an ETC the main of which are the heat pipe, the U-pipe, and the coaxial flow configuration. Ayompe and Duffy [13] made a thermal performance analysis of a heat pipe evacuated tube system while Zheng et al. [14] studied on how the emissivity of the back receiver's surface influences the heat losses of a heat pipe application. The U-pipe system has, also, been investigated by Kim and Seo [15] and Pei et al. [16]. Gao et al. [17] put forward a mathematical model so as to describe the thermal behavior of a U-pipe evacuated tube collector, while Liangdong Ma et al. [18] conducted a thermal investigation on a U-type evacuated tube application by analytical method.

As far as the coaxial flow system is concerned, there are not many studies conducted in that field. For instance, Kim et al. [19] evaluated analytically the thermal performance of such a system while Glembin et al. [20] analyzed the impact of the internal thermal coupling between the fluid in the annuli and the fluid in the inner tube of a counter flow ETC on the temperature profile and the thermal efficiency. Zhang et al. [21] examined the performance of a direct flow coaxial evacuated tube collector with and without a heat shield and found that the collector performs better with the shield, while Ataee and Ameri [22] conducted an energy and exergy analysis of a similar collector. Finally, Han et al. [23] used a three-dimensional analytical model to investigate the thermal performance of an all-glass ETC with a coaxial flow conduit.

The aim of this work is to add a different prospect in the field of the coaxial flow ETC analysis through the investigation of the thermal performance and the convection regime of a coaxial flow ETC with a mini-CPC reflector in several operating conditions.

47.2 Collector's Geometry and Data

A coaxial flow evacuated tube collector with a mini-compound parabolic concentrator was designed and simulated in SolidWorks. The geometry and the main dimensions of the collector are depicted on Fig. 47.1.

As Fig. 47.1 suggests, the working medium enters the collector through the inner tube and leaves it via the annulus passage which is formed between the last one and the receiver, while vacuum regime prevails at the interior of the glass tube.

The reflector's geometry is of considerable interest since it optimally cooperates with the absorber tube. More specifically, the focuses and the focal distances of the reflector have not been designed by chance, but the first were deliberately located on

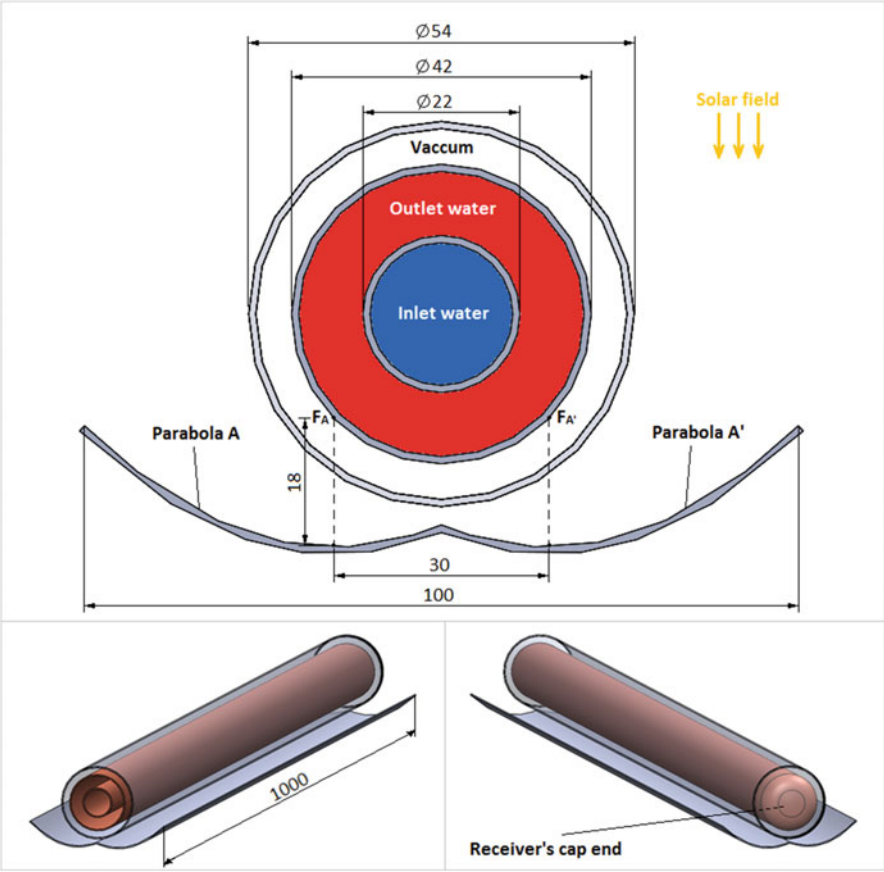

Fig. 47.1 Coaxial evacuated tube collector with a mini-CPC concentrator

Table 47.1 Thermal and optical properties

Component	Material	Thermal properties	Optical properties
Reflector	Aluminum	–	$\rho = 1$
Glass tube	Glass	$\varepsilon_g = 0.88$	$\tau = 1$
Outer tube	Copper	$\varepsilon_p = 0.1$	$\alpha = 0.8$
Inner tube	Copper	–	–

the receiver, while the second were considered to be perpendicular to the aperture plane. This design makes all the perpendicular to the aperture incident solar rays end up on the absorber.

The main characteristics and properties of each component are given bellow in Table 47.1.

Table 47.2 Operating conditions of the collector

Variable	Value	Units
Environment temperature	10	°C
Inlet water temperature range	10–100	°C
Water mass flow rate	0.004	kg/s
Wind heat transfer coefficient	10	$W/m^2/K$
Global irradiance	1000	W/m^2

The cover's transmittance and the reflectance of the concentrator take the unit value because we have set all the optical losses on the receiver's outer surface. Hence, the value of 0.8 on the above table does not represent only the absorptance of the receiver tube but also includes the mirror and the glass optical losses. The thickness of all the components is 1 mm.

47.3 Analysis

At this chapter the operating conditions under which our collector is examined are described. Also, the methodology we are going to use so as to analyze the thermal behavior of the collector and to determine the efficiency and the convection regime inside the coaxial conduit is presented.

The collector was tested in ten different inlet water temperatures (T_i) considering that the global irradiance (G_T) is constant and perpendicular to the aperture plane. The operating conditions are given in Table 47.2.

47.3.1 Energy Balance

In Fig. 47.2 a detailed view of the coaxial flow tube and the conditions that prevail in there are depicted while the symbolization we are going to use in our analysis is given too.

Tube energy balance

$$Q_{u,t} = \dot{m} \cdot C_p \cdot (T_{o,t} - T_i) = h_{f,1} \cdot A_{s,1} \cdot (T_{s,1} - T_{f,t}), \tag{47.1}$$

Cap end energy balance

$$Q_{u,cap} = \dot{m} \cdot C_p \cdot (T_{i,an} - T_{o,t}), \tag{47.2}$$

Annuli energy balance

$$Q_{u,an} = \dot{m} \cdot C_p \cdot (T_o - T_{i,an}) = h_{f,2} \cdot A_{s,2} \cdot (T_{s,2} - T_{f,an}) - Q_{u,t}, \tag{47.3}$$

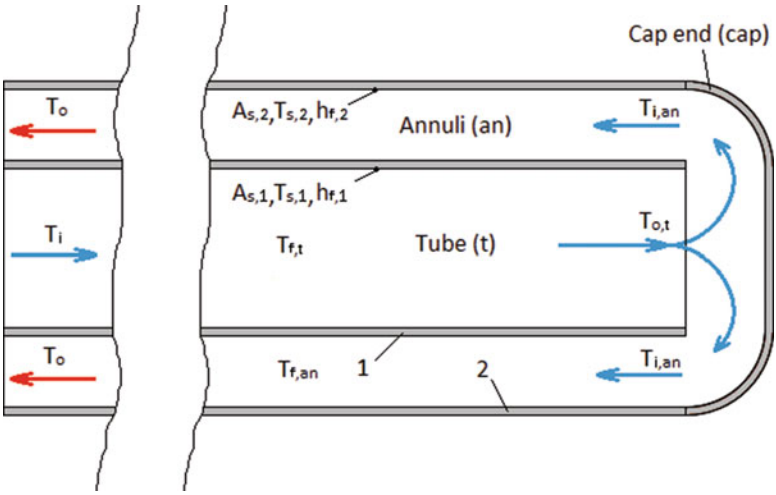

Fig. 47.2 Coaxial flow tube

Total energy balance

$$Q_{\mathrm{u,tot}} = \dot{m} \cdot C_{\mathrm{p}} \cdot (T_{\mathrm{o}} - T_{\mathrm{i}}) = Q_{\mathrm{u,an}} + Q_{\mathrm{u,t}} + Q_{\mathrm{u,cap}}, \tag{47.4}$$

Overall heat losses

$$Q_{\mathrm{L}} = \left[h_{\mathrm{w}} \cdot \left(T_{\mathrm{g}} - T_{\alpha}\right) + \varepsilon_{\mathrm{g}} \cdot \sigma \cdot \left(T_{\mathrm{g}}^4 - T_{\alpha}^4\right)\right] \cdot A_{\mathrm{g,o}} = \frac{A_{\mathrm{p}} \cdot \sigma \cdot \left(T_{\mathrm{p}}^4 - T_{\mathrm{g}}^4\right)}{\frac{1}{\varepsilon_{\mathrm{p}}} + \frac{1-\varepsilon_{\mathrm{g}}}{\varepsilon_{\mathrm{g}}} \cdot \frac{D_{\mathrm{p,o}}}{D_{\mathrm{g,i}}}}, \tag{47.5}$$

Overall heat loss coefficient

$$U_{\mathrm{L}} = \frac{Q_{\mathrm{L}}}{T_{\mathrm{p}} - T_{\mathrm{a}}} \cdot \frac{1}{A_{\mathrm{p}}}, \tag{47.6}$$

Thermal efficiency

$$\eta = \frac{Q_{\mathrm{u,tot}}}{A_{\mathrm{a}} \cdot G_{\mathrm{T}}}, \tag{47.7}$$

Equations (47.1, 47.2, and 47.3) express the useful energy which is conveyed on the water in each specific region of the counter flow conduit, while Eq. (47.4) gives the total water heat gain from the inlet to the outlet of the collector. The overall heat losses, the losses coefficient, and the thermal performance of the system appear on Eqs. 47.5, 47.6, and 47.7, respectively. T_{α}, T_{p}, and T_{g} express the temperatures of the ambient, the absorber, and the glass, respectively.

We have to state that in the specific simulation tool, the bodies which do not have any radiative specification are considered as gray bodies, while thermal radiation emittance is diffusive by default. The second part of Eq. (47.5) holds for such conditions between two long coaxial cylinders (Bergman et al. [24]), so why we used it to calculate the overall heat losses. In addition, the flow inside the tube was considered as laminar due to the low velocity fields.

47.3.2 Efficiency and Losses of the Collector

Figure 47.3 that follows gives the thermal performance of the collector, and the useful energy is conveyed on the heat transfer fluid desperately for each of the three areas of the coaxial tube as a function of the inlet water temperature.

As we can see from Fig. 47.3b, the useful power the water gains at the tube region (Q_{u_tube}) is getting greater as the inlet temperature increases in contrast to the power in the cap (Q_{u_cap}) and the annuli region (Q_{u_annuli}). This happens because the difference between the power that passes from the outer tube to the working medium and the annuli useful power become greater as T_i increases. From Fig. 47.3a we observe that the efficiency reduces itself as the inlet water temperature takes greater values. This reduction seems to be quite gently due to the absence of convection inside the glass tube and happens because of the fact that the overall heat losses become greater with T_i as this is depicted in Fig. 47.4.

The main reason that causes this increment in the collector's thermal losses is the receiver's temperature increase which reasonably takes place since the thermal level of the inlet water increases too.

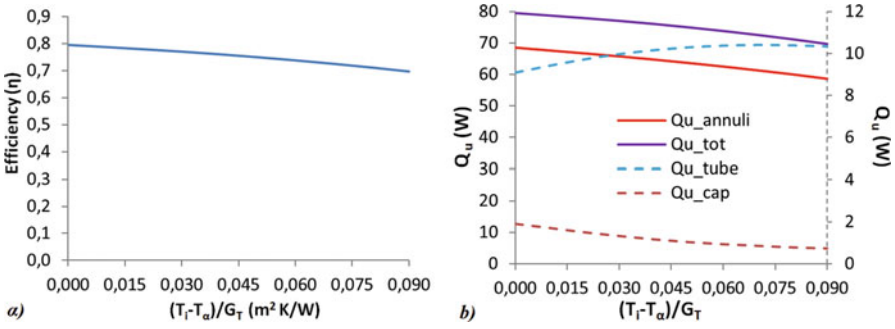

Fig. 47.3 (**a**) Thermal efficiency and (**b**) useful power the water gains totally and separately in each region

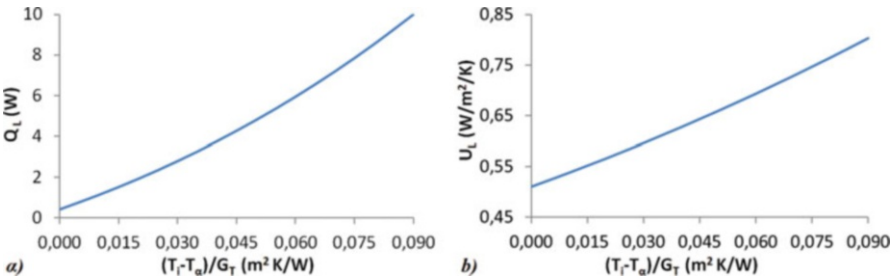

Fig. 47.4 (**a**) Overall heat losses and (**b**) overall heat loss coefficient

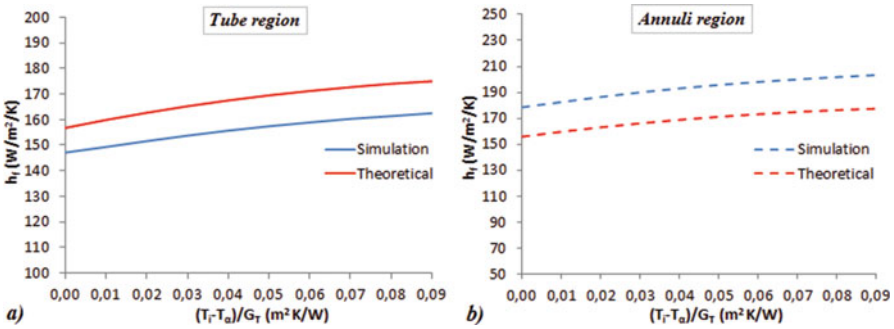

Fig. 47.5 Convective heat transfer coefficient (**a**) in the tube and (**b**) in the annuli

47.3.3 Convection Regime Inside the Coaxial Tube

Here we will determine two different heat transfer coefficients inside the tube. In particular, we are going to calculate the heat transfer coefficient at the inner side of the inner tube and the one at the outer tube (Fig. 47.5). For this calculation, Eqs. 47.1 and 47.3 were solved as below:

$$h_{\mathrm{f},1} = \frac{Q_{\mathrm{u,t}}}{A_{\mathrm{s},1} \cdot (T_{\mathrm{s},1} - T_{\mathrm{f,t}})}, \tag{47.8}$$

$$h_{\mathrm{f},2} = \frac{Q_{\mathrm{u,an}} + Q_{\mathrm{u,t}}}{A_{\mathrm{s},2} \cdot (T_{\mathrm{s},2} - T_{\mathrm{f,an}})} = \frac{Q_{\mathrm{u,tot}} - Q_{\mathrm{u,cap}}}{A_{\mathrm{s},2} \cdot (T_{\mathrm{s},2} - T_{\mathrm{f,an}})}, \tag{47.9}$$

We, also, validated the specific coefficients through two models of the heat transfer theory. In the tube region, we used the theoretical approach that considers constant surface temperature since the temperature of the inner tube does not change significantly along the flow, while for the annuli area, we considered constant heat

flux conditions since the outer tube is exposed on a constant solar field. These models are described on Eqs. 47.10 and 47.11 that follow:

Tube region

$$h_{f\_T=\mathrm{ct}} = \left(3.66 + \frac{0.0668 \cdot Re_{D_{1,i}} \cdot Pr \cdot D_{1,i}/L_t}{1 + 0.04 \cdot \left(Re_{D_{1,i}} \cdot Pr \cdot D_{1,i}/L_t\right)^{2/3}}\right) \cdot \frac{k_f}{D_{1,i}} \tag{47.10}$$

Annuli region

$$h_{f\_H=\mathrm{ct}} = \left(4.364 + \frac{0.036 \cdot Re_{D_{h,an}} \cdot Pr \cdot D_{h,an}/L_t}{1 + 0.0011 \cdot Re_{D_{h,an}} \cdot Pr \cdot D_{h,an}/L_t}\right) \cdot \frac{k_f}{D_{h,an}} \tag{47.11}$$

where $D_{h,an} = D_{2,i} - D_{1,o}$

The values of *Re* and *Pr* were taken for the mean water temperature of each region (from simulation).

It is obvious that the two theoretical curves approach sufficiently the simulation curves. Particularly, there is a mean declination of about 12.6% for the coefficient in the outer tube and 7.5% for the respective at the inner tube. Generally, the convective coefficient increases with T_i because of the thermal conductivity increment.

47.4 Inner Tube Effect

In the specific paragraph, the inner tube's diameter effect on the useful output of the collector is investigated. More specifically, we are going to apply seven different inner diameters of the inner tube (5, 10, 15, 20, 25, 30, and 35 mm) and make a comparison among them in order to determine the best choice. We should mention that for the particular investigation, we removed the glass tube and considered that the outer tube is exposed directly on the environment conditions Table 47.2 suggests. This was done because the examined modifications do not affect significantly the evacuated configuration. Next, a comprehensive table (Table 47.3) which

Table 47.3 Collector's performance and maximum possible efficiency increase dependent on the inner tube diameter and the inlet water temperature

η (%)		$D_{1,i}$ (m)							$\delta\eta_{max}$ (%)
		0.005	0.010	0.015	0.020	0.025	0.030	0.035	
T_i (°C)	10	70.81	70.86	71.51	72.22	72.99	73.84	74.83	5.7
	20	58.19	58.36	58.99	59.43	60.14	60.93	61.70	6.0
	30	45.52	45.84	46.37	46.88	47.37	47.89	48.44	6.4
	40	32.99	33.36	33.79	33.83	34.34	34.93	35.30	7.0
	50	20.39	20.71	20.97	21.21	21.42	21.66	21.87	7.2

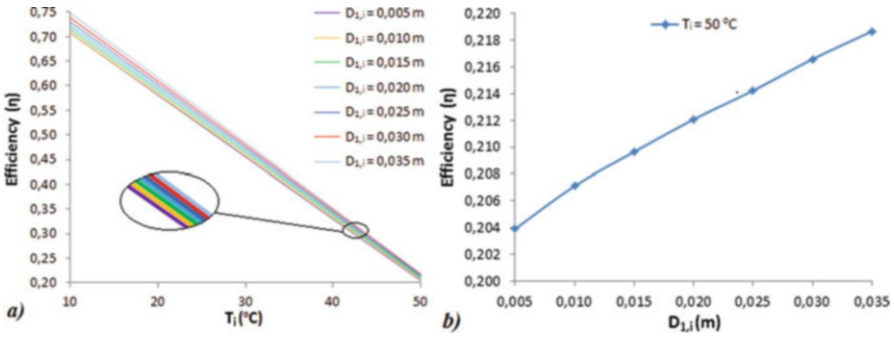

Fig. 47.6 Efficiency of the collector dependent on (**a**) $D_{1,i}$ and T_i and (**b**) $D_{1,i}$ for $T_i = 50\ ^\circ C$

presents the collector's efficiency and the maximum possible increase of it in each examined case is given.

As we can see from Table 47.3, the collector's efficiency increases as the inner tube approaches the outer one while decreases with T_i because the overall heat losses become greater. The maximum possible performance increment is presented in the last column of Table 47.3 and expresses how much could the efficiency of the collector increase going directly from the worst to the best diameter scenario. So, according to Table 47.3, we have a significant change on the efficiency for all the examined inlet water temperatures by changing the inner tube's inner diameter value from 5 mm to 35 mm. A briefly depiction of the above table is presented bellow on Fig. 47.6 in order to get a more clear view of the problem.

47.5 Allocations and Diagrams

In this chapter a global overview of the collector's thermal behavior is provided via several diagrams and allocations. Figure 47.7 shows the peripheral absorber's temperature and the coaxial tubes' temperature distribution.

As we can observe from Fig. 47.7a, the temperature of the receiver takes its highest values directly at the reflector's parabolas' focal points something that indicates the sufficiency of the simulation.

The receiver's temperature field, on Fig. 47.7b, is depicted as we expected since the temperature increases along the flow. The inner tube seems to follow the receiver's temperature fields something that happens because of the internal thermal coupling between the water and the tubes.

In Fig. 47.8 the bulk average water temperature from the inlet to the outlet of the collector for $T_i = 50\ ^\circ C$ and the temperature of the water, the cover, and the glass for each operating point are presented.

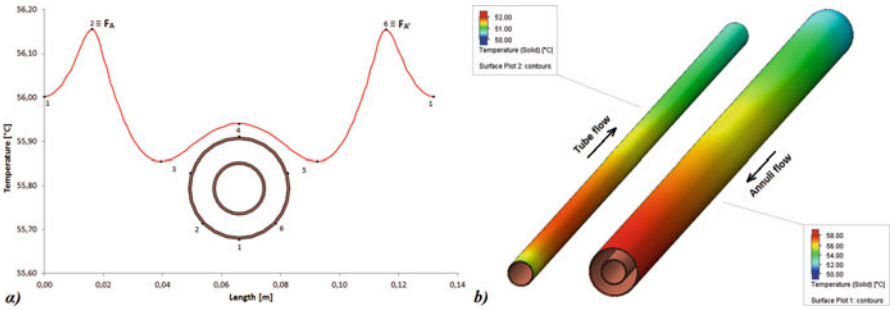

Fig. 47.7 (**a**) Peripheral absorber's temperature and (**b**) delivery and receiver tube wall temperature distribution for $T_i = 50$ °C

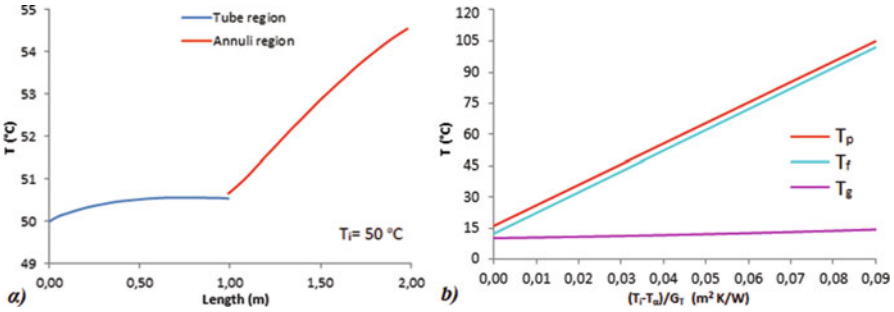

Fig. 47.8 (**a**) Bulk average water temperature along the flow for $T_i = 50$ °C; (**b**) water, receiver, and glass temperatures

It is obvious that the water temperature increases slightly on the tube region and rapidly on the annuli one since the last one is exposed on the solar heat flux through the outer tube. Regarding Fig. 47.8b the cover temperature is very low compared to the rest temperatures while the divergence between receiver and water temperature is kept almost constant as T_i increases. These two phenomena have to do with the absence of convection at the interior of the glass tube which leads to the elimination of the thermal losses.

The velocity fields are of considerable interest due to the complexity of the flow regime inside the coaxial tube (Fig. 47.9).

The allocations of Fig. 47.9a give a clue about how the flow takes place at the inner tube outfall region. More specifically, as the water exits the inner tube and goes to the annuli, vortices are developed due to the abrupt direction change, something that is depicted clearly at Fig. 47.9b. These vortices seem to behave as a solid body since extremely low velocity fields prevail in them. Hence, Fig. 47.9 gives us an idea on how the main stream of the water is formed by taking into consideration the vortex regime which is an obstacle for the main flow.

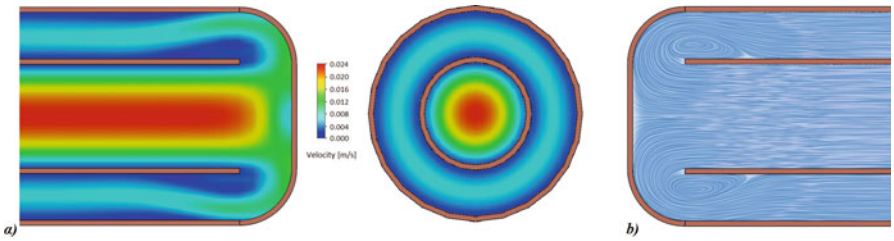

Fig. 47.9 (**a**) Velocity fields inside the coaxial tube for $T_i = 50$ °C; (**b**) flow streamlines

47.6 Concluding Remarks

In the specific investigation, a coaxial flow ETC with a mini-CPC reflector was examined at several different operating conditions. The thermal performance was determined and found to decrease with the inlet water temperature rise, due to the increment of the overall heat losses. The heat transfer coefficients inside the inner tube and the annuli were both calculated and validated by two theoretical heat transfer models. Particularly, the two respective coefficients diverge from the theoretical values 7.5% and 12.6%, respectively.

In an attempt to examine how the distance between the inner and the outer tube affects the collector's performance, we conducted a relative investigation considering absence of the glass tube. The results were unexpectedly interesting since significant changes in the thermal efficiency were taken place by modifying this diameters' distance. In particular, the thermal performance increases as the inner tube comes closer to the outer one, while this increment becomes greater as the inlet water temperature increases. Specifically, we could have up to 7.2% increment at the thermal performance of the coaxial tube. Hence, the most optimal solution that could provide with high thermal performances that kind of collectors is to bring the coaxial tubes close to each other.

Nomenclature

General Parameters

A	Area (m^2)
C_p	Specific heat (kJ/kg/K)
D	Diameter (m)
G_T	Global irradiance (W/m^2)
h	Convective coefficient ($W/m^2/K$)
k	Thermal conductivity (W/m/K)
L	Length (m)
$\dot{m}$	Mass flow rate (kg/s)
Pr	Prandtl number (−)
Q	Heat flux (W)

Re	Reynolds number (−)
T	Temperature (°C)
U	Thermal transmittance (W/m^2/K)

Greek Letters

α	Absorptance (−)
ε	Emittance (−)
η	Thermal efficiency (−)
ρ	Reflectance (−)
σ	Boltzmann constant (W/m^2/K^4)
τ	Transmittance (−)

Subscripts

a	Aperture
α	Environment
an	Annuli
cap	Cap end
f	Water
g	Glass
h	Hydraulic
i	Inlet/inner
L	Overall heat losses
o	Outlet/outer
p	Receiver
s	Walls
t	Tube
tot	Total
u	Useful
w	Wind
1	Inner tube
2	Outer tube without the cap end

References

1. Korres D, Tzivanidis C (2016) Thermal analysis of an entire flat plate collector with a serpentine flow system and determination of the water and air flow and convection regime. In: ECOS 2016: Proceedings of 29th international conference on efficiency, cost, optimization, simulation, and environmental impact of energy systems, Portoroz, Slovenia
2. Cooper PI (1981) The effect of inclination on the heat loss from flat-plate solar collectors. Solar Energy 27:413–420
3. Bellos E, Tzivanidis C, Korres D, Antonopoulos KA (2015) Thermal analysis of a flat plate collector with Solidworks and determination of convection heat coefficient between water and absorber. In: ECOS 2016: Proceedings of 28th international conference on efficiency, cost, optimization, simulation, and environmental impact of energy systems, Pau, France
4. Subiantoro A, Tiow OK (2013) Analytical models for the computation and optimization of single and double glazing flat plate solar collectors with normal and small air gap spacing. Applied Energy 104:392–399

5. Korres D, Tzivanidis C (2017) A new mini-CPC under thermal and optical investigation, IC-SCCE 2016: Renewable Energy, article in press
6. Korres D, Tzivanidis C (2016) Optical and thermal analysis of a new U-type evacuated tube collector with a mini-compound parabolic concentrator and a cylindrical absorber. In: ECOS 2016: Proceedings of 29th international conference on efficiency, cost, optimization, simulation, and environmental impact of energy systems, Portoroz, Slovenia
7. Korres D, Tzivanidis C, Alexopoulos J, Mitsopoulos G (2016) Thermal and optical investigation of a U-type evacuated tube collector with a mini-compound parabolic concentrator and a flat absorber. In: IC-SCCE 2016: Proceedings of 7th international conference from scientific computing to computational engineering, Athens, Greece
8. Li X, Dai YJ, Li Y, Wang RZ (2013) Comparative study on two novel intermediate temperature CPC solar collectors with the U-shape evacuated tubular absorber. Solar Energy 93:220–234
9. Buttinger F, Beikircher T, Pröll M, Schölkopf W (2010) Development of a new flat stationary evacuated CPC-collector for process heat applications. Solar Energy 84:1166–1174
10. Antonelli M, Francesconi M, Di Marco P, Desideri U (2016) Analysis of heat transfer in different CPC solar collectors: a CFD approach. Applied Thermal Engineering 101:479–489
11. Wang Y, Liu Q, Lei J, Jin J (2014) A three-dimensional simulation of a parabolic trough solar collector system using molten salt as heat transfer fluid. Applied Thermal Engineering 70:464–476
12. Tzivanidis C, Bellos E, Korres D, Antonopoulos KA, Mitsopoulos G (2015) Thermal and optical efficiency investigation of a parabolic trough collector. Case Studies in Thermal Engineering 6:226–237
13. Ayompe LM, Duffy A (2013) Thermal performance analysis of a solar water heating system with heat pipe evacuated tube collector using data from a field trial. Solar Energy 90:17–28
14. Zheng H, Xiong J, Su Y, Zhang H (2014) Influence of the receiver's back surface radiative characteristics on the performance of a heat-pipe evacuated-tube solar collector. Applied Energy 116:159–166
15. Kim Y, Seo T (2007) Thermal performances comparisons of the glass evacuated tube solar collectors with shapes of absorber tube. Renewable Energy 32:772–795
16. Pei G, Li G, Zhou X, Ji J, Su Y (2012) Comparative experimental analysis of the thermal performance of evacuated tube solar water heater systems with and without a mini-compound parabolic concentrating (CPC) reflector(C=LT(1)). Energies:911–924
17. Gao Y, Fan R, Zhang XY, AN YJ, Wang MX, Gao YK, Yua Y (2014) Thermal performance and parameter analysis of a U-pipe evacuated solar tube collector. Solar Energy 107:714–727
18. Ma L, Lu Z, Zhang J, Liang R (2010) Thermal performance analysis of the glass evacuated tube solar collector with U-tube. Building and Environment 45:1959–1967
19. Kim JT, Ahn HT, Han H, Kim HT, Chun W (2007) The performance simulation of all-glass vacuum tubes with coaxial fluid conduit. Heat and mass transfer 34:587–597
20. Glembin J, Rockendorf G, ScheurenInternal J (2010) Internal thermal coupling in direct-flow coaxial vacuum tube collectors. Solar Energy 84:1137–1146
21. Zhang X, You S, Ge H, Gao Y, Xu W, Wangb M, He T, Zheng X (2014) Thermal performance of direct-flow coaxial evacuated-tube solar collectors with and without a heat shield. Energy Conversion and Management 84:80–87
22. Ataee S, Ameri M (2015) Energy and exergy analysis of all-glass evacuated solar collector tubes with coaxial fluid conduit. Solar Energy 118:575–591
23. Han H, Kim JT, Ahn HT, Lee SJ (2008) A three-dimensional performance analysis of all-glass vacuum tube with coaxial fluid conduit. Heat and mass transfer 35:589–596
24. Bergman TL, Lavine AS, Incropera FP, Dewitt DP (2011) Fundamentals of heat and mass transfer, 7th edn. John Wiley & Sons Inc, (2011)

Chapter 48
Exergetic Optimization of a Parabolic Trough Solar Collector

Ceyda Gunay, Anil Erdogan, and C. Ozgur Colpan

48.1 Introduction

Parabolic trough solar collectors (PTSCs) are one of the most promising technologies among the different types of solar collectors (e.g., flat plate, evacuated tube, solar dishes) [1]. PTSCs are widely used in many engineering applications such as heating buildings, hybridization with geothermal power plants, and other types of energy systems. The first usage of PTSC in power plant was in 1984 in California [2]. Since then, its usage in power plants has increased significantly. The schematics of the PTSC and its components are shown in Fig. 48.1. As can be seen in this figure, the collector is made of a reflective material sheet which has a form of parabola. The receiver is a metal tube, which is surrounded by a glass cover. Glass cover reduces the heat losses. Collector performance is significantly affected by reflectivity, absorptivity, operating conditions of the heat transfer fluid, tracking mechanism, and so on [3].

There are several studies on the modeling of PTSCs. Manikandan et al. [4] conducted a thermal model for PTSC and obtained the thermal performance of the PTSC. In addition, a parametric study was conducted using the following parameters: mass flow rate, concentration ratio, heat transfer fluid (HTF), heat removal factor, and the solar radiation. The results of this study showed that when the inlet temperature of PTSC fluid increases, the efficiency of the collector decreases for various mass flow rates and different HTF. In addition, when collector temperature increases, radiation losses increase. Qu et al. [5] programed a single dimensional model by using EES and considered the effect of solar intensity, incident angle,

C. Gunay (✉) · A. Erdogan
Dokuz Eylul University, The Graduate School of Natural and Applied Sciences, Buca, Izmir

C. Ozgur Colpan
Dokuz Eylul University, Faculty of Engineering, Department of Mechanical Engineering, Buca, Izmir

S. Nižetić, A. Papadopoulos (eds.), *The Role of Exergy in Energy and the Environment*, Green Energy and Technology,
https://doi.org/10.1007/978-3-319-89845-2_48

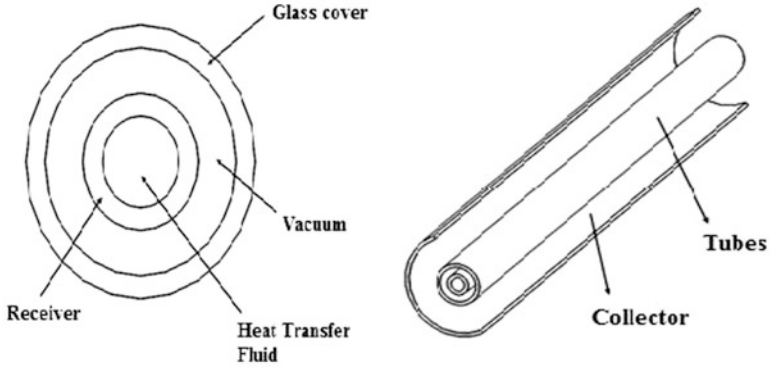

Fig. 48.1 The schematics of PTSC and its layers

collector dimensions, and fluid properties on the performance of the PTSC. The model is validated by the experimental data. After that, the model is used to improve PTSC design and to optimize system operation. Yılmaz and Söylemez [6] developed solar, optical, and thermal models by differential and non-algebraic correlations. Differential equations were solved simultaneously using EES. The developed model was compared to the experimental data. The results showed that the optical loss is the most effective parameter on the collector efficiency. From a theoretical viewpoint, the best suggestion to reduce the heat loss was given as vacuuming the annulus. However, when the vacuuming is used, maintenance is more difficult. As a result of this study, using less-conductive fluid to decrease heat losses through the annulus was recommended. The required pumping power increases when mass flow rate increases; hence, for more efficient PTSC, the optimal range of mass flow rate should be considered. Padilla et al. [7] developed a one-dimensional numerical heat transfer model of a PTSC. To analyze the receiver and glass envelope by using mass and energy balances, both of these components were divided into segments. Their numerical model compared well with experimental data. Kalogirou [8] proposed a thermal model of the PTSC and solved it using EES. This model was compared with the known performance of existing collectors, which were tested in Sandia National Laboratories. Finally, the model is used for installation of the collector at the Archimedes Solar Energy Laboratory of the Cyprus University of Technology. Conrado et al. [9] presented a review of thermal and mathematical models for components of PTSC. Abbas et al. [1] developed a model using Monte Carlo ray-trace code to compare PTSCs and linear Fresnel collectors in terms of energy effectiveness and flux intensity map at the receiver for different days and orientations. Their results showed that the maximum efficiency is obtained from PTSCs when the linear Fresnel collectors have multitube receivers. In addition, NS orientation ensures higher efficiency for PTSCs, but orientation type has not affected the linear Fresnel collectors' efficiency.

Literature survey conducted shows that there is very limited study on the detailed optical and thermal models of PTSC and its optimization. In the first part of this

study, detailed thermal and optical models are first developed; then an exergy analysis is conducted; and finally parametric studies were conducted. The effect of some key design and operating parameters, which are the outer diameter of receiver, the aperture width, the wind speed, the type of heat transfer fluid, and the solar radiation, on the performance of the PTSC is assessed. The performance parameters are the outlet temperature of receiver and the exergetic efficiency of the PTSC. In the second part of this paper, an optimization study was carried out using Taguchi method to find the optimum design parameters that maximize the exergetic efficiency of the PTSC.

48.2 Modeling

In this section, modeling equations and approach for PTSCs are presented. The operating principles of PTSCs are as follows. When the solar rays reach the parabolic mirror, these rays are focused onto the receiver tube. The concentrated radiation heats the heat transfer fluid; in this way, the solar radiation transforms to useful energy. When the solar beams reach to the receiver from the mirror, optical and thermal losses are observed. These optical and thermal losses are calculated as discussed in the following subsections.

48.2.1 Optical Model

The aim of the optical model is to find the optical efficiency of the PTSC. Therefore, the heat absorbed by the receiver should be first found by using Eq. (48.1) [8].

$$S = G_b \cdot \eta_r \tag{48.1}$$

The optical efficiency for PTSC is given by Eq. (48.2).

$$\eta_r = \rho \cdot \gamma \cdot \tau \cdot \alpha \cdot ((1 - A_f \cdot \tan(\Theta)) \cdot \cos(\Theta)) \tag{48.2}$$

where A_f is geometric factor and is given in Eq. (48.3).

$$A_f = \frac{A_{loss}}{A_a} \tag{48.3}$$

The geometric factor is caused due to the shaded area of the PTSC. Total shaded area can be obtained from Eq. (48.4).

$$A_{loss} = \frac{2}{3} W_a \cdot h_p + f \cdot W_a \cdot \left[1 + \frac{{W_a}^2}{48 \cdot f^2}\right] \tag{48.4}$$

48.2.2 Thermal Model

Thermal losses should be first found to find the useful energy of PTSC. The loss coefficient, U_L, is used to estimate the thermal losses from the receiver. This loss coefficient is given in Eq. (48.5) [10].

$$U_L = h_w + h_r + h_c \tag{48.5}$$

where h_r, radiation loss, is given in Eq. (48.6).

$$h_r = 4\sigma\varepsilon T_r^3 \tag{48.6}$$

To find the wind loss coefficient, Nusselt correlations can be used and as shown below.

For $0.1 < Re < 1000$,

$$Nu = \frac{h_w}{D_g \cdot k} = 0.4 + 0.54(Re)^{0.52} \tag{48.7}$$

For $1000 < Re < 50{,}000$,

$$Nu = \frac{h_w}{D_g \cdot k} = 0.3(Re)^{0.6} \tag{48.8}$$

The convection losses from the receiver to air are negligible, when the space between the glass cover and the receiver is evacuated.

The loss coefficient can be estimated using Eq. (48.9).

$$U_L = \left[\frac{A_r}{(h_w + h_{r,c-a})A_c} + \frac{1}{h_{r,r-c}}\right]^{-1} \tag{48.9}$$

where $h_{r,\ c\ -\ a}$ is the radiation coefficient from cover to ambient which can be obtained from Eq. (48.10).

$$h_{r,c-a} = \varepsilon_g \cdot \sigma \cdot \left(T_g + T_a\right) \cdot \left(T_g^2 + T_a^2\right) \tag{48.10}$$

where $h_{r,\ r\ -\ c}$ is the radiation coefficient from the glass cover to the receiver which can be estimated by using Eq. (48.11).

$$h_{r,r-c} = \frac{\sigma(T_r + T_c)\left(T_r^2 + T_c^2\right)}{\frac{1}{\varepsilon_r} + \frac{A_r}{A_c}}\left(\frac{1}{\varepsilon_c} - 1\right) \tag{48.11}$$

T_c is required to solve the previous equations. When the radiation absorbed by the cover is ignored, Tc can be estimated by using Eq. (48.12).

Table 48.1 Correlations to calculate Nusselt number for the heat transfer fluid in the receiver [11]

Equations	Limitations
$\mathrm{Nu} = 4.36$	$\mathrm{Re} < 2300$
$\mathrm{Nu} = \dfrac{(f/8)\cdot(\mathrm{Re}-1000)\mathrm{Pr}}{1+1.27\cdot(f/8)^{1/2}\left(\mathrm{Pr}^{2/3}-1\right)}$	$\mathrm{Re} > 2300$
$f = [0.79\cdot\ \ln(\mathrm{Re}) - 1.64]^{-2}$	

$$T_c = \frac{A_r h_{r,r-c} T_r + A_g (h_{r.c-a} + h_w) T_a}{A_r h_{r,r-c} + A_g (h_{r.c-a} + h_w)} \tag{48.12}$$

The result obtained from this equation must be iterated until the accepted value is very close to it. The overall heat transfer coefficient, U_o, must be obtained to find collector efficiency factor and useful energy after this iteration by using Eq. (48.13).

$$U_o = \left(\frac{1}{U_L} + \frac{D_o}{h_{fi}\cdot D_i} + \frac{D_o \cdot \ln(D_o/D_i)}{2\cdot k}\right)^{-1} \tag{48.13}$$

where h_{fi} is convective heat transfer coefficient inside the receiver which can be obtained from Eq. (48.14).

$$\mathrm{Nu} = \frac{h_{fi} D_i}{k} \tag{48.14}$$

Nu given in Eq. (48.14) can be obtained from Table 48.1.

The collector efficiency is required to calculate the heat removal factor, which can be estimated using Eq. (48.15).

$$F' = \frac{1/U_L}{\frac{1}{U_L} + \frac{D_o}{h_{fi}\cdot D_i}} + \left(\frac{D_o}{2\cdot k}\ln\left(\frac{D_o}{D_i}\right)\right) \tag{48.15}$$

The heat removal factor is calculated from Eq. (48.16)

$$F_R = \frac{c_p \cdot \dot{m}}{A_r \cdot U_l}\cdot\left(1 - \exp\left(-\frac{U_L \cdot A_r \cdot F'}{c_p \cdot \dot{m}}\right)\right) \tag{48.16}$$

Finally, the useful energy is estimated by using Eq. (48.17).

$$Q_u = F_R \cdot [S \cdot A_a - A_r \cdot U_L \cdot (T_i - T_a)] \tag{48.17}$$

T_o can be obtained from energy balance around the PTSC as follows.

$$T_o = T_i + \frac{Q_u}{c_p \cdot \dot{m}} \tag{48.18}$$

The collector efficiency is calculated by Eq. (48.19).

$$\eta = F_R \cdot \left[\eta_r - U_L \cdot \left(\frac{T_i - T_a}{G_B \cdot C}\right)\right] \tag{48.19}$$

In Eq. (48.19), C is the concentration ratio and can be calculated using Eq. (48.20).

$$C = \frac{A_a}{A_r} \tag{48.20}$$

48.2.3 Exergy Analysis of PTSC

Exergy analysis is required to calculate the flow exergy change of the thermal oil and the exergetic efficiency of PTSC. Total exergy gained by PTSC can be obtained from Eq. (48.21)

$$\dot{E}x_{solar} = A_a \cdot N \cdot S \cdot \left[1 + \frac{1}{3}\left(\frac{T_a}{T_{sun}}\right)^4 - \frac{4}{3}\left(\frac{T_a}{T_s}\right)\right] \tag{48.21}$$

Flow exergy change is given by Eq. (48.22):

$$\dot{E}x_{flow} = \dot{m} \cdot (h_{out} - h_{in}) - T_a \cdot \dot{m} \cdot (s_{out} - s_{in}) \tag{48.22}$$

Exergetic efficiency can be calculated by using Eq. (48.23):

$$\eta_{exergetic} = \frac{\dot{E}x_{flow}}{\dot{E}x_{solar}} \tag{48.23}$$

48.3 Results and Discussion

The optical, thermal, and exergetic models of PTSC are solved for various geometric and environmental parameters by using different heat transfer fluids. The maximum and minimum values of these parameters are shown in Table 48.2.

Table 48.2 Value range for parameters

Parameter	Minimum value	Maximum value
Outer diameter of the receiver	0.04 m	0.09 m
Aperture width	3 m	10 m
Wind speed	1 m/s	9 m/s
Solar radiation	400 W/m^{22}	1100 W/m^2

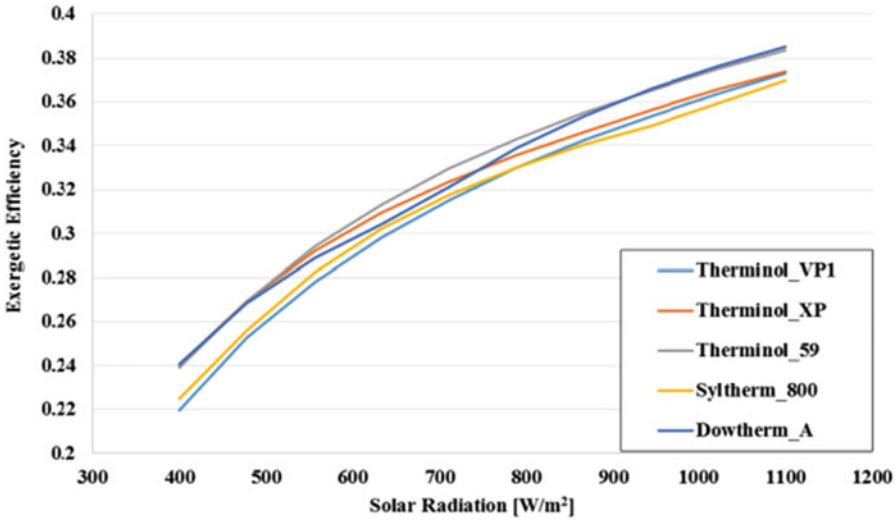

Fig. 48.2 Exergetic efficiency vs. solar radiation for various heat transfer fluids

The fluid selection is one of the key factors affecting the performance of the PTSC. In general, a suitable heat transfer fluid should have the following properties in order to have favorable thermodynamic characteristics and low environmental impact: high working temperature range, high thermal conductivity, low viscosity, and non-corrosiveness. For this purpose, five different heat transfer fluids as PTSC fluid are chosen, which are Therminol VP1, Therminol XP, Therminol 59, Syltherm 800, and Dowtherm A.

The effect of the solar radiation on the exergetic efficiency is shown in Fig. 48.2. It is clear from Fig. 48.2 that the exergetic efficiency increases with an increase in the solar irradiation for various heat transfer fluids. These efficiency differences of the heat transfer fluids are due to their specific heat value at a given working temperature. When the solar radiation increases, the useful energy also increases. This increase causes a higher outlet temperature of PTSC. On the other hand, the maximum exergetic efficiency is provided by using Dowtherm A for various solar radiations as shown in the Fig. 48.2.

The exergetic efficiency of the PTSC for different wind speed is plotted in Fig. 48.3. When the wind speed increases, convective heat transfer coefficient and heat removal factor decrease. As a result, useful energy and output temperature also decrease. Figure 48.3 shows that the exergetic efficiency decreases as the useful energy increases. For the same wind speed, the highest exergetic efficiency is obtained by using Dowtherm A or Therminol 59.

The unshaded area of the PTSC increases when the aperture width of the parabola increases. When the unshaded area increases, the useful energy gain and the flow exergy increase. Consequently, the exergetic efficiency increases as the aperture width increases as shown in the Fig. 48.4. On the other hand, Dowtherm A yields the highest exergetic efficiency for the same aperture width.

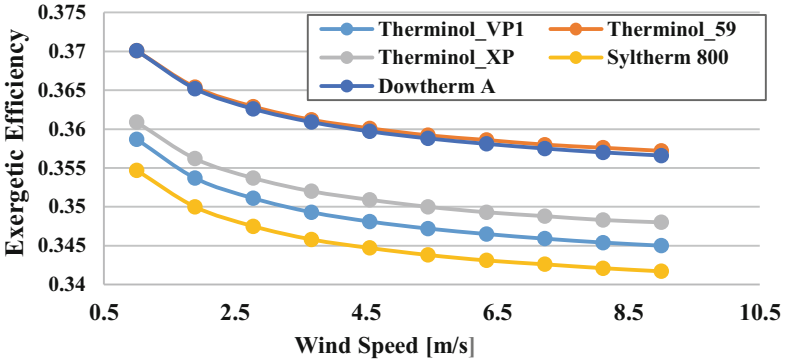

Fig. 48.3 Exergetic efficiency vs. wind speed for various heat transfer fluids

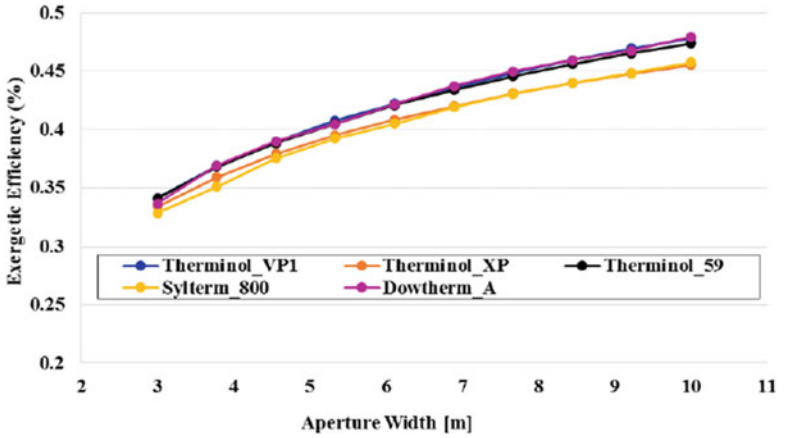

Fig. 48.4 The effect of aperture width on the exergetic efficiency of the PTSC for different heat transfer fluids

The effect of the outer diameter of the receiver on the exergetic efficiency is shown in Fig. 48.5. When the outer diameter of the receiver increases, the outlet temperature, heat removal factor, and useful energy decrease. As a result, when the outer diameter of the receiver increases, the exergetic efficiency of PTSC increases. Additionally, Therminol VP1 ensures the highest exergetic efficiency for the selected receiver diameters.

The outlet temperature of the heat transfer fluids, which are used in this study, is shown in Fig. 48.6. These fluids are used because of their compatibility for wide temperature range. The heat transfer fluids must remain in the liquid phase to achieve the correct results for the exergetic efficiency [13]. According to Fig. 48.6, when the Syltherm 800 is used as the PTSC fluid, it is found that the outlet temperature of receiver has the highest value (547.8 K) among the other type of fluids. This trend is mainly due to the fact that Syltherm 800 has favorable thermophysical properties (e.g., specific heat and enthalpy).

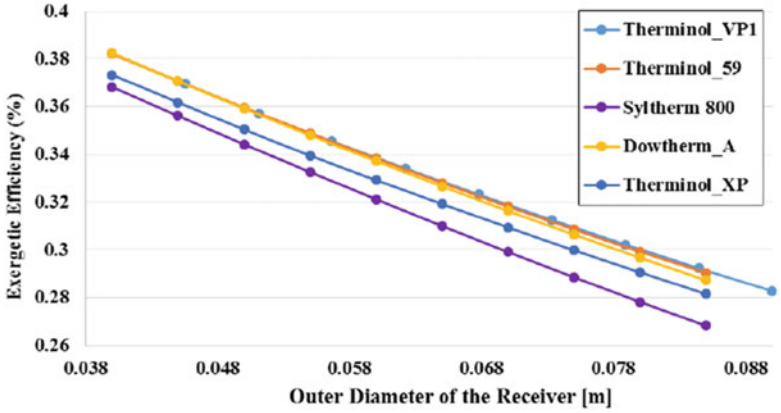

Fig. 48.5 The effect of outer diameter of receiver on the exergetic efficiency for different heat transfer fluids

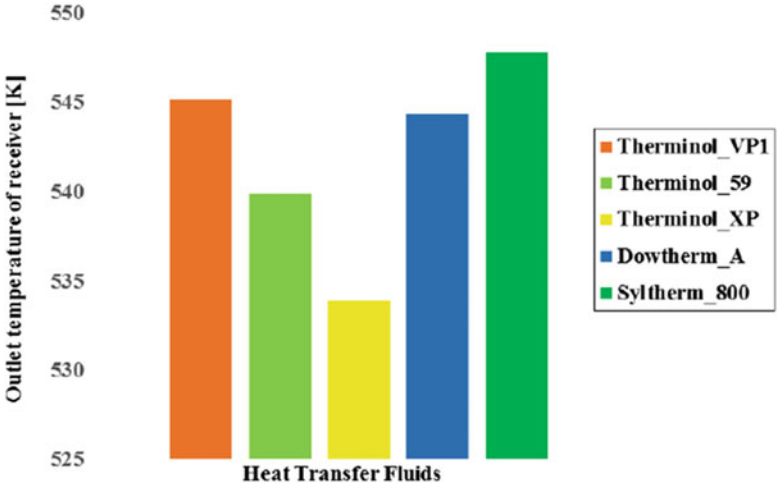

Fig. 48.6 Outlet temperatures for various heat transfer fluids

48.4 Optimization by Using Taguchi Method

The exergetic efficiency of the PTSC is calculated by using different values of the mentioned parameters. In this paper, optimization study is conducted to calculate the maximum exergetic efficiency for chosen conditions. The optimization of this system is done with Minitab 17 software by using Taguchi method. Taguchi method is an experimental optimization method and developed by Dr. Genichi Taguchi [12, 13]. In this study, standard L9 orthogonal array for a three-level design is selected. Four different design parameters (factors) were chosen for the Taguchi method as follows: the type of PTSC fluids, receiver diameter, aperture width, and

Table 48.3 The design parameters of Taguchi method

Heat transfer fluids	Receiver diameter (m)	Aperture width (m)	Wind speed (m/s)	Exergetic efficiency
Therminol VP1	0.04	3	1	0.3729
Therminol VP1	0.065	6.5	5	0.4026
Therminol VP1	0.09	10	9	0.4073
Dowtherm A	0.04	6.5	9	0.4482
Dowtherm A	0.065	10	1	0.4649
Dowtherm A	0.09	3	5	0.2516
Sylthern 800	0.04	10	5	0.4802
Sylthern 800	0.065	3	9	0.2873
Sylthern 800	0.09	6.5	1	0.3526

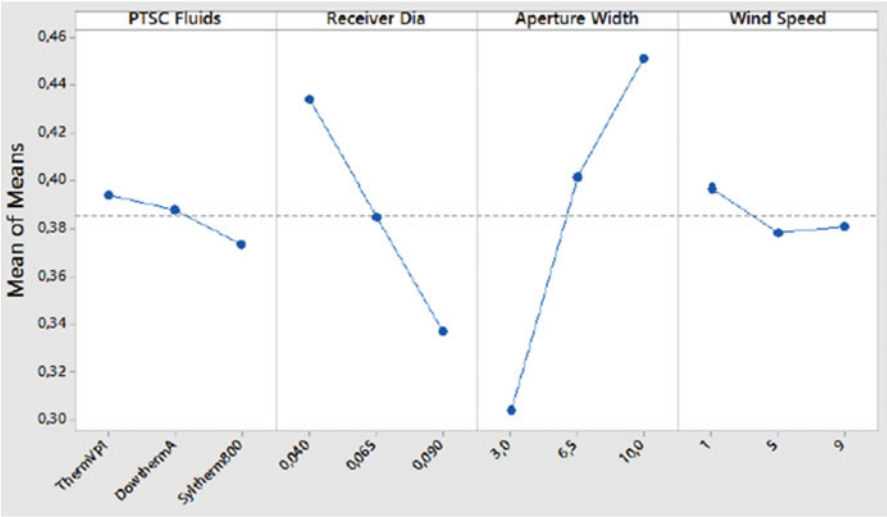

Fig. 48.7 S/N plot for the Taguchi method for maximized exergetic efficiency

wind speed. Three different values (levels) for each factor that represent a low, medium, and high value in a given range were taken. The Taguchi method gives us nine different types of parameter sets to be used in simulations. These simulations are then run in EES software to find the desired performance parameters (exergetic efficiency). The design parameters of this optimization are shown in Table 48.3.

In this study, heat transfer fluids, outer diameter of the receiver, aperture width of the parabola, and wind speed are used as design parameters (factors). The exergetic efficiency is calculated for these factors.

The change of S/N ratios for each factor is shown in Fig. 48.7. The higher ratio corresponding to a level for each factor is taken to find the set of the parameters that gives the optimum performance. According to Fig. 48.7, Therminol VP1 as the heat

transfer fluid, 0.04 m as the outer diameter of the receiver, 10 m as the aperture width, and 1 m/s as the wind speed are chosen to maximize the exergetic efficiency. After these selections, the obtained values are recalculated with EES. When chosen values are used in the EES code, the exergetic efficiency is found as 0.5019.

48.5 Conclusions

In this chapter, the optical, thermal, and exergetic analyses of PTSC were carried out, and the equations were solved using EES. Parametric studies were conducted to calculate the effect of some key parameters on the outlet temperature of PTSC and the exergetic efficiency of PTSC. Then, the optimization of the PTSC using Taguchi method was done to maximize the exergetic efficiency of the PTSC. The main conclusions from this study are shown below.

- The parametric studies show that the exergetic efficiency increases when the solar radiation and aperture width increase for all the heat transfer fluids which are used in this study. In addition, when the outer diameter and wind speed increase, the exergetic efficiency decreases.
- Taguchi analysis shows that the effect of aperture width on the exergetic efficiency is the most dominant parameter, and Therminol VP1 is the most optimal heat transfer fluid for various working temperature.
- The maximum exergetic efficiency was obtained by using Dowtherm A as 38.51%.
- The parametric studies show that Syltherm 800 yields the lowest exergetic efficiency for different conditions (e.g., solar radiation, wind speed, or aperture width).

Nomenclature

A_a	Total aperture area (m^2)
A_f	Geometric factor (m^2)
A_{loss}	Total loss in aperture area (m^2)
A_r	Receiver area (m^2)
D_g	Glass cover diameter (m)
D_i	Inside diameter of the receiver (m)
D_o	Outside diameter of the receiver (m)
$\dot{E}x_{flow}$	Flow exergy rate (kW)
$\dot{E}x_{solar}$	Exergy rate from the sun (kW)
f	Focal distance of the parabola, friction factor (m)
F_R	Heat removal factor
G_b	Solar radiation (W/m^2)
h	Specific enthalpy (kJ/kg)
h_c	Conduction loss from the tubes (W/m^2K)
h_{fi}	Convective heat transfer coefficient inside the receiver (W/m^2K)

h_p	Parabola height (m)
h_r	Radiation loss (W/m^{2}K)
$h_{r,\ c\ -\ a}$	Radiation coefficient from glass cover to ambient (W/m^{2}K)
$h_{r,\ r\ -\ c}$	Radiation coefficient from receiver to the glass cover (W/m^{2}K)
h_w	Wind loss coefficient (W/m^{2}K)
k	Thermal conductivity of fluid (W/mK)
N	Number of PTSC
Nu	Nusselt number
Pr	Prandtl number
Re	Reynolds number
S	The heat absorbed by the receiver (W/m^2)
s	Specific entropy (kJ/kgK)
T_a	Ambient temperature (K)
T_c	Glass cover temperature (K)
T_{sun}	The temperature of the sun (K)
T_i	Inlet temperature of the heat transfer fluid (K)
U_o	Overall heat transfer coefficient (W/m^{2}K)
W_a	Aperture of parabola (m)

Subscripts

a	Ambient, aperture
i	Inner, inlet
o	Outer
r	Radiation

Greek Letters

α	Absorptance of the receiver
γ	Intercept factor
$\eta_{exergetic}$	Exergetic efficiency of PTSC
η_r	Optical efficiency
ε_g	Emissivity of the glass cover
ρ	Reflectance of the mirror
σ	Stefan–Boltzmann constant (W/m^2·K^4)
τ	Transmittance of the glass cover
θ	Incidence angle

References

1. Abbas R, Montes MJ, Rovira A, Martínez-Val JM (2016) Parabolic trough collector or linear Fresnel collector? A comparison of optical features including thermal quality based on commercial solutions. Sol Energy 124:198–215
2. Mokheimer EM, Dabwan YN, Habib MA, Said SA, Al-Sulaiman FA (2014) Techno-economic performance analysis of parabolic trough collector in Dhahran, Saudi Arabia. Energy Convers Manag 86:622–633

3. Kalogirou SA (2004) Solar energy engineering: processes and systems. Elsevier Academic Press, San Diego
4. Manikandan KS, Kumaresan G, Velraj R, Iniyan S (2012) Parametric study of solar parabolic trough collector system. Asian J Appl Sci 5(6):384–393
5. Qu M, Archer DH, Yin H (2007) A linear parabolic trough solar collector performance model. In: ASME 2007 energy sustainability conference, pp 663–670. American Society of Mechanical Engineers Long Beach, California, USA, July 27–30, 2007
6. Yılmaz İH, Söylemez MS (2014) Thermo-mathematical modelling of parabolic trough collector. Energy Convers Manag 88:768–784
7. Padilla RV, Demirkaya G, Goswami DY, Stefanakos E, Rahman MM (2011) Heat transfer analysis of parabolic trough solar receiver. Appl Energy 88(12):5097–5110
8. Kalogirou SA (2012) A detailed thermal model of a parabolic trough collector receiver. Energy 48(1):298–306
9. Conrado LS, Rodriguez-Pulido A, Calderón G (2017) Thermal performance of parabolic trough solar collectors. Renew Sust Energ Rev 67:445–459
10. Cakici DM, Erdogan A, Colpan CO (2017) Thermodynamic performance assessment of an integrated geothermal powered supercritical regenerative organic Rankine cycle and parabolic trough solar collectors. Energy 120:306–319
11. Bergman TL, Incropera FP (2011) Fundamentals of heat and mass transfer. Wiley, Hoboken
12. Taguchi G (1986) Introduction to quality engineering: designing quality into products and processes, vol 191. ARRB Group Limited, White Plains
13. Erdogan A, Colpan CO, Cakici DM (2017) Thermal design and analysis of a shell and tube heat exchanger integrating a geothermal based organic Rankine cycle and parabolic trough solar collectors. Renew Energy 109:372–391

Part V
Energy Efficiency in the Building Sector

Chapter 49
Experimental Estimation of Factors Influencing the Equivalent Outdoor Temperature for the Multifamily Building

Tomasz Cholewa

49.1 Introduction

Nowadays considerable attention is paid to increasing energy efficiency in buildings, particularly in the residential sector (EU-Directive 2012/27/EU [1]). Taking this into account, the effective management of heat in terms of building and forecasting the heat consumption for buildings becomes more and more important [2–5].

The equivalent outdoor temperature is used in a lot of municipal heat supply companies by forecasting the process of heat power which should be delivered to buildings for the heating purpose and taking into account estimated corrective coefficients considering the wind speed and level of cloudiness.

That is why this paper presents the method of estimating factors (wind speed and insolation) influencing the equivalent outdoor temperature for one multifamily building on the basis of long-term exploitive research.

49.2 Materials and Methods

Experimental research was performed for one multifamily building in the heating season 2015/2016. The building is located in Poland and has heated floor surface area of 2150 m^2. The central heating installation is a traditional one (with vertical risers in each flat and convective radiators) and supplied with the heating medium (80/60 °C).

T. Cholewa (✉)
Lublin University of Technology, Faculty of Environmental Engineering, Lublin, Poland
e-mail: t.cholewa@wis.pol.lublin.pl

S. Nižetić, A. Papadopoulos (eds.), *The Role of Exergy in Energy and the Environment*, Green Energy and Technology,
https://doi.org/10.1007/978-3-319-89845-2_49

An individual thermal station for heating and hot water purposes is located in the building, which is supplied from a high-temperature district heating network. There are two calibrated heat metres which measure hourly heat consumption used in heating and hot water systems. But for the purposes of this article, only hourly heat power delivered to the heating system is analysed. Additionally, the weather data, particularly the outside temperature, the average and maximum wind speed (v) and the level of the cloudiness were measured hourly in the near location of analysed multifamily building.

The data were specially gathered taking into account the large amount of data for the analysis and the goal to clearly show the influence of different weather factors and the methodologies of the analysis on the heat power and then the calculation of the equivalent outdoor temperature. Namely, the heat power delivered for heating purposes was presented for average and maximum wind speed below 3 m/s, between 3 m/s and 6 m/s and higher than 6 m/s.

Different times of the day and night were taken into account, and the attention to the accuracy of obtained results was paid. The level of cloudiness was also taken into account by the following assumptions: low, 0–2 octant; average, 3–5 octant; high, 6–7 octant; and total, 8 octant. The specified linear equations and their correlation coefficients were obtained by regression and are analysed in details in section 3 of this paper.

49.3 Results and Discussion

Firstly, the analysis is related to the influence of wind speed (average, maximum) on the heat power delivered to analysed building for heating purpose by taking into account all hourly data from analysed heating season 2015/2016 (Fig. 49.1 and Fig. 49.2). It may be noticed that higher coefficients of correlation are obtained for maximum wind speed than for average one. Furthermore, it was observed that the higher level of correlation was for the lowest value of wind speed (wind speed below 3 m/s). The correlation between wind speed and delivered heat power decreases parallel with the increase of wind speed (v).

In order to show that the methodology of data analysis is a very important factor in getting proper correlation coefficient between particular factors and heat power delivered, the results of correlation between wind speed and heat power depending on the time of the day included in the data analysis are presented in Figs. 49.3 and 49.4 (for hours 6.00–18.00) and Figs. 49.5 and 49.6 (for hours 18.00–6.00).

Based on the results (Fig. 49.3, 49.4, 49.5, and 49.6), also in these cases, it can be noticed that much higher accuracy (R^2 higher between 0.080 and 0.4331) of heat power forecasting is obtained for maximum wind speed than for average wind speed. Besides, the higher correlation is elaborated when taking into account data of heat power and weather conditions only for night hours (18.00–6.00) rather than day hours (6.00–18.00). It may be connected with the fact that the users of heating

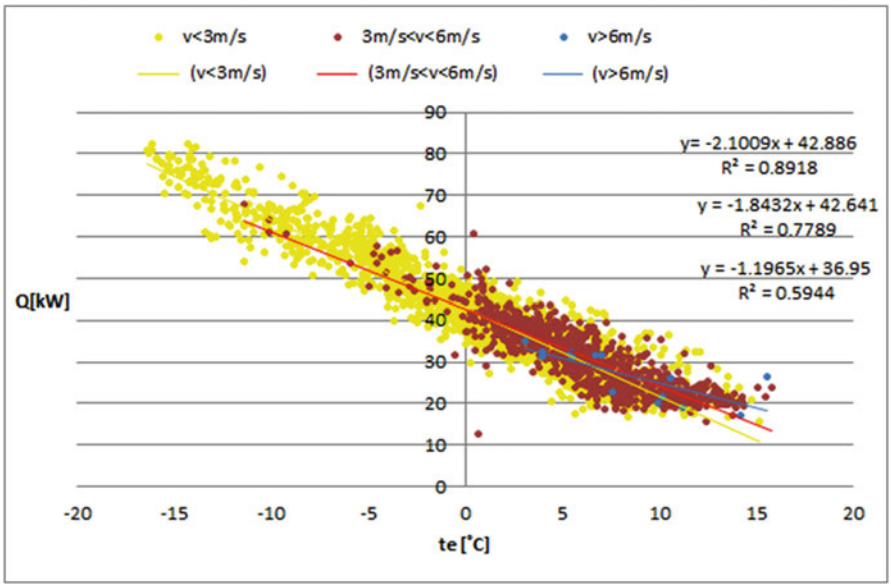

Fig. 49.1 Heat power delivered to the heating system between hours 0.00 and 23.59 by average wind speed

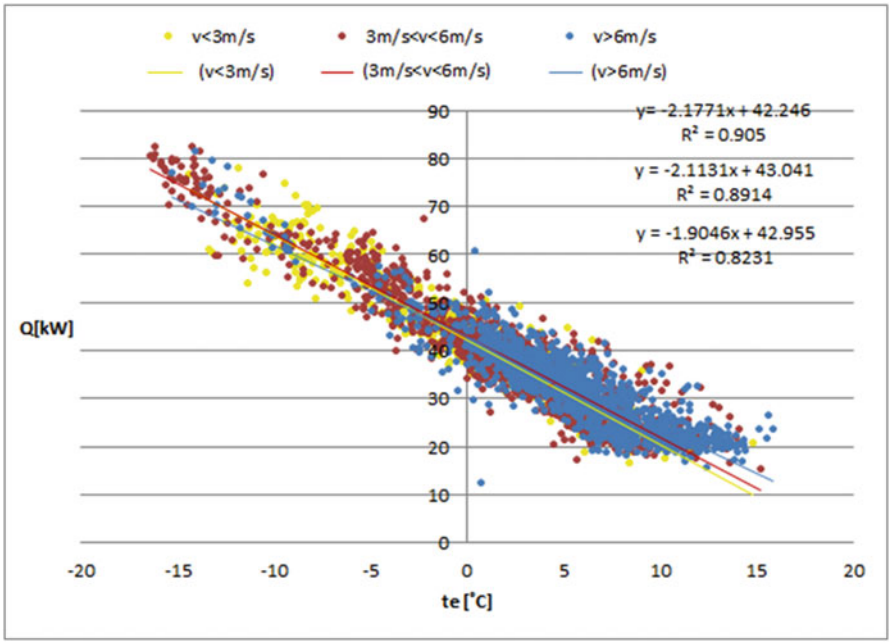

Fig. 49.2 Heat power of the heating system between hours 0.00 and 23.59 by maximum wind speed

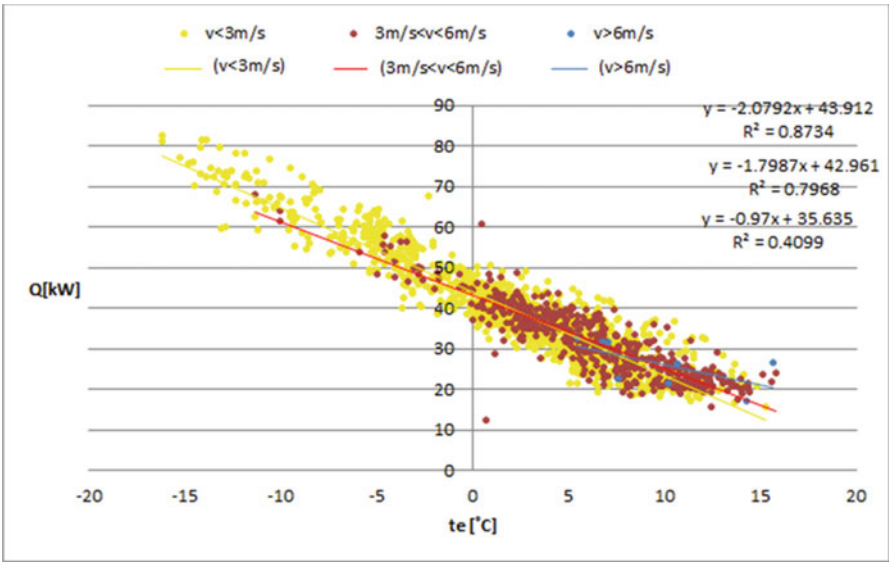

Fig. 49.3 Heat power of the heating system between hours 6.00 and 18.00 by average wind speed

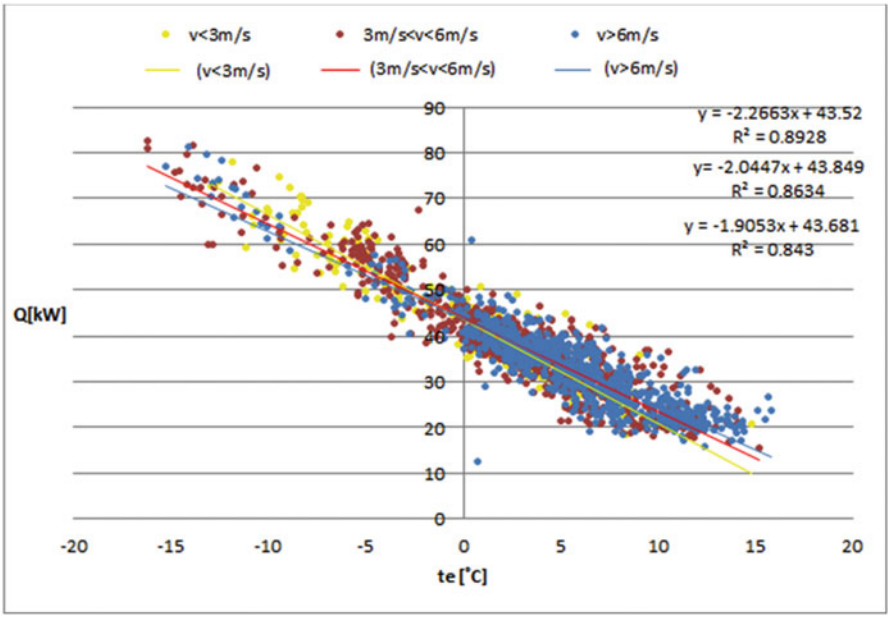

Fig. 49.4 Heat power of the heating system between hours 6.00 and 18.00 by maximum wind speed

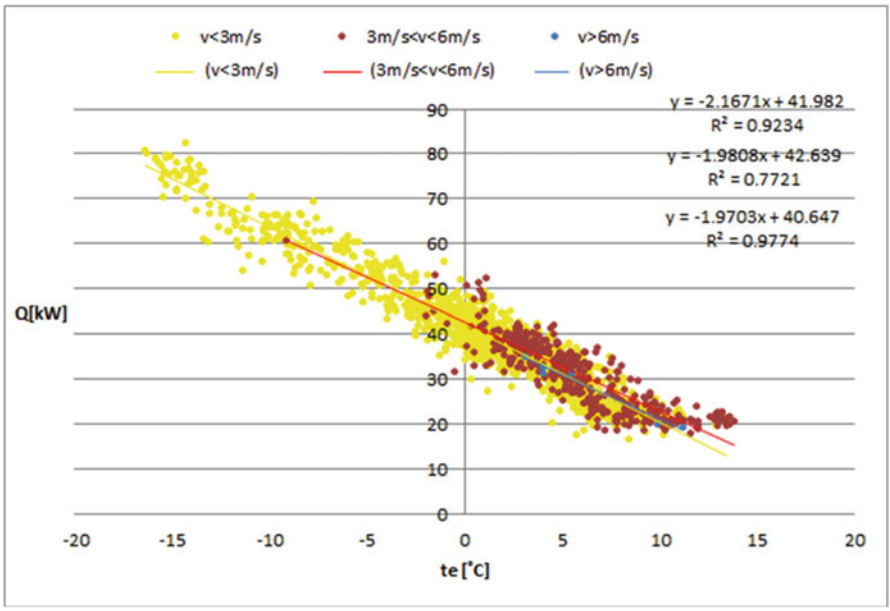

Fig. 49.5 Heat power of the heating system between hours 18.00 and 6.00 by average wind speed

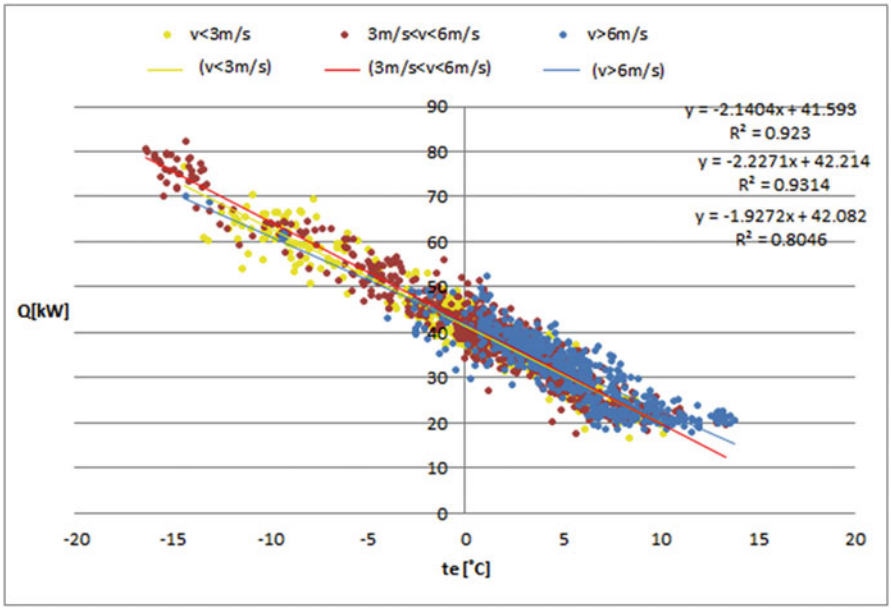

Fig. 49.6 Heat power of the heating system between hours 18.00 and 6.00 by maximum wind speed

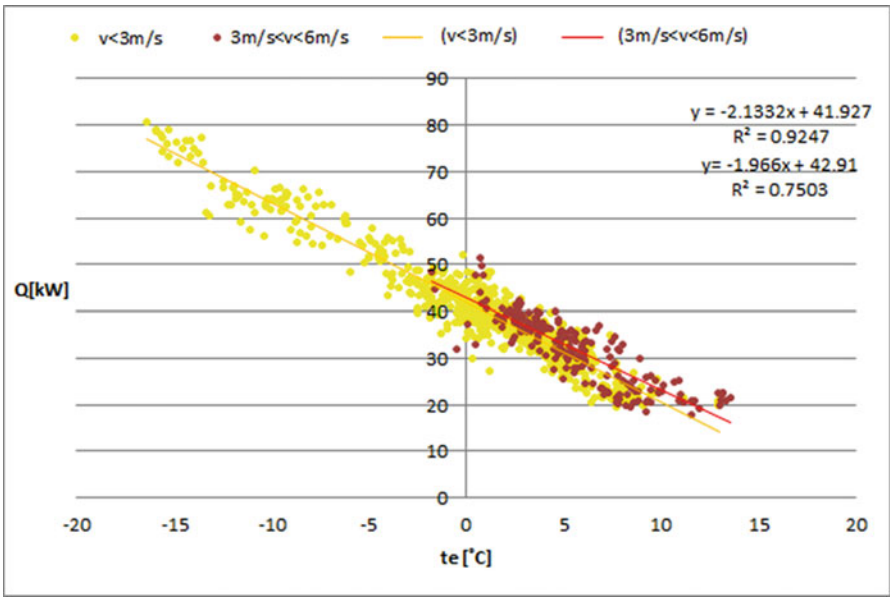

Fig. 49.7 Heat power of the heating system between hours 0.00 and 4.00 by average wind speed

installation may use the thermostatic radiator valves (TRVs) more during the day than at night, and also the influence of the sun may deface the level of correlation.

In order to show this more precisely, additional correlations were presented only for late night hours (0.00–4.00) in Fig. 49.7 and 49.8 and for the level of cloudiness (Figs. 49.9 and 49.10).

It was noticed (Fig. 49.7 and 49.8) that the correlation of heat power delivered to the heating system for analysed building is higher exactly for the night hours and maximum wind speed (Table 49.1) than for other analysed cases. This is connected with the minimalization of the influence of other weather and human conditions for this time at night.

Additionally, it was reported that there is no logical correlation and influence of the level of cloudiness on the heat power demand for analysed building.

49.4 Conclusions

In engineering practice the equivalent outdoor temperature is mostly calculated based on all available data of heat power supplied to the building or district heating system, which may generate low accuracy of forecasting of heat power. That is why, taking into account the results of this study, it was proposed to use only night data (0.00–4.00) when evaluating the correlation between heat power and wind speed,

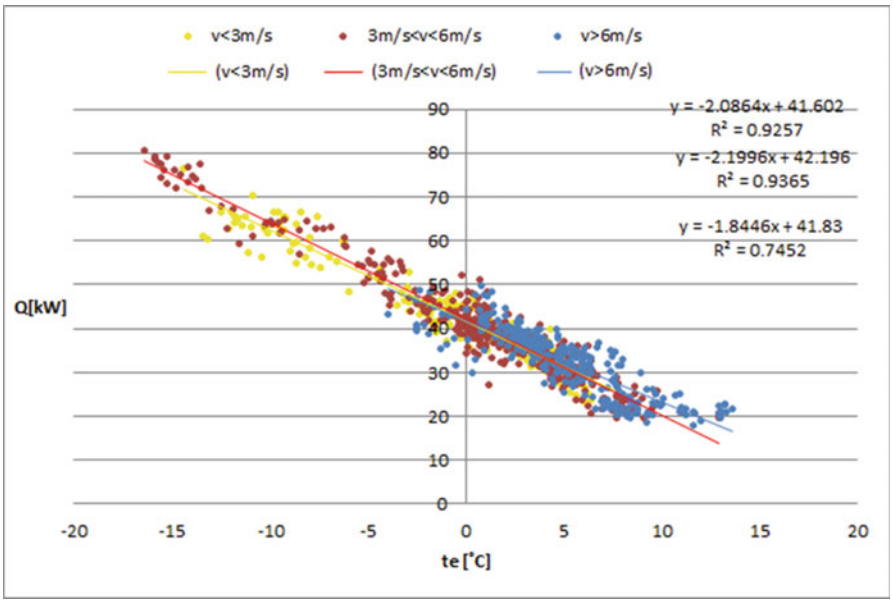

Fig. 49.8 Heat power of the heating system between hours 0.00 and 4.00 by maximum wind speed

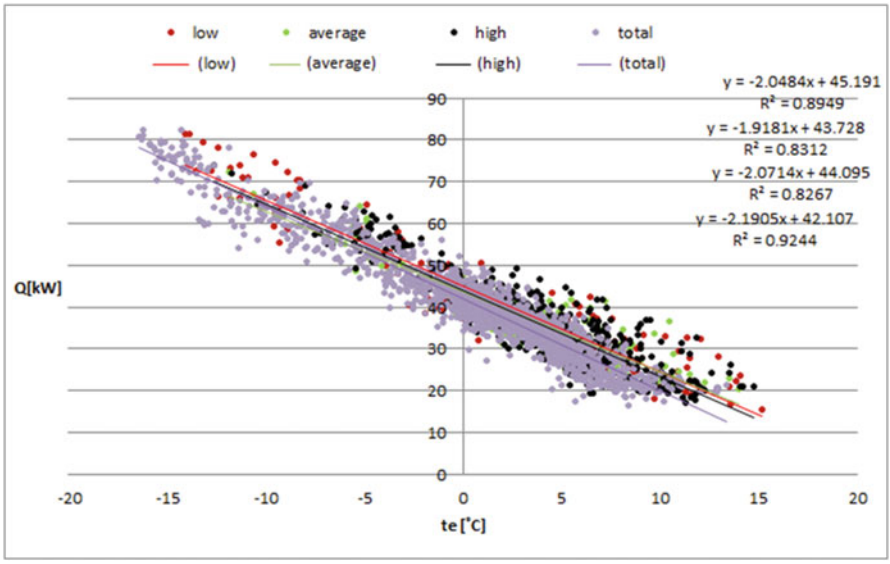

Fig. 49.9 Heat power of the heating system for analysed levels of cloudiness by average wind speed below 3 m/s

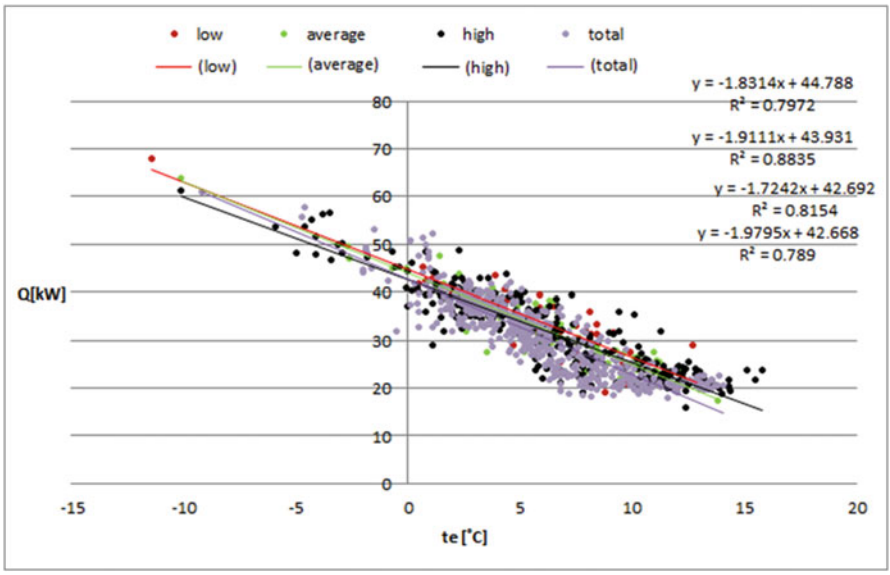

Fig. 49.10 Heat power of the heating system for analysed levels of cloudiness by average wind speed between 3 m/s and 6 m/s

Table 49.1 The regression coefficients for analysed cases

Time	Wind speed (v)	v < 3	3 < v < 6	v > 6
0.00–23.59	Average	0.8918	0.7789	0.5944
	Maximum	0.905	0.8914	0.8231
6.00–18.00	Average	0.8734	0.7968	0.4099
	Maximum	0.8928	0.8634	0.8430
18.00–6.00	Average	0.843	0.7721	0.9774
	Maximum	0.923	0.9314	0.8046
0.00–4.00	Average	0.9247	0.7503	–
	Maximum	0.9257	0.9365	0.7452

which is one of the most influencing factors of weather conditions. Then the R^2 is on the level of 0.9365 for maximum wind speed, and its range is between 3 m/s and 6 m/s.

The much lower level of correlation is obtained when average wind speed level is taken into account instead of maximum value.

It was not observed that the level of cloudiness may have important influence on heat power delivered to the heating system.

Acknowledgements This study was supported by research project, financed by the Polish Ministry of Science and Higher Education.

References

1. Directive 2012/27/EU of the European Parliament and of the Council of 25 October 2012 on energy efficiency
2. Freire R, Oliveira G, Mendes N (2008) Predictive controllers for thermal comfort optimization and energy savings. Energ Buildings 40:1353–1365
3. Prívara S, Siroky J, Ferkl L, Cigler J (2011) Model predictive control of a building heating system: the first experience. Energ Buildings 43:564–572
4. Široky J, Oldewurtel F, Cigler J, Prívara S (2011) Experimental analysis of model predictive control for an energy efficient building heating system. Appl Energy 88:3079–3087
5. Wojdyga K (2008) An influence of weather conditions on heat demand in district heating systems. Energ Buildings 40:2009–2014

Chapter 50
From Energy Demand Calculation to Life Cycle Environmental Performance Assessment for Buildings: Status and Trends

Thomas Lützkendorf and Maria Balouktsi

50.1 Introduction

Climate change, resource depletion, and fuel poverty are only some of the major challenges in the construction industry that must be managed responsibly today and over the long term. In the attempt to tackle them, designing, constructing, and operating buildings in a sustainable and energy-efficient manner are becoming increasingly important. This is also reflected in broader international activities linking sustainable building activity to wider sustainable development goals (SDGs). For example, aspects of sustainable building are referenced in several UN SDGs, such as SDG 11 "Sustainable Cities and Communities"; SDG 3 "Good Health and Well-being"; SDG 6 "Clean Water and Sanitation"; SDG 7 "Affordable and Clean Energy"; SDG 9 "Industry, Innovation, and Infrastructure"; SDG 12 "Responsible Consumption and Production"; and SDG 13 "Climate Action" [1].

With this regard, it is expected that in the near future, sustainable building design, construction, and operation will leap from being a state-of-the-art "alternative" to becoming the norm in the building sector. Starting with the aspect of energy, it is already the case that operational energy demand for buildings has steadily fallen over the past decades. The first oil crisis in the early 1970s was a driving force for most countries to implement building codes with stricter requirements. This development grew from a tightening of thermal insulation requirements of individual building components to the introduction of requirements for a maximum allowed heating demand and even a maximum allowed nonrenewable primary energy demand per square meter of a building. This has resulted in massive energy savings for building operation – especially heating and cooling. At the same time, technological

T. Lützkendorf · M. Balouktsi (✉)
Karlsruhe Institute of Technology, Centre for Real Estate, Karlsruhe, Germany
e-mail: maria.balouktsi@kit.edu

S. Nižetić, A. Papadopoulos (eds.), *The Role of Exergy in Energy and the Environment*, Green Energy and Technology,
https://doi.org/10.1007/978-3-319-89845-2_50

development in construction materials, products, and technologies (i.e., HVAC systems and other building services), as well as modern design methods, has enabled to reduce buildings' operational energy consumption to net-zero or net-energy-plus levels. This has led to the emergence of several related regional standards and initiatives over the last decade, such as the European Union guidelines (2010/31/EU) that require all new buildings to be nearly zero-energy level by the end of 2020 (public buildings by the end of 2018).

As a consequence of these changes, the energy required to construct and maintain/repair such buildings – as well as to produce, transport, install, remove, dispose, or possibly recycle the materials that comprise them – the so-called embodied energy, is gaining relative importance from a life cycle perspective [2]. Hence, discussions of widening the scope of energy saving from a former exclusive focus on operational energy in the use phase to the inclusion of embodied energy are currently relevant both at EU level and internationally. A similar view is expressed in the latest EU Communication on Resource Efficiency Opportunities in the Building Sector [3], which includes embodied energy in the core list of recommended indicators.

50.1.1 Additional Targets and Indicators

Driven by climate change, however, there is a shift in focus for many building practitioners and decision makers toward the consideration of greenhouse gas (GHG) emissions as the primary environmental metric and as a proxy for broad environmental consequences of primary energy consumption. To this end, the "carbon footprint" indicator has gained tremendous popularity over the last few years. This has also been identified as a trend in research and publications by Lützkendorf et al. [4]. Therefore, a great emphasis is nowadays placed not only on the aspect of resource conservation but also on climate protection, either in combination or separately.

Nevertheless, an assessment of the life cycle-related environmental performance of buildings typically should not be solely focused on primary energy and GHG emissions but to cover a broad range of environmental (and in addition health-related) issues. This requires a transition to the use of life cycle analysis as a basis for assessing the contributions of single buildings to sustainable development. In this context, this paper provides an overview of the topics and trends that have shaped the current approaches to the assessment of the environmental performance of buildings as part of sustainability or overall performance assessment. More specifically, the discussion is revolving around two main trends: (1) the extended system boundaries when considering the full life cycle of buildings and (2) the extended assessment scope when looking at a building's environmental performance beyond primary energy demand.

The results of the paper are partly built on the discussions for the initiation and preparation of the new international project of the IEA EBC program, Annex

72 "Assessing life cycle-related environmental impacts caused by buildings," in which the authors have been actively involved. This project also makes use of the results of previous IEA activities (i.e., EBC Annex 31 [5] and EBC Annex 57 [6]).

50.2 Clarification of Terms: Difference Between "Energy Efficient", "Green," and "Sustainable"

There are still uncertainties and misunderstandings associated with the use of the terms "energy efficient," "green," and "sustainable," when describing advanced building concepts. However, a uniform understanding of these terms is necessary to formulate appropriate project objectives, to select and apply assessment criteria, to measure the building performance, and to indicate appropriate building features to third parties. The situation is further complicated by the fact that other terms such as "climate neutral" or "high performance" are used without clearly defining them. (From the authors' point of view, climate-neutral buildings are the ones with a net-zero emission balance in the operation phase or in the complete life cycle, while high-performance buildings are the ones with an above-average technological and functional quality.)

Energy-efficient and energy-saving buildings are nowadays considered to be the same. However, the term "efficiency" always involves the consideration of the balance between benefits and effort. The benefits consist, among others, in ensuring the building's essential functions and retaining its durability and value by avoiding structural damage while providing adequate thermal comfort, indoor air quality, and visual comfort (adequate provision of daylight and artificial light). For purely energy considerations, on the other side of the balance is the energy consumed by the building. This raises the question of how much energy is required to maintain an adequate level of occupant's thermal and visual comfort, as well as indoor air quality, under specific site and use conditions during the operation phase. The assessment of energy consumption of such building concepts requires that this is itemized into the type of energy use (e.g., space heating, lighting and other appliances, etc.) and the type of energy sources/carriers consumed (e.g., gas, coal, renewable, etc.). In a larger scope, it is possible to also consider the associated adverse effects on the global and local environment (e.g., global warming, ozone depletion, and other impacts), including risks to the local environment and health. Analyzing the amount of energy costs saved and discussing the potentially higher costs for their construction and maintenance is also typical for this type of buildings.

While the concept of an "energy-efficient" building focuses on the aspect of energy (and comfort), the "green building" approach goes beyond this. It is based on the traditions of design for environment (DfE) [7] and design for deconstruction (DfC) [8], among other similar strategies, leading to the use of terms like "ecological," "resource efficient," "environmentally friendly," or "healthy" to further characterize it. In addition to the aspects of energy and comfort, also issues related to the

use of resources (e.g., through the selection of construction products, water consumption, etc.), changes in land use, and interactions between buildings and the local environment (heat islands, impacts on the groundwater) are taken into account, among others. The selection and use of insulation materials is often discussed as a specific topic.

Thus, the analysis in the case of "green buildings" is focused on the question of what building materials consumption is required to achieve a good energy standard and whether potential environmental and health hazards are caused. A further aspect is the consideration of the ease of dismantling and recycling. Currently, the overall environmental compatibility of "green buildings" can be assessed through an environmental performance assessment and with the help of binding international and European standards on this subject (e.g., ISO 21931-1:2010, EN 15643-2:2011 and EN 15978:2011). Social aspects like comfort, security, and user satisfaction are also partly considered in these concepts.

On the other hand, the "sustainable building" concept considers environmental, economic, and social aspects simultaneously and in an equal manner, but under the condition of fulfilling certain technical and functional requirements first. ISO 15392:2008 provides the general principles for this. The main difference with the green building concept lies in the addition of the economic aspects to the analysis.

Regardless of a building's energy standard, an assessment according to "sustainable building" principles would provide the most complete picture of its overall performance. This is the main argument around which the paper centers. The energy quality of a building is closely connected to its contribution to sustainable development and particularly has an effect on:

- Resource use/depletion (energy sources) and adverse effects on the environment in the use stage (environmental dimension)
- Resource use/depletion and adverse effects on the environment as a result of the building life cycle stages other than the operation, being the production, construction, maintenance, repair, and EoL (environmental dimension)
- The service life of the building envelope (technical dimension)
- Health, comfort, and satisfaction of users (social dimension)
- The aesthetics of the building (social dimension)
- The energy costs (economic dimension)
- The affordability of housing by reducing the energy cost burden (sociopolitical dimension)
- The maintenance and servicing costs (economic dimension)
- The design and construction costs (economic dimension)
- The marketability/rentability and price of the rent (economic dimension)
- The value stability and value development (economic dimension)

50.3 First Trend: Consideration of the Whole Building and Its Life Cycle

50.3.1 Shift to Whole Building Considerations

Since the late 1970s, following the oil crisis of 1973, the debate on the appropriate use of energy resources arose, leading to several efforts on the improvement of the energy performance of buildings. These were initially focused on the heating demand, looking at two different elements of the building: the building envelope (e.g., increase of the insulation thickness, reduction of heat losses, etc.) and the heating system (e.g., requirements to the dimensioning of central heating systems, etc.).

Later on, the growing importance of electricity due to the increase in the use of electrical equipment and devices in buildings, including air-conditioning, led to a more comprehensive approach to building energy. Not only requirements for different elements (e.g., building envelope) or energy uses (e.g., annual heating demand) have been set in the codes but also requirements for the whole building performance (e.g., a maximum allowed nonrenewable primary energy demand). For example, in Europe, there are series of standards (already published or under development) covering both the evaluation of product characteristics and the overall energy use, e.g.:

- CEN TC 48, TC 57, TC 89, etc. include standards evaluating product characteristics.
- CEN TC 156, TC 169, TC 228, TC 247, etc. include standards for the calculation of energy needs and losses associated with typical building services.
- CEN/TC 371 includes standards for the overall energy performance of buildings (in line with the EU guidelines (2010/31/EU)).

This trend is also evident in the international standardization activities with several standards being already developed by the technical committee ISO/TC 163. As in the case of CEN standardization activities, this includes both standards dealing with individual aspects of the building (thermal performance of materials, products, components and buildings, calculation methods of individual building services, etc.) and standards dealing with the assessment of the overall energy performance of buildings (i.e., ISO 16346:2013). Therefore, nowadays, besides the description of the building envelope, a detailed description of the building services is also considered equally essential.

50.3.2 Shift to Life Cycle Thinking

As significant efforts in this area continue, the accuracy of the assessment of the operational energy of buildings increases and their regulation becomes more elaborate, making the design and construction of more energy-efficient building a norm in the building and real estate industry. This means that the relative importance of the

energy consumption associated with the nonoperational stages of a building, the so-called embodied energy, is becoming larger. For example, research has shown that the embodied energy in modern, well-insulated, energy-efficient buildings can add up to 40% of the total life cycle energy consumption and can even exceed the operational energy in certain cases [9]. Considering also that some of the building materials used in energy-efficient concepts are themselves highly energy intensive to produce and have short lifetimes (and thus require frequent replacement), embodied energy is gaining importance also in absolute terms.

The analysis of a specific case study elaborated by Ascona GbR in collaboration with the authors for the purposes of the IEA EBC Annex 57 (and shortly presented here as an example) leads to the same conclusion [10]. The selected case study building is a German primary school located in Hohen Neuendorf, in the district area of Berlin, which was designed by the planning office IBUS to be a "plus energy" building (and with a final energy demand lower than the energy demand of a passive house – around 42 kWh/m^2 treated floor area/year) [11]. To this aim, a photovoltaic system of 410 m^2 was installed, while the heating system used is a wood pellet boiler. The ventilation and cooling is supported by an adiabatic system, and the lighting is done partly with the use of LED lights. The selected reference study period was 50 years. For the calculation of embodied energy demand, the life cycle stages of production (Modules A1–3, Fig. 50.2), replacement (Module B4, Fig. 50.2), waste processing and disposal (Modules C3–4, Fig. 50.2), and recovery/reuse/recycling potential (Module D, Fig. 50.2) of the building were considered. Construction elements and material contents were calculated with the help of LEGEP tool [12], and LCA data were taken from the German national database ökobau.dat (the 2013 version) [13].

The case study examined the trade-offs between embodied and operational impacts considering three different indicators: the nonrenewable primary energy consumption (PEnren), the total primary energy consumption (PEtot), and the global warming potential (GWP). From the analysis of the results (partly shown in Fig. 50.1), the following significant shares occurred for embodied impacts: 91% for PEnren, 44% for PEtot, and 88% for GWP. These figures clearly indicate the importance of the nonoperation life cycle stages, especially in the case of low-energy concepts.

The need to shift toward a life cycle approach to the quantification of the energy consumption of a building to reduce the overall energy impact of energy-efficient buildings has already been acknowledged by several organizations in the building industry (e.g., by RICS [14], ICE [15], etc.). A challenge is that there is still a lot of confusion in relation to the calculation and assessment of embodied energy, partly owing to the fact that there are no clear and commonly accepted definitions and system boundaries. An analysis of the existing definitions, system boundaries, as well as guidelines specific to different building-industry stakeholder groups dealing with LCA as a whole, or only with the aspects of embodied energy and embodied GHG emissions, can be found in Lützkendorf et al. [4]. The spectrum of definitions ranges from accounting only for initial embodied impacts resulting from the production of building materials and components (raw material extraction, transport, and manufacture) to accounting for the whole life cycle (production, construction,

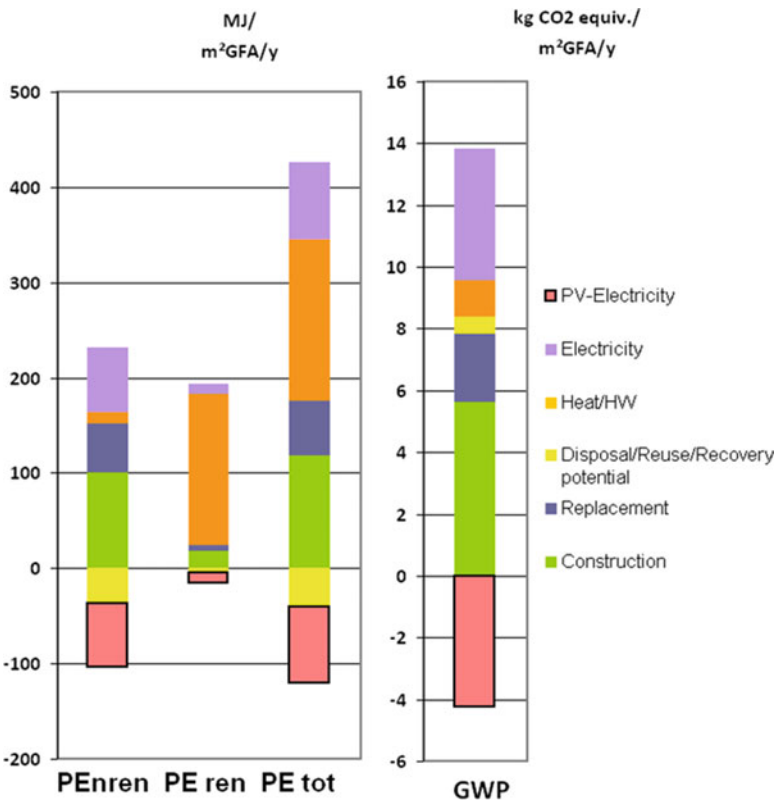

Fig. 50.1 Distribution of shares between embodied and operational impacts. The yellow column is in the "bonus" area (under 0) for PE due to recycling potentials of wood, plastic, and metals. The electricity produced by the PV system is highlighted and also shown in the "bonus" area

maintenance, and end of life of the building). Sometimes, even the net benefits of recycling and recovery are considered in this type of energy. There is no one-size-fits-all approach, and usually system boundaries are defined subjectively in each study to accommodate specific purposes.

There is already a well-established modular life cycle model from EN 15978:2011 (ISO 21931-1:2010 follows more or less the same concept) describing the different system boundaries in a consistent and widely accepted way. According to this model, a building's life cycle consists of four main stages: product stage (Module A1–3), construction process stage (Module A4–5), use stage (Module B1–7), and end-of-life stage (Module C1–4). There is also an additional and separate information module (Module D: benefits and loads beyond the system boundary). Each stage is further divided into several sub-modules. This is illustrated in Fig. 50.2.

In stages A and C, the included modules describe a linear sequence of building-creation and end-of-life processes, while in stage B, the processes occur usually in parallel (use, operational energy use, operational water use, etc.) or cyclically/

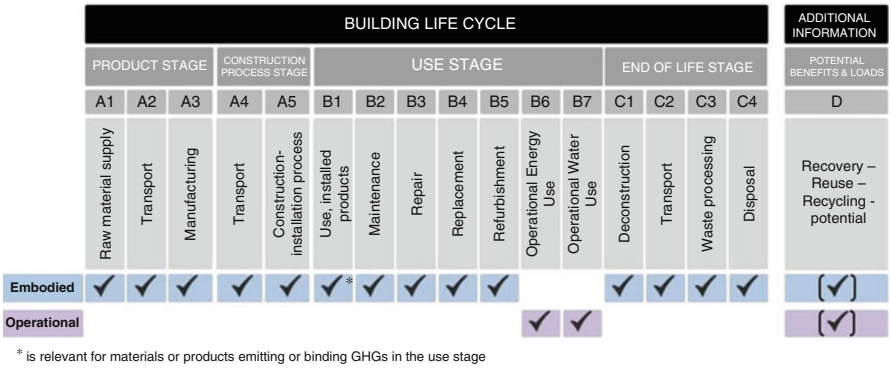

Fig. 50.2 Illustration of the life cycle of buildings based on the modular approach of EN 15978:2011. The embodied and operational components of the life cycle impacts are indicated. (The figure has been borrowed from Balouktsi et al. [16])

regularly during the building use (e.g., use – maintenance – use). This results in a diversity of interactions [16]. For example, replacement (B4) includes the production, transportation, and installation (replacement process) of the replaced components (Modules A1–5 for replaced components) and the end-of-life stage of the removed component (Modules C1–4 for the removed component). Assumptions for the useful service life and the reference study period have a significant influence on the embodied energy associated with this module, because they form the basis for defining the number of replacements of each building component. Furthermore, exploiting the recycling potential of recyclable construction products and materials (environmental benefits reported in module D) requires selective deconstruction processes (Module C1).

Therefore, for increased transparency in system boundary definition, declaring exactly the type and scope of the life cycle stages involved in every study is important and should be the norm in future.

50.4 Second Trend: Extension of the Assessment Scope

However, besides the gradual shift from operational to life cycle energy considerations, a more recent trend is the widening of the assessment scope to include additional environmental indicators in the assessment of buildings. Assessing only the performance of buildings from an energy point of view is a very limited scope. This goes along with the increasing consideration of global warming as an issue of high political importance. Meanwhile, the last decade has also seen the overwhelmingly increasing popularity of carbon footprint (CF), mainly among real estate industry stakeholders, as an easy to measure and understand indicator [4]. This was followed by the development of related international standards (e.g., ISO/TS 14067:2013 and ISO 16745:2015).

This trend is also evident in the most recent study by WBCSD [1] claiming that energy and GHG emissions are the most popular life cycle categories of indicators used by stakeholders in the built environment sector. However, an assessment of the life cycle-related environmental performance of buildings typically should not be focused solely on primary energy and GHG emissions but to cover a broad range of environmental issues. This is of crucial importance also from the point of view of considering potential trade-offs or target conflicts among different objectives.

A typical target conflict is between reducing the air exchange to save energy (environmental aspect) and ensuring an adequate indoor air quality (social aspect). A trade-off/target conflict effect can also be observed between the reduction of calculated GHG emissions by switching to wood-fired heating systems, on the one hand, and the increase in fine particulate matter as a result of this practice, on the other hand [17]. Particulate matter is relevant both for climate and health [18, 19]. In Germany, to reduce the possible adverse health effects associated with wood combustion for heating, regulations considering appropriate standards (lower threshold of emissions) and requirements (in production, quality, use, and maintenance) for such heating systems, especially for older models, have already been introduced since 2010 [20, 21]. Besides wood-based bioenergy, also the case of nuclear energy is controversial. Although it is an almost "carbon-free" source, the problem of safe long-term storage of nuclear waste has not been solved yet [22]. The indicator "amount of radioactive waste" is therefore important in order to adequately illustrate this problem.

With regard to renewable and energy-saving technologies (e.g., insulation materials, PV panels, etc.), the impact of extraction of critical raw materials for their production together with their waste management at the end of their life is of concern [23]. During these processes, possible toxic and harmful pollutants can be released into air, soil, and water. Moreover, it is still difficult to assess the impacts of current and future recycling procedures due to lack of data and inadequate experience. For example, although some decades from now the amount of PV waste will be significant, recycling PV systems is currently challenging due to the associated high costs, among others [23]. Another potential conflict arises between using bioenergy as a renewable energy carrier and the land use required to produce such bioenergy.

Future consideration of the potential of a building for deconstruction and disassembly is a new and challenging concept for design teams and clients. The recycling and reuse potential of materials and products cannot be fully exploited, if the dismantling processes are complicated. Uncertainty relating to end-of-life scenarios for building materials suggests that there may be value in establishing the disassembly potential of a building and its key elements as a prerequisite for claiming Module D benefits according to EN 15978:2011 and EN 15804:2012. However, there are currently no mature indicators to measure disassembly, but it is a concept that is already practiced for some building types in the Netherlands [24]. This problem could be possibly solved in the future with the introduction of ISO 20887 Design for Disassembly and Adaptability of Buildings that is currently under development by TC 59/SC17/WG1.

All the above trade-off effects suggest that there is a need to go beyond just energy and GHG analyses in sustainability assessments and, at a minimum, include all the environment- and health-related consequences of all the energy sources utilized by a building. A balance between embodied and operational impacts, including the consideration of local climate and health and well-being factors, must be aimed for. It is important to consider this balance in the light of the relationships between different stakeholders (e.g., planning authorities, owners and occupiers, financers, insurers), who may have many conflicting interests.

However, this is only the beginning. This can be seen as the first step toward making life cycle-based sustainability assessments an integral part of the design process of buildings. This means that in future, all the environmental, economic, and social issues/indicators (and thus the full spectrum of target conflicts) identified in the current CEN TC 350 and ISO/TC 59/SC 17 standards should be covered and investigated along the entire building life cycle.

50.5 Methodological Issues and Recommendations for Practice

Making life cycle sustainability assessment approaches the standard practice in the building industry takes several steps. First, it is essential to improve the description of the energy performance of buildings in their operation and include information beyond the final and useful energy, which is nowadays used as the basis. It is important to identify separately the final energy need per final energy source and to avoid summing up all the final energy needs into a total value. Additionally, the following information should be given as the minimum requirement, e.g., in Energy Performance Certificates (EPCs):

- Primary energy demand, nonrenewable
- Primary energy demand, renewable
- GHG emissions
- Emission of other air pollutants
- Amount of radioactive waste
- Thermal comfort in the heating period
- Thermal comfort in the cooling period

For the determination and presentation of GHG emissions, an orientation toward ISO 16745: 2015 “Environmental performance of buildings – Carbon metric of a building – Use stage” is recommended. Second comes the transition to environmental performance assessments covering the complete life cycle of buildings. Already standards are available for this purpose within ISO/TC 59/SC 17 (mainly ISO 21931-1:2010) and CEN TC 350 (mainly EN 15978:2011). Selected standards out of these sets of standards are currently under review. For stakeholders wishing to make this transition gradually through initially focusing on the identification and

assessment of embodied energy and GHG emissions as part of the environmental performance of buildings, the results of the international project IEA EBC Annex 57 "Evaluation of Embodied Energy and CO_2 Equivalent Emissions for Building Construction" can be used (see also [25]). The ultimate aim should, however, be the assessment of the contribution of buildings to sustainable development. This should be based on the core list of indicators according to ISO 21921-1:2011 – entitled "Sustainability in building construction – Sustainability indicators – Part 1: Framework for the development of indicators and a core set of indicators for buildings."

50.6 Discussion and Conclusion

The sole consideration of the operational energy performance of buildings is no longer sufficient to meet all sustainable development goals. There is always the danger of ending up with sub-optimal solutions and ignoring the conflicting goals. In order to avoid such problems, it is sensible to fully cover the building and its life cycle, on the one hand, and to include several criteria for determining and assessing the use of resources, as well as the effects on the environment and health, on the other. However, this also raises new questions such as: (1) Is there a trade-off between the operational and embodied energy? (2) Can benchmarks for resource consumption and environmental impacts be identified and used for the complete life cycle? (3) Is there a weighting factor for effects that occur far in the future? (4) How can the technical progress be considered in life cycle models? (5) What data and tools exist to support designers in a life cycle analysis? These questions, among others, will be discussed in the recently launched international project IEA EBC Annex 72 [26].

From the authors' point of view, the inclusion of embodied impacts (embodied energy and embodied GHG emissions) is the next logical step toward the further development of the EPBD in Europe. In the German climate protection plan 2050 [27], it is already proposed to include issues of sustainable construction in the consideration of the improvement of energy efficiency and to take into account the life cycle phases upstream and downstream of the use phase in the design and assessment of buildings. In summary, based on the recommendations provided within the context of this paper, to strive for an almost climate-neutral building stock (one of Germany's 2050 goals [27]) is not sufficient. Energy-saving and climate-neutral building concepts should always be subject to complete sustainability assessments in future.

References

1. WBCSD (2016) The business case for the use of life cycle metrics in construction and real estate, World Business Council for Sustainable Development, Geneva, Switzerland
2. Balouktsi M, Lützkendorf T (2016) Energy efficiency of buildings: the aspect of embodied energy. Energ Technol 4:31–43

3. European Commission (2014) Communication from the Commission to the European Parliament, the Council, the European Economic and Social Committee and the Committee of the Regions on resource efficiency opportunities in the building sector, The European Commission, COM (2014) 445 final
4. Lützkendorf T, Balouktsi M, Frischknecht R (2016) Evaluation of embodied energy and CO2eq for building construction (Annex 57), Subtask 1: Basics, Actors and Concepts, Institute for Building Environment and Energy Conservation, Tokyo, Japan
5. EBC Annex 31 Energy Related Environmental Impact of Buildings, Link: http://www.iea-ebc.org/projects/completed-projects/ebc-annex-31/ Last accessed day: 20 Oct 2017
6. EBC Annex 57 Evaluation of Embodied Energy and CO2 Equivalent Emissions for Building Construction, Link: http://www.iea-ebc.org/projects/completed-projects/ebc-annex-57/ Last accessed day: 20 Oct 2017
7. Kolb B (1991) Aktueller Praxisratgeber für umweltverträgliches Bauen. WEKA Baufachverlage/Verlag für Architektur, Kissing
8. Crowther P (2001) Developing and inclusive model for design for deconstruction. In: Chini AR (ed) Deconstruction and materials reuse: technology, economic, and policy. CIB Publication 266, Proceedings of the CIB TG39, Wellington, pp 1–26
9. Dixit MK, Fernandez-Solis JL, Lavy S, Culp CH (2010) Identification of parameters for embodied energy measurement: a literature review. Energ Buildings 42:1238–1247
10. König H (2016) Analyse von Fallbeispielen zum IEA EBC Annex 57. Unpublished internal report
11. Legep, Energy-Plus School, Hohen Neuendorf, Link: https://legep.de/projekte/grundschule-niederheide-hohen-neuendorf/?lang=en Last accessed day: 20.10.2017
12. Legep, Link: https://legep.de/?lang=en Last accessed day: 20 Oct 2017
13. BMUB, ÖKOBAUDAT 2013, Link: http://www.oekobaudat.de/archiv/oekobaudat-2013.html Last accessed day: 06.03.2017
14. RICS (2012) Methodology to calculate embodied carbon of materials, RICS QS & Construction Standards, 1st edn, Coventry, UK
15. ICE (2015) Energy briefing sheet: embodied energy and carbon. Institution of Civil Engineers, London, UK
16. Balouktsi M, Lützkendorf T, Seongwon S, Foliente G (2016) Embodied energy and global warming potential in construction: perspectives and interpretations. In: Proceedings of CESB16 Prague, pp. 661–668, ISBN 978-80-271-0248-8
17. Boman B, Forsberg A, Jarvholm B (2003) Adverse health effects from ambient air pollution in relation to residential wood combustion in modern society. Scand J Work Environ Health 29:251–260
18. WHO (2015) Residential heating with wood and coal: health impacts and policy options in Europe and North America, World Health Organization, Copenhagen, Denmark
19. Smith KR, Frumkin H, Balakrishnan K, Butler CD, Chafe ZA, Fairlie I, Kinney P, Kjellstrom T, Mauzerall DL, McKone TE, McMichael AJ, Schneider M (2013) Energy and human health. Annu Rev Public Health 34:159–188
20. BMUB (2010) Erste Verordnung zur Durchführung des Bundes- Immissionsschutzgesetzes (Verordnung über kleine und mittlere Feuerungsanlagen-1. BImSchV). Bundesministerium für Umwelt, Naturschutz, Bau und Reaktorsicherheit, Berlin
21. Sutcliffe R, Orban E, McDonald K, Moebus S (2012) The German Energiewende: a matter for health? Eur J Public Health 26(4):707–712
22. Muradov N (2014) Liberating energy from carbon: introduction to decarbonization. Springer, New York
23. Latunussa C, Mancini L, Blengini G, Ardente F, Pennington D (2016) Analysis of material recovery from photovoltaic panels. Publications Office of the European Union, Luxembourg
24. Dodd N, Gama-Caldas M, Van de Vyver I, Stranger M, Dugrosprez O, Allacker K (2016) Summary findings and indicator proposals for the life cycle environmental performance, quality

and value of EU office and residential buildings, Joint Research Centre, European Commission, Seville, Spain
25. Birgisdottir H, Moncaster A, Houlihan Wiberg A, Chae C, Yokoyama K, Balouktsi M, Seo S, Oka T, Lützkendorf T, Malmqvist T (2017) IEA EBC annex 57 'evaluation of embodied energy and CO_{2eq} for building construction'. Energ Buildings 154:72–80
26. EBC Annex 72 Assessing life cycle related environmental impacts caused by buildings, Link: http://www.iea-ebc.org/projects/ongoing-projects/ebc-annex-72/ Last accessed day: 20 Oct 2017
27. BMUB (2016) Klimaschutzplan 2050, Klimaschutzpolitische Grundsätze und Ziele der Bundesregierung. Bundesministerium für Umwelt, Naturschutz, Bau und Reaktorsicherheit, Berlin

Chapter 51
Providing a Scientific Arm to Renewable Energy Cooperatives

Georgios Chalkiadakis, Charilaos Akasiadis, Nikolaos Savvakis, Theocharis Tsoutsos, Thomas Hoppe, and Frans Coenen

51.1 Introduction

Recent research on sustainable energy and development planning indicates a shift towards renewable energy resources, and the adoption of energy conservation techniques is gaining ground towards tackling energy poverty and meeting large-scale energy efficiency (EE) [1]. However, for EE to be attained, stakeholders (i.e. utility companies, grid regulators, end users) need to get actively involved.

One of the most significant parts of the current energy market is the European renewable energy sources cooperatives (REScoops). More than 2397 REScoops across Europe, collectively having more than 650,000 members,[1] provide participating citizens the opportunity to buy renewably generated electricity at fair prices, to democratically react with other members and co-decide the cooperative's future, and to be autonomous and independent with respect to energy. Given these features and benefits, REScoops organize events, such as meetings, conventions, etc., in order to raise their members' energy awareness. Thus, it is expected that when end users join forces in an energy cooperative, they become more active regarding energy conservation and efficiency.

[1]Data according to the European Federation of REScoops (REScoop.eu).

G. Chalkiadakis · C. Akasiadis · N. Savvakis · T. Tsoutsos (✉)
Technical University of Crete, Chania, Greece
e-mail: theocharis.tsoutsos@enveng.tuc.gr

T. Hoppe
TU Delft, Department of Multi-Actor Systems, Delft, The Netherlands

F. Coenen
University of Twente, Department of Government and Technology for Sustainability, Enschede, The Netherlands

S. Nižetić, A. Papadopoulos (eds.), *The Role of Exergy in Energy and the Environment*, Green Energy and Technology,
https://doi.org/10.1007/978-3-319-89845-2_51

This anticipated REScoops' "high energy efficiency potential" has, of course, to be realized and showcased in practice. To this end, the use of scientific tools and methods to (a) evaluate REScoops' EE performance and (b) boost their capabilities to actually achieve exceptional EE behaviour, is imperative so as they can meet their wider environmental, societal, and economic set targets. In particular, three key axes of scientific research are in interplay when one attempts to study and positively influence REScoops' EE behaviour. First, there is a need to employ statistical analysis tools to quantitatively assess the level of REScoops' EE effectiveness. Second, behavioural analysis techniques need to be used in order to support the statistical analysis findings and obtain additional quantitative as well as qualitative intuitions regarding REScoops' best practices (current and future ones). Third, *modern artificial intelligence* methods (including techniques from machine learning, game theory, decision theory, and multi-agent systems) can be key *(i)* to automate REScoop business and also *(ii)* to enable their participation in complex *demand-side management* schemes that require advance or real-time rational decisions regarding providing or consuming energy, in order to promote renewable energy use and avoid imbalances in the electricity grid load [2–4].

Indirect mirroring of this view, the REScoop Plus H2020 project (https://rescoop.eu/european-project/rescoop-plus) aims to gather available information and data from various European REScoops and demonstrate that participation in such a cooperative raises energy awareness and contributes to the accomplishment of the challenging goal of EE. Moreover, a central REScoop Plus goal is to promote a better understanding and cultivate the behavioural change of the cooperatives' engagement. In order for those goals to be met, it was essential to conduct a careful logging of and *statistical analysis* over the energy data stored by the REScoops, as well as the current state of their engagement in energy efficiency. Such tasks are imperative in order to support the claim that REScoop engagement promotes energy sobriety; and associate consumption reduction with specific behaviours, ICT tools, and EE practices. Second, it was essential to conduct an *in-depth behavioural analysis* regarding current EE practices and lay the ground for identifying "best practices" to be adopted. Third, there is a need to equip REScoops with modern *intelligent decision-aiding tools* that will assist them in their current business and expand it to include participation in automated demand-side management schemes. In the remainder of this chapter, we provide more intuitions on these key scientific axes and tools and showcase their use on the REScoop Plus project and other real-world settings.

51.2 Statistical Analysis of REScoops' Data and Behavioural Patterns

In this section, we present in brief the statistical analysis conducted in REScoop Plus. Specifically, we outline the methodology and statistical techniques used; and we present the key results of this analysis.

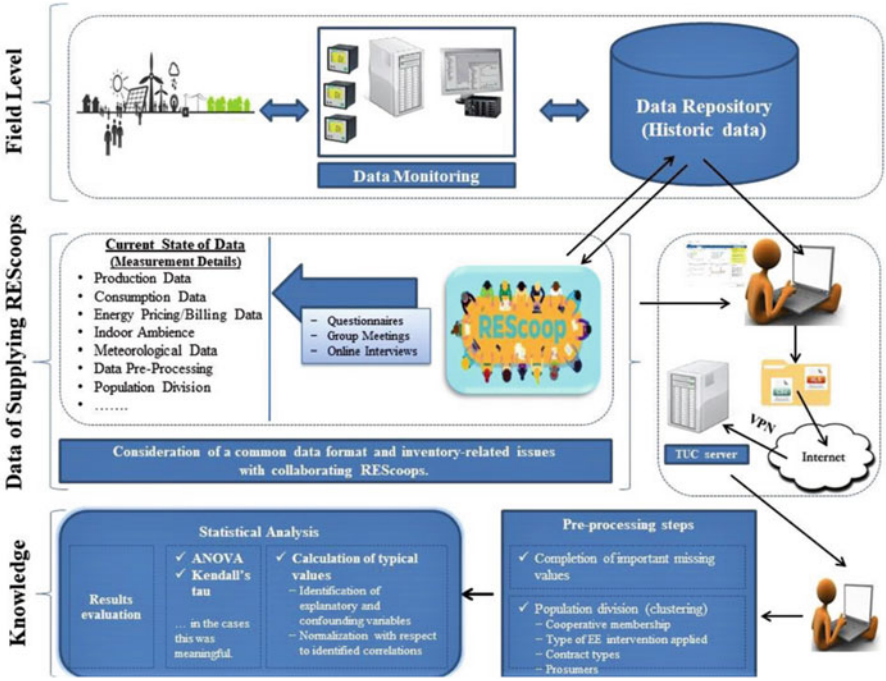

Fig. 51.1 Overview of a statistical analysis methodology for REScoops [5]

The design of a research methodology in order to conduct a statistical analysis of energy-related data is a complex process that requires significant technical expertise. There are many adjustments required in order to reach the optimum balance between reliability, accuracy, and significance. In this section, the methodological approach and critical issues to be considered are outlined. In brief, our approach in the REScoop Plus project consists of the following steps, also depicted in Fig. 51.1:

- Identification of the current state of the data from the participating REScoops
- Specification and adoption of a common data format and settling of inventory-related issues
- Receiving the datasets: Potential completion of values missing from third-party sources
- Analysing the development of the average yearly consumption for all cooperatives and separating all possible variables that might influence consumption (climate, habitual changes, etc.): Population clustering, identification of explanatory and confounding variables
- Validating the decrease in average consumption. Also, potentially checking whether there is a decrease in usage of conventionally produced energy (from non-renewable resources); performing hypothesis testing, following, e.g. n-way ANOVA [6] (includes identification of degree of correlation among variables); derivation of typical consumption curves for each cluster (includes normalization with respect to identified correlations)

51.2.1 Conducting the Actual Statistical Analysis

Given an identified methodology, one then needs to make choices regarding the actual statistical tools to be used for data analysis. In the REScoop Plus case, we utilize two well-known approaches, i.e. statistical hypothesis testing and analysis of variance (ANOVA). The latter is the main method we adopt in our work. According to this procedure, multiple subject groups are compared against each other with respect to average values and variances of certain measures [6]. For our purposes, the subject members are going to be divided into control and testing groups, i.e. some are going to apply EE interventions, while others are not. ANOVA is going to be used to assess the effectiveness of each EE intervention type when applied to different member groups. In some detail, we can use ANOVA to test how different EE interventions and incentives (factors) influence consumption for each energy end user (observations). By filling the ANOVA table with the observations corresponding to the various factors, we will find out the correlations between these variables and discover if the factors are additive. Also, if information on non-REScoop members is available, we can use ANOVA to compare the performance of groups of REScoop members with that of non-REScoop ones.

However, the exact analysis methodology strongly depends on the actual data that REScoops offer; thus, the final decision regarding the statistical analysis method is always anticipated to be subject to changes until the actual datasets are obtained. Also, ANOVA assumes that the data come from normal distributions, which is not always the case when it comes to electricity consumption data. Alternative methods for hypothesis testing are the Student's *t*-tests and the calculation of *p*-values [6].

To summarize, the statistical analysis technique used in REScoop Plus is in general as follows:

(a) Divide samples (i.e. members and clients of REScoops) into similarity groups with respect to (*wrt.*) factors such as contract type, type of EE intervention applied, etc.
(b) For each group: *(i)* calculate normalized average consumption for each individual consumer before and after the application of the EE intervention in question; *(ii)* calculate average reductions in normalized average consumption as a result of the EE intervention; and *(iii)* test statistical significance with appropriate techniques from the literature (according to the assumptions that the available data fulfil).
(c) Draw conclusions regarding the effectiveness of each EE intervention.

51.2.2 Preliminary REScoop Plus Project Statistical Analysis Results

In this section,[2] we present the results from the data gathering process, as well as some results regarding *(i)* a large Danish district heating cooperative, EBO, and *(ii)* a large Belgian electricity cooperative, Ecopower.

The submitted EBO dataset included monthly heating consumption values from 300 residential customers, which are cooperative members, for the period of May 2012 to September 2016. Additionally, EBO responded to past yearly consumption values of the members before joining EBO and also with a dataset from a non-cooperative company, containing monthly data samples that indicate the consumption of 1000 non-cooperative members. Most EBO member measurements were accompanied by information regarding the buildings' surface in square metres, the number of residents, additional building characteristics, and meteorological data, e.g. minimum, maximum, and average temperature values and heating degree days. The EE intervention that EBO has applied to their members is termed as "technical support". This intervention includes technical inspections by experts, suggestions for equipment or insulation upgrades, etc. As our results illustrate, this particular EE intervention was effective in reducing consumption when applied to the cooperative members. In particular, the treated customers achieved *20% reductions in their monthly kWh normalized by heating degree days' consumption on average*, after receiving the intervention. This indicates that "technical support" can be proven a valuable tool for other REScoops that also deal with district heating. Regarding statistical significance, we observed a $p\text{-value} < 0.05$, indicating that there is a significant difference between the sample distributions of the consumption measurements before and after applying this particular EE intervention. In addition, *Kendall's τ value* was <1, meaning that the two vectors containing the values before and after the EE intervention are only to an extent correlated; thus, given the observed significant reduction, actual changes in consumption behaviour have indeed occurred. Furthermore, our results show that the customers who became cooperative members *reduced their consumption (in kWh/m^2) by 19.92%*, as compared to the time before joining. Receiving technical support led to *a reduction of 21.42%* in *average heating energy consumption in $kWh/(m^2 * HDD)$* and to *reduced CO_2 emissions by 274.13 kg* on average for the receiving members [5].

As far as Ecopower is concerned, consumption measurements were gathered on a yearly basis. The number of customers with measurements was significantly larger, totalling to 33,596 customers. The reported period regarded the years 2011–2015, and the number of residents for each building was included. Now, although Ecopower does not gather monthly data itself, some of their customers have

[2]We note that we actually have preliminary results for seven REScoops across Europe, but presenting these is obviously not the focus of this chapter. However, the reader can find those results in the public deliverables of the REScoop Plus project.

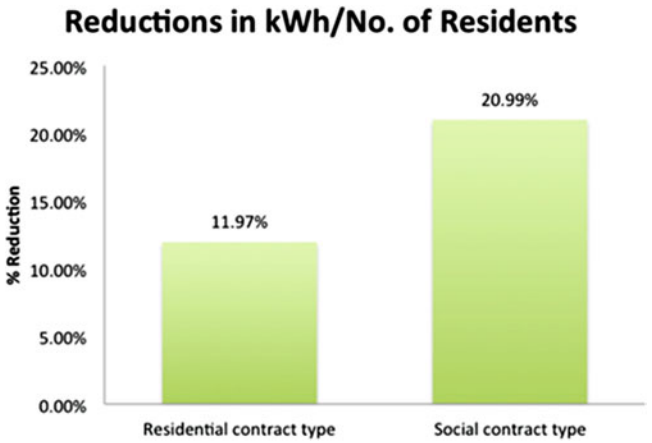

Fig. 51.2 Reductions in average yearly consumption of Ecopower customers adopting EnergieID [5]

Table 51.1 Significance tests regarding yearly average reductions achieved in *kWh/No. of residents* after applying the EnergieID EE intervention (two main categories of Ecopower customers) [5]

Contract type	Significance test	Result
Residential	p-value	2.105e−07
	Kendall's τ	0.572
Social	p-value	0.256
	Kendall's τ	0.578

subscribed to EnergieID,[3] a consumption monitoring and analysis software service, which includes the gathering of monthly consumption data, and also the buildings' surface in square metres, which is used as a normalizer for the consumption of these members. EnergieID service itself is the EE intervention analysed for its effectiveness in reducing electricity consumption [5].

Reduction results after applying the EnergieID EE intervention are summarized in Fig. 51.2 for two main categories of Ecopower customers and related significance tests are presented in Table 51.1.

Given these results, it is obvious that subscribing to EnergieID leads to significant reduction in the yearly average measurements for both main Ecopower contract types. Moreover, Ecopower clients who became cooperative members produced *235.12 fewer kg of* CO_2 *per year* [5].

[3]Energie ID is a digital platform for monitoring energy-related data, which offers the ability to consumers to manage efficiently their energy consumption.

Table 51.2 Presentation of integrated intervention framework

Strategy Types	Intervention	Type of policy instrument
Antecedent strategies	Commitment	Symbolic and hortatory tools
	Goal setting	Symbolic and hortatory tools
	Information Modelling	Capacity tools Capacity tools
	Tariffs Collective purchasing	Incentive tools Incentive tools
	Services	Incentive tools
Consequence strategies	Feedback Learning tools	Capacity tools
	Rewards	Incentive tools

51.3 Behavioural Analysis of REScoops Energy-Saving Policies

The transition to sustainable energy systems is not only a technological and economic challenge. It also requires a behavioural change, so that energy users use energy in more rational and efficient ways. Users' behavioural determinants can be targeted with policy measures to *(a)* encourage voluntary behaviour change and/or *(b)* to change the conditions under which they make decisions on energy use. Although the activities that REScoops undertake to some extent resemble those of other organizations, because of their particular organizational and business model as citizens' initiatives, REScoops, the cooperative model, are assumed to be well positioned for activities to influence and help their members and potential other energy consumers to save energy. This section discusses arguments why the REScoop model in energy supply can be an important contributor to reduce energy use by their members. Further, this section discusses measures that have been undertaken by REScoops studied in the REScoop Plus project.

REScoops use particular business and organizational models based on the cooperative model, a jointly owned and democratically controlled enterprise (see below). Therefore not all of the potential interventions are conceivable, like regulations. This raises the question, *whether REScoops are in a relatively good position to take certain measures and succeed in persuading customers to lower their energy consumption level*. In the REScoop Plus project, we compare in the first place REScoop members with other (commercial) energy users and non-REScoop members and not REScoops with other energy agents. We theorize that if REScoop members save more energy than conventional energy consumers, this might be due to one (or a combination) of the factors outlined below.

51.3.1 The Added Value of REScoops as Locally Based Energy Communities

The following arguments can be given why REScoops as a particular organizational or business model are in a relatively good position to stimulate energy among householders based on the lessons drawn from best practices (e.g. [7, 8]), REScoop policy documents [9], and the academic and professional literature (e.g. [10, 11]). We formulate seven arguments why the REScoop model in energy supply can be an important contributor to reduce energy use by their members [12].

A first argument would be that REScoops are in a good position to stimulate energy saving because of the scale level of their activities, which is mostly on the local level, i.e. close to citizens. Even if REScoops are national organizations, they often work with locally organized groups. In the literature on local sustainability, often the argument of proximity to citizens is used as an argument to take measures at a lower geographical level [13]. The REScoop model provides a good scale to run relevant local energy efficiency projects, such as investing in thermal insulation of dwellings, and that this would be a source of inspiration for others, including non-members [12]. Research shows that participating in decision-making related to sustainable consumption makes people more willing to cooperate in implementation actions and contribute to attaining energy efficiency goals [14].

A second argument would be that REScoops have a specific capacity and critical mass to stimulate energy saving among their members. Implementing and using measures and equipment to save energy takes a lot of time and requires both technological expertise and bureaucratic competence (e.g. to grant legal permits or subsidies). Sharing experiences, not reinventing the wheel, and the advantages of participating in activities together (in terms of costs or time) add to the capacity for action. For REScoops, it means that by facilitating consumers with measures like technological advice, administrative support, or upfront investments, a larger group of consumers can be motivated to actually participate in energy-saving activities. REScoops also have a certain critical mass to acquire the necessary expertise and motivate and assist citizens who are less motivated than those who are devoted to pursue sustainability goals [12]. A third argument we can label is social networking. REScoops are in an excellent position to share and link their activities, including their energy-saving actions, with other local actors like schools, sport clubs, local business firms, and housing associations. These organizations also have a stake in the energy and low carbon debates and are willing to take their own responsibility [15]. REScoops do not pursue profit maximization and often have similar idealistic and collective, community goals. Moreover, given their expertise, REScoops are often viewed by the other local organizations as good partners for energy and low carbon projects [12].

A fourth argument is the potential for awareness raising and education of the REScoop members. REScoops are in a good position to make their consumers more aware of energy use. They can also educate the larger community on the importance of energy efficiency by organizing and showing visible pilot projects in public

buildings such as office buildings and schools, but also in individual consumer projects, and, for instance, the local community building [7]. Becoming a member of a REScoop presupposes already to be more aware of the importance of using energy than just being a passive consumer of a traditional energy supplier [12]. A fifth argument would be that REScoops are not only in a good position to make consumers aware of energy use, but they also tend to set energy saving as a social norm, viz. energy not only becomes a significant issue to the consumer and his/her household, but relative energy use and savings become less anonymous actions once users share their experiences with peers [16]. In this sense, REScoop energy-saving goals and average group energy-saving behaviour can become an element of goal steering, as a reference point for behaviour. A sixth argument is that REScoops are in a good position to generate trust towards citizens for them to take measures themselves and invest in energy efficiency or renewable energy technology appliances. This is especially important if these activities involve financial risks to be taken by the consumers in terms of making investments. Dealing with REScoops, who are often viewed as a very trustworthy partner to give advice and supply energy systems and appliances, might make people more willing and able to take investment risks [17].

Finally, in particular cases, e.g. "energy islands", the common argument in sustainable energy production might occur. Commons are natural resources which are accessible to all members of a given community; they are not privately owned and therefore can potentially be consumed by all of them, presenting the risk of overexploitation and depletion of the natural resource pool [18]. If the energy produced by the REScoop is seen as a common good, saving energy by individual consumers also makes it possible for more people to make use of the available renewable energy production [12].

51.3.2 Energy-Savings Measures Used by REScoops

In this section, we summarize what energy-saving tools and actions thus far have been developed by the REScoops participating in the REScoop Plus project and subdivided into antecedent and consequence strategies [12, 19].

Figure 51.3 shows the number of a large variety of *social and communicative antecedent strategies* we found among eight REScoops that were analysed. Most commonly used antecedent interventions concerned awareness raising, education, and behavioural change campaigns. Information (newsletters, social media, etc.) and (local) ambassadors were also used but more infrequently. Overall, 16 different interventions were identified.

There were certain incentive antecedent strategies that were used, most commonly transparent and single pricing (of renewable energy sold to householders), simple tariffs, and collective purchasing. Bonuses, giving out shares, and lending of money were also used only incidentally.

Fig. 51.3 Overview of social and communicative interventions (antecedent strategy)

Fig. 51.4 Overview of (technical) feedback tools used by REScoop

The infrequent use of economic incentives might point to the fact that many of the REScoops observed were in the phase of starting off and experimenting with local projects and related business models. Finally, it is surprising that only one of the studied REScoops mentioned giving out shares as an incentive, since this forms a key principle of cooperatives.

The main *technical tools* deployed by the studied REScoops cover both direct and indirect feedback tools (see Fig. 51.4). At least half of the REScoop surveyed conveyed the use of consequence strategies, i.e. electronic billing, using online client accounts, smart metering, and organizing energy audits. As may be expected with consequence strategies, all tools and interventions used were technical or technology supported, often using smart (ICT) technology. Feedback from the REScoop staff to their members appears to mostly happen indirectly, i.e. via billing and online accounts on a web-based platform. There is no groupwise feedback or learning systems.

The overview shows that particular many antecedent strategies were used by REScoops. Compared with overviews of measures used by other energy agents,

these measures are however not unique [20]. Particularly, many of the information tools used by REScoops are rather similar to what other energy supplier or governments and NGOs use. Consequence strategies were used less than antecedent strategies. Notwithstanding this fact, the consequence strategies' use varied a lot, and included both direct and indirect feedback tools. Consequence strategies were found to be well supported by online platforms and smart technology (i.e. smart metering). However, many REScoops are just on the verge of using feedback tools. REScoops were found to use a lot of technical equipment to provide feedback on energy consumption to their customers. REScoop members are more willing to use this equipment. This is not only technical equipment (but also uses other feedback mechanisms).

Measures are related to attaining goals, and one measure could serve different goals. Strictly speaking, we look for measures that address the goals investing in RES (producing more renewable energy) and saving energy. However, our inventory showed that for the studied REScoops, also other goals like delivering (energy) services, enlarging the size of total REScoop membership, stimulating the green energy transition, and climate change awareness raising are important. In the end, these other goals will contribute to the attainment of the first two main goals. A mix of existing policies aimed at stimulating reductions in energy can be called a policy package [21]. The overview is based on single measures or interventions on not measure packages. Additionally, one has to address situational factors like laws, regulations, neighbourhood factors, dwelling size, household size, income, employment status of occupants, ownership, stage of family life cycle, geographical locations, and personal comfort. Studies show that they all correlate significantly with household energy consumption (e.g. [22]).

51.4 Intelligent Agents and Game Theory of Demand-Side Management

Managing conventional electricity grids requires the continuous control of energy supply in real time, in order to keep the balance with demand undisturbed regardless of the demand levels. However, the integration of renewable energy sources (RES) entails that generation cannot be easily controlled because it heavily relies on weather conditions and is performed by large numbers of RES distributed across the network [2]. Moreover, electricity consumer preferences are complex due to distribution-related constraints and variable electricity prices and will become even more complex in the future due to electric vehicles' (EVs) usage [23]. All these call for the widespread use of effective demand-side management (DSM), that is, the use of schemes aiming to move electricity demand, to periods where consumption is lower or RES production more abundant [2, 4, 24].

This increased complexity requires replacing human intervention with intelligent agents and multi-agent systems [25]. By incorporating intelligent autonomous

agents employing artificial intelligence and machine learning in the picture, important procedures—such as forecasting, real-time monitoring, and immediate reaction to emergent situations—become more effective, and reliability can be improved [3]. At the same time, although large industrial facilities might be, at least in principle, easy to incorporate in DSM schemes, this does not hold for every type of consumer. Especially for residential customers, daily habits can create negative incentives for DSM participation [26], since behavioural change also impacts customer comfort, not only finances. Here, intelligent agents can also be used to weigh individual costs and preferences, optimize individual consumption schedules, and deliver positive DSM impacts to scheme participants [3].

Now, optimizing individual consumption schedules is not enough: individual consumption is a very small world aggregate; thus, a single individual's actions induce imperceptible changes; and even when all individual actions do coordinate, herding effects may occur and new imbalances between supply and demand can arise at different points of the demand curve [3]. As a result, DSM operations have to be not only large scale but also coordinated. To this end, DSM contributors often join forces in cooperatives or virtual power plants so as to either consume or produce electricity in a coordinated fashion, mimicking the performance of a single large entity meeting the grid requirements [4]. The smooth operation of such entities and schemes is aided by the existence of rules and incentives that lead potentially selfish individuals to adopt a cooperative behaviour and coordinate their actions.

This is exactly the problem studied by mechanism design (MD) [27], a subfield of game theory that explores how to design a setting (viewed as a game) so that rational actors (or players) adopt a behaviour that helps meet the designer's objectives. In other words, MD schemes seek to offer incentives or counter-incentives for achieving desired social outcomes, to individuals that aim to maximize their own utility. Typically, such schemes strive to be incentive compatible, meaning that participants are incentivized to be truthful regarding their private preferences and that "gaming" the scheme leads to worse outcomes for "misbehaving" actors. As such, MD can be used to create DSM schemes that promote more efficient network operation, by granting economic and/or social gains to the participating individuals. Of course, scheme participation is determined by each actor individually; and the incentives must be sophisticated, so as to drive changes to human consumption habits while maintaining the profitability of energy sector businesses.

The emergence of effective, large-scale DSM is not a thing for the future. The requirement for large-scale, coordinated consumer action lies at the foundations of the fledging REScoops industry. REScoop activities include producing and trading renewable energy and also, already to some extent, providing DSM services. As such, they can naturally benefit from incorporating AI, MD, and other GT methods, in order to select the most appropriate participants for DSM actions, take individual preferences into account, and redistribute profits in a "fair" manner, rewarding truthful and accurate participants more than "unhelpful" and "misbehaving" ones.

An example of a day-ahead "electricity consumption shifting" scheme that employs mechanism design and machine learning solutions and which can be potentially adopted by REScoops that envisage expanding their business to

demand-side management appears in [28]. Results presented there, obtained via simulations over datasets including real consumption data from a Greek municipality and real production data from a Spanish renewable energy generation site,[4] indicate that *(i)* the consumption curve can be effectively trimmed and that *(ii)* participating consumers can actually enjoy considerable monetary gains. Specifically, a REScoop that adopts DSM can reduce the daily peak load by 85.99% on average. This is achieved by shifting the consumption of 1.2 MWh and results in almost half the cost per kWh, for consuming this energy during nonpeak hours throughout the day. In more detail, cooperative members that participate regularly, and consistently meet their consumption shifting promises, achieve up to 19.3% monthly bill reductions in a typical industrial case. Highly engaged residential members manage to reduce their monthly bills by 22.67%.

51.5 Conclusions

Providing state-of-the-art scientific solutions to the fledging REScoops industry is key to REScoops' viability and success in meeting their goals, including realizing their anticipated energy efficiency potential. In turn, such a success will be a significant step towards a sustainable energy future. To this end, in this chapter, we identified three axes of scientific research, deriving from various scientific disciplines, which can collectively provide the aforementioned solutions. We demonstrated how solutions linked to these axes can be applied to real-world REScoops' problems and showed that these solutions can actually provide benefits to real-world REScoops and their members. Naturally, there is a great deal of work remaining to be done, in order to improve existing scientific methods and test them in the real-world, even more extensively, and in order to communicate these and related ideas effectively to REScoops and the wider public. In any case, we are convinced that science working hand in hand with the REScoops industry will result to outcomes beneficial to our societies at large.

Nomenclature

AI, MD, GT	Artificial intelligence, mechanism design, game theory
ANOVA	Analysis of variance
DSM	Demand-side management
EE	Energy efficiency
HDD	Heating degree days
ICT	Information and communications technology
REScoop	Renewable energy sources cooperative

[4]The dataset comprised 8000 consumers from Kissamos, Greece, and wind and solar generator production patterns from Galicia, Spain. Please see [28] for more details.

References

1. Schüle R, Arens C, Breuer T, Fülöp O, Höfele V, Rudolph F, Becker D, Jaeger J, Jaworski P, Kleßmann C (2009) Energy Efficiency Watch Final Report on the Evaluation of national energy efficiency action plans. http://www.energy-efficiency-watch.org/
2. Strbac G (2008) Demand side management: benefits and challenges. Energy Policy 36 (12):4419–4426
3. Ramchurn SD, Vytelingum P, Rogers A, Jennings NR (2012) Putting the 'smarts' into the smart grid: a grand challenge for artificial intelligence. ACM Commun 55(4):86–97
4. Akasiadis C, Chalkiadakis G (2013) Agent cooperatives for effective power consumption shifting. In: Proceedings of the 27th AAAI conference on artificial intelligence (AAAI-2013), Bellevue, WA, USA, pp 1263–1269
5. Akasiadis C, Savvakis N, Mamakos M, Hoppe T, Coenen F, Chalkiadakis G, Tsoutsos T (2017) Analyzing statistically the energy consumption and production patterns of European REScoop members: results from the H2020 project REScoop Plus. In: 9th international exergy, energy and environment symposium (IEEES-9) conference proceedings, Split, Croatia, pp 372–378
6. DeGroot MH, Schervish MJ (2010) Probability and statistics, 4th edn. Addison-Wesley, Reading. ISBN 0-321-50046-6
7. Hoppe T, Graf A, Warbroek B, Lammers I, Lepping I (2015) Local governments supporting local energy initiatives; lessons from the best practices of Saerbeck (Germany) and Lochem (the Netherlands). Sustainability 7(2):1900–1931
8. Hufen J, Koppenjan J (2015) Local renewable energy cooperatives: revolution in disguise? Energy Sustain Soc 5(1):1–18
9. REScoop.eu REScoop.eu (2016) Liege, Retrieved from https://rescoop.eu/
10. Bauwens T (2016) Explaining the diversity of motivations behind community renewable energy. Energy Policy 93:278–290
11. Walker G, Devine-Wright P (2008) Community renewable energy: what should it mean? Energy Policy 36(2):497–500
12. Coenen F, Hoppe T (2016) D3.1 report on specific tools of supplying REScoops in Europe. Horizon 2020 project 'REScoop PLUS'. Grant agreement number 696084. University of Twente/Delft University of Technology, Enschede/Delft, pp. 1–82.
13. Coenen F (2009) Local agenda 21: 'meaningful and effective' participation? In: Public participation and better environmental decisions. Springer, Dordrecht, pp 165–182
14. Coenen F, Huitema D, Woltjer J (2009) Participatory decision-making for sustainable consumption. In: Coenen F (ed) Public participation and better environmental decisions. Springer, Dordrecht, pp 89–110
15. Seyfang G, Park JJ, Smith A (2013) A thousand flowers blooming? An examination of community energy in the UK. Energy Policy 61:977–989
16. Abrahamse W, Steg L, Vlek C, Rothengatter T (2005) A review of intervention studies aimed at household energy conservation. J Environ Psychol 25:273–291
17. Walker G, Devine-Wright P, Hunter S, High H, Evans B (2008) Trust and community: exploring the meanings, contexts and dynamics of community renewable energy. Energy Policy 38(6):2655–2663
18. Hardin G (2009) The tragedy of the commons. J Nat Res Policy Res 1(3):243–253
19. Hoppe T, Coenen FHJM (2016) Exploring interventions and tools used by REScoops to lower householders' energy consumption and stimulate investment in RES projects. Paper presented at the Annual Work Conference 2016 of the Netherlands Institute of Government (NIG), 24 November 2016, University of Antwerp, Department of Political Sciences, Antwerp, Belgium. Panel session on 'Energy and climate governance', pp. 1–27.
20. European Environment Agency (2013) Achieving energy efficiency through behaviour change: what does it take?. EEA technical report no 5
21. Kerna F, Kivimaaa P, Martiskainen M (2017) Policy packaging or policy patching? The development of complex energy efficiency policy mixes. Energy Res Soc Sci 23:11–25

22. Frederiks ER, Stenner K, Hobman EV (2015) The socio-demographic and psychological predictors of residential energy consumption: a comprehensive review. Energies 8(1):573–609
23. Finn P, Fitzpatrick C, Connolly D (2012) Demand side management of electric car charging: benefits for consumer and grid. Energy 42(1):358–363
24. Urieli D, Stone P, (2016) Autonomous electricity trading using time-of-use tariffs in a competitive market. In: Proceedings of the 30th AAAI conference on artificial intelligence (AAAI-2016), Phoenix, AZ, USA, pp 345–351
25. Palensky P, Dietrich D (2011) Demand side management: demand response, intelligent energy systems, and smart loads. IEEE Trans Ind Inform 7(3):381–388
26. Spence A, Demski C, Butler C, Parkhill K, Pidgeon N (2015) Public perceptions of demand-side management and a smarter energy future. Nat Clim Chang 5(6):550–554
27. Nisan N (2007) Introduction to mechanism design. In: Algorithmic game theory. Cambridge University Press, Cambridge, pp 209–242
28. Akasiadis C, Chalkiadakis G (2017) Cooperative electricity consumption shifting. Sustain Energy, Grids and Netw 9:38–58

Chapter 52
Potential of Energy Performance Contracting for Tertiary Sector Energy Efficiency and Sustainable Energy Projects in Southern European Countries

Maria Frangou, Maria Aryblia, Stavroula Tournaki, and Theocharis Tsoutsos

52.1 Introduction

The European Union (EU) is bounded to a 20% reduction of overall energy consumption by 2020, according to the 2012/27/EU Energy Efficiency Directive. With the new package of measures, announced on 30 November 2016 [1], the EU wants to lead the clean energy transition, not only adapt to it, by putting energy efficiency (EE) at first, achieving global leadership in renewable energies and providing a fair deal for consumers. The European Commission proposes a 30% binding energy efficiency target by 2030, with a simultaneous cut in CO_2 emissions by at least 40% and an increase of renewable energy sources (RES) share to at least 27% of the final energy consumption. The package includes proposals for the revisions of the Energy Efficiency Directive, the Energy Performance of Buildings Directive, the Renewable Energy Directive and the Electricity Directive, as well as measures on eco-design and others.

Even though the EU is on its way to reaching the 20% primary energy-saving target by 2020, there is still a risk that hinders the efforts of the EU member states to stick to their commitments and that is the insufficient public and private investment in EE. Indeed, financial barriers are commonly reported as the main barriers to realize EE projects, especially for SMEs in the tertiary sector.

Energy consumption in the tertiary sector increased significantly in the early 2000s and was then rather stable until 2008. In 2009, it decreased by 2,3%, as a result of the EU policies and the member states efforts to increase energy efficiency, as well as due to the economic recession. Different trends are observed within the

M. Frangou · M. Aryblia · S. Tournaki · T. Tsoutsos (✉)
Renewable and Sustainable Energy Systems Laboratory, School of Environmental Engineering, Technical University of Crete, Chania, Greece
e-mail: theocharis.tsoutsos@enveng.tuc.gr

S. Nižetić, A. Papadopoulos (eds.), *The Role of Exergy in Energy and the Environment*, Green Energy and Technology,
https://doi.org/10.1007/978-3-319-89845-2_52

EU. Although the energy intensity has been decreasing in most countries, several Southeast and Mediterranean countries present an increasing trend. The data suggest that there is a significant potential for energy efficiency improvement in the tertiary sector of these countries. However, in the current economic stagnation, difficult access to financing, combined with a limited investors' confidence, slows down the pace of investments in EE.

In this context, flexible financial schemes and mechanisms can contribute to mobilize funds from the financial sector to EE projects. Such a mechanism is Energy Performance Contracting (EPC), which offers an integrated solution for financing, planning, installing and monitoring of EE measures. Even though the EPC market is working relatively well in several EU countries (such as Germany, Sweden and Austria), lighthouse projects are still rare in the tertiary sector of Southern European countries. In order to increase trust amongst involved parties and unlock access to third-party financing, proper certification, validation and assessment tools are required [2].

52.2 EPC Demand Insight

52.2.1 Overview of EPC Demand in South Europe

In this part, the results of a demand analysis study, which included more than 180 interviews with tertiary sector representatives, EPC providers/facilitators and financial institutions in six Southern European countries, are presented. The study [3] was carried out in the context of the Trust EPC South European initiative. The analysis included also a review of the National Energy Efficiency Action Plans, statistical data and strategic documents.

Electricity and natural gas are the most used energy forms and represent 86% of overall energy needs of the tertiary sector of the analysed countries (Fig. 52.1). Electricity is used for cooling, heating and domestic hot water (DHW) production in coastal regions, lighting, cooking and equipment. Natural gas is dominantly used for

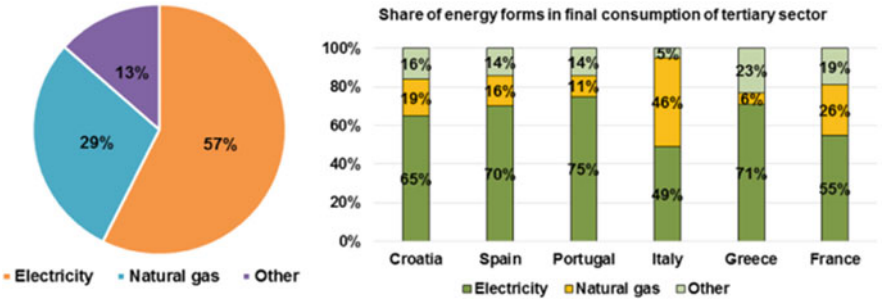

Fig. 52.1 Shares of dominantly used energy forms in tertiary sector, overall and per country [4]

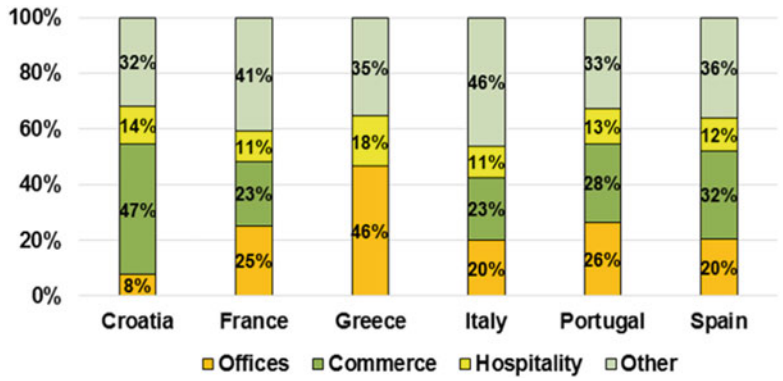

Fig. 52.2 Shares of energy consumption per segment in total final consumption of the tertiary sector in the analysed countries

Table 52.1 EPC demand in the private tertiary sector in the analysed countries [5]

Country	Expected EPC market by 2020, M€	EPC market potential, M€[a]
Croatia	40–80	600
France	750–1.000	19.600
Greece	400–600	1.600
Italy	2.600	9.300
Portugal	630	1.600
Spain	1.600	9.800

[a]Calculated according to energy consumption, average savings and energy prices methodology

heating. In lesser percentage, it is used for cooking and DHW production. Gas, oil-derived heat and other energy sources represent less than 14% of the overall energy needs of the tertiary sector.

In all the analysed countries, three segments of the tertiary sector have been pointed out as dominant, in terms of energy consumption – offices, commercial (retail) and hospitality (Fig. 52.2); other segments are country-specific and in majority represent energy consumption in public sector. In Greece, energy consumption of offices and retail is shown together, as available statistical data cannot be separated.

The analysis showed that large buildings such as hospitals, offices, hotels and shopping centres are of great interest for EPC providers. More specifically, in Croatia and Spain, retail is the most lucrative segment and offices in France. In Greece, hotels, offices and retail are of equal interest. In Portugal and Italy, offices and retail are the segments with the highest demand.

Based on the demand analysis findings, EPC projects usually have a duration of 3–8 years, with the value between 100.000 € and 1 M€.

The EPC demand in the six countries is presented in Table 52.1.

In general, the EPC market has not yet developed to its full potential in the six countries, showing a significant degree of development in the larger ones (France,

Italy and Spain) and an early stage of development in the smaller ones (Croatia, Greece and Portugal).

From the tertiary sector side, interviews showed that an EPC concept is known in general, but very few have actually been involved in one or have a deeper understanding. SMEs are willing to engage in EE/RES measures but are usually constrained by limited investment capacities, while EPC providers usually do not regard them as good business cases, due to relatively high transaction costs. Medium and large enterprises, with high energy consumption, are usually more appealing clients, due to higher profits and lower risk. Nevertheless, such companies usually invest in EE/RES measures themselves, when those are economically appealing. The low level of knowledge on EPC projects and scarcity of successful examples in the private tertiary sector cause a lack of trust and disinterest for this type of solution.

On the financing side, the interviews' findings indicate that the majority of key stakeholders is familiar with the EPC business model. One of the common conclusions obtained was that all interviewees considered EE/RES projects as either low risk or with as much risk as any other project. However, when talking specifically about EPCs, none of the small organisations had developed such projects in the past and some large institutions considered these as high risk or not suitable for them.

The creditworthiness of the client is the most relevant aspect evaluated before offering any finance solution; this is closely followed by technical aspects and financial performance. The investments are considered interesting if they exceed the minimum threshold defined by each institution (scaling from 100.000 € to >20 M €), and the main fields considered of high potential are private retail, hospitals and industry.

52.2.2 Overview of EPC Demand in Greece

In Greece, the total final energy consumption amounted to 17,1 Mtoe (199,2 TWh) in 2012 and 15,3 Mtoe in 2013 [6], showing a 30,5% reduction over the period 2007–2013 as the result of both the implementation of EE measures and the impact of the economic downturn in the Greek economy.

The services (tertiary) sector accounts for 12% of the final energy consumption and 75% of the sector's buildings are privately owned. Over half of them were constructed before 1980, providing opportunities for EE interventions. As shown in Table 52.2, offices and stores are the main market segments in terms of floor area, the number of buildings and primary energy consumption, followed by hotels.

Hospitals are the highest energy consumers per unit area (kWh/m^2) followed by offices and stores (Fig. 52.3). The most common energy-saving measures are roof insulation and lighting, BEMS and automatic controls when it comes to HVAC. The most common RES applications are photovoltaics (PV) for electricity production, solar collectors for DHW production and heat pumps.

The EPC market in Greece is at an early stage; EPC projects are limited, estimated to 70–100 often as pilots through EU or national-funded projects [10], with only a

Table 52.2 Number and floor area per type of building use

Tertiary sector segment	No. of buildings	Floor area[a] (m^2, 2012)	Primary energy consumption[b] (TWh)
Hotels	43.516	31.800.000	8,20
Hospitals/health	1.973	2.390.000	2,15
Schools, education	21.853	53.200.000	2,19
Offices and stores	206.254	67.300.000	22,71

[a][7]
[b][8]

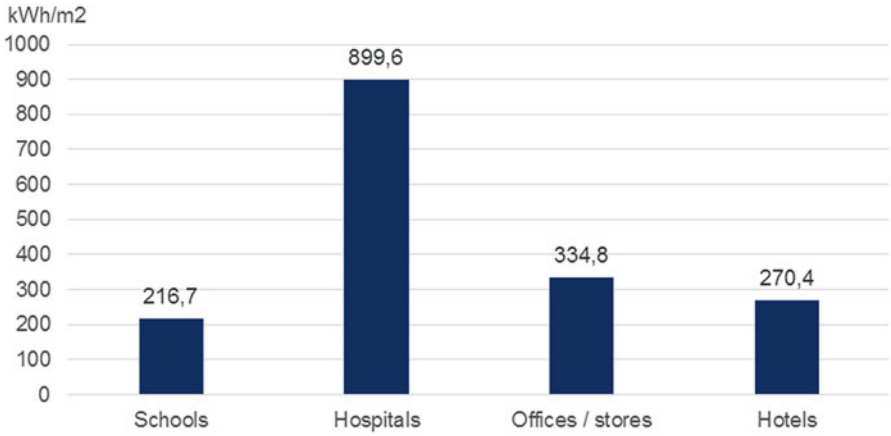

Fig. 52.3 Average energy consumption per building type (kWh/m^2/year), 2011–2014. (Data retrieved from [9])

few of them completed. The pilot projects have been focused on schools, local administrations, healthcare facilities and hotels, while a few projects are implemented in the industry, mainly including RES solutions combined with improvement in the building envelope and equipment.

The market uptake has been delayed mainly due to the financial crisis and market uncertainty. Technical and financial risks are perceived as high and banks are reluctant to finance projects due to their smaller size. Recently, the number of initiating projects seems to increase. A regeneration of the market is expected due to positive legislative changes.

According to a recent study by the Ministry of Environment, Energy and Climate Change, the tertiary sector in Greece could reach 72% energy savings compared to 2011 due to renovations in 170.000 buildings with an investment cost of 26 billion € till 2050.

The total national energy-saving target set for 2020 is 3.332,7 ktoe (38,8 TWh) according to the National Energy Efficiency Action Plan [11]. The investment costs in EE/RES interventions in the private tertiary sector by 2020 are estimated at 2.100–3.200 M€.

Table 52.3 Estimation of the annual energy efficiency potential for the tertiary sector in Greece, M€ [12]

Segment	Scenario 1: average energy savings 20%	Scenario 2: average energy savings 30%
Offices/commercial stores	195,70	293,55
Hotels	70,66	105,99
Educational/research	18,87	28,31
Health	18,52	27,79
Total	**303,76**	**455,64**

In order to simulate the energy-saving potential of the existing building stock per tertiary sector segment, the following baseline data and assumptions were taken into account:

- Reference year: 2012.
- Total energy.
- Cost of electricity bills estimated to 0,147 €/kWh in 2014.
- Primary energy factor of electricity: 2,9.
- Fifteen per cent discount on the current energy-saving cost was considered, based on the standard pricing, as a driver to create interest and increase competitiveness.
- Each facility in the sector was assumed to implement energy-saving measures.
- Two levels of potential energy saving were considered (20% and 30%).

Based on the above, the potential annual EPC demand is estimated between 300 and 450 M€ in the medium term (Table 52.3).

Hotels, private offices, stores and hospitals are perceived as the most interesting segments of the tertiary sector by the EPC market actors. The energy cost reduction is the main motive for implementing EE projects. The opportunity of reaching public subsidies or other investment incentives and the availability of funding is a critical factor for decision-making. Strengthening the company's green profile and supporting environmental policy are also main drivers.

The interviewed financial institutes consider the EPC market as a new lucrative business segment. The financing options offered are mostly custom options or grant-based loans; specific products or services to finance EPC-based projects are not available. The creditworthiness of the client, legal aspects and the foreseen financial performance of the project are the main aspects assessed for decision-making related to the financing of an EPC project.

The main roadblocks for the EPC market uptake, as perceived by the involved parts (Figs. 52.4, 52.5, and 52.6), are the low market liquidity and the difficulties to access financing, the scarcity of flagship projects, the shortage of supporting regulatory frameworks, the absence of tailored bank products, the lack of credible verification and measurement tools/methods and the complexity of the EPC concept/processes. Potential EPC beneficiaries mentioned also the lack of trust and transparency. The lack of guarantees and equity, the shortage of specific capacity

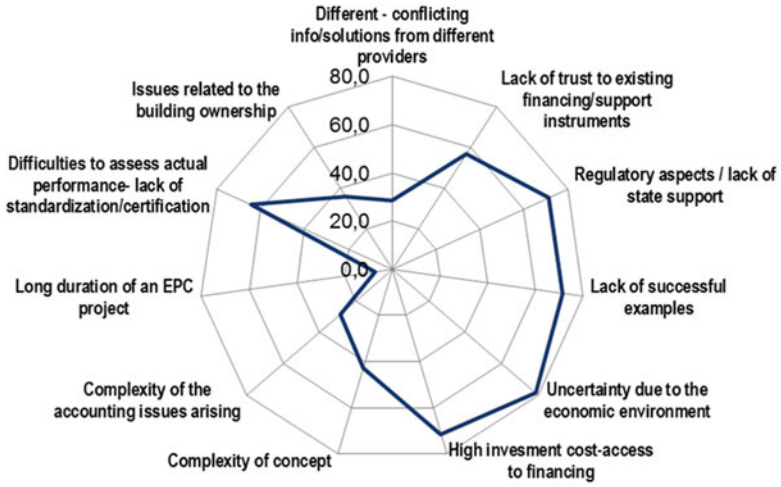

Fig. 52.4 Clients' main concerns about EPCs, EPC providers/facilitators' point of view

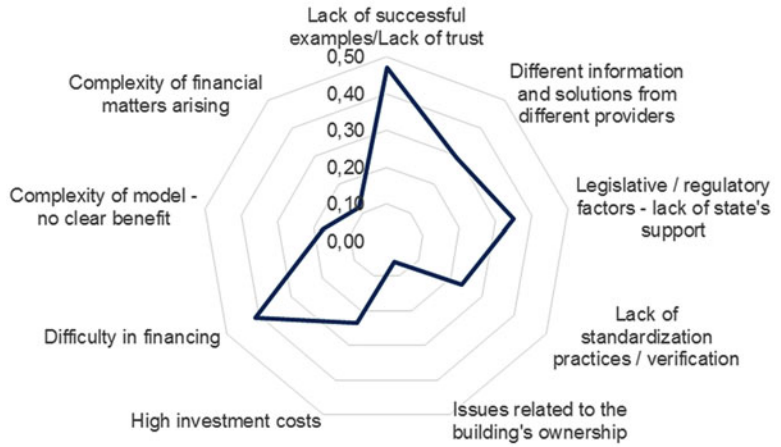

Fig. 52.5 Perception of roadblocks, the tertiary sector's point of view

to deal with the complexity of an EPC project and the small level of investments (which makes the handling of an EPC-based product less profitable) are also noted by the financial actors as blocking factors.

Potential solutions to eliminate roadblocks were proposed by the interviewed stakeholders in Greece, some of them being the following:

- Improve access to financing: funding of EE investments as a priority in the structural funds; public financing instruments to compensate part of the risks; loans with favourable terms and lower guarantees; a more active role of the financial institutions offering specialised products; international acknowledged energy-savings verification body to increase trust and confidence.

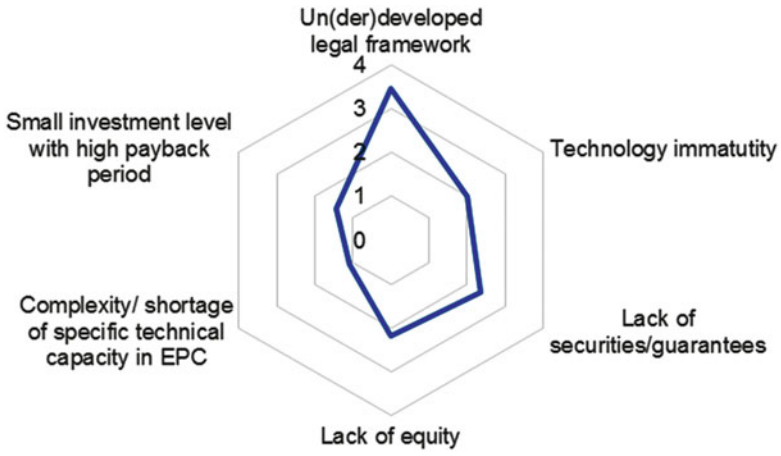

Fig. 52.6 Perceived risks/roadblocks in financing EPC-based projects, financing sector view

- Improve regulatory framework: clear and stable regulatory framework to be adopted in a long-term perspective; national standards and clear procedures to be regulated in the EPC market; mandatory registration of EPC providers in the official registry with appropriate validation procedures; tax incentives for entities adopting EPC approach; EE measures as a basic criterion for co-funded investments in the private sector.
- Increase trust: standardization practices and certification protocols in the EPC market; pilot projects to test the feasibility of the model; information and training on EPC procedures, models, benefits, risks and technical issues; transparent and credible processes for assessing EPC providers, including certification of competence and compliance.
- Flagship examples: demonstration of successful models in national or similar markets; state funding of ambitious EPC projects in the public sector; dissemination of information and credible results on implemented projects.
- Training/capacity building: tailored training sessions/capacity building activities to provide an understanding of EPC basics; specific standardised products to facilitate cooperation between EPC stakeholders.

52.3 EPC Applications in Tertiary Sector Buildings in Greece

In this chapter, the possible application of EPC in buildings in Greece is presented. The assessment was done using GREPCon, a new investment assessment and benchmarking tool, developed in the frame of the Trust EPC South project [13], based on the existing Green Rating™ methodology by Bureau Veritas. The tool offers a standardized technical and financial assessment of Energy Performance Contracts.

The methodology followed in the analysis comprises the following steps:

- Detailed audit of the facilities, including building equipment inventory, gathering of energy bills and building plans, recording of operation times and occupancy levels
- Dynamic thermal simulation of the building, to establish the heating and cooling needs
- Technical analysis using GREPCon, to establish the energy breakdown and the savings achieved by standardized EE and RES measures that can be applied in the building
- Financial assessment using GREPCon, to evaluate the potential for EPC
- Elaboration of standardization and benchmarking report

The examined buildings are two hotel complexes and two office buildings, which belong to promising segments of the tertiary sector as regards their EPC potential, based on the demand analysis presented previously. Figure 52.7 shows indicatively one of the cases.

After evaluating the energy profile and the technical features of the building and the equipment, a series of energy efficiency scenarios involving active and passive solutions, as well as RES, have been studied using the aforementioned standardized approach. The collective results of the analysis are presented comparatively in Table 52.4.

In seasonal-operating Mediterranean hotels, commonly found in Southern European countries, it is a usual case for cooling to reach high shares of energy use, more than 60% of the total primary energy use, as shown in previous work [14, 15]. Therefore, passive measures, such as substitution of windows and building envelope insulation, targeted the reduction of cooling needs. The substitution of single-glazing with double-glazing windows with thermal break exhibits a good index of investment cost versus energy saved. However, this is not the case for building insulation, which has a very high payback in this type of hotel and cannot be part of an EPC contract, at least without the support of incentives. Taking into

Fig. 52.7 (**a**) View of hotel roof with installed solar thermal panels, (**b**) Thermal simulation of hotel buildings

Table 52.4 Energy efficiency scenarios for tertiary sector buildings

Building type		Hotel	Hotel	Office	Office
Location		Crete, urban	Crete, coastal	Crete, urban	Athens, urban
Area of reference (m^2)		4.450	18.018	1.545	6.575
Year of construction		1989, refurbished in 2004	1996, refurbished in 2004	1968	2008
Main features		7 buildings complex, 324 beds, restaurant, 3 pools	15 buildings complex, 1.036 beds, restaurants, bars, spa, kids club, pools (1 indoor, 5 outdoor, 21 private)	4 floors, 1 basement	7 floors, 1 basement, 5 level underground parking
Operation		May–October	April–October	All year	All year
Green certifications		ISO 14001:2004, green key	ISO 14001:2004, Travelife gold	–	ISO 50001:2011
Energy sources and main uses		Electricity (cooling, restaurant, laundry), LPG (DHW, restaurant)	Electricity (cooling, lighting), biomass (DHW, restaurant, spa), LPG (restaurant), oil (DHW), solar (DHW)	Electricity (heating, cooling, lighting)	Natural gas (heating), electricity (cooling, lighting, servers)
Total energy consumption (kWh/yr)		516.888	1.603.217	97.242	942.554
Energy consumption per m^2 ($kWh/m^2/yr$)		119	95	63	143
CO_2 emissions ($kgCO_2eq/m^2/yr$)		89	77	62	123
Energy efficiency scenarios					
Passive interventions (kWh/yr & savings %)	Thermal insulation of building envelope	7.919 (1,5%)	47.507 (3%)	Not implemented	Already implemented
	Substitution of windows	Already implemented	47.508 (3%)	25.219 (26%)	Already implemented
	Substitution of doors (automatic door)	Not implemented	Not implemented	6.467 (6,7%)	Not implemented
	Improve solar factor	Not implemented	45.507 (3%)	Not implemented	49.768 (5,3%)
	Installation of ceiling fans	32.000 (6%)	Not implemented	Not implemented	Not implemented

Active systems (kWh/yr & savings %)	Substitution of conventional lamps	7.207 (1,5%)	42.324 (2,6%)	10.551 (11%)	81.028 (9%)
	Sensors (occupancy & presence)	819 (0,2%)	Not implemented	332 (0,3%)	7.678 (1%)
	Substitution of appliances – laundry	16.107 (3%)	Not implemented	na	na
	Substitution of appliances – kitchen	63.518 (12,5%)	Not implemented	na	na
	Substitution of low-efficiency chiller	Not implemented	390.073 (24,5%)	Not implemented	Not implemented
Renewables (kWh/yr & savings %)	Solar thermal plant	3.960 (1%)	152.413 (10%)	Not implemented	Not implemented
	Photovoltaic plant	75.000 (15%)	75.000 (5%)	Not implemented	86.717 (9,2%)
Technical - Economical - Sustainability indices					
Technical – economical	Investment cost (€/kWh saved during the system lifetime)	Substitution of conv. lamps with LED*	Substitution of conv. lamps with LED*	Substitution of conv. lamps with LED*	Substitution of conv. lamps with LED*
		0,03	0,09	0,14	0,05
		Occupancy sensors	Heat pumps installation	Occupancy sensors	Improve solar factor
		0,11	0,03	0,13	0,01
		Thermal insulation of building envelope	Substitution of windows	Substitution of doors	Solar thermal plant
		0,11	0,03	0,09	0,04
		Substitution of appliances	Thermal insulation of building envelope	Substitution of windows	PV plant
		0,06	0,05	0,04	0,04
		PV plant	Heat recovery systems		
		0,04	0,01		

(continued)

Table 52.4 (continued)

			Swim. pool heat cover		
			0,04		
			Solar thermal plant		
			0,02		
			PV plant		
			0,04		
Sustainability indices	Investment cost (€/kg CO_2eq saved during the system lifetime)	Substitution of conv lamps with LED*	Substitution of conv lamps with LED*	Substitution of conv lamps with LED*	Substitution of conv lamps with LED*
		0,03	0,10	0,14	0,05
		Occupancy sensors	Heat pumps installation	Occupancy sensors	Improve solar factor
		0,11	0,03	0,13	0,02
		Thermal insulation of building envelope	Substitution of windows	Substitution of doors	Solar thermal plant
		0,11	0,03	0,09	0,04
		Substitution of appliances	Thermal insulation of building envelope	Substitution of windows	PV plant
		0,06	0,05	0,04	0,04
		PV plant	Swim. pool heat cover		
		0,03	0,14		
			PV plant		
			0,04		
		*150 units	*3.111 units	*577 units	*3.027 units

account though the improvement of indoor environmental conditions that can be achieved through this intervention, for hotel guests, then the benefits and motives for hotel management to proceed with such investment are multiplied. In hotels with a year-round operation, where heating also plays a major role, building insulation could exhibit better economic indices.

Another major energy use in hotels proves to be the restaurant and other non-hosting functions, as demonstrated in previous works [16]; therefore, measures targeting this energy use, such as replacement of appliances, achieve important energy savings. Active measures and RES solutions, such as the installation of heat pumps, photovoltaics and solar thermal panels, have good paybacks and represent a high potential for EPC applications in Mediterranean hotels.

Finally, it is worth mentioning that in all types of buildings, the replacement of conventional lamps with LED was very profitable in terms of savings and is usually one of the first measures examined for EPC.

52.4 Conclusions

The potential EPC applications in the Greek tertiary sector buildings demonstrate the viability of several passive and active solutions, as well as renewable energy systems through the standardized approach.

The total expected EPC demand in the private tertiary sector of the six Southern European countries studied reaches to 6.000–6.500 M€ by 2020. The total EPC potential rises to 42.500 M€. It is clear that there is a large untapped potential that can be exploited, if concerns and barriers faced by EPC market stakeholders (EPC providers, tertiary sector potential clients and financial institutions) are addressed.

In order for EPCs to become a standard practice in the EE market, trust amongst involved stakeholders needs to be reinforced, and one way to achieve this is through appropriate investment assessment and standardization practices for EPC projects and through demonstration of lighthouse examples.

Nomenclature

BEMS	Building energy management system
DHW	Domestic hot water
EE	Energy efficiency
EPC	Energy Performance Contracting
EU	European Union
HVAC	Heating, ventilation and air-conditioning
LPG	Liquefied petroleum gas
PV	Photovoltaics

RES	Renewable energy sources
SME	Small- and medium-sized enterprise

Acknowledgements This publication has been developed within the framework of the Trust EPC South project funded by the European Union's Horizon 2020 research and innovation programme under grant agreement number 649772. The sole responsibility for the content of this publication lies with the authors. It does not necessarily reflect the opinion of the European Union. Neither the EASME nor the European Commission is responsible for any use that may be made of the information contained therein.

References

1. European Commission. https://ec.europa.eu/energy/en/news/commission-proposes-new-rules-consumer-centred-clean-energy-transition. Last accessed 11. 2016
2. Energy Efficiency Financial Institutions Group. The EEFIG report. eefig.eu/index.php/the-eefig-report. Last accessed 11. 2016
3. Trust EPC South (2016) Overview of national EPC market reports. www.trustepc.eu/en/public-deliverables
4. Tsoutsos T, Tournaki S, Frangou M, Sonvilla PM, Bišćan M (2017) Building trust in energy performance contracting for tertiary sector energy efficiency and sustainable energy projects in Southern European Countries. The Trust EPC South European initiative. In: 9th international exergy, energy and environment symposium (IEEES-9) conference proceedings, Split, Croatia
5. Tsoutsos T, Tournaki S, Farmaki E, Sonvilla P, Lensing P, Bartnicki J, Cobos A, Biscan M (2017) Benchmarking framework to encourage energy efficiency investments in South Europe. The Trust EPC South approach. Environ Sci Procedia 38:413–419
6. European Commission Energy statistics. https://ec.europa.eu/energy/en/statistics/country. Last accessed 11. 2015
7. Odyssee database. www.indicators.odyssee-mure.eu/energy-efficiency-database.html Last accessed 11.2015
8. Ministry of Environment, Energy and Climate Change (YPEKA) (2014). Report on long-term strategy for mobilizing investment for the renovation of residential and commercial buildings, public and private national building stock. https://ec.europa.eu/energy/sites/ener/files/documents/GreekReportBuildingsArticle4_en.pdf
9. Centre for Renewable Energy Sources and Saving (2015) Building energy audits and auditors. http://bpes.ypeka.gr/wp-content/uploads/presentationpetroliagki10032015.pdf
10. Joint Research Centre (JRC) (2013) ESCO market report. https://ec.europa.eu/jrc/en/publication/eur-scientific-and-technical-research-reports/european-esco-market-report-2013
11. Ministry of Environment, Energy and Climate Change of Greece (YPEKA) (2014) National energy efficiency action plan. https://ec.europa.eu/energy/sites/ener/files/documents/EL_NEEAP_en%20version.pdf
12. Trust EPC South (2016) National EPC market report – Greece. http://www.trustepc.eu/en/wp-content/uploads/sites/3/2016/02/TRH_WP2_D2.2_National_report_GR_FINAL.pdf
13. Trust EPC South (2017) White Paper: Green Rating™ approach for EPC assessment and verification. http://www.trustepc.eu/en/wp-content/uploads/sites/3/2017/03/200317_TRH_White-paper.pdf
14. Tsoutsos T, Tournaki S, Frangou M, Morell R, Guerrero Hernandez I, Derjanecz A (2016) Cooling in Mediterranean hotels during summertime. Experience from the neZEH (nearly Zero

Energy Hotels) project. In: 4th IIR conference on sustainability & the cold chain conference proceedings. International Institute of Refrigeration, Auckland, New Zealand
15. Tsoutsos T, Tournaki S, Avellaner de Santos C, Vercellotti R (2013) Nearly zero energy buildings. Application in Mediterranean hotels. Energy Procedia 42:230–238
16. neZEH (2016) nearly Zero Energy Hotels in Europe – Flagship projects and tools for hoteliers. http://www.nezeh.eu/assets/media/PDF/D1491.5%20neZEH%20result-oriented%20report.pdf

Chapter 53
Effective Envelope Insulation and Heating Strategies in Apartment Buildings in Mid-temperate Regions: A Case Study of Nova Scotia, Canada

Hamid Jamili, Danurachman Krishana, Jesus Rubio, Gabriela Tristan, and Luis Rojas-Solórzano

53.1 Introduction and Objectives

The nation of Canada faces different challenges in terms of climate change, mainly driven by growing population, extreme temperatures, a large landmass, and a diversified growing economy [1, 2].

Particularly, in the region of Nova Scotia, located in the mid-latitude (44.7° N) of the country, there was a review of the province's electricity system in 2013 with commitment by 2020 of promoting and improving energy efficiency measures in residential and industry sector and the transition to renewable energy production [3]. As a mid-temperate region, most of the electricity consumption in Nova Scotia is due to space heating. As it is shown in Fig. 53.1, almost 63% of total energy consumption represents the space heating used at homes, institutions, and offices during peak season (December to February) [1].

Nova Scotia has the second largest population among all 4 provinces, with 24 inhabitants per square kilometer [1]. The case study here presented focuses on envelope insulation and heating source for a residential multifamily building. The insulation retrofit will be considered as implemented on walls and floors since those parts have potential for improving the energy efficiency.

A life-cycle cost analysis (LCCA) will be used to assess the total economic benefit of each option as opposed to not implementing it. It takes into account all costs of acquiring, owning, and disposing of a building or building system. LCCA is

H. Jamili · D. Krishana · J. Rubio · G. Tristan
Ecole des Mines de Nantes, Engineering, Energy Systems and Environment Department, Nantes, France

L. Rojas-Solórzano (✉)
Nazarbayev University, School of Engineering, Astana, Kazakhstan
e-mail: luis.rojas@nu.edu.kz

S. Nižetić, A. Papadopoulos (eds.), *The Role of Exergy in Energy and the Environment*, Green Energy and Technology,
https://doi.org/10.1007/978-3-319-89845-2_53

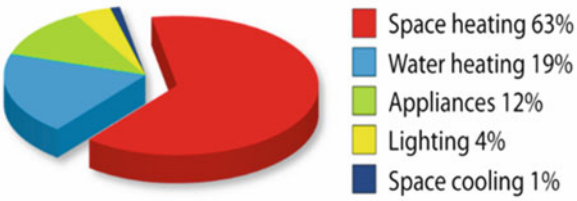

Fig. 53.1 Distribution of residential energy use in Canada [3]

Fig. 53.2 Kent Fields Estates eight-unit apartment building plan. (Source: Equilibrium Engineering Inc.)

Table 53.1 Building envelope area

	Building area per sectors
Floors	156 m^2
Walls	588 m^2
Windows	31.59 m^2
Doors	30.50 m^2
Roof	428 m^2

especially useful when project alternatives that fulfill the same performance requirements, but differ with respect to initial costs and operating costs, have to be compared in order to select the one that maximizes net savings [4]. The feasibility study is conducted via LCCA using RETScreen, a Clean Energy Management Software system for energy efficiency, renewable energy, and cogeneration project feasibility analysis. This Excel-based software has proven to be very helpful to decision-makers in technical and financial viability of potential clean energy projects [5, 6].

53.2 Building Characteristics

The analysis here presented is held for an existing building with eight apartments located in the region of Nova Scotia, Kentville. The building plan is shown in Fig. 53.2. The dimensions of building areas are shown in Table 53.1.

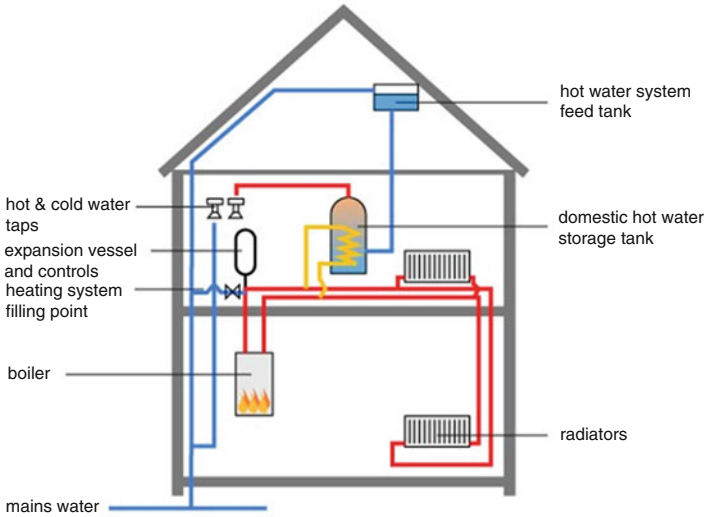

Fig. 53.3 Existing heating system. (Source: greenspec.co.uk)

The existing combination of space-water heating consists of a main water boiler and the distribution of centralized steam by radiators throughout the building, as shown in Fig. 53.3.

Current insulation in the building has the following characteristics:

- Insulation $2'' \times 6''$ $16''$ O.C. (on center)
- Double pane low-e vinyl in windows
- Low resistance insulation in under slab
- Insulation in walls R20 = 3.52 m^2 K/W
- Insulation in roof R40 = 7.04 m^2 K/W

Actual R-values of the insulation are shown in Fig. 53.4.

53.3 Technical-Economic Analysis

In order to reduce the heating-oil consumption, two options are presented and compared. These two options consist of improving envelope insulation and introducing electric heating to complement the existing heating-oil heating system. Both options are displayed in Figs. 53.5 and 53.6. The model includes fuel type (heating oil or electricity), cost of each fuel, occupancy, and comfort temperature. Table 53.2 shows the values used for the analysis.

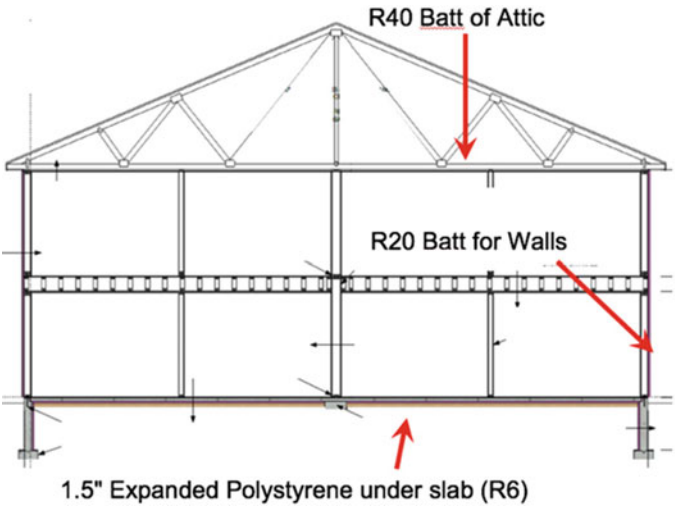

Fig. 53.4 Original insulation in building. (Source: Equilibrium Engineering Inc.)

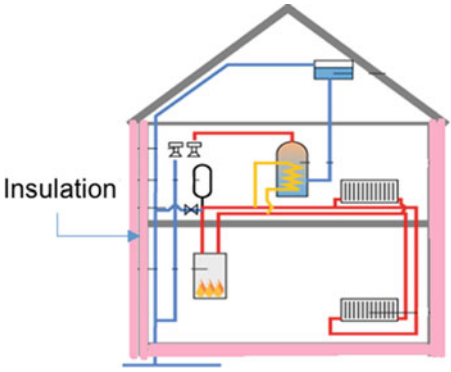

Fig. 53.5 Option 1 insulation replacement in floor and walls. (Source: greenspec.co.uk)

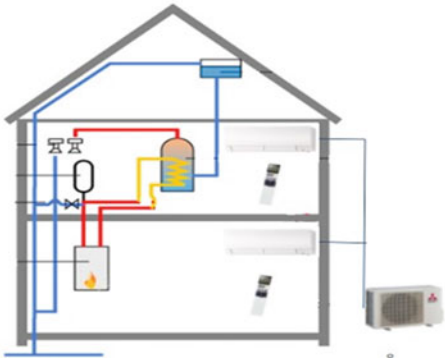

Fig. 53.6 Option 2 heating system replacement. (Source: greenspec.co.uk)

Table 53.2 Parameter used in technical-economic analysis

Parameters	
Fuel type	Option 1: • Proposal A: diesel #2 • Proposal B: diesel #2 Option 2: • Electricity
Cost of fuel	Option 1: • Proposal A: 0.89€/L[a] • Proposal B: 0.89€/L[a] Option 2: • 0.104€/kWh[a]
Occupancy	24 h, 7 days a week
Comfort temperature	18 °C
Inflation rate [7]	1.5%
Discount rate [8]	2.5%

[a][9]

53.3.1 Option 1 Insulation Replacement

Option 1 consists of upgrading the existing insulation with material of higher thermal resistance. There are several types of insulation materials with different thermal resistance, from R2.08 = 0.37 m^2 K/W until R40 = 7.04 m^2 K/W. For this study, there will be two types of thermal resistance. Firstly, Proposal A corresponds to low thermal resistance (R30 = 5.28 m^2 K/W for the walls and R13 = 2.29 m^2 K/W for the floor). Secondly, Proposal B corresponds to high thermal resistance (R38 = 6.69 m^2 K/W for the walls and the floor).

53.3.2 Option 2 Heating System Replacement

Option 2 consists of complementing the current heating system that works with fuel oil by an electrical heating system. The prices for the electrical heating system, including installation but excluding the boiler, were given by the company EEI. The price for the boiler was taken from "domotelec.fr."

53.4 Results and Discussions

- *Option 1 (insulation replacement): Insulation A (R30 for the walls and R13 for the floor)* vs *Insulation B (R38 for the walls and R38 for the floor)*

Although Proposal B requires a major investment (5019.59 €) in comparison with Proposal A (3,720.5 €), the LCCA shows that in long terms the Insulation B has more economic benefits with a net present value NPV_B = 28,284 € and a benefit-cost

Table 53.3 Results of the LCCA for Option 1 (A and B) and Option 2

Description		Option 1		Option 2
		Proposal A	Proposal B	
Technical spec.	*R*-value [10]	R30 = 5.28 m^2 K/W (wall)	R38 = 6.69 m^2 K/W (wall)	Electrical heater
		R13 = 2.29 m^2 K/W (floor)	R38 = 6.69 m^2 K/W (floor)	
Capital cost	€	3721	5020	35,744
Fuel saving	%	7%	11%	39.8%
After-tax IRR – equity	%	50.6%	53.7%	19.8%
Simple payback	Yr	2.1	2.0	5.7
Equity payback	Yr	2.0	1.9	5.3
Net present value (NPV)	€	18,534	28,284	18,402
Annual life cycle savings	€/yr	1347	2055	2284
Benefit-cost (B-C) ratio		5.62	6.63	1.51

ratio B-C = 6.63 compared with Proposal A which results to NPV_A = 18,534 € and B-C = 5.62. Also, it is easy to appreciate that the payback period of the Proposal A (2.1 years) is bigger than the Proposal B (2.0 years). This demonstrates that in this case, it is better to invest in long term with high R-value insulation (Option 1-B).

- *Option 2 (heating system replacement): Fuel oil heater* vs *fuel oil + electric heaters*

For Option 2 with a new electrical heating system complementing the existing fuel oil heating system, the study shows that this case has a NPV = 18,402 €, payback period of 5.7 years, and B-C = 1.5. Compared to Option 1-B, this option demonstrates that insulation replacement is the most feasible option given that the electrical heating system has significantly less economic benefits than either Options 1-A or 1-B. The summary of Options 1 and 2 are shown in Table 53.3.

53.5 Conclusions

A technical-economic assessment of using better thermal insulation and electric heating instead of oil heating for space heating in mid-latitude countries is presented. An eight-unit residential building located in Nova Scotia, Canada, is considered for the analysis. Three scenarios are evaluated based on perspectives. Option 1-A (replacing building envelope insulation with a low thermal-resistant and low-cost insulation) and Option 1-B (replacing the building envelope insulation with a higher thermal-resistant and higher-cost insulation) are intended to decrease building

heating load, while Option 2 (installation of electric boilers to complement current oil-consuming boilers) is aimed at reduction of cost of energy. The LCCA show the much better outcome economic and environmental outcome coming from upgrading envelope insulation (Option 1-B).

In Options 1-A and 1-B, the simple payback is around 2 years for both, but when the B-C ratios are analyzed and compared, Proposal B has the best B-C ratio which is 18% higher than Proposal A. Proposal B NPV is 28,284€ (52.6% higher than Proposal A). Therefore, retrofitting the insulation demonstrated to be a more attractive mechanism, both technically and economically, than electric heating supply to reduce lifetime space heating costs for apartment buildings located in Nova Scotia, Canada. Preference should be given to higher resistance insulation over lower resistance insulation, despite CAPEX might be obviously larger, because lifetime costs for the former will render larger financial benefits to householders.

Nomenclature

B-C	Benefit-cost ratio
€	Euros
EEI	Equilibrium Engineering Inc.
EMN	Ecole des Mines de Nantes
IRR	Internal rate of return
kWh	kW-hour
L	Liter
LCCA	Life-cycle cost analysis
NPV	Net present value
OC	On center. Construction term that indicates the measurement from the center of one wood plank to the center of the next one

Acknowledgments The research was adopted from a real case, for which the data was provided by Equilibrium Engineering Inc. (EEI), a Nova Scotia-based energy services firm rooted in sustainable building design and energy conservation. EEI partners with their customers to help reduce energy costs and overall ecological footprint. Special thanks to EMN master's program for conducting RETScreen courses and paving the way to this publication.

References

1. INDC., Canada's INDC submission to the UNFCCC (2014) http://www4.unfccc.int/submissions/INDC/Published%20Documents/Canada/1/INDC%20-%20Canada%20%20English.pdf
2. Cohen JE, Small C (2012) Hypsographic demography: The distribution of human population by altitude. In: Proceedings of the National Academy of Sciences of the United States of America, vol 95. The Academy, Washington, DC, pp 14009–14014
3. NSpower, Nova Scotia Nova Scotia Electricity System Review (2013) http://0-nsleg-edeposit.gov.ns.ca.legcat.gov.ns.ca/deposit/b1067231x.pdf
4. NIST-National Institute of Standards and Technology, Life-cycle cost analysis (2016) https://www.wbdg.org/resources/lifecycle-cost-analysis-lcca

5. Benavides S, Bitosova M, De Gregorio J, Welschbillig A, Rojas-Solórzano L (2015) Technical-economic assessment of energy efficiency measures in a mid-size industry. Proceedings of 7th international exergy, energy and environment symposium IEEES7, Valenciennes, France
6. RETScreen, Canada, RETScreen Energy Project Analysis Software (2016) http://en.openei.org/wiki/RETScreen_Clean_Energy_Project_Analysis_Software
7. Trading economics. Canada inflation rate (2016) http://www.tradingeconomics.com/canada/inflation-cpi
8. Trading economics. Canada interest rate (2017) http://www.tradingeconomics.com/canada/interest-rate
9. Statcan, Gasoline and fuel oil, average retail prices by urban centre (2016) http://www.statcan.gc.ca/tablestableaux/sum-som/l01/cst01/econ154a-eng.htm
10. Groupe Isolofoam, R and RSI value converter (2016) http://www.isolofoam.com/english/r-and-rsi-valueconverter

Chapter 54
Numerical Simulation of Building Wall Integrated with Phase Change Material: A Case Study of a Mediterranean City Izmir, Turkey

Mustafa Asker, Ersin Alptekin, Ayça Tokuç, Mehmet Akif Ezan, and Hadi Ganjehsarabi

54.1 Introduction

The ever-increasing energy consumption by buildings has received increasing attention on the thermal performance of buildings. Decreasing energy consumption that arises due to heating and cooling utilities of a building and keeping heat loss/gain to lowest level can play a major role in saving energy in buildings. During the past decade, several researchers have focused their attention on utilizing the phase change material (PCM) plates inside the exterior walls of the buildings. Darkwa and Kim [1] investigated two different PCM drywall configurations for having better heat transfers between solid and liquid phases at the moving interface. Their results showed that the laminated PCM wallboard system has a considerable advantage of enhancing thermal performance, which leads to improving heat transfer rates under a narrow temperature range.

Zhang et al. [2] analyzed the impact of thermal physical properties of the PCM on overcooling and overheating during the winter and summer, respectively. Huang et al. [3] numerically examined the energy conservation potential and temperature fluctuation effects due to the utilization of PCMs in a building cavity wall. Alawadhi [4] analyzed a two-dimensional model for a common building brick with cylindrical

M. Asker (✉) · M. A. Ezan
Department of Mechanical Engineering, Adnan Menderes University, Aydın, Turkey
e-mail: mustafa.asker@adu.edu.tr

E. Alptekin
Department of Mechanical Engineering, Dokuz Eylül University, Izmir, Turkey

A. Tokuç
Department of Architecture, Dokuz Eylul University, Izmir, Turkey

H. Ganjehsarabi
Department of Mechanical Engineering, Erzincan University, Erzincan, Turkey

S. Nižetić, A. Papadopoulos (eds.), *The Role of Exergy in Energy and the Environment*, Green Energy and Technology,
https://doi.org/10.1007/978-3-319-89845-2_54

holes containing PCM. He conducted a parametric study to investigate the effect of different design parameters, such as the PCM's quantity, type, and location in the brick, and showed that the heat gain is significantly reduced when the PCM is incorporated into the brick. Kuznik et al. [5] experimentally examined light building envelope with a wall containing PCM material. Their results showed that 5 mm of PCM wallboard correspond to an equivalent of 8 cm of concrete with respect to indoor air temperature fluctuations.

Zhou et al. [6] investigated the thermal performance for a "direct-gain room" utilizing PCM plates as inner linings. The effects of various design parameters such as melting temperature, location, and board thickness on the thermal performance were studied. Their results showed that the PCM plates are more advantageous in direct-gain passive solar buildings. Zhang et al. [7] studied the impacts of various design parameters such as thermal conductivity, melting temperature, and heat of fusion of the PCM on the building thermal performance of a PCM-embedded wallboard. Their results showed that the internal wall of the building should contain PCM, which leads to having higher energy efficiency in a solar house. Haghshenaskashani and Pasdarshahri [8] developed and examined two-dimensional model of brick incorporated PCM. Their results showed that utilizing PCM in the buildings leads to a decline in maximum entering heat flux to the building. Kara and Kurnuc [9] used test room to investigate the performance of coupled novel triple glass (NTG) and PCM wall. PCM used are GR35 and GR41 and were incorporated into the plaster of the walls. They found that overall efficiency of the PCM walls varied from 20% to 36%, and solar transmittance of the NTG ranged from 0.45 to 0.55 during the heating period. In another work, Kara and Kurnuc [10] evaluated the performance of PCM walls in the summer only. They found that the solar transmittance of the triple glass unit (TGU) decreased approximately 100% during summer compared to winter. Izquierdo-Barrientos et al. [11] examined the effect of melting temperature of PCM, the position of PCM layer, the orientation of the wall, and environmental condition on thermal performance. Chwieduk [12] examined the applicability of replacing the thick and weighty thermal mass external walls utilized in high-latitude climates by thin and light thermal mass ones containing PCM, without compromising the indoor comfort throughout the year. Their results show that external light mass walls must contain insulation in an outer layer if it is combined with a PCM panel in high-latitude countries. Jin et al. [13] experimentally studied the performance of a gypsum wall with reference and six different PCM layer locations. They showed a possible 41% reduction in the average peak heat flux, yet concluded that in addition to layer location, the state of the PCM significantly affected the thermal performance of the wall. Lei et al. [14] studied the incorporation of PCM in a building located in a tropical climate with a concrete wall for cooling load reduction through the whole year. They show the importance of phase change temperature for performance and state that the location, thickness, and enthalpy curve of PCM are critical for the selection of optimum phase change temperature. In this chapter, a numerical analysis is carried out to evaluate the effect of PCM layer location on the thermal performance of the wall. In this content, a one-

dimensional model is developed, and parametric results are represented in the case of a city with Mediterranean climate, Izmir, Turkey.

54.2 Material and Method

54.2.1 Definition of the Problem

A model room with dimensions of 4 m long, 4 m wide, and 2.5 m height is selected. The room contains one window. By following the recent work of Chwieduk [12], the total surface area of the wall and the area of the glass are taken to be $A_{wall} = 38$ m^2 and $A_{glass} = 2$ m^2, respectively. The overall heat transfer coefficient for the glass is defined to be $U_{glass} = 0.6$ W/m^2.K by Çengel and Ghajar [15]. The layers of the building wall are retrieved from the Turkish standards [16], which is schematically represented in Fig. 54.1. It consists of (1) 3 cm cement plaster layer (the left-most layer adjacent to the outdoor), (2) 19 cm aerated concrete, (3) 9 cm thermal insulation, and (4) 2 cm cement-lime plaster (the right-most layer adjacent to the indoor).

The thermophysical properties of the building wall materials are assumed independent of temperature variations except for the PCM. The corresponding properties are defined according to the Turkish standards and listed in Table 54.1. The PCM has been integrated with the insulation part (layer 3) in various configurations; the parametric cases are defined by incorporating PCM into the wall in place of a part

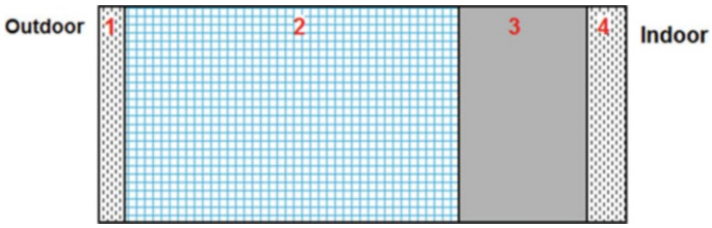

Fig. 54.1 Schematic diagram for the building wall layers (1) cement plaster, (2) aerated concrete, (3) insulation, (4) cement-lime plaster

Table 54.1 Thermophysical properties of the building materials [16, 17]

Layer #	Type of material	Thickness (cm)	Thermal conductivity (W/m.K)	Specific heat (J/kg.K)	Density (kg/m^3)
1	Cement plaster	3	1.4	1116	2100
2	Aerated concrete	19	0.13	1116	400
3	Insulation	9	0.1	1116	400
4	Cement-lime plaster	2	0.9	1116	1800

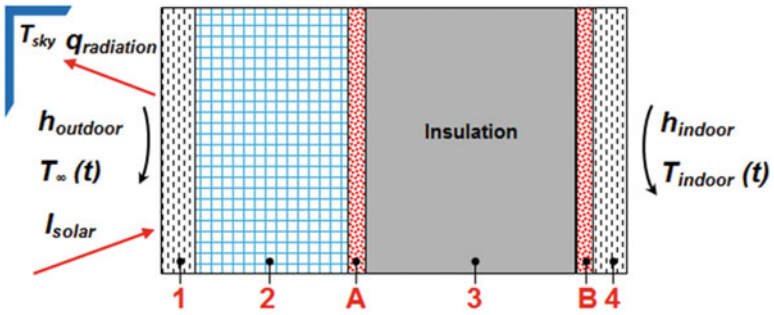

Fig. 54.2 General configuration of building wall with PCM

Table 54.2 Thermophysical properties of the phase change material [18]

Properties	Paraffin wax
Melting temperature, °C	32
Latent heat of fusion, kJ/kg	251
Specific heat of solid, kJ/kg.K	1.92
Specific heat of liquid, kJ/kg.K	3.26
Thermal conductivity of solid, W/m.K	0.514
Thermal conductivity of liquid, W/m.K	0.224
Density of solid, kg/m^3	830
Density of liquid, kg/m^3	830

of the insulation as given in Fig. 54.2. The thermophysical properties for the PCM are given in Table 54.2.

The volume of the air inside the room are $V_{air} = 40$ m^3, and the thermophysical properties of air are the density $\rho_{air} = 1.1$ kg/m^3 and the specific heat $c_{p,\ air} = 1005$ J/kg.K [15]. The outdoor surface of the wall is exposed to solar radiation and combined forced and natural convection, while on the indoor face of the wall, natural convection is the only heat transfer mechanism between the wall surface and the indoor air. In numerical analyses, the real weather data for the city of Izmir is defined at the exterior wall. The data for the ambient temperature, solar load, and wind speed are used in the analysis for July as shown in Fig. 54.3.

54.2.2 Mathematical Modeling

A one-dimensional time-dependent mathematical model for the wall integrated with PCM is developed. The energy equation for the building wall layers with PCM can be written as follows:

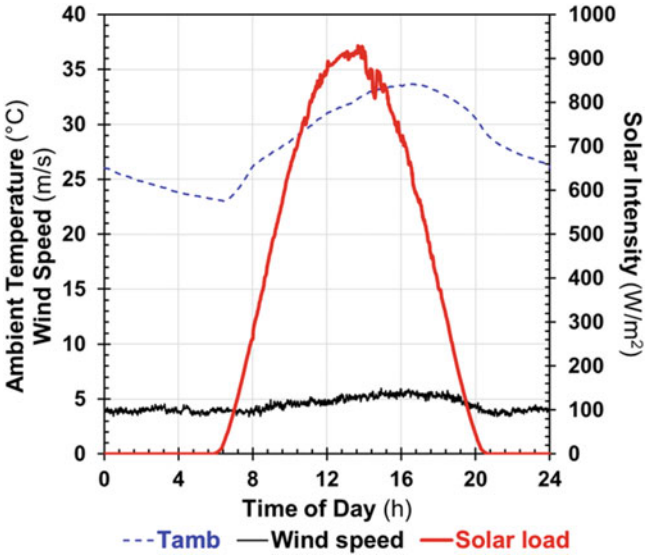

Fig. 54.3 Weather data for Izmir (July)

$$\frac{\partial}{\partial t}(\rho cT) = \frac{\partial}{\partial x}\left(k\frac{\partial T}{\partial x}\right) \tag{54.1}$$

By following the apparent heat capacity approach of Alawadhi [4], the volumetric heat capacity of the PCM can be expressed as a function of temperature as follows:

$$C_{\text{PCM}} = \begin{cases} C_{\text{solid}} & T < T_{\text{solidus}} \quad \text{Solid} \\ \dfrac{C_{\text{solid}} + C_{\text{liquid}}}{2} + \dfrac{\rho_{\text{solid}} + \rho_{\text{liquid}}}{2}\left(\dfrac{h_{sf}{}^{sf}}{\Delta T}\right) & T_{\text{solidus}} \le T \le T_{\text{liquidus}} \quad \text{Mushy} \\ C_{\text{liquid}} & T > T_{\text{liquidus}} \quad \text{Liquid} \end{cases} \tag{54.2}$$

The energy balance of air in the room can be written as follows:

$$\frac{\partial}{\partial t}(\rho cVT)_{\text{air}} = q_{\text{conv}} + q_{\text{glass}} \tag{54.3}$$

where q_{conv} represents the heat transfer by convection between the inner surface and the interior air. The term q_{glass} in Eq. (54.3), on the other hand, accounts for the heat transfer through the glass as follows:

$$q_{\text{glass}} = U_{\text{glass}}A_{\text{glass}}(\text{T}_{\text{indoor}} - T_{\text{amb}}) \tag{54.4}$$

On the exterior surface of the wall, a mixed boundary condition is defined as follows:

$$-k\frac{\partial T}{\partial x}\bigg|_{\text{exterior wall}} = q''_{\text{conv}} + q''_{\text{rad}} + I_{\text{solar}} \tag{54.5}$$

where the convective heat transfer is evaluated as the sum of the natural and forced components

$$q''_{\text{conv}} = h_{\text{total}}(T_s - T_{\text{amb}}) \tag{54.6}$$

where h_{total} indicates the combined forced and natural convection heat transfer coefficient between the outer surface and ambient. Hendricks and van Sark [19] define the combined convective heat transfer coefficient as follows:

$$h_{\text{total}} = \left(h^3_{\text{natural}} + h^3_{\text{forced}}\right)^{1/3} \tag{54.7}$$

The heat transfer coefficients for the natural (caused by buoyancy) and forced (caused by the wind) convections on the outdoor building wall are obtained from the following equations of Hendricks and van Sark [19].

$$h_{\text{natural}} = 1.78(T_s - T_{\text{amb}})^{1/3} \tag{54.8}$$

$$h_{\text{forced}} = 2.8 + 3.0v \tag{54.9}$$

where v is the wind speed. The heat transfer by radiation from the surface is calculated using the well-known Stefan-Boltzmann equation [20]. The sky temperature (T_{sky}), on the other hand, is defined using a modified Swinbank equation [21, 22]

$$T_{\text{sky}} = 0.037536\ T^{1.5}_{\text{amb}} + 0.32T_{\text{amb}} \tag{54.10}$$

54.2.3 Solution Method

Numerical analyses were conducted in ANSYS FLUENT [23] software by resolving the Eqs. (54.1 to 54.10) iteratively. A set of user-defined functions (UDF) is coded in C++ language to incorporate the boundary conditions adequately on the inner and outer walls. According to the preliminary runs, the time step size and convergence criterion are decided as 10 s and 1E-7, respectively.

54.3 Results and Discussion

Time-wise temperature variations and temperature distributions within the wall are evaluated for four different envelope designs. As listed in Table 54.3, Case 1 considers the reference case without PCM layer. In Case 2 and Case 4, 1 cm of PCM is placed in layers B and A, respectively (see Fig. 54.2). Case 3, on the other hand, has the highest storage capacity since it includes PCM in layers A and B.

Figure 54.4 demonstrates the time-wise variations of the ambient and sky temperatures with the indoor, inner and outer wall temperatures of the wall throughout 15 days. Due to the higher thermal inertia of the wall, it takes nearly 7 days to reach cyclic temperature variation under the current conditions. The surface temperatures and the indoor air temperature are close to each other and fluctuate around 38 °C under periodic steady-state condition.

Figure 54.5 compares the indoor temperature variations for each case. The implementation of PCM mass into the wall shifts the time to reach the periodic steady-state condition. In Case 1, in which there is no PCM mass, the indoor temperature variation settles to a cyclic regime in a shorter time in comparison with the ones which incorporate PCM. In Case 2, the temperature history resembles with Case 1 for the first 40 h. Beyond this time, the thermal inertia of PCM (both sensible and latent) prevents the increase of indoor temperature, and indoor temperature maintains at the melting temperature of the PCM for an extended period. In

Table 54.3 Configuration of each case

Case	Layer A	Layer B	Total PCM thickness (cm)
1	Insulation	Insulation	**No PCM**
2	Insulation	**PCM**	1
3	**PCM**	**PCM**	2
4	**PCM**	Insulation	1

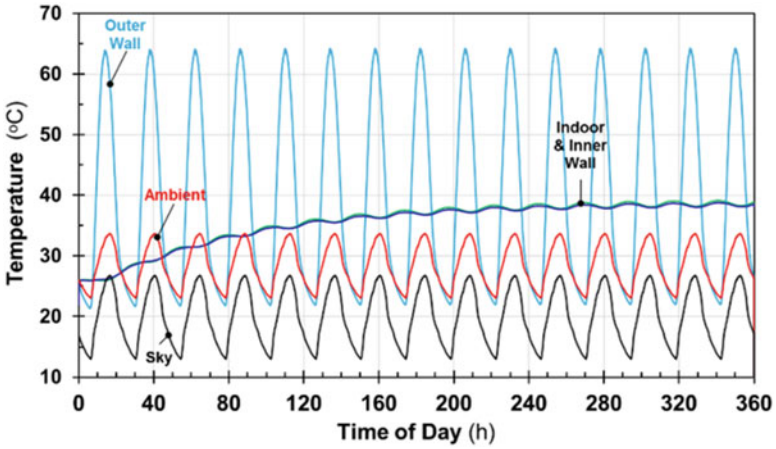

Fig. 54.4 Temperature variations for Case 1

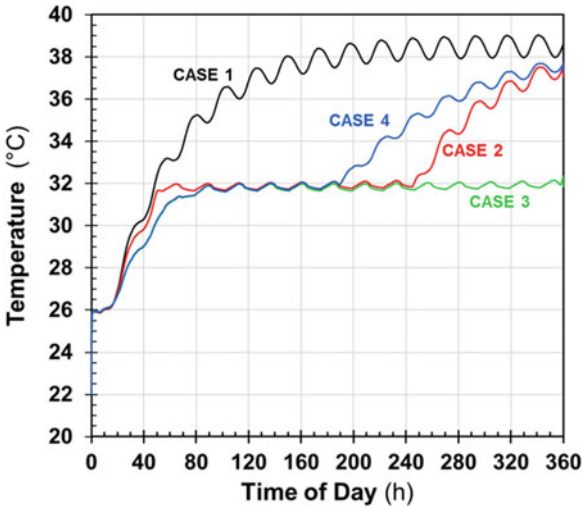

Fig. 54.5 Evolution of indoor temperature

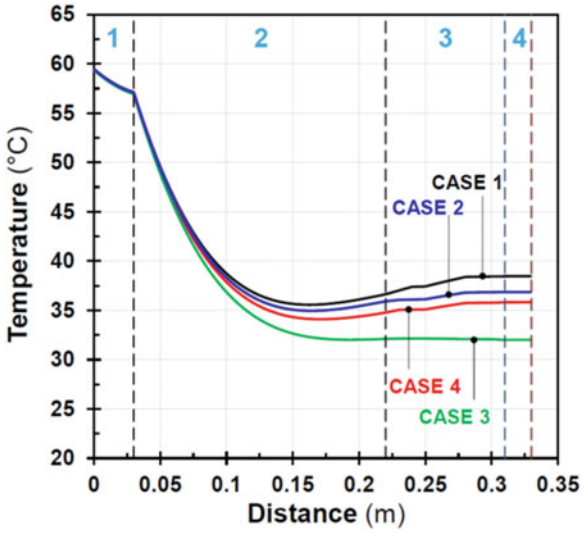

Fig. 54.6 Variation of temperature inside the wall at 12 am in 13th day

Case 2, the complete melting occurs on day 10 and the indoor temperature gradually increases beyond this point. For Case 3 and Case 4, indoor temperature variations differ from the others, particularly in the early stages of the process, since the PCM mass in Layer A delays the sudden increase in indoor temperature. Besides, since Case 3 involves the highest amount of PCM, the indoor temperature remains at 32 °C throughout the 1 days.

In Fig. 54.6, local temperature variations are given for each case at the noon of the 13th day. It is clear that the outer wall temperature is same in all of the cases independent of being with or without PCM. The influence of PCM on the

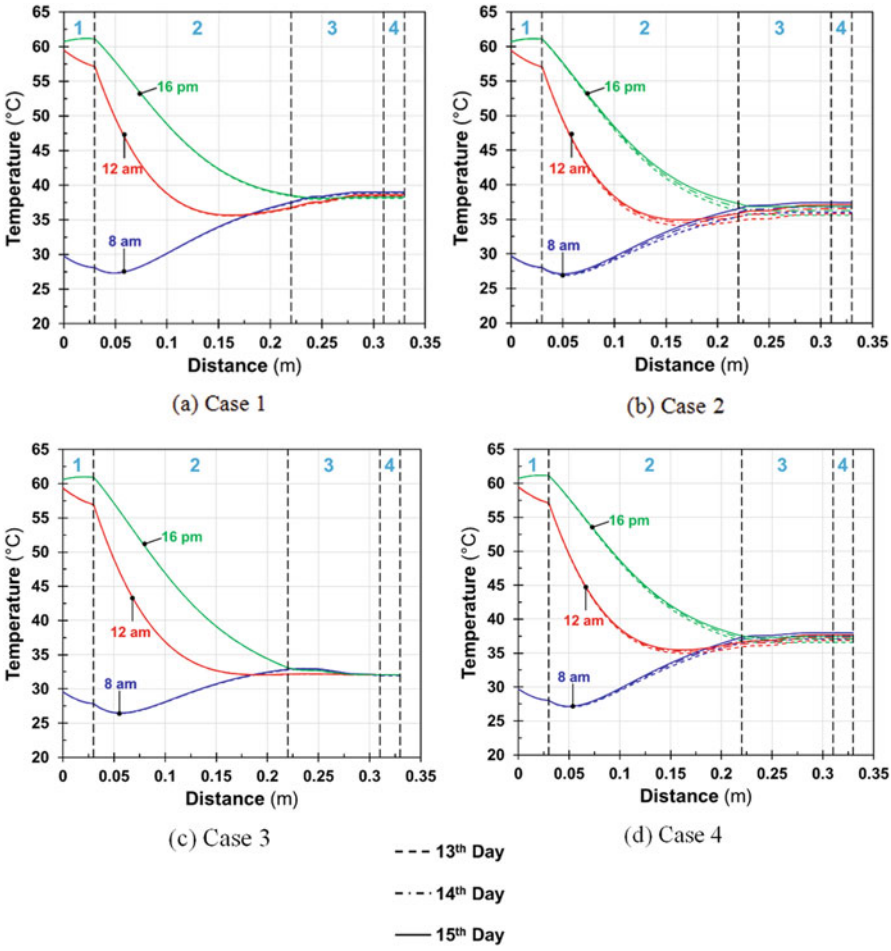

Fig. 54.7 Comparison of local temperature variations at selected hours of the last 3 days (**a**) Case 1 (**b**) Case 2 (**c**) Case 3 (**d**) Case 4

temperature distribution becomes apparent at the mid-width of Layer 2 and in Layers 3 and 4. The lowest temperatures are observed for Case 3, which includes the highest PCM mass. Case 3 reduces the wall temperature significantly. The reduction in indoor wall temperature is nearly 6 °C. Besides, the temperature distributions in Case 2 and Case 4 look similar, and regarding the indoor wall temperature, the difference between each case is 1 °C.

Lastly, Fig. 54.7 compares the local temperature variations at three selected hours of the last 3 days (13th, 14th, and 15th). It is clear that for Cases 1 and 3, the temperature variations for each day overlap. Since the transient temperature variations do not reach a periodic steady-state condition for Cases 2 and 4 (see Fig. 54.5), the local variations for each day have different trends especially nearby the inner

wall. Even though literature studies usually give results after 3 or 5 days, longer periods are necessary to reach steady-state condition for PCM incorporation.

It is interesting to note that from 8 a.m. to 16 p.m., even if the outer wall temperatures vary by nearly 30 °C, the variation of the inner wall surface temperatures is less than 5 °C. The thermal inertia of the insulation layer dampens the sudden temperature alterations of the indoors, and even in the case without PCM, the variation of the inner wall surface temperatures is very limited.

54.4 Conclusions

In this chapter, a one-dimensional model for a PCM-embedded building wall is developed in ANSYS FLUENT to simulate the transient indoor temperature variations for four different envelope designs. Unlike the previous works in the literature, both spatial and temporal temperature variations inside the wall are considered. For cooling under the Mediterranean climatic conditions, the following conclusions can be listed:

- Due to the higher thermal inertia of the building wall, transient analyses should be carried out longer periods to obtain a periodic steady-state condition for interpretation,
- The implementation of 1 cm PCM, either closer to indoors or outdoors, is not sufficient to hold the indoor temperature at the desired lower values.
- Incorporating 2 cm PCM significantly inhibits the heat transfer to the indoors and maintains the indoor temperature at 32 °C, which is 6 °C lower than the reference case. Usage of PCM in the building walls is a quite promising technology to reduce the energy consumption of the air-conditioning units and decrease the required cooling system implementation costs.
- While the PCM absorbs solar energy during the day, the main energy damping takes place in the thermal insulation material due to its amount; therefore the optimization of the amount of thermal insulation material would improve results.

Further studies should be conducted to discuss the influence of PCM under different climatic conditions and for various PCMs and wall configurations. In these studies, the energetic and economic aspects would also be considered in addition to the heat transfer physics. The current model in CFD software is quite promising since it allows the researchers to investigate complicated designs, such as 2D or 3D models, irregular geometries, and various climatic conditions.

Nomenclature

A	Area (m^2)
c	Specific heat (J/kg.K)
k	Thermal conductivity (W/m.K)
q	Heat transfer rate (W)
T	Temperature (K)

U	Overall Heat transfer coefficient (W/m^2.K)
V	Volume (m^3)
v	Wind speed (m/s)

Greek letters

ρ	Density (kg/m^3)
μ	Viscosity (Pa.s)
ΔT	Phase change temperature range K

Subscripts

air	Air
amb	Ambient
glass	Glass
m	Melting
s	Surface
sky	Sky

References

1. Darkwa K, Kim JS (2004) Heat transfer in neuron-composite laminated phase-change drywall. J Power Energy Proc Inst of Mech Eng Part A 218:83–88
2. Zhang YP, Lin K, Zhang Q, Di H (2006) Ideal thermal physical properties for free cooling (or heating) buildings with constant thermal physical property material. Energ Buildings 38 (10):1164–1170
3. Huang MJ, Eames PC, Hewitt NJ (2006) The application of a validated numerical model to predict the energy conservation potential of using phase change materials in the fabric of a building. Sol Energy Mater Sol Cells 90(13):1951–1960
4. Alawadhi EM (2008) Thermal analysis of a building brick containing phase change material. Energ Buildings 40:351–357
5. Kuznik F, Virgone J, Roux JJ (2008) Energetic efficiency of room wall containing PCM wallboard: a full-scale experimental investigation. Energ Buildings 40:148–156
6. Zhou G, Zhang Y, Lin K, Xiao W (2008) Thermal analysis of a direct-gain room with shape-stabilized PCM plates. Renew Energy 33:1228–1236
7. Zhang YP, Lin KP, Jiang Y, Zhou GB (2008) Thermal storage and nonlinear heat transfer characteristics of PCM wallboard. Energ Buildings 40:1771–1779
8. Haghshenaskashani S, Pasdarshahri H (2009) Simulation of thermal storage phase change material in buildings. World Acad Sci Eng Technol 58:111–115
9. Kara YA, Kurnuc SA (2012) Performance of coupled novel triple glass and phase change material wall in the heating season: an experimental study. Sol Energy 86:2432–2442
10. Kara YA, Kurnuç SA (2012) Performance of coupled novel triple glass unit and PCM wall. Appl Therm Eng 35:243–246
11. Izquierdo-Barrientos MA, Belmonte JF, Rodríguez-Sanchez D, Molina AE, Almendros-Ibáñez J (2012) A numerical study of external building walls containing phase change materials (PCM). Appl Therm Eng 47:73–85
12. Chwieduk DA (2013) Dynamics of external wall structures with a PCM (phase change materials) in high latitude countries. Energy 59:301–313
13. Jin X, Zhang S, Xu X, Zhang X (2014) Effects of PCM state on its phase change performance and the thermal performance of building walls. Build Environ 81:334–339

14. Lei J, Yang J, Yang EH (2016) Energy performance of building envelopes integrated with phase change materials for cooling load reduction in tropical Singapore. Appl Energy 162:207–217
15. Çengel YA, Ghajar A (2015) Heat and mass transfer: fundamentals and applications, 5th edn. McGraw-Hill Education, New York
16. Turkish Standarts Instititon (2008) TS 825, Thermal insulation requirements for buildings
17. Movida (2017) http://www.movida-project.eu. Last Accessed Day: 07.04.2017
18. Agyenim F, Hewitt N, Eames P, Smyth M (2010) A review of materials, heat transfer and phase change problem formulation for latent heat thermal energy storage systems (LHTESS). Renew Sust Energ Rev 14:615–628
19. Hendricks JHC, van Sark WGJHM (2013) Annual performance enhancement of building integrated photovoltaic modules by applying phase change materials. Prog Photovolt Res Appl 21(4):620–630
20. Incropera F, DeWitt DP, Bergman TL, Lavine AS (2006) Fundamental of heat and mass transfer, 6th edn. Wiley Inc, New York
21. Anderson T, Duke M, Morrison G, Carson J (2009) Performance of building integrated photovoltaic/thermal (BIPVT) solar collector. Sol Energy 83:445–455
22. Eicker U (2003) Solar technologies for buildings. Wiley, Chichester
23. Ansys Inc (2009) Ansys-Fluent 14.0 theory guide, ANSYS Inc.

Chapter 55
Improving Energy Efficiency in a Municipal Building: Case Study of Ekurhuleni Metropolitan Municipality Buildings in South Africa

Johanna Pérez, Fernando Alay, Aashis Joshi, Rocío Nallim, Lucas Chacha, and Luis Rojas-Solórzano

55.1 Introduction

Power and heat generation are the largest greenhouse gases (GHG) emitting activities, accounting up to 55% of global GHG emissions, according to the Fifth Assessment Report of the Intergovernmental Panel on Climate Change (IPCC) [1]. Besides transitioning to renewable sources of energy to limit fossil fuel use, reducing energy demand through energy efficiency improvement is key to limiting global temperature increase.

According to the United Nations Development Program (UNDP), residential, commercial, and public buildings account for 30–40% of global energy consumption and are responsible for nearly 30% of total GHG emissions including energy end-use emissions, electricity generation emissions, and district heat [2]. Energy end use in buildings vary among building types (residential, commercial, and public); however, the top three largest shares correspond to heating, ventilation, and air conditioning (HVAC) systems (32–39%), followed by lighting (12–25%) and water heating (6–12%) [3].

Technological advancements in energy-demanding systems, along with decreasing costs, mean that more effective measures can be implemented in buildings to enhance energy efficiency. As stated by the Global Environment Facility (GEF), "retrofitted buildings can reduce heating and cooling energy requirements by 50–90%." In a study done for the city of Hong Kong, Li and Lam (2003) claim that artificial lighting can account for 20–30% of the electricity consumption in typical nonresidential buildings [4]. Principi and Fioretti (2014) show that LEDs can

J. Pérez (✉) · F. Alay · A. Joshi · R. Nallim · L. Chacha
École des Mines de Nantes, Department of Energy Systems and Environment, Nantes, France

L. Rojas-Solórzano
Nazarbayev University, School of Engineering, Astana, Republic of Kazakhstan

S. Nižetić, A. Papadopoulos (eds.), *The Role of Exergy in Energy and the Environment*, Green Energy and Technology,
https://doi.org/10.1007/978-3-319-89845-2_55

provide a 41–50% reduction in electricity demand and global warming potential compared with CFL lighting systems [5].

In South Africa (SA), municipal and commercial buildings account for 12% of the national electricity demand [6], and typically 40% of the electricity is used in lighting and water heating. Electricity generation in SA relies heavily on fossil fuels, especially coal. Therefore, reducing electric consumption in these two systems could have a substantial impact on energy consumption and carbon emissions. In this work, the case of retrofitting the Germiston Civic Center and the EGSC buildings in the city of Ekurhuleni, South Africa, is presented as an example of energy efficiency improvement in a municipal building.

55.2 Background

Ekurhuleni is a city of 3.2 million people in Gauteng, SA [7], and it is a member of the International Council for Local Environmental Initiatives (ICLEI) Cities for Climate Protection Campaign (CCP). In 2005, a retrofitting project in the Ekurhuleni Metropolitan Municipality (EMM) buildings took place, involving the replacement of incandescent light bulbs with fluorescent light bulbs, installation of timers for the lighting and hot water systems (geysers), and substitution of kettles with hydroboils. The original project developed in 2005 received a capital incentive of 50% of the initial cost through a grant secured by ICLEI, achieving a payback period of 1.2 years [8]. Thus, the retrofit project attained energy savings of 53% and emissions reduction of 308 tonnes of CO_2 eq., 3 tonnes of SOx and 1 tonne of NOx.

In this work, a new project is evaluated in which current fluorescent lighting is replaced by LED and motion sensors. The possibility of replacing the existing geysers with a solar water heating system is also investigated. For both the lighting and hot water scenarios, an analysis of the energy, cost, and CO_2 emissions savings, as well as financial indicators to evaluate the financial feasibility of the project, is presented. In addition, the impact of existing energy efficiency policies of the South African government on the financial outlook of the project is assessed.

55.3 Methodology

Life-cycle cost assessment (LCCA) is a tool for assessing the total cost of acquiring, operating, and disposing of an investment. It allows estimating the overall costs of project alternatives to compare and select the one with the lowest overall cost. Based on the available information from 2005, a retrofitting project for the year 2016 is proposed and a LCCA of energy efficiency measures in the EMM buildings is performed, thus evaluating the impact of current technologies, costs, and policies in the financial behavior of the project.

The data gathered for this project included the location, current energy consumption of each system, current and proposed equipment technical data, and costs.

Given the level of completeness of the data, this work is considered as a feasibility study, and therefore the results obtained from the methodology described below are expected to have an accuracy of ±25%.

55.3.1 Lighting System

55.3.1.1 Changing Technology: From Fluorescent to LED (Scenario 1A)

The EMM buildings consist of office spaces and workspace with different lighting needs. The goal is to propose a LED lighting system that provides the same or greater illumination (measured in lumens) as the fluorescent system in place (base case).

For the office area, the proposal is to install the same number of LED lamps as the CFLs, to make use of all the current lighting fixtures and layout. The workspace area has 5-foot fluorescent tubes, and it is proposed to install LED tubes of the same length to avoid costs associated with installing new fixtures. The methodology is outlined below.

- *For the office space:*

With data including yearly energy consumption and operation time of lighting system in this area, as well as the number of CFLs in place, it is possible to estimate the power load of each CFL, by using Eqs. (55.1) and (55.2).

$$P_{\text{tot,CFL}} = \frac{Q_{\text{tot,CFL}}}{t} \tag{55.1}$$

$$P_{\text{CFL}} = \frac{P_{\text{tot,CFL}}}{N_{\text{CFL}}} \tag{55.2}$$

With the average value of lumen rating (R_{CFL}) and the power, the lumen output of each CFL is determined.

$$L_{\text{CFL}} = P_{\text{CFL}} \times R_{\text{CFL}} \tag{55.3}$$

Since the LEDs are expected to provide the same lumen output as the CFLs, the average value of lumen rating (R_{LED}) is used to estimate the power required per LED with Eq. (55.4), as follows:

$$P_{\text{LED}} = \frac{L_{\text{LED}}}{R_{\text{LED}}} \tag{55.4}$$

By keeping the number of light bulbs and the operation time constant, it is possible to estimate the yearly energy consumption of the new lighting system using a rearrangement of Eq. (55.1).

- *For the workspace:*

Like the office space, the data for the workspace allowed to estimate the load of the existing system of T5 fluorescent tubes:

$$P_{\text{tot, T5}} = \frac{Q_{\text{tot, T5}}}{t} \tag{55.5}$$

Since each fixture in the workspace holds two T5 tubes, the number of tubes is determined by Eq. (55.6):

$$N_{\text{FT}} = N_{\text{T5}} \times 2 \tag{55.6}$$

The power of each existing fluorescent tube is estimated with Eq. (55.7) and the lumen rating (R_{FT}) is considered to determine the lumen output of the existing system with Eq. (55.8):

$$P_{\text{FT}} = \frac{P_{\text{tot, T5}}}{N_{\text{FT}}} \tag{55.7}$$

$$L_{\text{FT}} = P_{\text{FT}} \times R_{\text{FT}} \tag{55.8}$$

Since the LED tubes are expected to provide the same lumen output as the fluorescent, the average value of lumen rating ($R_{\text{T5, LED}}$) is used to estimate the power of the tube with Eq. (55.9) as follows:

$$P_{\text{T5,LED}} = \frac{L_{\text{T5,LED}}}{R_{\text{T5, LED}}} \tag{55.9}$$

These calculations, for both the offices and workspace, allow to estimate the wattage of the new LED light bulbs and tubes. This serves as a guide to search products commercially available to define the final system.

Finally, the total cost of purchase, installation, and operation and maintenance (O&M) of the LEDs is compared with the savings resulting from decreased electricity consumption and decreased O&M costs, to assess the feasibility of the project.

55.3.1.2 Changing Technology: From Fluorescent to LED with Motion Sensors (Scenario 1B)

Motion sensors allow switching lights on and off depending on the occupancy of a space. Each motion sensor can detect movement within a certain area range. Installing motion sensors reduces electricity consumption by around 32% [9]. LEDs used in conjunction with motion sensors therefore achieve greater energy efficiency and reduce electricity expenditure, which enhances the feasibility of the project.

The number of sensors required is calculated based on the coverage area (A_{cov}) and the total floor space area. The number of sensors is calculated with Eq. (55.10):

$$N_{\text{sensor}} = \frac{A_{\text{floor}}}{A_{\text{cov}}} \tag{55.10}$$

Passive infrared (PIR) motion or vacancy sensors are proposed for both the office and workspaces. These have an average power consumption of approximately 0.002 W, which amounts to 0.006 kWh/year per sensor in electrical energy consumption.

55.3.2 Hot Water System

55.3.2.1 Changing Technology: From Electric Heaters to Solar Water Heater (Scenario 2)

The current hot water system consists of electric heaters operated with timers that limit the electric resistance consumption to a fraction of hours a day. Although further efficiency may be achieved by installing new electric heaters, the aim of this work is to explore the possibility of using a renewable energy technology, such as a solar water heating system. This allows reducing the energy demand from conventional electricity (which is originated mostly from fossil fuels).

55.3.2.2 Hot Water Estimation

Since data about the volume of annual hot water consumed or number of occupants were not available, the electric system dimension (average daily hot water used) was estimated based on the operation hours and the current yearly energy consumption reported for the electric heaters.

First, the daily energy consumption of the water heaters is estimated using daily and yearly operation times as in Eq. (55.11):

$$Q_{\text{day}} = \frac{Q_{\text{year}} \times t_{\text{day}}}{t_{\text{year}}} \tag{55.11}$$

To estimate the hot water consumption, an average water inlet temperature ($T_{\text{in}} = 14\ ^{\circ}\text{C}$) and outlet temperature ($T_{\text{out}} = 60\ ^{\circ}\text{C}$) are assumed.

$$V_{\text{day}} = \frac{Q_{\text{day}}}{C_{\text{p}} \times \Delta T \times \rho} \tag{55.12}$$

The value obtained for the hot water estimation was entered to RETScreen (2013) model platform by adjusting parameters such as load type (office), number of occupants, occupancy rate, and schedule. RETScreen possesses an integrated climate database of the location in SA, which allows estimating the yearly energy

consumption for the base case (electric heating). This value coincided with the original data available for the base case of the project, which served to validate the assumptions and as a basis for dimensioning the solar water heating system.

The proposed solar water heating system can replace 74% of the use of the electric heaters. The system consists of an evacuated heating system, given the temperature gradient required during the winter season (increase from 10 °C to 60 °C), since evacuated systems can deliver larger heating than glazed and unglazed heaters. In addition, environmental temperature does not involve a risk of water freezing in the heating system; thus a direct system is proposed.

55.3.3 Implementing Energy Efficiency Policies

Over the last few years, the Government of the Republic of South Africa has been actively implementing policies to promote energy efficiency. The National Energy Efficiency Strategy of the Department of Energy set a national target for an energy efficiency improvement of 12% by 2015, using the consumption in 2000 as the baseline. A target of 15% improvement in energy efficiency in commercial and public buildings is part of this strategy [10].

South Africa's electricity public utility, Eskom, has a rebate model that offers consumers an incentive for converting their energy inefficient technologies to efficient ones. Its Standard Offer, which is available to consumers who can achieve verifiable energy savings in projects consuming from 50 kW to 5 MW, covers both lighting and solar water heating systems. For implementing LED light bulbs, Eskom offers a rebate of 0.04 USD per kWh saved, and for hot water systems, the rebate is 0.03 USD per kWh saved [11].

55.3.3.1 Effect of Policies on Lighting System Project (Scenario 3A)

Based on the amount of energy saved, the total amount of incentives possible for the project are calculated and added to the cash flow as a reduction in the cost of the project. According to the Policy, this incentive is received during the first 3 years after the installation of the new technology. The incentives are applied to the more attractive financial scenario (in this case, installation of LED technology and motion sensors, scenario 1B).

55.3.3.2 Effect of Policies on Solar Water Heater Project (Scenario 3B)

In addition to the rebates offered by Eskom, the National Energy Regulator of South Africa (NERSA) plans to save 1730 MW in the 5-year period from 2013–2014 to 2017–2018. To this end, it has approved US$ 670 million in funding, which amounts to US$ 387 per kW installed of solar water heating systems [11]. As

in the lighting project, the rebates are calculated based on the amount of energy saved and added to the cash flow, considering it as a reduction in the cost of the project.

55.4 Results and Discussions

55.4.1 Technical Design

55.4.1.1 Lighting System

The calculations proposed in the previous section allowed to define the lighting system configuration for both the office and workspace. Table 55.1 below shows these results and the data used for the energy and cost assessment for the workspace and the office area, respectively.

The data for this project included the area (m^2) for the spaces evaluated and this allows to estimate the power load (W/m^2), which is the coefficient of the sum of the loads of all the lamps in an area, and the area. This parameter is the main input for the energy and environmental analysis for lighting retrofit projects in RETScreen.

55.4.1.2 Solar Water Heating

From the daily hot water use estimated, the solar water heater configuration is determined, including collector area, storage tank capacity, and the elements required for the energy and cost evaluation.

Table 55.1 Lighting system configuration

Scenario	Base Case (2005)	Proposed Case
Workspace		
Floor area, m^2	3200	3200
Lighting technology	5-ft fluorescent tubes	5-ft LED tubes
Lamp power, W	32	20
Lamp quantity, units	192	212
Power load, W/m^2	1.9	1.3
Office area		
Floor area, m^2	11,700	11,700
Lighting technology	CFL	LED
Lamp power, W	15	9
Lamp quantity, unit	2003	2003
Power load, W/m^2	2.6	1.6
Power load (sensors), W/m^2	–	1.1

Table 55.2 Solar water heating system configuration

	Solar water heating
Load type	Office
Number of units, person	290
Occupancy rate, %	85
Daily hot water use, L/d	937
System technology	Evacuated, direct
Number of collectors, units	3
Solar collector area, m^2	14.43
Capacity, kW	8.74
Storage capacity, L	936
Heating delivered, MWh	9.3

Table 55.3 Energy savings and environmental results (from RETScreen)

Scenario.	1A	1B	2
Pre-retrofit energy use (kWh/yr.)	114,000	114,000	12,600
Post-retrofit energy use (kWh/yr.)	72,000	49,000	3300
Energy savings (kWh/yr.)	43,000	65,000	9300
Energy saving (%)	37.3	56.8	73.8
Emission reduction (tonnes CO_2)	41.6	63.3	9.2

The model available in RETScreen allows entering data such as a detailed operational schedule and consumption parameters. It also has embedded the technical specifications of commercially available heaters which provide important data for the design. The proposed solar water heating system is outlined in the Table 55.2 below.

55.4.2 Energy Savings

The results of the energy analysis for each proposed scenario shown in Table 55.3 evidence the improvement in energy savings, due to the change in the technology. It is possible to save up to 37.3% of total energy usage and to achieve emissions reduction of 41.6 tonnes CO_2 eq., only by changing CFL to LED technology (scenario 1A) and up to 56.8% energy saving and 63.3 tonnes CO_2 eq. when motion sensors are incorporated (scenario 1B).

The use of solar water heaters as an alternative thermal energy source allows reducing the energy consumption in geysers by 73.8% (scenario 2).

Table 55.4 Financial results (From RETScreen)

Scenario.	1A	1B	3A	2	3B
Investment (thousand USD)	12.1	15.7	15.7	9.0	9.0
Incentives (thousand USD)	–	–	6.6	–	4.1
NPV (thousand USD)	17.2	29.7	36.3	3.4	7.5
IRR (%)	35.6	43.4	75.0	11.7	20.5
Benefit–cost (ratio)	2.4	2.9	3.3	1.4	1.8
Equity payback (yrs.)	2.8	2.4	1.4	9.2	5.7

55.4.3 Financial Results

By making use of publicly available information on the costs of the systems suggested, as well as other variables such as electricity cost in SA, inflation rate, and discount rate, a financial analysis for the scenarios 1A, 1B, and 2 is built.

For the most energy-efficient scenario for lighting (scenario 1B) and for the solar water heater (scenario 2), the effect of energy policies is included in the project financial indicators. From this, scenarios 3A and 3B are obtained. Table 55.4 shows the financial results.

In scenario 3A, replacing CFLs with LEDs and motion sensors, the policy allows obtaining a rebate that increases the NPV to USD 36,263; this is a 22% increment from the NPV without incentives (scenario 1B). Also, the payback period of this retrofit drops from 2.4 to 1.4 years.

The scenario 3B, replacing geysers with a solar water heating system, allows receiving a rebate that rises the NPV to USD 7515, thus increasing 120% the NPV of the project without incentives (scenario 2) and lowering the payback period from 9.2 to 5.7 years.

55.5 Conclusions

In this work, the life-cycle cost assessment for the water heating and lighting retrofitting in a municipal building in Ekurhuleni, South Africa, is presented. The change from fluorescent to LEDs (including motion sensors) and from electric to solar water heating allows for significant energy savings (56.8% and 73.8%, respectively). Combined, these two measures could achieve 72.5 tonnes CO_2 eq. emissions reduction yearly.

For the lighting system project, the decrease in electricity consumption leads to enough cost savings to cover the capital costs within a reasonable payback period of 2.8 years and an NPV of 17,163 USD. These indicators improve to 2.4 years and 29,682 USD with the use of motion sensors. The water heating retrofit project has a payback period of 9.2 years with an NPV of 3417 USD.

The financial outlook for both projects improve significantly when the incentives and grants offered by Eskom and NERSA are considered, with the payback period decreasing to 1.4 and 5.7 years for the lighting and hot water projects, respectively, and the NPVs increasing to 36,263 and 7515 USD, accordingly.

Nomenclature

P	Power (W)
Q	Energy (J)
t	Operation time (s)
N	Number
L	Luminous flux (lm)
R	Lumen rating (lm/W)
A	Area (m2)
V	Volume (liter)
?	Density of water (kg/liter)
Cp	Specific heat capacity of water (kJ/kg/°C)
ΔT	Temperature difference (°C)

Subscripts

CFL	Compact fluorescent lamp
Tot	Total
LED	Light-emitting diode
FT	Fluorescent tube
T5	T5 fixture
Floor	Floor space
Cov	Coverage area for sensor
sensor	Motion sensor

References

1. Intergovernmental Panel on Climate Change (IPCC) (2015) Intergovernmental Panel on Climate Change (IPCC) [Online]. Available: https://www.ipcc.ch/pdf/assessment-report/ar5/syr/SYR_AR5_FINAL_full_wcover.pdf. [Accessed 5 October 2017]
2. United Nations Development Program (2009) Promoting energy efficiency in buildings: lessons learned from international experience, March 2009. [Online]. Available: https://www.thegef.org/sites/default/files/publications/EEBuilding_WEB_2.pdf. [Accessed 9 October 2017]
3. Center for Climate and Energy Solutions (2009) Center for Climate and Energy Solutions, May 2009. [Online]. Available: https://www.c2es.org/docUploads/Buildings%20Overview%20Final.pdf. [Accessed 5 October 2017]
4. Li D, Lam J (2003) An analysis of lighting energy savings and switching frequency for a daylit corridor under various indoor design illuminance levels. Appl Energy 76:363–378
5. Principi P, Fioretti R (2014) A comparative life cycle assessment of luminaires for general lighting for the office compact fluorescent (CFL) vs light emitting diode (LED) a case study. J Clean Prod 83:96–107

6. Eskom Holdings Limited (2010) Mind your own business: energy efficiency in commercial properties, May 2010. [Online]. Available: http://www.eskom.co.za/sites/idm/Documents/126455ESKD_Brochure_May_2010.pdf
7. Statistics South Africa (2016) "Ekurhuleni," 17 Dec 2016. [Online]. Available: http://www.statssa.gov.za/?page_id=1021&id=ekurhuleni-municipality
8. Parra M, Williams R (2006) Improving energy efficiency in Ekurhuleni metropolitan municipal buildings, April 2006. [Online]. Available: https://www.ase.org/sites/ase.org/files/ekurhuleni_ee_case_study_4_06.pdf
9. Ray J (2014) Energy-wise homes. An economic and policy analysis, 29.10.2014. [Online]. Available: http://www.academia.edu/12828409/Energy_Wise_Homes
10. Department of Energy Republic of South Africa (2013) Overview on the National Energy Efficiency Strategy (NEES) Post 2015, 26 Sept 2013. [Online]. Available: http://www.energy.gov.za/files/IEP/jhb_workshop/Overview-on-the-National-Energy-Efficiency-Strategy-Post2015-26Sep2013.pdf
11. Rue C (2013) Energy efficiency country study: republic of South Africa. Lawrence Berkeley National Laboratory, Berkeley

Chapter 56
Assessment of Energy Consumption in Spanish Hospitals

Justo García-Sanz-Calcedo, Alfonso G. González, and David R. Salgado

56.1 Introduction

At present, there is a global commitment to reduce carbon dioxide emissions in order to avoid novice global levels of 450 ppm CO_2 in our planet. This could prevent the rise of the global temperature on Earth [1].

According to the Spanish Institute for Diversification and Saving of Energy (IDAE), the building sector represents one of the areas with the highest influence on carbon dioxide emissions to the atmosphere [2].

The US Department of Energy estimates that hospitals are buildings within the tertiary sector, which, because of their infrastructure and purpose, consume large energy resources [3].

The saving and energy efficiency guide for hospitals in 2010 issued by Energy Madrid Foundation indicates that the annual energy consumption in a small hospital reaches 40.000 kWh with an annual expense of €8400 [4].

Santamouris et al. (2008) carried out a detailed analysis of audits for 30 healthcare buildings in Greece (Hellas). The results show that it is possible to save up to 20% of energy [5].

J. García-Sanz-Calcedo (✉)
Graphical Expression Department, University of Extremadura, Badajoz, Spain
e-mail: jgsanz@unex.es

A. G. González
Department of Mechanical, Energy and Materials Engineering, University of Extremadura, Mérida, Spain

D. R. Salgado
Department of Mechanical, Energy and Materials Engineering, University of Extremadura, Badajoz, Spain

S. Nižetić, A. Papadopoulos (eds.), *The Role of Exergy in Energy and the Environment*, Green Energy and Technology,
https://doi.org/10.1007/978-3-319-89845-2_56

Vanhoudt et al. (2011) demonstrated that in a hospital in Belgium, potentially it is possible to save up to 71% of the primary energy system by using thermal energy storage in combination with a heat pump compared to a gas-based boilers and water chiller [6].

Szklo et al. (2004) analysed the energy consumption indicators and CHP technical potential in the Brazilian hospital sector and determined that the average ratio between electric and thermal loads in the hospitals was suitable for a cogeneration system operation [7]. An analysis performed for a non-optimized cogeneration system predicted large potential for energy savings and CO_2 reduction. Short et al. (2012) showed that the UK health sector accounts for 30% of public sector emissions [8].

Hu et al. studied energy consumption at a large acute care hospital in Taiwan (Hu, Chen and Chuah, 2004). They concluded that the use of air conditioning (HVAC) has a great impact on the electricity consumption, since it comprises more than 50% of the total energy used [9]. Other research studies carried out by Natural Resources Canada indicated that the highest energy consumption was due to how heating, lighting and ventilation were managed [10].

Kapoor and Kumar (2011) showed that heating, ventilation and air conditioning (HVAC) generate the highest energy consumption in hospitals, followed by illumination, with a percentage between 30–65% and 30–40%, respectively [11]. The Australian Department of Health in a study performed in 2012 on a suburban hospital concluded that HVAC is the most contributory to energy consumption and emissions, adding up to 65 and 47%, respectively [12].

In Spain, the savings potential derived from the energy management in hospitals has not been studied systematically. However, studies of other smaller types of sanitary buildings, such as healthcare centres, were carried out. Authors reported on the analysis of energy efficiency in healthcare buildings to conclude that the potential to reduce the energy consumption of a healthcare building sized 1000 m^2 is 10,801 kWh by making an average investment of €11,601, thus saving €2961/year with 3.92 years average payback time [13].

The aim of this paper is to analyse and quantify the final average energy consumption in hospitals in Spain, according to different variables.

56.2 Methodology

An analytical study was carried out between 2005 and 2014 in 18 hospitals located in Spain. They were built between 1980 and 2005.

The data analysed were obtained from EMAS Regulation (European Parliament, 2009), a voluntary European Union standard that recognizes organizations that have implemented an environmental management system (EMS), and they have a commitment to continuous improvement, verified by independent audits [14]. Eco-Management and Audit Scheme (EMAS) statements from hospitals have been analysed.

The correlation coefficient was obtained by dividing the covariance of the two variables by the product of their standard deviations [15]. The population correlation coefficient $\rho_{X,Y}$ between two random variables X and Y with expected values μ_X and μ_Y and standard deviations σ_X and σ_Y is defined by Eq. 56.1:

$$\rho_{X,Y} = \frac{\operatorname{corr}(X,Y)}{\sigma_X \sigma_Y} = \frac{E[(X-\mu_X)(Y-\mu_Y)]}{\sigma_X \sigma_Y} \tag{56.1}$$

where E is the expected value operator, cov means covariance, and corr is a widely used alternative notation for the correlation coefficient.

If we have a series of n measurements of X and Y written as x_i and y_i for $i = 1, 2,..., n$, then the sample correlation coefficient can be used to estimate the population Pearson correlation r between X and Y. The sample correlation coefficient was written as shown in Eq. 56.2:

$$r_{xy} = \frac{\sum_{i=1}^{n}\left(x_i-\bar{x}\right)\left(y_i-\bar{y}\right)}{(n-1)s_x s_y} = \frac{\sum_{i=1}^{n}\left(x_i-\bar{x}\right)\left(y_i-\bar{y}\right)}{\sqrt{\sum_{i=1}^{n}\left(x_i-\bar{x}\right)^2 \sum_{i=1}^{n}\left(y_i-\bar{y}\right)^2}} \tag{56.2}$$

where x and y are the sample means of X and Y, and s_x and s_y are the corrected sample standard deviations of X and Y.

The final energy consumption was obtained after conversion of the corresponding thermal energy consumption into its equivalent electrical energy. In order to do so, a relationship between both energies was set as a function of the coefficient of performance (COP) of a conventional air condensation heat pump [16] to yield the following expression:

$$C = \mathrm{Ct}/2.6 + \mathrm{Ce}, \tag{56.3}$$

where C, Ct and Ce represent the annual consumptions for final, thermal and electric energies, respectively, expressed in kWh.

56.3 Results

The correlation between the average annual energy consumption and the three indicators selected (built surface area, number of employees and number of beds) is now presented.

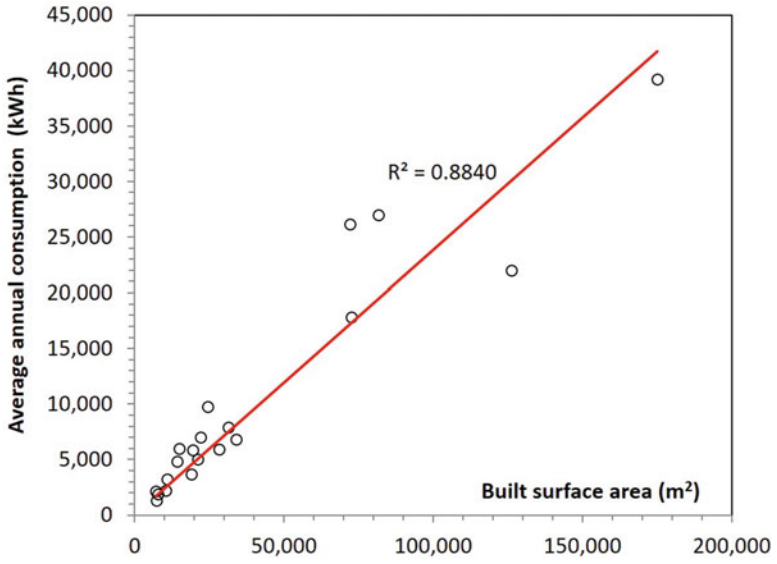

Fig. 56.1 Relationship between the average annual final energy consumption and the built surface area

56.3.1 Relationship Between Average Annual Final Energy Consumption and Built Surface Area per Hospital

Figure 56.1 shows the final energy consumption and built surface area of the analysed sample. A high correlation ($R^2 = 0.8840$) was observed between the average annual consumption and built surface area.

Equation 56.4 defines the relationship between the average annual final energy consumption as a function of the built surface area per hospital:

$$EC = 0.23A + 1,261.9 \tag{56.4}$$

where EC represents the average annual final energy consumption, expressed in MWh, and A is the value of the built surface area, expressed in m^2.

56.3.2 Relationship Between Average Annual Final Energy Consumption and Number of Employees per Hospital

Figure 56.2 shows the energy consumption and the number of employees per hospital. A clear correlation between those two variables was noted, showing a Pearson coefficient of 0.8630. Equation 56.5 defines the relationship between

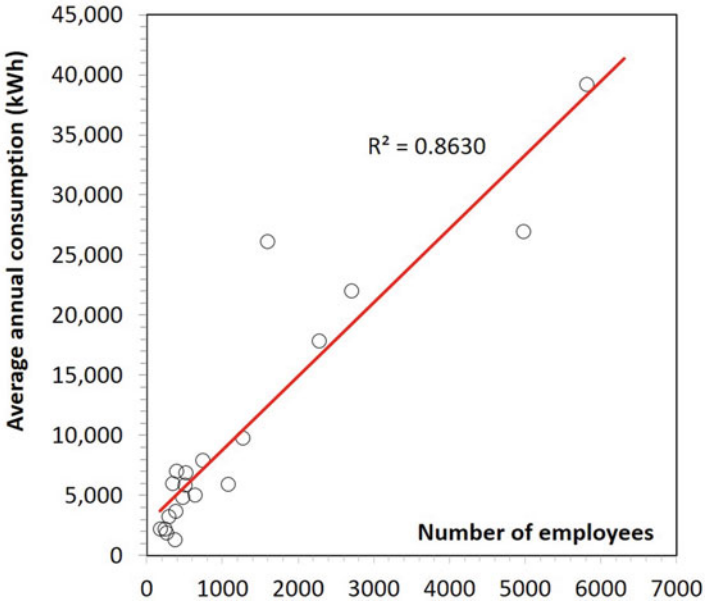

Fig. 56.2 Relationship between the average annual final energy consumption and the number of employees

average annual energy consumption as a function of the number of employees per hospital:

$$\mathrm{EC} = 6.20\,\mathrm{NW} + 2,437.60 \tag{56.5}$$

where EC represents the average annual consumption of final energy, expressed in MWh, and NW indicates the number of employees per year and hospital.

56.3.3 Relationship Between Average Annual Final Energy Consumption and Number of Beds per Hospital

In Fig. 56.3, we can see the relationship between the average annual final energy consumption (in kWh) and the number of beds (NB). In this case, although the correlation remains high, the result for the Pearson coefficient (0.8380) is the lowest of the three indicators analysed to estimate final energy consumption in a hospital.

Equation 56.6 defines the relationship between the average annual final energy consumption as a function of the number of beds per hospital:

$$\mathrm{EC} = 31.67\,\mathrm{NB} + 679 \tag{56.6}$$

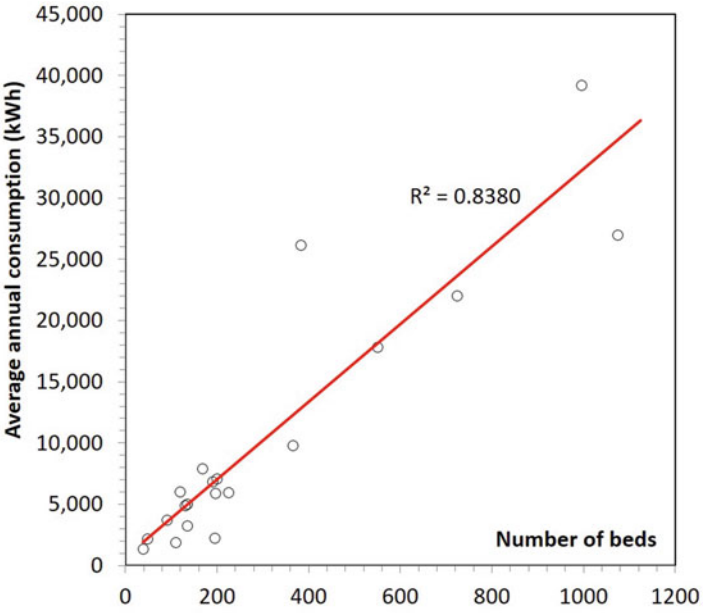

Fig. 56.3 Relationship between the average annual final energy consumption and the number of hospital beds

where EC represents the average annual energy consumption, expressed in MWh, and NB is the number of beds per hospital.

56.3.4 Relationship Between Number of Hospitals and Mean Consumption Values

The ratios of the average annual final energy consumption shown in Figs. 56.4, 56.5 and 56.6 have been collected according to the built surface area, the number of employees and the number of beds per hospital.

The average annual final energy consumption according to the built surface area is 271.69 kWh/m^2.

Figure 56.5 shows the average annual final energy consumption according to the number of employee, with a value of 9992.45 kWh/employee.

Similarly, the above figure represents the average annual final energy consumption according to the number of beds (34,609.98 kWh/bed).

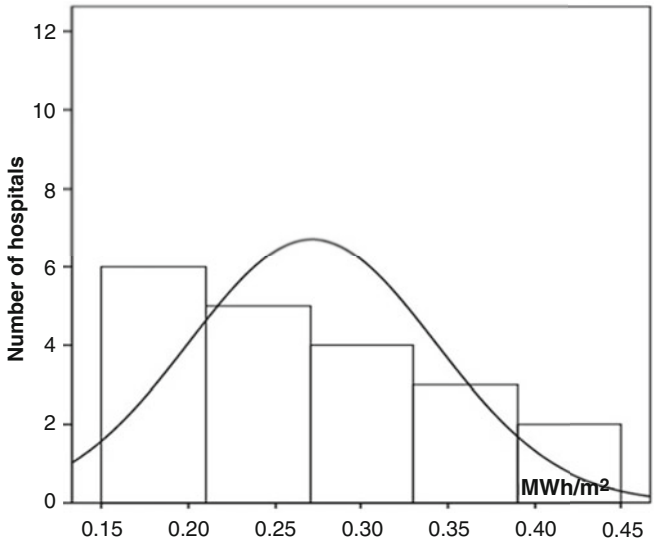

Fig. 56.4 Average energy consumption per built surface area of the hospital (MWh/m^2)

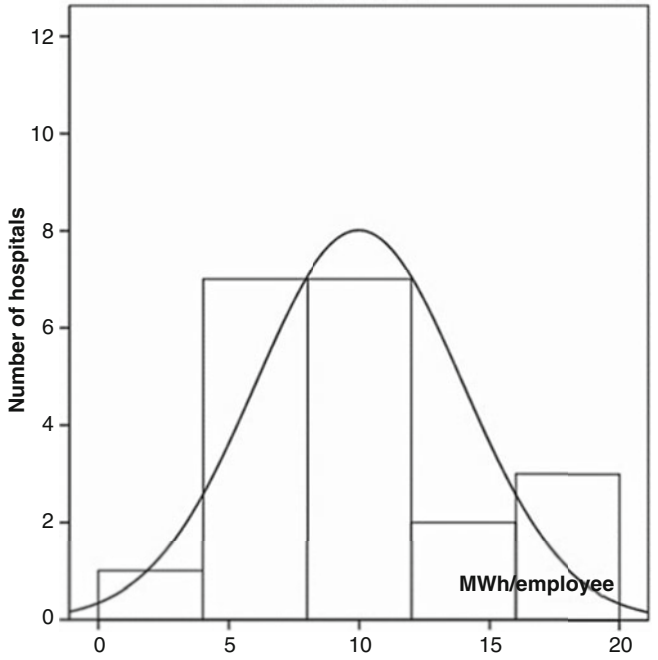

Fig. 56.5 Average energy consumption per employee (MWh/employee)

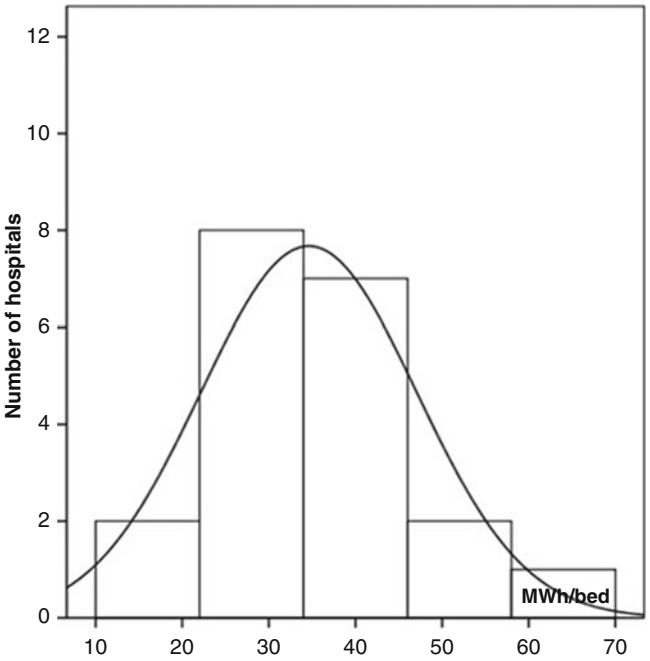

Fig. 56.6 Average energy consumption per bed (MWh/bed)

56.4 Discussion

Any measures taken in order to improve the energy efficiency of a hospital must consider the climatic and the proper operating conditions of this type of buildings. They should not contravene other essential requirements, such as accessibility, safety and reliability of their facilities. The prevailing indoor conditions should ensure air quality and thermal and visual comfort, in order to have a healing effect on patients [17].

It has been detected in general that a large amount of the budget is directly used for to the daily management of the hospital [18]. It is advisable to promote awareness campaigns for energy-saving measures. Also, reasonable goals should be set in order to improve energy-saving motivation, which would preferably involve the change of user habits.

Healthcare engineering has a relevant issue in hospital management, since one of its objectives is focused on energy and environmental efficiency of the building [19]. Also objective is fulfilment of the Environmental Biosafety conditions, keeping the perspective of patient safety [20].

It is recommended to perform periodic maintenance audits in order to determine whether building management actions are adequate and to anticipate the trend for maintenance demand in the future [21].

An appropriate selection of energy service companies for the implementation and financing of energy efficiency measures would improve the management of this type of public buildings. It is necessary to take into account to carry out a correct planning of the hospital projects [22].

However, thermal discomfort or inadequate lighting levels may affect medical diagnosis [23], and appropriate infection control measures could be directly affected by insufficient ventilation. Taking into account the particular characteristics of this type of public building, none of the energy-saving measures can compromise the health and comfort of users.

56.5 Conclusions

In this chapter, assessment of energy consumption in Spanish hospitals was analysed by using Pearson's product-moment coefficient. The results show that the average annual energy consumption in normal operation conditions in the hospitals under study can serve as a starting point for the development of indicators in order to quantify the exact consumption of energy. They can also help to set optimal hospital infrastructure through healthcare engineering.

The results obtained in this research will allow us to have average reference indicators on energy consumption. With these indicators are able to know which are saving measures more effective to reduce the energy consumption in hospitals. Table 56.1 shows the average energy consumption as a function of the different variables studied.

The results of this research may serve as a starting point for the development of indicators to quantify the exact consumption of energy in a given hospital. A comparative research study in different types of organizations and hospitals in other countries may be of interest to establish a more thorough comparison in energy building efficiency, particularly in the correlation of thermal comfort with energy consumption.

The data and results of this research have been provided to the regional health authorities so that they can serve to improve the management of hospital facilities.

Table 56.1 Consumption ratios

Ratio	Average
$\frac{\text{average energy consumption (kWh)})}{\text{built surface area (m}^2\text{)}}$	270
$\frac{\text{average energy consumption (kWh)}}{\text{number of employees}}$	10,000
$\frac{\text{average energy consumption (kWh)}}{\text{number of beds}}$	35,000

Nomenclature

A	Built surface area (m^2)
C	Annual consumptions for final energy (kWh)
Ce	Annual consumptions for electric energy (kWh)
Ct	Annual consumptions for thermal energy (kWh)
EC	Average annual final energy consumption (MWh)
NB	Number of beds per hospital.
NW	Number of employees per year and hospital

Acknowledgements The authors wish to acknowledge to the Junta de Extremadura for the support of this research work, which was supported by Project GR-15057 from the Regional Government of Extremadura and the European ESIF funds, linked to the V Research and Development Regional Plan (2014–2017).

References

1. European Council (2002) Directive 2002/91 of the European Parliament and of the Council on the energy performance of buildings
2. National Action Plan for Energy Efficiency 2017–2020 in Spain (2016)
3. American Society for Healthcare Engineering (2015) High performance hospital partnerships: reaching the 2030 challenge and improving the health, and healing environment
4. Madrid Energy Foundation (2010) Guía de Ahorro y Eficiencia Energética en Hospitales
5. Santamouris M, Dascalaki E, Balaras C et al (2008) Energy performance and energy conservation in health care buildings in Hellas. Energy Convers Manag 35(4):293–305
6. Vanhoudt D, Desmedt J, Van Bael J et al (2011) An aquifer thermal storage system in a Belgian hospital: long-term experimental evaluation of energy and cost savings. Energ Buildings 43:3657–3665
7. Szklo AS, Soares JB, Tolmasquim MT (2004) Energy consumption indicators and CHP technical potential in the Brazilian hospital sector. Energy Convers Manag 45:2075–2091
8. Short CA, Lomas KJ, Giridharan R, Fair AJ (2012) Building resilience to overheating into 1960's UK hospital buildings within the constraint of the national carbon reduction target: adaptive strategies. Build Environ 55:73–95
9. Hu SC, Chen JD, Chuah YK (2004) Energy cost and consumption in large acute hospital. Int J Archit Sci 5:11–19
10. Natural Resources Canada (2003) Benchmarks and best practices for acute and extended health care facilities: a guide for energy managers and finance officers: Natural Resources Canada1/4Ressources naturelles, Ottawa
11. Kappor R, Kumar S (2011) Energy efficiency in hospitals best practice guide (p 52). New Delhi, India: USAID, ECO-III project
12. Australia Department of Health (2012) Sustainability in healthcare. Victoria Department of Health
13. García Sanz-Calcedo J (2014) Analysis on energy efficiency in healthcare buildings. J Healthc Eng 5(3):361–373
14. European Parliament (2009) Regulation (EC) No 1221/2009 of the European Parliament and of the Council of 25 November 2009 on the voluntary participation by organizations in a Community eco-management and audit scheme (EMAS), repealing Regulation (EC) No 761/2001 and Commission Decision 2001/681/EC, Bruxelles

15. Adler J, Parmryd I (2010) Quantifying colocalization by correlation: the Pearson correlation coefficient is superior to the Mander's overlap coefficient. Cytometry A 77(8):733–742
16. Garcia-Sanz-Calcedo J, López F, Cuadros F (2014) Quantitative analysis on energy efficiency of health centers according to their size. Energ Buildings 73:7–12
17. Papadopoulos AM (2016) Energy efficiency in hospitals: historical development, trends and perspectives. In: Boemi SN, Irulegi O, Santamouris M (eds) Energy performance of buildings. Springer, Cham
18. García Sanz-Calcedo J, Cuadros F, López-Rodríguez F (2011) Energy audit: a management tool in health centers. Gac Sanit 25(6):549–551
19. Chyu MC, Austin T, Calisir F, Chanjaplammootil S, Davis MJ, Favela J, Gan J, Gefen A, Haddas R, Hahn-Goldberg S et al (2015) Healthcare engineering defined: a white paper. J Healthc Eng 6:635–648
20. Fraile JC, San-José J, González-Alonso A (2014) A boiler room in a 600-bed hospital complex: study, analysis, and implementation of energy efficiency improvements. Energy 7:3282–3303
21. Garcia Sanz-Calcedo J, Gómez CM (2017) Quantitative analysis of the impact of maintenance management on the energy consumption of a Hospital in Extremadura (Spain). Sustain Cities Soc 35:217–222
22. Candelario-Garrido A, Garcia-Sanz-Calcedo J, Reyes AM (2017) A quantitative analysis on the feasibility of 4D planning graphic systems versus conventional systems in building projects. Sustain Cities Soc 35:378–384
23. Joseph A (2006) Impact of light on outcomes in healthcare settings. The Center for Health Design Volume August 1:12

Chapter 57
Energy Efficiency in the Building Sector: The Effect of Residential Progressive Electricity Tariffs on the Economic Performance of the Building-Integrated Photovoltaic Blind

Jeongyoon Oh, Choongwan Koo, and Taehoon Hong

57.1 Introduction

South Korea is implementing the residential progressive electricity tariffs (RPET), which imposes different electricity rates on residential buildings based on the amount of electricity consumption [1]. RPET can greatly affect the economic performance of the photovoltaic (PV) system in residential buildings [2]. As the RPET was revised in December 2016, the economic performance of the PV system, which had been evaluated based on the conventional RPET (RPET conventional), would change. In this regard, it is necessary to analyze the effect of RPET on the economic performance of the PV system. This study focused on building-integrated photovoltaic blind (BIPB) among the PV system, which can be applied to residential building facade with a considerable amount of area and effectively reduce the air-conditioning loads in buildings through the awning function [3–5].

The previous studies on the PV system can be summarized from two perspectives (i.e., technical analysis and economic analysis). First, some previous studies analyzed the technical performance of the PV system [6–11]. Bueno et al. [3] proposed the optimized installation of the PV panel over building surfaces and estimated the total amount of electricity generated from the PV system through the "Autodesk Ecotect" simulation program. Hussein et al. [6] conducted a performance evaluation of monocrystalline silicon-type PV modules at different tilt angles and orientations

J. Oh · T. Hong
Department of Architecture and Architectural Engineering, College of Engineering, Yonsei University, Seoul, Republic of Korea

C. Koo (✉)
Department of Architectural Engineering, College of Creative Engineering, Kyonggi University, Suwon, Republic of Korea
e-mail: cwkoo@kgu.ac.kr

S. Nižetić, A. Papadopoulos (eds.), *The Role of Exergy in Energy and the Environment*, Green Energy and Technology,
https://doi.org/10.1007/978-3-319-89845-2_57

using the "TRNSYS" simulation program. Second, other previous studies analyzed the economic performance of the PV system considering its technical performance [12–16]. Bhuiyan et al. [2] conducted an economic evaluation of a stand-alone residential PV system in a rural area in Bangladesh and compared renewable generators with nonrenewable generators via life cycle cost (LCC) analysis. Kazem and Khatib [14] assessed the techno-economic performance and the productivity of grid-connected PV systems in Oman considering the capacity factor and cost of energy.

Based on the literature review, the previous studies had the following limitations. First, most of studies, having focused on the technical performance of the PV system, mainly used energy simulation tools. However, it is difficult for decision-makers (e.g., designer or construction manager) to predict the technical performance of the PV system through energy simulation at the early design stage. Second, few of studies focused on RPET in analyzing the economic performance of the PV system since RPET was not considered in the target countries, or there was a minimal difference in the electricity rates according to the amount of electricity consumption. Therefore, this study aimed to develop a finite element model for estimating the techno-economic performance of BIPB, in which the economic performance of BIPB was analyzed considering RPET.

57.2 Materials and Methods

This study was conducted in three steps: (i) step 1, development of a finite element model for estimating the techno-economic performance of BIPB; (ii) step 2, establishment of representative household types; and (iii) step 3, impact analysis of RPET on the economic performance of BIPB.

57.2.1 Finite Element Model for Estimating the Techno-economic Performance of the BIPB

This study developed a four-node-based Lagrangian finite element model for estimating the techno-economic performance of BIPB ($FEM_{4\text{-node}}$BIPB) for residential buildings. $FEM_{4\text{-node}}$BIPB was developed in three steps: (i) estimation of the technical performance of BIPB, (ii) estimation of the economic performance of BIPB, and (iii) systemization of the proposed model.

57.2.1.1 Estimation of the Technical Performance of BIPB

In this study, the technical performance of BIPB was estimated in the following process: (i) definition of variables, (ii) establishment of a standard database using energy simulation, and (iii) estimation of the technical performance of BIPB using FEM.

First, the design variables affecting the amount of electricity generated from BIPB (EG_{BIPB}) were defined as follows: (i) architectural design elements (i.e., the region and orientation), (ii) window design elements (i.e., the visible transmittance (VT) and exterior window area), and (iii) BIPB design elements (i.e., the window-to-PV panel ratio and efficiency of the PV panel) [17, 18]. In addition, the design variables can be categorized into the nominal-scale design variables (i.e., orientation, VT) and ratio-scale design variables (i.e., exterior window area, window-to-PV panel ratio).

Second, a standard database was established using the "Autodesk Ecotect" software program in the following process: (i) definition of the reference model and (ii) establishment of a standard database.

(i) *Definition of reference model*: The reference model of BIPB was defined considering three aspects (i.e., the size of the reference model, the blind type of the reference model, and the efficiency of the PV panel in the reference model). First, the size of the reference model was determined to be 1 m^2 (1000 × 1000 mm) by considering the linear relationship between the amount of EG_{BIPB} and the installation area of the BIPB. Second, the blind type of the reference model was set as a 50-mm-wide venetian blind. Third, the copper indium gallium selenide (CIGS) PV panel with 11.70% efficiency was determined to be used in the reference model by considering the usability and constructability of the PV panels to be applied to the BIPB [19].

(ii) *Establishment of a standard database*: Based on the defined reference model, this study established a standard database using the "Autodesk Ecotect Analysis" software program. A standard database was set by considering three nominal-scale variables (i.e., region (3 types), orientation (8 types), and VT (6 types)) and the monthly EG_{BIPB} (12 types). Accordingly, a total of 1728 standard databases (3 × 8 × 6 × 12) were generated. Table 57.1 shows an example of a standard database for the amount of EG_{BIPB} under the following conditions: southern part of the region, 1m^2 of the exterior wall area, 100% of the window-to-PV panel ratio, and 11.70% of the CIGS PV panel efficiency.

Finally, the technical performance of BIPB using FEM was estimated in the following process: (i) definition of the independent variables to be applied to FEM, (ii) discretization of the continuum of the independent variables, and (iii) determination of the shape and interpolation function.

(i) *Definition of the independent variables to be applied to FEM*: Among the six design variables (i.e., the region, orientation, VT, exterior window area, window-to-PV panel ratio, and efficiency of the PV panel), the orientation (ξ)

Table 57.1 Standard database for the amount of EG_{BIPB}

[a] VT	Month	Orientation [b] S: 0°	[c] SE: 45°	[d] E: 90°	[e] NE: 135°	[f] N: 180°	[g] NW: 225°	[h] W: 270°	[i] SW: 315°
0.8	January	8722	7759	4469	1967	1822	1829	2962	5778
	February	8908	7492	4571	2114	1918	1964	3700	6721
	March	7543	7331	5878	3656	3026	3259	4956	6636
	April	5937	7035	7019	5240	3738	4385	6012	6579
	May	5101	6703	7688	6296	4220	5504	6911	6594
	June	4700	6221	7347	6486	4714	5493	6051	5559
	July	4408	5285	5860	5270	4238	4915	5552	5247
	August	4916	6392	7050	5662	3892	4583	5718	5763
	September	5593	6124	5429	3793	3026	3377	4545	5290
	October	8651	8130	5779	2965	2428	2569	4500	6850
	November	8544	7059	4242	1846	1639	1666	3416	6294
	December	9698	7604	3856	1634	1569	1569	3075	6712

Note: [a]*VT* stands for the visible transmittance, [b]*S* stands for the south, [c]*SE* stands for the southeast, [d]*E* stands for the east, [e]*NE* stands for the northeast, [f]*N* stands for the north, [g]*NW* stands for the northwest, [h]*W* stands for the west, and [i]*SW* stands for the southwest. Unit (Wh/m^2)

Table 57.2 $\xi-\eta$ matrix of the amount of EG_{BIPB} (in January)

[a] VT (η)	Orientation (ξ) [b] S:0°	[c] SE: 45°	[d] E: 90°	[e] NE: 135°	[f] N: 180°	[g] NW: 225°	[h] W: 270°	[i] SW: 315°
0.3	6777	5904	3138	1418	1335	1340	2081	4324
0.4	7126	6231	3323	1473	1379	1384	2171	4599
0.5	7463	6644	3578	1738	1477	1482	2288	4871
0.6	7898	7026	3886	1716	1606	1612	2527	5188
0.7	8281	7371	4154	1821	1694	1699	2729	5463
0.8	8722	7759	4469	1967	1822	1829	2962	5778

Note: [a]*VT* stands for the visible transmittance, [b]*S* stands for the south, [c]*SE* stands for the southeast, [d]*E* stands for the east, [e]*NE* stands for the northeast, [f]*N* stands for the north, [g]*NW* stands for the northwest, [h]*W* stands for the west, and [i]*SW* stands for the southwest. Unit (Wh/m^2)

and VT (η) were selected as the design variables to be applied to FEM, which can affect the amount of EG_{BIPB}.

(ii) *Discretization of the continuum of the independent variables*: This study conducted the discretization for the continuum of the independent variables (i.e., the orientation (ξ) and VT (η)). As a result, the orientation between 0 and 360° was divided into 8 intervals in 45° unit (i.e., south, 0°; southeast, 45°; east, 90°; northeast, 135°; north, 180°; northwest, 225°; west, 270°; and southwest, 315°), and the VT between 0.3 and 0.8 was divided into 6 intervals in 0.1 unit (i.e., 0.3, 0.4, 0.5, 0.6, 0.7, and 0.8). The $\xi-\eta$ matrix for the amount of EG_{BIPB} was established on the basis of the results of discretization. Table 57.2 shows an example of the $\xi-\eta$ matrix for the amount of EG_{BIPB} in January. In addition,

based on the $\xi-\eta$ matrix for the amount of EG_{BIPB}, the four extreme points, which should be used for the determination of the shape and interpolation function, could be derived.

(iii) *Determination of the shape and interpolation function*: The shape function was derived from the variable configuration (i.e., ξ and η were defined as the orientation and VT, respectively), and the function configuration (i.e., ϕ (ξ, η) was defined as the amount of EG_{BIPB}). Also, based on the derived shape function, the interpolation function was defined. The general expression of the four-node-based *Lagrangian* shape function was defined in Eq. (57.1). By applying the four extreme points in the $\xi-\eta$ matrix to Eq. (57.1), four polynomial equations can be derived. As shown in Eq. (57.2), the interpolation function can be defined with the four polynomial equations. Also, the coefficients of the four-node-based *Lagrangian* shape function can be calculated using the inverse matrix in Eq. (57.3).

$$\varphi(\xi,\eta) = \alpha_1 \times \xi + \alpha_2 \times \xi \cdot \eta + \alpha_3 \times \eta + \alpha_4 \tag{57.1}$$

$$\begin{bmatrix} \xi_n & \xi_n \cdot \eta_n & \eta_n & 1 \\ \xi_{n+1} & \xi_{n+1} \cdot \eta_n & \eta_n & 1 \\ \xi_n & \xi_n \cdot \eta_{n+1} & \eta_{n+1} & 1 \\ \xi_{n+1} & \xi_{n+1} \cdot \eta_{n+1} & \eta_{n+1} & 1 \end{bmatrix} \begin{bmatrix} \alpha_1 \\ \alpha_2 \\ \alpha_3 \\ \alpha_4 \end{bmatrix} = \begin{bmatrix} \varphi_1(\xi_n,\eta_n) \\ \varphi_2(\xi_{n+1},\eta_n) \\ \varphi_3(\xi_n,\eta_{n+1}) \\ \varphi_4(\xi_{n+1},\eta_{n+1}) \end{bmatrix} \tag{57.2}$$

$$\begin{bmatrix} \alpha_1 \\ \alpha_2 \\ \alpha_3 \\ \alpha_4 \end{bmatrix} = \begin{bmatrix} \xi_n & \xi_n \cdot \eta_n & \eta_n & 1 \\ \xi_{n+1} & \xi_{n+1} \cdot \eta_n & \eta_n & 1 \\ \xi_n & \xi_n \cdot \eta_{n+1} & \eta_{n+1} & 1 \\ \xi_{n+1} & \xi_{n+1} \cdot \eta_{n+1} & \eta_{n+1} & 1 \end{bmatrix}^{-1} \begin{bmatrix} \varphi_1(\xi_n,\eta_n) \\ \varphi_2(\xi_{n+1},\eta_n) \\ \varphi_3(\xi_n,\eta_{n+1}) \\ \varphi_4(\xi_{n+1},\eta_{n+1}) \end{bmatrix} \tag{57.3}$$

where, ϕ stands for the amount of electricity generated from BIPB (EG_{BIPB}); ξ stands for the orientation as design variable; η stands for the VT as design variable; and $\alpha_1-\alpha_4$ stand for the coefficients of the four-node-based *Lagrangian* shape function.

57.2.1.2 Estimation of the Economic Performance of BIPB

In this study, the economic performance of BIPB was evaluated using LCC analysis. As shown in Table 57.3, this study established five main assumptions: (i) analysis approach, (ii) starting point of analysis, (iii) analysis period, (iv) real discount rate, and (v) significant costs of ownership [1, 19].

The economic performance of BIPB can be provided in three ways: (i) the net present value (NPV) as an absolute value, (ii) the saving-to-investment ratio (SIR) as relative values, and (iii) the payback period. Also, if "NPV $\geq$ 0" or "SIR$\geq$1", it could be reasonable to apply BIPB to residential buildings in terms of economic viability (refer to Eqs. (57.4) and (57.5)).

Table 57.3 Main assumption of the LCC analysis

Classification			**Detailed description**	
Analysis approach			*Present worth method*	
Starting point of analysis			*2017*	
Analysis period			*25 years*	
Real discount rate	Inflation rate		*3.30%*	
	Electricity price growth rate		*0.66%*	
	CO_2 trading price growth rate		*2.66%*	
Significant costs of ownership	Cost	[a]IIC	*[b]BIPB using [c]CIGS PV panel: 258.11 US$/m^2*	
		Repair cost	*0.5% of IIC/year*	
	Benefit	Electricity-saving benefit	*[d]$RPET_{conventional}$*	*[e]$RPET_{revised}$*
			• *Under 100kWh: 0.050 US$/kWh* • *101~200kWh: 0.105 US$/kWh* • *201~300kWh: 0.156 US$/kWh* • *301~400kWh: 0.233 US$/kWh* • *401~500kWh: 0.347 US$/kWh* • *Over 500kWh: 0.590 US$/kWh*	• *Under 200kWh: 0.078 US$/kWh* • *201~400kWh: 0.156 US$/kWh* • *Over 400kWh: 0.233 US$/kWh*
		[f]KCERs	*8.77 US$/t$CO_{2eq}$*	*8.77 US$/t$CO_{2eq}$*

Note: [a]*IIC* stands for the initial investment cost, [b]*BIPB* stands for the building-integrated photovoltaic blind, [c]*CIGS* stands for the copper indium gallium selenide, [d]$RPET_{\text{conventional}}$ stands for the conventional residential progressive electricity tariffs, [e]$RPET_{\text{revised}}$ stands for the revised residential progressive electricity tariffs, and [f]*KCERs* stand for the Korean certified emission reductions. The exchange rate (KRW/USD) is 1203.00 won to a US dollar (as of January 4, 2017)

$$\mathrm{NPV}_n = \sum_{t=0}^{n} \frac{\mathrm{EG}_t + \mathrm{ET}_t}{(1+r)^{\mathrm{t}}} - \sum_{t=0}^{n} \frac{\mathrm{IIC} + \mathrm{RC}_t}{(1+r)^t} \tag{57.4}$$

$$\mathrm{SIR}_n = \left(\sum_{t=0}^{n} \frac{\mathrm{EG}_t + \mathrm{ET}_t}{(1+r)^t} \right) / \left(\sum_{t=0}^{n} \frac{\mathrm{IIC} + \mathrm{RC}_t}{(1+r)^t} \right) \tag{57.5}$$

where NPV_n stands for net present value during n years, SIR_n stands for saving-to-investment ratio during n years, r stands for real discount rate, n stands for LCC analysis period, EG_t stands for the benefit from the electricity generation in year t, ET_t stands for the benefit from the emission trading in year t, IIC stands for initial investment cost in year t, and RC_t stands for repair cost in year t.

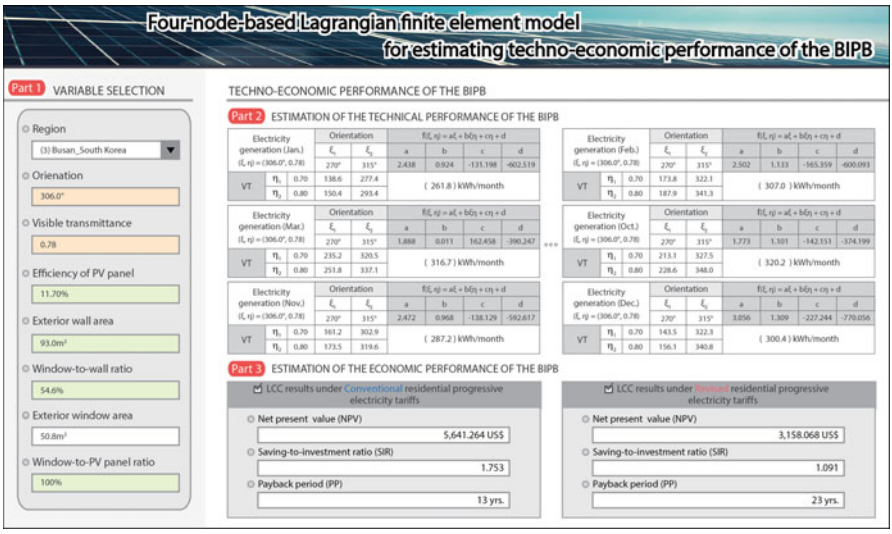

Fig. 57.1 The graphic user interface for the proposed model ($FEM_{4\text{-node}}$BIPB for residential buildings)

57.2.1.3 Systemization of the Proposed Model

This study conducted the systemization of the proposed model ($FEM_{4\text{-node}}$BIPB) for residential buildings. Since it is difficult for decision-makers to carry out the aforementioned complex process (i.e., estimation of the techno-economic performance of BIPB using FEM and LCC analysis), especially at the early design stage, the developed system will be very useful for them. The systemization of the proposed model can be conducted using the "Microsoft-Excel-based Visual Basic for Application."

As shown in Fig. 57.1, if decision-makers select design variables for a residential building in Part 1 (i.e., variable selection), the model can provide them with the techno-economic performance of BIPB, which can be estimated through both FEM in Part 2 (i.e., estimation of the technical performance of BIPB) and LCC analysis in Part 3 (i.e., estimation of the economic performance of BIPB).

57.2.2 Establishment of Representative Household Types

This study established representative household types to analyze the impact of RPET on the economic performance of BIPB, which was conducted in two steps: (i) data collection and (ii) definition of the representative household types.

57.2.2.1 Data Collection

Data collection was conducted in the following process: (i) definition of the facade design variables of residential building and (ii) establishment of database. First, the electricity consumption in a household ($EC_{household}$) and the EG_{BIPB} can be affected by the facade design variables of residential buildings [17, 18, 20]. Thus, this study defined the facade design variables of residential buildings from the four viewpoints: (i) architectural design elements (i.e., the region and orientation, which can affect both $EC_{household}$ and EG_{BIPB}, and the household floor area, which can affect only $EC_{household}$), (ii) exterior wall design elements (i.e., the number of exterior walls, U-value of the exterior wall, wall-to-floor ratio, and exterior wall area by orientation, which can affect only $EC_{household}$), (iii) window design elements (i.e., the U-value of the windows, solar heat gain coefficient, direct solar transmittance, VT, window-to-wall ratio, and window area by orientation, which can affect both $EC_{household}$ and EG_{BIPB}), and (iv) BIPB design elements (i.e., the window-to-PV panel ratio and efficiency of the PV panel, which can affect only EG_{BIPB}) [20–31]. Second, this study established a database for 5002 households, including the facade design variables of residential buildings, $EC_{household}$, and EG_{BIPB}. The databases on the facade design variables were established using design drawings. The database of $EC_{household}$ was established through the energy service provider (i.e., Korea Electric Power Corporation). Based on the defined facade design variables, this study established a database of EG_{BIPB} using $FEM_{4\text{-}node}$BIPB for residential buildings.

57.2.2.2 Definition of Representative Household Types

Based on the established database for 5,002 households, representative household types were defined in the following process: (i) clustering of 5,002 households considering the facade design variables of residential buildings and (ii) selection of representative household types. First, the households with the identical facade design variables were classified into the same group. Accordingly, a total of 57 clusters were generated. Second, using Monte Carlo simulation, this study estimated the probability density function for $EC_{household}$ by each cluster. Based on the results, the median value of $EC_{household}$ by each cluster was established as a representative value by each cluster. Accordingly, a total of 57 representative household types were defined.

57.2.3 Economic Impact Analysis of Residential Progressive Electricity Tariffs on the BIPB

In this study, the economic performance of BIPB was analyzed with focus on RPET in two ways: (i) conventional residential progressive electricity tariffs

Table 57.4 Electricity rates in South Korea by $RPET_{conventional}$ and $RPET_{revised}$

Classification		Basic charge (US $/household)	Electricity rates (US$/kWh)
[a]$RPET_{conventional}$	Under 100kWh (tariff zone "A")	0.341	0.050
	101~200kWh (tariff zone "B")	0.756	0.105
	201~300kWh (tariff zone "C")	1.330	0.156
	301~400kWh (tariff zone "D")	3.200	0.233
	401~500kWh (tariff zone "E")	6.068	0.347
	Over 500kWh (tariff zone "F")	10.756	0.590
[b]$RPET_{revised}$	Under 200kWh (tariff zones "A" and "B")	0.756	0.078
	201~400kWh (tariff zones "C" and "D")	1.330	0.156
	Over 400kWh (tariff zone "F")	6.068	0.233

Note: [a]$RPET_{conventional}$ stands for the conventional residential progressive electricity tariffs, [b]$RPET_{revised}$ stands for the revised residential progressive electricity tariffs. The exchange rate (KRW/USD) is 1203.00 won to a US dollar (as of January 4, 2017)

($RPET_{conventional}$) and (ii) revised residential progressive electricity tariffs ($RPET_{revised}$). In terms of $RPET_{conventional}$, the standard for electricity rates consists of six zones in 100kWh unit, based on the monthly $EC_{household}$. On the other hand, in terms of $RPET_{revised}$, the standard for electricity rates consists of three zones in 200kWh unit, based on the monthly $EC_{household}$. As shown in Table 57.4, in case of $RPET_{conventional}$, the maximum electricity rate (US$0.590/kWh) was 11.3 times higher than the minimum electricity rate (US$0.050/kWh). In case of $RPET_{revised}$, however, the maximum electricity rate (US$0.233/kWh) was 2.98 times higher than the minimum electricity rate (US$0.078/kWh).

As shown in Fig. 57.2, there are remarkable differences between $RPET_{conventional}$ and $RPET_{revised}$ in accordance with the amount of monthly $EC_{household}$. First, when $RPET_{conventional}$ was applied to the households whose monthly $EC_{household}$ was under 200 kWh (i.e., tariff zones "A" and "B"), the electricity rates decreased by a small margin compared to those based on $RPET_{revised}$. Second, the electricity rates before and after the revision of RPET were identical for the households whose monthly $EC_{household}$ was between 201 and 300 kWh (i.e., tariff zone "C"). Third, when $RPET_{conventional}$ was applied to the households whose monthly $EC_{household}$ was over 300 kWh (i.e., tariff zones "D," "E," and "F"), the electricity rates considerably increased compared to $RPET_{revised}$ [1].

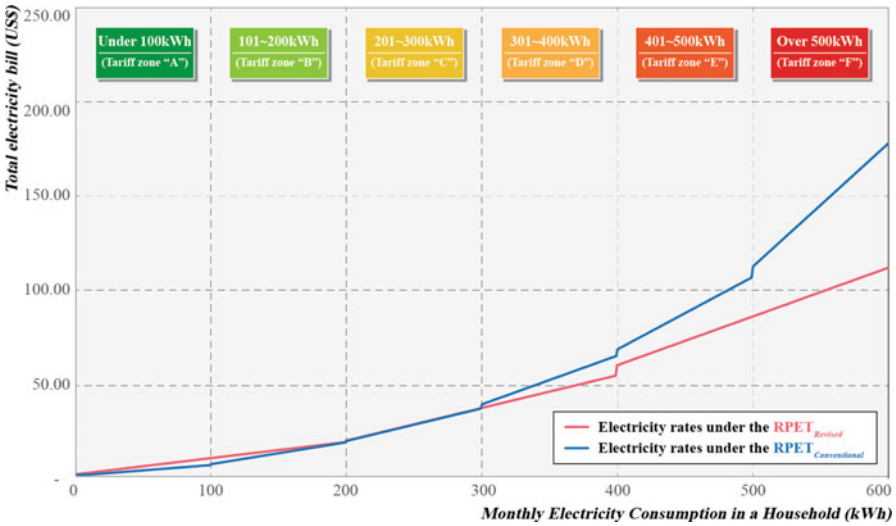

Fig. 57.2 Analysis on the electricity rates by considering residential progressive electricity tariffs (RPET)

57.3 Results and Discussion

The feasibility of $FEM_{4\text{-node}}BIPB$ was verified based on the comparison between the energy simulation (i.e., *Autodesk Ecotect* software program) and the developed model. In addition, the impact of RPET on the economic performance of BIPB was analyzed by using the developed $FEM_{4\text{-node}}BIPB$ for residential buildings. To do this, the $EC_{household}$ and the EG_{BIPB} of the 57 representative household types were used. The results can be explained in detail from two perspectives: (i) economic performance of BIPB under $RPET_{conventional}$ and (ii) economic performance of BIPB under $RPET_{revised}$.

57.3.1 Validation of the Proposed Model

In order to verify the feasibility of the developed $FEM_{4\text{-node}}BIPB$, the EG_{BIPB} from the energy simulation (i.e., *Autodesk Ecotect* software program) was compared with that from the developed model in terms of MAPE (mean absolute percentage error) (refer to Eq. (57.6)). The validation was conducted by using the EG_{BIPB} at the following points: (i) orientation (ξ) 22.5, 67.5, 112.5, 137.5, 202.5, 247.5, 292.5, and 337.5° and (ii) VT (η) 35, 45, 55, 65, and 75%.

Table 57.5 The results of validation on $FEM_{4\text{-node}}BIPB$

Classification	[a]MAPE	
	Monthly	Yearly
January	6.00%	4.54%
February	5.07%	
March	3.09%	
April	3.54%	
May	4.94%	
June	3.42%	
July	3.19%	
August	3.99%	
September	2.80%	
October	4.02%	
November	6.67%	
December	7.79%	

Note: [a]*MAPE* stands for the mean absolute percentage error

$$f_{\text{MAPE}} = \left(\sum_{i=1}^{n} \left| \frac{\text{SEG}_i - \text{FEG}_i}{\text{SEG}_i} \right| \times \frac{1}{n} \right) \times 100 \tag{57.6}$$

Table 57.5 shows the results of validation for the $FEM_{4\text{-node}}BIPB$. As shown in Table 57.5, the yearly based MAPE was determined to be 4.54%. In addition, the $FEM_{4\text{-node}}BIPB$ can provide the estimated techno-economic performance of the BIPB within a short time in an easy way. Therefore, the feasibility of $FEM_{4\text{-node}}BIPB$ was verified in terms of two aspects: (i) the effectiveness (i.e., its superior estimation accuracy) and (ii) the efficiency (i.e., computational time).

57.3.2 *Economic Performance of BIPB under $RPET_{conventional}$*

As shown in blue circle in Fig. 57.3 and green circle in Fig. 57.4, this study analyzed the correlation between $EC_{household}$ and the economic performance of BIPB (i.e., SIR and payback period) under $RPET_{conventional}$. It showed that as the $EC_{household}$ increased, the SIR improved and the payback period became shorter. Such results can be explained in detail by focusing on the economic performance of BIPB based on each zone of $EC_{household}$ (e.g., tariff zones "C," "D," "E," and "F").

In case of the households in tariff zone "F" (dark blue circle in Fig. 57.3 and dark green circle in Fig. 57.4), the economic performance of BIPB (i.e., SIR and payback period) was shown to have much superior, compared to those in tariff zone "D" (light blue circle in Fig. 57.3 and light green circle in Fig. 57.4). As the $EC_{household}$ increased, the total electricity bills rose sharply under $RPET_{conventional}$. This is because the electricity rates increase by 100kWh unit of $EC_{household}$. In other words, the electricity-saving benefit generated from EG_{BIPB} is higher for the

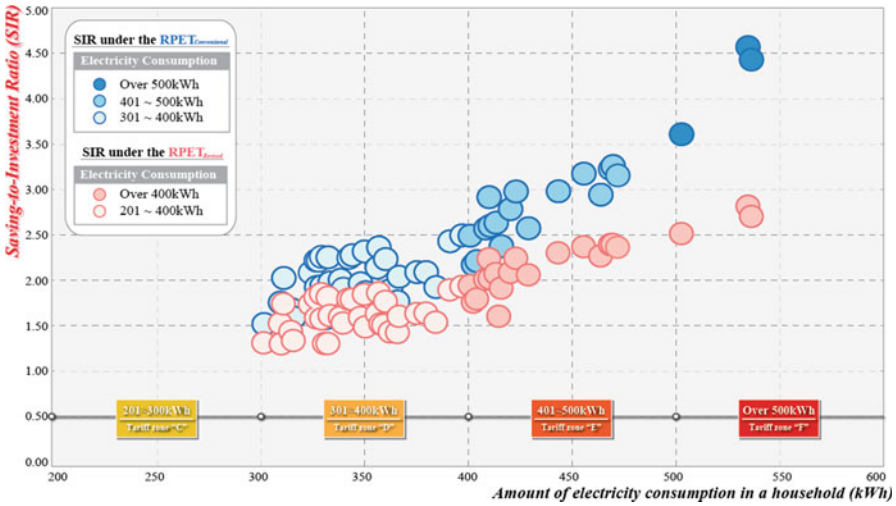

Fig. 57.3 Correlation between the $EC_{household}$ and the SIR of the BIPB for 57 representative household types

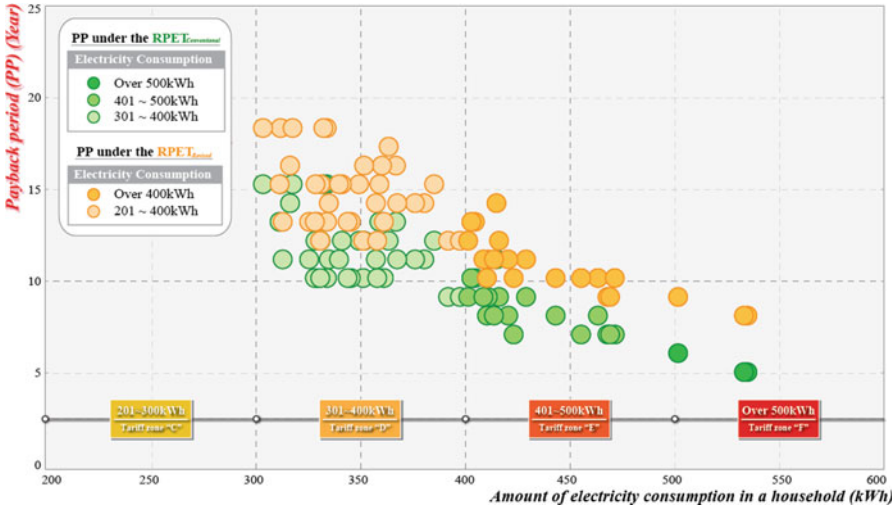

Fig. 57.4 Correlation between the $EC_{household}$ and the PP of the BIPB for 57 representative household types

households in tariff zone "F" (dark blue circle in Fig. 57.3 and dark green circle in Fig. 57.4), compared to those in tariff zone "D" (light blue circle in Fig. 57.3 and light green circle in Fig. 57.4). As a result, it was determined that it would be more effective to apply BIPB to households with higher $EC_{household}$ than to those with lower $EC_{household}$.

57.3.3 Economic Performance of BIPB under $RPET_{revised}$

As shown in red circle in Fig. 57.3 and yellow circle in Fig. 57.4, this study analyzed the correlation between $EC_{household}$ and the economic performance of BIPB (i.e., SIR and payback period) under $RPET_{revised}$. It showed that as the $EC_{household}$ increased, the economic performance of BIPB (i.e., SIR and payback period) improved in common with the case of $RPET_{conventional}$.

However, as RPET was reorganized to increase the electricity rates by 200kWh unit of $EC_{household}$, the margin of increase in the electricity rates in accordance with the amount of $EC_{household}$ decreased, compared to that under $RPET_{conventional}$. In other words, the ratio of the maximum electricity rates to the minimum electricity rates decreased from 11.3 to 2.98 as RPET was reorganized. Since the $EC_{household}$ of all the 57 representative household types were included in tariff zones "D," "E," and "F," the total electricity bills under $RPET_{revised}$ (refer to red circle in Fig. 57.3) decreased, compared to those under $RPET_{conventional}$ (refer to blue circle in Fig. 57.3). As a result, it was determined that the overall economic performance of BIPB (i.e., SIR and payback period) decreased under $RPET_{revised}$, which was caused by the reduction of the electricity-saving benefit from the application of BIPB.

57.3.4 Discussion

As RPET was reorganized in December 2016, the potential of electricity-saving benefit by applying BIPB to residential buildings was reduced. Accordingly, the economic performance of BIPB of the 57 representative household types was decreased. Nevertheless, as the electricity rate changes based on $EC_{household}$, the economic performance of BIPB is expected to increase for the households with a large floor area. That is, it will be more economical to apply BIPB to households with higher $EC_{household}$. It is because $EC_{household}$ and the household floor area generally have a positive correlation.

57.4 Conclusions

This study developed $FEM_{4\text{-node}}$BIPB for residential buildings, which used to analyze the economic performance of BIPB considering RPET. This study was conducted in three steps: (i) step 1, development of a finite element model for estimating the techno-economic performance of BIPB; (ii) step 2, establishment of representative household types; and (iii) step 3, impact analysis of RPET on the economic performance of BIPB. The main findings can be summarized as follows:

- Compared to the energy simulation, the yearly based MAPE of the $FEM_{4\text{-}node}BIPB$ was determined to be 4.54%. Therefore, the developed model appeared to have excellent prediction accuracy.
- As for the economic performance of BIPB based on the 57 representative household types, the households with a higher $EC_{household}$ showed to be superior due to the effect of RPET. Namely, it will be more economical to apply BIPB to households with a larger household floor area.
- As the electricity rates were lowered after the reorganization of RPET, the electricity-saving benefit through the application of BIPB to the 57 representative household types decreased. As a result, the economic performance of BIPB under $RPET_{revised}$ tended to decrease, compared to $RPET_{conventional}$.

This study provided intuitive results on the economic performance of BIPB considering RPET in accordance with the household properties (i.e., the $EC_{household}$ and household floor area). This study focused on the self-consumed utilization plan for EG_{BIPB}. The results showed that the economic performance of BIPB would decrease after the reorganization of RPET in South Korea. In this regard, it is necessary to conduct further research not only for the self-consumed utilization plan but also for the grid-connected utilization plan. Toward this end, the developed model ($FEM_{4\text{-}node}BIPB$ for residential buildings) should be expected to conduct a multilateral economic analysis, for which the research team is conducting a follow-up study.

Nomenclature

BIPB	Building-integrated photovoltaic blind
$EC_{household}$	Electricity consumption in a household
EG_{BIPB}	Electricity generated from BIPB
FEM	Finite element model
$FEM_{4\text{-}node}BIPB$	Four-node-based *Lagrangian* finite element model for estimating the techno-economic performance of BIPB
RPET	Residential progressive electricity tariffs
$RPET_{conventional}$	Conventional residential progressive electricity tariffs
$RPET_{revised}$	Revised residential progressive electricity tariffs
VT	Visible transmittance

Acknowledgments This research was supported by the National Research Foundation of Korea (NRF) grant funded by the Korean government (MSIP; Ministry of Science, ICT and Future Planning) (NRF-2016R1C1B2007941).

References

1. Bahr W (2014) A comprehensive assessment methodology of the building integrated photovoltaic blind system. Energ Buildings 82:703–708
2. Bhuiyan MMH, Asgar MA, Mazumder RK, Hussain M (2000) Economic evaluation of a stand-alone residential photovoltaic power system in Bangladesh. Renew Energy 21(3):403–410

3. Bueno L, Ibliha M, Vizcarra B, Chaudhry GM, Siddiki MK (2015) Feasibility analysis of a solar photovoltaic array integrated on façades of a commercial building. In Photovoltaic Specialist Conference (PVSC), 2015 IEEE 42nd, 1–4
4. EPBD (The Energy Performance of Buildings Directive) (2005) Improving the energy efficiency of the existing housing stock. In: Delft Universit of Technology (DUT)
5. GFE (Glass for Europe) (2010) The energy performance of buildings directive: business opportunities for the glass industry and national implementation challenges. In: Brussels
6. Hussein HMS, Ahmad GE, El-Ghetany HH (2004) Performance evaluation of photovoltaic modules at different tilt angles and orientations. Energ Convers Manag 45(15):2441–2452
7. Hwang T, Kang S, Kim JT (2012) Optimization of the building integrated photovoltaic system in office buildings-focus on the orientation, inclined angle and installed area. Energ Buildings 46:92–104
8. Hong T, Koo C, Kim D, Lee M, Kim J (2015) An estimation methodology for the dynamic operational rating of a new residential building using the advanced case-based reasoning and stochastic approaches. Appl Energ 150:308–322
9. Hummon M, Denholm P, Margolis R (2012) Impact of photovoltaic on orientation on its relative economic value in wholesale energy markets. Prog Photovolt Res Appl 21(7):1531–1540
10. Kacira M, Simsek M, Babur Y, Demirkol S (2004) Determining optimum tilt angles and orientations of photovoltaic panels in Sanliurfa, Turkey. Renew Energ 29(8):1265–1275
11. Hong T, Koo C, Oh J, Jeong K (2017) Nonlinearity analysis of the shading effect on the technical–economic performance of the building-integrated photovoltaic blind. Appl Energ 194:467–480
12. KEPCO (Korea Electric Power Corporation), The electricity rates. Available at http://home.kepco.co.kr/ (January 4, 2017)
13. Kaldellis J, Zafirakis D (2012) Experimental investigation of the optimum photovoltaic panels' tilt angle during the summer period. Energy 38(1):305–314
14. Kazem HA, Khatib T (2013) Techno-economical assessment of grid connected photovoltaic power systems productivity in Sohar, Oman. Sust Energ Technol Assessments 3:61–65
15. Koo C, Hong T, Lee M, Kim J (2016) An integrated multi-objective optimization model for determining the optimal solution in implementing the rooftop photovoltaic system. Renew Sust Energ Rev 57:822–837
16. Koo C, Hong T, Jeong K, Ban C, Oh J (2017) Development of the smart photovoltaic system blind and its impact on net-zero energy solar buildings using technical-economic-political analyses. Energy 124:382–396
17. Koo C, Hong T, Park H, Yun G (2014) Framework for the analysis of the potential of the rooftop photovoltaic system to achieve the net-zero energy solar buildings. Prog Photovolt Res Appl 22(4):462–478
18. Koo C, Park S, Hong T, Park H (2014) An estimation model for the heating and cooling demand of a residential building with a different envelope design using the finite element method. Appl Energ 115:205–215
19. Lee H, Park J, Yoon J, Shin U (2013) A study on the economic evaluation of photovoltaic system in the greenhome. Korean Solar Energy Soc 4:47–52
20. ZCH (Zero Carbon Hub) (2011) Energy performance of building directive: Introductory guide to the recast EPBD-2. London
21. Lee J (2010) A study on support policy for popularization of BIPV. In: Korean J (ed) The Korean Journal of Air-Conditioning and Refrigeration Engineering, pp 1608–1612
22. Mandalaki M, Tsoutsos T, Papamanolis N (2014) Integrated PV in shading systems for Mediterranean countries: Balance between energy production and visual comfort. Energ Buildings 77:445–456
23. Ordóñez J, Jadraque E, Alegre J, Martínez G (2010) Analysis of the photovoltaic solar energy capacity of residential rooftops in Andalusia (Spain). Renew Sust Energ Rev 14(7):2122–2130

24. Shukla A, Sudhakar K, Baredar P (2016) Simulation and performance analysis of 110 kW p grid-connected photovoltaic system for residential building in India: a comparative analysis of various PV technology. Energy Reports 2:82–88
25. Pillai G, Putrus G, Georgitsioti T, Pearsall N (2014) Near-term economic benefits from grid-connected residential PV (photovoltaic) systems. Energy 68:832–843
26. Vieira F, Moura P, de Almeida A (2017) Energy storage system for self-consumption of photovoltaic energy in residential zero energy buildings. Renew Energ 103:308–320
27. Park H, Koo C, Hong T, Oh J, Jeong K (2016) A finite element model for estimating the techno-economic performance of the building-integrated photovoltaic blind. Appl Energ 179:211–227
28. Masa-Bote D, Caamaño-Martín E (2014) Methodology for estimating building integrated photovoltaics electricity production under shadowing conditions and case study. Renew Sust Energ Rev 31:492–500
29. MLTM (Ministry of Land, Transport, and Maritime Affairs) (2010) Standard for the design and performance evaluation of residential green buildings. Seoul (South Korea)
30. MLTM (Ministry of Land, Transport, and Maritime Affairs) (2012) Building envelope design guidelines for achieving energy savings. Seoul (South Korea)
31. Siraki AG, Pillay P (2012) Study of optimum tilt angles for solar panels in different latitudes for urban applications. Sol Energ 86(6):1920–1928

Chapter 58
Numerical Models for Prediction of Energy Performance and Noise Emissions of Building Roof Fan

Ivo Marinić-Kragić, Zoran Milas, and Damir Vučina

58.1 Introduction

Until recently, centrifugal roof fans did not attract much attention since they were considered as "small" machines (installed power is usually bellow 2 kW). Nevertheless, they account for 30% of all nonresidential ventilation [1]. If we consider them on a large scale, this makes them large energy consumers. The centrifugal roof fans have efficiency between 30% and 50%, which means that large space for improvement exists. These facts attracted researchers mostly from areas of fluid mechanics and numerical optimization. Recent numerical studies consider various centrifugal fan sizes (and designs), ranging from very small (outer diameter smaller than 100 mm) to large (outer diameter up to 500 mm). Numerical simulation of a very small centrifugal fan (used for CPU cooling) was conducted in [2]. This study includes numerical simulation of performance and noise emissions and a comparison with experimental results. Experimental and numerical study of a fan similar in size (centrifugal fan for a refrigerator) was conducted by [3]. They adopted an URANS CFD model for performance analysis. The results from CFD simulation were subsequently used for acoustic noise calculation using Ffowcs Williams-Hawkings equations [4]. This noise calculation model in combination with URANS is also used for larger centrifugal fans, for example, in [5] for a fan which has 510 mm outer diameter. Some authors have also used a similar but computationally more efficient noise estimation model developed by [6]. Example is the study by [7]. Additionally, for flow simulation they used SAS turbulence model [8]. This is a hybrid LES-RANS turbulence model which uses the RANS $k\omega$–SST model in the areas

I. Marinić-Kragić (✉) · Z. Milas · D. Vučina
Faculty of Electrical Engineering, Mechanical Engineering and Naval Architecture, Univeristy of Split, Split, Croatia
e-mail: imarinic@fesb.hr

S. Nižetić, A. Papadopoulos (eds.), *The Role of Exergy in Energy and the Environment*, Green Energy and Technology,
https://doi.org/10.1007/978-3-319-89845-2_58

near the solid walls and the LES far away. Recent studies also include numerical optimization of energy conversion efficiency and acoustic emissions [9, 10]. It was shown that single-objective (fan efficiency) optimization case has a very low sensitivity in the area near the optimal solution. This means that multiple different solutions exist with almost the same efficiency. The first approach in solving the low sensitivity problem was to define the efficiency as an average over multiple operating regime. The second approach implemented multi-objective optimization with noise emission as a second criterion. The use of an appropriate numerical model is important in all optimization scenarios. Here, we tested various CFD models regarding the prediction of fan pressure, efficiency, and noise emission. Steady-state RANS, URANS, and LES turbulence models were investigated. Frozen rotor approach was used in all cases.

58.2 Roof Fan Design and Performance

58.2.1 Design and Geometry

Since roof fans expel the air directly into the ambient, they do not require a scroll housing. Roof fan housing is usually a simple axisymmetric cap, used merely as a weather shield as illustrated in Fig. 58.1. Electric motor usually drives the impeller by a direct drive without a belt or gears. In any case, the far-field flow conditions are axisymmetric.

58.2.2 Performance Definition

The most important fan performance parameters are the total pressure increase and the corresponding fan efficiency. Since roof fans do not have a pressure duct, the

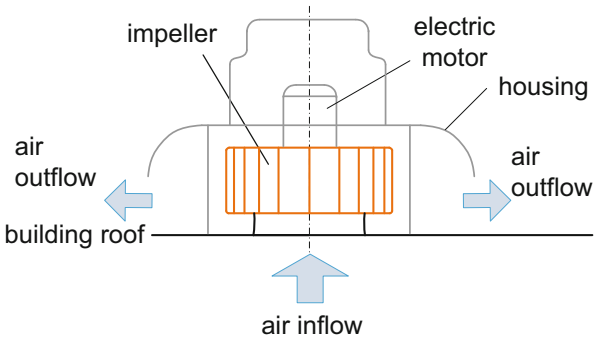

Fig. 58.1 Simplified roof fan schematic

outlet dynamic pressure is ignored. Hence, the total pressure increase Δp_t is defined as:

$$\Delta p_t = \int_{Ao} p_o \left(\vec{v}_o d\bar{A}_o\right)/\dot{V} - \int_{Ai} \left(p_i + \frac{1}{2}\rho v_i^2\right)\left(\bar{v}_i d\bar{A}_i\right)/\dot{V} \tag{58.1}$$

where p_o is static pressure at outlet and p_i is the static pressures at inlet. The absolute velocities at outlet and inlet are designated by $\vec{v}_o$ and $\vec{v}_i$, respectively. Area of fan outlet section is designated A_o while the inlet section area is designated by A_i, ρ is the air density, and $\dot{V}$ is the volume flow rate.

The fan efficiency is defined as:

$$\eta = \dot{V}\,\Delta p_t / P \tag{58.2}$$

where P is the fan power. The fan power Pcan be calculated by:

$$M_i \omega + M_{fd}\omega \tag{58.3}$$

where M_i is the torque due to the aerodynamic forces acting on the inside impeller surface and M_{fd} the disc friction torque. In reality, additional power is required due to the volumetric and mechanical losses (which have only a minor impact on the overall efficiency). To calculate the torque, pressure and shear stress are integrated along the fan impeller walls according to:

$$M_i + M_{fd} = \int_A \left(\vec{r} \times \vec{n}\right)_y p dA + \left(\vec{r} \times \vec{\tau}_w\right)_y dA \tag{58.4}$$

58.2.3 Experimental Results

This section presents the experimental results from [10]. The experiments include measurements of pressure and efficiency as defined by Eqs. (58.1) and (58.2), respectively. Table 58.1 defines the geometric characteristics of the investigated fan. This geometry was later used for constructing the numerical model.

Table 58.1 Fan geometric characteristics [10]

Impeller diameter (outlet)	D (mm)	325
Impeller eye	D_o (mm)	235
External rotor (el. motor)	d_{er} (mm)	138
Impeller width	b (mm)	75
Number of vanes	z	14
Vane outlet angle	β (^{O})	45
Vane thickness	t (mm)	1,5

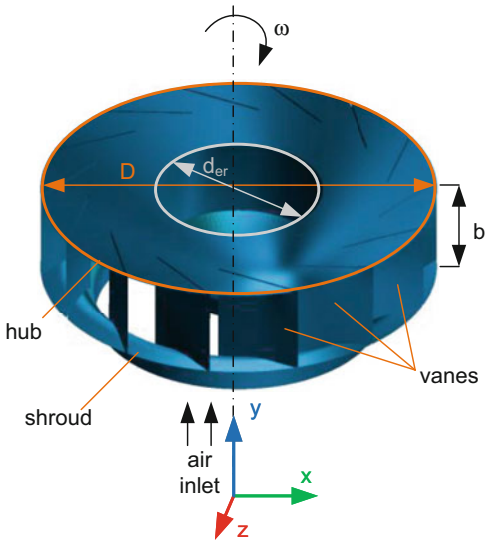

Fig. 58.2 Impeller geometry

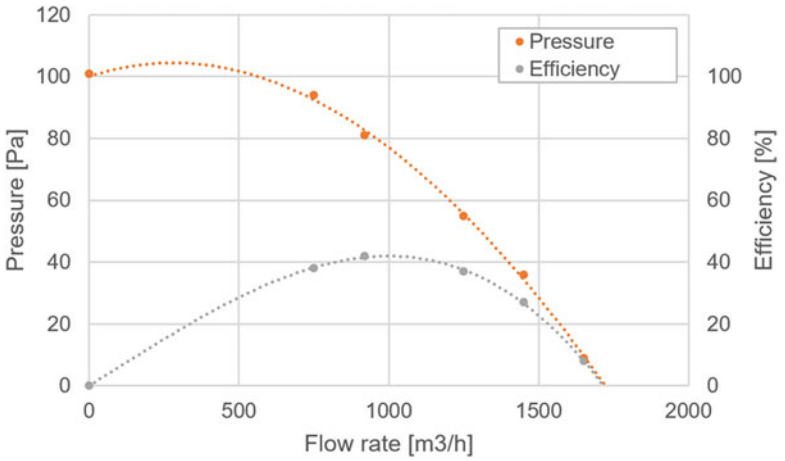

Fig. 58.3 Experimental fan characteristics from [10]

The impeller outer diameter and the impeller width are shown in Fig. 58.2, while the impeller eye is only visible from the bottom view (not shown).

Measurements were conducted for multiple flow rates and the results are shown in Fig. 58.3. This small roof fan was tested in laboratory conditions. The fan "housing" was only a simple axisymmetric horizontal cap, and far-field conditions can also be regarded as axisymmetric. The peak efficiency (42%) was measured at flow rate of 918 m^3/h, with the pressure increase 81 Pa. Measurements were conducted up to flow rate of 1650 m^3/h where efficiency drops to near zero. Rotational speed was constant in all tests $\omega = 103$ rad/s. These results were compared with the numerical as shown later in results section.

58.3 Numerical Model

58.3.1 Computational Domain

Computational domain is selected such that it encapsulates only one vane. This is sufficient since the periodic boundary conditions can be used. A single segment of impeller computational sub-domain is illustrated in Fig. 58.4. In addition to impeller sub-domain, intake pipe and outflow atmospheric domain has to be modeled. Again, only one segment is modeled. Intake pipe segment with length twice the impeller diameter (D) was used, while the diameter of the atmospheric domain was six times the impeller diameter. Atmospheric sub-domain is divided in two domains so that different element sizes can be used near the fan outlet and far away. The impeller sub-domain and the inner atmospheric sub-domain were analyzed in a rotating

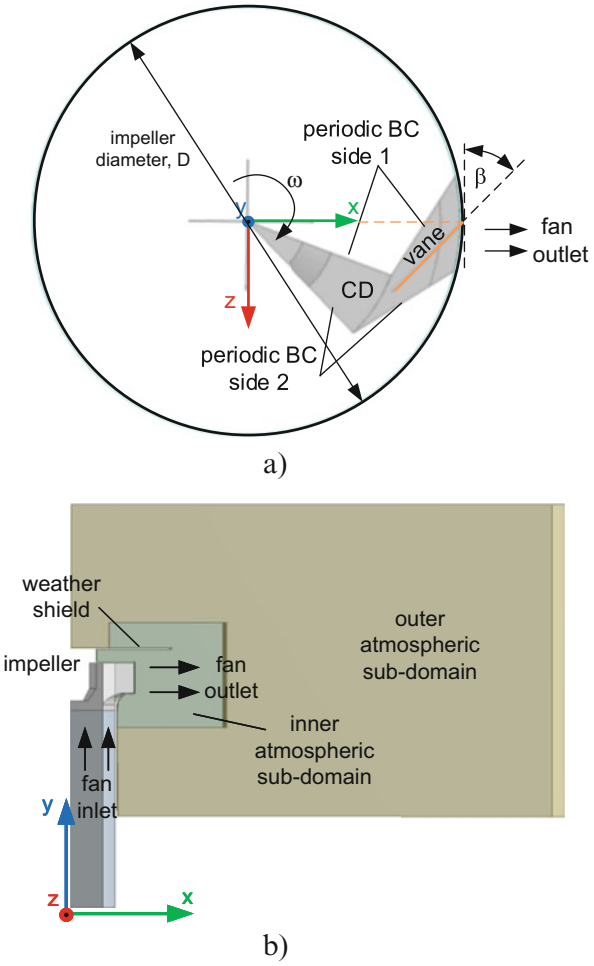

Fig. 58.4 Computational (sub-)domains: (**a**) impeller computational domain (CD) segment with periodic boundary conditions (BC) and (**b**) remaining computational sub-domains

reference frame, while the rest of the computational domain was stationary. Mass flow boundary condition was set at the pipe inlet section, while the pressure outlet (zero pressure) was prescribed at the outer atmospheric sub-domain.

58.3.2 Domain Discretization

The computational domain is discretized by the finite volumes using the ANSYS Meshing. Regarding the number of elements, two different domain discretizations were used. A courser mesh is used for the RANS simulations while finer mesh was used for LES. Structured mesh with hexahedral elements was used in the atmosphere domains. Intake pipe domain was constructed with unstructured swept mesh with inflation zone near the pipe wall. In the impeller domain, tetrahedral elements were used with prism inflation layers near the wall surfaces. In RANS model, 17 inflation layers were used. The first layer height was set to 0.015 mm and growth rate was set to 1.17. For LES model, inflation zone with 30 layers and growth rate of 1.035 were used. Figure 58.5 illustrates the mesh at half-height of the impeller (Fig. 58.6).

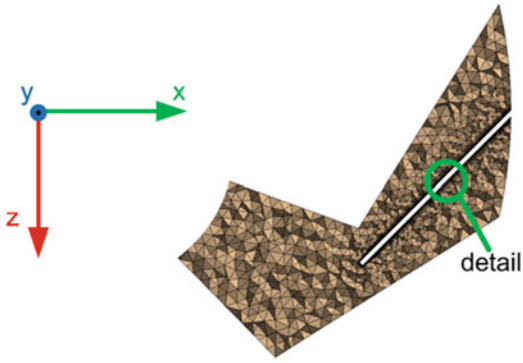

Fig. 58.5 Mesh at half-height of impeller domain for RANS model – whole impeller view

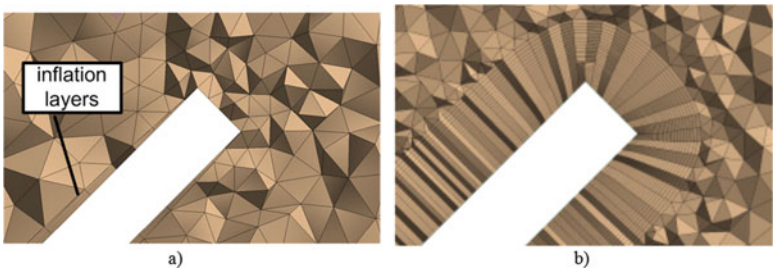

Fig. 58.6 Mesh near the vane leading edge at half-height of impeller domain: (**a**) RANS model and (**b**) LES model

Table 58.2 Number of finite volume elements per sub-domain for mesh used with RANS and LES models

Sub-domain	Number of elements	
	RANS model	LES model
Inlet pipe	31,416	186,873
Impeller	336,812	40,780,027
Atmosphere (inner)	90,600	2,213,843
Atmosphere (outer)	167,859	6,322,836

While the total number of elements required for RANS simulation is about 0.5 million, LES (LES-WALE) requires a mesh with about 50 million elements (almost 700 million elements without the periodic boundary conditions). The distribution of elements per sub-domain is shown in Table 58.2.

58.3.3 Flow and Acoustics Modeling

The averaged continuity and momentum equations in the case of incompressible flows (and body forces excluded) can be written in index notation and Cartesian coordinates as:

$$\frac{\partial \rho \overline{u_i}}{\partial x_i} = 0 \tag{58.5}$$

$$\frac{\partial \rho \overline{u_i}}{\partial t} + \frac{\partial}{\partial x_j}\left(\rho \overline{u_i u_j} + \rho \overline{u_i' u_j'}\right) = -\frac{\partial \bar{p}}{\partial x_i} + \frac{\partial \overline{\tau_{ij}}}{\partial x_j} \tag{58.6}$$

where ρ, p, and $\bar{u}_i$ are the time-averaged flow density, pressure, and the Cartesian velocity components, respectively: x_i is the Cartesian coordinate; $\overline{\tau_{ij}}$ are the time-averaged viscous stress tensor components:

$$\overline{\tau_{ij}} = \mu\left(\frac{\partial \overline{u_i}}{\partial x_j} + \frac{\partial \overline{u_j}}{\partial x_j}\right) \tag{58.7}$$

The generalized transport equation for the time averaged of a scalar quantity ϕ (velocity u for momentum conservation and *1* for mass conservation) can be written as:

$$\frac{\partial \rho \overline{\phi}}{\partial t} + \frac{\partial}{\partial x_j}\left(\rho \overline{u_i}\overline{\phi} + \rho \overline{u_j' \phi'}\right) = \frac{\partial}{\partial x_j}\left(\Gamma \frac{\partial \overline{\phi}}{\partial x_j}\right) \tag{58.8}$$

The presence of fluctuating terms in the conservation equations, namely, Reynolds stresses and turbulent scalar flux, means that the equations are not closed. The closure requires the use of some approximations, which usually take the form of prescribing the Reynolds stress tensor and turbulent scalar fluxes in terms of the time-averaged flow quantities. The effect of turbulence can be represented as an

increased viscosity (which is called turbulence viscosity μ_t) [11]. This leads to the Boussinesq eddy-viscosity model for the Reynolds stress R_{ij}:

$$R_{ij} = -\rho\overline{u_i' u_j'} = \mu_t\left(\frac{\partial \overline{u_i}}{\partial x_j} + \frac{\partial \overline{u_j}}{\partial x_i} - \frac{2}{3}\frac{\partial \overline{u_k}}{\partial x_k}\delta_{ij}\right) - \frac{2}{3}\rho\delta_{ij}k \tag{58.9}$$

In (58.9), k is the turbulence kinetic energy:

$$k = \frac{1}{2}\overline{u_i' u_i'} \tag{58.10}$$

The eddy-viscosity hypothesis is widely used due to easy to implement and its application has shown reasonably good results for many types of flows. Turbulent viscosity μ_t and turbulence kinetic energy k are determined by the turbulence model. The system of time-averaged equations with time term is also termed as unsteady RANS (URANS). Specifically, this chapter implemented $k-\omega$ SST [12] as RANS turbulence model. In addition to RANS turbulence model, this chapter presents the results obtained by model LES (large-eddy simulation). LES equations are derived by averaging (in space and time) only on scales with a prescribed limit (usually defined indirectly by the mesh size). The LES equations result in a system similar to RANS equations but with different definition of turbulence viscosity and Reynolds stresses. The LES-WALE model [13] was selected for LES. Convergence criteria were set to 10^{-4} for residuals in all cases. In unsteady simulations, time step was $2°/\omega$.

The selected method for modeling the noise problem is the Ffowcs Williams and Hawkings (FW-H) method [4]. The FW-H method uses the most general form of the Lighthill's acoustic analogy. This method is appropriate for the prediction of sound generated by rigid bodies moving at subsonic velocities. FW-H method was implemented using the ANSYS Fluent. Stationary observer was set at 1 m distance from the rotational axis. In order to calculate the overall pressure caused by all vanes, multiple observers were to be used (one for each vane).

58.4 Results and Discussions

58.4.1 Steady State Model

First test case was steady-state RANS simulation with SST turbulence model. First-order upwind discretization scheme was used. Figure 58.7 shows the comparison of the results obtained by numerical simulation and experiment. A very good agreement is evident especially near the maximum efficiency point (flow rate 900 m^3/h).

The following figure (Fig. 58.8) shows the flow field velocities at two sub-domains for the flow rate 1650 m^3/h. Apparently, no or very little flow separation appears at the vane surface. Looking at the outlet flow, it can be observed that the flow direction is slightly axial.

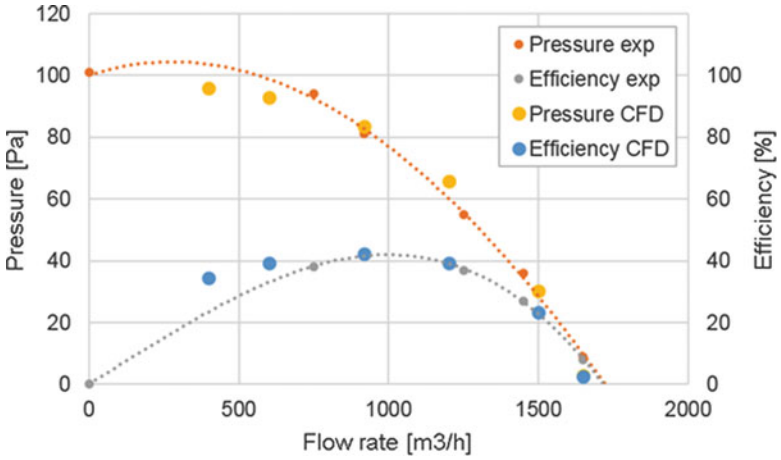

Fig. 58.7 Comparison of experimental results (exp) and steady-state RANS numerical (CFD) simulation

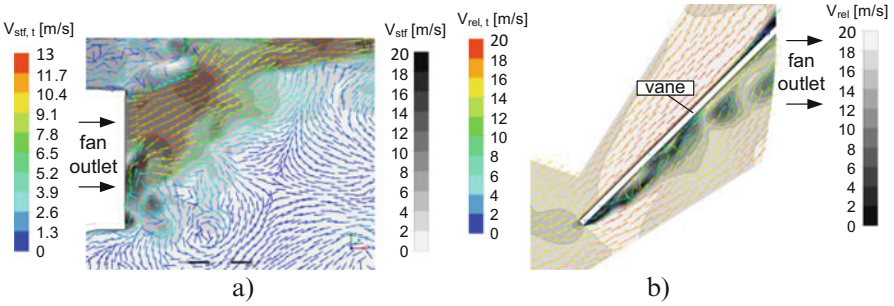

Fig. 58.8 Flow field velocities for RANS simulation at flow rate 1650 m^3/h (V_{stf}, velocity in stationary frame; $V_{stf,t}$, velocity in stationary frame tangential to current plane; V_{rel}, relative velocity; $V_{rel,t}$, relative velocity tangential to current plane): (**a**) x–y plane section at $z = 0$ and (**b**) x–z plane section at half vane height

The data from the CFD simulation can now be used for calculation of the acoustic pressure at the observer point. This requires "virtual" rotation of the vane since only steady-state solution exists. The observer point was set at 1 m distance from the rotation axis. The result of the acoustic pressure for a single vane at the flow rate 918 m^3/h is illustrated in Fig. 58.9a. This is the acoustic pressure that would appear at the observer location if there was only a single vane. Since multiple vanes exist, the FW-H equation has to be integrated over the whole fan. Since periodic conditions are assumed, this does not require additional CFD simulation. To obtain the acoustic pressure caused by the remaining vanes, the single-vane acoustic pressure result is time-translated ($\Delta t = 2*\pi/14/\omega$). By summing the results over all vanes, the overall acoustic pressure for the whole fan can be obtained. By conducting a Fourier

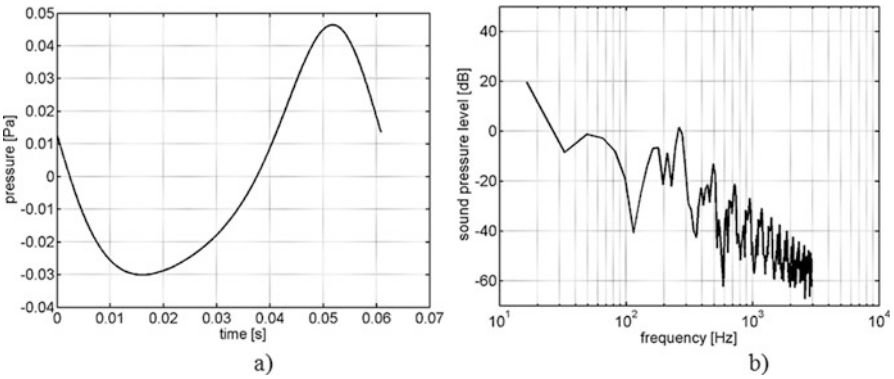

Fig. 58.9 Acoustic noise for observer at 1 m distance using RANS model at flow rate 918 m^3/h: (**a**) acoustic pressure caused by single vane (**b**) sound pressure level as a function of frequency

transformation, sound pressure level as a function of frequency can be calculated as shown in Fig. 58.9b.

As already mentioned, this solution was obtained by using the first-order upwind discretization scheme. When the same simulation was conducted using higher-order discretization schemes, residuals did not converge to the defined criterion 10^{-4}. Upwind scheme is known to introduce lots of numerical dissipation (stability). This means that physically unsteady solution can become a steady-state solution. Thus, the next case conducts an unsteady RANS simulation with a higher-order discretization scheme.

58.4.2 URANS Model

Next, transient RANS simulation was conducted with the same settings as earlier but with $2°/\omega$ time step. Simulation was conducted for approximately two rotations and the results were averaged. The results are illustrated in Fig. 58.10. Compared to the previous case, CFD prediction capability for pressure and efficiency has deteriorated. For example, earlier the maximum fan flow rate was about 1650 m^3/h, while now it is approximately 10% lower and amounts approximately 1500 m^3/h. The pressure obtained at maximum efficiency point has also reduced from about 80 Pa to 65 Pa. Since this was not an expected result, various test cases with different mesh sizes and domain shapes were conducted, but the results did not improve.

In order to evaluate acoustic pressure, now a transient solution is required. Since FW-H equation only uses surface integration, this requires storage of transient solution only at the selected source surfaces which is a considerable memory saving in comparison to storing full 3D transient solution. The observer point was again set at 1 m distance from the rotation axis. The result of the acoustic pressure for a single vane at the flow rate 918 m^3/h is illustrated in Fig. 58.11a. In total, 14 observer points

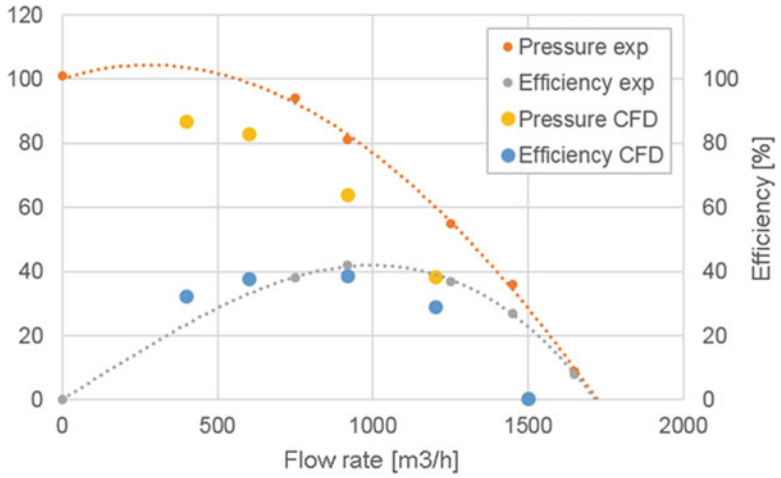

Fig. 58.10 Comparison of experimental results (exp) and averaged transient URANS numerical (CFD) simulation

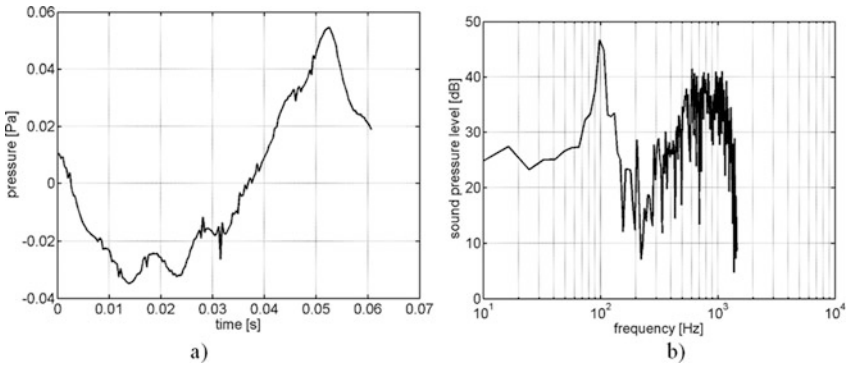

Fig. 58.11 Acoustic noise for observer at 1 m distance using URANS model at flow rate 918 m^3/h: (**a**) acoustic pressure caused by single vane (**b**) overall fan sound pressure level as a function of frequency

were set at equidistant angles for calculating the acoustic pressure. Assuming periodic conditions, the data from these 14 points can be used to integrate the acoustic pressure for the overall fan. Next, sound pressure level as a function of frequency is shown in Fig. 58.11b. In comparison to earlier case, URANS results in wider spectrum of acoustic noise and much higher sound pressure levels. Experimental data for the fan noise emissions is not available, but this is clearly a much more realistic result.

58.4.3 LES Model

Next, the LES WALE turbulence model is used. This model requires a very fine computational mesh with about 50 million elements which is about 100 times more than required for RANS simulation. The same time step $2°/\omega$ was used. The pressure and efficiency results are shown in Fig. 58.12. Still, the maximum fan flow is approximately 10% lower than experimental, but the result at the maximum efficiency point is considerably improved in comparison to URANS simulation.

The flow field for the LES simulation at the flow rate 1650 m^3/h is shown in Fig. 58.13. Now, the flow field contains lots of turbulent eddies. Some of these eddies are apparently generated near the leading edge at the pressure side of the vane.

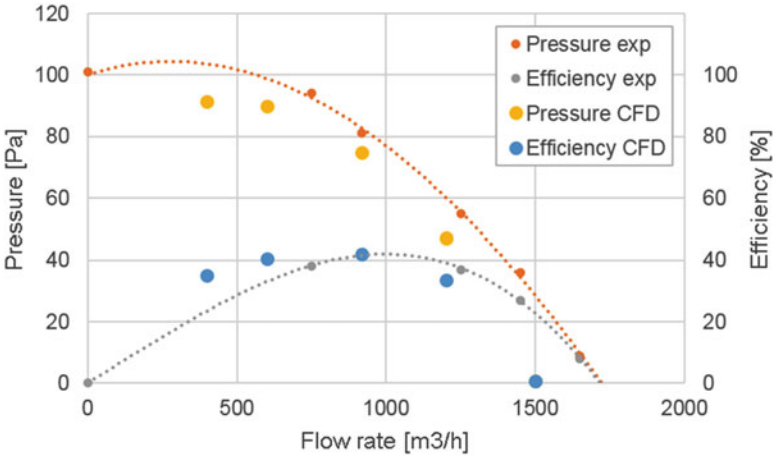

Fig. 58.12 Comparison of experimental results (exp) and averaged transient LES numerical (CFD) simulation

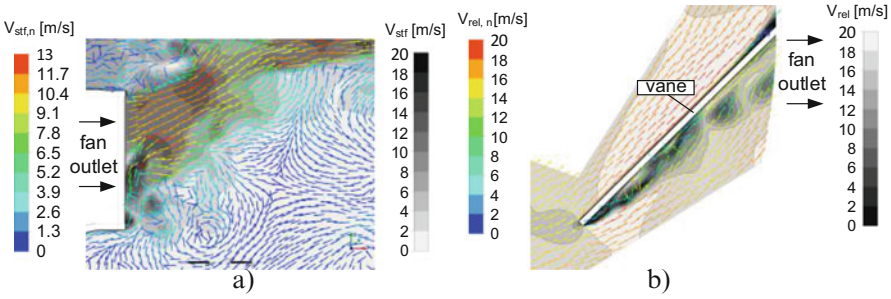

Fig. 58.13 Flow field velocities for LES simulation at flow rate 1650 m^3/h (V_{stf}, velocity in stationary frame; $V_{stf,t}$, velocity in stationary frame tangential to current plane; V_{rel}, relative velocity; $V_{rel,t}$, relative velocity tangential to current plane): (**a**) x–y plane section at $z = 0$ and (**b**) x–z plane section at half vane height

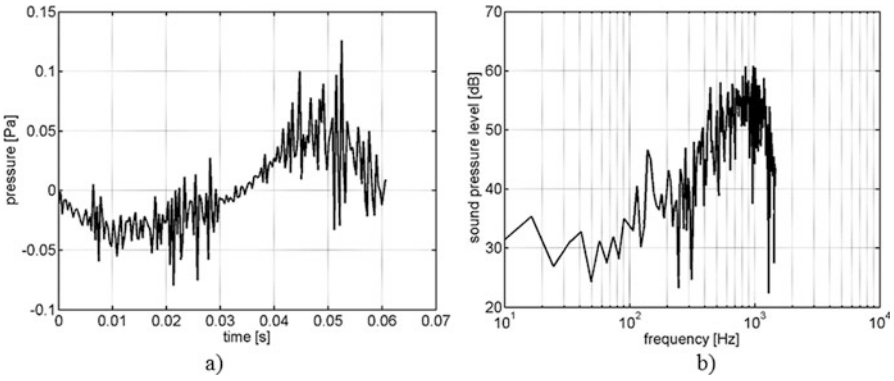

Fig. 58.14 Acoustic noise for observer at 1 m distance using LES model at flow rate 918 m^3/h: (**a**) acoustic pressure caused by single vane (**b**) overall fan sound pressure level as a function of frequency

This kind of flow field is expected to produce more acoustic emissions especially at higher frequencies.

As was the case in URANS simulation, in order to calculate the acoustic pressure by FW-H equation, the transient solution at the selected source surfaces needs to be stored. Figure 58.14a shows the acoustic noise for observer at 1 m distance using the LES model. Flow rate 918 m^3/h was used. Figure 58.14b shows the sound pressure level as a function of frequency for full fan. It is visible that up to about 100 Hz, the solution is approximately the same as was when using URANS. While the URANS simulation predicted that peak acoustic emissions would be generated at 100 Hz, the LES predicts that the most noise will be generated at 800 Hz frequency. In order to confirm these results, future work would have to include experimental acoustic measurements.

58.5 Conclusions

This chapter presented the evaluation of RANS, URANS, and LES turbulence models for simulating the centrifugal roof fan performance and noise emissions, and the results were compared to the available experimental results. The best performance prediction model is obtained by using the steady-state RANS model with the first-order upwind discretization. The first-order scheme introduces lots of numerical dissipation; thus, higher-order schemes are usually recommended. But, when using higher-order schemes, it was shown that the solution does not converge to a steady state. Instead of steady state, high-order scheme can be used solved in a transient simulation (URANS). The results obtained by the URANS do not achieve as good performance prediction as the RANS with the first-order discretization scheme. In comparison with the URANS, it was shown that the LES achieves

improved performance predictions. The fan noise emission was also predicted using RANS, URANS, and LES models. It was shown that steady-state RANS model results in unrealistically small sound pressure levels. Meanwhile, the URANS and the LES models predict more noise emissions especially at higher frequencies.

In this chapter, only the frozen rotor approach was used. Future work will investigate also the sliding-mesh approach. Since LES is very computationally demanding, hybrid approaches such as DES will be tested. These hybrid turbulence models might achieve as good results but with considerably reduced computational requirements.

References

1. Radgen P, Oberschmidt J, Cory WTW EuP Lot 11: Fans for ventilation in non residential buildings Final Report
2. Tsai BJ, Wu CL (2007) Investigation of a miniature centrifugal fan. Appl Therm Eng 27 (1):229–239
3. Heo S, Cheong C, Kim T-H (2011) Development of low-noise centrifugal fans for a refrigerator using inclined S-shaped trailing edge. Int J Refrig 34(8):2076–2091
4. Williams JEF, Hawkings DL, Ffowcs JE, And W, Hawkingst DL (1969) Sound Generation by turbulence and surfaces in arbitrary Motion [321] Sound generation by turbulence and surfaces in arbitfrary motion. Philos Trans R Soc London Ser A Math Phys Sci 264(1151):321–342
5. Zhang J, Chu W, Zhang H, Wu Y, Dong X (2016) Numerical and experimental investigations of the unsteady aerodynamics and aero-acoustics characteristics of a backward curved blade centrifugal fan. Appl Acoust 110:256–267
6. Lowson MV (1970) Theoretical analysis of compressor noise. J Acoust Soc Am 47 (1B):371–385
7. Buccieri BM, Richards CM (2016) Application of the aeroacoustic analogy to a shrouded, subsonic, radial fan. J Sound Vib 385:125–137
8. Menter F, Egorov Y (2005) A scale adaptive simulation model using two-equation models. In: 43rd AIAA aerospace sciences meeting and exhibit
9. Marinić-Kragić I, Vučina D, Milas Z (2016) 3D shape optimization of fan vanes for multiple operating regimes subject to efficiency and noise-related excellence criteria and constraints. Eng Appl Comput Fluid Mech 10(1):210–228
10. Milas Z, Vučina D, Marinić-Kragić I (2014) Multi-regime shape optimization of fan vanes for energy conversion efficiency using CFD, 3D optical scanning and parameterization. Eng Appl Comput Fluid Mech 8(3):407–421
11. Ferziger JH, Peric M (2002) Computational methods for fluid dynamics. Springer, New York
12. Menter F (1993) Zonal two equation k-w turbulence models for aerodynamic flows. In: 23rd fluid dynamics, plasmadynamics, and lasers conference
13. Nicoud F, Ducros F (1999) Subgrid-scale stress modelling based on the square of the velocity gradient tensor. Flow Turbul Combust 62(3):183–200

Chapter 59
Improving the Energy and Environmental Efficiency of the Hotel Sector

Effrosyni Giama, Dimitris Karakasidis, and Agis M. Papadopoulos

59.1 Introduction

Energy management in complex and large commercial buildings with strongly varying heat/cold and/or electricity loads, such as big urban hotels, requires a holistic optimization approach in order to ensure economic, environmental and operational efficiency as well as natural resource conservation. In general, buildings contribute approximately 30% to total global GHG emissions. In efforts to reduce global warming, GHG reductions in this area would make a significant contribution [1]. According to the Intergovernmental Panel on Climate Change (IPCC), there are three areas to focus on in reducing emissions from buildings: reducing energy consumption and building embodied energy, switching to renewable energy and controlling non-CO2 emissions [2].

Hotels are typically purpose-dedicated pieces of infrastructure handling facilities, installations and equipment to serve the overall variety of tasks required by contemporary logistics services but also quite extensive retail and leisure services. In that sense, they have to satisfy commercial as well as entrainment services for visitors. For these reasons, hotels, especially the bigger one, show significant demand for energy. The energy demand is composed mainly of electricity, space cooling and heating and hot water provision. Given these high-energy requirements but also its quite significant variation on a daily and seasonal basis depending especially on the local climatic conditions, energy conservation measures as well as the implementation of renewables and state-of-the-art energy management can contribute to reduce the energy demand by increasing energy efficiency, by optimizing the overall

E. Giama (✉) · D. Karakasidis · A. M. Papadopoulos
Department of Mechanical Engineering, Aristotle University of Thessaloniki, Process Equipment Design Laboratory, Thessaloniki, Greece
e-mail: fgiama@auth.gr

S. Nižetić, A. Papadopoulos (eds.), *The Role of Exergy in Energy and the Environment*, Green Energy and Technology,
https://doi.org/10.1007/978-3-319-89845-2_59

environmental performance, by lowering operational cost and by improving the level of services provided. Moreover hotels are demanding energy consumers due to their 24-hour-based operation the variety of facilities and functions provided [3].

Despite this, not intensive research has been made based on environmental assessment with carbon footprint analysis methodology. Carbon footprint analysis is focusing on mapping greenhouse gas emissions throughout the products or processes, targeting at sustainability and economic benefits. A "carbon footprint" is in that sense a measure of the greenhouse gas emissions associated with an activity or group of activities of a product or process. This study discusses the potential environmental assessment of tourism accommodation facilities and their contribution to global carbon footprint. The carbon footprint analysis was used as a tool to define the processes, supported by Gabi Software, taking into consideration the most significant energy consumption, and improve the present situation of a hotel studied in Greece. Energy and environmental goals were set to improve the environmental and consequently the energy efficiency processes [4]. The results produced were compared with other similar cases reported in the literature considering the hotel sector in Europe. For the accomodation cluster (that means for hotels), reductions in carbon emissions, in energy consumption, in cost can be achieved by using the existing, state of the art technologies, in processes such as lighting, heating, cooling which are important for hotels' energy efficiency.

59.2 Carbon Footprint Analysis Methodology

The task of calculating carbon footprints can be approached methodologically from two different directions: (a) bottom-up, based on process analysis (PA), and (b) top-down, based on environmental input-output (EIO) analysis. Both PA and EIO deal with the aforementioned challenges and strive to capture the full life cycle impacts [4]. Wiedmann [5] describes two methods to calculate the carbon footprint using LCA: process analysis (PA) and environmental input-output (EIO) analysis. The process analysis is a bottom-up approach to analyse a product from creation to the end of its life, taking into account direct and some secondary emissions but having the disadvantage of double counting. EIO involves a top-down approach and is applied on sectoral level, expanding boundaries and eliminating the problem of double counting. The authors recommend the application of a hybrid model, combining advantages of the two methods: using EIO as primary method and locally applying the PA [6].

The analysed emissions within such a model are divided into three levels, depending on the control power of the organization/community on their sources: scope 1, direct emissions, for activities directly controlled by the organization/community; scope 2, indirect emissions, derived from the use of electricity, heat and cooling; and scope 3, other indirect emissions, from downstream and upstream (along the supply and retail chain).

A number of internationally organized standards for reporting in GHG emissions exist: The Greenhouse Gas Protocol Initiative (GHG Protocol) is more popular in the USA where it is recognized as a primary GHG emission accounting and reporting tool for organizations. It provides indicators for a number of processes of business sector including services. Another approach to calculate carbon footprint indicator is the ISO 14064–65 series of standards. These standards are fully compatible to the standards adopted by the GHG Protocol. The Intergovernmental Panel on Climate Change (IPCC) has also developed guidelines for calculating carbon footprint indicator. IPCC makes activity- or process-specific estimates of carbon impacts on the basis of the GHG emission coefficients retrieved from a range of sources, including governmental agencies (US EPA, European Environment Agency (EEA)), industry-related databases, academic publications and surveys as well as consultation with experts. All these have been summarized in a special IPCC emission factor database [7]. The UK's Department of Environment, Food and Rural Affairs (DEFRA) has developed independent standards for carbon footprint accounting and reporting, the DEFRA's GHG conversion factors. The GHG conversion factors from DEFRA's guide are also based on a number of the previous mentioned sources such as IPCC, IEA and EEA. An attempt to make a holistic approach estimation of the carbon footprint indicator by applying a universal GHG emission reporting tool has been undertaken in the UK where the Carbon Trust together with DEFRA has appointed the British Standards Institute to develop the Publicly Available Specification (PAS) 2050 [8]. The main objective of this initiative was to provide a simplified standardized approach for carbon footprint estimation and reporting that could be used from a boarder audience.

59.3 Environmental Assessment at the Hotel Sector

In order to perform environmental assessment by implemented life cycle analysis or carbon footprint analysis on hotels, it is necessary to identify the critical aspects of energy use. The operational energy of a commercial building is associated with energy consumption in the form of heating, ventilation and air conditioning, use of elevators, use of electric appliances and lightning the building. In the hotel sector, these activities may account for up to 85% of the total energy use. Other popular and energy-consuming activities related to the hotel sector are cooking and catering facilities and laundry and transportation services [9].

To measure the extent to which hotels have addressed environmental sustainability and implemented green practices and to calculate their carbon footprint, a statistical analysis regarding 5-star hotels in six major European cities (London, Paris, Rome, Madrid, Berlin, Amsterdam) was conducted. As a source, we used the official websites of the hotels to extract the necessary information and also several Internet websites that promote sustainable tourism. In total, the 5-star hotels in these six cities amounted to 262. From the data collected and presented in Table 59.1 and the following charts, we can see that more than ¾ of the hotels (76%) apply some

Table 59.1 Total emissions (Kg CO2) and carbon footprint indicator per month

Month	Total emissions	Guest nights	kg CO_2 eq./guest night
May	8157,78	2006	4,07
June	12645,16	3521	3,59
July	16340,00	3932	4,16
August	19581,45	3889	5,04
September	11740,33	2830	4,15

kind of "green" practice, while slightly fewer (69%) are those that have been awarded an official environmental certification (Ecolabel, Green Key, etc.). Additionally, 39% of the units report that they have proceeded to calculate the carbon emissions from their operations, and 27% of them publish a full sustainability report. In general, however, most hotels that are positively graded in the four categories belong to one of the major hotel chains (Accor, Marriott, InterContinental, Hilton, Hyatt, Wyndham), while in the privately owned units, the situation is somewhat different, with many of them already applying environmentally friendly practices, but very few have quantified their carbon emissions.

Separate analysis for each city suggests that the most environmentally friendly hotels are located in Berlin and Amsterdam. For the German capital, 24 of the 29 5-star hotels (83%) report that they have already applied green practices and they are also certified by an international or domestic organization. Also, 18 of them (62%) say they have calculated their carbon footprint. The situation is similar for the capital of the Netherlands, with 17 out of 21 hotels (81%) applying measures for energy saving and environmental protection, while 16 of them have an official certification. About a half of the hotels (52%) have calculated their emissions to the atmosphere.

The hotels in Berlin and Amsterdam are followed by those in London and Paris, the two cities in which the most 5-star hotels in Europe are located (75 and 71, respectively). Finally, Madrid and Rome occupy the last two positions of the list, with their rates for implementation of "green" practices and certifications being below 70%. This is probably because many units in these cities do not belong to large hotel chains, which as mentioned are those involved to a greater extent to the environmental consequences of their properties. We should not neglect the fact that these two countries (Spain and Italy) were affected by the economic crisis in a much greater extent than the others, so the main priority of their operators is the survival of their units, leaving no room for environmental improvements.

The majority of the hotels in Greece are operating seasonally, with the peak being monitored at high season (July and August), and are located in areas enjoying high levels of solar radiation and of sunshine such as the Cycladic islands, Peloponnese and Chalkidiki. Within the sample, 67% of the hotels are big units (with more than 100 beds), 33,3% are 5-star hotels (luxury hotels), 40,6% are 4-star hotels, 23,2% are 3-star hotels and only 2,9% are 2-star hotels. The total number of hotels in Greece is 9.677 (773.445 beds). Only 19% of the hotels were built after 2004. Nevertheless and despite the economic recession, after 2012, there is a significant activity in construction of 5-star hotels in Greece [10].

59.4 Results and Discussion

The statistical analysis is divided in two main aspects; initially a descriptive analysis is conducted and then an inferential focusing on the correlations among comfort sensation and environmental parameters.

The population under evaluation is composed of both male and female occupants with 43,4% of the respondents being men and 56,6% women. The age range of the respondents specified is typical for office buildings as it varies from 26- to 73-year-old occupants with a mean of 45 years and a standard deviation of 8.239.

The evaluation of the indoor environmental conditions for winter and summer period focused on the occupants' perception concerning air temperature, indoor air quality, lighting, noise and comfort conditions. In detail, the indoor air temperature conditions are determined as comfortable during winter by 71,8% of the respondents while during summer are described as moderate by 50,6% and comfortable by 39,2% of the respondents. Moreover, the indoor air quality is evaluated, and the analysis denoted that 55% of the respondents describe it as moderate and moderate to satisfied 76,9% during winter and summer period, respectively.

Furthermore, the majority of the respondents for both winter and summer period specify the lighting conditions as satisfactory for 81,9% and 80,8%, respectively. Considering noise, 57,1% of the respondents consider it as moderate, while 33,3% as satisfactory during winter period, whereas during summer the majority of the respondents (54,4%) are satisfied. Regarding the perceived comfort sensation, the analysis deduced that in both seasons under evaluation, the respondents are moderately to highly satisfied. Therefore, as deduced from the analysis concerning indoor environmental parameters, the respondents are satisfied with the existing conditions.

Energy and consequently the environmental performance of hotels vary depending on their size, class, types of energy used and services and facilities provided [11]. The hotel used for the energy and environmental evaluation case study is a Greek 4-star hotel.

Hotel Porto Koufo is located in the second leg of Chalkidiki, an area also known as Sithonia. The region is the largest tourist destination in northern Greece and in the summer attracts both residents of Thessaloniki and other major cities of Macedonia, as well as guests from other cities. Also, in the last few years, foreign tourist arrivals have increased from countries bordering or relatively close to Greece to the northern border, due to the small distances that make the area easy to reach by car. The hotel unit is situated just outside the village of Koufos, near the end of the second leg, about 155 km from Thessaloniki Centre and 140 km from the airport. The hotel started operating in 1993, and the most recent renovation was completed in March 2011.

It belongs to the 3-star category and is built on an area of 3000 square metres, surrounded by pine trees, palm trees and a garden, with the beach and the sea just in front of the hotel. The total area of the building, consisting of two floors, is 1600 square metres. The hotel offers private parking, fitness centre, conference room with audiovisual equipment suitable for presentations, bar and free Internet in all rooms.

Fig. 59.1 Hotel located in Porto Koufo, Chalkidiki, Greece

Fig. 59.2 Overall view of the hotel building studied

Available from May to the end of September, the hotel offers a total of 36 rooms, 3 junior suites and 10 studios, all recently renovated and with excellent view. The rooms are fully equipped with air conditioning, and each of them has a satellite TV, hairdryer, refrigerator, telephone, TV, safe and balcony with sea view (Fig. 59.1).

The system's boundaries include input data for all the types of energy used, raw materials, personnel and guests. The processes connected to the input data studied were heating, cooling, air conditioning, lighting, electric appliance use, catering services, laundry and transportation of the guests and personnel. The outputs calculated based on the processes studied are CO2 emissions, solid waste and waste water. The functional unit suggested for the environmental analysis is the energy used registered in kWh or MJ and associated GHG emissions in kg CO2 eq per one guest night. The "per guest night" benchmarking indicator is the most commonly used indicator in the tourism accommodation sector (Fig. 59.2).

The carbon footprint indicator was calculated with GaBi software with Ecoinvent database. Gabi is a next-generation software sustainability solution with a powerful

Table 59.2 Total emissions (Kg CO_2) from electric energy use

Year	2013	2014	2015
Electric energy (kWh)	98.559	102.543	110.790
Electric energy emissions (kg CO_2)	70.786,4	73.647,3	79.570,5
Transmission & Distribution Emissions (kg CO_2)	2.192	2.280,5	2.464
Total emissions (kg CO_2)	72.978,4	75.927,9	82.034,5

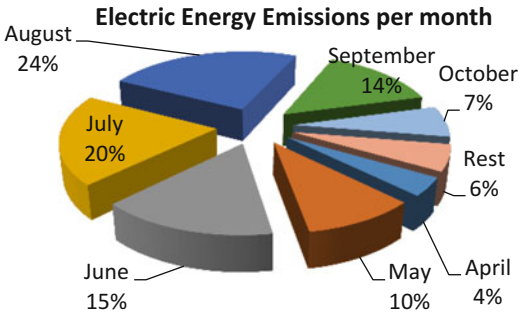

Fig. 59.3 Electric energy emissions per month

life cycle assessment engine to support the following business applications: life cycle assessment; design for environment; eco-efficiency, reducing material, energy and resource use in the most cost-effective way; as well as eco-design, developing products with smaller environmental footprints such as fewer GHG emissions and reduced water consumption and waste.

All the input data for all the types of energy used, raw materials, personnel and guests related to the processes studied (heating, cooling, air conditioning, lighting, electric appliances use, catering services, laundry, transportation of the guests and personnel) were registered based on the system's boundaries defined above. The energy consumption was translated to carbon footprint with the Gabi software tool, and for ensuring results reliability, the carbon footprint was also calculated with DEFRA impact factor emissions. As the transportation parameter was taken into consideration for the carbon footprint analysis, a list of all the tourists and their origin country was registered. Stays of 16.235 were listed for 2015, majority of them belong to Bulgarian tourists with 3.518 stays and και 21,67% of the total. Greek and Turkish follow with 16,47% and 9,74%, respectively (Table 59.2).

Based on the input energy data concerning the operational hotel's energy, the 4 months responsible for the 74% of the total CO2 emissions are August, September, June and July. If we normalize the CO2 emission results with the total guest nights, it derives 3,73 kg CO2 eq./guest night in June, while in August which is a peak-season month, the carbon footprint per month is increased to 5,05 kg CO2 eq./guest night. The average CO2 emission per guest night is 4,25 kg CO2 eq./guest night for the year 2015. Electric energy consupmtion registered includes all the processes such as air conditioning, laundry, catering services, lighting, small electric appliances. There is no separate thermal system used as the hotel is not used during winter. So the main energy consumption is electric energy consumption (Fig. 59.3).

Table 59.3 CO_2 emissions from transport process

Month	Car emissions	Airplane emissions	Total emissions
April	2.318,19	9.134,33	11.452,52
May	32.413,72	130.709,16	163.122,88
June	43.113,94	144.970,27	188.084,20
July	42.294,00	105.057,21	147.351,21
August	33.241,11	110.879,52	144.120,63
September	42.730,06	121.396,61	164.126,66
Total	196.111,01	622.147,10	818.258,11

The transport process is the process from which the majority of the CO2 emissions were registered. More specific 69,7% of the total CO2 emissions derive from airplane use and 22% from road transportation. The major pollutant process responsible for the carbon footprint of the hotel is the transportation process if we take into consideration that electricity is responsible for the 7,8% of CO2 emissions.

The total CO2 emissions calculated with Gabi software tool are 894,5 tn CO2 eq annually, while the DEFRA emission factors methodology estimated 617,5 tn CO2 eq. In correspondence the carbon footprint indicator for the annual operation of the Greek hotel studied reached the 55,1 kg CO2 eq./guest night και 38 kg CO2 eq./guest night, respectively. The difference is not important as different emission factors were used (Table 59.3).

It is also concluded that actually the carbon footprint analysis is a more energy-focused LCA, a life cycle energy analysis (LCEA) which can evaluate the environmental profile of the building and services and estimate the carbon footprint of the system studied. Conversion emission factors are the multipliers used to convert a quantifiable unit of resource into mass of carbon. Most of the conversion factors are based upon an LCA methodology. This means that the conversion factor for each aspect measured in a carbon footprint analysis arises from a previous life cycle study of the particular aspect, e.g. the conversion factor for 1 kWh of gas would be obtained from LCA of gas extraction and distribution.

59.5 Conclusions

Europe faces multiple socio-economic challenges, which have a direct impact on the energy and the financial sector. The increase in energy demand, observed in the past years, led to the gradual depletion of fossil fuels. Furthermore, the significant increase in gas pollutants (e.g. CO2 and NOx) has had major impacts on climate and environmental quality (e.g. global warming). Therefore, and also because of the strict European legislation framework, global climate change and carbon emissions as indicative environmental factors have been a top priority in the decision-making process for governments and companies.

Environmental sustainability has emerged as a key issue amongst governments, policymakers, researchers and the public. Increasing efforts and resources have been devoted to research and environmental policies in order to identify, evaluate and assess harmful environment impacts. This study discusses the potential environmental assessment of tourism accommodation facilities and their contribution to global carbon footprint. The carbon footprint analysis was used as a tool to define the processes, supported by Gabi Software, taking into consideration the most significant energy consumption, and improve the present situation of a hotel studied in Greece. Energy and environmental goals were set to improve the environmental and consequently the energy efficiency processes. The results produced were compared with other similar cases reported in the literature considering the hotel sector in Europe. For the accomodation cluster (that means for hotels), reductions in carbon emissions, in energy consumption, in cost can be achieved by using the existing, state of the art technologies, in processes such as lighting, heating, cooling which are important for hotels' energy efficiency.

It is within this context that carbon footprint analysis has emerged as a more targeted method to assess the environmental impact and to foster sustainability in a broad range of activities. Moreover, and in spite of the rather volatile international financial background, there is evidence for a positive trend: many companies and organizations seem to recognize that applying environmental management schemes and implementing sustainability policies help to reduce energy consumption as well as the use of raw and auxiliary materials and can therefore lead to a cleaner, leaner and more cost-efficient production, a recognition that is mirrored in the continual increase of the energy and environmental management certificates. In that sense, sustainability is essential for the hotel industry as well, for two main reasons: (a) as a means for the improvement of the quality of services and (b) as a major tool for marketing and promoting. On a broader scale, one cannot omit to mention the increasing concern about global climate change, which is reflected in the European legislative framework, carbon emissions being the major causal factor.

Companies and organizations are therefore pursuing “carbon footprint” indicators to estimate their own contributions to global climate change and to assess the saving potential. The results of hotels refurbishments and renovation is focused on energy reduction and environmental management as a tool for reducing cost and attracting visitors.

References

1. UNEP (2009) Buildings and climate change – summary for decision makers. UNEP DTIE, Sustainable Consupmtion and Production Branch, Paris
2. Biswas WK (2014) Carbon footprint and embodied energy consumption assessment of building construction works in Western Australia. Int J Sustain Built Environ 3:179–186
3. Cucek L, Klemes JJ, Kravanja Z (2012) A review of footprint analysis tools for monitoring impact on sustainability. J Clean Prod 34:9–20

4. Gabi Software, Life Cycle Analysis Software (2016) http://www.gabi-software.com/international/index/
5. Wiedmann T (2014) Editorial carbon footprint and input-output analysis – an introduction. Econ Syst Res, p. 175–186. https://doi.org/10.1080/09535310903541256
6. Giama E (2016) Energy performance of buildings – energy efficiency and built environment in temperate climates. In: Santamouris M (ed) Chap. 6, Life cycle vs carbon footprint analysis for construction materials. Springer Science & Business Media. ISBN 978-3-319-20830-5, ISBN 978-3319-20831-2 (eBook), New York, pp 95–106. https://doi.org/10.1007/978-3-319-20831-2
7. Filimonau V, Dickinson J, Robbins D, Huijbregts MAJ (2011) Reviewing the carbon footprint analysis of hotels: life cycle energy analysis (LCEA) as a holistic method for carbon impact appraisal of tourist accommodation. J Clean Prod 19:1917–1930
8. Radu AL, Scrieciu MA, Caracota DM (2013) Carbon footprint analysis: towards a projects evaluation model for promoting sustainable development. Procedia Econ Financ 6:353–363
9. Dascalaki E, Balaras CA (2004) XENIOS- a methodology for assessing refurbishment scenarios and the potential of application of RES and RUE in hotels. Energ Buildings 36:1091–1105
10. Kyriaki E, Drosou V, Papadopoulos AM (2015) Solar thermal systems for low energy hotel buildings: state of the art, perspectives and challenges. Energy Procedia 78C:1968–1973. https://doi.org/10.1016/j.egypro.2015.11.385
11. Moss J, Lambert CG, Rennie AEW (2008) SME application of LCA bsed carbon footprints. Int J Sustain Eng 1(2):132–141

Chapter 60
Comfort Sensation Versus Environmental Aspects in Office Buildings

Panagiota Antoniadou, Effrosyni Giama, Sandro Nižetić, and Agis M. Papadopoulos

60.1 Introduction

Indoor environment conditions of both working and living areas are extremely important as they can affect the occupants' health and well-being. In this framework, the determination of the buildings' energy and construction profile is imperative. As stated by Eurostat, the existing building stock, despite its improvement regarding energy performance, is responsible for 38% of the total final energy consumption [1, 2]. In this line of approach, the decrease of the consumed energy and in parallel the maintenance and even increase of the occupants' comfort is imperative and stated through a variety of international standards (EN ISO 7730:2005, EN ISO 15251:2006) and European Directives (91/2002, 31/2010) [3–8].

In order to achieve an integrated and effective institutional framework, the determination of the existing building stock is essential. The European buildings are classified among three periods, before 1960, from 1961 to 1990, and from 1991 to 2010, with the majority of the buildings constructed in the first two periods corresponding to the 38% and 45.3% of the buildings, respectively [2]. An approximately similar building distribution regarding their construction period is determined in case of Greece with only 32% of the buildings being constructed in accordance to a national thermal insulation regulation [9, 10]. Therefore, the need to upgrade the energy and comfort profile of the existing building stock is profound,

P. Antoniadou (✉) · E. Giama · A. M. Papadopoulos
Department of Mechanical Engineering, Aristotle University of Thessaloniki, Process Equipment Design Laboratory, Thessaloniki, Greece
e-mail: pantoniadou@auth.gr

S. Nižetić
Department of Electrical Engineering, Mechanical Engineering and Naval Architecture, LTEF – Laboratory for Thermodynamics and Energy Efficiency, University of Split, Split, Croatia, Croatia

S. Nižetić, A. Papadopoulos (eds.), *The Role of Exergy in Energy and the Environment*, Green Energy and Technology,
https://doi.org/10.1007/978-3-319-89845-2_60

as comfort constitutes a parameter that affects the occupants' concentration, productivity levels, health, and well-being [6]. Moreover, as research indicates, comfort is an aspect of constant and intense development, with the majority of the researchers especially during the last years focusing on a more personalized approach, where both the indoor conditions and the occupants' characteristics are considered [11–14].

A series of studies were performed in this field, determining probable correlations among occupants' characteristics and thermal comfort. In detail, Indraganti et al. investigated probable correlations among behavioral adaptation of the occupants and their age and gender in India, determining statistical important correlations among the parameters [15]. Moreover, Kim and de Dear identified the nonlinear relationship between individual indoor environmental quality and workspace satisfaction, whereas Antoniadou et al. determined a binary logistic regression model between the expression of complaints for ventilation and the social and building characteristics [16, 17]. As research shows, further analysis on the buildings evaluation and occupants' interaction is appropriate.

Building rating systems are environmental and management tools that aid in focusing on the construction sector and aiming at sustainability, as well as at economic and social benefits. Rating systems for buildings have incorporated the expertise and knowledge from environmental methodologies, decision-making, and management tools, which have been used in other productive sectors and were therefore influenced by those. It is therefore only reasonable that a majority of the rating systems are based on the concept of life cycle analysis (LCA) methodology and demonstrate similarities with the environmental management systems. They also include the energy audit part and extend this philosophy to other environmental issues, such as water conservation, indoor air quality, materials' selection, and waste management.

In this sense, rating systems are scoring systems designed to evaluate new and existing buildings based on a selected standard of assessing environmental performance. The most popular certification schemes based on the number of certifications accredited are Building Research Establishment Environmental Assessment Method (BREEAM) [18]: It is a European rating system developed in the UK, but also available and applicable to any other country, with measurable evaluation characteristics and practical to be implemented for the users. Together with Leadership in Energy and Environmental Design (LEED), they are the most widespread schemes. BREEAM was created in 1990 by the British organization BRE, and since then more than 200,000 buildings have been certified, while more than 500 have been registered for evaluation in and outside the UK. BREEAM assesses the overall performance of buildings using environmental aspects such as energy efficiency, water consumption, internal environment (health and well-being), pollution, transport, and materials, awarding credits in each area according to buildings' performances. LEED [19]: It was developed in America in 2000 by the US Green Building Council and is more popular in North America (USA and Canada). Still, it is also used in other regions around the world, such as South America, Europe, and Asia. The main advantage of the assessment method is the user-friendly interface adopted in the

evaluation procedure which is used for quantifying the buildings' environmental performances.

In correspondence to BREEAM, LEED assesses the overall performances of buildings using environmental aspects such as energy efficiency, water consumption, indoor air quality, pollution, transport, and sustainable sites selection, awarding credits for each environmental criterion according to the building's performance [20]. Moreover, as depicted from integrated green certification schemes for buildings such as BREEAM and LEED, a variety of environmental parameters are to be taken into consideration during certification as they influence the occupants' well-being and health [18, 19]. In detail, in case of BREEAM certification, 14 parameters are evaluated regarding the occupants' health and welfare. Those parameters are concentrating on the indoor environment conditions (air quality, lighting, acoustics, ventilation, and comfort), office space, and windows' view, parameters that establish preferable work environment conditions [18]. Additionally, in the framework of an environmental evaluation, aspects as neatness and waste management are of high priority with recycling, composting, and reuse of material being the most popular and green applied methodologies.

Within this study, two main goals are to be met: (a) the evaluation of indoor conditions in cases of office buildings through qualitative analysis and (b) the linkage of the occupants' perception of comfort to environmental parameters. This approach enables both a qualitative evaluation of the buildings, depicting the parameters that need to be taken into account by the policy makers and also outlining the perceived existing indoor conditions, so that appropriate strategies and plans can be applied for achieving in the near future nZEB status. Concerning the indoor conditions evaluation, the under evaluation parameters for both winter and summer periods are the indoor air temperature, air quality, lighting, and noise levels. Therefore, it can easily be outlined whether the perceived indoor conditions are in compliance with the constructions characteristics and HVAC systems.

Finally, during the qualitative evaluation, except for the traditional indices of thermal comfort, as set by P.O. Fanger, probable linkage between the occupants' perception of comfort and a variety of environmental characteristics are studied [21]. In this line of approach, an integrated evaluation of the office buildings is presented, considering both the buildings' energy and structural capabilities, along with the occupants' needs and well-being.

60.2 Case Study

For evaluating the indoor environmental conditions of the existing building stock, three office buildings were evaluated through a revealed preference survey. They all are public buildings and located in the Municipality of Pylaia-Hortiatis, a suburb of Thessaloniki, Greece. Thessaloniki is a typical Mediterranean, coastal city with both mild winter and warm and humid summer periods.

Fig. 60.1 Main facade of Building A

60.2.1 Building A

Building A houses the municipality's technical services. It is a two-storied building with a basement, ground floor, and two upper floors, as shown in Fig. 60.1. The entire building is occupied by offices; its construction was completed in 1998, and it is in compliance with the first Greek Thermal Insulation Regulation, issued in 1979. Its successor is the regulation on the energy performance of buildings, known as KENAK, which was issued in 2010, as part of the implementation of the initial European Energy Performance of Buildings Directive. Then, in 2013, the Greek Law 4122/2013 was published, introducing the definition of the net zero energy buildings for both commercial and private buildings [22], in accordance with the requirements of the recast Energy Performance of Buildings Directive.

Concerning the current state of the building, the two main areas of interest are (a) the building's envelope and (b) the HVAC systems. Building A is a cornered, square building with a variety of openings in all facades and double glazed, aluminum framed windows, with no external sun protection systems but internal blinds. The number and dimensions of openings in every office are considered to be sufficient for lighting and ventilation, based on the offices' dimensions, number of employees, and usage.

In order to achieve the appropriate indoor conditions during winter, a central gas boiler with autonomy per zone is used, which feeds radiator panels. Furthermore, local heat pumps (room air conditioners) are installed almost in every office and are occasionally used for heating. The operation schedule of the central heating system corresponds with the office hours of the Municipality, namely, from 07:00 am to

Fig. 60.2 Main facade of Building B

04:00 pm. During summer period, cooling is achieved by means of natural ventilation and by the aforementioned local air conditioning unit. Concerning the artificial lighting, the majority of the lamps used are fluorescent, and the total level of lighting in all offices can be characterized as adequate. However, there is neither occupancy nor lighting intensity sensors.

60.2.2 Building B

The second Building B is the former Town Hall of Pylaia-Hortiatis' Municipality, which was constructed in 1995. It can be seen in Fig. 60.2 and is a two-building complex with a ground floor and two upper floors; they are connected with an external corridor.

Concerning the architectural characteristics of the building, it features openings in every façade, and all windows are aluminum framed, with tinted double glazing, to ensure low thermal losses and sufficient natural lighting. Given its construction period, the building can be considered to be adequately insulated, with respect to contemporary requirements.

In order to achieve a better understanding of the building, the HVAC systems should also be mentioned. During the winter period, heating in Building B is achieved by means of a geothermal system, heat pumps, and fan-coils as terminal units; its operation schedule is from 7:00 am to 4:00 pm. Moreover, in addition to the central heating system, portable heating means are used (e.g., electric heaters). The

Fig. 60.3 Main facade of Building C

geothermal system is also being used for the cooling period. It should be noted, that this building was the first Greek public building to be heated and cooled by means of geothermal energy. The performance of the building was measured and evaluated by the Process Equipment Design Laboratory of the Aristotle University Thessaloniki over a 4-year period: As it was found out, annual primary energy savings between 45% and 97% where achieved for the heating period, compared to a conventional oil boiler heating. With respect to cooling, savings between 28% and 55% were achieved compared to conventional air-to-air heat pumps by Michopoulos et al. [23].

Finally, concerning the artificial lighting, fluorescent tubes are used, and the total level of lighting in offices is found to be adequate. In cases of corridors, an autonomous artificial lighting system is implemented that detects movement, to achieve decrease of the energy consumed for lighting.

60.2.3 Building C

The last building under evaluation is the Town Hall of Pylaia-Hortiatis Municipality (Building C, Fig. 60.3). This construction is a two-building structure with basement, ground floor, and first floor, which are connected with an external corridor. The building was constructed in 2002 and is well insulated, based on the regulatory requirements valid then, but also with respect to contemporary ones. In both structures, offices are located, but in the East building, the majority of areas are art and culture halls.

Both structures have openings in all their external façades, with sliding, aluminum framed, double glazed windows for achieving a satisfactory level of energy efficiency. In order to achieve adequate daylight control, internal and external blinds are installed and used. Moreover, the number and dimensions of openings in the offices are considered sufficient for lighting and ventilation, based on the offices' dimensions, number of employees, and usage.

Concerning the HVAC systems of the buildings, heating and cooling are achieved by means of a central, natural gas fired boiler and a central chiller, respectively. A dual air duct system is being used to circulate the warm and cold, respectively. The same duct system is also being used for the building's ventilation. In addition, natural ventilation is being carried out through the windows, particularly in the spring and fall period. Finally, concerning the artificial lighting, fluorescent tubes are used, and the total level of lighting in offices is found to be adequate.

60.3 Qualitative Environmental Evaluation

In order to conduct a qualitative evaluation of the indoor environment conditions, a revealed preference survey was carried out specifying the occupants' perception of indoor environment conditions during winter and summer period. The implementation of this methodological approach is exceptionally popular and widely applied for the specification of indirect conditions and goods [24]. The applied methodology is outlined in four different stages: (a) evaluation of criteria, (b) construction of questionnaires, (c) data collection, and (d) data analysis. The structure of the questionnaire is divided in three main aspects: (a) general social characteristics, (b) personalized evaluation of indoor conditions during winter and summer period, and (c) a variety of parameters focusing on the interaction between occupants and HVAC systems.

Main goal of the analysis is the determination of the environmental parameters and their influence on the occupants' comfort sensation during winter and summer period. The collected sample consists of 106 questionnaires with an error of 4% and a confidential interval of 95% based on the population.

The respondents were asked to evaluate the indoor environmental conditions and to express through a Likert scale their opinion concerning six indirect environmental parameters that as outlined from green building certifications, BREEAM and LEED, affect the occupants' well-being. Those parameters are (a) how productive the occupants feel during they stay in their offices, (b) in which scale does the indoor environment conditions contribute to their concentration level, (c) whether they are satisfied with their work environment conditions, (d) neatness and (e) window view of their offices, and finally (f) the frequency of recycling.

The qualitative evaluation of the indoor environment conditions along with the correlation of occupants' comfort sensation and environmental parameters is carried through statistical analysis. Initially, a descriptive analysis is conducted determining the occupants' attitude and perspective concerning the indoor conditions. Second stage of the analysis is the specification of probable correlations between occupants' comfort sensation and the aforementioned environmental parameters. This methodological approach can lead to a successful determination of the linkage between the occupants' comfort sensation and the environmental parameters, enabling the aforementioned effect of those parameters on the occupants'.

60.4 Results and Discussion

The statistical analysis is divided in two main aspects; a descriptive analysis is conducted and then an inferential focusing on the correlations among comfort sensation and environmental parameters. The under evaluation population is composed of both male and female occupants with 43.4% of the respondents being men and 56.6% women. Regarding the age of the respondents, it varies from 26 to 73 years old with a mean of 45 years and a standard deviation of 8.239.

Through the analysis, a variety of personal characteristics and indoor conditions are evaluated. Regarding the evaluation of indoor environment conditions, the occupants' perception concerning air temperature, indoor air quality, lighting, noise, and comfort conditions for winter and summer period are evaluated. In detail, the indoor air temperature conditions are determined as comfortable in case of winter by 71.8% of the respondents, while during summer are described as moderate by 50.6% and comfortable by 39.2% of the respondents. Moreover, the indoor air quality is evaluated, and the analysis denoted that 55% of the respondents describe it as moderate and moderate to satisfied 76.9% during winter and summer period, respectively.

Furthermore, the majority of the respondents for both winter and summer period specify the lighting conditions as satisfactory for 81.9% and 80.8%, respectively. Considering noise, 57.1% of the respondents consider it as moderate, while 33.3% as satisfactory during winter period, whereas during summer the majority of the respondents (54.4%) are satisfied. Regarding the perceived comfort sensation, the analysis deduced that in both under evaluation seasons, the respondents are moderately to highly satisfied. Therefore, as deduced from the analysis concerning indoor environmental parameters, the respondents are satisfied with the existing conditions.

In addition to the qualitative evaluation of the indoor environment conditions, an inferential analysis is carried out, determining probable correlations among perceived comfort sensation during winter and summer period and a variety of environmental parameters. The respondents were asked to determine their perceived level of comfort for both winter and summer in a Likert scale from 1 (unsatisfactory) to 7 (satisfactory) and their satisfaction of the aforementioned parameters in a Likert scale from 1 (unsatisfactory) to 7 (satisfactory). Due to the nature of the data, a nonparametric Wilcoxon analysis is conducted, and the results of the analysis are depicted in Table 60.1.

As deduced from the analysis, all the presented correlations in Table 60.1 are statistically important but the occupants' concertation and point of view about neatness in correlation to the total comfort sensation during summer. The rest correlations have a confidentiality interval of 99% ($p < 0.05$).

The analysis depicts a positive correlation among the occupants perception of comfort during winter and summer period and the aforementioned environmental parameters. In detail, the analysis deduced that the more productive the occupants fell, the higher their comfort perception is in both under evaluation season. Moreover, the more concentrated the occupants fell in their office area, the higher their

Table 60.1 Correlations among occupants' comfort perception and environmental parameters

Correlations	*Z*	Asymp. Sig. (2-tailed)
Felt of productivity in the office – total comfort sensation during winter	−2.063	0.039
Concentration in the office – total comfort sensation during winter	−2.272	0.023
Point of view for work environment – total comfort sensation during winter	−3.923	0.000
Point of view for neatness – total comfort sensation during winter	−2.454	0.014
Window view – total comfort sensation during winter	−2.872	0.004
Frequency of recycle – total comfort sensation during winter	−4.859	0.000
Felt of productivity in the office – total comfort sensation during summer	−3.082	0.002
Concentration in the office – total comfort sensation during summer	−1.129	0.259
Point of view for work environment – total comfort sensation during summer	−2.990	0.003
Point of view for neatness – total comfort sensation during summer	−1.255	0.209
Window view – total comfort sensation during summer	−2.084	0.037
Frequency of recycle – total comfort sensation during summer	−4.033	0.000

comfort sensation during winter is (Fig. 60.4a). Another parameter under evaluation is the neatness of the area. From the analysis is outlined that the more satisfied the occupants are with the neatness of their office area, the higher their comfort sensation during winter is (Fig. 60.4b).

Moreover, the work environment conditions are analyzed. In this case the majority of the respondents are satisfied with their work environment conditions (plants, pictures, etc.), and as deduced from the analysis, the more satisfied the occupants are with the indoor decoration and office environment, the higher the level of comfort sensation in both seasons is. Regarding the occupants' satisfaction concerning their window view, it is outlined that the more satisfied the occupants are with the existing view, the higher their comfort sensation during winter and summer period is (Fig. 60.5). The final under evaluation correlation is the one among the frequency of recycling and the comfort sensation. In this case, the correlation among the variables is once more positive with increase of the comfort sensation when the recycling frequency is high (Fig. 60.6).

Therefore, it is safe to say that as expected and depicted from the literature research, those environmental parameters are strongly and positively correlated with the occupants' comfort sensation, but in the summer period, not all parameters under evaluation are correlated with the occupants' comfort sensation.

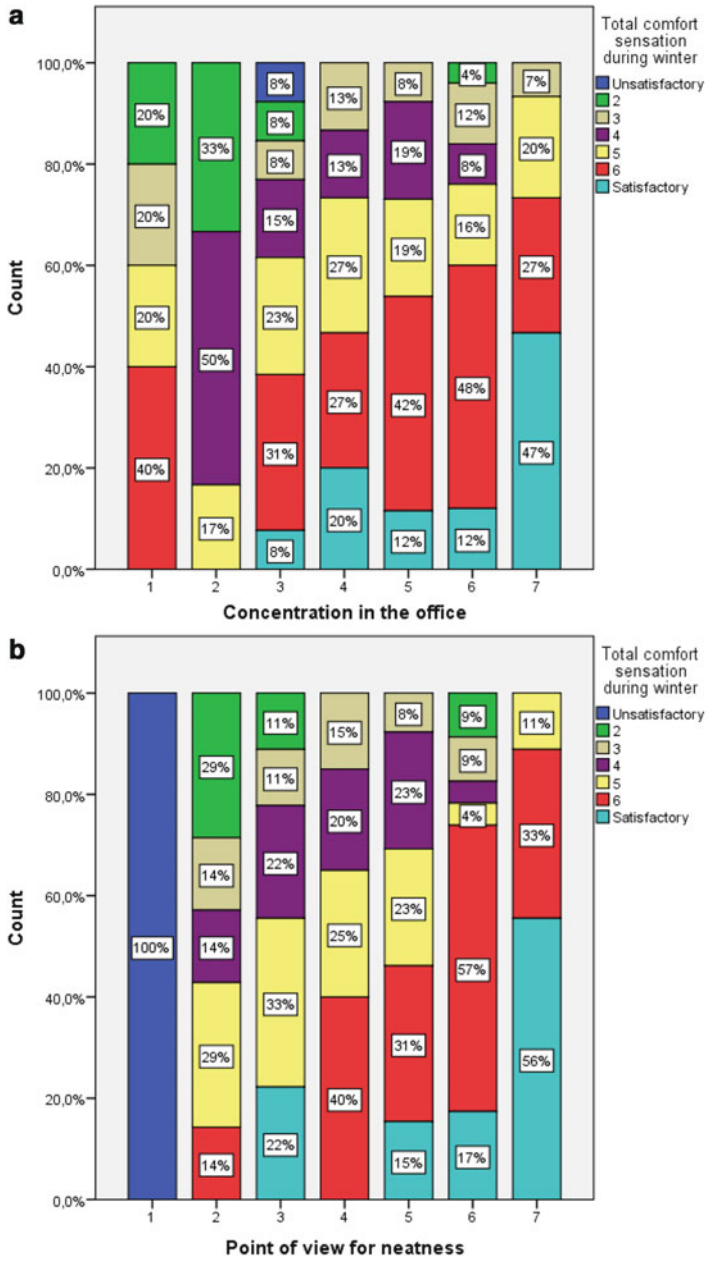

Fig. 60.4 Relation between the total comfort sensation during winter and (**a**) the concentration level of occupants in their office area and (**b**) the point of neatness in the office area

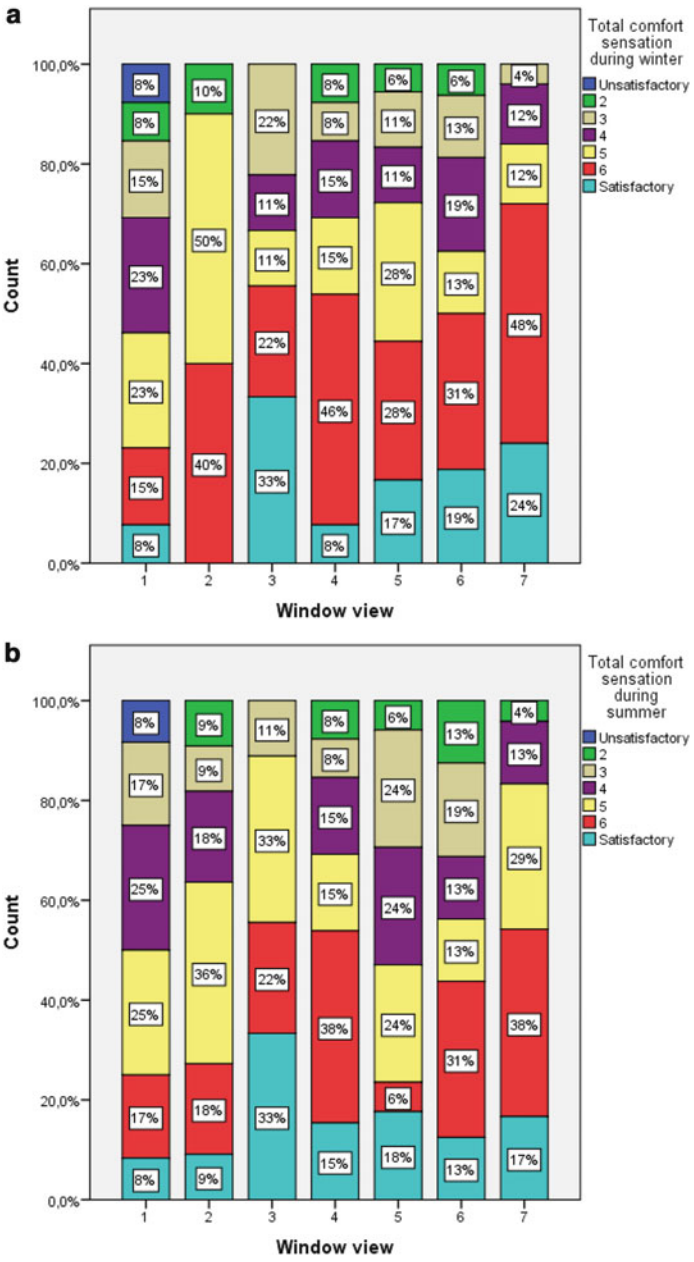

Fig. 60.5 Relation between the occupants' satisfaction regarding window view during (**a**) winter and (**b**) summer period

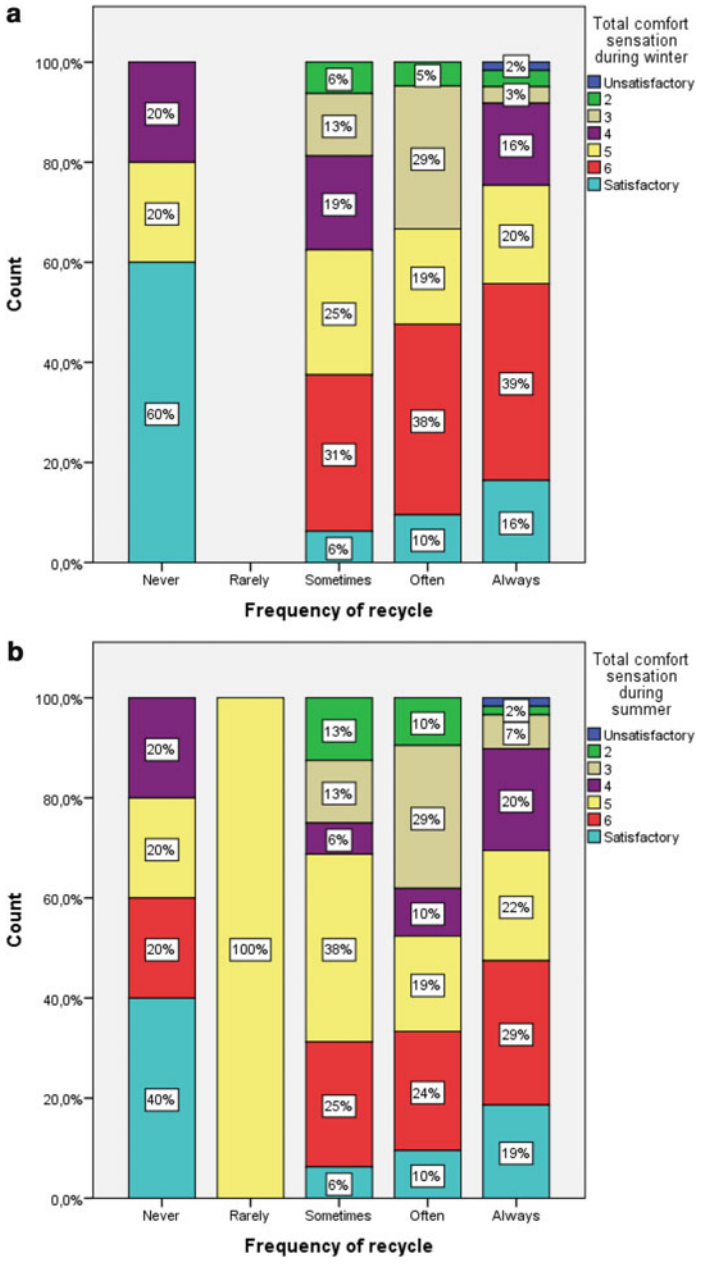

Fig. 60.6 Relation between the occupants' frequency of recycle during (**a**) winter and (**b**) summer period

60.5 Conclusions

Determination and evaluation of the indoor environmental parameters along with the environmental parameters that affect the occupants' perception of comfort sensation in case of office buildings are essential, as main goal of the existing and forthcoming legislation is the energy upgrade of the existing and new constructed buildings, creating an environmental friendly and with low energy footprint building. It was within this line of approach that an extensive qualitative evaluation of three office buildings in northern Greece was carried out.

Regarding the results of the study, a revealed preference survey was carried out and an evaluation of the indoor environment conditions was conducted, to determine the occupants' perception of indoor air temperature, air quality, lighting, and noise conditions along with their general sense of comfort during winter and summer period. Taking into account the construction period of the buildings, a satisfactory level of thermal protection and a good heating and cooling ability of the buildings was confirmed. This prevision is successful as for both under evaluation periods, the majority of the respondents are moderately to highly satisfied, for all parameters considered.

In addition to the aforementioned qualitative evaluation, an inferential statistical analysis was conducted, determining the existence and nature of probable correlations among the occupants' comfort sensation and a variety of environmental parameters. The analysis depicted that all parameters under evaluation are positively correlated with the occupants' comfort sensation during winter. In case of summer period, all under evaluation parameters but the concentration and neatness in the office area are specified as statistically important correlated. The deduced correlations also during summer period are positive with the upgrade of any environmental parameter leading to an upgrade of the occupants' comfort sensation.

Concluding, the analysis highlighted the need to determine and evaluate the existing correlations between the perceived comfort sensation and the environmental parameters that affect the occupants' well-being and productivity. Linking those parameters to the decision-making stage of the design and construction process is essential. Moreover, the adaptation and creation of a healthy and comfortable work environment that fosters the occupants' productivity and well-being is imperative, as they can help the policy makers accomplish the vision of a green building, not only concerning energy consumption but the occupants.

Acknowledgments The authors would like to express their gratitude to the Mayor of Pylaia-Hortiatis Municipality, Greece, and to the employees of the technical service, the former Town Hall, and the Town Hall, for their support and their participation in the survey.

The survey and study were carried out within the framework of the research project "Identification and Evaluation of the perceived level of comfort in office buildings using hybrid, personalized models". The project was funded under the "RESEARCH PROJECT FOR EXCELLENCE IKY/SIEMENS"; the authors want to express their gratitude to IKY/State Scholarships Foundation for this.

References

1. Eurostat (2015) Final energy consumption by sector. Retrieved June 26, 2017, from http://ec.europa.eu/eurostat/tgm/table.do?tab=table&init=1&language=en&pcode=teina225&plugin=1
2. Economidou M, Atanasiu B, Despret C, Maio J, Nolte I, Ralf O, . . . Staniaszek D (2011) Europe 's Buildings Under the Microscope: a country-by-country review of the energy performance of buildings. Buildings Performance Institute Europe (BPIE)
3. Eurostat (2017) Europe 2020 indicators – research and development. Eurostat Statistics Explained. Retrieved June 5, 2017, from http://ec.europa.eu/eurostat/statistics-explained/index.php/Europe_2020_indicators_-_research_and_development
4. Papadopoulos AM (2016) Forty years of regulations on the thermal performance of the building envelope in Europe: achievements, perspectives and challenges. Energ Buildings 127:942–952. https://doi.org/10.1016/j.enbuild.2016.06.051
5. CEN (European Committee for Standardization) (2005) ISO 7730: Ergonomics of the thermal environment analytical determination and interpretation of thermal comfort using calculation of the PMV and PPD indices and local thermal comfort criteria. Geneva: International Standard Organization, 3, 605–615. https://doi.org/10.1016/j.soildyn.2004.11.005
6. CEN (European Committee for Standardization) (2007) DS/EN 15251: Indoor environmental input parameters for design and assessment of energy performance of buildings addressing indoor air quality, thermal environment, lighting and acoustics. Geneva: International Standard Organization, 54. https://doi.org/10.1520/E2019-03R13.Copyright
7. European Commision (2010) Directive 2010/31/EU of the European Parliament and of the Council of 19 May 2010 on the energy performance of buildings (recast). Off J Eur Union:13–35. https://doi.org/10.3000/17252555.L_2010.153.eng
8. European Commision (2002) Directive 2002/91/EC of the European Parliament and of the council of 16 December 2002 on the energy performance of buildings. Off J Eur Union:65–71. https://doi.org/10.1039/ap9842100196
9. Hellenic Statistical Authority (2011) National Population Census of 2011. Retrieved April 18, 2017, from http://www.statistics.gr/
10. Theodoridou I, Papadopoulos AM, Hegger M (2011) A typological classification of the Greek residential building stock. Energ Buildings 43(10):2779–2787. https://doi.org/10.1016/j.enbuild.2011.06.036
11. Antoniadou P, Papadopoulos AM (2017) Occupants' thermal comfort: state of the art and the prospects of personalized assessment in office buildings. Energ Buildings 153(C):136–149. https://doi.org/10.1016/j.enbuild.2017.08.001
12. De Dear RJ, Akimoto T, Arens EA, Brager G, Candido C, Cheong KWD, Li B, Nishihara N, Sekhar SC, Tanabe S, Toftum J, Zhang H, Zhu Y (2013) Progress in thermal comfort research over the last twenty years. Indoor Air 23(6):442–461. https://doi.org/10.1111/ina.12046
13. Gossauer E, Wagner A (2007) Post-occupancy evaluation and thermal comfort: state of the art and new approaches. Adv Building Energy Res 1(1):151–175. https://doi.org/10.1080/17512549.2007.9687273
14. Frontczak M, Wargocki P (2011) Literature survey on how different factors influence human comfort in indoor environments. Build Environ 46(4):922–937. https://doi.org/10.1016/j.buildenv.2010.10.021
15. Indraganti M, Ooka R, Rijal HB (2015) Thermal comfort in offices in India: behavioral adaptation and the effect of age and gender. Energ Buildings 103:284–295. https://doi.org/10.1016/j.enbuild.2015.05.042
16. Kim J, de Dear R (2012) Nonlinear relationships between individual IEQ factors and overall workspace satisfaction. Build Environ 49(1):33–40. https://doi.org/10.1016/j.buildenv.2011.09.022

17. Antoniadou P, Kyriaki E, Manoloudis A, Papadopoulos AM (2017) Evaluation of thermal sensation in office buildings : a case study in the Mediterranean. Procedia Environ Sci 38:28–35. https://doi.org/10.1016/j.proenv.2017.03.071
18. BRE (n.d.) BREEAM. Retrieved January 15, 2017, from http://www.breeam.com/
19. U. S. Green Building Certification (n.d.) LEED. Retrieved Jan 15, 2017, from http://www.usgbc.org/leed
20. Giama E, Papadopoulos AM (2012) Sustainable building management: an overview of certification schemes and standards. Adv Building Energy Res 6(2):242–258. https://doi.org/10.1080/17512549.2012.740905
21. Fanger PO (1970). Thermal comfort. Analysis and applications in environmental engineering. Thermal comfort. Analysis and applications in environmental engineering
22. Greek Law 4122 (2013) Energy efficiency in buildings-in accordance to directive 2010/31/EC of the European Parliament and the council. Off J Greek Gov 42(A):639–654
23. Michopoulos A, Bozis D, Kikidis P, Papakostas K, Kyriakis NA (2007) Three-years operation experience of a ground source heat pump system in Northern Greece. Energ Buildings 39 (3):328–334. https://doi.org/10.1016/j.enbuild.2006.08.002
24. Samuelson PA (1938) A note on the pure theory of consumer's behaviour. Economica 5 (17):61–71

Chapter 61
Evaluation of Thermal and Visual Comfort: Bioclimatic Strategies for Office Buildings

David C. Avila

61.1 Introduction

The starting point of this research project, funded by the National Council of Science and Technology (CONACYT), was an analysis of the conditions of use and consumption of energy at administrative and educational sites, taking as an example the physical spaces of the Cultural Building and Administrative Building at the University of Guadalajara, by interdisciplinary researchers from different universities to propose adequate solutions for each case in the process of achieving comprehensive energy saving.

The analysis was based mainly on the energy used in air conditioning, artificial lighting, and the connected equipment in each unit. On the basis of the results obtained through the various stages of the research, it has been possible to perform an energy audit and, in the process, propose recommendations for environmental adaptation of the architectural spaces at the institution in search of energy saving and optimization of the institutional resources, as well as improvement of the working conditions of the users.

The methodology is described below in three steps:

A. General inspection of the present condition of the analyzed buildings and observation of the physical characteristics of spaces, the daylighting, and the electrical power conditions. The kind of electrical installation is also analyzed, making it feasible to determine the annual energy consumption, percentages of annual costs, and kinds of energy used.
B. Diagnosis to determine the loss or excessive use of electrical energy inside the buildings by means of the specific consumption by electrical installations, artificial lighting, connected equipment, and special equipment. Besides that,

D. C. Avila (✉)
University of Guadalajara Mexico, Department of Urbanism, Guadalajara, Mexico

S. Nižetić, A. Papadopoulos (eds.), *The Role of Exergy in Energy and the Environment*, Green Energy and Technology,
https://doi.org/10.1007/978-3-319-89845-2_61

Building space	levels	Area (square meters)	
		by level	by building
A. Parking lot	1	10,200	10,200
B. Green areas and small square	1	16,575	16,575
C. Auditorium	3	variable (see F3)	1,512
D. Hall	2	variable (see F3)	1,083
E. Tower	8	variable (see F3)	2,680
F. Calssrooms, South wing	3	variable (see F3)	4,103
G. Calssrooms, North wing	4	variable (see F3)	7,708
H. Workshops	3	variable (see F3)	3,138
I. Research modules	2	variable (see F3)	250
		Total (m^2)	47,249
		Surfase of the area (m^2)	41,275

Fig. 61.1 Census of building facilities

the available daylight and the bioclimatic conditions are delimited in the spaces, according to the layout of openings and the facades orentation.

Proposals are devised, mainly based on readjustment of previously established architectonic spaces (classroom type), as well as implementation of energy-saving systems in the aforementioned spaces.

C. Analysis.

Characteristics of the building: The building analyzed is located at a latitude of 20° north and 1450 meters above sea level. It is used as a teaching center, and activities such as reading, writing, and painting take place there. The total built surface is 18,017 square meters, distributed across nine buildings. A maximum of 1300 people congregate in it.

The areas are divided as shown in Fig. 61.1.

61.2 Census of Facilities

To obtain information on the total energy consumption of the existing electrical facilities in the School of Architecture buildings, we carried out a registration of the lighting system and all electrical equipment in each building. The results of the census showed, in a general way, that more than a third of the electricity consumption was used for artificial lighting at the School of Architecture. Two thirds of that lighting consumption occurred in buildings F and G, the classrooms. To reduce the consumption in these classrooms, a potential savings would be obtained by the implementation of energy-saving systems and by taking advantage of natural lighting (Fig. 61.2).

Concept	Consumo (kw-h/month)	Charge (kw)
Lightning	32,361.11	154.26
Air conditioned	2,898.43	40.88
Connections	13,008.86	116.59
Power	4,843.78	163.63
TOTAL	53,112.18	475.36

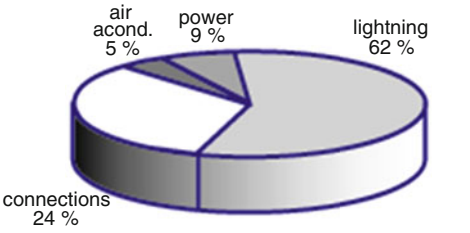

Dustribution of enegy consumption in the school building

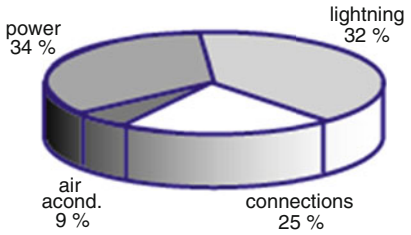

Distribution in the charge installed in the school building

Fig. 61.2 Energy consumption and electric charge installed

61.2.1 Air Conditioning Requirements

Energy requirements depend on activities. It is necessary to define acclimatization strategies according to the seasons of the year to obtain environmental comfort:

In the hot season:

- Ventilation needs to be maximized (0.3–2.5 m/s) to obtain an internal building temperature within the comfort range.
- The external ambience of the building needs to be humidified (2–3.5 kg/cm^2) to improve internal comfort.
- Direct sun radiation over inhabitable spaces needs to be avoided.
- The air is humid.
- Cross-ventilation needs to be optimized (0.3–2 m/s) to avoid humidity inside the buildings.
- Protection is needed to avoid direct sun radiation, which results in an undesired calorific contribution to the building.

In the dry and temperate seasons:

- An adequate reduction between external and internal temperatures to optimize the entire comfort of the building (thermic delay).

- Direct solar radiation is favored only in the early morning in order to obtain light heating of the buildings (70–3500 W).

Such recommendations allow us to define the means of environmental control in the buildings by examining the constructive elements in an analytical way or by tests in models in simulated environments.

61.2.2 Available Natural Illumination

The setting of the applicable illumination grade is made using a Dresler graphic. Here it is observed that at a latitude of 20°N we can easily obtain high levels of illumination (9000–13,000 lux) of 90–95% during the working day, which determines the daylight factor (DLF). This graphic is based on average conditions of time and climate. If seasons are drier or more humid, it is obvious that these values are only a design guide, because absolute values are not usable for adequate lightning design anyway. Once the abovementioned information is analyzed, it is feasible to know the lighting strategies needed according to the energy saving program [1] (Fig. 61.3).

61.3 Diagnostics

Energy revision: For the present work, classrooms of the same kind as those in the north and south wings were chosen as ones that summarize the light and climatic conditions of all classrooms (general characteristics), as well as its place on the whole and general characteristics. The results obtained here would be used in all of the center's educational spaces since, according to the initial analysis, they were considered suitable for this area survey.

Measurements of available electrical power: There is a need to know the energetic behavior of the consumption curve and the demand for electrical power, obtained by means of measurements of the feed transforms. Such measurements produce two basic graphs: the energy demand and the power factor. The behavior of the demand of the 300 kVA transformer is connected to the charges of equipment and lighting that correspond to Buildings A, B, C, D, E, F, and I. It is shown that a maximum value of 75 kW is reached near the hour of highest demand (19.00 h).

Making a detailed forecast of energy consumption based on measurements during a typical day, it is shown that the hour of highest demand for energy at the center is the hour of maximum demand established by the CFE (Federal Commission of Electricity). The foregoing means that the energy consumption in this hour represents a higher cost (Fig. 61.4).

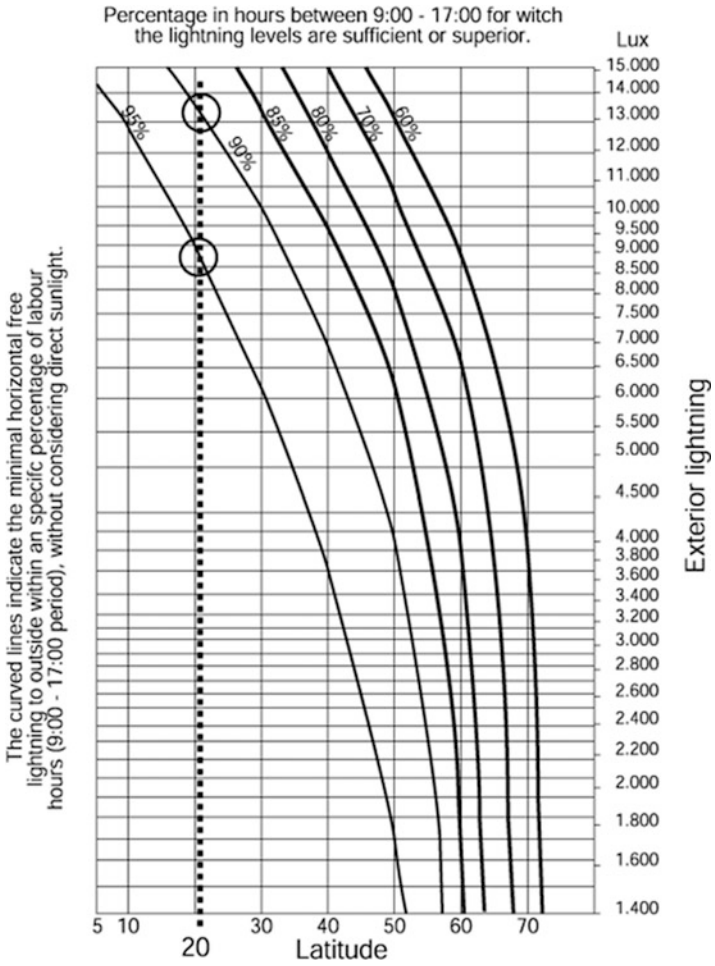

Fig. 61.3 Dresler graphic

Behavior of electrical demand: On the other hand, we must consider—besides the demand cost, which coincides in a proportional way during most of the year—the electrical demand in kilowatts. Except in the months of January and April, the real cost of the energy is greater that the demand, which means that with the highest demand, the energy cost is greater per kilowatt hour. Regarding energy consumption for each kilowatt hour, the proportional cost of energy is presented during the whole year. For example, in January the consumption is higher and so is the cost [2].

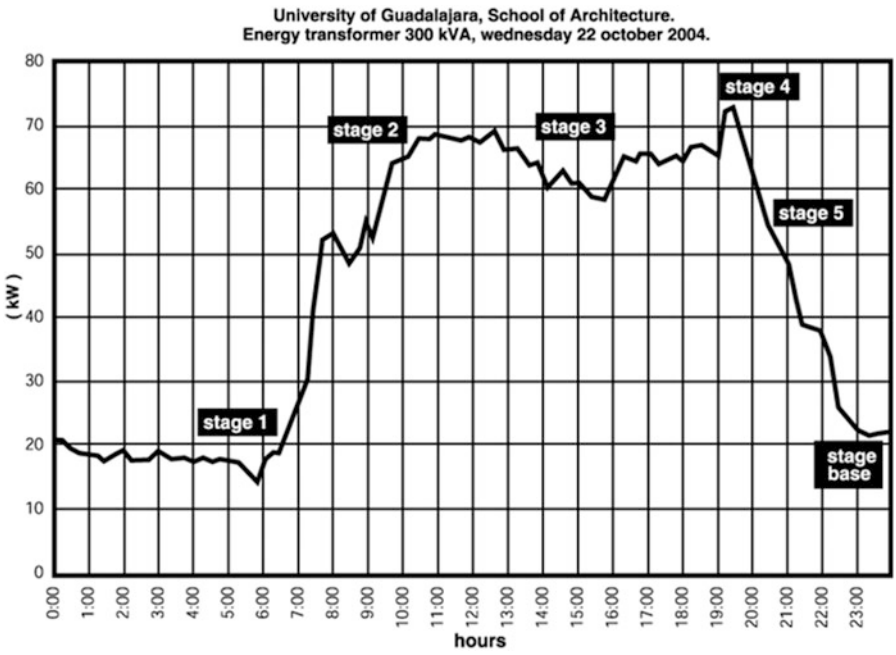

Fig. 61.4 Behavior of electrical demand

61.3.1 Lightning Behavior of Real Measurements in Model Classrooms

The analyses of real conditions in model classrooms are performed taking into account two aspects: measurement at 16 points of work levels using luxometers in real conditions of the sky CIE and through graphic analysis of fisheye photos regarding the resulting daylight (Fig. 61.5).

The abovementioned helps to establish certain criteria for the proportions of the optimum size, form, and placement of windows. Using the lecture survey and the position of such measurement points (fisheye), it was intended to make a proposal to modify classrooms. The parameters analyzed in the openings were:

- Coefficient and proportion of windows
- Form and geometry
- Layout and location
- Illumination of working levels
- External reflected levels

For the two points of view of the analysis in model classrooms, they could be divided into two groups: those referring to aspects of opening and those related to receptor surfaces [3].

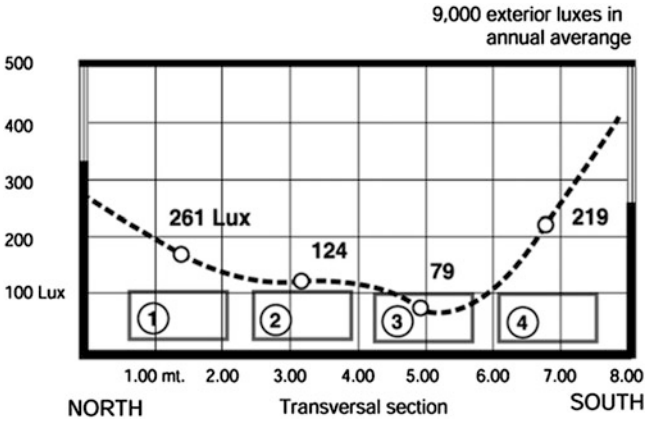

Fig. 61.5 Percentages of available natural lighting

61.4 Proposals

Selection of the components of the steps: First, it is convenient to remember the main principles that must guide the steps in the analysis of natural illumination of the architectural project; three different objectives can be observed:

- Optimization of the reception of diffusion of light
- Selection of direct sun penetrations according to the season
- Homogeneous distribution of light in spaces of interest

It can be seen that there are two great groups of natural illumination components: the lateral and the zenithal. The available light in a spot in the space depends on the sky type, the horizontal exterior component, the solid angle of the opening, and the cosine of the angle of media incidence of that light over a respective level.

It is deduced, by this relation, that zenithal openings are more effective in a horizontal plane than lateral openings, because they produce high interior illumination over the horizontal surface. Concerning the direct sun incidences (sunlight) it can be said that lateral openings are more favorable because the penetration is selective depending on the season of the year, the day, and the hour, as opposed to zenithal openings where the incidence in summer is critical and in winter it is lower, even though in the case of the classrooms we contemplated only the lateral analysis of the sky CIE classification (2; covered sky), which means the diffusion of light. This also takes into account consideration of control devices for direct solar incidence. The bioclimatic criteria mark the guides to reach this preconclusion regarding the percentages of windows and their geometry and disposition on different walls. Even though the proportion is marked according to climatic matters, illumination levels that can be reached with these proportions are well accepted to accomplish visual tasks in solar orientation. The results

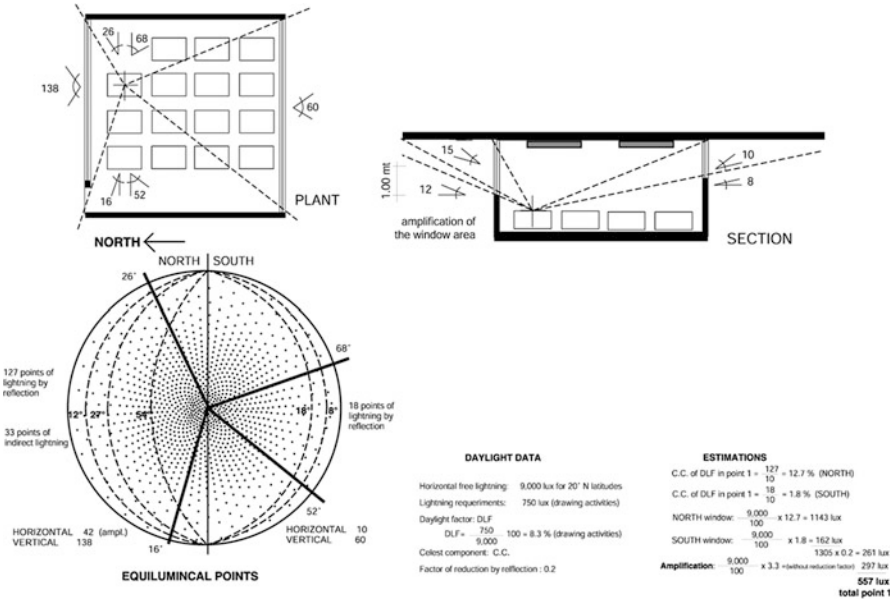

Fig. 61.6 Daylight data and estimation

obtained show that the proportions of the original north–south windows provide only 261 lux in the position shown in, which are the activity visual requirements in drawing 750 lux (Fig. 61.6).

61.4.1 Complementary Saving Measures

Some complementary measures are set forth in the readjustment of typical spaces to obtain an integral saving inside the buildings, from which are obtained a series of savings in consumption, in maximum demand, and in costs, besides the percentages of consumption and maximum demand [4] (Fig. 61.7).

Photometry of the interior surfaces: The factor of reflection of the light in a space depends to a great extent on the materials used for construction of the walls, floor, and roof. The light consequences due to the factor of reflection off the walls are in direct relation to the light comfort that will be had in the space. With the help of the computer program GENELUX, we verified the aerial map-making of the coating materials' effects on the distribution of light inside a given volume (Fig. 61.8).

The top figure shows the light distribution (in curves) of different finishes. In the aforementioned analysis it appeared that between curve 2 and curve 3 there was a decrease of 20% in the part close to the window and that at the back of the space, both diminished by 100%. From this it is possible to conclude that half of the available lighting at the back of the space comes only from interreflections of light

Measure	initial investment (US dollars)	Savings				
		Consumption kw-h/month	Maximum demand	Economic $/month	% of consumption	maximum demand
Advantage of natural lightning in WC, F and G buildings	$ 0.00	249	0	85	1%	0%
Advantage of natural lightning in building E	$ 0.00	584	0	200	2%	0%
Elimination of innecesary incandescent lamps	$ 0.00	23	0	10	9%	0%
Adequate lightning levels in surveillance corridor	$ 122.10	2,2260	0	768	9%	0%
Substitute lamps and balasts by lamps T8 and electron balasts	$ 900.00	441	1	219	2%	2%

Fig. 61.7 Savings in the different buildings

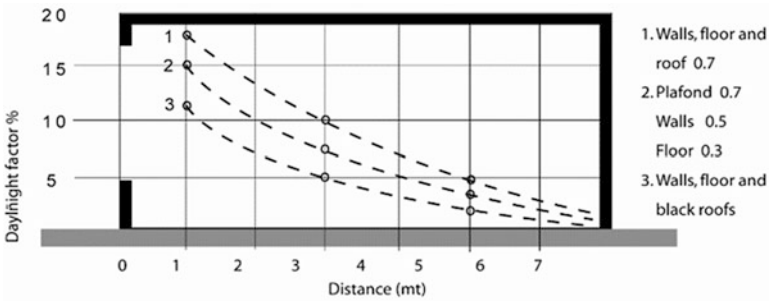

Fig. 61.8 Materials of coating photometry

on the walls, floor, and roof of the space. If we compare curves 1 and 2, it can be appreciated that the available quantities of light at the back of the space are of the order of multiplication by two, or half of a totally white space. Both comparisons show the importance of bearing in mind the aerial map-making of the coating materials in an architectural space.

Therefore, it is possible to affirm that with different interior surfaces the behavior would be as described below.

Clear sky: In general, the roof does not receive natural lighting in a direct way; it does not intervene in an important way in the distribution of the light. On the other hand, in cases where light is turned upward (mantelpieces of light), it receives a certain quantity that it can redistribute in turn to the whole space. As a consequence, the factor of reflection of this surface will have to be raised (0.7–0.8).

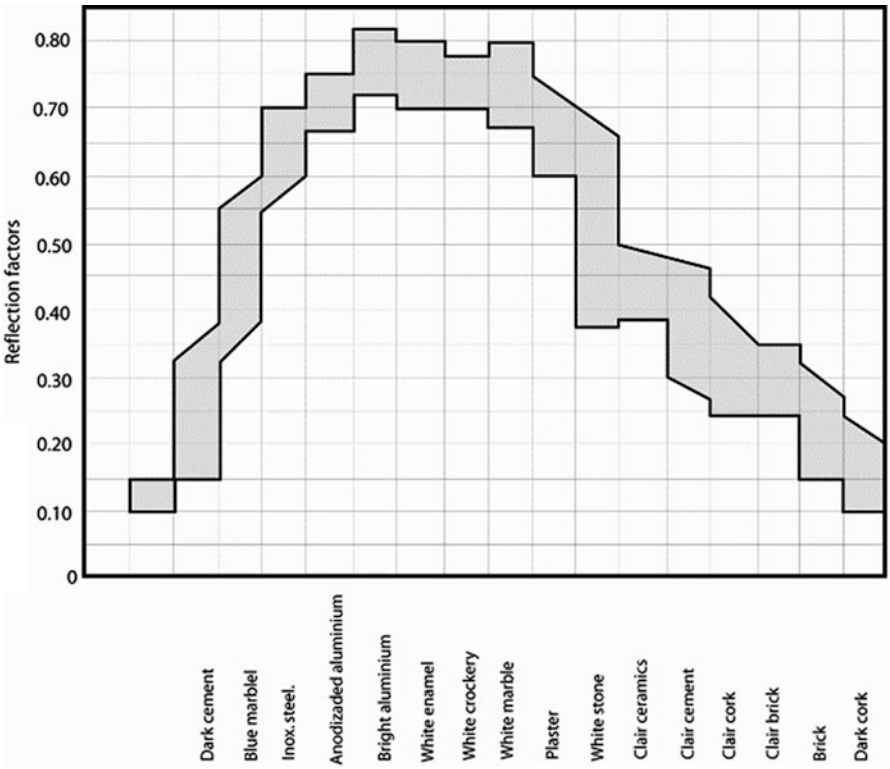

Fig. 61.9 Reflection factors of materials. (Source: Damelincourt et Rangueil, Universite Paul Sabatier. Adapted by David Carlos Avila)

Floor: First of all, it suits to add in a general way that the surfaces of the floors are strange free or clear. The furniture and especially the tables (levels) of work cover a great part of the surface.

The analysis centers on considering the horizontal levels of work, which are those that will receive the most important quantity of light, and it places major importance on taking care that there are not high levels of lighting that provoke discomfort by dazzling the eye (Fig. 61.9).

61.4.2 Walls

Since it is verified in the simulations that the walls receive both direct and diffuse lighting, they play the most important role in the architectural space in terms of distributing the aforementioned light to the interior. As a general rule, it is possible to say that if the factor of reflection of the walls is lower than 0.5, it will be difficult for the lighting to adequately illuminate the back of the space in question (Fig. 61.10).

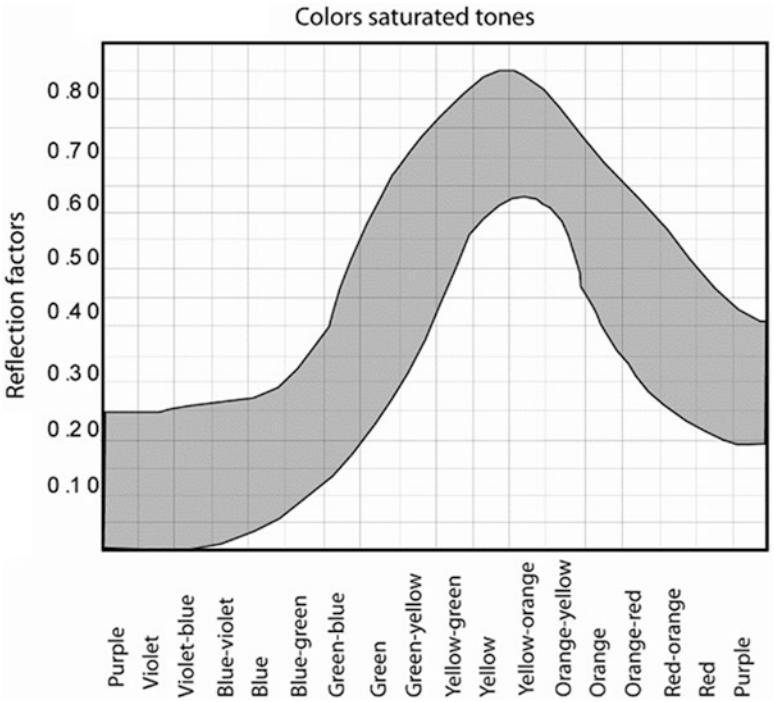

Fig. 61.10 Reflection factors of different paint colors. (Source: Damelincourt et Rangueil, Universite Paul Sabatier)

With regard to the variety of available materials in the construction market, where it is possible to compare the characteristics of each of them (Fig. 61.11).

61.5 Conclusion

For a suitable saving in energy consumption for artificial lighting, it becomes necessary to take into account all of the variables that intervene in the distribution of the luminous flow, from the disposition of the windows (form, size, orientation, and location) to the architectural elements that intervene in the process, and the materials, the textures, the colors, the proportions, etc.

- Physical readjustments in classrooms can obtain a substantial saving by taking maximum advantage of natural illumination.
- Taking into account integration of the five saving measures that were introduced, it has been deduced that with an initial investment of US$1022.00 and a useful lifetime of 6.6 years, the savings are 3556.63 KWh/month or 42,679.5 KWh/year,

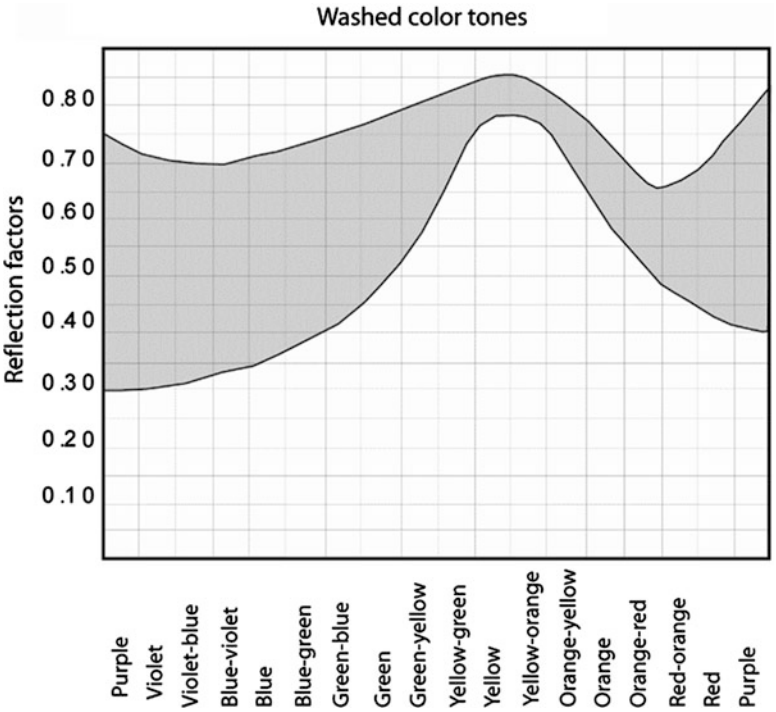

Fig. 61.11 Reflection factors of different paint colors. (Source: Damelincourt et Rangueil, Universite Paul Sabatier. Adapted by David Carlos Avila)

recovering the investment in only 0.75 years (9 months), as well as saving expenses of US$128/month or US$1539/year.

In addition, the following ecological benefits are obtained during the lifetime of the project, estimated at 6.6 years:

Reduction of CO^2: 128,848 kg
Reduction of SO^2: 2343 kg
Reduction of NO_X: 264 kg
Conservation of hydrocarbons: 53,858 kg
Reduction in water consumption: 662,637 kg

Acknowledgements The author appreciates the financial support received from the National Council of Science and Technology (CONACYT), the contribution of the technical consultancy made by the Commission for the Saving of Energy (CONAE), and the support of the University of Guadalajara.

References

1. Moore F (1989) Concepts and practice of architectural daylighting. Nostrand Van Reinhold, New York, pp 23–34
2. Gomez G (1998) Solar geometry, UDC, Mexico, University of Colima, Mexico
3. Mur R (1982) Natural geometry and natural lightning, ESTAB, Spain, University of Catalonia
4. Arias S, Avila DC (2004) Natural lightning in the architecture, UDG, Mexico, University of Guadalajara, Mexico

Chapter 62
LED Lighting for Healthcare Facilities

Canan Perdahci

62.1 Introduction

Good healing environments can be created through efficient lighting, and therefore lighting design plays an important role in multifunction and diverse habitat environments like hospitals. In a hospital environment, a wide variety of activities can be differentiated so in the design step of the lighting system, the following objectives are needed to be considered: the physical and emotional comfort of patients, motivation and the critical visual requirements for hospital staff and visitor experience [1]. A sensitive design of lighting schemes that is used in lighting systems enables significant energy cost savings in addition to above-mentioned targets.

Performance and comfort limits defined by the relevant standards must be established prior to a productive system. This improves patient's comfort as well as employee's performance.

Lighting criteria in hospitals are much more complex than a general environment. Within the hospital structure, there are many areas with different functionalities and many groups (such as patients, staff and doctors) with different needs. Most of the hospital structures, which are used 24 h a day and have a constant dynamic structure, are very important for the patient and health personnel. These environments must provide comfort and performance conditions for all patients and hospital personnel at all times.

In hospitals, lighting systems perform several functions:

– By bringing the appropriate degree of visibility and visual comfort, lighting systems offer a prestigious design which satisfies patients in terms of the expectation of well-being.

C. Perdahci (✉)
Kocaeli University, Electrical Engineering, Kocaeli, Turkey
e-mail: perdahci@kocaeli.edu.tr

S. Nižetić, A. Papadopoulos (eds.), *The Role of Exergy in Energy and the Environment*, Green Energy and Technology,
https://doi.org/10.1007/978-3-319-89845-2_62

– For doctors and nursing staff, lighting should meet the visual task requirements in each area of the hospital and also heighten motivation.
– Emotions and well-being feelings of non-medical personnel can be affected by a good lighting system design [2].

The determination of lighting demands is based on the saturation of visual comfort (i.e. where the workers have a feeling of well-being which can also conduce to a high productivity level), visual performance (i.e. where the workers are able to perform their visual tasks, even under difficult circumstances and during longer periods.) and safety (EN 12464-1 2002) [3].

Large amounts of energy for heating, ventilation, air conditioning, lighting and operating medical equipment are consumed in hospitals and care facilities with several hundreds of beds. Hospitals are responsible for high amount of energy due to the continuous operation, and it would be very desirable to reduce this consumption. Consuming energy for artificial lighting is a large percentage of the overall energy; estimates range from 26% to about 36% [4]. Thus, the total energy balance is significantly affected by lighting. Modern lighting technologies, which have a long service life and low-energy and maintenance requirements, are the basis for energy saving. A huge improvement of lighting quality is achieved by modern light sources and luminaires which provide energy consumption.

Hospitals are places where people are not willing to go and where they have to be under compulsory conditions and on the other hand are places where people work and spend their time. These spaces should be illuminated by considering the different needs of people and not affecting their working performances during the day. Illuminations that are usually applied only to illuminate a single level and have no other factor in mind can negatively affect patients and doctors. Optimum yield from the employees and making the patients feel as comfortable and peaceful as possible with the preference of the lighting are important aspects of the hospital lighting.

Another issue of today, energy saving, is the fast-changing process with LED lighting system. High-energy savings achieved through regeneration efforts accelerate this process. It is not difficult to raise the savings to 70% in LED lighting system with intelligent automation systems by integrating the opening, closing and throttling operations where necessary.

For this reason, performance and comfort are as important as energy efficient use. Studies show that lighting is one of the important systems in healthcare, and in many cases lighting has a positive effect on psychology and indirectly on the patient treatment process. Energy saving in lighting should be ensured by reducing energy consumption without changing the desired or required light level. For this reason, LED lighting luminaires are now the most popular projects in the lighting industry (Perdahci) [5].

DIALux 4.8 simulation software as per the international standards is used to present hospital lighting system design procedure. This study focuses on the most appropriate selection of lighting type which is visually and financially viable.

62.2 Patient Room Lighting

Apart from the treatment facilities, the atmosphere and the appearance of rooms are important criteria for the patients' hospital choice.

The right general lighting can make a perceptible contribution towards creating a pleasant and homely atmosphere in patient rooms, and the right general lighting should suffice to allow simple nursing duties. A number of separately switched lighting systems should fulfil the lighting requirements of patients' rooms: general comfort lighting, reading light for the patient, lighting for bedside examinations and treatment, night/observation lighting and orientation lighting.

Providing indirect lighting delivering at least 100 lux illuminance and warm white light can encourage comfortable atmosphere in patient rooms. As a result of indirect lighting, rooms look larger which is favoured by the patients. Furthermore, another positive effect is the calming one. The risk of direct glare for bedridden patients can be eliminated by limiting the average luminance of luminaires visible from the bed to 1000 candela per square metre according to DIN 5035-3. Another general lighting requirement for patient rooms is that 500 candela per square metre is the maximum permissible brightness produced by the indirect lighting at the ceiling [6].

In order to perform personal activities such as reading and manual activities, patients need sufficient lighting provided by the lighting integrated in each bed (indirect lighting and reading lighting from headboard) [1]. The reading lamps – which are required for every hospital bed –with a minimum of 300 lux on the reading plane create pleasant reading conditions. The reading lamps are to be switched one by one or separately, so as not to bother other patients hosted at the same room as well [6]. Especially the patients staying at their bed always on resting position need to see a variety of colours on the ceiling with reflection factor of not less than 0.7 [1]. Patients will be appreciated by using a kind of potential control at their ambience with immediate effect in terms of local lighting control [7].

Adequate luminance levels for the medical and auxiliary staff are required in patient rooms to ensure performance of medical examinations and care activities on the patients. Lighting system should provide optimal illumination with high levels of visual comfort and the absence of glare against the staff, since the visual task have the difficulties. When considered from this point of view, it is also important to use lighting sources with colour rendering as close as possible to the natural light [1]. DIN EN 12464-1 and DIN 5035-3 recommend illuminance of around 300lux on the examination plane for nursing tasks and simple examinations. It is also important to note that the uniformity – the ratio of maximum to average illuminance – should be minimum 1:2. The recommended illuminance for examinations and treatments or emergencies is a minimum of 1000 lux [6].

Night/observation lighting systems are possible solution to how patient rooms are lit at night when patients are asleep. The required average illuminance is 5lux on a plane 0.85 m above floor level. At night the staff need to be able to check patients

without unnecessarily disturbing them and perform simple tasks; a very low level of light is therefore necessary [6].

In order to help patients find their way at night without disturbing sleeping patients in unfamiliar surroundings, the quality of orientation lighting has to be taken into account. The wide-angled LED lighting luminaires mounted below bed level and the vicinity of the door are able to comply with requirements in patient rooms or care facilities as needed [6].

Patients require lighting that is tailored to their needs and individually adjustable so that all luminaires need to be separately switched in patient rooms [6].

Owing to light colour's and dynamic lighting scenes' positive influences on biological well-being of patients and staff, biologically effective artificial lighting solutions need to be installed in hospitals apart from the functional lighting essential for hospital operations. A patient's sleep/wake rhythm (human circadian system) can be positively impacted by changing brightness and light colour. Patients' natural active and resting phases, good night's sleep and a swifter recovery are supported by biologically effective artificial lighting (Lichtwissen) [6].

In patient rooms different numbers of patients have to share the same room. In such a case, hygiene is important. It is necessary to prevent bacterial formation in luminaires using antibacterial dyes. The protection type of the luminaire used should be IP65 so that people can be accommodated in clean hygiene rooms.

The recommended principles of lighting requirements of indoor workplaces for visual comfort and visual performance purposes are set out in the European Standard EN 12464-1 titled – European Committee for Standardization: EN 12464-1, Light and Lighting- Lighting of work places – Part 1: Indoor work places‖. Within the frame of this standard, some reference values from EN 12464-1 for healthcare premises are shown in Table 62.1. Table 62.1 defines the most important requirements that need to be met by lighting in terms of parameters such as the minimum values of average maintained illuminance (Em), the illuminance uniformity (U0), the colour rendering index (Ra) of the lamps and the maximum values of discomfort glare (UGRL). Visual sign boards for especially health usage are subject to change in required areas with illuminance level range from 100 lux to usual lighting to 1000 lux in accordance with EN12464-1 [8]. The lowest of Em indicated in the EN12464-1 is adjusted from the bottom levels (e.g. 5 lx, for night lighting) to normal level for absolute environment (e.g.100 lx, for general lighting) to the highest levels (e.g. 1000 lx, for examination and treatment performed by medical staff).

Table 62.1 Recommended lighting requirements for patient rooms in hospitals according to EN12464-1

Task or activity	E_m (lx)	UGR_L	U_0	R_a
General lighting	100	19	0.4	80
Reading lighting	300	19	0.7	80
Simple examinations	300	19	0.6	80
Examination and treatment	1.000	19	0.7	90
Night lighting	5	–	–	80

62.3 Case Study

The case study has been conducted in a patient room in Istanbul. The length, breadth and height of the rectangle patient room are 12,61 m, 5,87 m and 3 m, respectively. The reflection coefficients (supposed diffuse) of the walls are ρwall = 0.5, floor ρfloor = 0.2 and the ceiling ρceiling = 0.70. As seen in Table 62.1, the required lux level for the examination and treatment is 1000 lx, and the required lux level for the general lighting is 100 lux. The measurement of required illumination was taken on a workplane that has a height 0.850 m. The lighting scheme is designed with an assumed maintenance factor 0.9. An experimental procedure based on measurement of different types of lamps like T8 (T26) FL and LED lamps has been performed in order to assess the visual comfort through glare effect, colour rendering and the power consumption of the patient room of the hospital. In the design, hospitals are considered to deliver high-quality care sustainable 24 h a day, 7 days a week. The lighting scheme for the study has been designed by using DIALux 4.8 simulation software, and the simulation results are presented for each scenario.

Scenario 1
LITPA product LITPA 200331881 FGS 300/4x18W-WP is used for the illumination of patient room of the hospital.

The lighting distribution values in lux are illustrated in Fig. 62.1. The luminous flux of used luminaire is 2581 lumen, and the power is 64 W. The luminous flux of lamps of luminaire is 5400 lumen. The energy efficiency can be calculated as 2581lumen/5400lumen = %48. Totally seven luminaires were used for the study. So the total luminous flux is the sum of all the flux emitted by seven luminaires and equals 18067lumen. Also the total used power equals:

$$Pt = n.P = 7.64\ W = 448\ W$$

According to result of DIALux program, the average illuminance measured at workplane Eav [lx] = 215 lux, the minimum illuminance measured at workplane Emin[lx] = 53 lux and the maximum illuminance measured at workplane Emax [lx] = 326 lux.

Figure 62.2 presents photometric data. Figure 62.3 illustrates the luminaire layout plan. Figure 62.4 is 3D colour rendering and presents the effect of lighting on different area in the room. Figure 62.5 presents false colour rendering scheme, and Fig. 62.6 presents the value chart for this scenario.

Scenario 2
LITPA product LITPA 200331882 HFC /38 W-WP LED is used for the illumination of patient room of hospital.

The lighting distribution values in lux are illustrated in Fig. 62.7. The luminous flux of used luminaire is 3696 lumen, and the power is 44 W. The luminous flux of lamps of luminaire is 4400 lumen. The energy efficiency can be calculated as 3696lumen/4400lumen = %84. Totally seven luminaires were used for the study. The total luminous flux is the sum of all the flux emitted by seven luminaires and equals 25,872 lumen. Also the total used power equals:

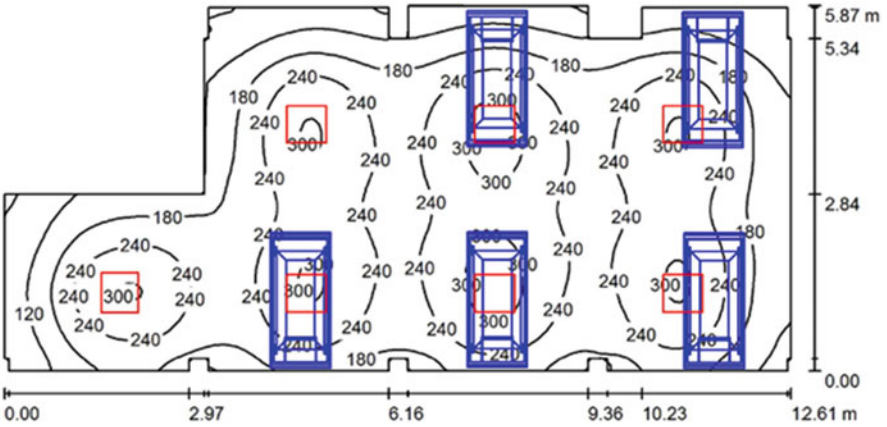

Height of Room: 3.000 m, Mounting Height: 3.090 m, Maintenance factor: 0.80

Values in Lux, Scale 1:91

Surface	ρ [%]	E_{av} [lx]	E_{min} [lx]	E_{max} [lx]	u0
Workplane	/	215	53	326	0.245
Floor	20	152	9.01	276	0.059
Ceiling	70	35	20	44	0.577
Walls (34)	50	62	13	174	/

Workplane:

Height:	0.850 m
Grid:	128 x 64 Points
Boundary Zone:	0.000 m

Luminaire Parts List

No.	Pieces	Designation (Correction Factor)	Φ (Luminaire) [lm]	Φ (Lamps) [lm]	P [W]
1	7	LITPA 200331881 FGS 300/4x18W-WP (1.000)	2581	5400	64.0
			Total: 18070	Total: 37800	448.0

Specific connected load: 7.08 W/m² = 3.29 W/m²/100 lx (Ground area: 63.29 m²)

Fig. 62.1 Lighting distribution values in Lux

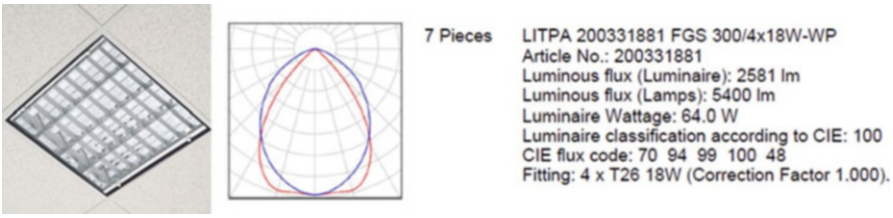

7 Pieces

LITPA 200331881 FGS 300/4x18W-WP
Article No.: 200331881
Luminous flux (Luminaire): 2581 lm
Luminous flux (Lamps): 5400 lm
Luminaire Wattage: 64.0 W
Luminaire classification according to CIE: 100
CIE flux code: 70 94 99 100 48
Fitting: 4 x T26 18W (Correction Factor 1.000).

Fig. 62.2 Photometric data

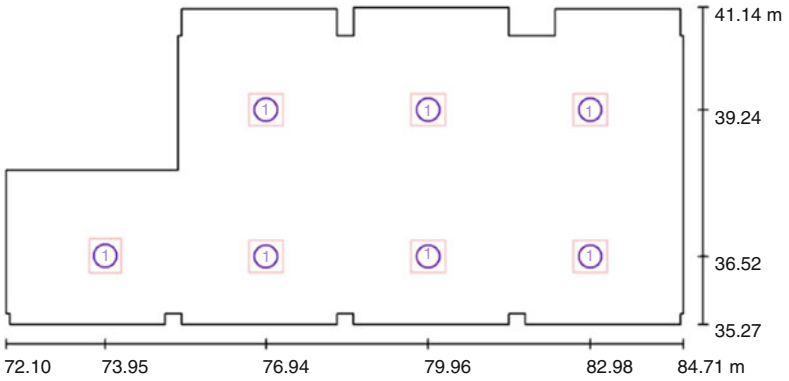

Fig. 62.3 Layout plan

Fig. 62.4 3D rendering

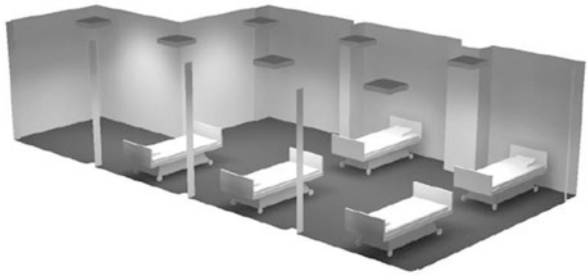

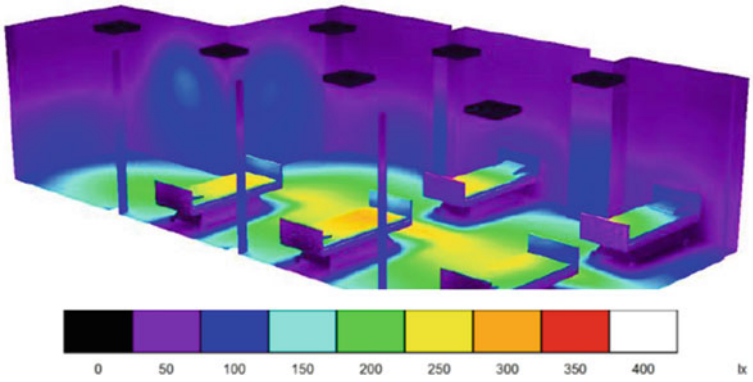

Fig. 62.5 False colour rendering (lighting level distribution - lux)

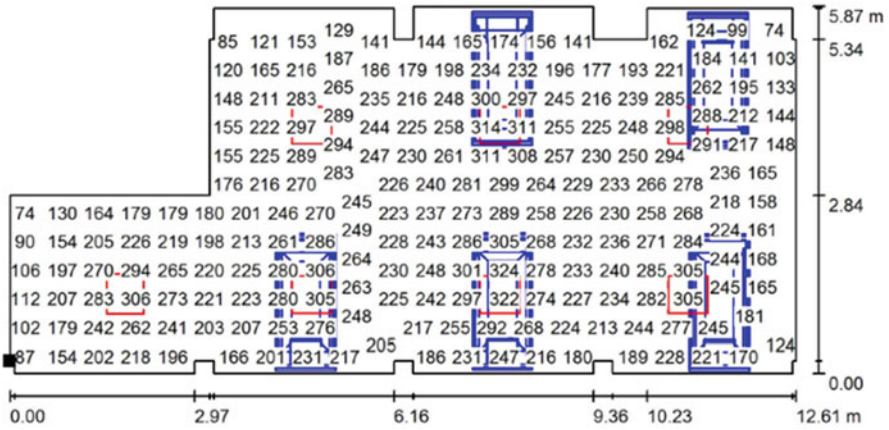

Fig. 62.6 Value chart (metre)

$$Pt = n.P = 7.44\ W = 308\ W$$

According to result of DIAlux program, the average illuminance measured at workplane Eav [lx] = 347 lux, the minimum illuminance measured at workplane Emin [lx] = 84 lux and the maximum illuminance measured at workplane Emax [lx] = 524 lux.

Figure 62.8 presents photometric data. Figure 62.9 illustrates the luminaire layout plan. Figure 62.10 is 3D colour rendering and presents the effect of lighting on different area in the room. Figure 62.11 presents false colour rendering scheme, and Fig. 62.12 presents the value chart for this scenario.

62.4 Results and Conclusions

The aim of the study presented herein was to analyse efficiency using simulation method. In this study, the lighting project in the patient rooms in the hospital is designed using antibacterial LED panel and fluorescent lamp connected to electronic ballast. Their consumed power (W), luminous flux (lumen) and luminous efficacy were measured. Luminous flux (lum) values were compared to the amount of power consumed by using two types of luminaires. Electrical power consumption has been analysed.

Table 62.2 illustrates the summary of the simulation results of the lighting system design in order to assess the efficiency of fluorescent lamp and LED. The most important conclusion from the Table 62.2 is that fluorescent lamp luminaire (40 lm/W) has lower lumen/watt value when compared with LED luminaire (84 lm/W) (Table 62.3).

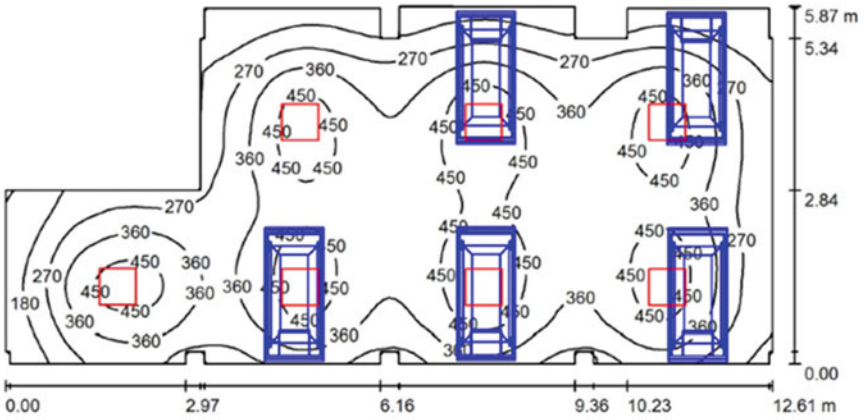

Height of Room: 3.000 m, Mounting Height: 3.090 m, Maintenance factor: 0.90 Values in Lux, Scale 1:91

Surface	ρ [%]	E_{av} [lx]	E_{min} [lx]	E_{max} [lx]	u0
Workplane	/	347	84	524	0.243
Floor	20	245	13	447	0.055
Ceiling	70	57	29	81	0.512
Walls (34)	50	101	22	282	/

Workplane:
Height: 0.850 m
Grid: 128 x 64 Points
Boundary Zone: 0.000 m

Luminaire Parts List

No.	Pieces	Designation (Correction Factor)	Φ (Luminaire) [lm]	Φ (Lamps) [lm]	P [W]
1	7	LITPA 200331882 HFC /38W-WP (1.000)	3696	4400	44.0
			Total: 25872	Total: 30800	308.0

Specific connected load: 4.87 W/m² = 1.40 W/m²/100 lx (Ground area: 63.29 m²)

Fig. 62.7 Lighting distribution values in lux

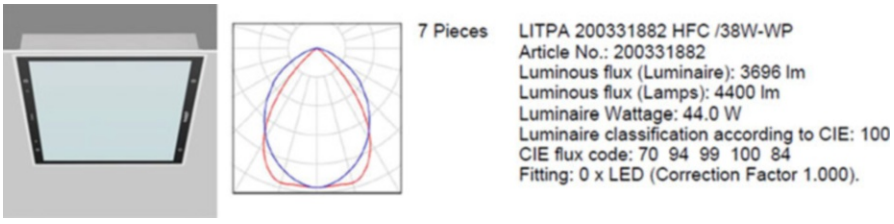

Fig. 62.8 Photometric data

In scenario 1, FLs are utilized, and the design is requiring seven luminaires to give 326 lx levels. In scenario 2, LED luminaires are introduced, and the design is requiring seven luminaires to give 524 lx levels (Table 62.4).

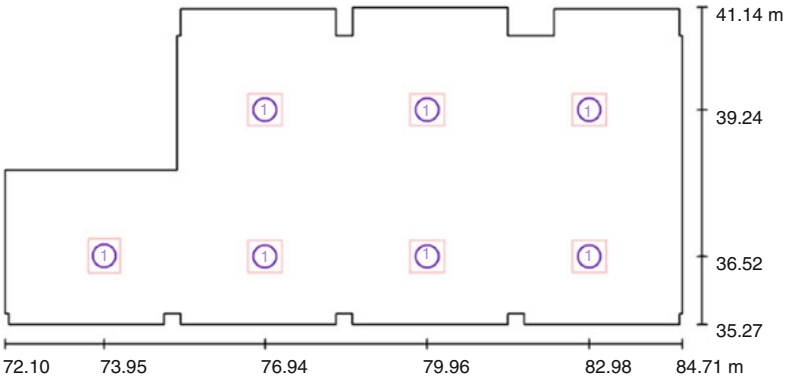

Fig. 62.9 Layout plan

Fig. 62.10 3D rendering

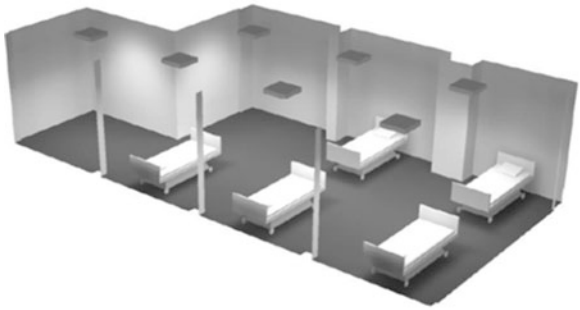

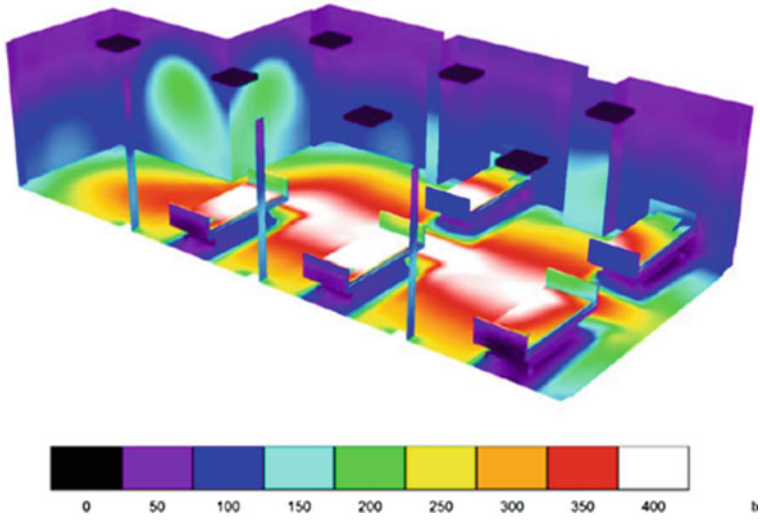

Fig. 62.11 False colour rendering (lighting level distribution - lux)

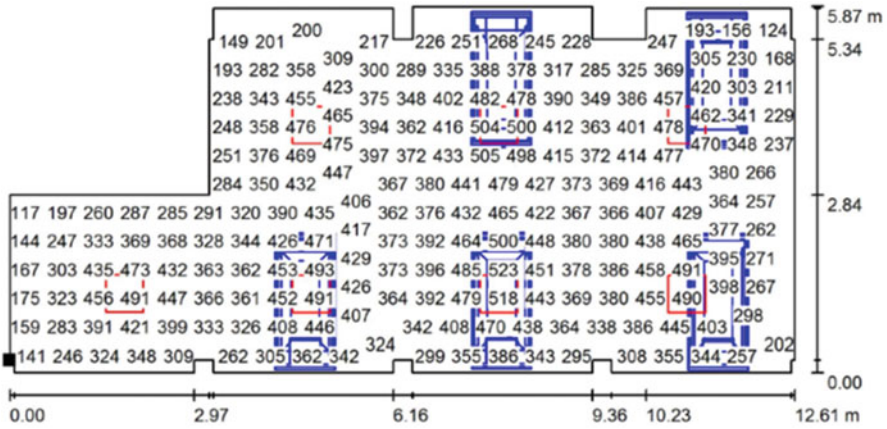

Fig. 62.12 Value chart (metre)

Table 62.2 Simulation results summary

Type	Φ (Lamps) [lm]	Φ (Luminaire) [lm]	Luminous efficacy (lm/W)	Total Φ (7Luminaire) [lm]
FL	5400	2581	40	18,067
LED	4400	3696	84	25,872

Table 62.3 Photometric results

Luminaire	Eav	Emin	Emax	*Uo*
FL	215 lux	53 lux	326 lux	0.245
LED	347 lux	84 lux	524 lux	0.243

Table 62.4 Lum/W values for FL and LED luminaires

Type	Power consumed *P* (W)	Total power consumed *P* (W)	Luminaire efficacy	Total Φ (7 luminaire) [lm]	Luminous efficacy (lm/W)
FL	64 W	448 W	48	18,067	40,32
LED	44 W	308 W	84	25,872	84

In scenario 1, the total luminous flux of the fluorescent luminaire lamps equals 5400lumen, and the luminous flux of the fluorescent luminaire equals 2581lumen. Based on the luminous fluxes measured for the fluorescent luminaires, one can infer that the efficiency of the fluorescent luminaire is 48%. In scenario 2, the total luminous flux of the LED luminaire lamps equals 4400lumen, and the luminous flux of the LED luminaire equals 3696lumen. Based on the luminous fluxes measured for the LED luminaires, one can infer that the efficiency of the LED luminaire is 84%. Therefore, in terms of luminaire efficiency, LED lamp luminaires are 57% more efficient than fluorescent lamp luminaires.

Table 62.5 Lum/W values in the same active power consumption

Type	Total power consumed *P* (W)	Total Φ (luminaire) [lm]	Luminous efficacy (lm/W)
FL (LITPA 200331881 FGS 300/4x18W-WP)	448 W	18,067	40,32
LED (LITPA 200331882 HFC /38 W-WP LED)	440 W	36,960	84

In order to compare two lamp types, we can either obtain the same lumen values and compare the amount of power consumed or we can compare the luminous flux values using the lamps at the same power. When we replace the fluorescent lamps with LED luminaires in a hospital that is being used in this study, we have to replace seven fluorescent lamp luminaires with seven LED luminaires. Because using different luminaire sizes and numbers during this replacement would require renovation in the hospital room, this would lead to both an economic expense and an unwanted situation by the administrators of the hospital. So we used LED lamp luminaires in the same sizes of fluorescent lamp luminaires that are being used in this replacement.

For these reasons, seven luminaires were used in the above tables. However, in order to make comparison, we used the same power to compare lumens in both luminaires. In other words, while a total of seven fluorescent lamp luminaires consume 448 W, a total of 10 LED lamp fixtures consume 440 W. In two scenarios with approximately equal power consumption, the luminaries in Scenario 1 produce 18,067 lum, while the luminaries in Scenario 2 produce 36,960 lum. Therefore, as can be seen from Table 62.5, LED lamp luminaires are 48.9% more efficient than fluorescent lamp luminaires at approximate power.

Accordingly, in order to achieve the same luminous level, the same luminous level can be achieved by consuming 229 W instead of 448 W using LED lamps which are about 49% efficient. A total savings of 220 Wh is achieved. This is approximately 1425.6kWh for a single room, and this saves energy of 1425.6kWh per annum for luminaires used at 18 h per day at about this luminous level.

Acknowledgement The author would like to also thank University of Kocaeli and LITPA Lighting Co. for their valuable contributions to the present study.

References

1. Francesco L, Carlo M, Sergio I, Michele R, Giacomo S (2016) Quality of lighting in hospital environments: a wide survey through in situ measurements. J Light Vis Environ 40:1–14
2. Fördergemeinschaft Gutes Licht, Good Lighting for Health Care Premises, 7, http://www.licht.de/fileadmin/Publikationen_Downloads/lichtwissen07_healthcare_premises.pdf

3. European Standard EN 12464-1-Lighting of work places – part 1: Indoor Work Places, November 2014, http://www.licht.de/fileadmin/Publikationen_Downloads/Guide_DIN-EN-12464-1.pdf
4. Pimkamol M, Thorbjörn L, Maria J (2016) Factors affecting optimal lighting use in shared hospital environments: a case-study. Build Environ 96:260–269
5. Perdahci C (2016) Hastane Aydınlatma Sistemleri, Üsküdar Üniversitesi Sağlık Bilimleri Enstitüsü Nörobilim Anabilim Dalı Yüksek Lisans Bitirme Projesi
6. Fördergemeinschaft Gutes Licht, licht.wissen, Light as a Factor in Health, 7 (2012), http://en.licht.de/fileadmin/shop-downloads/Lichtwissen07_E.pdf
7. Hilary D, Jenny L, Elga N, Nilgun C, Guillaume S, Sarah H, Laura S (2006) Colour and lighting in hospital design. Opt Laser Technol 38:343–365
8. Iman D, Ali S, Javad B, Mohammad AJ, Alex WS (2013) Objective and subjective assessments of lighting in a hospital setting: implications for health, safety and performance. Ergonomics 56 (10):1535–1545

Chapter 63
Thermoeconomic Analysis and Evaluation of a Building-Integrated Photovoltaic (BIPV) System Based on Actual Operational Data

Arif Hepbasli, Mustafa Araz, Emrah Biyik, Runming Yao, Mehdi Shahrestani, Emmanuel Essah, Li Shao, Armando C. Oliveira, Teodosio del Caño, Elena Rico, and Juan Luis Lechón

63.1 Introduction

Photovoltaic (PV) systems used on buildings can be classified into two main groups, namely, building-attached PVs (BAPVs) and BIPVs. It is rather difficult to identify whether a PV system is a building-attached (BA) or building-integrated (BI) system, if the mounting method of the system is not clearly stated [1]. BAPVs are added on the building and have no direct effect on structure's functions. On the other hand, BIPVs are defined as PV modules, which can be integrated in the building envelope (into the roof or façade) by replacing conventional building materials (e.g., tiles) [2–4].

BIPV technology is a promising addition to the mix of renewable energy generation technologies. The majority of the BIPV performance assessment efforts have focused on energetic aspects, while exergetic studies are very low in numbers and have not been comprehensively performed. There is a wide range of BIPV electric generation capacity reported, ranging from a few MWh/yr to more than 100 MWh/yr, with efficiency values ranging from 5% to 18%. In addition, both façade and rooftop BIPV applications are equally common in the literature [4].

The term thermoeconomics (in the United States), also referred to as exergoeconomics (in Europe), is a kind of engineering branch, which combines

A. Hepbasli (✉) · M. Araz · E. Biyik
Yasar University, Energy Systems Engineering, Izmir, Turkey
e-mail: arif.hepbasli@yasar.edu.tr

R. Yao · M. Shahrestani · E. Essah · L. Shao
University of Reading, School of the Built Environment, Reading, UK

A. C. Oliveira
University of Porto, Mechanical Engineering, Porto, Portugal

T. del Caño · E. Rico · J. L. Lechón
Onyx Solar Energy, Avila, Spain

S. Nižetić, A. Papadopoulos (eds.), *The Role of Exergy in Energy and the Environment*, Green Energy and Technology,
https://doi.org/10.1007/978-3-319-89845-2_63

exergy analysis and economic principles. It has been widely used for more than 20 years to support the design, synthesis, and operation of energy-related systems with higher exergetic efficiency and lower unit production costs. It also provides the system designer or operator with valuable information, which cannot be obtained from conventional energy analysis and economic assessments [5].

Shukla et al. [6] reviewed studies on energy and exergy analyses of BIPV modules to evaluate the electrical performance, exergy destruction, and exergy efficiency with photonic method. They concluded that exergetic assessment of BIPV systems was highly dependent on the daily solar radiation and radiation intensity, while the BIPV module temperature had a great effect on the exergy efficiency.

As far as exergoeconomic analyses and assessments of BIPV systems are concerned, Gaur and Tiwari [7] proposed the modified EXCEM method. They calculated annual electricity and net present values for the composite climatic conditions of New Delhi, India. Irrespective of the solar cell type, the semitransparent PV modules showed higher net energy and exergy loss rates compared to the opaque ones. Among all types of solar modules, the one based on c-Si had minimum energy and exergy loss rate values. Hepbasli et al. [1] used the exergy, cost, energy, and mass (EXCEM) analysis method to assess the BIPV system installed at Yasar University. Exergoeconomic parameters based on energetic and exergetic terms ranged from 0.001 to 0.714 W/€ and 0.001 to 0.664 W/€, with daily average values of 0.315 and 0.293, respectively.

Based on the literature review we performed, some limited studies on exergetic assessment of BIPV/T systems have been conducted, while any studies on the thermoeconomic analysis and evaluation of a BIPV system using the SPECO method based on the actual operational data have not appeared in the open literature to the best of the authors' knowledge. This was the primary motivation behind this contribution.

63.2 System Description

The BIPV system installed at Yasar University, Izmir, Turkey, consists of a total of 48 crystalline silicon (c-Si) modules in 4 rows and 12 columns, with a gap of 150 mm between the modules and the wall [8]. There are shading effects that were considered, as the southeast façade lies on the lower part of the building. The total façade area is 57.6 m^2 with a cell area of 42.08 m^2, while the total peak installed power is 7.44 kW with a peak power per PV unit of 155 W_p. A picture of the system is given in Fig. 63.1 [8].

This system is called as a ventilated façade and increases the efficiency of the system due to cooling effect. A 7 kW three-phase inverter with two independent MPPT inputs was selected for the system. The inverter converts the DC input to AC and feeds the building grid. It also serves as a measuring instrument, and all electrical data are recorded to the integrated FTP server inside the inverter with 5-minute intervals.

Fig. 63.1 A picture of the BIPV system installed [8]

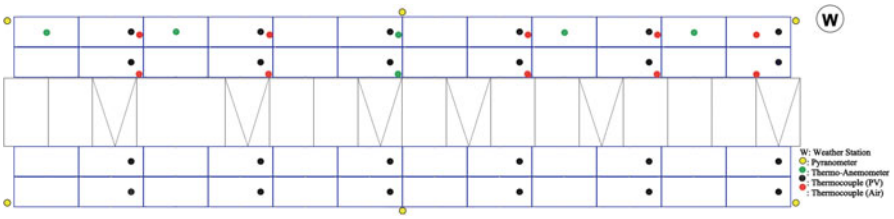

Fig. 63.2 A schematic diagram of the BIPV system investigated [8]

As can be seen in Fig. 63.2 [8], the surface temperatures of the PV modules are measured on 24 points, while the air temperatures between the wall and the modules are measured at 16 different locations. The air velocity behind the modules is also measured on six points. For the irradiation measurements, six pyranometers are mounted on the system (four in the corners and two at midpoints), and one pyranometer is located on top of the building horizontally, where there is no shadow. Also, a weather station is located just next to the upper string. Wind velocity and direction, air temperature, and humidity are measured at this point. All these measurements are continuously recorded on a 60-channel internet-connected data logger.

The single line diagram of the system is illustrated in Fig. 63.3 [8] where panels are connected in two series to the inverter. The installation of the BIPV system was completed on February 8, 2016, and since then, the performance of the system has been monitored through Sunny Portal, while a total electrical energy of 10009.67 kWh was produced as of October 12, 2017 (15:16 PM).

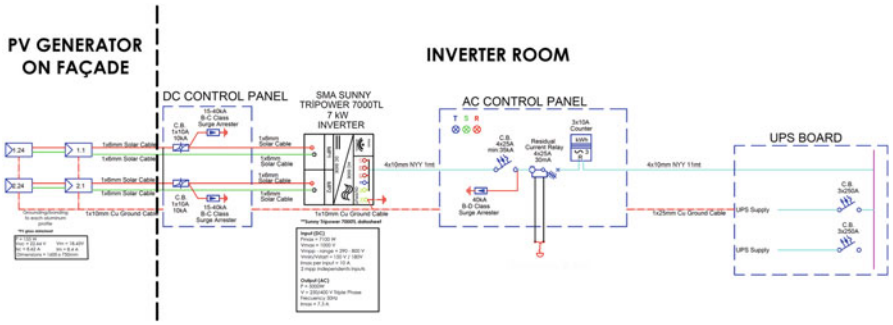

Fig. 63.3 Single line diagram of the BIPV system [8]

63.3 Analysis

The following assumptions are made during the analysis:

(a) The salvage value of the system is neglected.
(b) The interest rate is taken as 10%.
(c) The expected lifetime of the BIPV panels is 30 years, while that of the inverter is taken to be 15 years. This means that the inverter will be replaced two times within the lifetimes of BIPVs.
(d) Yearly operation and maintenance costs are taken as 40 €/kW$_p$, which includes the replacement of the inverter after the 15th year.
(e) The yearly degradation of the system is taken to be 0.6%.

The performance of a BIPV system can be evaluated using both the first and second laws of thermodynamics. The energetic efficiency of the system can be defined as the ratio of power produced at maximum power point by the BIPV system (W) to the irradiation (G) received over the BIPV area (A) [9]. Because the panels used in the BIPV system studied are partially transparent, two different efficiencies based on the total area and cell area are determined in this study.

$$\eta = \frac{\dot{W}}{AG} \tag{63.1}$$

The exergy efficiency of the system is the ratio of the exergetic output of the system (power produced) to the exergy of the irradiation received (Ex_{sol}), [9].

$$\psi = \frac{\dot{E}x_{BIPV}}{\dot{E}x_{sol}} = \frac{\dot{W}}{\dot{E}x_{sol}} \tag{63.2}$$

There are various ways of determining the exergy of solar irradiation. In this study, the following relation developed and proposed by Petela was used [10].

$$\dot{\mathrm{Ex}}_{\mathrm{sol}} = AG\left[1 - \frac{4}{3}\left(\frac{T_0}{T_{\mathrm{sun}}}\right) + \frac{1}{3}\left(\frac{T_0}{T_{\mathrm{sun}}}\right)^4\right] \tag{63.3}$$

where T_{sun} is taken as 6000 K. Energetic and exergetic efficiencies over a time period can be calculated using Eqs. (63.4) and (63.5) [9].

$$\overline{\eta} = \frac{\sum \dot{W}}{\sum AG} \tag{63.4}$$

$$\overline{\psi} = \frac{\sum \dot{W}}{\sum \dot{\mathrm{Ex}}_{\mathrm{sol}}} \tag{63.5}$$

In this study, the SPECO method was applied to the system. The most general form of the equation used in this method is given as follows [11, 12]:

$$\sum_{\mathrm{e}} \left(c_{\mathrm{e}}.\dot{\mathrm{Ex}}_{\mathrm{e}}\right)_k + c_{\mathrm{w},k}\,\dot{\mathrm{W}}_k = c_{\mathrm{q},k}.\dot{\mathrm{Ex}}_{\mathrm{q},k} + \sum_{\mathrm{i}} \left(c_{\mathrm{i}}.\dot{\mathrm{Ex}}_{\mathrm{i}}\right)_k + \dot{Z}_k \tag{63.6}$$

where c_{i}, c_{e}, c_{w}, and c_{q} denote average costs per unit of exergy in Euros per kWh, while $\dot{Z}_k$ is the total cost rate of the kth component, which is the sum of capital investment and operation and maintenance cost rates, as given below [11, 12].

$$\dot{Z} = \dot{Z}^{\mathrm{CI}} + \dot{Z}^{\mathrm{OM}} \tag{63.7}$$

Because there are only two main pieces of equipment, namely, the BIPV panels and the inverter in the BIPV system, one needs to use Eq. (63.6) for both of them. For the BIPV panels, Eq. (63.6) can be written as follows:

$$c_{\mathrm{sun}}\dot{\mathrm{Ex}}_{\mathrm{sun}} + \dot{Z}_{\mathrm{BIPV}} = c_{\mathrm{DC}}\dot{\mathrm{Ex}}_{\mathrm{DC}} \tag{63.8}$$

On the other hand, inverters are used to convert the generated electricity from DC to AC, and during this process, some amount of exergy is always destroyed. The exergetic efficiencies of such devices are always zero and they are regarded as dissipative devices.

The cost associated with dissipative devices should be charged to productive components being responsible for its use, which are the BIPV panels in the present study. The following equation should be used for this purpose [12]:

$$\dot{C}_{\mathrm{e}} + \dot{C}_{\mathrm{diff,dc}} = \dot{C}_{\mathrm{i}} + \dot{Z}_{\mathrm{dc}} \tag{63.9}$$

Rewriting Eq. (63.9) for the inverter, one can get:

$$c_{\mathrm{DC}}\dot{\mathrm{Ex}}_{\mathrm{DC}} + \dot{Z}_{\mathrm{inv}} = c_{\mathrm{AC}}\dot{\mathrm{Ex}}_{\mathrm{AC}} + \dot{C}_{\mathrm{diff,dc}} \tag{63.10}$$

If one takes $\dot{C}_{\mathrm{diff,dc}}$ from Eq. (63.10) and uses the F principle ($c_{\mathrm{DC}} = c_{\mathrm{AC}}$), the following is obtained:

$$\dot{C}_{\text{diff,dc}} = c_{\text{AC}}\left(\dot{\text{Ex}}_{\text{AC}} - \dot{\text{Ex}}_{\text{DC}}\right) + \dot{Z}_{\text{inv}} \tag{63.11}$$

Adding this cost to the cost of the BIPV panels, one can write:

$$\dot{Z}_{\text{BIPV}} = \dot{Z}^{\text{CI}} + \dot{Z}^{\text{OM}} + c_{\text{AC}}\left(\dot{\text{Ex}}_{\text{AC}} - \dot{\text{Ex}}_{\text{DC}}\right) + \dot{Z}_{\text{inv}} \tag{63.12}$$

Inserting Eq. (63.12) into Eq. (63.8), one can get the following:

$$c_{\text{sun}}\dot{\text{Ex}}_{\text{sun}} + \dot{Z}^{\text{CI}} + \dot{Z}^{\text{OM}} + \dot{Z}_{\text{inv}} = c_{\text{AC}}\dot{\text{Ex}}_{\text{AC}} \tag{63.13}$$

where $c_{\text{sun}} = 0$. This approach is assuming that instantaneous or average hourly exergy flows are constant throughout the operating period and is reliable for large power plants. However, due to discontinuous profile of renewable energy sources, the exergy flows should be cumulatively calculated over a defined time period [13]:

$$Ex = \int_{\text{period}} \dot{Ex} \tag{63.14}$$

On the other hand, the costs of the inverter and BIPV panels can be calculated using the following equations [13]:

$$\dot{Z}^{\text{CI}} = Z.\text{CRF}.\frac{\tau_{\text{operation}}}{8760} \tag{63.15}$$

where τ is the operation period and CRF is the capital recovery factor.

$$\text{CRF} = \frac{i(i+1)^n}{(i+1)^n - 1} \tag{63.16}$$

where i is the interest rate and n is the lifetime of the system. Because the expected lifetime of the inverter is 10 years, it should be replaced two times during the lifetime of the BIPV panels. Therefore, a replacement cost should also be added to the total cost [14].

$$Z_{\text{R}} = Z_{\text{inv}}\left[\frac{1}{(1+i)^{10}}\right] + Z_{\text{inv}}\left[\frac{1}{(1+i)^{20}}\right] \tag{63.17}$$

63.4 Results and Discussion

In the first part of the study, energetic and exergetic analyses were performed for September 17, 2016. The daily distribution of the irradiation, the exergy of solar irradiation, and the power generation are shown in Fig. 63.4.

Figure 63.5 illustrates a variation of the power conversion and exergy efficiencies based on cell and module (total) areas with a measurement period of 15 min.

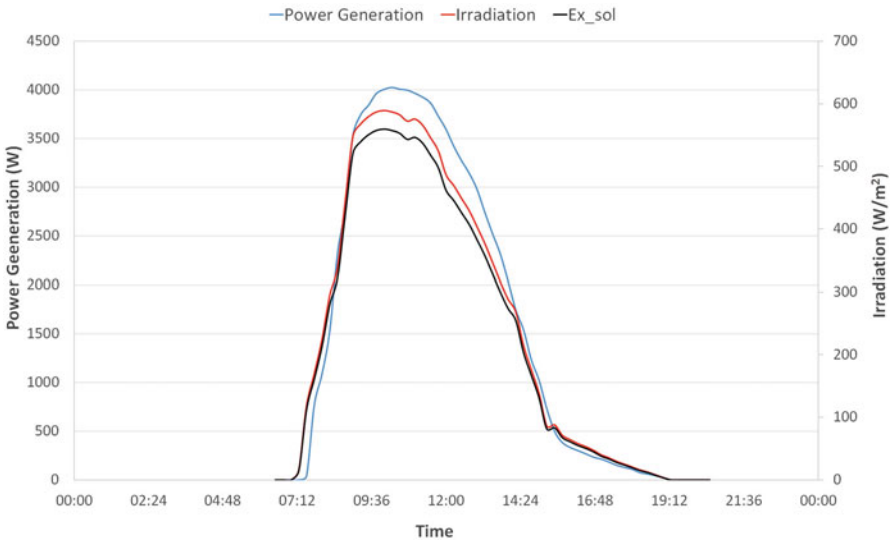

Fig. 63.4 Daily power generation and irradiation variations on September 17, 2016

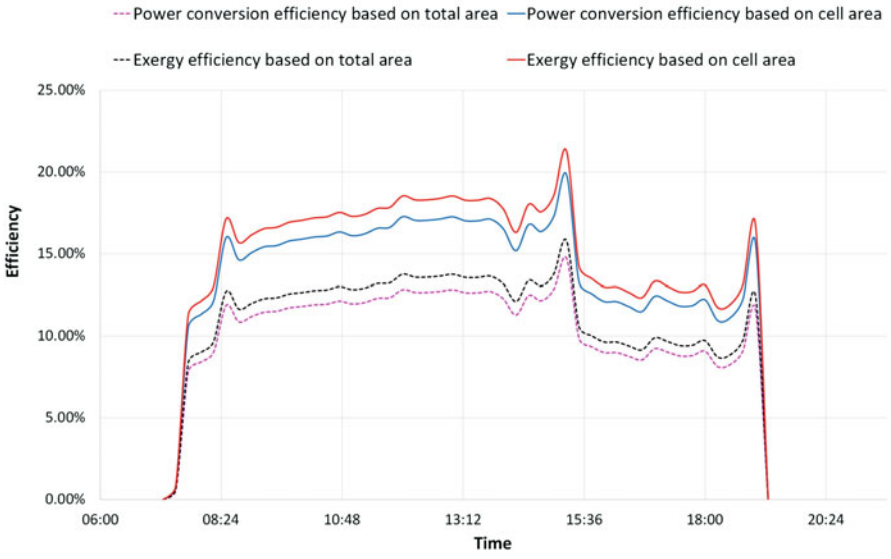

Fig. 63.5 Daily variation of power conversion and exergy efficiencies on September 17, 2016

As can be seen from the figure, there is a good agreement between the power conversion and the exergy efficiencies, while the difference in the efficiencies based on cell area and module area is about 4%. Also, the exergy efficiencies are always higher than the corresponding power conversion efficiencies. That is expected because the exergy of solar irradiation is always lower than the energy of solar irradiation.

Table 63.1 Some monthly thermoeconomic analysis results of the selected days

	T_0 (°C)	η_{sys} (%)	φ_{sys} (%)	Ex_{dest} (kWh)	W (kWh)	c_{AC} (Euro/kWh)
Jan	10.38	0.117	0.125	153.33	21.82	0.24
Feb	8.52	0.114	0.121	181.43	25.05	0.21
Mar	13.29	0.108	0.115	187.76	24.41	0.22
Apr	27.12	0.107	0.115	166.04	21.62	0.25
May	26.33	0.107	0.115	140.63	18.25	0.29
Jun	32.65	0.107	0.115	115.17	14.96	0.36
Jul	31.57	0.110	0.118	119.72	15.96	0.33
Aug	33.06	0.109	0.117	122.90	16.32	0.56
Sept	30.36	0.119	0.127	134.23	19.58	0.27
Oct	21.79	0.107	0.114	152.15	19.66	0.27
Nov	18.07	0.127	0.136	119.09	18.75	0.28
Dec	10.27	0.120	0.129	115.68	17.06	0.31

In the second part of the study, an uncloudy day was selected from each month, and the efficiencies based on total area and the exergetic cost associated with the generated electricity (c_{AC}) are calculated. The results are given in Table 63.1.

As can be seen in the table, the daily average energetic and exergetic efficiencies are in the range of 10.7%–12.7% and 11.4%–13.6%, respectively. According to the exergoeconomic analysis, the exergetic cost of generated electricity varies between 0.21 and 0.36 €/kWh$_{ex}$ for the selected days. c_{AC} is also calculated for the whole year, i.e., for 8760 h of operation time, and obtained to be 0.368 €/kWh$_{ex}$.

63.5 Conclusions

In this study, a BIPV system installed at Yasar University, Izmir, Turkey, was considered. The performance of the system was evaluated using energy, exergy, and exergoeconomic analysis methods.

The main conclusions we have drawn from the results of the present study may be summarized as follows:

(a) The exergy efficiencies were determined to be higher than the power conversion efficiencies during the whole day, while there is an average difference of 4% between the total and cell area-based efficiencies.
(b) Exergetic costs associated with the generated electricity ranged between 0.21 and 0.36 €/kWh$_{ex}$ for the selected days, while the average exergetic cost for the whole year is found to be 0.368 €/kWh$_{ex}$.
(c) The authors expect that this study would be beneficial to the researchers, designers, and manufacturers, who are interested in applying exergy-based economic analysis methods to BIPV systems.

Nomenclature

A	Area (m^2)
c	Average costs per unit exergy (€/kWh)
$\dot{C}$	Exergetic cost rate (€/h)
CRF	Capital recovery factor
Ex	Amount of exergy (kWh)
$\dot{Ex}$	Exergy rate (kW)
G	Solar irradiation (W/m^2)
i	Inflation rate (−)
T	Temperature (°C or K)
$\dot{W}$	Power (kW)
Z	Cost (€)
$\dot{Z}$	Cost rate (€/day or €/year)

Greek Letters

η	Energy efficiency (−)
φ	Exergy efficiency (−)
$\tau_{\text{operation}}$	Operation period (h)

Acknowledgments The presented work was developed within the framework of project "REELCOOP – Research Cooperation in Renewable Energy Technologies for Electricity Generation," co-funded by the European Commission (FP7 ENERGY.2013.2.9.1, Grant agreement no: 608466). The authors would like to thank the three reviewers for their constructive and valuable comments, which have been very useful in improving the quality of the paper.

References

1. Hepbasli A, Biyik E, Araz M, Shahrestani M, Yao R, Essah E, Shao L, Oliveira AC Del Caño T, Rico E, Lechón JL (2016) Exergoeconomic assessment of a building integrated photovoltaic (BIPV) system: a case study of Yasar University, Izmir, Turkey. In: The international conference of SDB16, Chongqing, China, 5–6 November 2016
2. Barkaszi S, Dunlop J (2001) Discussion of strategies for mounting photovoltaic arrays on rooftops. In: International solar energy conference, Washington, DC, USA, pp 333–338
3. Henemann A (2008) BIPV: Built-in solar energy. Renew Energy Focus 9(14):16–19
4. Biyik E, Araz M, Hepbasli A, Shahrestani M, Yao R, Shao L, Essah E, Oliveira AC, Del Caño T, Rico E, Lechón JL, Andrade L, Mendes A, Atli YB (2017) A key review of building integrated photovoltaic (BIPV) systems. Int J Eng Sci Technol 20(3):833–858
5. Tsatsaronis G (2007) Definition and nomenclature in exergy analysis and exergoeconomics. Energy 32(4):249–253
6. Shukla AK, Sudhakar K, Baredar P (2016) Exergetic assessment of BIPV module using parametric and photonic energy methods: a review. Energ Buildings 119:62–73
7. Gaur A, Tiwari GN (2014) Exergoeconomic and enviroeconomic analysis of photovoltaic modules of different solar cells. J Sol Energy. Article ID 719424, 8 pages, https://doi.org/10.1155/2014/719424

8. REELCOOP (2015) Research cooperation in renewable energy technologies for electricity generation report. Seventh Framework Programme of the European Union
9. Rawat R, Lamba R, Kaushik SC (2017) Thermodynamic study of solar photovoltaic energy conversion: an overview. Renew Sust Energ Rev 71:630–638
10. Petela R (2003) Exergy of undiluted thermal radiation. Sol Energy 74:469–488
11. Bejan A, Tsatsaronis G, Moran M (1996) Thermal design and optimization. Wiley, New York
12. Lazzaretto A, Tsatsaronis G (2006) SPECO: a systematic and general methodology for calculating efficiencies and costs in thermal systems. Energy 31:1257–1289
13. Calise F, d'Accadia MD, Macaluso A, Piacentiono A, Vanol L (2016) Exergetic and exergoeconomic analysis of a novel hybrid solar-geothermal polygeneration system producing energy and water. Energy Convers Manag 115:200–220
14. Agrawal B, Tiwari GN (2011) Building integrated photovoltaic thermal systems for sustainable developments, RSC Energy Series No. 4, The Royal Society of Chemistry, Cambridge, UK

Index

S. Nižetić, A. Papadopoulos (eds.), *The Role of Exergy in Energy and the Environment*, Green Energy and Technology,
https://doi.org/10.1007/978-3-319-89845-2